HEDH
HEAT EXCHANGER DESIGN HANDBOOK

2

Fluid mechanics and heat transfer

VDI-Verlag GmbH
Verlag des Vereins Deutscher Ingenieure • Düsseldorf
Hemisphere Publishing Corporation Washington New York London

EDITORIAL BOARD

Ernst U. Schlünder, Editor-in-Chief
Lehrstuhl und Institut für Thermische Verfahrenstechnik der Universitat Karlsruhe TH, D-7500 Karlsruhe 1, Kaiserstrasse 12, Postfach 6380, F.R. Germany

Kenneth J. Bell
School of Chemical Engineering, Oklahoma State University, Stillwater, Oklahoma 74078, U.S.A.

Duncan Chisholm
Department of Trade and Industry, National Engineering Laboratory, East Kilbride, Glasgow G75 OQU, Scotland

Geoffrey F. Hewitt
Engineering Sciences Division, Atomic Energy Research Establishment, Harwell OX110RA, U.K.

Frank W. Schmidt
Mechanical Engineering Department, Pennsylvania State University, University Park, Pennsylvania 16802, U.S.A.

D. Brian Spalding
Department of Mechanical Engineering, Imperial College of Science and Technology, Exhibition Road, London SW7 2BX, U.K.

Jerry Taborek
Heat Transfer Research, Inc., 1000 South Fremont Avenue, Alhambra, California 91802, U.S.A.

Algirdas Žukauskas
The Academy of Sciences of the Lithuanian SSR, MTP-1, Lenino pr. 3, 232600 Vilnius, U.S.S.R.

V. Gnielinski, Associate Editor
Lehrstuhl und Institut für Thermische Verfahrenstechnik der Universitat Karlsruhe TH, D-7500 Karlsruhe 1, Kaiserstrasse 12, Postfach 6380, F.R. Germany

PUBLISHED UNDER THE AUSPICES OF THE INTERNATIONAL CENTRE FOR HEAT AND MASS TRANSFER

Heat Exchanger Design Handbook

Copyright © 1983 by Hemisphere Publishing Corporation. All rights reserved. Printed in the United States of America. Except as permitted under the United States Copyright Act of 1976, no part of this publication may be reproduced or distributed in any form or by any means, or stored in a data base or retrieval system, without the prior permission of the publisher.

1 2 3 4 5 6 7 8 9 0 BCBC 8 9 8 7 6 5 4 3 2

This book was set in Press Roman by Hemisphere Publishing Corporation.
Editors: Brenda Munz Brienza, Judith B. Gandy, and Lynne Lackenbach.
Production supervisor: Miriam Gonzalez.
Compositors: Peggy M. Rote, Sandra F. Watts, Shirley J. McNett, and Wayne Hutchins.
BookCrafters, Inc., was printer and binder.

Distribution outside the U.S.A., Canada, Mexico, U.K., and Ireland, by VDI-Verlag, Dusseldorf.

The publisher, editors, and authors have maintained the highest possible level of scientific and technical scholarship and accuracy in this work, which is not intended to supplant professional engineering design or related technical services, and/or industrial or international codes and standards of any kind. The publisher, editors, and authors assume no liability for the application of data, specifications, standards or codes published herein

Library of Congress Cataloging in Publication Data

Main entry under title:

Fluid mechanics and heat transfer.

(Heat exchanger design handbook ; 2)
Kept up to date by supplements.
Includes index.
1. Fluid mechanics. 2. Heat-Transmission. 3. Heat exchangers. I. Armstrong, Robert Calvin, date-
II. Series.
TJ263.H38 1983 vol. 2 621.402 5s 82-9266
[TA357] [621.402'2] AACR2
ISBN 3-18-41-9082-X (VDI Part 2)
ISBN 3-1841-9080-3 (VDI set)
ISBN O-89116-125-2 (Hemisphere set)

HEDH CONTENTS

1 Heat exchanger theory

Contributors xiii
General Preface xv
Part 1 Preface xvii
Nomenclature xix
International System of Units (SI): Rules, Practices, and Conversion Charts, J. Taborek xxv

1.1 DESCRIPTION OF HEAT EXCHANGER TYPES

1.1.0 Structure of the Section, D. Brian Spalding
1.1.1 Types of Fiow Configuration, D. Brian Spalding
1.1.2 Types of Interactions between Streams, D. Brian Spalding
1.1.3 Types of Temperature Change Pattern, D. Brian Spalding
1.1.4 Types of Interface between Streams, D. Brian Spalding
1.1.5 Types of Heat Exchange Equipment, D. Brian Spalding
1.1.6 Unsteady Operation, D. Brian Spalding

1.2 DEFINITIONS AND QUANTITATIVE RELATIONSHIPS FOR HEAT EXCHANGERS

1.2.0 Structure of the Section, D. Brian Spalding
1.2.1 Thermodynamics: Brief Notes on Important Concepts, D. Brian Spalding
1.2.2 Flux Relationships, D. Brian Spalding
1.2.3 Transfer Coefficient Dependences, D. Brian Spalding
1.2.4 Balance Equations Applied to Complete Equipment, D. Brian Spalding
1.2.5 The Differential Equations Governing Streams, D. Brian Spalding
1.2.6 Partial Differential Equations for Interpenetrating Continua, D. Brian Spalding

1.3 ANALYTIC SOLUTIONS TO HEAT EXCHANGER EQUATIONS

1.3.1 Uniform-Transfer-Coefficient Solutions for the No-Phase-Change Heat Exchanger, D. Brian Spalding
1.3.2 Other Analytic Solutions, D. Brian Spalding

1.4 NUMERICAL SOLUTION PROCEDURES FOR HEAT EXCHANGER EQUATIONS

1.4.1 Cases with Prescribed Flow Patterns, D. Brian Spalding

Rev. 1966

1.4.2 **Cases in Which the Flow Patterns Must Be Calculated,** D. Brian Spalding
1.4.3 **Special Applications of Numerical Solution Procedures,** D. Brian Spalding

1.5 CHARTS FOR MEAN TEMPERATURE DIFFERENCE IN INDUSTRIAL HEAT EXCHANGER CONFIGURATIONS

1.5.1 **Introduction,** J. Taborek
1.5.2 ***F* and θ Charts for Shell-and-Tube Exchangers,** J. Taborek
1.5.3 ***F* and θ Charts for Cross-Flow Arrangements,** J. Taborek

1.6 EFFECTIVENESS OF MULTIPASS SHELL–AND–TUBE HEAT EXCHANGERS WITH SEGMENTAL BAFFLES (CELL METHOD)

1.6.1 **Introduction,** E. S. Gaddis
1.6.2 **Calculation Procedure,** E. S. Gaddis
1.6.3 **Numerical Examples,** E. S. Gaddis
1.6.4 **Rules for Highest Heat Exchanger Effectiveness,** E. S. Gaddis
1.6.5 **Special Case of Two Tube Passes,** E. S. Gaddis
1.6.6 **Heat Exchangers with Longitudinal Baffles,** E. S. Gaddis
1.6.7 **Cell Effectiveness,** E. S. Gaddis
1.6.8 **Comparison of the Conventional Method and the Cell Method,** E. S. Gaddis
1.6.9 **General Remarks,** E. S. Gaddis

Index I-l

2
Fluid mechanics and heat transfer

Contributors xiii
General Preface xv
Part 2 Preface xvii
Nomenclature xix
International System of Units (SI): Rules, Practices, and Conversion Charts, J. Taborek xxv

2.1 FUNDAMENTALS OF HEAT AND MASS TRANSFER

2.1.0 **Introduction,** E. U. Schliinder
2.1.1 **Physical Mechanisms of Transport Phenomena,** E. U. Schliinder
2.1.2 **Industrial Applications of Heat and Mass Transfer,** E. U. Schliinder
2.1.3 **Presentation of Heat and Mass Transfer Data,** E. U. Schliinder
2.1.4 **Heat and Mass Transfer in Uniform and Nonuniform Systems,** E. U. Schliinder
2.1.5 **Analogy between Heat and Mass Transfer and Its Limitations,** E. U. Schlünder
2.1.6 **Combined Heat and Mass Transfer,** E. U. Schliinder
2.1.7 **State of the Art of Heat and Mass Transfer,** E. U. Schliinder

2.2 SINGLE–PHASE FLUID FLOW

2.2.1 **Introduction and Fundamentals,** K. Gersten
2.2.2 **Ducts,** K. Gersten
2.2.3 **Immersed Bodies,** K. Gersten
2.2.4 **Banks of Plain and Finned Tubes,** A. Žukauskas and R. Ulinskas
2.2.5 **Fixed Beds, P.** J. Heggs
2.2.6 **Fluidized Beds, 0.** Molerus
2.2.7 **Headers, Nozzles, and Turnarounds,** J. A. R. Henry
2.2.8 **Non-Newtonian Fluids,** Robert C. Armstrong

2.3 MULTIPHASE FLUID FLOW AND PRESSURE DROP

2.3.1 **Introduction and Fundamentals,** G. F. Hewitt
2.3.2 **Gas-Liquid Flow, G.** F. Hewitt
2.3.3 **Solid-Gas Flow,** M. Weber and W. Stegmaier
2.3.4 **Solid-Liquid Flow,** M. Weber and W. Stegmaier

2.4 HEAT CONDUCTION

2.4.1 **Basic Equations,** H. Martin
2.4.2 **Steady State,** H. Martin
2.4.3 **Transient Response to a Step Change of Temperature,** H. Martin
2.4.4 **Melting and Solidification,** H. Martin
2.4.5 **Periodic Change of Temperature,** H. Martin
2.4.6 **Thermal Contact Resistance,** T. F. Irvine, Jr.

2.5 SINGLE–PHASE CONVECTIVE HEAT TRANSFER

2.5.1 **Forced Convection in Ducts,** V. Gnielinski

2.5.2 **Forced Convection around Immersed Bodies,** V. Gnielinski
2.5.3 **Banks of Plain and Finned Tubes**
A. Single Rows and Tube Banks in Cross Flow, V. Gnielinski
B. Finned Tubes, A. Žukauskas and A. Skrinska
2.5.4 **Fixed Beds,** V. Gnielinski
2.5.5 **Fluid-to-Particle Heat Transfer in Fluidized Beds,** S. S. Zabrodsky with revisions by H. Martin
2.5.6 **Impinging Jets,** H. Martin
2.5.7 **Free Convection around Immersed Bodies,** S. W. Churchill
2.5.8 **Free Convection in Layers and Enclosures,** S. W. Churchill
2.5.9 **Combined Free and Forced Convection around Immersed Bodies,** S. W. Churchill
2.5.10 **Combined Free and Forced Convection in Channels,** S. W. Churchill
2.5.11 **Augmentation of Heat Transfer,** Arthur E. Bergles
2.5.12 **Heat Transfer for Non-Newtonian Fluids,** Robert C. Armstrong and H. H. Winter
2.5.13 **Heat Transfer in Liquid Metals,** V. M. Borishanski and E. V. Firsova

2.6 **CONDENSATION**

2.6.1 **General Introduction,** D. Butterworth
2.6.2 **Film Condensation of Pure Vapor,** D . Butterworth
2.6.3 **Condensation of Vapor Mixtures,** D . Butterworth
2.6.4 **Condensation of Vapor Mixtures Forming Immiscible Liquids,** R. G. Sardesai
2.6.5 **Dropwise Condensation,** P. Griffith
2.6.6 **Augmentation of Condensation,** Arthur E. Bergles
2.6.7 **Fogging,** D. Chisholm
2.6.8 **Direct-Contact Condensers,** Harold R. Jacobs

2.7 **BOILING AND EVAPORATION**

2.7.1 **Boiling of Single Component Liquids: Basic** Processes, J. G. Collier
2.7.2 **Pool Boiling,** J. G. Collier
2.7.3 **Boiling within Vertical Tubes,** J. G. Collier
2.7.4 **Convective Boiling inside Horizontal Tubes,** J. G. Collier
2.7.5 **Boiling outside Tubes and Tube Bundles,** J. G. Collier
2.7.6 **Boiling of Binary and Multicomponent Mixtures: Basic Processes,** J. G. Collier
2.7.7 **Boiling of Binary and Multicomponent Mixtures: Pool Boiling,** J. G. Collier
2.7.8 **Boiling of Binary and Multicomponent Mixtures: Forced Convection Boiling,** J. G. Collier
2.7.9 **Augmentation of Boiling and Evaporation,** Arthur E. Bergles

2.8 **HEAT TRANSFER TO GAS-SOLID SYSTEMS**

2.8.1 **Stagnant Packed Beds,** R. Bauer
2.8.2 **Packed Beds with a Gas Flowing Through,** R. Bauer
2.8.3 **Packed and Agitated Packed Beds,** E. Muchowski
2.8.4 **Fluidized Beds,** J. S. M. Botterill

2.9 **HEAT TRANSFER BY RADIATION**

2.9.1 **Introduction,** D. K. Edwards
2.9.2 **Surface Radiation Characteristics,** D. K. Edwards
2.9.3 **Radiation Transfer between Perfectly Diffuse Surfaces,** D. K. Edwards
2.9.4 **Radiation Transfer between Specular and Imperfectly Diffuse Surfaces,** D. K. Edwards
2.9.5 **Gas Radiation Properties,** D. K. Edwards
2.9.6 **Radiation Transfer with an Isothermal Gas,** D. K. Edwards
2.9.7 **Nonisothermal Gas Radiation,** D. K. Edwards
2.9.8 **Radiation Acting with Conduction or Convection,** D. K. Edwards

Index I-l

3

Thermal and hydraulic design of heat exchangers

Contributors xiii
General Preface xv
Part 3 Preface xvii
Nomenclature xix
International System of Units (SI): Rules, Practices, and Conversion Charts, J. Taborek xxv

3.1 INTRODUCTION TO HEAT EXCHANGER DESIGN

3.1.1 **Fundamental Concepts,** Kenneth J. Bell
3.1.2 **Types of Heat Exchangers and Their Applications,** Kenneth J. Bell
3.1.3 **Logic of the Design Process,** Kenneth J. Bell
3.1.4 **Approximate Sizing of Shell-and-Tube Heat Exchangers,** Kenneth J. Bell

3.2 DOUBLE-PIPE HEAT EXCHANGERS

3.2.1 **Introduction,** A. R. Guy
3.2.2 **Applications of Double-Pipe Heat Exchangers,** A. R. Guy
3.2.3 **Design Parameters,** A. R. Guy
3.2.4 **Types Available,** A. R. Guy
3.2.5 **Construction/Mechanical Design,** A. R. Guy
3.2.6 **Operational Advantages,** A. R. Guy

3.3 SHELL-AND-TUBE HEAT EXCHANGERS: SINGLE-PHASE FLOW

3.3.1 **Objectives and Background,** J. Taborek
3.3.2 **Survey of Shell-Side Flow Correlations,** J. Taborek
3.3.3 **Recommended Method: Principles and Limitations,** J. Taborek
3.3.4 **Practices of Shell-and-Tube Heat Exchanger Design,** J. Taborek
3.3.5 **Input Data and Recommended Practices,** J. Taborek
3.3.6 **Auxiliary Calculations,** J. Taborek
3.3.7 **Ideal Tube Bank Correlations for Heat Transfer and Pressure Drop,** J. Taborek
3.3.8 **Calculation of Shell-Side Heat Transfer Coefficient and Pressure Drop,** J. Taborek
3.3.9 **Performance Evaluation of a Geometrically Specified Exchanger,** J. Taborek
3.3.10 **Design Procedures for Segmentally Baffled Heat Exchangers,** J. Taborek
3.3.11 **Extension of the Method to Other Shell, Baffle, and Tube Bundle Geometries,** J. Taborek

3.4 CONDENSERS

3.4.1 **Introduction,** A. C. Mueller
3.4.2 **Selection of Condenser Types,** A. C. Mueller
3.4.3 **Discussion of Condenser Types,** A. C. Mueller
3.4.4 **Mixtures,** A. C. Mueller
3.4.5 **Operational Problems,** A. C. Mueller
3.4.6 **Heat Transfer,** A. C. Mueller
3.4.7 **Pressure Drop,** A. C. Mueller
3.4.8 **Mean Temperature Difference,** A. C. Mueller
3.4.9 **Design Procedure,** A. C. Mueller

3.5 EVAPORATORS

3.5.1 **Introduction,** R. A. Smith
3.5.2 **Types of Evaporators,** R. A. Smith
3.5.3 **Arrangements,** R. A. Smith
3.5.4 **Design Details,** R. A. Smith
3.5.5 **Choice of Type,** R. A. Smith
3.5.6 **Estimation of Pressure Drop and Circulation Rate,** R. A. Smith
3.5.7 **Estimation of Heat Transfer Coefficients,** R. A. Smith
3.5.8 **Estimation of Surface Area,** R. A. Smith

3.6 SHELL-AND-TUBE REBOILERS

3.6.1 **Introduction,** J. W. Palen
3.6.2 **Thermal Design,** J. W. Palen
3.6.3 **Pressure Drop,** J. W. Palen
3.6.4 **Special Design Considerations,** J. W. Palen
3.6.5 **Calculation Procedures,** J. W. Palen

3.7 PLATE HEAT EXCHANGERS

3.7.1 **Construction and Operation,** Anthony Cooper and J. Dennis Usher
3.7.2 **Factors Governing Plate Specification,** Anthony Cooper and J. Dennis Usher
3.7.3 **Corrugation Design,** Anthony Cooper and J. Dennis Usher
3.7.4 **Friction Factor Correlations,** Anthony Cooper and J. Dennis Usher
3.7.5 **Heat Transfer Correlations,** Anthony Cooper and J. Dennis Usher
3.7.6 **Factors Affecting Plate Design,** Anthony Cooper and J. Dennis Usher
3.7.7 **Overall Plate Design,** Anthony Cooper and J. Dennis Usher
3.7.8 **Plate Arrangement and Correction Factors,** Anthony Cooper and J. Dennis Usher
3.7.9 **Fouling,** Anthony Cooper and J. Dennis Usher
3.7.10 **Methods of Surface Area Calculation,** Anthony Cooper and J. Dennis Usher
3.7.11 **Thermal Mixing,** Anthony Cooper and J. Dennis Usher
3.7.12 **Two-Phase Fiow Applications,** Anthony Cooper and J. Dennis Usher

3.8 AIR-COOLED HEAT EXCHANGERS

3.8.1 **Air as Coolant for Industrial Processes:** Comparison to Water, P. Paikert
3.8.2 **Custom-Built Units,** P. Paikert
3.8.3 **Fin-Tube Systems for Air Coolers,** P. Paikert
3.8.4 **Fin-Tube Bundles,** P. Paikert
3.8.5 Thermal Rating, P. Paikert
3.8.6 **Tube-Side Flow Arrangements,** P. Paikert
3.8.7 Cooling **Air Supply** by Fans, P. Paikert
3.8.8 **Cooling Air Supply in Natural Draft Towers,** P. Paikert
3.8.9 **Special Features of Air Coolers,** P. Paikert

3.9 COMPACT HEAT EXCHANGERS

3.9.1 Introduction, R. L. Webb
3.9.2 Definition of Geometric Terms, R. L. Webb
3.9.3 **Plate Fin Surface Geometries,** R. L. Webb
3.9.4 Surface Performance Data, R. L. Webb
3.9.5 **Laminar Flow Surfaces,** R. L. Webb
3.9.6 **Correlation of Heat Transfer and Friction** Data, R. L. Webb
3.9.7 **Goodness Factor Comparisons,** R. L. Webb
3.9.8 **Specification of Rating and Sizing Problems,** R. L. Webb
3.9.9 **Calculation Procedure for a Rating Problem,** R. L. Webb
3.9.10 **Pressure Drop Calculation,** R. L. Webb
3.9.11 **Procedures for the Thermal Sizing Problem,** R. L. Webb
3.9.12 **Multifluid Service,** R. L. Webb
3.9.13 **Recent Theory and Data on Vaporization and Condensation,** R. L. Webb

3.10 HEAT PIPES

3.10.1 **Introduction,** D. Chisholm
3.10.2 **Circulation and Axial Heat Transfer,** D . Chisholm
3.10.3 **Temperature Distributions and Radial Heat Transfer Flux,** D. Chisholm
3.10.4 **Axial Heat Transfer and the Operational Envelope,** D . Chisholm
3.10.5 **Selection of Working Fluid,** D. Chisholm
3.10.6 **Characteristics of Wicks,** D. Chisholm
3.10.7 **Start-up and Control,** D. Chisholm

3.11 FURNACES AND COMBUSTION CHAMBERS

3.11.1 Introduction, J. S. Truelove
3.11.2 **Process Heaters and Boilers,** J. S. Truelove
3.11.3 **Heat Transfer in Furnaces,** J. S. Truelove
3.11.4 **The Stirred-Reactor Furnace Model,** J. S. Truelove
3.11.5 **The Plug-Flow Furnace Model,** J. S. Truelove
3.11.6 **The Multizone Furnace Model,** J. S. Truelove
3.11.7 Advanced Furnace Models, J. S. Truelove

3.12 COOLING TOWERS

3.12.1 **Introduction,** J. R. Singham
3.12.2 **The Packing Region,** J. R. Singham
3.12.3 **Natural Draft Towers,** J. R. Singham
3.12.4 **Mechanical Draft Towers,** J. R. Singham
3.12.5 **Hybrid Towers,** J. R. Singham
3.12.6 **Further Topics,** J. R. Singham

3.13 DRYERS

3.13.1 **Introduction,** E. U. Schliinder
3.13.2 Classification and Selection, E. U. Schliinder
3.13.3 **Layout and Performance Data,** E. U. Schlünder
3.13.4 **Prediction of Drying Rates,** E. U. Schliinder
3.13.5 **Prediction of Residence Times with Prescribed Material** Flow, E. U. Schlünder
3.13.6 **Prediction of Residence Times with Nonprescribed Material Flow,** E. U. Schlünder
3.13.7 **Practical Dryer Design,** D. Reay

3.14 AGITATED VESSELS

3.14.1 **Introduction,** W. R. Penney
3.14.2 **Equipment,** W. R. Penney
3.14.3 **Heat Transfer Correlations,** W. R. Penney

3.15 REGENERATION AND THERMAL ENERGY STORAGE

3.15.0 **Introduction,** F. W. Schmidt
3.15.1 **Operation of Regenerators,** A. J. Willmott
3.15.2 **Construction of Regenerator Packing,** A. J. Willmott
3.15.3 **Internal Behavior of a Regenerator: Development of the Mathematical Model,** A. J. Willmott
3.15.4 **Heat Transfer Coefficient,** A. J. Willmott
3.15.5 Use of Bulk or Overall Heat Transfer **Coefficient,** A. J. Willmott
3.15.6 **Development of Dimensionless Parameters,** A. J. Willmott
3.15.7 **Calculation of Regenerator Thermal Performance,** A. J. Willmott

3.15.8 Effect of Longitudinal Conduction in the Packing of the Regenerator, A. J. Willmott
3.15.9 Dealing with Heat Losses, A. J. Willmott
3.15.10 Transient Characteristics of Regenerators. A. J. Wiilmott
3.15.1 1 Explicit Design of Balanced Regenerators, B. Kulakowski
3.15.1.2 Single-Blow Operation, F. W. Schmidt

3.16 WASTE HEAT BOILER SYSTEMS

3.16.1 Description of Typical System, P. Hinchley
3.16.2 Key Aspects of the Design and Specification of Individual Items of Plant, P. Hinchley
3.16.3 Detailed Mechanical Design and Fabrication of Equipment, P. Hinchley
3.16.4 Precommissioning of Waste Heat Boiler Systems, P. Hinchley

3.17 FOULING IN HEAT EXCHANGERS

3.17.1 Overview and Summary, James G. Knudsen
3.17.2 Types of Fouling, James G. Knudsen
3.17.3 Analysis of the Fouling Process, James G. Knudsen
3.17.4 Fouling Control Measures, James G. Knudsen
3.17.5 Cleaning of Heat Exchangers, James G. Knudsen
3.17.6 Measurement of Fouling Resistances, James G. Knudsen
3.17.7 Recommended Fouling Resistances for Design, James G. Knudsen

Index I-l

4 Mechanical design of heat exchangers

Contributors xiii
General Preface xv
Part 4 Preface xvii
Nomenclature xix
International System of Units (SI): Rules, Practices, and Conversion Charts, J. Taborek xxv

4.1 BASIC MECHANICAL PRINCIPLES

4.1.1 Introduction, C . Ruiz
4.1.2 Methods of Analysis, C. Ruiz
4.1.3 Shells, C. Ruiz
4.1.4 Tube Plates, C. Ruiz
4.1.5 Tubes, C. Ruiz
4.1.6 Expansion Joints, C. Ruiz
4.1.7 Flanges, C. Ruiz
4.1.8 Heads, Openings, and Branches, C. Ruiz

4.2 SHELL–AND–TUBE HEAT EXCHANGERS: ELEMENTS OF CONSTRUCTION

4.2.1 Introduction, E. A. D. Saunders
4.2.2 Design and Construction Codes, E. A. D. Saunders
4.2.3 Types of Shell-and-Tube Heat Exchangers, E. A. D. Saunders
4.2.4 Head Types, E. A. D. Saunders
4.2.5 Features Related to Thermal Design, E. A. D. Saunders
4.2.6 Features Relating to Mechanical Design and Fabrication, E. A. D. Saunders

4.3 SHELL–AND–TUBE HEAT EXCHANGERS: REVIEW OF MECHANICAL DESIGN CODES

4.3.1 Mechanical Design Codes, M. Morris
4.3.2 Index to U.S., U.K., and F.R.G. Codes, M. Morris
4.3.3 Analytic Basis of Code Rules, M. Morris
4.3.4 Comparison of Principal Codes, M. Morris
4.3.5 Guides to National Practice, M. Morris
4.3.6 Design Example: Floating-Head Heat Exchanger, TEMA Type AJS, D. Harris

4.4 MECHANICAL DESIGN: GENERAL FORMS OF HEAT EXCHANGERS

4.4.1 Mechanical Design of Air-Cooled Heat Exchangers, K. V. Shipes
4.4.2 Mechanical Design of Plate Heat Exchangers, J. Dennis Usher
4.4.3 Plate Fin Heat Exchangers, R. L. Webb
4.4.4 Other Types of Heat Exchangers, I. Murray

4.5 MATERIALS OF CONSTRUCTION AND CORROSION

4.5.1 Introduction, J. F. Lancaster
4.5.2 Materials of Construction, J. F. Lancaster
4.5.3 Corrosion and Other Types of Damage, J. J. Lancaster

4.6 FLOW–INDUCED VIBRATION

4.6.1 Introduction, J. M. Chenoweth

4.6.2 **Tube Bundle Vibration Characteristics,** J. M. Chenoweth
4.6.3 **Shell-Side Velocities in Shell-and-Tube Exchangers,** J. M. Chenoweth
4.6.4 **Flow-induced Vibration Phenomena,** J. M. Chenoweth
4.6.5 **Procedure for Vibration Predictions,** J. M. Chenoweth
4.6.6 **Design Considerations,** J. M. Chenoweth

4.7 **TESTING AND INSPECTION**

4.7.1 **Objectives of Inspection, Testing, and Drawing Approval,** A. Illingworth
4.7.2 **Materials,** A. Illingworth
4.7.3 **Welding,** A. Illingworth
4.7.4 **Stages of Inspection,** A. Illingworth
4.7.5 **Construction,** A. Illingworth
4.7.6 **Nondestructive Testing,** A. Illingworth
4.7.7 **Certification,** A. Illingworth
4.7.8 **Fittings,** A. Illingworth
4.7.9 **Cleanliness and Storage,** A. Illingworth
4.7.10 **Preparation and Dispatch,** A. Illingworth
4.7.11 **Quality Control and Inspection Disciplines,** R. S. M. Moffatt

4.8 COSTING OF SHELL–AND–TUBE HEAT EXCHANGERS

4.8.1 Introduction, D. Chisholm
4.8.2 **Costing of Shell-and-Tube Heat Exchangers,** R. C. Cowie
4.8.3 **Costing of Air Coolers, C.** North
4.8.4 **Costing of Plate Heat Exchangers,** J. Dennis Usher

4.9 **SPECIFICATIONS AND TENDERS**

4.9.1 **Introduction,** D . Edge
4.9.2 **Specifications,** D. Edge
4.9.3 **Tenders,** D. Edge

4.10 **EXPANSION BELLOWS**

4.10.1 **Introduction,** M. Morris
4.10.2 **Expansion Bellows,** M. Morris

Index I-l

5
Physical properties

Contributors xiii
General Preface xv
Part 5 Preface xvii
Nomenclature xix
International System of Units (SI): Rules, Practices, and Conversion Charts, J. Taborek xxv

5.1 PROPERTIES OF PURE FLUIDS

5.1.0 **Introduction,** M. Schunck
5.1.1 **Critical Data,** M. Schunck
5.1.2 **Specific Volume, p-$\tilde{V}$-T Correlations,** M. Schunck
5.1.3 **Thermodynamic Properties,** M. Schunck
5.1.4 Transport **Properties,** M. Schunck
5.1.5 **Surface Tension,** M. Schunck

5.2 PROPERTIES OF MIXTURES OF FLUIDS

5.2.1 **Phase Behavior of Mixtures,** R. N. Maddox
5.2.2 **Thermodynamic Properties,** R. N. Maddox
5.2.3 **Thermophysical Properties,** R. N. Maddox
5.2.4 **Interfacial Tension,** R. N. Maddox
5.2.5 **Diffuse Coeffkients,** R. N. Maddox

5.3 PROPERTIES OF RHEOLOGICALLY COMPLEX MEDIA

5.3.1 **Disperse Compositions,** Z. P. Shulman
5.3.2 **Classification of Lubricants,** Z. P. Shulman
5.3.3 **Oils,** Z. I? Shulman
5.3.4 **Plastic Lubricants,** Z. P. Shulman
5.3.5 **Lubricant-Cooling Liquids,** Z. P. Shulman
5.3.6 **Polymers,** Z. P. Shulman
5.3.7 **Oriented Polymers,** Z. P. Shulman
5.3.8 **Effect of External Electric and Magnetic Fields,** Z. P. Shulman

5.4 **PROPERTIES OF SOLIDS**

5.4.0 **Introduction,** M . Schunck
5.4.1 **Density of Solids,** M. Schunck
5.4.2 **Specific Heat of Solids,** M. Schunck
5.4.3 **Thermal Conductivity of Solids,** M. Schunck
5.4.4 **Emissivity of Solids,** M. Schunck
5.4.5 **Elastic Properties, S.** F. Pugh

5.5 **PHYSICAL PROPERTY DATA TABLES**

5.5.0 **Index to Compounds and Properties by Section,** Clive F. Beaton
5.5.1 **Properties of Saturated Fluids,** R. N. Maddox

5.5.2 Properties of Superheated Gases, R. N. Maddox
5.5.3 **Steam Tables,** Clive F. Beaton
5.5.4 Constants for Binary Mixtures, R. N. Maddox
5.5.5 Emissivity Data for Gases, D. K. Edwards and Robert Matavosian
5.5.6 Thermal Conductivity of Solids, l? E. Liley
5.5.7 Emissivity of Solids, P. E. Liley
5.5.8 Elastic Properties of Solids, S. F. Pugh
5.5.9 Properties of Liquid Heavy Water, G. Ulrych
5.5.10 Physical Properties of Liquids at Temperatures below Their Boiling Point, Clive F. Beaton
5.5.11 Transport Properties of Superheated Gases, G. F. Hewitt
5.5.12 Thermal and Mechanical Properties of Heat Exchanger Construction Materials, Clive F. Beaton
5.5.13 Properties of Seawater, Clive F. Beaton

Index I-l

2 Contributors

Robert C. Armstrong
Department of Chemical Engineering, Massachusetts Institute of Technology, Cambridge, Massachusetts 02139 U.S.A.

R. Bauer
BASF Aktiengesellschaft TAF/A, Im Hemshofcenter, D-6700 Ludwigshafen/Rhein F.R. Germany

Arthur E. Bergles
Department of Mechanical Engineering, Iowa State University, Ames, Iowa 50010 U.S.A.

V. M. Borishanski
Vsesojuznoje Agentstva, po Avtorskim Pravam/VAAP, USSR 103104 Moskwa, K-104, B. Bronnaja 6A U.S.S.R.

J. S. M. Botterill
Department of Chemical Engineering, University of Birmingham, POB 363, Edgbaston, GB-Birmingham B15 2TT U.K.

D. Butterworth
Heat Transfer and Fluid Flow Service, Atomic Energy Research Establishment, Harwell, Oxfordshire OX1 1 0RA U.K.

D. Chisholm
Department of Trade and Industry, National Engineering Laboratory, East Kilbride, Glasgow G75 OQU Scotland

S. W. Churchill
Department of Chemical Engineering, University of Pennsylvania, Philadelphia, Pennsylvania 19 104 U.S.A.

J. G. Collier
Atomic Energy Technical Unit, Atomic Energy Research Establishment, Harwell, Oxfordshire OX1 1 0RA U.K.

D. K. Edwards
Mechanical Engineering Department, University of California, Irvine, California 92707 U.S.A.

E. V. Firsova
Leningrad Central Boiler Turbine Research Institute, Polytechnitcheskaya 24, Leningrad K-21 U.S.S.R.

K. Gersten
Institut für Thermo- und Fluiddynamik, Ruhr-Universität Bochum, Universitätsstrasse 150, Gebäude IB, D-4630 Bochum F.R. Germany

V. Gnielinski
Institut für Thermische Verfahrenstechnik der Universität Karlsruhe, Postfach 6380, D-7500 Karlsruhe 1 F.R. Germany

P. Griffith
Mechanical Engineering Department, Massachusetts Institute of Technology, Cambridge, Massachusetts 02139 U.S.A.

P. J. Heggs
Chemical Engineering Department, University of Leeds, Leeds LS2 9JT U.K.

J. A. R. Henry
Department of Industry, National Engineering Laboratory, East Kilbride, Glasgow G75 OQU Scotland

G. F. Hewitt
Engineering Sciences Division, Atomic Energy Research Establishment, Harwell, Oxfordshire OX1 1 0RA U.K.

T. F. Irvine, Jr.
Mechanical Engineering Department, State University of New York, Stony Brook, Long Island, New York 11790 U.S.A.

H. Martin
lnstitut für Thermische Verfahrenstechnik der Universitat Karlsruhe, Postfach 6380, D-7500 Karlsruhe 1 F.R. Germany

0. **Molerus**
Institut für Mechanische Verfahrenstechnik der Universitat Erlangen-Niirnberg, Martensstrasse 9, D-8520 Erlangen F.R. Germany

E. Muchowski
Anger 2, D-802 1 Strasslach F .R. Germany

R. G. **Sardesai**
Heat Transfer and Fluid Flow Service, Atomic Energy Research Establishment, Harwell, Oxfordshire OX1 1 0RA U.K.

E. U. Schlünder
Lehrstuhl und Institut fur Thermische Verfahrenstechnik der Universitat Karlsruhe TH, Postfach 6380, D-7500 Karlsruhe 1 F.R. Germany

A. Skrinska
Thermoinsulation Research Institute, Linkmenu St. 28, 232657 Vilnius, Lithuanian SSR U.S.S.R.

W. Stegmaier
BASF Aktiengesellschaft, D-6700 Ludwigshafen F.R. Germany

R. Ulinskas
Institute of Physical and Technical Problems of Energetics, Metalo 4, 233684 Kaunas, Lithuanian SSR U.S.S.R.

M. **Weber**
Institut für Fördertechnik, Abteilung Strömungsfördertechnik, Universitat Karlsruhe, Hertzstrasse 16, D-7500 Karlsruhe 21 F.R. Germany

H. H. Winter
Chemical Engineering Department, University of Massachusetts, Amherst, Massachusetts 01003 U.S.A.

S. S. Zabrodsky
Luikov Heat and Mass Transfer Institute, 15 Podlesnaya, Minsk U.S.S.R.

A. Žukauskas
The Academy of Sciences, MTP 1, Lenino Pr. 3, 232600 Vilnius U.S.S.R.

HEDH
GENERAL PREFACE

Ernst U. Schlünder

■ The idea to create a Heat Exchanger Design Handbook originated at the seminar Recent Developments in Heat Exchangers. organized by the International Centre for Heat and Mass Transfer (ICHMT) in Trogir, Yugoslavia in 1972.

Even though much heat transfer data and correlations were available, this information was scattered throughout the open literature or buried in the files of proprietary organizations. For manufacturers, vendors, and users of heat transfer equipment it was becoming more and more difficult not only to keep up with the continually growing heat transfer information but also to compare data and correlations from various sources. In addition, these sources were often inconsistent, and it was difficult for users to decide which data and correlations would serve their own purposes best. Moreover, over the years many heat transfer publications had become more analytical and more academic, which delayed their immediate application by practicing heat transfer engineers.

Because of this situation, a group of heat transfer specialists decided to collect heat transfer information available in the existing open literature and also-as far as possible-from proprietary sources in order to create a heat transfer information base. Recommended correlations based on selected experimental material would then be provided for all heat exchanger design data.

Although there was great enthusiasm for this project, not much progress was made until 1974, at the Fifth International Heat Transfer Conference in Tokyo. The idea was formulated then of publishing the information base under the auspices of the ICHMT by Hemisphere Publishing Corporation, the publisher of the Centre. Eight representatives of universities, industry, and proprietary organizations formed the Editorial Board, which immediately started working on the scope and organization of this Handbook. As a result of these joint efforts the following five parts were planned:

Part I presents the theory of heat exchangers defining and explaining all parameters and concepts needed for thermal and hydraulic design and rating.

Part 2 contains recommended correlations for design and rating parameters based on evaluated available information. As far as possible experimental data are presented together with the recommended correlations in order to reveal both the consistency of the data as well as the reliability of the correlations.

Part 3 shows how to apply the material given in Parts 1 and 2 when solving actual heat exchanger design and rating problems. Because of the volume of material, it would be impossible for this part to cover all known kinds of heat exchangers. Nevertheless, most of the commonly used types of equipment are discussed in detail together with related installations such as cooling towers and combustion chambers.

Part 4 is devoted to the mechanical design of heat exchangers, which actually cannot be separated from thermal and hydraulic design. A useful comparison of some major national standards is included.

Part *5* contains physical property data that are needed in design calculations in the other four parts.

For each of the five parts, a member of the Editorial Board agreed to act as Lead Editor. Although each Lead Editor accepted additional administrative responsibility for his particular part, the whole Handbook has been a

cooperative effort with each editor sharing the reviewing and editorial work for all the material.

A large number of authors-well-known experts in their fields-have contributed to this Handbook. Each manuscript went through a review procedure and many of them were discussed during the regular meetings of the Editorial Board, which have been held every six months since 1975.

Nevertheless, this Handbook must be considered as a first step rather than as a final result. Though the concept was clear, the realization has not been easy and there is still room for improvement. Additionally, because new heat transfer data and correlations are published each year, a permanent updating procedure has been established to keep this Handbook current. This supplementary material will be offered regularly to the subscribers. To ensure that any future material (including personal remarks and comments) can be added easily, a loose-leaf ring binder format was chosen for the Handbook.

The users of this Handbook are urged to communicate with us about what is missing and to make suggestions for improving the contents of the book and its applicability. This kind of interaction and cooperation between users and editors not only should improve the quality of the Handbook but also should stimulate further research work guided by the requirements of heat exchanger design.

The Editorial Board wishes to thank the publisher as well as the contributing authors for their most valuable cooperation.

2

Preface

Frank W. Schmidt

■ The thermal design engineer is forced to base his or her design on published or proprietary correlations or on experimental results. It is recognized that there is uncertainty in the accuracy of many of these correlations. The primary objective of this part of the Handbook is to evaluate and present the best available correlations. Whenever possible, the expected accuracy of the correlations is indicated by comparison with reliable experimental results.

A number of authors have included a discussion of the basic phenomena, recognizing that in many instances an engineer unfamiliar with a technical area will refer to the Handbook for design assistance. Words of caution are also given when special considerations must be given to avoid an undesirable or faulty design. Although space limitations required that only the most general correlations be given, most authors have included an extensive list of references which will assist users of the Handbook in their search for more detailed information.

Heat exchangers take so many varied forms that their design requires correlations that are applicable over a wide range of transfer processes and exchanger geometries. The Editorial Board, recognizing this, attempted to cover as completely as possible all the significant areas associated with thermal transfer devices. As a result, this part will be of considerable value not only to engineers concerned with the design and rating of heat exchangers but to those interested in all aspects of thermal design.

Section 2.1 reviews the fundamentals of heat, mass, and momentum transfer. Single phase fluid flow in ducts, in banks of plain and finned tubes, and over immersed bodies is discussed in Sec. 2.2 for both Newtonian and non-Newtonian fluids. A discussion of flow in fixed and fluidized beds is also presented in this section.

Extensive coverage of multiphase fluid flow and pressure drop is given in Sec. 2.3. A discussion of the fundamentals of these types of flows is followed by a detailed discussion of gas-liquid, solid-gas, and solid-liquid flows.

Heat conduction is covered in Sec. 2.4. Steady-state and transient heat conduction with and without changes in phase are discussed. A section on contact resistance is also included.

Section 2.5 presents correlations for single phase convective heat transfer. These include force, free, and combined free and forced convection. Heat transfer in Newtonian, non-Newtonian, and liquid metals systems are discussed. Techniques used to augment heat transfer are also described.

A very complete section on condensation of pure vapor, vapor mixtures, and vapor mixtures forming immiscible liquids is presented in Sec. 2.6. Dropwise condensation, fogging, and enhancement devices are also discussed in this section.

Boiling and evaporation is the subject of Sec. 2.7. The techniques required to predict heat transfer and vapor formation rate in pool boiling, boiling inside and outside tubes, and tube bundles of single component liquids are presented. Boiling if binary and multicomponent mixtures is also discussed.

Section 2.8 discusses heat transfer to gas-solid systems in fixed beds with and without gas movement, fluidized beds, and agitated packed beds.

A very thorough discussion of radiation heat transfer is presented in Sec. 2.9. Surface radiation characteristics, radiation heat transfer between specular and diffuse surfaces and gaseous radiation are discussed in detail in the section.

NOMENCLATURE

The most frequently used symbols for quantities in heat and mass transfer are listed here according to the following principles:

1. Capital Roman letters (not italic) denote absolute quantities expressed in either SI basic units or derived units, e.g., N = kg m/s^2, J = N m, W = J/s.

Exceptions: Time (t), variables, coordinates (x, y, z, r), characteristic lengths in dimensionless numbers (l, d, s).

2. Lowercase Roman letters (not italic) denote the corresponding specific quantities per unit mass, mole. length, area, or volume (but not time). A dot over the symbol denotes an absolute or specific quantity per unit time.

Exception: Velocity (u, v, w).

A function will be indicated by ( ).

Molar quantities are denoted by a tilde (~) over the symbol.

Exceptions: Gas constant ($\tilde{R}$), Loschmidt number ($\tilde{L}$), molecular weight ($\tilde{M}$), chemical potential (y).

3. Lowercase Greek letters are used for coefficients and physical propertics.

Exceptions: Overall heat transfer coefficient (U), heat capacity (c_p, c,).

Capital Greek letters refer to eddy (turbulent) quantities; e.g., A denotes eddy thermal conductivity.

4. Dimensionless variables should be denoted by a superscript $^+$ following the corresponding symbol. e.g., y^+ for a dimensionless coordinate.

5. Decimal fractions or multiples of the SI units may be denoted by the corresponding symbol preceding the SI unit, e.g. MW = 10^6 W.

© 1983 Hemisphere Publishing Corporation

Basic Quantities

Quantity	Symbol	Unit
Heat rate	$\dot{Q}$	W
Heat quantity	$Q = \int \dot{Q}\, dt$	J
Heat flux	$\dot{q} = \dot{Q}/A$	W/m^2
Time	t	s
Frequency	f	1/s
Mass	M	kg
Mass flow rate	$\dot{M}$	kg/s
Mass velocity (mass flow per unit area)	$ni = \dot{M}/S$	$kg/m^2 s$
Mass flux	$\dot{m}_n = \dot{M}_n/A$	$kg/m^2 s$
Number of moles	N	mol
Molar mass flow rate	$\dot{N}$	mol/s
Molar mass velocity	$\dot{n} = \dot{N}/S$	$mol/m^2 s$
Molecular weight	$\tilde{M}$	g/mol
Density	ρ	kg/m^3
Concentration	c	kg/m^3
Molar density	$\tilde{\rho}$	mol/m^3
Molar concentration	$\tilde{c}$	mol/m^3
Mass fraction	x_i, Yi	kg_i/kg
Mass loading	X_i, Y_i	kg_i/kg_j
Molar mass fraction	$\tilde{x}_i, \tilde{y}_i$	mol_i/mol
Molar mass loading	$\tilde{X}_i, \tilde{Y}_i$	mol_i/mol_j
Volume	V	m^3
Volume flow rate	$\dot{V}$	m^3/s
Velocity	u, v, w	m/s
Surface area	A	m^2
Cross-sectional area	S	m^2
Length or diameter	L, D, l, d, s	m
Coordinate	$\psi, \varphi, r, x, y, z$	
Void fraction	ϵ	
Fraction of volume flow rate	$\dot{\epsilon}$	—
Quality	x	—
Flow quality	$\dot{x}$	—
Work	W	J

© 1983 Hemisphere Publishing Corporation

Transport coefficients

Quantity	Symbol	Unit
Heat transfer coefficient	α	$W/m^2 K$
Mass transfer coefficient	β	m/s
Overall heat transfer coefficient	U	$W/m^2 K$
Drag coefficient	ξ	—
Friction factor	f	—
Emissivity	ϵ	—
View factor	φ_{12}	—
Thermal conductivity	λ	W/m K
Diffusivity	δ	m^2/s
Kinematic viscosity	ν	m^2/s
Dynamic (absolute) viscosity	η	kg/m s
Thermal diffusivity	$\kappa \equiv \lambda/\rho c_p$	m^2/s
Surface tension	σ	N/m
Shear stress	τ	Pa (N/m^2)
Pressure	p	Pa (N/m^2)
Pressure drop	Δp	Pa (N/m^2)

Thermodynamic quantities

Quantity	Symbol*	Unit
Enthalpy (specific)	h	J/kg
Internal energy (specific)	u	J/kg
Gibbs function free enthalpy (specific)	$g = h - Ts$	J/kg
Free energy (specific)	$f = u - Ts$	J/kg
Entropy (specific)	s	J/kg K
Chemical potential	μ	J/kg
Specific heat capacity	c_p, c_v	J/kg K
Temperature	T	K, °C
Mean logarithmic temperature difference	ΔT_{LM}	K, °C

*For totals, letters are capitalized, H, U.

© 1983 Hemisphere Publishing Corporation

Chemical reactions

Quantity	Symbol	unit
Reaction enthalpy; phase-change enthalpy; latent heat	Δh	J/kg
Energy of activation	ΔE	J/kg
Equilibrium constant	K	Various
Rate constant	k	Various
Rate of reaction	$\dot{r}$	$mol/m^3 s$
Activity coefficient	γ_l	—
Fugacity coefficient	γ_g	—
Stoichiometric factors	ν_i	—

Physical constants

Quantity	Symbol	Unit
Gas constant	$\tilde{R}$	8.314 J/mol K
Loschmidt number	$\tilde{L}$	$6.0252 \cdot 10^{23}$
Avogadro number	$\tilde{L}$	1/mol
Stefan-Boltzmann constant	C_s	$5.6697 \cdot 10^{-8}$ $W/m^2 K^4$
Acceleration of gravity	g	m/s^2
Standard acceleration of gravity	$g_n = 9.8 \ldots$	m/s^2

Subscripts

Quantity	Symbol
Wall	w
Bulk	b
Mean	m
Solid	s
Liquid	ℓ
Gas	g
Inlet	in
Outlet	out

© 1983 Hemisphere Publishing Corporation

Dimensionless numbers (most frequently used)

Name	Symbol and definition
Archimedes number	$Ar = gl^3 \Delta\rho/\nu^2 \rho = gl^3 \rho\Delta\rho/\eta^2$
Biot number	$Bi = \alpha_g l/\lambda_s$ or $\alpha_l l/\lambda_s$
Effectiveness	E
Euler number	$Eu = \Delta p/(\rho u^2/2)$
Fourier number	$Fo = \kappa t/l^2 = \lambda t/\rho c_p l^2$
Froude number	$Fr = u^2/gl$
Galileo number	$Ga = l^3 g/\nu^2 = l^3 g\rho^2/\eta^2$
Grashof number	$Gr = gl^3 \Delta\rho/\nu^2 \rho = gl^3 \rho\Delta\rho/\eta^2$
Graetz number	$Gz = ud^2/\kappa l = ud^2 \rho c_p/\lambda l = Re\ Pr\ d/l$
Knudsen number	$Kn = l_0/l$, where l_0 is the molecular mean free path
Lewis number	$Le = \kappa/\delta = \lambda/\rho c_p \delta$
Mach number	$Ma = u/u_{sound}$
Number of transfer units	NTU
Nusselt number	$Nu = \alpha l/\lambda$
Péclet number	$Pe = ul/\kappa = ul\rho c_p/\lambda = Re\ Pr$
Phase change number	$Ph = c_p AT/Ah_{,,}$
Prandtl number	$Pr = \nu/\kappa = \eta c_p/\lambda$
Rayleigh number	$Ra = Gr\,Pr$
Reynolds number	$Re = ul/\nu = ul\rho/\eta = \dot{m}l/\eta$
Schmidt number	$SC = \nu/\delta = \eta/\rho\delta$
Sherwood number	$Sh = \beta l/\delta$
Stanton number	$St = \alpha/\rho u c_p = Nu/Re\ Pr$
Strouhal number	$Sr = fl/u$
Weber number	$We = u^2 \rho l/\sigma$

Dimensionless mass transfer numbers are distinguished from dimensionless heat transfer numbers by a prime (′), e.g., $Bi = \beta l/\delta$. Exceptions: $Nu = \beta l/\delta = Sh$ and $Pr' = \nu/\delta = \eta/\rho\delta = SC$

© 1983 Hemisphere Publishing Corporation

INTERNATIONAL SYSTEM OF UNITS (SI): RULES, PRACTICES, AND CONVERSION CHARTS

J. Taborek

■ HEDH is written in SI units because this system has been officially adopted by all countries and is replacing the older metric engineering system, the cgs system, as well as the U.S. customary system. In this section we shall review the basic rules for use of the SI. However, recognizing the fact that many references are written in other unit systems, comprehensive unit conversion charts are included.

A. Basic SI units

SI is absolute in the sense that there are only seven fundamental, precisely defined basic units from which all others are derived. The following five units are important to heat transfer and fluid flow.

length (meter, m): defined in terms of krypton-86 wavelength

mass (kilogram, kg): the mass of an international prototype, approximately equal to the weight of 1 liter H_2 0 at 4° C

time (second, s): defined in terms of radiation frequency of the cesium-133 atom

temperature (kelvin, K): defined in terms of the triple point of water (ice point = 273.15 K)

amount of substance (mole, mol): amount of substance that contains as many elementary entities as there are atoms in 0.012 kg of carbon-12. The elementary entities must be identified when the mole is used (atoms, molecules, ions).

B. Derived SI units with special names

Because SI is defined by the basic units only, there is a need for establishing definitions for the most frequently used composite or derived units, mainly for the purpose of simplifying unit notation. Thus, for example, newton, N, replaces kg m/s^2.

There are a number of derived units that have special names, signifying their importance: newton, joule, watt, pascal, and many others. While the unit symbols are capital letters (N, J, W, Pa), the spelled out unit names begin with lowercase letters, that is, newton, joule, watt, and pascal.

The most frequently used derived SI units with special names in the area of heat transfer and fluid flow are shown in Table 1.

Table 1 Most frequently used derived SI units

Quantity	Unit	Symbol	Dimension
Force	newton	N	kg m/s^2
Energy, work, heat (also power x time)	joule	J	N m or kg m^2/s^2 W s = J s/s
Power	watt	W	J/s = kg m^2/s^3
Pressure	pascal	Pa	N/m^2 = kg/m s^2
Frequency	hertz	Hz	1/s
Dynamic viscosity	poise	P	0.1 Pa s
	centipoise	cP	mPa s

© 1984 Hemisphere Publishing Corporation

C. Prefixes and specification rules

The magnitude of the basic units may often not fit the practice of specific applications without using a large number of decimal digits or power of ten multipliers. SI provides for this by assigning prefixes to the basic units, as shown in Table 2.

Thus, for example, to express very high pressures (stresses) in Pa, the megapascal, **MPa**, is used instead of 10^6 Pa. The preferred graduation is in powers of 10^3, and there are only a few exceptions to this rule, such as for units that are deeply ingrained in common use, such as centimeter. Some of these are discussed later.

(a) Punctuation and spelling rules

The following general rules should be carefully followed to maintain SI consistency.

1. **Prefixes** are attached directly to the base unit symbol or a derived unit symbol with a special name, such as km for kilometer or MW for megawatt.

2. Prefixed units are spelled out in text as one word, without hyphen, such as meganewton, not **mega**-newton.

3. The multiplication of base units can be expressed by leaving a space between the symbols, such as N s for newton X second. However, for better clarity, a center dot is often used, for example, **N·s.** This usage becomes especially important when the symbol m is used, which can stand for **milli** or for meter. Thus **mN** (millinewton) is clearly distinguished from **m·N** (meter X newton).

4. A prefix applied to a base unit constitutes a new unit. When a power is applied to such a unit, the exponent operates on the prefixed unit as an entity, i.e., $mm^2 = (mm)^2$.

5. The unit of length in SI is correctly spelled metre (French spelling). This rule will be hard to enforce in U.S. literature, however, and meter will probably be more commonly used.

Table 2 SI prefixes

Factor	Prefix	Symbol	Status
10^{12}	tera	T	Preferred
10^9	giga	G	Preferred
10^6	mega	M	Preferred
10^3	kilo	k	Preferred
10^2	hecto	h	Accepted
10^1	deka	da	Accepted
10^{-1}	deci	d	Accepted
10^{-2}	centi	c	Accepted
10^{-3}	milli	m	Preferred
10^{-6}	micro	μ	Preferred
10^{-9}	nano	n	Preferred
10^{-12}	pico	p	Preferred

6. Multiple **prefixes** are prohibited. This presents some problems with the unit kilogram (kg), where the k stands for the **prefix** kilo and is one of the very few inconsistencies in **SI** (a carryover from the older cgs system). Thus k (for kilo) cannot be used in connection with kg, as this would result in the unacceptable term kkg. Equally incorrect is the use of Mg (megagram), as gram is not a basic SI unit. Thus, the unit used is 10^3 kg or the equivalent unit, metric ton (see below).

Similarly, mkg is not an acceptable way to express 10^{-3} kg, and the more common alternate unit of gram (g) is used.

D. Alternate units and supplementary comments

There are as many derived units as the technology demands, as SI is particularly suitable for this purpose by the clearly defined unit relations. The Nomenclature of this handbook contains practically all such units used in heat transfer and fluid flow, showing the appropriate **SI** dimensions. Consequently, these are not repeated here.

In some cases, strict SI rules are relaxed to respect generally accepted and deeply established practices. The following list presents most frequently used exceptions, together with some additional comments to alternate units, their definition, and their usage.

length: The unit centimeter (cm) is a very practical measure for everyday usage (person s height, 6 ft≃ 183 cm), and will probably remain in perpetual use.

mass: The unit of kilogram is often too small for expressing quantities of mass experienced in many engineering applications. One of the few weaknesses of SI is the lack of a well-defined alternate unit of mass. As explained above, the prefixed units (kkg, Mg) are not acceptable. Instead, an alternate unit for large quantities of mass is introduced, designated metric ton (symbol t), t = 1000 kg. While this unit has not yet been accepted as a recognized SI unit, it is very much in common use.

In the U.S. customary lb,-based system, several definitions of a unit of mass similar in magnitude to the metric ton exist. In engineering practice, the following two definitions of the lb,-based ton are most frequently used:

short ton, which is equal to 2 000 lb, (exact) and therefore approximately = 907.2 kg

long ton, which is equal to 2 240 lb,,, (exact), and therefore approximately = 1 016 kg

It is important to be aware of these differences in the inconsistently defined U.S. customary system.

For small quantities of mass, gram (g) is also often used in place of 10^{-3} kg.

©1984 Hemisphere Publishing Corporation

time: The unit second (s) should be used whenever possible, as the alternates of minutes, hours, and days are nondecimal entities, and thus complicate the system.

However, to express large quantities of mass per unit of time, the unit hour (h), 3 600 seconds, or the unit day (d), 86 400 seconds, must be used sometimes. The time unit minute (min), often used in the U.S. customary system (gal/min), has no real justification, except that it is ingrained in some industrial practices. Otherwise, the differential quantity of a minute, as compared to a second, can be readily expressed by prefixes in SI units, to obtain a number with reasonable digits.

force: The newton is a very small unit of force, approximately equal to the weight of water in a small glass. Thus the more practical units of force are often the kN or MN.

volume: The liter, defined as dm^3, is a very popular unit of volume for everyday use, such as for water and gasoline. Liter (L) is accepted as a common alternate unit.

amount of substance: The frequently used units of the metric engineering system, gram-mol and kg-mol, are designated in SI as follows: 1 gram-mol = 1 mol (SI), and 1 kg-mol = 1 kmol (SI). Thus 1 mol = 6.023 X 10^{23} molecules.

pressure: The basic unit of pressure, pascal (Pa = N/m^2), is a very small quantity, equal to the pressure exerted by about O.l-mm layer of water over 1 m^2 Thus in most engineering applications kPa or MPa is more useful.

Many derived units of pressure are firmly established in various branches of engineering and will probably remain in use indefinitely. The most important metric-based units are:

bar: has exact relationship to SI (=100 kPa)

torr = 1 mmHg = 0.133 kPa: used for gas pressure measurements

mm water = 9.8067 Pa: used for very small gas pressure measurements

at (technical atmosphere) = kg_f/cm^3 = 98.066 kPa

atm (normal or barometric atmosphere) = 760 mmHg = 101.3 kPa

temperature: In many engineering applications it is more convenient to use degrees Celsius rather than the absolute unit kelvin. The use of Celsius is permitted as an alternate, with the relationship

$T(°C) = T(K) - 273.16$ and $\Delta T(°C) = \Delta T(°K)$

Table 3 Unit conversion

Physical quantity	Given in → / Gives ←	Multiplied by → / Divided by ←	Gives → / Given in	Approximate or useful relationship
Length	ft	0.3048	m	$3\frac{1}{4}$ ft ≃ 1 m
	in	25.4 (exact)	mm	1 inr 25 mm
	mil	0.0254	mm	
	yard	0.9144	m	
	mile (mi)	1609.3	m	1 mi ≃ 1.6 km
	km	0.621388	mi	
Area	ft^2	0.092903	m^2	100 ft^2 ≃ 9 m^2
	in^2	645.16	mm^2	1 in* ≃ 650 mm^2
	acre	4 047.0	m^2	
Volume	ft^3	0.028317	m^3	35 ft ≃ 1 m^3
	U.S. gal	0.003785	m^3	260 gal ≃ 1 m^3
	U.S. gal	3.785	liter (L)	1 gal ≃ $3\frac{3}{4}$ L
	L (liter)	0.2642	U.S. gal	1 L ≃ 0.26 gal
	Brit. gal	0.004546	m^3	
	U.S. gal	0.13368	ft^3	
	barrel (U.S. pet.)	0.15898	m^3	
	barrel (U.S. pet.)	42	U.S. gal	
Velocity	ft/s[a]	0.3048	m/s	10 ft/s ≃ 3 m/s
	m/s	3.2808	ft/s	
	ft/min	0.00508	m/s	100 ft/min ≃ 0.5 m/s
	mi/h	1.6093	km/h	30 mi/h ≃ 48 km/h
	km/h	0.6214	mi/h	50 km/h ≃ 31 mi/h
	knots	1.852	km/h	

(See *footnotes on page xxix.*)

©1984 Hemisphere Publishing Corporation

Table 3 Unit conversion (*Continued*)

Physical quantity	Given in → / Gives ←	Multiplied by → / Divided by ←	Gives → / Given in	Approximate or useful relationship
Mass	**lb_m**	0.45359	**kg**	1 lb, r.45 kg
	kg	2.2046	**lb_m**	1 kg- 2.2 lb,
	metric ton	2 204.6	**lb_m**	metric ton = **10^3** kg
	ton (2 000 lb,)	907.18	**kg**	
Force	**lb_f**	4.44822	N = kg **m/s^2**	
	lb_f	0.45359	**kg_f**	**1 N ≈ 0.1 kg_f**
	kg_f	2.2046	**lb_f**	**≈** 0.22 **lb_f**
	kg_f	9.80665	N	
	dyne	0.00001 (exact)	N	
Amount of substance	**lb_m-mol**	453.6	kmol	
	g-mol	1.000	mol	
	kg-mol	1.000	kmol	
	mol	1 000	**kmol**	
Mass flow rate	**lb_m/h**	0.0001260	**kg/s**	**10^3 lb/h ≃ .13** kg/s
	kg/s	7 936.51	**lb_m/h**	
	lb_m/s	0.4536	**kg/s**	
	lb_m/min	0.00756	**kg/s**	
Volume flow rate	U.S. **gal/min**	6.309 x **10^{-5}**	**m^3/s**	
	U.S. **bbl/day**	0.15899	**m^3** /day	
	U.S. **bbl/day**	1.84 x **10^{-6}**	**m^3/s**	
	ft^3/s	0.02832	**m^3/s**	
	ft^3/min	0.000472	**m^3/s**	
Mass velocity (mass flux)	**$lb_m/h\ ft^2$**	1.356 x IO-	kg/s **m^2**	
	kg/s **m^2**	737.5	**$lb_m/h\ ft^2$**	
Energy (work) (heat)	**Btu**[b]	1 055.056	J = N m = W s	**1 Btu ≃ 1 000 J**
	Btu	0.2520	**kcal**	1 **kcal** ≃ 4 Btu
	Btu	778.28	ft **lb_f**	
	kcal	4 186.8	J	1 **kcal ≃ 4** 000 J
	ft **lb_f**	1.3558	J	
	W h	3 600	J	
Power	**Btu/h**	0.2931	W = J/s	**10^6 Btu/h ≃** 300 **kW**
	W	3.4118	**Btu/h**	
	kcal/h	1.163	W	
	ft **lb_f/s**	1.3558	W	1 000 **kW ≃** 3.5 x **10^6**
	hp (metric)	735.5	W	**Btu/h**
	Btu/h	0.2520	**kcal/h**	
	tons refrig.	3 5 16.9	W	
Heat flux	**$Btu/h\ ft^2$**	3.1546	**W/m^2**	1 000 **$Btu/h\ ft^2 ≃$** 3.2
	W/m^2	0.317	**Btu/h** ft	**kW/m^2**
	$kcal/cm^2$ s	41.868	W/m*	
Heat transfer coefficient	**$Btu/h\ ft^2\ °F$**	5.6784	W/m* K	1 000 **$Btu/h\ ft^2\ °F ≃$**
	W/m^2 K	0.1761	**$Btu/h\ ft^2\ °F$**	5 600 **W/m^2** K
	$kcal/cm^2$ s °C	41.868	**W/m^2** K	
Heat transfer resistance	**$(Btu/h\ ft^2\ °F)^{-1}$**	0.1761	$(W/m^*\ K)^{-1}$	0.001 **$(Btu/h\ ft^2\ °F)^{-1} ≃$**
	$(W/m^2\ K)^{-1}$	5.6784	**$(Btu/h\ ft^2\ °F)^{-1}$**	0.000 18 **$(W/m^2\ K)^{-1}$**
Pressure	**lb_f/in^2** (psi)	6.8948	**kN/m^2 = kPa**	1 psi ≃ 7 kPa
	kPa	0.1450	psi	14.5 psi ≃ 100 **kPa**
	bar	100	**kPa**	

(See footnotes on page xxix.)

© 1984 Hemisphere Publishing Corporation

Table 3 Unit conversion *(Continued)*

Physical quantity	Given in → / Gives ←	Multiplied by → / Divided by ←	Gives → / Given in ←	Approximate or useful relationship
Pressure *(Continued)*	lb_f/ft^2	0.0479	kPa	
	mm Hg (torr)	0.1333	kPa	1 000 kPa = 1 MPa ≃
	in Hg	3.3866	kPa	150 psi
	mm H_2O	9.8067	Pa	
	in H_2O	249.09	Pa	1 in H_2O ≃ .25 kPa
	at (kg_f/cm^2)	98.0665	kPa	
	atm (normal)	101.325	kPa	atm = 760 mmHg
Mass flux	lb_m/ft^2 s	4.8824	kg/m^2 s	
	lb_m/ft^2 h	0.001356	kg/m^2 s	
	Physical and Transport Properties			
Thermal conductivity	Btu/ft h °F	1.7308	W/m K	steel ≃ 50 W/m K
	W/m K	0.5778	Btu/ft h °F	water (20° C)≈ 0.6 W/m K
	kcal/m h °C	1.163	W/m K	air (STP) ≃ 24 mW/m K
Density	lb_m/ft^3	16.0185	kg/m^3	
	kg/m^3	0.06243	lb_m/ft^3	62.4 lb_m/ft^3 ≃ 1 000
	lb_m/U.S. gal	119.7	kg/m^3	kg/m^3
Specific heat capacity	B tu/lb_m °F	4 186.8	J/kg K	1 Btu/lb_m °F ≃ 4.2
	kcal/kg °C	4 186.8	J/kg K	kJ/kg K
Enthalpy	Btu/lb_m	2 326	J/kg	
	kcal/kg_m	4 186.8	J/kg	
Dynamic (absolute) viscosity	centipoise (cP)	0.001	kg/m s	kg/m s = N s/m^2 = Pa s
	poise (P)	0.1	Pa s	
	cP	1.000	mPa s	
	cP	1 000	μPa s	water (100°C), 0.31 cP
	lb_m/ft h	0.0004 134	Pa s	
	lb_m/ft h	0.4134	cP	
	cP	2.4189	lb_m/ft h	air (100°C), 0.021 cP
	lb_m/ft s	1.4482	Pa s	
Kinematic viscosity	stoke (St), cm^2s	0.0001	m^2/s	
	centistoke (cSt)	10^{-6}	m^2/s	
	ft^2/s	0.092903	m^2/s	
Diffusivity	ft^2/s	0.092903	m^2/s	
Thermal diffusivity	m^2/h	0.0002778	m^2/s	
	ft^2/s	0.092903	m^2/s	
	ft^2/h	25.81 x 10^{-6}	m^2/s	
Surface tension	dyne/cm	0.001	N/m	
	dyne/cm	6.852 x 10^{-5}	lb_f/ft	
	lb_f/ft	14.954	N/m	

Temperature relations: $°C = \frac{5}{9}[°F - 32]$ $°C = (°F + 40)\frac{5}{9} - 40$ $\Delta T(°C) = \frac{9}{5}\Delta T(°F)$ $K = °C + 273.15$

$°F = \frac{9}{5}(°C) + 32$ $°F = (°C + 40)\frac{9}{5} - 40$ $\Delta T(°F) = \frac{5}{9}\Delta T(°C)$ $R = °F + 459.67$

Miscellaneous:

Acceleration of gravity (standard):	g = 9.806 65	m/s^2
Gas constant:	R = 8 314.3	m N/K kmol
Stefan-Boltzmann constant:	5.669 7 x 10^{-8}	$W/m^2 K^4$
	1.714 x 10^{-9}	Btu/ft^2 h R^4

[b] Even though the abbreviations s and h were introduced only with the SI, they are used here throughout for consistency.

Note: the calorie and Btu are based on the International Standard Table values. The thermochemical calorie equals 4.184 J (exact) and is used in some older texts.

© 1984 Hemisphere Publishing Corporation

LENGTH: meter, m; foot, ft

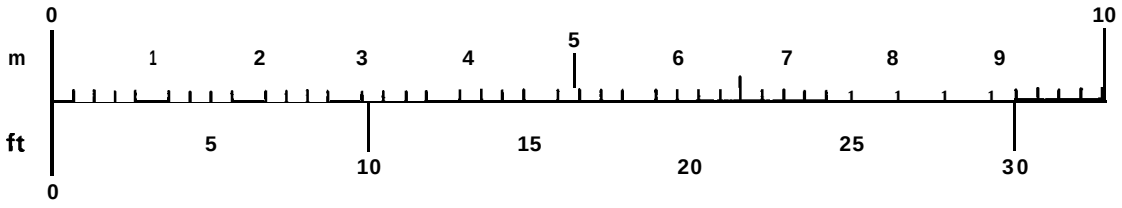

m X 3.2803 = ft
ft X 0.3048 = m

AREA: square meter, m^2; square foot, ft^2

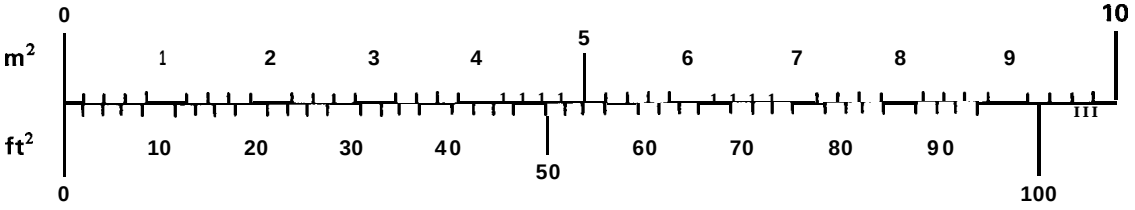

m^2 X 10.764 = ft^2
ft^2 X 0.0929 = m^2

VOLUME: cubic meter, m^3; cubic foot, ft^3

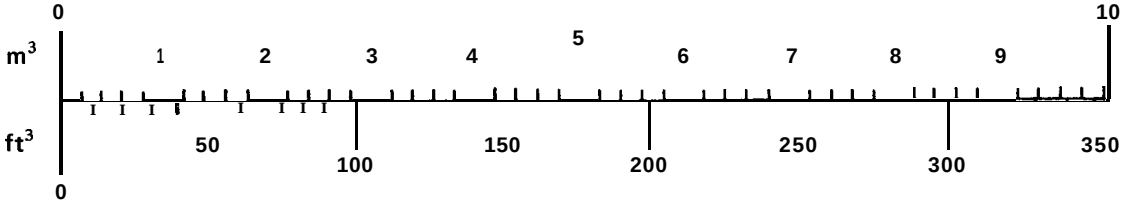

m^3 X 35.314 = ft^3
ft^3 X 0.083 = m^3

MASS: kilogram, kg; pound-mass, $lb_{,,,}$

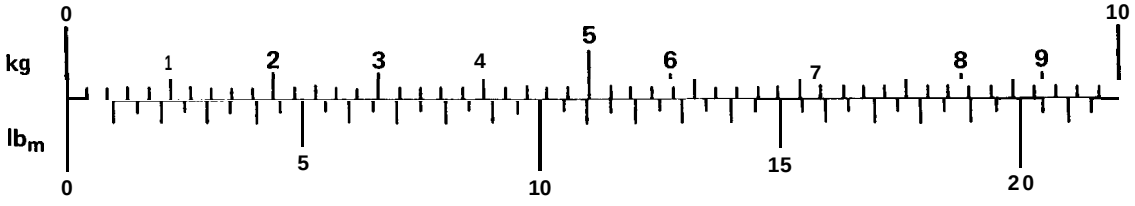

kg X 2.205 = $lb_{,,,}$
$lb_{,,,}$ X 0.454 = kg

© 1984 Hemisphere Publishing Corporation

VOLUME FLOW RATE: $\frac{m^3}{s}$; $\frac{gal(U.S.)}{min}$

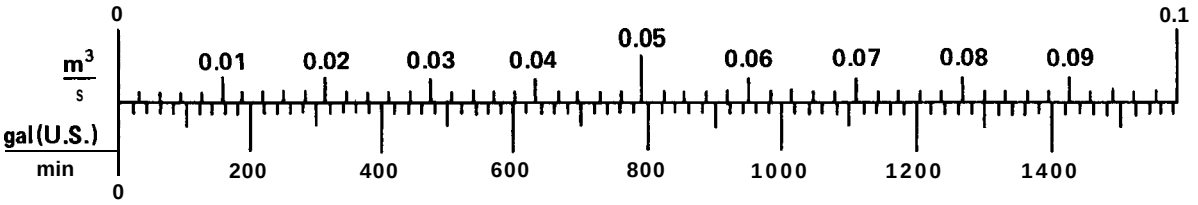

$$\frac{m^3}{s} \times 1.585(10^4) = \frac{gal(U.S.)}{min}$$

$$\frac{gal(U.S.)}{min} \times 6.31(10^{-5}) = \frac{m^3}{s}$$

VELOCITY: $\frac{m}{s}$; $\frac{ft}{s}$

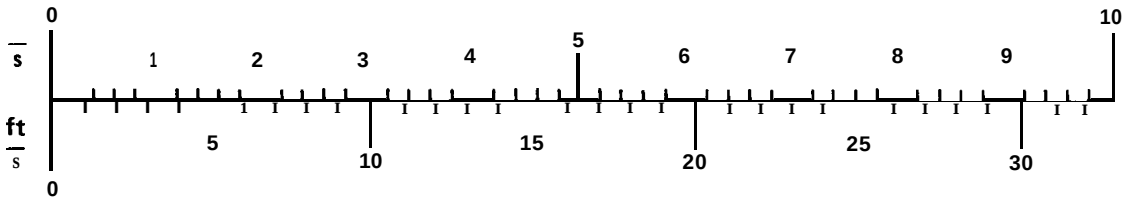

$$\frac{m}{s} \times 3.28 = \frac{ft}{s}$$

$$\frac{ft}{s} \times 0.305 = \frac{m}{s}$$

MASS VELOCITY: $\frac{kg}{s\,m^2}$; $\frac{10^3\ lb_m}{h\,ft^2}$

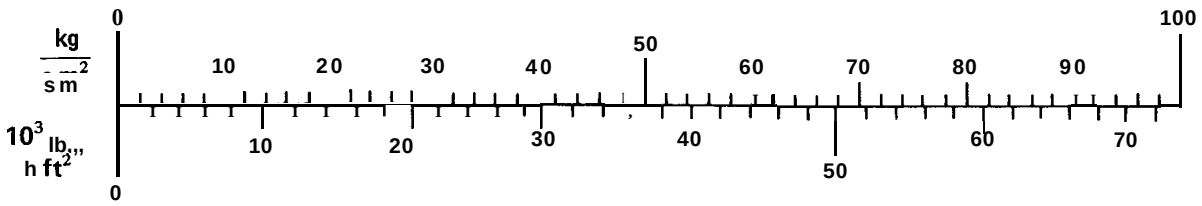

$$\frac{kg}{s\,m^2} \times 0.737 = \frac{10^3\ lb_m}{h\,ft^2}$$

$$\frac{10^3\ lb_m}{h\,ft^2} \times 1.356 = \frac{kg}{s\,m^2}$$

© 1984 Hemisphere Publishing Corporation

MASS FLOW RATE: $\frac{kg}{s}$; $\frac{10^3\ lb_m}{h}$

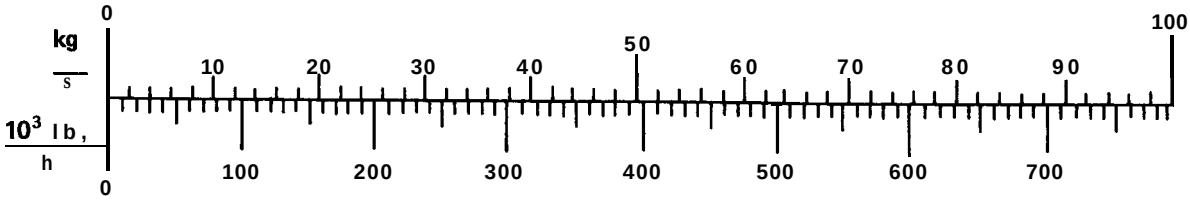

$$\frac{kg}{s} \times 7.937 = \frac{10^3\ lb_m}{h}$$

$$\frac{10^3\ lb_m}{h} \times 0.126 = \frac{kg}{s}$$

FORCE: newton, N = $\frac{kg\ m}{s^2}$; pound-force, lb_f

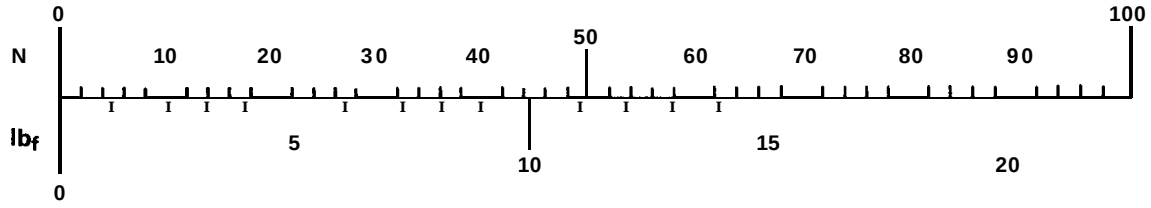

N X 0.225 = lb_f

lb_f X 4.448 = N

ENERGY (WORK): joule, J = N m; Btu

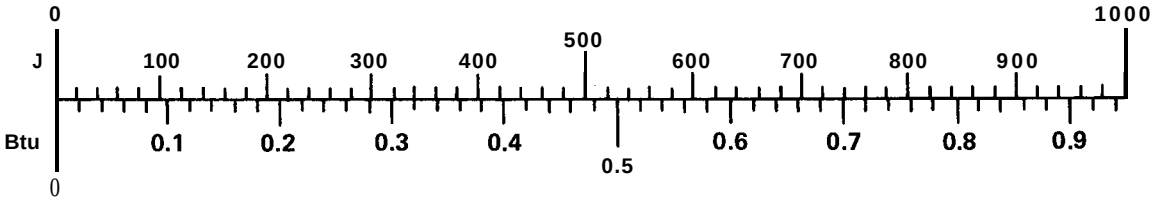

J X $0.948(10^{-3})$ = Btu

Btu X 1055 = J

POWER OR ENERGY FLOW RATE: kilowatt, kW = $\frac{kJ}{s}$ · $\frac{10^6\ Btu}{h}$

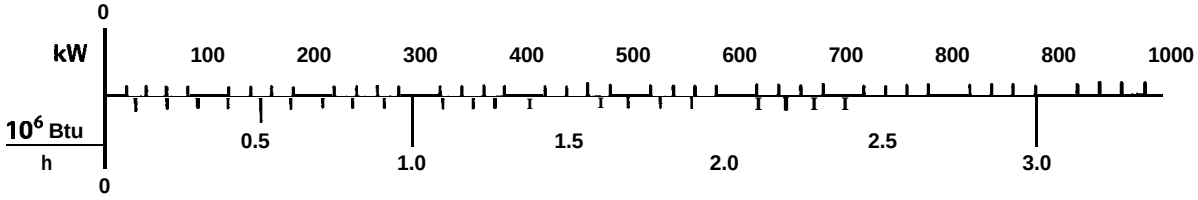

$$kW \times 3.412(10^{-3}) = \frac{10^6\ Btu}{h}$$

$$\frac{10^6\ Btu}{h} \times 293 = kW$$

© 1984 Hemisphere Publishing Corporation

HEAT TRANSFER COEFFICIENT: $\frac{W}{m^2 K}$; $\frac{Btu}{h\ ft^2\ °F}$

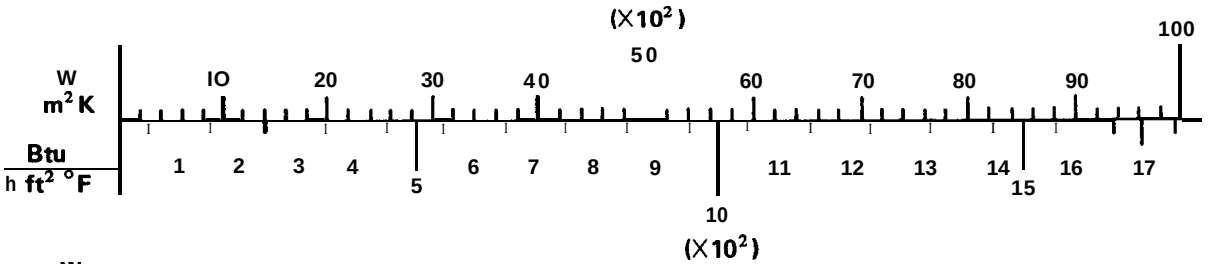

$\frac{W}{m^2 K} \times 0.176 = \frac{Btu}{h\ ft^2\ °F}$

$\frac{Btu}{h\ ft^2\ °F} \times 5.68 = \frac{W}{m^2 K}$

HEAT FLUX: $\frac{W}{m^2}$; $\frac{Btu}{h\ ft^2}$

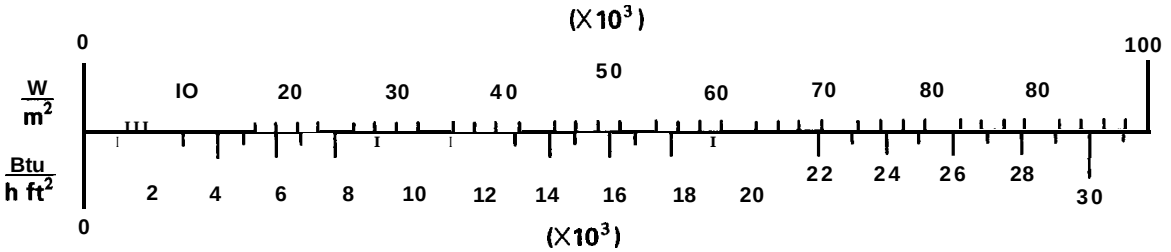

$\frac{W}{m^2} \times 0.316 = \frac{Btu}{h\ ft^2}$

$\frac{Btu}{h\ ft^2} \times 3.16 = \frac{W}{m^2}$

DENSITY: $\frac{kg}{m^3}$; $\frac{lb_m}{ft^3}$

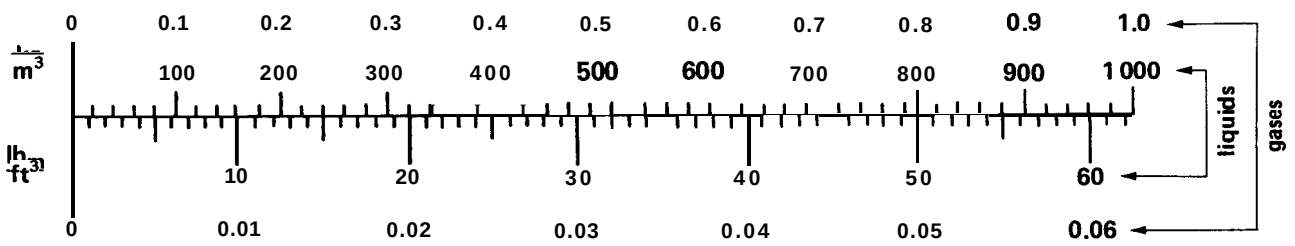

$\frac{kg}{m^3} \times 0.0624 = \frac{lb_m}{ft^3}$

$\frac{lb_m}{ft^3} \times 16.02 = \frac{kg}{m^3}$

© 1984 Hemisphere Publishing Corporation

SPECIFIC HEAT CAPACITY: $\frac{kJ}{kg\,K}$; $\frac{Btu}{lb_m\,°F}$

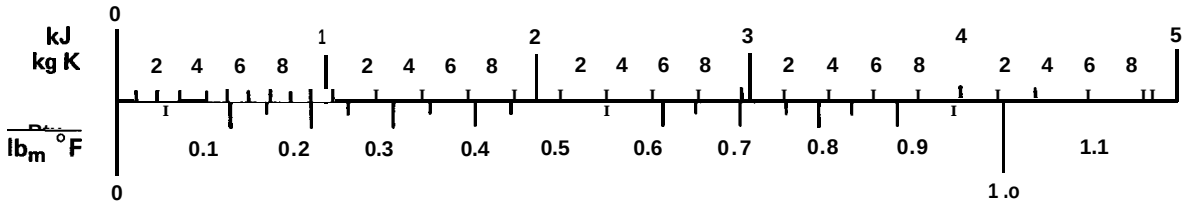

$$\frac{kJ}{kg\,K} \times 0.239 = \frac{Btu}{lb_m\,°F}$$

$$\frac{Btu}{lb_m\,°F} \times 4.187 = \frac{kJ}{kg\,K}$$

THERMAL CONDUCTIVITY: $\frac{W}{m\,K}$; $\frac{Btu}{h\,ft\,°F}$

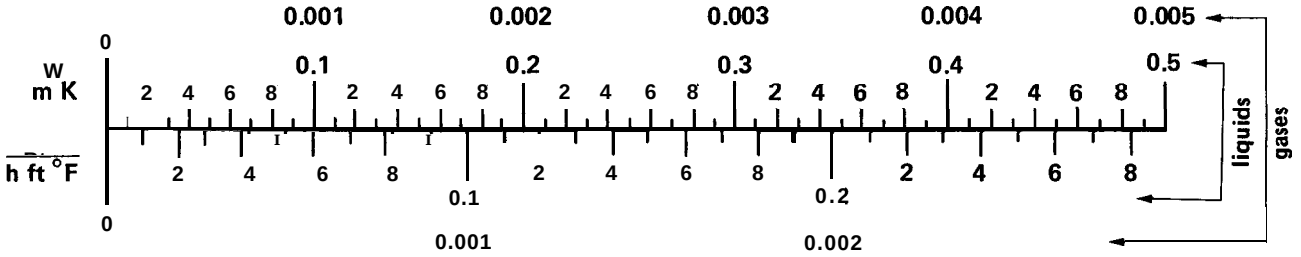

$$\frac{W}{m\,K} \times 0.578 = \frac{Btu}{h\,ft\,°F}$$

$$\frac{Btu}{h\,ft\,°F} \times 1.731 = \frac{W}{m\,K}$$

DYNAMIC (ABSOLUTE) VISCOSITY: $\frac{N\,s}{m^2}$; $\frac{lb_m}{h\,ft}$

centipoise $cP = 10^{-3}\frac{N\,s}{m^2} = mPa\,s$

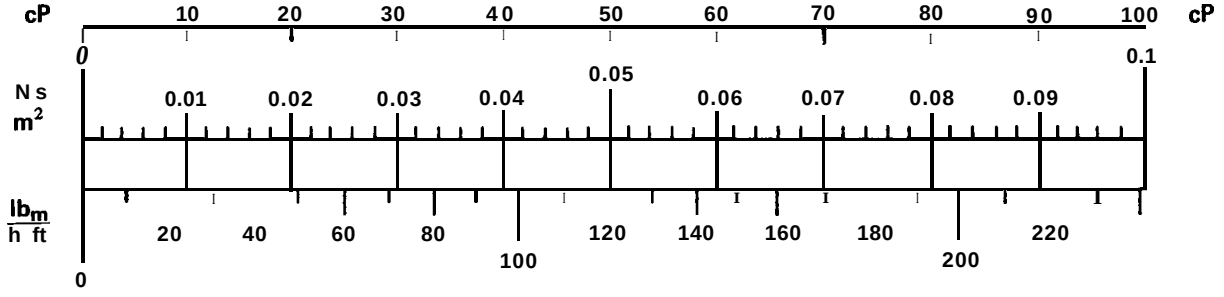

$$cP \times 2.42 = \frac{lb_m}{h\,ft}$$

$$\frac{lb_m}{hff} \times 0.413 = cP$$

© 1984 Hemisphere Publishing Corporation

ENTHALPY: $\frac{kJ}{kg}$, Btu/lb$_m$

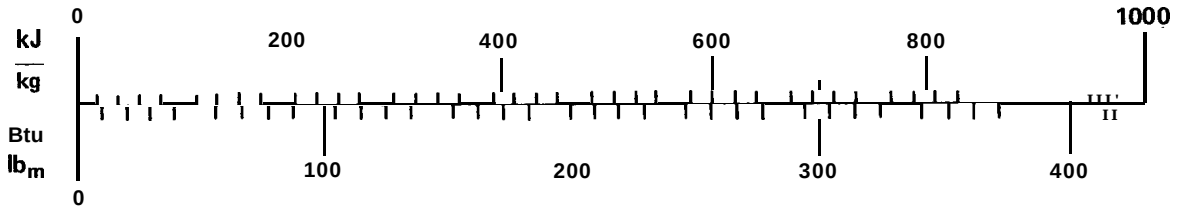

$$\frac{kJ}{kg} \times 0.430 = \frac{Btu}{lb_m}$$

$$\frac{Btu}{lb_m} \times 2.326 = \frac{kJ}{kg}$$

PRESSURE CONVERSION CHART
(top line = 1 Pa on all charts)

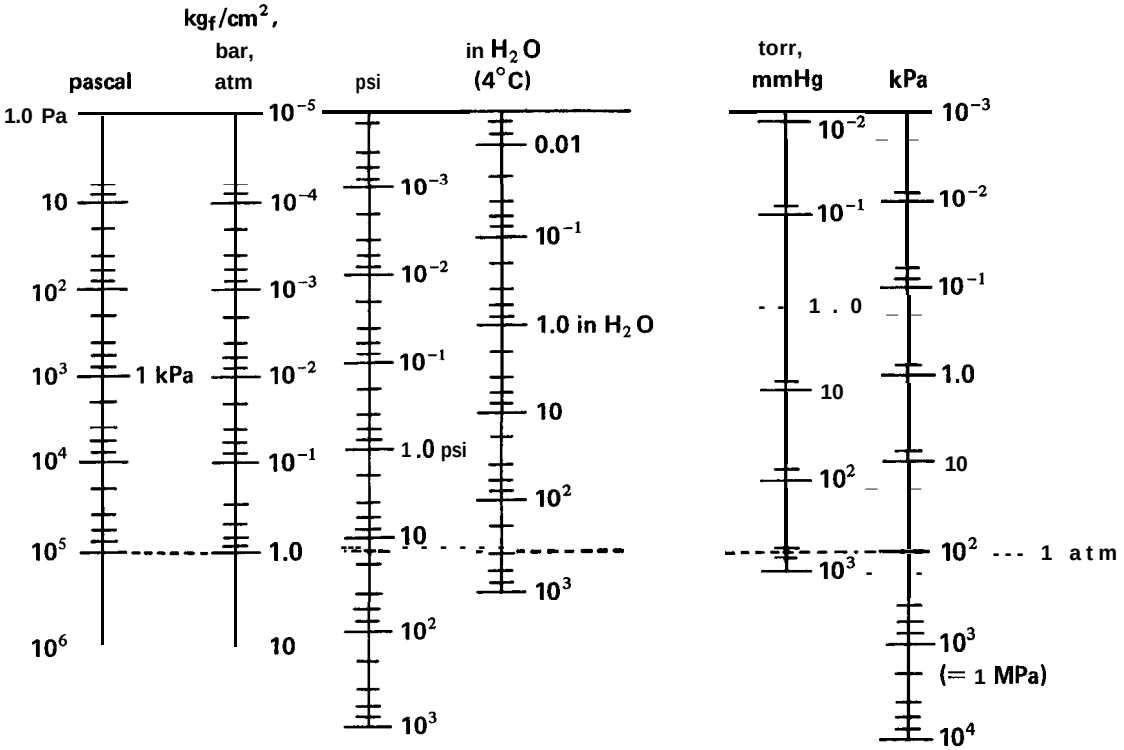

*NOTE: only bar is exact (1 bar = 10^5 Pa); however, atm and kg$_f$/cm^2 are within 2% accuracy (see list below).

1 atm = 1.01325 X 10^5 Pa
1 psi = 6.89476 X 10^3 Pa
1 in H_2O = 2.49082 X 10^2 Pa
1 kg$_f$/cm^2 = 9.80665 X 10^4 Pa
1 bar= 10^5 Pa
1 mmHg = 1.33322 X 10^2 Pa

1 Pa = 9.86923 X IO atm
1 Pa = 1.45038 X 10^{-4} psi
1 Pa = 4.01474 X 10^{-3} in H_2O
1 Pa = 1.01972 X 10^{-5} kg$_f$/cm^2
1 Pa = 10^{-5} bar
1 Pa = 7.50064 X 10^{-3} mmHg

© 1984 Hemisphere Publishing Corporation

TEMPERATURE COMPARISON
(NOT TO SCALE)

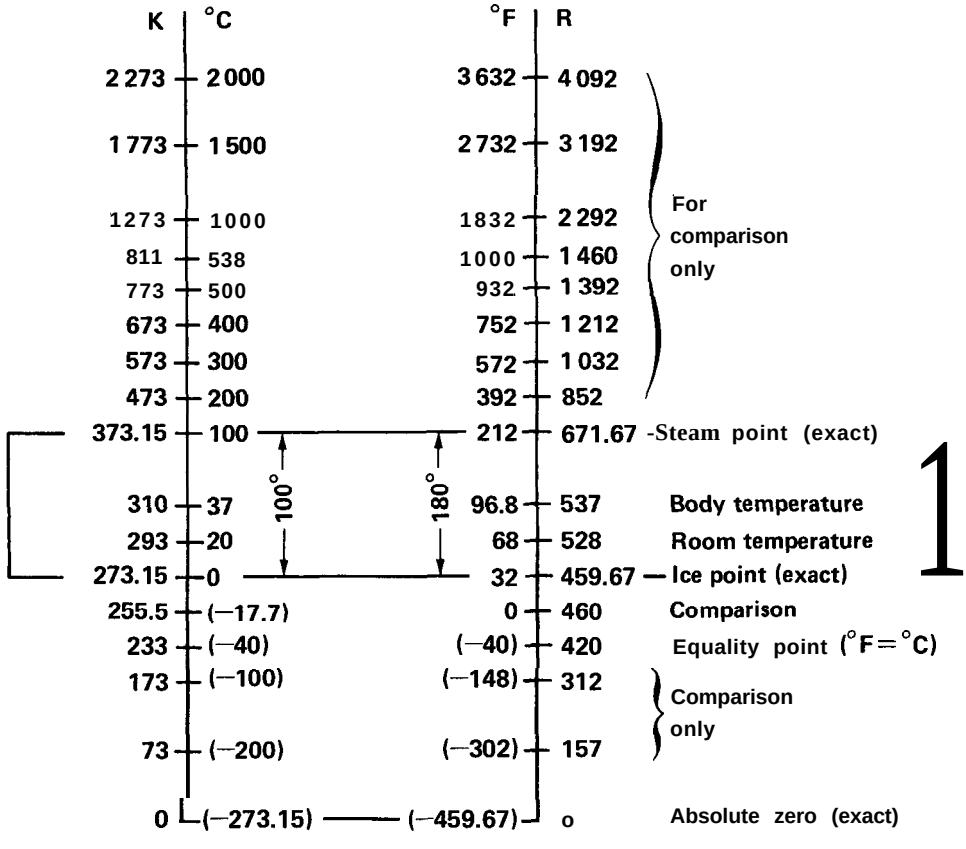

$T(°F) = (°C + 40)\frac{9}{5} - 40$ T(R) = $T(°F)$ + 460

$T(°C) = (°F + 40)\frac{5}{9} - 40$ T(K) = $T(°C)$ + 273.15

$AT: °C = \frac{5}{9}(°F)$ $°F = \frac{9}{5}(°C)$

© 1984 Hemisphere Publishing Corporation

2.1
Fundamentals of heat and mass transfer

Contents

2.1.0
INTRODUCTION, E. U. Schliinder 2.1.0-l

2.1.1
PHYSICAL MECHANISMS OF TRANSPORT PHENOMENA,
E. U. Schliinder 2.1.1-1

A. Limitation of phenomenological laws by discontinuity effects **2.1.1-1**
B. Limitation of phenomenological laws by turbulence **2.1.1-3**

2.1.2
INDUSTRIAL APPLICATIONS OF HEAT AND MASS TRANSFER,
E. U. Schliinder 2.1.2-l

A. The $\bar{U}$ method **2.1.2-1**
B. The $\bar{U}$-$\bar{\alpha}$ method **2.1.2-5**
C. The U-α method **2.1.2-7**
D. Summary **2.1.2-9**

2.1.3
PRESENTATION OF HEAT AND MASS TRANSFER DATA,
E. U. Schliinder 2.1.3-l

2.1.4
HEAT AND MASS TRANSFER IN UNIFORM AND NONUNIFORM SYSTEMS, E. U. Schliinder 2.1.4-l

2.15
ANALOGY BETWEEN HEAT AND MASS TRANSFER AND ITS LIMITATIONS, E. U. Schliinder 2.1.5-l

2.1.6
COMBINED HEAT AND MASS TRANSFER, E. U. Schliinder 2.1.6-l

A. Drying **2.1.6-1**
B. Condensation of mixtures **2.1.6-2**

2.1.7
STATE OF THE ART OF HEAT AND MASS TRANSFER, E. U. Schliinder 2.1.7-l

A. Heat and mass transfer to solids and fluids in prototype channel flow and flow past immersed bodies, forced and free convection **2.1.7-1**
B. Heat and mass transfer in packed, agitated, and fluidized beds **2.1.7-2**
C. Condensation **2.1.7-4**
D. Evaporation and boiling **2.1.7-6**

References for Sections 2. I .O-2.1.7 **2.1.7-8**

© 1983 Hemisphere Publishing Corporation

HEDH

2.1.0
Introduction

E. U. Schlünder

■ The procedures of thermal and hydraulic design of heat exchangers are based on the laws of thermodynamics and the laws of transport phenomena. The laws of thermodynamics tell us the conditions under which a system is in equilibrium, thus establishing the limits to which extent energy or mass can ultimately be exchanged in any type of heat exchanger. These laws, however, cannot tell us how fast the system moves to the state of equilibrium, and therefore they cannot tell us the time that a medium must stay within a heat exchanger in order to approach the state of equilibrium. The size of a heat exchanger is directly proportional to the required residence time of the respective medium, and therefore prediction of the required residence time is one of the main objectives in heat exchanger design. To accomplish those predictions we need additional information, which is supplied by the equations of energy, mass, and momentum transfer. These equations of transport phenomena connect the fluxes of energy, mass, and momentum with the deviation from the state of equilibrium by the introduction of appropriate phenomenological flux equations.

The laws of thermodynamics apply a priori and are well established. They will be referred to as far as necessary in this part of the book, but they will not be derived or explained. The equations of transport phenomena apply a posteriori and are less established. In some cases they are hypothetical and, to a certain degree, unproved and therefore the subject of current research. These relationships, however, are necessary, and often they provide the missing links in the design procedures.

The importance of these equations in the field of engineering was pointed out by Wilhelm Nusselt as early as 1923 [1] . Nusselt was a mechanical engineer, and most of his publications were devoted to the solution of problems in this field. Since 1923 the field of chemical engineering has evolved, raising an awareness of a vast number of new heat transfer problems. Some examples are heat transfer with and without phase change, heat and mass transfer in separation processes, heat transfer in tubular reactors for catalytic reactions, heat and mass transfer in porous media and in drying, and so on.

Heat transfer is also important to those working in nonengineering fields. Examples of some of these areas include geology, meteorology, astrophysics, medicine, and biology. The same statement may be made about mass transfer and momentum transfer.

The objective of Part 2 of this handbook is to supply engineers and scientists with the basic laws for the prediction of energy, mass, and momentum transfer rates. These may then be used together with the laws of thermodynamics for the design and rating of heat exchangers. In the terminology used in this book, heat exchangers include all types of equipment in which the transfer of heat is important or even the rate-controlling process. As a result, equipment such as dryers, tubular reactors, and so on, are discussed in detail.

Besides the laws of heat and mass transfer, the laws of momentum transfer are an essential tool needed in heat exchanger design. The contents of Part 2 are organized so that the following section deals with the laws of momentum transfer in fluid flow. Successive sections then cover the laws of heat transfer by conduction, convection, multiphase heat transfer, combined

© 1983 Hemisphere Publishing Corporation

heat and mass transfer, and heat transfer by radiation. As a result of this structure some overlapping is unavoidable, particularly where combined heat and mass transfer occurs, such as in the condensation of mixtures. In these cases reference to related sections will be given. This arrangement follows the classical approach adopted in other textbooks, as well as handbooks on heat and mass transfer in heat exchanger design.

A general remark on the various modes of heat transfer, such as convection and radiation, might be appropriate. Wilhelm Nusselt pointed out in 1915 [2]:

> In the literature one finds very often the statement that the heat transfer from a solid body to the surrounding follows in general three different mechanisms: radiation, heat conduction and convection. It is said that, either by buoyancy forces or by forced air flow, permanently cold eddies of the air contact the surface of the heated body and heat is removed from the surface. By the distinction between heat transfer through conduction and convection it is suggested that these are two independent mechanisms. Consequently, one might conclude that heat could be transferred by convection only without the help of thermal conduction. However, this is not true. The truth is, that the basic equation of Fourier $dQ = -\lambda(\partial T/\partial n)\, dA\, dt$ applies to both heat conduction and convection. If the thermal conductivity, λ, of the ambient medium is zero, there would be no heat transfer, neither through conduction nor through forced convection. If, however, the thermal conductivity of the ambient medium is not zero, then all the heat, except that transferred by radiation, will be transferred through conduction. However, the amount of heat transferred may be increased by the fact that the surrounding medium has a certain flow velocity and this velocity affects the $\partial T/\partial n$ at the surface of the body.

There is no doubt that Nusselt was completely right and that only two mechanisms of heat transfer can be distinguished physically: heat transfer by conduction, and heat transfer by radiation. In the first case the carrier of the heat energy is the matter; in the latter case the heat energy is carried by electromagnetic waves. Nevertheless, the terms conduction, convection, and radiation are so commonly used that all three will be also referred to in this handbook. We shall rely on the reader to recognize the correct physical meaning of these terms.

References for Section 2.1.0 appear at the end of Section 2.1.7.

© 1983 Hemisphere Publishing Corporation

2.1.1

Physical mechanisms of transport phenomena

E. U. Schlünder

■ A few introductory remarks on the physical mechanisms of the transport of energy, mass, and momentum will be made. These may assist the reader in obtaining a clearer understanding of the concepts of conduction, diffusion, convection, and radiation.

In stagnant media the transport phenomenon can be described as a macroscopic effect that is the statistically smoothed result of a large number of microscopic events that certain elements of the matter permanently undergo. Those elements may be molecules, ions, atoms, electrons, phonons, or photons. The events are usually collisions between those elements resulting from their permanent random motions maintained by the principle of microscopic reversibility. The phenomenological laws of heat, mass, and momentum transfer have been established by Fourier (conduction), Fick (diffusion), and Newton (shear), and are applicable as long as two conditions are fulfilled:

1. The number of collisions between the elements themselves in a given volume must be large compared to the number of collisions between the elements and the confining walls of the volume.
2. The medium inside a given volume must be either stagnant or, if moving, the motion must be reversible.

The first condition may be violated as soon as the number of elements within a given volume falls below a certain critical value. This may occur if the given volume is sufficiently small or if the medium is at a very low pressure. The second condition may be violated as soon as turbulent motion appears.† These two limitations will be discussed in the following sections.

A. Limitation of phenomenological laws by discontinuity effects

Transport phenomena in diluted gases are fairly well understood. They will be treated first, followed by a few remarks on transport phenomena in solids and liquids.

Transport phenomena in dilute gases are based on the collisions of randomly moving molecules. A very much simplified model gives the following expressions for the heat flux $\dot{q}$, the diffusional flux $\dot{n}_j$, and the shear stress τ due to a flux of momentum (see also [3]):

$$q = -\frac{1}{3}\bar{\rho}\bar{c}_v w_m \sigma \frac{\partial T}{\partial z} \quad (1)^{\ddagger}$$

$$\dot{n}_j = -\frac{1}{3}\tilde{\rho} w_m \sigma \frac{\partial \tilde{x}_j}{\partial z} \quad (2)$$

$$\tau = -\frac{1}{3}\tilde{\rho}\tilde{M} w_m \sigma \frac{\partial u}{\partial z} \quad (3)$$

where $\tilde{\rho}$ is the molar density, w_m is the average velocity of the gas molecules, σ is the mean free path of the

†Potential flow and laminar flow are hydrodynamically reversible; e.g., the Euler and Navier-Stokes equations remain unaffected as the sign of the time coordinate is reversed.

*Within a three-digit section the equation, figure, and table numbers do not have the three-digit identifier; for cross-references between sections, the appropriate threedigit number will be given.

© 1983 Hemisphere Publishing Corporation

molecules, $\tilde{M}$ is the molecular mass, $\tilde{c}_v$ is the specific heat capacity per mole, $\partial T/\partial z$ is the temperature gradient, $\partial \tilde{x}_j/\partial z$ is the gradient of the mole fraction of species j, and $\partial u/\partial z$ is the velocity gradient. The respective phenomenological laws are

$$\dot{q} = -\lambda \frac{\partial T}{\partial z} \quad \text{(Fourier, 1821)} \tag{4}$$

$$\dot{n}_j = -\tilde{\rho}\delta \frac{\partial \tilde{x}_j}{\partial z} \quad \text{(Fick, 1855)} \tag{5}$$

$$\tau = -\eta \frac{\partial u}{\partial z} \quad \text{(Newton, 1687)} \tag{6}$$

Comparison of these two sets of equations gives the transport properties λ, δ, and η in terms of the molecular properties $\tilde{\rho}, w_m, \sigma, \tilde{M}$, and $\tilde{c}_v$. These relationships do not predict the transport properties as set forth in Part 5 of this handbook, but they show the limitations of the phenomenological laws themselves.

Let us consider the conduction of heat through a gaseous gap of width s. Integration of Eq. (4) yields

$$\dot{q} = \lambda \frac{T_1 - T_2}{s} \tag{7}$$

The smaller the gap width, the greater the heat flux, provided that s is much larger than σ so that the gas in the gap can be considered as a continuum. However, when the gap width s becomes small with respect to σ, collisions between gas molecules are less frequent and the heat flux becomes independent of s and reaches a limiting maximum value $\dot{q}_{max}$:

$$q_{max} = -\tfrac{1}{6}\tilde{\rho}\tilde{c}_v w_m (T_1 - T_2) \tag{8}$$

For a gas at normal pressure, σ is of the order of 0.1 μm. Usually s is much larger than σ, so the Fourier equation (7) normally applies for steady-state conditions. However, the situation may become completely different if we look at fine powders under vacuum.

The very poor apparent thermal conductivity of powders under vacuum is due to the fact that Eq. (8) becomes rate-controlling. This phenomenon is well known as the Smoluchowski effect (see Sec. 2.8 and also Sec. 2.1.7). At normal pressure and with particles of about a millimeter in diameter, Eq. (8) may become rate-controlling when the heat is transferred under transient conditions and the contact time of the particles is rather short (a few seconds or less). This occurs in fluidized beds, where the particles collide with immersed heating or cooling coils. It also occurs in other contact heat transfer devices such as rotary kilns and rotary dryers.

Similar expressions for a maximum mass flux and a maximum shear stress may be developed. Again, as s becomes small relative to σ, Eqs. (2) and (3) give

$$n_{j,max} = -\tfrac{1}{6}\tilde{\rho} w_m (\tilde{x}_{j,1} - \tilde{x}_{j,2}) \tag{9}$$

and

$$\tau_{max} = -\tfrac{1}{6}\tilde{\rho}\tilde{M} w_m u \tag{10}$$

As an illustration, if a pure substance evaporates into an absolute vacuum, $\tilde{x}_{j,1}$ is unity and $\tilde{x}_{j,2}$ is zero. Therefore, the maximum rate of evaporation is

$$n_{max,evap} = -\tfrac{1}{6} w_m \tilde{\rho} \tag{11}$$

Usually this maximum rate of evaporation is much higher (3.5 kmol/m^2 s at normal pressure and temperature) than the rates occurring in technical equipment. This is the justification for the commonly introduced concept that phase equilibrium can be assumed at the gas-liquid interface in evaporators and condensers. However, this may not be true if evaporation occurs under vacuum or in the case of rapid evaporation under transient conditions such as a flashing process.

The shear stress at the walls of a circular duct in laminar gas flow according to the Hagen-Poiseuilles law, which is based on Eq. (6), is

$$\frac{\tau}{u} = 8\frac{\eta}{d} \tag{12}$$

where d is the tube diameter. At atmospheric pressure and room temperature, τ/u is of the order of 10^{-2} kg/m^2 s if the tube diameter d is assumed to be of the order of centimeters. The maximum value for τ/u at the same conditions is, according to Eq. (10), of the order of 200 kg/m^2 s. Therefore, the shear stress is usually controlled by Eq. (12). However, if gas flows through vacuum ducts or through porous media, molecular flow as represented by Eq. (10) becomes the controlling mechanism.

Heat conduction in solids is accomplished either by phonon transport (nonmetallic solids) or by electron transport (metallic solids). In the case of phonon transport the velocity of energy propagation is the velocity of sound. Therefore the maximum heat flux is given by

$$q_{max} = -\tfrac{1}{6}\tilde{\rho}\tilde{c}_v w_s (T_1 - T_2) \tag{13}$$

where w_s is the velocity of sound.

In the case of electron transport one obtains

$$q_{max} = -\tfrac{1}{6}\tilde{\rho}\tilde{c}_v w_e (T_1 - T_2) \tag{14}$$

where w_e is the average thermal velocity of the electrons. Comparing the maximum heat fluxes in gases and solids, both nonmetallic and metallic, one finds the following numbers:

© 1983 Hemisphere publishing Corporation

Gas,† 1 bar, 300 K:

$$\dot{q}_{max} = 0.10 \times 10^6 (T_1 - T_2)\ W/m^2$$

Solid,‡ nonmetallic:

$$\dot{q}_{max} = 1.25 \times 10^9 (T_1 - T_2)\ W/m^2$$

Solid, § metallic :

$$\dot{q}_{max} = 0.50 \times 10^{11} (T_1 - T_2)\ W/m^2$$

The maximum heat flux for nonmetallic liquids is of the same order of magnitude as for nonmetallic solids. In any case the maximum heat fluxes for solids and liquids are considerably higher than those obtainable in actual equipment and thus are of little practical value.

The maximum heat flux in the case of radiation occurs when the surfaces of the energy-exchanging bodies are thermally black. Further, if the energy exchange by radiation is perfect, that is, there are no radiative losses to the surroundings, the rate of heat transfer is given by the Stefan-Boltzmann law,

$$4_{max} = C_s(T_1^4 - T_2^4) \tag{15}$$

where all temperatures are in kelvins.

The radiation constant C_s is known as the Stefan-Boltzmann constant and is equal to [4]

$$C_s = 5.67 \times 10^{-8}\ W/m^2K^4 \tag{16}$$

For moderate temperature differences $(T_1^4 - T_2^4)$, Eq. (15) may be approximated by

$$4_{max} = 4C_sT_m^3(T_1 - T_2) \tag{17}$$

where $T_m = \frac{1}{2}(T_1 + T_2)$. At room temperature we obtain

$$\dot{q}_{max} = 5.8(T_1 - T_2)\ W/m^2$$

Although this value is comparatively low, heat transfer by radiation may become rate-controlling at low temperature differences in a free convection system.

†Calculated with

$$w_m = \sqrt{\frac{8}{\pi}\frac{\tilde{R}T}{\tilde{M}}}$$

‡Calculated for glass with

$w_s = 4\,000$ m/s

§Calculated with

$$w_e = \sqrt{3\frac{\tilde{R}T}{\tilde{M}}} = 100\ 000\ m/s$$

B. Limitation of phenomenological laws by turbulence

Another limitation of the applicability of the flux equations (4)-(6) containing the molecular transport properties λ, δ, and η is the phenomenon of turbulence. Turbulence occurs in gases and liquids as a random motion of so-called eddies, the size of which is of the order of a few percent of the confining system. This may be of the order of millimeters in heat exchanger tubes, centimeters in a large cooling tower, or even meters in the open atmosphere. The eddies appear in fluids at high flow velocities, within ducts of large diameters, behind obstacles, and so on. The criterion for the onset of turbulence is the critical Reynolds number,

$$Re_{crit} = \left(\frac{\rho u L}{\eta}\right)_{crit} \tag{18}$$

where L is a characteristic dimension. For tube flow the value of the critical Reynolds number is 2 300 with L equal to the tube diameter. The molecular transport equations (4)-(6) apply as long as the actual Reynolds number is less than 2 300. Above this number the turbulent eddies will appear and contribute to the transport of heat, mass, and momentum.

A large number of models have been suggested to describe turbulent transport phenomena. None of them, however, is able to derive the turbulent fluxes completely from the physical properties of the fluids. One widely used model involves the introduction of the turbulent transport properties λ_t, δ_t, and η_t. The phenomenological flux equations (4)-(6) are then extended to

$$\dot{q}_t = -(\lambda + \lambda_t)\frac{\partial T}{\partial z} \tag{19}$$

$$n_{j,t} = -\tilde{\rho}(\delta + \delta_t)\frac{\partial \tilde{x}_j}{\partial z} \tag{20}$$

$$\tau_t = -(\eta + \eta_t)\frac{\partial u}{\partial z} \tag{21}$$

The turbulent transport properties, however, are not physical properties of the fluid, but depend on the flow velocity, the distance from rigid walls, and the geometric shape of the duct, immersed body, free-stream jet, and so on. They must be evaluated from experiment for each individual case. In any case, however, the turbulent fluxes are larger than the molecular fluxes $(\Delta z \gg \sigma)$ but less than the maximum molecular fluxes $(\Delta z \ll \sigma)$:

$$\dot{q} < \dot{q}_t < \dot{q}_{max} \tag{22}$$

$$t_{ij} < \dot{n}_{j,t} < \dot{n}_{j,max} \tag{23}$$

$$\tau < \tau_t < \tau_{max} \tag{24}$$

© 1983 Hemisphere Publishing Corporation

A rough estimate is that the turbulent fluxes may become from 10 to 100 times greater than the molecular fluxes.

As a concluding remark, it should be pointed out that the shear stress in a fluid due to molecular momentum transport does not always follow Newton s law, Eq. (6). Sometimes the viscosity η depends on the shear stress itself. Elastic effects are also observed in flowing fluids. The theory of molecular momentum transfer in so-called non-Newtonian and viscoelastic fluids is given in several books [5, 6] and is discussed in Sec. 2.2.8.

Nomenclature for Section 2.1.1 appears at the beginning of Part 2. References appear at the end of Section 2.1.7.

© 1983 Hemisphere Publishing Corporation

2.1.2

Industrial applications of heat and mass transfer

E. U. Schlünder

■ After having briefly discussed the physical mechanisms of heat, mass, and momentum transfer, it seems appropriate to make a few comments on these transfer processes as they are used in heat exchanger design. The flux equations given in the previous section apply both locally and instantaneously and must be integrated with respect to time and position in order to predict the total flux over the surface of the heat exchanger. This integration, if done rigorously, is a very complex procedure, involving the simultaneous solution of coupled differential equations. This can be done only with the help of computers. Today a number of computer programs are available. In addition to these computer-aided rating and design procedures, shortcut or hand methods are also available. These represent a reasonable first approximation. In many cases the hand-method results are of sufficient accuracy.

In the following sections a brief description of these various methods will be given, starting with the simpler ones and proceeding to the more sophisticated ones.

A. The $\bar{U}$ method

If heat is to be transferred from medium 1 to medium 2, both being separated by a solid wall (see Fig. 1), one starts with the following flux equation:

$$\dot{q} = \bar{U}(T_{1,\mathrm{av}} - T_{2,\mathrm{av}}) \tag{1}$$

Here $\bar{U}$ is the overall heat transfer coefficient. It is assumed to be independent of the average fluid temperatures $T_{1,\mathrm{av}}$ and $T_{2,\mathrm{av}}$, time ♦ and position x, y. It is

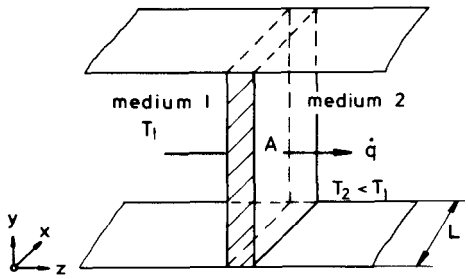

Figure 1 Heat transfer from medium 1 to medium 2, separated by a solid wall.

further assumed that medium 1 and medium 2 are stagnant fluids occupying the volumes V_1 and V_2, exchanging sensible heat only, and having constant heat capacities c_1 and c_2, respectively. At the beginning $(t = 0)$ the initial temperatures may be given by $T_{1,0}$ and $T_{2,0}$. The important questions are how $T_{1,\mathrm{av}}$ and $T_{2,\mathrm{av}}$ vary with time and what is the time averaged heat flux $\dot{q}_{\mathrm{av}}$. To answer these questions we need, in addition to the flux equation (1), the law of energy conservation for the two fluids,

$$-\frac{dH_1}{dt} = \dot{q}A \tag{2}$$

$$\frac{dH_2}{dt} = \dot{q}A \tag{3}$$

where A is the heat exchanger surface area, $H_j = (\rho c V T_{\mathrm{av}})_j$ is the enthalpy of the respective medium, and t is the time. The simultaneous solution of Eqs. (1)-(3) for medium 1 is

© 1983 Hemisphere Publishing Corporation

$$\frac{T_{1,av} - T_{1,0}}{T_{2,0} - T_{1,0}} = \frac{W_2}{W_2 + W_1} \times \left\{1 - \exp\left[-\left(\frac{1}{W_1} + \frac{1}{W_2}\right)\bar{U}At\right]\right\} \quad (4)$$

where $W_j = (\rho c V)_j$. The groups

$$\frac{\bar{U}A}{W_1}t \quad \text{and} \quad \frac{\bar{U}A}{W_2}t \quad (5)$$

are the so-called number of transfer units NTU_j of the heat exchanger with respect to mediums 1 and 2, respectively. The NTU is a dimensionless contact time, where $W_j/\bar{U}A$ are the so-called relaxation times of mediums 1 and 2, respectively. The amount of heat transferred Q during time t is

$$Q = \bar{U}At\,\frac{(T_{1,0} - T_{2,0}) - (T_{1,av} - T_{2,av})}{\ln[(T_{1,0} - T_{2,0})/(T_{1,av} - T_{2,av})]} \quad (6)$$

where the last factor is called the logarithmic mean temperature difference ΔT_{LM} (see Sec. 1.3.1):

$$Q = \bar{U}At\ \mathrm{AT}_{,,} \quad (6a)$$

The time-averaged heat flux is

$$\dot{q}_{av} = \frac{Q}{At} = \bar{U}\,\Delta T_{LM} \quad (7)$$

The same analysis applies if both media flow in the x direction parallel to the surface ***A,*** as long as steady-state conditions are considered and dispersion of energy in the x direction is negligible. Let $\dot{V}_j$ be the volume flow rates of the mediums, $\dot{H}_j = (\rho c \dot{V} T_{av})_j$ and $\dot{W}_j = (\rho c \dot{V})_j$. The energy balances are

$$-\frac{d\dot{H}_1}{dA} = \dot{q} \quad (8)$$

$$\frac{d\dot{H}_2}{dA} = \dot{q} \quad (9)$$

The solution of Eqs. (1), (8), and (9) is

$$\frac{T_1 - T_{1,0}}{T_{2,0} - T_{1,0}} = \frac{\dot{W}_2}{\dot{W}_2 + \dot{W}_1} \times \left\{1 - \exp\left[-\left(\frac{1}{\dot{W}_1} + \frac{1}{\dot{W}_2}\right)\bar{U}A\right]\right\} \quad (10)$$

for medium 1. An analogous expression can be obtained for medium 2. The subscript 0 refers to the inlet position at x = 0, whereas no subscript refers to the outlet position at x = L in Fig. 1. The average heat flux betweenx=Oandx= 1 is

$$\dot{q}_{av} = \frac{\dot{Q}_{av}}{A} = \bar{U}\,\Delta T_{LM} \quad (11)$$

which is exactly the same expression as given by Eq. (7) for the stagnant fluids. This is no surprise, since the case of the moving mediums can be transformed into the case of the stagnant mediums by introducing the residence time t. This is given as the ratio of the hold-up volume V and the flow rate $\dot{V}$,

$$t_1 = \frac{V_1}{\dot{V}} \text{ for medium 1}$$

and (12)

$$t_2 = \frac{V_2}{\dot{V}_2} \text{ for medium 2}$$

Thus we find that

$$\frac{\bar{U}A}{\dot{W}_1} = \frac{\bar{U}A}{W_1}t_1 = \mathrm{NTU}_1 \quad (13)$$

$$\frac{\bar{U}A}{W_2} = \frac{\bar{U}A}{W_2}t_2 = \mathrm{NTU}_2 \quad (14)$$

which indicates the equivalence of Eqs. (10) and (4) for the moving and stagnant mediums, respectively.

In summary, the benefits and the limitations of the $\bar{U}$ method are these: As long as the presuppositions hold, which means that $\bar{U}$ must not depend on the temperatures, the time, or the position, the $\bar{U}$ method allows the solution of scale-up problems with respect to temperature variations. Once the overall heat transfer coefficient $\bar{U}$ has been determined-for example, by evaluation of experimental data obtained with a full-size heat exchanger-one can scale up or down for the same fluids within a certain range of temperature differences. Approximate overall heat transfer coefficients for various types of heat exchangers are given in Table 1. The lower values apply to lower flow velocities and poorly conducting fluids.

The $\bar{U}$ method is a one-parameter method that is appropriate for the first approximation. It also allows the establishment of a relationship between the effectiveness of the heat transfer process and the number of transfer units for various flow configurations. For cocurrent flow this correlation has been given by Eq. (10). The effectiveness ***E*** is defined as the ratio of the temperature change to the maximum temperature difference:

$$E_1 = \frac{T_1 - T_{1,0}}{T_{2,0} - T_{1,0}} \quad (15)$$

By introducing $\dot{W}_1/\dot{W}_2 = \dot{R}$, this correlation becomes

$$E_1 = \frac{1}{1 + \dot{R}}\{1 - \exp[-(1 + \dot{R})\mathrm{NTU}_1]\} \quad (16)$$

Similar expressions for counter-current flow, cross flow, flow with back mixing of the fluids, and various

© 1983 Hemisphere I blishing Corporation

Table 1 Approximate overall heat transfer coefficients for various types of heat exchangers

Type	Performance	$\bar{U}$, W/m² K
Shell-and-tube heat exchanger 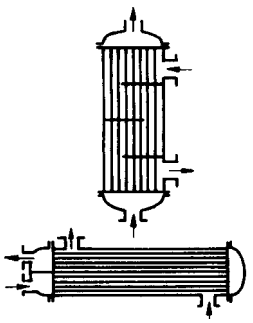	Gas (1 bar)-gas (1 bar)	5-35
	Gas (250 bar)-gas (250 bar)	150–500
	Liquid-gas (1 bar)	15-70
	Liquid-gas (250 bar)	200-400
	Liquid-liquid	150-1 200
	Liquid-condensing vapor	300-1 200
Reboiler 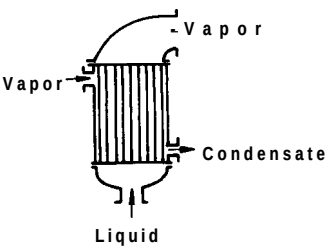	Natural recirculation	
	(a) Viscous liquids	300-900
	(b) Water	600-1 700
	Forced recirculation	900-3 000
	NH,evaporator-brine	200-800
Condenser 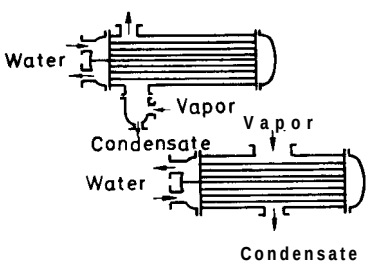	Organic vapor, NH,	300-1 200
	Power plant steam condenser, brass tubes	1 500–4 000
	Inert gas reduces $\bar{U}$	
Gas heater 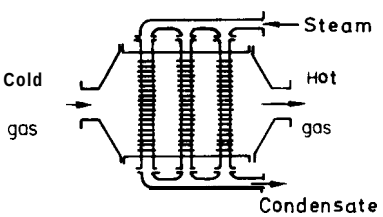	Forced convection	12-50
Double-pipe heat exchanger 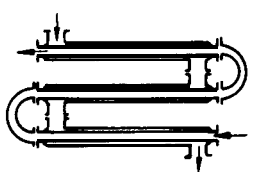	Gas (1 bar)-gas (1 bar)	10-35
	Gas (1 bar)-gas (250 bar)	20-60
	Gas (250 bar)-gas (250 bar)	150–500
	Gas (250 bar)-liquid	200-600
	Liquid-liquid	300-1 400

© 1983 Hemisphere Publishing Corporation

Table 1 Approximate overall heat transfer coefficients for various types of heat exchangers ***(Continued)***

Type	Performance	$\bar{U}$, W/m² K
Film cooler 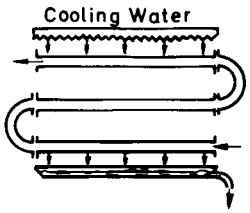	Water-gas (1 bar) Water-gas (250 bar) Water-liquid Water-cooled condenser	20-60 150-350 300-900 300-l 200
Helical coil cooler 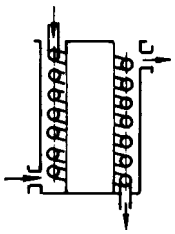	Water-gas (1 bar) Water-gas (250 bar) Water-liquid Water-condensing steam	20-60 150-500 200-700 350-900
Plate heat exchanger 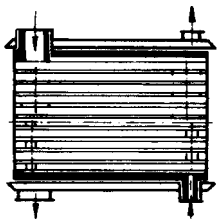	Water-gas (1 bar) Water-liquid	20-60 350-l 200
Matrix heat exchanger 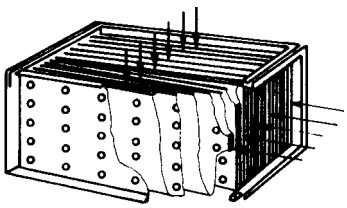	Gas (1 bar)-gas (1 bar) Gas (1 bar)-liquid	10-35 20-60
Spiral heat exchanger 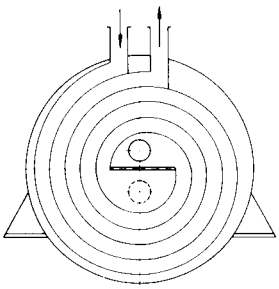	Liquid-liquid Condensing steam-liquid	700-2 500 900-3 500

© 1983 Hemisphere Publishing Corporation

Table 1 Approximate overall heat transfer coefficients for various types of heat exchangers *(Continued)*

Type	Performance	$\bar{U}$, W/m² K
Agitated vessel		
A. Double jacket B. Coil inside 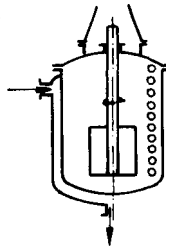	A. Double jacket	
	Condensing steam-liquid	500-1 500
	Condensing steam-boiling liquid	700-1 700
	Cooling water-liquid	150-350
	B. Coil inside	
	Condensing steam-liquid	700-2 500
	Cooling water-liquid	500-1 200
C. Welded coil outside 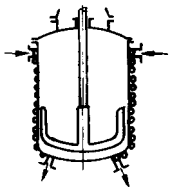	C. Welded coil outside	
	Condensing steam-Iiquid	500-1 700
	Condensing steam-boiling liquid	700-2 300
	Cooling water-liquid	350-900

combinations of these are shown in Fig. 2 and are discussed in Sec. 1.3.

Figure 2 shows that there are two distinguishable regimes. At low NTU_1, say, less than 0.2, the effectiveness E_1 is purely heat transfer-controlled, and the flow configuration has no influence on E_1. At high NTU_1, however, the effectiveness is controlled primarily by the flow configuration and is only minimally influenced by the overall heat transfer coefficient $\bar{U}$ and by the heat exchanger surface area A. This is a very important relationship to consider when selecting the type of heat exchanger for a given application.

The limitation of the $\bar{U}$ method for scale-up or scale-down is that it is applicable only for a given type of heat exchanger with similar fluids and flow velocities. A more refined analysis, using the overall heat transfer coefficient $\bar{U}$, leads to the development of an expression for $\bar{U}$ in terms of the individual heat transfer coefficients $\bar{\alpha}_j$. The individual heat transfer coefficients take into account the fluid properties and the flow velocities.

B. The $\bar{U}$-$\bar{\alpha}$ method

The overall heat transfer coefficient $\bar{U}$ is expressed in terms of the individual average heat transfer coefficients $\bar{\alpha}_j$ according to the following flux equations+:

$$\dot{q} = \bar{\alpha}_1 (T_1 - T_{1,w}) \quad (17)$$

$$\dot{q} = \bar{\alpha}_w (T_{1,w} - T_{2,w}) \quad (18)$$

$$\dot{q} = \bar{\alpha}_2 (T_{2,w} - T_2) \quad (19)$$

(see Fig. 3). Since the overall heat transfer coefficient $\bar{U}$ is defined by

$$\dot{q} = \bar{U}(T_1 - T_2) \quad (20)$$

elimination of the intermediate temperature at the wall $T_{1,w}$ and $T_{w,2}$ leads to

$$\frac{1}{\bar{U}} = \frac{1}{\alpha_1} + \frac{1}{\alpha_w} + \frac{1}{\alpha_2} \quad (21)$$

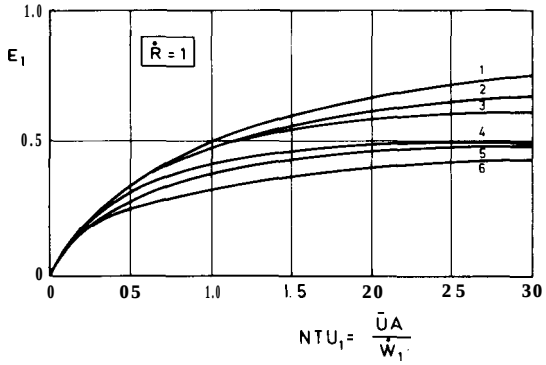

Figure 2 Effectiveness of heat transfer E_1 depending on the number of transfer units NTU, for various flow configurations in a heat exchanger. (1) Counter-current flow. (2) Ideal cross flow. (3) Cross flow, medium 2 partly mixed. (4) Cocurrent flow. (5) Cross flqw, medjum 2 totally mixed. (6) Both mediums perfectly mixed. $R = (\rho c \dot{V})_1 / (\rho c \dot{V})_2 = 1$.

+These equations apply to plane walls. For circular walls see Part 1.

© 1983 Hemisphere Publishing Corporation

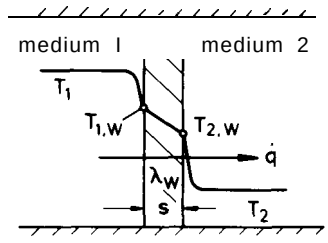

Figure 3 Illustration of individual heat transfer resistances and corresponding temperature profiles.

This indicates that the overall heat transfer resistance $1/\bar{U}$, is equal to the sum of the individual resistances, $1/\bar{\alpha}_j$. Usually the wall is a metal having a fairly high thermal conductivity λ_w.

Since

$$\alpha_w = \frac{\lambda_w}{s} \quad \text{or} \quad \frac{1}{\bar{\alpha}_w} = \frac{s}{\lambda_w} \tag{22}$$

the resistance offered by the wall is often negligibly small when compared with that offered by the fluid streams $1/\bar{\alpha}_1$ and $1/\bar{\alpha}_2$. However, the metal wall may become coated with a layer of poor conducting material, which precipitates out during the operation of the unit. This process is called fouling. The overall heat transfer resistance $1/\bar{U}$ might be essentially controlled by heat conduction through the precipitated layers:

$$\frac{1}{\bar{U}} = \frac{1}{\bar{\alpha}_1} + \frac{1}{\bar{\alpha}_{\text{foul},1}} + \frac{1}{\bar{\alpha}_w} + \frac{1}{\bar{\alpha}_{\text{foul},2}} + \frac{1}{\bar{\alpha}_2} \tag{23}$$

Assume that a 2-mm copper wall with λ_w = 200 W/m K is covered with a O.lO-mm layer of calcium carbonate with λ_{foul} = 1 W/m K. Then $1/\bar{\alpha}_{\text{foul}}$ is 10 times as much as $1/\bar{\alpha}_w$.

The fluid heat transfer coefficients $\bar{\alpha}_1$ and $\bar{\alpha}_2$ are dependent on the fluid properties and the fluid flow velocities. They are also affected by a phase change such as evaporation or condensation. The most important physical fluid properties with regard to heat transfer are the thermal conductivity λ, the density ρ, and the viscosity η. This is clearly shown in Table 2. Although λ and η for air are almost independent of pressure, $\bar{\alpha}$ is much higher for compressed air flowing at the same velocity because of the higher mass velocity (ρu). For all liquids, however, ρ is practically a constant. In this case the mass flow rate ρu is limited by the viscosity η. Except for very viscous liquids, the predominant property in this case is the thermal conductivity λ. For water λ is five times as much as for practically any organic liquid. Therefore the heat transfer coefficients $\bar{\alpha}$ for water are also five times larger, as shown in Table 2.

The heat transfer coefficients for evaporation and condensation are greatly dependent on the thermal conductivity and the viscosity of the liquid phase. The lower $\bar{\alpha}$ values apply for poorly conducting and highly viscous fluids.

The heat transfer coefficients between particles frequently contacting walls, as in fluidized beds, rotary dryers, and so on, depend essentially on the particle size and the gas pressure. The lower value in Table 2 applies for vacuum (0.001 mbar) operation, whereas the larger value is for normal pressure and particles a few millimeters in diameter.

The heat transfer coefficient for radiative heat transfer applies for small temperature differences and follows from Eq. 2.1.1(17):

$$\bar{\alpha}_{\text{rad}} = 4\epsilon C_s T_m^3 \tag{24}$$

It depends on the emisivity ($0.001 < \epsilon < 1$) and on the average temperature T_m.

Knowing the individual heat transfer coefficients $\bar{\alpha}$, one can predict the overall coefficient $\bar{U}$ for various combinations of individual heat transfer processes. This is the important advantage of the $\bar{U}$-$\bar{\alpha}$ method compared with the $\bar{U}$ method. However, the $\bar{U}$-$\bar{\alpha}$ method also applies only if the individual heat transfer coefficients are independent of the temperatures, the temperature differences, and the surface area.

In many practical cases this is not true. If the variations of $\bar{\alpha}$ are relatively small or rapidly converge to a constant value, one may apply averaged α and consider them to be quasiconstants.

For transient heat conduction, $\bar{\alpha}$ is a function of time t. For steady-state heat transfer in laminar flow, $\bar{\alpha}$ is a function of the downstream position x. The average quantities to be used in the $\bar{U}$-$\bar{\alpha}$ method are defined as

$$\bar{\alpha} = \frac{1}{t}\int_0^t \alpha(t')\,dt \quad \text{or} \quad \bar{\alpha} = \frac{1}{L}\int_0^L \alpha(x)\,dx \tag{25}$$

Table 2 Range of average heat transfer coefficients

Medium	$\bar{\alpha}$, W/m² K
Air (1 bar), free convection	2-20
Air (1 bar), forced convection	10–200
Air (250 bar), forced convection	200-I 000
Water	500-S 000
Organic liquids	100-l 000
Condensation (water)	2 000-50 000
Condensation (organic vapor)	500-10 000
Evaporation (water)	2000-100000
Evaporation (organic liquids)	500-50 000
Particle-gas-wall	S-500
Radiation at room temperature, black surface	5
Radiation at 2 000 K, black surface	1 500

© 1983 Hemisphere Publishing Corporation

In the case of free convection, condensation, and evaporation, the individual heat transfer coefficients depend on the temperature difference between fluid and wall AT,. The most common averaging used is to take the arithmetic mean value:

$$\bar{\alpha} = \tfrac{1}{2}[\alpha\{\Delta T_{w,1}\} + \alpha\{\Delta T_{w,2}\}] \tag{26}$$

In the case of temperaturedependent fluid properties, the individual heat transfer coefficients depend on the fluid temperature T_1 and/or T_2, respectively. Usually the arithmetic mean is taken as the so-called reference temperature in evaluating the fluid properties:

$$T_{\text{ref}} = \tfrac{1}{2}(T_{\text{in}} + \text{Tout}) \tag{27}$$

The average individual heat transfer coefficients also depend on the thermal boundary conditions, that is, constant wall temperature or constant heat flux, and so on. If the $\bar{U}$-$\bar{\alpha}$ method is used, this effect is ignored. Therefore, a more rigorous analysis of the heat transfer process that takes into account the effects of these items on the heat transfer coefficients must start with the instantaneous or local heat transfer coefficients α and the instantaneous or local overall heat transfer coefficient U.

C. The U-α method

The overall instantaneous or local heat transfer coefficient U is split up into instantaneous or local individual heat transfer coefficients in the same way as in the $\bar{U}$-$\bar{\alpha}$ method described in the previous section:

$$\frac{1}{U} = \Sigma \frac{1}{\alpha_j} \tag{28}$$

Since α_j is a function of t, x, T_w, and AT, U is also a function of those quantities. Combining the flux equations for the instantaneous or local heat flux,

$$\dot{q} = U(T_1 - T_2) \tag{29}$$

with the instantaneous or local energy balance as given by Eqs. (2) and (3) yields the basic equations required to calculate the change of temperature T_1 and T_2. A practical example will illustrate this in a straightforward way. Figure 4 shows a double-pipe water cooler with evaporating Freon in the inner tube. In the forced convection boiling regime the individual boiling heat transfer coefficient α_2 increases with increasing vapor quality $\dot{x}$. As a rough approximation one could assume a linear relationship between α_2 and $\dot{x}$. The energy balance yields

$$\dot{M}_2 \Delta h_v(\dot{x}' - \dot{x}) = -\dot{M}_1 c_{p1}[(T_1' - T_2) - (T_1'' - T_2)] \tag{30}$$

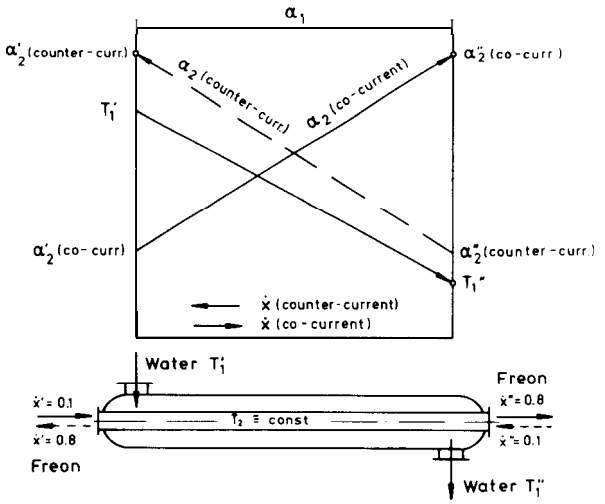

Figure 4 Linear variation of one individual heat transfer coefficient with respect to the local temperature difference.

Here $\dot{x}$ is a linear function of $T_1 - T_2$, hence α_2 is a linear function of $T_1 - T_2$. This class of problem, where the heat transfer coefficient depends linearly on the driving temperature difference, has been solved by Colburn [7] . He obtained the following expression for the total heat flux $\dot{Q}$:

$$\frac{A(T_1' - T_2)}{\dot{Q}} = \frac{1}{\alpha_1}\frac{\ln\theta}{\theta - 1} + \frac{\ln(\alpha_2'/\alpha_2'')\theta}{\alpha_2'\theta - 1} \tag{31}$$

where

$$\theta = \frac{T_1'' - T_2}{T_1' - T_2}$$

For small temperature changes $T_1' = T_1''$, which means that $\theta \to 1$ and Eq. (31) yields

$$\lim_{\theta \to 1} \frac{A(T_1' - T_2)}{\dot{Q}} = \frac{\ln\theta}{\theta - 1}\left(\frac{1}{\alpha_1} + \frac{1}{\alpha_2}\right) \tag{32}$$

where

$$\bar{\alpha}_2 = \frac{\alpha_2' - \alpha_2''}{\ln(\alpha_2'/\alpha_2'')}$$

One recognizes that only in the latter case does the $\bar{U}$-$\bar{\alpha}$ method described in the previous section give a good approximation; in general, no $\bar{U}$ can be defined in this case. The most important effect, however, is that the total heat flux $\dot{Q}$ depends on the flow direction of the Freon and is larger for cocurrent flow than for counter-current flow. This can be shown by forming the ratio

$$\frac{\dot{Q}}{\lim_{\theta \to 1} \dot{Q}} \tag{33}$$

© 1983 Hemisphere Publishing Corporation

$$= \frac{(1 + \mathrm{Bi})(\ln \theta)/(\theta - 1)}{[(\ln \theta)/(\theta - 1)] + \mathrm{Bi}\,[(\mu - 1)/(\ln \mu)][(\ln \mu\theta)/(\mu\theta - 1)]} \quad (33)$$

(Cont.)

where the Biot number $\mathrm{Bi} = \alpha_1/\bar{\alpha}_2$ and $\mu = \alpha_2'/\alpha_2''$. Figure 5 shows this ratio as a function of θ with Bi and μ as parameters. Comparisons with the $\bar{U}$-$\bar{\alpha}$ method indicate that errors could be of the order of ±30%.

The U-α method can also be extended to nonlinear or even arbitrary relationships between α and the local temperature difference. Those relationships appear with nucleate boiling, condensation, and free convection heat transfer and have the form

$$\dot{q} = \alpha_1^*(T_1 - T_w)^{n_1} \quad (34)$$

$$\dot{q} = \alpha_2^*(T_w - T_2)^{n_2} \quad (35)$$

These generalized local flux equations can be transformed and combined with the local energy balance to give an expression for predicting the total heat flux. Transformation gives

$$T_1 - T_2 = \left(\frac{\dot{q}}{\alpha_1^*}\right)^{1/n_1} + \left(\frac{\dot{q}}{\alpha_2^*}\right)^{1/n_2} = f(\dot{q}) \quad (36)$$

and combination yields, for cocurrent flow,

$$\dot{Q} = A\,\frac{(T_{1,0} - T_{2,0}) - (T_1 - T_2)}{\varphi(\dot{q}_0, \dot{q})} \quad (37)$$

where

$$\varphi = \int_{\dot{q}_0}^{\dot{q}} \frac{f'(\dot{q})}{\dot{q}}\, d\dot{q} \quad (38)$$

with $\dot{q}_0 = U_0(T_{1,0} - T_{2,0})$ and $\dot{q} = U(T_1 - T_2)$. In case the flux equations are linear, that is, $n_1 = n_2 = 1$, then the function φ becomes

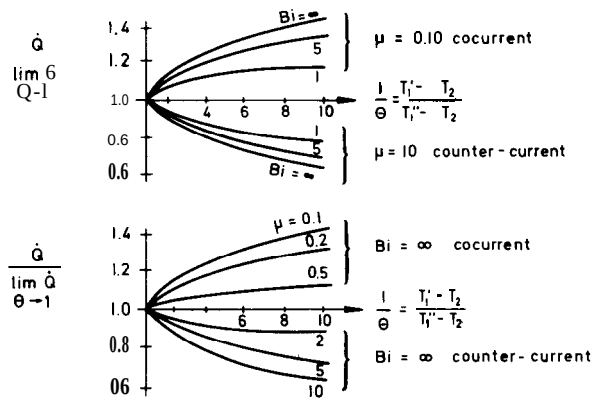

Figure 5 Effect of co- and counter-current flow in case of linear variation of one individual heat transfer coefficient with respect to the temperature difference.

$$\varphi_{n_1=1,n_2=1} = \frac{1}{\bar{U}} \ln \frac{T_{1,0} - T_{2,0}}{T_1 - T_2} \quad (39)$$

which means that the total heat flux could also be predicted by the $\bar{U}$-$\bar{\alpha}$ method.

Summarizing the result of the U-α analyses in this case indicates that if α depends on AT,,,, one always should attempt to combine low local α's with large local ΔT_w's and vice versa, thus achieving, whenever possible, a uniform heat flux within the heat exchanger. This gives a maximum heat flux or a minimum required surface area. In the example given above, the heat flux is more uniform in the case of cocurrent flow, which means that this flow direction gives higher performance of the heat exchanger. This result could never have been found with the $\bar{U}$-$\bar{\alpha}$ method and shows clearly the benefit of the more sophisticated U-α method.

It may happen, however, that even the local heat transfer coefficients do not permit correct prediction of heat exchanger performance, because no local overall heat transfer coefficient U can be defined. This is because any local heat transfer coefficient depends on the thermal boundary conditions, particularly in laminar flow. The standard boundary condition for calculating local heat transfer coefficients is constant wall temperature. In practice, however, the wall temperature may vary considerably, depending on the heat conductivity of the wall and on the heat transfer coefficients α_1 and α_2 on both sides of the wall. Therefore medium 1, medium 2, and the wall form a thermally coupled system, where the local heat flux must be evaluated pointwise and then integrated. Such a situation may occur, particularly in laminar flow, as has been shown by Stein and Shastri [8].

This situation may also arise in two-phase flow heat transfer. Consider, for example, evaporation in a horizontal tube. Assume separated flow with 50% of the perimeter wetted (Fig. 6). The heat transfer coefficient for the liquid phase is usually much higher than that for the vapor phase. Consequently, there is a heat

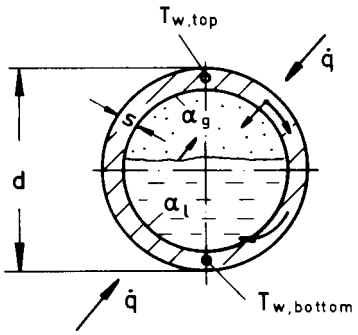

Figure 6 Evaporation in a horizontal tube, separated flow. Effect of heat conduction in the tube wall.

© 1983 Hemisphere Publishing Corporation

flux variation around the perimeter of the tube from top to bottom, if heat is supplied at some rate $\dot{q}$. Of course, the wall temperature also varies from top to bottom. There are two limiting cases:

1. The heat flux variation along the tube perimeter may be negligible; $\dot{q}$ is uniform all around the tube.
2. The heat flux along the perimeter may become infinitely large; the wall temperature around the tube is uniform.

The perimeter-averaged heat transfer coefficient for the evaporating fluid may be defined as

$$\alpha = \frac{\dot{q}}{T_{w,\mathrm{av}} - T} \tag{40}$$

where $T_{w,\mathrm{av}}$ is the average wall temperature:

$$T_{w,\mathrm{av}} = \tfrac{1}{2}(T_{w,\mathrm{top}} + T_{w,\mathrm{bottom}}) \tag{41}$$

This gives for the uniform heat flux case 1

$$\frac{1}{\alpha_{\dot{q}=\mathrm{const}}} = \frac{1}{2}\left(\frac{1}{\alpha_g} + \frac{1}{\alpha_\ell}\right) \tag{42}$$

whereas for constant wall temperature, case 2, the result is

$$\alpha_{T_w=\mathrm{const}} = \tfrac{1}{2}(\alpha_g + \alpha_\ell) \tag{43}$$

Practical cases fall in between, depending on the thermal conductivity and the thickness of the tube wall as well as on the external heat flux distribution or boundary conditions. Forming the ratio of $\alpha_{T_w=\mathrm{const}}/\alpha_{\dot{q}=\mathrm{const}}$ gives

$$\frac{\alpha_{T_w=\mathrm{const}}}{\alpha_{\dot{q}=\mathrm{const}}} = \frac{1}{4}\left(1 + \frac{\alpha_\ell}{\alpha_g}\right)\left(1 + \frac{\alpha_g}{\alpha_\ell}\right) \tag{44}$$

Assume that $\alpha_\ell/\alpha_g = 10$. The ratio according to Eq. (44) will be about 3, which means that the perimeter-averaged internal heat transfer coefficient may vary by a few hundred percent depending on, for example, the thickness and the thermal conductivity of the tube wall. The basic information that would be needed for the prediction of heat exchanger performance data would be the local heat transfer coefficients α_g and α_ℓ as well as the percentage of the tube perimeter that is dry as a function of all the external variables.

D. Summary

The $\bar{U}$ method as well as the $\bar{U}$-$\bar{\alpha}$ method use average transfer coefficients both in the flow direction of the fluids as well as perpendicular to it. These flux equations are easy to handle, and the mathematical implications are kept to a minimum. These methods are fully sufficient to solve many standard heat transfer problems and are also useful for first estimations in more complicated cases. They are hand calculation methods. The U-α method uses local transfer coefficients with respect to the flow direction (or time). Yet those coefficients are still averaged along the perimeter perpendicular to the flow direction. This method should be applied if the local transfer coefficients vary strongly with temperature, temperature difference, time, and position. It requires a deeper insight into the mechanism of the transfer process and more experimental information, but in return it provides a wider range of applicability and scale-up. In most cases the U-α method is to be considered a computer method. However, the rapid development of desk computers will create a growing demand for local transfer coefficients.

The next step toward sophistication may become necessary if the local transfer coefficients also vary perpendicular to the flow direction, for example, along the tube perimeter. In this case local values in two directions, so-called point coefficients, are needed. Once more the required experimental information increases and the mathematical treatment becomes more difficult.

At present the $\bar{U}$-$\bar{\alpha}$ and the U-α methods are the most widely used ones. Therefore, the transfer coefficients presented in this handbook are usually either average $\bar{\alpha}$ or local α values.

Nomenclature for Section 2.1.2 appears at the beginning of Part 2. References appear at the end of Section 2.1.7.

© 1983 Hemisphere Publishing Corporation

2.1.3

Presentation of heat and mass transfer data

E. U. Schlünder

■ Heat and mass transfer coefficients are as far as possible expressed as dimensionless numbers (see Sec. 1.2.3). This not only reduces the number of parameters but also gives guidelines for solving scale-up problems. In this section the most important dimensionless numbers in heat and mass transfer will be discussed and their physical significance explained. In explaining the physical significance of these numbers it is useful to use some examples, which are treated in a way that may be somewhat unfamiliar to many heat transfer engineers. The first such case is that of the cooling of a slab of solid material whose thermal conductivity is λ. The slab illustrated in Fig. 1 is assumed to have an initial temperature T_0 at time $t = 0$, whereas the wall temperature is reduced to T_w and maintained at that value. The heat flux $\dot{q}$ is given by the $\bar{\alpha}$ method as

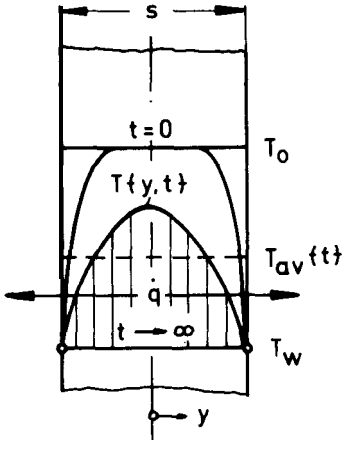

Figure 1 Temperature distribution in a slab kept at constant wall temperature T_w. Initial temperature T_0. Average temperature $T_{av}(t)$.

$$\dot{q} = \bar{\alpha}(T_{av} - T_w) \tag{1}$$

where T_{av} is the average temperature (see Fig. 1).

The energy balance can be written

$$\dot{q}A = -\rho c V \frac{dT_{av}}{dt} \tag{2}$$

where V is the volume of the slab. Combining Eqs. (1) and (2) gives the basic equation for predicting the variation of temperature with time:

$$\frac{d(T_{av} - T_w)}{dt} + \frac{\alpha A}{\rho c V}(T_{av} - T_w) = 0 \tag{3}$$

Integration of Eq. (3) gives

$$\ln \frac{T_{av} - T_w}{(T_{av} - T_w)_0} = -\frac{A}{\rho c V} \int_0^t \bar{\alpha}\, dt \tag{4}$$

The right-hand side,

$$\frac{A}{\rho c V} \int_0^t \bar{\alpha}\, dt = \frac{A\bar{\alpha}t}{\rho c V} \tag{5}$$

is identical to the number of transfer units:

$$\frac{A\bar{\alpha}t}{\rho c V} = \mathrm{NTU} \tag{6}$$

The solution is then

$$\frac{T_{av} - T_w}{(T_{av} - T_w)_0} = \exp(-\mathrm{NTU}) \tag{7}$$

© 1983 Hemisphere Publishing Corporation

HEDH

The NTU may also be interpreted as the product of two other dimensionless numbers. With

$$\frac{A}{v} = \frac{2}{s} \tag{8}$$

Eq. (6) may be expanded to

$$2\frac{\bar{\alpha}S}{\lambda}\frac{\kappa t}{s^2} = 2\,\overline{\mathrm{Nu}}\,\mathrm{Fo} \tag{9}$$

where $\bar{\alpha}S/\lambda$ is the average Nusselt number $\overline{\mathrm{Nu}}$, and $\kappa t/s^2$ is the Fourier number Fo. Therefore we have by definition in this case,

$$\mathrm{NTU} = 2\,\overline{\mathrm{Nu}}\,\mathrm{Fo} \tag{10}$$

The Fourier number represents the ratio of the cooling time to the thermal relaxation time s^2/κ of the slab. The Nusselt number may be interpreted as the ratio of the thickness s of the slab to an average effective depth of heat penetration into the slab, $\bar{\alpha} = \lambda/s_{\mathrm{eff}}$.

Comparing Eq. (7) with Eq. (3), one recognizes that the number of parameters has been reduced from five to one by introducing the dimensionless quantity NTU. Moreover, if NTU = 2 $\overline{\mathrm{Nu}}$ Fo is large, say, larger than 5, the temperature T_{av} is very nearly equal to the equilibrium temperature T_w, which means that for large NTUs the whole system is in equilibrium.

The time-averaged heat transfer coefficient can be evaluated from a rigorous solution of Fourier s law in combination with the energy balance for a volume element. For practical purposes a semitheoretical correlation can be recommended, which, for a slab, is as follows:

$$\overline{\mathrm{Nu}} = \sqrt{\frac{\pi^4}{4} + \frac{4}{\pi}\frac{1}{\mathrm{Fo}}} \tag{11}$$

(see Sec. 2.4.3).

The same correlation also applies to a moving solid, for example, a moving plastic belt coming from an extruder and running through a cold water bath as shown in Fig. **2.** This problem becomes identical with the problem described in Fig. 1 if heat conduction in the x direction is negligible and if the cooling time t is calculated using the residence time:

$$t = \frac{L}{u_s} \tag{12}$$

Thus Eq. (11) also applies to the moving belt. For convenience, however, Eq. (11) may be rewritten in terms of the Graetz number Gz, by substituting the residence time in the definition of the Fourier number according to Eq. (12):

$$\mathrm{Fo} = \frac{\kappa L}{u_s s^2} = \frac{1}{\mathrm{Gz}} \tag{13}$$

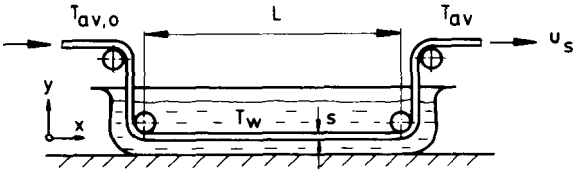

Figure 2 Heat transfer from a moving plastic belt or wire to a water bath kept at t_w = const.

The Graetz number is the reciprocal of the Fourier number and obviously has the same physical interpretation; that is, it is the ratio of the thermal relaxation time s^2/κ to the cooling time t. Equation (11) can then be written as

$$\overline{\mathrm{Nu}} = \sqrt{\frac{\pi^4}{4} + \frac{4}{\pi}\mathrm{Gz}} \tag{14}$$

Now assume that the belt is built up by a number of thinner belts forming a laminated structure as shown in Fig. 3 and consider the case in which the velocity of each layer with thickness As may be different. As a result, the residence time of the material of the whole belt with thickness s will no longer be uniform. The question arises as to how the temperatures in the individual layers change with position z and how much heat will be transferred to the surrounding water bath.

Figure 3 shows the whole belt, which is composed of six layers. Because of symmetry, only three layers are depicted. The temperature gradient at the center line is zero, thus the heat flux through the center plane, $\dot{q}_0$, is also zero. The temperature T_3 is identical to the surface temperature T_w of the whole belt. Applying the energy balance and Fourier s law of heat conduction, one obtains the following set of equations:

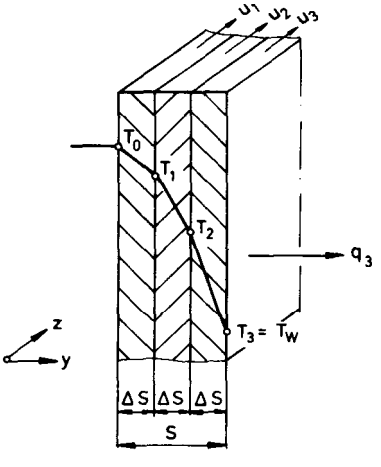

Figure 3 Heat transfer from a laminated belt to a water bath with each layer moving at a different velocity u_j.

© 1983 Hemisphere Publishing Corporation

$$\dot{q}_0 - \dot{q}_1 = \Delta s \rho c u_1 \frac{\Delta T_1}{\Delta z} = \lambda \left(0 - \frac{T_0 - T_1}{s} \right)$$

$$\dot{q}_1 - \dot{q}_2 = \Delta s \rho c u_2 \frac{\Delta T_2}{\Delta z} = \lambda \left(\frac{T_0 - T_1}{\Delta s} - \frac{T_1 - T_2}{\Delta s} \right) \quad (15)$$

$$\dot{q}_2 - \dot{q}_3 = \Delta s \rho c u_3 \frac{\Delta T_3}{\Delta z} = \lambda \left(\frac{T_1 - T_2}{\Delta s} - \frac{T_2 - T_3}{\Delta s} \right)$$

Summing the left-hand side of these equations, one finds that

$$-\dot{q}_3 = \rho c \sum_1^3 \Delta s u_j \frac{\partial T_j}{\partial z} \quad (16)$$

Since

$$\sum_1^3 \Delta s = s$$

$$p \sum_1^3 \Delta s u_j = \rho s u_{av}$$

$$\rho c \sum_1^3 \Delta s u_j T_j = \rho c s u_{av} T_{av} \quad (17)$$

Equation (16) can also be written as

$$_0 - _{43} = s \rho c u_{av} \frac{\partial T_{av}}{\partial z} \quad (18)$$

where T_{av} is the mean calorimetric temperature of the whole belt at any position z, whereas $\dot{q}_3 = \dot{q}_w$ is the heat flux from the outer surface of the whole belt into the water bath.

The right-hand side of Eq. (15) can be written as

$$\lambda \left(\frac{T_{j-1} - T_j}{\Delta s} - \frac{T_i - T_{j+1}}{\Delta s} \right) = \lambda \frac{\partial}{\partial y} \left(\frac{\partial T}{\partial y} \right) \Delta s \quad (19)$$

and one obtains the basic differential equation for the prediction of the temperature distribution with respect to the coordinates y and z:

$$\rho c u(y) \frac{\partial T}{\partial z} = \lambda \frac{\partial^2 T}{\partial y^2} \quad (20)$$

which applies as soon as the number of layers is sufficiently large. The residence time for each layer is $z/u(y)$. The local velocity $u(y) = u_{av} f(y/s)$, so Eq. (20) can be written in dimensionless form as

$$\mathrm{Gz} \frac{\partial T}{\partial (z/L)} = \frac{1}{f(y/s)} \frac{\partial^2 T}{\partial (y/s)^2} \quad (21)$$

where

$$\mathrm{Gz} = \frac{u_{av} s^2}{\kappa L} \quad (22)$$

Equation (21) indicates that the temperature distribution and the heat flux into the water bath for a laminated belt with different velocities for the individual layers depend on the Graetz number only, This is the same result as that obtained previously for the nonlarninated belt. Obviously the form of the velocity distribution function $u(y)$ does not influence the fact that the Graetz number is the only parameter.

Assume as a next step that the laminated belt is replaced by a stationary duct through which air is entering with an inlet temperature $T_{av,0}$ and an outlet temperature T_{av}. The problem is exactly the same as described in Fig. 3 for the laminated belt as long as the airflow is laminar and fully developed, that is, that the air velocity is a function of the coordinate y only. Near the entrance of the duct, however, the flow is not developed and the air velocity is a function of both coordinates y and z. In this region the fluid viscosity ν becomes an additional variable. This is taken into account by the ratio ν/κ, which is called the Prandtl number Pr. The Prandtl number is a ratio of molecular momentum transport to molecular energy transport. For the developing laminar-flow region in ducts, the Nusselt number is a function of the Graetz number and the Prandtl number.

With higher air velocities the flow in the duct becomes turbulent. In this case the heat transfer coefficient depends not only on the residence time t, that is, the Graetz number, but also on the absolute flow velocity u, that is, on the Reynolds number $\mathrm{Re} = us/\nu$. The physical meaning of the Reynolds number can be interpreted on both a macroscopic and a microscopic level. The first requires that we express the Reynolds number in the following way:

$$\mathrm{Re} = \frac{\rho u^2}{\eta (u/s)} = \frac{p}{\tau} \quad (23)$$

This equation indicates that the Reynolds number can be interpreted as the ratio of momentum p associated with the flow to the shear stress τ that the flow exerts onto the wall of the confining duct.

On the microscopic level we refer to the collision theory, which gives the following expression for the viscosity [compare Eqs. 2.1.1(3) and (6)], where w_m is the average velocity of the microscopic particles and σ is the mean free path between two collisions of the particles. The Reynolds number may be rewritten as

$$\mathrm{Re} = 3 \frac{us}{w_m \sigma} = 3 \frac{t_{rad}}{t_{ax}} \quad (24)$$

where $t_{rad} = s/w_m$ is the traveling time of the particle

© 1983 Hemisphere I blishing Corporation

from wall to wall in the radial direction, whereas $t_{ax} = \sigma/u$ is the traveling time of the particle in the axial direction along the net path σ. Assume s to be of the order of 0.10 m. For gases the particles are molecules having an average velocity of 500 m/s and a mean free path at normal pressure and temperature of $\sigma = 0.1\ \mu m$. Usual gas velocities in heat exchangers are about 10 m/s. This gives $t_{rad} = 2 \times 10^{-4}$ s and $t_{ax} = 10^{-8}$ s, which yields a Reynolds number of 60 000. For liquids the particles are phonons having an average velocity of about 5 000 m/s (velocity of sound) and a mean free path of the order of 10^{-9} m (close to the crystal lattice of a solid). Usual liquid velocities in heat exchangers are 1 m/s. This gives $t_{rad} = 2 \times 10^{-5}$ s and $t_{ax} = 10^{-9}$ s, which again yields a Reynolds number of 60 000. These numbers show that in practice the order of magnitude of the Reynolds number is around 10^4-10^5.

Summarizing the various modes of heat transfer from the fluid to the walls of a plane duct gives the following relationships:

Plug flow and fully developed laminar flow:

$$\overline{Nu} = f_p(Gz) \tag{25}$$

Developing laminar flow:

$$\overline{Nu} = f_l(Gz, Pr) \tag{26}$$

Turbulent flow :

$$\overline{Nu} = f_t(Gz, Pr, Re) \tag{27}$$

A general correlation for the Nusselt number must contain three independent variables, as Eq. (27) shows. However, it is a matter of convenience as to which variables are eventually chosen. The set Gz, Pr, Re is very unusual, since the mean fluid velocity appears in both Gz and Re. Combining Gz, Re, and Pr gives a new dimensionless variable,

$$\frac{Gz}{Re\ Pr} = \frac{s}{L} \tag{28}$$

which is merely a geometric relationship. The expression for turbulent flow is thus

$$\overline{Nu} = f_t\left(Gz, Pr, \frac{s}{L}\right) \tag{29}$$

For numerical calculations the set Re, Pr, s/L is most widely used. In U.S. literature one often finds a modified Nusselt number, the Colbourn j factor,

$$j = \frac{\overline{Nu}}{Re\ Pr^{1/3}} \tag{30}$$

which is expressed as a function of the variables Re, Pr, and s/L. If the plane duct is replaced by a circular tube, s/L is replaced by d/L. Remember that in turbulent flow $\overline{Nu}$ is proportional to $Re^{0.8}$, Eq. 1.2.3(21), so that the j factor is proportional to $Re^{-0.20}$. This reveals an analogy to the friction factor, which for turbulent flow in smooth tubes is also proportional to $Re^{-0.20}$, Eq. 1.2.3(12). Since the pressure drop is as important in heat exchanger design as heat transfer, the use of the j factor alleviates the simultaneous consideration of both phenomena.

The Prandtl number is characteristically about 0.7 for gases, about 7 for liquids such as water, and up to 1 000 for very viscous liquids. For a quick orientation, four graphic representations of $\overline{Nu} = \overline{Nu}(Gz, d/L)_{Pr=const}$ or $Nu = Nu(Re, d/L)_{Pr=const}$ might be quite useful. The four graphs in Fig. 4 show the Nusselt number as a function of the Graetz number according to the equations given above. This representation takes advantage of the fact that the number of transfer units NTU is connected with Nu and Gz by definition. For tube flow one obtains

$$\overline{Nu} = \overline{NTU}\,\frac{Gz}{4} \tag{31}$$

Consequently, Fig. 4 also shows lines of constant NTU, which is useful information, indicating how close the heat transfer process has come to an equilibrium.

The Nusselt number is a measure of the intensiveness of the heat transfer process. The number of transfer units is a measure of the effectiveness of the heat transfer process. In laminar flow a high effectiveness is paid for by a low intensiveness, whereas a high intensiveness is always accompanied by a low effectiveness of the heat transfer process. It is only in turbulent flow that both high effectiveness and high intensiveness may be achieved simultaneously.

Some interpretation of the graphs in Fig. 4 might be useful:

1. In the transition regime between laminar and fully developed turbulent flow, the Nu number varies almost linearly with the Graetz number. Since the Graetz number is directly proportional to the volume flow rate $\dot{V}$ in the tube ($Gz = ud^2/\kappa L = 4\dot{V}/\pi\kappa L$), this has the consequence that a variation of the volume flow rate $\dot{V}$ does not effect the outlet temperature of the fluid (NTU = const).

2. Within this regime one may also change the tube length, say, by a factor of 10, without experiencing a significant change in the $\overline{NTU}$. Keeping d/L constant means that when L is changed by a factor of 10, d is also changed by a factor of 10. Thus the surface area A is changed by a factor of 100 without any significant change in NTU and the outlet temperature of the fluid. Of course, keeping the flow rate constant under these conditions means that the pressure drop will be changed by a factor of 10^4. This example shows that the rating and design of heat

© 1983 Hemisphere publishing Corporation

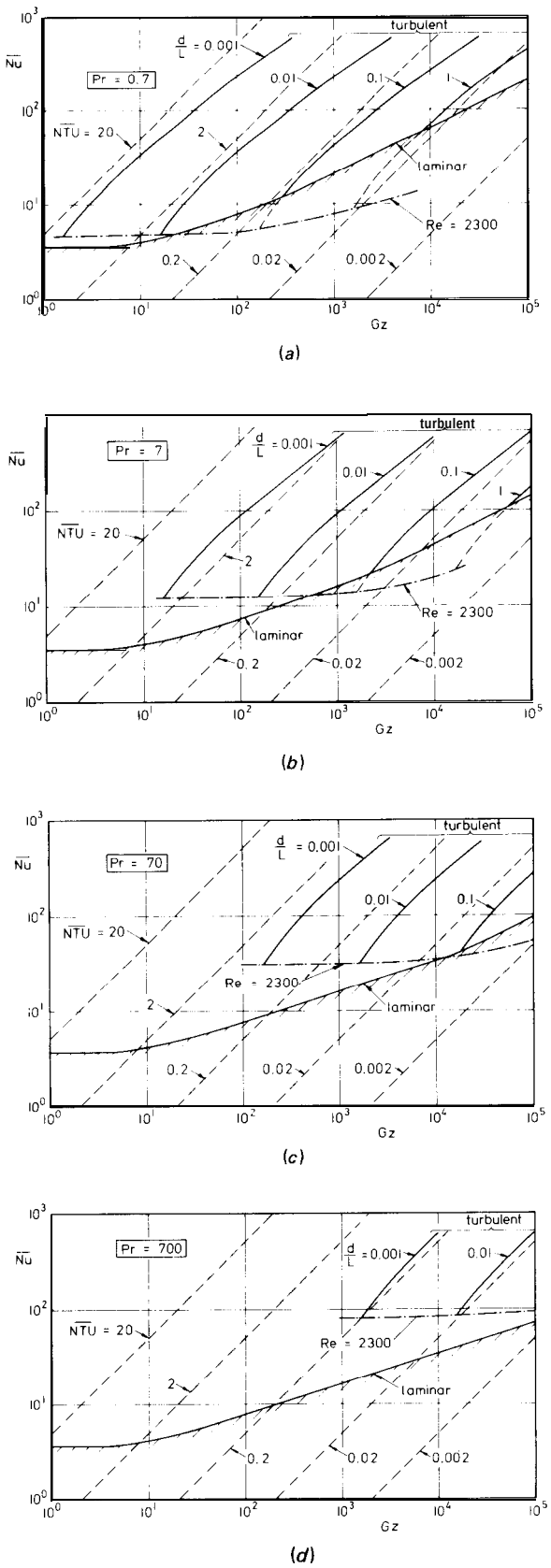

Figure 4 Heat transfer in laminar and turbulent tube flow in the form Nu = Nu(Gz, Pr, *d/L*) for constant wall temperature.

exchanger may be not a heat transfer but a hydraulic problem.

3. The NTU has a twofold meaning, which can be demonstrated by writing the equation

$$\frac{T_{in} - T_{out}}{\Delta T_{LM}} = \overline{NTU} = \frac{\bar{\alpha} A}{\rho c \dot{V}} \qquad (32)$$

The left-hand side is the ratio of temperature change to temperature difference. This ratio represents the thermal requirements that are to be matched by the heat exchanger. The right-hand side is the ratio of heat transfer capacity to heat storage capacity and represents a combined property of the heat exchanger that is to match the thermal requirements.

Assume that the left-hand side is given. A countercurrent heat exchanger in an air liquifier has to cool the incoming air down to -180° C and simultaneously to warm up the exhaust air from -178° C to +20°C. With a temperature difference of, say, 2°C, the NTU is 100.

One can see immediately from Fig. 4*a* (Pr = 0.7) that the heat exchanger must be built up with a number of very thin and long tubes ($L > 1\,000d$). This is actually true; such heat exchangers have tubes of about 6-10 mm diameter and up to 100 m length ($L \sim 10^4 d$).

4. For any given NTU there is always a Graetz number at which this NTU can be realized in laminar flow. For any given total flow rate $\dot{V}$ and any simultaneously given flow velocity u, one is free to choose a small number of parallel tubes of large diameter or a large number of tubes of small diameter in order to build a heat exchanger that can match the given NTU. It may be asked if there is an optimum number of parallel tubes. The answer can be obtained as follows:

Let n be the arbitrary number of parallel tubes. The Graetz number is

$$Gz = \frac{4}{\pi} \frac{V}{nd^2} \frac{d^2}{\kappa L} = f(\overline{NTU}) = \text{const} \qquad (33)$$

This means that

$$nL = \text{const}$$

On the other hand, the pressure drop in laminar flow is given by the Hagen-Poiseuille law,

$$\Delta P = 32\eta \frac{4}{\pi} \frac{\dot{V}}{nd^2} \frac{L}{d^2}$$

Assume as a second requirement that ΔP is to be kept at a given finite value. Then one obtains a second condition:

$$nd^2 = \text{const}$$

© 1983 Hemisphere Publishing Corporation

Combining the two conditions yields $d^2/L = \text{const.}$ As long as this resulting condition is fulfilled, one may choose any number n of parallel tubes; NTU, as well as ΔP, will remain unaffected. In the limit n may go to infinity while L and d go to zero. This means that a finite amount of heat can be transferred with a finite pressure drop in a heat exchanger of finite cross-sectional area, but with zero length and therefore with zero surface area. The problem, however, is how to distribute the second medium within the heat exchanger having a large number of very small and very short tubes. One realizes that in this case the problem is to design appropriate headers and turnarounds.

Figure 5 shows an alternative presentation of the same correlations as given in Sec. 2.5.1, but in the form

$$\text{Nu} = \text{Nu}\left(\text{Re}, \text{Pr}, \frac{d}{L}\right)$$

The same interrelationships can also be given in the form of the j factor in Fig. 6. All these three-parameter presentations, $\text{Nu}(\text{Gz}, \text{Pr}, d/L)$, $\text{Nu}(\text{Re}, \text{Pr}, d/L)$, and $j(\text{Re}, \text{Pr}, d/L)$, are equivalent.

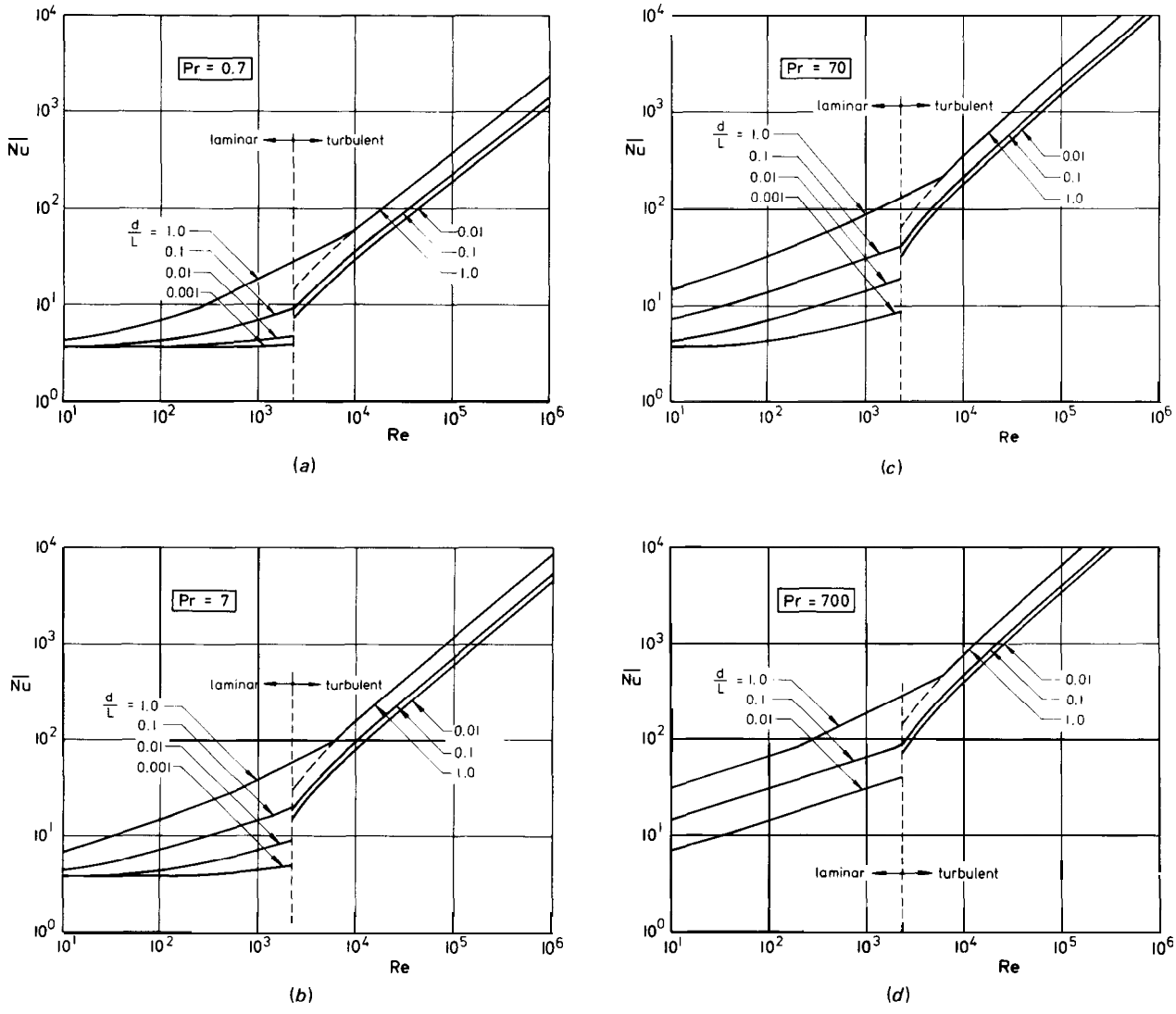

Figure 5 Heat transfer in laminar and turbulent tube flow in the form $\text{Nu} = \overline{\text{Nu}}(\text{Re}, \text{Pr}, d/L)$ for constant wall temperature.

© 1983 Hemisphere Publishing Corporation

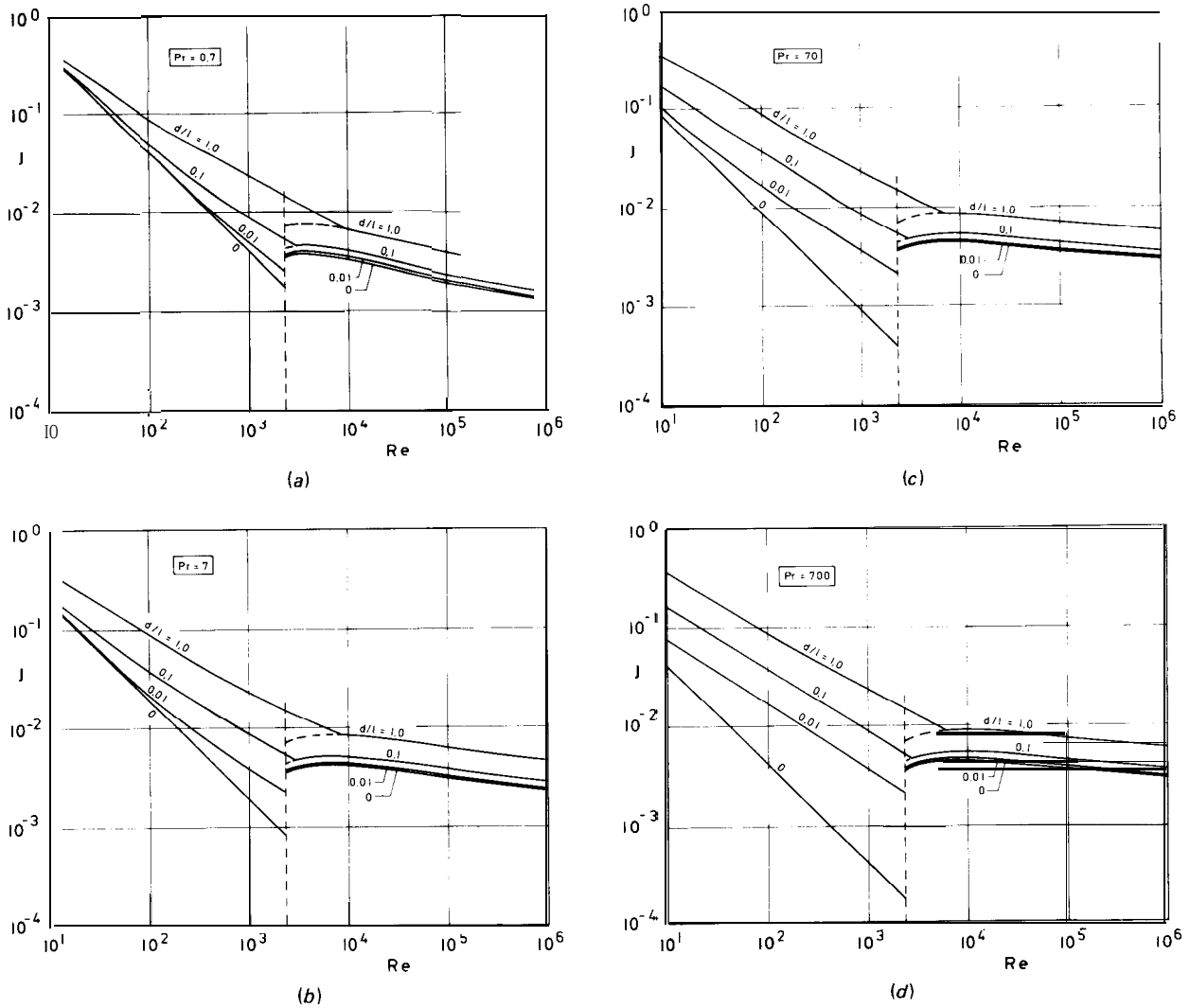

Figure 6 Heat transfer in laminar and turbulent tube flow in the form $j = j(\mathrm{Re}, \mathrm{Pr}, d/L)$ for constant wall temperature.

Nomenclature for Section 2.1.3 appears at the beginning of Part 2.

© 1983 Hemisphere Publishing Corporation

2.1.4

Heat and mass transfer in uniform and nonuniform systems

E. U. Schlünder

■ Standard formulas for average as well as for local heat transfer coefficients are calculated not only for standard boundary conditions, such as constant wall temperature, but also for standard geometric configurations. The prototype for heat transfer in channel flow is the circular tube, whereas the prototypes for external flow are the flat plate, the cylinder, and the sphere. In general, all types of heat exchangers and equivalent equipment (tubular reactors, dryers, etc.) are more or less regular assemblies of standard elements such as tube bundles, tube banks, double pipes, packed beds, and so on.

As long as such assemblies are uniformly arranged, one may expect the heat and mass transfer to each element within the assembly to be the same or at least proportional to the heat and mass transfer to a single element. This can be demonstrated by the following example. Consider a shell-and-tube heat exchanger with the shell side held at constant temperature by some evaporating liquid (Fig. 1). If the tube-side heat transfer coefficient is the rate-controlling one, the $\bar{U}$-$\bar{\alpha}$ method applies. The heat transfer coefficient for flow in a single tube, laminar or turbulent flow, can be predicted for a given fluid velocity. If all tubes are of the same size and if the flow resistance in the tubes controls the fluid velocity, the heat transfer coefficients $\bar{\alpha}_1$ are the same for each tube. The fluid temperature will change from $T_{1,0}$ at the inlet to T_1 at the outlet according to

$$\frac{T_1 - T_2}{T_{1,0} - T_2} = \exp\left(-\frac{\bar{\alpha}_1 A}{\rho_1 c_1 \dot{V}_1}\right) \tag{1}$$

which follows immediately by combining the flux equation $\dot{q} = \bar{\alpha}_1 (T_1 - T_2)$ and the energy balance $(\rho c \dot{V})_1 dT_1 = -\dot{q}\, dA$ for a single tube. The group

$$\frac{\bar{\alpha}_1 A}{(\rho c \dot{V})_1} = \overline{\mathrm{NTU}}, \tag{2}$$

is the number of transfer units for a single tube, which is identical to that for the whole bundle. T_1 approaches the wall temperature T_2 as NTU_1 increases, which indicates that either $\bar{\alpha}_1 A$ is large or that $(\rho c \dot{V})_1$ is small. This is the typical behavior of a uniform tube system.

Now we shall consider a tube bundle with n smaller tubes all having diameter d_s and one larger tube having diameter d_ℓ, thus forming a prototype of a nonuniform system. Since the pressure drop of the fluid is the same in each tube, the volume flow rate in the larger tube will be larger. The respective flow rates are related as

$$\frac{\dot{V}_\ell}{\dot{V}_s} = \left(\frac{d_\ell}{d_s}\right)^m \tag{3}$$

where m is equal to 4 in laminar flow and 2.5 in

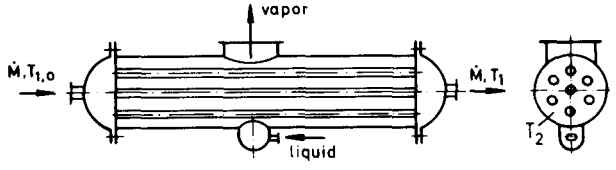

Figure 1 Shell-and-tube heat exchanger with shell-side evaporation cooling as an example for a uniform system (all tubes having the same diameter) and a nonuniform system (one tube may have a larger diameter than all the others).

© 1983 Hemisphere Publishing Corporation

turbulent flow. Consequently, according to Eq. (2), the NTU of the large tube is smaller than that of the small ones. The change in the fluid temperature T_1 is smaller in the large tube, since

$$\left(\frac{T_1 - T_2}{T_{1,0} - T_2}\right)_{\text{large}} = \exp\left(-\overline{\text{NTU}}_{\text{large}}\right) \tag{4}$$

whereas for the small tubes

$$\left(\frac{T_1 - T_2}{T_{1,0} - T_2}\right)_{\text{small}} = \exp\left(-\overline{\text{NTU}}_{\text{small}}\right) \tag{5}$$

applies. The average fluid outlet temperature is the mixing cup temperature of the two different outlet temperatures as given above:

$$\frac{T_{1,\text{av}} - T_2}{T_{1,0} - T_2} = \frac{\dot{V}_\varrho}{\dot{V}_\varrho + n\dot{V}_s}\left(\frac{T_1 - T_2}{T_{1,0} - T_2}\right)_\varrho + \frac{n\dot{V}_s}{\dot{V}_\varrho + n\dot{V}_s}\left(\frac{T_1 - T_2}{T_{1,0} - T_2}\right)_s \tag{6}$$

The average number of transfer units of the nonuniform system correlates to the average outlet temperature:

$$\text{NTU}_{\text{av}} = -\ln\frac{T_{1,\text{av}} - T_2}{T_{1,0} - T_2} \tag{7}$$

Combining Eq. (7) with Eqs. (6), (5), and (4) yields

$$\text{NTU}, = -\ln\left[\frac{V_\varrho}{\dot{V}_\varrho + n\dot{V}_s}\exp\left(-\text{NTU}\right)_\varrho + \frac{n\dot{V}_s}{\dot{V}_\varrho + n\dot{V}_s}\exp\left(-\text{NTU}\right)_s\right] \tag{8}$$

Defining an average Graetz number Gz, by, for example, introducing an average hydraulic diameter, one obtains by definition an average Nusselt number $\overline{\text{Nu}},$:

$$\overline{\text{Nu}}_{\text{av}} = \text{NTU}_{\text{av}}\tfrac{1}{4}\,\text{Gz},, \tag{9}$$

The same definition applies to

$$\overline{\text{Nu}}_\varrho = \text{NTU}_\varrho\tfrac{1}{4}\,\text{Gz} \tag{10}$$

and

$$\overline{\text{Nu}}_s = \text{NTU}_s\tfrac{1}{4}\,\text{Gz}, \tag{11}$$

Thus, combining Eq. (8) and Eqs. (9)-(11) with the general correlations $\text{Nu}\{\text{Gr}, \text{Pr}, d/L\}$, given in Sec. 2.5.1 for single tubes, allows prediction of the average quantities NTU,, and $\overline{\text{Nu}}_{\text{av}}$ from the individual quantities $\text{NTU}_{\varrho,s}$ and $\overline{\text{Nu}}_{\varrho,s}$.

A discussion of Eq. (8) in more detail leads to the following conclusions:

1. If both individual NTUs are low, that is, the whole system is far from equilibrium, Taylor series expansion of Eq. (8) gives

$$\text{NTU}_{\text{av}} = \frac{V_\varrho}{\dot{V}_\varrho + n\dot{V}_s}\overline{\text{NTU}}_\varrho + \frac{n\dot{V}_s}{\dot{V}_\varrho + n\dot{V}_s}\overline{\text{NTU}}_s \tag{12}$$

and

$$\overline{\text{Nu}},, = \frac{A_\varrho}{A_\varrho + nA_s}\overline{\text{Nu}}_\varrho + \frac{nA_s}{A_\varrho + nA_s}\overline{\text{Nu}}_s \tag{13}$$

This means that the average number of transfer units is the flow rate-weighted arithmetic mean of the individual NTUs, whereas the average Nusselt number is the surface area-weighted arithmetic mean of the individual $\overline{\text{Nu}}$'s.

Transfer processes in this regime, where the individual NTUs are low. are called ***kinetically controlled processes.***

2. If both individual NTUs are high, that is, the whole system is very close to equilibrium, Eq. (8) yields

$$\text{NTU},, = \boldsymbol{K}\frac{\overline{\text{Nu}}_\infty}{\frac{1}{4}\,\text{Gz}_{\text{av}}} \tag{14}$$

and

$$\overline{\text{Nu}},, = \boldsymbol{K}\,\overline{\text{Nu}}_\infty \tag{15}$$

with $\boldsymbol{K} = [1 + n(d_s/d_\varrho)^4]/(1 + n)$ and $\overline{\text{Nu}}_\infty = 3.65$ for laminar flow. $\overline{\text{Nu}},$ is the terminal value of the Nusselt number for a single tube.

The average Nusselt number could fall far below this terminal value, since depending on n and d_s/d_ϱ the number $\boldsymbol{K}$ could be less than 1 by orders of magnitude. Transfer processes in this regime, where all the individual NTUs are high, are called *equilibrium-controlled processes.*

3. If NTU_ϱ is low, however, and NTU, is high, Eq. (8) yields

$$\overline{\text{NTU}}_{\text{av}} = -\ln\frac{\dot{V}_\varrho}{\dot{V}_\varrho + n\dot{V}_s} \tag{16}$$

and

$$\overline{\text{Nu}}_{\text{av}} = \frac{\text{Gz}_{\text{av}}}{4}\left(-\ln\frac{\dot{V}_\varrho}{\dot{V}_\varrho + n\dot{V}_s}\right) \tag{17}$$

This means that the average number of transfer units NTU,, does not depend on the heat transfer coefficient $\bar{\alpha}$, the surface area A, the throughput $\dot{V}$, or the thermal properties of the fluid, but only on the throughput ratio $\dot{V}_\varrho/(\dot{V}_\varrho + n\dot{V}_s)$. This throughput ratio depends on the diameter ratio d_ϱ/d_s and the friction factors f_ϱ and f_s. Since these are purely hydraulic properties, the average number of transfer units, NTU_{av}, as well as the average Nusselt number $\overline{\text{Nu}},$,

© 1983 Hemisphere Publishing Corporation

are purely hydraulic properties of the nonuniform system.

Transfer processes in this regime, where one individual NTU is high while the other is low, are called ***hydraulically controlled processes.***

What happens physically in this regime is that the small tubes perform an almost perfect equilibrium, while the fluid temperature in the large tube remains practically unchanged. So, one might say, if the diameter distribution in a nonuniform system is wide enough, this system produces nothing but a mixture of perfect equilibria and perfect nonequilibria. This makes it comprehensible that the average NTU of the nonuniform system does not depend on the transport properties of the fluid, the surface area, and so on. For a more detailed analysis, see [9,10].

Figures 2 and 3 show an evaluation of Eq. (8) for various parameters n and d_ℓ/d_s. One recognizes the hydraulically controlled regime, where NTU, is almost constant. One even recognizes that to some extent NTU_{av} decreases with decreasing Gz, that is, with decreasing throughput, which is quite the opposite behavior to that expected for a uniform system. The reason for this is again a purely hydraulic effect. Since the friction factor for the small tubes increases more than that for the large tube as the throughput (and thus the Reynolds number or the Graetz number) decreases, the flow rate ratio $\dot{V}_\ell/(\dot{V}_\ell + n\dot{V}_s)$ will increase, thus giving a lower effectiveness for the whole system. This is also the reason that in the hydraulically controlled regime, $\overline{Nu}_{av} \sim Gz^{(1+x)}$ with x up to 0.5, as can be seen from Figs. 2 and 3.

The most important statement, however, is that the average Nusselt number $\overline{Nu}_{av}$ in the hydraulically

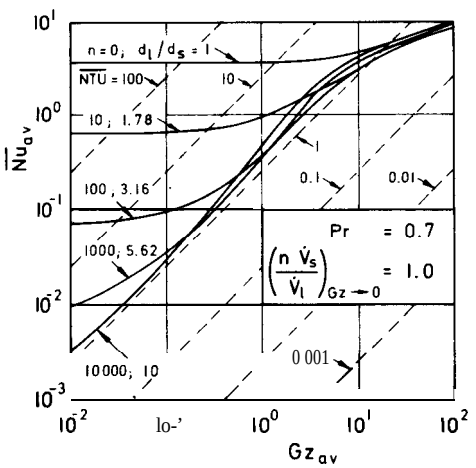

Figure 2 Heat transfer in nonuniform systems represented by a tube bundle having n smaller tubes of diameter d_s and one larger tube of diameter d_ℓ. Fifty percent of the total throughput is passing through the one larger tube as the total throughput goes to zero.

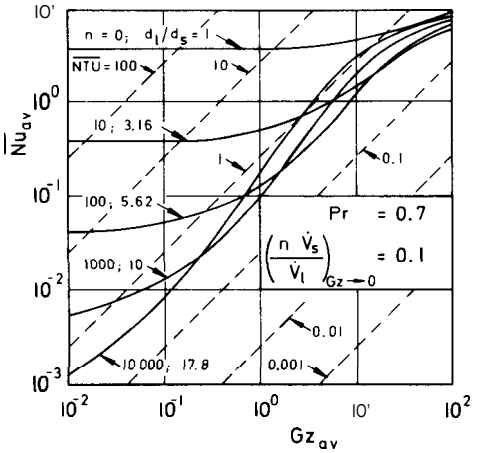

Figure 3 As Fig. 2, except that 91% of the total throughput is passing through the one larger tube as the total throughput goes to zero.

controlled regime no longer has the physical meaning of a heat transfer coefficient. It would be completely wrong to compare such an average transfer coefficient, with, for example, the rate constant of a chemical reaction in order to decide whether the reaction is transfer- or reaction-controlled. In such cases one has to evaluate the individual process in each channel separately.

Most industrial equipment such as heat exchangers, dryers, tubular reactors, packed towers, fluidized beds, and spray and bubble columns are more or less nonuniform systems. For a tubular reactor, for example, it is well known that the void fraction near the tube wall is larger than in the middle of the tube. If this is modeled according to Fig. 4 and assuming that the void fraction near the wall is 0.5 while in the bulk it is 0.4 for a randomly packed bed of spherical particles, the model predicts a very drastic drop in the average Nusselt number for the low Reynolds number region (see Fig. 5). This is in quite good agreement with many experimental results (see [11] and Sec. 2.5.4).

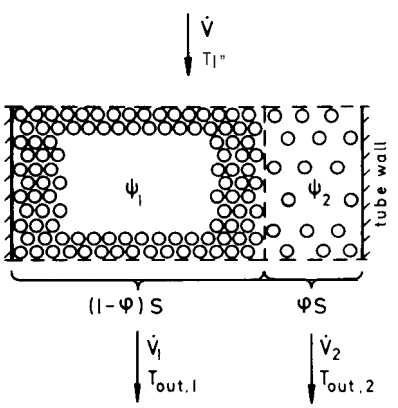

Figure 4 Modeling of a packed bed as a nonuniform system.

© 1983 Hemisphere Publishing Corporation

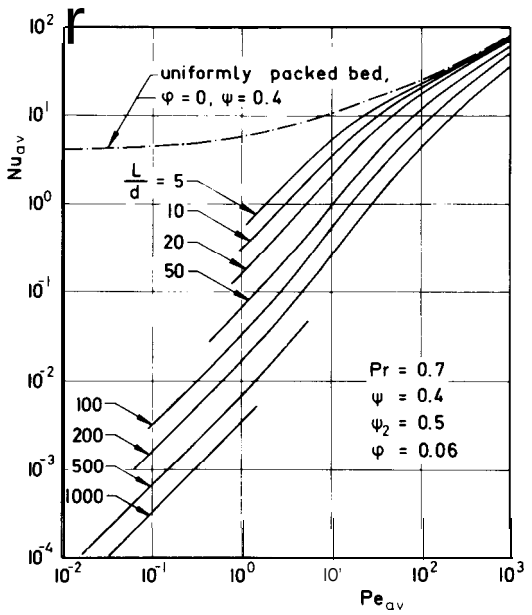

Figure 5 Heat transfer in a packed bed of spheres confined by rigid walls, e.g., as in a tubular reactor. L = height of the packed bed and d = particle diameter.

This result is remarkable since only a slight nonuniformity of the void fraction, that is, 6% of the total cross-sectional area, has a 25% larger void fraction and may cause the packed beds to operate in the hydraulically controlled region, where the average Nusselt number can no longer be interpreted as a heat transfer coefficient. Similar results have also been obtained for fluidized beds (see Sec. 2.5.5). Heat transfer in tube banks as well as in shell-and-tube heat exchangers may be seriously affected through nonuniform flow rate distributions.

The nonuniform system may show, not only quantitatively but also physically, completely different heat and mass transfer characteristics from the uniform system. It may be completely misleading to treat a nonuniform system as a quasiuniform one by introducing average quantities, such as average hydraulic diameters, average fluid velocities, or average heat transfer coefficients. In such cases only a so-called microflow analysis will lead to physically reasonable results, which may be used for more reliable scale-up predictions.

Nomenclature for Section 2.1.4 appears at the beginning of Part 2. References appear at the end of Section 2.1.7.

© 1983 Hemisphere Publishing Corporation

2.1.5

Analogy between heat and mass transfer and its limitations

E. U. Schlünder

■ In Secs. 2.1 .l-2.1.4, single-phase heat transfer without phase change has been considered. In many practical cases, such as in condensation, evaporation, drying, and chemical reactions, phase changes occur. In all these cases, in particular if mixtures are involved, the heat transfer process is accompanied, and also affected by, the mass transfer processes. Therefore it seems appropriate to make a few remarks on the fundamentals of mass transfer and also on combined heat and mass transfer, which may be helpful to a better understanding of a number of technical transfer processes involving mass transfer.

The basic law controlling all types of contact heat transfer is Fourier s law of heat conduction [see Eq. 2.1.1(4)] . The basic law for mass transfer is Fick s law of diffusion as given by Eq. 2.1.1(5). However, Eq. 2.1.1(5) represents only a special case, in which the diffusivities of all species are equal, and the net flux

$$\dot{n} = \Sigma \dot{n}_j \tag{1}$$

vanishes. In general, the situation is not always that simple. If $\dot{n} \neq 0$ and the binary diffusivities δ_{ji} are different, one should start with the Stefan-Maxwell equations, which have been derived for dilute gases [12]:

$$A \frac{\partial \tilde{x}_j}{\partial z} = \sum_{i=1} \frac{1}{\tilde{\rho}\delta_{ji}} (\tilde{x}_j \dot{N}_i - \tilde{x}_i \dot{N}_j) \tag{2}$$

where A = surface area perpendicular to the fluxes $\dot{N}_i$
$\dot{N}$ = molar flux
$\tilde{\rho}$ = molar density
$\tilde{x}$ = mole fraction
z = direction of the flux
δ_{ji} = binary diffusivities

If all binary diffusivities are equal, that is, $\delta_{ji} = 6$, Eq. (3) can be rewritten explicitly with respect to the flux:

$$\dot{N}_j = -A\tilde{\rho}\delta \frac{\partial x_j}{\partial z} + \dot{N}\tilde{x}_j \tag{3}$$

where $\dot{N}$ is the net flux according to Eq. (1).

Alternatively, defining a quasibinary multicomponent diffusivity δ_{jm} by the equation

$$\dot{N}_j = -A\tilde{\rho}\delta_{jm} \frac{\partial x_j}{\partial z} + \dot{N}\tilde{x}_j \tag{4}$$

one finds by comparison with Eq. (2) that

$$\frac{1}{\delta_{jm}} = \frac{\sum_i (1/\tilde{\rho}\delta_{ji})(\tilde{x}_i \dot{N}_j - \tilde{x}_j \dot{N}_i)}{\dot{N}_j - \tilde{x}_j \dot{N}} \tag{5}$$

Equation (5) is particularly convenient if, say, component 1 is in large excess. Then

$$\delta_{jm} = \delta_{ji} \tag{6}$$

In binary mixtures δ_{ji} always equals δ_{ij} by definition. The basic equations (2) and (4) have been written in molar quantities, which is convenient in many cases and always applies as long as momentum transfer by diffusional processes is negligible. If, however, momentum transfer is to be taken into account, as for example in boundary-layer phenomena, the basic equations (2) and (4) must be written in mass quantities. It may happen that, although the net flux in the molar

© 1983 Hemisphere Publishing Corporation

system is zero, the net flux in the mass system does not vanish, due to different molar masses of the various species.

The analogy between heat and mass transfer is perfect as long as the net mass flux is zero and all binary diffusivities are equal. Furthermore, the boundary conditions for each component j must be the same as for the analogous heat transfer problem. If one of these conditions is not fulfilled, the analogy between heat and mass transfer is more or less imperfect. As long as the analogy is perfect, the same correlations as given for an equivalent heat transfer problem will hold.

Consider a leaching process for a slab as described in Fig. 1. The initial mole fraction of component 1 may be $\tilde{x}_{1,0}$, the mole fraction of the surface of the slab is kept at $x_{1,w}$; for example by continuous rinsing. Component 1 diffuses toward the wall, while component 2 (water) diffuses toward the center of the slab with the same flux, that is, $\dot{n}_1 = -\dot{n}_2$, so that the molar net flux is zero. Defining a (time-dependent) mass transfer coefficient β by the flux equations

$$\dot{n}_1 = \tilde{\rho}\beta(\tilde{x}_{1,\mathrm{av}} - \tilde{x}_{1,w}) \tag{7}$$

and

$$\dot{n}_2 = \tilde{\rho}\beta(\tilde{x}_{2,w} - \tilde{x}_{2,\mathrm{av}}) \tag{8}$$

makes this mass transfer problem physically and formally analogous to the respective heat transfer problem as described by Fig. 2.1.3(1), the cooling of a slab. Therefore, the same correlations that have been given for the heat transfer coefficient $\bar{\alpha}$ [see Fig. 2.1.3(4a)], apply also to the prediction of the required leaching time, if the thermal properties in these correlations are replaced by the respective diffusional properties. Thus we obtain the following set of equivalent dimensionless numbers for heat and mass transfer:

Heat transfer	Mass transfer
$\mathrm{Nu} = \frac{\alpha s}{\lambda}$, Nusselt	$\mathrm{Sh} = \frac{\beta s}{\delta}$, Sherwood
$\mathrm{Pr} = \frac{\nu}{\kappa}$, Prandtl	$\mathrm{Sc} = \frac{\nu}{\delta}$, Schmidt
$\mathrm{Fo} = \frac{\kappa t}{s^2}$, Fourier	$\mathrm{Fo} = \frac{\delta t}{s^2}$
$\mathrm{Pe} = \frac{us}{\kappa}$, Péclet	$\mathrm{Pe} = \frac{us}{\delta}$
$\mathrm{Gz} = \frac{us^2}{\kappa L}$, Graetz	$\mathrm{Gz} = \frac{us^2}{\delta L}$

Equation 2.1.3(4) can be rewritten for the solution of the equivalent mass transfer problem:

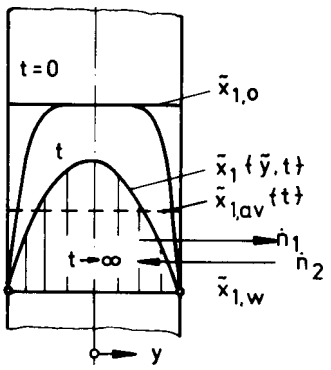

Figure 1 Concentration profiles when leaching a slab-analogy to the temperature profiles when cooling a slab as shown in Fig. 2.1.3(1).

$$\mathrm{Sh} = \sqrt{\frac{\pi^4}{4} + \frac{4}{\pi}\frac{1}{\mathrm{Fo}}} \tag{9}$$

The situation is different if the net flux $\dot{n}$ is not negligible. This is the case in many technical processes such as drying, catalysis, absorption, and combustion. For a binary mixture, such as vapor and air in a drying process, Eq. (3) applies, since $\delta_{12} = \delta_{21} = 6$. With $CH_4 \rightarrow 2H_2 + C$ at a carbon interface, a binary mixture is formed to which Eq. (3) applies. (See Figs. 2 and 3.)

Integration of this equation for steady-state diffusion through a stagnant fluid film yields for the diffusional flux of species j:

$$\dot{n}_j = \tilde{\rho}\frac{\delta}{s}\dot{\nu}_j \ln\frac{\dot{\nu}_j - \tilde{x}_j}{\dot{\nu}_j - \tilde{x}_{j,0}} \tag{10}$$

where

$$\nu_j = \frac{\dot{n}_j}{\Sigma \dot{n}_i} \tag{11}$$

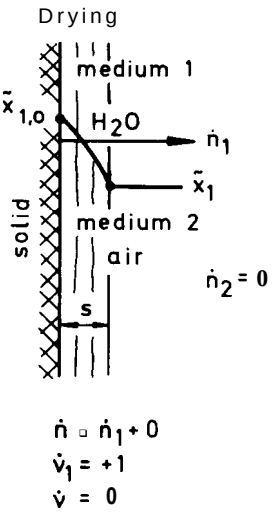

Figure 2 Vapor concentration profile $\tilde{x}_1(s)$ in a viscous sublayer of air flowing over a wet solid.

© 1983 Hemisphere Publishing Corporation

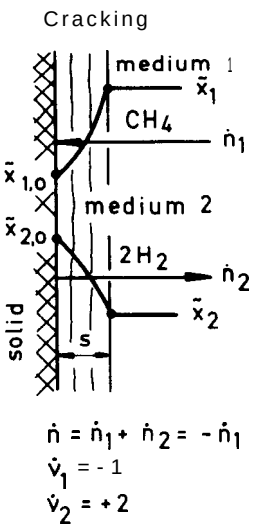

Figure 3 Concentration profiles of methane and hydrogen in a viscous sublayer of the reaction gas flowing over a catalytic solid surface.

are the stoichiometric factors. $\tilde{x}_{j,0}$ is the mole fraction at the solid interface, and $\tilde{x}_j$ is the bulk concentration.

The unsteady-state solution of Eq. (3) gives an approximate equation for the time-averaged flux of

$$\dot{n}_j \cong \tilde{\rho}\,\frac{2}{\sqrt{\pi}}\sqrt{\frac{\delta}{t}}\,\dot{\nu}_j \ln\frac{\dot{\nu}_j - \tilde{x}_{j,0}}{\dot{\nu}_j - \tilde{x}_j} \tag{12}$$

assuming a constant mole fraction at the interface $x_{j,0}$.

Introducing a mass transfer coefficient for the steady state,

$$\bar{\beta}_{t\to\infty} = \frac{\delta}{s} \tag{13}$$

and for the transient state,

$$\bar{\beta}_{t\to 0} = \frac{2}{\sqrt{\pi}}\sqrt{\frac{\delta}{t}} \tag{14}$$

we could again apply the $\bar{\beta}$ concept and obtain as a basic flux equation

$$\dot{n}_j = \tilde{\rho}\bar{\beta}\dot{\nu}_j \ln\frac{\dot{\nu}_j - \tilde{x}_{j,0}}{\dot{\nu}_j - \tilde{x}_j} \tag{15}$$

The value of $\bar{\beta}$ can be obtained from Eq. (9), and the flux equation predicts the flux of each species in a binary mixture in a manner perfectly analogous to that used in prediction of a heat flux. The only difference is that the driving potential has a logarithmic form instead of a linear one as in Eqs. (7) and (8). However, if the mole fractions $\tilde{x}_j$ are low compared to the stoichiometric factors $\dot{\nu}_j$, Eq. (15) may be expanded to give

$$\lim_{\tilde{x}_j/\dot{\nu}_j\to 0} \dot{n}_j = \tilde{\rho}\beta(\tilde{x}_{j,0} - \tilde{x}_j) \tag{16}$$

which is again the simpler linear relationship.

In the literature one finds the ratio

$$\frac{\dot{n}_j}{\lim_{\tilde{x}_j/\dot{\nu}_j\to 0} n_j} = \frac{\dot{\nu}_j \ln(\dot{\nu}_j - \tilde{x}_{i,0})/(\dot{\nu}_j - \tilde{x}_j)}{\tilde{x}_{j,0} - \tilde{x}_j} = \phi \tag{17}$$

called an ***enhancement factor.*** It may also be referred to as the Ackermann correction factor or the Stefan flow correction factor. This factor ϕ is applied to the basic flux equation in the following fashion:

$$\dot{n}_j = \tilde{\rho}\,\bar{\beta}^0(\tilde{x}_{j,0} - \tilde{x}_j) \tag{18}$$

where (see [12])

$$\bar{\beta}^0 = \bar{\beta}\phi \tag{19}$$

The analogy between heat and mass transfer also applies as a first approximation to binary mass transfer problems with a nonvanishing net flux.

The situation becomes more difficult in the case of multicomponent mass transfer. However, the analogy still holds if one component is in large excess. Equations (4) and (5) apply and we obtain ***k flux*** equations of the type (***k*** = number of components)

$$\dot{n}_j = \tilde{\rho}\,\bar{\beta}_j\dot{\nu}_j \ln\frac{\dot{\nu}_j - \tilde{x}_{j,0}}{\dot{\nu}_j - \tilde{x}_j} \tag{20}$$

which can usually be reduced to the linear equation (16), since all $\tilde{x}_j$'s are smaller than the $\dot{\nu}_j$ except for those of the excess component.

Another special case of multicomponent mass transfer is obtained when all binary diffusivities are equal. Equation (4) and the analogy also applies. However, one must notice that a component might be transferred with a ***negative linear*** concentration difference, which means that the logarithmic driving potential is always applied in order to obtain correct results.

A special case of multicomponent mass transfer also appears if one component diffuses much faster than all the others. This is particularly true if hydrogen is a constituent of the mixture, because hydrogen diffuses about 10 times faster than, say, benzene. In such cases the concentration of the very-fast-diffusing component is practically constant in the boundary layer and equal to the bulk concentration, so that the whole set of equations for the diffusional flux can be greatly simplified. As an example the catalytic hydrogenation of benzene may be considered (see Fig. 4). Although the bulk concentrations $\tilde{x}_{H_2}$ and $\tilde{x}_{C_6H_6}$ are stoichiometric, the hydrogen concentration at the interface is practically the same as in the bulk. If the diffusivity of hydrogen had been the same as those of the other components, the hydrogen concentration

© 1983 Hemisphere I blishing Corporation

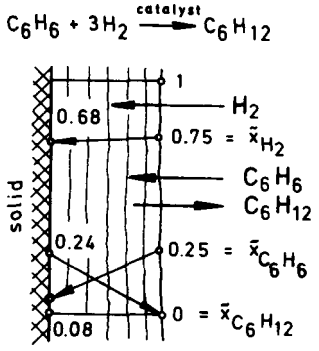

Figure 4 Concentration profiles of hydrogen, benzene, and cyclohexane in a viscous sublayer of the reacting gas flowing over a catalytic solid surface.

would have been zero. Consequently, the ternary mixture H_2, C_6H_6, C_6H_{12} might be treated as a binary one with hydrogen as an inert buffer gas.

Summarizing, one may say that in most practical cases the analogy between heat and mass transfer applies, provided that the correct driving potential in the flux equation is used. This is, in general, of the logarithmic form as given in Eqs. (15) and (20), which although not rigorously developed can usually be introduced without introducing appreciable errors. The analogy breaks down in the most general case, when all binary diffusivities are different, but not too different, and all mole fractions are of the same order of magnitude.

The basic flux equations for multicomponent diffusion Eqs. (2) and (4) have been derived for dilute gases. They might also be applied to multicomponent liquid diffusion, as long as all binary diffusivities are equal. If not, the basic diffusional flux equations must also take into account higher-order effects, which cannot be represented by the analogy.

Nomenclature for Section 2.1.5 appears at the beginning of Part 2. References appear at the end of Section 2.1.7.

© 1983 Hemisphere Publishing Corporation

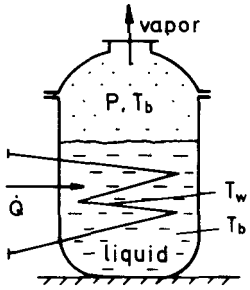

Figure 6 Pool boiling.

temperature difference $AT_{,,}$ where the natural convection regime ends one may use those quantities as parameters to correlate the heat transfer coefficients in the nucleate boiling regime where $AT > AT_{,,}$ and $\alpha > \alpha_{ce}$. A widely used correlation has the form

$$\alpha = \alpha_{ce} \left(\frac{\Delta T}{\Delta T} \right)^m_{ce} \tag{24}$$

where the exponent m may vary from, say, 1 to 4 depending on the pressure, the physical properties of the liquid, and the surface. On the average, $m = 2.5$ may be a fairly good estimate. Also, the critical temperature difference $AT_{,,}$ depends on the same variables as m, and in general these two parameters must be found by experiment.

As the temperature difference AT is further increased, a second critical value, the so-called burnout point, is reached. At this temperature difference ΔT_{cb} the bubbles coalesce, forming a vapor film between the surface and the liquid. Consequently, the heat transfer coefficient goes down by orders of magnitude. Figure 7 shows the heat transfer coefficient α depending on the temperature difference AT for water at 1 bar pressure in a pool boiling experiment for the three regimes described above. A fourth regime appears if

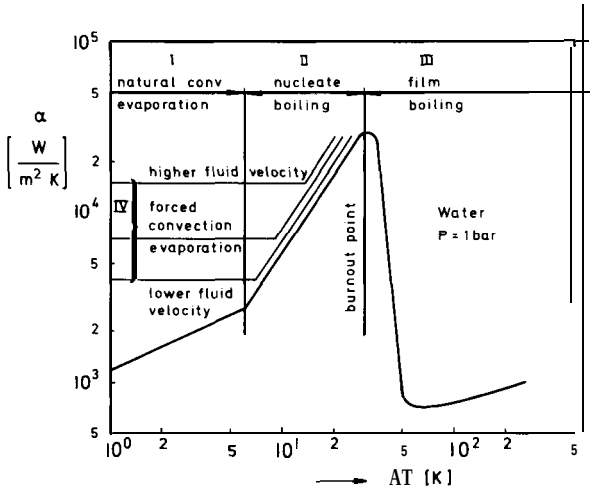

Figure 7 Pool boiling heat transfer coefficient: distinction of various boiling regimes.

by, for example, a stirrer, forced convection is superimposed to the liquid. In this regime no bubble formation occurs and the heat transfer coefficient depends mainly on the fluid velocity but not at all on the temperature difference. Also, in the nucleate boiling regime forced convection enhances the heat transfer up to about 100%. The regimes IV and II normally occur when the liquid evaporates inside horizontal or vertical tubes. As long as the vapor flow quality $\dot{\epsilon}$ is low, regime II prevails, whereas as $\dot{\epsilon}$ becomes larger, regime IV becomes predominant, since the vapor velocity increases considerably with increasing $\dot{\epsilon}$. The heat transfer coefficient in regime IV inside tubes, $\alpha_{2\mathrm{Ph}}$, can be predicted by empirical correlations based on the two-phase flow frictional pressure drop in tubes:

$$\frac{\alpha_{2\mathrm{Ph}}}{\alpha_{1\mathrm{Ph},\ell}} = C(\mathrm{Pr}_\ell) \left(\frac{\Delta P_{2\mathrm{Ph}}}{\Delta P_{1\mathrm{Ph},\ell}} \right)^n \tag{25}$$

The subscript $1\mathrm{Ph},\ell$ in Eq. (25) means single-phase liquid flow. The exponent n is of the order of 0.4-0.5, whereas the coefficient C depends on the Prandtl number for the liquid. The pressure drop $\Delta P_{2\mathrm{Ph}}$ can be predicted by the empirical correlations as given in Sec. 2.3.2.

One should bear in mind, however, that both experimental data as well as the correlations for two-phase flow pressure drop and the respective heat transfer coefficients show a fairly large scatter (±100% and sometimes even more). This is due to the fact that two-phase flow is much less stable than single-phase flow. Even with single-phase flow we have deviations of as much as 100% and more, especially in the transition regime between laminar and turbulent flow. Although we have only one limited transition regime in single-phase flow, we might have many transition regimes in two-phase flow because of the great number of different flow patterns.

The burnout point or second critical temperature difference is of great practical interest when the heat flux $\dot{q} = \alpha$ AT is a prescribed quantity. If the heat flux exceeds the second critical value, the temperature difference will increase by many hundred degrees and, consequently, the heating surface may be destroyed. The prediction of the critical heat flux in the case of pool boiling is based on empirical correlations, which contain basic physical properties. In horizontal tubes the critical heat flux may be decreased up to a factor of 10 by the incomplete wetting of the inner tube surface. In vertical tubes the critical heat flux comes much closer to the pool boiling data.

Evaporation of liquid mixtures involves the same problem as condensing of vapor mixtures, which is the prediction of the liquid temperature. Again one may

© 1983 Hemisphere Publishing Corporation

distinguish various special cases that correspond to certain limiting values of the dimensionless groups $\phi_g = \dot{n}/\tilde{\rho}_g\tilde{\beta}_g = -\ln(\dot{v}_1 - \tilde{y}_1^*)/(\dot{v}_1 - \tilde{y}_1)$ and $\phi_\ell = \dot{n}/\tilde{\rho}_\ell\beta_\ell = -\ln(\dot{v}_1 - \tilde{x}_1)/(\dot{v}_1 - \tilde{x}_1^*)$. In the case of $\phi_g > 5$ and $\phi_\ell < 0.1$, one will achieve the largest separation effect in the case of particle evaporation. Usually these conditions are realized in autoclaves as shown in Fig. 6, since in both regimes-natural convection and nucleate boiling-the phase change occurs at the gas-liquid interface. Then ϕ_g may be estimated as follows*

The evaporation flux at the liquid level is given by

$$\dot{n} = \frac{\alpha_{\text{boiling}} \quad \Delta T \quad A_{\text{coil}}}{\Delta h_{g\ell} \quad A_{\text{liquid interface}}} \tag{26}$$

With α_{boiling} = 5 000 W/m² K, AT = 10 K, $\Delta h_{g\ell}$ = 2 260 kJ/kg, and $A_{\text{coil}}/A_{\text{liquid level}} \cong 10$, one calculates $\dot{n} = 0.22$ kg/m² s. The vapor-side mass transfer coefficient $\rho_g\beta_g$ may be estimated from the Lewis law $\rho_g\beta_g = \alpha_g/c_{pg}$ = 5 X 10^{-3} kg/m² s, with α_g = 10 W/m² K and c_{pg} = 2 kJ/kg K. This gives ϕ_g = 44 > 5. One may also estimate ϕ_ℓ. Boiling water at 1 bar has a temperature at the interface of 100°C, whereas the bulk is slightly superheated and has a temperature of 100.4°C at the most. From these data we estimate a liquid-phase heat transfer coefficient at the liquid interface of $\alpha_{\text{interface}} = \alpha_{\text{boiling}}(A_{\text{coil}}/A_{\text{interface}})(\Delta T/\Delta T_{\text{interface}})$, which gives $\alpha_{\text{interface}} = 1.25 \times 10^6$ W/m² K. The Lewis number of the liquid (water) is $\text{Le}_\ell = \kappa_\ell/\delta_\ell$, which gives $\text{Le}_\ell = 140$ with $\kappa_\ell = 1.4 \times 10^{-3}$ cm²/s and $\delta_\ell = 10^{-5}$ cm²/s. Applying the Lewis law gives $\rho_\ell\beta_\ell = \text{Le}^{-0.6}\,\alpha_{\text{interface}}/c_{p\ell} = 15$ kg/m² s. This gives $\phi_\ell = 0.22/15 = 0.015$ <O.l.

These numbers mean that in the liquid the composition at the interface $\tilde{x}_1^*$ is equal to the bulk composition $\tilde{x}_1$, whereas the instantaneous vapor flux v_1 is always in equilibrium with the liquid; that is, $\dot{v}_1 = \tilde{y}_1^*(\tilde{x}_1)$. This kind of evaporation is also called an ***open distillation process.*** The corresponding condensation process is case I as described in connection with Fig. 5.

The situation is somewhat different in a falling film evaporator as shown in Fig. 8. The evaporation **flux** $\dot{n}$ is of the order of $\dot{n} = \alpha_{\text{film}}\Delta T/\Delta h_{g\ell} \simeq 0.008$ 8 kg/m² s, where $\alpha_{\text{film}} = 2\,000$ W/m² K, $\Delta T = 10$ K, and $\Delta h_{g\ell}$ = 2 260 kJ/kg. Assuming that $\rho_\ell\beta_\ell$ = 15 kg/m² s gives $\phi_\ell = 5.8 \times 10^{-4} < 0.1$ as in pool boiling. However, in the vapor phase one may estimate $\rho_g\beta_g$ = 5 X 10^{-2} kg/m² s, again from the Lewis law, with α_g = 100 W/m² K and c_{pg} = 2 kJ/kg K. This gives ϕ_g = 0.17, which is fairly low. These numbers mean that in both phases bulk and interface compositions are equal and in equilibrium; that is, $\tilde{y}_1 = \tilde{y}_1(x_1)$ and $x_1 = \tilde{x}_1^*(y_1)$. This process is also called closed ***distillation process*** and corresponds to case II in condensation. The separation effect in a falling film evaporator is less than in an autoclave because of the higher vapor-phase mass transfer.

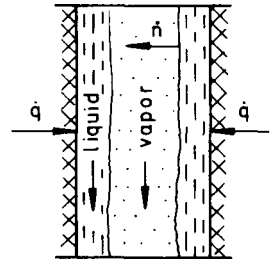

Figure 8 Falling film evaporator.

Nomenclature for Section 2.1.7 appears at the beginning of Part 2.

REFERENCES FOR SECTIONS 2.1 .O-2.1.7

1. Nusselt, W., Bedeutung der Lehre vom Warmedurchgang für die Maschinentechnik, *Z.Ver.Dtsch.Ing.*, vol. 67, pp. 885-886, 1923.
2. Nusselt, W., Das Grundgesetz des Wärmeüberganges, *Gesund.Ing.*, vol. 38, pp. 477–482, 490–496, 1915.
3. Hirschfelder, J., Curtis, L., and B. Bird, ***Molecular Theory of Gases and Liquids,*** Wiley, New York, 1965.
4. Planck, M., Zur Theorie des Gesetzes der Energieverteilung im Normalspectrum, *Verh.Dtsch.Phys.Ges.*, ***vol. 2,*** pp. 237-245, 1900.
5. Schowalter, W., ***Mechanics of Non-Newtonian Fluids,*** Pergamon, Elmsford, N.Y., 1978.
6. Wilkinson, W. L., *Non-Newtonian Fluids*, International ***Series*** of Monographs ***on*** Chemical Engineering, vol. 1, Pergamon, Elmsford, N.Y., 1960.
7. Colburn, A. P., Mean Temperature Difference and Heat Transfer Coefficient in Liquid Heat Exchangers, ***Ind.*** *Eng.Chem.*, ***vol.*** 25, pp. 873-877, 1933.
8. Stein, R. P., and Shastri, V. M. K., A Heat Transfer Analysis of Heat Exchangers with Laminar Tube-Side and Turbulent Shell-Side Flows-A New Heat Exchanger Graetz Problem, 12th Natl. Heat Transfer Conf., Tulsa, AICHE Preprint 1.5, 1971.
9. Schhinder, E. U., On the Mechanism of Mass Transfer in Heterogeneous Systems-In Particular in Fixed Beds, Fluidized Beds and on Bubble Trays, ***Chem.*** *Eng.Sci.*, ***vol. 32,*** pp. 845-851, 1977.
10. Martin, H., Low Péclet Number Particle-to-Fluid Heat and Mass Transfer in Packed Beds, *Chem.* Eng. *Sci.*, vol. 33, pp. 913–919, 1978.

© 1983 Hemisphere 1 blishing Corporation

11. Kunii, D., and Suzuki, M., Particle-to-Fluid Heat and Mass Transfer in Packed Beds of Fine Particles, *Int. J. Heat Mass Transfer*, vol. 10, pp. 845-852, 1967.
12. Bird, B., Stewart, W., and Lightfoot, E., *Transport* **Phenomena,** Wiley, New York, 1960.
13. Nusselt, W., Die Oberflächenkondensation des Wasserdampfes, *Z. Ver. Dtsch.* ***Ing., vol. 27,*** pp. 542-575, 1916.
14. Blangetti, F. Lokaler Wärmeübergang bei der Kondensation mit überlagerter Konvektion im vertikalen Rohr. Ph.D. thesis, Univ. Karlsruhe, 1979.

© 1983 Hemisphere Publishing Corporation

2.2 Single-phase fluid flow

Contents

2.2.1
INTRODUCTION AND FUNDAMENTALS, K. Gersten 2.2.1-1

A. Equations governing the motion of a fluid **2.2.1-1**
B. Dimensional analysis and theory of similarity **2.2.1-10**
C. Fundamentals of turbulent flow **2.2.1-13**
D. Boundary-layer theory **2.2.1-16**

Nomenclature for Section 2.2.1 **2.2.1-30**
References for Section 2.2.1 **2.2.1-31**

2.2.2
DUCTS, K. Gersten 2.2.2-1

A. Fully developed circular pipe flow 2.2.2-1
B. Fully developed noncircular pipe flow **2.2.2-7**
C. Developing duct flow **2.2.2-10**
D. Compressible duct flow **2.2.2-12**
E. Unsteady duct flow **2.2.2-14**
F. Losses of piping components **2.2.2-14**

Nomenclature for Section 2.2.2 **2.2.2-20**
References for Section 2.2.2 **2.2.2-21**

2.2.3
IMMERSED BODIES, K. Gersten 2.2.3-1

A. Flow regimes **2.2.3-1**
B. Forces exerted on the body **2.2.3-2**
C. Flow around a circular cylinder **2.2.3-3**
D. Flow around variously shaped cylinders **2.2.3-6**

Nomenclature for Section 2.2.3 **2.2.3-7**
References for Section 2.2.3 **2.2.3-8**

2.2.4
BANKS OF PLAIN AND FINNED TUBES, A. Žukauskas and R. Ulinskas 2.2.4-1

A. Introduction **2.2.4-1**
B. Drag and pressure drop in banks of tubes **2.2.4-3**
C. Pressure drop in banks of finned and rough-surfaced tubes **2.2.4-13**
D. Hydrodynamic parameters of separated flows in banks of tubes **2.2.4-15**

Nomenclature for Section 2.2.4 **2.2.4-16**
References for Section 2.2.4 **2.2.4-16**

2.2.5
FIXED BEDS, P. J. Heggs 2.2.5-1

References for Section 2.2.5 **2.2.5-4**

2.2.6
FLUIDIZED BEDS, 0. Molerus 2.2.6-1

A. Overall behavior **2.2.6-1**
B. Local structure of gas-solid fluidized beds **2.2.6-3**

Nomenclature for Section 2.2.6 **2.2.6-8**
References for section 2.2.6 **2.2.6-9**

2.2.7
HEADERS, NOZZLES, AND TURNAROUNDS, J. A. R. Henry 2.2.7-1

A. Introduction **2.2.7-1**
B. Nozzles **2.2.7-2**

© 1983 Hemisphere Publishing Corporation

HEDH

C. Headers 2.2.7-4
D. Turnarounds 2.2.7-8
E. Example 2.2.7-9

Nomenclature for Section 2.2.7 2.2.7-10
References for Section 2.2.7 2.2.7-11

2.2.8
NON-NEWTONIAN FLUIDS,
Robert C. Armstrong 2.2.8-1

A. Introduction 2.2.8-1
B. Experimental characterization of non-Newtonian fluids 2.2.8-1
C. Models for non-Newtonian fluids 2.2.8-6
D. Volume flow rate/pressure drop relations 2.2.8-9
E. Turbulent flow of non-Newtonian fluids 2.2.8-11

References for Section 2.2.8 2.2.8-12

© 1983 Hemisphere Publishing Corporation

2.2.1

Introduction and fundamentals

K. Gersten

A. Equations governing the motion of a fluid

(a) Basic concepts and definitions

A fluid is considered a continuous isotropic substance, the individual elements of which continue to deform as the result of applied tangential surface stresses. Fluids comprise both liquids and gases.

Although fluid matter, whether liquid or gaseous, is discrete on a microscopic-i.e., molecular-scale, it is convenient-and will be done in the following-to consider small fluid elements to contain many molecules, and to work with the average statistical properties of such large numbers of molecules; that is, the detailed molecular structure is not taken into account but is replaced by a continuous model of the fluid, assuming that the smallest relevant length scale considered is still very large compared with the average intermolecular distance (continuum model of fluids).t

The physical behavior of a fluid can be described by its thermodynamic and transport properties. The density $\boldsymbol{p}$ is such a continuum property of the fluid, defmed by the following limiting process, which is typical in continuum mechanics:

$$\rho = \lim_{\Delta V \to 0} \frac{\Delta M}{\Delta V} \tag{1}$$

According to this definition, the density is the ratio of mass to volume for the case in which the volume tends to an extremely small value but remains large enough to contain a large number of molecules.

The continuum local properties describing the behavior of the fluid that may depend on the temperature $\boldsymbol{T}$ and on the pressure p are as follows:

Thermodynamic properties:
- Density: ρ
- Speed of sound: $u_{\text{sound}} = \sqrt{(\partial p/\partial \rho)_s}$
- Heat capacities: $c_p = (\partial h/\partial T)_p, c_v = (\partial u/\partial T)_\rho$
- Coefficient of expansion: $\beta = -(\partial \rho/\partial T)_p/\rho$

Transport properties:
- Dynamic viscosity: η
- Kinematic viscosity: $\nu = \eta/\rho$
- Thermal conductivity: λ
- Prandtl number: $\mathrm{Pr} = \eta c_p/\lambda$

In addition, a thermal equation of state,

$$\rho = \rho(p, T) \tag{2}$$

or a caloric equation of state,

$$h = h(p, T) \tag{3}$$

have to be known. The fluid is assumed to be locally in thermodynamic equilibrium; that is, each point of the flow field has one definite thermodynamic equilibrium temperature.

In fluid mechanics, generally the so-called Eulerian description of fluid motion is used; that is, one does not follow individual fluid particles but describes instead what happens at every fixed point in space as a function of time. All quantities are considered field quantities that depend on the position vector $\mathbf{r}$ and the time t.

†The continuum model is valid for gases as long as the Knudsen number is small, i.e., $\mathrm{Kn} = l_0/l < 0.1$, where I, is the mean free path for the molecules, and I is the characteristic length of the flow field; see (6, 7].

© 1983 Hemisphere Publishing Corporation

HEDH

For the velocity vector, we obtain

$$\mathbf{w} = \mathbf{wfr,\ I)} \tag{4}$$

If w does not depend on the time t, the flow is called steady, otherwise it is unsteady. Curves the tangents of which are everywhere parallel to the local velocity vectors are denoted as streamlines.

Using the Eulerian formulation to describe the fluid motion, it is desired to calculate the time rate of change of a field quantity connected with a particular particle. For any scalar field quantity f (e.g., density, temperature, velocity component), this substantial derivative, also called material or particle derivative, is†

$$\frac{Df}{Dt} = \frac{\partial f}{\partial t} + \mathrm{w} \cdot \mathrm{grad}\ f \tag{5}$$

where the first part is denoted as local derivative and the second part as convective derivative. If f is a velocity component, then Df/Dt is the corresponding substantial acceleration component and consists of a local and a convective contribution.

The stress tensor **S** is represented by a symmetrical matrix (i.e., six components). The sum of the diagonal elements is zero. Assume that the fluid is cut by a plane surface at position **r** and time t. The normal unit vector on the planar surface is n. The resultant force (with components normal and tangential to the surface) per unit area exerted on that plane is then

$$\mathbf{s} = \mathrm{Sn} - \mathbf{pn} \tag{6}$$

For Newtonian fluids, the stress tensor **S** is connected with the rate-of-strain tensor **W** by the simple linear relationship

$$\mathrm{s} = \eta \mathbf{W} \tag{7}$$

where η is the dynamic (or shear) ***viscosity.***

In principle, another coefficient of viscosity, the bulk viscosity (also denoted as expansion viscosity or second coefficient of viscosity), should appear in Eq. (7). The bulk viscosity induces stress due to changes of the volume of the fluid element. It vanishes for incompressible flow (ρ = const). However, even for compressible flows, the bulk viscosity is generally so small that it can be neglected for the most cases of application; see Hirschfelder et al. [1].

The matrices of the tensors **S** and W depend on the coordinate system. For a Cartesian coordinate system, we obtain

$$\mathrm{w} = (u, v, w)$$

$$\mathrm{div}\ \mathbf{w} = \nabla \cdot \mathbf{w} = \frac{\partial u}{\partial x} + \frac{\partial v}{\partial y} + \frac{\partial w}{\partial z} \tag{8}$$

†Where **grad** f = **V**f.

$$\mathrm{grad}\ f = \nabla f = \left(\frac{\partial f}{\partial x}, \frac{\partial f}{\partial y}, \frac{\partial f}{\partial z} \right) \tag{9}$$

$$\mathbf{S} = \begin{pmatrix} \tau_{xx} & \tau_{xy} & \tau_{xz} \\ \tau_{yx} & \tau_{yy} & \tau_{yz} \\ \tau_{zx} & \tau_{zy} & \tau_{zz} \end{pmatrix} \tag{10}$$

$$\mathrm{w} = \begin{vmatrix} 2\frac{\partial u}{\partial x} - \frac{2}{3}\mathrm{div}\ \mathbf{w} & \frac{\partial u}{\partial y} + \frac{\partial v}{\partial x} & \frac{\partial u}{\partial z} + \frac{\partial w}{\partial x} \\ \frac{\partial v}{\partial x} + \frac{\partial u}{\partial y} & 2\frac{\partial v}{\partial y} - \frac{2}{3}\mathrm{div}\ \mathbf{w} & \frac{\partial v}{\partial z} + \frac{\partial w}{\partial y} \\ \frac{\partial w}{\partial x} + \frac{\partial u}{\partial z} & \frac{\partial w}{\partial y} + \frac{\partial v}{\partial z} & 2\frac{\partial w}{\partial z} - \frac{2}{3}\mathrm{div}\ \mathbf{w} \end{vmatrix} \tag{11}$$

For other coordinate systems see, for instance, Bird et al. [2].

(b) Basic flow equations in integral form

In most problems in fluid mechanics it is convenient to consider a ***control volume*** fixed in space through which the fluid flows. This is in accordance with the Eulerian description of the fluid motion. The control volume V has a closed surface of area S as a boundary. A surface element can be represented by the vector n dS, where n is the unit outward normal vector and dS the area of a surface element. For the fluid contained in the control volume, the following conservation laws may be written leading to integral froms of the basic flow equations:

. Continuity equation

$$\frac{d}{dt} \iiint_V \rho\, dV + \iint_S \rho \mathbf{w} \cdot \mathbf{n}\, dS = 0 \tag{12}$$

The mass inside the control volume changes only by mass flux over the surface. The first term vanishes for steady flows.

2. Momentum equation (equation of motion)

$$\frac{d}{dt} \iiint_V \mathbf{w}\rho\, dV + \iint_S \mathbf{w}\rho\mathbf{w} \cdot \mathbf{n}\, dA = \mathbf{F}_B + \mathbf{F}_S \tag{13}$$

The change of fluid momentum in the control volume is equal to the sum of the body force $\mathbf{F}_B$ acting on the control volume and the surface force $\mathbf{F}_S$, which is the resultant of all the stress forces acting on the surface.

$$\mathbf{F}_B = \iiint_V \mathbf{k}\, dV \tag{14}$$

© 1983 Hemisphere I blishing Corporation

Here k is the body force per unit volume which, in case of the gravity field with g as gravitational acceleration, leads to

$$\mathbf{k} = \rho \mathbf{g} \tag{15}$$

$$\mathbf{F}_A = \iint_S \mathbf{s}\, dS \tag{16}$$

where **s** is the stress force according to Eq. (6).

2a. Equation of moment of momentum

$$\frac{d}{dt}\iiint_V \rho(\mathbf{r} \times \mathbf{w})\, dV + \iint_S (\mathbf{r} \times \mathbf{w})\rho \mathbf{w} \cdot \mathbf{n}\, dS = \mathbf{M}_B + \mathbf{M}_S \tag{17}$$

The change of the moment of momentum in the control volume is equal to the sum of the moment of the body force $\mathbf{M}_B$ and the moment of the surface force $\mathbf{M}_S$. The position of a volume element or a surface element relative to the reference point of the moment is given by the position vector **r**.

$$\mathbf{M}_B = \iiint_V (\mathbf{r} \times \mathbf{k})\, dV \tag{18}$$

$$\mathbf{M}_S = \iint (\mathbf{r} \times \mathbf{s})\, dS \tag{19}$$

3. Energy equation (first law of thermodynamics)

$$\frac{d}{dt}\iiint_V \left(\frac{1}{2}w^2 + u\right)\rho\, dV + \iint_S \left(\frac{1}{2}w^2 + h\right)\rho \mathbf{w} \cdot \mathbf{n}\, dS = P_B + P_M + P_H \quad \textbf{(20)}$$

The change of kinetic and internal energy inside the control volume is equal to the sum of energies that are added to the control system from its surroundings. The so-called egoistic sign notation is used; that is, energy addition to the system from outside is counted positive. The power terms (energy per unit time) have the following meanings:

$$P_B = \iiint_V \mathbf{w} \cdot \mathbf{k}\, dV \tag{21}$$

is the work done by body forces (potential energy); P_M is the mechanical work done on the fluid by a pump, shaft work (negative for turbines); and P_H is the rate of heat added to the system by conduction or radiation from the surroundings. The notation $\dot{Q}$ is also used for the rate of heat.

The work done by shear forces on the surface of the control volume has been neglected in Eq. (20). In most practical cases this can be done, when the control volume is chosen properly.

4. Equation of kinetic energy (mechanical energy)

$$\frac{d}{dt}\iiint_V \frac{1}{2}w^2\rho\, dV + \iint_S \frac{1}{2}w^2\rho \mathbf{w} \cdot \mathbf{n}\, dS = P_S + P_B + P_M - P_D - P_\rho \tag{22}$$

The three terms on the right-hand side that appears in addition to Eq. ***(20)*** are as follows:

P_S is the work done by all stress forces on the surface. If again all shear forces are neglected, P_S is given by

$$P_S = -\iint_A p\mathbf{w} \cdot \mathbf{n}\, dS \tag{23}$$

P_D is dissipation, the loss of mechanical energy due to friction and turbulent mixing. From the second law of thermodynamics, it follows that P_D must always be positive.

P_ρ is the work done to change the density. In order to increase the density inside the control volume, compression work has to be done. It is a compressibility effect.

$$P_\rho = \iiint_V \frac{p}{\rho}\frac{D\rho}{Dt}\, dV = -\iiint_V p\, \mathrm{div}\, \mathbf{w}\, dV \tag{24}$$

5. Equation of internal energy

$$\frac{d}{dt}\iiint_V u\rho\, dV + \iint_S u\rho \mathbf{w} \cdot \mathbf{n}\, dS = P_H + P_D + P_\rho \tag{25}$$

The internal energy of the control volume can be changed only by heat addition P_H, dissipation P_D, or compression P_ρ (or expansion). Equations (12)-(25) are universal. They are valid for gases and for liquids, and also for non-Newtonian fluids. They are independent of the thermodynamic and transport properties of the fluid. The flow can be laminar or turbulent. Even discontinuities (e.g., shocks) are covered by these balance equations in integral form.

Example: conservation equations for a duct

The equations in integral form will be specialized to the flow of a duct according to Fig. 1. The flow is assumed to be steady. The inlet area S_1 and the exit area S_2 are small compared to the height difference $z_2 - z_1$. The gravitational acceleration g is constant and directed in the negative z direction. Shear stresses in inlet and exit

© 1983 Hemisphere Publishing Corporation

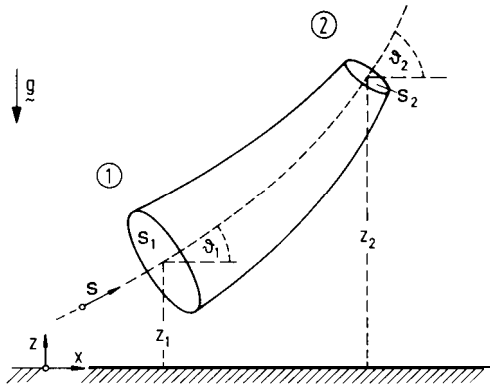

Figure 1 Flow in a stream tube: geometry.

areas are neglected. The static pressure p is assumed to be constant over the cross section, whereas w, ρ, T, h, and u may vary over the cross section. The following mean values over the cross-sectional areas are used:

Mean velocity:
$$\bar{w} = \frac{1}{S}\iint_S w\, dS \tag{26}$$

Mean density:
$$\bar{\rho} = \frac{1}{\bar{w}S}\iint_S \rho w\, dS \tag{27}$$

Mean temperature:
$$\bar{T} = \frac{1}{\bar{\rho}\bar{w}S}\iint_S T\rho w\, dS \tag{28}$$

Kinetic energy correction factor:
$$\alpha = \frac{1}{\bar{\rho}\bar{w}^3 S}\iint_S \rho w^3\, dS \tag{29}$$

Momentum correction factor:
$$\beta = \frac{1}{\bar{\rho}\bar{w}^2 S}\iint_S \rho w^2\, dS \tag{30}$$

Mean specific enthalpy:
$$\bar{h} = \frac{1}{\bar{\rho}\bar{w}S}\iint_S hpw\, dS$$

The mean value $\bar{h}$ is called bulk enthalpy. The corresponding bulk density and bulk temperature are in general different from $\bar{\rho}$ and $\bar{T}$, respectively. For constant density (incompressible fluid), Eqs. (27)–(30) are simplified so that the mean values depend only on the velocity distribution over the cross-section area. The control volume is the duct volume between the cross-sections 1 (inlet) and 2 (exit). Using these mean values, the following equations hold for a duct according to Fig. 1:

Conservation of mass:
$$\bar{\rho}_2\bar{w}_2 S_2 = \bar{\rho}_1\bar{w}_1 S_1 = \dot{M} \tag{31}$$

where $\dot{M}$ is the mass flow rate in the duct.

Momentum equation:
x direction (horizontal):
$$(p_2 + \beta_2\bar{\rho}_2\bar{w}_2^2) S_2 \cos\theta_2 = (p_1 + \beta_1\bar{\rho}_1\bar{w}_1^2) S_1 \cos\theta_1 - F_x \tag{32}$$

z direction (vertical):
$$(p_2 + \beta_2\bar{\rho}_2\bar{w}_2^2) S_2 \sin\theta_2 = (p_1 + \beta_1\bar{\rho}_1\bar{w}_1^2) S_1 \sin\theta_1 - gM - F_z \tag{33}$$

F_x and F_z are the components in the x and z directions, respectively, of the force (normal and tangential) exerted by the fluid on the duct wall. The total mass of the fluid in the control volume is M.

Energy equation:
$$\bar{h}_2 + \alpha_2(\tfrac{1}{2})\bar{w}_2^2 + gz_2 = \bar{h}_1 + \alpha_1(\tfrac{1}{2})\bar{w}_1^2 + gz_1 + w_{t12} + q_{12} \tag{34}$$

where
$$w_{t12} = \frac{P_M}{\dot{M}} \tag{35}$$

is the specific technical work (specific shaft work) done by a pump or agitator between the cross sections 1 and 2. The term
$$q_{12} = \frac{P_H}{\dot{M}} \tag{36}$$

is the specific heat (not to be confused with the specific capacities of heat, c_p and c,). It is the rate of heat added to the fluid between the cross sections 1 and 2 based on the mass flow rate in the duct. According to the energy equation (34), the sum of specific enthalpy h, kinetic energy $\alpha(1/2)\bar{w}^2$, and potential energy gz can be changed only by applying either technical work or heat addition. It is worth mentioning that this equation is valid for all duct flows, viscous or inviscid.

Kinetic energy equation:
$$\frac{p_2}{\bar{\rho}_2} + \alpha_2\left(\frac{1}{2}\right)\bar{w}_2^2 + gz_2 = \frac{p_1}{\bar{\rho}_1} + \alpha_1\left(\frac{1}{2}\right)\bar{w}_1^2 + gz_1 - \phi_{12} - \frac{P_\rho}{\dot{M}} \tag{37}$$

where
$$\phi_{12} = \frac{P_D}{\dot{M}} \tag{38}$$

is the specific dissipation. The most difficult part of Eq. (37) is the compression work P_ρ. It vanishes for incompressible fluids (ρ = const). For compressible fluids, P_ρ depends on the kind of process by which the fluid changes its thermodynamic properties on its way

© 1983 Hemisphere Publishing Corporation

from cross section 1 to cross section 2. If the density is constant over the cross-sectional area, one obtains

$$\frac{P_\rho}{\dot{M}} = -\int_{s_1}^{s_2} p(s)\, d\left(\frac{1}{\rho}\right) \tag{39}$$

This integral can be determined when $p(\rho)$ is a function of p only. Combination of Eq. (39) and the relationship

$$\frac{p}{p_1} = \left(\frac{\rho}{\rho_1}\right)^n \tag{40}$$

leads to

$$\frac{P_\rho}{\dot{M}} = \frac{1}{n-1}\frac{p_2}{\rho_2} - \frac{1}{n-1}\frac{p_1}{\rho_1} \qquad (\text{for } n \neq 1) \tag{41}$$

For the special case $n = 1$, which is the isothermal case, the corresponding equation is

$$\frac{P_\rho}{\dot{M}} = \frac{p_2}{\rho_2}\ln p_2 - \frac{p_1}{\rho_1}\ln p_1 \qquad (\text{for } n = 1) \tag{42}$$

It is obvious that Eq. (37) is particularly suitable for incompressible fluids (p = const) because of vanishing compression work P_ρ.

Internal energy equation:

$$\bar{u}_2 = \bar{u}_1 + q_{12} + \phi_{12} + \frac{P_\rho}{\dot{M}} \tag{43}$$

For flows of incompressible fluids ($P_\rho = 0$), the specific internal energy $\bar{u}$ can be increased by heat addition q_{12} and dissipation ϕ_{12}, but not by body forces.

Equations (31)-(34), (37), and (39) are fairly universal. They are valid regardless of the particular thermodynamic properties of the fluids. They can be simplified for so-called one-dimensional flows, where all variables are constant over the cross-sectional areas (so-called stream-filament assumption). In this case, the correction factors α and β are equal to unity. For compressible fluids the energy equation (34) is used, whereas for incompressible fluids Eq. (37) is preferred.

The specialization to ducts of constant cross-sectional area ($S_2 = S_1$) simplifies the equations further. When F_x and w_{t12} are neglected, Eqs. (31), (32), and (33) reduce to the well-known relationships for the normal shock, which represents a discontinuity of the physical properties in the duct flow.

The combination of Eqs. (32) and (37) for the incompressible flow in a horizontal duct of constant cross-sectional area S leads to a connection of the fluid force F_x exerted on the duct wall with the specific dissipation:

$$\phi_{12} = \left(\frac{F_x}{\rho \bar{w}^2 S} + \frac{\alpha_1 - \alpha_2}{2} + \beta_2 - \beta_1\right)\bar{w}^2 \tag{44}$$

Assuming the wall shear stress τ_w to be constant along the perimeter P_r of the not necessarily circular duct, the axial force F_x can be written as

$$F_x = P_r \int_{s_1}^{s_2} \tau_w(s)\, ds \tag{45}$$

where $L = s_2 - s_1$ is the length of the duct. Defining the hydraulic diameter d_h by

$$d_h = \frac{4S}{P_r} \tag{46}$$

the specific dissipation can be determined as

$$\phi_{12} = \left[\frac{4}{\rho \bar{w}^2 d_h}\int_{s_1}^{s_2} \tau_w(s)\, ds + \frac{1}{2}(\alpha_1 - \alpha_2) + \beta_2 - \beta_1\right]\bar{w}^2 \tag{47}$$

Dissipation can be caused either by skin friction or by change of the velocity profile due to mixing if the flow is not fully developed. In the case of fully developed flow (τ_w, α and β independent of s), Eq. (47) reduces to

$$\phi_{12} = \frac{8\tau_w}{\rho \bar{w}^2}\frac{L}{d_h}\frac{\bar{w}^2}{2} = \hat{f}\,\frac{L}{d_h}\frac{\bar{w}^2}{2} \tag{48}$$

where the dimensionless quantity

$$\hat{f} = \frac{8\tau_w}{\rho \bar{w}^2} \tag{49}$$

is the friction factor of the duct. For further details about duct flows, see Sec. 2.2.2.

(c) Basic flow equations in differential form

The control volume is now an infinitesimally small fluid element. In this case, the balance equations become differential equations. In vector notation, the equations have the following form regardless of the coordinate system:

Continuity equation:

$$\frac{\partial \rho}{\partial t} + \text{div}\,(\rho w) = 0 \tag{50}$$

Momentum equation (Navier-Stokes equation):

$$\rho \frac{Dw}{Dt} = k - \text{grad}\, p + \text{div}\, S \tag{51}$$

Inertia force | Body force | Pressure force | Viscous force

where†

$$\frac{Dw}{Dt} = \frac{\partial w}{\partial t} + \text{grad}\,\frac{w^2}{2} - w \times \text{curl}\, w \tag{52}$$

†Here curl w = rot w = V X w

© 1983 Hemisphere Publishing Corporation

Hence the inertia force balances the sum of body force, pressure force, and viscous force.

Kinetic energy equation:

$$\rho \frac{D(w^2/2)}{Dt} = \mathrm{w} \cdot \mathbf{k} - \mathrm{w} \cdot \mathrm{grad}\ p + \boldsymbol{w} \cdot \mathrm{div}\ \mathrm{S} \tag{53}$$

(Internal) energy equation:

$$\rho c_p \frac{DT}{Dt} = \mathrm{div}\ (\lambda\ \mathrm{grad}\ T) + \beta T \frac{Dp}{Dt} + \eta\Phi \tag{54}$$

The dissipation function Φ in Eq. (54) is always positive.† Here β is the coefficient of expansion.

The sum of Eqs. (53) and (54) leads to the equation for the total energy.

In the case of three-dimensional flow, Eqs. (SO), (5 I), and (54) are five scalar equations for the following unknowns: w, ***p,*** and ***T.*** These unknowns depend on position **r** and time t. In order to close the system of equations, some thermodynamic and transport properties of the fluid have to be known. In particular, the dependence of the quantities $\rho(T, p)$, $c_p(T, p)$, $\beta(T, p)$, $\eta(T, p)$, and $\lambda(T, p)$ on temperature and pressure have to be given. These relationships of the properties of the fluid close the system of 10 equations in 10 unknowns.

The boundary conditions of the unknowns depend on the problem considered. At solid walls, the no-slip condition

$$(\mathbf{w})_w = 0 \tag{55}$$

has to be satisfied.‡ When permeable walls are considered, generally a permeation velocity v_n,

$$v_n(\mathbf{r}_w, t) = (\mathbf{w} \cdot \mathbf{n})_w \tag{56}$$

must be prescribed. In the case of injection, v_n is positive. In the case of suction, v_n is negative.

In analogous form, a boundary condition for the temperature $T(\mathbf{r}, t)$ has to be specified at the wall. Either the wall temperature $T_w(\mathbf{r}_w, t)$ or the heat flux at the wall,

$$\dot{q}_w = -(\lambda \mathbf{n} \cdot \mathrm{grad}\ T)_w \tag{57}$$

or a combination of wall temperature and heat flux are prescribed.

So far the basic equations have been presented in vector notation; they are valid regardless of the coordinate systems. In the following, the details of the basic equations are given for the two most important coordinate systems.

I. Cartesian coordinates $(x, y, z; u, v, \mathrm{w})$

Continuity equation:

$$\frac{\partial \rho}{\partial t} + \frac{\partial(\rho u)}{\partial x} + \frac{\partial(\rho v)}{\partial y} + \frac{\partial(\rho w)}{\partial z} = 0 \tag{58}$$

Momentum equations:

$$\rho\left(\frac{\partial u}{\partial t} + u\frac{\partial u}{\partial x} + v\frac{\partial u}{\partial y} + w\frac{\partial u}{\partial z}\right) = k_x - \frac{\partial p}{\partial x} + \frac{\partial}{\partial x}\left[\eta\left(2\frac{\partial u}{\partial x} - \frac{2}{3}\nabla\mathbf{w}\right)\right] + \frac{\partial}{\partial y}\left[\eta\left(\frac{\partial u}{\partial y} + \frac{\partial v}{\partial x}\right)\right] + \frac{\partial}{\partial z}\left[\eta\left(\frac{\partial w}{\partial x} + \frac{\partial u}{\partial z}\right)\right] \tag{59a}$$

$$\rho\left(\frac{\partial v}{\partial t} + u\frac{\partial v}{\partial x} + v\frac{\partial v}{\partial y} + w\frac{\partial v}{\partial z}\right) = k_y - \frac{\partial p}{\partial y} + \frac{\partial}{\partial y}\left[\eta\left(2\frac{\partial v}{\partial y} - \frac{2}{3}\nabla\mathbf{w}\right)\right] + \frac{\partial}{\partial z}\left[\eta\left(\frac{\partial v}{\partial z} + \frac{\partial w}{\partial y}\right)\right] + \frac{\partial}{\partial x}\left[\eta\left(\frac{\partial v}{\partial x} + \frac{\partial u}{\partial y}\right)\right] \tag{59b}$$

$$\rho\left(\frac{\partial w}{\partial t} + u\frac{\partial w}{\partial x} + v\frac{\partial w}{\partial y} + w\frac{\partial w}{\partial z}\right) = k_z - \frac{\partial p}{\partial z} + \frac{\partial}{\partial z}\left[\eta\left(2\frac{\partial w}{\partial z} - \frac{2}{3}\nabla\mathbf{w}\right)\right] + \frac{\partial}{\partial x}\left[\eta\left(\frac{\partial w}{\partial x} + \frac{\partial u}{\partial z}\right)\right] + \frac{\partial}{\partial y}\left[\eta\left(\frac{\partial v}{\partial z} + \frac{\partial w}{\partial y}\right)\right] \tag{59c}$$

where

$$\nabla\mathbf{w} = \frac{\partial u}{\partial x} + \frac{\partial v}{\partial y} + \frac{\partial w}{\partial z} \tag{59d}$$

†More precisely, the internal energy equation has the form

$$\underset{\text{Change of internal energy}}{\rho \frac{Du}{Dt}} = \underset{\text{Conduction}}{\mathrm{div}\ (\lambda\ \mathrm{grad}\ T)} \underset{\text{Compression (reversible)}}{- p\ \mathrm{div}\ \mathrm{w}} + \underset{\text{Dissipation (irreversible)}}{\eta\Phi}$$

which is equivalent to Eq. (54). Another equivalent form of this equation is

$$\rho \frac{Dh}{Dt} = \mathrm{div}\ (\lambda\ \mathrm{grad}\ T) + \frac{Dp}{Dt} + \eta\Phi$$

Additional terms for sources of energy, for instance, due to dissociation and ionization (see Dorrance [3] and Pai [4] or radiation (see Pai [5]), have been neglected.

‡For Knudsen numbers $0.1 < \mathrm{Kn} < 1$, the so-called slip flow regime, the equations based on a continuum model can still be used. However, the boundary condition at the wall has to be modified because of the slip at the wall. See footnote on page 2.2.1-1 and [6] and [7].

© 1983 Hemisphere Publishing Corporation

Energy equation:

$$\rho c_p \left(\frac{\partial T}{\partial t} + u\,\frac{\partial T}{\partial x} + v\,\frac{\partial T}{\partial y} + w\,\frac{\partial T}{\partial z}\right) = \frac{\partial}{\partial x}\left(\lambda\,\frac{\partial T}{\partial x}\right) + \frac{\partial}{\partial y}\left(\lambda\,\frac{\partial T}{\partial y}\right) + \frac{\partial}{\partial z}\left(\lambda\,\frac{\partial T}{\partial z}\right) + \beta T\left(\frac{\partial p}{\partial t} + u\,\frac{\partial p}{\partial x} + v\,\frac{\partial p}{\partial y} + w\,\frac{\partial p}{\partial z}\right) + \eta\Phi \tag{60}$$

where

$$\Phi = 2\left[\left(\frac{\partial u}{\partial x}\right)^2 + \left(\frac{\partial v}{\partial y}\right)^2 + \left(\frac{\partial w}{\partial z}\right)^2\right] + \left(\frac{\partial v}{\partial x} + \frac{\partial u}{\partial y}\right)^2 + \left(\frac{\partial w}{\partial y} + \frac{\partial v}{\partial z}\right)^2 + \left(\frac{\partial u}{\partial z} + \frac{\partial w}{\partial x}\right)^2 - \frac{2}{3}(\nabla \mathbf{w})^2 \tag{61}$$

II. Cylindrical coordinates $(r, \theta, z; v_r, v_\theta, v_z)$

Continuity equation:

$$\frac{\partial \rho}{\partial t} + \frac{1}{r}\,\frac{\partial(\rho r v_r)}{\partial r} + \frac{1}{r}\,\frac{\partial(\rho v_\theta)}{\partial \theta} + \frac{\partial(\rho v_z)}{\partial z} = 0 \tag{62}$$

Momentum equations:

$$\rho\left(\frac{\partial v_r}{\partial t} + v_r\,\frac{\partial v_r}{\partial r} + \frac{v_\theta}{r}\,\frac{\partial v_r}{\partial \theta} - \frac{v_\theta^2}{r} + v_z\,\frac{\partial v_r}{\partial z}\right) = k_r - \frac{\partial p}{\partial r} + \frac{1}{r}\,\frac{\partial}{\partial r}\left[\eta r\left(2\,\frac{\partial v_r}{\partial r} - \frac{2}{3}\,\nabla \mathbf{w}\right)\right] + \frac{1}{r}\,\frac{\partial}{\partial \theta}\left[\eta\left\{r\,\frac{\partial}{\partial r}\left(\frac{v_\theta}{r}\right) + \frac{1}{r}\,\frac{\partial v_r}{\partial \theta}\right\}\right] - \frac{\eta}{r}\left[2\left(\frac{1}{r}\,\frac{\partial v_\theta}{\partial \theta} + \frac{v_r}{r}\right) - \frac{2}{3}\,\nabla \mathbf{w}\right] + \frac{\partial}{\partial z}\left[\eta\left(\frac{\partial v_z}{\partial r} + \frac{\partial v_r}{\partial z}\right)\right] \tag{63a}$$

$$\rho\left(\frac{\partial v_\theta}{\partial t} + v_r\,\frac{\partial v_\theta}{\partial r} + \frac{v_\theta}{r}\,\frac{\partial v_\theta}{\partial \theta} + \frac{v_r v_\theta}{r} + v_z\,\frac{\partial v_\theta}{\partial z}\right) = k_\theta - \frac{1}{r}\,\frac{\partial p}{\partial \theta} + \frac{1}{r^2}\,\frac{\partial}{\partial r}\left[r^2\eta\left\{r\,\frac{\partial}{\partial r}\left(\frac{v_\theta}{r}\right) + \frac{1}{r}\,\frac{\partial v_r}{\partial \theta}\right\}\right] + \frac{1}{r}\,\frac{\partial}{\partial \theta}\left[\eta\left\{2\left(\frac{1}{r}\,\frac{\partial v_\theta}{\partial \theta} + \frac{v_r}{r}\right) - \frac{2}{3}\,\nabla \mathbf{w}\right\}\right] + \frac{\partial}{\partial z}\,\eta\left(\frac{\partial v_\theta}{\partial z} + \frac{1}{r}\,\frac{\partial v_z}{\partial \theta}\right) \tag{63b}$$

$$\rho\left(\frac{\partial v_z}{\partial t} + v_r\,\frac{\partial v_z}{\partial r} + \frac{v_\theta}{r}\,\frac{\partial v_z}{\partial \theta} + v_z\,\frac{\partial v_z}{\partial \theta}\right) = k_z - \frac{\partial p}{\partial z} + \frac{1}{r}\,\frac{\partial}{\partial r}\left[r\eta\left(\frac{\partial v_z}{\partial r} + \frac{\partial v_r}{\partial z}\right)\right] + \frac{1}{r}\,\frac{\partial}{\partial \theta}\,\eta\left(\frac{\partial v_\theta}{\partial z} + \frac{1}{r}\,\frac{\partial v_z}{\partial \theta}\right)\Bigg] + \frac{\partial}{\partial z}\left[\eta\left(2\,\frac{\partial v_z}{\partial z} - \frac{2}{3}\,\nabla \mathbf{w}\right)\right] \tag{63c}$$

where

$$\nabla \mathbf{w} = \frac{1}{r}\,\frac{\partial(r v_r)}{\partial r} + \frac{1}{r}\,\frac{\partial v_\theta}{\partial \theta} + \frac{\partial v_z}{\partial z} \tag{63d}$$

Energy equation:

$$\rho c_p\left(\frac{\partial T}{\partial t} + v_r\,\frac{\partial T}{\partial r} + \frac{v_\theta}{r}\,\frac{\partial T}{\partial \theta} + v_z\,\frac{\partial T}{\partial z}\right) = \frac{1}{r}\,\frac{\partial}{\partial r}\left(\lambda r\,\frac{\partial T}{\partial r}\right) + \frac{1}{r}\,\frac{\partial}{\partial \theta}\left(\lambda\,\frac{1}{r}\,\frac{\partial T}{\partial \theta}\right) + \frac{\partial}{\partial z}\left(\lambda\,\frac{\partial T}{\partial z}\right) + \beta T\left(\frac{\partial p}{\partial t} + v_r\,\frac{\partial p}{\partial r} + \frac{v_\theta}{r}\,\frac{\partial p}{\partial \theta} + v_z\,\frac{\partial p}{\partial z}\right) + \eta\Phi \tag{64}$$

where

$$\Phi = 2\left[\left(\frac{\partial v_r}{\partial r}\right)^2 + \left(\frac{1}{r}\,\frac{\partial v_\theta}{\partial \theta} + \frac{v_r}{r}\right)^2 + \left(\frac{\partial v_z}{\partial z}\right)^2\right] + \left[r\,\frac{\partial}{\partial r}\left(\frac{v_\theta}{r}\right) + \frac{1}{r}\,\frac{\partial v_r}{\partial \theta}\right]^2 + \left(\frac{1}{r}\,\frac{\partial v_z}{\partial \theta} + \frac{\partial v_\theta}{\partial z}\right)^2 + \left(\frac{\partial v_r}{\partial z} + \frac{\partial v_z}{\partial r}\right)^2 - \frac{2}{3}\,(\nabla \mathbf{w})^2 \tag{65}$$

The equations of motions for more general coordinate systems can be found in Tsien [8] and Bird et al. [2].

(d) Models of fluids

The equations of motion presented in the previous sections are most general when the thermodynamic and transport properties of the fluid are specified as functions of temperature and pressure. In practice, these functions are usually given in convenient mathematical form depending on the model used for the fluid.

The ***thermodynamic properties*** $\rho, \beta, c_p, c_v, \gamma$, and u_{sound} of the fluid are generally described by the following models.

I. Perfect gas (ideal gas)

$$\frac{p}{\rho} = RT \tag{66}$$

where

$$R = c_p(T) - c_v(T) = \frac{\gamma(T) - 1}{\gamma(T)}\,c_p(T) \tag{67}$$

© 1983 Hemisphere Publishing Corporation

$$\beta = \frac{1}{T} \tag{68}$$

$$u^2_{\text{sound}} = \gamma(T)RT = \gamma(T)\frac{p}{\rho} \tag{69}$$

Hence, the quantities $c_p(T)$, $c_v(T)$, $\beta(T)$, and $u_{\text{sound}}(T)$ are functions of temperature only.

Example:

Air 500 K< T < **2000** K

1.4 > $\gamma(T)$ > 1.27

R = **287** m²/s² K

II. Calorically perfect gas

A calorically perfect gas is a perfect gas with constant heat capacities. The speed of sound is proportional to the square root of the temperature.

Example :

Air 50 K < T< **500** K

R = 287 m²/s² K

γ = 1.4

c_p = 1005 m²/s² K

III. Small density variations

The density function $\rho(T, p)$ can be expanded in a Taylor series in the vicinity of a reference state denoted by the subscript ∞:

$$\rho(T,p) = \rho_\infty + \left(\frac{\partial\rho}{\partial T}\right)_{p_\infty}(T-T_\infty) + \left(\frac{\partial\rho}{\partial p}\right)_{T_\infty} \times (p-p_\infty) + \left(\frac{\partial^2\rho}{\partial T\,\partial p}\right)_\infty (T-T_\infty) \times (p-p_\infty) + \frac{1}{2}\left(\frac{\partial^2\rho}{\partial T^2}\right)_{p_\infty}(T-T_\infty)^2 + \frac{1}{2}\left(\frac{\partial^2\rho}{\partial p^2}\right)_{T_\infty}(p-p_\infty)^2 + \cdots \tag{70}$$

All derivatives are taken at the reference point p_∞, T_∞.

Usually, only the linear terms of this expansion are taken into account. Introducing the coefficient of expansion,

$$\beta = -\frac{1}{\rho}\left(\frac{\partial\rho}{\partial T}\right)_p \tag{71}$$

and using the general relationship

$$\left(\frac{\partial\rho}{\partial p}\right)_T = \frac{c_p}{c_v}\left(\frac{\partial\rho}{\partial p}\right)_s = \frac{\gamma}{u^2_{\text{sound}}} \tag{72}$$

the linear terms of Eq. (70) yield

$$\rho = \rho_m - \rho_\infty\beta_\infty(T-T_\infty) + \frac{\gamma_\infty}{u^2_{\text{sound},\infty}}(p-p_\infty) \tag{73}$$

This equation is usually applied when nonisothermal fluid flows affected by buoyancy forces are investigated; see Sec. A(e).

Examples: (T_∞ = 293 K, p_∞ = 1 bar)

Air:	Water:
ρ_∞ = 1.188 kg/m³	ρ_∞ = 998.4 kg/m³
β_∞ = 3.419 X 10^{-3} K^{-1}	β_∞ = 2.067 X 10^{-4} K^{-1}
γ_∞ = 1.401	γ_∞ = 1.006
$u_{\text{sound},\infty}$ = 343.4 m/s	$u_{\text{sound},\infty}$ = 1 460 m/s

The other thermodynamic properties $\beta(T,p)$, and $c_p(T,p)$ and also the transport properties $\eta(T,p)$ and $\lambda(T,p)$ can be expanded in Taylor series analogous to Eq. (70). The linear derivatives of these Taylor series are listed in Table 1 for air and water at T_∞ = **293** K (20° C) and p_∞ = 1 bar. At least for these two fluids at the particular thermodynamic state chosen, the table shows very clearly which dependencies can be neglected and which have to be taken into account:

Air: Dependence on temperature and pressure: $\rho(T,p)$
Dependence on temperature only: $\beta(T)$, $\eta(T)$, $\lambda(T)$
Constant: c_p, Pr

Water: Dependence on temperature only: $\eta(T)$, $\lambda(T)$, $\beta(T)$, Pr(T)
Constant: p, c_p

In most practical cases, a constant c_p is obviously a very good approximation.

IV. Constant-density fluid

In many cases, liquids and also gases can be considered as fluids of constant density, if the temperature variations in the flow field are very small. According to Eq. (73), this means that β = 0 or $T = T_\infty$ and $u_{\text{sound}} \to \infty$.

The ***transport properties*** η, λ, and the Prandtl number Pr = $\eta c_p/\lambda$ of the fluid are described by the following models:

(i) Independence of pressure. In most cases it is assumed that $\eta(T)$, $\lambda(T)$, and Pr(T) are functions of temperature only; see Table 1.

(ii) Constant Prandtl number. In addition to the assumption of constant Prandtl number Pr, usually c_p is assumed to be constant, in which case λ is proportional to η.

© 1983 Hemisphere Publishing Corporation

Table 1 Variation of physical properties with temperature and pressure for air and water at $T_\infty = 293$ K and $p_\infty = 1$ bar

	Air	Water
$\frac{T}{\rho}\left(\frac{\partial\rho}{\partial T}\right)_p = -\beta T$	-1.01	-0.06
$\frac{T}{\beta}\left(\frac{\partial\beta}{\partial T}\right)_p$	-1.01	15.8
$\frac{T}{c_p}\left(\frac{c_p}{T}\right)_p$	0.01	−0.05
$\frac{T}{\eta}\left(\frac{\partial\eta}{\partial T}\right)_p$	0.70	−7.37
$\frac{T}{\lambda}\left(\frac{\partial\lambda}{\partial T}\right)_p$		0.75
$\frac{T}{\mathrm{Pr}}\left(\frac{\partial \mathrm{Pr}}{\partial T}\right)_p$	4.12	−8.17
$\frac{T}{\rho\eta}\left(\frac{\partial(\rho\eta)}{\partial T}\right)_p$	−0.31	−7.43
$\frac{p}{\rho}\left(\frac{\partial\rho}{\partial p}\right)_T$	1	5.4×10^{-5}
$\frac{p}{\beta}\left(\frac{\partial\beta}{\partial p}\right)_T$	-2×10^{-3}	5.7×10^{-4}
$\frac{p}{c_p}\left(\frac{\partial c_p}{\partial p}\right)_T$	1.8×10^{-3}	-4.4×10^{-5}
$\frac{p}{\eta}\left(\frac{\partial\eta}{\partial p}\right)_T$	8.5×10^{-3}	10^{-6}
$\frac{p}{\lambda}\left(\frac{\partial\lambda}{\partial p}\right)_T$	1.3×10^{-3}	1.5×10^{-4}
$\frac{p}{\mathrm{Pr}}\left(\frac{\partial \mathrm{Pr}}{\partial p}\right)$	1.3×10^{-3}	-1.9×10^{-4}
$\frac{p}{\rho\eta}\left(\frac{\partial(\rho\eta)}{\partial p}\right)$	1	5.4×10^{-5}

Examples :

Air (50 K < T < 1 600 K): Pr = 0.71

Water ($T = 293$ K): Pr = 6.92

(iii) Sutherland formula. For gases the following formula may be used:

$$\frac{\eta}{\eta_\infty} = \left(\frac{T}{T_\infty}\right)^{3/2} \frac{T_\infty + S}{T + S} \qquad (74)$$

where S is a specific constant for each gas.

Example:

Air ($T_\infty = 293$ K)

$\eta_\infty = 18 \times 10^{-6}$ kg/m s

s = 116K

(iv) Power law formula. Very often the following formula is used for gases:

$$\frac{\eta}{\eta_\infty} = \left(\frac{T}{T_\infty}\right)^{\omega} \qquad 0.5 < \omega \leqslant 1 \qquad (75)$$

Example :

Air ($T_\infty = 293$ K) $\omega = 0.8$

For $\omega = 1$, the viscosity is proportional to temperature, in which case the equations of motions can be drastically simplified.

(v) Density-viscosity function. The product of density and viscosity,

$$\zeta = \frac{\rho\eta}{\rho_\infty \eta_\infty} \qquad (76)$$

is nearly constant for gases, if pressure changes are small. At constant pressure, we obtain exactly $\zeta = 1$ for perfect gases and $\omega = 1$.

(vi) Chapman-Rubesin formula. The relationship

$$\frac{\eta}{\eta_\infty} = C\frac{T}{T_\infty} \qquad (77)$$

has the advantage that η is proportional to temperature. The Chapman-Rubesin parameter C can be chosen such that at a certain temperature T_r different from T_∞, the viscosity has the value η_r, which leads to $C = \eta_r T_\infty / \eta_\infty T_r$ or

$$\frac{\eta}{\eta_r} = \frac{T}{T_r} \qquad (78)$$

Frequently, it is convenient to have a reference state for η (index r) different from that of the rest of the properties (index ∞), see Sec. D(f).

(vii) Small viscosity variations. Assuming small variations of temperature lead to the Taylor series expansion

$$\eta(T) = \eta_\infty + \left(\frac{d\eta}{dT}\right)_\infty (T - T_\infty) + \frac{1}{2}\left(\frac{d^2\eta}{dT^2}\right)_\infty (T - T_\infty)^2 + \cdots \qquad (79)$$

© 1983 Hemisphere Publishing Corporation

Examples:

Air $(T_\infty = 293$ K, $\eta_\infty = 18 \times 10^{-6}$ kg/m s)

$$\left(\frac{d\eta}{dT}\right)_\infty = 4.32 \times 10^{-8} \text{ kg/m s K}$$

$$\left(\frac{d^2\eta}{dT^2}\right)_\infty = -5 \times 10^{-11} \text{ kg/m s K}^2$$

Water $(T_\infty = 293$ K, $\eta_\infty = 10^{-3}$ kg/m s)

$$\left(\frac{d\eta}{dT}\right)_\infty = -25 \text{ kg/m s K}$$

$$\left(\frac{d^2\eta}{dT^2}\right)_\infty = 10^{-6} \text{ kg/m s K}^2$$

The value $(d\eta/dT)_\infty$ is positive for gases and negative for liquids; see Table 1.

(viii) Constant viscosity. In isothermal flows of constant-density fluids, constant viscosity is usually assumed, too. In this case, the velocity and pressure fields are independent of the temperature field.

(e) Flows affected by buoyancy forces

The body force in the Navier-Stokes equation, Eq. (51), is usually the gravity force.

$$\mathbf{k} = \rho \mathbf{g} \tag{80}$$

If gravity forces have an effect on the flow, it is common to account for this effect in an approximate way called the Boussinesq approximation.

The equation of momentum, Eq. (51), is also valid for the fluid at rest. Assuming that the static field (w = 0) is steady and isothermal (T_{st} = const), the static pressure field p_{st} and the static density ρ_{st} are connected by

$$\text{grad } p_{st} = \rho_{st} \cdot \mathbf{g} \tag{81}$$

and after multiplying with the velocity w:

$$\frac{Dp_{st}}{Dt} = \mathbf{w} \cdot \text{grad } p_{st} = \rho_{st} \mathbf{w} \cdot \mathbf{g} \tag{82}$$

As equation of state, Eq. (73) is applied using the assumption of small variations of temperature and pressure. Hence, the density of the isothermal static field is given by

$$\rho_{st} = \rho_\infty + \frac{\gamma_\infty}{u^2_{\text{sound},\infty}} (p_{st} - p_\infty) \tag{83}$$

which, combined with Eq. (73), leads to the density relation

$$\rho = \rho_{st} - \rho_\infty \beta_\infty (T - T_\infty) + \underline{\frac{\gamma_\infty}{u^2_{\text{sound},\infty}} (p - p_{st})} \tag{84}$$

Introducing the pressure due to fluid motion by

$$p_{dyn} = p - p_{st} \tag{85}$$

Eqs. (5 1) and (54) become

$$\rho \frac{D\mathbf{w}}{Dt} = -\rho_\infty \beta_\infty (T - T_\infty)\mathbf{g} + \underline{\frac{\gamma_\infty}{u^2_{\text{sound},\infty}} p_{dyn}\mathbf{g}} - \text{grad } p_{dyn} + \text{div S} \tag{86}$$

and

$$\rho c_p \frac{DT}{Dt} = \text{div } (\lambda \text{ grad } T) + \eta\Phi + \underline{\beta T \frac{Dp_{dyn}}{Dt}} + \beta T \rho_{st} \mathbf{w} \cdot \mathbf{g} \tag{87}$$

In these equations, the pressure as thermodynamic property does not appear. Only p_{dyn}, the pressure due to the fluid motion, appears. The density ρ is connected with p_{dyn} and T by Eq. (84).

If gravity forces are taken into account, the values of p_{dyn} can usually be assumed to be small compared to the square of the speed of sound; that is, the terms underlined in Eqs. (84), (86), and (87) are negligible.

If the flow of the fluid is due only to buoyancy forces, the flow is called free convection flow (or natural convection flow). In this case, the unknowns w, p_{dyn}, $T - T_\infty$ [for example, $\eta(T)$ according to Eq. (79), c_p = const, Pr = const] are proportional to some given temperature difference, for example, $T_w - T_\infty$. Since this temperature difference is assumed to be small [to allow for the Taylor series in Eq. (70)], the density ρ in Eqs. (86) and (87) can be replaced by the known function ρ_{st} (Boussinesq approximation).

B. Dimensional analysis and theory of similarity

(a) Dimensionless parameters

The equations of motion, Eqs. (50), (51), and (54), are five scalar equations for the five unknowns w. p, and T in three-dimensional flows. The fluid properties ρ, c_p, β, η, and λ that appear in these equations are known functions of temperature and pressure. In general, all 10 unknowns are functions of position $\mathbf{r}$ and time t as well as functions of all initial and boundary values of the unknowns.

The large number of independent variables can be reduced considerably by introducing dimensionless variables and by writing the equations of motion in a dimensionless form.

We introduce the dimensionless variables

$$\mathbf{r}^* = \frac{\mathbf{r}}{l}, \quad t^* = \frac{U_\infty t}{l}, \quad \mathbf{w}^* = \frac{\mathbf{w}}{U_\infty}, \quad p^* = \frac{p - p_\infty}{\rho_\infty U^2_\infty},$$

@ 1983 Hemisphere I blishing Corporation

$$T^* = \frac{T}{T_\infty}, \quad \rho^* = \frac{\rho}{\rho_\infty}, \quad c_p^* = \frac{c_p}{c_{p\infty}} \quad \beta^* = \frac{\beta}{\beta_\infty},$$

$$\eta^* = \frac{\eta}{\eta_\infty}, \quad \lambda^* = \frac{\lambda}{\lambda_\infty} \tag{88}$$

where l is a characteristic length of the flow field. The subscript ∞ denotes the reference state. In the dimensionless form of the equations of motions, certain dimensionless combinations of the reference values will occur. These combinations are listed in Table 2 as items 1-5. The general solution of the equations of motions in dimensionless form will then be

$$\mathbf{w}^* = \mathbf{w}^*(\mathbf{r}^*, t^*, \text{Re}, \text{Pr}, \text{Ec}, \text{Fr}, \beta_\infty T_\infty) \tag{89}$$

and similarly for the other seven unknowns.

Combinations of the powers of the dimensionless groups result again in dimensionless groups. The dependence on new dimensionless combinations is completely equivalent to the original dependence. For instance, the relationship

$$\mathbf{w}^* = \mathbf{w}^*(\mathbf{r}^*, t^*, \text{Re}, \text{Pe}, \text{Ec}, \text{Ga}, \beta_\infty T_\infty) \tag{90}$$

is equivalent to Eq. (89). Items 6-l 1 in Table 2 are such combinations of groups l-5 of the table.

When additional boundary conditions are prescribed, more dimensionless numbers will appear. Examples are the Euler number Eu, which is a dimensionless pressure difference, and the Damköhler number, which is a dimensionless specific heat; see Sec. 2.2.2D(b).

In heat transfer problems, the Nusselt number plays an important role as a dimensionless heat flux at the wall. When perfect gases are considered, the Eckert number may be replaced by a combination of the Mach number and the ratio of the heat capacities, γ.

Periodic flow phenomena are characterized by the Strouhal number, which is a dimensionless frequency.

The description of a flow problem by relationships between dimensionless quantities reduces the number of variables and, hence, simplifies the understanding of the problem.

Instead of varying the four values ρ_∞, U_∞, I, and η_∞ independently, it is sufficient to vary only one dimensionless group, the Reynolds number.

(b) The pi theorem

Each problem can be described by relations between dimensionless variables. When a mathematical description in the form of differential, integral, or algebraic equations is available, these dimensionless variables can easily be found, as was shown in Sec. (a).

If no mathematical description of the problem is available, it is still possible to determine the proper dimensionless variables. This can be done using the so-called pi theorem, which can be stated as follows:

The general functional relation

$$f(a_1, a_2, a_3, \ldots, a_n) = 0 \tag{91}$$

between n geometric or physical variables a_n, the units of which are combinations of m independent

Table 2 Dimensionless numbers

No.	Name	Symbol and definition	Comments
1	Reynolds number	$\text{Re} = \rho Ul/\eta = Ul/\nu$	
2	Prandtl number	$\text{Pr} = \eta c_p/\lambda$	
3	Froude number	$\text{Fr} = U^2/gl$	
4	Eckert number	$\text{Ec} = U^2/c_pT$	
5	Grashof number	$\text{Gr} = gl^3\beta T/\nu^2$	
6	Galileo number	$\text{Ga} = \rho^2 l^3 g/\eta^2 = l^3 g/\nu^2$	$\text{Ga} = \text{Re}^2/\text{Fr}$
7	Péclet number	$\text{Pe} = \rho Ulc_p/\lambda$	$\text{Pe} = \text{Re Pr}$
8	Fourier number	$\text{Fo} = \lambda t/\rho c_p l^2$	$\text{Fo} = t^*/\text{Pe}, t^* = Ut/l$
9	Graetz number	$\text{Gz} = Ul^2\rho c_p/\lambda x$	$\text{Gz} = \text{Pe}/x^*, x^* = x/l$
10	Rayleigh number	$\text{Ra} = \rho^2 gl^3\beta T c_p/\eta\lambda$	$\text{Ra} = \text{Gr Pr}$
11	Archimedes number	$\text{Ar} = gl\beta T/U^2$	$\text{Ar} = \text{Gr}/\text{Re}^2 = \beta T/\text{Fr}$
12	Euler number	$\text{Eu} = 2\,\Delta p/\rho U^2$	Ap: pressure difference
13	Damköhler number	$\text{Da} = q/c_pT$	q: see Eq. (36)
14	Nusselt number	$\mathbf{Nu} = \dot{q}_w l/\lambda T$	
15	Stanton number	$\text{St} = \dot{q}_w/\rho Uc_pT$	$\text{St} = \text{Nu}/\text{Re Pr} = \text{Nu}/\text{Pe}$
16	Mach number	$\text{Ma} = U/u_{\text{sound}}$	$\text{Ma}^2 = \text{Ec}/(\gamma - 1)$ (perfect gases)
17	Strouhal number	$\text{Sr} = fl/U$	f: frequency
18	Knudsen number	$\text{Kn} = l_0/l$	l_0: mean free path of molecules
19	Rossby number	$\text{Ro} = Ul/\omega$	ω: angular velocity
20	Richardson number	$\text{Ri} = -g\rho(dU/dy)^{-2}(d\rho/dy)$	$(d\rho/dy)$: density gradient (dU/dy): velocity gradient

© 1983 Hemisphere Publishing Corporation

basic units (basic units are m, s, kg, K, etc.), can always be written in the form

$$F(\Pi_1, \Pi_2, \Pi_3, \ldots, \Pi_{n-m}) = 0 \qquad (92)$$

where $\Pi_1, \Pi_2, \ldots, \Pi_{n-m}$ are dimensionless combinations of the original variables $a_1, a_2, \ldots, a_n$.

The theorem states that the number of variables can be reduced from n to $n - m$, where m is the number of independent basic units. In the flow problems considered above, we have m = 4.

The procedure to determine the dimensionless combinations $\Pi_1, \Pi_2, \ldots$ may be demonstrated in an example.

The steady flow past a flat plate of length l at zero incidence is considered. The mean heat flux at the wall $\bar{q}_w$ of the plate has to be found when the wall temperature of the plate T_w is slightly different from the temperature of the free stream T_∞. For this problem, a general relation of the following form must exist :

$$f(\bar{q}_w, l, U_\infty, T_w - T_\infty, \rho_\infty, c_{p\infty}, \eta_\infty, \lambda_\infty) = 0 \qquad (93)$$

Since the number of basic units is four, this relation among eight variables can be reduced to a relation among four dimensionless variables.

The dimensionless variables to be determined are combinations of the given variables; that is, they have the form

$$(\bar{q}_w)^{\alpha_1} l^{\alpha_2} U_\infty^{\alpha_3} (T_w - T_\infty)^{\alpha_4} \rho_\infty^{\alpha_5} c_{p\infty}^{\alpha_6} \eta_\infty^{\alpha_7} \lambda_\infty^{\alpha_8} = 0 \qquad (94)$$

Since the combinations must be dimensionless, the units have to satisfy the relation

$$\left(\frac{\mathrm{N}}{\mathrm{m\,s}}\right)^{\alpha_1} \mathrm{m}^{\alpha_2} \left(\frac{\mathrm{m}}{\mathrm{s}}\right)^{\alpha_3} \mathrm{K}^{\alpha_4} \left(\frac{\mathrm{N\,s^2}}{\mathrm{m^4}}\right)^{\alpha_5} \left(\frac{\mathrm{m^2}}{\mathrm{s^2\,K}}\right)^{\alpha_6} \times \left(\frac{\mathrm{N\,s}}{\mathrm{m^2}}\right)^{\alpha_7} \left(\frac{\mathrm{N}}{\mathrm{s\,K}}\right)^{\alpha_8} = \mathrm{N}^0\ \mathrm{s}^0\ \mathrm{m}^0\ \mathrm{K}^0 \qquad (95)$$

which has to be fulfilled separately for each of the four basic units. Hence, we obtain four equations:

$$\begin{aligned}
&\text{Unit K:} && \alpha_4 - \alpha_6 - \alpha_8 = 0\\
&\text{Unit N:} && \alpha_1 + \alpha_5 + \alpha_8 = 0\\
&\text{Unit s:} && -\alpha_1 - \alpha_3 + 2\alpha_5 - 2\alpha_6 + \alpha_7 - \alpha_8 = 0\\
&\text{Unit m:} && -\alpha_1 + \alpha_2 + \alpha_3 - 4\alpha_5 + 2\alpha_6 - 2\alpha_7 = 0
\end{aligned} \qquad (96)$$

These are four homogeneous linear algebraic equations in eight unknowns $\alpha_1, \alpha_2, \ldots, \alpha_8$. There are precisely four independent solutions, as long as the rank of the matrix of the coefficients of the system of equations is m. (Here $m = 4$.) This is in practice always the case. The four solutions correspond to the four dimensionless groups:

1. $\alpha_1 = 1, \alpha_2 = 1, \alpha_3 = 0, \alpha_4 = -1,$
   $\alpha_5 = 0, \alpha_6 = 0, \alpha_7 = 0, \alpha_8 = -1$
   $$\mathrm{Nu} = \frac{\bar{q}_w l}{(T_w - T_\infty)\lambda_\infty}$$ Nusselt number

2. $\alpha_1 = 0, \alpha_2 = 1, \alpha_3 = 1, \alpha_4 = 0,$
   $\alpha_5 = 1, \alpha_6 = 0, \alpha_7 = -1, \alpha_8 = 0$
   $$\mathrm{Re} = \frac{\rho_\infty U_\infty l}{\eta_\infty}$$ Reynolds number

3. $\alpha_1 = 0, \alpha_2 = 0, \alpha_3 = 0, \alpha_4 = 0,$
   $\alpha_5 = 0, \alpha_6 = 1, \alpha_7 = 1, \alpha_8 = -1$
   $$\mathrm{Pr} = \frac{c_{p\infty}\eta_\infty}{\lambda_\infty}$$ Prandtl number

4. $\alpha_1 = 0, \alpha_2 = 0, \alpha_3 = 2, \alpha_4 = -1,$
   $\alpha_5 = 0, \alpha_6 = -1, \alpha_7 = 0, \alpha_8 = 0$
   $$\mathrm{Ec} = \frac{U_\infty^2}{c_{p\infty}(T_w - T_\infty)}$$ Eckert number

The new functional relation is

$$F(\mathrm{Nu}, \mathrm{Re}, \mathrm{Pr}, \mathrm{Ec}) = 0 \qquad (97)$$

For further details regarding the pi theorem, see texts on dimensional analysis, such as [9-22].

(c) Theory of models

In the previous section, dimensional analysis was used to show that each flow problem is characterized by dimensionless numbers. All phenomena that are determined by the same values of the dimensionless numbers and cannot be distinguished in a dimensionless description are called ***similar.***

Dimensionless numbers that contain the length ***l,*** such as the Reynolds number, can have the same value for different values of the length. Thus a flow of a given fluid has the same value of Reynolds number for twice the length and half the velocity.

This is the principle that underlies modeling. Instead of studying flow phenomena with full-scale models, smaller models may be used as long as the proper dimensionless numbers, such as the Reynolds number, are the same. This scaling can exactly reproduce full-scale conditions in the laboratory. The condition of similitude of the full-scale problem and the model problem include two types of similitude, the geometric similitude (linear scaling) and the dynamic similitude (same values of dimensionless variables at corresponding points).

© 1983 Hemisphere I blishing Corporation

Sometimes it is not easy to obtain full-scale Reynolds numbers with small models. Changing the fluid (e.g., from air to water) or lowering the temperature of the fluid for gas flows (cryogenic wind tunnels; see [23]) may be possible means to achieve higher Reynolds numbers.

Frequently, it is not possible to obtain complete similitude between model and full scale. A typical example is the case where the Reynolds number and the Froude number should be the same for the same fluid. According to Reynolds similitude, the model must have higher velocity, whereas according to Froude similitude, the velocity must be lower in the model. Therefore, in many investigations of models there will be only a partial similitude. In these cases formulas that correct the violation of complete similitude have to be used when applying the model results to full scale.

In several flow situations, the number of dimensionless numbers can be reduced, which is equivalent to an approximation to the complete similitude. Such a reduction is usually possible by considering the asymptotic behavior of the physical phenomenon for large or small values of the dimensionless numbers. The dimensionless variables in the new reduced functional relation are then combinations of the original dimensionless numbers.

In the following, a few demonstrating examples related to Eq. (97) will be considered:

1. Laminar flow at large Reynolds numbers (boundary-layer theory)

$$F\left(\frac{\mathrm{Nu}}{\sqrt{\mathrm{Re}}}, \mathrm{Pr}, \mathrm{Ec}\right) = 0 \tag{98}$$

2. Laminar flow at large Reynolds numbers and large Eckert numbers

$$F\left(\frac{\mathrm{Nu}}{\sqrt{\mathrm{Re}}\ \mathrm{Ec}}, \mathrm{Pr}\right) = 0 \tag{99}$$

3. Laminar flow at large Reynolds, Eckert, and Prandtl numbers

$$\frac{\mathrm{Nu}}{\sqrt{\mathrm{Re}}\ \mathrm{Ec}\ \mathrm{Pr}^{2/3}} = \text{const} \tag{100}$$

4. Laminar flow at large Reynolds and Prandtl numbers for $\mathrm{Ec} = 0$

$$\frac{\mathrm{Nu}}{\sqrt{\mathrm{Re}}\ \mathrm{Pr}^{1/3}} = \text{const} \tag{101}$$

If a reduction of the number of coordinates (including time) is possible, the flows are called self-similar; see Sec. D(c).

Dimensional analysis and similitude have been described in many textbooks; see, for example, [9–21].

C. Fundamentals of turbulent flow

(a) Conservation equations for turbulent flows

Most flows that occur in practical applications are turbulent. The main characteristic feature of turbulent flow is the irregular fluctuation of all variables which is superimposed on the mean values. The instantaneous quantities of turbulent flow are replaced by their mean and by their fluctuating quantities. If $f(\mathbf{r}, t)$ is a typical flow quantity, we may write:

$$f(\mathbf{r}, t) = \tilde{f}(\mathbf{r}) + f'(\mathbf{r}, t) = \bar{f}(\mathbf{r}) + f''(\mathbf{r}, t) \tag{102}$$

Here, two different ways of averaging appear: the time average,

$$\bar{f}(\mathbf{r}) = \frac{1}{\Delta t}\int_{t_0}^{t_0+\Delta t} f(\mathbf{r}, t)\, dt \tag{103}$$

and the mass-weighted time average,

$$\tilde{f}(\mathbf{r}) = \frac{1}{\bar{\rho}\,\Delta t}\int_{t_0}^{t_0+\Delta t} \rho(\mathbf{r}, t)\, f(\mathbf{r}, t)\, dt \tag{104}$$

For constant-density fluids, the two averages are identical.

The averages must be independent of the averaging time At. In practice, averaging times At are of the order of a few seconds. Within that time the mean value should be constant. If the mean values are at all independent of time, as was assumed in Eqs. (102)–(104), the flow is called statistically stationary. If the mean values change slowly with time, for example, noticeable within-time periods large compared with the averaging time ***At,*** the concept of averaging can still be applied. Such flows are called unsteady turbulent flows, where the term unsteady refers to the mean motion. For the more difficult case that the mean values change rapidly, ensemble averages must be used; see Bradshaw [24, 25].

From the definitions, Eqs. (102)–(104), it follows that

$$\overline{f'} = -\frac{\overline{\rho'' f''}}{\bar{\rho}} \neq 0 \qquad \overline{\rho f'} = 0 \tag{105a}$$

$$\overline{f''} = 0 \qquad \overline{\rho f''} = \bar{\rho}(\tilde{f} - \bar{f}) \tag{105b}$$

$$\tilde{f} - \bar{f} = \frac{\overline{\rho'' f''}}{\bar{\rho}} = \frac{\overline{\rho'' f'}}{\bar{\rho}} = -\overline{f'} \tag{105c}$$

The fluctuating motion of turbulent flows is much too complicated to describe the detailed behavior of the

© 1983 Hemisphere Publishing Corporation

flow with time. In practice, however, often only the mean motion is of interest. In order to deduce the equations of motion, which must be satisfied by the mean flow, the turbulent motion is assumed to consist of the sum of the mean part and a fluctuating part. That is, the physical unknowns are replaced by the following sums:

$$\begin{aligned} \rho &= \bar{\rho} + \rho'' \\ p &= \bar{p} + p'' \\ \eta &= \bar{\eta} + \eta'' \\ \mathbf{w} &= \tilde{\mathbf{w}} + \mathbf{w}' \\ T &= \tilde{T} + T' \end{aligned} \tag{106}$$

The other variables are replaced by similar expressions. Introducing these sums into the equations of motions, Eqs. (50), (51), (53), and (54), provides the following equations for the mean flow, after proper time averaging of these equations.

Continuity equation:

$$\frac{\partial \bar{\rho}}{\partial t} + \operatorname{div}(\bar{\rho}\tilde{\mathbf{w}}) = 0 \tag{107}$$

Momentum equation:

$$\bar{\rho}\frac{D\tilde{\mathbf{w}}}{Dt} = \bar{\rho}\mathbf{g} - \operatorname{grad}\bar{p} + \operatorname{div}(\bar{\mathbf{S}} + \bar{\mathbf{S}}_t) \tag{108}$$

Kinetic energy equation of the mean motion:

$$\bar{\rho}\frac{D(\tilde{\mathbf{w}}^2/2)}{Dt} = \bar{\rho}\tilde{\mathbf{w}}\cdot\mathrm{g} - \tilde{\mathbf{w}}\operatorname{grad}\bar{p} + \tilde{\mathbf{w}}\operatorname{div}(\bar{\mathbf{S}} + \bar{\mathbf{S}}_t) - \overline{\mathrm{w}\ \operatorname{grad}\mathrm{p} + \mathrm{w}\ \operatorname{div}\mathrm{S}} \tag{109}$$

Internal energy equation:

$$\bar{\rho}c_p\frac{DT}{Dt} = \operatorname{div}(\overline{\lambda\ \operatorname{grad}\ T} - c_p\rho\overline{T'\mathbf{w}'}) + \beta T\frac{D\bar{p}}{Dt} + \overline{\mathbf{w}'\ \operatorname{grad}\ \mathrm{p}} + \bar{\eta}\bar{\Phi} \tag{110}$$

For the derivation of the last equation, it was assumed that βT and c_p were not fluctuating.†

The equations of the mean motion of turbulent flow are the same as those of laminar flow with one exception: Instead of the shear tensor, the sum of the time-averaged shear tensor $\bar{S}$ and an additional shear tensor $\bar{S}_t$ appears in the equations of motions. Similarly, the additional terms $c_p\rho\overline{T'\mathbf{w}'}$ and $\overline{\mathbf{w}'\ \operatorname{grad}\ \mathrm{p}}$ appear in the equation of internal energy. These additional terms are caused by the fluctuating turbulent motion. In other words, the effect of turbulent fluctuation on the mean motion is like an increase of viscosity and heat conductivity.

The tensor $\bar{S}_t$ of the additional turbulent shear stresses due to the turbulent fluctuation is denoted as ***Reynolds shear stress tensor*** (also: tensor of ***apparent*** or ***virtual stresses).*** In Cartesian coordinates, it has the form

$$\bar{\mathbf{S}}_t = \begin{pmatrix} -\bar{\rho}\overline{u'^2} & -\bar{\rho}\overline{u'v'} & -\bar{\rho}\overline{u'w'} \\ -\bar{\rho}\overline{u'v'} & -\bar{\rho}\overline{v'^2} & -\bar{\rho}\overline{v'w'} \\ -\bar{\rho}\overline{u'w'} & -\bar{\rho}\overline{v'w'} & -\bar{\rho}\overline{w'^2} \end{pmatrix} \tag{111}$$

The main problem in the theory of turbulent shear flows is the so-called closure problem. That is, the Reynolds shear stresses and the other terms due to the fluctuations have to be connected with values of the mean motion (turbulence modeling).

In turbulence modeling, the equation of the mean kinetic energy of the velocity fluctuations is sometimes used. This equation is usually denoted as the ***turbulent-energy equation,*** which can be written as

$$\frac{Dk}{Dt} = P + D - \epsilon \tag{112}$$

Advection Production Diffusion Dissipation

where

$$k = \tfrac{1}{2}\overline{\rho(u'^2 + v'^2 + w'^2)} \tag{113}$$

is the time-averaged turbulent kinetic energy. The convective term on the left-hand side is denoted advection. It is equal to the combination of production P, diffusion D, and dissipation ϵ. For more details on this equation and additional equations concerning other components of the Reynolds shear stress tensor, Eq. (111), see Cebeci and Smith [26], Schubauer and Tchen [28], or Favre et al. [29] and Bradshaw [25].

(b) Turbulence modeling

In the equations of turbulent mean motion of Eqs. (107)-(110), terms appear that follow from the turbulent fluctuation. They represent correlations between the fluctuating quantities, that is, correlations between the fluctuation of velocity components, pressure, temperature, or viscosity and velocity component fluctuations.

The aim of turbulence modeling is to find a mathematical description of the connection between these correlation terms due to turbulent fluctuation and the mean motion. Considering only Eqs. (107)-(109), it is apparent that these equations have the same form term by term as those for an incompressible flow with two exceptions: The viscous stresses and the Reynolds

†If c_p and βT are fluctuating, the balance equation of specific enthalpy (see footnote on page 2.2.1-6) is used; see Cebeci and Smith [26].

© 1983 Hemisphere publishing Corporation

stresses include fluctuations in viscosity and in density, respectively.

For flows that are not too extreme (Mach numbers less than 5, see Laufer [27]), the following assumptions regarding these terms can usually be made (Morkovin hypothesis, see [128]):

1. Pressure fluctuations in Eqs. (109) and (1 10), produced by velocity fluctuations, can be neglected.

$$\overline{|\mathbf{w}' \text{ grad } p''|} \ll |\tilde{\mathbf{w}} \text{ grad } \bar{p}| \tag{114}$$

2. The following assumptions based on observation,

$$\overline{\eta' \frac{\partial u'}{\partial x}} \ll \bar{\eta} \frac{\partial \tilde{u}}{\partial x}, \quad \overline{\eta' \frac{\partial u'}{\partial y}} \ll \bar{\eta} \frac{\partial \tilde{u}}{\partial y}, \text{ etc.} \tag{115}$$

have the consequence that the viscosity-to-velocity gradient correlation are negligible.

3. The assumptions

$$\overline{\rho' u' v'} \ll \bar{\rho} \overline{u' v'}, \overline{\rho' u'^2} \ll \bar{\rho} \overline{u'^2}, \text{ etc.} \tag{116}$$

lead to neglecting the triple correlation involving the density fluctuations.

When these three assumptions are used, Eqs. (107)-(109) and (112) do not depend explicitly on the temperature (or density) fluctuations.

For implicit dependence of the mean velocity field on the temperature fluctuation, the turbulent dissipation, that is, the term ϵ in Eq. (112), could lead to such an interaction. The dissipation, increased by turbulence, modifies the mean temperature distribution and therefore the mean density. This in turn produces changes in the mean velocity distribution. Such a feedback mechanism is believed to be negligible in flows under consideration. The temperature fluctuations produced by velocity fluctuations do not react back upon the mean velocity field; that is, they are ***passive.***

Introducing the assumptions of Eqs. (114) and (115), the shear stress tensors have the following form:

1. In Cartesian coordinates:

$$\bar{\mathbf{S}} = \begin{pmatrix} \bar{\eta}\left(2\frac{\partial \tilde{u}}{\partial x} - \frac{3}{2} \text{ div } \tilde{\mathbf{w}}\right) & \bar{\eta}\left(\frac{\partial \tilde{u}}{\partial y} + \frac{\partial \tilde{v}}{\partial x}\right) & \bar{\eta}\left(\frac{\partial \tilde{u}}{\partial z} + \frac{\partial \tilde{w}}{\partial x}\right) \\ \bar{\eta}\left(\frac{\partial \tilde{v}}{\partial x} + \frac{\partial \tilde{u}}{\partial y}\right) & \bar{\eta}\left(2\frac{\partial \tilde{v}}{\partial y} - \frac{2}{3} \text{ div } \tilde{\mathbf{w}}\right) & \bar{\eta}\left(\frac{\partial \tilde{v}}{\partial z} + \frac{\partial \tilde{w}}{\partial y}\right) \\ \bar{\eta}\left(\frac{\partial \tilde{w}}{\partial x} + \frac{\partial \tilde{u}}{\partial z}\right) & \bar{\eta}\left(\frac{\partial \tilde{w}}{\partial y} + \frac{\partial \tilde{v}}{\partial z}\right) & \bar{\eta}\left(2\frac{\partial \tilde{w}}{\partial z} - \frac{2}{3} \text{ div } \tilde{\mathbf{w}}\right) \end{pmatrix} \tag{117}$$

$$\bar{\mathbf{S}}_t = \begin{pmatrix} -\bar{\rho}\overline{u'^2} & -\bar{\rho}\overline{u'v'} & -\bar{\rho}\overline{u'w'} \\ -\bar{\rho}\overline{v'u'} & -\bar{\rho}\overline{v'^2} & -\bar{\rho}\overline{v'w'} \\ -\bar{\rho}\overline{w'u'} - \bar{p}\overline{w'} & \overline{v'} & -\bar{\rho}\overline{u'^2} \end{pmatrix} = \begin{pmatrix} \epsilon_{xx}\left(2\frac{\partial \tilde{u}}{\partial x} - \frac{2}{3} \text{ div } \tilde{\mathbf{w}}\right) & \epsilon_{xy}\left(\frac{\partial \tilde{u}}{\partial y} + \frac{\partial \tilde{v}}{\partial x}\right) & \epsilon_{xz}\left(\frac{\partial \tilde{u}}{\partial z} + \frac{\partial \tilde{w}}{\partial x}\right) \\ \epsilon_{yx}\left(\frac{\partial \tilde{v}}{\partial x} + \frac{\partial \tilde{u}}{\partial y}\right) & \epsilon_{yy}\left(2\frac{\partial \tilde{u}}{\partial y} - \frac{2}{3} \text{ div } \tilde{\mathbf{w}}\right) & \epsilon_{yz}\left(\frac{\partial \tilde{v}}{\partial z} + \frac{\partial \tilde{w}}{\partial y}\right) \\ \epsilon_{zx}\left(\frac{\partial \tilde{w}}{\partial x} + \frac{\partial \tilde{u}}{\partial z}\right) & \epsilon_{zy}\left(\frac{\partial \tilde{w}}{\partial y} + \frac{\partial \tilde{v}}{\partial z}\right) & \epsilon_{zz}\left(2\frac{\partial \tilde{w}}{\partial z} - \frac{2}{3} \text{ div } \tilde{\mathbf{w}}\right) \end{pmatrix} \tag{118}$$

2. In cylindrical coordinates:

$$\bar{\mathbf{S}} = \begin{pmatrix} \bar{\eta}\left(2\frac{\partial \tilde{v}_r}{\partial r} - \frac{2}{3} \text{ div } \tilde{\mathbf{w}}\right) & \bar{\eta}\left[\frac{1}{r}\frac{\partial \tilde{v}_r}{\partial \theta} + r\frac{\partial}{\partial r}\left(\frac{\tilde{v}_\theta}{r}\right)\right] & \bar{\eta}\left(\frac{\partial \tilde{v}_r}{\partial z} + \frac{\partial \tilde{v}_z}{\partial r}\right) \\ \bar{\eta}\left[r\frac{\partial}{\partial r}\left(\frac{\tilde{v}_\theta}{r}\right) + \frac{1}{r}\frac{\partial \tilde{v}_r}{\partial \theta}\right] & \bar{\eta}\left[2\left(\frac{1}{r}\frac{\partial \tilde{v}_\theta}{\partial \theta} + \frac{\tilde{v}_r}{r}\right) - \frac{2}{3} \text{ div } \tilde{\mathbf{w}}\right] & \bar{\eta}\left(\frac{\partial \tilde{v}_\theta}{\partial z} + \frac{1}{r}\frac{\partial \tilde{v}_z}{\partial \theta}\right) \\ \bar{\eta}\left(\frac{\partial \tilde{v}_z}{\partial r} + \frac{\partial \tilde{v}_r}{\partial z}\right) & \bar{\eta}\left(\frac{1}{r}\frac{\partial \tilde{v}_z}{\partial \theta} + \frac{\partial \tilde{v}_\theta}{\partial z}\right) & \bar{\eta}\left(2\frac{\partial \tilde{v}_z}{\partial z} - \frac{2}{3} \text{ div } \tilde{\mathbf{w}}\right) \end{pmatrix} \tag{119}$$

$$\bar{\mathbf{S}}_t = \begin{pmatrix} -\bar{\rho}\overline{v_r'^2} & -\bar{\rho}\overline{v_r'v_\theta'} & -\bar{\rho}\overline{v_r'v_z'} \\ -\bar{\rho}\overline{v_\theta'v_r'} & -\bar{\rho}\overline{v_\theta'^2} & -\bar{\rho}\overline{v_\theta'v_z'} \\ -\bar{\rho}\overline{v_z'v_r'} & -\bar{\rho}\overline{v_z'v_\theta'} & -\bar{\rho}\overline{v_z'^2} \end{pmatrix}$$

© 1983 Hemisphere Publishing Corporation

$$
\begin{aligned}
&\epsilon_{rr}\left(2\frac{\partial \bar{v}_r}{\partial r}-\frac{2}{3}\,\mathrm{div}\,\tilde{\mathbf{w}}\right) \quad \epsilon_{r\theta}\left(\frac{1}{r}\frac{\partial \bar{v}_r}{\partial \theta}+r\frac{\partial}{\partial r}\frac{\bar{v}_\theta}{r}\right) \quad \epsilon_{rz}\left(\frac{\partial \bar{v}_r}{\partial z}+\frac{\partial \bar{v}_z}{\partial r}\right)\\
=\;&\epsilon_{\theta r}\left(r\frac{\partial}{\partial r}\frac{\bar{v}_\theta}{r}+\frac{1}{r}\frac{\partial \bar{v}_r}{\partial \theta}\right) \quad \epsilon_{\theta\theta}\left(2\frac{1}{r}\frac{\partial \bar{v}_\theta}{\partial \theta}+\frac{\bar{v}_r}{r}-\frac{2}{3}\,\mathrm{div}\,\tilde{\mathbf{w}}\right) \quad \epsilon_{\theta z}\left(\frac{\partial \bar{v}_\theta}{\partial z}+\frac{1}{r}\frac{\partial \bar{v}_z}{\partial \theta}\right) \qquad (120)\\
&\epsilon_{zr}\left(\frac{\partial \bar{v}_z}{\partial r}+\frac{\partial \bar{v}_r}{\partial z}\right) \quad \epsilon_{z\theta}\left(\frac{1}{r}\frac{\partial \bar{v}_z}{\partial \theta}+\frac{\partial \bar{v}_\theta}{\partial z}\right) \quad \epsilon_{zz}\left(2\frac{\partial \bar{v}_z}{\partial z}-\frac{2}{3}\,\mathrm{div}\,\tilde{\mathbf{w}}\right)
\end{aligned}
$$

The coefficients $\epsilon_{xx}, \ldots$ are denoted as apparent viscosities or eddy viscosities. They are usually functions of the position in the flow field. Turbulence modeling means finding connections between these values ϵ_{xx}, $\epsilon_{xy}, \ldots$ and the quantities of the mean motions.

A simplification is possible in so-called free turbulent flow fields, where no walls are present as boundaries of the flow field. Examples are turbulent free jets and wakes. In these cases, the molecular viscosity can be neglected in comparison to the eddy viscosities. For details of applications, see Abramovich [30], Rodi [31], and Townsend [32].

For turbulent shear flows where walls are boundaries of the flow field, the eddy viscosities vanish at the wall, which has the consequence that the eddy viscosities are more complicated functions of space and time. The theory of eddy viscosities for such turbulent flow fields is still in a very preliminary status. For details see, for example, the book by Gosman et al. [33]. More reliable turbulence modeling is possible for turbulent boundary layers; see Sec. D.

In flow fields with simple geometries (ducts, etc.) or simplified flow conditions (rotational symmetry or fully developed flow, where the dependence of one or more independent variables vanishes), turbulence modeling is much easier. Details will be discussed in Sec. 2.2.3.

In principle, turbulent motion is an unsteady process. Near boundaries of turbulent flow fields, the flow at a given point may become intermittently turbulent; that is, the flow is turbulent only for a certain percentage of time, and is laminar for the rest of the time. The fraction of time for which the flow is turbulent at a given location is called the intermittency factor γ; see Sec. D(h). This on-off character of turbulence is very difficult to model. For further details on turbulence modeling, see [31-41].

Corresponding to the continuous development of speed and storage of computers, there is a tendency, although not yet in engineering practice, to calculate solutions of the full time-averaged Navier-Stokes equations. For more details on computational fluid dynamics, see [42-46].

(c) Origin of turbulence

Flows become turbulent at high Reynolds numbers. The reason is an instability of laminar flows at sufficiently high Reynolds numbers. If the flow becomes unstable, it does not change abruptly into fully developed turbulence. There is a regime in between of so-called transitional flow. The transition from laminar to turbulent flow is a gradual process from instability over transitional flow into the fully developed turbulent flow.

The onset of instability can be computed by stability theory, in particular by linear stability theory; see the books [47-49] and surveys [50-55].

For the transitional flow and hence for transition, no theory is available today. Empirical and semi-empirical methods have to be applied to determine the transition from laminar to turbulent flow. For more details, see Schlichting [50]. Regarding transition in boundary layers, see Sec. D(g); transition in ducts is mentioned in Sec. 2.2.3A and F.

In particular flow situations a turbulent flow may become laminar again. This is called *relaminarization*. It may happen in highly accelerated flows or by stabilizing effects such as suction, cooling, and so on. Especially for boundary layers, relaminarizaton may become important; see Sec. D(g) and Sec. 2.2.2C(b).

D. Boundary-layer theory

(a) Boundary-layer concept

In Sec. B it was shown that in real fluid flows the Reynolds number Re is the most important parameter. It is the dimensionless group containing the viscosity.

In many practical flow situations the Reynolds number is rather high, that is, of the order of 1 000 and more. Therefore, it is appropriate to study the asymptotic behavior of the solutions of the flow equations for the limit $\mathrm{Re} \to \infty$.

In 1904 L. Prandtl developed the ***boundary-layer*** concept for flows past bodies at high Reynolds numbers. According to this concept, the entire flow field can be

© 1983 Hemisphere Publishing Corporation

divided into two different regions. In the larger of these two regions, which is almost the entire flow field, the viscosity can be neglected. In other words, the flow is inviscid in this region. The second region is a very narrow layer close to the wall, the *boundary layer,* where the viscosity effects are essential. The thickness δ of the boundary layer is extremely small. The following estimates can be made:

$$\delta \sim \mathrm{Re}^{-1/n} \qquad n = 2 \text{ (laminar)},\ n > 5 \text{ (turbulent)} \tag{121}$$

The two regions of the flow field, the outer inviscid flow and the boundary-layer flow, close to the body wall, have to be matched properly in a small overlapping region at the outer edge of the boundary layer.

In both regions the flow equations can be simplified. In the outer flow, viscosity and heat conductivity can be neglected. Within the boundary layer, the flow equations can also be simplified. The main simplifications, which are a consequence of the extremely small thickness of the boundary layer, are as follows.

1. The pressure is constant across the boundary layer.
2. The momentum and energy transfer parallel to the wall are negligibly small compared to the transfer perpendicular to the wall.
3. A Cartesian coordinate system that follows the wall contour can be used to develop the boundary-layer equations.

In the following, it is assumed that the equations for the outer inviscid flow have been solved. Only the boundary-layer flow will be considered in detail.

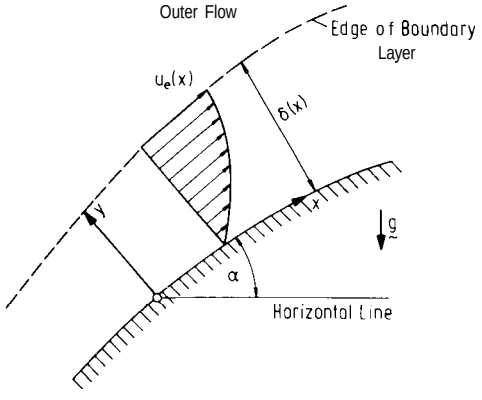

Figure 2 Flow in a boundary layer. geometry.

(b) Boundary-layer equations
(two-dimensional mean flow)

The flow within the boundary layer can be laminar or turbulent, where the first can formally be considered a special case of the latter. Therefore, the more general equations for the mean motion of the turbulent boundary will be given. Only two-dimensional mean flows will be considered. For general three-dimensional boundary layers, see [56-62].

It can be shown that, in the boundary layer,

$$\tilde{u} = \bar{u} \qquad \tilde{T} = \bar{T} \tag{122}$$

which, according to Eq. (105*c*), means that $\overline{\rho'' u''}$ and $\rho'' T''$ are extremely small compared to $\bar{\rho}$; see [26]. Figure 2 shows the Cartesian coordinate system used. The equations, which result from simplifications of the flow equations given in Secs. A and C, are as follows.

Continuity equation:

$$\frac{\partial \bar{\rho}}{\partial t} + \frac{\partial}{\partial x}(\bar{\rho}\bar{u}) + \frac{\partial}{\partial y}(\bar{\rho}\bar{v}) = 0 \tag{123}$$

Momentum equations:

$$\bar{\rho}\frac{\partial \bar{u}}{\partial t} + \bar{\rho}\bar{u}\frac{\partial \bar{u}}{\partial x} + \bar{\rho}\bar{v}\frac{\partial \bar{u}}{\partial y} = -\bar{\rho}g\sin\alpha - \frac{\partial \bar{p}}{\partial x} + \frac{\partial}{\partial y}\left(\bar{\eta}\frac{\partial \bar{u}}{\partial y} - \bar{\rho}\overline{u'v'}\right) \tag{124a}$$

$$0 = -\frac{\partial \bar{p}}{\partial y} - \frac{\partial}{\partial y}(\bar{\rho}\overline{v'^2}) \tag{124b}$$

In laminar boundary layers the pressure is constant across the layer, whereas in turbulent boundary layers the combination $\bar{p} + \bar{\rho}\overline{v'^2}$ is a constant across the layer. For low-turbulence outer flow, however, the pressure at the outer edge of the boundary layer is equal to the pressure at the wall.

Mean kinetic energy equation:

$$\bar{\rho}\frac{\partial}{\partial t}\left(\frac{1}{2}\bar{u}^2\right) + \bar{\rho}\bar{u}\frac{\partial}{\partial x}\left(\frac{1}{2}\bar{u}^2\right) + \bar{\rho}\bar{v}\frac{\partial}{\partial y}\left(\frac{1}{2}\bar{u}^2\right) = \underbrace{-\bar{\rho}\bar{u}g\sin\alpha}_{\text{Potential energy}} \underbrace{-\bar{u}\frac{\partial \bar{p}}{\partial x}}_{\text{Displacement work}} + \underbrace{\frac{\partial}{\partial y}\left[\bar{u}\left(\bar{\eta}\frac{\partial \bar{u}}{\partial y} - \bar{\rho}\overline{u'v'}\right)\right]}_{\text{Diffusion (momentum)}} + \underbrace{\bar{\rho}\overline{u'v'}\frac{\partial \bar{u}}{\partial y}}_{\text{Production of turbulent energy}} \underbrace{-\bar{\eta}\left(\frac{\partial \bar{u}}{\partial y}\right)^2}_{\text{Dissipation}} \tag{125}$$

© 1983 Hemisphere Publishing Corporation

A reduction of the kinetic energy of the mean flow in the boundary layer can result because of five reasons: (1) increase of potential energy (inviscid effect); (2) increase of pressure (inviscid effect); (3) diffusion; (4) production of turbulent kinetic energy, which will eventually change into heat via a cascade process of the turbulent fluctuation; (5) dissipation, that is, direct change into internal energy.

Internal energy equation: †

$$c_p\left(\bar{\rho}\frac{\partial \bar{T}}{\partial t}+\bar{\rho}\bar{u}\frac{\partial \bar{T}}{\partial x}+\bar{\rho}\bar{v}\frac{\partial \bar{T}}{\partial y}\right)=\beta T\left(\frac{\partial \bar{p}}{\partial t}+\bar{u}\frac{\partial \bar{p}}{\partial x}\right)$$

Compression

$$+\frac{\partial}{\partial y}\left(\lambda\frac{\partial \bar{T}}{\partial y}-\bar{\rho}c_p\overline{T'v'}\right)+\left(\bar{\eta}\frac{\partial \bar{u}}{\partial y}-\bar{\rho}\overline{u'v'}\right)\frac{\partial \bar{u}}{\partial y} \tag{126}$$

Diffusion (energy, heat) Dissipation

Turbulent kinetic energy equation:

$$\bar{\rho}\frac{\partial}{\partial t}\left(\frac{\overline{q^2}}{2}\right)+\bar{\rho}\bar{u}\frac{\partial}{\partial x}\left(\frac{\overline{q^2}}{2}\right)+\bar{\rho}\bar{v}\frac{\partial}{\partial y}\left(\frac{\overline{q^2}}{2}\right)=-\bar{\rho}\overline{u'v'}\frac{\partial \bar{u}}{\partial y}$$

Advection Turbulent energy production

$$+\frac{\partial \delta}{\partial y}\left[\bar{\eta}\frac{\partial}{\partial y}\left(\frac{1}{2}\overline{q^2}+\overline{v'^2}\right)\right]-\frac{\partial}{\partial y}\left[\overline{v'\left(\frac{1}{2}\bar{\rho}q^2+p\right)}\right]$$

Viscous diffusion Kinetic Pressure diffusion diff.

$$-\overline{\rho\Phi} \tag{127}$$

Turbulent energy dissipation

where

$$q^2=u'^2+v'^2+w'^2 \tag{127a}$$

The unknowns in the boundary layer have to satisfy the boundary conditions:

At the wall, y = 0:

$$\bar{u}=0,\ \bar{v}=\bar{v}_w(x),\ \bar{T}=\bar{T}_w,\ \bar{\rho}=\bar{\rho}_w,\ \bar{\eta}=\bar{\eta}_w,\ \bar{\lambda}=\bar{\lambda}_w \tag{128}$$

At the outer edge of the boundary layer, y = δ:

$$\bar{u}=u_e(x),\ \bar{T}=T_e(x),\ \bar{\rho}=\rho_e(x),\ p=p_e(x) \tag{129}$$

where the index e refers to the edge of the boundary layer or to the outer inviscid flow. It is assumed that $u_e(x), T_e(x)$, and so on, are already known from calculations of the outer flow. At the outer edge of the boundary layer the equations lead to

$$\rho_e\left(\frac{\partial u_e}{\partial t}+u_e\frac{\partial u_e}{\partial x}\right)=-\frac{\partial p_e}{\partial x} \tag{130}$$

$$\rho_e c_{pe}\left(\frac{\partial T_e}{\partial t}+u_e\frac{\partial T_e}{\partial x}\right)=\beta_e T_e\left(\frac{\partial p_e}{\partial t}+u_e\frac{\partial p_e}{\partial x}\right) \tag{131}$$

The main problem of modeling of turbulent boundary layers is finding connections of the correlation terms

$$\overline{u'v'} \quad \text{and} \quad \overline{T'v'}$$

with quantities of the mean flow. These terms vanish for laminar flows.

For further details on boundary-layer theory, see books [26, 63–68] and surveys [69–72].

(c) The Levy-Lees transformation‡

For steady, low-speed (Ma $\ll$ 1) boundary layers without buoyancy effects and constant c_p, Eqs. (123), (124*a*), and (125) can be reduced by the transformation

$$d\xi=\rho_e\eta_e u_e\,dx \tag{132a}$$

$$d\eta_s=\frac{\bar{\rho}u_e}{(2\xi)^{1/2}}\,dy \tag{132b}$$

The continuity equation can be satisfied by using a stream function defined by

$$\bar{\rho}\bar{u}=\frac{\partial \psi}{\partial y} \qquad \bar{\rho}\bar{v}=-\frac{\partial \psi}{\partial x} \tag{133}$$

Introducing the functions $f(\xi,\eta_s)$ and $g(\xi,\eta_s)$ by the definitions

$$\psi(x,y)=(2\xi)^{1/2}f(\xi,\eta_s) \tag{134}$$

$$\bar{u}(x,y)=u_e(\xi)f'(\xi,\eta_s) \tag{135a}$$

$$\bar{\rho}\bar{v}(x,y)=-\rho_e\eta_e u_e(2\xi)^{1/2}\left[\frac{f}{2\xi}+\frac{\partial f}{\partial \xi}+f'\left(\frac{\partial \eta_s}{\partial \xi}\right)_y\right] \tag{135b}$$

$$\bar{T}(x,y)=T_e g(\xi,\eta_s) \tag{136}$$

the boundary-layer equations reduce to

$$(bf'')+ff''+\beta_s(c-f'^2)=2\xi\left(f'\frac{\partial f'}{\partial \xi}-f''\frac{\partial f}{\partial \xi}\right) \tag{137a}$$

$$(ag')'+fg'=2\xi\left(f'\frac{\partial g}{\partial \xi}-g'\frac{\partial f}{\partial \xi}\right) \tag{137b}$$

†It is assumed that c_p and βT are not fluctuating in the boundary layer; see footnote on page 2.2.1-6.

‡The transformation is also called after Dorodnitsyn. Illingworth, Howarth, and Stewartson; see Dorrance [3].

© 1983 Hemisphere Publishing Corporation

The boundary conditions are

$$\eta_s = 0: \quad f = f_w \quad (f_w \neq 0 \text{ for suction or injection})$$

$$f' = 0,\ g = g_w \text{ or } g = g'_w$$

$$\eta_s \to \infty: \quad f' = 1,\ g = 1 \tag{138}$$

The primes refer here to differentiation with respect to η_s. The following abbreviations were used in the differential equations:

$$b(\xi, \eta_s) = \frac{\bar{\rho}\bar{\eta}}{\rho_e \eta_e}(1 + \epsilon_m^+) \tag{139a}$$

$$\beta_s(\xi) = \frac{2\xi}{u_e}\frac{du_e}{d\xi} \tag{139b}$$

$$c(\xi, \eta_s) = \frac{\rho_e}{\bar{\rho}} \tag{139c}$$

$$a(\xi, \eta_s) = \frac{\bar{\rho}\bar{\eta}}{\rho_e \eta_e}\mathrm{Pr}^{-1}\left(1 + \frac{\epsilon_m^+ \mathrm{Pr}}{\mathrm{Pr}_t}\right) \tag{139d}$$

The equations are valid for laminar and turbulent boundary layers under the assumptions that the flow is steady, independent of buoyancy effects, and at low speeds, that is, that the velocity in the flow field is always very small compared to the local sound speed. As a consequence of the assumptions, the terms for compression and dissipation in Eq. (126) have been neglected. Furthermore, constant c_p and Pr are assumed. This is a very good approximation for gases. When c_p of the fluid considered varies strongly with temperature (or less likely with pressure), a boundary-layer equation for the specific enthalpy has to be used instead of Eq. (126): see the footnote on page 2.2.1-6. For higher flow velocities, when compressibility effects become important, the reader is referred to the special literature on transsonic, supersonic, and even hypersonic boundary layers; see Cebeci and Smith [26] and Dorrance [3].

For laminar boundary layers, the bars on the symbols for density ρ and viscosity η will be left out. Furthermore, the terms ϵ_m^+ and Pr_t will vanish, which are characteristics describing the additional effects due to turbulence. Analogous to the mean molecular kinematic viscosity $\bar{\nu} = \bar{\eta}/\bar{\rho}$ in turbulent flow, the so-called eddy viscosity is defined as†

$$\nu_t = -\frac{\overline{u'v'}}{\partial\bar{u}/\partial y} \tag{140}$$

The term ϵ_m^+ in Eqs. (139a) and (139d) is defined as the ratio of the eddy viscosity ν_t and the mean molecular kinematic viscosity $\bar{\nu}$:

$$\epsilon_m^+ = \frac{\nu_t}{\bar{\nu}} = -\frac{\rho u'v'}{\bar{\eta}\,\partial\bar{u}/\partial y} \tag{141}$$

Similarly, the ***eddy thermal conductivity*** can be defined as‡

$$\lambda_t = -\bar{\rho}c_p\frac{\overline{T'v'}}{\partial\bar{T}/\partial y} \tag{142}$$

The ***turbulent Prandtl number*** Pr_t used in Eq. (139d) is defined as

$$\mathrm{Pr}_t = \frac{\bar{\rho}c_p\nu_t}{\lambda_t} = \frac{\overline{u'v'}}{\overline{T'v'}}\frac{\partial\bar{T}}{\partial\bar{u}} \tag{143}$$

Once the function $f(\xi, \eta_s)$ and $g(\xi, \eta_s)$ and their derivatives are determined, the boundary-layer parameters can be calculated. As examples, the following equations can be used:

Local skin friction coefficient:

$$c_f = \frac{\tau_w}{(1/2)\rho_e u_e^2} = \left(\frac{2}{\xi}\right)^{1/2}\eta_e\left(\frac{\bar{\rho}_w\bar{\eta}_w}{\rho_e\eta_e}\right)f''_w \tag{144}$$

Stanton number:

$$\mathrm{St} = \frac{-q_w}{\rho_e u_e c_p(T_e - T_w)} = \frac{g'_w}{\mathrm{Pr}}\frac{\bar{\rho}_w\bar{\eta}_w}{\rho_e\eta_e}\frac{\eta_e}{(2\xi)^{1/2}} \quad 1 - g_w \tag{145}$$

It is immediately apparent from Eqs. ***(137a)*** and ***(137b)*** that, if $\beta = 0$ (flat plate) and $\mathrm{Pr} = \mathrm{Pr}_t = 1$, a solution to Eq. (137*b*) is

$$g = Af' + B \tag{146}$$

where A and ***B*** are constants of integration. This formula is called ***Crocco's integral.***

If the values ***b,*** β, c, and ***a*** are independent of ξ, Eqs. ***(137a)*** and ***(137b)*** reduce to a system of ordinary differential equations. Their solutions are called self-similar or similar. For those, two velocity profiles located at different locations x differ only by scale factors in $\bar{u}$ and y. The temperature profiles have an equivalent behavior. Many self-similar solutions have been determined numerically; for surveys, see [72-75].

Most important cases of self-similar solutions are the flow along a flat plate ($\beta = 0$) and the stagnation point flow ($\beta = 1$).

Application of the Levy-Lees transformation has the following advantages:

1. The singularity at the leading edge disappears, which occurs in the flow along the flat plate and in similar flows.

2. The coordinate $\eta_{se}(\xi)$, corresponding to the outer edge of the boundary layer, changes much less due

†Sometimes the symbol ϵ or ϵ_m is used for the eddy viscosity.

‡Sometimes the symbol ϵ_H or A is used for the eddy conductivity.

© 1983 Hemisphere Publishing Corporation

to boundary-layer development than the analogous coordinate $y_e(x) = \delta(x)$.

3. The well-known differential equations for self-similar solutions are special cases of the general equations.

(d) Integral equations of the boundary layers

Integration of the equations ofmotions across the boundary layer, that is, integration with respect toy from 0 to y, lead to the following integral equations of the steady boundary layer (buoyancy effects are neglected):

Momentum integral equation:

$$\frac{d\delta_2}{dx} + \frac{\delta_2}{u_e}\frac{du_e}{dx}\left(2 + H_{12} + \frac{u_e}{\rho_e}\frac{d\rho_e/dx}{du_e/dx}\right) = \frac{c_f}{2} \qquad (147)$$

Mean kinetic energy integral equation:

$$\frac{d\delta_3}{dx} + \frac{\delta_3}{u_e}\frac{du_e}{dx}\left(3 + 2H_{43} + \frac{u_e}{\rho_e}\frac{d\rho_e/dx}{du_e/dx}\right) = D \qquad (148)$$

Internal energy integral equation:

$$\frac{d\delta_5}{dx} + \frac{\delta_5}{u_e}\frac{du_e}{dx}\left[1 + \left(\frac{u_e^2}{c_{pe}T_e} + \frac{u_e}{\rho_e c_{pe}T_e}\right.\right.$$
$$\left.\left.\times \frac{d(\rho_e c_{pe}T_e)/dx}{du_e/dx}\right)\right] = D\frac{u_e^2}{2c_{pe}T_e} + \frac{q_w}{\rho_e c_{pe}T_e u_e} \qquad (149)$$

Turbulent energy integral equation:

$$\frac{d[(1/2)IQ^2]}{dx} = \underset{\text{Production}}{\bar{P}} - \underset{\text{Dissipation}}{d} \qquad (150)$$

The abbreviations used above are

Displacement thickness:

$$\delta_1 = \int_0^\delta \left(1 - \frac{\bar{\rho}\bar{u}}{\rho_e u_e}\right) dy \qquad (151)$$

Momentum thickness:

$$\delta_2 = \int_0^\delta \frac{\bar{\rho}\bar{u}}{\rho_e u_e}\left(1 - \frac{\bar{u}}{u_e}\right) dy \qquad (152)$$

Energy thickness:

$$\delta_3 = \int_0^\delta \frac{\bar{\rho}\bar{u}}{\rho_e u_e}\left(1 - \frac{\bar{u}^2}{u_e^2}\right) dy \qquad (153)$$

Density thickness:

$$\delta_4 = \int_0^\delta \frac{\bar{\rho}\bar{u}}{\rho_e u_e}\left(\frac{\rho_e}{\bar{\rho}} - 1\right) dy \qquad (154)$$

Temperature thickness:

$$\delta_5 = \int_0^\delta \frac{\bar{\rho}\bar{u}}{\rho_e u_e}\left(\frac{\bar{T}}{T_e} - 1\right) dy \qquad (155)$$

Shape parameter:

$$H_{12} = \frac{\delta_1}{\delta_2} \qquad H_{43} = \frac{\delta_4}{\delta_3} \qquad (156)$$

Dissipation integral:

$$D = \frac{2}{\rho_e u_e^3}\int_0^\delta \left(\bar{\eta}\frac{\partial \bar{u}}{\partial y} - \overline{\rho u' v'}\right)\frac{\partial \bar{u}}{\partial y}\, dy \qquad (157)$$

An integral scale for the turbulence:

$$IQ^2 = 2\int_0^\delta \overline{ii}k\, dy \qquad (158)$$

Production of turbulent energy:

$$P = -\int_0^\delta \overline{\rho u' v'}\frac{\partial \bar{u}}{\partial y}\, dy \qquad (159)$$

Dissipation of turbulent energy:

$$d = \int_0^\delta \bar{\rho}\bar{\epsilon}\, dy \qquad (160)$$

Skin friction coefficient [see also Eq. (144)]

$$c_f = \frac{2\tau_w}{\rho_e u_e^2} \qquad (161)$$

These integral equations are valid for impermeable walls. When suction or injection is applied on a permeable wall, see Cebeci and Smith [26].

For unsteady boundary layers, see Schlichting [65].

It is noteworthy that the integral equations do not depend explicitly on the density when the outer flow has constant density ($d\rho_e/dx = 0$). The density variation within the boundary layer, for instance, due to heat transfer, appears only in the definition of the various thicknesses and, therefore, affects the flow field only indirectly.

(e) Solutions of the equations for laminar boundary layers

Numerical methods for solving nonlinear partial differential equations and computer techniques have reached a standard that in practice the complete equations, Eqs. (123)–(125), are being solved numerically. Various procedures, based on finite difference methods, and more recently also on finite element methods, have been developed. Many authors solve Eqs. (137*a*) and (137*b*),

© 1983 Hemisphere Publishing Corporation

which are easier to handle than the equations in the original coordinate system. For details of various numerical procedures, see [43-45, 76, 77]. In the past, approximate solutions of the boundary-layer equations have been developed by using the integral equations given in Sec. D(d). Their application is becoming rare. By assuming simple profiles for velocity and temperature, the integral equations can lead to approximations, which are very useful for a rough estimation.

I. Thwaites method

For incompressible fluids (constant properties), the following simple formulas can be used:

$$\frac{u_e(x)\,\delta_2^2(x)}{\nu} = 0.45\,\frac{\int_0^x u_e^5(x)\,dx}{u_e^5(x)} \tag{162}$$

$$\frac{\tau_w(x)\,\delta_2(x)}{\eta u_e(x)} = l(\lambda) \tag{163}$$

where

$$\lambda = \frac{\delta_2^2(x)}{\nu}\,\frac{du_e}{dx} \tag{164}$$

The functions $l(\lambda)$ and $H_{12}(\lambda)$, where $H_{12} = \delta_1/\delta_2$ is the shape parameter, are given in Table 3. When $u_e(x)$ and hence du_e/dx are given, $\delta_2(x)$, $\tau_w(x)$ and $H(x)$ can be determined. Separation ($\tau_w = 0$) occurs at $\lambda = -0.09$.

II. Stratford s method

An even more explicit formula for skin friction and separation was given by Stratford:

$$c_p(x - x_0)\,\frac{dc_p}{dx} = 0.0104\left(1 - \frac{\tau_w}{\tau_B}\right)^3 \left(1 + 2.02\,\frac{\tau_w}{\tau_B}\right) \tag{165}$$

where

$$\tau_B = 0.332\eta u_{eB}\left(\frac{u_{eB}}{\nu(x_B - x_0)}\right)^{1/2} \tag{166}$$

$$c_p = \frac{p - p(x = x_B)}{(1/2)\rho u_{eB}^2} \tag{167}$$

By this formula skin friction can be determined directly from the outer-flow pressure distribution for boundary layers with adverse pressure gradients, when the skin friction τ_B in the point of minimum pressure (Index B) is given. Equation (166) yields x_0, the location of a fictitious origin. Separation occurs when

$$c_p(x - x_B)\,\frac{dc_p}{dx} = 0.010\,4 \qquad \text{(separation)} \tag{168}$$

Table 3 Values of $H_{12}(\lambda)$ and $l(\lambda)$ according to Eq. (163), after Thwaites

λ	H_{12}	I
-0.090	3.55	0
-0.088	3.49	0.015
-0.086	3.44	0.021
-0.084	3.39	0.038
-0.080	3.30	0.056
-0.076	3.22	0.072
-0.072	3.15	0.085
-0.068	3.09	0.095
-0.064	3.04	0.104
-0.060	2.99	0.113
-0.056	2.94	0.122
—0.048	2.87	0.138
-0.032	2.75	0.168
-0.016	2.67	0.195
0	2.61	0.220
+0.016	2.55	0.244
+0.032	2.49	0.268
+0.048	2.44	0.291
+0.064	2.39	0.313
+0.075	2.36	0.327

III. Special literature

So far, only two-dimensional boundary layers have been discussed. The following books and review articles contain more information on special topics of laminar boundary layers.

1. Three-dimensional boundary layers: [56-59].
2. Unsteady boundary layers: [78-80, 131].
3. Boundary layers with suction or injection: Suction is used to thin the boundary layer (avoiding turbulence, *laminar* flow ***control*** or LFC) and increase the skin friction (avoiding separation). Injection, also of different fluids, is used mainly for cooling systems ***(transpiration cooling); see*** [81].
4. Free convection flow: Motions caused solely by density gradients created by temperature differences also display, in most cases, a boundary-layer structure, particularly if the viscosity and conductivity of the fluid are small. The flow along a vertical hot plate is a typical example; see [82,83].
5. Free shear layers: Shear layers that occur in the absence of walls. They also have boundary-layer character for fluids having small viscosity. Mixing layers between jets of different velocity, free jets, and wakes are typical examples; see [30,84, 85].
6. High-speed flows: Laminar boundary layers in transsonic, supersonic, and even hypersonic flows have applications mainly in aeronautics. But boundary layers with chemical reactions also have applications in other fields; see [3,132].
7. Higher-order effects: Prandtl s boundary-layer

© 1983 Hemisphere I blishing Corporation

theory, an asymptotic theory of the Navier-Stokes equations for high Reynolds numbers, can be extended to lower Reynolds numbers by higher-order boundary-layer theory; see [86, 87]. Singularities of the boundary-layer solutions can be avoided by the concept of multistructured boundary layers, see [88], which is particularly important at separation, [89, 90]; see also [91] and [92].

(f) Laminar flow along the flat plate

The boundary-layer equations reduce considerably for the flow along a flat plate. The pressure gradient vanishes; that is, $\beta = 0$. By assuming $b = \rho\eta/\rho_e\eta_e$ to be independent of $\xi = \rho_e\eta_e u_e x$, the flow is self-similar; that is, Eqs. (140) and (141) become ordinary differential equations:

$$(bf'')' + ff'' = 0 \qquad (169a)$$

$$\left(\frac{b}{\mathrm{Pr}}\,g'\right)' + fg' = 0 \qquad (169b)$$

The boundary conditions are

$$\begin{aligned} \eta_s = 0: &\quad f = f_w,\ f' = 0,\ g = g_w \\ \eta_s \to \infty: &\quad f' = 1,\ g = 1 \end{aligned} \qquad (170)$$

The given wall temperature $T_w = T_e g_w$ is assumed to be constant. If suction or injection is applied, the mass flux at the wall has to be proportional to $1/\sqrt{x}$, in order to get self-similar solutions:

$$\rho_w v_w = -\sqrt{\frac{\rho_e\eta_e u_e}{2x}}\,f_w \qquad (171)$$

The solutions $f(\eta)$ and $g(\eta)$ and hence the skin friction coefficient

$$c_f = \frac{\tau_w}{(1/2)\rho_e u_e^2} = \sqrt{\frac{2\eta_e}{x\rho_e u_e}\,\frac{\rho_w\eta_w}{\rho_e\eta_e}}\,f_w'' \qquad (172)$$

depend on Prandtl number Pr, wall temperature T_w/T_e, mass transfer parameter f_w, and the particular density-viscosity relationship used.

Several authors have solved this system, mainly for ideal gases and by using power laws or the Sutherland formula for the viscosity (see [72-75], where comprehensive tables of solutions of this system can be found).

In the following, various special cases will be considered:

I. Effect of density-viscosity function

When $b = C = \text{const}$, the two equations are uncoupled, and the skin friction coefficient is independent of the temperature distribution in the boundary layer.

The solution for the impermeable flat plate ($f_w = 0$) leads to $f_w'' = 0.469\,6/\sqrt{C}$ and hence to the skin friction coefficient

$$c_f\sqrt{\mathrm{Re}_x} = \frac{0.664}{\sqrt{C}}\,\frac{\rho_w\eta_w}{\rho_e\eta_e} \qquad (173)$$

where

$$\mathrm{Re}_x = \frac{\rho_e u_e x}{\eta_e} \qquad (174)$$

is the Reynolds number based on the coordinate x. In particular, C is called the Chapman-Rubesin parameter when

$$C = \frac{\rho_w\eta_w}{\rho_e\eta_e} \qquad (175)$$

(see Dorrance [3]).

The skin friction coefficient becomes

$$c_f\sqrt{\mathrm{Re}_x} = 0.664\,\sqrt{\frac{\rho_w\eta_w}{\rho_e\eta_e}} \qquad (176)$$

which is supposed to give a better approximation for the flat-plate flow with heat transfer than the equation for the constant property flow (C= 1). Equation (176) is a special case of a more general formula

$$c_f\sqrt{\mathrm{Re}_x} = 0.664\left(\frac{\rho_w\eta_w}{\rho_e\eta_e}\right)^{a_T(\mathrm{Pr})} \qquad (177)$$

of the so-called property ratio method [see also Sec. 2.2.2A(d)]. This formula was derived by assuming a linear dependence of density and viscosity on temperature and a small difference between wall temperature T_w and free-stream temperature T_e. These assumptions lead also to

$$b = 1 + \left[\frac{T}{\rho\eta}\,\frac{d(\rho\eta)}{dT}\right]_e (g - 1) \qquad (178)$$

(see Table 1) and hence to the skin friction coefficient

$$c_f\sqrt{\mathrm{Re}_x} = 0.664 \times \left\{1 + a_T(\mathrm{Pr})\left[\frac{T}{\rho\eta}\,\frac{d(\rho\eta)}{dT}\right]_e \frac{T_w - T_e}{T_e}\right\} \qquad (179)$$

which is (within the above-mentioned assumptions) equivalent to Eq. (177). The function $a_T(\mathrm{Pr})$ is shown in Fig. 3. It can be seen that Eq. (176), using the Chapman-Rubesin parameter, is a very good approximation for $\mathrm{Pr} \to 0$.

II. Effect of wall temperature

When the wall temperature is only slightly different from free-stream temperature, Eq. (179) shows the

© 1983 Hemisphere Publishing Corporation

first-order wall temperature effect on skin friction. ***Since*** $[(T/\rho\eta)\, d(\rho\eta)/dT]_e$ is in practice always negative, heating the plate decreases the friction, whereas cooling results in increase of friction. This effect is usually more pronounced for liquids than for gases (see also Table 1). According to the formula, temperature has no effect when $\rho\eta = \text{const}$. This is, for instance, the case for perfect gases ($\beta_e = 1/T_e$) and a linear viscosity-temperature law ($\eta \sim T$).

III. The reference temperature

In heat transfer investigations, ***reference temperature*** is very often used. This is a suitably chosen temperature such that the formulas derived for isothermal conditions give the same results as the exact formulas found by a complete theory. We define the reference temperature T_r such that the wall shear stress, calculated by the isothermal formula, Eq. (177), is the same as the result given in Eq. (179). After combining Eqs. (176) and (178), this condition leads to

$$T_r = T_e + 2a_T(T_w - T_e) \tag{180}$$

The reference temperature is about the arithmetic mean value of outer and wall temperature (also called film temperature) when Pr ≈ 1. Increasing Prandtl number shifts the reference temperature to the outer flow temperature. Very low Prandtl numbers lead to reference temperatures closer to the wall temperature.

It is worth mentioning that the reference temperature, derived in this way, is independent of the fluid properties and a function of Prandtl number only. For further discussion on reference temperature, also for high-speed flow and free convection flow, see [93-96].

IV. Effect of Prandtl number

For a given fluid and a given not-too-large difference of wall temperature and free-stream temperature, the effect of Prandtl number can be seen from Eq. (179). The deviation of the skin friction coefficient from the value found in incompressible flow decreases with increasing Prandtl number, as shown in Fig. 3.

V. Effect of suction or injection

The value f_w in Eq. (171) represents the quantity of suction or injection. Solutions of Eqs. (169) and (170) for $f_w \neq 0$ can be found in [73-75]. Suction increases skin friction, whereas injection decreases it. It turns out that at f_w = -0.875 7, the skin friction vanishes (separated flow), and no solutions exist for $f_w <$ −0.875 7. The function $a_T(\text{Pr})$ in Eq. (179) depends also on the parameter f_w, which means that the reference temperature is a function of the mass transfer parameter f_w.

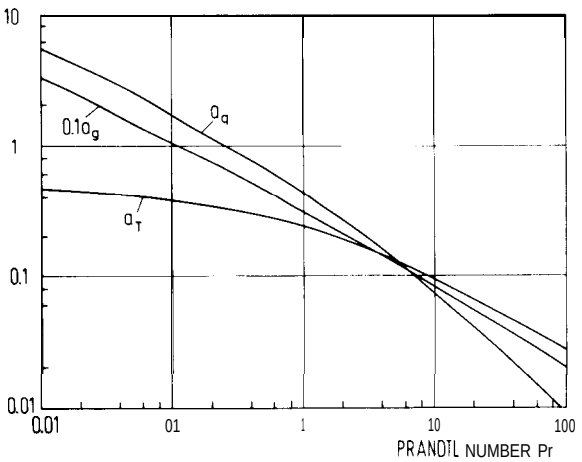

Figure 3 Functions $a_T(\text{Pr})$, $a_q(\text{Pr})$, and $a_g(\text{Pr})$, according to Eqs. (179), (182), and (183), respectively.

The plate flows considered so far are still special cases. In more general cases, additional effects, which are not covered by Eqs. (169) and (170), may appear, a few of which are described in the following.

VI. Effect of Mach number

At higher speed, when the velocities are no longer small compared to sound velocity, the terms for compression and dissipation cannot be neglected in the internal energy equation, Eq. (126). Even when the wall temperature and free-stream temperature are the same, there will be heat transfer due to viscous heating (dissipation). The skin friction coefficient is in this case ($T_w = T_e$)

$$c_f \sqrt{\text{Re}_x} = 0.664(1 + A(\omega)\, \text{Ma}_e^2) \tag{181}$$

where the Mach number Ma, is the ratio of the velocity and sound velocity at free stream. For perfect gases, the factor $A(\omega)$ is a function of the exponent ω in the viscosity-temperature relationship. The factor $A(\omega)$ vanishes for $\omega = 1$. As an example, Af0.7) = 0.016 (Pr = 0.7, $\gamma = 1.4$), see [75].

VII. Effect of wall temperature distribution

So far, only constant wall temperature of the flat plate has been considered. Generally, the wall temperature $T_w(x)$ can be any function of x. The flow always leads to self-similar solutions as long as the wall temperature is a power series of x; see [74]. In particular, the heat flux at the wall is constant for $T_w \sim \sqrt{x}$, which leads to the skin friction coefficient analogous to Eq. (179):

© 1983 Hemisphere Publishing Corporation

$$c_f \sqrt{\mathrm{Re}_x} = 0.664 \left[1 + a_q(\mathrm{Pr}) \left(\frac{T}{\eta\rho} \frac{d(\eta\rho)}{dT}\right)_e \frac{\mathrm{Nu}_x}{\sqrt{\mathrm{Re}_x}}\right] \quad (182)$$

where Nu, = (&,x)/(X, T_∞). The parameter $a_q(\mathrm{Pr})$ is shown in Fig. 3. Cooling the flat plate (Nu, <0) increases the skin friction, whereas heating (Nu, > 0) reduces the skin friction.

VIII. Effect of buoyancy forces

According to boundary layer theory, wall forces perpendicular to the main flow direction are neglected within the boundary layer. Therefore, buoyancy forces are neglected in horizontal boundary layers. By extending the classical boundary-layer theory to a higher-order theory, buoyancy forces in horizontal boundary layers can be taken into account; see Gersten and d'Avila [97]. For small differences of the flat-plate temperature T_w and outer flow temperature T_e, the skin friction coefficient can be approximated by

$$c_f \sqrt{\mathrm{Re}_x} = 0.664 \left(1 \pm a_g(\mathrm{Pr}) \frac{\mathrm{Ar}_x}{\sqrt{\mathrm{Re}_x}}\right) \quad (183)$$

where Ar_x is the Archimedes number based on $(T_w - T_e)$ and the coordinate x. The upper sign refers to the upper side of the flat plate. Hence, a heated flat plate experiences a higher skin friction on the upper side, and a lower skin friction on the lower side. Furthermore, buoyancy forces result in a pressure difference across the flat plate such that a lift force on the heated flat plate occurs; see [98].

IX. Higher-order effects

Prandtl s boundary-layer theory yields asymptotic solutions for the limit $\mathrm{Re}_x \to \infty$. In practice, formulas such as Eq. (177) are valid for about $\mathrm{Re}_x > 10^3$. To get solutions for lower Reynolds numbers, higher-order boundary-layer theory has to be applied; see [86]. In the case of flat-plate flow, the main correction of Prandtl s theory refers to the flow near the trailing edge of the plate. Prandtl s theory does not distinguish between a semiinfmite flat plate and a flat plate of finite length. Higher-order theory yields the following formula for the drag coefficient based on the length of the plate l (see [88]),

$$\bar{c}_f = \frac{D}{(\rho_e/2) u_e^2 l} = \frac{1.328}{\mathrm{Re}^{1/2}} + \frac{2.668}{\mathrm{Re}^{7/8}} \quad (184)$$

Figure 4, reproduced from Melnik and Chow [99], shows that the values of $\overline{c_f}$ computed with the aid of Eq. (184) agree very well with the results obtained from the complete Navier-Stokes equations as well as with those of measurements down to Re = 10.

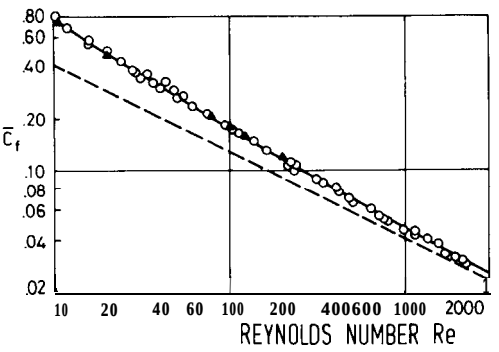

Figure 4 Drag coefficient of a flat plate of finite length, according to Eq. (184). --- First-order solution, $\bar{c}_f = 1.328\ \mathrm{Re}^{-1/2}$. ▲ Solution of full Navier-Stokes equations; see [100]. ○ Measurements, after Janour [101].

(g) Transition laminar-turbulent

There is no theory available to predict transition from laminar to turbulent flow. For incompressible flows, there are several empirical methods for predicting the transition point in two-dimensional flows; see [26] and Sec. C(b). One of these empirical methods was proposed by Michel [102]. It is based on the assumption that the variation of the transition momentum-thickness Reynolds number $\mathrm{Re}_{\delta 2} = u_e(x)\,\delta_2(x)/\nu$ with the Reynolds number $\mathrm{Re}_x = u_e(x)\,x/\nu$ is a universal curve, which after [26] can be described by the following formula:

$$\mathrm{Re}_{\delta 2} = 1.174 \left[1 + \left(\frac{22\,400}{\mathrm{Re}_x}\right)\right] \mathrm{Re}_x^{0.46}$$

$$10^5 \leqslant \mathrm{Re}_x \leqslant 4 \times 10^7 \quad (185)$$

If the value $\mathrm{Re}_{\delta 2}(x)$, calculated by a prediction method for laminar incompressible two-dimensional boundary layers, exceeds the values given in Eq. (185), the flow becomes turbulent. This universal curve is valid only when the turbulence intensity in the outer flow is extremely low.

The following effects can influence the location of transition.

I. Pressure gradient

Adverse (positive) pressure gradient or deceleration of the flow destabilizes the boundary layer and hence promotes transition. Favorable (negative) pressure gradient or acceleration of the flow leads to stable boundary layers.

© 1983 Hemisphere Publishing Corporation

II. Outer flow turbulence

Usually transition is encouraged by outer flow turbulence. In laboratory experiments, outer flow turbulence is sometimes produced artificially by grids to enforce transition on a model, in order to simulate flows at higher Reynolds numbers. Here, grid size and location of the grid with regard to the model is essential, because at certain arrangements grids can reduce the turbulence and hence suppress transiton; see [103].

III. Surface roughness

Continuous roughness (sandpaper roughness) or single roughness elements (trip wires) will both promote transition from laminar to turbulent. Again, artificial roughness mounted on models is often used in laboratory experiments to fix the location of transition on the model; see [104].

In this connection it is important to know the maximum roughness height that will not change the local skin friction (hydraulically smooth); see [105].

IV. Suction or blowing

Continuous or discontinuous (slot suction) suction has a stabilizing, blowing a destabilizing effect. Laminarization by continuous suction, called *laminar flow* ***control*** (LFC), has been used in aeronautics to reduce airfoil drag; see [106].

V. Heat transfer

Heat transfer at the body surface influences the stability and hence the transition due to temperature dependence of the viscosity. For gases, cooling stabilizes the boundary layer, whereas in liquids cooling has a destabilizing effect.

For further effects, such as those due to surface curvature, compressibility, density stratification, and so on, see Sec. C(c).

One simple way to determine the location of transition is measuring the velocity profiles and calculating the shape parameter H_{12}, defined in Eq. (156). For H_{12} the following ranges can be distinguished

Laminar flow: $2.5 < H_{12} < 3.5$

Turbulent flow: $1.2 < H_{12} < 2.4$

Transition is not a discontinuous change of the boundary layer, but takes place within a certain region of finite length. Predicting such a transitional boundary layer is still one of the unsolved problems of boundary-layer theory.

The reverse, the transition from turbulent to laminar flow condition, called ***reluminarization,*** can also occur. In particular, turbulent boundary layers under very strong favorable pressure gradient (strong acceleration) may become laminar when $\mathrm{Re}_{\delta 2}$ reaches values below a certain critical value, say, $\mathrm{Re}_{\delta 2 cr} \approx 370$, see [107].

(h) Universal laws for velocity, temperature, and shear stress distributions in turbulent boundary layers

The main problem in the theory of turbulent boundary layers is to find a connection between the eddy viscosity ν_t defined in Eq. (140) and quantities of the mean motion in the boundary layer (turbulence modeling). This problem is simplified by the empirical observation that in most turbulent boundary layers the connection between ν_t and mean-motion quantities is a local one; that is, it is in a very good approximation independent of the upstream development of the boundary layer. In other words, in many cases history effects can be neglected in a first approximation. As a consequence, universal laws for the distributions of the mean velocity, mean temperature, and shear stress can be formulated.

In contrast to laminar boundary layers, however, two different length scales exist in turbulent boundary layers:

Boundary layer thickness: δ

Wall layer thickness: $\delta_w = \dfrac{\nu_w}{u_\tau}$

where

$$u_\tau = \sqrt{\frac{\tau_w}{\rho_w}} \tag{186}$$

is called *friction* ***velocity.***

Accordingly, two different layers are distinguished in turbulent boundary layers, the wall (inner) layer ($0 < y < 300\delta_w \approx 0.16$) and the outer layer ($0.16 < y < \delta$); see Fig. 5. In these two layers the physical phenomena and the distributions of various flow quantities are different. For two-dimensional low-speed turbulent boundary layers, the different formulas are given in Table 4.

Most important is the logarithmic law region within the inner layer, where the velocity and temperature are logarithmic functions of the wall distance (law of ***the wall***). The mixing length is about proportional to wall distance, and the turbulent Prandtl number is nearly constant. The constants in the logarithmic laws are usually functions of the heat transfer parameter,

$$B_q = \frac{q_w}{\rho_w c_p u_\tau T_w} \tag{187}$$

© 1983 Hemisphere I blishing Corporation

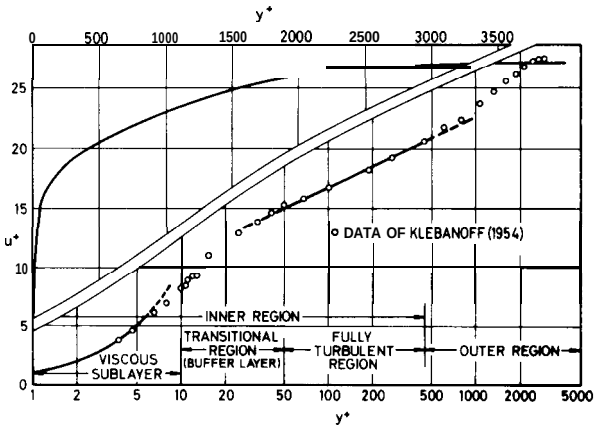

Figure 5 Semilogarithmic and linear plots of mean velocity distribution across a turbulent boundary layer with zero pressure gradient. o Measurements, after Klebanoff [126].

and of the roughness parameter,

$$k^+ = \frac{k_r u_\tau}{\nu_w} \tag{188}$$

where k_r is the roughness height. In a semilogarithmic plot, the velocity distribution corresponds to a straight line. Heat transfer or surface roughness lead only to a parallel shifting of the straight line.

This logarithmic behavior of the velocity law is often used to determine the wall shear stress in turbulent boundary layers. By rearranging the formula for $\bar{u}$ in the logarithmic law region, we get

$$\frac{\bar{u}}{u_e} = \frac{1}{\kappa\kappa}\frac{u_\tau}{u_e}\ln\frac{y u_e}{\nu} + \frac{u_\tau}{u_e}\left(C + \frac{1}{\kappa}\ln\frac{u_\tau}{u_e}\right) \tag{189}$$

A plot of $\bar{u}/u_e$ against $\ln(yu_e/\nu)$ must therefore be linear (*Clauser* plot). The slope of the straight line is equal to $u_\tau/\kappa u_e$, from which τ_w can be calculated.

In order to use probes for determining the wall shear stress (for instance, the Preston tube), it has to be assumed that the logarithmic law of the wall is valid at the station of the measurement; see [108].

The outer layer, about 90% of the boundary layer, is governed by the ***velocity defect law*** of von Karman, and by the law ***of the wake*** of D. Coles, respectively.

The defect law is independent of viscosity, roughness, and heat transfer. Only the pressure gradient influences the wake parameter II.

Combining the law of the wall and the law of the wake leads to a universal velocity law for turbulent boundary layers:

$$u^+ = \frac{\bar{u}}{u_\tau} = \frac{1}{\kappa}\ln y^+ + C(k^+, B_q) + \frac{2\Pi}{\kappa}\sin^2\left(\frac{\pi}{2}\frac{y}{\delta}\right) \tag{190}$$

where

$$y^+ = \frac{y}{\delta_w,} = \frac{y u_\tau}{\nu_w} \tag{191}$$

This universal law is valid over the whole thickness of the boundary layer except an extremely small region very close to the wall ($y < 0.026$).

Using this universal velocity profile for the whole boundary layer, integral values such as $\delta_1, \delta_2, H_{12}$, and so on, can be determined as functions of u_τ, δ, k^+, and B_q. For smooth and isolated surfaces ***(k' = 0, B_q = 0),*** a universal relationship between local skin friction coefficient, see Eq. (161), and Reynolds number based on δ_2 can be derived. This relationship is the well-known Ludwieg-Tillmann formula,

$$c_f = 0.246\,\mathrm{Re}_{\delta 2}^{-0.268} \times 10^{-0.678 H_{12}} \tag{192}$$

where $H_{12} = \delta_1/\delta_2$ is the shape parameter defined in Eq. (156). This formula can be used to determine the skin friction coefficient by measuring the velocity profile and calculating δ_1, δ_2, and hence $\mathrm{Re}_{\delta 2}$ and H_{12}.

The boundary-layer thickness is usually defined as the wall distance where the velocity is a certain given percentage (say, 99.5%) of the outer flow velocity. For $y < \delta$, the flow is not always turbulent. In the region $0.4 < y/\delta < 1.2$, the flow condition changes randomly from laminar to turbulent and back. The intermittency [see Sec. C(b)] is $\gamma = 0.5$ at about $y = 0.86$. If the velocity profiles, properly nondimensionalized, are independent of the downstream distance (self-similarity). the turbulent boundary layers are called self-preserving or equilibrium layers; see also Sec. D(c). The turbulent boundary layer past a flat plate is in equilibrium only if there is roughness on the plate surface with a roughness height proportional to the downstream distance x; see [114].

(i) Prediction methods for turbulent boundary layers

The prediction methods for turbulent boundary layers can be classified into two main groups, the integral methods and the differential methods, depending on the form of the governing equations used.

Although integral methods are preferred in engineering practice today, the development of computers and advanced techniques to measure details in turbulent flows (real-time measuring techniques, Laser-Doppler technique) led more and more to a superiority of the differential methods; see [115].

I. Integral methods

The integral methods use the momentum integral equation, Eq. (147), and some other integral equations. As a second governing equation, often the mean kinetic

© 1983 Hemisphere Publishing Corporation

Table 4 Universal distribution of velocity, shear stress, and temperature in turbulent boundary layers[a]

	Inner (wall) layer			outer layer
	Viscous sublayer	Buffer layer	Logarithmic law region (Law of the wall)	(Law of the wake) (defect law)
Range within boundary layer (roughly)	$0 < y^+ < 5$ $0 < \frac{y}{\delta} < 0.002$	$5 < y^+ < 60$ $0.002 < \frac{y}{\delta} < 0.02$	$60 < y^+ < 300$ $0.02 < \frac{y}{\delta} < 0.1$	$300 < y^+ < 3\,000$ $0.1 < \frac{y}{\delta} < 1$
Velocity distribution	$\frac{\bar{u}}{u_\tau} = y^+$	$\frac{\bar{u}}{u_\tau} = 11 \arctan \frac{y^+}{11}$ $(B_q = 0, k+ = 0)$	$\frac{\bar{u}}{u_\tau} = \frac{1}{\kappa} \ln y^+ + C(B_q, k^+)$	$\frac{u_e - \bar{u}}{u_\tau} = -2.5 \ln\left(\frac{y}{\delta}\right) + \frac{\Pi(B_q)}{\kappa}\left[2 - w\left(\frac{y}{\delta}\right)\right]$
Eddy viscosity ν_t	$\nu_t = \kappa u_\tau y$			$\nu_t = \alpha_1 u_\tau \delta$ $0.06 \leqslant \alpha_1 \leqslant 0.075$
Mixing length I	$l = \kappa y D$			$I \approx 0.096$
Turbulent Prandtl number Pr_t (Pr > 0.6)	$0.90 < \mathrm{Pr}_t < 1.02$			$\mathrm{Pr}_t = 0.95 - 0.45 \frac{y}{0^\delta}^2$
Temperature distribution $\bar{T}$	$T = T_w(1 - B_q \mathrm{Pr}_w y^+)$		$\bar{T} = T_w - \frac{\kappa q_w}{\kappa_\theta c_p \tau_w} - \frac{\kappa \bar{u}^2}{2\kappa_\theta c_p}$	
Remarks	Depending on viscosity Independent of pressure gradient		Velocity gradient Independent of ν	Dependent on pressure gradient via Π

[a] κ = 0.41 (von Karman constant).
$\kappa_\theta \equiv 0.45$.
B_q according to Eq. (187).
k^+ according to Eq. (188).
D according to Eq. (204).
$w(y/\delta) = 2 \sin^2(\pi y/2\delta)$.
$C(B_q, k^+) = 5.2 + 30.7B_q + 226B_q^2$, $0 < k^+ < 5$, hydraulically smooth.
$C(0, k^+) = 8.5 - 2.5 \ln k^+$, $60 < k^+$, fully rough.

energy equation, Eq. (148), is used. The latter equation requires some assumption about the turbulent shear stress to permit calculation of the dissipation function D, defined in Eq. (157). If one uses, for instance, the universal shear stress distribution given in Table 5, the integral equations for momentum and mean kinetic energy together with the Ludwieg-Tillmann formula can be considered as three equations for the three unknown values of the boundary layer $\mathrm{Re}_{\delta 2}$, H_{12}, and c_f.

In the case of incompressible, two-dimensional turbulent boundary layers, the two integral equations lead to the following ordinary differential equations:

$$\frac{d\delta_2}{dx} + (2 + H_{12})\frac{\delta_2}{u_e}\frac{du_e}{dx} = \frac{c_f}{2} = \frac{1}{2}\alpha(H_{32})\,\mathrm{Re}_{\delta 2}^{-0.268} \tag{193}$$

$$\frac{d\delta_3}{dx} + 3\frac{\delta_3}{u_e}\frac{du_e}{dx} = 2c_D = 2\beta(H_{32})\,\mathrm{Re}_{\delta 2}^{-0.168} \tag{194}$$

where

$$H_{12}(H_{32}) = 1 + 1.48(2 - H_{32}) + 104(2 - H_{32})^{6.7} \tag{195}$$

$$\alpha(H_{32}) = 0.056\,6H_{32} - 0.084\,2 \tag{196}$$

$$\beta(H_{32}) = 0.004\,81 + 0.082\,2(H_{32} - 1.5)^{4.81} \tag{197}$$

These are two equations for the two unknowns δ_2 and $\delta_3 = H_{32} \cdot \delta_2$, when the external flow velocity distribution $u_e(x)$ is given. The calculation starts at the transition point, determined by Eq. (185). At this point $\delta_2 = \delta_{2,\mathrm{lam}}$ and $H_{32} = H_{32,\mathrm{lam}}$. The criterion for separation is

$$H_{32,\mathrm{sep}} \approx 1.53\text{-}1.57 \tag{198}$$

Analogous to Eq. (168), separation of turbulent boundary layers can also be calculated from given

© 1983 Hemisphere Publishing Corporation

pressure distribution directly. Stratford, see [109], developed the criterion for separation:

$$c_p \left(\frac{dc_p}{dx} \right)^{1/2} (10^{-6}\ \mathrm{Re}_x)^{-1/10} = 0.3\text{-}0.5 \qquad (199)$$

Here c_p is defined as

$$c_p = 1 - \left(\frac{u_e}{u_0} \right)^2 \qquad (200)$$

where u_0 is the outer flow velocity at the beginning of the adverse pressure gradient. The formula assumes an adverse pressure gradient starting from the leading edge, as well as fully turbulent flow everywhere. When there is a region of laminar flow or a region of turbulent flow with a favorable pressure gradient, a fictitious origin for the coordinate x has to be determined before Eq. (199) can be applied; see [109] and Sec. D(e).

Integral methods for predicting turbulent boundary layers are available that take into account further effects such as history effects, heat transfer, and compressibility. For further information, the reader is referred to the book by Walz [68], and also to the literature surveys in [110-114].

II. Differential methods

The velocity components or the stream functions are governed by partial differential equations. Depending on the modeling of the turbulence, the following levels of turbulent-flow models can be distinguished; see [111] and [119].

(i) Zero-equation models. Zero-equation models use only the partial differential equations for the mean velocity field, where the shear stress is given by an algebraic equation. Most of these methods are based on the eddy viscosity concept, see Eq. (140), or on Prandtl s mixing length formula,

$$\frac{\tau_t}{\rho} = -\overline{u'v'} = l^2 \left| \frac{\partial \bar{u}}{\partial y} \right| \frac{\partial \bar{u}}{\partial y} \qquad (201)$$

The latter equation is the definition of the mixing length l, which, in simple flows, is simpler to correlate than $\overline{u'v'}$ itself. The connection between ν_t and l is

$$\nu_t = l^2 \left| \frac{\partial \bar{u}}{\partial y} \right| \qquad (202)$$

In most methods of modeling eddy viscosity ν_t or the mixing length l, the viewpoint of Sec. D(h) is adopted; that is, the turbulent boundary layer is regarded as a composite layer consisting of inner and outer regions, and the distributions of ν_t or l are described by two separate empirical expressions in each region. As an example, the following expressions have been used in the method by Patankar and Spalding [116]:

$$l = \kappa y D \qquad 0 \leqslant \frac{y}{\delta} \leqslant \frac{\lambda}{\kappa} \qquad (203a)$$

$$l = \lambda \delta \qquad \frac{\lambda}{\kappa} \leqslant \frac{y}{\delta} \leqslant 1 \qquad (203b)$$

where

$$D = 1 - \exp\left[-\frac{y(\tau_w \rho_w)^{1/2}}{A^+ \eta_w} \right] \qquad (204)$$

is the Van Driest damping factor. The constants are

$\kappa = 0.435$ (von Karman constant)

$\lambda = 0.09$ or $\frac{\lambda}{\kappa} = 0.2$

$A+ = 25.3$

For other equations modeling ν_t or l, see [26, 110, 111].

(ii) One-equation models. One-equation models use a partial differential equation for the shear stress $\tau(x, y)$. The turbulence kinetic energy equation, Eq. (127), is used as a basis for a model equation of the shear stress. The shear stress and the turbulent kinetic energy have to be connected by an appropriate relationship. Such models have been developed by Bradshaw et al. [117] and by a group at Stanford University [115, 121].

Bradshaw uses the following partial differential equation for the shear stress $\tau(x, y)$ derived from the turbulent kinetic energy equation:

$$\underbrace{\bar{u} \frac{\partial}{\partial x} \left(\frac{\tau}{2a_1 \rho} \right) + \bar{v} \frac{\partial}{\partial y} \left(\frac{\tau}{2a_1 \rho} \right)}_{\text{Advection}} \underbrace{- \frac{\tau}{\rho} \frac{\partial \bar{u}}{\partial y}}_{\text{Production}} \underbrace{+ \frac{(\tau/\rho)^{3/2}}{L}}_{\text{dissipation}}$$

$$\underbrace{+ \left(\frac{\tau_{\max}}{\rho} \right)^{1/2} \frac{\partial}{\partial y} \left[\left(\frac{\tau_{\max}}{\rho u_e^2} \right)^{1/2} \phi \frac{\tau}{\rho} \right]}_{\text{Diffusion}} = 0 \qquad (205)$$

where $L/6$ and ϕ are given universal functions of the dimensionless wall distance y/S.

It is worth mentioning that neglecting the transport terms due to advection and due to diffusion, the equation reduces to a much simpler equation, representing the equality of production and dissipation. This equation is identical with the mixing-length formula, Eq. (201).

(iii) Two-equation models. Two-equation models use partial differential equations for $\tau(x, y)$ and a turbulent length scale $l(x, y)$. Whereas $\tau(x, y)$ is calculated from the turbulent kinetic energy equation (k equation), $l(x, y)$ is determined by an equation for the isotropic dissipation ϵ. This equation can be developed from the Navier-Stokes equations by appropriate differentia-

© 1983 Hemisphere F blishing Corporation

tion, multiplication, and averaging. Such two-equation models, sometimes called k-e-equation models, have been developed by groups at Imperial College and at Stanford University; see [115, 12 13 .

(iv) Stress-equation models. Stress-equation models use partial differential equations for all components of the turbulent stress tensor. One special model has been developed by Rotta [118], who uses partial differential equations for the mean velocity components, $\bar{u}(x, y)$, $\bar{v}(x, y)$, for the shear stress $\tau(x, y)$, for the turbulence kinetic energy $k(x, y)$ and for the turbulence length scale $L(x, y)$.

(v) Large-eddy simulations. Large-eddy simulation methods compute the three-dimensional time-dependent large-eddy structure and use a low-level model for the small-scale turbulence. Large computers are necessary, and the development of these methods is in an early stage [129].

Class (i) is also called the class of ***mean** field* closures, classes (ii)-(iv) being ***transport-equation*** closures. An alternative classification is based on the highest order of velocity product for which a transport equation is used. Zero-equation models use partial differential equations for ii, $\bar{v}$ only and are therefore first-order models, classes (ii)-(iv) use partial differential equations for $u'v'$, and so on. and are second-order closures.

For curvature effects see [127].

(j) Turbulent boundary layer on a flat plate

The relationship given in the last two sections can be specialized for the flow past a flat plate, where the pressure gradient is equal to zero. The shape parameters for the smooth flat plate without heat transfer are nearly constant:

$H_{12} = 1.3$

$H_{32} = 1.75$

$\Pi = 0.55 \qquad (\mathrm{Re}_{\delta 2} > 5\,000)$

For lower Reynolds numbers, II is a function of $\mathrm{Re}_{\delta 2}$, see [26]. The Ludwieg-Tillmann formula, Eq. (192), reduces to the simple relationship

$$c_f = 0.037\,4\,\mathrm{Re}_{\delta 2}^{-0.268} \tag{206}$$

Since the momentum integral equation, Eq. (147), reduces to

$$c_f = 2\,\frac{d\delta_2}{dx} \tag{207}$$

the local skin friction coefficient becomes approximately

$$c_f = 0.059\,2\,\mathrm{Re}_x^{-1/5} \qquad (5 \times 10^5 \leqslant \mathrm{Re}_x \leqslant 10^7) \tag{208}$$

This equation is in good agreement with experiments up to Re, = 10 .

$$c_f = 0.270(\log \mathrm{Re}_x)^{-2.584}$$
$$c_f = (2 \log \mathrm{Re}_x - 0.65)^{-2/3} \tag{209}$$

The integration of the wall shear stress over the cord length of the flat plate leads to the skin friction drag coefficient,

$$c_f = \frac{D}{(\rho_e/2)u_e^2 l} = \frac{\int_{J0}^{l} \tau_w\, dx}{(\rho_e/2)u_e^2 l} = \frac{\delta_2(l)}{l} \tag{210}$$

In Fig. 6 this drag coefficient is shown as a function of Reynolds number $\mathrm{Re} = u_e l/\nu$ and the relative roughness height k_r/l. The broken curve shown in the diagram corresponds to the limit of complete roughness, beyond which the drag coefficient is independent of Reynolds number. It is noted from Fig. 6 that a given relative roughness causes the coefficient of skin friction to increase only if the Reynolds number exceeds a certain value. The roughness height k_{radm} is called ***admissible*** if it causes no increase in drag compared with a smooth wall. From Fig. 6, the following simple formula can be derived:

$$\frac{u_e k_{\mathrm{radm}}}{\nu_e} \leqslant 100 \tag{211}$$

In Table 5 the equivalent sand roughness heights for several types of technically rough surfaces are given.

The following effects may influence the turbulent flow on the flat plate.

I. Heat transfer

The simplest way to determine the drag coefficient taking heat transfer into account is the use of the ***reference temperature Tr,*** which lies between the highest and the lowest values of the temperature encountered within the boundary layer.

$$T_r = T_e + j(T_w - T_e) \qquad 0 \leqslant j \leqslant 1 \tag{212}$$

When $j = 0.5$ is used, the reference temperature is called *film* ***temperature; see*** [119] and also Sec. D(f). The formulas derived for isothermal flow are also used for the case of heat transfer, but the values for ρ and η are taken at the reference temperature.

A formula has been derived by Van Driest [120], which takes the heat transfer into account assuming a power law viscosity-temperature relationship $\eta \sim T^{\omega}$:

$$\frac{2}{(T_w/T_e)^{1/2} + 1}\,\frac{1}{\sqrt{\bar{c}_f}} = 0.41 + \log(\mathrm{Re}_x \bar{c}_f) - \omega \log \frac{T_w}{T_e} \tag{213}$$

This formula, specialized for the isothermal case $T_w = T_e$, reduces to a relationship that is equivalent to the one given in Fig. 6; see also [130].

© 1983 Hemisphere Publishing Corporation

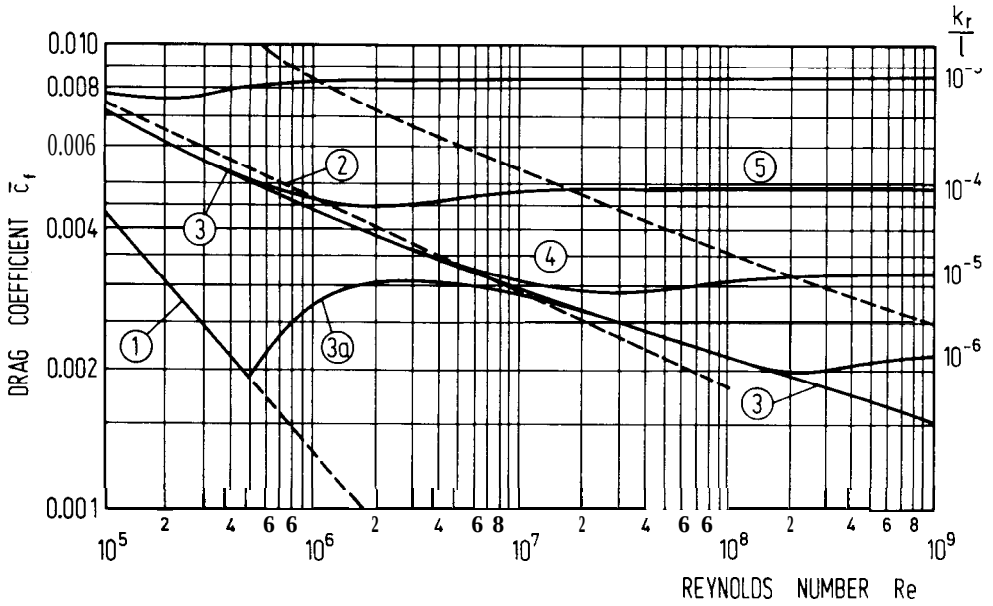

Figure 6 Drag coefficient of the flat plate. (1) Blasius: $\bar{c}_f = 1.328\ \mathrm{Re}^{-1/2}$ (laminar). (2) Prandtl: $\bar{c}_f = 0.074\ \mathrm{Re}^{-1/5}$ (turbulent hydraulically smooth). (3) Prandtl-Schlichting: $\bar{c}_f = 0.455\ (\log \mathrm{Re})^{-2.58}$ (turbulent hydraulically smooth). (3a) $\bar{c}_f = 0.455\ (\log \mathrm{Re})^{-2.58} - 1700\ \mathrm{Re}^{-1}$ (turbulent hydraulically smooth). (5) $\bar{c}_f = [1.89 + 1.62 \log (l/k_r)]^{-2.5}$ (fully rough).

Table 5 Equivalent sand roughness for several types of surfaces

Type of surface	k_r, mm
Polished metal or wood	$0.5\text{-}2 \times 10^{-3}$
Natural sheet metal	4×10^{-3}
Smooth matte paint, carefully applied	6×10^{-3}
Standard camouflage paint, average application	10^{-2}
Camouflage paint, mass production spray	3×10^{-2}
Dip-galvanized metal surface	0.15
Natural surface of cast iron	0.25

II. Suction or injection

As in laminar flow, suction increases skin friction, whereas injection decreases it and leads eventually to flow separation. Further details can be found in [121-123].

III. Mach number effect

High-speed flows are characterized by the Mach number. In particular, for air the Mach number effects I-rave been studied extensively; see surveys in [124] and [125].

NOMENCLATURE FOR SECTION 2.2.1

$a_g(\mathrm{Pr})$ factor in Eq. (183)
$a_q(\mathrm{Pr})$ factor in Eq. (182)
$a_T(\mathrm{Pr})$ factor in Eqs. (178)-(180)
$a(\xi, \eta_s)$ factor, Eq. (139*d*)
$A(\omega)$ factor in Eq. (18 1)
A' dimensionless Van Driest constant [Eq. (204)]
Ar Archimedes number
Ar_x Archimedes number based on x [Eq. (183)]
$b(\xi, \eta_s)$ factor, Eq. (139*a*)
B_q heat transfer parameter [Eq. (187)]
c reciprocal density ratio [Eq. (139c)]
c_D dimensionless dissipation [Eq. (194)]
c_f skin friction coefficient [Eq. (172)]
$\bar{c}_f$ friction drag coefficient [Eq. (210)]
c_p heat capacity at constant pressure, J/kg K
c_p pressure coefficient [Eq. (200)]
c_v heat capacity at constant volume, J/kg K
C Chapman-Rubesin parameter [Eq. (175)]
$C(k^+, B_q)$ constant in law of the wall [Eq. (190)]
d dissipation [Eq. (160)], kg/s^3
d_n hydraulic diameter [Eq. (46)], m
D diffusion [Eq. (112)], kg/m s^3
D Van Driest damping factor [Eq. (204)]
D dissipation integral [Eq. (15 7)]
D drag per unit span [Eq. (184)], N/m
Da Damköhler number
Ec Eckert number
Eu Euler number

© 1983 Hemisphere F blishing Corporation

$\hat{f}$ friction factor [Eq. (49)]
f frequency, s^{-1}
$f(\xi, \eta_s)$ dimensionless stream function [Eq. (134)]
F force, N
Fo Fourier number
Fr Froude number
$g(\xi, \eta_s)$ dimensionless temperature [Eq. (136)]
g gravitational acceleration, m/s^2
Ga Galilei number
Gr Grashof number
Gz Graetz number
h specific enthalpy, m^2/s^2
$H = H_{12}$ shape parameter [Eq. (156)]
H_{32} shape parameter [Eq. (197)]
H_{43} shape parameter [Eq. (156)]
IQ^2 integral scale for turbulence [Eq. (158)], kg/m
k time-averaged turbulent kinetic energy [Eq. (113)], $kg/m\,s^2$
k^+ roughness parameter [Eq. (188)]
k_r roughness height, m
$k_{r,adm}$ admissible roughness height, m
k_r, k_θ, k_z components of body force per unit volume in cylindrical coordinate system, N/m^3
k_x, k_y, k_z Cartesian components of body force per unit volume, N/m^3
k body force per unit volume, N/m^3
Kn Knudsen number
l characteristic length [Eq. (88)], m
I mixing length [Eq. (201)], m
l_0 mean free path, m
$l(\lambda)$ Thwaites function [Eq. (163)]
L length of duct [Eq. (48)], m
$L(y)$ Bradshaw function [Eq. (205)], m
M mass, kg
$\dot{M}$ mass flow rate, kg/s
M moment, N/m
Ma Mach number
n polytropic exponent [Eq. (40)]
n normal unit vector
Nu Nusselt number
p static pressure, N/m^2
p_{dyn} pressure due to fluid motion [Eq. (85)], N/m^2
p_{st} pressure in static field, N/m^2
P production of turbulence [Eq. (112)], $kg/m\,s^3$
P power, J/s = W
P_S work done by all stress forces on the surface [Eq. (23)], W
P_B work done by body forces [Eq. (21)], W
P_D dissipation [Eq. (22)], W
P_H rate of heat added to system, W
P_M mechanical work done on fluid, W
P_ρ work done to change density, W
$\bar{P}$ integral of turbulence production [Eq. (159)], kg/s^3
P_r perimeter, m
Pe Péclet number
Pr Prandtl number
Pr_t turbulent Prandtl number [Eq. (143)]
q_{12} specific heat [Eq. (36)], m^2/s^2
$q(t)$ resultant fluctuation velocity [Eq. (127a)], m/s
$\dot{q}$ heat flux per unit area, $J/m^2\,s$
r position vector, m
r, θ, z cylindrical coordinates, m, –, m
R specific gas constant, J/kg K
Ra Rayleigh number
Re Reynolds number
Re_x Reynolds number based on x
$Re_{\delta 2}$ Reynolds number based on δ_2
Ri Richardson number
Ro Rossby number
s coordinate along mean flow direction, m
s force per unit area, N/m^2
S cross-sectional flow area, m^2; Sutherland constant [Eq. (74)]
$\overline{S_t}$ Reynolds shear stress tensor [Eqs. (111),(118), (120)], N/m^2
S stress tensor [Eqs. (117) and (119)], N/m^2
Sr Strouhal number
St Stanton number
t time, s
T (absolute) temperature, K
$\bar{T}$ mean (bulk) temperature [Eq. (28)], K
u specific internal energy, J/kg K
u_{sound} speed of sound, m/s
u_τ friction velocity [Eq. (186)], m/s
u, v, w Cartesian velocity components, m/s
U reference velocity, m/s
U_∞ free stream velocity, m/s
v_r, v_θ, v_z cylindrical polar velocity components, m/s
V volume, m^3
w wake function (Table 4)
$\bar{w}$ mean velocity [Eq. (26)], m/s
W velocity vector, m/s
w_{t12} specific technical work [Eq. (35)], m^2/s^2
W rate-of-strain tensor, s^{-1}
x, y, z Cartesian coordinates, m
y^+ dimensionless distance from wall [Eq. (191)]
α angle of coordinate system against horizontal [Eqs. (124), (125)]
α kinetic energy correction factor [Eq. (29)]
$\alpha(H_{32})$ skin friction factor [Eq. (196)]
β coefficient of thermal expansion [Eq. (71)], K^{-1}
β momentum correction factor [Eq. (30)]
$\beta(H_{32})$ dissipation factor [Eq. (197)]
$\beta_s(\xi)$ dimensionless pressure gradient [Eq. (139b)]
γ heat capacity ratio
γ intermittency factor [Sec. C(b)]

© 1983 Hemisphere Publishing Corporation

δ boundary-layer thickness, m
δ_1 displacement thickness [Eq. (15 1)], m
δ_2 momentum thickness [Eq. (152)], m
δ_3 energy thickness [Eq. (153)], m
δ_4 density thickness [Eq. (155)], m
δ_5 temperature thickness [Eq. (155)], m
δ_w wall-layer thickness [Eq. (19 1)], m
Ap pressure loss, N/m^2
ϵ dissipation [Eq. (112)], kg/m s^3
$\epsilon_{ij}(i, j = x, y, z)$ Cartesian components of eddy viscosity tensor [Eq. (11 8)], kg/m s
$\epsilon_{ij}(i, j = r, \theta, z)$ cylindrical polar components of eddy viscosity tensor [Eq. (120)], kg/m s
ϵ_m^+ viscosity ratio [Eq. (141)]
ζ dimensionless product of density and viscosity [Eq. (76)]
η (dynamic) viscosity, kg/m s
η_s similarity variable [Eq. (132*b*)]
θ angle of coordinate system against horizontal [Eqs. (32), (33)]
κ von Karman constant [Eq. (189)]
κ_θ constant in universal temperature distribution (Table 4)
λ thermal conductivity, J/m s K
λ Thwaites function [Eq. (164)]
λ factor in Spalding s mixing length formula [Eq. (203*b*)]
λ_t eddy thermal conductivity [Eq. (142)], J/m s K
ν kinematic viscosity, m^2/s
ν_t eddy kinematic viscosity [Eq. (140)], m^2/s
ξ transformed coordinate, Eq. (132*a*), $kg^2/m^2 s^2$
Π factor in law of the wake [Eq. (190)]
ρ density, kg/m^3
$\bar{\rho}$ mean density [Eq. (27)], kg/m^3
τ shear stress, N/m^2
τ_w wall shear stress, N/m^2
$\tau_{ij}(i, j = x, y, z)$ Cartesian components of stress tensor [Eq. (IO)], N/m^2
ϕ Bradshaw function [Eq. (205)]
ϕ_{12} specific dissipation between stations 1 and 2 [Eq. (38)], m^2/s^2
Φ dissipation function [Eq. (61)], s^{-2}
ψ stream function [Eq. (133)], kg/m s
ω viscosity law exponent [Eq. (75)]

Subscripts

B body force
B Blasius solution [Eqs. (165)-(168)]
cr critical
e outer edge of boundary layer
n normal to the wall
r reference state
s at constant entropy
S cross-sectional flow area
sep separation
t turbulent
w wall
x, z x axis, z axis
∞ far field

Superscripts

$\bar{\ }$ time mean or spatial mean
$\tilde{\ }$ mass-weighted time average [Eq. (104)]
$*$ dimensionless values [Eq. (88)]
$'$ turbulent fluctuation [Eq. (106)]
$''$ turbulent fluctuation [Eq. (106)]
$+$ dimensionless value, based on δ_w

REFERENCES FOR SECTION 2.2.1

1. Hirschfelder, J. O., Curtiss, C. F., and Bird, R. B., ***The Molecular Theory of Gases and Liquids,*** Wiley, New York, 1954.
2. Bird, R. B., Stewart, W. E., and Lightfoot, E. ***N., Transport Phenomena,*** Wiley, New York, 1960.
3. Dorrance, W. H., ***Viscous Hypersonic*** Flow, McGraw-Hill, New York, 1962.
4. Pai, ***S. I., Magnetogasdynamics and Plasma Dynamics,*** Springer-Verlag, Vienna, 1962.
5. Pai, ***S. I., Radiation Gasdynamics,*** Springer-Verlag, Berlin, 1965.
6. Schaaf, S. A., and Chambrt, P. L., Flow of Rarefied Gases, ***in Fundamentals of Gas Dynamics,*** ed. H. W. Emmons, High Speed Aerodynamics and Jet Propulsion, vol. 3, pp. 687-739, Princeton University Press, Princeton, N.J., 1958.
7. Schaaf, S. A., Mechanics of Rarefied Gases, ***in Handbook of Physics,*** ed. S. Flügge, vol. 8, 2, pp. 591-624, Springer-Verlag, Berlin, 1958.
8. Tsien, H. S., The Equations of Gas Dynamics, in ***Fundamentals of Gasdynamics.*** ed. H. W. Emmons, High Speed Aerodynamics and Jet Propulsion, vol. 3, pp. 3-63, Princeton University Press, Princeton, N.J., 1958.
9. Comolet, R., ***Introduction l'Analyse Dimensionelle et Aux Problèmes de Similitude en Mécanique des Fluides,*** Masson, Paris, 1958.
10. Duncan, W. J., ***Physical Similarity and Dimensional Analysis,*** Edward Arnold, London, 1953.
11. Gukhman, A. A., ***Introduction to the Theory of Similarity,*** Academic Press, New York, 1965.
12. Huntley, H. E., ***Dimensional Analysis,*** Dover, New York, 1967.
13. Ipsen, D. ***C., Units, Dimensions and Dimensionless Numbers,*** McGraw-Hill, New York, 1960.
14. Isaacson, E. de St. Q., and Isaacson, M. de ***St. Q., Dimensional Methods in Engineering and Physics,*** Edward Arnold, London, 1975.
15. Kline, ***S.*** J., ***Similitude and Approximation*** Theory, McGraw-Hill, New York, 1965.
16. Langhaar, H. L., ***Dimensional Analysis and the Theory of Models,*** Wiley, New York, 195 1.
17. Pankhurst, R. ***C., Dimensional Analysis and Scale Factors,*** Chapman and Hall, London, 1964.

© 1983 Hemisphere Publishing Corporation

18. Pawlowski, J., ***Die Ahnlichkeitstheorie in der physikalisch-technischen*** *Forschung*, Springer-Verlag, Berlin, 197 1.
19. Sedov, A. ***I., Similarity and Dimensional Methods in Mechanics,*** Academic Press, New York, 1959.
20. Taylor, E. ***S., Dimensional*** *Analysis* ***for Engineers,*** Clarendon Press, Oxford, 1973.
21. Zierep, J.. *Ähnlichkeitsgesetze* ***und*** *Modellregeln* ***der*** *Strömungslehre*, Braun, Karlsruhe, 1972.
22. Schneider, W., Über die Rolle der Flüssigkeits- und Gaseigenschaften in der Theorie mechanisch ähnlicher Strömungen, *Acta Mech.*, vol. 12, pp. 275-305. 1971.
23. Howell, R. R., and McKinney, W., The U.S. 2.5Meter Cryogenic High Reynolds Number Tunnel, ***Proc.10th Congr. Int. Council Aeronaut. Sci. (ICAS), Ottawa,*** pp. 77-87, 1976.
24. Bradshaw, P., ***An Introduction to Turbulence and Its Measurement,*** Pergamon, New York, 1971.
2.5. Bradshaw, P., Introduction, in ***Turbulence, Topics in Applied Physics,*** ed. P. Bradshaw, vol. 12, pp. l-44, Springer-Verlag, Berlin, 1976.
26. Cebeci, T., and Smith, A. M. ***O., Analysis of Turbulent Boundary Layers,*** Academic Press, New York, 1974.
27. Laufer, J., Thoughts on Compressible Turbulent Boundary Layers, ***in Compressible Turbulent Boundary Layers,*** NASA SP-216, pp. 1-14, Washington, D.C., 1969.
28. Schubauer, G. B., and Tchen, C. M., Turbulent Flow, in ***Turbulent*** *Flows* ***and Heat Transfer,*** ed. C. C. Lin, High Speed Aerodynamics and Jet Propulsion, vol. 5, pp. 75-195, Princeton University Press, Princeton, N.J., 1959.
29. Favre, A., Kovasznay, L. S. G., Dumas, R., Gaviglio, J., and Coantic, M., ***La Turbulence en*** *Mécanique* ***des*** *Fluides*, Gauthier-Villars, Paris, 1976.
30. Abramovich, ***G. N., The Theory of Turbulent Jets,*** Massachusetts Institute of Technology Press, Cambridge, Mass., 1963.
31. Rodi, W., A Review of Experimental Data of Uniform Density Free Turbulent Boundary Layers, ***in Studies in Convection,*** ed. B. E. Launder, vol. 1, pp. 79-166, Academic Press, London, 1975.
32. Townsend, A. A., ***The Structure of Turbulent Shear Flow,*** Cambridge University Press, New York, 1976.
33. Gosman. A. D., Pun, W. M., Runchal, A. K., Spalding, D. B., and Wolfshtein, M., ***Recirculating*** *Flows*, Academic Press, London, 1969.
34. Tennekes, H., and Lumley, J. L., ***A First Course in Turbulence,*** Massachusetts Institute of Technology Press, Cambridge, Mass., 1972.
35. Reynolds, A. J., ***Turbulent Flows in Engineering,*** Wiley, London, 1974.
36. Monin, A. S., and Yaglom, A. M., ***Statistical Fluid Mechanics: Mechanics of Turbulence,*** vols. 1 and 2, Masschusetts Institute of Technology Press, Cambridge, Mass., 197 1.
37. Davies, J. T., ***Turbulence Phenomena,*** Academic Press, New York, 1972.
38. Bradshaw, P., Compressible Turbulent Shear Layers, *Annu.* ***Rev. Fluid*** *Mech.*, ***vol. 9,*** pp. 33-54, 1977.
39. Launder, B. E., and Spalding, D. B., ***Lectures in*** *Mathematical Models* ***of Turbulence,*** Academic Press, London, 1972.
40. Launder, B. E., Recce, C. J.. and Rodi, W., Progress in the Development of a Reynolds-Stress Turbulence Closure, ***J. Fluid*** *Mech.*, vol. 68, pp. 537-566, 1975.
41. Mellor, G. L., and Herring, H. J., A Survey of Mean Turbulent Field Closure Models, ***AIAA*** *J.*, vol. 11, pp. 590-599, 1973.
42. Patankar, S. V., Numerical Prediction of Three-Dimensional Flows, in ***Studies in Convection,*** ed. B. E. Launder, vol. 1, pp. l-78, Academic Press, London, 1975.
43. Roache, P. J., ***Computational Fluid*** *Dynamics*, Hermosa, Albuquerque, N.M., 1972.
44. Taylor, T. D., ***Numerical Methods for Predicting Subsonic, Transonic and Supersonic Flow,*** AGARDograph no. 187, 1974.
45. Shen, S. F., Finite-Element Methods in Fluid Mechanics, ***Annu. Rev. Fluid*** *Mech.*, ***vol. 9,*** pp. 421-446, 1977.
46. Peyret, R., and Viviand, H., ***Computation of Viscous Compressible Flows Based on the Navier-Stokes Equations,*** AGARDograph no. 212, 1975.
47. Lin, ***C. C., The Theory of*** *Hydrodynamic Stability*, Cambridge University Press, Cambridge, 1955.
48. Betchov, R., and Criminale, W. ***O., Stability of Parallel Flows,*** Academic Press, New York, 1967.
49. Chandrasekkar, S., ***Hydrodynamic and Hydromagnetic Stability,*** Clarendon Press, Oxford, 1961.
50. Schlichting, H., Enstehung der Turbulenz, in ***Handbook of Physics,*** ed. S. Flügge, vol. 8, 1, pp. 351-450, Springer-Verlag, Berlin, 1959.
51. Shen, S. F., Stability of Laminar Flows, in ***Theory of Laminar Flows,*** ed. F. K. Moore, High Speed Aerodynamics and Jet Propulsion. vol. 4, pp. 719-854, Princeton University Press, Princeton, N.J., 1964.
52. Tani, I., Boundary-Layer Transition, ***Annu. Rev. Fluid*** *Mech.*, vol. 1, pp. 169-196, 1969.
53. Reshotko, E., Boundary Layer Stability and Transition. *Annu.* ***Rev. Fluid*** *Mech.*, ***vol. 8,*** pp. 31 l-350, 1976.
54. Morkovin, M. V., Instability, Transition to Turbulence and Predictability, AGARDograph no. 236, 1978.
55. Stuart, J. T., Hydrodynamic Stability, in ***Laminar Boundary Lavers,*** ed. L. Rosenhead, Clarendon Press. Oxford, 1963.
56. Moore, F. K.. Three-Dimensional Boundary Layer Theory, ***in Adv. Applied*** *Mech.*, ***vol. 4,*** pp. 160-228, 1956.
57. Cooke, J. C., and Hall, M. G., Boundary Layers in Three Dimensions, in ***Prog. Aeronaut.*** *Sci.*, ***vol. 2,*** pp. 221-282. 1962.
58. Mager, A., Three-Dimensional Laminar Boundary Layers, in ***Theory of Laminar Flows,*** ed. F. K. Moore, High Speed Aerodynamics and Jet Propulsion, vol. 4, pp. 286-394, Princeton University Press, Princeton, N.J., 1964.
59. Crabtree, L. F., Kiichemann, D., and Sowerby, L., Three-Dimensional Boundary Layers, in ***Laminar Boundary Layers,*** ed. L. Rosenhead, Clarendon Press, Oxford, 1963.
60. Nash, J. F., and Patel, V. C., ***Three Dimensional Turbulent Boundary Layers,*** SBC Technical Book, Atlanta, Ga., 1972.
61. Eichelbrenner, E. A., Three-Dimensional Boundary Layers, *Annu.* ***Rev.*** *Fluid Mech.*, vol. 5, pp. 339-360, 1974.
62. Fannelöp, T. K., and Krogstad, P. A., Three-Dimensional Boundary Layers in External Flows, A Report on Euromech 60, ***J. Fluid*** *Mech.*, vol. 71, pp. 815-826, 1975.
63. Stewartson, K., ***The Theory of Laminar Boundary Layers in Compressible Fluids,*** Oxford University Press, London, 1964.
64. Loitsianski, L. G., ***Laminare Grenzschichten*** (tr from Russian), Akademie-Verlag, Berlin, 1967.

© 1983 Hemisphere Publishing Corporation

65. Schlichting, H., *Grenzschicht-Theorie,* Braun, Karlsruhe, 196.5; English ed.: ***Boundary*** Layer Theory, McGraw-Hill, New York, 1969.
66. Persen, L. ***N., Introduction to Boundary Layer*** Theory, Tapir Forlag, Trondheim, 1972.
67. Cebeci, T., and Bradshaw, P., ***Momentum Transfer in Boundary Layers,*** Hemisphere, Washington, DC.. 1977.
68. Walz, A., ***Strömungs- und Temperaturgrenzschichten,*** Braun, Karlsruhe, 1966.
69. Lagerstrom, P. A., Laminar Flow Theory, in ***Theory of Laminar Flows,*** ed. F. K. Moore, High Speed Aerodynamics and Jet Propulsion, vol. 4, pp. 20-285, Princeton University Press, Princeton, N. J., 1964.
70. Jones, C. W., and Watson, E. J., Two-Dimensional Boundary Layers, in ***Laminar Boundary Layers,*** ed. L. Rosenhead. Clarendon Press, Oxford, 1963.
71. Gadd, G. E., Jones, C. W., and Watson, E. J., Approximate Methods of Solution, in ***Laminar Boundary Layers,*** ed. L. Rosenhead, Clarendon Press, Oxford, 1963.
72. Evans, H. L., ***Laminar Boundary-Layer Theory,*** Addison-Wesley, Reading, Mass., 1968.
73. Stewart, E. E., and Prober, R., Heat Transfer and Diffusion in Wedge Flows with Rapid Mass Transfer, *Int. J. **Heat Mass Transfer,*** vol. 5, pp. 1149-1163, 1962.
74. Gersten, K., and Körner, H., Wärmeübergang unter Berücksichtigung der Reibungswärme bei laminaren Keilströmungen mit veränderlicher Temperatur und Normalgeschwindigkeit entlang der Wand. *Int. J. **Heat Mass Transfer,*** vol. 11, pp. 655-673. 1968.
75. Dewey, C. F., Jr., and Gross, J. F., Exact Similar Solutions of the Laminar Boundary-Layer Equations, ***Adv. Heat Transfer, vol. 4,*** pp. 317-446, 1967.
76. Keller, H. B., Numerical Methods in Boundary-Layer Theory, ***Annu. Rev. Fluid** Mech., **vol.*** 10, pp. 417-434, 1978.
77. Jaffee, N. A., and Smith, A. M. O., Calculation of Laminar Boundary Layers by Means of a Differential-Difference Method. in *Prog. **Aerospace** Sci.,* vol. 12, pp. 49-212, 1972.
78. Stuart, J. T., Unsteady Boundary Layers, in ***Laminar Boundary*** Layers, ed. L. Rosenhead, Clarendon Press, Oxford, 1963.
79. Rott, N., Theory of Time-Dependent Laminar Flows, in ***Theory of Laminar Flows,*** ed. F. K. Moore, High Speed Aerodynamics and Jet Propulsion, vol. 4, pp. 395-438, Princeton University Press, Princeton, N.J., 1964.
80. Telionis, D. P., Calculations of Time-Dependent Boundary Layers, in ***Unsteady Aerodynamics,*** ed. R. B. Kinney. vol. 1, pp. 155–190, University of Arizona, Tucson, Ariz., 1975.
81. Wuest, W., Theory of Boundary Layer Suction to Prevent Separation, in ***Boundary Layer and Flow Control,*** ed. G. V. Lachmann, vol. 2, pp. 196-208, Pergamon Press, Oxford, 1961.
82. Ostrach, S., Laminar Flows with Body Forces, in Theory ***of Laminar*** Flows, ed. F. K. Moore, High Speed Aerodynamics and Jet Propulsion, vol. 4, pp. 528-718, Princeton University Press, Princeton, N.J., 1964.
83. Ede, A. J., Advances in Free Convection, in ***Adv. Heat Transfer,*** vol. 4, pp. l-64, 1967.
84. Pai, ***S. I., Fluid Dynamics of Jets,*** Van Nostrand, Toronto, 1954.
85. Berger, ***S.*** A., ***Laminar Wakes,*** American Elsevier, New York, 1971.
86. Van Dyke, M., Higher-Order Boundary-Layer Theory, ***Annu. Rev.*** *Fluid Mech.,* vol. 1, pp. 265-292, 1969.
87. Gersten, K., and Gross, J. F., Higher Order Boundary Layer Theory, in ***Fluid Dynamics Transactions,*** ed. W. Fiszdon, vol. 7, pt. II, pp. 7-36, Polish Scientific Publishers, Warsaw, 1976.
88. Stewartson, K., Multistructured Boundary Layers on Flat Plates and Related Bodies, in ***Adv. Appl.*** *Mech., **vol.*** 14, pp. 146-239, 1974.
89. Brown, S. N., and Stewartson, K., Laminar Separation, ***Annu. Rev. Fluid*** *Mech., **vol.*** 1, pp. 45-72, 1969.
90. Williams, J. C., HI, Incompressible Boundary-Layer Separation, *Annu. **Rev. Fluid** Mech.,* vol. 9, pp. 13-32, 1977.
91. ***Chang,*** P. K., ***Separation of*** *Flow,* Pergamon Press, Oxford, 1970.
92. Chang, P. K., ***Control of Flow Separation,*** Hemisphere, Washington, D.C., 1976.
93. Eckert, E. R. G., Engineering Relations for Friction and Heat Transfer to Surface in High Velocity Flow, ***J. Aeronaut. Sci,*** vol. 22, pp. 585-587, 1955.
94. Eckert, E. R. G., and Drake, R. M., ***Heat and Mass Transfer,*** McGraw-Hill, New York, 1959.
95. Knuth, E. L., Use of Reference States and Constant Property Solutions in Predicting Mass, Momentum and Energy Transfer Rates in High-Speed Laminar Flow, ***Int. J. Heat Mass Transfer, vol. 6,*** pp. l-22, 1963.
96. Miyamoto, M., Influence of Variable Properties upon Transient and Steady-Free Convection, *Int. J. **Heat Mass Transfer, vol. 20,*** pp. 1258–1261, 1977.
97. Gersten, K., and d'Avila, J. S., Grenzschichteffekte höherer Ordnung bei kombinierter freier und erzwungener Konvektion, DLR-FB 77-16, pp. 85-90, 1977.
98. Chen, T. S., Sparrow, E. M., and Mucoglu, A., Mixed Convection in Boundary Layer Flow on a Horizontal Plate. *J. **Heat Transfer,*** vol. 99, pp. 66-71, 1977.
99. Melnik, R. E., and Chow, R., Asymptotic Theory of Two-Dimensional Trailing Edge Flows, NASA SP-347, pp. 177-250, 1975.
100. Veldmann, A. E. P., and Van de Vooren, A. I., Drag of a Finite Flat Plate, Proc. 4th Int. Conf. Numerical Methods in Fluid Dynamics, ***Lecture Notes in Physics,*** vol. 35, pp. 135-144, Springer-Verlag, Berlin, 1976.
101. Janour, Z., Resistance of a Flat Plate at Low Reynolds Numbers, NACA TM 1316, 1951.
102. Michel, R., Etude de la Transition sur les Profiles d'Aile, Establissement d un Critere de Determination de Point de Transition et Calcul de la Trainée de Profile Incompressible. ONERA Rept. 1/1578 A, 195 1.
103. Laws, E. M., and Livesey, J. L., Flows Through Screens, ***Annu. Rev. Fluid*** *Mech.,* vol. 10, pp. 247-266, 1978.
104. Von Doenhoff, A. E., and Braslow, A. L., The Effect of Distributed Surface Roughness on Laminar Flow, in ***Boundary Layer and Flow Control,*** ed. G. V. Lachmann, vol. 2, pp. 657-681, Pergamon Press, Oxford, 1961.
105. Gibbings, J. C., and Hall, D. J., Criterion for Tolerable Roughness in a Laminar Boundary Layer, *J. Aircraft,* vol. 6, pp. 171-173, 1969.
106. Pfenninger, W., Laminar Flow Control, Laminarization, in Special Course on Concepts for Drag Reduction, AGARD Rept. 654, pp. 3-l to 3-75, 1977.

© 1983 Hemisphere Publishing Corporation

107. Narasimha, R., The Three Archetypes of Relaminarization, *Proc. 6th Can. Congr. Appl. Mech.*, *Vancouver,* pp. 503–527.
108. Head, M. R., and Vasanta Ram, V., Simplified Presentation of Preston Tube Calibration, *Aeronaut. Quart.,* vol. 22, pp. 295-300, 1971.
109. Stratford, B. S., The Prediction of Separation of a Turbulent Boundary Layer, *J. Fluid Mech.,* vol. 5, pp. l-16, 1959.
110. Kline, S. J., et *al.,* eds., *Proc. Computation of Turbulent Boundary Layers-1968,* AFOSR-IFP-Stanford Conference, vol. 1: Methods, Predictions Evaluation and Flow Structure (eds. S. J. Kline, M. V. Morkovin, G. Sovrnn, D. J. Cockrell); vol. 2: Compiled Data (eds. D. C. Coles, A. E. Hirst), Stanford University, Stanford, Calif., 1959.
111. Reynolds, W. C., and Cebeci, T., Calculation of Turbulent Flows, in *Turbulence,* ed. P. Bradshaw, Topics in Applied Physics, vol. 12, pp. 193-231, Springer-Verlag, Berlin, 1976.
112. Fernholz, H. H., External Flows, in *Turbulence,* ed. P. Bradshaw, Topics in Applied Physics, vol. 12, pp. 45-108, Springer-Verlag:, Berlin, 1976.
113. Rotta, J. C., Turbulent Boundary Layers in Incompressible Flow, *Prog. Aeronaut. Sci,* vol. 2, pp. 3-220, 1962.
114. Rotta, J. *C., Turbulente Strömungen,* Teubner, Stuttgart, 1972.
115. Reynolds, W. C., Computation of Turbulent Flows, *Annu. Rev. Fluid Mech.,* vol. 8, pp. 183-208, 1976.
116. Patankar, S. V., and Spalding, D. B., *Heat and Mass Transfer in Boundary Layers,* Intertext, London, 1970.
117. Bradshaw, P., Ferriss, D. H., and Altwell, N. P., Calculation of Boundary-Layer Development Using the Turbulent Energy Equation, *J. Fluid Mech.*, vol. 28, pp. 593-616, 1967.
118. Rotta, J. C., Turbulent Shear Layer Prediction on the Basis of the Transport Equations for the Reynolds Stresses, in *Theoretical and Applied Mechanics,* Proc. XIII. Int. Congr. Theor. Appl. Mech., ed. E. Becker and G. K. Mikhailov, pp. 295–308, Springer-Verlag, Berlin, 1973.
119. Knuth, E. L., and Dershin, H., Use of Reference States in Predicting Transport Rates in High-Speed Turbulent Flows with Mass Transfer, *Int. J. Heat Mass Transfer,* vol. 6, pp. 999-1018, 1963.
120. Van Driest, E. R., Convective Heat Transfer *in* Gases, *in Turbulent Flows and Heat Transfer,* High Speed Aerodynamics and Jet Propulsion. ed. C. C. Lin, vol. 5, pp. 339-540, Princeton University Press, Princeton, N.J., 1959.
121. Kays, W. M., and Moffat, R. J., The Behaviour of Transpired Turbulent Boundary Layers, in *Studies in Convection,* ed. B. E. Launder, vol. 1, pp. 223-320, Academic Press, London, 1975.
122. Jeromin, L. 0. F., The Status of Research in Turbulent Boundary Layers with Fluid Injection, in *Prog. Aeronaut. Sci.,* vol. 10, pp. 65-189, 1970.
123. Simpson, R. L., Some Important Physical Phenomena in Flows with Separated Turbulent Boundary Layers, in *Turbulence in Internal Flows,* ed. S. N. B. Murthy, pp. 31 l-346, Hemisphere, Washington, DC., 1976.
124. Kutateladze, S. S., and Leont ev, A. I.,*Turbulent Boundary Layers in Compressible Gases,* Edward Arnold, London, 1964.
125. Fernholz, H. H., and Finley, P. J., A Critical Compilation of Compressible Turbulent Boundary Layer Data, AGARDograph no. 223, 1977.
126. Klebanoff, P. S., Characteristics of Turbulence in a Boundary Layer with Zero Pressure Gradient. NACA TN 3178, 1954.
127. Bradshaw, P., Effects of Streamline Curvature on Turbulent Flow, AGARDograph no. 169, 1973.
128. Morkovin, M. V., Effects of Compressibility on Turbulent Flows, *in Mécanique de la Turbulence,* Colloque Internationaux no. 108. ed. A. Favre, Editions du Centre Nationale de la Recherche Scientifique, Paris, 1962.
129. Kim, J. and Moin, P., Large Eddy Simulation of Turbulent Channel Flow-ILIAC N Calculation, in AGARD Conf. Proc. no. 271, *Turbulent Boundary Layers, Experiments, Theory and Modelling,* ed. H. W. Liepmann, pp. 14-l to 14-18, 1980.
130. Rotta, J. C., Die turbulente Grenzschicht an einer stark geheizten ebenen Platte bei Unterschallströmung, *Wärme-und Stoffiibertragung,* vol. 7, pp. 133-144, 1974.
13 1. Telionis, D. P., *Unsteady Viscous Flows,* Springer-Verlag, Berlin, 198 1.
132. Libby, P. A., ed., *Turbulent Reacting Flows,* Springer-Verlag, Berlin, 1981.

© 1983 Hemisphere Publishing Corporation

2.2.2
Ducts

K. Gersten

A. Fully developed circular pipe flow

(a) Friction factor (Moody chart)

The flow in a straight circular pipe of constant diameter $d = 2R$ is called fully developed if the velocity distribution $u(r)$ and hence wall shear stress τ_w are independent of the streamwise coordinate x.

The pressure loss Ap between two stations of distance L is given as

$$\Delta p = \hat{f}\,\frac{L}{d}\,\frac{\rho}{2}\,\bar{u}^2 \tag{1}$$

The dimensionless value $\hat{f}$ is called ***friction coefficient*** or ***friction factor,*** which is connected with the wall shear stress [see Eq. 2.2.1(49)] by

$$\hat{f} = \frac{8\tau_w}{\rho\bar{u}^2} \tag{2}$$

where

$$\bar{u} = \frac{2}{R^2}\int_0^R u(r)\,r\,dr = \frac{Q}{\pi R^2} \tag{3}$$

is the mean velocity. According to Eq. 2.2.1(48), the pressure loss is proportional to the dissipation in the pipe, that is, the change from mechanical energy into internal energy. In this section, constant physical quantities ρ and η are assumed; that is, isothermal flow is considered. The friction coefficient $\hat{f}$ is a function of the Reynolds number,

$$\mathrm{Re} = \frac{\rho\bar{u}d}{\eta} \tag{4}$$

and the relative roughness ***k/d.*** This dependence is given by the Moody chart shown in Fig. 1; see [1] . The formulas describing the velocity profiles and other flow characteristics for the various flow regimes are given in Table 1. Five flow regimes can be distinguished, as described below.

1. Laminar flow (Re < 2 400). If the Reynolds number is less than about 2 400, the flow is laminar and if disturbed will return to the laminar condition. For this flow the Navier-Stokes equations, Eqs. 2.2.1(62)–2.2.1(65), can be drastically simplified; the solution leads to Hagen-Poiseuille's law.

2. Turbulent flow, hydraulically smooth surface (2 400 < Re < 3 X 10^6). It was found empirically that in this flow regime the velocity profiles could be described by power law distributions. The exponent of the power law is decreasing with increasing Reynolds number, as can be seen from Table 2.

3. Turbulent flow, hydraulically smooth surface ***(2 400*** < Re, $k^+ < 5$***).*** The flow is very similar to the turbulent boundary-layer flow at high Reynolds numbers; see Sec. 2.2.1D(h), particularly Table 2.2.1(4) and Fig. 2.2.1(5). The flow again can be divided into three layers:

The viscous sublayer ($y < 5\delta_w$)
The buffer layer (56, $< y <$ 606,)
The logarithmic law region ($y > 606\,_w$)

where

$$\delta_w = \frac{\nu}{u_\tau} \tag{5}$$

is the characteristic length scale of the wall region.

© 1983 Hemisphere Publishing Corporation

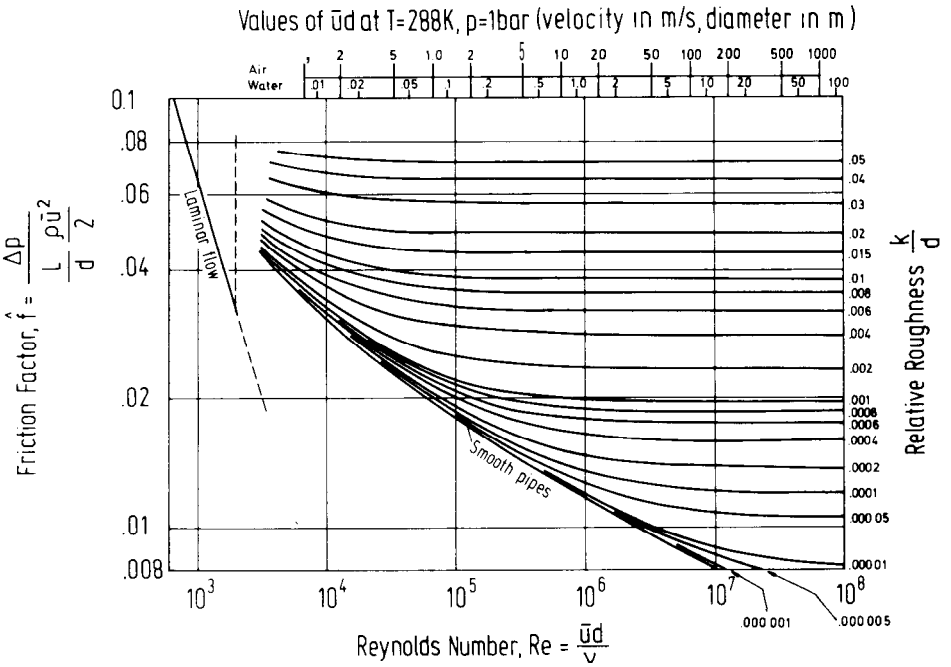

Figure 1 Moody chart for the friction factor of fully developed circular pipe flow. After Moody [1]. Δp, pressure drop over the distance L; d, diameter; $\bar{u}$, mean velocity according to Eq. 2.2.1(26); k, roughness height; ν, kinematic viscosity.

Principally, there is a fourth layer near the pipe center corresponding to the law of the wake-see Table 2.2.1(4)--but its effect is almost negligibly small in pipe flow-see Cebeci and Bradshaw [2].

The flow is called hydraulically smooth if the roughness has no effect on the friction coefficient. This is the case when the roughness is so small that all protrusions are contained within the viscous sublayer, that is, when $k < 56$, or $k^+ = k/\delta_w < 5$.

4. Turbulent flow, rough surface (2 400 < Re, $5 < k^+ < 60$). The protrusions of the rough surface extend partly outside the viscous sublayer. The additional resistance, as compared with a smooth pipe, is due mainly to the form drag experienced by the protrusions in the buffer layer. In this flow regime the friction coefficient is a function of Reynolds number as well as relative roughness k/d.

5. Turbulent flow, completely rough surface (2 400 < Re, $60 < k^+$). In this flow regime all protrusions reach outside the viscous sublayer and by far the largest part of the resistance is due to the form drag that acts on them. For this reason, the viscosity has no effect on the resistance, and the friction coefficient becomes a function of relative roughness only. The pressure loss is now exactly a quadratic function of the mean velocity.

The value of k is not necessarily the height of roughness elements in technically rough pipes. It is the ***equivalent sand roughness,*** which has to be determined experimentally for a given rough surface. The curves in the Moody chart correspond to so-called commercially rough pipes as they occur in practice [1].

Very extensive measurements on rough pipes have been carried out by Nikuradse [3], who used circular pipes covered on the inside as tightly as possible with sand of a definite grain size glued to the wall. In the Moody chart the values k are the height of the equivalent sand roughness elements.

In Table 3 examples of equivalent relative sand roughness for commercial pipes are given.

(b) Turbulence characteristics

The universal defect law, stated in Table 1, is independent of Reynolds number for Re $>10^5$. In Fig. 2, measurements after Nikuradse [3] are shown and compared with the formula

$$\frac{u_c - u}{u_\tau} = \frac{1}{\kappa} \ln \frac{y}{R} \tag{6}$$

According to the balance between pressure forces and friction forces, the shear stress is proportional to the radius

$$\tau = \tau_l + \tau_t = \rho(\nu + \nu_t) \frac{du}{dy} = \frac{\tau_w}{R} r \tag{7}$$

where y is the wall distance and the eddy viscosity ν_t is defined as [see Eq. 2.2.1(140)]

$$\nu_t = -\frac{\overline{u'v'}}{du/dy} \tag{8}$$

Velocity v is positive in y-direction.

© 1983 Hemisphere publishing Corporation

Table 1 Flow characteristics of fully developed circular pipe flow[a]

Flow regime	Reynolds number Re	Roughness k^+	Friction coefficient $\hat{f}$	Velocity distribution u (r)	Turbulent characteristics for smooth and rough pipes (Re > 10^5)
1. Laminar flow	0 < Re < 2 400		Hagen-Poiseuille $\hat{f} = \frac{64}{\mathrm{Re}}$	$u(r) = 2\left[1 - \left(\frac{r}{R}\right)^2\right]$	
2. Turbulent flow	**2 400** < Re < 10^5 < **3 x** 10^6	$k^+ < 5$	Blasius $\hat{f} = \frac{0.316}{\mathrm{Re}^{1/4}}$ (Re < 10^5) $\hat{f} = \frac{0.184}{\mathrm{Re}^{1/5}}$ (Re > 10^5)	$u(r) = u_C(n)\left(1 - \frac{r}{R}\right)^{1/n}$ $\frac{u(y)}{u_\tau} = C(n)(y^+)^{1/n}$ $u_C(n), C(n)$, in Table 2	
3. Hydraulically smooth surface	**2 400** < Re	$k^+ < 5$	$\frac{1}{\sqrt{\hat{f}}} = 2.0 \log (\mathrm{Re}\sqrt{\hat{f}}) - 0.8$	$u^+ = \frac{u(y)}{u_\tau}$ $\frac{1}{\kappa}\ln y^+ + 5.5$ $y^+ > 60$ $u^+ = y^+$ $0 < y^+ < 5$	Mixing length $\frac{l}{R} = 0.14 - 0.08\left(\frac{r}{R}\right)^2 - 0.06\left(\frac{r}{R}\right)^4$ $\frac{l}{R} = \kappa\frac{y}{R} - 0.44\left(\frac{y}{R}\right)^2$ $0 < y < 0.2R$ (independent of Reynolds number for Re > 10^5)
4. Turbulent flow, rough surface	**2 400** < Re	$5 < k^+ < 60$	Colebrook-White $\frac{1}{\sqrt{\hat{f}}} = 1.74 - 2\log\left(\frac{2k}{d} + \frac{18.7}{\mathrm{Re}\sqrt{\hat{f}}}\right)$ Miller $\hat{f} = \frac{0.25}{[\log(k/3.7d) + (5.74/\mathrm{Re}^{0.9})]^2}$	$u^+ = \frac{1}{\kappa}\ln y^+ + C^+(k^+)$ $C^+(k^+) + \frac{1}{\kappa}\ln k^+$ 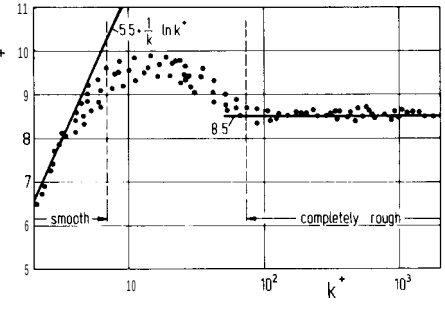 	Universal velocity defect law $\frac{u_C - u}{u_\tau} = \frac{1}{\kappa}\ln\frac{R}{Y}$ $y^+ > 60$, $y^+ > k^+$ $\bar{u} = u_C - 4.07u_\tau$ $\frac{\bar{u}}{u_C} = (1 + 1.44\sqrt{\hat{f}})^{-1}$
5. Turbulent flow, fully rough surface	**2 400** < Re	$60 < k^+$	von Karman $\frac{1}{\sqrt{\hat{f}}} = 1.74 - 2\log\frac{2k}{d}$	$u^+ = \frac{1}{\kappa}\ln\frac{y}{k} + 8.5$	

[a] $d = 2R$, diameter; $\hat{f}$ = friction factor according to Eq. (1); **k,** roughness height; $k^+ = ku_\tau/\nu$, dimensionless roughness height: l, mixing length according to Eq. (9); n = exponent of power law velocity distribution; r, radial coordinate; **R,** radius of pipe; Re = $\bar{u}d/\nu$, Reynolds number; u, axial velocity; $\bar{u} = Q/\pi R^2$, mean velocity; Q, volume flux; u_C, center velocity; $u_\tau = \sqrt{\tau_W/\rho}$, friction velocity; $y = R - r$, wall distance; $y^+ = yu_\tau/\nu$, dimensionless wall distance; $\kappa = 1.4$, von Karman constant; ν, kinematic viscosity; ρ, density; τ_W, wall shear stress.

© 1983 Hemisphere Publishing Corporation

Table 2 Characteristic values of turbulent pipe flow having power law velocity distributions

Re	4 x 10^3	1.1 x 10^5	4.7 x 10^5	1.3 x 10^6	3 x 10
n	6	7	8	9	10
$\frac{\bar{u}}{u_c}$	0.791	0.817	0.837	0.852	0.865
α	1.077	1.058	1.046	1.037	1.031
β	1.027	1.020	1.016	1.013	1.011
$Cf\frac{n}{2}$	7.76	8.74	9.71	10.6	11.5

[a] $C_f(n), n, \mathrm{Re}, \bar{u}, u_c$, see Table 1; α, energy correction factor according to Eq. 2.2.1(29); β, momentum correction factor according to Eq. 2.2.1(30).

Table 3 Roughness values k^a

	k, mm
1. Smooth pipes[b]	
Drawn brass, copper, aluminum, etc.	0.002 5
Glass, plastic, perspex, fiber glass, etc.	0.002 5
2. Steel pipes	
New smooth pipes	0.025
Centrifugally applied enamals	0.025
Light rust	0.25
Heavy brush asphalts, enamals, and tars	0.5
Water mains with general tuberculations	1.2
3. Concrete pipes	
New. unusually smooth concrete with smooth joints	0.025
Steel forms, first-class workmanship, with smooth joints	0.025
New, or fairly new, smooth concrete and joints	0.1
Steel forms, average workmanship, smooth joints	0.1
Wood, floated or brushed surface, in good condition, with good joints	0.25
Eroded by sharp material in transit, marks visible from wooden forms	0.5
Precast pipes, good surface finish, average joints	0.25
4. Other pipes	
Sheet metal ducts with smooth joints	0.002 5
Galvanized metals, normal finish	0.15
Galvanized metals, smooth finish	0.025
Cast iron, uncoated and coated	0.15
Asbestos cement	0.025
Flexible straight rubber pipe with a smooth bore	0.025
Corrugated plastic pipes[c] (apparent roughness)	3.5
Mature foul sewers	3.0

[a] After Miller [4].

[b] Extruded. cast, and pipes formed on mandrels may have imperfections that can increase roughness by a factor of 10.

Commercial corrugated plastic pipes in the 40-100 mm diameter size range have corrugation crest length-to-depth ratios of about 1.5. Increasing the crest length-to-depth ratio from 1.5 to 5 may double the friction coefficient.

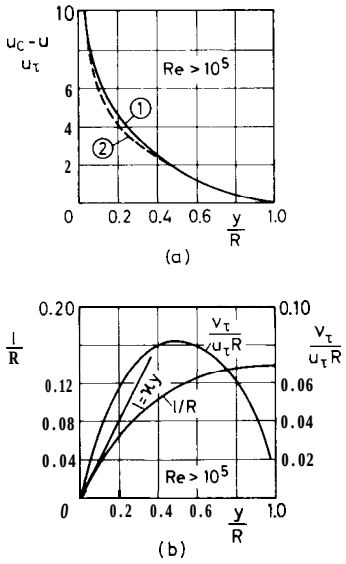

Figure 2 Fully developed turbulent pipe flow with smooth or rough walls (Re > 10^5). (a) Universal velocity defect law. Curve 1 corresponds to Eq. (6), curve 2 corresponds to measurements of Nikuradse [3]. (h) Mixing length l and eddy viscosity ν_t. After measurements of Nikuradse [3]. R, pipe radius; u_τ, friction velocity.

From the mixing length hypothesis [Eq. 2.2.1(201)], the eddy viscosity ν_t and mixing length l are connected by

$$\nu_t = l^2 \frac{du}{dy} \tag{9}$$

The dimensionless eddy viscosity $\nu_t/u_\tau R$ and the mixing length l/R are also shown in Fig. 2. The formulas for l/R given in Table 1 are valid for Re > 10^5. At lower Reynolds numbers, the mixing length distribution depends on Reynolds number.

Figure 3 relates the shear stress τ_t and eddy viscosity generated within the turbulent pipe flow from measurements of Laufer [5]. The central part of the pipe (defect law region) and the thin wall layer region are considered separately. For the former, the velocities are based on u_c, the maximum velocity at the center of the pipe, whereas for the wall layer region the friction velocity u_τ is used as the reference velocity. The turbulent shear stress $\tau_t = -\rho\overline{u'v'}$ is almost a linear function of y except very close to the wall, but at the outer edge of the wall region we have $\tau_t \approx \tau_w$.

Figure 4 shows how the mean velocity u and the fluctuation values $\sqrt{\overline{u'^2}}, \sqrt{\overline{v'^2}}$, and $\sqrt{\overline{w'^2}}$ vary between pipe wall and axis. The axial fluctuation intensity $\sqrt{\overline{u'^2}}$ is the largest over the entire flow. Its maximum of $\sqrt{\overline{u'^2}}/u_c = 0.08$ is located within the buffer layer (at about $y^+ = 15$). From this figure it can be seen that within the wall layer region the turbulence is neither

© 1983 Hemisphere Publishing Corporation

homogeneous ($\overline{u'^2} = \overline{v'^2} = w'^2$) nor isotropic ($\overline{u'v'} = \overline{v'w'} = \overline{u'w'} = 0$).

Figure 5 shows the mechanical energy balance in turbulent pipe flow, based on measurements of Laufer [5] for Re = 5×10^5. Positive values represent a gain of energy by the turbulence.

The turbulent kinetic energy equation, analogous to that for boundary layers, Eq. 2.2.1(127), can be derived for fully developed turbulent pipe as

$$\overline{u'v'}\frac{du}{dr} + \frac{1}{r}\frac{d}{dr}\left[r\overline{\left(\frac{q^2}{2} + \frac{p'}{\rho}\right)v'}\right] + \frac{\nu}{r}\frac{d}{dr}\left[r\frac{d}{dr}\left(\frac{\overline{q^2}}{2} + \overline{v'^2}\right)\right] - \epsilon_t = 0 \qquad (10)$$

Production; Kinetic diffusion; Pressure diffusion; Viscous diffusion; Dissipation

It describes the balance of the five effects: production, kinetic diffusion, pressure diffusion, viscous diffusion, and dissipation. In a first approximation, production and dissipation are in balance except in the center of the pipe where the turbulence is maintained by diffusion of kinetic energy. All of the contributions change rapidly as the wall layer is approached. The diffusion terms change sign. In the wall layer region the two turbulent diffusion terms are large but have opposite signs, so that their combined effect on the energy balance is comparatively small.

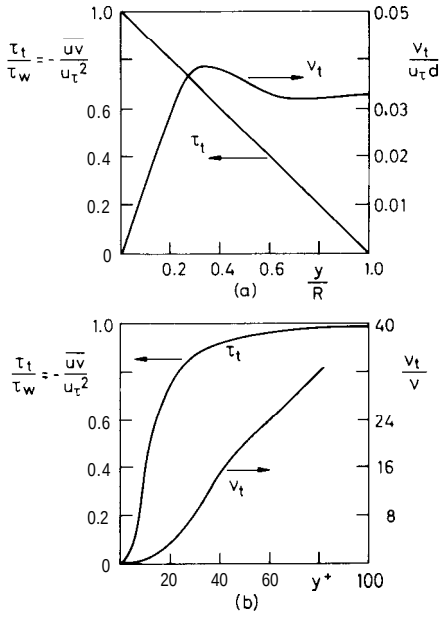

Figure 3 Fully developed turbulent pipe flow. Variation of turbulent shear stress τ_t and eddy viscosity ν_t according to Eq. (7). After measurements of Laufer [5], Re = 5×10^5. (a) Fully turbulent region. (b) Wall layer region. $y^+ = yu_\tau/\nu$, dimensionless wall distance; u_τ, friction velocity.

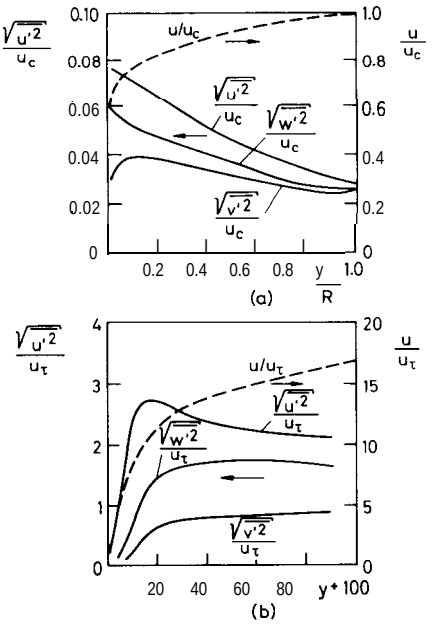

Figure4 Fully developed turbulent pipe flow. Variations of velocity $u(y)$ and turbulent fluctuation intensities $\sqrt{u'^2}, \sqrt{v'^2}, \sqrt{w'^2}$. Based on measurements of Laufer [5]. Re = 5 X 10 .(*a*) Fully turbulent region. (b) Wall layer region. u', v', w , fluctuation velocity components: u_c, center velocity; y, wall distance; $y^+ = yu_\tau/\nu$, dimensionless wall distance; u_τ, friction velocity; $\overline{u'^2}$, time average of the squared axial fluctuation velocity component.

A review by Reethof [6] on turbulence-generated noise in pipe flow is worth mentioning.

(c) Influence of superimposed free convection in horizontal pipes

So far only isothermal pipe flow has been considered. If a radial temperature distribution develops as a result of viscous heating or heat transfer between the fluid and the pipe wall, free convection effects may become important, particularly if the Reynolds number is small or if high temperature differences are employed. The effect of the superimposed free convection may be important, primarily in the laminar flow region, and is discussed in detail in Sec. 2.5.10.

When heat transfer is involved, the temperature field is always developing in axial direction and so are the free convection forces. If, however, constant heat flux is assumed, the radial temperature distribution will asymptotically become independent of the axial coordinate although the level of temperature still varies linearly downstream. If, furthermore, the BOUSSINESQ approximation is used [see Sec. 2.2.1A(e)], assuming constant fluid properties except the temperature dependence of the density in the buoyancy force term in the equation of vertical momentum], far downstream a fully developed flow situation is reached, including

© 1983 Hemisphere publishing Corporation

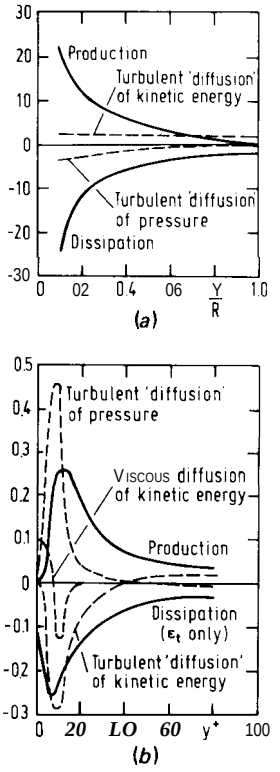

Figure 5 Fully developed turbulent pipe flow. Mechanical energy balance. Based on measurements of Laufer [5]. Re = 5×10^4. Positive values represent a gain of energy by turbulence; see Eq. (10). (*a*) Fully turbulent region. The terms of Eq. (10) have been nondimensionalized by u_τ^3/R; y, wall distance. (b) Wall layer region. The terms of Eq. (10) have been nondimensionalized by u_τ^4/ν; $y^+ = yu_\tau/\nu$.

forced and free convection. The effect of free convection is correlated by combinations of the following two dimensionless parameters:

Grashof number:

$$\mathrm{Gr} = \frac{g\rho^2 d^3 \beta (T_w - T_b)}{\eta^2} \tag{11}$$

Rayleigh number:

$$\mathrm{Ra} = \mathrm{Gr}\ \mathrm{Pr} = \frac{g\rho^2 d^3 \beta (T_w - T_b)}{\eta\lambda}\, c_p \tag{12}$$

where the fluid properties density ρ, coefficient of expansion β, viscosity η, and thermal conductivity λ have to be taken at the bulk temperature T_b; see Eq. 2.2.1(28).

Metais and Eckert [7] studied the available literature and found the boundary where free convection effects become important in pipe flow. Figure 6 shows their results for horizontal pipe flow.

The boundary between the forced convection regime and the mixed convection regime is defined such that the actual heat flux under the combined influence of the forces does not deviate by more than 10% from the heat flux that would be caused by the external forces alone.

Principally, two different boundary conditions can be distinguished:

1. Uniform heat flux axially and circumferentially (zero conductivity)
2. Uniform average heat flux along the pipe, but uniform temperature circumferentially at each axial location (infinite conductivity)

Figure 6 refers to the latter case. In the first case, significant circumferential wall temperature variations can occur, as have been shown by Morcos and Bergles [8]. They found an increase of the friction factor with Rayleigh number:

$$\frac{\hat{f}_f}{\hat{f}_{\mathrm{iso}}} = [1 + (0.195\ \mathrm{Ra}_f^{0.15})^{15}]^{1/15} \tag{13}$$

where the index f refers to the film temperature, which is the arithmetic mean value of average circumferential wall temperature and bulk temperature. The isothermal friction factor is given by $\hat{f}_{\mathrm{iso}} = 64/\mathrm{Re}$, also based on film temperature.

The Rayleigh number is based on the difference between wall temperature and bulk temperature.

Approximately, the film temperature is given by

$$T_f = \frac{T_w + T_b}{2} = T_b + \frac{11}{48}\,\frac{\dot{q}_w d}{\lambda} \tag{14}$$

which is an exact relationship for fully developed pipe flow when fluid properties are constant and only small heat flux values $\dot{q}_w$ are considered.

The experiments show good agreement with theoretical results of Newell and Bergles [9] for the boundary condition of constant circumferential temperature (infinite conductivity). According to Faris and Viskanta [10] the correction in Eq. (13) depends on another combination of Gr, Pr, and Re.

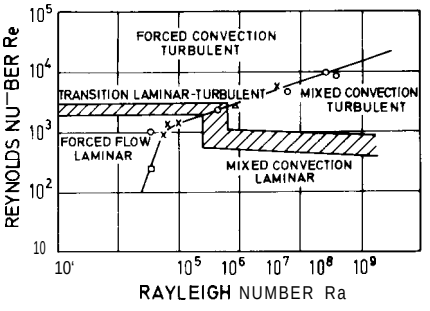

Figure 6 Influence of free convection on fully developed horizontal circular pipe flow. Free, forced, and mixed convection flow regimes after Metais and Eckert [7]. Ra, Rayleigh number according to Eq. (12).

© 1983 Hemisphere Publishing Corporation

The reason for the increase of pipe resistance in the case of heating is the occurrence of a secondary flow in the pipe such that the heated fluid close to the wall rises, whereas the fluid descends in the vertical symmetry plane. The streamlines have the form of spirals in the two cells of secondary flow side by side. This secondary flow is very similar to that occurring in curved pipes; see Sec. D. Actually, there exists a more general analogy between free convection effects and curvature effects; see [127] in Sec. 2.2.1.

Obviously, the free convection effects are much less pronounced in turbulent pipe flow compared to laminar flow. A theoretical investigation of turbulent pipe flow with buoyancy effects has been carried out by Abdelmeguid and Spalding [11].

Free convection effects become important when the heat flux is high and hence temperature increases are high. For these cases, usually variable properties of the fluid must be taken into account; see review of Shah and London [12] and the following section.

(d) Influence of temperature-dependent fluid properties

One of the basic assumptions made in the preceding sections is that the fluid properties are constant. Since the transport properties of most fluids vary with temperature [see Sec. 2.2.1A(d) and Table 2.2.1(2)], the constant-property assumption provides a good approximation for heat transfer problems involving small temperature differences. For those problems involving large temperature differences, variable properties have to be taken into account.

For fully developed axisymmetric pipe flow, the flow equations in cylindrical coordinates (coordinates x, r, axial velocity u [see Eqs. 2.2.1(62)-2.2.1(65)]) reduce to

$$\frac{dp}{dx} = \frac{1}{r}\frac{d}{dr}\left[r\eta\left(1 + \frac{\nu_t}{\nu}\right)\frac{du}{dr}\right] \tag{15}$$

Changes in pipe flow resistance will occur mainly due to the temperature dependence of the viscosity $\eta(T)$.

It is common practice to use constant-property results and then to apply some kind of correction to account for property variations.

Three schemes for such correction are commonly used:

1. Property ratio method. In the property ratio method, all properties are evaluated at the bulk mean temperature, and then all of the variable properties effects are lumped into a function of a ratio of some pertinent property evaluated at the surface temperature to that property evaluated at the bulk temperature.

2. Reference temperature method. In the reference temperature method, a temperature is specified at which the properties appearing in the dimensionless groups may be evaluated such that the constant-property results may be used to evaluate variable property behavior [see Sec. 2.2.1D(e)]. Typically, this may be the film average temperature T_f.

3. Linear approximation. Using linear approximation of the variable properties (first term of a Taylor series) and assuming small temperature difference leads to simple linear corrections of the constant-property relationships; see Sec. 2.2.1D(e). In Table 2.2.1(2), the gradients of the properties for air and water are given.

The third method is the most universal one, because the corrections are independent of the fluid. In the first two methods, a distinction between gases and liquids is usually necessary. As discussed by Kays and Perkins [13], the property ratio method leads to less ambiguity and awkwardness for the internal duct flow problem.

In Table 4 typical correction formulas are given.

(e) Influence of additives on fluid friction

It has been found experimentally that very small concentrations, on the order of a few parts per million by weight, of a dissolved high-polymer substance can reduce the frictional resistance in turbulent flow to as low as one-fourth that of the pure solvent. In laminar flow, similar additives leave the pressure drop practically unchanged. The extent of drag reduction depends on the molecular weight of the polymer and on its concentration. As the concentration increases, the reduced friction factor tends to a curve of maximum reduction,

$$\frac{1}{\sqrt{\hat{f}}} = 9.5 \log (\mathrm{Re}\sqrt{\hat{f}}) - 19 \tag{16}$$

as has been indicated by Virk et al. [21]. The polymer particles obviously have some damping effect on the turbulent fluctuation, at least in a certain range of the turbulence spectrum. A complete and satisfactory explanation of the phenomenon of drag reduction has not yet been advanced. For further details, see the reviews in [22-25].

B. Fully developed noncircular pipe flow

(a) Laminar flow

In a duct of arbitrary cross section, the axial velocity distribution $u(y,z)$ is a solution of the following linear partial differential equation

$$\frac{\partial}{\partial y}\left(\eta\frac{\partial u}{\partial y}\right) + \frac{\partial}{\partial z}\left(\eta\frac{\partial u}{\partial z}\right) = \frac{dp}{dx} = \text{const} \tag{17}$$

© 1983 Hemisphere Publishing Corporation

Table 4 Influence of temperature-dependent fluid properties on friction factor of fully developed flow[a]

Flow	Formula	Remarks	References
Laminar flow, gases and liquids	$\frac{\hat{f}}{\hat{f}_{iso}} = 1 + \frac{6}{11}\left(\frac{d\eta}{dT}\frac{T}{\eta}\right)\frac{T_w - T_b}{T_b} - \frac{14}{33\,\mathrm{Pr}}\left(\frac{d\rho}{dT}\frac{T}{\rho}\right)_b\frac{T_w - T_b}{T_b}$	$\eta = \eta_b + \left(\frac{d\eta}{dT}\frac{T}{\eta}\right)_b\frac{T - T_b}{T_b}$; $\hat{f}_{iso}$ at T_b; $T_w - T_b$ small	
Laminar flow, gases and liquids	$\hat{f} = \frac{64}{\mathrm{Re}}$ Gases: $j = 0.58$; Petroleum oil: $j = 0.25$; Liquid metals: $j = 0.54$	η at temperature $T_r = T_b + j(T_w - T_b)$	Roshenow and Choi [14]
Laminar flow, gases	$\frac{\hat{f}}{\hat{f}_{iso}} = \left(\frac{T_w}{T_b}\right)^m$ $m = 0.81$ $0.5 < \frac{T_w}{T_b} < 1$; $m = 1$ $1 < \frac{T_w}{T_b} < 3$	$\hat{f}_{iso}$ at T_b	Kays and Perkins [13]
Laminar flow, liquids	$\frac{\hat{f}}{\hat{f}_{iso}} = \left(\frac{\eta_w}{\eta_b}\right)^m$ $m = 0.50$ $\frac{T_w}{T_b} < 1$; $m = 0.58$ $\frac{T_w}{T_b} > 1$	$\hat{f}_{iso}$ at T_b	Kays and Perkins [13]
Laminar flow (viscous heating only)	$\frac{\hat{f}}{\hat{f}_{iso}} = 1 - 7.833\left(\frac{d\eta}{dT}\frac{T}{\eta}\right)_b \mathrm{Pr\,Ec}$	$\mathrm{Ec} = \frac{\bar{u}^2}{c_p T_b}$; $T_w - T_b$ small	Hausenblas [15]
Turbulent flow, gases	$\frac{\hat{f}}{\hat{f}_{iso}} = \left(\frac{T_b}{T_w}\right)^m$ $m = 0.5$; $m = 0.6$	$\hat{f}_{iso}$ at T_w	Taylor [16]; Perkins and Worsoe-Schmidt [17]
Turbulent flow, liquids	$\frac{\hat{f}}{\hat{f}_{iso}} = \left(\frac{\eta_w}{\eta_b}\right)^m \left(\frac{\rho_w}{\rho_b}\right)^{0.5}$ Water: $m = 10\hat{f}_{iso}$; $\frac{T_w}{T_b} > 1$	$\hat{f}_{iso}$ at T_b	Maurer and Tourneau [18]
	$\frac{\hat{f}}{\hat{f}_{iso}} = \left(\frac{\eta_w}{\eta_b}\right)^{0.14}$ Oils: $\frac{T_w}{T_b} > 1$	$\hat{f}_{iso}$ at T_b	Waggener [19]
	$\frac{\hat{f}}{\hat{f}_{iso}} = \left(\frac{\eta_w}{\eta_b}\right)^{0.24}$ $\frac{T_w}{T_b} < 1$	$\hat{f}_{iso}$ at T_b	Petukhov [20]

[a] $\mathrm{Ec} = \bar{u}^2/c_p T_b$, Eckert number; ii, mean velocity; c_p, heat capacity; $\hat{f}$, friction factor including the influence of temperature-dependent fluid properties; $\hat{f}_{iso}$, friction factor for isothermal flow, fluid properties taken at T_b or at T_w; Pr, Prandtl number, taken at bulk temperature T_b; T_w, wall temperature, η, viscosity; ρ, density; index b, taken at T_b; index w, taken at T_w; $[(d\eta/dT)/(T/\eta)]$, dimensionless variation of viscosity with temperature at T_b; see Table 2.2.1(2).

where x is the main flow direction parallel to the duct axis. On the periphery of the cross section, the no-slip condition $u = 0$ has to be satisfied. For isothermal flows this equation reduces to Poisson s equation, where the constant on the right-hand side is proportional to the pressure gradient and hence to the friction factor.

The reference length for noncircular cross section is the ***equivalent diameter*** or ***hydraulic diameter***

$$d_h = \frac{4S}{P_r} \tag{18}$$

as defined in Eq. 2.2.1(46), where P_r is the wetted perimeter of the cross section. The hydraulic diameter reduces to the diameter for circular cross section.

Using the reference length d_h in the definitions of the friction factor and of the Reynolds number, the friction factor can be given as

$$\hat{f} = \frac{K_f}{\mathrm{Re}} \tag{19}$$

where K_f is a constant dependent on the geometry of the duct cross section (for a circular duct, $K_f = 64$).

© 1983 Hemisphere Publishing Corporation

For many cross-section shapes this constant Kf has been determined. Table 5 contains information about these constants and the hydraulic diameters.

(b) Turbulent flow

The determination of the friction factor for turbulent flow in a noncircular duct is much more complex than in laminar flow. Since the flow is no longer axisymmetric, asymmetries in the turbulent flow field cause secondary flows that move fluid from low to high shear stress regions, evening out the shear stress distribution on the periphery. Figure 7 illustrates the secondary flow paths in a square section. Secondary flow velocities reach a maximum of 1–2% of the axial velocity. The secondary flows continuously transport momentum from the center to the corners and generate high velocities there. Prandtl has called this ***secondary flow of the second kind,*** contrary to the secondary flow occurring due to free convection [see Sec. A(c)] or due to curvature [see Sec. D] .

The advantage of the secondary flow in turbulent noncircular duct flow is that the circumferential shear stress distribution is fairly constant. If the shear stress were exactly constant over the periphery, the friction would be the same as that of a circular pipe with the same perimeter. Therefore, for many noncircular cross sections a satisfactory procedure for determining the friction factor is to replace the pipe diameter d in the friction factor definition and in the Reynolds number by the hydraulic diameter d_h.

The hydraulic diameter concept is adequate provided that the cross section sP_r/A^3 is not significantly

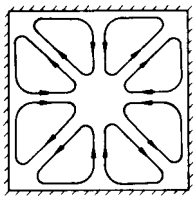

Figure 7 Secondary flow paths in a square cross section. Secondary flow of second kind.

greater than that of any other cross section that can be drawn inside it. In calculating pressure losses, the minimum P_r/A^3 has to be found, and its associated perimeter and area should be used for calculating the Reynolds number, the mean velocity, and the pressure loss; see Miller [4].

When the cross section of the duct contains a narrow region, transition from laminar to turbulent does not occur simultaneously over the whole of the flow. For example, in the region within an acute angle of a triangular cross section, the flow remains larninar to very large Reynolds numbers, whereas in the bulk it turns turbulent at a much lower Reynolds number; see Irvine [26].

For the following cross sections, turbulent duct flows have been investigated:

1. Two-dimensional channel flow. The velocity profiles and the friction factor are slightly different from those of the circular pipe; see Laufer [27], Dean [28], Povarnitsyn [29], Schumann [30], Meyer [31].

2. Annular ducts. There is no secondary flow of the second kind in concentric annular ducts; see Macagno and McDougall [32], Eifler [33], Levy [34].

Table 5 Characteristic values of noncircular laminar pipe flows[a]

Cross section	Geometry	d_h	K_f	$K(\infty)$	$\frac{L_{hy}}{d_h \mathrm{Re}}$
Circle	Diameter d	d	64	1.25	0.057
Square	Side a	a	56.9	1.43	0.033
Rectangle (sides a, b)	$a/b = 2$	$\frac{2}{3}a = \frac{4}{3}b$	62.2	1.28	0.028
	$a/b = 5$	$\frac{1}{3}a = \frac{5}{3}b$	76.3	0.931	0.019
Two-dimensional channel	Height h	$2h$	96	0.674	0.011
Equilateral triangle	Side a	$0.577a$	53.3	1.69	0.040
Concentric annulus (outer diameter d_O, inner diameter d_i)	$d_i/d_O = 0.05$	$0.95d_O = 19d_i$	86.3	0.830	0.021
	$d_i/d_O = 0.1$	$0.9d_O = 9d_i$	89.4	0.784	0.019
	$d_i/d_O = 0.5$	$0.5d_O = d_i$	95.2	0.688	0.012
	$d_i/d_O = 0.75$	$0.25d_O = 0.33d_i$	95.9	0.678	0.011
	$d_i/d_O = 1$	$d_O - d_i$	96	0.674	0.011

[a] d_h, hydraulic diameter according to Eq. 2.2.1(46); K_f, constant in Eq. (19), for friction factor of fully developed flow; $K(\infty)$, asymptotic incremental pressure drop number according to Eq. (21) for hydrodynamically developing flow; L_{hy}, entrance length of hydrodynamically developing flow, where maximum velocity achieves 99% of its asymptotic value.

© 1983 Hemisphere Publishing Corporation

3. Rectangular ducts. See Naot et al. [35], Launder and Ying [36], Gessner and Jones [37], Jones [38], Wilkie et al. [39].

4. Rod bundles. See Eifler [33], Carnavos [40], Carajilescov and Tondreas [41], Rehme [42], Dwyer [43].

5. Various cross sections. For eccentric annular ducts, see Jonsson and Sparrow [44], Eifler [33]. For triangular ducts, see Gosman and Rapley [45].

C. Developing duct flow

(a) Hydrodynamic entrance region of isothermal duct flow

In many practical cases the flow in pipes is not fully developed, but rather in the process of developing and hence eventually reaching the fully developed state.

One typical example of such a developing flow is the flow in the entrance region of a pipe. At the entrance section of the pipe the flow is assumed to have constant velocity over the whole cross section. In the inlet region of the pipe the velocity profile is gradually transformed and tends, under the influence of viscous forces, to assume the asymptotic velocity profile at the fully developed pipe flow, discussed in the previous sections.

The hydrodynamic entrance region of isothermal flow in a pipe of constant cross section will be considered here.

According to Eqs. 2.2.1(37) and 2.2.1(47), the pressure drop between the entrance section (index 1, $x = 0$) and the section at station x is given by

$$\frac{p_1 - p(x)}{(\rho/2)\bar{u}^2} = \frac{4}{d_h}\int_0^x \frac{\tau_w(x)}{(\rho/2)\bar{u}^2}dx + 2\,[\beta(x) - 1] \tag{20}$$

where $\beta(x)$ is the momentum correction factor of the velocity distribution at station x. The pressure drop results from the wall shear and the change in momentum flow rate across the two relevant duct sections. The shear stress within the entrance region is higher than the shear stress of the fully developed flow. The pressure drop can be considered as consisting of two components: (1) the pressure drops based on the fully developed flow, and (2) additional pressure drop due to momentum change and accumulated increment in wall shear between developing flow and developed flow. The second contribution to the pressure drop, in a dimensionless form, is designated as the ***incremental pressure drop number*** $K(x)$, sometimes called the ***pressure defect,*** defined by

$$\frac{p_1 - p(x)}{(\rho/2)\bar{u}^2} = \hat{f}\,\frac{x}{d_h} + K(x) \tag{21}$$

An alternative way of characterizing the pressure drop of the flow in the entrance region defines an ***apparent friction factor*** f_{app} as

$$\frac{p_1 - p(x)}{(\rho/2)\bar{u}^2} = \hat{f}_{\text{app}}(x)\,\frac{x}{d_h} \tag{22}$$

$K(x)$ increases monotonically from 0 at $x = 0$ to a constant value $K(\infty)$ in the fully developed region. The ***hydrodynamic entrance length*** L_{hy} is defined, somewhat arbitrarily, as the duct length required to achieve a duct section maximum velocity of 99% of the corresponding fully developed magnitude when the entering flow is uniform. There are a number of other definitions used in the literature for L_{hy}, but the foregoing definition is most commonly used.

In a long duct, that is, longer than L_{hy}, the knowledge of $K(\infty)$ is sufficient to determine the additional pressure drops in the inlet. To calculate $K(\infty)$ and the details of the developing velocity and pressure field, usually the boundary-layer approximation is applied; that is, shear stresses are important only in directions perpendicular to the flow and hence $\partial^2 u/\partial x^2$ is negligible. Therefore, the results found in the literature are valid for large Reynolds numbers. For example, such a calculation has been carried out by Cebeci and Chang [46].

For a circular pipe the following results can be used:

Laminar circular pipe flow:

$$K(\infty) = 1.25$$

$$\frac{L_{\text{hy}}}{d_h} = 0.057\ \text{Re} \tag{23}$$

Turbulent circular pipe flow:

$$K(\infty) = 0.065$$

$$\frac{L_{\text{hy}}}{d_h} \simeq 45 \tag{24}$$

As can easily be seen, the inlet length is much shorter for turbulent flow compared to laminar flow.

For lower Reynolds numbers (Re < 250), there are deviations from the results given, because the boundary-layer assumptions mentioned above are no longer valid. The problem of the proper mathematical treatment of inlet flow problems was examined critically by Van Dyke [47]. He gave a solution for the entrance region of the two-dimensional channel.

The case in which flow in the pipe starts as laminar flow, but becomes turbulent further downstream within the entrance region, has also been investigated by Cebeci and Chang [46].

Values of $K(\infty)$ and L_{hy} for laminar flow in entrance regions of ducts of arbitrary cross section are given in Table 4; see also Shah [48].

© 1983 Hemisphere Publishing Corporation

The equivalent values for turbulent flow are in most cases not available. Since they are practically not very important, the concept of hydraulic diameter can be used; that is, the values of the circular pipe entrance region can be taken.

(b) Various forms of developing duct flo w

The inlet flow is only one but typical example of a developing duct flow. There are many other possibilities of developing flow that are of practical importance.

The following examples of developing duct flow may occur in practice.

I. Hydrodynamically developing flow including buoyancy forces

The developing flow described in the previous section can be influenced by free convection effects when heat transfer and hence temperature differences are present. These additional effects can occur on horizontal as well as on vertical pipes. As a first approximation, the apparent friction factor $\hat{f}_{app}$ could be corrected due to buoyancy effects the same way as the normal friction factor for fully developed flow; see Sec. A(c).

II. Hydrodynamically developing flow taking into account temperature-dependent fluid properties

As in the previous case, the apparent friction factor could be corrected due to variable fluid properties by using the correction formulas for fully developed flows.

As far as the temperature field is concerned, the flow may also develop thermally, leading to a thermal inlet problem.

Thermal entrance length problems are of two categories: (1) The velocity and temperature profiles develop simultaneously, and (2) the temperature profile starts developing at some station in the hydrodynamic entry region.

III. Vertical pipe flow including free convection effects

If heat transfer is involved in vertical duct flow, the buoyancy forces have to be taken into account. In the case of heating (T_w/T_b > I), the buoyancy drives the fluid in an upflow in the direction of the mean flow, whereas in a downflow the buoyancy tends to force the fluid opposite to the mean flow. This heating in upflow is similar to cooling in downflow, whereas cooling in upflow is similar to heating in downflow.

Because of this additional force acting on the fluid, the flow never becomes fully developed but changes continually along the channel.

Vertical channel flows including buoyancy effects have been investigated by Chato [49], Petukhov [50], Jackson and Fewster [51], and Campbell and Perkins [52]. The latter investigation concerned ducts with triangular cross-section. In most cases variable properties of the fluid have to be taken into account. When the temperature increases rapidly, the local Reynolds number may become quite low for gas flows, which can result in *relaminarization* of the flow; see McEligot et al. [53].

IV. Axial change of geometry or wall roughness

The flow will be developing when it has to adjust to new boundary conditions. Siuru and Logan [54] investigated the turbulent pipe flow when the roughness of the wall changes. Roberts and Forester [55] considered the flow in a duct whose shape of cross section changes continuously downstream, where the cross-section area may even be constant.

In such a process of adjusting to a new, eventually fully developed flow condition, the various flow parameters need different distances downstream to reach their asymptotic values. As Vasanta Ram and von Schulz-Hausmann [56] have shown in a study of a turbulent channel flow with a change in wall roughness, the adjustment of the pressure gradient occurs almost immediately, the mean velocities need more time, but the turbulent shear stress and other characteristic values of the turbulent fluctuation reach their new equilibrium state very slowly. For a sudden change of the boundary condition (for instance, change of roughness), the turbulence structure reaches its new state at a station about 40 diameters downstream.

V. Distorted inlet velocity distribution

When the velocity profile at the entrance station is highly inhomogeneous (for instance, due to fluid injection), the flow will need a certain distance downstream to reach a fully developed state. Such a turbulent mixing process in a duct has been investigated by Ahmed [57]. According to the momentum theorem, Eq. 2.2.1(32), this mixing process in a duct of constant cross-section area is connected with a pressure ***increase,*** when wall shear stresses are neglected.

When there is a ***swirl*** in the inlet region of the flow, again a certain distance downstream is necessary to dissipate this swirl completely. The main characteristic of such a swirl flow is the radial pressure gradient (lower pressure at the axis) due to centrifugal forces. The laminar flow with swirl has been investigated by Collatz and Görtler [58], whereas the turbulent case was studied by Vasilescu [59].

© 1983 Hemisphere Publishing Corporation

D. Compressible duct flow

(a) Basic equations

The main characteristic of compressible pipe flow is the change of the mean density in the flow direction. This can be caused by heat transfer and/or by high mean velocities. Compressibility effects have to be considered when the mean pipe velocity is larger than about 30% of the speed of sound.

The basic equations for general duct flows have been given in Sec. 2.2.1 A(b).

For simplification, the following assumptions will be made:

1. The cross-section area is constant, $S = \text{const}$.
2. Buoyancy forces are neglected.
3. Velocity and density are constant across the cross section, i.e., $\alpha = 1, \beta = 1$.
4. Calorically perfect gases are considered [see Sec. 2.2.1A(d)].
5. The friction factor $\hat{f}$ is constant, i.e., independent of the axial coordinate x. For variable $\hat{f}(x)$, a mean value over the length considered has to be taken.
6. Wall shear stress τ_w and heat flux $\dot{q}_w$ (if it is nonzero) are constant around the perimeter.

Under these conditions, the basic differential equations for the flow are as follows.

Continuity equation:

$$\frac{d}{dx}(\rho u) = 0 \tag{25}$$

Momentum equation:

$$\rho u \frac{du}{dx} + \frac{dp}{dx} = -\frac{4\tau_w}{d_h} \tag{26}$$

Energy equation:

$$\frac{d}{dx}\left(c_p T + \frac{1}{2}u^2\right) = \frac{4\dot{q}_w}{\rho u d_h} \tag{27}$$

According to the momentum equation, there are two reasons for a static pressure drop: (1) the skin friction, and (2) an acceleration of the flow due to decreasing density downstream.

Instead of velocity u, very often the local Mach number,

$$\mathrm{Ma} = \frac{u}{u_{\text{sound}}} = \frac{u}{\sqrt{\gamma R T}} \tag{28}$$

is used as the dimensionless velocity.

(b) Constant heat transfer

The heat transfer with constant $\dot{q}_w$ may start at station x_1. At this section the velocity u_1 and the temperature T_1 and hence the Mach number Ma_1 are given.

Using the dimensionless axial coordinate,

$$\bar{x} = \hat{f}\frac{x - x_1}{d_h} \tag{29}$$

and a modified Damkijhler number,

$$\overline{\mathrm{Da}} = \frac{4q_w}{\hat{f}\rho u c_p T_1} \tag{30}$$

it can be shown that the local Mach number Ma is a function of the inlet Mach number Ma_1, the modified Damkijhler number $\overline{\mathrm{Da}}$, and the dimensionless axial coordinate $\bar{x}$:

$$\mathrm{Ma} = F(\mathrm{Ma}_1, \overline{\mathrm{Da}}, \bar{x}) \tag{31}$$

The axial gradient of the Mach number is given by

$$\frac{d\mathrm{Ma}}{d\bar{x}} = \frac{\mathrm{M}}{2}\,\mathrm{a}\,\frac{1+\gamma\,\mathrm{Ma}^2}{1-\mathrm{Ma}^2}\,\overline{\mathrm{Da}}\,\frac{T_1}{T} + \gamma\,\mathrm{Ma}^3 \times \frac{1+[(\gamma-1)/2]\mathrm{Ma}^2}{1-\mathrm{Ma}^2} \tag{32}$$

where

$$\frac{T}{T_1} = \frac{1+[(\gamma-1)/2]\mathrm{Ma}_1^2 + \overline{\mathrm{Da}}\,\bar{x}}{1+[(\gamma-1)/2]\mathrm{Ma}^2} \tag{33}$$

From the Mach number $\mathrm{Ma}(\bar{x})$ and the temperature $T(\bar{x})$, the velocity $u(\bar{x})$ and density $\rho(\bar{x})$ can be found using Eq. (28) and Eq. (25), respectively.

The momentum equation determines the modified pressure gradient

$$\frac{dp}{d\bar{x}} = -\frac{\rho}{2}u^2 \cdot {}_{p}\,{}_{u}\frac{du}{d\bar{x}}$$

In Fig. 8 the results are given for the inlet Mach number $\mathrm{Ma}_1 = 0.5$.

It is interesting to note that the flow ends at a ***critical condition*** defined by Ma = 1, when the gradient $d\mathrm{Ma}/d\bar{x}$ becomes infinite.

The variation of the temperature is determined by two effects: (1) increasing temperature due to heating and (2) decreasing temperature due to decreasing pressure and hence decreasing density. Therefore the temperature distribution has for $\overline{\mathrm{Da}} > 0$ (heating) a maximum, because in the front part of the pipe the temperature increases because of the heating whereas in the rear part of the pipe the temperature decreases because of decreasing pressure predominating.

Figure 9 shows the temperature distributions at a given modified Damköhler number $\overline{\mathrm{Da}} = 0.4$ for differ-

© 1983 Hemisphere Publishing Corporation

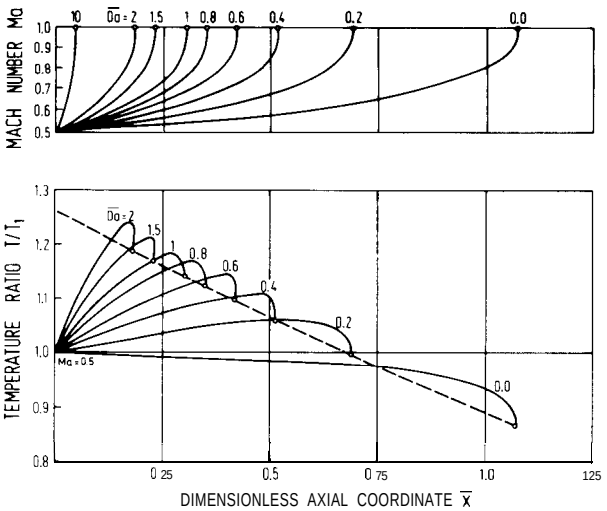

Figure 8 Compressible pipe flow with constant heat flux. Axial distribution of Mach number Ma and temperature ratio T/T_1. Ma, local Mach number according to Eq. (28); $\overline{Da}$, modified Damköhler number according to Eq. (30); $\bar{x}$, dimensionless axial coordinate according to Eq. (29); $\hat{f}$, friction factor assumed to be constant. Example: $Ma_1 = 0.5$ at the beginning of heating.

ent inlet Mach numbers Ma_1. At very low Mach numbers (incompressible flow), the temperature increases linearly. Because of compressibility effects, the temperature increase is reduced, and at a certain inlet Mach number Ma, (in the example, about $Ma_1 = 0.6$), there is eventually no increase of temperature although the fluid has been heated from the wall.

(c) Adiabatic flow (Fanno flow)

One limiting case of the flows considered in the previous section is the adiabatic flow, that is, the flow without heat transfer, $\overline{Da} = 0$. This flow is called Fanno flow. According to Eq. (32), the Mach number gradient becomes independent of $\bar{x}$. The integration can be done analytically (see Oswatitsch [60]), and one universal curve $Ma = F(\bar{x})$ can be found. This function is shown in Fig. 10, and has been tabulated by Shapiro and Hawthorne [61]; see also the review by Cambel [62].

(d) Isothermal flow

In order to keep the fluid temperature equal to a constant, $T = T_1$, a certain amount of heat has to be transferred to the fluid. Since p/ρ is constant, the momentum equation can be integrated easily to give

$$\frac{1}{\gamma\, Ma_1^2}\left[1-\left(\frac{u_1}{u_2}\right)^2\right]+\ln\left(\frac{u_1}{u_2}\right)^2=\hat{f}\,\frac{L}{d_h} \tag{34a}$$

$$\frac{p_2}{p_1}=\frac{\rho_2}{\rho_1}=\frac{w_1}{w_2} \tag{34b}$$

The flow ends when $Ma_2 = 1/\sqrt{\gamma}$, which leads to

$$\lim_{u_1 \to 0}\frac{u_2}{u_1}=\frac{1}{\sqrt{\gamma}\,Ma_1} \tag{35}$$

The energy equation can be used to determine the heat that had to be transferred to keep the temperature constant.

(e) Low-density effects

For Reynolds numbers smaller than about Re = 25, low-density effects become important, with the consequence that the no-slip condition at the wall is no longer valid. Information about the laminar tube flow in the so-called slip flow regime can be found in [14].

(f) Inviscid flow with heat addition

Inviscid compressible flow in ducts will not be considered here. It is particularly important in connection with ***dejlagration*** and ***shock-induced combustion*** (detonation). For more details, see Cambel [62], Bartlmä [63], or Oswatitsch [60].

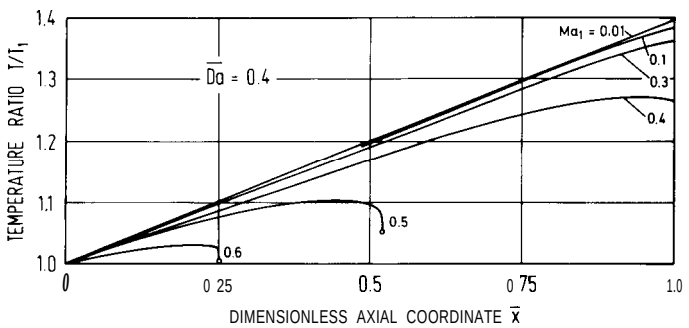

Figure 9 Compressible pipe flow with constant heat flux. Axial distribution of temperature ratio, T/T_1, for various inlet Mach numbers Ma, Example: Da = 0.4. Symbols as in Fig. 8.

© 1983 Hemisphere I blishing Corporation

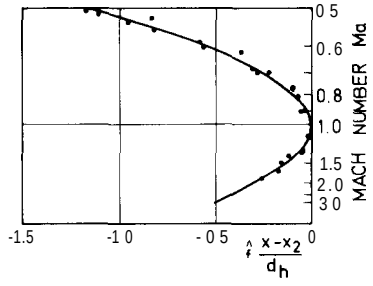

Figure 10 Compressible pipe flow with adiabatic wall condition. Axial distribution of Mach number. Curve corresponds to Eq. (34). Points refer to measurements; see Oswatitsch [60]. $\hat{f}$, friction factor assumed to be constant.

E. Unsteady duct flow

Unsteady duct flow occurs when the driving pressure difference is a function of time. A special case is the oscillating flow in a pipe under the influence of a periodic pressure difference. Transient flows can be originated by dynamic events such as the closing of a valve or the loss of power of a pump. Calculations of transient flows are more involved than steady-state calculations, because the complete history of the system has to be calculated from the initiation of the transient to the time of interest. The concept of the friction factor, used in steady-state flow, is generally not applicable, since there might be a time lag between the pressure gradient and the wall shear stress. In turbulent flow the time-averaging procedure is not trivial, because the mean values (e.g., the mean velocities) are still time dependent. Therefore, ***ensemble averages*** have to be used; see Sec. 2.2.1C(a).

Surveys on unsteady pipe flow have been given by Rich [64], Wylie and Streeter [65], Paynter [66], and Kalinin and Dreitser [67].

Oscillating pipe flows have been investigated by Uchida [68] and Richardson and Tyler [69] for the laminar case and Schultz-Grunow [70] for the turbulent case.

Zielke [71] studied the laminar transient pipe flow, whereas the turbulent case has been investigated by Brown et al. [72], Hirose [73], and Margolis and Brown [74].

F. Losses in piping components

(a) Loss coefficient

A system loss coefficient is defined as the difference of the nondimensionalized total pressure loss between the extreme ends of two long straight pipes or passages when there is a zero loss component between the two pipes or passages and when the real component is installed; see Miller [4]. In nondimensionalizing the pressure loss, the convention is to use the component s inlet dynamic pressure, except when the component is an inlet from a large space the outlet dynamic pressure is used. The long pipe before the component ensures a developed flow at inlet and the long pipe at outlet from the component ensures that losses caused by flow redevelopment after the component are debited to the component. Figure 11 illustrates the procedure for establishing the loss coefficient. The inlet and outlet developed friction gradients are projected to the component and the difference between the projected total pressures at the component is established.

The ***loss coefficient K*** is given by

$$K = \frac{\Delta p_t}{(\rho/2)\bar{u}^2} \tag{36}$$

where Δp_t is the total pressure loss.

Obviously, many components do not have inlet or outlet pipes. Experience shows that if inlet and outlet pipes or passages are 30 or more diameters long, loss coefficients typically lie within about 0.02 of their value with much longer pipes or passages. When the inlet and outlet length requirements are not met, corrections have to be applied to system loss coefficients.

When the cross section of the pipe is the same in the inlet and in the outlet, the total pressure loss is identical with the static pressure loss. The static pressure difference, however, is not sufficient to determine the loss coefficient in enlargements (diffusers) or contractions (nozzles); see Sec. (c).

(b) Curved ducts

I. Flow characteristics

When flow is turned, static pressure and velocity distributions change. To compensate the centrifugal forces, a pressure gradient perpendicular to the main flow occurs such that on the inner side of the turned pipe or bend the pressure is lower. Consequently, two adverse pressure gradients parallel the main flow and hence danger of ***flow separation occurs,*** one at the outer side in front of the turning and one on the inner side beyond the turning. The low-energy fluid close to the

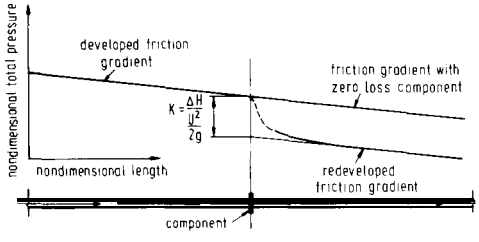

Figure 11 Definition of loss coefficient.

© 1983 Hemisphere Publishing Corporation

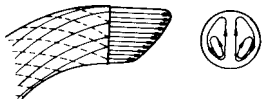

Figure 12 Flow in a curved pipe showing secondary flow of the first kind.

wall has to follow the pressure gradient within a cross section leading to a ***secondary flow (secondary flow of the first kind)*** shown in Fig. 12. The secondary flow is directed outward in the center and inward (i.e., toward the center of curvature) near the wall. The shape of the cross section has a strong influence on the secondary flow, as can be seen from the velocity distributions shown in Fig. 13.

It is obvious that flow turning affects the ***turbulence structure*** of the flow due to secondary flow and local separation, if the curvature is strong enough. Curvature causes the flow on convex surfaces to be stabilized with a reduction in turbulent shear stresses and to be destabilized on concave surfaces with an increase in turbulence shear stress; see Bradshaw, Sec. 2.2.1 [127].

Bend outlet velocity and turbulence distributions differ substantially from those of developed pipe or passage flows. Additional losses are involved in establishing developed flow conditions after a bend. Some 30 diameters from the bend, a steady-state pressure gradient is reestablished. Although the static pressure gradient becomes constant after 30 diameters, weak secondary flows are usually present and continue to be detectable 50 to 100 -diameters after the bend. In some circumstances nearly all the pressure loss is associated with reestablishing developed flow after a bend.

Considering 90 bends of circular cross section, the main experimental observations of the distribution of losses between the bend and the outlet pipe are, according to Miller [4]:

1. In bends of $r/d < 0.8$, serious flow separation can be expected. Most of the loss is the result of the separated flow expanding immediately after the bend. Intense turbulence generated by the expanding flow tends to destroy secondary flows.
2. For bends of $0.8 < r/d < 1.5$, about 80% of all losses occur in the bend and the first two pipe diameters after the bend.
3. For $1.5 < r/d < 3$, about 40% of the loss occurs downstream of the bend.
4. For $r/d > 3$, increasing contribution of wall friction reduces the percentage contribution of the downstream loss to the total loss.

II. Fully developed flow

In helically coiled pipes a fully developed flow will be established. The friction factor according to Eq. (1) can be applied for suchflows. Thefollowingformulas can be used:

(i) Laminar flow

$$\hat{f}_s = 0.106\ De^{0.5} \qquad De > 300 \qquad \text{Adler [75]} \tag{37}$$

$$\hat{f}_s = 0.37\ De^{0.36} \qquad 80 < De < 2\,000 \qquad \text{Prandtl [76]} \tag{38}$$

Here the characteristic dimensionless parameter, which determines the influence of curvature in the laminar case, is the Dean number,

$$De = \frac{1}{2}\ Re \sqrt{\frac{R}{r}}$$

where R is the radius of the cross section and r is the radius of curvature of the centerline of the bend.

In Eqs. (37) and (38) f_s refers to the straight duct, whereas the index c corresponds to the flow with curvature.

Further investigations on fully developed laminar flow in curved pipes and with noncircular cross section have been carried out by Ito [77], Patankar et al. [78], Cheng et al. [79], Ghia and Sokhey [80], Taborrek and Lin [81], Cheng [82], Austin and Seader [83], Greenspan [84], Zapryanov et al. [85], Dravid et al. [86], Srinivason et al. [87], and Humphrey et al. [88]. The critical Reynolds numqer is

$$Re_{cr} = 2\,400 \left[1 + 8.6 \left(\frac{R}{r}\right)^{0.45}\right]^{0.45}$$

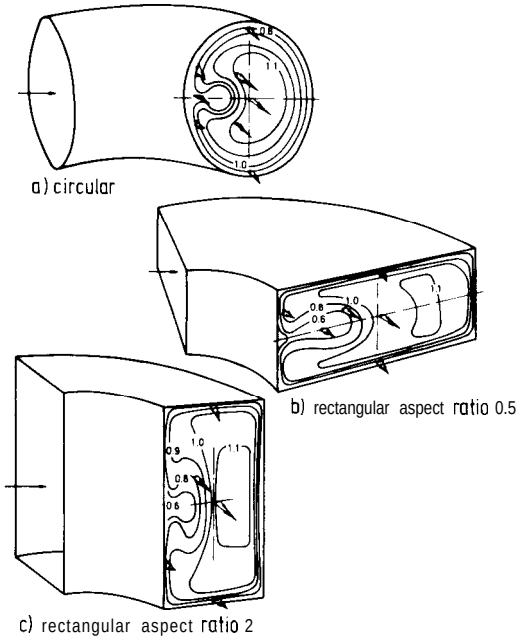

Figure 13 Effect of cross-sectional shape on velocity distributions (contours of local to mean velocity). After Miller [4].

© 1983 Hemisphere Publishing Corporation

(ii) Turbulent flow

$$\frac{\hat{f}_c}{\hat{f}_s} = 1 + 0.075\left[\mathrm{Re}\left(\frac{R}{r}\right)^2\right]^{0.25} \tag{39}$$

White [89]

$$\frac{\hat{f}_c}{\hat{f}_s} = \left[\mathrm{Re}\left(\frac{R}{r}\right)^2\right]^{0.05} \qquad \mathrm{Re}\left(\frac{R}{r}\right)^2 > 6 \tag{40}$$

Ito [90]

$$\hat{f}_c = \left(\frac{R}{r}\right)^{0.5}\left\{0.029 + 0.304\left[\mathrm{Re}\left(\frac{R}{r}\right)^2\right]^{-0.25}\right\} \tag{41}$$

$$0.034 < \mathrm{Re}\left(\frac{R}{r}\right)^2 < 300$$

There are no curvature effects for $\mathrm{Re}(R/r)^2 < 0.034$.

III. Loss coefficient

Figure 14 shows the loss coefficient K_b for circular cross-section bends at Reynolds number Re = 10^6 according to Miller [4]. The loss coefficient was defined for bends with long and hydraulically smooth inlet and outlet pipes. Correction factors are given by Miller [4] to correct the loss coefficient to any other Reynolds number and outlet pipe length. Allowance is made for roughness by multiplying the smooth friction factor as found in Sec. A(a), as long as the roughness correction does not exceed 1.4; see Miller [4].

Empirical equations for the loss coefficient in turbulent flow (smooth walls) that well represent Ito's [90,91] very accurate and systematic experimental results, and that agree with that of many other experimenters, have the form

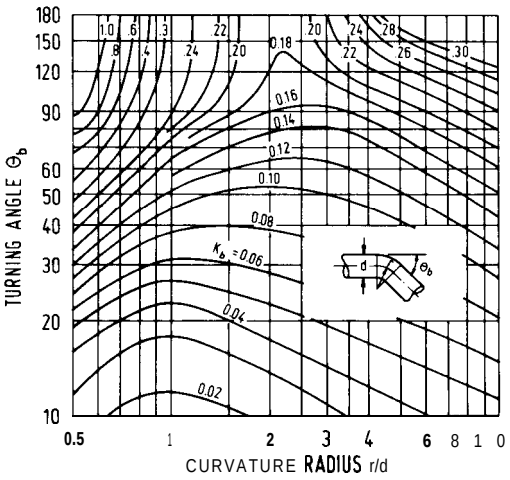

Figure 14 Bend performance chart-circular cross section (Re = 10^6). After Miller [4]. K_b, loss coefficient of the bend.

(i) $\mathrm{Re}(R/r)^2 < 91$

$$K = 0.008\ 73\ \alpha\theta\frac{r}{R}\hat{f}_c \tag{42}$$

where θ is the bend angle in degrees and $\hat{f}_c$ is the friction factor of the fully developed curved flow.

The empirical factor α has been given by Ito as

$$\alpha_{\theta=45^\circ} = 1 + 14.2\left(\frac{r}{R}\right)^{1.47} \tag{43}$$

$$\alpha_{\theta=90^\circ} = 0.95 + 17.2\left(\frac{r}{R}\right)^{1.96} \tag{44}$$

According to this formula, the dependence of the loss coefficient on Reynolds number is the same as that of the friction factor $\hat{f}_c$ of the fully developed curved flow.

(ii) $\mathrm{Re}(R/r)^2 > 91$

$$K = 0.002\ 4\ \alpha\theta\left(\frac{r}{R}\right)^{0.84}\mathrm{Re}^{-0.17} \tag{45}$$

The loss coefficient of bends with the turning angle θ can also be determined by using the results of the 90 bend and applying a correction factor C_θ as

$$K_\theta = C_\theta K_{90^\circ}$$

The values of C_θ are as follows [92]:

θ	20°	40°	60°	80°	100	120	140	160	180
C_θ	IO.29	0.56	0.77	0.93	1.06	1.16	1.25	1.32	1.38

When a bend is located in close proximity to other components, corrections for interaction effects are necessary. For bend-bend interactions and bend-diffuser interactions, see Miller [4].

For more information about bends, and also mitre bends with various cross sections, see Miller [4], Idel chik[93], and Ananyan [94].

IV. Vaned bends

By using vanes, the loss coefficient of a mitre bend can be reduced to that of the lowest-loss circular-arc bend. Ideally, vanes should be closer together on the inside of the bend, but because of strength requirements the vane thickness may be such as to cause excessive blockage on the inside of the bend.

Vanes within circular arc bends are justified only if the bend radius, r/d, is less than 1 and the vanes are thin and occupy less than 5% of the cross-sectional area. For radius ratios $r/d > 0.7$, a single vane located at $r_m = \sqrt{r_i r_o}$ should be used, r_i and r_o being the inner and outer bend radii, respectively. A vane at this location reduces the loss coefficient of a $r/d = 0.7$ bend by half and a $r/d = 1$ bend by 20%; see Miller [4].

© 1983 Hemisphere Publishing Corporation

Instead of vanes, airfoil blades can be used to reduce the loss coefficient even further. An optimal blade geometry for 90 turning has been found by Wolf[95] and Collar [96], who could reduce the loss coefficient down to about ***K = 0.04.***

(c) Enlargements

I. Diffuser performance

Diffusers are tapered enlargements. They are devices for converting dynamic pressure to static pressure and for reducing velocities (in subsonic flow).

The performance of a diffuser in incompressible flow can be characterized by

Loss coefficient:

$$K_d = \frac{\Delta p_t}{(\rho/2)\bar{u}_1^2} = \frac{p_1 + \alpha_1(\rho/2)\bar{u}_1^2 - p_2 - \alpha_2(\rho/2)\bar{u}^2}{(\rho/2)\bar{u}_1^2}$$

$$= \frac{\phi_{12}}{(1/2)\bar{u}_1^2} \tag{46}$$

see Eqs. 2.2.1(37) and (38). Since the Reynolds numbers in the inlet and outlet pipe are different, α_1 and α_2 may usually be different.

Pressure recovery coefficient:

$$c_p = \frac{p_2 - p_1}{(\rho/2)\bar{u}_1^2} \tag{47}$$

Diffuser efficiency:

$$\eta_d = \frac{c_p}{c_{pi}} = \frac{p_2 - p_1}{[1 - (S_1/S_2)^2](\rho/2)\bar{u}_1^2} \tag{48}$$

where

$$c_{pi} = 1 - \left(\frac{S_1}{S_2}\right)^2 \tag{49}$$

is the ideal recovery coefficient.

These performance parameters are connected by

$$K_d = \alpha_1 - \alpha_2 \frac{S_1}{S_2}^2 - c_p \tag{50}$$

and

$$K_d = (\alpha_1 - \eta_d) - (\alpha_2 - \eta_d)\left(\frac{S_1}{S_2}\right)^2 \tag{51}$$

where the latter equation for $\alpha_1 = \alpha_2$ reduces to

$$K_d = (\alpha - \eta_d)\left[1 - \frac{S_1}{S_2}^2\right] \tag{52}$$

In practical applications the factor $\alpha - \eta_d$ has values of 0.05-0.2.

Figure 15 shows the loss coefficient K_d for cornical diffusers with an outlet pipe at a Reynolds number of Re = 10^6 according to Miller [4]. The loss coefficient is a function of two geometric parameters, the ***area ratio,***

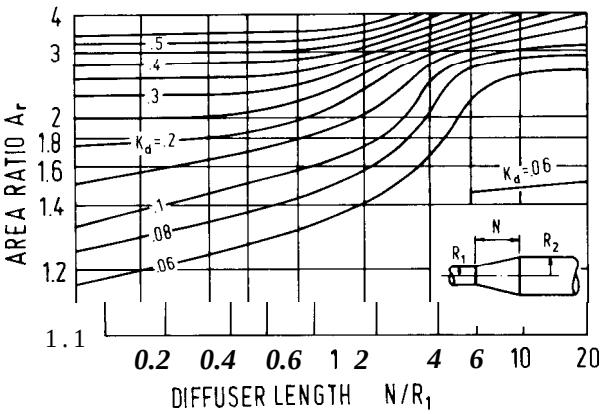

Figure **15** Loss coefficient K_d for conical diffusers with an outlet pipe and fully developed inlet flow (Re = 10). After Miller [4]. $A_r = (R_2/R_1)^2$, area ratio.

$$A_r = \frac{S_2}{S_1} \tag{53}$$

and the length of the diffuser N based on the inlet radius R_1. The half angle, θ_d, of the diffuser is connected with the area ratio and diffuser length by

$$\tan\theta_d = \frac{\sqrt{S_2/S_1} - 1}{N/R_1} \tag{54}$$

These loss coefficients are valid for diffusers with inlet pipe lengths of five diameters or more and with outlet pipe of four diameters or more.

Generally, loss coefficients increase for lower Reynolds numbers, but K_d values are practically independent of Reynolds number for Re > 10^5 [4, 97]. For corrections with regard to Reynolds number, see Miller [4].

II. Diffusers with free discharge

In practical applications very often diffusers with free discharge are used. For diffusers with free discharge, the dynamic pressure at the outlet must be considered as additional loss. Therefore the loss coefficient is defined as

$$K_d = \frac{\phi_{12} + (1/2)\alpha_2\bar{u}_2^2}{(1/2)\bar{u}_1^2} = \alpha_1 - \eta_d\left[1 - \left(\frac{S_1}{S_2}\right)^2\right]$$

$$= \alpha_1 - c_p \tag{55}$$

Figure 16 shows the loss coefficient chart of conical diffusers with a free discharge at a Reynolds number Re = 10^6 according to Miller [4].

There exist optimum geometries of diffusers of given area ratio (A in Fig. 17) and for given length to inlet

© 1983 Hemisphere Publishing Corporation

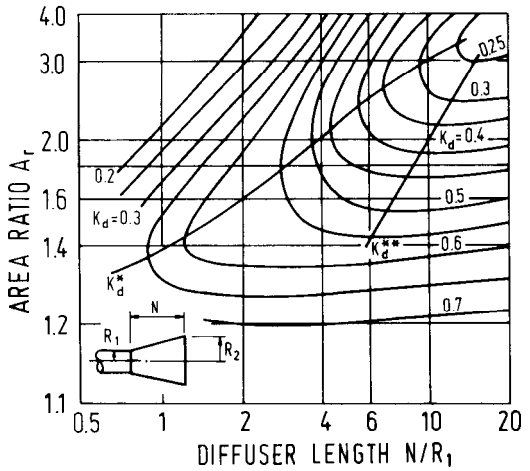

Figure 16 Loss coefficients K_d for conical diffusers with a free discharge and fully developed inlet flow (Re = 10^6). After Miller [4]. K_d^*, line of minimum loss coefficients in a given length; K_d^{**}, line of minimum loss coefficients in a given area ratio.

radius ratio (curve B); the curve $2\theta_b = 6$ is located between these two optimum curves.

Optimum diffusers have an optimum performance total diffuser angle of about $2\theta_b = 6°$. For higher Reynolds numbers the optimal diffuser angle becomes smaller; see Schlichting and Gersten [98]. Nikuradse [99] gave the relation

$$(2\theta_d)_{opt} \approx 150\ \mathrm{Re}^{-0.25} \tag{56}$$

for diffusers of rectangular cross section where the optimum diffuser angle is slightly higher than that of conical diffusers.

At higher diffuser angles, flow separation occurs leading to strongly unsteady flow characteristics. For quantifying the frequency of pressure fluctuations the time period At can be used, within which the flow traverses a distance of one pipe diameter at the diffuser inlet velocity; that is,

$$\boldsymbol{At} = \frac{d_1}{\bar{u}_1} \tag{57}$$

According to Miller [4], the lines in Fig. 17 indicate roughly the following regions:

Line 1: To the right of this line, the flow is steady.

Line 2: Onset of small areas of flow separation with small amplitude fluctuations with a period of about 20 ***At.***

Line 3: Flow very unsteady, with areas of stall moving around the diffuser and penetrating far into the flow. Period of pressure fluctuations about 100 ***At.***

Line 4: Extremely unstable flow conditions, large eddies or stall moving violently in the diffuser. Period of pressure fluctuation 200 ***At*** with amplitudes in excess of 10% of the inlet dynamic pressure.

Line 5: Very unstable flow, with low-frequency, large-amplitude movements of the whole flow. Period of fluctuation about 2 000 ***At.***

An equivalent description of the various regions for straight two-dimensional diffusers is given by Reneau et al. [97]. For calculating the flow below line 1, see, for instance, Roberts and Forester [100]. A very careful experimental investigation of the turbulence characteristics of a conical diffuser ($2\theta_b = 6$) has been carried out by Pozzorini [101]. Regarding two-dimensional diffusers, the systematic investigations by Kline and his group [120],[97,102-108] should be mentioned.

III. Inlet conditions of diffusers

A diffuser s performance depends strongly on the velocity distribution at its inlet. The diagram in Fig. 18 represents the variation of efficiency with the ratio $26_{11}/d_1$ for diffusers with circular cross section according to Sprenger [109]. The symbol δ_{11} denotes the displacement thickness [see Eq. 2.2.1(151)] at the inlet, and d_1 is the inlet diameter. The diffuser efficiency decreases more strongly for curved diffusers than for straight diffusers.

For thin inlet boundary layers, the diffuser efficiency can be calculated using the boundary-layer concept; see Sec. 2.2.1D. The flow field can be divided into an inviscid core and the boundary layer close to the wall. There is a strong interaction between the two fields, because they depend on each other. Such calculations have been carried out for axisymmetric diffusers by Schlichting and Gersten [98] and for two-

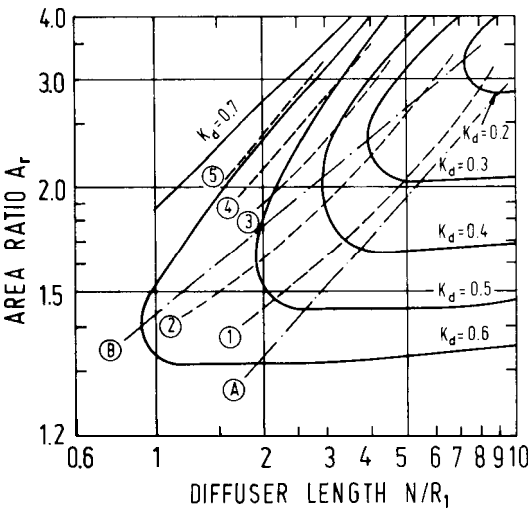

Figure 17 Flow regimes. Conical diffusers with a free discharge and thin inlet boundary layer (Re = 10^6). After Miller [4]. Curve A, line of minimum loss coefficients in a given area ratio; curve B, line of minimum loss coefficients in a given length.

© 1983 Hemisphere Publishing Corporation

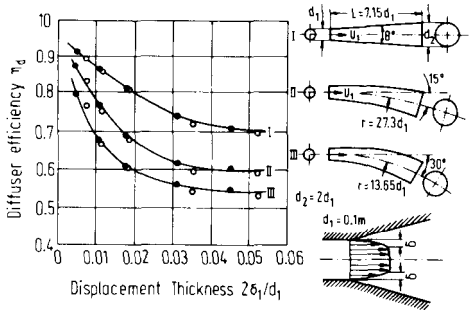

Figure 18 Diffuser efficiency in straight and curved diffusers with circular cross sections. After Sprenger [109]. Efficiency defined in Eq. (48). Diagram represents dependence on ratio of boundary-layer displacement thickness to radius of cross section at entry.

dimensional diffusers by Ackeret [110] and by Kline and his co-workers [106–108] and Weber [111].

It is worth mentioning that for larger diffuser angles the pressure is not constant across the cross section, but varies radially as a result of the curvature of the flow. This radial pressure distribution has to be taken into account in the calculation of the inviscid core region; see Gersten et al. [112].

For further details of the effect of inlet conditions of diffusers, see Robertson and Ross [113], Winternitz and Ramsay [114], Miller [4], and Idel chik[93].

Optimum diffusers have been investigated by Sovran and Klomp [115], Fernholz [116], and Ghose and Kline [107].

Reviews about diffusers have been given by Patterson [117], Cockrell and King [118], Cockrell and Markland [119], Miller [4], and Idel chik[93].

IV. Methods of improving performance

Diffuser performance can be improved by the following five methods.

(i) Curved wall diffusers. The basic shapes for curved wall diffusers are the trumpet shape and the bell shape. From theoretical results of Schlichting and Gersten [98], it can be concluded that the bell-shape diffuser can in some cases be better than the conical diffuser; see Adkins [120].

For diffusers that are connected with coolers at their outlet section, trumpet-shape diffusers have much better performance than the bell-shape diffusers, as has been shown by Küchemann and Weber [121]. They give the coordinates of such a bell-shape diffuser, called a ***streamline diffuser.*** They showed that, for instance, for an area ratio of A, = 2.5 and a length $N/R_1 = 3$, the flow of the streamline diffuser would not separate, whereas the flow in a conventional diffuser of the same area ratio and length would already be extremely separated.

(ii) Application of vortex generators. See the review by Adkins [120].

(iii) Diffuser with swirl. Swirl can improve the performance of diffusers; see Liepe [122], Cockrell and King [118].

(iv) Application of suction. Boundary control by suction (see Furuya et al. [123]) or blowing can improve the performance of diffusers; see Sec. 2.2.1 [92] and Adkins [120].

(v) Vaned diffusers. See Miller [4], Idel chik[93], and Albring [124].

V. Sudden enlargement

The loss coefficient of sudden enlargement is given by

$$K = C\left(1 - \frac{S_1}{S_2}\right)^2 \tag{58}$$

where the factor C is slightly larger than 1, which takes into account that the ***base pressure*** in the separated region is slightly smaller than the inlet pressure p_1. Under the assumption that the base pressure and the inlet pressure are the same (C = 1), Eq. (58) is called the Carnot formula.

Since these losses are wasteful, the use of sudden enlargements should be avoided.

(d) Pipe fittings

There are numerous publications about loss coefficients of all kinds of pipe fittings. Typical examples for results are the loss coefficients of combining flow and dividing

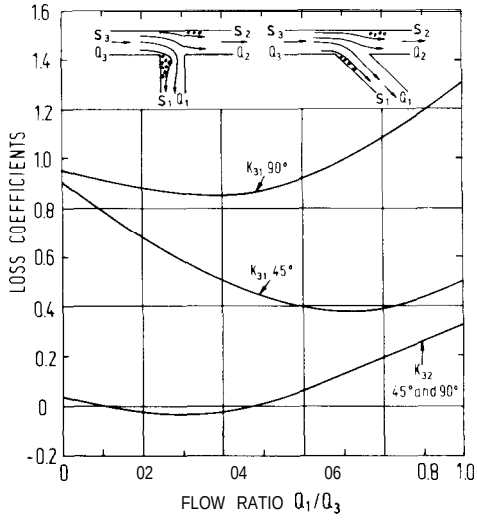

Figure 19 Loss coefficients for sharp-edged 45 and 90 dividing junctions. After Miller [4].

© 1983 Hemisphere Publishing Corporation

flow in Figs. 19 and 20, respectively, as given by Miller [4].

Further details about loss coefficients of pipe fittings can be found in books by Miller [4], Idel chik

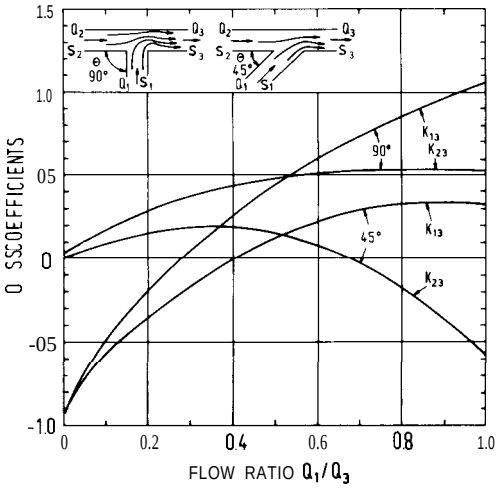

Figure 20 Loss coefficients for sharp-edged 45 and 90 combining junctions. After Miller [4].

Table 6 References presenting loss coefficients of pipe fittings

Pipe fitting	References
Sudden enlargement	[133–135]
Nozzles	[136–143]
Sudden contraction (inlets)	[4, 92, 133]
Orifices	[137–140]
Perforated plates	[144, 145]
Screens	[92, 146–151], Sec. 2.2.1 [103]
Honeycombs	[149, 150]
Branching (T junctions)	[152–154]
Manifolds	[4, 93, 125]
Valves	[124, 127, 129, 155]

[93], Kamininski [125], Benedict and Carlucci [126], Zoebl and Kruschik [127], Schweigerer [128], Volk [129], Benedict [92], and in books on hydraulics [130–132].

In Table 6 special references for various types of pipe fittings are collected.

NOMENCLATURE FOR SECTION 2.2.2

A_r area ratio
c_p heat capacity at constant pressure, J/kg K
c_p pressure recovery coefficient [Eq. (47)]
c_{pi} ideal pressure recovery coefficient [Eq. (49)]
C factor [Eq. (58)]
C_θ correction factor for curved ducts [Sec. F(b), III]
$C(n)$ factor for power law velocity distribution (Table 2)
d diameter, m
d_h hydraulic diameter, m
Da modified Damköhler number [Eq. (38)]
De Dean number [Eq. (38)]
Ec Eckert number (Table 4)
$\hat{f}$ friction coefficient [Eq. (2)]
g gravitational acceleration, m/s^2
Gr Grashof number [Eq. (11)]
k roughness height, m
k^+ dimensionless roughness height [Eq. 2.2.1(188)]
K loss coefficient [Eq. (36)]
K_b loss coefficient of bend (Fig. 14)
K_d loss coefficient of diffuser [Eq. (46)]
K_d^* loss coefficient of optimal diffusers at given length (Fig. 16)
K_d^{**} loss coefficient of optimal diffusers at given area ratio (Fig. 16)
Kf cross-section geometry factor [Eq. (19)]
K_θ loss coefficient of bend with bend angle θ [Eq. (45)]
K_{31}, K_{32} loss coefficients of dividing flow (Fig. 19)
K_{13}, K_{23} loss coefficients of combining flow (Fig. 20)
l mixing length [Eq. (9)], m
L length [Eq. (1)], m
L_{hy} hydrodynamic entrance length [Sec. C(a)]
Ma Mach number [Eq. (28)]
n exponent of power law velocity distribution
N diffuser length (Fig. 15), m
p static pressure, N/m^2
P_r perimeter, m
Pr Prandtl number
$q(t)$ resultant fluctuation velocity [Eq. 2.2.1(127a)]
$\dot{q}$ heat flux per unit area, $J/m^2 s$
Q flow rate, m^3/s
r local radius, m
R pipe radius, m
R specific gas constant, J/kg K
Ra Rayleigh number [Eq. (12)]
Re Reynolds number [Eq. (4)]
S cross-sectional flow area
T temperature, K
u velocity in main flow direction, m/s
$\bar{u}$ mean flow velocity [Eq. (3)], m/s
u_c velocity at center, m/s
u_{sound} speed of sound, m/s
u_τ friction velocity [Eq. 2.2.1 (186)], m/s
u', v', w fluctuation velocity components, m/s

© 1983 Hemisphere Publishing Corporation

$\overline{u'v'}$ temporal mean of product of two fluctuation velocity components, m^2/s^2
v velocity perpendicular to the wall, positive away from the wall, m/s
x coordinate along duct axis, m
$\bar{x}$ dimensionless axial coordinate [Eq. (29)]
y distance from wall, m
y^+ dimensionless distance from wall [Eq. 2.2.1(191)]

α kinetic energy correction factor [Eq. 2.2.1(29)]
β momentum correction factor [Eq. 2.2.1(30)]
γ heat capacity ratio
δ_1 displacement thickness [Eq. 2.2.1(151)], m
δ_w wall layer thickness [Eq. (5)], m
Δp pressure loss, N/m^2
Δp_t total pressure loss, N/m^2
Δt time interval, s
ϵ_t dissipation, m^2/s^3
η (dynamic) viscosity, kg/m s
η_d efficiency of diffuser [Eq. (48)]
θ, θ_b bend angle
θ_d half-angle of conical diffuser
κ von Karman constant
λ thermal conductivity, J/m s K
ν kinematic viscosity, m^2/s
ν_t eddy viscosity [Eq. (9)], m^2/s
ρ density, kg/m^3
τ shear stress, N/m^2
τ_l laminar shear stress [Eq. (7)], N/m^2
τ_t turbulent shear stress [Eq. (7)], N/m^2
τ_w wall shear stress, N/m^2
ϕ_{12} specific dissipiation between stations 1 and 2 [Eq. 2.2.1(38)], m^2/s^2

Subscripts

b bulk temperature
c curved, center
f film temperature
is0 isotherm
s straight, not curved
t turbulent
W wall

Superscripts

$\bar{}$ time average
' fluctuation
+ dimensionless value, based on δ_w

REFERENCES FOR SECTION 2.2.2

1. Moody, L. F., Friction Factors for Pipe Flow, *J. Heat Transfer,* vol. 66, pp. 671-684, 1944.
2. Cebeci, T., and Bradshaw, P., ***Momentum Transfer** in **Boundary** Layers,* Hemisphere, Washington, D.C., 1977.
3. Nikuradse, J., Strömungsgesetz in rauhen Rohren, *Forsch. **Arb.** Ing.-Wes.,* no. 361, 1933.
4. Miller, D. S., Internal Flow Systems, British Hydromechanics Research Association (BHRA) Fluid Engineering, Bedford, U.K., 1978.
5. Laufer, J., The Structure of Turbulence in Fully Developed Pipe Flow, NACA Rept. 1174, 1954.
6. Reethof, G., Turbulence-Generated Noise in Pipe Flow, *Annu. **Rev. Fluid** Mech.,* vol. 10. pp. 333-367, 1978.
7. Metais, B., and Eckert, E. R. G., Forced. Mixed, and Free Convection Regimes, ***J. Heat Transfer, vol. 86,*** pp. 295-296, 1964.
8. Morcos, S. M., and Bergles, A. E., Experimental Investigation of Combined Forced and Free Laminar Convection in Horizontal Tubes, ***J. Heat Transfer,*** vol. 97, pp. 212-219, 1975.
9. Newell, P. H., and Bergles, A. E., Analysis of Combined Free and Forced Convection for Fully Developed Laminar Flow in Horizontal Tubes, ***J. Heat Transfer,*** Ser. C, vol. 92, pp. 83-93, 1970.
10. Faris, G. N., and Viskanta, R.. An Analysis of Laminar Combined Forced and Free Convection Heat Transfer in a Horizontal Tube, *Int. J. **Heat Mass Transfer, vol.*** 12, pp. 1295-1309, 1969.
11. Abdelmeguid, A. M., and Spalding, D. B.. Turbulent Flow and Heat Transfer in Pipes with Buoyancy Effects, ***J. Fluid** Mech., **vol.** **94,*** pp. 383-400, 1979.
12. Shah, R. K., and London, A. L., ***Laminar Flow Forced*** Convection ***in Ducts,*** Supplement 1 to Advances in Heat Transfer, ed. T. F. Irvine. Jr., and J. P. Hartnett, Academic Press, New York, 1978.
13. Kays, W. M., and Perkins, H. C., Forced Convection, Internal Flow in Ducts, in ***Handbook of Heat** Transfer,* ed. W. M. Roshenow and I. P. Hartnett. p. 193. McGraw-Hill, New York, 1973.
14. Roshenow, W. M., and Choi, H. ***Y., Heat, Mass. and Momentum Transfer,*** Prentice-Hall, Englewood Cliffs, N.J., 1961.
15. Hausenblas, H., Die nichtisotherme laminare Strömung einer zähen Flüssigkeit durch enge Spalte und Kapillarröhren, *Ing.-Archiv,* vol. 18, pp. 151-166, 1950.
16. Taylor, M. F., Correlation of Friction Coefficient for Laminar and Turbulent Flow with Ratios of Surface to Bulk Temperature from 0.35 to 7.35, NASA TR R-267, 1967.
17. Perkins, H. C., and Worsoe-Schmidt, P., Turbulent Heat and Momentum Transfer for Gases in a Circular Tube at Wall to Bulk Temperature Ratios to Seven. ***Int. J. Heat Muss Transfer,*** vol. 8, pp. 1011-1031, 1965.
18. Maurer, G. W., and Le Tourneau, B. W., Friction Factors for Fully Developed Turbulent Flow in Ducts with and without Heat Transfer, ***J. Basic** Eng.,* Ser. D, vol. 86, pp. 627-636, 1964.
19. Waggener, J. P., Friction Factors for Pressure-Drop Calculations, ***Nucleonics,*** vol. 19, pp. 145-147, 1961.
20. Petukhov, B. S.. Heat Transfer and Friction in Turbulent Pipe Flow with Variable Physical Properties. in *Adv. Heat **Transfer,*** vol. **6,** pp. 503-564, 1970.

© 1983 Hemisphere Publishing Corporation

21. Virk, P. S., Merrill, E. W., Mickley, H. S., Smith, K. A., and Mollo-Christensen. E. L., The Toms Phenomenon: Turbulent Pipe Flow of Dilute Polymer Solutions, *J. Fluid Mech.*, vol. 30, pp. 305-328, 1967.
22. Landahl, M. T., Drag Reduction by Polymer Addition, in *Proc. 13th Int. Congr. Theor. Appl. Mech., Moscow, 1972,* ed. E. Becker and G. K. Mikhailov, pp. 177-199, Springer-Verlag, 1973.
23. Lumley, J. L., Drag Reduction by Additives, *Annu. Rev. Fluid Mech.,* vol. 1, pp. 367-384, 1969.
24. Frankiel, F. N., Landahl, M. T., and Lumley, J. L., eds., Structure of Turbulence and Drag Reduction, IUTAM Symp., Washington, D.C., 1976, ***The Physics of Fluids,*** vol. 20, no. 10, pt. II, pp. S1-S292, 1977.
25. Berman, N. S., Drag Reduction by Polymers, *Annu. Rev. Fluid Mech.,* vol. 10, pp. 47-64, 1978.
26. Irvine, T. F., Noncircular Duct Convective Heat Transfer. in ***Modern Developments in Heat Transfer,*** ed. W. Ibele, pp. 1-18. Academic Press, New York, 1963.
27. Laufer, J., Investigation of Turbulent Flow in a Two-Dimensional Channel, NACA Rept. 1053. 1951.
28. Dean, R. B., Reynolds Number Dependence of Skin Friction and Other Bulk Flow Variables in Two-Dimensional Rectangular Duct Flow, *J. Fluids Eng.,* Ser. I, vol. 100, pp. 215-223, 1978.
29. Povarnitsyn, M. S., Developed Flow and Drag in Planar Channel with Rough Walls, ***Fluid Dynamics,*** vol. 13, pp. 13-18. 1978.
30. Schumann, V., A Procedure for the Direct Numerical Simulation of Turbulent Flows in Plane and Annular Channels and Its Application in the Development of Turbulence Models, NASA TT-F-15391, 1974.
31. Meyer, L., Turbulent Flow in a Plane Channel Having One or Two Rough Walls, *Int. J. Heat Mass Transfer,* vol. 23. pp. 591-608, 1980.
32. Macagno, E. O., and McDougall, D. W., Turbulent Flow in Annular Pipes, *AIChE J.*, vol. 12, pp. 437-445, 1966.
33. Eifler, W., Über die turbulente Geschwindigkeitsverteilung und Wandreibung in Strömungskanälen verschiedener Querschnitte, Dissertation, Tech. University Darmstadt, 1968.
34. Levy, S., Turbulent Flow in an Annulus, *J. Heat Transfer,* Ser. C, vol. 89, pp. 25-31, 1967.
35. Naot, D., Shavit, A., and Wolfshtein, M., Numerical Calculation of Reynolds Stresses in a Square Duct with Secondary Flow, *Wärme Stoffübertrag.*, vol. 7, pp. 151-161, 1974.
36. Launder, B. E., and Ying, W. M., Secondary Flows in Ducts of Square Cross Section, *J. Fluid Mech.*, ***vol. 54,*** pp. 289-295. 1972.
37. Gessner, F. B., and Jones, J. B., On Some Aspects of Fully-Developed Turbulent Flow in Rectangular Channels. *J. Fluid Mech.*, vol. 23, pp. 689-713, **1965.**
38. Jones, 0. C., An Improvement in the Calculation of Turbulent Friction in Rectangular Ducts, *J. Fluids Eng.*, Ser. I, vol. 98, no. 2, pp. 173-181, 1976.
39. Wilkie, D., Cowin, M., Burnett, P., and Burgoyne, T., Friction Factor Measurements in a Rectangular Channel with Walls of Identical and Non-Identical Roughness, ***Znt. J. Heat Mass Transfer,*** vol. 10, pp. 611-621, 1967.
40. Carnavos, T. C., Some Recent Developments in Augmented Heat Exchange Elements, in ***Heat Exchangers,*** ed. N. Afgan and E. V. Schltinder, pp. 441-489, Hemisphere, Washington, D.C., 1974.
41. Carajilescov, P., and Tondreas, N. E., Experimental and Analytical Study of Axial Turbulent Flows in an Interior Subchannel of a Bare Rod Bundle, *J. Heat Transfer,* Ser. C. vol. 98, pp. 262-268, 1976.
42. Rehme, K., Anisotropic Eddy Viscosities in the Turbulent Flow Through a Rod Bundle, *Proc. First Symp. Turbulent Shear Flow, Pennsylvania State University, vol.* I, pp. 8.41-8.48, 1977.
43. Dwyer, 0. E., ed., Longitudinal Flow Through Rod Bundles, in *Progress in Heat and Mass Transfer.* pp. 115-264, Pergamon Press. Oxford, 1973.
44. Jonsson, V. K., and Sparrow, E. M., Experiments on Turbulent-Flow Phenomena in Eccentric Annular Ducts, *J. Fluid Mech.*, ***vol.*** **25,** no. 2, pp. 65-86, 1966.
45. Gosman, A. D., and C. W. Rapley, A Prediction Method for Fully-Developed Flow Through Non-Circular Passages. in Numerical Methods in Laminar and Turbulent Flow, *Proc. First Znt. Conf. at University College Swansea,* pp. 271-285. Prentice Press. London, 1978.
46. Cebeci, T., and Chang, K. C., A General Method for Calculating Momentum and Heat Transfer in Laminar and Turbulent Duct Flows, ***Num. Heat Transfer,*** vol. 1, pp. 39-68, 1978.
47. Van Dyke, M., Entry Flow in a Channel, *J. Fluid Mech.*, vol. 44, pp. 813-823, 1970.
48. Shah, R. K., A Correlation for Laminar Hydrodynamic Entry Length Solutions for Circular and Noncircular Ducts, *J. Fluid Eng.*, Ser. I, vol. 100, pp. 177-179, 1978.
49. Chato, J. C., Combined Free and Forced Convection Flow in Channels, in ***Advanced Heat Transfer,*** ed. B. T. Chao, pp. 439-459, University of Illinois Press, Urbana, 1969.
50. Petukhov, B. S., Turbulent Heat Transfer in Tubes with Variable Fluid Properties, in ***Heat Exchangers,*** ed. N. Afgan and E. V. Schltinder, pp. 239-263, Hemisphere, Washington, D.C.
51. Jackson, J. D., and Fewster, J., Enhancement of Turbulent Heat Transfer Due to Buoyancy for Downward Flow of Water in Vertical Tubes, in ***Heat Transfer and Turbulent Buoyant Convection,*** ed. D. B. Spalding and N. Afgan, vol. II, pp. 759-775, Hemisphere, Washington, D.C., 1977.
52. Campbell, D. A., and Perkins, H. C., Variable Property Turbulent Heat and Momentum Transfer for Air in a Vertical Rounded Corner Triangular Duct, ***Znt. J. Heat Mass Transfer,*** vol. 11, pp. 1003-1012, 1968.
53. McEligot, D. M., Coon, C. W., and Perkins, H. C., Relaminarization in Tubes, *Int. J. Heat Mass Transfer,* vol. 13, pp. 431-433. 1970.
54. Siuru, W. D., and Logan, E., Response of a Turbulent Pipe Flow to a Change in Roughness, *J. Fluid Eng.*, Ser. 1, vol. 99, pp. **548-555, 1977,**
55. Roberts, D. W., and Forester, C. K., Parabolic Procedure for Flows in Ducts with Arbitrary Cross-Sections, ***AZAA J.***, vol. 17, pp. 30-40, 1979.
56. Vasanta Ram, V., and von Schulz-Hausmann, F., A Study of the Relaxation Process in Turbulent Channel Flow, *Proc. Symp. Turbulent Shear Flows, Pennsylvania State University,* pp. 8.19-8.27, 1977.

© 1983 Hemisphere Publishing Corporation

57. Ahmed, S. R., Die Vermischung von koaxialen, turbulenten Strahlen verschiedener Geschwindigkeit und Temperatur in einem Rohr, VDI-Forschungsheft 547, VDI-Verlag, Düsseldorf, 197 1.
58. Collatz, L., and Görtler, M., Rohrströmung mit schwachem Drall. Z. *Angew. Math. Phys.,* vol. 5, pp. 95-110, 1954.
59. Vasilescu, D., Ein Beitrag zur Drallströmung im Rohr hinter dem unstetigen Übergang von einem Ringquerschnitt in einen Kreisquerschnitt, Dissertation, University of Karlsruhe, 1977.
60. Oswatitsch, K., ***Gasdynamik,*** Springer-Verlag, Vienna, 1978.
61. Shapiro, A. A., and Hawthorne, W. R., The Mechanics and Thermodynamics of Steady One-Dimensional Gas Flow, *J. Appl. Mech.,* ***vol.*** 14, pp. 317-336, 1947.
62. Cambel, A. B., Compressible Flow, in ***Handbook*** of ***Fluid Dynamics,*** ed. V. L. Streeter. pp. 8-1 to 8-70, McGraw-Hill, New York, 1961.
63. Bartlmä, F., ***Gasdynamik der*** *Verbrennung,* Springer-Verlag, Vienna, 1975.
64. Rich, G. R., ***Hydraulic Transients,*** Dover, New York, 1963.
65. Wylie, E. B., and Streeter, V. L., ***Fluid Transients,*** McGraw-Hill. New York, 1978.
66. Paynter, H. M., Fluid Transients in Engineering Systems, in ***Handbook of Fluid*** *Dynamics,* ed. V. L. Streeter, pp. 20-l to 20-47, McGraw-Hill, New York, 1961.
67. Kalinin, E. K., and Dreitser, G. A., Unsteady Convective Heat Transfer and Hydrodynamics ***in*** Channels. in *Adv. Heat* ***Transfer.*** vol. 6. pp. 367–502, 1970.
68. Uchida, S., The Pulsating Viscous Flow Superposed on the Steady Laminar Motion of Incompressible Fluid in a Circular Pipe. Z. ***Angew. Math. Phys.,*** vol. 7, pp. 403-422, 1950.
69. Richardson, E. G., and Tyler, E., The Transverse Velocity Gradient Near the Mouths of Pipes in Which an Alternating or Continuous Flow of Air Is Established, *Proc. Phys. Soc.* ***London,*** vol. 42, pp. l-15, 1929.
70. Schultz-Grunow, F., Pulsierender Durchfluss durch Rohre, *Forsch.* ***Ingenieurwes.,*** vol. 11, pp. 170-187, 1940.
71. Zielke, W., Frequency-Dependent Friction in Transient Pipe Flow, *J.* ***Basic*** *Eng.,* ***Ser.*** D, vol. 90, pp. 109-l 15, 1968.
72. Brown, F. T., Margolis, D. L., and Shah, R. P., Small Amplitude Frequency Behavior of Fluid Lines with Turbulent Flow. *J.* ***Basic*** *Eng.,* Ser. D, vol. 91, pp. 678-693, 1969.
73. Hirose, T., Frequency-Dependent Wall Shear in Transient Fluid Flow Simulation of Unsteady Turbulent Flow, Master s thesis, Massachusetts Institute of Technology, Cambridge, Mass., 1971.
74. Margolis, D. L., and Brown, F. T., Measurement of the Propagation of Long-Wave Length Disturbances Through Turbulent Flow in Tubes, ASME paper 15-FE-22, ***Fluid Eng.*** *Conf.* ***Minneapolis,*** May 5-7, 1975.
75. Adler, M., Strömung in gekriimmten Rohren, *Z.* ***Angew. Math.*** *Mech.,* vol. 14, pp. 257-275, 1934.
76. Prandtl, L., *Führer* ***durch die*** *Strömungslehre,* Vieweg, Braunschweig, 1949.
77. Ito, H., Laminar Flow in Curved Pipes, Z. ***Angew. Math.*** *Mech.,* vol. 49, pp. 653-663, 1969.
78. Patankar, S. V., Pratap, V. S., and Spalding, D. B., Prediction of Laminar Flow and Heat Transfer in Helically Coiled Pipes, *J.* ***Fluid*** *Mech.,* ***vol. 62,*** pp. 539-551, 1974.
79. Cheng, K. C., Lin, R. C., and Ou, J. W., Fully Developed Laminar Flow in Curved Rectangular Channels, *J. Fluids Eng.,* ***Ser. I, vol.*** 98, pp. 41–48, 1976.
80. Ghia, K. N., and Sokhey, J. S., Laminar Incompressible Viscous Flow in Curved Ducts of Regular Cross-Sections, *J.* ***Fluids*** *Eng.,* Ser. I, vol. 99, pp. 640-648, 1977.
81. Taborrek, B., and Lin, R. C., Laminar Flow and Heat Transfer in Curved Ducts, in ***Applied Numerical*** *Modelling,* ed. C. A. Brebbia, pp. 499-513, Pentech, London, 1978.
82. Cheng, K. C., Fully Developed Laminar Flow Curved Rectangular Channels, *J.* ***Fluids Eng., Ser.*** I, vol. 98, pp. 41-48, 1977.
83. Austin, L. R., and Seader, J. D., Fully Developed Viscous Flow in Coiled Circular Pipes, *AIChE J.,* vol. 19, pp. 85-94, 1973.
84. Greenspan, D., Secondary Flow in a Curved Tube, *J.* ***Fluid*** *Mech.,* vol. 57, pp. 167-176, 1973.
85. Zapryanov, Z., Christov, Ch., and Toshev, E., Fully Developed Laminar Flow and Heat Transfer in Curved Tubes, ***Int.*** *J.* ***Heat Mass*** *Transfer,* vol. 23, pp. 873-880, 1980.
86. Dravid, A. N., Smith, K. A., Merrill, E. W., and Brian, P. L. T., Effect of Secondary Fluid Motion on Laminar Flow Heat Transfer in Helically Coiled Circular Pipes, *AIChE J.,* vol. 17, pp. 1114-l 122, 1971.
87. Srinivason, P. S., Nandapakar, S. S., and Holland, F. A., Friction Factor for Coils, ***Trans. Inst. Chem.*** *Eng.,* vol. 48, no. 4-6, pp. T156–T161, 1970.
88. Humphrey, J. A. C., Taylor, A. M. K., and Whitelaw, J. H., Laminar Flow on a Square Duct of Strong Curvature, *J.* ***Fluid*** *Mech.,* vol. 83, pp. 509-527, 1977.
89. White, C. M., Streamline Flow Through Curved Pipes, *Proc. R. Soc.* ***London,*** A123, pp. 645-663, 1929.
90. Ito, H., Friction Factors for Turbulent Flow in Curved Pipes, *J.* ***Basic Eng.,*** Ser. D, vol. 81, pp. 123-l 34, 1959.
91. Ito, H., Pressure Losses in Smooth Pipe Bends, *J.* ***Basic En.,*** Ser. D, vol. 82, pp. 131-143, 1960.
92. Benedict, R. P., ***Fundamentals of Pipe Flow,*** Wiley, New York, 1980.
93. Idel chik, ***I.*** E., ***Handbook of Hydraulic Resistance,*** AEC-TR-6630, NTIS, U.S. Department of Commerce, Washington, D.C.. 1966.
94. Ananyan, A. K., ***Fluid Flow in Bends of Conduits*** (tr. from Russian), Israel Program for Scientific Translations, Jerusalem, 1965.
95. Wolf, H., Messung im Nachlauf eines Gleichdruckgitters für 90 Umlenkung, ***Maschinenhautechnik,*** p. 539, 1957.
96. Collar, A. R., Some Experiments with Cascades of Aerofoils, Air Ministry R & M, no. 1768. 1937.
97. Reneau, L. R., Johnston, I. P., and Kline, S. J.. Performance and Design of Straight, Two Dimensional Diffusers. *J.* ***Basic*** *Eng.,* Ser. D, vol. 89, pp. 141-150, 1967.
98. Schlichting, H., and Gersten, K., Berechnung der Strömung in rotationssymmetrischen Diffusoren mit Hilfe der Grenzschicht-theorie, Z. *Flugwiss.,* ***vol. 23,*** pp. 135-140, 1961.
99. Nikuradse, J., Untersuchung iiber die Strömungen des Wassers in konvergenten und divergenten Kanälen, *Forsch. Ing.-Wes.,* VDI no. 281, 1926; VDI no. 356, 1932; VDI no. 361, 1933.

© 1983 Hemisphere Publishing Corporation

100. Roberts, D. W., and Forester, C. K., Numerical Prediction of Three-Dimensional Subsonic Diffuser Flows, ***Symp. Flow in Primary, Non-Rotating Passages in Turbomachines, ASME Winter Annual Meeting,*** pp. 133-l 39, 1979.
101. Pozzorini, R., Das turbulente Strömungsfeld in einem langen Kreiskegel-Diffusor, Dissertation, ETH Ziirich, 1976.
102. Moore, C. A., and Kline, S. J., Some Effects of Vanes and of Turbulence on Two-Dimensional Wide-Angle Subsonic Diffusers, NACA TN 4080, 1958.
103. Kline, S. J., Abbott, D., and Fox, R., Optimum Design of Straight-Walled Diffusers, ***J. Basic Eng.. Ser.*** D, pp. 321-329, 1959.
104. Fox, R. W., and Kline, S. J., Flow Regime Data and Design Methods for Curved Subsonic Diffusers, ***J. Basic Eng.,*** Ser. D, vol. 84, 1962.
105. Wolf, S., and Johnston, J. P., Effects of Nonuniform Inlet Velocity Profiles on Flow Regimes and Performance in Two-Dimensional Diffusers, ***J. Basic Eng.,*** Ser. D, vol. 91, pp. 462-474, 1969.
106. Kline, S. J., and Ghose, S., The Computation of Separated Diffusors Flows, in Beiträge zu Transportphänomene in der Strömungsmechanik und anverwandten Gebieten, DLR-FB 77-16, pp. 139-149, 1977.
107. Ghose, S., and Kline, S. J., The Computation of Optimum Pressure Recovery in Two-Dimensional Diffusers, ***J. Fluids Eng.,*** Ser. I, vol. 100, pp. 419-426, 1978.
108. Woolley, R. L., and Kline, S. J., A Procedure for Computation of Fully Stalled Flows in Two-Dimensional Passages, ***J. Fluid Eng.,*** Ser. I, vol. 100, pp. 180-186, 1978.
109. Sprenger, H., Experimentelle Untersuchungen an geraden und gekriimmten Diffusoren, Mitt. Inst. Aero. ETH Zürich, no. 27, 1959.
110. Ackeret, J., Grenzschichten in geraden und gekriimmten Diffusoren, ***IUTAM Symp.,*** Freiburg/br., ed. H. Görtler, pp. 22-37, Springer-Verlag, Berlin, 1958.
111. Weber, H. E., Boundary Layer Calculations for Analysis and Design, ***J. Fluids Eng.,*** Ser. I, vol. 100, pp. 232-236, 1978.
112. Gersten, K., Herwig, H., and Wauschkuhn, P., Theoretical and Experimental Investigations of Two-Dimensional Flows with Separated Regions of Finite Length, AGARD CP, 128, pp. 23-1 to 23-13, 1980.
113. Robertson, J. M., and Ross, D., Effect of Entrance Conditions on Diffusor Flow, ***Proc. ASCE,*** vol. 78, 1952.
114. Winternitz, F. A.. and Ramsay, W. J., Effects of Inlet Boundary Layer on Pressure Recovery Energy Conversion and Losses in Conical Diffusers, ***J. R. Aero. Soc.,*** vol. 61, pp. 116-124, 1957.
115. Sovran, G., and Klomp, E. D., Experimentally Determined Optimum Geometries for Rectilinear Diffusors with Rectangular, Conical or Annular Cross-Section, in ***Fluid Mechanics of Internal Flow,*** ed. G. Sovran, pp. 270-319, Elsevier, Amsterdam, 1967.
116. Fernholz, H., Grenzschichttheoretische Untersuchung optimaler Unterschalldiffusoren, ***Ing.-Archiv,*** vol. 35, pp. 192-201, 1966.
117. Patterson, G. N., Modern Diffusor Design, ***Aircraft Eng.,*** vol. 10, pp. 267-273, 1938.
118. Cockrell, D. J., and King, A. L., A Review of the Literature on Subsonic Fluid Flow Through Diffusers, Br. Hyd. Res. Ass., B.H.R.A. Rept. TN 902, 1967.
119. Cockrell, D. J., and Markland, E., A Review of Incompressible Diffuser Flow, ***Aircraft Eng.,*** vol. 35, pp. 286-292, 1963.
120. Adkins, R. C. Diffusers and Their Performance Improvement by Means of Boundary Layer Control, in Special Course on Concepts for Drag Reduction, AGARD-R-654, pp. 6-l to 6-53, 1977.
121. Küchemann, D.. and Weber, J., ***Aerodynamics of Propulsion,*** McGraw-Hill, New York, 1953.
122. Liepe, F., Untersuchungen über das Verhalten von Drallströmungen in Kegeldiffusoren, ***Masch.-bautechn.,*** vol. 12, pp. 137-147, 1963.
123. Furuya, Y., Nakamura, I., and Yamada, H., On the Characteristics of the Two-Dimensional Diffusers with Suctions Through Parallel Porous Side Walls, ***Mem. Faculty Eng., Nagoya University,*** vol. 29, pp. 232-245, 1977.
124. Albring, W., ***Angewandte Strömungslehre,*** Verlag Theodor Steinkopff, Dresden, 1970.
125. Kaminski, D. A., ed., ***Fluid Flow Data Book,*** General Electric, Schenectady, N.Y., 1979.
126. Benedict, R. P. and Carlucci, ***N.*** A., ***Handbook of Specific Losses in*** Flow ***Systems,*** Plenum, New York, 1966.
127. Zoebl, H., and Kruschik, J., ***Strömung durch Rohre und Ventile,*** Springer-Verlag, Vienna, New York, 1978.
128. Schweigerer, ***S., Rohrleitungen, Theorie und Praxis,*** Springer-Verlag, Berlin, 1967.
129. Volk, W., ***Absperrorgane in Rohrleitungen,*** Springer-Verlag, Berlin, 1959.
130. Richter, H., ***Rohrhydraulik,*** 4th ed., Springer-Verlag, Berlin, 1962.
131. Kozeny, J., ***Hydraulik,*** Springer-Verlag, Vienna, 1953.
132. Jaeger, ***C., Technische Hydraulik,*** Birkhäuser-Verlag, Basel, 1949.
133. Benedict, R. P., Carlucci, N. A., and Swetz, S. D., Flow Losses in Abrupt Enlargements and Contractions, ***J. Eng. Power,*** Ser. A, vol. 88, pp. 73-81, 1966.
134. Moon, L. F., and Rudinger, G., Velocity Distribution in an Abruptly Expanding Circular Duct, ***J. Fluids Eng.,*** Ser. I, vol. 99, pp. 226-230, 1966.
135. Cherdron, W., Durst, F., and Whitelaw, J. H., Asymmetric Flows and Instabilities in Symmetric Ducts with Sudden Expansions, ***J. Fluid Mech.,*** vol. 84, pp. 13-31, 1978.
136. Benedict, R. P., and Wyler, J. S., Analytical and Experimental Studies of ASME Flow Nozzles, ***J. Fluids Eng.,*** Ser. I, vol. 100, pp. 265-275, 1978.
137. Alvi, S. H., Sridharan, K., and Lakshmana Rao, N. S., Loss Characteristics of Orifices and Nozzles, ***J. Fluids Eng.,*** Ser. I, vol. 100, pp. 299-307, 1978.
138. Benedict, R. P., Loss Coefficient for Fluid Meters, ***J. Fluid Eng.,*** Ser. I, vol. 99, pp. 245-248, 1977.
139. Alvi, S. H., Sridharan, K., and Lakshmana Rao, N. S., Loss Characteristics of Orifices and Nozzles, ***J. Fluids Eng.,*** Ser. I, vol. 100, pp. 299-307, 1978.
140. VDI Durchflussmessregeln, DIN 1952, Düsseldorf, 1971.
141. Börger, G. G., Optimierung von Windkanaldüsen für den Unterschallbereich, Z. ***Flugwiss.,*** vol. 23, pp. 45-50 and 282, 1975.
142. Morel, T., Design of Two-Dimensional Wind Tunnel Contractions, ***J. Fluids Eng.,*** Ser. I, vol. 99, pp. 371-378, 1977.
143. Morel, T., Comprehension Design of Axisymmetric Wind Tunnel Contractions, ***J. Fluids Eng.,*** Ser. I, vol. 97, pp. 225-233, 1975. ***See*** also ***J. Fluids Eng.,*** Ser. I, vol. 98, pp. 131-133, 1976.

© 1983 Hemisphere Publishing Corporation

144. Kolodzie, P. A., and van Winkle, M., Discharge Coefficients Through Perforated Plates, *AIChE J.*, vol. 3, pp. 305-312, 1957.
145. Smith, P. L., and van Winkle, M., Discharge Coefficients Through Perforated Plates at Reynolds Numbers of 400 to 3 000. *AIChE J.*, vol. 4, pp. 266-268, 1958.
146. Bernardi, R. T., Linehan, J. H., and Hamilton, L. H., Low Reynolds Number Loss Coefficient for Fine Mesh Screens, *J. Fluids Eng.*, Ser. I, vol. 98, pp. 762–764, 1976.
147. Cornell, W. G., Loss in Flow Normal to Plane Screens, *J. Heat Transfer*, vol. 80, pp. 791-799, 1958.
148. Wieghardt, K., Über den Strijmungswiderstand von Sieben, *Z. Angew. Math. Mech.*, **vol. 33,** pp. 312-314, 1953.
149. Pope, A., ***Wind Tunnel Testing,*** Wiley, New York, 1954.
150. Pankhurst, R. C., and Holder, D. W., ***Wind-Tunnel Technique,*** Pitman, London, 1952.
151. Papworth, M., The Effects of Screens on Flow Characteristics, Br. Hyd. Res. Ass., B.H.R.A. TN 1198, 1972.
1.52. Wharton, R., Division and Combination of Flow, Br. Hyd. Res. Ass., B.H.R.A. TN 937, 1968.
153. Williams, J. V., and Rhone, T. J., Dividing Flow in Branches and Wyes, *J. Hyd. Div.,* vol. 99, pp. 747-769, 1973.
154. Katz, S., Mechanical Potential Drops at a Fluid Branch, ***J. Basic Eng.,*** Ser. D, vol. 89, pp. 732-736, 1967.
155. Dodge, L., Fluid Throttling Devices, ***Prod. Eng.,*** p. 81, 1964.

© 1983 Hemisphere Publishing Corporation

2.2.3
Immersed bodies

K. Gersten

A. Flow regimes

In this section, flows past bodies of finite length will be considered. The emphasis will be on low-speed flow, which means that the velocity in the whole flow field should not exceed 30% of the speed of sound.

For high-speed flows past bodies, the reader is referred to special literature on gas dynamics; see Liepmann and Roshko [1], Oswatitsch [2,3], Becker [4], Zierep [5], Shapiro [6], and Tsien, Sec. 2.2.1 [8].

The flow pattern past immersed bodies is characterized by the Reynolds number, defined as

$$\mathrm{Re} = \frac{\rho V l}{\eta} = \frac{V l}{\nu} \tag{1}$$

where l is the characteristic length of the body, V is the flow velocity, ρ, η, and ν are density, dynamic (absolute) viscosity, and kinematic viscosity, respectively, taken at conditions far upstream of the body.

Two limiting cases can be distinguished, where $\mathrm{Re} \to \infty$ and where $\mathrm{Re} \to 0$.

(a) Re → ∞: Boundary-layer theory

The basic concept of boundary-layer theory has been described in Sec. 2.2.1D. As a consequence of this asymptotic theory according to Prandtl, the flow field can be divided into two different regions, the inviscid outer region and the very narrow viscous boundary layer close to the wall. Two fluid dynamical phenomena have so far limited the application of this theory, turbulence and separation.

I. Turbulence

There is no theory available to predict the laminar-turbulent transition of the boundary layer. Furthermore, the turbulent boundary layer needs empirical or semi-empirical modeling of turbulence; see Sec. 2.2.1C and 2.2.1D(g)-2.2.1D(j).

Turbulence modeling is still one of the major activities in fluid dynamics research.

II. Separation

When the boundary layer separates, the original boundary-layer concept breaks down. In these cases, additional modeling of the separated region and of the wake of the flow past the body is necessary. By applying such additional modeling, the boundary-Iayer concept can be used in a modified and more extended form by dividing the flow field into several regions, which interact with each other. These regions are the inviscid outer flow, the attached boundary layer, a free shear layer beyond separation, the separated regions (dead water), and the wake beyond the separated region of finite length.

This asymptotic theory for high Reynolds numbers, including separation, is still in a preliminary stage; for more information see Smith [7], Stewartson, Sec. 2.2.1 [88], Brown and Stewartson, Sec. 2.2.1 [89], and Williams, Sec. 2.2.1[90]. Flows exhibiting separation are still the domain of experiments and empirical relationships; see Chang, Sec. 2.2.1 [91, 92].

When the location of separation is not fixed, the

© 1983 Hemisphere Publishing Corporation

flow field usually becomes unsteady, although the free-stream velocity is independent of time; see Sec. B.

(b) Re → 0: Low Reynolds number flow

In this limit the inertial terms in the Navier-Stokes equation are usually very small and negligible (Stokes flow, ***creeping*** motion). However, the classical theory of Stokes, in which the inertial terms are dropped from the Navier-Stokes equations, is deficient for the case of a body in an unbounded stream, in that Stokes flow cannot properly represent conditions both at the body and at infinity; see Langlois [8], and Happel and Brenner [9]. This difficulty of Stokes theory has been resolved by use of the method of matched asymptotic expansions; see Van Dyke [10], and Schneider [11].

Van Dyke has compared the two-term expansion with both numerical and experimental results for the flow behind a sphere, and good agreement is observed for Reynolds numbers up to at least Re = 2. As far as the shape and length of the standing eddy is concerned, which appears at the rear part of the sphere at about Re = 16, agreement exists for even higher Reynolds numbers.

(c) Intermediate Reynolds number range

For flows in the intermediate range, only experimental investigations leading to empirical relationships are usually possible. Because of the rapid development of high-speed computers, there is a tendency to replace experiments more and more by numerical computations. Current research activity is concentrated on the numerical solutions of the so-called Reynolds-averaged Navier-Stokes equations [Sec. 2.2.1C(a), using more or less sophisticated turbulence modeling [Sec. 2.2.1C(b)]. The final aim for the future is the numerical solution of the complete time-dependent Navier-Stokes equations, including a direct numerical simulation of the large turbulent eddies. Only the small, subgrid-scale eddies are modeled. Assuming that projected trends of computer development continue, it has been estimated that turbulent eddy simulations of aerodynamic flows with the order of 10^9-10^{10} grid point would become feasible in the late 1990s; see Chapman [12].

B. Forces exerted on the body

(a) Total force

In the flow past a fixed body in a stream that is steady and uniform at infinity, the total force exerted on the body by the fluid is of most practical interest. Contributions to this total force are made by the tangential stress and by the normal stress at the body surface, integrated over that surface.

Considering an elementary area dA of the body surface, the resultant force (with components normal and tangential to the surface) exerted on that area is given by

$$\mathbf{s} = S\mathbf{n} - p\mathbf{n} \tag{2}$$

where $\mathbf{n}$ is the normal unit vector on that surface element and S is the stress tensor [see Eq. 2.2.1(10)]. Integration over the body surface leads to the total force

$$\mathbf{F} = \iint_A \mathbf{s}\, dA \tag{3}$$

[see Eq. 2.2.1(16)]. Since the resultant force $\mathbf{s}$ per unit area consists of pressure force (normal force) and tangential force, the total force can be split into a pressure force and a viscous force. The component of the total force in the free-stream direction is called ***drag D;*** the component normal to it is called ***lift L***.

(b) Drag

In the same way as the total force, the drag consists of two parts, the *friction* ***drug*** (integration of tangential forces) and the ***pressure drag*** (integration of normal forces), the latter also being called *form* ***drag.*** A dimensionless ***drag coefficient*** c_D is defined by

$$c_D = \frac{D}{(\rho/2)V^2 A} \tag{4}$$

where ***A*** is a characteristic reference area.

For a two-dimensional symmetric body of span ***b*** and length l in symmetric two-dimensional flow, the drag coefficient can be determined using the formula

$$c_D = 2\int_0^1 c_f\, d\left(\frac{x}{l}\right) + 2\int_0^1 c_p \frac{dy_c}{dx}\, d\left(\frac{x}{l}\right) \tag{5}$$

Friction drag Pressure drag

where the following definitions have been used. The skin friction coefficient based on the free-stream velocity V is

$$c_f = \frac{\tau_w(x)}{(\rho/2)V^2} \tag{6}$$

and the pressure coefficient is

$$c_p = \frac{p(x) - p_\infty}{(\rho/2)V^2} \tag{7}$$

where p_∞ is the undisturbed free-stream pressure far upstream of the body. The contour of the upper side of the two-dimensional body is given by the function $y_c(x)$ satisfying the conditions $y_c(0) = y_c(l) = 0$.

In inviscid flow the friction drag is equal to zero. But the pressure drag also vanishes in inviscid (subsonic) flows. The latter result is called *d'Alembert's* ***paradox.*** In

© 1983 Hemisphere Publishing Corporation

flows of high Reynolds numbers, where the boundary layer is applicable, separation might be avoided when the body is simple and slender enough such that the adverse pressure gradients are not sufficiently strong. Then the pressure distribution can be calculated by inviscid potential theory leading to zero pressure drag. The boundary-layer calculation ends up with the wall shear-stress distribution $\tau_w(x)$ and hence, according to Eq. (5), with the friction drag.

In most practical cases, however, boundary-layer separation will occur. As a consequence, a separated region at the rear part of the body develops, which changes the pattern of the complete flow field considerably. The pressure distribution around the body will change such that the pressure drag becomes a finite value. Since there is no theory available to calculate separated flows, drag coefficients of most bodies have to be determined experimentally. The most comprehensive collection of drag coefficient data has been given by Hoerner [13]. For the simple case of a sphere, the drag coefficient data are given in Table 1.

(c) Lift

The component of the total force normal to the free-stream direction is called lift. Hoerner and Borst [14] have collected all kinds of data on lift of immersed bodies.

If high lift values are desirable, the bodies have the special form of airfoils or wings to serve this purpose. For more detailed information on airfoils, see Riegels [15].

Although the mean value of the lift exerted on the body by the flow might be equal to zero, there is a possibility of nonzero timedependent lift values due to unsteady oscillatory separation of the boundary layer. This phenomenon can-even for symmetric bodies-lead to flow-induced movements of the body. The reader is referred to special literature on flow-induced vibrations and aeroelasticity [16-18].

Table 1 Drag coefficient of sphere[a]

Reynolds number Re	Drag coefficient c_D	Flow regime
$Re < 1$	$\frac{24}{Re}\left[1 + \frac{3}{16}Re + O(Re^2 \ln Re)\right]$	Low Reynolds number flow
$1 < Re < 10^3$ First separation at Re = 20	$0.4 < CD < 28$ See formula in [22]	
$10 < Re < 3 \times 10^5$	≈ 0.4	Subcritical
$3 \times 10^5 < Re < 10$	$0.08 < CD < 0.4$ See [36]	Critical and postcritical
$10 < Re$	≈ 0.2	Transcritical (supercritical)

[a] Sphere diameter, D; frontal area, $A = (\pi/4)D^2$; Reynolds number, $Re = VD/\nu$.

C. Flow around a circular cylinder

(a) Flow regimes

The flow around a circular cylinder is considered in detail as a typical example of the flow past a bluff body, where flow separation has an essential effect on the overall features of the flow. Table 2 presents the various regimes of flow experienced by a circular cylinder immersed in an incompressible fluid [19]. The Reynolds number is based on the diameter D of the cylinder. In the limit of very low Reynolds numbers, the flow exhibits complete fore-and-aft symmetry. At about Re = 3, flow separation occurs at the rear of the cylinder, forming two steady recirculating eddies. The steady recirculating wake persists for at least two decades in Reynolds number, growing in length until oscillations in the downstream wake progress forward to the recirculating eddy. The steady flow then breaks down into the familiar ***von Karman vortex street*** for Re of the order of 100. This pattern of alternating vortices exists up to about Re = 300, breaking down into an irregular unsteady wake, and finally into a completely turbulent wake for high Reynolds numbers. As noted in Table 2, the limits on these flow regimens are not fixed, since they depend strongly on the conditions of the experiment.

In several flow regimes the flow exhibits more or less pronounced periodicity due to vortex shedding, which is characterized by the Strouhal number,

$$Sr = \frac{fD}{V} \tag{8}$$

where f is the vortex shedding frequency. Values of Strouhal numbers for various flow regimes are also given in Table 2.

(b) Drag coefficient

The drag coefficient of circular cylinders as a function of the Reynolds number is shown in Fig. 1. The drag coefficient defined in Eq. (4) is based on the frontal area, that is, the product of diameter D and span b of the cylinder. There is excellent agreement between experiment and theory for Re < 1. The theoretical curve corresponds to a two-term expansion for low Reynolds numbers based on the method of matched asymptotic expansions (see Van Dyke [IO]):

© 1983 Hemisphere Publishing Corporation

Table 2 Flow characteristics of a circular cylinder[a]

Reynolds number Re	Flow regime	Flow pattern	Flow characteristics	Strouhal number Sr	Drag coefficient c_D	Separation angle θ_s
$Re \to 0$	Very low Reynolds number flow	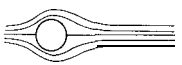	Steady flow, no wake, fore-and-aft symmetry, theory available		Eq. (9)	
3-4 < Re < 30-40	Twin vortex stage	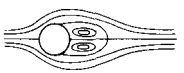	Steady flow, separation, recirculating eddies		$1.59 < c_D < 4.52$ (Re = 30) (Re = 4) (numerical)	$130 < \theta_s < 180$ (Re = 35) (Re = 5)
30 40 < Re < 80 90	Incipient von Karman range	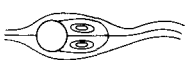	Laminar wake, instability		$1.17 < c_D < 1.59$ (Re = 100) (Re = 30) (numerical)	$115 < \theta_s < 130$ (Re = 90) (Re = 35)
80 90 < Re < 150 300	Pure von Karman range		von Karman vortex street	0.14 < Sr < 0.21		
150 300 < Re < 100000 130 000	Subcritical regime	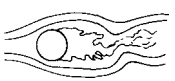	Laminar near-wake with vortex street instability	Sr = 0.21	≈ 1.2	≈ 80
100 000 130 000 < Re < 3 500 000	Critical and post-critical regime		Laminar separation, turbulent reattachment (bubble), final turbulent separation, turbulent wake	Loss of dominant periodicity	$0.2 < c_D < 1.2$	$80 < \theta_s < 140$
3 500 000 < Re	Transcritical regime (supercritical)		Transition to turbulent boundary layer, turbulent separation	0.25 < Sr < 0.30	≈ 0.6	≈ 115°

Cylinder diameter, D; cylinder span, b; frontal area, $A = Db$; Reynolds number, $Re = VD/\nu$, Strouhal number, $Sr = Df/V$.

© 1983 Hemisphere Publishing Corporation

$$c_D \approx \frac{8\pi}{\mathrm{Re}} [\Delta_1(\mathrm{Re}) - 0.87\ \Delta_1^3(\mathrm{Re}) + 0(\Delta_1^4)] \quad (9)$$

where

$$\Delta_1(\mathrm{Re}) = \left(\ln \frac{8}{\mathrm{Re}} + 0.0772\right)^{-1} = \left(\ln \frac{7.406}{\mathrm{Re}}\right)^{-1} \quad (10)$$

In this regime the friction drag is about half the total drag.

Assuming steady flow, the drag coefficients of circular cylinders have been determined by solving numerically the complete Navier-Stokes equations up to about Re = 100. Numerical results of Hamiele and Raal [20] are shown in Fig. 1. At Re = 100, the friction drag is only 36% of the total drag. Due to the high unsteadiness in the von Karman street regime, no numerical solution of the Navier-Stokes equations for Re > 100 is available. In the range between Re = 10^3 and about Re = 1.3 X 10^5, the total drag is almost constant, but the ratio of friction drag to total drag is decreasing rapidly. At Re = 10^5 the friction drag is less than 1% of the total drag; see Achenbach [21]. In the critical regime (1.5 X 10^5 < Re < 3.5 X 10^6), the drag coefficient is reduced drastically. The explanation lies in the behavior of the boundary layer at the surface of the cylinder. When the Reynolds number exceeds a certain value, the separated laminar shear layer may become turbulent followed by a reattachment forming a separation bubble. Finally, the turbulent boundary layer will separate, but far more backwards. The largest angle of separation (measured from forward stagnation point) is about $\theta_s = 140°$, corresponding to the lowest drag coefficient of about $c_D \approx 0.2$. For higher Reynolds number the boundary layer becomes turbulent before laminar separation, leading to turbulent separation and a turbulent wake. In this transcritical regime the drag coefficient is again a constant, the value being about $c_D = 0.6$. The friction drag in this regime is still of the order of 1% of the total drag.

The critical Reynolds number, defined at the steepest slope of the drag coefficient curve in the critical regime, is a function of turbulence intensity Tu of the free stream, which is defined as the ratio of the time-averaged turbulent kinetic energy [see Eq. 2.2.1(113)] and the dynamic pressure of the free stream. Brauer and Sucker [22] found the formula

$$\mathrm{Re}_s = 3.78 \text{ X } 10^5 e^{-6\sqrt{\mathrm{Tu}}} \quad (11)$$

for

$$0 \leqslant \mathrm{Tu} \leqslant 0.05 \quad (12)$$

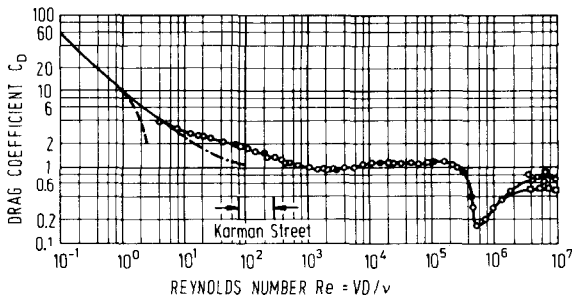

Figure 1 Drag coefficient for circular cylinders. Measurements after Wieselsberger, Flachsbart, Roshko, and Jones and Walker; see Schlichting, Sec. 2.2.1 [65]. – – – Theory according to Eq. (9); –·–·– numerical solution after Hamielec and Raal [20].

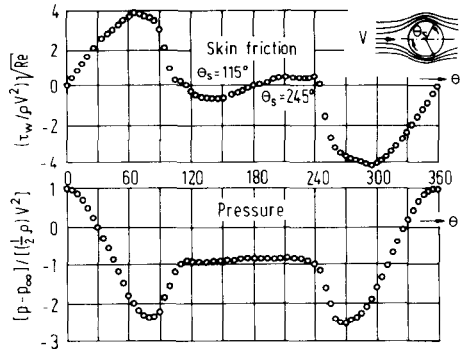

Figure 2 Skin friction and pressure distribution around a circular cylinder at Re = 10^5 (subcritical). θ_S, separation angle. After Achenbach [2 1]

(c) Distributions of *pressure and shear stress at the wall*

Achenbach [21] has made measurements of the pressure and the shear stress at the wall around the circumference of the cylinder for several Reynolds numbers. Figures 2 and 3 show examples of results. Figure 2 refers to a subcritical Reynolds number, Re = 10^5, and Fig. 3 to a supercritical Reynolds number, Re = 3.6 X 10^6. The considerable difference between these two cases can

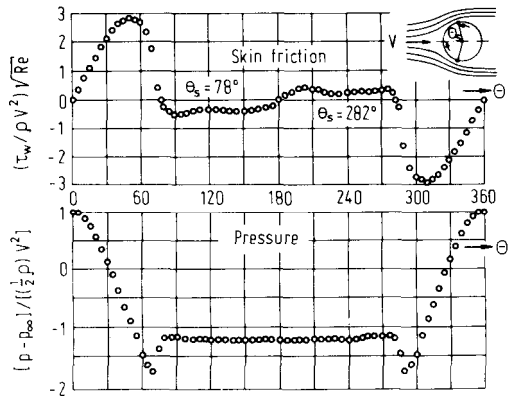

Figure 3 Skin friction and pressure distribution around a circular cylinder at Re = 3.6 X 10^6 (supercritical). θ_S, separation angle. After Achenbach [21].

© 1983 Hemisphere Publishing Corporation

easily be seen. In the first case (laminar separation at $\theta_s = 78°, c_D = 1.2$), the drag is about 60% higher than in the second case (turbulent separation at $\theta_s = 115°$, $c_D = 0.76$).

(d) Effect of roughness

The effect of roughness on the flow around circular cylinders has been investigated by Achenbach [23], Fage and Warsap [24], Szechenyi [25], and Güven et al. [26]. Figure 4 shows the drag coefficient of rough circular cylinders in cross flow versus Reynolds number according to Achenbach [23]. The parameter is the relative roughness k_s/D. Each curve representing the variation with Reynolds number covers three regimes, the subcritical, the critical, and the transcritical. Obviously, the subcritical flow regime is not influenced by the surface roughness. Because of increasing Reynolds number, the laminar separation is followed by a closed bubble leading to a backward shifting of the separation point and hence to a reduction in drag. This process takes place at lower Reynolds number when the surface is rough because of additional disturbances in the boundary layer caused by roughness elements. The reduction of drag in the critical region is not so pronounced for rough surfaces compared to smooth ones. Achenbach has also measured the distributions of static pressure and shear stress at the wall around rough circular cylinders, as well as the locations of the points of laminar-turbulent transition.

(e) Effects of various parameters

The following effects on flows around circular cylinders are worth mentioning.

I. Free-stream turbulence

As already noted, the main effect of free-stream turbulence is on critical Reynolds number according to Eq. (11); see also Fage and Warsap [24].

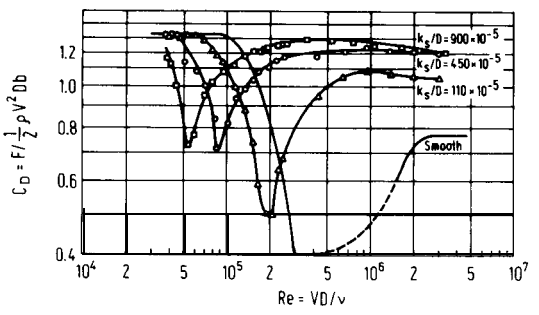

Fire 4 Drag coefficient of rough circular cylinders. After Achenbach [23]. ***D,*** cylinder diameter; ***F,*** drag; k_s, sand roughness.

II. Compressibility

When the fluid is compressible, the drag coefficient and other flow parameters also depend on the Mach number Ma; see Eq. 2.2.2(28). Measurements of Naumann and Pfeiffer [27] have shown that the Mach number has no effect for $Ma < 0.3$.

On the other hand, at higher Mach numbers the influence is large. The effect of Reynolds number recedes more and more as the Mach number is increased. For Mach numbers larger than Ma = 0.8, the drag coefficient is independent of Reynolds number.

III. Temperature-dependent fluid properties

For flows around circular cylinders with heat transfer, the fluid properties are usually taken at a reference temperature; see Eq. 2.2.1(212). Often the film temperature-i.e., the mean value of wall temperature and free-stream temperature-is used; see Morgan [28]. Zukauskas [29] reports the effect of heat transfer on the skin friction distribution and hence on friction drag, which, however, is only a very small percentage of the total drag.

IV. Unsteady flow

It has been noted that even for steady free-stream flow, unsteadiness occurs in the flow field in various Reynolds number regimes. This can lead to oscillatory lift coefficients that are of the same order of magnitude as the drag coefficient; see Morkovin [19]. The flow characteristics become even more complex when the cylinder performs small lateral oscillations, for example, as a consequence of aeroelastic effects. The reader is referred to special publications on this subject; see McCroskey [30], Morkovin [19], and literature mentioned earlier [17, 18].

V. Fins

The flow around circular cylinders having fins parallel to the free-stream direction is extremely complicated because of the mutual interaction of the boundary-layer flows on the fins and on the cylinder, respectively; see Keefe [31]. Since the boundary layer on the fin is similar to the boundary layer on the flat plate, many investigations have been carried out on circular cylinders mounted perpendicular to a flat plate. For more details of this flow see, for instance, [32,33].

D. Flow around variously shaped cylinders

The drag of blunt bodies is due mainly to its pressure distribution (pressure drag over 90%), which differs

© 1983 Hemisphere Publishing Corporation

radically from that for inviscid flow because of flow separation. Separation on the body occurs either at sharp edges or at positions of large adverse pressure gradients.

In the range of Reynolds numbers $10^3 < \mathrm{Re} < 10^8$, blunt bodies with sharp edges show little variation in drag coefficient with Reynolds number. The drag coefficients for some typical cases are given in Table 3.

The Strouhal number for blunt bodies is given by

$$\mathrm{Sr} = \frac{0.21}{c_D^{3/4}} \qquad (13)$$

found by a composite empirical fit to the data from a wide range of blunt bodies.

Blunt but rounded forms show a remarkable reduction in drag coefficient over a small range of Reynolds numbers in which transition from laminar to turbulent separation occurs (critical Reynolds number). The designations subcritical and supercritical are used to indicate the Reynolds number ranges in which laminar or turbulent separation occurs. In Table 4, drag coefficients for some rounded shapes are given in the subcritical regime. For more information, see Hoerner [13] and Heddleson et al. [34].

Table 3 Drag coefficients of various blunt cylinders[a]

Shape	c_D
	1.98
	2.30
	1.16
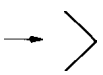	2.20
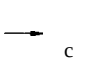 c l	2.05
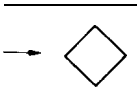	1.55

[a] $\mathrm{Re} > 10^3$ based on frontal height.

Table 4 Drag coefficients for rounded cylinders

Flow direction	Fineness ratio (c_0 lb,)	Corner radius ratio *(r/b,)*	c_D at Re = 10
	1:1	0.50	1.00
	1:2		1.6
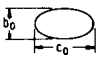	2:1		0.6
	1:2	0.021	2.2
	1:2	0.083	1.9
	1:2	0.250	1.6
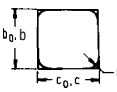	1:1	0.021	2.0
	1:1	0.167	1.2[b]
	1:1	0.333	1.0
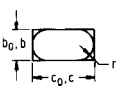	2:1	0.042	1.4
	2:1	0.167	0.7[b]
	2:1	0.500	0.4
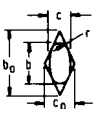	1:2	0.021	1.8
	1:2	0.083	1.7
	1:2	0.167	1.7
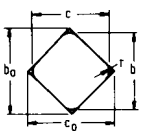	1:1	0.015	1.5
	1:1	0.118	1.5[b]
	1:1	0.235	1.5
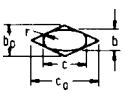	2:1	0.042	1.1
	2:1	0.167	1.1[b]
	2:1	0.333	1.1
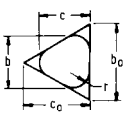	1:1	0.021	1.2
	1:1	0.083	1.3[b]
	1:1	0.250	1.1
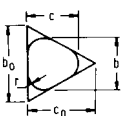	1:1	0.021	2.0
	1:1	0.083	1.9[b]
	1:1	0.250	1.3

[b] After Fraas and Ozisik [35].
[b] $\mathrm{Re} = 2 \times 10^5$.

NOMENCLATURE FOR SECTION 2.2.3

A	surface area, m^2	D	diameter, m
b	span, m	D	drag, N
c_D	drag coefficient	f	frequency, s^{-1}
c_f	skin friction coefficient	F	drag force, N
c_p	pressure coefficient	$\mathbf{F}$	force, N

© 1983 Hemisphere Publishing Corporation

k_s	(sandpaper) roughness height, m
l	length, m
L	lift, N
Ma	Mach number
n	normal unit vector
p	static pressure, N/m^2
p_∞	static pressure in far field, N/m^2
Re	Reynolds number
Re_c	critical Reynolds number
s	force per unit area, N/m^2
S	stress tensor, N/m^2
Sr	Strouhal number
Tu	turbulence intensity, Tu = $2k/\rho U_\infty^2$ [Eq. 2.2.1-(113)1
V	velocity, m/s
x, Y	Cartesian coordinates, m
Yc	contour coordinate, m
η	dynamic (absolute) viscosity, kg/m s
θ	angle (circular cylinder)
θ_s	angle at flow separation
ν	kinematic viscosity, m^2/s
ρ	density, kg/m^3
τ_w	wall shear stress, N/m^2

REFERENCES FOR SECTION 2.2.3

1. Licpmann, H. W., and Roshko, A., ***Elements of Gasdynamics.*** Wiley, New York, 1957.
2. Oswatitsch, K., ***Grundlagen der Gasdynamik,*** Springer-Verlag, Vienna, 1976.
3. Oswatitsch, K., ***Spezialgebiete der Gasdvnamik,*** Springer-Verlag, Vienna, 1977.
4. Becker, E., ***Gasdynamik,*** Teubner, Stuttgart, 1966.
5. Zierep, J., ***Vorlesungen iiber theoretische Gasdynamik,*** Braun, Karlsruhe, 1976.
6. Shapiro, A. H., *The Dynamics* ***and Thermodynamics of Compressible Fluid Flow, 2*** vols., Ronald Press, New York, 1953, 1954.
7. Smith, F. T., Laminar Flow of an Incompressible Fluid Past a Bluff Body: The Separation, Reattachment, Eddy Properties and Drag. ***J. Fluid Mech., vol. 92,*** pp. 171-205, 1979.
8. Langlois, W. E., Slow ***Viscous Flow,*** Macmillan, New York, 1964.
9. Happel, L., and Brenner, H., ***Low Reynolds Number Hydrodynamics,*** Prentice-Hall, Englewood Cliffs, N.J., 1965.
10. Van Dyke, M., ***Perturbation Methods in Fluid Mechanics,*** Parabolic Press, Stanford, Calif., 1975.
11. Schneider, W., ***Mathematische*** *Methoden* ***der Strömungsmechanik,*** Vieweg, Braunschweig, 1978.
12. Chapman, D. R., Computational Aerodynamics Development and Outlook, *AIAA J.,* vol. 17, pp. 1293-1313, 1979.
13. Hoerner, ***S.*** F., ***Fluid-Dynamic Drag,*** S. F. Hoerner, Midland Park, N.J., 1957.
14. Hoerner, S. F., and Borst, H. V., ***Fluid Dynamic Lift,*** L. A. Hoerner, Brick Town, N.J., 1975.
15. Riegels, F. W., ***Aerodynamische Profile,*** Oldenbourg, Munich, 1958, English tr. by D. G. Randall, ***Aerofoil Sections,*** Butterworths, London, 1961.
16. Naudascher, E., ed., Flow-Induced Structural Vibrations, ***IUTAM/IAHR Symp. Karlsruhe, August*** 1972, Springer-Verlag, Berlin, 1974.
17. Sachs, P., ***Wind Forces in Engineering,*** Pergamon Press, Oxford, 1972.
18. Förshing, H. W., ***Grundlagen der Aeroelastik,*** Springer-Verlag, Berlin, 1974.
19. Morkovin, M. V., Flow Around Circular Cylinder-A Kaleidoscope of Challenging Fluid Phenomena, in *Symp.* ***Fully Separated Flows,*** American Society of Mechanical Engineers, pp. 102-118, 1964.
20. Hamielec, A. E., and Raal, J. D., Numerical Studies of Viscous Flow Around Circular Cylinders, ***Phys. Fluids,*** vol. 12, pp. 11-17, 1969.
21. Achenbach, E., Distribution of Local Pressure and Skin Friction Around a Circular Cylinder in Cross Flow up to Re = 5×10^6, ***J. Fluid Mech.,*** vol. 34, pp. 625-639, 1968.
22. Brauer, H., and Sucker, D., Umströmung von Platten, Zylindern und Kugeln, ***Chem. Ing. Tech.,*** vol. 48, pp. 665-736, 1976.
23. Achenbach, E., Influence of Surface Roughness on the Cross-Flow Around a Circular Cylinder, ***J. Fluid Mech.,*** vol. 46, pp. 321-335, 1971.
24. Fage, A., and Warsap, J. H., The Effects of Turbulence and Surface Roughness on the Drag of Circular Cylinders, ARC RM 1283, 1930.
25. Szechenyi, E., Supercritical Reynolds Number Simulation for Two-Dimensional Flow over Circular Cylinders, ***J. Fluid Mech.,*** vol. 70, pp. 529-542, 1975.
26. Güven, O., Patel, V. C., and Farrel, C., A Model for High-Reynolds-Number Flow Past Rough-Walled Circular Cylinders, ***J. Fluids Eng.,*** vol. 99, pp. 480-494, 1977.
27. Naumann, A., and Pfeiffer, H., Über die Grenzschichtströmung am Zylinder bei hohen Geschwindigkeiten, ***Adv. Aeronaut. Sci.,*** vol. 3, pp. 185-206, 1962.
28. Morgan, V. T., The Overall Convective Heat Transfer from Smooth Circular Cylinders, ***Adv. Heat Transfer,*** vol. 11, pp. 199-264. 1975.
29. Zukauskas, A., Heat Transfer from Tubes in Crossflow, ***Adu. Heat Transfer,*** vol. 8, pp. 93-160, 1972.
30. McCroskey, W. J., Some Current Research in Unsteady Fluid Dynamics-The 1976 FREEMAN Scholar Lecture, ***J. Fluids*** *Eng.,* ***vol.*** 99, pp. 8-39, 1977.
31. Keefe, R. T., An Investigation of the Fluctuating Forces Acting on a Stationary Circular Cylinder in a Subsonic Stream and of the Associated Sound Field, University of Toronto, UTIA Rept. 76, 1961.
32. Thwaites, B., ***Incompressible Aerodynamics,*** Clarendon Press, Oxford, 1960.

© 1983 Hemisphere Publishing Corporation

33. Hornung, H. G., and Joubert, P. N., The Mean Velocity Profile in Three-Dimensional Turbulent Boundary Layers, *J. Fluid Mech.*, vol. 15, pp. 368-384, 1963.
34. Heddleson, Brown, and Cliffe, Summary of Drag Coefficients for Various Shaped Cylinders, Clearing House for Federal Scientific and Technical Information, Springfield, XDC 56-2-19, 1955.
35. Fraas, A. P., and Ozisik, M. ***N., Heat Exchanger Design,*** Wiley, New York, 1965.
36. Achenbach, E., Experiments on the Flow Past Spheres at Very High Reynolds Numbers. ***J. Fluid Mech., vol. 54,*** pp. 565-575, 1972.

© 1983 Hemisphere Publishing Corporation

2.2.5
Fixed beds

P. J. Heggs

■ The structural properties of fixed beds have been extensively reviewed by Haughey and Beveridge [1]. Two categories of fixed bed exist: regular and random packed. Regular packings provide complete control of bed voidage and surface area, but assembly is expensive. Regular packings are used, however, in thermal regenerators, checkerwork in high-temperature stoves in the glass and steel industries, and metallic matrix arrangements in the Ljungstrom rotary regenerators used in the power generation industry. In all these situations the pressure drop across the fixed bed must be small.

Random packings are found in a wide range of industrial operations: adsorption, catalysis, combustion, filtration, separation, and solid-fluid contacting in general. They are formed by the haphazard positioning of particles to provide a bed and the average bed properties are largely dependent on the mode of assembly [2]. Only an infinitely sized bed is wholly random, but this is closely approached when the ratios of container diameter (D) and container length (L) to the particle diameter (d) are greater than 10 [3]. Random beds are simple in design, assembly is cheap, and construction is rugged.

Fixed beds are normally characterized by the specific surface area of the bed S_B and the fractional voidage of the bed ϵ. The latter is defined as the free volume of the bed divided by the volume of the bed, that is,

$$\epsilon = \frac{\text{bed volume} - \text{packing volume}}{\text{bed volume}} \tag{1}$$

and the specific surface area of the bed is strictly dependent on the value of ϵ. The specific surface area of the particles S is defined as the surface area of the particles divided by the volume of the particles. For a sphere,

$$S = \frac{6}{d} \tag{2}$$

Thus the specific surface area of the bed is less than the specific surface area of the particles, and hence

$$S_B = S(1 - \epsilon) \tag{3}$$

For nonspherical particles, a characteristic dimension d is employed, and is defined as 6 divided by the specific surface area of the particles. The properties of beds of some regular-shaped materials are listed in Table 1[4, 5].

Even for regular-shaped packings there is a wide range of bed specific areas and bed voidages. The bed voidage can vary for each individual packing shape and size depending on the mode of assembly, and the results in Table 1 were obtained for beds that were continuously tamped during assembly.

In all fixed-bed operations, one of the major operating costs is related directly to the pressure drop across the fixed bed. The following variables affect pressure drop in fixed beds: fluid velocity; density and viscosity; the size, shape, and orientation of the packing; the bed voidage, surface roughness, and possible wall effects. Two main approaches to the interpretation of experimental data have been developed:

1. The bed consists of an assembly of tortuous channels of varying cross section-the channel model

© 1983 Hemisphere Publishing Corporation

Table 1 Properties of beds of some regular-shaped packings

Packing no.	Description	S, m^2/m^3	ϵ	S_B, m^2/m^3	d, mm
	Spheres				
1	3 mm diam.	2 000	0.36	1 280	3.0
2	6 mm diam.	1 000	0.37	630	6.0
3	9 mm diam.	500	0.38	310	9.0
	Cylinders				
4	4.76 mm diam. X 4.76 mm	1 261	0.30	882	4.76
5	6.35 mm diam. X 6.35 mm	945	0.31	652	6.35
6	6.35 mm diam. X 12.7 mm	787	0.34	520	7.62
	Plates 3.175 mm thick				
7	1.32 mm spacing	576	0.31	398	10.41
8	2.64 mm spacing	576	0.46	311	10.41
9	5.94 mm spacing	576	0.63	213	10.41
	Lessing rings				
10	6.35 mm diam. X 6.35 mm steel	4 444	0.71	1 022	1.35
11	6.35 mm diam. X 6.35 mm porcelain	2 490	0.62	946	2.41
12	9.35 mm diam. X 9.35 mm porcelain	1432	0.56	630	4.19

2. The bed is regarded as consisting of an assembly of particles submerged in the flowing fluid, each particle processing its own boundary layer

The first model is more widely used, although the second is conceptually closer to the physical situation.

The best-known equation, which represents the channel model, is the Ergun equation [6]. It includes all the variables affecting the pressure drop, except surface roughness and wall effects, and is as follows:

$$\frac{\Delta p}{L} = \frac{150\eta u(1-\epsilon)^2}{d^2\epsilon^3} + \frac{1.75\rho u^2(1-\epsilon)}{d\epsilon^3} \quad (4)$$

The pressure drop is the sum of two terms; the first term represents the effects of skin friction, and the second, the effect of form drag. The constants 150 and 1.75, respectively, were found by linearly fitting the data of Ergun [7], Burke and Plummer [8], and Morcom [9]. The particle shapes considered in these investigations included spheres, cylinders, tablets, nodules, marble chips, and graded coke. Hence the characteristic particle dimension, d, is used in Eq. (4).

Equation (4) can be easily manipulated into two linear equations, each of which provides a linear relationship of a friction factor with a particle Reynolds number ($\mathrm{Re} = ud\rho/\eta$), first

$$f_v = 150 + 1.75\frac{\mathrm{Re}}{1-\epsilon} \quad (5)$$

and second

$$f_k = 150\frac{1-\epsilon}{\mathrm{Re}} + 1.75 \quad (6)$$

where $f_v = \Delta p d^2\epsilon^3/[L\eta u(1-\epsilon)^2]$, which represents the ratio of the pressure drop to the viscous energy term, and $f_k = \Delta p d\epsilon^3/[L\rho u^2(1-\epsilon)]$, which represents the ratio of the pressure drop to the kinetic energy term. f_k is similar to the commonly used Fanning friction factor used for flow in pipes.

At a low Reynolds number, Eq. (4) reduces to the Blake [10]-Carmen [11]-Kozeny [12] equation for laminar flow, and at high Reynolds numbers to the Burke-Plummer [8] equation for turbulent flow.

However, the generality of the Ergun equation constants, 150 and 1.75. have been shown to be suspect. Bradshaw and Myers [13] presented pressure drop measurements for fixed beds of Celite cylinders of dimensions 0.617 mm diameter X 0.488 mm, d = 0.566 mm, in the Ergun manner, but the results were almost 50% higher than the curve representing the Ergun equation. Handley and Heggs [14] also found that the Ergun equation did not predict the pressure drop for random fixed beds of spheres, cylinders, rings, and plates. The Ergun-type expression correlated the experimental data extremely well, but for each particle shape a different pair of constants were obtained.

Hicks [15] showed that the constants in the Ergun-type equation are also functions of Reynolds number and not true constants, as is commonly accepted. In addition. the importance of the Reynolds number range of the experimental data, the subsequent correlation of the data, and the applicability of using the correlation outside its Reynolds number range is shown in Fig. 1. This is a plot off, against $\mathrm{Re}/(1-\epsilon)$ for the following correlations for randomly dumped spheres:

Ergun [6]:

$$f_v = 150 + 1.75\frac{\mathrm{Re}}{1-\epsilon} \qquad 1 < \frac{\mathrm{Re}}{1-\epsilon} < 2\,000 \quad (7)$$

© 1983 Hemisphere Publishing Corporation

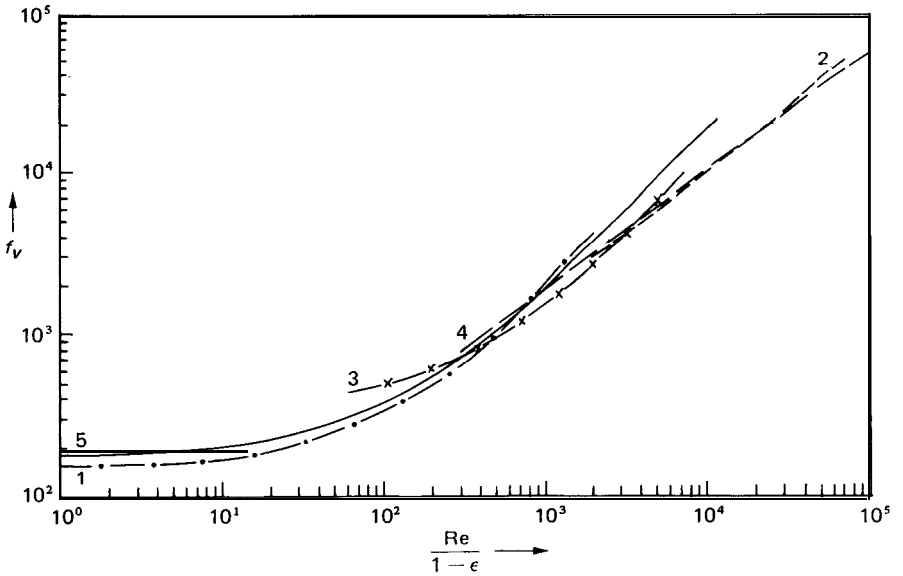

Figure 1 Pressure drop correlations for dumped spherical packings. 1, Ergun [6]; 2, Wentz and Thodos [16]; 3, Handley and Heggs [14]; 4, Hicks [15]; 5, Macdonald et al. [17].

Wentz and Thodos [16]:

$$f_v = 0.396\frac{\mathrm{Re}/(1-\epsilon)}{[\mathrm{Re}/(1-\epsilon)]^{0.05}-1.20}$$

$$2\,000 < \frac{\mathrm{Re}}{1-\epsilon} < 65\,000 \qquad (8)$$

Handley and Heggs [14]:

$$f_v = 368 + 1.24\,\frac{\mathrm{Re}}{1-\epsilon} \qquad 60 < \frac{\mathrm{Re}}{1-\epsilon} < 7\,000 \qquad (9)$$

Hicks [15]:

$$f_v = 6.8\left(\frac{\mathrm{Re}}{1-\epsilon}\right)^{0.8} \qquad 300 < \frac{\mathrm{Re}}{1-\epsilon} < 6\,500 \qquad (10)$$

Macdonald et al. [17]:

$$f_v = 180 + 1.8\,\frac{\mathrm{Re}}{1-\epsilon} \qquad 0.1 < \frac{\mathrm{Re}}{1-\epsilon} < 10000 \qquad (11)$$

The correlation of Macdonald et al. covers the widest Reynolds number range and for the majority of the range provides the largest prediction of the pressure drop. This correlation is recommended for predicting the pressure drop through fixed beds of randomly dumped spherical packing. The other correlations, although providing excellent fits for the data, should not be used outside their Reynolds number ranges.

However, the correlations listed above for spherical packings can lead to serious errors in the prediction of the pressure drop for fixed beds of random nonspherical packings. Figure 2 shows the data and best line fits for the cylinders and Lessing rings listed in Table 1 [14]. Also included in Fig. 2 are lines representing the correlations of Handley and Heggs for dumped spheres, Eq. (9), and that of Macdonald, et al., Eq. (11). Neither of the sphere correlations provides good predictions of the nonsphere pressure drop over their respective Reynolds number range. Table 2 lists the values of the constants obtained by least-squares fitting of the data by the rearranged Ergun equation (5) and the respective Reynolds number ranges. These fixed beds were assembled in an identical manner to the spherical packed beds of Handley and Heggs [14], and over the entire Reynolds number range the values of the viscous friction factor are greater for the nonspherical packing.

Figure 3 shows a plot of f_v against $\mathrm{Re}/(1-\epsilon)$ for the plates 3.175 mm thick and spaced 1.32 mm apart (no. 7) listed in Table 1. Six sets of data are shown for plates of differing lengths: 6.35, 12.7, 25.4, 50.8,

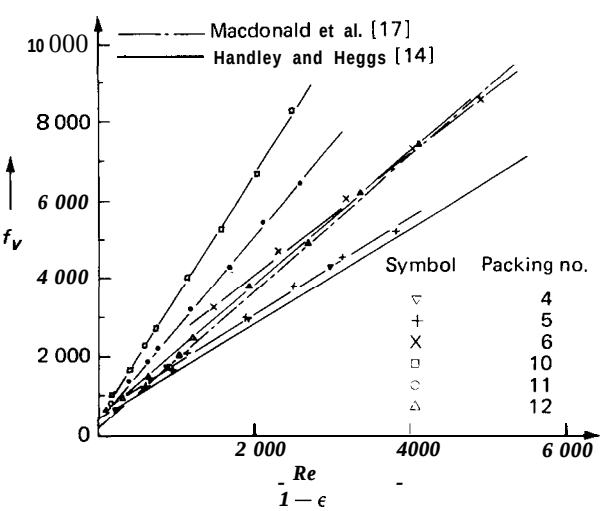

Figure 2 Pressure drop data for nonspherical packings.

© 1983 Hemisphere Publishing Corporation

Table 2 Pressure drop correlations for cylindrical and Lessing ring packings

Packing no.	m	c	$Re/(1-\epsilon)$ range
4	1.25	598	200-3 000
5	1.28	458	600-3 900
6	1.54	1 083	1 500-4 900
10	3.15	410	200-2 500
11	2.37	356	200-2600
12	1.72	452	300-4 100

101.6, and 203.2 mm. It is quite obvious that the rearranged Ergun equation (5) fits each individual set of data, but with widely differing constants. In all cases the values of the viscous friction factor fall well below the correlation line of the Macdonald et al. equation (11). The correlation constants for the rearranged Ergun equation (5) for these plate dimensions and the other two plate spacings listed in Table 1 may be found in [14]. For other arranged packings, such as woven screens and compact heat exchanger matrices, Kays and London [18] present extensive design data.

The wall effect can be accounted for in fixed beds, when the column diameter to particle characteristic dimension is less than 7, by including a parameter M in the Ergun-type equation (5) as recommended by Mehta and Hawley [19]. M accounts for the column surface in the evaluation of the hydraulic radius of the channel model and is given by

$$M = 1 + \frac{4d}{6D(1-\epsilon)} \tag{12}$$

where D is the column diameter, and the rearranged Ergun equation becomes

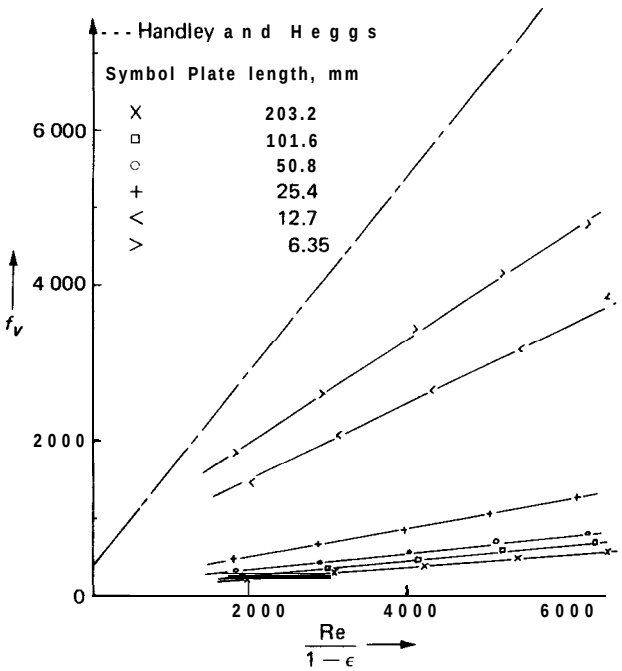

Figure 3 Pressure drop data for parallel-plate packings.

$$f_v = 150M^2 + 1.75M\frac{Re}{1-\epsilon} \tag{13}$$

The constants in Eq. (13) may be changed according to the packing shape being investigated.

No similar modification is available for particle roughness, although Macdonald et al. [17] have correlated rough particles by the Ergun-type equation (5) and only the value 1.8 is changed to 4, the other constant remaining fixed at 180. This infers that roughness affects only the inertia contribution to the overall pressure drop.

Nomenclature for Section 2.2.5 appears at the beginning of Part 2.

REFERENCES FOR SECTION 2.2.5

1. Haughey, D. P., and Beveridge, G. S. G., Structured Properties of Packed Beds-A Review, *Can. J. Chem. Eng.*, vol. 47, p. 130, 1969.
2. Debbas, S., and Rumpf, H., On the Randomness of Beds Packed with Spheres or Irregular Shaped Particles, *Chem. Eng. Sci.*, vol. 21, p. 583, 1966.
3. Ridgway, K., and Tarbuck, K. J., The Random Packing of Spheres, *BCE*, vol. 12, p. 384, 1967.
4. Heggs, P. J., Transfer Processes in Packings Used in Thermal Regenerators, Ph.D. thesis, University of Leeds, 1967.
5. Main, A. J. St. J., An Experimental Investigation into Heat Transfer and Momentum Effects in Packed Beds, Ph.D. thesis, University of Leeds, 1978.
6. Ergun, S., and Orning, A. A., Fluid Flow through Randomly Packed Columns and Fluidised Beds. *2nd. Eng. Chem., vol.* 41, p. 179, 1949.
7. Ergun, S., Fluid Flow through Packed Columns, *Chem. Eng. Prog.*, vol. 48, p. 89, 1952.
8. Burke, S. P., and Plummer, W. B., Gas Flow through Packed Columns, *Ind. Eng. Chem., vol. 20,* p. 196, 1928.
9. Morcom, A. R., Fluid Flow through Granular Materials, *Trans. Inst. Chem. Eng.*, *vol. 24,* p. 30, 1946.
10. Blake, F. E., The Resistance of Packing to Fluid Flow, *Trans. AIChE*, vol. 14, p. 415, 1922.
11. Carmen, P. C., Fluid Flow through Granular Beds, *Trans. AIChE*, vol. 29, p. 150, 1937.
12. Kozeny, J., Uber Kapillars Leitung des Wassers in Boden, *Ber. Wien Akad.*, vol. 136, p. 271, 1927.
13. Bradshaw, R. D., and Myers, J. E., Heat and Mass Transfer in Fixed and Fluidised Beds of Large Particles, *AIChE J.*, *vol.* 9, p. 590, 1963.

© 1983 Hemisphere Publishing Corporation

14. Handley, D., and Heggs, P. J., Momentum and Heat Transfer Mechanisms in Regular Shaped Packings, ***Trans. Inst. Chem. Eng., vol. 46,*** p. T251, 1968.
15. Hicks, R. E., Pressure Drop in Packed Beds of Spheres, ***Ind. Eng. Chem. Fund., vol. 9,*** p. 500, 1970.
16. Wentz, C. A., and Thodos, G., Pressure Drops in the Flow of Gases through Packed and Distended Beds of Spherical Particles, ***AIChE J., vol. 9,*** p. **81, 1963.**
17. Macdonald, I. F., El-Sayed, M. S., Mow, K., and Dullen, F. A. L., Flow through Porous Media-the Ergun Equation Revised, ***Ind. Eng. Chem. Fund., vol. 18,*** p. 198, 1979.
18. Kays, W. M., and London, A. **L., *Compact Hear Exchangers,* McGraw-Hill, New York, 1964.**
19. Mehta, D., and Hawley, M. C., Wall Effect in Packed Columns, ***Ind. Eng. Chem. Process Des. Dev.,*** vol. 8, p. 281, 1969.

© 1983 Hemisphere Publishing Corporation

2.2.6
Fluidized beds

O. Molerus

A. Overall behavior

(a) Types of fluidization

In a fluidized bed consisting of fine-grained particles, the upward flow of a fluid just balances the weight of the particles, which are not, therefore, in permanent contact with one another. The mobility of the particles thus achieved gives rise to a liquidlike behavior of the fluidized bed as a whole.

At low flow rates the fluid percolates the voids of the bed without changing its structure (Fig. la). An increase in flow rate, and thereby in the forces exerted by the fluid on the solid material, results in individual particles beginning to move within narrowly bounded regions, whereas the majority of the particles remain in permanent contact as a solid bed. With a further increase in the throughput of fluid, a situation is reached where the particles are not in permanent contact with one another and are supported by the fluid. In this state, the fluid pressure drop measured between two horizontal reference planes is in equilibrium with the weight of the solid and fluid contained between these planes when expressed in terms of unit area. The bed has now attained fluidization (see Fig. lb) and is characterized by the voidage ϵ_{mf} and the height h_{mf}.

With a further increase in the throughput of fluid, two different types of fluidization are observed. Liquid-solid systems continue, in general, to expand uniformly and exhibit homogeneous particle distribution (Fig. lc). This type of fluidization is referred to as ***particulate.***

With gas-solid systems, however, additional throughput of gas above the minimum amount required for fluidization takes place essentially in the form of bubbles free from solid (see Fig. 1*d*). This type of fluidization is referred to as ***aggregative.*** In the state of fluidization, both voidage and height of the fluidized bed are greater than ϵ_{mf} and h_{mf}, respectively.

The rising gas bubbles grow rapidly by coalescence unless baffles are incorporated to promote bubble splitting. With columns that are sufficiently narrow and tall, the bubble diameter may approach the column diameter, so that gas seals off the whole cross section. The fluidized bed is then said to be ***slugging*** (Fig. le).

As long as a more or less well-defined, upper bed surface is observed, dense-phase fluidization prevails. As the superficial upward velocity of a fluidizing liquid approaches the free-falling velocity of the particles, the bed contents will be carried over.

In a gas-solid fluidized system with high voidage, bubble formation and a defined, upper bed surface disappear. As a result of the appearance of particle strands, however, circulating fluidized beds may operate

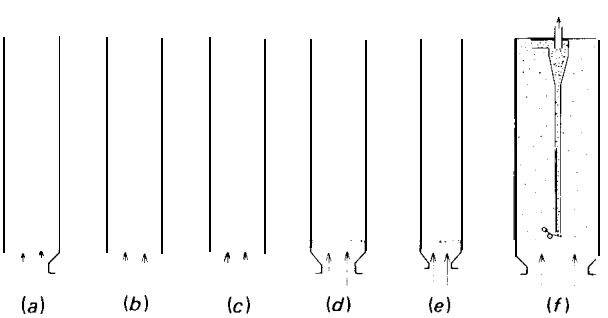

Figure 1 Types of fluidization.

© 1983 Hemisphere Publishing Corporation

at superficial gas velocities that exceed considerably the free-falling velocity of single particles (Fig. 1*f*).

(b) Pressure drop and minimum jkidization

In a fluidized bed, the pressure drop Ap across a bed of height h just balances the total weight of fluid and particles in the bed. Thus,

$$\frac{\Delta p}{h} = [(1-\epsilon)\rho_S + \epsilon\rho_f]g \qquad (1)$$

For gas-solid systems, the total weight is approximately equal to the weight of the particles alone.

With a well-fluidized bed consisting of approximately equal-sized particles with low cohesion, the dimensionless pressure drop is related to the superficial velocity u (normalized by means of the minimum velocity for fluidization u_{mf}) as shown in Fig. 2.

In particular, with gas-solid systems and with fine-grained particles, however, the bed is consolidated by its own gravitational load, giving rise to increased cohesive forces between adjacent particles. The pressure drop curve will thus pass through a maximum before reaching the horizontal equilibrium line in the fluidized region. This excess pressure drop is necessary to break up the consolidated, fixed-bed structure.

With decreasing fluid velocity in the fixed-bed region, the pressure drop velocity curve lies below the curve obtained initially for the consolidated bed, because the fixed bed then remains at a bed voidage ϵ_{mf} that is higher than that of the consolidated fixed bed

Usually, the transition from the horizontal, fluidized-bed, pressure drop line to the inclined, fixed-bed pressure drop curve is continuous. The minimum velocity for fluidization is therefore defined as the point of intersection of the respective, extrapolated pressure drop curves for fixed and fluidized beds (see Fig. 2).

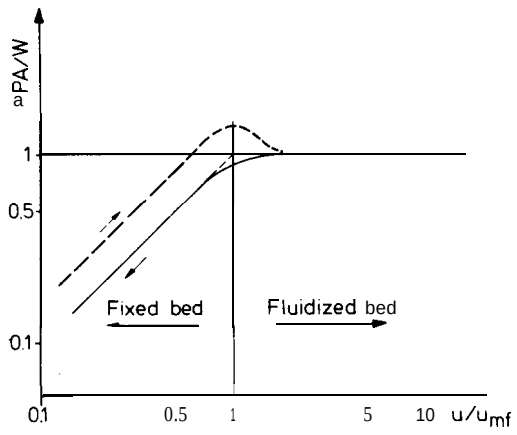

Figure 2 Pressure drop velocity curve.

(c) Calculation of *the minimum velocity for fluidization*

In technical fluidized beds, particles of irregular shape are used and size distributions may be narrow or broad.

At minimum fluidization, the bed is in the state of loosest packing. The voidage ϵ_{mf} increases with a decrease in the average particle size and with a decrease in the shape factor Φ_S, but no general rule for ϵ_{mf} can be given.

For particles with a given mass distribution density $q_3(d_p)$, an appropriate average diameter can be defined by

$$\overline{d_p} = \frac{1}{\int_{d_{p\min}}^{d_{p\max}} d_p^{-1} q_3(d_p)\, d(d_p)} \qquad (2)$$

The state of minimum fluidization may be considered as the limiting state of the fixed bed. Thus, equating the pressure drop corresponding to Ergun s equation [1] and the fluidized-bed pressure drop according to Eq. (1) yields

$$\mathrm{Re}_{mf} = 42.9\,\frac{1-\epsilon_{mf}}{\Phi_S} \times \left[\sqrt{1 + 3.1\times 10^{-4}\,\frac{\Phi_S^3\epsilon_{mf}^3}{(1-\epsilon_{mf})^2}\,\mathrm{Ar}} - 1\right] \qquad (3)$$

This equation, together with a knowledge of the data for both solid and fluidizing media, allows the superficial velocity of the fluid at the point of minimum fluidization to be calculated.

(d) State diagram and nondimensional groups

At a fluidized spherical particle, the average drag force and buoyancy balance the particle s weight:

$$C_D(\mathrm{Re},\epsilon)\,\frac{\pi d_p^2}{4}\,\frac{\rho_F}{2}\left(\frac{u}{\epsilon}\right)^2 + \frac{\pi d_p^3}{6}\rho_F g = \frac{\pi d_p^3}{6}\rho_S g \qquad (4)$$

In the fluidized state, the particle s drag coefficient C_D depends on the Reynolds number $\mathrm{Re} = ud_p/\nu$ and on the voidage ϵ.

Rearrangement of Eq. (4) yields

$$\frac{3}{4}\,\frac{U^2}{d_p g}\,\frac{\rho_F}{\rho_S - \rho_F} = \frac{\epsilon^2}{C_D(\mathrm{Re},\epsilon)}$$

which is equivalent to

$$\frac{3}{4}\,\mathrm{Fr}\,\frac{\rho_F}{\rho_S - \rho_F} = f(\mathrm{Re},\epsilon) \qquad (5)$$

By evaluating measurements on the basis of Eq. (5), Reh [2] developed a state diagram that describes the

© 1983 Hemisphere Publishing Corporation

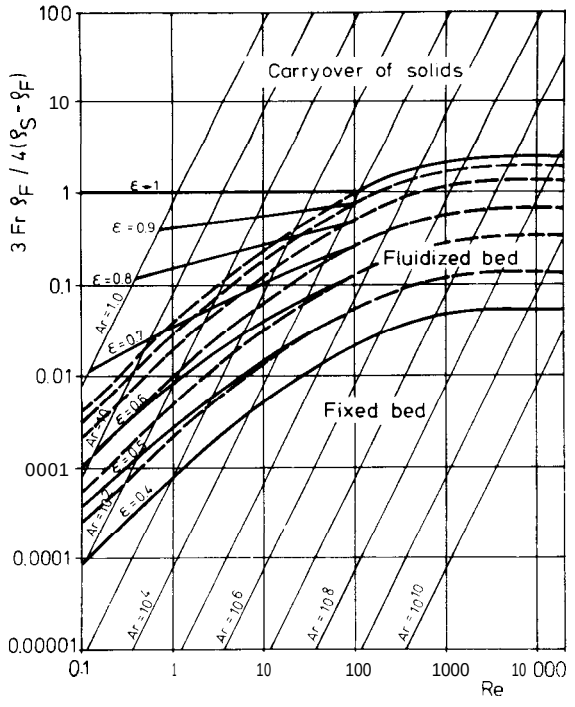

Figure 3 State diagram for the fluidization of monosized spheres.

fluidization of monosized spheres (Fig. 3). This state diagram is not single-valued, because the dashed lines represent particulate fluidization and the solid lines describe aggregative fluidization.

In the simpler case of particulate fluidization, the values indicated by the dashed lines are numerically correct. For a given particle-liquid system, bed expansion follows a line Ar = const beginning with $\epsilon \approx 0.4$ for minimum fluidization up to a limit of $\epsilon = 1$, which describes a floating, single particle.

The more complex behavior of aggregative fluidization depends largely on bed diameter, bed height, and distributor design. The numerical accuracy of the values of ϵ predicted by the full lines ϵ = const should not, therefore, be overestimated. They indicate, however, some important differences between particulate and aggregative fluidization. The lines ϵ = const for aggregative fluidization lie above those for particulate fluidization, i.e., an aggregatively fluidized bed expands less than a particulately fluidized bed of the same Archimedes number at the same Reynolds number.

Very important for practical applications is the finding that, for low Archimedes numbers, there exists a region above the line describing a floating, single particle in which gas-solid fluidized systems can exist. As a result of gas-solid demixing in this range, the so-called fast fluidized bed [3] can operate with recirculation of the particles.

The ambiguity of the state diagram Fig. 3 means that a purely static view, taking into account only the three nondimensional groups of Eq. (5), is not sufficient to describe aggregative fluidization.

Wilhelm and Kwauk [4] concluded from experimental results that the Froude number $\mathrm{Fr}_{mf} = u_{mf}^2/d_p g$ is a rough criterion for distinguishing between the two types of fluidization. Accordingly,

$\mathrm{Fr}_{mf} \lesssim 1$ holds for particulate fluidization

and (6)

$\mathrm{Fr}_{mf} \gtrsim 1$ holds for aggregative fluidization

B. Local structure of gas-solid fluidized beds

The overwhelming majority of industrial applications for fluidized-bed technology involve gas-solid systems.

In gas-solid systems, rapid mixing of solid occurs, so that coefficients for heat transfer at the walls or at immersed surfaces are relatively high.

Heat transfer mechanisms in gas-solid fluidized beds may be largely understood from a knowledge of the local flow patterns for gas and solid. (Compare Sec. 2.8.4 of this handbook.)

(a) Types of powders

According to Geldart [5], with gas-solid fluidized systems one has to distinguish among the following four types of powders (see Fig. 4).

I. Group A

Materials having a small mean size and/or a low particle density (less than about 1.4 g/cm^3) generally exhibit the type of behavior described below, some cracking catalysts being typical examples.

Beds of powders in this group expand considerably before bubbling commences. When the gas supply is suddenly cut off, the bed collapses slowly, typically at a rate of 0.3-0.6 cm/s, this being similar to the superficial velocity of the gas in the dense phase. All bubbles rise more rapidly than the interstitial gas velocity. The mean size of bubbles may be reduced in two ways, i.e., by having a wide particle size distribution and/or a small mean particle size. A maximum bubble size does appear to exist.

II. Group B

Group B contains most materials in the mean size and density ranges, i.e.,

$40\ \mu\mathrm{m} \lesssim d_p \lesssim 500\ \mu\mathrm{m}$

$1.4\ \mathrm{g/cm^3} \lesssim \rho_s \lesssim 4\ \mathrm{g/cm^3}$

© 1983 Hemisphere Publishing Corporation

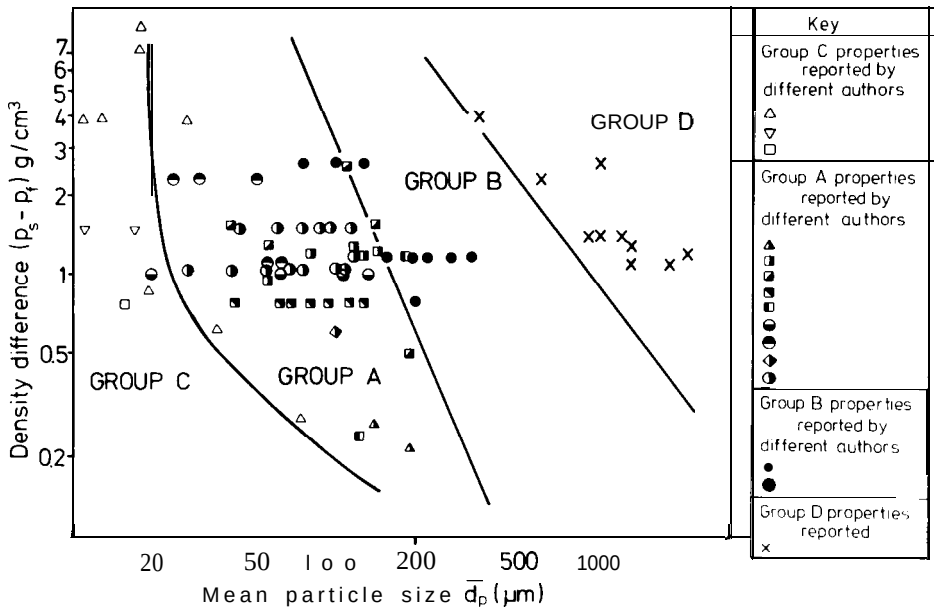

Figure 4 Powder classification diagram according to Geldart [5] for fluidization by air.

In contrast with group A powders, naturally occurring bubbles start to form in this type of powder at or only slightly above minimum fluidization velocity. Bed expansion is small, and the bed collapses very rapidly when the gas supply is cut off. Most bubbles rise more quickly than the interstitial gas velocity. There is no evidence of a maximum bubble size. At comparable conditions, i.e., at the same distance from the distributor, bubble size seems to be independent of particle size.

III. Group C

Powders that are in any way cohesive belong to group C.

Normal fluidization of such powders is extremely difficult. The powder lifts as a plug in small-diameter tubes, or channels badly; i.e., the gas passes up voids extending from distributor to bed surface. This difficulty arises because the interparticle forces are considerably greater than those that the fluid can exert on the particle.

Fluidization can generally be made possible or improved by the use of mechanical stirrers [6].

IV. Group D

This further group of powders is confined to large and/or very dense particles. Certainly all but the largest bubbles rise more slowly than the interstitial fluidizing gas, so that gas flows into the base of the bubble and out of the top, providing a mode of gas exchange and bypassing different from that observed with group A or B powders. The gas velocity in the dense phase is high. If gas is admitted only through a centrally positioned hole, group D powders can be made to spout.

The powder classification diagram (Fig. 4) evaluated by Geldart [5] from experiments with air as fluidizing agent shows that, in general, decreasing density difference shifts the boundaries between the regimes observed to larger particle sizes.

Usually, fluidization is confined to group A and group B particles. The main difference between group A and group B particles consists of the onset of bubbling and the limited maximum bubble size of group A powders.

In the following the behavior of bubbling fluidized beds is reported with restriction mainly to group B powders.

(b) Single bubbles

The characteristic property of gas-solid systems is the appearance of gas bubble swarms. Because of the lack of transparency, measurements of the local structure of such fluidized beds are extremely complicated. However, the essential details of the influence of gas bubbles on the properties of fluidized beds may be understood from the investigation of single bubbles existing in fluidized beds at superficial velocities slightly above the minimum velocity for fluidization. A comprehensive survey of the present state of knowledge has been given by Jackson [7] and by Rowe [8] for theoretical and experimental investigations, respectively.

Theoretical and experimental results may be summarized as follows (see Fig. 5).

The bubble shape is essentially spherical but with an

© 1983 Hemisphere Publishing Corporation

indented base. The bubble rise velocity is given approximately by

$$u_b \approx \sqrt{0.95 g r_b} \tag{7}$$

so that, as long as the bubble is not too small, u_b is large compared with the interstitial gas velocity in the surrounding suspension in the case of type A and type B powders.

Viewed within a frame moving upward with the bubble s rise velocity, the particles flow around the bubble within steady streamlines.

In analogy to the fluid flow pattern around a solid sphere at Re $>$ 1, a wake, in which particles are carried upward, exists at the lower end of the bubble.

This flow pattern is in accordance with the pressure distribution inside a bubble, which was carefully measured by Reuter [9].

As shown in Fig. 5, the dashed line represents the pressure distribution within the undisturbed bed far removed from the bubble, whereas the solid line represents the pressure distribution along the bubble s vertical axis of symmetry.

Following the pressure gradient, gas flows from the bottom into the bubble and carries with it particles from underneath into the wake. The bubbles are therefore flattened at the base, with a little hump at the vertical axis of symmetry. Since unlimited enrichment of particles in the wake is not possible, particle shedding occurs after a certain rise distance.

In accordance with the pressure gradient in the upper part of the bubble, gas penetrates into the surrounding suspension. Except for very small bubbles, the bubble rise velocity substantially exceeds the interstitial gas velocity in the suspension, so that gas penetrating from the rising bubble into the surrounding suspension is carried downward and reenters the bubble from underneath.

The existence of the circulation of gas within a

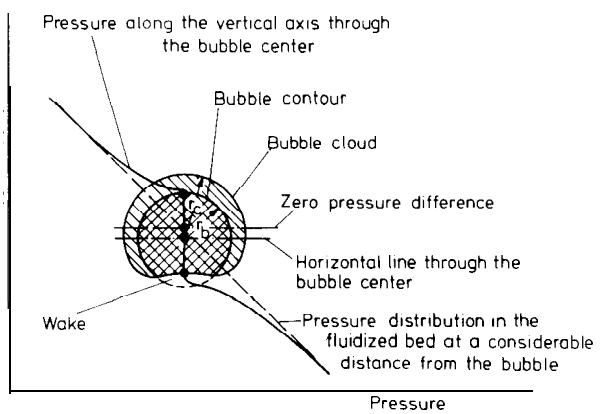

Figure 5 Cloud formation and pressure distribution for a single bubble.

relatively small cloud surrounding the bubble was predicted theoretically by Davidson [10] and confirmed experimentally for gas-solid systems by Rowe and Partridge [11]. With increasing bubble size, the relative depth of penetration into the surrounding suspension is steadily reduced.

The results achieved from single-bubble investigations yield the following important insights into the overall behavior of gas-solid fluidized systems of type A and type B powders:

1. Gas bubbles carry particles upward in their wake. As a consequence of the motion around rising bubbles, even particles not captured in the wake are moved some distance in an upward direction, as can be seen from observations of total particle movement.
2. Gas circulation inside the bubble gives rise to a bypass effect, whereby the gas inside the bubble does not come into direct contact with the particles.
3. As a consequence of the lower pressure at the bottom of the bubble, a larger and faster-rising bubble will, in overtaking, absorb a smaller one into its base. The consequence of this coalescence is rapid bubble growth in the direction of upward movement.

(c) Bubble coalescence

Using miniaturized capacitance probes of a shape that did not disturb the state of fluidization, Werther and Molerus [12] investigated the local structure of large-diameter (D_B = 1 m) fluidized beds.

Figure 6 shows the two cumulative number distributions of the bubbles passing two points in the bed at heights of 8 and 30 cm above the distributor.

As may be seen, both the average bubble diameter and the width of the bubble size distribution increase with distance above the distributor.

In Fig. 7, measurements of local, average bubble volumes reported by Werther [13] are depicted. The results reveal that in a fluidized bed of D_B = 1 m bed diameter, the average bubble volume increases over a distance of almost 1 m by a factor of about 100 (filled circles: u = 10 cm/s superficial velocity; open circles: u = 20 cm/s superficial velocity).

Using measurements as depicted in Fig. 7, Werther [13] developed a statistical model of bubble coalescence that yields the following empirical correlation :

$$\frac{d_b}{\text{cm}} = 0.853 \sqrt[3]{1 + 0.272 \frac{u - u_{mf}}{\text{cm/s}}} \times \left(1 + 0.068\,4 \frac{x}{\text{cm}}\right)^{1.21} \tag{8}$$

Equation (8) relates the local, average bubble diameter to the excess, superficial gas velocity u $-\,u_{mf}$ and to the

© 1983 Hemisphere Publishing Corporation

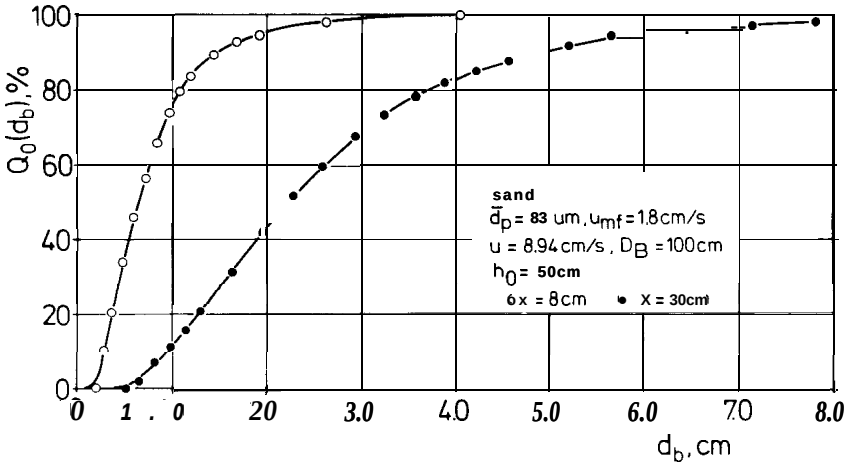

Figure 6 Bubble size distribution at two different heights x above the distributor.

height x above the distributor. In this equation, the properties of the fluidlzed solid appear only in the form of the minimum velocity for fluidization u_{mf}. Furthermore, in contrast to the opinion often expressed in the published literature, the excess, superficial gas velocity and not the fluidization number u/u_{mf} is seen to be the determining factor. Figure 8 shows a comparison of values predicted by Eq. (8) with results obtained experimentally.

The bubble growth rate investigations reported here deal with fluidized beds without any baffles or immersed tubes, although the latter are often present of necessity for purposes of heat transfer. Disadvantages of these and similar attachments include the possibility of erosion, the formation of deposits or encrustations of solid, and the hindrance to fluid flow and to particle movement. Apart from the qualitative knowledge that baffles or immersed tubes are suitable for the control of bubble growth, no detailed, quantitative information on this problem of significant practical importance is at present available.

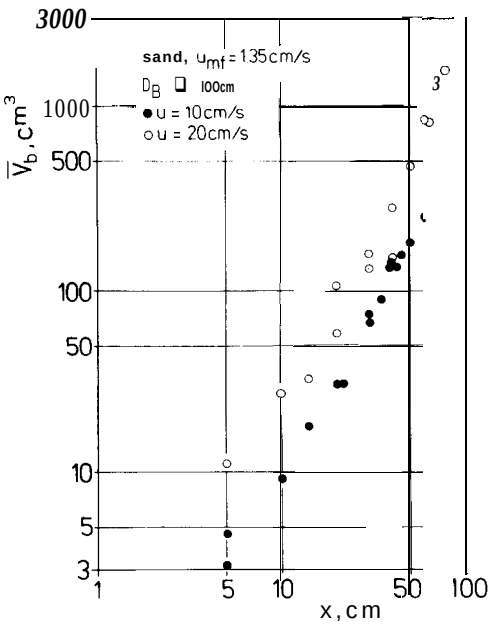

Figure 7 Local average bubble volume as a function of height above the distributor for two different superficial gas velocities u [13].

(d) Spatial distribution of bubbles and circulation of solids

In the preceding paragraph, only the dependence of bubble size on height above the distributor was considered. Another effect that gives rise to a further complication in the flow pattern of gas and solid in a fluidized bed is the typically nonuniform distribution of rising bubbles over the bed s cross section.

The left side of Fig. 9 shows the results of measurements made by Werther [15] of the dependence of local gas flow rates on the radial distance from the central axis of the tube. The curves indicate increased bubble formation at the walls of the vessel, close to the distributor plate. With increasing height above the plate, this peak in the gas flow rate is shifted toward the middle of the tube. Associated with this effect is a characteristic pattern for the circulation of solids, as depicted schematically on the right side of Fig. 10.

Calculations carried out by Johnson [16] show that this characteristic flow profile is caused by the influence of the walls on bubble coalescence. This interaction, however, indicates only the initiating mechanism, because the bubbles carry particles in their wakes that are ejected at the bed surface and sink down preferentially in the zones of reduced bubble development. As a consequence of this circulation pattern shown in Fig. 9 the nonuniform distribution of the bubbles over the bed s cross section is further increased and stabilized.

© 1983 Hemisphere Publishing Corporation

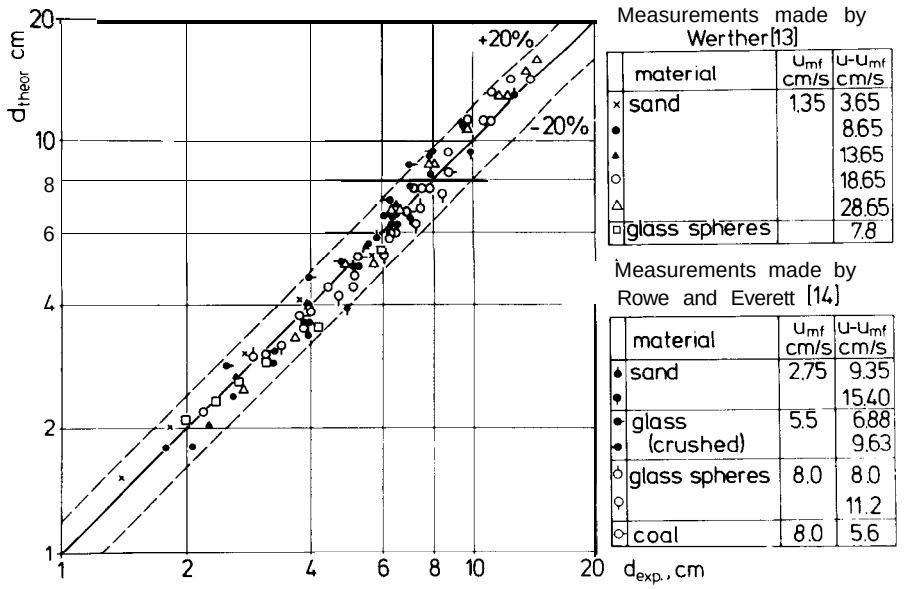

Figure 8 Comparison of measured bubble diameters with bubble diameters predicted by Eq. (8).

The circulation pattern described above gives rise both to intensive, convective mixing of solids and to back mixing of gas, an effect that may be of disadvantage in catalytic fluidized beds because it results in the reentry of exhausted gas associated with the downward-flowing solid. In other applications, however, the intensive mixing in the solid phase is of great benefit.

By adjusting the inlet gas distribution over the cross section of the bed, it is possible to increase the circulation of solids as described by Merry and Davidson [17]. It is very difficult, however, to reduce the circulation of solids, because the underlying mechanism of preferential bubble coalescence near the walls, which is typical for all bubbling fluidized beds, means that the influence of the distributor on the flow distribution of the gas transported in bubbles is very limited.

On the other hand, as indicated in the literature [18-20], all measures that limit bubble growth or that promote bubble splitting-i.e., baffles, immersed tubes; increased static pressure; and increased fraction of fines in the solid phase-give rise to a more uniform bubble development.

(e) Influence of distributor design

As a criterion for good gas distribution, a very high ratio of distributor pressure drop to bed pressure drop is often recommended. Relevant measurements [21], however, show that an increase in distributor pressure

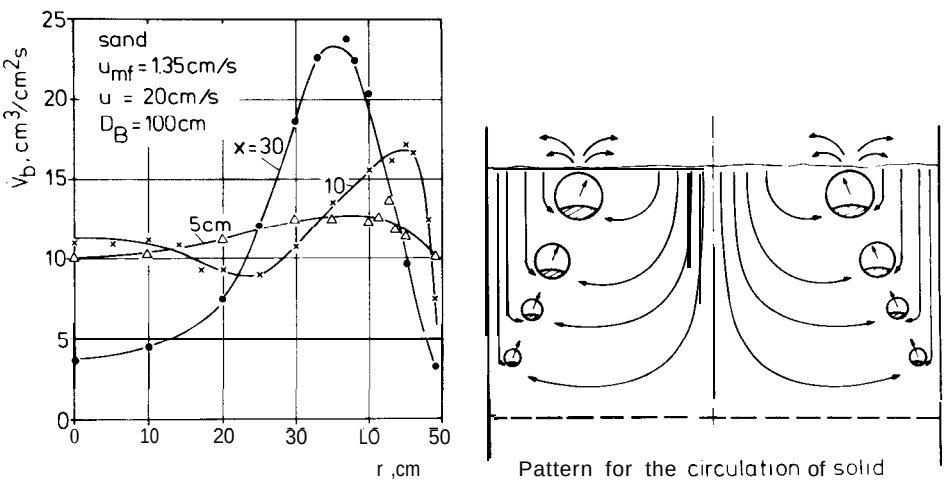

Figure 9 Spatial distribution of gas flow in the form of bubbles at different heights h above the distributor (left) and the associated pattern (right) for the circulation of solids. From Werther [15].

© 1983 Hemisphere Publishing Corporation

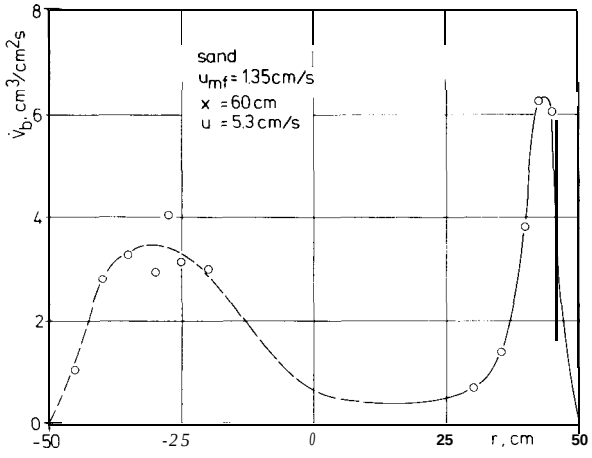

Figure 10 Measured irregularities in the flow distribution of gas transported in bubbles at a ratio of distributor pressure drop to bed pressure drop = 0.19 [15].

drop above a certain limit does not result in a further improvement in gas distribution, whereas below a certain minimum distributor pressure drop, distinct irregularities and instabilities in the flow distribution of gas transported in bubbles are observed (see Fig. 10). In general, minimum ratios of distributor pressure drop to bed pressure drop of between 0.1 and 0.4 are recommended [21-23], but Fig. 10 reveals that such recommendations should be treated with caution.

Investigations of Whitehead et al. [18] on a multituyere distributor indicate a dependence of the necessary minimum distributor pressure drop not only on the bed pressure drop, but also on the superficial gas velocity and on the pressure drop velocity characteristics of the distributor.

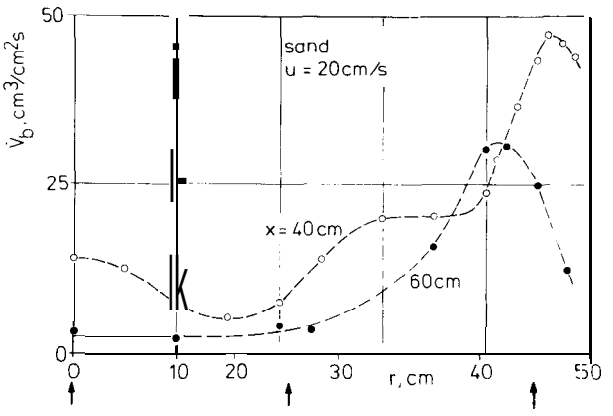

Figure 11 Influence of distributor design on the flow distribution of gas transported in bubbles [24].

Figure 11 shows the results of measurements of gas flow rates of gas transported in bubbles [24] at two different heights x above a multihole distributor. The arrows at the bottom of the figure indicate the position of three distributor holes in the vertical plane of the measurements. It is apparent that at a distance of x = 40 cm above the distributor, the influence of the location of the holes is discernible, whereas at a height of x = 60 cm the typically nonuniform distribution of flow rate of gas transported in bubbles as associated with porous plate distributors prevails (compare Fig. 9).

NOMENCLATURE FOR SECTION 2.2.6

Ar	Archimedes number [= $gd_p^3(\rho_S-\rho_F)/\nu^2\rho_F$]
C_D	coefficient of drag, defined by Eq. (4)
d_b	bubble diameter
d_p	particle diameter
$\overline{d_p}$	average particle diameter, defined by Eq. (2)
d_{pmax}	maximum particle diameter
d_{pmin}	minimum particle diameter
D_B	bed diameter
Fr	Froude number (= u^2/d_pg)
Fr_{mf}	Froude number at the point of minimum fluidization (= u_{mf}^2/d_pg)
g	gravitational acceleration
h	bed height
ho	fixed bed height
h_{mf}	bed height at minimum fluidization
Δp	pressure drop across the bed
q_3	mass distribution density for a particle size distribution
Qo	cumulative number of distribution curve of bubble diameters
r	radial distance from tube center
r_b	bubble radius
r_c	cloud radius
Re	Reynolds number (= ud_p/ν)
Re_{mf}	Reynolds number at the point of minimum fluidization (= $u_{mf}\overline{d_p}/\nu$)
u	superficial velocity
u_b	bubble rise velocity
u_{mf}	superficial velocity at the point of minimum fluidlzation
$\overline{V_b}$	average bubble volume
$\dot{V}_b$	flow rate of gas transported in bubbles
x	height above the distributor
ϵ	bed voidage
ϵ_{mf}	bed voidage at the point of minimum fluidization
ν	kinematic viscosity
ρ_F	fluid density
ρ_S	solid density
Φ_S	sphericity

© 1983 Hemisphere Publishing Corporation

REFERENCES FOR SECTION 2.2.6

1. Ergun, S., Fluid Flow through Packed Columns, *Ind. Eng. Chem.*, vol. 41, pp. 1179-1184, 1949.
2. Reh, L., Verbrennung in der Wirbelschicht, *Chem. Ing.* Tech., vol. 40, pp. 509-515, 1968.
3. Yerushahni, I., Turner, D. H., and Squires, A. M., The Fast Fluidized Bed, *Ind. Eng. Chem. Process Des. Dev.*, vol. 15, no. 1, pp. 47-53, 1976.
4. Wilhelm, R. H., and Kwauk, M., Fluidization of Solid Particles, ***Chem. Eng. Prog., vol. 44,*** pp. 201-218, 1948.
5. Geldart, D., Types of Gas Fluidization, ***Powder Technol.,*** vol. 7, pp. 285-292, 1973.
6. Novosad, J., Smid, V., and Smid, J., The Fluidization of Powders by Rotating Nozzles, ***Preprints European Congress Transfer Processes in Particle Systems, Nuremberg, 1977, vol.*** 1, pp. E2–E11, 1977.
7. Jackson, R., Fluid Mechanical Theory, in ***Fluidization,*** eds. J. F. Davidson and D. Harrison, pp. 65-119, Academic, London, 1971.
8. Rowe, P. N., Experimental Properties of Bubbles, ***in Fluidization***, eds. J. F. Davidson and D. Harrison, pp. 121-191, Academic, London, 1971.
9. Reuter, H., Druckverteilung urn Blasen im Gas-Feststoff-Fliessbett, ***Chem. Ing. Tech., vol. 3.5,*** pp. 98-103, 1963.
10. Davidson, J. F., Symp. Interaction between Fluids and Particles-Discussion, ***Trans. Inst. Chem. Eng.***, vol. 39, pp. 230-232, 1961.
11. Rowe, P. N., and Partridge, B. A., The Effect of Bubbles on Gas Solids Contacting in Fluidized-Beds, ***Chem. Eng. Prog. Symp. Ser.,*** vol. 58, no. 38, pp. 42-56, 1962.
12. Werther, J., and Molerus, O., The Local Structure of Gas Fluidized Beds, I. A Statistically Based Measuring System, *Int. J.* ***Multiphase Flow,*** vol. 1, pp. 103-122, 1973.
13. Werther, J., Die Bedeutung der Blasenkoaleszenz für die Auslegung von Gas-Feststoff-Wirbelschichten, *Chem. Ing.* ***Tech.,*** vol. 48, p. 339, MS 349/76, 1976.
14. Rowe, P. N., and Everett, D. J., Fluidized Bed Bubbles Viewed by X-Rays, Part III-Bubble Size and Number when Unrestrained Three-dimensional Growth Occurs, ***Trans. Inst. Chem. Eng.,*** vol. 50, pp. 55-60, 1972.
15. Werther, J., The Hydrodynamics of Fluidization in a Large Diameter Fluidized Bed, GVC/AIChE-Joint Meeting, München 1974, Preprints, vol. 3, E2–2, pp. 1-12, 1974.
16. Johnson, J. E., Bubble Distributions in Fluidized Beds, M. Eng. thesis, McGill University, Montreal, 1973.
17. Merry, J. M. D., and Davidson, J. F., Gulf Stream Circulation in Shallow Fluidized Beds, *Proc. Int. Symp.* ***Fluidization Its Application, Toulouse,*** 1973, pp. 196-206, Sté Chimie Industrielle, 1974.
18. Whitehead, A. D., Gartside, G., and Dent, D. C., Flow and Pressure Maldistribution at the Distributor Level of a Gas-Solid Fluidized Bed, ***Chem. Eng. J.***, vol. 1, pp. 175-185, 1970.
19. Knowlton, T. M., High Pressure Fluidization Characteristics of Several Particulate Solids Primarily Coal and Coal Derived Material, 67th Annual Meet. AIChE, Washington, D.C., Paper No. 9b,1.-5., December 1974.
20. Matsen, J. M., Evidence of Maximum Stable Bubble Size in a Fluidized Bed, *AIChE Symp.* ***Ser., vol. 69,*** no. 128, pp. 30-33, 1973.
21. Van Swaaij, W. P. M., and Zuiderweg, F. J., The Design of Gas-Solids Fluidized Beds-Prediction of Chemical Conversion, *Proc. Int. Symp.* ***Fluidization Its Applications, Toulouse, 1973,*** pp. 454-467, Sté Chimie Industrielle, 1974.
22. Zenz, F. A., and Othmer, D. F., ***Fluidization and Fluid Particle Systems,*** p. 260, Reinhold, New York, 1960.
23. Gregory, S. A., The Distribution Plate Problem, *Proc. Int.* ***Symp. Fluidization, Eindhoven,*** 1967, pp. 751-758, Netherlands University Press, 1967.
24. Werther, J., Der Einfluss des Anströmbodens auf die Strömungsmechanik von Gas-Feststoff-Wirbelschichten, ***Preprints European Congress Transfer Processes in Particle Systems, Nuremberg, 1977, vol.*** 1, pp. E32–E59, 1977.

© 1983 Hemisphere Publishing Corporation

2.2.7

Headers, nozzles, and turnarounds

J. A. R. Henry

A. Introduction

The prime purpose of nozzles, headers, and turnarounds is to distribute fluid through a heat exchanger matrix, as shown in Fig. 1 for a typical case.

The indirect purpose of these components, in common with the others making up the structure, is to contain the process fluids, which may be under high pressure. Hence, although their prime function is to direct and distribute flow, it is often found that their design is dictated by strength, cheapness, or ease of manufacture, rather than by considerations of fluid dynamics. In many instances this approach results in poor distribution of the fluid within the heat exchanger.

Poor distribution may or may not result in unsatisfactory performance, which in the past has usually been of secondary importance. However, with the increasing cost of energy and materials, it is desirable to utilize equipment to maximum efficiency during its lifetime. This requires a balanced performance, one aspect of which is achieving more uniform flow distribution. Associated with this is the need to predict pressure drop with some accuracy.

The prime purpose of a nozzle is to provide a connecting point between the heat exchanger shell and its supply pipework, both at inlet and outlet.

The inlet nozzle supplies process fluid to the inlet header, whence it is distributed to individual tubes comprising the tube bank. The inlet nozzle usually represents an expansion in the flow path and the dynamic head of the entering fluid tends to create a pressure gradient within the header box. This is, of course, strongly dependent on the position of the nozzle on the header box, as will be evident from Fig. 2; it might be expected that arrangement (a) would result in a different pressure profile across the face of the tube

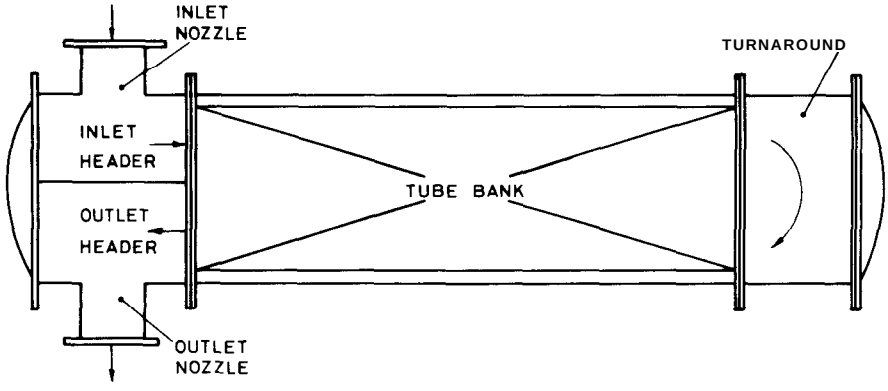

Figure 1 Definition of terms.

© 1983 Hemisphere Publishing Corporation

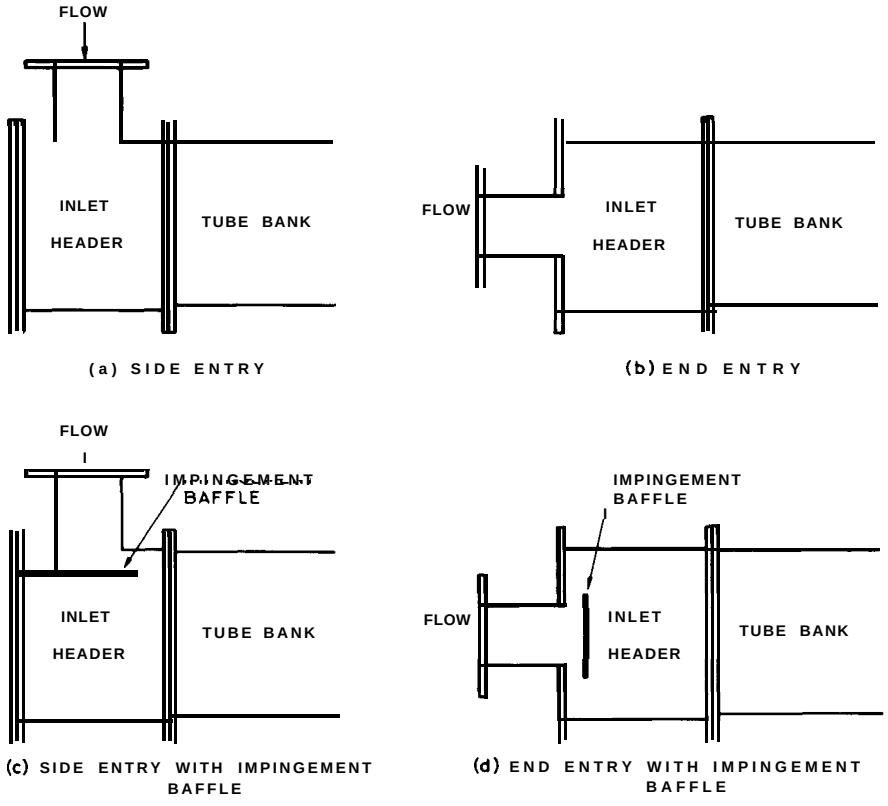

Figure 2 Inlet nozzle arrangements with and without impingement baffles.

plate than arrangement (b), and hence a different flow distribution. In arrangement (a), tubes at the bottom of the tube bank will tend to have greater flow through them than the tubes at the top; whereas in arrangement (b), tubes in the center of the tube bank will have greater flow than those at the periphery.

An outlet nozzle usually represents a contraction in the flow path. Its position in the outlet header also affects flow distribution by imposing a specific pressure distribution across the outlet header of the tube bank.

It is difficult to divorce the design of these components from one another. Hence the behavior of the combination of them must be considered.

Tolerable distribution can always be attained in single-phase flow by the simple expedient of increasing the overall system pressure drop by throttling at a suitable point in the flow path. This represents increased running costs, and possibly increased capital cost, because of the increased pumping power required. Good distribution could also be achieved by experimentation-for instance, flow visualization tests-but there are so many possible configurations that each case would probably have to be considered in isolation. It is therefore the decision of the design engineer to assess how important it is that good distribution be obtained and to decide what further steps would be reasonable to achieve it.

The cause of flow maldistribution is contained in the momentum and frictional forces acting on the flow. Hence some indication of a satisfactory solution can be obtained by considering these equations. Some sources of pressure loss will therefore be considered.

B. Nozzles

(a) Inlet nozzle pressure change

The pressure drop at the inlet nozzle is usually a relatively small part of the total heat exchanger pressure loss and is normally assumed to be due to a sudden expansion from the nozzle flow area S_n to the appropriate downstream area S_D. The change in static pressure caused by the change of section has two components, the first owing to irreversibilities and the second to the change in velocity. These are, respectively,

$$\frac{p_n - p_D}{\rho} = \left[K_e + \left(\frac{S_n}{S_D}\right)^2 - 1\right]\frac{v_n^2}{2} \tag{1}$$

For fully developed turbulent flow in the nozzle, Re, > 4 000, the irreversibility coefficient K_e is given by the Borda-Carnot equation

$$K_e = \left(1 - \frac{S_n}{S_D}\right)^2 \tag{2}$$

© 1983 Hemisphere Publishing Corporation

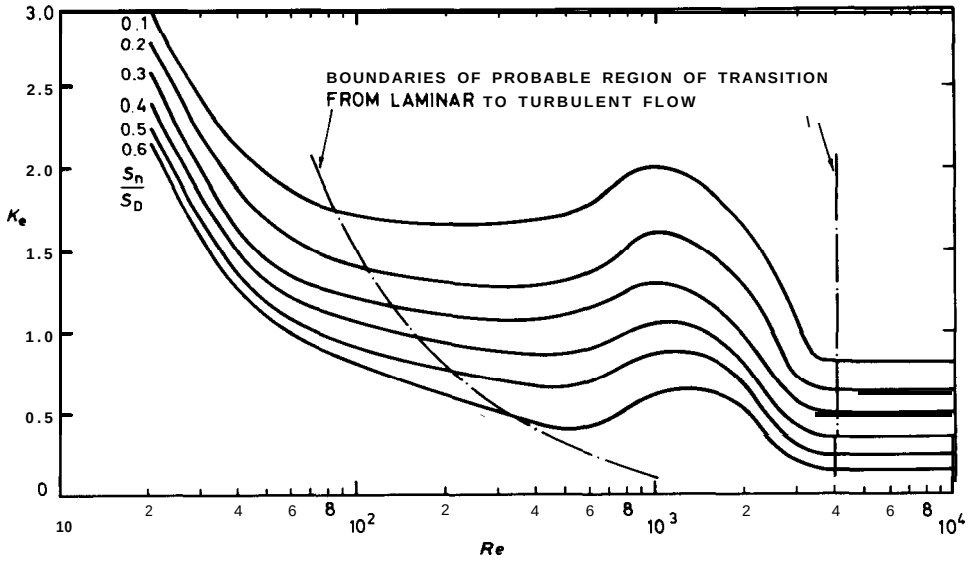

Figure 3 Energy loss coefficient for a sudden expansion. From ESDU [1].

When the nozzle area is small compared with the downstream area, that is, $S_n/S_D \approx 0$, it can be seen that Eq. (2) indicates that the change in specific energy amounts to one nozzle velocity head, that is, $\frac{1}{2}v_n^2$. When flow through the nozzle is not turbulent, Re < 4 000, K_e is given by Fig. 3 [1].

(b) Outlet nozzle pressure change

The pressure drop at the outlet nozzle is normally calculated on the assumption of a sudden contraction from flow area S_U to nozzle area S_n, and the static pressure difference is given by

$$\frac{p_U - p_n}{\rho} = \left[1 - \left(\frac{S_n}{S_U}\right)^2 + \lambda K_C\right] \frac{v_n^2}{2} \tag{3}$$

the coefficient K_C being given by Figs. 4 and 5 [2]

The energy loss associated with a sudden contraction is strongly affected by the radius of curvature of the contraction edge. This can be tentatively taken into account using the factor λ, which is presented in Fig. ***5b*** [2]. Little research has been carried out on

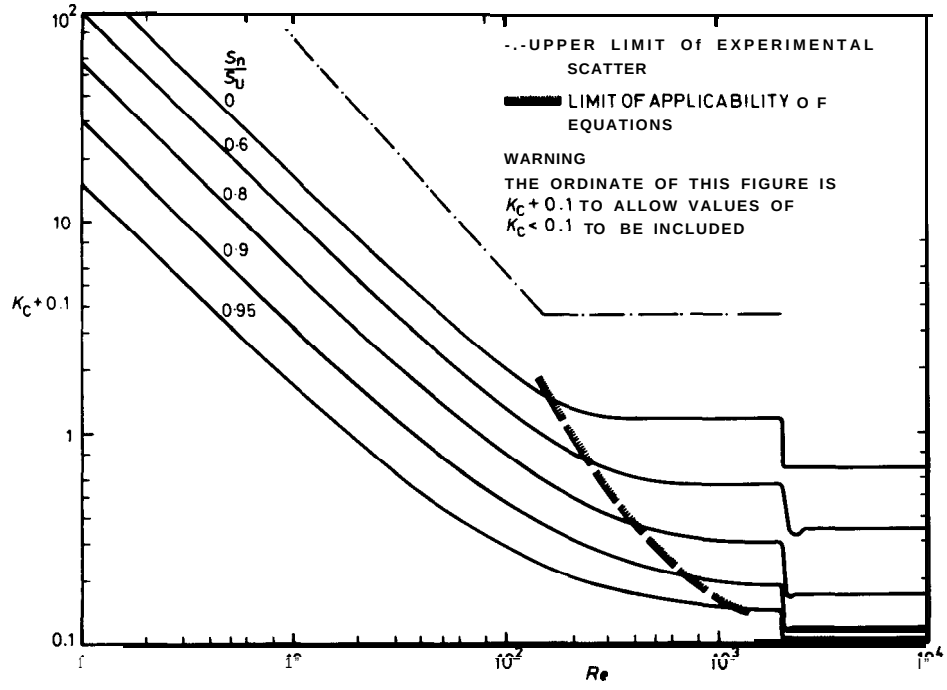

Figure 4 Energy loss coefficient for a sudden contraction for Re < 10^4 (incompressible flow). From ESDU [2].

© 1983 Hemisphere Publishing Corporation

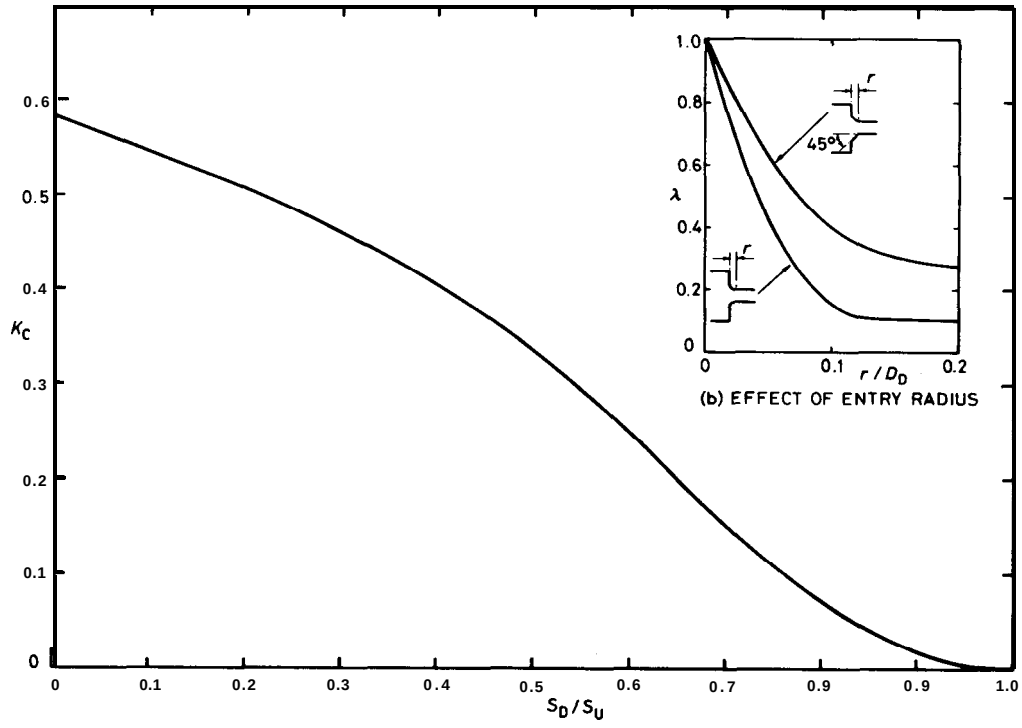

(b) EFFECT OF ENTRY RADIUS

(a) LOSS COEFFICIENT FOR INCOMPRESSIBLE FLOW

Figure 5 Energy loss coefficient for a sudden contraction for Re $\geq 10^4$ (incompressible flow). From ESDU [2].

this aspect of heat exchanger design. One of the few papers that deals with this subject in passing is that of lshigai and Nishikawa [3], who recommend that the ***sum*** of the inlet and outlet nozzle energy losses can be calculated from

$$\frac{\Delta p}{\rho} = 1.5\,\frac{v_n^2}{2} \tag{4}$$

This compares fairly well with the values given by Eqs. (1) and (3) for the case Re, > 4 000 and

$$\frac{S_n}{S_D} = 0 \qquad \frac{S_n}{S_U} = 0$$

That is,

$$\frac{\Delta p}{\rho} = 1.58\,v_n^2 \tag{5}$$

(c) Effect of impingement plate

There are occasions when it is necessary to fit an impingement plate to the inlet nozzle. The purpose of the impingement plate is to protect the tubes directly in line with the inlet nozzle from the abrading effects of the jet of fluid.

An impingement plate is normally fitted when the value of ρv^2 exceeds the following [4]:

Noncorrosive, nonabrasive, single-phase fluids: ***2 235*** N/m^2

All other liquids, including a liquid at its boiling point: 745 N/m^2.

For all other gases and vapors and two-phase mixtures, impingement protection is required regardless of the value of ρv^2.

The impingement plate is normally positioned not less than $D_n/4$ below the lower tip of the nozzle, as shown in Fig. 6, which means that there is no change in flow area caused by the impingement plate. Under such circumstances the static pressure change is given approximately by the normal equation for a square right-angled bend:

$$\frac{p_n - p_D}{\rho} = \left[\left(\frac{S_n}{S_D}\right)^2 + 0.3\right]\frac{v_n^2}{2} \tag{6}$$

In the absence of an impingement plate, the inlet nozzle will discharge directly into the tube bank. The pressure drop in this case is not well defined owing to the complex flow field downstream, but to some extent may be allowed for by basing the downstream velocity on the flow area between the tubes.

Although the prime purpose of an impingement plate on the shell side of a heat exchanger is to protect the neighboring tubes from erosion, it is also often used in the tube-side inlet header as shown in Figs. 2*c* and 2*d* to dissipate the kinetic head of the entering

© 1983 Hemisphere 1 blishing Corporation

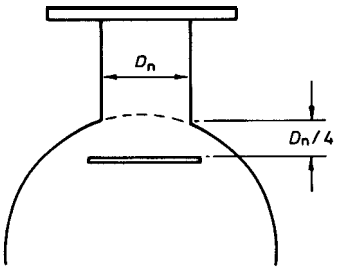

Figure 6 Position of impingement plate.

fluid stream and so promote a more uniform pressure distribution within the inlet header. As will be seen in a later section, this can greatly improve the distribution of fluid through individual tubes.

C. Headers

The function of a header is to distribute fluid to a number of closely spaced tubes such as in a tube bank, and also to recombine the flow from a number of tubes into one stream, as at exit from the tube bank, as shown in Fig. 1. Normally the ideal is to ensure that every tube has the same flow rate and, under most circumstances, ±5% of the mean flow would be regarded as uniform distribution. Some consequences of maldistribution are considered by Mueller [5]

Unless the flow is one-dimensional, designing a header from theory is not straightforward, and it is more usual to resort to experiment to obtain a design with the desired characteristics. In most cases the flow field is three-dimensional and must be solved by computer. Up till now this has not been reported in the literature in the context of heat exchanger headers.

To some extent it is possible to quantify the potential for the maldistribution of flow within a tube bank by relating it to the overall pressure drop across the tube bank and the dynamic head of the fluid at entry to the header. Hence,

$$\frac{\text{Maximum velocity through a tube}}{\text{Mean velocity through a tube}} = \sqrt{\frac{\Delta p_T + (\frac{1}{2}\rho v^2)_{in}}{\Delta p_T}} \tag{7}$$

This shows that distribution can be improved in two ways :

1. By increasing the overall pressure drop until it is large compared with the inlet dynamic head, that is,

$$\Delta p_T \gg (\tfrac{1}{2}\rho v^2)_{in}$$

2. By ensuring that the inlet dynamic head is small by suitable sizing of the header

Unfortunately, these obvious steps are not always acceptable because of the higher pumping power in the first case and to the large physical size of the header resulting in the second. If flow maldistribution must not exceed ±5% of the mean flow rate, then Eq. (7) shows that the inlet dynamic head should not be greater than 10% of the overall pressure drop [6].

In general, the variation in pressure over the face of the inlet tube plate will be less than the inlet dynamic head and can be reduced still further by taking suitable steps to dissipate the dynamic head before the tube plate is encountered. An impingement baffle as shown in Figs. 2*c* and 2*d* is one way of achieving this.

For cases in which the flow can be considered one-dimensional, a more theoretical analysis is possible, provided that certain, largely empirical quantities are known. Very little such data have been published in the open literature.

When flow encounters a branch, there are two pressure changes that have to be taken into account: that of the main stream, and that of the branch flow.

(a) Inlet distribution header

An inlet header distributes flow to a number of branches as shown in Fig. 7. In this case the main flow suffers a deceleration as part of it divides to flow through the branch pipe.

Applying the energy equation across the junction control volume gives [7]

$$\frac{p_D - p_U}{\frac{1}{2}\rho v_U^2} = 1 - \left(\frac{v_D}{v_U}\right)^2 - \frac{E_f}{\frac{1}{2}v_U^2} = K_{MD} \tag{8}$$

The pressure change across the junction in the direction of the main flow can be related to the upstream velocity by the constant K_{MD}. As shown in Fig. 8, this is a function of the fraction of the total flow that leaves through the branch and also the ratio of the branch diameter to the main header diameter. The solid lines on Fig. 8 agree well with the data of McNown [7] and of Rouse [8]. The data points have been omitted for clarity.

The part of the flow that enters the branch also undergoes a pressure change, which can be related to the flow velocity in the main header by the constant K_{SD} as follows:

$$\frac{p_U - p_B}{\frac{1}{2}\rho v_U^2} + 1 - \left(\frac{S_U}{S_B}\right)^2 = K_{SD} \tag{9}$$

Values of K_{SD} are given in Fig. 9.

© 1983 Hemisphere Publishing Corporation

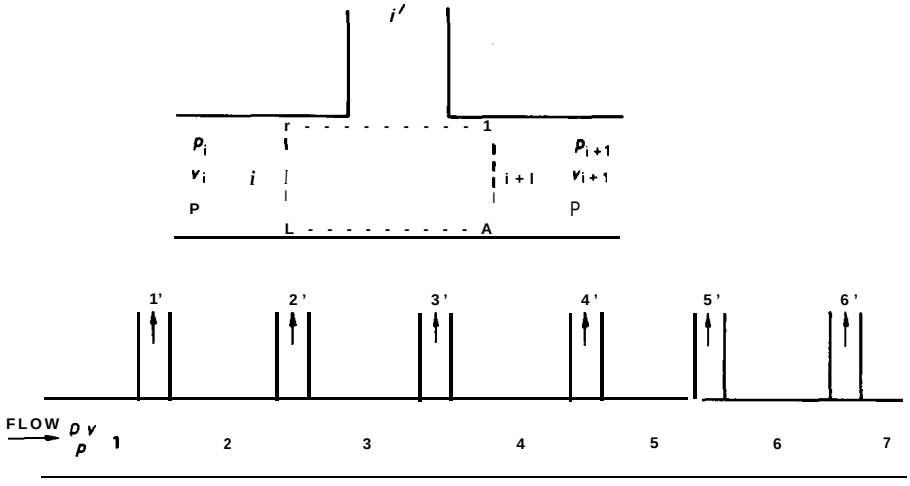

Figure 7 One-dimensional dividing header.

(b) Outlet (combining) header

An outlet header takes the flow from several branches and combines them as shown in Fig. 10. In this case the main flow is accelerated as the branch flow joins it; the resulting pressure change can be calculated from the energy equation

$$\frac{p_U - p_D}{\frac{1}{2}\rho v_D^2} = 1 - \left(\frac{v_U}{v_D}\right)^2 + \frac{E_f}{\frac{1}{2}v_D^2} = K_{MC} \tag{10}$$

The momentum coefficient for combining flow, K_{MC}, is given in Fig. 11 and is once again a function of $\dot{M}_B/\dot{M}_D$ and the diameter ratio ***d/D.***

The side-stream loss coefficient for combining flow is defined as

$$\frac{p_B - p_D}{\frac{1}{2}\rho v_D^2} - 1 + \frac{S_D}{0S_B}^2 = K_{SC} \tag{11}$$

Values of K_{SC} can be represented by the curves given in Fig. 12.

(c) One-dimensional continuously dividing header

For the case in which the removal of fluid from a constant-diameter header is continuous (or can be regarded as continuous), the equations governing flow within the header can be written in differential form [9] as

$$\frac{d^2V}{dZ^2}\frac{dV}{dZ} + V\frac{dV}{dZ} + FV^{7/4} = 0 \tag{12}$$

where V is the ratio of the local axial velocity to the header inlet velocity, and Z is a dimensionless distance along the header.

$$Z \equiv \frac{4\alpha C}{D}\sqrt{(2K_{MD})X} \tag{13}$$

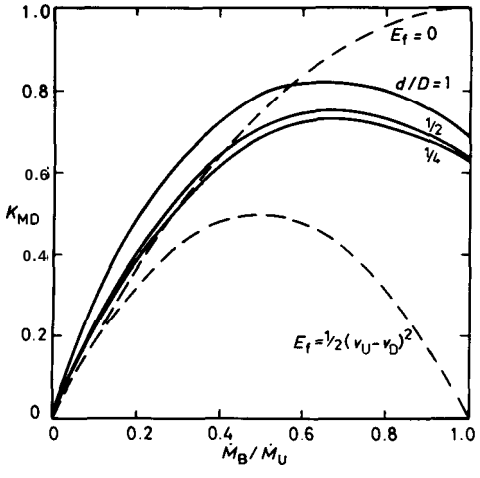

Figure 8 Momentum coefficient for dividing flow.

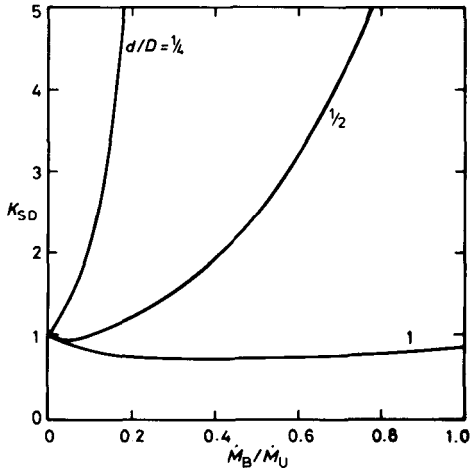

Figure 9 Branch loss coefficient for dividing flow.

© 1983 Hemisphere Publishing Corporation

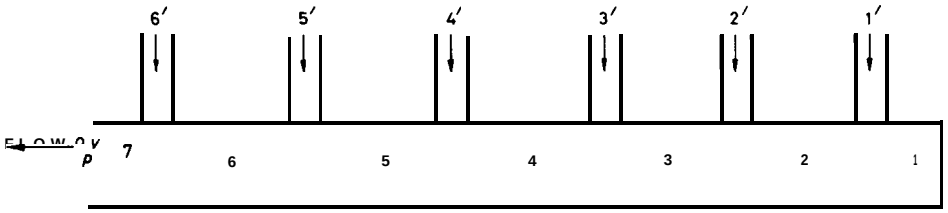

Figure 10 One-dimensional combining header.

and

$$F \equiv \frac{f_1}{\sqrt{(2^5 K_{MD}^3)\alpha C}} \tag{14}$$

The boundary conditions for solving Eq. (12) are that at Z = 0 (that is, X = 0, inlet of manifold),

$$\text{v= } 1 \qquad \frac{dV}{dZ} = -M \tag{15}$$

The parameter ***M*** relates the pressure difference causing branch flow at the start of the header to the fluid momentum (along the header axis) at that position, and is defined as

$$M = \sqrt{\frac{\Delta p_B}{K_{MD}\rho v_D^2}} \tag{16}$$

Equation (12) can be solved for various values of M and ***F.*** Typical variation of branch flow along the header axial direction is shown in Fig. 13. The range of side flow is shown in Fig. 14. It is apparent that approximately uniform flow division can be attained by choosing the value of the inlet condition parameters ***F*** and ***M.*** In all cases, however, the distribution is best when M is large, which has already been noticed from Eq. (7), this being the condition in which the branching flow pressure drop is large in comparison to the dynamic head at inlet to the distributing device.

For the case of a combining header as shown in Fig. 10, Eq. (12) can be rewritten [9] as

$$\frac{d^2V}{dZ^2}\frac{dV}{dZ} - V\frac{dV}{dZ} + FV^{7/4} = 0 \tag{17}$$

This equation, together with Eqs. (13)-(16), can be solved numerically as before; the result is shown in Fig. 1.5.

In a combining manifold the friction and momentum forces act in the same direction, and this is reflected in that the solution no longer displays a turning point as it did in the case of the dividing manifold. For a given pair of ***M*** and ***F*** values, Fig. 13 shows that the maldistribution is worse in the case of the combining manifold, all other parameters being equal. Hence, for similar flow distribution to a dividing manifold to be achieved, a combining manifold would need to be larger in cross-sectional area.

(d) Calculation of tube entry pressure loss

Tube entry pressure loss can usually be adequately calculated from the equation for a sudden contraction, that is, from Eq. (3),

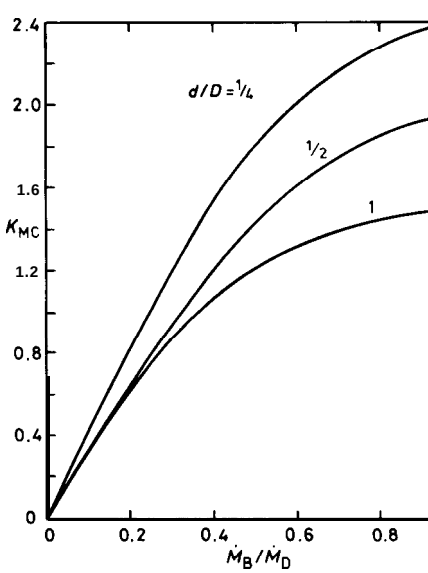

Figure 11 Momentum coefficient for combining flow.

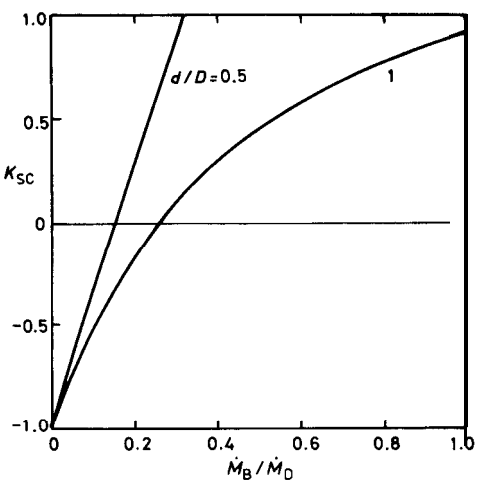

Figure 12 Branch loss coefficient for combining flow.

© 1983 Hemisphere Publishing Corporation

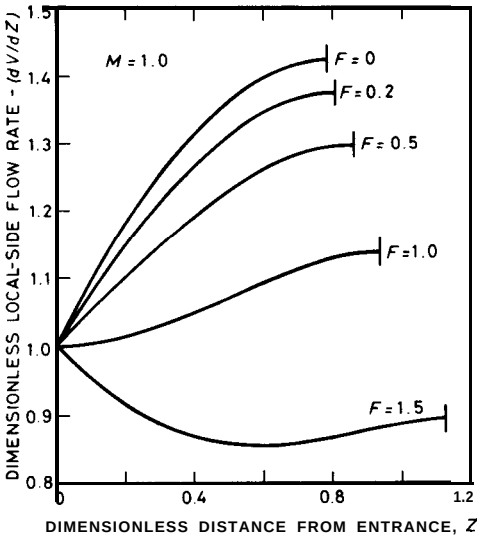

Figure 13 Variation of local flow rate with position (dividing flow).

$$\frac{p_U - p_D}{P} = \left[\lambda K_C + 1 - \left(\frac{S_D}{S_U}\right)^2\right]\frac{v^2}{2}$$

in which v is the mean tube velocity. The coefficient K_C is given by Figs. 4 and 5, depending on the value of the tube Reynolds number. The downstream/upstream area ratio can be evaluated from

For triangular tube pitch: $$\frac{S_D}{S_U} = 0.907\left(\frac{d}{P}\right)^2 \qquad (18)$$

For square tube pitch: $$\frac{S_D}{S_U} = 0.785\left(\frac{d}{P}\right)^2$$

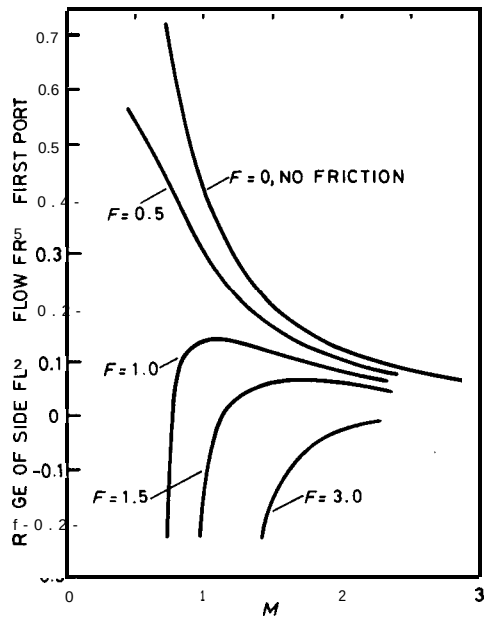

Figure 14 Range of flow rate as a function of position (dividing flow).

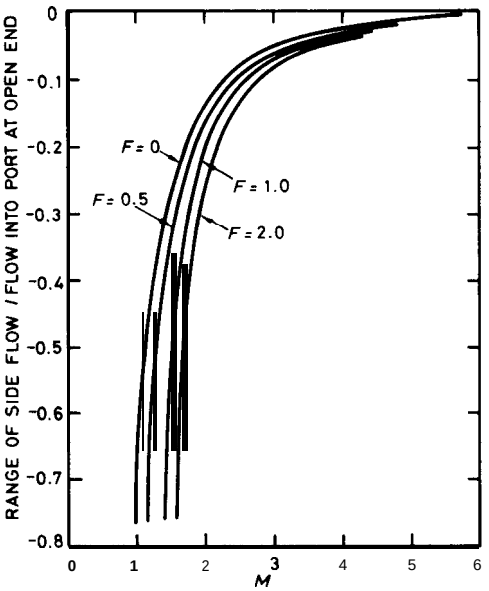

Figure **15** Range of flow rate as a function of position (combining flow).

The pressure loss at entry to the tube bank is rarely controlling, but if it is then it will also be necessary to include the effect of the constant λ, which makes allowance for the radius of curvature at entry to a tube.

(e) Calculation of tube exit pressure loss

Flow leaving a tube to enter the downstream header undergoes a sudden expansion, and the pressure loss can be well calculated by Eq. (1).

$$\frac{p_U - p_D}{P} = \left[K_e + \left(\frac{S_U}{S_D}\right)^2 - 1\right]\frac{v_U^2}{2} \qquad (19)$$

in which v is the mean tube velocity and the expansion coefficient K_e is given by Fig. 3, in which the ratio of upstream/downstream flow area ratio is given by

For triangular tube pitch: $$\frac{S_U}{S_D} = 0.907\left(\frac{d}{P}\right)^2 \qquad (20)$$

For square tube pitch: $$\frac{S_U}{S_D} = 0.785\left(\frac{d}{P}\right)^2$$

When these equations are applied to tube entrance and exit losses it is, of course, implied that all tubes behave in a similar manner, that is, that there is ideal flow distribution.

D. Turnarounds

It is normal practice for each pass of a multiple-pass heat exchanger to contain approximately the same number of tubes. The turnaround receives the flow

© 1983 Hemisphere Publishing Corporation

from a pass of the heat exchanger and distributes it to the next pass. The turnaround therefore represents an even more complex flow situation than either the inlet or outlet header, since it combines both functions, and it is unlikely that the flow can be considered to be one- or even two-dimensional.

The entry and exit pressure loss can be calculated as described above in Secs. C(d) and C(e). As well as these losses, the flow direction is being changed through 180° in a rather complex manner. There appears to be no experimental information in the literature covering this specific problem, and it seems reasonable that 1.5 velocity heads be allowed (based on the tube velocity); this is equivalent to a 180 bend.

The effect of the turnaround on flow distribution is also difficult to quantify in the absence of experimental data. It seems unlikely, however, that it will be greater than that of the entry header, and hence the same criteria should apply. Steps should therefore be taken to ensure that the dynamic head within the turnaround is small compared with the pressure drop through the pass downstream of it. The extent to which this can be carried out, however, depends on the overall pressure drop that can be tolerated.

E. Example

Some of the foregoing can be illustrated by an example.

(a) Example

Calculate the pressure drop and possible maldistribution that will occur in a heat exchanger as follows:

Header inside diameter = 400 mm
Tube length = 1 500 mm
Header depth = 300 mm
Inlet and outlet nozzle diameter = 100 mm

The shell contains 150 tubes in a single pass and the tubes are 17 mm in inside diameter and are on a pitch/diameter ratio of 1.25. Liquid of density 1 000 kg/m^3 and viscosity 1 cP flows through the tubes at a rate of 25 kg/s.

Nozzle flow area $S_n = \frac{\pi}{4} 0.1^2 = 0.007\ 85\ \text{m}^2$

Nozzle velocity $v_n = \frac{25}{1000 \times 0.007\ 85} = 3.18$ m/s

(b) Inlet nozzle pressure drop

From Eq. (1),

$$\frac{p_n - p_D}{\rho} = \left[K_e + \left(\frac{S_n}{S_D}\right)^2 - 1\right]\frac{v_n^2}{2}$$

The nozzle Reynolds number

$$\text{Re}_n = \frac{\rho v_n d}{\mu} = \frac{1\ 000 \times 3.18 \times 0.1}{0.001} = 3.18 \times 10^5$$

The coefficient K_e can therefore be calculated from Eq. (2):

$$K_e = \left(1 - \frac{S_n}{S_D}\right)^2 = 0.87$$

Hence

$$p_n - p_D = \left[0.87 + \left(\frac{0.007\ 85}{0.12}\right)^2 - 1\right]\frac{3.18^2}{2} \times 1\ 000$$

$$= -633\ \text{N/m}^2$$

That is the pressure increases owing to momentum effects.

(c) Outlet nozzle pressure drop

From Eq. (3),

$$\frac{p_U - p_n}{\rho} = \left[1 - \left(\frac{S_n}{S_U}\right)^2 + \lambda K_C\right]\frac{v_n^2}{2}$$

Again the Reynolds number is 3.18 X 10^5, hence K_C may be obtained from Fig. 5 for

$$\frac{S_n}{S_U} = \frac{0.007\ 85}{0.12} = 0.065\ 5$$

and is

$K_C = 0.56$

It is assumed that the nozzle edge is sharp, therefore $\lambda = 1$.

$$p_U - p_n = [1 - (0.065\ 5)^2 + 0.56]\frac{3.18^2}{2} \times 1\ 000$$

$$= 7\ 866\ \text{N/m}^2$$

(d) Mean flow through tubes

Total flow area $S_T = 150\frac{\pi}{4}(0.017)^2 = 0.034\ \text{m}^2$

Mean velocity $\bar{v} = \frac{25}{1\ 000 \times 0.034} = 0.73$ m/s

Hence the Reynolds number

$$\text{Re} = \frac{1\ 000 \times 0.73 \times 0.017}{0.001} = 12\ 410$$

© 1983 Hemisphere Publishing Corporation

(e) Tube entry pressure change

Regarding as a sudden contraction, use Eq. (3).

$$\frac{p_U - p_D}{\rho} = \left[1 - \left(\frac{S_D}{S_U}\right)^2 + \lambda K_C\right]\frac{v_n^2}{2}$$

From Eq. (18),

$$\frac{S_D}{S_U} = 0.907\left(\frac{d}{P}\right)^2$$

that is,

$$\frac{S_D}{S_U} = 0.907\left(\frac{1}{1.25}\right)^2 = 0.58$$

Hence, from Fig. 5,

$$K_C = 0.275$$

and

$$p_U - p_D = (0.275 + 1 - 0.58^2)\frac{0.73^2}{2} \times 1\,000$$

$$= 250 \text{ N/m}^2$$

(f) Tube exit pressure change

Since Re > 10^4, Eq.(2) may be used.

$$K_e = \left(1 - \frac{S_U}{S_D}\right)^2 = (1 - 0.58)^2 = 0.176$$

The pressure change may be calculated from Eq. (1).

$$p_U - p_D = \left[K_C + \left(\frac{S_U}{S_D}\right)^2 - 1\right]\frac{v_U^2}{2}$$

$$= (0.176 + 0.58^2 - 1\text{ j}\frac{0.73^2}{2} = -130 \text{ N/m}^2$$

The tube pressure drop may be calculated from the Darcy equation

$$\Delta p = \frac{4flv^2\rho}{2d}$$

where the friction factor

$$f = \frac{0.046}{\text{Re}^{0.2}} = \frac{0.046}{12\,410^{0.2}} = 0.007$$

$$\Delta p = \frac{4 \times 0.007 \times 1.5 \times 0.73^2 \times 1000}{2 \times 0.017} = 658 \text{ N/m}^2$$

Hence the total pressure drop is

$$\Delta p_T = -633 + 7\,866 + 250 - 130 + 658$$

$$-8\,011 \text{ N/m}^2$$

The possible level of maldistribution may be evaluated from Eq. (7).

$$\frac{\text{Maximum velocity}}{\text{Mean velocity}} = \sqrt{\frac{\Delta p_T + \frac{1}{2}\rho v_n^2}{\Delta p_T}}$$

$$= \sqrt{\frac{8\,011 + \frac{1}{2}8011 \times 1\,000(3.18)^2}{8\,011}}$$

$$= 1.28$$

Hence there is a possibility that the flow through some tubes is 28% greater than the ideal, other tubes taking correspondingly less.

NOMENCLATURE FOR SECTION 2.2.7

C	contraction coefficient
D	header diameter or equivalent diameter, m
d	branch diameter, m
E_f	specific energy loss due to viscous dissipation, J/kg
F	defined by Eq. (14)
f_1	fanning friction factor
K	loss coefficient
M	defined by Eq. (16)
$\dot{M}$	mass flow rate, kg/s
P	pitch [Eqs. (18) and (20)], m
p	pressure, N/m^2
Δp	pressure difference, N/m^2
Re	Reynolds number
S	flow area, m^2
V	dimensionless velocity
v	velocity, m/s
X	distance along flow path, m
Z	dimensionless distance [Eq. (13)]
α	fraction of internal area of header occupied by branches, assumed uniformly spaced
ρ	density, kg/m^3
λ	correction factor for entry radius

Subscripts

B	branch
c	contraction; combining
D	downstream of junction

© 1983 Hemisphere Publishing Corporation

e	expansion	S	sidestream
M	momentum	***T***	total
n	nozzle	***U***	upstream

REFERENCES FOR SECTION 2.2.7

1. ESDU, Flow through a Sudden Enlargement of Area in a Duct, in ***Fluid Mechanics, Internal Flow,*** vol. 4, Engineering Sciences Data Unit, Item 72011, London, 1972.
2. ESDU, Pressure Losses in Flow through a Sudden Contraction of Duct Area, in ***Fluid Mechanics, Infernal Flow,*** vol. 4, Engineering Sciences Data Unit, Item 78007, London, 1977.
3. Ishigai, S., and Nishikawa, Y., Shell-Side Pressure Drop in Multi-baffled Shell-and-Tube Heat Exchangers, ***Bull. JSME,*** vol. 8, pp. 644-651, 1965.
4. ***Standards of Tubular Exchanger Manufacturers Association,*** TEMA, New York, 1978, 6th Edition.
5. Mueller, A. C., An Enquiry of Selected Topics on Heat Exchanger Design, 16th National Heat Transfer Conf., St. Louis, ***Can. Soc. Chem. Eng./Can Soc. Mech. Eng., 1976.***
6. Senecal, V. E., Fluid Distribution in Process Equipment, ***Ind. Eng. Chem.***, vol. 49, no. 6, pp. 993-997, 1957.
7. McNown, J. S., Mechanics of Manifold Flow, ***Trans. Am. Soc. Civil Eng.,*** vol. 79, no. 258, 1953.
8. Rouse, H., ***Engineering Hydraulics,*** p. ***437,*** Wiley, New York, 1950.
9. Acrivos, A., Babcock, B. D., and Pigford, R. L., Flow Distribution in Manifolds, ***Chem. Eng. Sci.,*** vol. 10, pp. 112-124, 1959.

© 1983 Hemisphere Publishing Corporation

2.2.8

Non-Newtonian fluids

Robert C. Armstrong

A. Introduction

Many fluids do not obey Newton s law of viscosity; these materials are commonly grouped together under the broad heading of non-Newtonian fluids. Examples of non-Newtonian fluids include polymer solutions and melts, paints, soaps, biological fluids, greases, pastes, and suspensions. The field of study that is aimed at understanding the deformation and flow behavior of these substances is known as rheology. Because they make up the most commonly encountered subgroup of non-Newtonian materials, polymers will be emphasized in this section.

There are many simple experiments that can serve to illustrate the often dramatic differences in behavior between Newtonian and non-Newtonian fluids. If, for example, the viscosity of a polymer solution were determined in a falling-ball viscometer and in a tube flow experiment, different results might be obtained. If a rotating shaft is inserted into a beaker of polymeric fluid, the polymer climbs the rod. Polymer extruded through a circular orifice may swell to a diameter several times that of the hole. If a filament of molten polymer is suddenly stretched and then released, it will snap back nearly to its original length [1].

Because of the very high viscosities exhibited by most concentrated polymer solutions and melts, the flow of these fluids is laminar in most applications, and laminar flow will be the primary focus of this section. In Sec. B, experimental methods for characterizing non-Newtonian fluids are described. Section C then presents models for describing these properties, and Sec. D gives examples to illustrate the calculation of quantities of engineering importance. In Sec. E, turbulent tube flow of non-Newtonian fluids is discussed.

B. Experimental characterization of non-Newtonian fluids

Most currently used experimental methods for characterization of non-Newtonian fluids involve measurement of the stress/rate-of-strain behavior of the material in either a shear flow or a shear-free flow. Shear flow is found in pipe flow, flow through slits, and flow in runners and mold cavities. Approximations to shear-free flows are found in stagnation flow, fiber spinning, blow molding, vacuum forming, and film blowing.

(a) Shear flow

As an example of shearing flow, consider the velocity field (see Fig. 1)

$$v_x = \dot{\gamma} y \qquad v_y = 0 \qquad v_z = 0 \tag{1}$$

which can be generated in a fluid contained between parallel plates that are made to undergo a relative sliding motion. The velocity gradient $\dot{\gamma}$ is known as the ***shear rate;*** when $\dot{\gamma}$ is constant, the flow is steady shear or viscometric flow.

In the time interval between t' and t, the cube in Fig. ***la*** is sheared by an amount $(t - t')\dot{\gamma}$, but the lengths of the edges of the cube along x and z do not change. There is no shear present in Fig. lb, and in the interval $(t - t')$ the length of the cube in the direction

© 1983 Hemisphere Publishing Corporation

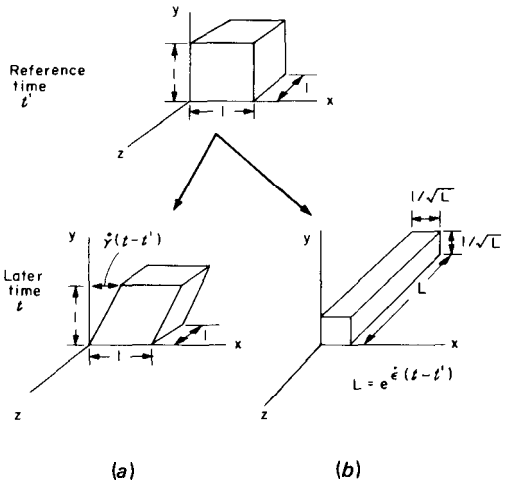

Figure 1 Deformation of an isolated unit cube of fluid undergoing (a) steady shear flow with shear rate $\dot{\gamma}$ and (b) steady elongational flow with elongation rate $\dot{\epsilon}$ (see text).

of stretching increases by a factor $e^{\dot{\epsilon}(t-t')}$. The volume is unchanged in either flow.

For a fluid undergoing shear flow, it can be shown that the only stresses that can be nonzero are the shearing stress $T_{yx} = \tau$ and the three normal stresses T_{xx}, T_{yy}, and T_{zz}. Here the T_{ij} are components of the extra stress tensor and are defined to be positive when a fluid element is in tension. If the fluid is incompressible (a good assumption for most non-Newtonian flow problems), it is not possible to measure normal stress components individually; instead, normal stress differences can be found. It is customary to use for these differences $T_{xx} - T_{yy} = N_1$ and $T_{yy} - T_{zz} = N_2$, known as the primary (first) and secondary (second) normal stress differences, respectively. The steady shear flow behavior of non-Newtonian fluids can thus be reported in terms of three stress coefficients η, Ψ_1, and Ψ_2, defined by

$$\tau = \eta(\dot{\gamma})\dot{\gamma} \tag{2}$$

$$N_1 = \Psi_1(\dot{\gamma})\dot{\gamma}^2 \tag{3}$$

$$N_2 = \Psi_2(\dot{\gamma})\dot{\gamma}^2 \tag{4}$$

In these equations, η is the (non-Newtonian) viscosity, and Ψ_1 and Ψ_2 are the first and second normal stress coefficients, respectively. Note that for a Newtonian fluid in steady shear flow, η is the constant viscosity μ, and Ψ_1 and Ψ_2 are both zero. For most non-Newtonian fluids η, Ψ_1 and Ψ_2 depend on the shear rate $\dot{\gamma}$.

In Fig. 2 results are shown for $\eta(\dot{\gamma})$ for two polymer solutions and a soap solution; these data are typical of the behavior shown by a wide variety of non-Newtonian fluids. At low shear rates it is seen that the viscosity approaches a constant value η_0 known as the zero-shear-rate viscosity. As the shear rate is increased, the viscosity shows a dramatic decrease; η can decrease by three or four orders of magnitude with increasing shear rate. In the region of steepest descent, log η is a linear function of log $\dot{\gamma}$, and this range of shear rates is often called the *power law* region. This is a particularly important zone because the shear rates in many applications fall into this region.

Materials that show this decreasing viscosity are called shear-thinning or pseudoplastic. A few fluids exhibit the opposite behavior, with η increasing with increasing $\dot{\gamma}$; such fluids are called shear-thickening or dilatant. This behavior is exhibited by fairly concentrated suspensions of very small particles, two examples being titanium oxide in a sucrose solution and corn starch in an ethylene glycol/water mixture.

In Fig. 3 the first normal stress coefficient Ψ_1 is shown for the same solutions as in Fig. 2. At low shear rates, Ψ_1 also approaches a limiting value $\Psi_{1,0}$; and at high shear rates it shows a power law region. Most often, the rate of decline of Ψ_1 with $\dot{\gamma}$ is greater than that of η with $\dot{\gamma}$. Moreover, Ψ_1 can decrease by as much as a factor of 10^6 in the power law region.

The second normal stress coefficient is much more difficult to measure than η or Ψ_1, and consequently much less is known about it. Available data on polymer solutions suggest that its magnitude is roughly 10% of Ψ_1 and it is opposite in sign. For most engineering applications. it is probably safe to ignore Ψ_2; however, the second normal stress difference may be important in hydrodynamic stability problems and in calculating secondary flows.

In addition to steady shear flow, a wide variety of nonsteady shear flow experiments can be performed. A sampling of these is given in Table 1, where $\dot{\gamma}(t)$ is

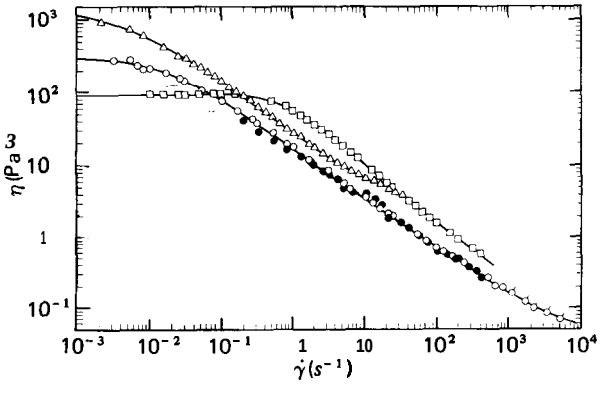

Figure 2 Dependence of viscosity on shear rate for two polymer solutions and an aluminum soap solution. ○ 1.5% polyacrylamide (Separan AP 30) in a 50/50 mixture by weight of water and glycerin, △ 2.0% polyisobutylene in Primol, and □ 7% aluminum laurate in a mixture of decalin and m-cresol. The data shown by ◁ were taken on a Ferranti-Shirley viscometer; all others are from a Weissenberg Rheogoniometer. All data were taken at 298 K. From [2].

© 1983 Hemisphere Publishing Corporation

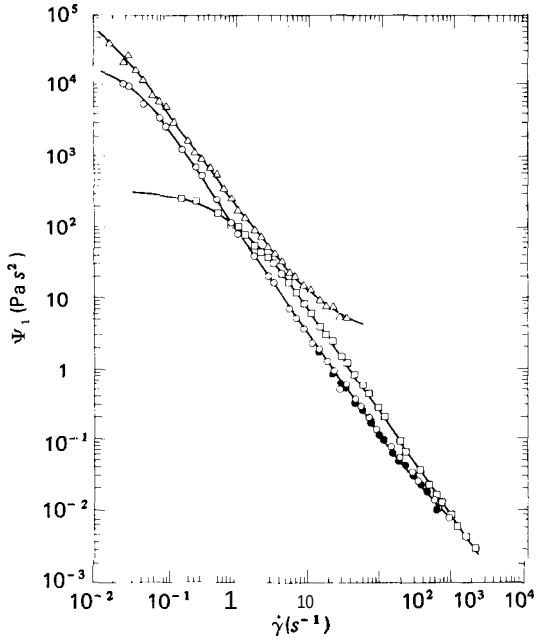

Figure 3 Dependence of the primary normal stress coefficient on shear rate for two polymer solutions and a soap solution. ○ 1.5% polyacrylamide in a water/glycerine mixture. △ 2.0% polyisobutylene in Primol, and ▫ 7% aluminum laurate in decalin and m-cresol. All data taken at 298 K. From [2].

given for each. Stress coefficients analogous to η, Ψ_1, and Ψ_2 can be defined and measured for each of these flows. In some of these experiments-for example, constrained recovery after steady shear flow-it is possible to observe directly the elastic character of non-Newtonian fluids. Quite a lot of information has been developed interrelating results from the small-amplitude oscillatory experiment and molecular structure, with the result that this area, a part of linear viscoelasticity, now constitutes a form of mechanical spectroscopy. A survey of this field is given by Ferry [3].

A number of standard experimental geometries for measuring shear flow properties are listed in Table 2. A particularly convenient arrangement for obtaining both η and Ψ_1 is the cone-and-plate instrument. If the cone is rotated at angular velocity W and makes angle θ_0 with the plate ($\theta_0 \ll 1$), then the shear rate is everywhere W/θ_0 in the gap. The values of the torque $\mathcal{T}$ required to hold the lower plate fixed and the total thrust exerted downward on the lower plate can be used to calculate η and Ψ_1 at this shear rate from the formulas

$$\eta = \frac{3\mathcal{T}}{2\pi R^3 \dot{\gamma}} \tag{5}$$

$$\Psi_1 = \frac{2\mathcal{F}}{\pi R^2 \dot{\gamma}^2} \tag{6}$$

where R is the radius of the plate. If the radial dependence of pressure on the lower plate were measured, then Ψ_2 could also be determined. These pressure measurements are very difficult, however, and provisions for them are not included on commercially available instruments.

Formulas for reduction of data in other geometrics are available in [1], [4], and [28].

(b) Shear-free flow

Shear-free flow is characterized by the absence of rotational motion in the fluid. As an example we

Table 1 Shear flow experiments used in rheology

Name	$t < 0$	$t \geq 0$
1. Steady shear flow	$\dot{\gamma}$ = constant ($\dot{\gamma}_0$) measure $T_{ij}(\dot{\gamma}_0)$	
2. Small-amplitude oscillatory shear flow	$\dot{\gamma} = \dot{\gamma}^0 \cos \omega t$ $\dot{\gamma}^0$ = shear rate amplitude ω = angular frequency	
3. Stress growth upon inception of steady shear flow	$\dot{\gamma} = 0$	$\dot{\gamma}$ = constant ($\dot{\gamma}_0$) measure $T_{ij}(t)$
4. Stress relaxation after cessation of steady shear flow	$\dot{\gamma}$ = constant ($\dot{\gamma}_0$)	$\dot{\gamma} = 0$ measure $T_{ij}(t)$
5. Stress relaxation after a step shear strain	$\dot{\gamma} = 0$	$\dot{\gamma} = \gamma_0 \delta(t)$ γ_0 = magnitude of shear strain measure $T_{ij}(t)$
6. Creep	$\dot{\gamma} = 0$	T_{yx} = constant (τ_0) measure $\dot{\gamma}(t)$
7. Constrained recoil after steady shear flow	$\dot{\gamma}$ = constant ($\dot{\gamma}_0$)	$T_{yx} = 0$ measure $\dot{\gamma}(t), T_{ii}(t)$

Flow: $v_x = \dot{\gamma}(t)y; v_y = 0; v_z = 0$.
Stresses: $T_{yx} = \tau; T_{xx} - T_{yy} = N_1; T_{yy} - T_{zz} = N_2$.

© 1983 Hemisphere Publishing Corporation

Table 2 Methods for determining viscometric functions

Geometry	Measure	Compute
Capillary viscometer 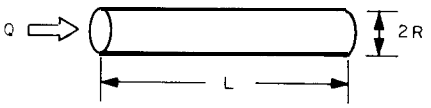	Q = volume flow rate $\Delta p/L$ = pressure gradient	$\tau_w = \Delta pR/2L$ $\dot{\gamma}_a = 4Q/\pi R^3$ $\dot{\gamma}_w = \frac{1}{4\tau_w^2}\frac{d}{d\tau_w}(\tau_w^3\dot{\gamma}_a)$ $\eta(\dot{\gamma}_w) = \frac{\tau_w}{\dot{\gamma}_a}\left(\frac{3}{4} + \frac{1}{4}\frac{d\ln\dot{\gamma}_a}{d\ln\tau_w}\right)^{-1}$
Cone and plate instrument 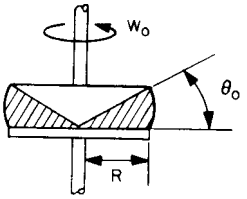	W_0 = angular velocity of cone 3 = torque on plate $\mathfrak{F}$ = downward force exerted on plate	$\dot{\gamma} = W_0/\theta_0$ $\eta(\dot{\gamma}) = \frac{3\mathfrak{I}}{2\pi R^3\dot{\gamma}}$ $\Psi_1(\dot{\gamma}) = \frac{2\mathfrak{F}}{\pi R^2\dot{\gamma}^2}$
Parallel-disk instrument 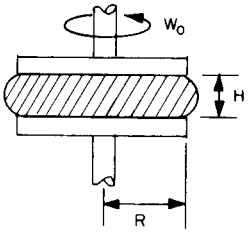	W_0 = angular velocity of upper disk 3 = torque on lower disk $\mathfrak{F}$ = downward force exerted on lower disk	$\dot{\gamma}_R = W_0R/H$ $\eta(\dot{\gamma}_R) = \frac{t}{\dot{\gamma}_R}\left(3 + \frac{d\ln t}{d\ln\dot{\gamma}_R}\right)$ $(t = \mathfrak{I}/2\pi R^3)$ $\Psi_1(\dot{\gamma}_R) - \Psi_2(\dot{\gamma}_R) = \frac{f}{\dot{\gamma}_R^2}\left[2 + \frac{d\ln f}{d\ln\dot{\gamma}_R}\right]$ $(f = \mathfrak{F}/\pi R^2)$
Couette viscometer 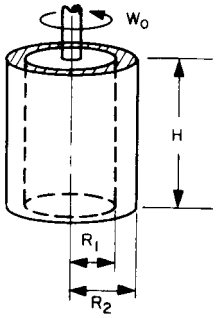 $(R_2 - R_1 \ll R_2)$	W_0 = angular velocity of inner cylinder $\mathfrak{I}$ = torque on outer cylinder	$\dot{\gamma} = \frac{W_0R_1}{R_2 - R_1}$ $\eta(\dot{\gamma}) = \frac{\mathfrak{I}(R_2 - R_1)}{2\pi R_1^3 W_0}$
Slit die 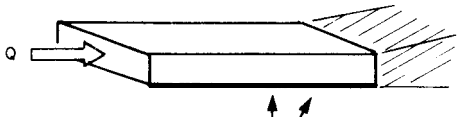 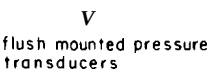 W = width $2B$ = gap L = length	Q = volume flow rate $\frac{dp}{dz}$ = pressure gradient $-S_{BL}$ = pressure reading at exit	$\tau_w = (-dp/dz)B$ $\dot{\gamma}_a = 3Q/2WB^2$ $\dot{\gamma}_w = \frac{2}{3}\dot{\gamma}_a\left(1 + \frac{3d\ln\dot{\gamma}_a}{2\,d\ln\tau_w}\right)$ $\eta(\dot{\gamma}_w) = \tau_w/\dot{\gamma}_w$ $\Psi_1(\dot{\gamma}_w) = \frac{-1}{\dot{\gamma}_w^2}\left(S_{BL} + \frac{\partial S_{BL}}{\partial\ln\tau_w}\right)$ (for low Reynolds number)

© 1983 Hemisphere Publishing Corporation

consider the simple elongational flow given by the velocity components

$$v_x = -\tfrac{1}{2}\dot{\epsilon}x \qquad v_y = -\tfrac{1}{2}\dot{\epsilon}y \qquad v_z = \dot{\epsilon}z \tag{7}$$

in which $\dot{\epsilon}$ is the elongation rate. A sketch of the deformation in a fluid element undergoing this flow in shown in Fig. 1.

In simple elongational flow there are no shear stresses; and for incompressible fluids, the only measurable combination of normal stresses is $T_{zz} - T_{xx} = T_{zz} - T_{yy}$. For steady flow in which $\dot{\epsilon}$ is constant for all times, the state of stress is customarily reported in terms of the elongational viscosity $\bar{\eta}$, defined by

$$\bar{\eta}(\dot{\epsilon}) = \frac{T_{zz} - T_{xx}}{\dot{\epsilon}} \tag{8}$$

For Newtonian fluids $\bar{\eta}$ is constant and given by

$$\bar{\eta} = 3\mu \tag{9}$$

so that elongational flow experiments do not give any new information about the fluid. For non-Newtonian fluids, $\bar{\eta}$ is a function of the elongation rate and is not simply related to the viscosity $\eta(\dot{\gamma})$.

Figure 4 shows the elongational viscosity for a low-density polyethylene melt as a function of $\dot{\epsilon}$. At low elongation rates, $\bar{\eta}$ approaches a constant value equal to $3\eta_0$. As the strain rate is increased, $\bar{\eta}$ first rises, then levels off, and finally decreases with increasing $\dot{\epsilon}$ at a rate similar to $\eta(\dot{\gamma})$ at large $\dot{\gamma}$. The strain-rate thickening in $\bar{\eta}$ that polymeric fluids exhibit is associated with the alignment and extension of the macromolecules in the direction of the stretching. In this configuration they offer increased resistance to the deformation.

Measurements of $\bar{\eta}$ are not easy to make because of the difficulty in reaching steady state. Indeed, recent evidence [6] suggests that perhaps steady state was not reached in the experiments reported in Fig. 4. From Fig. 1 it is seen that in steady flow, the length

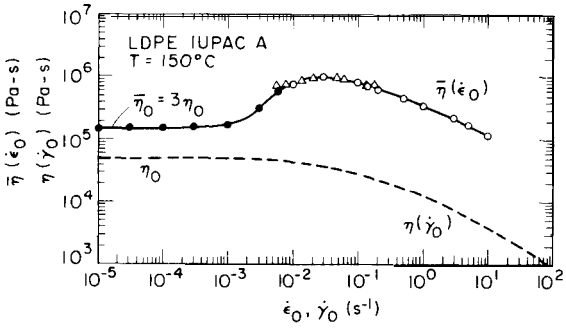

Figure 4 Dependence of elongational viscosity on elongation rate and viscosity on shear rate for a low-density polyethylene melt (IUPAC A). Data from [5].

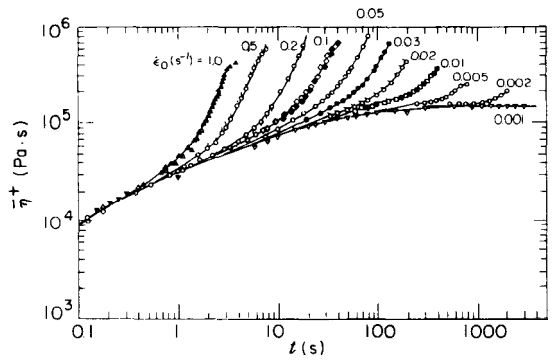

Figure 5 Elongational stress growth coefficient $\bar{\eta}^+$ versus time at various elongation rates for a low-density polyethylene melt (melt I). Data from [7].

of an element of fluid lying along the stretching direction increases exponentially with time. At moderate elongation rates the cross-sectional area of a test specimen rapidly decreases to the point that either the sample breaks or the total force transmitted through it is too small to be measured accurately.

Two types of devices are presently used for measuring $\bar{\eta}$; they differ in whether or not the clamps that hold the sample move relative to one another or not (see, for example, [5]). With movable clamps, the specimen is elongated by separating the clamps at an exponential rate. With fixed-separation clamps, one or both clamping devices are rotated in such a way that sample is removed from between the clamps at a constant velocity. This latter method seems capable of producing larger strains $\epsilon = \dot{\epsilon}t$ in the sample, and can thus give steady flow at higher values of strain rate.

In elongational flow, transient measurements are particularly important, both because steady state is hard to achieve in the laboratory and because it is doubtful that steady state (in a material sense) is achieved in processing applications. The most common transient experiment is the sudden startup of steady elongation with constant elongation rate $\dot{\epsilon}_0$. In this test the growth of the tensile stress toward its steady-state value is observed. Results are given in terms of an elongational stress growth coefficient $\bar{\eta}^+$, defined by

$$\bar{\eta}^+(t; \dot{\epsilon}_0) = \frac{T_{zz}(t) - T_{xx}(t)}{\dot{\epsilon}_0} \tag{10}$$

which approaches $\bar{\eta}$ as $t \to \infty$. Some illustrative data are shown in Fig. 5 for a low-density polyethylene melt. The monotone increasing curve observed for low strain rates is the linear viscoelastic response. For high strain rates, sudden upturns in $\bar{\eta}^+$ are seen at a roughly constant value of imposed strain $\dot{\epsilon}_0 t$.

It is important to emphasize that methods for measuring elongational flow properties of non-Newtonian fluids are still under active development.

© 1983 Hemisphere Publishing Corporation

There is very little elongational viscosity data available on polymer melts, and none for polymer solutions. Reviews of theoretical and experimental aspects of shear-free flows can be found in [4], [8], and [9].

C. Models for non-Newtonian fluids

Attempts to construct constitutive equations or rheological equations of state that are capable of describing the diverse stress/strain behavior of non-Newtonian fluids have been a major activity in rheology over the past two decades. Although progress has been made in incorporating a variety of viscoelastic behavior into a single model, this has come at the expense of increased complexity in the constitutive equation and added difficulty in its use for solving hydrodynamic flow problems. Thus this section begins with a discussion of the generalized Newtonian fluid which, though it is one of the oldest and simplest non-Newtonian models, is one of the most useful for engineering calculations. A brief outline is then given of some of the more recent models and an indication of useful limiting forms of these.

(a) Generalized Newtonian fluid

The generalized Newtonian fluid is a modification of Newton s law of viscosity, which describes theshear-rate-dependent viscosity of non-Newtonian fluids. The constitutive equation is

$$\mathbf{T} = \eta(\dot{\gamma})\dot{\boldsymbol{\gamma}} \tag{11}$$

in which $\dot{\boldsymbol{\gamma}} = \nabla\mathbf{v} + (\nabla\mathbf{v})^{\dagger}$ is the rate-of-strain tensor. Equation (11) is identical to Newton s law of viscosity except that the viscosity η is dependent on the magnitude $\dot{\gamma}$ of the rate-of-strain tensor, defined by

$$\dot{\gamma} = \left(\tfrac{1}{2}\,\dot{\boldsymbol{\gamma}}:\dot{\boldsymbol{\gamma}}\right)^{1/2} = \sqrt{\tfrac{1}{2}\,\Sigma_i\Sigma_j\dot{\gamma}_{ij}\dot{\gamma}_{ji}} \tag{12}$$

For the simple shear flow in Eq. (1), the quantity defined by Eq. (12) is identical to the shear rate.

A number of empirical expressions are available to describe the dependence of viscosity on $\dot{\gamma}$. By far the best known and most widely used of these is the power law of Ostwald and de Waele:

$$\eta(\dot{\gamma}) = m\dot{\gamma}^{n-1} \tag{13}$$

Equation (13) describes the important region of the viscosity where log η decreases linearly with log $\dot{\gamma}$. The quantities m (with units of N s^n/m^2) and n (dimensionless) serve to characterize each non-Newtonian fluid. In Table 3 the values of m and n are given for the three fluids illustrated in Fig. 2. Note that m gives the magnitude of the viscosity and n gives the slope of the power law region. For pseudoplastic fluids n lies between 0 and 1; for dilatant fluids n is larger than 1. If $n = 1$, then the Newtonian fluid is recovered, and m is equal to the viscosity μ. For most polymeric fluids n lies between 0.15 and 0.6.

Table 3 Power law parameters for fluids in Figure 2

Fluid	m, N s^n/m^2	n
1.5% polyacrylamide in water/glycerin	18	0.320
2.0% polyisobutylene in Primol	27	0.295
7.0% aluminum Laurate in decalin/ m-cresol	62	0.207

The power law model is deficient in its failure to describe the limiting value of viscosity at low shear rates and also in its lack of a time constant. This latter problem means that it is not possible to correlate viscous and elastic behavior for this model. A variety of other models have been proposed to resolve these problems, and some of the most common of these are listed in Table 4.

The temperature dependence of the viscosity can be described by giving the variation in m and n with temperature. Experimentally it is found that the power law slope is not nearly as sensitive to temperature variations as is m. The following empiricisms have been found useful [10]:

$$m = m^0 e^{-A(T-T_0)/T_0} \tag{14}$$

$$n = n^0 + B\,\frac{(T - T_0)}{T_0} \tag{15}$$

where T_0 is a reference temperature and m^0 and n^0 are the power law parameters at this temperature. The constants A and B must be determined from experimental data for each fluid. The assumption that $B = 0$ is often quite reasonable.

The generalized Newtonian fluid is capable of giving exact results for volume flow rate versus pressure drop for flow through straight ducts of constant cross-sectional area inasmuch as the shear stress can be described arbitrarily well. This model, however, is not capable of describing any of the time-dependent or elastic phenomena discussed in the previous section. Nonetheless, the generalized Newtonian model has been used for a wide variety of calculations in which the flow is not steady state and in which more than just the shear stress is computed. Unfortunately, it is not possible at this time to assess the errors associated with using this model outside of the range for which it was intended.

(b) Modern continuum theories

It is an objective of modern continuum theories to produce constitutive equations for non-Newtonian

© 1983 Hemisphere Publishing Corporation

Table 4 Viscosity models for use in the generalized Newtonian fluid

Model	Parameters	$\eta(\dot{\gamma})$	Comments
Power law	m, n	$m\dot{\gamma}^{n-1}$	No time constant and no zero-shear-rate viscosity
Truncated power law	$\eta_0, \dot{\gamma}_0, n$	η_0 for $\dot{\gamma} \leqslant \dot{\gamma}_0$ $\eta_0 \left(\frac{\dot{\gamma}}{\dot{\gamma}_0}\right)^{n-1}$ for $\dot{\gamma} \geqslant \dot{\gamma}_0$	$(1/\dot{\gamma}_0)$ is a characteristic time: the slope of η versus $\dot{\gamma}$ is discontinuous at $\dot{\gamma}_0$
Carreau	$\eta_0, \lambda, n, \eta_\infty$	$\frac{\eta - \eta_\infty}{\eta_0 - \eta_\infty} = [1 + (\lambda\dot{\gamma})^2]^{(n-1)/2}$	Gives smooth transition from zero-shear-rate viscosity to power law region and then to infinite-shear-rate viscosity
Eyring	t_0, τ_0	$t_0\tau_0 \left(\frac{\text{arcsinh } t_0\dot{\gamma}}{t_0\dot{\gamma}}\right)$	t_0, τ_0 are characteristic time and stress; $t_0\tau_0$ is the zero-shear-rate viscosity
Ellis	$\tau_{1/2}, \eta_0, \alpha$	$\frac{\eta_0}{\eta(\tau)} = 1 + \left(\frac{\tau}{\tau_{1/2}}\right)^{\alpha-1}$	Model gives viscosity as function of shear stress rather than shear rate; $\tau_{1/2}$ is shear stress at which $\eta = \eta_0/2$
Bingham	μ_0, τ_0	$\eta = \infty \quad \tau \leqslant \tau_0$ $\eta = \mu_0 + \frac{\tau_0}{\dot{\gamma}} \quad \tau \geqslant \tau_0$	Useful model for slurries and pastes; τ_0 is a yield stress; there is no flow unless applied stress exceeds this value

fluids that contain the ideas of both viscosity and elasticity. It is hoped the wide range of experimental phenomena can be described with relatively few unknown functions (such as $\eta(\dot{\gamma})$ in the generalized Newtonian fluid) or constants (such as m and n in the power law model). To date, work in this area has concentrated on ***rheologicczlly simple fluids;*** these materials are defined as fluids in which the stress at a particular fluid element depends only on the deformation history of that element and not, for example, on the motion of neighboring elements. So far, it appears that this definition is sufficiently broad as to include all non-Newtonian fluids. This statement regarding the stress in simple fluids is not particularly useful from the point of view of making calculations. By making certain simplifying assumptions about either the flow under consideration or the material behavior itself, useful special forms of the simple fluid constitutive equation can be produced. Many of these are summarized in [1].

The convected Maxwell model can be obtained in this way by making some rather strong assumptions about the material behavior:

$$\mathbf{T} + \lambda_0 \frac{\delta}{\delta t}\mathbf{T} = \eta_0\dot{\boldsymbol{\gamma}} \tag{16}$$

where $\delta/\delta t$ is a convected derivative defined by

$$\frac{\delta}{\delta t}\mathbf{T} = \frac{\partial \mathbf{T}}{\partial t} + (\mathbf{v}\cdot\nabla\mathbf{T}) - [(\nabla\mathbf{v})^\dagger\cdot\mathbf{T} + \mathbf{T}\cdot\nabla\mathbf{v}] \tag{17}$$

The first two terms in $\delta/\delta t$ are the usual material or substantial derivative; the remainder takes into account the deformation of the fluid element for which $\mathbf{T}$ is being computed. The two constants in the model, η_0 and λ_0, are the zero-shear-rate viscosity and a time constant. In terms of these parameters the steady shear flow material functions are

$$\begin{aligned} \eta &= \eta_0 \\ \Psi_1 &= 2\lambda_0\eta_0 \\ \Psi_2 &= 0 \end{aligned} \tag{18}$$

Since η and Ψ_1 are both nonzero, the Maxwell model is seen to describe simultaneously the viscous and elastic characteristics of a fluid. However, the model is not capable of predicting the shear-rate dependence of η and Ψ_1, although it can be modified to do so. In elongational flow, strain-rate hardening is predicted by

$$\bar{\eta} = \frac{3\eta_0}{(1+\lambda_0\dot{\epsilon})(1-2\lambda_0\dot{\epsilon})} \tag{19}$$

although no steady state is approached for even moderate strain rates ($\dot{\epsilon} \geqslant 1/2\lambda_0$). In spite of its inability to describe non-Newtonian behavior quantitatively, the convected Maxwell model has been popular, because of its simplicity, for exploratory calculations in which it is desired to assess the relative importance of elastic and viscous forces. Examples of flows where the

© 1983 Hemisphere publishing Corporation

elasticity gives rise to interesting effects are converging and diverging flows, stagnation flows, and secondary flows produced in geometries with curved streamlines in the primary flow field.

An improvement in the convected Maxwell model is obtained by replacing η_0 in Eq. (16) with a shear-rate-dependent viscosity function $\eta(\dot{\gamma})$ and by replacing λ_0 by $\eta(\dot{\gamma})/G$, where G is a constant modulus. The function η can be either the experimentally determined viscosity or a convenient empirical expression such as one used in the generalized Newtonian fluid. The resulting model, known as the ***White-Metzner model,*** predicts that

$$\eta = \eta(\dot{\gamma})$$
$$\Psi_1 = \frac{2\eta^2(\dot{\gamma})}{G} \tag{20}$$
$$\Psi_2 = 0$$

A systematic procedure for improving the convected Maxwell model was given by Oldroyd [11]. Oldroyd suggested that since the convected derivative in Eq. (17) contains the product of velocity gradient and stress, one should include in such a model all possible terms that contain products of velocity gradient with stress and with itself. The resulting modification of the convected Maxwell model is the ***Oldroyd eight-constant model:***

$$\mathbf{T} + \lambda_1 \frac{\delta}{\delta t}\mathbf{T} + \frac{1}{2}\mu_0(\mathrm{tr}\,\mathbf{T})\dot{\gamma} - \frac{1}{2}\mu_1(\mathbf{T}\cdot\dot{\gamma} + \dot{\gamma}\cdot\mathbf{T}) + \frac{1}{2}\nu_1(\mathbf{T}:\dot{\gamma})\delta = \eta_0\left[\dot{\gamma} + \lambda_2\frac{\delta}{\delta t}\dot{\gamma} - \mu_2(\dot{\gamma}\cdot\dot{\gamma}) + \frac{1}{2}\nu_2(\dot{\gamma}:\dot{\gamma})\delta\right] \tag{21}$$

where tr denotes the trace of a tensor and δ is the unit tensor. Many of the popular models used for hydrodynamic calculations can be obtained from Eq. (21) by special choices of the constants $\lambda_1, \lambda_2, \mu_0, \mu_1, \mu_2, \nu_1, \nu_2$, and η_0 (see Table 8.1-1 in [1]). For example, the convected Maxwell model has $\mu_0 = \mu_1 = \mu_2 = \lambda_2 = \nu_1 = \nu_2 = 0$.

Most of the differential models presented above can be integrated to give explicit expressions for stress in terms of strain. For example, the integral form of the convected Maxwell model is

$$\mathbf{T} = -\int_{-\infty}^{t} M(t-t')\gamma_{[0]}(t')\,dt' \tag{22}$$

where

$$M(t-t') = \frac{\eta_0}{\lambda_0^2}e^{-(t-t')/\lambda_0} \tag{23}$$

is known as the memory function, and $\gamma_{[0]}$ is a finite strain tensor defined by

$$\gamma_{[0]}(t') = \delta - \mathbf{E}(t')\cdot\mathbf{E}^{\dagger}(t') \tag{24}$$

$$E_{ij}(t') = \frac{\partial x_i}{\partial x_j'} \tag{25}$$

in which x_i and x_i' are the Cartesian coordinates of a fluid particle at times t and t', respectively. The product $\mathbf{E}\cdot\mathbf{E}^{\dagger}$ is commonly known as the Finger strain tensor. From Eq. (23) we see the fading memory of a polymeric material expressed as a decaying exponential function.

Equation (22), with $M(t-t')$ unspecified, has been obtained from a network model of a polymeric fluid and is known as ***Lodge's rubberlike liquid*** [12]. Regardless of the form of $M(t-t')$, the rubberlike liquid is incapable of describing a non-Newtonian viscosity or shear-rate-dependent normal stress differences:

$$\eta = \int_0^{\infty} M(s)s\,ds$$
$$\Psi_1 = \int_0^{\infty} M(s)s^2\,ds \tag{26}$$
$$\Psi_2 = 0$$

A simple method for modifying Eq. (26) to account for shear rate dependence has been used by Wagner [13]:

$$\mathbf{T} = -\int_{-\infty}^{t} M(t-t')h(\mathrm{I},\mathrm{II})\gamma_{[0]}(t')\,dt' \tag{27}$$

where $h(\mathrm{I},\mathrm{II})$ is a function of the first two invariants, I and II, of $\gamma_{[0]}$ and describes the nonlinearity in the viscosity and first normal stress difference. The invariants I and II can be taken to be

$$\mathrm{I} = \mathrm{tr}\,\gamma_{[0]} = \sum_i \gamma_{[0]ii}$$
$$\mathrm{II} = \mathrm{tr}(\gamma_{[0]}\cdot\gamma_{[0]}) = \sum_i\sum_j (\gamma_{[0]ij}\gamma_{[0]ji}) \tag{28}$$

For simple shear flow, both invariants depend simply on the magnitude of shear $\gamma = \int_{t'}^{t}\dot{\gamma}(t'')dt''$, so that for shear flow h can be taken to depend only on γ. It further appears that for shear flows we can take [13, 14]

$$h(\gamma) = e^{-n\gamma} \tag{29}$$

where n is a constant that is fairly insensitive to molecular structure.

For elongational flow h is a different function of the strain invariants, and it is a disadvantage of the type of model in Eq. (27) that the function h cannot be measured directly. It is, however, possible to con-

© 1983 Hemisphere Publishing Corporation

struct an expression for $h(\mathrm{I}, \mathrm{II})$ that simplifies properly in the limiting cases of elongational and shearing flow [15]. Moreover, it has been shown that in flows where the strain is not always increasing with time, h may be a functional rather than a function of the strain invariants [15]. The Wagner model has been found capable of describing quantitatively a wide variety of shear and elongational flow data on low-density polyethylene.

D. Volume flow rate/pressure drop relations

In this section we consider how the models in Sec. C can be used to predict a quantity of engineering design interest such as volume flow rate through a circular tube or a slit. For either of these situations, the only non-Newtonian property that affects the flow rate is the relation between the shear stress and shear rate, that is, the shear-rate-dependent viscosity. For this reason, the generalized Newtonian model is as complex a model as need be considered. Note that the differential and integral models in Sec. C(b) which predict a constant viscosity will all give Poiseuille s law,

$$Q = \frac{\pi \Delta p R^4}{8 \eta_0 L} \tag{30}$$

for steady tube flow. In Eq. (30), Q is the volume flow rate, $\Delta p/L$ is the pressure gradient, R is the pipe radius, and η_0 is the constant (zero-shear-rate) viscosity. In slit flow the corresponding result is

$$Q = \frac{2}{3} \frac{\Delta p B^3 W}{\eta_0 L} \tag{31}$$

where W is the width of the slit and $2B$ is the gap thickness.

In Tables 5 and 6 results analogous to Eqs. (30) and (31) are presented for a number of viscosity models listed in Table 4. A method for estimating volume flow rate as a function of pressure drop for non-Newtonian fluids in ducts with irregular cross sections has been given by Miller [16] (see also Hanks [17]).

It should be emphasized that the results in these tables are restricted to laminar isothermal flow of the generalized Newtonian fluid. Because of the large viscosities that are typical in polymeric fluids, viscous dissipation is often significant in these flows, with the result that nonisothermal calculations are required. Generally these must be done numerically; a review of viscous heating in shear flows is given in [18]. Below are presented two examples that show how the entries in these tables can be used.

(a) Example I: Tube flow of a polystyrene melt

The viscosity of a polystyrene melt at 453 K is shown in Fig. 6 as a function of shear rate. It is desired to pump this melt at 453 K through a tube 8 cm long and 0.5 cm radius. If a pressure drop of 5.6 X 10^6 Pa can be applied, what is the resulting volume flow rate?

Solution. As a first approximation we model the

Table 5 Flow rates through slits

Model (constants)	$q = \frac{30}{2B^2 W}$	
Power law (m, n)	$\frac{3}{[(1/n)+2]} \frac{\tau_w}{0^m}^{1/n}$	(A)
Truncated power law $(\eta_0, \dot{\gamma}_0, n)$	$\frac{3\tau_w}{[(1/n)+2]\eta_0}\left[\left(\frac{\eta_0\dot{\gamma}_0}{\tau_w}\right)^{1-1/n} + \frac{1}{3}\left(\frac{1}{n}-1\right)\left(\frac{\eta_0\dot{\gamma}_0}{\tau_w}\right)^3\right]$ (for $\tau_w \gg \eta_0\dot{\gamma}_0$)	(B)
Eyring (t_0, τ_0)	$\frac{3}{t_0}\left(\frac{\tau_0}{\tau_w}\right)^2\left(\frac{\tau_0}{\tau_w}\cosh\frac{\tau_w}{\tau_0} - \sinh\frac{\tau_w}{\tau_0}\right)$	(C)
Ellis $(\tau_{1/2}, \eta_0, \alpha)$	$\frac{\tau_w}{\eta_0}\left[1 + \frac{3}{\alpha+2}\left(\frac{\tau_w}{\tau_{1/2}}\right)^{\alpha-1}\right]$	(D)
Bingham (μ_0, τ_0)	$\frac{\tau_w}{\mu_0}\left[1 - \frac{3}{2}\left(\frac{\tau_0}{\tau_w}\right) + \frac{1}{2}\left(\frac{\tau_0}{\tau_w}\right)^3\right]$ (for $\tau_w \geq \tau_0$)	(E)

Note: Q = volume flow rate; $2B$ = thickness of slit; W = width of slit; $\Delta p/L$ = pressure gradient; τ_w = wall shear stress $(\Delta p B/L)$.

© 1983 Hemisphere Publishing Corporation

Table 6 Flow rates through tubes

Model (constants)	$q = \frac{4Q}{\pi R^3}$	
Power law (m, n)	$\frac{4}{[(1/n) + 3]}\frac{\tau_w}{m}^{1/n}$	(A)
Truncated power law $(\eta_0, \dot{\gamma}_0, n)$	$\frac{4}{[(1/n)+31}\frac{\tau_w}{\eta_0}\left[\left(\frac{\eta_0\dot{\gamma}_0}{\tau_w}\right)^{1-1/n} + \frac{1}{4}\left(\frac{1}{n}-1\right)\left(\frac{\eta_0\dot{\gamma}_0}{\tau_w}\right)^4\right]$ (for $\tau_w \gg \eta_0\dot{\gamma}_0$)	(B)
Eyring (t_0, τ_0)	$\frac{8}{t_0}\left(\frac{\tau_0}{\tau_w}\right)^3\left\{\left[\frac{1}{2}\left(\frac{\tau_w}{\tau_0}\right)^2 + 1\right]\cosh\left(\frac{\tau_w}{\tau_0}\right) - \frac{\tau_w}{\tau_0}\sinh\left(\frac{\tau_w}{\tau_0}\right) - 1\right\}$	(C)
Ellis $(\tau_{1/2}, \eta_0, \alpha)$	$\frac{\tau_w}{\eta_0}\left[1 + \frac{4}{\alpha+3}\left(\frac{\tau_w}{\tau_{1/2}}\right)^{\alpha-1}\right]$	(D)
Bingham (μ_0, τ_0)	$\frac{\tau_w}{\mu_0}\left[1 - \frac{4}{3}\left(\frac{\tau_0}{\tau_w}\right) + \frac{1}{3}\left(\frac{\tau_0}{\tau_w}\right)^4\right]$ (for $\tau_w \geq \tau_0$)	(E)

Note: Q = volume flow rate; R = tube radius; $\Delta p/L$ = pressure gradient; τ_w = wall shear stress $(\Delta pR/2L)$.

polystyrene melt as a power law fluid. A power law fit of the viscosity is shown as the dashed line in Fig. 6. The slope of the power law region is found graphically to be

$$n - 1 = -0.6$$

$$[n = 0.4]$$

The value of the parameter m in the power law model is the value of the dashed line at $\dot{\gamma} = 1\ s^{-1}$. Thus

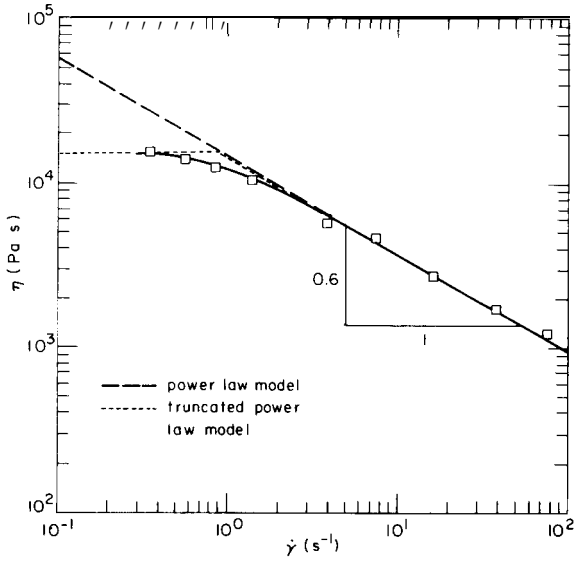

Figure 6 Viscosity of molten polystyrene at 453 K. The dashed line shows the power law approximation to the viscosity, and the dotted lines show the truncated power law approximation. The data are from [19].

$$m = 1.45 \times 10^4$$

The wall shear stress for the specified tube dimensions and pressure drop is

$$\tau_W = \frac{(\Delta p)R}{2L}$$

$$= \frac{(5.6 \times 10^6)(0.005)}{2(0.08)}$$

$$= 1.75 \times 10^5 \text{ Pa}$$

Finally, the volume flow rate is given by Eq. (A) in Table 6 to be

$$Q = \frac{\pi R^3}{[(1/n) + 3]}\left(\frac{\tau_w}{m}\right)^{1/n}$$

$$= \frac{\pi(0.005)^3}{[(1/0.4) + 3]}\left(\frac{1.75 \times 10^5}{1.45 \times 10^4}\right)^{1/0.4}$$

$$= 3.61 \times 10^{-5}\ m^3/s$$

$$= 36.1\ cm^3/s \quad (32)$$

To see how serious the neglect of η_0 in the volume flow rate calculation is, let us use the truncated power law model. In addition to $n = 0.4$, we now also need the zero-shear-rate viscosity η_0, which is seen from Fig. 6 to be

$$\eta_0 = 1.48 \times 10^4 \text{ Pa s}$$

and a critical shear rate $\dot{\gamma}_0$, which is the shear rate at which the power law line intersects η_0,

$$\dot{\gamma}_0 = 0.966\ s^{-1}$$

© 1983 Hemisphere Publishing Corporation

Then Eq. (B) in Table 6 gives

$$Q = \frac{\pi R^3 \tau_w}{[(1/n) + 3]\eta_0}\left[\left(\frac{\eta_0\dot{\gamma}_0}{\tau_w}\right)^{1-1/n} + \frac{1}{4}\left(\frac{1}{n} - 1\right)\left(\frac{\eta_0\dot{\gamma}_0}{\tau_w}\right)^4\right]$$

$$= (8.44 \times 10^{-7})(4.28 \times 10^1 + 1.6 \times 10^{-5})$$

$$= 3.6 \times 10^{-5}\ \mathrm{m^3/s}$$

$$= 36\ \mathrm{cm^3/s} \quad (33)$$

which is the same value of Q given by the power law model. Note that $\eta_0\gamma_0 = 1.43 \times 10^4$ is an order of magnitude less than τ_w, as required for use of the above expression for Q.

In general, the use of the power law model in place of a more complex viscosity expression that includes η_0 is reasonable as long as the apparent shear rate $\dot{\gamma}_a$, defined by

$$\dot{\gamma}_a = \frac{4Q}{\pi R^3} \quad (34)$$

is much greater than the characteristic shear rate at which η begins to decrease from η_0. In the above example,

$$\dot{\gamma}_a = \frac{(4)(4.5 \times 10^{-5})}{\pi(0.005)^3} = 460 \gg \dot{\gamma}_0$$

The apparent shear rate is just the wall shear rate that a Newtonian fluid would have for the same values of Q and R.

(b) Example 2: Axial annular flow of a carboxymethylcellulose solution

It is desired to force a 3.5% aqueous carboxymethylcellulose solution through the annular region between tubes of radius 6.80 cm and 7.0 cm at a volume flow rate of 50 $\mathrm{cm^3/s}$. This polymer solution can be described by an Ellis model with

$\eta_0 = 2.27$ Pa s

$\tau_{1/2} = 152$ Pa

$\alpha = 3.0$

Determine the required pressure gradient to obtain this flow rate.

Solution. We do not have an exact expression available that gives the relationship between Q and $\Delta p/L$ for annular flow of an Ellis model. However, an approximate solution can be obtained as follows.

Since the annular gap is small compared with the radius of either of the bounding tubes, we can replace the annulus by a rectangular slit of width $2\pi R_{av}$ and thickness $2B = \Delta R$. The result in Table 5, Eq. (D), can then be used. For the conditions of this problem,

$$\frac{3Q}{2WB^2}\eta_0 = \frac{3(50)(2.27)}{2(43.4)(0.1)^2} = 392\ \mathrm{Pa}$$

The wall shear stress τ_w must be such that

$$\tau_w\left[1 + \frac{3}{\alpha + 2}\left(\frac{\tau_w}{\tau_{1/2}}\right)^{\alpha-1}\right] = 392 \quad (35)$$

By trial and error it is easy to find that

$\tau_w = 196$ Pa

The required pressure gradient is then

$$\frac{\Delta p}{L} = \frac{\tau_w}{B} = 1.96 \times 10^5\ \mathrm{Pa/m} \quad (36)$$

Although it is not possible to assess precisely the errors associated with the slit approximation here, exact results for Newtonian fluids suggest that the error is about 2% for this problem (see Eq. 5.2-42) in [1]).

E. Turbulent flow of non-Newtonian fluids

In this final section we consider volume flow rate/pressure drop relations for pipe flow of non-Newtonian fluids in the turbulent regime. Because of the very high viscosities of most non-Newtonian fluids, turbulent flow is not typically encountered. One exception is for exceedingly dilute polymer solutions, where the phenomenon of drag reduction in turbulent flow is observed. The results in this section are presented in terms of a friction factor f, defined by

$$f = \frac{1}{4}\frac{D}{L}\frac{\Delta p}{\frac{1}{2}\rho V^2} \quad (37)$$

where Ap is the pressure drop over a length L of pipe and V is the average velocity in the pipe, and a generalized Reynolds number Re, , defined by [20]

$$\mathrm{Re}_n = \frac{D^n V^{2-n}\rho}{m} \quad (38)$$

The parameters m and n in Eq. (38) are the power law parameters; the form of Re, is suggested by dimensional analysis of the equation of motion coupled with the generalized Newtonian fluid model and power law viscosity [21]. Note that for Newtonian fluids, Eq. (38) reduces to the customary Re (= $DV\rho/\mu$).

(a) Drag reduction

Drag reduction refers to the substantial reduction in friction factor that results when a small amount of certain high-molecular-weight polymer additives are

© 1983 Hemisphere Publishing Corporation

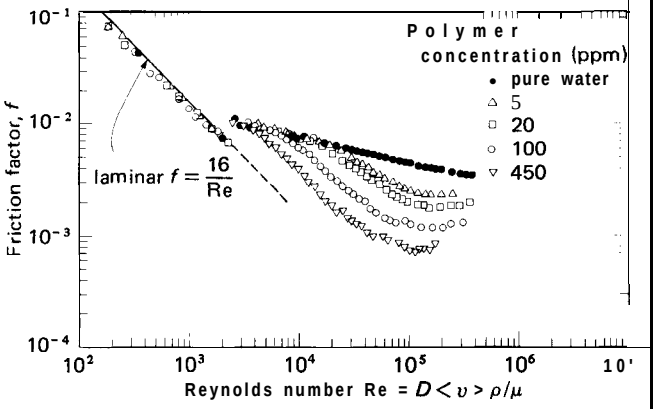

Figure 7 Friction factor versus Reynolds number for water and dilute aqueous solutions of poly(ethylene oxide), $\bar{M}_v$ = 6.1 X 10^6. In the turbulent regime, the curves for the polymer solutions lie below that of the solvent and illustrate drag reduction. Data replotted from [22].

added to Newtonian fluids undergoing turbulent tube flow. The magnitude of the effect is illustrated in Fig. 7, where f versus Re results for small amounts of poly(ethylene oxide) in water are shown. In this figure Re is the ordinary Reynolds number, since polymer solutions at these low concentration levels have virtually shear-rate-independent viscosities. There is no effect of the polymer on fin the laminar flow regime. After the onset of drag reduction at Re of about 3 000, the amount of drag reduction increases with increasing polymer concentration. There is a maximum amount of drag reduction that can be achieved, however, by adding more polymer. It can be seen in the figure that the addition of 5 ppm (by weight) of poly(ethylene oxide) to water reduces f by 40% at Re = 10^5, whereas the viscosity of the solution is increased by only 1% over that of water. Some other examples of drag-reducing systems are listed in Table 7. Additional information on drag reduction can be found in the reviews by Virk [23] and Berman [24].

(b) Concentrated solutions

For polymeric fluids transition from laminar to turbulent flow occurs at a generalized Reynolds number of about 2 100; somewhat higher values of Re, are found as n decreases from unity [25]. Dodge and Metzner have found that for fluids described by the generalized Newtonian fluid model, that is, that are not very elastic, Prandtl s universal law of friction should be modified as follows:

$$\frac{1}{\sqrt{f}} = \frac{4}{n^{3/4}} \log (\mathrm{Re}\, f^{(2-n)/2}) - \frac{0.4}{n^{1.2}} \tag{39}$$

The above result describes the frictional behavior of soft gels and suspensions.

Non-Newtonian fluids that are viscoelastic generally exhibit lower friction factors than nonelastic fluids with similar viscosities. A relatively simple correlation for these fluids is given by Shaver and Merrill [26]:

$$f = \frac{0.079}{n^5\, \mathrm{Re}^{\gamma}}$$

$$\gamma = \frac{2.63}{(10.5)} \tag{40}$$

A slight improvement in the predictions of f given by Eq. (40) can be obtained by the following pair of equations due to Meter [27]:

$$f = 0.0064 - 0.00425 \log\left(\frac{\tau_w}{\tau_{1/2}}\right) \quad \left(0.2 < \frac{\tau_w}{\tau_{1/2}} < 10\right) \tag{41}$$

$$f = 0.0117\left(\frac{\tau_w}{\tau_{1/2}}\right)^{-0.73} \quad \left(10 < \frac{\tau_w}{\tau_{1/2}} < 40\right) \tag{42}$$

where τ_w is the wall shear stress and $\tau_{1/2}$ is the Ellis model parameter given in Table 4. All of the above friction-factor expressions are restricted to flow through smooth pipes.

Table 7 Some polymer solvent systems that show drag reduction

Polymer	$M_w \times 10^{-6}$	Solvent
Poly(ethylene oxide)	0.30-8.45	Water
Poly(ethylene oxide)		Benzene
Polyacrylamide homopolymer	0.8-4.0	Water
Polyacrylamide partially hydrolyzed	1.0-10.0	1.0 *M* NaCl
Polyisobutylene	1.0-15.0	Cyclohexane
Polydimethylsiloxane		Toluene
Polymethylmethacrylate	0.4-3.3	Toluene
Polycisisoprene	0.07-1.0	Toluene
Guar gum	1.72	Water
Guaran triacetate	0.07-5.34	Acetonitrile
Hydroxyethylcellulose	0.08-0.63	Water

Nomenclature for Section 2.2.8 appears at the beginning of Part 2.

REFERENCES FOR SECTION 2.2.8

1. Bird, R. B., Armstrong, R. C., and Hassager, O., ***Dynamics of Polymeric Liquids, Vol. 1: Fluid Mechanics,*** Wiley, New York, 1977,

© 1983 Hemisphere Publishing Corporation

2. Hupler, J. D., Ashare, E., and Holmes, L. A., Rheological Properties of Three Solutions. Part 1. Non-Newtonian Viscosity, Normal Stresses, and Complex Viscosity, *Trans. Soc. Rheol., vol.* 11, pp. 159-179, 1967.
3. Ferry, J. D., *Viscoelastic Properties of Polymers,* 2d ed., Wiley, New York, 1970.
4. Walters, K., *Rheometry,* Chapman & Hall, London, 1975.
5. Laun, H. M., and Miindstedt, H., Elongational Behavior of a Low Density Polyethylene Melt, *Rheol. Acta,* vol. 17, pp. 415-425, 1978.
6. Raible, T., Demarmels, A., and Meissner, J., Stress and Recovery Maxima in LDPE Melt Elongation, *Polym. Bull.,* vol. 1, pp. 397-402, 1979.
7. Meissner, J., Dehnungsverhalten von Polyäthylen-Schmelzen, *Rheol. Acta,* vol. 10, pp. 230-242, 1971.
8. Petrie, *C.* J. *S., Elongational Flows,* Pitman, London, 1979.
9. Dealy, J. M., Extensional Flow of Non-Newtonian Fluids-A Review, *Polymer Eng. Sci.,* vol. 11, pp. 433-445, 1971.
10. Turian, R. M., *Thermal Phenomena in Non-Newtonian Viscometry*, Ph.D. thesis, University of Wisconsin, Madison, 1964.
11. Oldroyd, J. G., Non-Newtonian Effects in Steady Motion of Some Idealized Elastic-Viscous Liquids, *Proc. Roy. Soc. /London),* vol. A245, pp. 278-297, 1958.
12. Lodge, A. *S., Elastic Liquids,* Academic Press, New York, 1964.
13. Wagner, M. H., Analysis of Time Dependent Non-Linear Stress Growth Data for Shear and Elongational Flow of a Low Density Branched Polyethylene Melt, *Rheol. Acta,* vol. 15, pp. 136-142, 1976.
14. Wagner, M. H., Prediction of Primary Normal Stress Difference from Shear Viscosity Data Using a Single Integral Constitutive Equation, *Rheol. Acta, vol.* 16, pp. 43-50, 1977.
15. Wagner, M. H., and Stephenson, S. E., The Irreversibility Assumption of Network Disentanglement in Flowing Polymer Melts and Its Effects on Elastic Recoil Predictions, *J. Rheol., vol. 23,* pp. 489-504, 1979.
16. Miller, C., Predicting Non-Newtonian Flow Behavior in Ducts of Unusual Cross Section, *Znd. Eng. Chem. Fund.,* vol. 11, pp. 524-528, 1972.
17. Hanks, R. W., On the Prediction of Non-Newtonian Flow Behavior in Ducts of Noncircular Cross Section, *Ind. Eng. Chem. Fund.,* vol. 13, pp. 62-66, 1974.
18. Winter, H. H., Viscous Dissipation in Shear Flows of Molten Polymers, *Adv. Heat Transfer, vol.* 13, pp. 205-267, 1977.
19. Ballenger, T. F., Chen, I.-J., Crowder, J. W., Hagler, G. E., Bogue, D. C., and White, J. L., Polymer Melt Flow Instabilities in Extrusion: Investigation of the Mechanism and Material and Geometric Variables, *Trans. Soc. Rheol., vol.* 15, pp. 195-215, 1971.
20. Metzner, A. B., and Reed, J. C., Flow of Non-Newtonian Fluids–Correlation of the Laminar, Transition, and Turbulent Flow Regions, *AIChE J.,* vol. 1, pp. 434-440, 195.5.
21. Bird, R. B., Correlation of Friction Factors in Non-Newtonian Flow, *AIChE J.,* vol. 2, p. 428, 1956.
22. Virk, P. S., The Toms Phenomenon-Turbulent Pipe Flow of Dilute Polymer Solutions, Sc.D. thesis, Massachussetts Institute of Technology, 1966.
23. Virk, P. S., Drag Reduction Fundamentals, *AIChE J.,* vol. 21, pp. 625-655, 1975.
24. Berman, N. S., Drag Reduction by Polymers, *Ann. Rev. Fluid Mech.,* vol. 10, pp. 47-64, 1978.
25. Dodge, D. W., and Metzner, A. B., Turbulent Flow of Non-Newtonian Systems, *AIChE J.,* vol. 5, pp. 189-204, 1959.
26. Shaver, R. G., and Merrill, E. W., Turbulent Flow of Pseudoplastic Polymer Solutions in Straight Cylindrical Tubes, *AIChE J.,* vol. 5, pp. 181-188, 1959.
27. Meter, D. M., Tube Flow of Non-Newtonian Polymer Solutions: Part 11. Turbulent Flow, *AIChE J., vol.* 10, pp. 881-884, 1964.
28. Whorlow, R. W., *Rheological Techniques,* Ellis Horwood, Chichester, England, 1980.

© 1983 Hemisphere Publishing Corporation

2.3
Multiphase fluid flow and pressure drop

Contents

2.3.1
INTRODUCTION AND FUNDAMENTALS, G. F. Hewitt 2.3.1-1

A. Classification of multiphase flows **2.3.1-1**
B. Design parameters in multiphase flow systems **2.3.1-2**
C. Conservation equations for multiphase flows **2.3.1-3**
D. Drift flux and related models **2.3.1-7**

References for Section 2.3.1 **2.3.1-10**

2.3.2
GAS-LIQUID FLOW, G. F. Hewitt 2.3.2-l

A. General description of two-phase flows: flow patterns **2.3.2-1**
B. Applications of one-dimensional equations **2.3.2-7**
C. Hydrodynamics of specific flow regimes (vertical) **2.3.2-18**
D. Hydrodynamics of specific flow regimes (horizontal tubes) **2.3.2-23**
E. Critical two-phase flows **2.3.2-26**

Nomenclature for Sections 2.3.1-2.3.2 **2.3.2-29**
References for Section 2.3.2 **2.3.2-32**

2.3.3
SOLID-GAS FLOW, M. Weber and W. Stegmaier 2.3.3-l

A. Principle of pneumatic conveyance **2.3.3-1**
B. Flow patterns **2.3.3-2**
C. Schematic representation of pressure drop **2.3.3-2**
D. Air-activated gravity conveyor **2.3.3-2**
E. Principles of computation **2.3.3-3**

References for Section 2.3.3 **2.3.3-9**

2.3.4
SOLID-LIQUID FLOW, M. Weber and W. Stegniaier 2.3.4-l

A. Principle of hydraulic conveyance **2.3.4-1**
B. Flow patterns **2.3.4-1**
C. Flow regimes: Horizontal conveyance **2.3.4-1**
D. Basic relationships for pressure losses **2.3.4-2**

Nomenclature for Sections 2.3.3-2.3.4 **2.3.4-6**
References for Section 2.3.4 **2.3.4-7**

© 1983 Hemisphere Publishing Corporation

HEMISPHERE

2.3.3
Solid-gas flow

M. Weber and W. Stegmaier

A. Principle of pneumatic conveyance

Pneumatic conveyance is of great importance for the transport of grained and powdered materials, especially for short distances and in connection with heat exchange and mass transfer processes.

The physical principles involved are, however, very numerous. For this reason, only a few aspects of the phenomena will be treated here. A more exhaustive treatment of this principle of conveyance may be found in certain basic books [1-6].

(a) Pneumatic conveyance in vertical pipes

The principle of pneumatic conveyance may best be explained by referring to Fig. 1 for the case of vertically upward movement. The weight of a solid particle F_W and its inertial force $M_s\, dv_s/dt$ have to be compensated by the drag force F_D and the force due to the pressure gradient $V_s\, dp/dl$, which are both opposite to the flow direction of the particle. To bring this about, the velocity of the fluid medium v_g has to be greater than the free-fall velocity of the solid particle w_{so}.

$$v_g > w_{so} \tag{1}$$

(b) Pneumatic conveyance in horizontal pipes

In the horizontal pipe, relations are far more complex, for the main direction of the fluid flow is perpendicular to the gravity force acting on the solid particles.

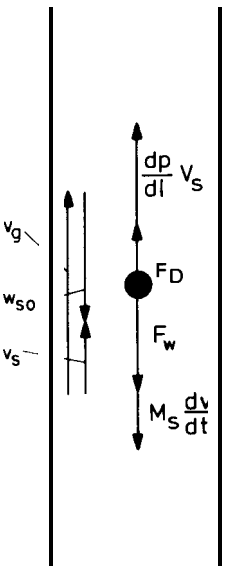

Figure 1 Force balance for vertical pneumatic conveying.

Short mention is therefore made solely of the effects essentially compensating the gravity force:

1. Transverse forces caused by the asymmetric direction of the fluid flow near the pipe wall due to the velocity gradient.
2. The Magnus force acting on spinning particles.
3. Transverse forces generated by the turbulent exchange of eddies.
4. The buoyant force is a minimum in pneumatic conveying, but it is of immense importance in hydraulic conveying.
5. Under certain circumstances, part of the axial

© 1983 Hemisphere Publishing Corporation

kinetic energy of the particles is converted into radial kinetic energy by their impact on the pipe wall.

6. In many cases the conveyed material is supported by the wall if it is sliding along the bottom of the pipe in the form of a settled layer.

The effects named under 1, 2, 3, and 5 would be neutral with regard to symmetry, but since particle concentration in the lower part of the pipe is higher due to gravity, upward-directed forces are the result.

(c) Pneumatic conveyance in inclined pipes

The above-described effects superpose each other in the case of an inclined pipe.

B. Flow patterns

Different flow patterns appear depending on gas velocity, free-fall velocity of a single particle, solids concentration, and position of the pipe. These are explained in the following example using a vertical pipe (Figs. 2 and 3).

1. Dilute-phase flow appears at low mass flow ratio ($\dot{x} < 10$) and the simultaneous condition of high gas velocities. The concentration distribution over the pipe cross section is nearly homogeneous (see Figs. 2*a* and Fig. 3, 3*a*).

2. Flow as clouds is experienced at higher mass flow ratio ($\dot{x} > 30$) combined with relatively low gas velocities. The solids distribution is inhomogeneous, the mode of flow is unsteady, and blockages are possible, if the characteristic of the blower is not stable (see Figs. 2, ***b-d*** and 3, ***b-d).***

3. Slugging dense-phase flow and packed-bed flow appear at low gas velocities ($v_g <$ w,) and high solids concentrations. The pressure loss that is found at conveying is considerable (see Figs. 2*e*, 2*f*, and Fig. 3, e and f).

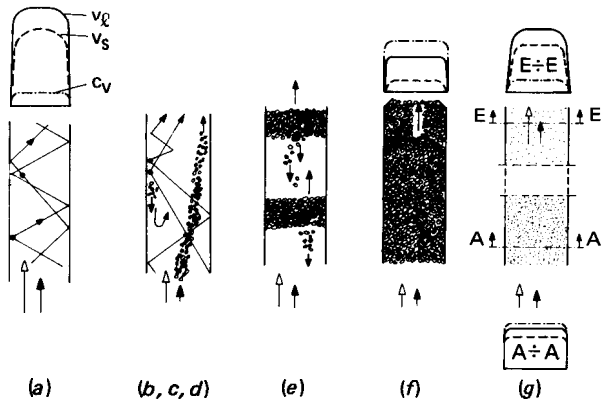

Figure 2 Flow patterns for vertical pneumatic conveying. See Fig. 3.

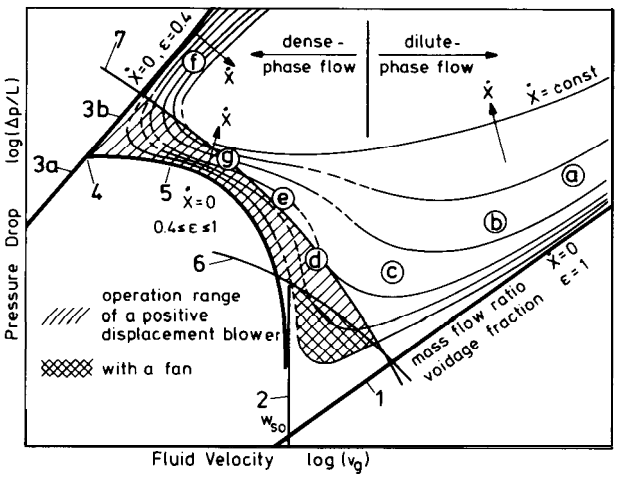

Figure 3 Schematic representation of pressure drop for pneumatic and hydraulic conveyance of medium- and coarse-grained materials in vertical pipes [2]. 1. Fluid phase alone. 2. Free-fall velocity of a single particle w_{so}. 3(a) Flow through a moved bed of solids. 3(b) Flow through a fiied bed. 4. Point of minimum fluidization velocity. 5. Expanded fluidized bed. 6. Characteristic of a fan. 7. Characteristic of a positive displacement blower. (a) Homogeneous. (*b*) Heterogeneous dilute-phase flow. (c)Cloud. (*d*) Layer. (*e*) Slug flow. (*f*) Packed-bed flow and hydraulic dense-phase flow. (*g*) Fluidized bed and hydraulic slurry conveyance.

4. Flow as a moving fluidized bed is possible with solids consisting of fine particles that can be easily fluidized. In this case high solids concentrations and low solids velocities can be achieved (see Figs. 2g and 3*g*).

C. Schematic representation of pressure drop

The conveying modes discussed in Sec. B can be characterized by the relationship between the pressure gradient dp/dl and the fluid velocity v_g. This is shown in Fig. 3 for the case of vertical pneumatic conveying of medium- and coarse-grained material.

D. Air-activated gravity conveyor

A particular case of pneumatic conveying is realized in the air-activated gravity conveyor. It is based on the principle of transforming the powdered material by vertical aeration into a fluidized-bed state. With a conventional inclination of the channel of from 2 to 6°, the material flows gravity-assisted in the desired direction (Fig. 4). Relatively low specific energy consumption (0.5-4 J/kg), little wear of the conveying duct, and a small amount of attrition due to low conveying velocities (OS-2 m/s) are advantages of these systems.

© 1983 Hemisphere Pu lishing *corporation*
HEDH

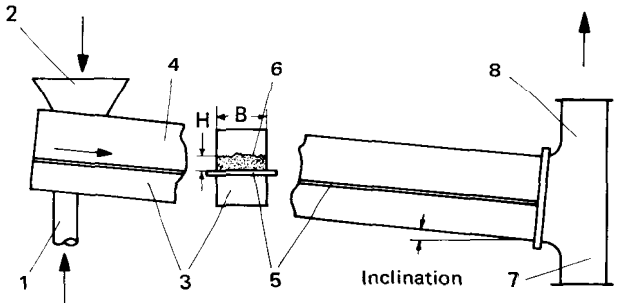

Figure 4 Air-activated gravity conveyor. 1. Air supply. 2. Feeding section. 3. Air supply channel. 4. Conveying channel. 5. Porous base. 6. Conveyed material. 7. Conveyed material exit. 8. Air exit.

E. Principles of computation

(a) Definition of important parameters

It is useful to define a number of parameters for the description and calculation of solid-fluid flows:

The volume of the fluid component is called V_g, and the total volume of the solid-fluid system is named $V_g + V_s$. The ratio of these two volumes is defined as voidage fraction or porosity:

$$\epsilon = \frac{V_g}{V_g + V_s} \tag{2}$$

For hydraulic conveying, however, the spatial concentration c_v is widely used:

$$c_v = 1 - \epsilon \tag{3}$$

In pneumatic conveying practice, the mass flow ratio $\dot{x}$ is commonly used, which is defined as the mass flow ratio of solid to fluid:

$$\dot{x} = \frac{\dot{M}_s}{\dot{M}_g} = \frac{(1-\epsilon)\rho_s v_s}{\epsilon \rho_g v_g} \tag{4}$$

In hydraulic transportation the delivered volume concentration c_T is normally employed,

$$c_T = \frac{\dot{V}_s}{\dot{V}_s + \dot{V}_{g,\mathrm{Q}}} \tag{5}$$

which is defined as the flow ratio of solid volume to total volume.

The conversion of the parameters as defined above from one into another can be seen in Table 1.

(b) Free-fall velocity

The free-fall velocity of particles is of multiple importance in hydraulic and pneumatic conveying. It can be computed by a force balance made up by weight, drag, and buoyancy.

The free-fall velocity of a spherical single particle w_{so} in an undisturbed static fluid without any influence of the pipe wall is given by

$$w_s = \sqrt{\frac{4}{3}\frac{d_s}{\xi}\frac{\rho_s - \rho_{g,\mathrm{Q}}}{\rho_{g,\mathrm{Q}}} g_n} \tag{6}$$

The drag coefficient ξ of a single particle depends on the Reynolds number, Re,:

$$\mathrm{Re}_s = \frac{d_s w_{so}}{\nu} \tag{7}$$

The correlation of the drag coefficient ξ and the Reynolds number Re, can be given as an empirical equation. Examples of this are shown in Table 2. For Reynolds numbers less than 2×10^4, an implicit equation results for the free-fall velocity w_s. This can be solved by iteration methods. Values for the free-fall velocity of single spherical particles in air at standardized conditions can be read off Fig. 5.

Frequently particles are not of a spherical shape. In this case an additional shape factor K must be taken into account. Empirical coefficients can be found from Torobin and Gauvin [8] and Heywood (cited in [8]). In some cases the influence of the pipe wall and solids concentration have to be considered. Clauss [9] provides equations that show a good fit with measured values.

Table 1 Conversion of parameters for gas and liquid flow

	ϵ	$\dot{x}$	c_v	c_T
ϵ		$\frac{1}{1 + \dot{x}(\rho_{g,\mathrm{Q}}/\rho_s)(v_{g,\mathrm{Q}}/v_s)}$	$1 - c_v$	$\frac{1}{1 + [c_T/(1-c_T)](v_{g,\mathrm{Q}}/v_s)}$
$\dot{x}$	$\frac{1-\epsilon}{\epsilon}\frac{v_s}{v_{g,\mathrm{Q}}}\frac{\rho_s}{\rho_{g,\mathrm{Q}}}$	–	$\frac{c_v}{1-c_v}\frac{v_s}{v_{g,\mathrm{Q}}}\frac{\rho_s}{\rho_{g,\mathrm{Q}}}$	$\frac{c_T}{1-c_T}\frac{\rho_s}{\rho_{g,\mathrm{Q}}}$
c_v	$1 - \epsilon$	$1 - \frac{1}{1+\dot{x}(\rho_{g,\mathrm{Q}}/\rho_s)(v_{g,\mathrm{Q}}/v_s)}$	–	$\frac{1}{1+[(1-c_T)/c_T](v_s/v_{g,\mathrm{Q}})}$
c_T	$\frac{1}{1+[\epsilon/(1-\epsilon)](v_{g,\mathrm{Q}}/v_s)}$	$\frac{1}{1 + (1/\dot{x})(\rho_s/\rho_{g,\mathrm{Q}})}$	$\frac{1}{1+[(1-c_v)/c_v](v_{g,\mathrm{Q}}/v_s)}$	–

© 1983 Hemisphere Publishing Corporation

Table 2 Correlations of drag coefficient of a single spherical particle

Equation	Defined range	Author
$\xi = \frac{24}{Re_s}$	$Re_s \leq 0.2$	Stokes [22]
$\xi = \frac{21}{Re_s} + \frac{6}{\sqrt{Re_s}} + 0.28$	$0.1 \leq Re_s \leq 4 \times 10^3$	Kürten et al. [7]
$\xi = 0.47$	$2 \times 10^4 \leq Re_s \leq 10$	

(c) Velocity ratio

According to the relationships shown in Sec. A(a), the solid velocity in a vertical pipe is given under certain simplified conditions $(v_g/w_{so} \leq 10)^{\dagger}$ by

$$v_s = v_g - w_{so} \tag{8}$$

From this the velocity ratio can be derived:

$$\frac{v_s}{v_g} = 1 - \frac{w_{so}}{v_g} \tag{9}$$

The relationships are more complicated in horizontal conveyance. For coarse-grained materials, Eq. (23) may be used.

(d) Pressure loss

I. General

The pressure drop $\Delta p/l$ along the conveying pipe is an essential parameter for the design of pneumatic conveying systems. This pressure drop is dependent on numerous parameters:

Ap = *f* (roughness of the pipe wall, conveyor length, pipe diameter, density and viscosity of the fluid, fluid velocity, material to be transported, material of the pipe, size and density of the particles, velocity of the particles, inclination of the pipe, particle size distribution, electrostatic properties, adhesiveness, cohesiveness, and moisture)

†At higher velocities $(v_g/w_{so} > 10)$, the influence of friction caused by particle-wall impacts and particle-particle impacts cannot be neglected any more. In these cases, the relative velocity w can be calculated with less simplified equations of motion according to Weidner [16], p. 148, equation (27); or Weber [2], p. 121, equation (4.7).

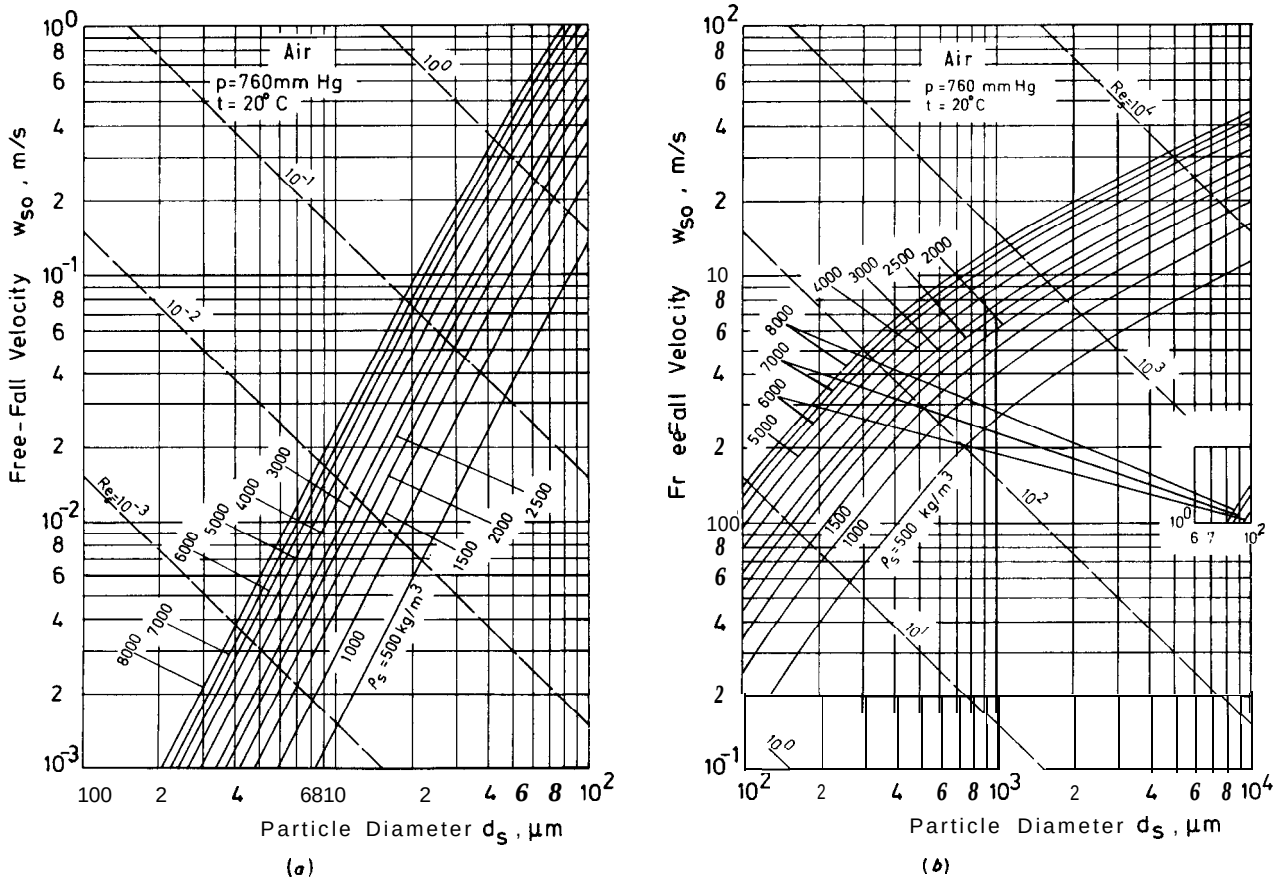

Figure 5 Free-fall velocity of a single particle in air [2]. (a) Low Reynolds numbers; (b) high Reynolds numbers.

© 1983 Hemisphere Publishing Corporation

In many cases it is therefore necessary to carry out experiments in a test rig because no computation formula gives sufficiently exact results. Only approximate values can be obtained by empirical equations shown in the following material.

Under some simplified assumptions the pressure drop may be regarded as being composed of the following parts:

1. Pressure loss $\Delta p_{g,\ell}$ of the fluid flow
2. Pressure loss Ap, generated by the solid friction
3. Pressure loss Δp_{sH} generated by the solids weight in a nonhorizontal pipe
4. Pressure loss Δp_{sA} generated by the acceleration of the solids at the beginning of the pipe
5. Pressure loss Δp_{sB} generated by the acceleration of the solids after bends

$$\Delta p = \Delta p_{g,\ell} + \Delta p_s + \Delta p_{sH} + \Delta p_{sA} + \Delta p_{sB} \tag{10}$$

According to Barth [10], the above equation may be written for gas-solid mixtures as follows, where the same sequence is valid:

$$\Delta p = \epsilon(f_g + \dot{x} f_s)\frac{l}{D}\frac{\rho_g}{2} v_g^2 + \dot{x}\frac{v_g}{v_s}\epsilon\rho_g g_n l \sin\delta + \epsilon\dot{x}\rho_g v_g(v_s + \Delta v_s) \tag{11}$$

The velocity of the gas is determined from the mass flow rate of the solids $\dot{M}_s$, the cross-sectional area of the pipe S, and a chosen mass flow ratio $\dot{x}$:

$$v_g = \frac{\dot{M}_s}{\dot{x}\rho_g S\epsilon} \tag{12}$$

For dilute phase flow, the most frequent case of pneumatic conveying $(\dot{x} < 30)$, the porosity approaches unity $(\epsilon \approx 1)$.

At higher mass flow ratios $(\dot{x} > 30)$, the velocity of the gas may be calculated more exactly by the following equation for vertical flow:

$$v_{gv} = \frac{\dot{M}_s}{\dot{x}\rho_g S}\left(1 + \frac{\rho_g/\rho_s}{1/\dot{x} - \rho_g w_{so} S/\dot{M}_s}\right) \tag{13}$$

In this case, the porosity follows from Eq. (12) and the velocity of the solid from Eq. (8). For horizontal pneumatic conveying at mass flow ratios $\dot{x} > 30$, Eq. (23) has to be used. By using Eq. (12) approximately with $\epsilon \approx 1$ to receive the Froude number, $\mathrm{Fr} = v_g^2/Dg_n$, an approximate velocity ratio $(v_g/v_s)^*$ follows from Eq. (23). This results in

$$v_{gh} = \frac{\dot{M}_s}{\dot{x}\rho_g S\{1/[1 + (v_g/v_s)^*(\rho_g/\rho_s)\dot{x}]\}} \tag{14}$$

Having obtained approximate values with $\epsilon \approx 1$, Eqs. (14) and (23) may be used iteratively to improve the accuracy of the results.

The friction factor $f_{g,\ell}$ for the fluid flow can be described by numerous empirical formulas. As an example, the correlation according to Blasius is given for smooth pipes:

$$f_{g,\ell} = 0.316\,4\sqrt[4]{\frac{1}{\mathrm{Re}}} \tag{15}$$

with

$$\mathrm{Re} = \frac{D v_{g,\ell}}{\nu} \tag{16}$$

II. Solid friction factor

The solid friction factor f_s, like the pressure loss Ap, depends on numerous parameters. In the following some examples of empirical correlations are given.

(i) Solid friction factor for horizontal pneumatic conveyance of powdered materials. The following correlation for the solid friction factor according to Stegmaier [11] is adapted for powdered materials $(d_s < 150\ \mu\mathrm{m})$ in horizontal conveying pipes. It is applicable to dilute and dense phase flow.

$$f_s = \frac{2.1(\mathrm{Fr}_w)^{0.25}}{\dot{x}^{0.3}(d_s/D)^{0.1}\mathrm{Fr}} \tag{17}$$

with

$$\mathrm{Fr}_w = \frac{w_{so}^2}{d_s g_n} \tag{18}$$

and

$$\mathrm{Fr} = \frac{v_g^2}{Dg_n} \tag{19}$$

Figure 6 shows $f_s\dot{x}^{0.3}(d_s/D)^{0.1}(\mathrm{Fr}_w)^{-0.25}$ versus $\sqrt{\mathrm{Fr}}$.

(ii) Solid friction factor for horizontal conveyance of coarse-grained materials. The subsequent correlation for the solid friction factor f_s may be used in the case of materials with grain sizes from 0 to 40 mm in horizontal pipes. It was derived by Schuchart [12].

$$f_s = 2.7\left(\dot{x} + \frac{\rho_s}{\rho_g}\right)^{-1}\frac{D}{d_s}\frac{v_g}{v_s}\left(1 - \frac{v_s}{v_g}\right)^2\frac{\xi}{K^2} \tag{20}$$

with K as the shape factor,

$$\xi = \frac{24}{\mathrm{Re}_s} + \frac{4}{\sqrt{\mathrm{Re}_s}} + 0.4 \tag{21}$$

and

$$\mathrm{Re}_s = \frac{d_s(v_g - v_s)}{\nu} \tag{22}$$

© 1983 Hemisphere publishing Corporation

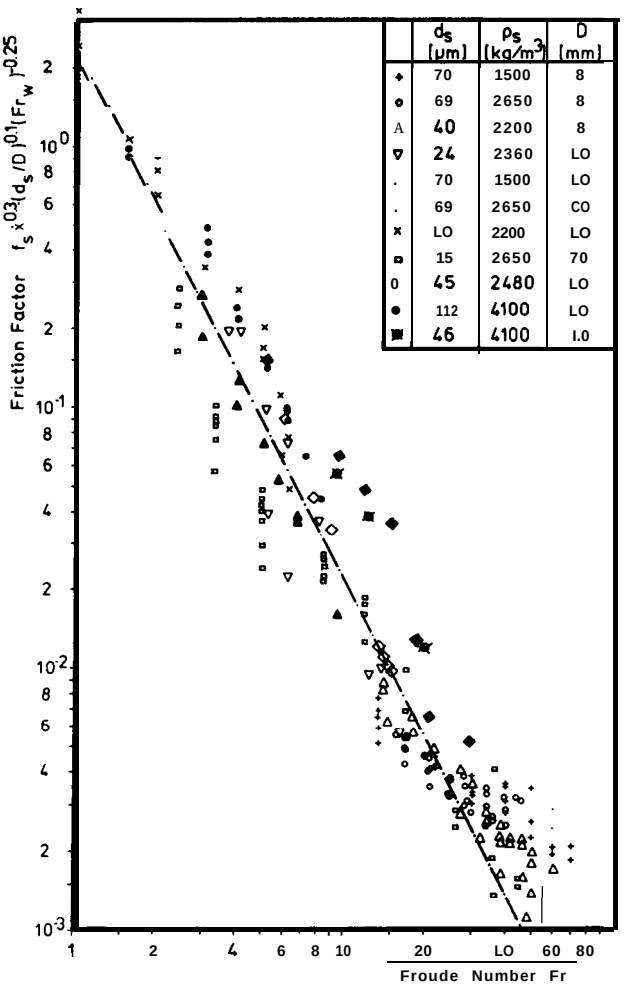

Figure 6 Correlation for the solid friction factor according to Stegmaier [11].

Equation (20) contains the velocity ratio v_g/v_s, which can be computed according to [12],

$$\frac{v_g}{v_s} = 1 + C^*\left(\frac{\rho_s}{\rho_g} - 1\right)^{2/3}\left(\frac{d_s}{D}\right)^{2/3}\left(1 + \frac{200}{\mathrm{Fr} - 100}\right) \quad (23)$$

with Eq. (19) for the Froude number,

$$\mathrm{Fr} = \frac{v_g^2}{Dg_n}$$

Empirical values for the factor C* amount to 0.014-0.09 (usually 0.015) depending on the material to be conveyed. In Figs. 7 and 8 the friction factor f_s and the velocity ratio v_g/v_s are shown.

(iii) Solid friction factor for vertical pneumatic conveyance. The solid friction factor f_s for vertical pneumatic conveyance and a relatively low mass flow ratio ($\dot{x}$ < 20) may be computed with relative high accuracy according to Kerker [13]:

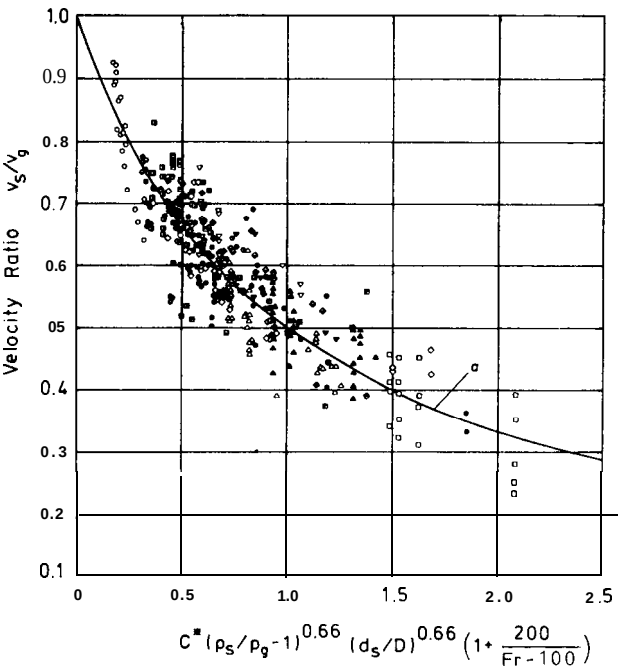

Figure 7 Velocity ratio for horizontal conveying according to Schuchart [12].

$$f_s = \frac{1}{1 + 217(1-\epsilon)}(3.13 \times 10^{-5})\left(\frac{g_n d_s^3}{\nu^2}\right)^{0.26}\frac{v_s}{v_g} \times \left[\left(\frac{v_{ss}}{v_s}\right)^{0.5}\left(\frac{v_s^2}{g_n d_s}\right)^{-0.25}\left(\frac{g_n d_s^3}{\nu^2}\right)^{0.16}\left(\frac{D}{d_s}\right) + (1.55 \times 10^{-3})\left(\frac{v_{ss}^2}{g_n d_s}\right)^{0.5}\right] \quad (24)$$

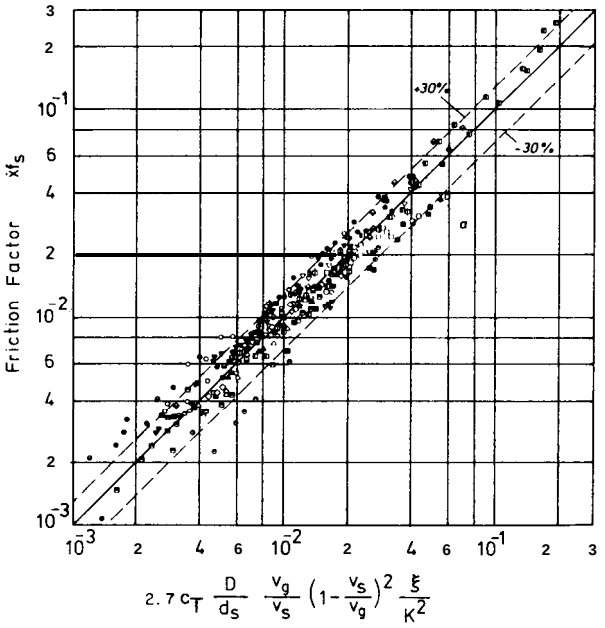

Figure 8 Solid friction factor for horizontal conveying according to Schuchart [12].

© 1983 Hemisphere Publishing Corporation

where v_{ss} is the sound velocity of the solid material. The accuracy is approximately 30%, as shown in Fig. 9, and is thus much higher than that obtained by other authors. The parameters varied as follows: D = 53 and 80 mm, $0.1 \leqslant d_s \leqslant 1.07$ mm, $1\,050 \leqslant \rho_s \leqslant 8\,650$ kg/m^3. For a simple estimate the correlation of Capes and Nakamura [14] may suffice in some cases. It gives good results on an average, but may show great differences in special cases when compared to experimental results.

$$f_s = \frac{0.193 v_s^{-1.22}}{\dot{x}} \qquad (25)$$

v_s is to be introduced in meters per second.

III. Pressure losses in bends

A certain separation of the solid material from the conveying fluid occurs due to the centrifugal forces acting on the solid-fluid mixture flowing in bends. The particles are decelerated owing to the higher wall friction. A pressure loss occurs in the adjoining straight section of the pipe because of the ensuing acceleration of the solids.

Velocity losses are different depending on the position of the bend (horizontal, horizontal-vertical, vertical-horizontal). The pressure losses in bends depend on the type of the material and the radius of the bend [16].

Investigations of pressure losses in bends were carried out by Uematu and Morikawa [1 S] , Weidner [16], Siegel [17], and Schuchart [12] . According to Weidner [16] , the additional pressure loss in the bend Δp_{sB} will amount to

$$\Delta p_{sB} = \dot{x} \rho_g (v_{sr} - v_{s,\,\mathrm{out}}) v_g \epsilon \qquad (26)$$

where v_{sr} is the velocity of solids after reacceleration.

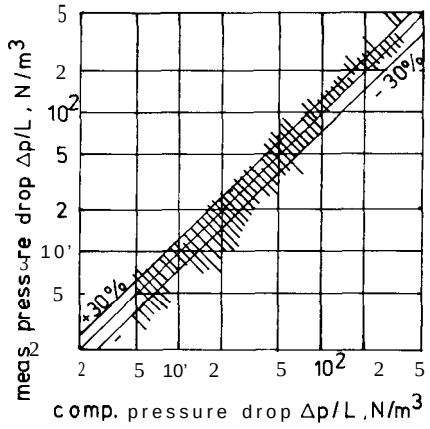

Figure 9 Comparison of measured and computed data according to Kerker [13].

Figure 10 shows the inlet and outlet velocities for different types of bends.

The influence of branching was studied by Jung [18] and Lempp [19].

IV. Layout of fluidized-bed gravity conveyors

Fluidization of the material may be computed according to the equations shown in Sec. 2.5.5. It should be mentioned here that the actual fluidization velocity should be 2.5-6 times the minimum fluidization velocity.

The mass flow conveyed by a fluidized-bed gravity conveyor may be approximately determined according to Muschelknautz et al. [20] as follows:

$$\dot{M}_s = \frac{H^{3.5} B^{1.5}}{K_R (1 + 2H/B)^2} [(1-\epsilon)\rho_s]^3 g_n \sin\delta \qquad (27)$$

where H is the height and B the width of the fluidized bed. The empirical factor K_R amounts to 15-20 N^2 s/m^4. A more accurate computation is possible according to the equations and empirical factors shown in [21].

(i) Example. In a pneumatic conveying plant consisting of three vertical and one horizontal pipe section according to Fig. 11, 3 600 kg/h of fine spherical grain is to be conveyed and simultaneously refrigerated with air at room temperature. The mixture ratio is assumed to be $\dot{x} = 5$:

$T = 293$ K	ρ_s = 2 500 kg/m^3
ρ_g = 1.2 kg/m^3	v_{ss} = 3 500 m/s
ν_g = 15.1 X 10^{-6} m^2/s	d_s = 200 μm

Since the pressure loss is not yet known, this example is calculated using the air density at atmospheric pressure (760 torr). This density and the corresponding kinematic viscosity will be kept constant to simplify matters. For the determination of the settling velocity w_{so}, diagram Fig. 5b can be used. For a more exact calculation and for discrete cases, the density and the viscosity along the conveying pipe must be corrected sectionwise to correspond more closely to the actual conditions. The density and viscosity of the air vary not only due to pressure loss but also due to heat transfer. The settling velocity of the solids must be determined using Eqs. (6) and (7) and using the drag coefficient ξ according to Table 2. Since in Eq. (6) the drag coefficient ξ is a function of Reynolds number, the calculation must of necessity be performed by successive approximation.

(ii) Calculational procedure. At first the settling velocity of the solids is determined from Fig. 5b for

© 1983 Hemisphere publishing Corporation

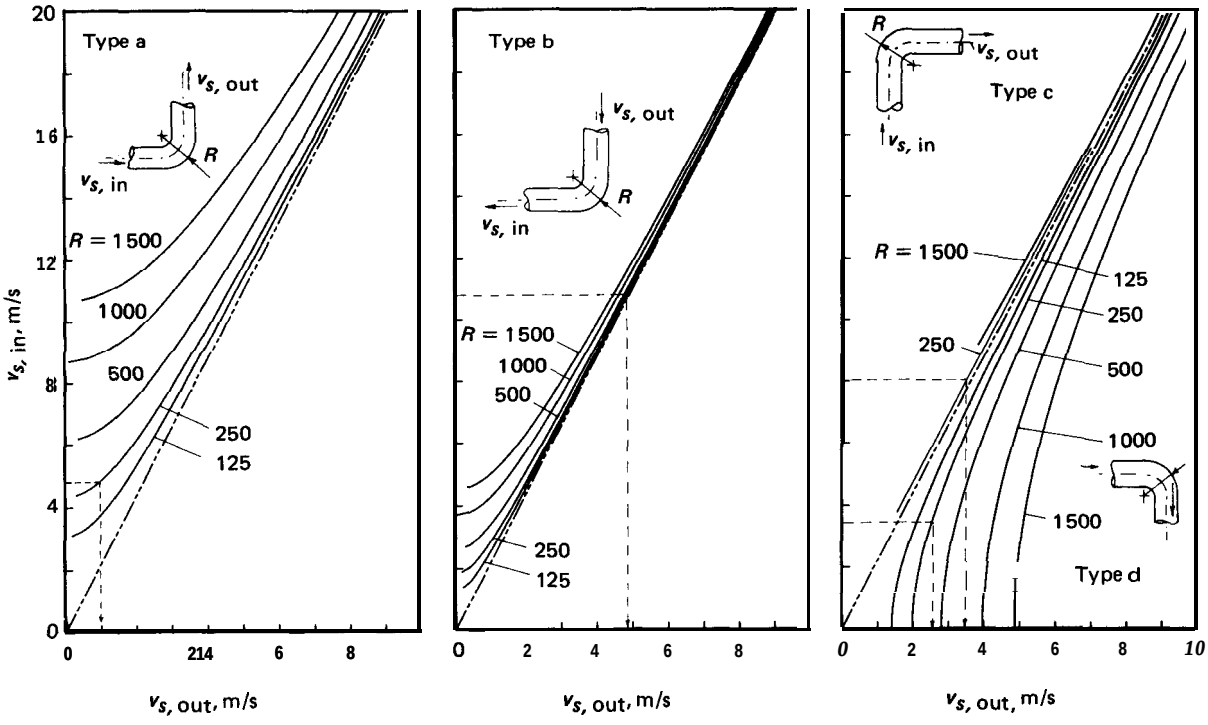

Figure 10 Computed exit velocities in bends according to Weidner [16], for different bend radii R and entry velocities. Medium: gas; Solid: sand. Bend angle AS = 90 . Mechanical friction factor ξ_F = 0.5 (horizontal bend interrupted line for all radii, bends in vertical plane full lines).

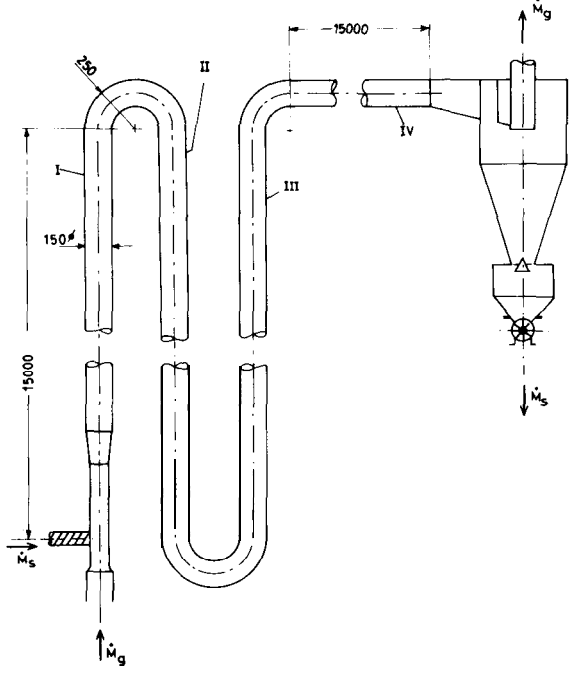

Figure 11 Layout of a pneumatic conveying plant with simultaneous refrigeration of the conveyed solids for the calculation example.

the given data for air and solids as

w_{s0} = 1.4 m/s

With $\epsilon \approx 1$ and D = 0.15 m, Eq. (12) yields the air velocity as

$v_g = 9.43$ m/s

With this the Reynolds number is given according to (16) as

Re = 9.36 X 10^4

and according to Eq. (15) the friction factor for pure air amounts to

f_g = 0.018

The solids velocity in pipe section I is given according to Eq. (8) as

$v_{s,I}$ = ***8.03*** m/s

According to Eq. (24), the solids friction factor f_s for pipe section I is given with $(1-\epsilon)_I$ = 2.81 X 10^{-3} according to Table 1:

$f_{s,I} = f_{s,III}$ = ***0.013 8***

For pipe section II (downward flow) the solids friction factor amounts to [with $v_{s,II}$ = 10.83 m/s and $(1-\epsilon)_{II}$ = ***2.08 X*** 10^{-3}]

© 1983 Hemisphere Publishing Corporation

$f_{s,\,II} = 0.015\,9$

For the horizontal pipe section IV, Eq. (17) yields

$f_{s,\,IV} = 0.233\,6$

Using the radius of the outer wall of the pipe bend as $R = 0.250$ m, the following solids velocities at entrance and exit are obtained according to Fig. 10 corresponding to the applicable bend types:

Type	1. Pipe bend c and d	2. Pipe bend b and a	3. Pipe bend C
v_s, in m/s	8.03	10.83	8.03
$v_{s,\,out}$, m/s	2.6	1.0	3.5

(iii) Pressure losses. For pipe section I the following pressure loss components are obtained using the above data and using Eqs. (10) and (11) ($l = 15$ m):

$$\Delta p_g = 0.018\frac{15}{0.15}\frac{1.2}{2}(9.43)^2 = 0.018 \text{ X } 5\,335.5$$

$$= 96 \text{ N/m}^2$$

$$\Delta p_s = 5 \text{ X } 0.013\,8 \text{ X } 5\,335.5 = 368 \text{ N/m}^2$$

$$\Delta p_{sH} = 5\,\frac{9.43}{8.03}\,1.2 \text{ X } 9.81 \text{ X } 15 = 1\,037 \text{ N/m}^2$$

$$\Delta p_{sA} = 5 \text{ X } 1.2 \text{ X } 9.43 \text{ X } 8.03 = 454 \text{ N/m}^2$$

$$\Sigma \Delta p_I = 1\,955 \text{ N/m}^2$$

For pipe section II,

$$\Delta p_g = 96 \text{ N/m}^2$$

$$\Delta p_s = 5 \text{ X } 0.015\,9 \text{ X } 5\,335.5 = 424 \text{ N/m}^2$$

$$\Delta p_H = -5\,\frac{9.43}{10.83}\,1.2 \text{ X } 9.8 \text{ X } 15 = -769 \text{ N/m}^2$$

$$\Delta p_{sB} = 5 \text{ X } 1.2 \text{ X } 9.43(10.83 - 2.6) = 466 \text{ N/m}^2$$

[Eq. (26)]

$$\Sigma \Delta p_{II} = 217 \text{ N/m}^2$$

For pipe section III,

$$\Delta p_g = 96 \text{ N/m}^2$$

$$Ap, = 368 \text{ N/m}^2$$

$$\Delta p_H = 1\,037 \text{ N/m}^2$$

$$\Delta p_{sB} = 5 \text{ X } 1.2 \text{ X } 9.43(8.03 - 1) = 398 \text{ N/m}^2$$

$$\Sigma \Delta p_{III} = 1\,899 \text{ N/m}^2$$

For pipe section IV,

$$\Delta p_g = 96 \text{ N/m}^2$$

$$\Delta p_s = 5 \text{ X } 0.233\,6 \text{ X } 5\,335.5 = 6\,232 \text{ N/m}^2$$

$$\Delta p_{sB} = 5 \text{ X } 1.2 \text{ X } 9.43(9.43 - 3.5) = 335 \text{ N/m}^2$$

$$\Sigma \Delta p_{IV} = 6\,663 \text{ N/m}^2$$

The total pressure loss for all four pipe sections amounts to

$$\Delta p_{tot} = 10\,734 \text{ N/m}^2$$

Nomenclature for Section 2.3.3 appears at the end of Section 2.3.4.

REFERENCES FOR SECTION 2.3.3

1. Brauer, H., ***Grundlagen der Einphasen- und Mehrphasenströmungen,*** Verlag Sauerländer, Frankfurt/Main, 1971.
2. Weber, M., ***Strömungsfördertechnik,*** Krausskopf Verlag, Mainz, 1974.
3. Boothroyd, R. ***G., Flowing Gas-Solids Suspensions,*** Chapman & Hall, London, 1971.
4. ***Soo, S.*** L., ***Fluid Dynamics of Multiphase Systems,*** Blaisdell, Waltham, Mass., 1967.
5. Zenz, F. A., and Othmer, D. F., ***Fluidization and Fluid-Particle Systems,*** Reinhold, New York, 1960.
6. Leva, M., ***Fluidization,*** McGraw-Hill, New York, 1959.
7. Kürten, H., Raasch, J., and Rumpf, H., Beschleunigung eines kugelformigen Feststoffteilchens im Strömungsfeld konstanter Geschwindigkeit, ***Chem Ing. Tech., vol. 9,*** pp. 941-948, 1966.
8. Torobin, L. B., and Gauvin, W. H., Fundamental Aspects of Solids-Gas-Flow, Part IV, The Effects of Particle Rotation, Roughness and Shape, ***Can J. Chem. Eng., vol. 39,*** pp. 142-153, 1960.
9. Clauss, G., Slip and Friction Losses in Deep Sea Hydraulic Lifting of Solids, ***Mar. Technol.,*** vol. 2, pp. 53-60, 1977.
10. Barth, W., Strömungstechnische Probleme der Verfahrenstechnik, ***Chem. Ing. Tech., vol. 26,*** pp. 29-34, 1954.
11. Stegmaier, W., Zur Berechnung der horizontalen pneumatischen Förderung feinkörniger Feststoffe, fördern und heben, vol. 28, pp. 363-366, 1978.
12. Schuchart, P., Widerstandsgesetze beim pneumatischen Transport durch gerade Rohre und Rohrkrümmer, Dissertation, Technische Universitlt Berlin, 1968, and ***Chem. Ing. Tech.,*** vol. 21/22, pp. 1060-1067, 1968.
13. Kerker, L., Druckverlust und Partikelgeschwindigkeit in der Anlaufstrecke bei der vertikalen Gas-Feststoffstromung, Dissertation, Universität Karlsruhe, 1977.
14. Capes, C. E., and Nakamura, K., Vertical Pneumatic Conveying, ***Can J. Chem. Eng.,*** vol. 51, pp. 31-38, 1973.
15. Uematu, T., and Morikawa, Y., Druckverluste in Krümmern einer waagrechten Förderung von körnigen Gütern, *Bull. JSME,* vol. 15, pp. 531-538, 1961.

© 1983 Hemisphere Publishing Corporation

16. Weidner, G., Grundsatzliche Untersuchungen iiber den pneumatischen Fördervorgang, insbesondere iiber die Verhältnisse bei Beschleunigung und Umlenkung, *Forsch. Ingenieurwes.*, vol. 21, pp. 145-155, 1955.
17. Siegel, W., Experimentelle Untersuchungen zur pneumatischen Förderung körniger Stoffe in waagrechten Rohren und Überprüfung der Ähnlichkeitsgesetze, VDI-Forsch.-Heft 538, VDI-Verlag, Dusseldorf, 1970.
18. Jung, R., Der Druckverlauf beim pneumatischen Staubtransport durch ein Kreisrohr veränderlichen Querschnitts, *Brennst. Waerme Kraft*, vol. 8, pp. 377-383, 1966.
19. Lempp, M., Die Strömungsverhältnisse von Gas-Feststoff-Cemischen in Verzweigungen pneumatischer Förderanlagen, *Aufbereit.* Tech., vol. 2, pp. 81-91, 1966.
20. Muschelknautz, E., Wojahn, H., Fördern, insbes. Fliessrinnenfiirderung *in Ullmanns Enzyklopädie der technischen Chemie, vol. 3,* pp. 131-184, Verlag Chemie, Weinheim, 1973.
21. Keunecke, K., Fluidisierung und Fliessbettforderung von Schüttgütern kleiner Teilchengrösse, VDI-Forschungsheft 509, VDI-Verlag Dusseldorf, 1965.
22. Stokes, G. G., On the Theories of Internal Friction of Fluids on the Motion of Pendulums, *Trans. Cam. Phil. Soc. 9, 1851.*

© 1983 Hemisphere Publishing Corporation

2.3.4
Solid-liquid flow

M. Weber and W. Stegmaier

A. Principle of hydraulic conveyance

Contrary to the pneumatic conveyance (Sec. 2.3.3), the hydraulic conveyance of granular and powdered solid materials can also be used for very long distances because the carrier fluid is so incompressible. The applied physical principles are similar to those of the pneumatic conveyance. In this section only some special aspects, different from pneumatic conveyance, will be treated.

The most essential differences between pneumatic and hydraulic conveying systems are the aforementioned incompressibility and the density of the carrier fluid. Because of the high density of the carrier fluid, the flow forces required for the transportation of solids can be achieved at relatively low flow velocities. In addition, the buoyancy of the particles in the liquid partly balances the gravitational forces. The effect on the settling velocity of the particles is apparent from Fig. 1 and Eq. 2.3.3(6).

B. Flow patterns

The flow patterns are in principle similar to those of pneumatic transportation. Differences due to the high density of the fluid exist and are manifested by higher solids concentrations for hydraulic conveyance, by lower velocities, and by solids movements that are much more attenuated.

For vertical transportation a relatively low tendency toward segregation exists as a result of the axial configuration of forces. Even for coarse material, a fairly uniform solids distribution can be expected in the pipe as long as the condition for conveyance is well satisfied. This means that the flow velocity must be much greater than the settling velocity of the solids. The vertical flow of the mixture can therefore be looked at as pseudo-homogeneous and the flow conditions can be correspondingly calculated with good accuracy.

For horizontal conveyance, gravity always assists the segregation of the solid particles, even when the corresponding transport condition is well satisfied. In this case this means that the flow velocity must be greater than a certain critical velocity at which the first single grain is deposited. In the horizontal pipe a more or less strong segregation appears depending on particle size and flow velocity. The segregation is characterized by a certain distribution of concentration.

C. Flow regimes: Horizontal conveyance

The classifications of Durand [2] and Newitt et al. [3] that have been established for hydraulic transportation of sand can be expressed in a more general manner. Fine granular material, whose characteristic Reynolds number is $Re_s < 0.02$, is nearly uniformly mixed with the carrier fluid and can be conveyed as a homogeneous suspension as long as there is turbulent flow.

The characteristic Reynolds number is calculated using the particle size, settling velocity, and kinematic viscosity of the fluid. Such a homogeneous suspension appears as a liquid with correspondingly higher density and viscosity. Only very fine solids with Re, $< 10^{-6}$ remain at rest in a uniform distribution, since they are

© 1983 Hemisphere Publishing Corporation

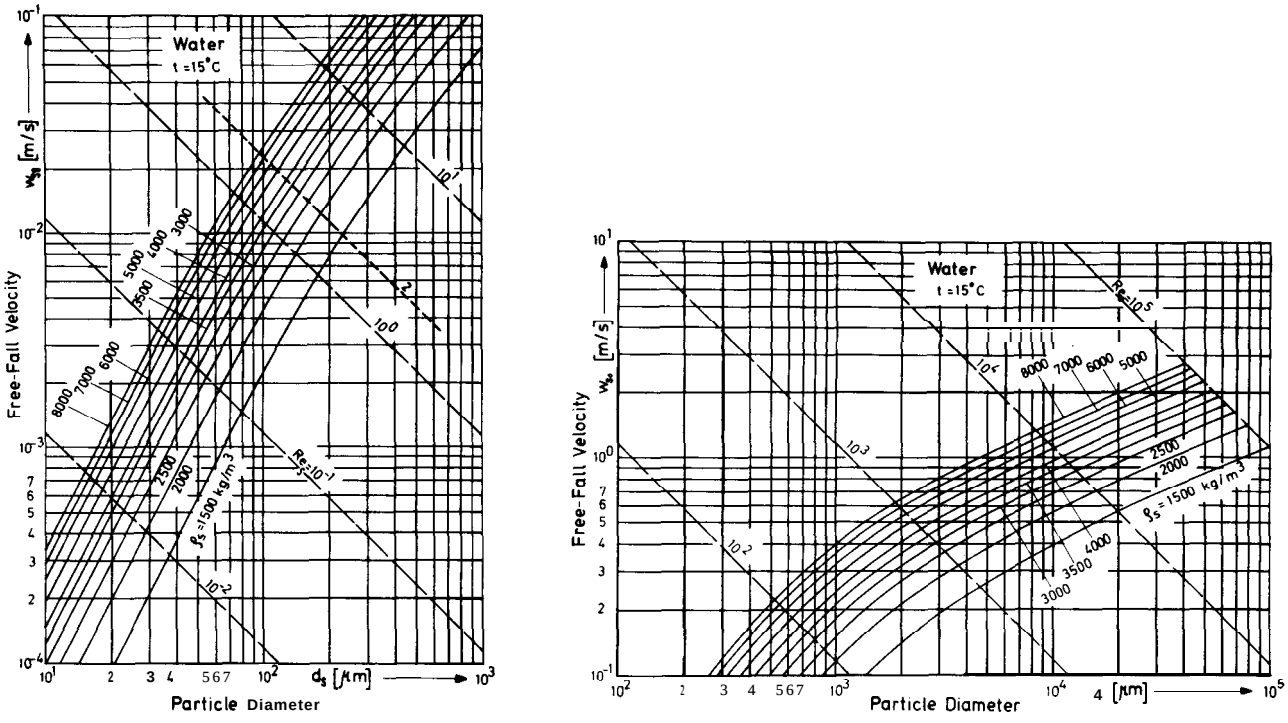

Figure 1 Free-fall velocity of a single particle in water [1].

already kept in suspension by the Brownian molecular movement (colloidal dispersion). Coarser solids cannot be kept completely in uniform suspension by turbulence. A certain degree of segregation is permitted. This type of suspension can exist at economically feasible transport velocities and is called pseudohomogeneous suspension. The Reynolds numbers range is $0.1 \leqslant \mathrm{Re}, \leqslant 2$. At these limits, in order to guarantee an equal degree of homogeneity for solids of any density, the ratio of the settling velocity and the fluid velocity, w_{so}/v_ϱ, must remain constant. The fluid velocities required for this condition can be obtained from Table 1. For larger Reynolds numbers, segregation is greater and transportation is more heterogeneous. This fact can lead to conveyance by saltation or dune movement. Normally such mixtures are differentiated according to their rheological behavior. Very fine solid-fluid mixtures display, at very high solids concentrations (c, > 35%), increasingly non-Newtonian behavior. For classification see the summary in Table 2.

D. Basic relationships for pressure losses

(a) Homogeneous and pseudohomogeneous conveyance

With Newtonian flow behavior, which means at solids concentrations of about $c_v < 35\%$ and turbulent flow, the pressure loss can be calculated for homogeneous and pseudohomogeneous transportation in the same way as for Newtonian fluids with an average density of

$$\rho_m = c_v \rho_s + (1 - c_v)\rho_\varrho \tag{1}$$

The pressure loss for the horizontal and the vertical case is

$$\frac{\Delta p}{l} = \left(\frac{\Delta p}{l}\right)_{\varrho h, \varrho v} \frac{\rho_m}{\rho_\varrho} \tag{2}$$

This is valid for homogeneous and pseudohomogeneous vertical and horizontal transportation and can also be applied to approximate the vertical conveyance of coarse material that is pseudohomogeneous relative to its solids distribution. The pressure gradient of the pure fluid must be entered correspondingly; for horizontal transportation,

$$\left(\frac{\Delta p}{l}\right)_{\varrho h} = f_\varrho \frac{\rho_\varrho}{2} \frac{v_m^2}{D} \tag{3}$$

and for vertical transportation,

$$\left(\frac{\Delta p}{l}\right)_{\varrho v} = f_\varrho \frac{\rho_\varrho}{2} \frac{v_m^2}{D} \pm g_n \rho_\varrho \tag{4}$$

v_m being the velocity of the mixture:

$$v_m = \frac{\dot{V}_s + \dot{V}_\varrho}{S} = c_v v_s + (1 - c_v) v_\varrho \tag{5}$$

where c_v is the spatial concentration of the solids.

The velocities of solids and carrier fluid are nearly

© 1983 Hemisphere Publishing Corporation

Table 1 Limits for pseudohomogeneous flow regime

ρ_s/ρ_ℓ		1.5	2	2.5	3	4	5	6	7	8
Re, = 2; w_{so}/v_ℓ = 0.005 6										
d_s	μm	231	184	162	147	128	116	108	101	96
w_{so}	cm/s	0.97	1.25	1.42	1.56	1.8	1.98	2.12	2.26	2.38
v_ℓ	m/s	1.73	2.23	2.53	2.78	3.21	3.53	3.78	4.03	4.25
Re_s = 0.1; w_{so}/v_ℓ= 0.001 46										
d_s	μm	80	63	55	49.5	43.5	39.5	36.5	34.5	33
w_{so}	cm/s	0.147	0.186	0.214	0.236	0.27	0.298	0.322	0.34	0.36
"Q	m/s	1.00	1.27	1.46	1.62	1.85	2.04	2.20	2.33	2.47

equal for homogeneous and pseudohomogeneous conveyance ($v_s \approx v_\ell \approx v_m$). Therefore, the discharge concentration c_T and the spatial concentration c_v are also nearly equal ($c_T \approx c_v$). This is no longer valid for vertical transportation of coarse solids, since in this case the settling velocity is not neglectable. Noticeable slip between solids and fluid will occur. In this case the solids velocity amounts to

$$v_s = v_\ell - w_{so} = v_m - (1 - c_v)w_{so} \tag{6}$$

The friction coefficient f_ℓ for smooth pipes can be calculated according to Eq. 2.3.3(12).

The following relationship exists between the spatial concentration and the discharge concentration:

$$c_v = c_T \frac{v_m}{v_s} = \frac{1}{1 + [(1 - c_T)/c_T](v_s/v_\ell)} \tag{7}$$

where c_T is defined by Eq. 2.3.3(5).

For higher concentrations ($c_v > 5\%$), the velocity of the solid has to be calculated by the following equation:

$$\frac{v_s}{v_m} = \frac{1}{2}\left(1 - \frac{w_s}{v_m}\right) + \sqrt{\frac{1}{4}\left(1 - \frac{w_s}{v_m}\right)^2 + c_T \frac{w_s}{v_m}} \tag{8}$$

where w_s is the settling velocity hindered by the mean density of the mixture :

$$w_s = \sqrt{\frac{4}{3}\frac{d_s}{c_w}\frac{\rho_s - \rho_m}{\rho_\ell} g_n} \tag{9}$$

(b) Heterogeneous horizontal conveyance

For heterogeneous horizontal hydraulic conveyance the pressure loss can be calculated by using Durand s relationship, which is given here in a generalized form for solids with variable density:

$$\phi = \frac{(\Delta p/l) - (\Delta p/l)_\ell}{(\Delta p/l)_\ell c_T} = K \left(\frac{gD}{v_m^2} \frac{(\rho_s - \rho_\ell)/\rho_\ell}{\sqrt{\xi}} \right)^n \tag{10}$$

where ξ is the drag coefficient of the particles. Durand supplies the values of K = 83 and n = 1.5 as a good approximation for 310 data points (see Fig. 2*a*). These measurements were made, however, using nearly uniform solids. For solids with a certain particle size distribution, which is the most common case in practice, completely different values of K and n are found. Therefore, in Fig. 2*a*, examples of a few more empirical results are given. It is recommended that tests be performed in cases of extremely wide particle size distributions and uncommon materials compositions of conveyed solids and pipe material. The results of these tests must then be correlated according to the equation above on double logarithmic paper to obtain the values of K and n for the specific combination of materials (see Fig. 2b).

The critical velocity, above which satisfactory conveyance is possible without deposition, is given according to tests made by Durand by the following formula:

Table 2 Classification of hydraulic flow regimes

Flow behavior	Rheologic behavior	Concentration by volume, %	Reynolds number, Re,
Homogeneous	Non-Newtonian	>35	co.1
Homogeneous	Newtonian	<30	
Pseudohomogeneous	Non-Newtonian	>35	0.1 ⩽ Re, ⩽ 2
Pseudohomogeneous	Newtonian	<30	
Heterogeneous	Newtonian	<30	>2

© 1983 Hemisphere Publishing Corporation

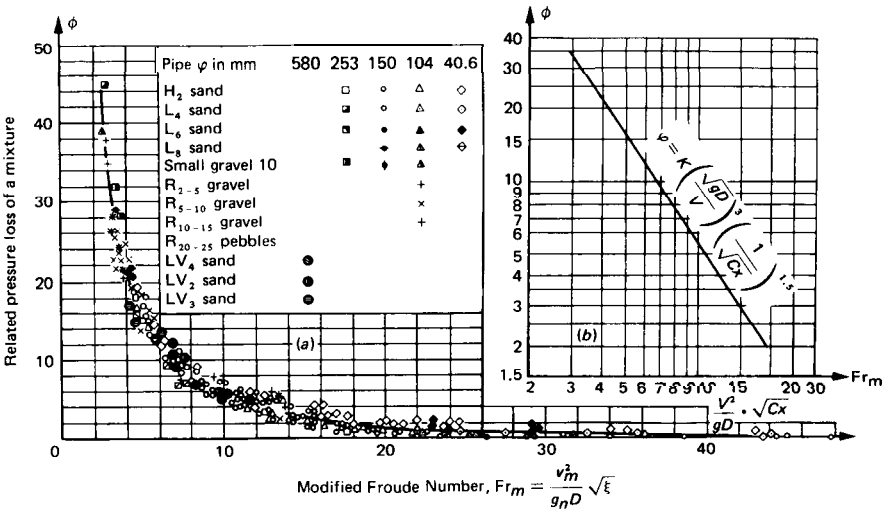

Figure 2 Durand s correlation of mixture friction losses according to[2] replotted from [4], where $\varphi = [\Delta p/l - (\Delta p/l)_{\varrho h}]/(\Delta p/l)_{\varrho h} c_T$. In this figure, adapted from Durand s original work, K amounts to K = 176, since K comprises $[(\rho_s - \rho_\varrho)/\rho_\varrho]^{1.5}$.

$$v_c = F_\varrho \sqrt{2gD\,\frac{\rho_s - \rho_\varrho}{\rho_\varrho}} \tag{11}$$

This formula has been confirmed in recent tests by Gödde [5]. F_ϱ is a function of particle diameter and concentration and can be read off Fig. 3.

The pressure losses due to acceleration can be calculated analogously to the last terms of Eq. 2.3.3(11). The initial acceleration is given by

$$\Delta p_{sA} = \frac{\dot{M}_s}{s} v_s \tag{12}$$

and the reacceleration after bends by

$$\Delta p_{sB} = \frac{\dot{M}_s}{s} \Delta v_s \tag{13}$$

where $s = \rho_s/\rho_\varrho$.

I. Example

In a hydraulic conveying plant consisting of three vertical and one horizontal pipe section according to Figs. 4 and 5, 36 t/h of fine spherical grain are to be conveyed. The transport concentration is assumed to be c_T = 5%:

$T = 288$ K $\qquad \rho_s = 2\,500$ kg/m^3

$\rho_\varrho = 1\,000$ kg/m^3 $\qquad d_s = 1$ mm

$v_\varrho = 10^{-6}$ m^2/s $\qquad D = 150$mm

For water at 288 K, the settling velocity w_{so} of various solids can be obtained from Fig. 1. For different water temperatures or different liquids, the settling velocity must be calculated using Eqs. 2.3.3(6), 2.3.3(7), and Table 2.3.3(2). For higher concentrations, Eq. (9) must be applied.

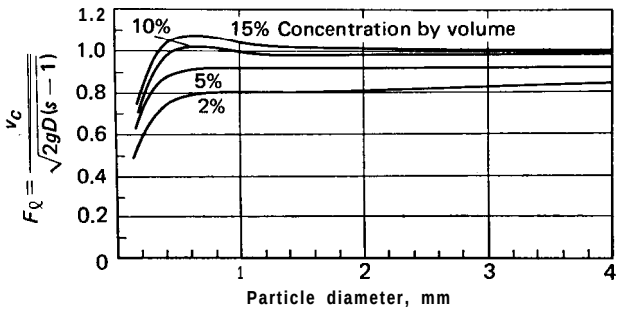

Figure 3 Critical velocity for heterogeneous mixtures according to [2] replotted from [4] ($s = \rho_s/\rho_\varrho$).

II. Calculational procedure

First the settling velocity of the solids is determined from Fig. 1 (right) for the given data for water and solids. It is found to be

w_{so} = 0.15 m/s

In this case, with the above-mentioned particle size, heterogeneous hydraulic conveyance is encountered especially in the horizontal section. The velocity of the mixture is given by Eq. 2.3.3(5) and Eq. (5) and the simple relationship $\dot{V}_s = \dot{M}_s/\rho_s$ as

$$v_m = \frac{\dot{M}_s}{s\rho_s c_T} = \frac{10}{0.017\,67 \times 2\,500 \times 0.05} = 4.53 \text{ m/s}$$

With this, the Reynolds number is given according to Eq. 2.3.3(16) as

Re = 5.9 X 10^5

© 1983 Hemisphere Publishing Corporation

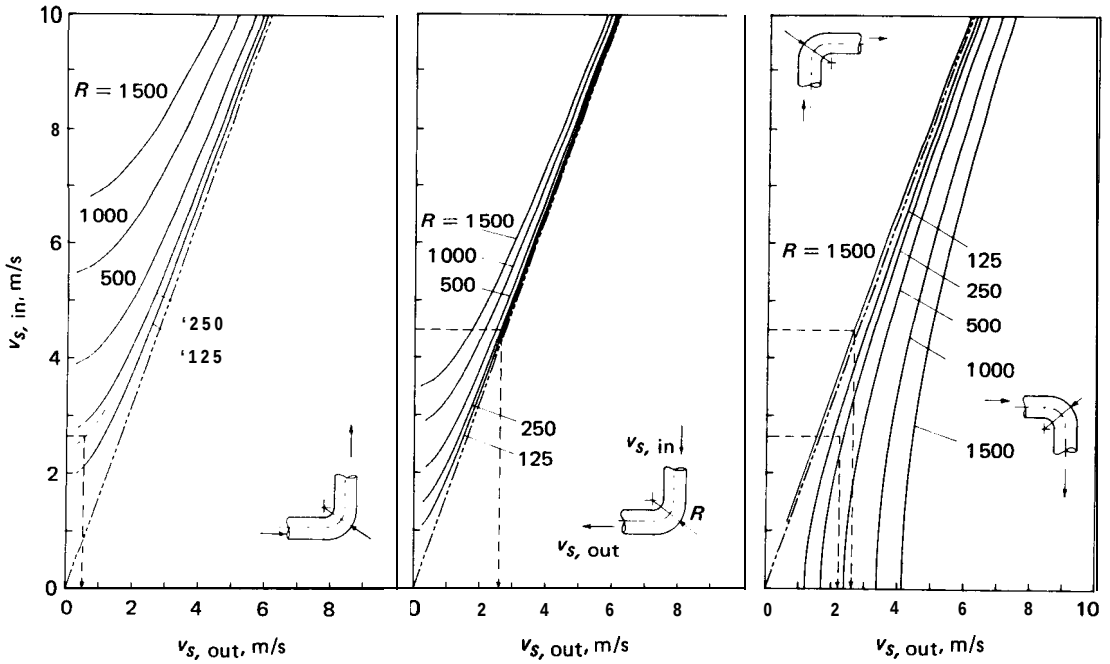

Figure 4 Computed exit velocities in bends for different bend radii R and entry velocities. Medium: water. Solid: sand. Bend angle Ad = 90°. Mechanical friction factor ξ_F = 0.5 (horizontal bend interrupted line for all radii).

and according to Eq. 2.3.3(15), the Blasius friction factor for the mixture amounts to

$f_\varrho = 0.011$

The pressure gradient of the mixture in the vertical sections I and III with upward flow is obtained from Eq. (2) using the pressure gradient of clear water according to Eq. (4) and the density of the mixture according to Eq. (1). These equations contain the influences due to friction and weight of both phases. Since the settling velocity is relatively small, $v_s \approx v_\varrho \approx v_m$ and $c_v \approx c_T$ are set with good approximation. Then the mixture density can be simply calculated as

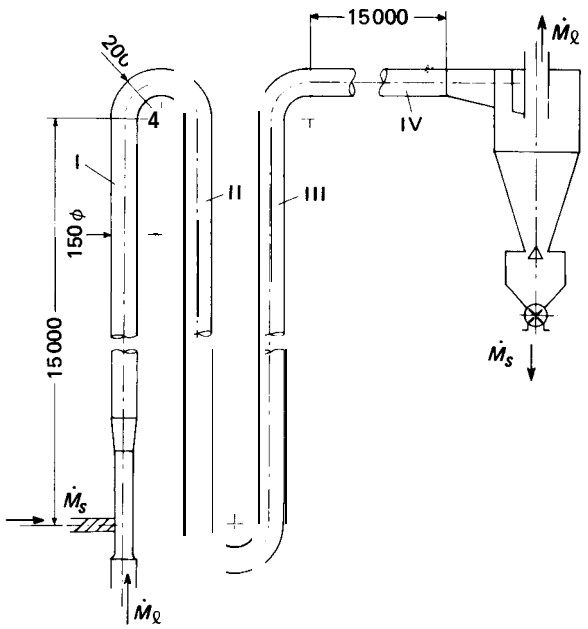

Figure 5 Layout of a hydraulic conveying plant for the calculation example.

$$\rho_m = 0.05 \times 2\,500 + 0.95 \times 1\,000$$
$$= 1\,075 \text{ kg/m}^3$$

$$\left(\frac{\Delta p}{l}\right)_{\varrho v\text{I}} = \left(\frac{\Delta p}{l}\right)_{\varrho v\text{III}} = 0.011 \frac{1\,000}{2} \frac{4.53^2}{0.15} + 9.81$$
$$\times\, 1\,000 = 10\,562 \text{ N/m}^3$$

$$\left(\frac{\Delta p}{l}\right)_{\text{I}} = \left(\frac{\Delta p}{l}\right)_{\text{III}} = 10\,562 \frac{1\,075}{1\,000} = 11\,355 \text{ N/m}^3$$

The pressure gradient of the pure liquid for pipe section II is given again by relationship (4) as

$$\left(\frac{\Delta p}{l}\right)_{\varrho v\text{II}} = 0.011 \cdot \frac{1\,000}{2} \cdot \frac{4.53^2}{0.15} \cdot 8 \cdot 1 \times 1000$$
$$= -9\,058 \text{ N/m}^3$$

and the pressure gradient of the mixture as

$$\left(\frac{\Delta p}{l}\right)_{\text{II}} = -9\,058 \frac{1\,075}{1\,000} = -9\,737 \text{ N/m}^3$$

© 1983 Hemisphere Publishing Corporation

For the horizontal section IV, Eq. (3) yields

$$\left(\frac{\Delta p}{l}\right)_{\varrho h} = 0.011 \frac{1\,000}{2} \frac{4.53^2}{0.15} = 752 \text{ N/m}^3$$

with Re, corresponding to expression 2.3.3(22) and Eq. 2.3.3(21):

Re, = 130

$$\xi = \frac{24}{130} + \frac{4}{\sqrt{130}} + 0.4 = 0.935$$

The pressure gradient is obtained by rearranging Eq. (10) to

$$\left(\frac{\Delta p}{l}\right)_{\text{IV}} = 83\left(\frac{9.81 \text{ x } 0.15\ 2\,500 - 1\ 000}{4.53^2 \quad 1\,000\sqrt{0.935}}\right)^{1.5} 752$$

$$\text{X } 0.05 + 752 = 868 \text{ N/m}^3$$

Pressure losses due to initial acceleration and reacceleration after pipe bends must be calculated from expressions (12) and (13).

With a bend radius of the outer wall of ***R = 200*** mm, Fig. 4 yields the following solids velocities at entry and exit (values are interpolated for ***R = 200*** mm):

	1. Pipe bend (2 x 90)	2. Pipe bend (2 x 90)	3. Pipe bend (1 x 90°)
$v_{s,\text{in}}$, m/s	4.53	4.53	4.53
$v_{s,\text{out}}$, m/s	-2.2	≈0.5	2.6

III. Pressure losses

For pipe section I, the following pressure loss components are obtained using the above data:

$$(\Delta p_\varrho + \Delta p_s + \Delta p_{sH} + \Delta p_{\varrho H})_{\text{I}} = 11\,355 \text{ X } 15$$

$$= 170\,325 \text{ N/m}^2$$

$$\Delta p_{sA} = \frac{4.53 \text{ X } 10}{0.017\ 67} = 2\,564 \text{ N/m}^2$$

$$\Sigma \Delta p_{\text{I}} = 172\,889 \text{ N/m}^2$$

Pipe section II:

$$(\Delta p_\varrho + \Delta p_s - \Delta p_{sH} - \Delta p_{\varrho H})_{\text{II}} = -9\,737 \text{ x } 15$$

$$= -146\,055 \text{ N/m}^2$$

$$\Delta p_{sB} = 1\,319 \text{ N/m}^2$$

$$\Sigma \Delta p_{\text{II}} = -144\,736 \text{ N/m}^2$$

Pipe section III:

$$(\Delta p_\varrho + \Delta p_s + \Delta p_{sH} + \Delta p_{\varrho H})_{\text{III}} = 170\,325 \text{ N/m}^2$$

$$\Delta p_{sB} = 2\,281 \text{ N/m}^2$$

$$\Sigma \Delta p_{\text{III}} = 172\,606 \text{ N/m}^2$$

Pipe section IV:

$$(\Delta p_\varrho + p_s)_{\text{IV}} = 868 \text{ X } 15 = 13\,020 \text{ N/m}^2$$

$$\Delta p_{sB} = 1\,092 \text{ N/m}^2$$

$$\Sigma \Delta p_{\text{IV}} = 14\,112 \text{ N/m}^2$$

The total pressure loss for all four pipe sections amounts to

$$\Delta p_{\text{tot}} = 214\,871 \text{ N/m}^2$$

NOMENCLATURE FOR SECTIONS 2.3.3-2.3.4

B	width of a fluidized-bed conveyor, m
c_T	delivered concentration by volume
c_v	concentration by volume
c *	constant
d_s	mean particle diameter, m
D	tube inside diameter, m
$f_{g,\varrho}$	Blasius friction factor of gas or liquid
f_S'	solid friction factor
F_D	drag force, N
F_W	gravitational force, N
Fr	Froude number
Fr_w	Froude number relative to a falling particle
g_n	gravitation acceleration, m
H	height of the fluidized bed in a conveyor, m
K	shape factor: ratio of free-fall velocities irregular grain to spherical grain with equal volume
K_R	constant factor, $\text{N}^2\text{s/m}^4$
l	length, m
$M_{g,\varrho}$	mass flow rate of gas or liquid phase, kg/s
$\dot{M}_s$	mass flow rate of particulate phase, kg/s
P	pressure, N/m^2
Re	Reynolds number related to fluid flow in the pipe
Re_s	Reynolds number related to a falling particle
S	cross-sectional area of pipe
$v_{g,\varrho}$	mean velocity of gas or liquid, m/s
v_m	mean velocity of the mixture, m/s
v_s	mean particle velocity, m/s
v_{ss}	velocity of sound of the solid material, m/s
$v_{s,\text{in}}$	particle velocity in bend entry, m/s
$v_{s,\text{out}}$	particle velocity in bend exit, m/s

© 1983 Hemisphere Publishing Corporation

v_{sr}	velocity of solids after reacceleration behind bends, m/s	Δp	pressure loss, N/m^2
$V_{g,\ell}$	volume of gas or liquid component, m^3	ϵ	voidage fraction
$\dot{V}_{g,\ell}$	volume flow rate of gas or liquid phase, m^3/s	ξ	drag coefficient of a single particle
V_s	volume of solid component, m^3	ξ_F	mechanical friction factor
$\dot{V}_s$	volume flow rate of particulate phase, m^3/s	$\rho_{g,Q}$	gas or liquid medium density, kg/m^3
w_s	settling velocity, m/s	ρ_S	particle density, kg/m^3
w_{so}	free-fall velocity of a single spherical particle, m/s	δ	inclination angle of the pipe
$\dot{x}$	mass flow ratio $(\dot{M}_s/\dot{M}_g)$	ν	kinematic viscosity, m^2/s

REFERENCES FOR SECTION 2.3.4

1. Weber, M., *Strömungsfördertechnik*, Krausskopf-Verlag, Mainz, 1974.
2. Durand, R., Basic Relationships of the Transport of Solids in Pipes. Experimental Research, *Proc. Minnesota Int. Hydr. Div. ASCE,* pp. 89-103, September 1953.
3. Newitt, D. M., Richardson, J. F., Abott, M., and Turtle, R. B., Hydraulic Conveying of Solids in Horizontal Pipes, *Trans. Inst. Chem. Eng.,* vol. 33, pp. 93-110, 1955.
4. Bain, A. G., and Bonnington, S. T., *The Hydraulic Transport of Solids by Pipelines,* Pergamon, New York, 1970.
5. Gödde, E., Untersuchungen zur kritischen Geschwindigkeit heterogener hydraulischer Feststofförderung in horizontalen Rohren, Dissertation, University of Karlsruhe, 1977.

© 1983 Hemisphere Publishing Corporation

2.4
Heat conduction

Contents

2.4.1
BASIC EQUATIONS, H. Martin 2.4.1-1

2.4.2
STEADY STATE, H. Martin 2.4.2-1

A. Plane, cylindrical, and spherical shells without internal heat sources **2.4.2-1**
B. Temperatures in standard bodies with internal heat sources **2.4.2-3**

2.4.3
TRANSIENT RESPONSE TO A STEP CHANGE OF TEMPERATURE, H. Martin 2.4.3-1

A. One-dimensional systems **2.4.3-1**
B. Multidimensional systems **2.4.3-10**
C. Coupled thermal fields **2.4.3-12**

2.4.4
MELTING AND SOLIDIFICATION, H. Martin 2.4.4-1

2.4.5
PERIODIC CHANGE OF TEMPERATURE, H. Martin 2.4.5-1

References for Sections 2.4.1-2.4.5 **2.4.5-4**

2.4.6
THERMAL CONTACT RESISTANCE, T. F. Irvine, Jr. 2.4.6-1

A. Introduction **2.4.6-1**
B. Thermal contact conductance **2.4.6-1**
C. Numerical example **2.4.6-3**
D. Discussion **2.4.6-4**

References for Section 2.4.6 **2.4.6-4**

© 1983 Hemisphere Publishing Corporation

HEDH

2.4.1

Basic equations

H. Martin

■ The analysis of the temperature distribution in a body is based on the first law of thermodynamics (the energy balance) and Fourier s equation of heat conduction (the rate equation). The energy balance, applied to an incremental volume of an incompressible medium at rest, may be written

$$\rho c_p \frac{\partial T}{\partial t} = -(\nabla \cdot \dot{\mathbf{q}}) \tag{1}$$

Equation (1) states that the internal energy, and so the temperature of the volume, will rise if the divergence of the heat flux is less than zero, that is, if the heat fluxes into the volume exceed the outward-directed ones.

Additional contributions to the internal energy- for example, by conversion of mechanical (viscous dissipation), electrical, chemical, or nuclear energy- may be accounted for by adding the appropriate source term to the right side of Eq. (1).

The heat flux vector can be expressed in terms of the temperature gradient by Fourier s equation:

$$\dot{\mathbf{q}} = -\lambda \nabla T \tag{2}$$

The direction of the heat flux coincides with that of the negative temperature gradient unless the thermal conductivity λ depends on direction as it does for anisotropic media such as crystals or wood.

Combining the energy balance Eq. (1) and the rate equation (2) yields a partial differential equation for the temperature distribution:

$$\rho c_p \frac{\partial T}{\partial t} = (\nabla \cdot \lambda \nabla T) \tag{3}$$

With constant thermal conductivity λ, Eq. (3) may be simplified, introducing the thermal diffusivity $\kappa = \lambda/(\rho c_p)$, to

$$\frac{\partial T}{\partial t} = \kappa \nabla^2 T \tag{3a}$$

The various differential vector operations symbolized in Eqs. (1) to ***(3a)*** by the nabla or del operator V are specified in Table 1 in Cartesian, cylindrical, and spherical coordinates for convenience.

© 1983 Hemisphere Publishing Corporation

HEDH

Table 1 Vector operations in cartesian, cylindrical, and spherical coordinates

	Cartesian coordinates (x, y, z)	Cylindrical coordinates (r, φ, z)	Spherical coordinates (r, ϑ, ψ)
Gradient $\nabla\vartheta$	$\mathbf{e}_x \frac{\partial\vartheta}{\partial x} + \mathbf{e}_y \frac{\partial\vartheta}{\partial y} + \mathbf{e}_z \frac{\partial\vartheta}{\partial z}$	$\mathbf{e}_r \frac{\partial\vartheta}{\partial r} + \mathbf{e}_\varphi \frac{1}{r}\frac{\partial\vartheta}{\partial\varphi} + \mathbf{e}_z \frac{\partial\vartheta}{\partial z}$	$\mathbf{e}_r \frac{\partial\vartheta}{\partial r} + \mathbf{e}_\varphi \frac{1}{r \sin\psi}\frac{\partial\vartheta}{\partial\varphi} + \mathbf{e}_\psi \frac{1}{r}\frac{\partial\vartheta}{\partial\psi}$
Divergence $\nabla\dot{q}$	$\frac{\partial\dot{q}_x}{\partial x} + \frac{\partial\dot{q}_y}{\partial y} + \frac{\partial\dot{q}_z}{\partial z}$	$\frac{1}{r}\frac{\partial}{\partial r}(r\dot{q}_r) + \frac{1}{r}\frac{\partial\dot{q}_\varphi}{\partial\varphi} + \frac{\partial\dot{q}_z}{\partial z}$	$\frac{1}{r^2}\frac{\partial}{\partial r}(r^2\dot{q}_r) + \frac{1}{r\sin\psi}\frac{\partial\dot{q}_\varphi}{\partial\varphi} + \frac{1}{r\sin\psi}\frac{\partial}{\partial\psi}(\dot{q}_\psi \sin\psi)$
Laplacian $\nabla^2\vartheta$	$\frac{\partial^2\vartheta}{\partial x^2} + \frac{\partial^2\vartheta}{\partial y^2} + \frac{\partial^2\vartheta}{\partial z^2}$	$\frac{1}{r}\frac{\partial}{\partial r}\left(r\frac{\partial\vartheta}{\partial r}\right) + \frac{1}{r^2}\frac{\partial^2\vartheta}{\partial\varphi^2} + \frac{\partial^2\vartheta}{\partial z^2}$	$\frac{1}{r^2}\frac{\partial}{\partial r}\left(r^2\frac{\partial\vartheta}{\partial r}\right) + \frac{1}{r^2\sin^2\psi}\frac{\partial^2\vartheta}{\partial\varphi^2} + \frac{1}{r^2\sin\psi}\frac{\partial}{\partial\psi}\left(\sin\psi\frac{\partial\vartheta}{\partial\psi}\right)$
Relation to Cartesian coordinates		$x = r\cos\varphi$ $y = r \sin 9$ z = z	$x = r\cos\varphi\sin\psi$ y = r sin 9 sin ψ z = r cos ψ

e unit vector

Nomenclature for Section 2.4.1 appears at the beginning of Part 2.

© 1983 Hemisphere Publishing Corporation

2.4.2
Steady state

H. Martin

A. Plane, cylindrical, and spherical shells without internal heat sources

For systems that are steady with respect to time, Eq. 2.4.1(3) reduces to

$$(\nabla \cdot \lambda \nabla T) = 0 \tag{1}$$

or

$$\nabla^2 T = 0 \tag{2}$$

if the thermal conductivity λ may be regarded as a constant.

If the thermal conductivity is a function of temperature but not of position, Eq. (1) can also be written in the form of Laplace s equation [Eq.(2)] by introducing a new temperature variable

$$T^* = \frac{1}{\lambda_0} \int_{T_0}^{T} \lambda(T)\, dT \tag{3}$$

where T_0 is an arbitrary reference temperature and λ_0 is the conductivity at that reference state $[\lambda_0 = \lambda(T_0)]$.

$$\nabla^2 T^* = 0 \tag{4}$$

Temperature distributions are easily calculated from Eq. (1), (2), or (4) if it is possible to define a coordinate system (x,y) in which one coordinate (say, x) coincides with the direction of the heat flux vector $\dot{q} = -\lambda \nabla T$.

For these one-dimensional problems Eq. (4) may be written

$$\frac{1}{A(x)} \frac{d}{dx}\left[A(x) \frac{dT^*}{dx}\right] = 0 \tag{5}$$

where $A(x)$ is the isothermal area perpendicular to x. Equation (5) can be integrated immediately to give

$$-\lambda(T) \cdot A(x) \frac{dT}{dx} = \dot{Q} = \text{const} \tag{6}$$

Equation (6) says that the heat rate $\dot{Q} = \dot{q}(x) \cdot A(x)$ in a steady one-dimensional system without sources or sinks is independent of the position x.

From Eq. (6) we can calculate the heat rates through plane cylindrical and spherical shells with given temperatures T_1 and T_2 at the inner and outer surfaces of the shell (x = x_1 and x = x_2, respectively; see Fig. 1).

$$Q = \frac{-\int_{T_1}^{T_2} \lambda(T)\, dT}{\int_{x_1}^{x_2} (dx/A(x))} \tag{7}$$

Equation (7) may be written in a more convenient way by introducing the following quantities: the integral average conductivity,

$$\bar{\lambda} = \frac{1}{T_2 - T_1} \int_{T_1}^{T_2} \lambda(T)\, dt \tag{8}$$

the shell thickness,

$$s = x_2 - x_1 \tag{9}$$

and a mean surface area A_m, defined by

© 1983 Hemisphere Publishing Corporation

HEDH

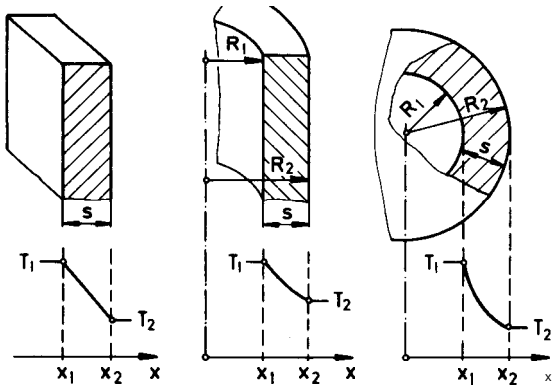

Figure 1 Steady-state conduction in plane, cylindrical, and spherical shells.

$$A_{,,,} = \frac{s}{\int_{x_1}^{x_2} (dx/A(x))} \tag{10}$$

With Eqs. (8), (9), and (10) the heat rate [in Eq. (7)] becomes

$$\dot{Q} = \frac{\bar{\lambda}}{s} A_m (T_1 - T_2) \tag{11}$$

The mean surface area defined by Eq. (10) is

$$A_{,} = \begin{cases} A = A_1 = A_2 & \text{plane shell} \\ \dfrac{A_2 - A_1}{\ln(A_2/A_1)} = \dfrac{2\pi \ell s}{\ln(R_2/R_1)} = \dfrac{2\pi R_1 \ell}{(R_1/s)\ln(1+s/R_1)} & \text{cylindrical shell} \\ \sqrt{A_1 \cdot A_2} = 4\pi R_1 R_2 = 4\pi R_1^2 \left(1 + \dfrac{s}{R_1}\right) & \text{spherical shell} \end{cases} \tag{12}$$

For the cylindrical shell $A_{,}$ is the logarithmic mean area between A_1 and A_2, whereas it is the geometric mean for spherical shells.

If the shell thickness s is small compared to the inner radius R_1 ($s \ll R_1$), then $A_{,}$ may be calculated approximately as the arithmetic mean

$$A_{,} \cong \tfrac{1}{2}(A_1 + A_2) \quad (s \ll R_1) \tag{13}$$

For the infinitely extended plane and cylindrical shells, the heat rates tend to zero as the shell thicknesses tend to infinity.

This is not true for the spherical shell. With a given inner radius R_1, the heat rate remains finite when s (or R_2) tends to infinity:

$$\min \dot{Q}_{\text{sphere}} = \lim_{s \to \infty} \frac{\bar{\lambda}}{s} 4\pi R_1 (R_1 + s)(T_1 - T_2)$$

$$\min \dot{Q}_{\text{sphere}} = \frac{\bar{\lambda}}{R_1} A_1 (T_1 - T_2) \tag{14}$$

From Eqs. (11) and (12) one can also find the temperature variation within the shell for a constant thermal conductivity λ:

$$\frac{T(x) - T_1}{T_2 - T_1} = \frac{A_m(x_1, x_2)}{A_m(x_1, x)} \frac{x - x_1}{x_2 - x_1} \tag{15}$$

$$\frac{T(x) - T_1}{T_2 - T_1} = \begin{cases} \dfrac{x - x_1}{x_2 - x_1} & \text{plane} \\ \dfrac{\ln(x/R_1)}{\ln(R_2/R_1)} & \text{cylindrical} \\ \dfrac{1 - R_1/x}{1 - R_1/R_2} & \text{spherical} \end{cases} \tag{16}$$

For temperature-dependent conductivity $\lambda(T)$, Eq. (16) has to be replaced by

$$\frac{\int_{T_1}^{T(x)} \lambda(T)\, dt}{\bar{\lambda}(T_2 - T_1)} = f(x) \tag{17}$$

where $f(x)$ denotes the same linear, logarithmic, or hyperbolic function as on the right-hand side of Eq. (16).

If we define a heat transfer coefficient for steady-state conduction through plane, cylindrical, and spherical shells by

$$\alpha \equiv \frac{\dot{Q}}{A_m (T_1 - T_2)} = \frac{\bar{\lambda}}{s} \tag{18}$$

The corresponding Nusselt number

$$\mathrm{Nu} \equiv \frac{\alpha s}{\bar{\lambda}} \tag{19}$$

always has the value Nu = 1 by definition.

If the shell consists of $n-2$ layers with thicknesses $s_{i,i+1}$ and average conductivities $\lambda_{i,i+1}$ (or heat transfer coefficients $\alpha_{i,i+1}$) the heat rate may be calculated from (see Fig. 2)

$$\dot{Q} = UA(T_0 - T_n) \tag{20}$$

where the overall heat transfer coefficient U is defined as

$$\frac{1}{U} = \sum_{i=0}^{n-1} \frac{A}{\alpha_{i,i+1} A_{m,i,i+1}} \tag{21}$$

In Eq. (21), $\alpha_{0,1}$ and $\alpha_{n-1,n}$ are the convective heat transfer coefficients at the inner and outer surfaces of

© 1983 Hemisphere Publishing Corporation

the shell. The corresponding mean surfaces are $A_{m,0,1} = A_1$ and $A_{m,n-1,n} = A_{n-1}$.

The choice of A in Eqs. (20) and (21) is arbitrary. It is not necessary to specify A, since the product UA is independent of that choice.

The temperature difference in one layer $(T_i - T_{i+1})$ may be found from the overall temperature difference $(T_0 - T_n)$ by

$$(T_i - T_{i+1}) = \frac{UA}{\alpha_{i,i+1} A_{m,i,i+1}} (T_0 - T_n) \tag{22}$$

B. Temperatures in standard bodies with internal heat sources

Conversion of other forms of energy (electrical, chemical, nuclear, etc.) inside a solid may be regarded as conduction with internal heat sources.

The rate of conversion of energy per volume will be denoted by $\dot{S}$ (in watts per cubic meter) (the strength of the heat source). In general, $\dot{S}$ may depend on temperature and position and therefore one has to start with a differential balance

$$-\frac{1}{A(x)} \frac{d}{dx} \left[A(x) \lambda \frac{dT}{dx} \right] = \dot{S}(x,T) \tag{23}$$

for one-dimensional steady-state conduction with internal sources.

If $\dot{S}$ is a function of position only, Eq. (23) can be solved by separating the variables:

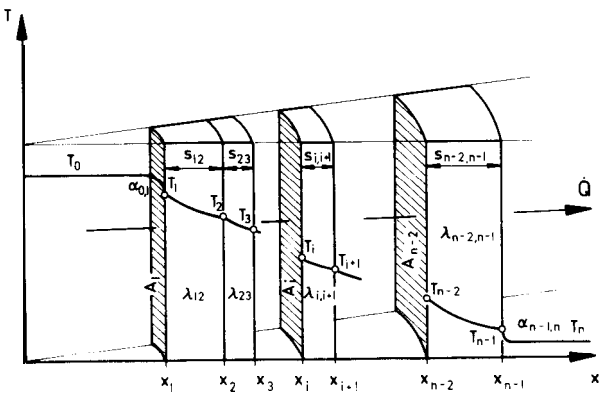

Figure 2 Steady-state conduction in multilayered shells.

$$-A(x) \lambda \frac{dT}{dx} = \int \dot{S}(x) A(x)\, dx + C_1$$

$$-\lambda\, dT = \frac{\int \dot{S}(x)\, dV + C_1}{A(x)} \tag{24}$$

where

$$A(x)\, dx = dV$$

For constant thermal conductivity we find the temperature variation inside the body by

$$T(x) = -\frac{1}{\lambda} \int \left[\frac{\int \dot{S}(x)\, dV + C_1}{A(x)} \right] dx + C_2 \tag{25}$$

where the two constants are to be determined from the boundary conditions.

Constant rate of energy conversion, $\dot{S}$ = const, in a slab of thickness $2R$ (infinitely extended in the other two directions), an infinitely long cylinder, or a sphere of radius R, with the surfaces held at a constant temperature T_0, leads to a parabolic temperature profile inside the body:

$$T(x) - T_0 = \frac{\dot{S} R V}{\lambda A} \frac{1}{2} \left[1 - \left(\frac{x}{R} \right)^2 \right] \tag{26}$$

The ratio A/V, that is, the surface area per volume, is inversely proportional to R:

$$\frac{A}{V} = \frac{n+1}{R} \qquad \text{with } n = \begin{cases} 0 \text{ for a slab} \\ 1 \text{ for a cylinder} \\ 2 \text{ for a sphere} \end{cases}$$

If we define a heat transfer coefficient

$$\alpha = \frac{\dot{Q}}{A(\bar{T} - T_0)} = \frac{\dot{S} V}{A(\bar{T} - T_0)} \tag{27}$$

where $\bar{T}$ is the integral caloric mean temperature

$$\bar{T} = \frac{1}{V} \int_v T\, dV \tag{28}$$

(for constant physical properties ρc = const), the corresponding Nusselt number becomes

$$\mathrm{Nu}_R \equiv \frac{\alpha R}{\lambda} = \frac{AR}{V} + 2 = \begin{cases} 3 \text{ for a slab} \\ 4 \text{ for a cylinder} \\ 5 \text{ for a sphere} \end{cases} \tag{29}$$

Nomenclature for Section 2.4.2 appears at the beginning of Part 2.

© 1983 Hemisphere Publishing Corporation

2.4.3

Transient response to a step change of temperature

H. Martin

A. One-dimensional systems

(a) Series solutions for the temperature field

Transient temperature distributions may always be considered to be due to a perturbation of an initially steady state. In general the perturbation consists of a change in the state of the surroundings at a certain time, $t = t_{\text{initial}}$. For convenience, $t_{\text{initial}} = 0$. The temperature distribution is then completely determined for any time $t > 0$ if the initial distribution is known,†

$$T(r,0) = T_I(r) \quad \text{(initial condition, I.C.)} \tag{1}$$

and if the state of the surroundings is given for any time greater than zero (boundary condition, B.C.). Generally the B.C.'s may be written

$$-\lambda\left(\frac{\partial T}{\partial n}\right)_B = \dot{q}_B \tag{2}$$

where $\partial T/\partial n$ denotes the component of the temperature gradient vector in the outward direction normal to the surface of the body under consideration. The heat flux $\dot{q}_B$, transferred across the surface, in turn has to be determined from the temperature distribution of the surroundings. Strictly speaking, a whole system of coupled thermal field equations [2.4.1(3)] has to be solved simultaneously. In practice one avoids those difficulties by suitably specifying the heat flux $\dot{q}_B$ in a simpler, idealizing way.

†r is a vector of space coordinates; for example, $r = (x,y,z)$ in Cartesian coordinates.

For example, by putting it proportional to the temperature difference between the surface and the surroundings (Newton s law),

$$\dot{q}_B = \alpha(T_B - T_\infty) \tag{3}$$

This form of B.C. with a constant heat transfer coefficient α and the temperature of the surroundings a prescribed function of time and position $T_\infty = T_\infty(r,t)$ contains the B.C. of a prescribed surface temperature as a special case, where the outer thermal resistance $(1/\alpha)$ is considered to vanish:

$$T_B = T_\infty(r,t) \tag{4}$$

This is referred to in the literature as a B.C. of the first kind. Prescribing the heat flux at the boundary, that is,

$$-\lambda\left(\frac{\partial T}{\partial n}\right)_B = \dot{q}_B(r,t) \tag{5}$$

is called a B.C. of the second kind, and the case already mentioned with

$$\left(\frac{\lambda}{\alpha}\frac{\partial T}{\partial n} + T\right)_B = T_\infty(r,t) \tag{6}$$

[from Eqs. (2) and (3)] is referred to as a B.C. of the third kind.

For bodies of simple shape a multitude of analytical solutions of Eq. 2.4.1(3a) with various forms of initial and boundary conditions may be found in textbooks on heat conduction [1-4]. Some of the simplest and most frequently encountered of these solutions will be treated here. Many problems may be treated, at least approximately, by assuming that the heat flux occurs only in one direction-for example,

© 1983 Hemisphere Publishing Corporation

HEMISPHERE

the x direction in Cartesian coordinates if the planes x = const. are isothermals, or the r direction in cylindrical and spherical coordinates if the cylindrical or spherical shells r = const. are isothermals. In these cases Eq. 2.4.1(3*a*) may be written [see Table 2.4.1(1)]:

$$\frac{\partial T}{\partial t} = \kappa \frac{\partial^2 T}{\partial x^2} \quad \text{for the plane field } T(x,t) \tag{7a}$$

$$\frac{\partial T}{\partial t} = \frac{\kappa}{r}\frac{\partial}{\partial r}\left(r\frac{\partial T}{\partial r}\right) \quad \text{for the cylindrically symmetric field } T(r,t) \tag{7b}$$

$$\frac{\partial T}{\partial t} = \frac{\kappa}{r^2}\frac{\partial}{\partial r}\left(r^2\frac{\partial T}{\partial r}\right) \quad \text{for the spherically symmetric field } T(r,t) \tag{7c}$$

Summarizing, one may write generally for one-dimensional heat flux (and constant thermal diffusivity κ):

$$\frac{\partial T}{\partial t} = \frac{\kappa}{x^n}\frac{\partial}{\partial x}\left(x^n\frac{\partial T}{\partial x}\right) \tag{7}$$

with n = 0, 1, 2 for the three main coordinate systems. The simplest bodies pertaining to these one-dimensional temperature fields are as follows:

1. $-L \leqslant x \leqslant L; -\infty < y,z < \infty$

The slab of thickness $2L$ extended infinitely in the y and z directions. (This will be referred to as the slab in the following.)

2. $0 \leqslant r \leqslant R; 0 \leqslant \varphi \leqslant 2\pi; -\infty < z < \infty$

The circular cylinder of diameter $2R$ extended infinitely in the z direction. (This will be referred to as the cylinder in the following.)

3. $0 \leqslant r \leqslant R; 0 \leqslant \varphi \leqslant 2\pi; 0 \leqslant \psi \leqslant \pi$

The sphere of diameter 2R.

The initial and boundary conditions may be taken to be

$$T(x,0) = T_I = \text{const.} \tag{8}$$

and

$$\left(\frac{\lambda}{\alpha}\frac{\partial T}{\partial x} + T\right)_B = \begin{cases} T_I \text{ for } t \leqslant 0 \\ T_\infty \text{ for } t > 0 \end{cases} \tag{9}$$

that is, a sudden step change of the temperature of the surroundings from the constant initial temperature T_I to the constant temperature T_∞ for all times greater than zero.

The one-dimensional thermal field equation (7) and the I.C. and B.C.'s of Eqs. (8) and (9) may be written in dimensionless form by introducing the following new variablesand parameters.

Dimensionless temperature:

$$T^+ = \frac{T(x,t) - T_\infty}{T_I - T_\infty} \tag{10}$$

Dimensionless distance from the center of symmetry:

$$x^+ = \frac{x}{L}\left(\text{or } \frac{r}{R}, \text{ resp}\right) \tag{11}$$

Dimensionless time (= Fourier number):

$$t^+ = \frac{\kappa t}{L^2} \quad \left(\text{or } \frac{\kappa t}{R^2}, \text{ resp.}\right) \tag{12}$$

Ratio of the internal conductive resistance (R/λ) to the outer heat transfer resistance (l/or) (Biot number):

$$\text{Bi} = \frac{\alpha L}{\lambda} \quad \left(\text{or } \frac{\alpha R}{\lambda}, \text{ resp.}\right) \tag{13}$$

D.E.:

$$\frac{\partial T^+}{\partial t^+} = \frac{1}{x^{+n}}\frac{\partial}{\partial x^+}\left(x^{+n}\frac{\partial T^+}{\partial x^+}\right) \quad \begin{cases} \text{slab. } n = 0 \\ \text{cylinder, } n = 1 \\ \text{sphere, } n = 2 \end{cases} \tag{14}$$

I.C.: $T^+(x^+,0) = 1$ (15)

B.C.'s:

$$\left(\frac{1}{\text{Bi}}\frac{\partial T^+}{\partial x^+} + T^+\right)_{x^+=1} = 0 \quad (t^+ > 0) \tag{16a}$$

$$\left(\frac{\partial T^+}{\partial x^+}\right)_{x^+=0} = 0 \text{ (symmetry)} \tag{16b}$$

With this normalized representation it makes no difference whether the body is heated $(T_\infty > T_I)$ or cooled $(T_\infty < T_I)$. In each case the normalized temperature T', Eq. (10), will go from unity (at $t^+ = 0$) to zero (when t^+ tends to infinity).

Figure 1 shows an example for a transient temperature distribution for the conditions described by Eqs. (14) through (16).

It may be helpful when plotting these temperature distributions to note that the tangents to the temperature curves at the surface of the body (x = 1)

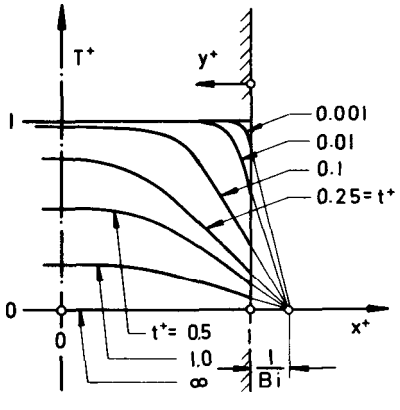

Figure 1 Temperature distribution $T^+(x^+, t^+, \text{Bi})$ in a slab. Boundary condition of the 3rd kind (calculated for Bi = 5).

© 1983 Hemisphere Publishing Corporation

intersect at one point. This may be seen immediately from the B.C.'s [Eq. (16a)]. The coordinates of the point of intersection are (see Fig. 1)

$$\left(T^+ = 0; x^+ = 1 + \frac{1}{\mathrm{Bi}}\right)$$

This point is situated the closer to the surface $(x^+ = 1)$, as the outside resistance ratio $(1/\mathrm{Bi})$ decreases, leading to B.C.'s of the first kind in the limit as $1/\mathrm{Bi}$ tends to zero. In this case $[T^+(x^+ = \pm 1) = 0]$ the variation of temperature inside the body is the maximum possible.

Example. Consider cooling or heating of a large body of poorly conducting material with a high outer heat transfer coefficient (as obtainable by evaporation or condensation on the surface).

If the resistance ratio $(1/\mathrm{Bi})$ increases, however, the point of intersection of the tangents of the temperature curves at the boundaries moves outward. The whole temperature variation inside the body becomes flatter and flatter. The maximum difference for the temperatures occurring within the body $\{\max [T^+(x^+ = 0) - T^+(x^+ = 1)] = \Delta T^+_{\max}\}$ may be estimated by simple geometric considerations to be less than $\mathrm{Bi}/(1 + \mathrm{Bi})$. For Biot numbers <0.1, the center and surface temperatures differ by less than 9% of the whole temperature step $(T_I - T_\infty)$.

Cooling or heating of a small body of good conducting material such as a metal in quiescent gas is an example of this type.

For short times t^+ the change in temperature is felt only in a small zone near the surface of the body (see Fig. 1). The thermal field may be said to be of the boundary-layer type. Since the boundary condition at the other side has no influence, the body may be considered to be semiinfinite. It is more appropriate to use a new length coordinate y with its origin at the surface and its direction opposite to x:

$$y = L - x \quad \text{or } (R - r), \text{ resp.} \tag{17}$$

Since there is no finite length involved in this problem, one may use the quantity $\sqrt{\kappa t}$, which has the dimension of length, to nondimensionalize the variables and parameters:

$$y^+ \equiv \frac{y}{2\sqrt{\kappa t}} \quad \left(= \frac{1 - x^+}{2\sqrt{t^+}}\right) \tag{18}$$

$$\mathrm{Bi}^* \equiv \frac{\alpha\sqrt{\kappa t}}{\lambda} \quad (= \mathrm{Bi}\sqrt{t^+}) \tag{19}$$

The temperature distribution $T^+(y^+, \mathrm{Bi}^*)$ may be written [1]:

$$T^+ = \operatorname{erfy} \quad + e^{-y^{+2}} \cdot F(y^+ + \mathrm{Bi}^*) \tag{20}$$

with

Table 1 The error function and related functions

Definitions: $\operatorname{erf}(z) = \frac{2}{\sqrt{\pi}} \int_0^z e^{-\xi^2}\, d\xi$

$\operatorname{erfc}(z) = 1 - \operatorname{erf}(z)$

$\operatorname{erf}(0) = 0 \quad \operatorname{erf}(\infty) = 1 \quad \operatorname{erf}(-z) = -\operatorname{erf}(z)$

Series expansions:

$$\operatorname{erf}(z) = \frac{2}{\sqrt{\pi}} \sum_{n=0}^{\infty} \frac{(-1)^n z^{2n+1}}{(2n+1)n!}$$

$$\operatorname{erf}(z) = \frac{2}{\sqrt{\pi}} e^{-z^2} \sum_{n=0}^{\infty} \frac{2^n z^{2n+1}}{1 \cdot 3 \cdot 5 \cdots (2n+1)}$$

Asymptotic expansion (for large arguments z):

$$e^{z^2} \operatorname{erfc}(z) = \frac{1}{\sqrt{\pi} z} \left\{ 1 + \sum_{n=1}^{N} (-1)^n \frac{1 \cdot 3 \cdot 5 \cdots (2n-1)}{(2z^2)^n} + R_N \right\}$$

with $|R_N| <$ | (the Nth term of the series) I

$$F(z) \equiv e^{z^2} \operatorname{erfc}(z) \tag{21}$$

Definitions and series expansions of $\operatorname{erf}(z), \operatorname{erfc}(z)$ $[= 1 - \operatorname{erf}(z)]$, and $F(z)$ are given in Table 1 for convenience.

Equation (20) is a rigorous solution for a semiinfinite body. For bodies of finite thickness $2L$ (or $2R$), it has to be considered an asymptotic one for small values oft+.

From Eq. (20), the surface temperature $T_B^+ = T^+(y^+ = 0)$ becomes

$$T_B^+ = F(\mathrm{Bi}^*) = e^{\mathrm{Bi}^{*2}} \operatorname{erfc}(\mathrm{Bi}^*) \tag{22}$$

For large values of Bi* [or $(y^+ + \mathrm{Bi}^*)$ in Eq. (20)], one may use the asymptotic expansion of F(z), which is valid for large arguments z (see Table 1).

The surface temperature may be written

$$T_B^+ \approx \frac{1}{\sqrt{\pi}} \frac{1}{\mathrm{Bi}^*} \quad \left(\text{error} < \frac{1}{\sqrt{\pi}} \frac{1}{2\,\mathrm{Bi}^{*3}}\right) \tag{23}$$

For $\mathrm{Bi}^* \to \infty, T_B^+$ becomes zero, that is, the B.C. is of the first kind and Eq. (20) reduces to

$$T^+ = \operatorname{erf}(y^+) \quad (\mathrm{Bi}^* \to \infty) \tag{24}$$

The instantaneous heat flux $\dot{q}_t$ across the surface may be obtained from (23) and (24):

$$\dot{q}_t = \frac{1}{\sqrt{\pi}} \frac{\lambda}{\sqrt{\kappa t}} (T_I - T_\infty) = \frac{1}{\sqrt{\pi}} \frac{\sqrt{\lambda\rho c}}{\sqrt{t}} (T_I - T_\infty) \tag{25}$$

So, for short times the heat flux decreases with $1/\sqrt{t}$ and is proportional to the quantity $\sqrt{\lambda\rho c}$, which is sometimes called the heat penetration coefficient.

© 1983 Hemisphere Publishing Corporation

The integral mean value of the heat flux, averaged over the time interval from $t = 0$ to $t(>0)$, is twice the instantaneous value at the same time:

$$\dot{q} = \frac{2}{\sqrt{\pi}} \frac{\lambda}{\sqrt{\kappa t}} (T_I - T_\infty) \tag{25a}$$

For sufficiently long times t^+, the temperature profiles inside the body of finite thickness become similar to each other (see Fig. 1). They all might be represented by the same function of the spatial variable $f(x^+)$, times a scaling factor $g(t^+)$ that is a decreasing function of time:

$$T^+ = g(t^+) \cdot f(x^+) \tag{26}$$

Substitution of this trial function into Eq. (14) transforms the partial differential equation into two ordinary ones for $g(t^+)$ and $f(x^+)$, respectively. The time function will be found to be

$$g(t^+) = e^{-m^2 t^+} \tag{27}$$

where m is a constant to be determined from the boundary conditions.

The form of the space function $f(x^+)$ depends on the shape of the body (see Table 2, last column). Of course, it is impossible to describe the thermal field for short times, especially the rectangular initial temperature distribution, by one of these parabolalike curves. Since there is an infinite number of values m_i that fulfill the boundary conditions (see the first column in Table 2), any of the functions $T_i^+ = C_i f(m_i^+) e^{-m_i^2 t^+}$ is a solution of Eq. (14), and, because of the linearity of this equation, the sum of these functions ΣT_i^+ is a solution, too. The yet unknown coefficients C_i can be determined to obtain a least-squares approximation to the initial temperature distribution by a finite series $\Sigma_i^n C_i(m_i) f(m_i x^+)$ with the errors approaching zero as n tends to infinity.

The so-called eigenvalues m_i are the roots of the transcendental equations given in the first column in Table 2. They have to be determined graphically or by iteration.

Table 2a gives the first four roots m_1 to m_4 for slab, cylinder, and sphere depending on the Biot number. Successive values m_i and m_{i+1} differ by an amount $\Delta m_i = m_{i+1} - m_i$ that tends to π for large numbers i. The fourth eigenvalue is always greater than (or equal to) 3π, and so the fourth term of the series Eq. (28) contains a scaling factor $e^{-m_4^2 t^+}$ that becomes very small unless the time is extremely short. This factor is less than 5×10^{-3} for $t^+ = 0.06$. Therefore it will often be sufficient to calculate the first three terms of the series if $t^+ > 0.06$, and only the first term if $t^+ > 0.6$. Figures 2 through 10 show the normalized center and surface temperatures T_c^+ and T_B^+ calculated from Eq. (28) with x+ = 0 and $x^+ = 1$ and the normalized average temperature $\bar{T}^+$ according to Eq. (29). The latter is related to the heat Q transferred across the surface from $t = 0$ to t.

$$(1 - \bar{T}^+) = \frac{T_I - \bar{T}}{T_I - T_\infty} = \frac{Q}{\rho c V (T_I - T_\infty)} \tag{30}$$

The average temperature $\bar{T}$ is defined by

$$\bar{T} \equiv \frac{\iiint_{(v)} (\rho c T)\, dV}{\iiint_{(v)} (\rho c)\, dV} \tag{31}$$

Table 2 Temperature distribution for one-dimensional heat flux in slab, cylinder, and sphere

The temperature distribution for one-dimensional heat flux in the slab, the cylinder, and the sphere after a step change in temperature of the surrounding medium from T_I (the constant initial temperature of the body) to the constant value T_∞, with a given, constant, outside heat transfer coefficient α (3rd B.C.).

$$T^+ = \sum_{i=1}^{\infty} C_i(m_i) f(m_i \xi) e^{-m_i^2 t^+} \tag{28}$$

$$\bar{T}^+ = \sum_{i=1}^{\infty} C_i(m_i) D_i(m_i) e^{-m_i^2 t^+} \tag{29}$$

	m_i to be determined from:	$C_i(m_i)$	$D_i(m_i)$	$f(m_i \xi)$
Slab	$m_i = \frac{\alpha X}{\lambda} \frac{\cos m_i}{\sin m_i}$	$2 \frac{\sin m_i}{m_i + \sin m_i \cos m_i}$	$1 \frac{\sin m_i}{m_i}$	$\cos\left(m_i \frac{x}{X}\right)$
Cylinder	$m_i = \frac{\alpha R}{\lambda} \frac{J_0(m_i)}{J_1(m_i)}$	$2 \frac{J_1(m_i)}{m_i [J_0^2(m_i) + J_1^2(m_i)]}$	$2 \frac{J_1(m_i)}{m_i}$	$J_0\left(m_i \frac{r}{R}\right)$
Sphere	$m_i = \left(1 - \frac{\alpha R}{\lambda}\right) \frac{\sin m_i}{\cos m_i}$	$2 \frac{\sin m_i - m_i \cos m_i}{m_i - \sin m_i \cos m_i}$	$3 \frac{\sin m_i - m_i \cos m_i}{m_i^3}$	$\frac{\sin [m_i (r/R)]}{m_i (r/R)}$

Tables and graphs of the Bessel functions J_0 and J_1 may be found in [7] and [8].

© 1983 Hemisphere Publishing Corporation

Table 2*a* **The first four roots m_i of the transcendental equations given in Table 2**

	Slab				Cylinder				Sphere			
Bi	m_1	m_2	m_3	m_4	m_1	m_2	m_3	m_4	m_1	m_2	m_3	m_4
0	0.000	π	2π	3π	0.000	3.832	7.016	10.174	0.000	4.493	7.725	10.904
0.001	0.032	3.142	6.283	9.425	0.045	3.832	7.016	10.174	0.055	4.494	7.725	10.904
0.002	0.044	3.142	6.284	9.425	0.063	3.832	7.016	10.174	0.077	4.494	7.725	10.904
0.005	0.071	3.143	6.284	9.425	0.100	3.833	7.016	10.174	0.122	4.495	7.726	10.905
0.01	0.100	3.145	6.285	9.426	0.141	3.834	7.017	10.175	0.173	4.496	7.727	10.905
0.02	0.141	3.148	6.286	9.427	0.200	2.837	7.019	10.176	0.242	4.498	7.728	10.906
0.05	0.222	3.157	6.291	9.430	0.314	3.845	7.023	10.178	0.385	4.504	7.732	10.908
0.1	0.311	3.173	6.299	9.435	0.442	3.858	7.030	10.183	0.542	4.516	7.739	10.913
0.2	0.433	3.204	6.315	9.446	0.617	3.884	7.044	10.193	0.759	4.538	7.761	10.923
0.5	0.653	3.292	6.362	9.477	0.941	3.959	7.086	10.222	1.166	4.604	7.790	10.950
1.0	0.861	3.426	6.437	9.529	1.256	4.079	7.156	10.271	$\pi/2$	3 n/2	5 n/2	$7\pi/2$
2.0	1.079	3.644	6.578	9.630	1.599	4.292	7.288	10.366	2.030	4.913	7.979	11.085
5.0	1.314	4.034	6.910	9.893	1.990	4.713	7.617	10.622	2.569	5.354	8.303	11.335
10	1.428	4.305	7.229	10.200	2.180	5.034	7.957	10.936	2.836	5.717	8.659	11.658
20	1.498	4.491	7.495	10.513	2.288	5.257	8.253	11.268	2.986	5.978	8.983	12.003
50	1.536	4.619	7.703	10.783	2.357	5.411	8.484	11.562	3.079	6.158	9.239	12.320
	$\pi/2$	3 n/2	5 n/2	7 n/2	2.405	5.520	8.653	11.792	π	2π	3π	4π

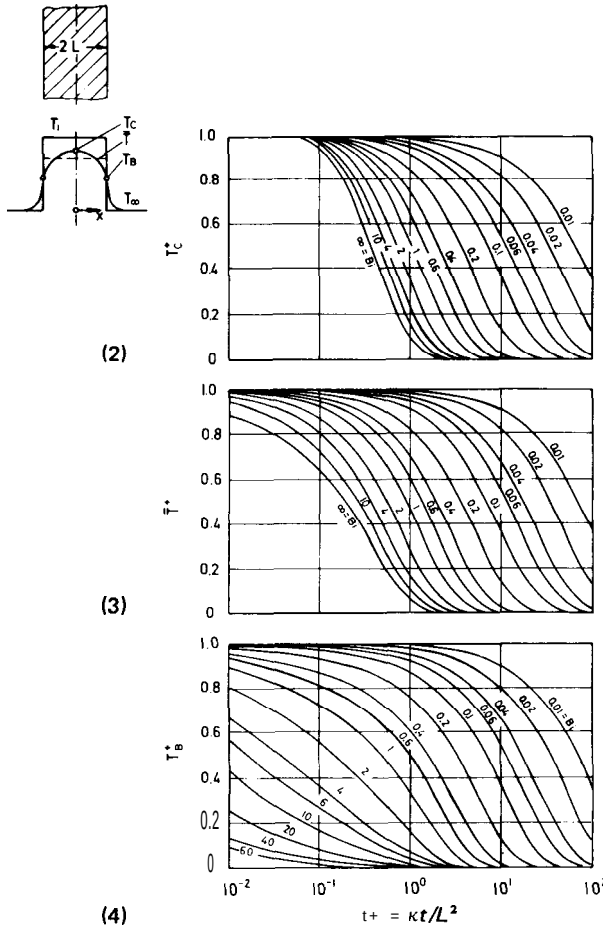

Figures 2, 3, 4 Normalized centerline, average, and surface temperatures in a slab as functions of dimensionless time t^+ with Bi = $\alpha L/\lambda$ as a parameter.

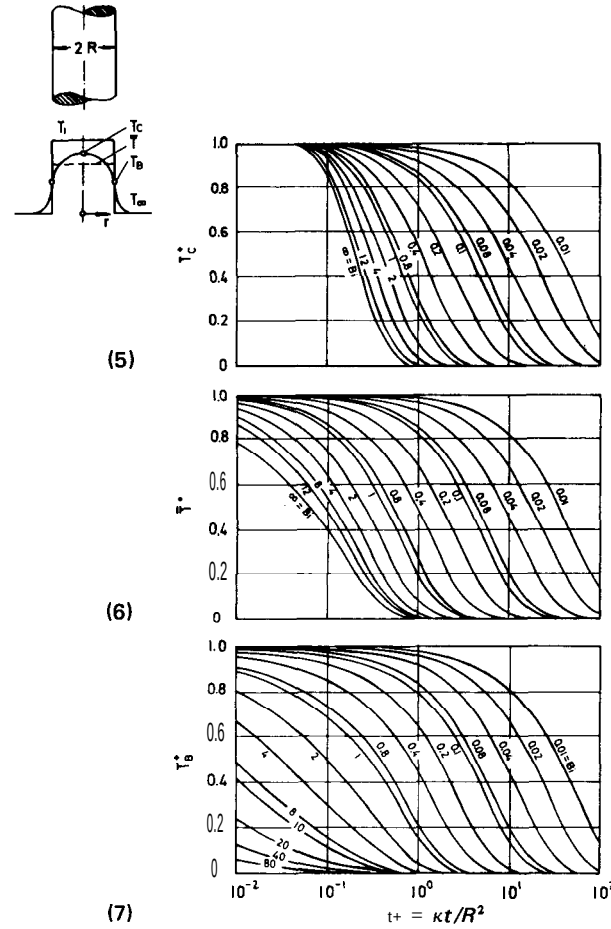

Figures **5, 6,** 7 Normalized centerline, average, and surface temperatures in a cylinder as functions of dimensionless time t^+ with Bi = $\alpha R/\lambda$ as a parameter.

© 1983 Hemisphere P ıblishing Corporation

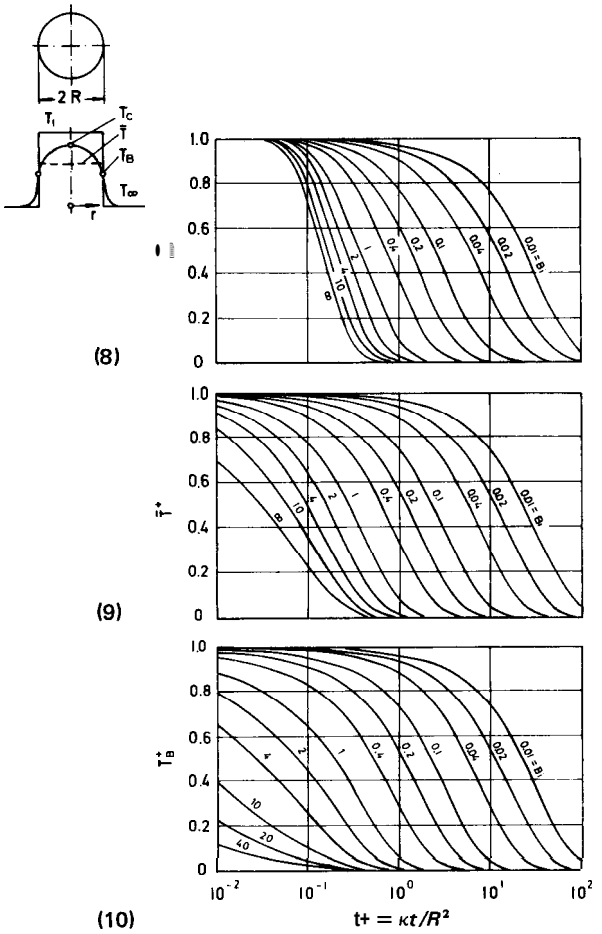

Figures 8, 9, 10 Normalized center, average, and surface temperatures in a sphere as functions of dimensionless time t^+ with Bi = $\alpha R/\lambda$ as a parameter.

With constant ρc and one-dimensional heat flux this may be written in dimensionless form for slab, cylinder, and sphere $(n = 0, 1, 2)$ as

$$\bar{T}^+ = (n+1)\int_0^1 T^+(x^+)x^{+n}\,dx^+ \tag{32}$$

From this the functions $D_i(m_i)$ in Table 2 were obtained. For sufficiently long times t^+, the first of these functions gives the ratio of $\bar{T}^+/T_c^+$.

$$D_1(m_1) = \frac{\bar{T}^+}{T_c^+} \qquad (t^+ \to \infty) \tag{33}$$

If the Biot number tends to zero, the series in Eqs. (28) and (29) reduce to a single term:

$$\lim_{\mathrm{Bi}\to 0} T^+ = \lim_{\mathrm{Bi}\to 0} \bar{T}^+ = \lim_{\mathrm{Bi}\to 0} e^{-(n+1)\mathrm{Bi}\,t^+} = 1 \tag{34}$$

This asymptotic solution may be used as an approximation for small Bi numbers (Bi < 0.05).

$$T^+ \cong e^{-(n+1)\mathrm{Bi}\,t^+} \qquad (\mathrm{Bi} < 0.05) \tag{35}$$

The same expression may be obtained immediately by considering the body to be a perfect conductor (or a well-stirred fluid). With $(n + 1) = AX/V$ and Bit+ = $(\alpha X/\lambda)(\kappa t/X^2) = \alpha t/(\rho c X)$, Eq. (35) may be seen to be independent of λ.†

$$T^+ \cong e^{-(\alpha A/\rho c V)t} \qquad \frac{\alpha X}{\lambda} < 0.05 \tag{36}$$

In the other limit, as Bi tends to infinity (B.C. of the first kind), the first terms of the series Eqs. (28) and (29) are (see Tables 2 and 2a) as follows:

Slab:

$$T^+ \cong \frac{4}{\pi}\cos\left(\frac{\pi}{2}\frac{x}{L}\right) e^{-(\pi/2)^2(\kappa t/L^2)} \tag{37}$$

$$\bar{T}^+ \cong \frac{2}{(\pi/2)^2}\, e^{-(\pi/2)^2(\kappa t/L^2)} \tag{38}$$

Cylinder:

$$T^+ \cong 1.613 J_0\left(2.405\frac{r}{R}\right) e^{-(2.405)^2(\kappa t/R^2)} \tag{39}$$

$$\bar{T}^+ \cong \frac{4}{(2.405)^2}\, e^{-(2.405)^2(\kappa t/R^2)} \tag{40}$$

Sphere:

$$T^+ \cong 2\frac{\sin(\pi\, r/R)}{(\pi\, r/R)}\, e^{-\pi^2(\kappa t/R^2)} \tag{41}$$

$$\bar{T}^+ \cong \frac{6}{\pi^2} e^{-\pi^2(\kappa t/R^2)} \tag{42}$$

for large values of $t^+(t^+ > 0.3)$ and Bi $\to \infty$. The relative errors of these long-time asymptotic solutions remain less than 1% if t^+ is greater.than 0.3 [5].

From these equations the heat flux across the surface can be determined:

Slab:

$$\dot{q} = 2\frac{\lambda}{L}(T_I - T_\infty)e^{-(\pi/2)^2 t^+} = \frac{\pi^2}{4}\frac{\lambda}{L}(\bar{T} - T_\infty) \tag{43}$$

Cylinder:

$$\dot{q} = 2\frac{\lambda}{R}(T_I - T_\infty)e^{-(2.405)^2 t^+}$$

$$= \frac{(2.405)^2}{2}\frac{\lambda}{R}(\bar{T} - T_\infty) \tag{44}$$

†X stands for the half-thickness L of a slab or the radius R of a cylinder and a sphere, respectively.

© 1983 Hemisphere Publishing Corporation

Sphere:

$$\dot{q} = 2\frac{\lambda}{R}(T_I - T_\infty)e^{-\pi^2 t^+} = \frac{\pi^2}{3}\frac{\lambda}{R}(\bar{T} - T_\infty) \quad (45)$$

for $t^+ > 0.3$ and Bi $\to \infty$.

In general, the calculation of the temperature distributions or heat fluxes involves the evaluation of infinite series [see Eqs. (28) and (29)].

Some limiting cases may be calculated much more easily by using asymptotic solutions [see Eqs. (20) through (2%) for $t^+ \to 0$, Eqs. (37) through (45) for $t^+ \to \infty$, and Eqs. (34) through (36) for Bi $\to 0$].

(b) Application of Internal Heat Transfer Coefficients in Transient Conduction

In order to simplify the calculations of nonsteady-state heat transfer in the whole range of variables ($0 < t^+ < \infty$; $0 < \text{Bi} < \infty$), one may apply a method that is well established in the calculation of steady-state convective heat transfer to a fluid passing through a channel. In steady-state problems of this type, one usually defines a heat transfer coefficient that depends on the length of the flow path and on the fluid velocity. From another viewpoint, one may say that they depend on the residence time (= flow path/velocity) of a fluid element. Analogously, we can use an internal heat transfer coefficient α_i to calculate nonsteady-state conductive heat transfer as well [6]. Clearly, these α_i have to depend on the time. Defining the instantaneous internal heat transfer coefficient $\alpha_{i,t}$ in terms of the temperature difference between the average temperature of the body and its surface temperature, we may write:

$$\dot{Q}_{B,t}(t) = \alpha_{i,t}(t)\,A[\bar{T}(t) - T_B(t)] \quad (46)$$

The same heat flux may be expressed by the outside temperature difference

$$Q_{B,t}(t) = \alpha A[T_B(t) - T_\infty] \quad (47)$$

Introducing an overall heat transfer coefficient U_t, with

$$\frac{1}{U_t(t)} = \frac{1}{\alpha} + \frac{1}{\alpha_{i,t}(t)} \quad (48)$$

the surface temperature T_B may be eliminated from Eqs. (46) and (47):

$$Q_{B,t}(t) = U_t(t)\,A[\bar{T}(t) - T_\infty] \quad (49)$$

Combining this with the energy balance

$$\dot{Q}_{B,t} = -\rho c V \frac{d\bar{T}}{dt} \quad (50)$$

yields

$$\int_{\bar{T}'}^{\bar{T}} \frac{d\bar{T}}{\bar{T} - T_\infty} = -\frac{A}{\rho c V}\int U_t(t)\,dt \quad (51)$$

Integration of Eq. (5 1) leads to the familiar exponential decay of temperature with time

$$\frac{\bar{T}(t) - T_\infty}{T_I - T_\infty} = \exp\left[-\frac{U(t)A}{\rho c V}t\right] \quad (52)$$

with

$$U(t) \equiv \frac{1}{t}\int_0^t U_t(t)\,dt \quad (53)$$

In principle, this average overall heat transfer coefficient could be determined exactly from Eqs. (28) and (29). This would make little sense, however, since its insertion in Eq. (52) must result in Eq. (29) again.

To simplify the calculation, we determine the internal heat transfer coefficient α_i for the limiting case Bi $\to \infty (1/\alpha \to 0)$ and assume it to be independent of the outside heat transfer coefficient a. The overall heat transfer coefficient U will be exact in this limit. In the other limit (Bi $\to$ 0), it is also exact, whether this assumption holds or not [see Eq. (48)].

The integral mean internal heat transfer coefficient for short times ($t^+ \to 0$) may be found from Eq. (25a) with $\bar{T} \approx T_I$:

$$t^+ \to 0: \quad \alpha_{i,0} = \frac{2}{\sqrt{\pi}}\frac{\lambda}{\sqrt{\kappa t}} \quad (54)$$

For long times one obtains, from Eqs. (43) through (45), $t^+ \to \infty$

$$\text{Slab:} \quad \alpha_{i,\infty} = \frac{\pi^2}{4}\frac{\lambda}{L} \quad (55)$$

$$\text{Cylinder:} \quad \alpha_{i,\infty} = \frac{(2.405)^2}{2}\frac{\lambda}{R} \quad (56)$$

$$\text{Sphere:} \quad \alpha_{i\infty} = \frac{\pi^2}{3}\frac{\lambda}{R} \quad (57)$$

A good approximation for the whole range of time may be obtained by the following interpolation formula:

$$\alpha_i(t) \cong [\alpha_{i,\infty}^2 + \alpha_{i,0}^2(t)]^{1/2} \quad (58)$$

With the dimensionless quantities defined by Eqs. (10), (12), and (13), and the dimensionless inside heat transfer coefficient

$$\text{Nu}_i \equiv \frac{\alpha_i R}{\lambda} \quad (59)$$

Eq. (52) becomes [with Eqs. (54) through (58)]

$$\bar{T}^+ \cong \exp\left[-a_v^+ \frac{t^+}{(1/\text{Bi}) + 1/\text{Nu}_i(t^+)}\right]$$
$$\text{Nu}_i(t^+) \cong \left[\text{Nu}_{i\infty}^2 + \frac{4}{\pi}\frac{1}{t^+}\right]^{1/2} \quad (60)$$

© 1983 Hemisphere Publishing Corporation

	a_v^+	$\mathrm{Nu}_{i\infty}$	$= C_\infty$
Slab	1	2.461	$= (\pi/2)^2$
Cylinder	2	2.892	$= (2.405)^2/2$
Sphere	3	3.290	$= \pi^2/3$

$$t^+ \equiv \frac{\kappa t}{X^2} = \frac{\lambda t}{\rho c X^2} \qquad T^+ \equiv \frac{T(x,t) - T_\infty}{T_I - T_\infty}$$

$$\mathrm{Bi} \equiv \frac{\alpha X}{\lambda} \qquad a_v^+ \equiv \frac{A \cdot X}{V} \quad \text{(dimensionless volume-specific surface area)}$$

This approximation is sufficiently exact for most engineering calculations, as one may see by comparison with the charts (Figs. 3, 6, and 9).

From the more rigorous series solutions one can find that the internal heat transfer coefficients α_i are not independent of the outside transfer coefficients α. The Nusselt numbers $\mathrm{Nu}_{i\infty}$ are functions of Bi and vary between the values of C_∞ given in Eq. (60) for ($\mathrm{Bi} \to \infty$) and the values

$$\lim_{\mathrm{Bi} \to 0} \mathrm{Nu}_{i\infty} = a_v^+ + 2 \tag{61}$$

in the other limit [see Eq. 2.4.2(29) for comparison].

The following empirical formula accounts for this functional relationship between inside and outside heat transfer coefficients:

$$\mathrm{Nu}_{i\infty}(\mathrm{Bi}) \cong C_\infty \frac{(a_v^+ + 2) + \mathrm{Bi}}{C_\infty + \mathrm{Bi}} \tag{62}$$

If this is used in Eq. (60), the accuracy of the approximation becomes even higher, especially in the range of intermediate Biot numbers.

Equations (60) through (62) may also be used to calculate the time required to heat or cool a body from an initial temperature T_I to an average temperature $\bar{T}$:

$$t^+ = \frac{1}{a_v^+}\left[\frac{1}{\mathrm{Bi}} + \frac{1}{\mathrm{Nu}_i(t^+)}\right] \ln \frac{T_I - T_\infty}{\bar{T} - T_\infty} \tag{63}$$

Equation (63) has to be solved by iteration, since the right-hand side depends on time [$\mathrm{Nu}_i(t^+)$]. Starting with $\mathrm{Nu}_i^{(0)}(t^+) = \mathrm{Nu}_{i\infty}$ as a first approximation, it converges rapidly.

To reach the same temperature in the center of the body, an additional time Δt_c^+ is required.

$$T_c^+(t^+ + \Delta t_c^+) = \bar{T}^+(t^+) \tag{64}$$

This time lag between average and center temperature turns out to be almost independent of the Biot number and the time:

$$\Delta t_c^+ \cong \begin{cases} \frac{1}{6} & \text{slab} \\ \frac{1}{8} & \text{cylinder} \\ \frac{1}{10} & \text{sphere} \end{cases} \tag{65}$$

For very high Biot numbers ($\mathrm{Bi} \to \infty$), Δt_c^+ becomes 0.183, 0.145, 0.121, respectively, instead of 0.167, 0.125, 0.100 according to Eq. (65). For very short times ($t^+ \ll \Delta t_c^+$), the center temperatures T_c^+ calculated from Eqs. (64) and (65) are higher than the exact ones.

(c) Numerical methods

In cases of more complex boundary conditions or geometric shapes, it is often very difficult or even impossible to find analytical solutions. Such problems may be solved by numerical methods. In the following we shall give only an example for a very simple and straightforward explicit finite difference method. For more sophisticated numerical techniques, such as implicit finite difference (FD), or finite element (FE) methods, the reader should consult textbooks on numerical methods such as Dusinberre [9] and Smith [10] for FD, Zienkiewicz [11] for FE, and Marsal [12] or Ames [13] for a comprehensive treatment of both FD and FE methods.

To illustrate the technique in principle, we start from the differential equation for one-dimensional conduction of heat, Eq. (7).

$$\frac{1}{\kappa}\frac{\partial T}{\partial t} = \frac{\partial^2 T}{\partial x^2} + \frac{n}{x}\frac{\partial T}{\partial x} \tag{66}$$

(The method can easily be generalized for multidimensional problems).

Using the following simple approximations for the time and space derivatives in Eq. (66),

$$\frac{\partial T}{\partial t} \cong \frac{T_{I+1,K} - T_{I,K}}{\Delta t} \tag{67}$$

$$\frac{\partial T}{\partial x} \cong \frac{T_{I,K+1} - T_{I,K-1}}{2\Delta x} \tag{68}$$

$$\frac{\partial^2 T}{\partial x^2} \cong \frac{(T_{I,K+1} - T_{I,K}) - (T_{I,K} - T_{I,K-1})}{(\Delta x)^2} \tag{69}$$

where the subscripts I and K refer to certain values of time ($t_{I+1} = t_I + \Delta t$) and position ($x_{K+1} = x_K + \Delta x$), we get an algebraic equation for the temperature $T_{I+1,K}$ as a function of $T_{I,K}$, $T_{I,K-1}$, and $T_{I,K+1}$:

$$T_{I+1,K} \cong M\left[T_{I,K-1}\left(1 - \frac{n}{2}\frac{\Delta x}{x_K}\right) + T_{I,K+1}\left(1 + \frac{n}{2}\frac{\Delta x}{x_K}\right)\right] + (1 - 2M)T_{I,K} \tag{70}$$

© 1983 Hemisphere Publishing Corporation

In Eq. (70), M is an abbreviation for a Fourier number formed with At and Ax:

$$M \equiv \frac{\kappa \cdot \mathrm{A\,t}}{(\Delta x)^2} \tag{71}$$

To assure stability of the numerical solution, M is required to be less than or equal to $\frac{1}{2}$. For $M > \frac{1}{2}$ the coefficient of $T_{I,K}$ in Eq. (70) would become negative, leading to a physically absurd result: The higher the temperature $T_{I,K}$, the lower it would become at a time interval At later.

Following Binder [14] and Schmidt [15], one may use the value $M = \frac{1}{2}$ to get an extremely simple finite difference method. In Cartesian coordinates ($n = 0$), Eq. (70) then becomes

$$T_{I+1,K} \cong \tfrac{1}{2}(T_{I,K-1} + T_{I,K+1}) \tag{71}$$

The new temperature $T_{I+1,K}$ at position x_K is found by simply taking the arithmetic mean of the temperatures at the two adjacent positions x_{K-1} and x_{K+1} at time t_I.

With two or three Cartesian space coordinates $(x_K, y_L), (x_K, y_L, z_M)$, taking

$$\Delta x = \Delta y = \Delta z \tag{72}$$

we get

$$T_{I+1,K,L} \cong M(T_{I,K-1,L} + T_{I,K+1,L} + T_{I,K,L-1} + T_{I,K,L+1}) + (1 - 4M)T_{I,K,L} \tag{73}$$

and

$$T_{I+1,K,L,M} \cong M(T_{I,K-1,L,M} + T_{I,K+1,L,M} + T_{I,K,L-1,M} + T_{I,K,L+1,M} + T_{I,K,L,M-1} + T_{I,K,L,M+1}) + (1 - 6M)T_{I,K,L,M} \tag{74}$$

with $M \leqslant \frac{1}{4}$ and $M \leqslant \frac{1}{6}$, respectively, to assure stability.

To show the application of the finite difference method, we start from the one-dimensional difference equation (70) in Cartesian ($n = 0$), cylindrical ($n = 1$), or spherical ($n = 2$) coordinates, taking $M = \frac{1}{2}$ for simplicity.

We subdivide the body (a slab, a cylinder, a sphere, or a hollow cylinder or sphere) in K_N shells of thickness Ax (see Fig. 11). The center(line) of the innermost shell must not coincide with the center(line) of a full sphere or cylinder [for $x_K = 0$, Eq. (70) cannot be used]. With the numbers K of the shells as shown in Fig. 11, we get the coordinate of the centerline of the Kth shell as

$$x_K = \Delta x(K - 0.5) \tag{75}$$

and Δx is related to the radius R (or the half-thickness L) and the total number of shells K_N by

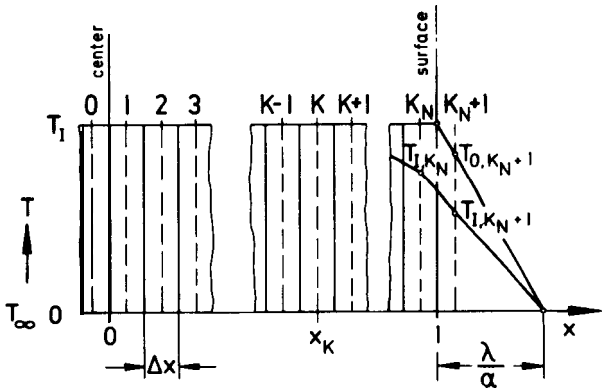

Figure 11 Subdivision of a body in K_N shells of thickness Ax for finite difference method.

$$\Delta x = \frac{R}{K_N} \tag{76}$$

To account for the boundary conditions we need the additional shell numbers $K = 0$ ($\Delta x/2$ left of the center) and $K_N + 1$ ($\Delta x/2$ outside the surface).

Assuming no heat flux (because of symmetry) at the center and the B.C. of the third kind at the surface (16), we get

$$T_{I,0} = T_{I,1} \quad \text{(symmetry)} \tag{77}$$

and

$$-\lambda \frac{T_{I,K_N+1} - T_{I,K_N}}{\Delta x} = \alpha(T_{I,K_N+1/2} - T_\infty) \tag{78}$$

For the first step ($I = 0$), the heat flux at the surface has to be expressed as

$$-\lambda \frac{T_{0,K_N+1} - T_{0,K_N+1/2}}{\Delta x/2} = \alpha(T_{0,K_N+1/2} - T_\infty) \tag{79}$$

Using the normalized temperatures T^+ [see Eq. (10)] with $T^+_\infty = 0$ and writing the surface temperature $T_{K_N+1/2}$ -which does not occur in the difference scheme-as the arithmetic mean of T_{K_N} and T_{K_N+1}, the boundary condition becomes

$$T^+_{0,K_N+1} = T^+_{0,K_N+1/2}\left(1 - \frac{\alpha\,\Delta x}{2\lambda}\right) \quad \text{for the first step } (I = 0) \tag{80}$$

$$T^+_{I,K_N+1} = T^+_{I,K_N}\frac{1 - \alpha\,\Delta x/2\lambda}{1 + \alpha\,\Delta x/2\lambda} \quad \text{for all succeeding steps } (I > 0) \tag{81}$$

With Eq. (76), the group $\alpha\,\Delta x/(2\lambda)$ may be written as

$$\frac{\alpha\,\Delta x}{2\lambda} = \frac{\alpha R}{\lambda}\frac{1}{2K_N} = \frac{\mathrm{i}}{2K_N} \tag{82}$$

From Eqs. (70) and (75) through (82), we get

© 1983 Hemisphere Publishing Corporation

$$T^+_{I+1,K} = \frac{(2K-1-n)T^+_{I,K-1} + (2K-1+n)T^+_{I,K+1}}{2(2K-1)} \tag{83}$$

$$T^+_{I,0} = T^+_{I,1} \tag{84}$$

$$T^+_{I,K_N+1} = \begin{cases} T^+_{0,K_N+1/2}\,\dfrac{2K_N - \mathrm{Bi}}{2K_N} & I = 0 \quad (85) \\ T^+_{I,K_N}\,\dfrac{2K_N - \mathrm{Bi}}{2K_N + \mathrm{Bi}} & I > 0 \quad (86) \end{cases}$$

Example. Consider cooling (or heating) of a sphere (n = 2) with constant initial temperature ($T^+_{0,K}$ = *I*), constant temperature of the surroundings (T^+_∞ = 0), and a Biot number of Bi = 1.

We want to know the temperature distribution in the sphere at a (dimensionless) time t^+ = 0.25. Choosing a relatively coarse subdivision of the sphere in only four shells (Ax $=\Delta x/R = \frac{1}{4}$) leads to a dimensionless time step of At $= \frac{1}{2}(\Delta x^+)^2 = \frac{1}{32}$. It is necessary to take eight steps in time to reach t^+ = 0.25 (t^+_8 = 8 . *At'* = 0.25). The calculation is carried out in tabular form in Table 3.

The expressions given in Eqs. (83) through (86) are used to obtain the temperatures at time $t^+_I = I\,\Delta t^+$ and position $x^+_K = (K-0.5)/K_N$. The surface temperature $T^+_{I,K_N+1/2}$ is calculated as the arithmetic mean of the temperature in the center of the outermost shell T_{I,K_N} ($\Delta x/2$ under the surface) and the (fictitious) temperature T_{I,K_N+1} ($\Delta x/2$ outside the surface). Figure 12 shows the results of the numerical calculation for Z = 2, 4, and 8 (*t'* = 0.062 5, 0.125, and 0.25), together with curves calculated from the exact analytical solution [Eq. (28)]. The agreement between numerical and analytic results is surprisingly good (less than 2% deviation for I = 8).

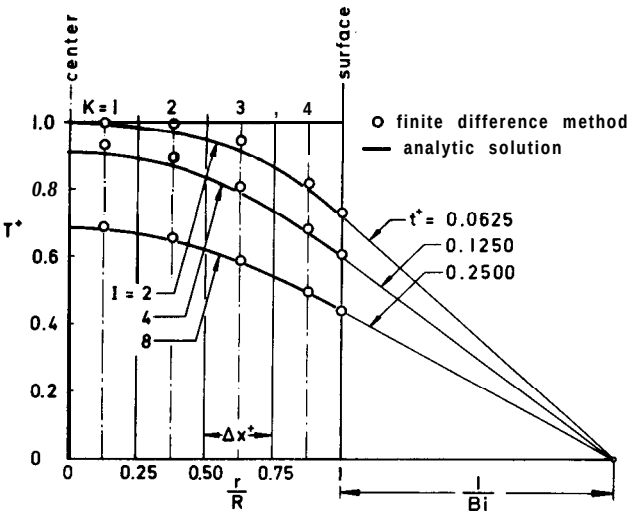

Figure 12 Comparison of numerical and analytical results for transient temperatures in a sphere.

B. Multidimensional systems

Solutions of Eq. 2.4.1(*3a*) for some multidimensional systems may be found by simply multiplying the corresponding one-dimensional solutions:

In Cartesian coordinates,

the temperature field $T^+(x,y,z,t)$

with the initial condition $T^+(x,y,z,0) = 1$ ***(87)***

and the boundary conditions (3rd B.C.):

$$\left(\frac{\lambda}{\alpha_1}\frac{\partial T^+}{\partial x} \pm T^+\right)_{x=\pm X} = 0 \qquad \left(\frac{\lambda}{\alpha_2}\frac{\partial T^+}{\partial y} \pm T^+\right)_{y=\pm Y} = 0$$

$$\left(\frac{\lambda}{\alpha_3}\frac{\partial T^+}{\partial z} \pm T^+\right)_{z=\pm Z} = 0 \tag{88}$$

Table 3 Finite difference calculation of transient temperatures in a sphere

	Center				Surface		
K	***0***	1	***2***	***3***	$K_N = 4$	$K_N + 1 = 5$	$K_{N+1/2}$
$T_{I(+1),K}$	$T_{I,1}$	$\dfrac{-T_{I,0} + 3T_{I,2}}{2}$	$\dfrac{T_{I,1} + 5T_{I,3}}{6}$	$\dfrac{3T_{I,2} + 7T_{I,4}}{10}$	$\dfrac{5T_{I,3} + 9T_{I,5}}{14}$	$\frac{7}{9}T_{I,4}$	$\dfrac{T_{I,4} + T_{I,5}}{2}$
$I = 0$	1	1	1	1	1	0.875[a]	1
1	1	1	1	1	***0.920***	0.715	0.818
2	1	**1**	1	***0.944***	0.817	***0.635***	***0.726***
3	**1**	1	***0.953***	***0.872***	***0.745***	***0.580***	***0.662***
4	***0.930***	***0.930***	***0.893***	***0.807***	***0.684***	***0.532***	***0.608***
5	***0.875***	***0.875***	***0.827***	***0.747***	***0.630***	***0.490***	***0.560***
6	***0.803***	***0.803***	***0.768***	***0.689***	***0.582***	***0.453***	0.517
7	*0.75* 1	***0.751***	***0.708***	***0.638***	***0.537***	***0.418***	***0.478***
8	***0.687***	***0.687***	***0.657***	***0.588***	***0.497***	***0.386***	0.441

[a] $\frac{7}{8}T_{0,K_N+1/2}$.

© 1983 Hemisphere Publishing Corporation

is given by

$$T^+(x,y,z,t) = T_1^+(x,t)T_2^+(y,t)T_3^+(z,t) \tag{89}$$

where T_1^+, T_2^+, and T_3^+ denote the solutions of the corresponding one-dimensional problems with the same initial and boundary conditions. Examples of systems of that kind include the following.

1. The quarterspace ($x > 0$, $y > 0$, $-\infty < z < \infty$) (a two-dimensional rectangular comer) with unit initial and zero surface temperature ($\lambda/\alpha \to 0$):

$$T^+(x,y,t) = \text{erf}\,\frac{x}{2\sqrt{\kappa t}}\,\text{erf}\,\frac{y}{2\sqrt{\kappa t}} \tag{90}$$

[see Eq. (20) with $\text{Bi} \to \infty$ for the corresponding one-dimensional problem, the semiinfinite body or half-space].

2. The octant ($x > 0$, $y > 0$, $z > 0$) (a three-dimensional rectangular comer) with unit initial and zero surface temperature:

$$T^+(x,y,z,t) = \text{erf}\,\frac{x}{2\sqrt{\kappa t}}\,\text{erf}\,\frac{Y}{2\sqrt{\kappa t}}\,\text{erf}\,\frac{z}{2\sqrt{\kappa t}} \tag{91}$$

3. The (infinitely) long bar of rectangular cross section ($-X < x < X$, $-Y < y < Y$, $-\infty < z < \infty$) with 3rd B.C.:

$$T^+(x,y,t) = T_1^+(x,t)T_2^+(y,t) \tag{92}$$

with $T_1^+(x,t)$ from Eq. (28) (slab of thickness 2X) and $T_2^+(y,t)$ from Eq. (28) (slab of thickness $2Y$).

4. The rectangular parallelepiped ($-X < x < X$, $-Y < y < Y$, $-Z < z < Z$) with 3rd B.C.:

$$T^+(x,y,z,t) = T_1^+(x,t)T_2^+(y,t)T_3^+(z,t) \tag{93}$$

with T_1^+, T_2^+, T_3^+ from Eq. (28) (slabs of thickness 2X, $2Y$, and $2Z$).

In cylindrical coordinates $T^+(r,z,t)$ with unit initial temperature

$$T^+(r,z,0) = 1 \tag{94}$$

and 3rd B.C.

$$\left(\frac{\lambda}{\alpha_1}\frac{T^+}{\partial r} + T^+\right)_{r=R} = 0 \tag{95}$$

$$\left(\frac{\lambda}{\alpha_2}\frac{\partial T^+}{\partial z} \pm T^+\right)_{z=\pm Z} = 0 \tag{96}$$

the finite cylinder ($0 \leqslant r < R$, $-Z < z < Z$) is given by

$$T^+(r,z,t) = T_1^+(r,t)T_2^+(z,t) \tag{97}$$

with $T_1^+(r,t)$ from Eq. (28) (infinite cylinder of radius R) and $T_2^+(z,t)$ from Eq. (28) (slab of thickness $2Z$).

The simple multiplication of one-dimensional solutions to get the multidimensional ones is also valid for the average temperature $\bar{T}$, so the method may be used with the approximative equation (60) as well.

Example. A solid foodstuff (thermal diffusivity $\kappa = 0.16 \times 10^{-6}\,\text{m}^2/\text{s}$, thermal conductivity $\lambda = 0.6$ W/m K) in thin-walled cylindrical tins of diameter $D = 2R = 100$ mm and height $H = 2Z = 50$ mm is to be sterilized by placing in a hot water bath at $T_\infty = 150°$ C (under pressure). We assume the heat transfer coefficient from the hot water to the tin surface to be $\alpha = 600\ \text{W/m}^2\,\text{K}$. What time is necessary to heat up the foodstuff from its initial temperature of 20° C to an average temperature of $\bar{T} = 100°\text{C}$?

From Eq. (97), we have

$$\bar{T}^+ = \bar{T}_1^+\bar{T}_2^+$$

with

$$\bar{T}_1^+ = \bar{T}^+\left(\frac{\kappa t}{R^2}, \frac{\alpha R}{\lambda}\right) \quad \text{(infinite cylinder)}$$

$$\bar{T}_2^+ = \bar{T}^+\left(\frac{\kappa t}{Z^2}, \frac{\alpha Z}{\lambda}\right) \quad \text{(slab of thickness } 2Z\text{)}$$

Since we wish to find the time, a solution using Eq. (29) or Figs. 3 and 6 can be found only by iteration. Also, the approximation (60) cannot be solved explicitly for the time in this case. The required iteration, however, is quite simple, and may be carried out in a few minutes with a pocket calculator.

With $e^a e^b = e^{a+b}$ we get, from (60) and (97),

$$\bar{T}^+ = \exp\left\{-\frac{t_Z^+}{(1/\text{Bi}_Z) + [1/\text{Nu}_{iZ}(t_Z^+)]} - \frac{2 \cdot t_R^+}{(1/\text{Bi}_R) + [1/\text{Nu}_{iR}(t_R^+)]}\right\} \tag{98}$$

Taking the logarithm and writing

$$t_R^+ \equiv \frac{\kappa t}{R^2} = \left(\frac{Z}{R}\right)^2 \frac{\kappa t}{Z^2} = \left(\frac{H}{D}\right)^2 t_Z^+ \tag{99}$$

we get an implicit equation for the heating (or cooling) time of a finite cylinder

$$t_Z^+ = \ln\left(\frac{1}{\bar{T}^+}\right)\left\{\frac{1}{(1/\text{Bi}_Z) + [\text{Nu}_{iZ\infty}^2 + (4/\pi)(1/t_Z^+)]^{-1/2}} + \frac{2(H/D)^2}{(1/\text{Bi}_R) + [\text{Nu}_{iR\infty}^2 + (4/\pi)(D/H)^2(1/t_Z^+)]^{-1/2}}\right\}^{-1} \tag{100}$$

With the given data we get:

$$\bar{T}^+ = \frac{100 - 150}{20 - 150} = \frac{5}{13}$$

$$\frac{H}{D} = 0.5 \qquad \text{Bi}_Z = \frac{600(25 \times 10^{-3})}{0.6} = 25 \qquad \text{Bi}_R = 50$$

© 1983 Hemisphere Publishing Corporation

$Nu^2_{iZ\infty} = 6.326 \qquad Nu^2_{iR\infty} = 8.718$ from Eq. (62)

$$t_Z^+ = \ln \frac{13}{5} \left\{ \frac{1}{0.04 + [6.326 + (4/\pi)(1/t_Z^+)]^{-1/2}} + \frac{0.5}{0.02 + [8.718 + (16/\pi)(1/t_Z^+)]^{-1/2}} \right\}^{-1}$$

This is easily solved by using the result of the right-hand side with $1/t_Z^+ = 0$ (i.e., $Nu_i = Nu$,) as a starting value for the iteration:

$t_Z^{+(0)} = 0.26$ rounded off to 0.2 and recalculated

yields $t_Z^{+(1)} = 0.167$ rounded off to 0.16 and recalculated

yields $t_Z^{+(2)} = 0.156\,5$ rounded off to 0.156 and recalculated

yields $t_Z^{+(3)} = 0.155\,3$ rounded off to 0.155 and recalculated

yields $t_Z^{+(4)} = 0.155\,0$

From this result the time required to heat up the foodstuff in the tins is found from the definition oft+:

$$t = \frac{Z^2}{\kappa} t_Z^+ = \frac{(25)^2}{0.16} 0.155\ \text{s} = 605\ \text{s} \cong 10\ \text{min}$$

Checking this with the more rigorous series solutions (or the charts) shows that the time calculated from the approximation is sufficient to heat the foodstuff to an average temperature of -105° C instead of 100° C. This seems to be a reasonable fair approximation if we keep in mind the uncertainties involved in the input data of our problem (physical properties of foodstuffs, heat transfer coefficient, etc.).

C. Coupled thermal fields

It is not always possible to specify the boundary conditions immediately on the surface of one homogeneous body, that is, the region under consideration, whose boundary conditions are known, may contain several bodies with different physical properties λ, ρ, c. Assuming these properties to be constant within each body, Eq. 2.4.1(3*a*) is valid for each body separately. At the interfaces the thermal fields are coupled by the following interface conditions:

$$T_i = T_{i+1} \tag{101}$$

$$\lambda_i \left(\frac{\partial T}{\partial n}\right)_i = \lambda_{i+1} \left(\frac{\partial T}{\partial n}\right)_{i+1} \tag{102}$$

(on the interface of bodies ***i*** and ***i + 1).***

Condition (101) is not necessarily fulfilled on the interfaces of real solids. Imperfect contact due to the surface roughness, oxide films, or sorption layers may result in additional contact resistances (see Sec. 2.4.6).

A simple example of coupled thermal fields is the contact of two semiinfinite bodies of different initial temperatures T_{I1} and T_{I2} with the plane x = 0 as interface (Fig. 13). The solution is

$$\frac{T_1 - T_0}{T_{I1} - T_0} = -\operatorname{erf} \frac{x}{2\sqrt{\kappa_1 t}} \qquad (x < 0) \tag{103}$$

$$\frac{T_2 - T_0}{T_{I2} - T_0} = +\operatorname{erf} \frac{x}{2\sqrt{\kappa_2 t}} \qquad (x > 0) \tag{104}$$

The contact temperature $T_1 (x = 0) = T_2 (x = 0) = T_0$ is found from these equations using the interface condition (102):

$$T_0 = \frac{T_{I1} + [\sqrt{(\lambda\rho c)_2}/\sqrt{(\lambda\rho c)_1}]T_{I2}}{1 + [\sqrt{(\lambda\rho c)_2}/\sqrt{(\lambda\rho c)_1}]} \tag{105}$$

The contact temperature depends on the ratio of $\sqrt{\lambda\rho c}$. It is always closer to the initial temperature of the body with the higher value of $\lambda\rho c$. The maximum temperature differences $(T_{I1} - T_0)$ and $(T_0 - T_{I2})$ in the two bodies are inversely proportional to that ratio:

$$\frac{T_{I1} - T_0}{T_0 - T_{I2}} = \frac{\sqrt{(\lambda\rho c)_2}}{\sqrt{(\lambda\rho c)_1}} \tag{105a}$$

Therefore wood seems to be warmer (cooler) than metal when touched by hand if both materials are at the same temperature below (above) the hand s temperature.

Other examples for coupled thermal fields such as multilayered slabs or bodies in contact with a well-stirred fluid of finite capacity are found in [1] and [2]. Analytical solutions may best be found by the method of Laplace transforms.

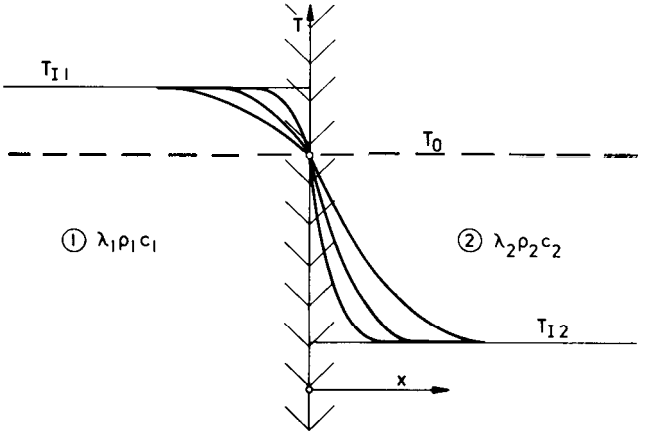

Figure 13 Coupled thermal fields of two semiinfinite bodies during contact.

Nomenclature for Section 2.4.3 appears at the beginning of Part 2. References appear at the end of Section 2.4.5.

© 1983 Hemisphere 1 blishing Corporation

2.4.4
Melting and solidification

H. Martin

■ If the temperature inside a body passes a melting point T_P (subscript P for phase change), the isothermal surface $T = T_P$ subdivides the body into two regions, each with a different phase and properties. The thermal fields in both phases are coupled (see Sec. 2.4.3C). Additionally, the position of the interface may change with time. Exact analytical solutions for these problems are known only for some simple special cases [1, chapter XI] . For practical applications it is often sufficient to know only the time required to solidify or melt a body completely, with the details of the temperature field of minor interest.

Solidifying times may be calculated by a simple approximation if the enthalpy change of the solid shell is small when compared with the latent enthalpy of solidification. Figure 1 shows the problem. It is assumed that the liquid (subscript 1) is initially at the phase-change temperature T_P.

The energy balance for this system may be written

$$-\dot{Q} \cong \rho_1 \, \Delta h_{12} \, \frac{dV_1(x)}{dx} \, \frac{dx}{dt} \tag{1}$$

where x denotes the position and dx/dt the velocity of the liquid-solid interface.

The change of enthalpy in the solid shell (subscript 2) is neglected in this balance, as we mentioned before $[c_{p2}(T_P - T_\infty) \ll \Delta h_{12}]$. In this case the temperature profiles in the solid shell are always like those for the steady state [Eq. 2.4.2(16)]. The heat rate $\dot{Q}$ may be expressed as

$$\dot{Q} = UA(T_P - T_\infty) \tag{2}$$

with

$$\frac{1}{U} = \frac{1}{\alpha_i(x)} + \underbrace{\left(\frac{s}{\lambda}\right)_{\text{wall}} + \frac{1}{\alpha_{\text{outside}}}}$$

or

$$\frac{1}{U} = \frac{1}{\alpha_i(x)} + \frac{1}{U_0} \tag{3}$$

The inside heat transfer resistance $1/\alpha_i$ as a function of the position of the interface is

$$\frac{1}{\alpha_i(x)} = \begin{cases} \dfrac{R}{\lambda_2}\left(1 - \dfrac{x}{R}\right) & \text{slab} \quad (4a) \\ \dfrac{R}{\lambda_2} \ln \dfrac{R}{x} & \text{cylinder} \quad (4b) \\ \dfrac{R}{\lambda_2}\left(\dfrac{R}{x} - 1\right) & \text{sphere} \quad (4c) \end{cases}$$

From Eqs. (1) through (4) we get a relation for the velocity of the interface dx/dt, which may be written in dimensionless form as

$$\frac{1}{\mathrm{Ph}} = -\left[\frac{1}{\mathrm{Bi}} + \frac{1}{\mathrm{Nu}(x^+)}\right] x^{+n} \frac{dx^+}{dt^+} \tag{5}$$

In Eq. (5) the dimensionless quantities are defined as follows:

Phase change number: $$\mathrm{Ph} \equiv \frac{\rho_1 \Delta h_{12}}{\rho_2 c_{p2}(T_P - T_\infty)} \tag{6}$$

Biot number: $$\mathrm{Bi} \equiv \frac{U_0 R}{\lambda_2} \tag{7}$$

Dimensionless interface position: $$x^+ \equiv \frac{x}{R} \tag{8}$$

© 1983 Hemisphere I blishing Corporation

HEDH

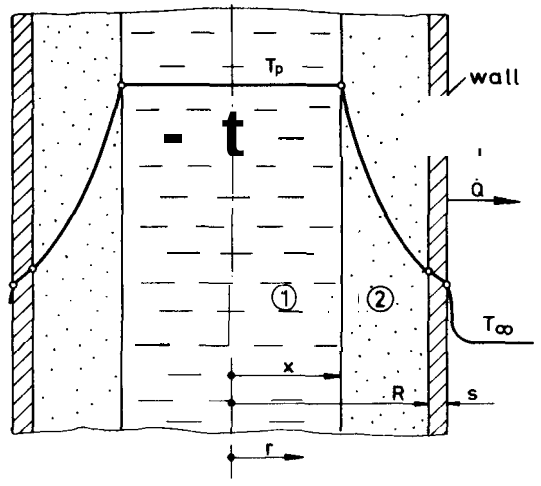

Figure 1 Solidification (or melting) of simple bodies.

Dimensionless time (Fourier number): $$t^+ \equiv \frac{\lambda_2 t}{\rho_2 c_{p2} R^2} \tag{9}$$

The dimensionless shell resistance $1/\mathrm{Nu}(x^+)$ follows from Eqs. (4*a*), (4*b*), and (4*c*):

$$\frac{1}{\mathrm{Nu}(x^+)} = \begin{cases} 1 - x^+ & n = 0 \quad \text{slab} & (10a) \\ -\ln(x^+) & n = 1 \quad \text{cylinder} & (10b) \\ \dfrac{1}{x^+} - 1 & n = 2 \quad \text{sphere} & (10c) \end{cases}$$

Integration of Eq. (5) with (10*a*), (10*b*), and (10*c*) in the limits $x^+ = 1$ to $x^+ = 0$ gives the solidification time t_s^+.

Since we neglected the enthalpy change of the shell, this calculation gives a minimum solidification time $t_{s,\min}^+$ (quasisteady-state solution):

$$t_{s,\min}^+ = \frac{\mathrm{Ph}}{2(n+1)} \left(1 + \frac{2}{\mathrm{Bi}}\right) \tag{11}$$

The same calculation may be used for melting (subscript 1 for solid, 2 for liquid) if there is no natural convection in the liquid shell.

The real solidification time is always greater than $t_{s,\min}$. It may be calculated from

$$t_s = \psi(\mathrm{Ph}, \mathrm{Bi}, n)\, t_{s,\min} \tag{12}$$

The function ψ can be determined from an exact analytical solution only for $n = 0$ (slab) and $\mathrm{Bi} = \infty$ (Neumann s solution, see [1], p. 285):

$$\psi(\mathrm{Ph}, \infty, 0) = \frac{1}{2\mathrm{Ph}\, v^2} \tag{13}$$

with v to be found from

$$\frac{1}{\mathrm{Ph}} = \sqrt{\pi}\, v e^{v^2} \operatorname{erf} v \tag{14}$$

Values of ψ for other n and Bi can be found only from numerical (finite difference) calculations. If one plots the numerical data of Linge [16] and Tao [17] for a slab [16], cylinder, and sphere [16, 17] in the form ψ versus $(n+1)/\mathrm{Ph}$ [with $(n+1) = AR/V$], one finds that the data for all three geometries may be represented by one curve with a reasonable degree of approximation (see Fig. 2). In Fig. 2, Neumann s solution [Eqs. (13) and (14)] is shown as a dotted line.

The full lines are calculated from the empirical equation

$$\psi\left(\frac{AR/V}{\mathrm{Ph}}, \mathrm{Bi}\right) \cong 1 + \frac{1}{2}\left(\frac{\mathrm{Bi}}{1+\mathrm{Bi}}\right)^{2/3} \times \left(\sqrt{1 + 2\frac{AR/V}{\mathrm{Ph}}} - 1\right) \tag{15}$$

The error of Eq. (15) is less than ±5% compared with Neumann s solution for $0 < 1/\mathrm{Ph} < 6$.

Solidification times calculated from Eq. (12) with (11) and (15) are in very good agreement with Tao s [17] numerically calculated charts for cylinders and spheres.

Example. For freezing water with a coolant temperature of $T_\infty = -18°\mathrm{C}$, the phase-change number Ph becomes

$$\mathrm{Ph} = \frac{(1\,000\ \mathrm{kg/m^3})(333\ \mathrm{kJ/kg})}{(917\ \mathrm{kg/m^3})(2.05\,\mathrm{kJ/kg\ K})[0 - (-18)]\,\mathrm{K}} = 9.84$$

that is, the reciprocal value $1/\mathrm{Ph} = 0.102$. So the freezing time can be calculated from Eq. (11). The correction ψ remains less than 14% for a sphere, less than 10% for a cylinder, and less than 5% for a slab with $\mathrm{Bi} \to \infty$. The time required to freeze a slab of thickness X (with a high heat transfer coefficient on one side) becomes

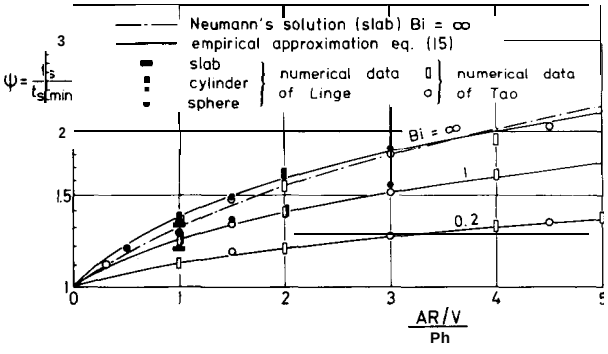

Figure 2 Correction ψ to calculate real solidification times from the minimum values *given* by the quasisteady-state solution equation (11).

© 1983 Hemisphere Publishing Corporation

$$t_{s,\min}\,(\mathrm{Bi}\to\infty)=\frac{\rho_2 c_{p2}}{\lambda_2}\,\frac{\rho_1\,\Delta h_{12}}{\rho_2 c_{p2}(T_P-T_\infty)}\,\frac{1}{2}\,X^2$$

With the physical properties and temperatures as given above, we get

$$t_{s,\min}=4.2\left(\frac{X}{\mathrm{mm}}\right)^2\ \mathrm{s}\qquad\begin{pmatrix}\text{for } T_\infty=-18^\circ\mathrm{C}\\ \text{and } U_0\gg\lambda_2/X\end{pmatrix}$$

So a layer of 10 mm thickness requires at least 7 min (420 s) to freeze. The formation of a 100-mm ice layer, however, takes about 12 h (4.2×10^4 s).

Considerably smaller values of the phase-change number Ph may be found for metals. According to Stephan [18], one can find [with T_∞ (or T_{wall}) = 80°C]:

	Ph	1/Ph
Tin	1.54	0.65
Zinc	0.11	1.30
Nickel	0.35	2.86
Steel (0.1%C)	0.33	3.03

In these cases the corrections ψ to the minimum solidification time may become considerably larger. Because of the high conductivity of the metals, however, the Biot number will often be very low and the solidification time again tends to its minimum value.

Nomenclature for Section 2.4.4 appears at the beginning of Part 2. References appear at the end of Section 2.4.5.

© 1983 Hemisphere Publishing Corporation

2.4.5

Periodic change of temperature

H. Martin

■ Another thermal boundary condition that frequently arises in natural as well as in engineering systems is the periodic change of the temperature of the surrounding medium. The daily and seasonal changes of solar radiation on the soil or on buildings, the periodic temperature changes in the cylinders of internal combustion engines, the (on-off) temperature control by a thermostat, and the periodic heat transfer in-a regenerator are examples for this kind of boundary condition.

The periodic change of temperature of the surroundings may be represented by a simple harmonic oscillation about an average value $\bar{T}$ with an amplitude $(T_{\infty,\max} - \bar{T})$:

$$T,(t) = \bar{T} + (T_{\infty,\max} - \bar{T}) \sin (\omega t) \qquad (1)$$

If this boundary condition has been maintained for a sufficiently large number of periods $(t_P = 2\pi/\omega) t \gg t_P$, the temperatures inside the body will undergo a periodic change too:

$$T(x,t) = \bar{T} + (T_{\infty,\max} - \bar{T}) \hat{A}(x) \sin [\omega t + \varphi(x)] \qquad (2)$$

The amplitude $\hat{A}$ and phase φ of this steady temperature oscillation are functions of the normalized position x^+, the Biot number, and a modulus M,

$$M \equiv \left(\frac{\omega}{2\kappa} R^2\right)^{1/2} = \sqrt{\left(\frac{\pi \rho c_p}{t_P \lambda}\right)} R \qquad (3)$$

which is the square root of a reciprocal Fourier number with $t_P/\pi = 2/\omega$ as the characteristic time.

For low values of M, that is, slow changes of the surrounding temperature (with a long period $t_P \gg \pi R^2/\kappa$), the amplitude $\hat{A}$ comes close to unity and the phase comes close to zero (no phase lag).

For large values of M, that is, rapid changes of the surrounding temperature, the amplitude $\hat{A}$ decreases from the surface (x = 1) toward the center $(x^+ = 0)$ of the body. In the same direction the negative phase of the oscillation increases (in its absolute value). For sufficiently large values of M, only a small layer near the surface of the body follows the outer oscillation.

The analytical expressions for amplitude and phase can be given in a generalized form for slab, cylinder, and sphere :

$$\hat{A}(x^+, M, \mathrm{Bi}) = \left[\frac{F_R^2(Mx^+) + F_I^2(Mx^+)}{G_R^2(M,\mathrm{Bi}) + G_I^2(M,\mathrm{Bi})}\right]^{1/2} \qquad (4)$$

$$\varphi(x^+, M, \mathrm{Bi}) = \arctan\left(\frac{F_I G_R - F_R G_I}{F_R G_R + F_I G_I}\right) \qquad (5)$$

The meaning of the symbols F_R, F_I, G_R, and G_I may be found from Table 1.

Figures 1 to 6 show amplitude and phase at the surface $(x^+ = 1)$ as functions of M with $\mathrm{Bi}_M = \mathrm{Bi}/M = (\alpha/\lambda)\sqrt{(2\kappa/\omega)}$ as a parameter.

From Figs. 7 and 8, $\hat{A}_c$ and φ_c, the amplitudes and phases in the center of the body, can be found.

For large values of Mx^+ (→ semiinfmite body), Eqs. (4) and (5) may be rewritten in a simpler way by introducing a new coordinate

$$\eta = M(1 - x^+) = \sqrt{\left(\frac{\omega}{2\kappa}\right)}\, y \qquad (6)$$

$(y = 0$ at the surface)

© 1983 Hemisphere 1 blishing Corporation

Table 1 Periodic change of temperature: Functions to calculate amplitude and phase of steady oscillations in slab, cylinder, and sphere

	Slab	Cylinder	Sphere
$F_R(M\xi)$	$\cosh(M\xi)\cos(M\xi)$	$\mathrm{ber}(\sqrt{2}M\xi)$	$\frac{\sinh(M\xi)}{\xi}\cos(M\xi)$
$F_I(M\xi)$	$\sinh(M\xi)\sin(M\xi)$	$\mathrm{bei}(\sqrt{2}M\xi)$	$\cosh(M\xi)\frac{\sin(M\xi)}{\xi}$
$\frac{dF_R}{d(M\xi)}_{\xi=1}$	$\sinh M\cos M-\cosh M\sin M$	$\mathrm{ber}_1(\sqrt{2}M)+\mathrm{bei}_1(\sqrt{2}M)$ $[=\sqrt{2}\,\mathrm{ber}'\sqrt{2}M)]$	$\left(\cosh M-\frac{\sinh M}{M}\right)\cos M-\sinh M\sin M$
$\frac{dF_I}{d(M\xi)}_{\xi=1}$	$\cosh M\sin M+\sinh M\cos M$	$\mathrm{bei}_1(\sqrt{2}M)-\mathrm{ber}_1(\sqrt{2}M)$ $[=\sqrt{2}\,\mathrm{bei}'(\sqrt{2}M)]$	$\sinh M\sin M+\left(\cos M-\frac{\sin M}{M}\right)\cosh M$

$$G_R(M,\mathrm{Bi})\equiv\left[F_R(M\xi)+\frac{M}{\mathrm{Bi}}\frac{dF_R}{d(M\xi)}\right]_{\xi=1}\qquad G_I(M,\mathrm{Bi})\equiv\left[F_I(M\xi)+\frac{M}{\mathrm{Bi}}\frac{dF_I}{d(M\xi)}\right]_{\xi=1}$$

Tables and graphs of the functions ber and bei (Kelvin s functions) are to be found in [7] and [8].

$$\hat{A}(\eta,\mathrm{Bi}_M)=\frac{e^{-\eta}}{\sqrt{1+2/\mathrm{Bi}_M+2/\mathrm{Bi}_M^2}} \tag{7}$$

$$\varphi(\eta,\mathrm{Bi}_M)=-\eta+\arctan\frac{1}{1+\mathrm{Bi}_M}\Big) \tag{8}$$

With the boundary condition (1), the direction of the heat flux changes after each half-period. The instantaneous heat flux follows a harmonic oscillation as the temperatures. Integration over a half-period yields the quantity of heat that is stored during this time interval as internal energy of the body and released to the surroundings in the next half-period:

$$Q_{tP/2}=\int_{t=0}^{tP/2}\dot{Q}(t)\,dt \tag{9}$$

After some algebraic rearrangement, this quantity of heat is found to be*

$$Q_{tP/2}=\lambda\sqrt{\left(\frac{\pi}{\kappa tP}\right)}\sqrt{\frac{(F_R')^2+(F_I')^2}{G_R^2+G_I^2}}\times A\,\frac{2}{\pi}(T_{\infty,\max}-\bar{T})\,\frac{t_P}{2} \tag{10}$$

Defining an overall heat transfer coefficient $U_{tP/2}$ by

$$Q_{tP/2}\equiv U_{tP/2}A\,\Delta\bar{T}\,\frac{t_P}{2} \tag{11}$$

with the time-averaged temperature difference $\Delta\bar{T}$ following the integration of Eq. (I),

$$\Delta\bar{T}=\frac{1}{t_P/2}\int_0^{tP/2}[T_\infty(t)-\bar{T}]\,dt=\frac{2}{\pi}(T_{\infty,\max}-\bar{T}) \tag{12}$$

one gets, by comparison of Eqs. (10) and (11),

$$U_{tP/2}=\lambda\sqrt{\frac{\pi}{\kappa t_P}}\sqrt{\frac{(F_R')^2+(F_I')^2}{G_R^2+G_I^2}} \tag{13}$$

The second square root on the right-hand side of Eq. (13) is a function of M and Bi_M (see Table 1).

For low values of Bi_M this function asymptotically approaches Bi_M itself, and the overall heat transfer coefficient $U_{tP/2}$ tends to the outside heat transfer coefficient α (inside resistance negligible).

$$\lim_{\mathrm{Bi}_M\to 0}U_{tP/2}=\alpha \tag{14}$$

In the other limit (i.e., for $\mathrm{Bi}_M\to\infty$), $U_{tP/2}$ tends to an inside heat transfer coefficient α_i that may be written in dimensionless form with $\sqrt{(\kappa tP/\pi)}$ as a characteristic length :

$$\lim_{\mathrm{Bi}_M\to\infty}\frac{U_{tP/2}}{\lambda}\sqrt{\frac{\kappa t_P}{\pi}}=\frac{\alpha_i}{\lambda}\sqrt{\frac{\kappa t_P}{\pi}}=\sqrt{\frac{(F_R')^2+(F_I')^2}{F_R^2+F_I^2}} \tag{15}$$

Figure 9 shows this dimensionless inside heat transfer coefficient

$$\mathrm{Nu}_{i,M}=\frac{\alpha_i}{\lambda}\sqrt{\frac{\kappa t_P}{\pi}}=\alpha_i\sqrt{\frac{t_P}{\pi\lambda\rho c}} \tag{16}$$

as a function of M for slab, cylinder, and sphere. For large values of M, $\mathrm{Nu}_{i,M}$ tends to a constant value,

*$F_R'=[dF_R(Mx^+)/d(Mx^+)]_{x^+=1}$ and $F_I'=[dF_I(Mx^+)/d(Mx^+)]_{x^+=1}$; see Table 1.

© 1983 Hemisphere Publishing Corporation

$$\lim_{M\to\infty} \mathrm{Nu}_{i,M} = \sqrt{2} \tag{17}$$

whereas it becomes linearly proportional to M for small values of M,

$$\lim_{M\to 0}\left(\frac{\mathrm{Nu}_{i,M}}{M}\right) = 2\frac{V}{AR} = \begin{cases} 2 & \text{slab} \\ 1 & \text{cylinder} \\ \frac{2}{3} & \text{sphere} \end{cases} \tag{18}$$

For the slab, $\mathrm{Nu}_{i,M}$ has a maximum a $M \cong 1.2$. For a given period t_P there exists a certain wall thickness $2X_{M=1.2} = 2.4\sqrt{\kappa t_P/\pi}$ with a maximum storage capacity. This optimal wall thickness is about 80 mm for a period of t_P = 2 h and firebrick with $\kappa = 16 \times 10^{-4}$ m^2/h (see [19], p. 96).

In practical applications the periodic boundary conditions will differ from the simple harmonic oscillation according to Eq. (1). In any case they can be represented as a sum of harmonic oscillations by a Fourier analysis. Equations (2) through (5) are then applied for each harmonic of the Fourier analysis and the resulting temperature variation is found by adding up these partial solutions.

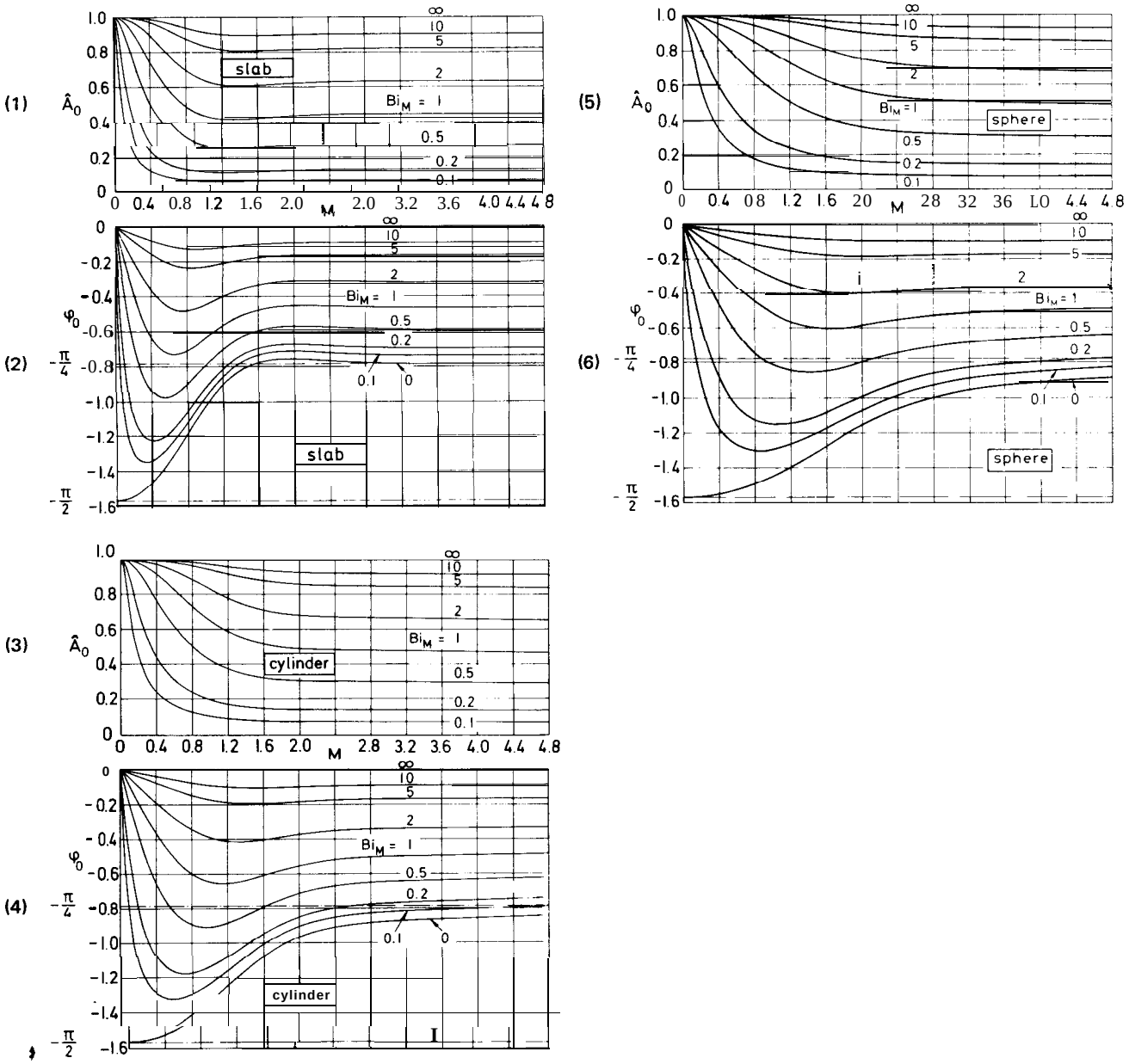

Figures 1 to 6 Amplitude $\hat{A}_o$ and phase. φ_0 of the steady temperature oscillation at the surface of a slab (1, 2), a cylinder (3, 4), and a sphere (5, 6) as functions of M with Bi_M as a parameter.

© 1983 Hemisphere Publishing Corporation

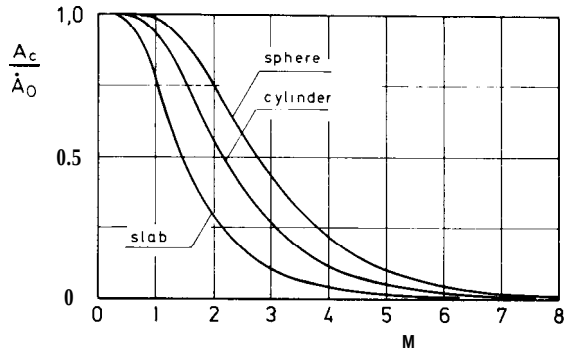

Figure 7 Amplitudes in the center as a function of *M*.

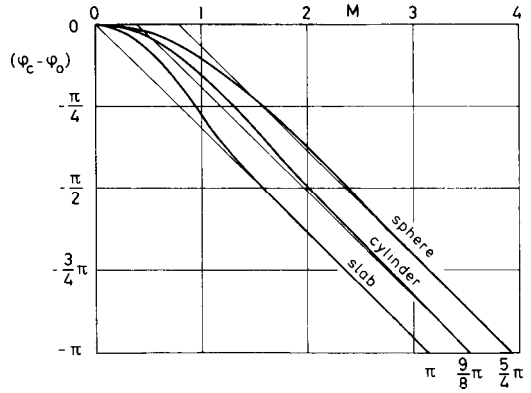

Figure 8 Phase in the center as a function of *M*.

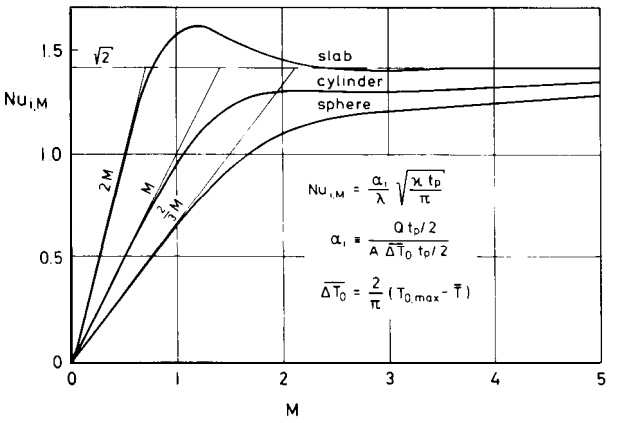

Figure 9 Dimensionless inside heat transfer coefficient for steady temperature oscillation as a function of *M*.

Nomenclature for Section 2.4.5 appears at the beginning of Part 2.

REFERENCES FOR SECTIONS 2.4.1-2.4.5

1. Carslaw, H. S., and Jaeger, J. C., ***Conduction of Heat in Solids,*** 2d ed., Oxford University Press, Oxford, 1959.
2. Tautz, H., ***Wärmeleitung und Temperaturausgleich,*** Verlag Chemie, Weinheim, 1971.
3. Arpaci, V. ***S., Conduction Heat Transfer,*** Addison-Wesley, Reading, Mass., 1966.
4. Grigull, U., and Sandner, H., ***Wiirmeleitung,*** Springer-Verlag, Berlin, Heidelberg, New York, 1979.
5. Pechoc, V., and Kanitra, E., Näherungslösungen des Temperaturausgleichs in einfachen Körpern, ***Forsch. Zngenieurwes.,*** vol. 39, pp. 45–49, 1973.
6. Schlünder, E. U., Über die Brauchbarkeit des Newtonschen Abktihlungsgesetzes im Lichte der Fourierschen Wärmeleitungstheorie, ***Wärme Stoffubertr.,*** vol. 5, pp. 9-14, 1972.
7. Jahnke, Emde, and Lösch, F., ***Tables of Higher Functions,*** 7th ed., Teubner Verlag, Stuttgart, 1966.
8. Abramowitz, M., and Stegun, J. A. (eds.), ***Handbook of Mathematical Functions,*** Dover, New York, 1965.
9. Dusinberre, ***G. M., Heat Transfer Calculations by Finite Differences,*** International Textbook, Scranton, Pa., 1961.
10. Smith, ***G.*** D., ***Numerical Solution of Partial Differential Equations,*** Oxford University Press, Oxford, 1971.
11. Zienkiewicz, ***0. C., The Finite Element Method in Engineering Science,*** McGraw-Hill, New York, 1971.
12. Marsal, D., ***Die numerische Lösung partieller Differentialgleichungen in Wissenschaft und Technik***, Bibliographisches Institut, Mannheim/Wien/Zürich, 1976.
13. Ames, W. F., ***Numerical Methods for Partial Differential Equations,*** 2d ed., Academic Press, New York, 1977.
14. Binder, L., Über äussere Wärmeleitung und Erwärmung elektrischer Maschinen, Dissertation, TH München, 1910.
15. Schmidt, E., Das Differenzenverfahren zur Lösung von Differentialgleichungen der nichtstationären Wärmeleitung, Diffusion und Impulsausbreitung, ***Forsch. Zngenieurwes., vol.*** 13, pp. 177-185, 1942.
16. Linge, V., Zum Problem der instationären Wärmeleitung im Gefrierbereich von Lebensmitteln, Dissertation, Universitlt Karlsruhe (TH), Karlsruhe, 1973.
17. Tao, L. C., Generalized Numerical Solutions of Freezing a Saturated Liquid in Cylinders and Spheres, *AIChE J.*, vol. 13, pp. 165-169,1967.
18. Stephan, K., Schmelzen und Erstarren geometrisch einfacher Körper, *Kältetech. Klim.*, vol. 23, pp. 42-46, 1971.
19. Gröber, Erk, and Grigull, ***Die Grundgesetze der Wiirmeiibertragung,*** 3d ed., Springer Verlag, Berlin, 1961.

© 1983 Hemisphere Publishing Corporation

2.4.6

Thermal contact resistance

T.F. Irvine, Jr.

A. Introduction

When two surfaces come into contact, as shown in Fig. 1, they remain separated by their roughness elements. A gas or a liquid may also fill the spaces between the surfaces, and if the interstitial fluid has a lower thermal conductivity than the surface materials a contact resistance may exist that can become a design consideration.

Figure 1 also illustrates the type of temperature distribution that is encountered in such situations where a sharp temperature gradient across the small interfacial separation distance is caused by the contact resistance.

The magnitude of the contact resistance depends mainly on the following:

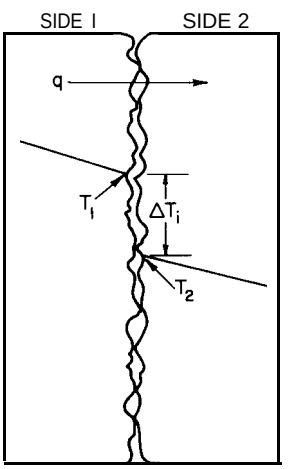

Figure 1 Interfacial contact.

1. The pressure with which the surfaces are pressed together
2. The thermal conductivity of the interstitial fluid if it is a liquid
3. The thermal conductivity of a gaseous interstitial fluid as well as the conditions that allow for an additional transfer of heat between the surfaces by thermal radiation
4. The surface finish, that is, the roughness of the surfaces
5. The hardness of the surface roughness elements that allow for deformations under pressure loading
6. The average temperature at the interface
7. At low pressures, the ratio between the mean free path of the gas molecules to the separation distance

Thus, the physical situation is quite complicated, and a great deal of effort has been expended in developing a general approach that is suitable and practical for engineering calculations.

B. Thermal contact conductance

A useful engineering quantity to describe the thermal conditions at the interface is the contact conductance U_i, which is defined as

$$q = U_i \, \Delta T_i \tag{1}$$

Veziroğlu [1] has analyzed a large number of experiments reported in the literature in order to develop a useful engineering correlation. The contact materials included iron, steel, stainless steel, aluminum, brass, bronze, gun metal, uranium, and magnox. The inter-

© 1983 Hemisph re Publishing Corporation

stitial fluids included air, argon, helium, water, glycerol, lubricating oil, and paraffin. The contact conductances ranged from 340 to 230 000 W/m^2 K, the contact pressures from 0.017 to 138 MPa, the mean contact temperatures from 27 to 316°C, the thermal conductivities of the materials from 22 to 216 W/m K, the thermal conductivities of the interstitial fluids from 0.017 to 0.62 W/m K, the Meyer hardness from 68.9 to 2 400 MPa, and the mean surface roughnesses from 0.08 to 838 μm. The correlation developed by Veziroğlu [1] is shown graphically in Fig. 2. The thermal contact conductance is included in the Nusselt number located on the ordinate, which also includes the effective gap thickness ℓ and the equivalent conductivity of the interstitial fluid λ_f. On the abscissa is the ratio of the gap number B to the conductivity number K. The parameter in the figure is the constriction number C.

Since all of the quantities listed in Fig. 2 are dimensionless, any consistent set of units may be used in calculating the thermal contact conductance.

In order to calculate a contact conductance from Fig. 2, the following information should be specified or estimated:

1. Material of the two surfaces
2. Interstitial fluid
3. Interface temperatures (T_1, T_2)
4. Root-mean-square (RMS) roughness of the surfaces (ℓ_1, ℓ_2)
5. Mean contact temperature $[(\bar{T}_i = (T_1 + T_2)/2]$
6. Contact pressure (P)
7. Meyer hardness (M)
8. Total area of the surface contact (one side) (A)
9. Total normal emissivities of the two surfaces if the interstitial fluid is transparent to thermal radiation (ϵ_1, ϵ_2)
10. Thermal conductivity of the surface materials (λ_1, λ_2)

The relations for calculating the quantities shown in Fig. 2 are given below.

(a) Constriction number (C)

$$C = \left(\frac{P}{M}\right)^{1/2} \tag{2}$$

where P = contact pressure

M = Meyer hardness of the softer surface

Meyer hardness information appropriate for these calculations is discussed in detail by Cetinkale [Veziroğlu] and Fishenden [3]. They consider both the effects of the time of pressure application and average interface temperature on the appropriate value to use for M. As a first approximation, which neglects the time and temperature effects, the values listed in Table 1 may be used [3].

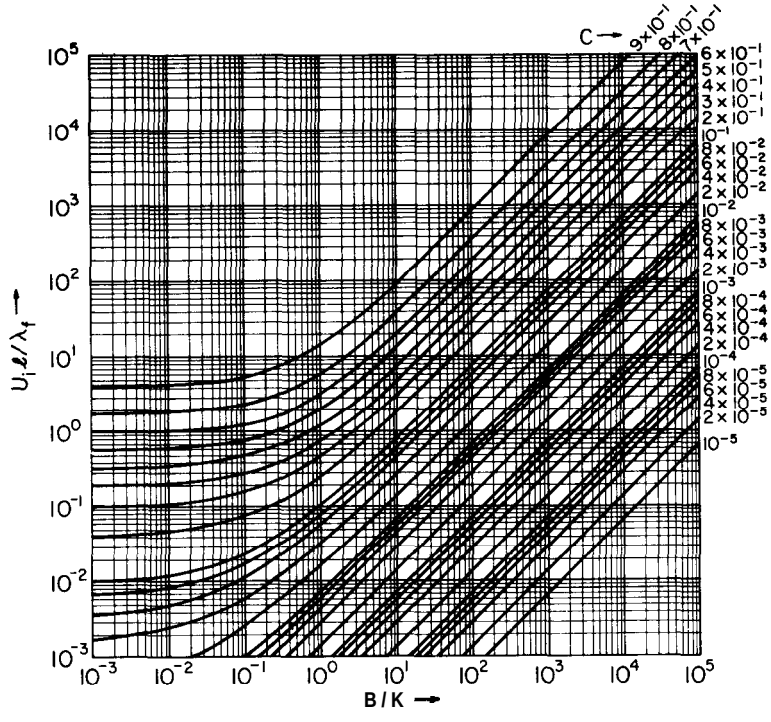

Figure 2 Thermal contact conductance correlation. (From Schneider [2], copyright 1973 by McGraw-Hill, Inc. Used with the permission of McGraw-Hill Book Company.)

© 1983 Hemisphere Publishing Corporation

Table 1 Meyer hardness for several materials

Material	*M*, MPa
Cast steel	3.52×10^3
Mild steel	1.64 X 10
Brass	1.18×10^3
Aluminum	1.04×10^3
Pure aluminum	0.32×10^3

(b) Gap thickness (ℓ)

If ℓ_1 and ℓ_2 are the RMS roughness values in micrometers of the two surfaces, then:

$$\ell = 3.56(\ell_1 + \ell_2) \quad \text{if } \ell_1 + \ell_2 < 7\ \mu\text{m} \tag{3}$$

$$\ell = 0.46(\ell_1 + \ell_2) \quad \text{if } \ell_1 + \ell_2 > 7\ \mu\text{m} \tag{4}$$

(c) Gap number (B)

B can be calculated from the constriction number and the gap thickness by the following relation:

$$B = 0\ 335C^{0.315(A^{1/2}/\ell)^{0.137}} \tag{5}$$

where A is the total interfacial area (one side).

(d) Equivalent conductivity (λ_f)

1. If the interstitial fluid is a liquid, then

$$\lambda_f = \lambda_0 \tag{6}$$

2. If the interstitial fluid is a gas transparent to thermal radiation, and if the ratio of the mean free path of the molecules, ℓ_0, to the gap thickness is less than 0.1, then

$$\lambda_f = \lambda_0 + \frac{4\sigma\ell\epsilon_1\epsilon_2\bar{T}_i^3}{\epsilon_1 + \epsilon_2 - \epsilon_1\epsilon_2} \tag{7}$$

where σ = 5.669 7 X 10^{-8} W/m^{2}k^4 (Stefan-Boltzmann constant).

Note: If $\ell_0/\ell > 0.1$, consult [1]. If the surface emissivities ϵ_1 and ϵ_2 are unknown, assume a value of 1 to yield a maximum thermal contact conductance. The minimum conductance will be obtained by assuming that $\lambda_f = \lambda_0$.

(e) Conductivity number (K)

$$K = \frac{\lambda_f(\lambda_1 + \lambda_2)}{2\lambda_1\lambda_2} \tag{8}$$

where the conductivities λ_1 and λ_2 of the contact solids may be evaluated at the average gap temperature $\bar{T}_i$.

When the above values have been determined, the quantity ***B/K*** is calculated and used to enter the abscissa of Fig. 2. Then, using the proper value of C as the parameter in the figure, the value of $U_i\ell/\lambda_f$ is read from the ordinate, from which the contact conductance can be calculated. The method is further illustrated by the following numerical example.

C. Numerical example

(a) Data

1. Materials: aluminum-aluminum
2. Interstitial fluid: air
3. Interface temperatures (est.): $T_1 = 80°C, T_2 = 66°C$
4. RMS roughness: $\ell_1 = \ell_2$ = 1.65 μm
5. Mean contact temperature: $\bar{T}_i$ = 73° C
6. Contact pressure: P = 0.7 MPa
7. Meyer hardness (from Table 1): $M = 1.04 \times 10^3$ MPa
8. Surface contact area: A = 6.45 cm^2 = 6.45 X 10^{-4} m^2
9. Surface emissivity (aluminum): $\epsilon_1 = \epsilon_2$ = 0.05

(b) Calculations

I. Constriction number (*C*)

From Eq. (2),

$$C = \left(\frac{P}{M}\right)^{1/2} = \left(\frac{0.7}{1.04 \times 10^3}\right)^{1/2} = 2.6 \times 10^{-2}$$

II. Gap thickness (Q)

Since $\ell_1 + \ell_2 = 3.3 < 7\ \mu$m, from Eq. (3),

$$\ell = 3.56(3.3 \times 10^{-6}) = 1.17 \times 10^{-5}\ \text{m}$$

III. Gap number (*B*)

From Eq. (5),

$$B = 0\ 335C^{0.315(A^{1/2}/\ell)^{0.137}} = 0.335 \times (2\ 6 \times 10^{-2})^{0.315[(6.45 \times 10^{-4})^{1/2}/1.17 \times 10^{-5}]^{0.137}}$$

$$= 1.25 \times 10^{-2}$$

IV. Equivalent conductivity (λ_f)

At $T_i = 73°C, \lambda_0 = 0.029$ W/m K. Then, from Eq. (7),

$$\lambda_f = 0\ 029 + \frac{4(5.669\ 7 \times 10^{-8})(0.05(0.05)(346)^3}{0.097\ 5}$$

$$= 0.029 + 2.8 \times 10^{-6} = 0.029 \text{ W/m K}$$

© 1983 Hemisphere Publishing Corporation

V. Conductivity number (K)

For aluminum at $73^{\circ}C, \lambda_1 = \lambda_2$ = 138.5 W/m K. Then, from Eq. (8),

$$K = \frac{0.029(277)}{2(138.5)(138.5)} = 2.1 \times 10^{-4}$$

Therefore the appropriate variables for Fig. 2 are

$$\frac{B}{K} = 59.5$$

$$C = 2.6 \times 10^{-2}$$

and, from Fig. 2,

$$\frac{U_i \ell}{\lambda_f} = 1.2$$

giving

$$U_i = \frac{1.2(0.029)}{1.17 \times 10^{-5}} = 2\,974 \text{ W/m}^2 \text{ K}$$

D. Discussion

The material presented above outlines a method for estimating the contact conductance in a situation that is often encountered in practice. Because of the type of model chosen in [1] and the variations in the reported data on which it is based, the average deviation between the actual and predicted contact conductances can be expected to be approximately 25%. For any single calculation, however, the deviation can be as much as a factor of 2.

Additional selected references that deal with other thermal contact resistance situations are the following: for contact resistances between thin laminated sheets [4,5]; for surfaces that are bolted or riveted together [6]; and for contact surfaces in a vacuum [7, 8].

Nomenclature for Section 2.4.6 appears at beginning of Part 2.

REFERENCES FOR SECTION 2.4.6

1. Veziroğlu, T. N., Correlation of Thermal Contact Conductance Experimental Results, ***Prog. Astron.*** Aero., vol. 20, Academic Press, New York, 1967.
2. Schneider, P. J., Conduction, ***in Handbook of Heat Transfer***, ed. Warren M. Rohsenow and James P. Hartnett, sec. 3, McGraw-Hill, New York, 1973.
3. Cetinkale, T. N., and Fishenden, M., Thermal Conductance of Metallic Surfaces in Contact, General Discussion of Heat Transfer, *Proc. **Inst. Mech. Eng. and** ASME*, pp. 271-275, 1951.
4. Veziroğlu, T. N., Williams, A., Kakac, S., and Nayak, P., Prediction and Measurement of the Thermal Conductance of Laminated Stacks, ***Int. J. Heat Mass Transfer,*** vol. 22, pp. 447–459, 1979.
5. Thomas, T. F., and Probert, S. D., Thermal Resistances of Some Multi-Layer Contacts Under Static Loads, ***Znt. J. Heat Mass Transfer,*** vol. 9, pp. 739-754, 1966.
6. Barzclay, M. E., Range of Interface Thermal Conductance for Aircraft Joints, NASA TN D-426, Washington, D.C., 1960.
7. Clausing, A. M., and Chao, B. T., Thermal Contact Resistance in a Vacuum Environment, ***J. Heat Transfer,*** vol. 27, pp. 243-251, 1965.
8. Yovanovich, M. M., and Fenech, H., Thermal Contact Conductance of Nominally-Flat, Rough Surfaces in a Vacuum Environment, AIAA Third Aerospace Sciences Meeting, Paper 6642, 1966.

© 1983 Hemisphere Publishing Corporation

2.5
Single-phase convective heat transfer

Contents

2.5.1
FORCED CONVECTION IN DUCTS, V. Gnielinski 2.5.1-1

A. Introduction **2.5.1-1**
B. Definition of the heat transfer coefficient **2.5.1-1**
C. Heat transfer for laminar flow **2.5.1-2**
D. Heat transfer for turbulent flow **2.5.1-5**

References for Section 2.5.1 **2.5.1-11**

2.5.2
FORCED CONVECTION AROUND IMMERSED BODIES, V. Gnielinski 2.5.2-1

A. Smooth flat plate **2.5.2-1**
B. Single bodies of various shapes **2.5.2-3**

References for Section 2.5.2 **2.5.2-8**

2.5.3
BANKS OF PLAIN AND FINNED TUBES 2.5.3-1

A. Single rows and tube banks in cross flow, *V. Gnielinski* **2.5.3-1**
B. Finned tubes, *A. Žukauskas and A. Skrinska* **2.5.3-6**

References for Section 2.5.3 **2.5.3-15**

2.5.4
FIXED BEDS, V. Gnielinski 2.5.4-1

A. Introduction **2.5.4-1**
B. The calculation process **2.5.4-1**
C. Remarks **2.5.4-2**
D. Comparison with experimental data **2.5.4-2**

References for Section 2.5.4 **2.5.4-6**

2.5.5
FLUID-TO-PARTICLE HEAT TRANSFER IN FLUIDIZED BEDS, S. S. Zabrodsky with revisions by H. Martin 2.5.5-1

A. Introduction, range of fluidization, bed expansion **2.5.5-1**
B. Recommended equations for fluid-to-particle heat transfer coefficients in fluidized beds **2.5.5-2**
C. Comparison with experimental data **2.5.5-2**
D. Some remarks on heat and mass transfer coefficients in the range of low Peclet numbers **2.5.5-3**
E. Illustrative example **2.5.5-5**

References for Section 2.5.5 **2.5.5-7**

2.5.6
IMPINGING JETS, H. Martin 2.5.6-1

A. Introduction **2.5.6-1**
B. Local variation of the transfer coefficients **2.5.6-2**
C. Average transfer coefficients **2.5.6-3**
D. Optimal spatial arrangements of nozzles **2.5.6-6**

References for Section 2.5.6 **2.5.6-9**

© 1983 Hemisphere Publishing Corporation

HEDH

2.5.7
FREE CONVECTION AROUND IMMERSED BODIES, S. W. Churchill 2.5.7-1

A. Vertical plates 2.5.7-2
B. inclined and horizontal surfaces 2.5.7-13
C. Buoyancy-induced flow in channels 2.5.7-19
D. Horizontal cylinders 2.5.7-20
E. Vertical and inclined cylinders 2.5.7-23
F. Vertical cones 2.5.7-24
G. Spheres 2.5.7-24
H. Other immersed shapes 2.5.7-25
I. Generalized solutions and correlations 2.5.7-25

References for Section 2.5.7 2.5.7-29

2.5.8
FREE CONVECTION IN LAYERS AND ENCLOSURES, S. W. Churchill 2.5.8-1

A. Infinite horizontal layers of fluid heated from below 2.5.8-1
B. Enclosures heated from below 2.5.8-3
C. Rectangular enclosures heated and cooled on the sides 2.5.8-6
D. Circular annuli heated and cooled on the vertical curved surfaces 2.5.8-13
E. Horizontal cylinders 2.5.8-14
F. Horizontal annuli 2.5.8-14
G. Concentric spheres 2.5.8-16
H. Inclined enclosures 2.5.8-17
I. Honeycombs 2.5.8-20

References for Section 2.5.8 2.5.8-23

2.5.9
COMBINED FREE AND FORCED CONVECTION AROUND IMMERSED BODIES, S. W. Churchill 2.5.9-1

A, Assisting convection 2.5.9-1
B. Opposing convection 2.5.9-4
C. Transverse convection 2.5.9-4

References for Section 2.5.9 2.5.9-6

2.5.10
COMBINED FREE AND FORCED CONVECTION IN CHANNELS, S. W. Churchill 2.5.10-1

A. Vertical channels 2.5.10-2
B. Horizontal channels 2.5.10-7

References for Section 2.5.10 2.5.10-12

2.5.11
AUGMENTATION OF HEAT TRANSFER, Arthur E. Bergles 2.5.1 l-1

A. Introduction 2.5.11-1
B. Free convection 2.5.11-3
C. Forced convection 2.5.11-4
D. Performance evaluation criteria 2.5.11-9

Nomenclature for Section 2.5.11 2.5.11-9
References for Section 2.5.11 2.5.11-10

2.5.12
HEAT TRANSFER FOR NON-NEWTONIAN FLUIDS, Robert C. Armstrong and H. H. Winter 2.5.12-1

A. Introduction 2.5.12-1
B. Physical properties 2.5.12-2
C. Governing equations and dimensionless groups 2.5.12-5
D. Heat transfer in steady confined channel flows without viscous heating 2.5.12-6
E. Influence of viscous heating on heat transfer 2.5.12-10
F. Heat transfer in turbulent flows of dilute polymer solutions 2.5.12-14

Nomenclature for Section 2.5.12 2.5.12-15
References for Section 2.5.12 2.5.12-15

2.5.13
HEAT TRANSFER IN LIQUID METALS, V. M. Borishanski and E. V. Firsova 2.5.13-1

A. Flow in channels 2.5.13-1
B. Liquid metal heat exchangers 2.5.13-3

References for Section 2.5.13 2.5.13-3

© 1983 Hemisphere Publishing Corporation

2.5.1

Forced convection in ducts

V. Gnielinski

A. Introduction

When fluids flow at very low velocities, all the individual particles are flowing in parallel lines. This type of flow is called laminar flow. If a fluid stream enters a duct with a uniform velocity profile, the velocity profile changes as the fluid moves down the tube. At a sufficient distance downstream from the inlet, the velocity pattern becomes fixed. The shape of the velocity distribution curve is parabolic for flow in a tube or between parallel plates.

If the velocity of the fluid is gradually increased, there will be a point at which the fluid no longer flows in parallel lines, but by a series of eddies that result in a complete mixing of all parts of the flow. This type of flow is called turbulent. The Reynolds number at which the flow changes from laminar to turbulent is the critical Reynolds number. The value of the critical Reynolds number in tubes is between 2 100 and 2 300. In long rectangular ducts and annular spaces, the transition from laminar to turbulent flow also starts at a Reynolds number of 2 100 when the hydraulic diameter of the duct is used as the characteristic geometric dimension in calculating the Reynolds number.

At Reynolds numbers greater than 10^4, the flow is turbulent. Between the lower and upper limits lies the zone of transition from laminar to turbulent flow. These limits are affected by the type of entry, initial disturbances in the fluid, roughness, and so on.

If the duct wall is at a temperature different from that of the fluid, heat will be transferred and a temperature profile will develop in the fluid. At a sufficient distance from the beginning of heating or cooling, the temperature profile becomes fully developed and therefore the heat transfer coefficient is constant. The rate of heat transfer is always greater in turbulent flow.

B. Definition of the heat transfer coefficient

The heat transfer between the wall of a duct and a fluid moving relative to the wall can be calculated at any position along the duct using a local heat transfer coefficient defined as

$$\alpha_x = \frac{\dot{q}_x}{(T_w - T_b)_x} \tag{1}$$

The local heat transfer coefficient is needed to calculate the axial variation in the wall temperature or heat flux. In design problems it is often mdre convenient to calculate the total heat transferred over a section or the whole length of a duct using a mean heat transfer coefficient defined as

$$\alpha = \frac{\dot{q}}{\Delta T_{LM}} \tag{2}$$

in which the logarithmic mean temperature difference ΔT_{LM} is given by

$$\mathrm{AT}_{,,} = \frac{(T_w - T_{b,\mathrm{in}}) - (T_w - T_{b,\mathrm{out}})}{\ln[(T_w - T_{b,\,in})/(T_w - T_{b,\,out})]} \tag{3}$$

$T_{b,\mathrm{in}}$ is the inlet bulk temperature. $T_{b,\mathrm{out}}$ is the outlet bulk temperature of the fluid, and T_w is the tempera-

@ 1983 Hemisphere Publishing Corporation

HEDH

ture of the duct wall. $T_{b,\text{out}}$ may be calculated from

$$T_{b,\text{out}} = T_{b,\text{in}} + \frac{Q}{\dot{M}c_p} \tag{4}$$

C. Heat transfer for laminar flow

(a) Introduction

The problems associated with fluid flow and heat transfer in laminar flow have been the subject of the analytic work of scientists for many years. Shah and London collected the analytic laminar flow solutions from the literature and have published them in a very comprehensive book [1]. They have presented the available analytic solutions for laminar fluid flow and forced convection in circular and noncircular pipes under many different boundary conditions. Because of this, the following sections summarize only the solutions that are of the most technical interest.

(b) Smooth straight tubes

I. Thermally developing and hydrodynamically developed flow

The well-known Nusselt-Graetz problem for heat transfer to an incompressible fluid with constant properties flowing through a circular tube having a uniform wall temperature and a fully developed laminar velocity profile was solved numerically by several authors. For the local Nusselt number the two asymptotes are

$$\text{Nu}_{x,T} = 1.077 \sqrt[3]{\text{Pe}\,\frac{d}{x}} \quad \text{for Pe}\,\frac{d}{x} > 10^2 \tag{5}$$

and

$$\text{Nu}_{x,T} = 3.66 \quad \text{for Pe}\,\frac{d}{x} < 10^2 \tag{6}$$

The asymptotes of the mean Nusselt number for a tube of the length L are

$$\text{Nu}_T = 1.6 \sqrt[3]{\text{Pe}\,\frac{d}{L}} \quad \text{for Pe}\,\frac{d}{L} > 10^3 \tag{7}$$

and

$$\text{NUT} = 3.66 \quad \text{for Pe}\,\frac{d}{L} < 10^2 \tag{8}$$

The superposition of the two asymptotes for the mean Nusselt number derived by Schlünder [2] gives sufficiently good results for most technical purposes:

$$\text{Nu}_T = \sqrt[3]{3.66^3 + 1.61^3\,\text{Pe}\,\frac{d}{L}} \tag{9}$$

The results of this equation deviate only slightly from the equation given by Hausen [3],

$$\text{Nu}_T = 3.66 + \frac{0.19[\text{Pe (d/L)}]^{0.8}}{1 + 0.117\,[\text{Pe (d/L)}]^{0.467}} \tag{10}$$

which is well-known in the literature. These equations may be used for the laminar flow of gases and liquids in the range $\text{Pe}(d/L)$ from 0.1 to 10^4. Axial conduction effects must be considered at $\text{Pe}(d/L) < 0.1$. The numerical values to be inserted for the physical properties are those at the mean temperature of the fluid,

$$T_b = \frac{T_{b,\text{in}} + T_{b,\text{out}}}{2} \tag{11}$$

Shah and London [1] also considered the case where a constant heat flux was applied at the wall. For the local Nusselt number they got the asymptotes

$$\text{Nu}_{x,H} = 1.302 \sqrt[3]{\text{Pe}\,\frac{d}{L}} \quad \text{for Pe}\,\frac{d}{L} > 10^4 \tag{12}$$

and

$$\text{Nu}_{x,H} = 4.36 \quad \text{for Pe}\,\frac{d}{L} < 10^3 \tag{13}$$

The asymptotes for the mean Nusselt numbers are

$$\text{Nu}_H = 1.953 \sqrt[3]{\text{Pe}\,\frac{d}{L}} \quad \text{for Pe}\,\frac{d}{L} > 10^2 \tag{14}$$

and

$$\text{Nu}_H = 4.36 \quad \text{for Pe}\,\frac{d}{L} < 10 \tag{15}$$

II. Thermally and hydrodynamically developing flow

Laminar flow develops very quickly. Only in very short tubes (d/L >O.l) and depending on the magnitude of the Prandtl number do the mean Nusselt numbers for thermally and hydrodynamically developing flow differ from the values calculated by Eq. (9) or (10). Shah and London [1] presented numerical values of the mean Nusselt number for this region. In the case of a short flow length, the values are represented by the asymptotic equation of Pohlhausen [4] for thermally and hydrodynamically developing flow over a flat plate. Transforming this equation to the tube, we obtain

$$\text{Nu} = 0.664 \frac{1}{\sqrt[6]{\text{Pr}}} \sqrt{\text{Pe}\,\frac{d}{L}} \tag{16}$$

For most engineering applications it is recommended that, for short tubes ($d/L > 0.1$), whichever of Eqs. (9), (10), or (16) yields the higher Nusselt number be used.

© 1983 Hemisphere Publishing Corporation

(c) Parallel plates

The parallel-plate duct geometry is a limiting geometry for rectangular ducts and also for concentric annular ducts. A great number of boundary conditions have been subjected to analytic solutions and were collected by Shah and London [1]. Only some simple cases are discussed in the following sections.

I. Thermally developing and hydrodynamically developed flow

Uniform wall temperature on both walls of the parallel-plate duct geometry, constant fluid properties, and a fully developed laminar velocity profile are assumed in the development of the following equations.

For the local Nusselt number $Nu = \alpha s/\lambda$, where s is the spacing of the plates, the two asymptotes are

$$Nu_{x,T} = 0.979\sqrt[3]{Pe\,\frac{s}{x}} \quad \text{for } Pe\,\frac{s}{x} > 10^3 \tag{17}$$

and

$$Nu_{x,T} = 3.78 \quad \text{for } Pe\,\frac{s}{x} < 10^2 \tag{18}$$

The asymptotes of the mean Nusselt number for a duct of length L are

$$Nu_T = 1.468\sqrt[3]{Pe\,\frac{s}{L}} \quad \text{for } Pe\,\frac{s}{L} > 10^3 \tag{19}$$

and

$$Nu_T = 3.78 \quad \text{for } Pe\,\frac{s}{L} < 10^2 \tag{20}$$

The asymptotes for the boundary condition of a uniform and equal heat flux on both walls are

$$Nu_{x,H} = 1.18\sqrt[3]{Pe\,\frac{s}{x}} \quad \text{for } Pe\,\frac{s}{x} > 10^4 \tag{21}$$

and

$$Nu_{x,H} = 4.12 \quad \text{for } Pe\,\frac{s}{x} < 10^3 \tag{22}$$

The asymptotes of the mean Nusselt number for a duct of length L are

$$Nu_H = 1.775\sqrt[3]{Pe\,\frac{s}{L}} \quad \text{for } Pe\,\frac{s}{L} > 10^3 \tag{23}$$

and

$$Nu_H = 4.12 \quad \text{for } Pe\,\frac{s}{L} < 10^2 \tag{24}$$

II. Thermally and hydrodynamically developing flow

For the parallel-plate duct geometry the solution of the differential equation with the constant wall temperature boundary condition obtained by Pohlhausen [4] gives the asymptote for a short flow length L. The mean Nusselt number is

$$Nu_T = \frac{0.664}{\sqrt[6]{Pr}}\sqrt{Pe\,\frac{s}{L}} \quad Pe\,\frac{s}{L} > 10^3 \tag{25}$$

The range of validity is $0.5 < Pr < 500$.

Stephan [5] obtained the following equation for the combined entry length problem at constant wall temperatures:

$$Nu_T = 3.78 + \frac{0.015\ 6[Pe\,(s/L)]^{1.14}}{1 + 0.058\ [Pe\ (s/L)]^{0.64}\,Pr^{0.17}} \tag{26}$$

This empirical equation is valid for the whole range of $Pe(s/L)$ and $0.1 < Pr < 10^3$.

(d) Concentric annular ducts

The simplest form of a two-fluid heat exchanger is a double pipe made up of two concentric circular tubes. One fluid flows through the inside tube and the other fluid flows through the annular passage. Heat may be transferred from one or from both walls of the passage. Figure 1 demonstrates the three different boundary conditions with which this section will deal. Heat may be transferred at the inner wall of the annular duct while the outer wall is insulated, Fig. *1a* (subscript i); at the outer wall while the inner wall is insulated, Fig. lb (subscript o); or at both walls of the passage, Fig. 1*c* (subscript b).

Heat transfer coefficients in annular ducts are dependent on the ratio of the diameters (d_i/d_o) because of the shape of the velocity profile. With annular flow the maximum velocity is shifted to the inner wall of the duct as d_i/d_o decreases. The limiting case, $d_i/d_o = 0$, is a circular duct with an infinitesimal thickness wire at the center [1]. The other limiting case of annular ducts, $d_i/d_o = 1$, is the parallel-plate geometry. The characteristic length used in the evaluation of the dimensionless numbers Nu, Pe, and Re is

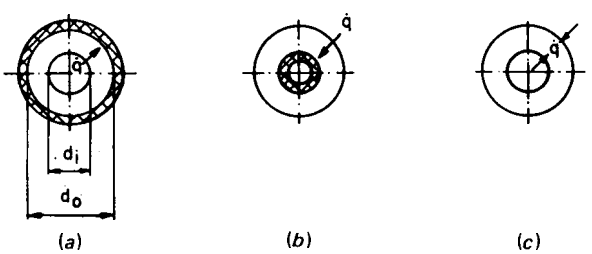

Figure 1 Boundary conditions for concentric annular duct flow.

© 1983 Hemisphere Publishing Corporation

the hydraulic diameter d_h of the annular duct. This is equal to

$$d_h = d_o - d_i \tag{27}$$

where d_o is the inner diameter of the outer tube and d_i is the outer diameter of the inner tube.

For the thermal boundary condition of constant wall temperature, Stephan [6] has developed the following equation based on Eq. (10) from Hausen [3]. The Nusselt number for fully developed laminar flow may be calculated from

$$\mathrm{Nu}_T = \mathrm{Nu}_\infty + f\left(\frac{d_i}{d_o}\right)\frac{0.19[\mathrm{Pe}\,(d_h/L)]^{0.8}}{1+0.117[\mathrm{Pe}\,(d_h/L)]^{0.467}} \tag{28}$$

The ranges of validity are $0.1 < \mathrm{Pr} < 10^3$, $0 < d_i/d_o < 1$, and laminar flow ($\mathrm{Re} < 2\,300$). The dimensionless numbers are $\mathrm{Nu} = \alpha d_h/\lambda$, $\mathrm{Re} = u d_h/\nu$. Nu_∞ is the value to which the Nusselt number tends when the length L of the annular duct becomes very large ($L \to \infty$).

In Fig. 2, Nu_∞ is presented graphically as a function of d_i/d_o for the three boundary conditions. Martin [7] has developed approximate expression for the three lines on Fig. 2, which are

Case I: $$\mathrm{Nu}_{i\infty} = 3.66 + 1.2\left(\frac{d_i}{d_o}\right)^{-0.8} \tag{29}$$

Case II: $$\mathrm{Nu}_{o\infty} = 3.66 + 1.2\left(\frac{d_i}{d_o}\right)^{0.5} \tag{30}$$

Case III: $$\mathrm{Nu}_{b\infty} = 3.66 + \left[4 - \frac{0.102}{(d_i/d_o)+0.2}\right]\left(\frac{d_i}{d_o}\right)^{0.04} \tag{31}$$

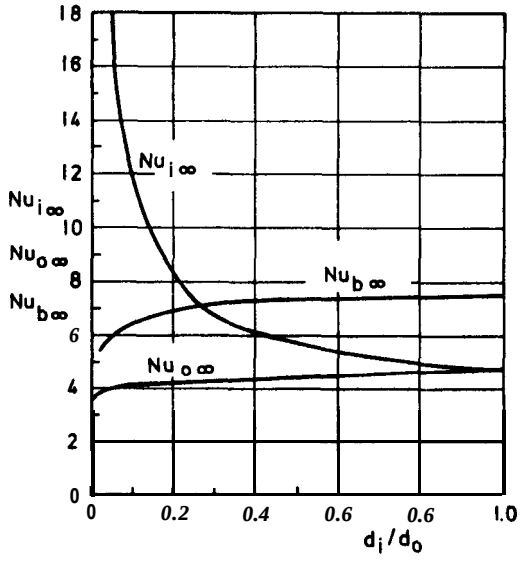

Figure 2 Dependence of the magnitude of Nu, on d_i/d_o in laminar flow for the three boundary conditions.

The function $f(d_i/d_o)$ is, according to Stephan [6],

Case I: $$f\left(\frac{d_i}{d_o}\right) = 1 + 0.14\left(\frac{d_i}{d_o}\right)^{-0.5} \tag{32}$$

Case II: $$f\left(\frac{d_i}{d_o}\right) = 1 + 0.14\left(\frac{d_i}{d_o}\right)^{1/3} \tag{33}$$

Case III: $$f\left(\frac{d_i}{d_o}\right) = 1 + 0.14\left(\frac{d_i}{d_o}\right)^{0.1} \tag{34}$$

Shah and London [1] report numerical values of Nusselt numbers on other hydrodynamic and thermal boundary conditions.

(e) Factors that influence the heat transfer coefficient

I. Variable physical properties

Experiments conducted by several authors [8-10] with air, nitrogen, and helium at wall-to-bulk temperature ratios in the range $0.5 < T_b/T_w < 2.0$ indicate that for gases the effect on heat transfer coefficient of radial property variations does not exceed 10%. Variable physical properties do effect the heat transfer coefficients for ***liquid*** flow. Heating of the liquid increases and cooling it decreases the velocity near the wall because of the temperature dependence of the viscosity. The distortion of the velocity profile results in a heat transfer coefficient which differs from that predicted by the above-mentioned equations. Sieder and Tate [11] correlated experimental data in tubes in the range $0.004 < \eta_b/\eta_w < 20$. They suggest that the following equation be used to correct values of Nu evaluated from the above-mentioned equations.

$$\mathrm{Nu}_c = \mathrm{Nu}\left(\frac{\eta_b}{\eta_w}\right)^{0.14} \tag{35}$$

The dynamic viscosity η_b is to be evaluated at the mean bulk temperature T_b of the liquid and η_w at the wall temperature T_w.

II. Free convection

Free convection effects may increase the heat transfer rate to a value of three or four times that for pure forced convection alone. This subject is discussed in detail in Sec. 2.5.10. The magnitude of the free convection contribution depends on many factors, especially the wall-to-bulk temperature difference, the tube diameter, the tube orientation (horizontal or vertical), the coefficient of volumetric expansion, and the flow velocity. The literature includes several attempts to take into consideration free convection effects. Because of the lack of systematic experimental

© 1983 Hemisphere I blishing Corporation
HDH

data suitable to test theoretically developed equations, the following equation should be used with care. Martinelli et al. [12] derived the following equation from a theoretical analysis.

$$\mathrm{Nu} = 1.61 \left[\mathrm{Pe}\,\frac{d}{L} + 0.0919 A F_1 \left(\mathrm{Gr}_w \mathrm{Pr}_w \frac{d}{L} \right)^{0.75} \right]^{1/3} \tag{36}$$

For aiding flow, vertical flow upward, A = +1 and for opposed flow, vertical flow downward, where the free convective forces act in the opposite direction to the forced circulation, A = -1. Opposed flow conditions occur when fluids in up flow are cooled or when fluids in down flow are heated. Equation (36) may be used for $(T_w - T_{b,\mathrm{in}})/(T_w - T_{b,\mathrm{out}}) < 3$. Pr, is the Prandtl number and Gr, the Grashof number evaluated with the physical properties at the wall temperature

$$\mathrm{Gr}, = \frac{g\zeta_w d^3 (T_w - T_{b,\mathrm{in}})}{\nu_w^2} \tag{37}$$

ζ_w is the coefficient of volumetric expansion and $(T_w - T_{b,\mathrm{in}})$ is the temperature difference at the inlet of the tube. F_1 is a function of $\mathrm{Nu}/\frac{1}{4}\mathrm{Pe}(d/L)$, as given in Fig. 3. A more comprehensive discussion of the problem is presented by McAdams [13] and in Sec. 2.5.10.

D. Heat transfer for turbulent flow

Transition to turbulent flow in ducts starts at Re = 2 300. The flow is fully turbulent at $5 \times 10^4 < \mathrm{Re} < 10^5$, depending on the turbulence of the incoming flow and the shape of the inlet section. Nusselt numbers for fully developed turbulent flow in ducts were correlated in many publications by functions of the type

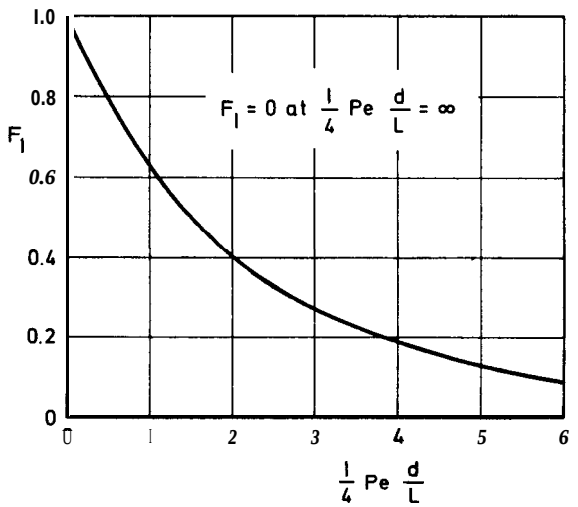

Figure 3 Function F_1 in Eq. (36).

$$\mathrm{Nu} = A\ \mathrm{Re}^m\ \mathrm{Pr}^n f\left(\frac{d}{L}\right) \tag{38}$$

The magnitude of the coefficient A and of the exponents m and n varied according to the experimental results on which the correlations were based.

No remarkable differences were found measuring heat transfer coefficients with the two boundary conditions of uniform wall temperature or constant wall heat flux. Because of this, the following equations are to be used independent of the thermal boundary condition.

(a) Smooth straight tubes

Comparing a great number of experimental data on heat transfer in tubes with the correlations included in the literature Gnielinski [14] found that a semiempirical type of equation similar to that proposed by Prandtl [15] correlates the data best. The equation of Prandtl for fully developed turbulent flow is of the form

$$\mathrm{Nu} = \frac{f/8\ \mathrm{Re}\ \mathrm{Pr}}{1 + 8.7\sqrt{f/8}(\mathrm{Pr} - 1)} \tag{39}$$

where f is the friction factor for turbulent flow. For smooth tubes f is a function of the Reynolds number only. A number of modifications of Eq. (39) are to be found in the literature and may be summarized by the equation

$$\mathrm{Nu} = \frac{f/8\ \mathrm{Re}\ \mathrm{Pr}}{k_1 + k_2\sqrt{f/8}(\mathrm{Pr}^n - 1)} \tag{40}$$

Petukhov and Popov [16] have suggested that $k_1 = 1$, $k_2 = 12.7$, and $n = \frac{2}{3}$ in Eq. (40). The data were correlated best [14] in the region of fully developed turbulent flow by this expression. Since Eq. (40) is based on a model for fully developed turbulent flow, it does not account for entrance effects and it is not applicable in the transition range between laminar and fully developed turbulent flow where the Reynolds numbers are between 2 300 and 5×10^4. To overcome these disadvantages of Eq. (40), Gnielinski [14] modified it by replacing Re by (Re − 1 000) and by multiplying with the entrance correction factor derived by Hausen [17]. The equation reads

$$\mathrm{Nu} = \frac{(f/8)(\mathrm{Re} - 1\,000)\,\mathrm{Pr}}{1 + 12.7\sqrt{f/8}(\mathrm{Pr}^{2/3} - 1)} \left[1 + \left(\frac{d}{L} \right)^{2/3} \right] \tag{41}$$

According to Filonenko [18], the friction factor for turbulent tube flow may be calculated from

$$f = (1.82 \log_{10} \mathrm{Re} - 1.64)^{-2} \tag{42}$$

Equation (41) in connection with Eq. (42) has been

© 1983 Hemisphere Publishing Corporation

shown to represent the majority of the experimental data within 20% [14].

Equation (41) is recommended in the following range of variables, $0 < d/L < 1$, $0.6 < Pr < 2\,000$, and $2\,300 < Re < 10^6$. Depending on the magnitude of d/L and the Prandtl number, Eq. (9) or (16) yields higher Nusselt numbers in the transition region than Eq. (41). This effect is shown for Pr = 0.7 in Fig. 4. In the above-mentioned case the higher Nusselt number should always be used. For estimation purposes Eq. (41) can be simplified by the following equations: $0.5 < Pr \leqslant 1.5$ by

$$Nu = 0.021\,4(Re^{0.8} - 100)\,Pr^{0.4}\left[1 + \left(\frac{d}{L}\right)^{2/3}\right] \quad (43)$$

$1.5 < Pr < 500$ by

$$Nu = 0.012(Re^{0.87} - 280)\,Pr^{0.4}\left[1 + \left(\frac{d}{L}\right)^{2/3}\right] \quad (44)$$

(b) Concentric annular ducts

Heat transfer coefficients for turbulent flow in concentric annular ducts are dependent on the ratio d_i/d_o in addition to Re, Pr, and d/L, since annuli are not geometrically similar unless the diameter ratio d_i/d_o is identical. Furthermore, they are dependent on the boundary conditions mentioned in Sec. C(d) and shown in Fig. 1. The heat transfer in turbulent flow of gases and liquids in concentric annuli may be obtained using a modified form of Eq. (41) for turbulent flow in tubes,

$$\frac{Nu_{ann}}{Nu_{tube}} = f\left(\frac{d_i}{d_o}\right) \quad (45)$$

using the hydraulic diameter $d_h = d_o - d_i$ to evaluate Nu, Re, and d/L in Eq. (41).

According to Petukhov and Roizen [19], the Nusselt number for boundary condition in Fig. la (heat transfer at the inner wall, outer wall insulated) may be calculated using

$$\frac{Nu_i}{Nu_{tube}} = 0.86\left(\frac{d_i}{d_o}\right)^{-0.16} \quad (46)$$

and for boundary condition in Fig. lb (heat transfer at the outer wall, inner wall insulated) using

$$\frac{Nu_o}{Nu_{tube}} = 1 - 0.14\left(\frac{d_i}{d_o}\right)^{0.6} \quad (47)$$

The Nusselt number for boundary condition in Fig. lc (heat transfer on both walls of the passage, equal temperatures on both walls) is to be calculated according to the relationship of Stephan [6] from the equation

$$\frac{Nu_b}{Nu_{tube}} = \frac{0.86(d_i/d_o)^{0.84} + [1 - 0.14(d_i/d_o)^{0.6}]}{1 + d_i/d_o} \quad (48)$$

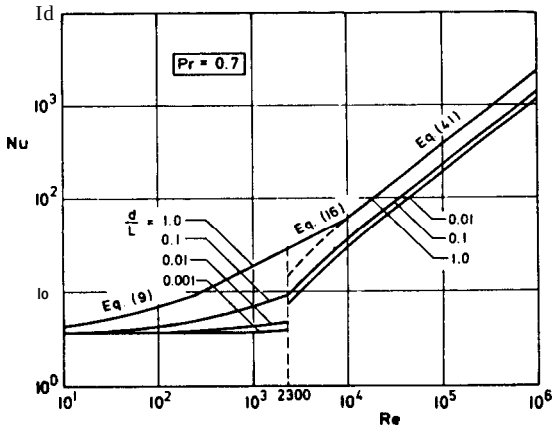

Figure 4 Variation of Eqs. (9), (16), and (41) as a function of the Reynolds number.

(c) Smooth straight ducts of various cross section

According to statements from the literature, the Nusselt numbers for heat transfer in smooth straight ducts of noncircular cross sections can also be calculated from Eq. (41) by using the hydraulic diameter of the duct in evaluating Nu, Re, and d/L. The hydraulic diameter is defined as

$$d_h = \frac{4S}{P} \quad (49)$$

where S is the flow cross-sectional area and P is the wetted perimeter of the duct.

(d) Factors that influence the heat transfer coefficient

I. Variable physical properties

The direction of heat flux (heating or cooling and fluid) influences the heat transfer when the physical properties are temperature-dependent. According to the literature, the influence can be taken into consideration by using a correction factor with the above-mentioned equations:

$$Nu_c = Nu\,K \quad (50)$$

For gases, the variation of fluid properties with temperature can be represented approximately by simple power laws, and the correction factor K can be written in the empirical form

$$K = \left(\frac{T_b}{T_w}\right)^n \quad (51)$$

© 1983 Hemisphere Publishing Corporation

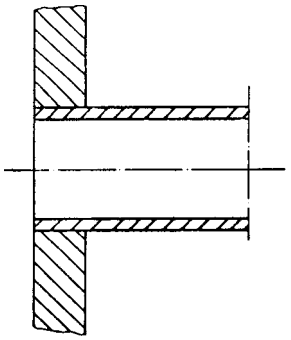

Figure 5 Tube fitting into the tube support plate.

where T_b is the absolute bulk temperature of the gas and T_w is the absolute wall temperature. The exponent n in Eq. (51) is $n = 0$ in the case of cooling a gas $[(T_b/T_w) > 1]$. Heating the gas $[(T_b/T_w) < 1]$ leads to different values of n for each gas. Gnielinski [14] correlated the data he collected for gases by taking $n = 0.45$ in the range $0 < T_b/T_w < 0.5$. According to the literature, n should be approximately equal to 0.15 for carbon dioxide and steam in the same temperature range. Gregorig [20] has derived a nomogram to take into account the influence of variable physical properties of gases.

For ***liquids,*** the variation of fluid properties with the temperature can be taken into account using

$$K = \left(\frac{\mathrm{Pr}}{\mathrm{Pr}_w}\right)^{0.11} \tag{52}$$

where Pr is the Prandtl number of the liquid at bulk temperature and Pr, at wall temperature, respectively. The range of validity of Eq. (52) is $0.1 < \mathrm{Pr}/\mathrm{Pr}_w < 10$.

II. Tube entrance effects

Equation (41) yields mean Nusselt numbers for tubes fitted without fillets in a tube support plate (Fig. 5). The influence of the shape of the tube inlet on the local Nusselt number was investigated by Grass [21] and by Boelter et al. [22].

(e) Comparison with experimental data

I. Smooth straight tubes

In the following figures, experimental data collected by Gnielinski [14] are shown in comparison to Eq. (41) and taking into account the influence of variable physical properties of the fluids according to Eqs. (50)-(52). Figures 6 and 7 show the data for heat transfer to various gases. The data shown in Figs. 8 and 9 were obtained for liquids flowing inside tubes. The data shown in Figs. 10 and 11 were obtained by

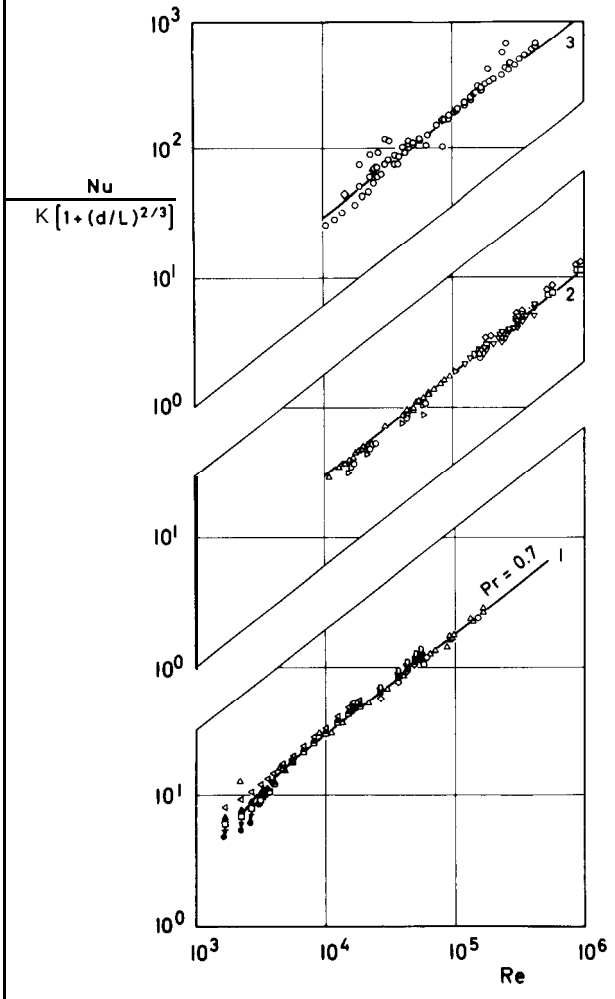

	Author	d/L	
1	Nusselt [23]	0.044	○
		0.037	△
	Cholette [24]	0.0952	▷
		0.0476	▲
		0.03175	□
		0.02381	+
		0.01905	x
		0.01587	○
	Boelter, Young, Iversen [22]	1.36	◇
		0.76	▯
		0.109	◆
		0.0588	■
	Bialokoz [25]	0.02	▽
	Kolar [26]	0.001	△
2	Delpont [27]	0.001	□
		0.001	◇
	Kirillov Malyugin [28]	0.014	▷
		0.0345	○
		0.0204	□
3	Ruppert [29]	0.001	○
	Sleicher [30]	0.001	◇

Figure 6 Comparison of Eq. (41) with the data of several authors for heat transfer of gases in tubes.

© 1983 Hemisphere Publishing Corporation

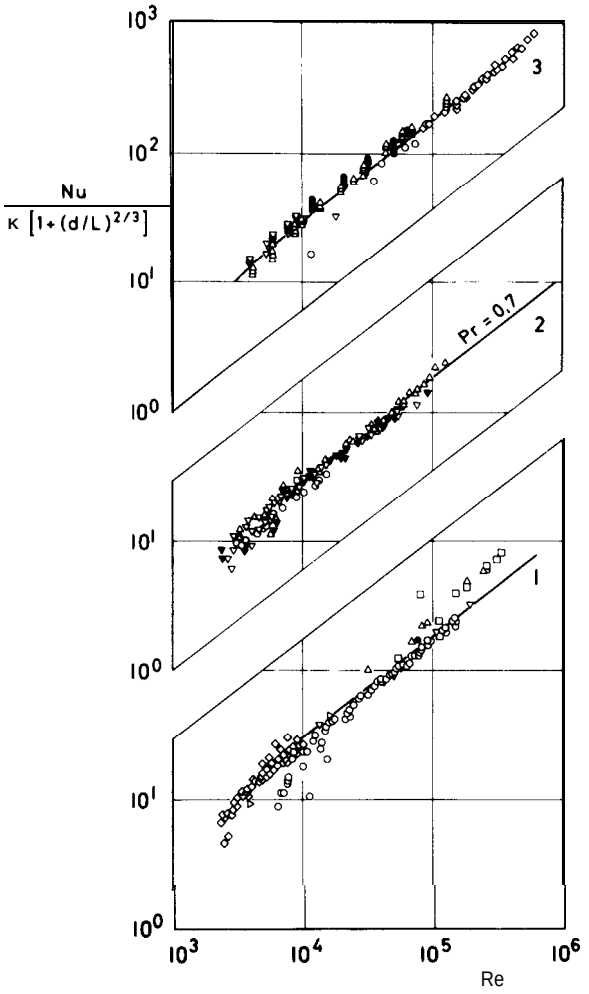

	Author		d/L
1	Humble et al. [31]	○	0.0166
	Taylor, [32] Kirchgessner	△ □	0.0166 0.011
	Mikheyev [33]	◇	0.01
	Mc Eligott et al. [34]	▽ ▷ ●	0.006 0.0128 0.02
2	Dalle-Donne, Bowditch [35]	▼ △ ▽	0.007 0.004 0.002
	Evans, Sarjant [36]	○	0.031
3	Barnes, Jackson [37]	● ▽ △	0.0095 0.012 0.01
	Perkins, [38] Worsoe-Sch.	○	0.007
	Lel'Chuk Dyadyakin [39]	◇	0.0072

Figure 7 Comparison of Eq. (41) with the data of several authors for heat transfer of gases in tubes.

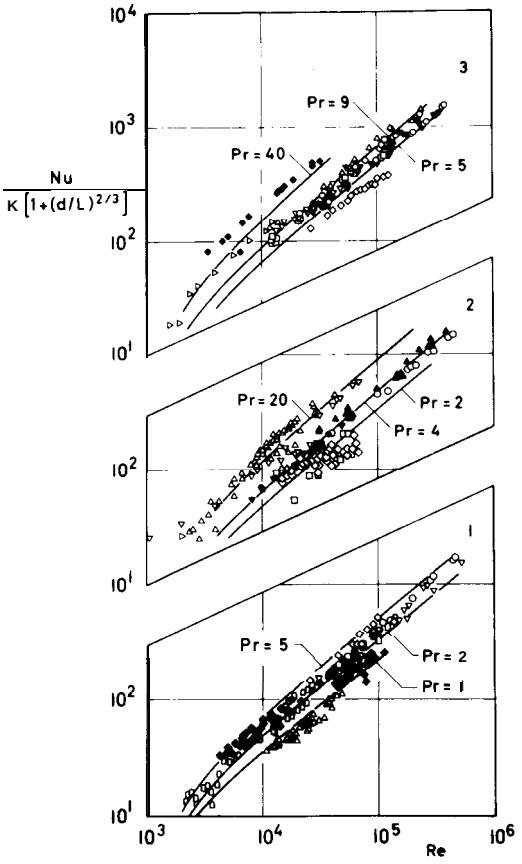

Author		d/L	Pr	
Sherwood and Petrie	[40]	0.0103	2 ÷ 4	◆
			3.8 ÷ 4.1	●
Hufschmidt et al.	[41]	0.0118	2.1 ÷ 4.0	▽
		0.0287	3 ÷ 6	◇
		0.01110	2.6 ÷ 4.2	○
Mikheyev	[33]	0 0 00	2 ÷ 5	□
Krischer	[42]	0.0200	4.0	□
Alad'jev et al.	[43]	0.0100	0.9 ÷ 1.2	△
Clapp et al.	[44]	0.0010	2 ÷ 5	□
Morris et al.	[45]	0.0050	2.8 ÷ 3.15	●
Sherwood	[40]	0.0103	2.0 ÷ 3.7	◇
Stone et al.	[46]	0.0010	4 ÷ 6	▲
Hufschmidt	[41]	0.0067	3.2 ÷ 4.1	○
Krischer	[42]	0.0045	4.0	▼
Morris et al.	[45]	0.0051	10 ÷ 71	▽
Sherwood	[40]	0.0103	12 ÷ 24	△
Lawrence and Sherwood	[47]	0.0017	8 ÷ 9	◇
		0.0045	5.3 ÷ 7.6	▽
Allen, Eckert	[48]	0.0010	7.0 ÷ 8.3	□
Stone, Ewing and Miller	[46]		5 ; 8 ; 10	○
			8 ; 13	△
			6 ; 8 ; 12	▼
Eagle et al.	[49]		5.0	●
Keevil	[50]		48 ÷ 62	◆
Morris and Whitman	[45]		32 ÷ 47	▷

Figure 8 Comparison of Eq. (41) with the data of several authors for heat transfer of liquids in tubes.

© 1983 Hemisphere publishing Corporation

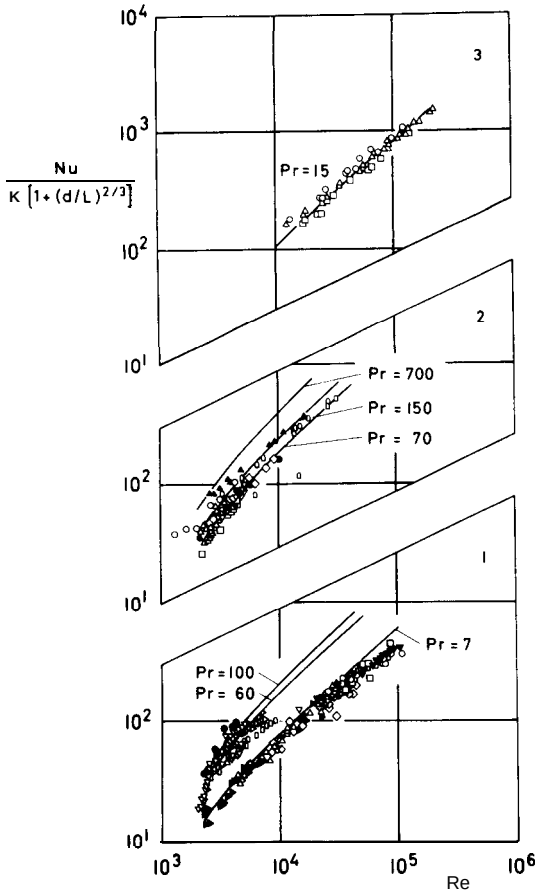

	Author		d/L	Pr
1	Lawrence and Sherwood [47]	▼	0.0082	6.0 - 8.5
		○	0.0055	6 - 8
	Sherwood and Petrie [40]	△	0.0103	5.7 - 7.9
		□	0.0103	5.5 - 8.1
	Ivanovskii [51]	◇	0.0100	4.1 - 7.0
	Mikheyev [33]	▶	0.0100	5 - 7
	Keevil [50]	▯	0.0010	60 - 100
		▽		99 - 130
		●		112 - 143
	Clapp et al.[44]	▷		71 - 120
2	Morris and Whitman [45]	○	0.0051	200 - 750
		◇	0.0051	87 - 164
	Kraussold [52]	●	0.0085	80 - 84.6
	Sherwood, Mangsen Kiley [53]	□	0.0043	92 - 110
		△	0.0083	132 - 160
		▽	0.0055	103 - 109
	Hufschmidt, Burck [54]	▯	0.0264	81 - 113
		▲		147 - 186
3	Stone, Ewing, Miller [46]	□	0.001	9, 12, 24
		△		11.5, 14-18
		○		15, 23

Figure 9 Comparison of Eq. (41) with the data of several authors for heat transfer of liquids in tubes.

Reinicke [55] for liquid flowing in short tubes. They demonstrate what was shown in Fig. 4, namely, that in the transition region the experimental data are more closely predicted using Eqs. (16) and (9), which give larger values for Nu than those obtained using Eq. (41).

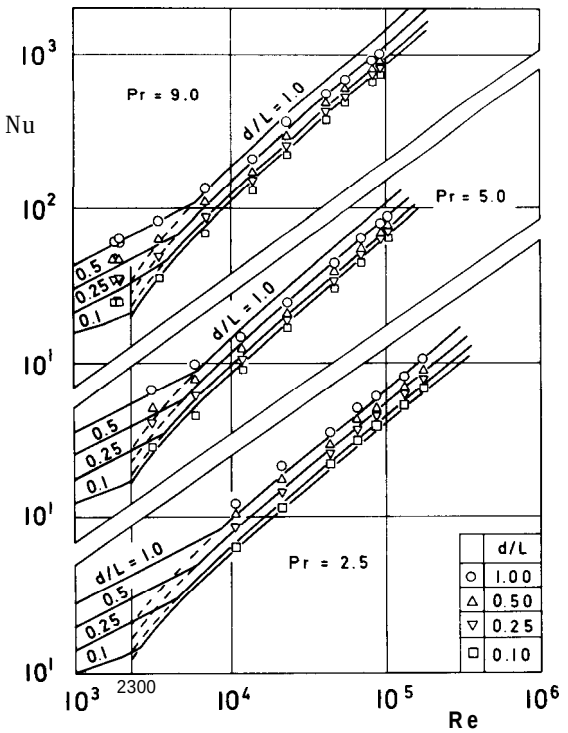

Figure 10 The data of Reinicke [55] compared with the variation of Eqs. (9), (16), and (41) for heat transfer of liquids flowing in short tubes.

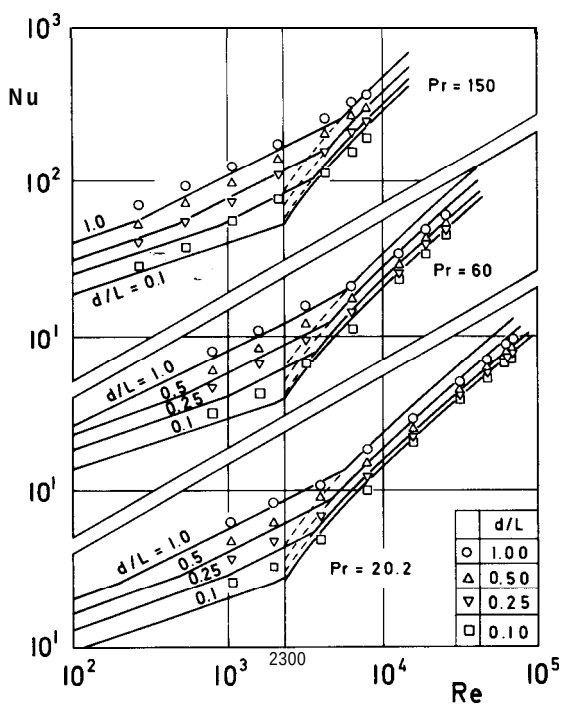

Figure 11 The data of Reinicke [55] compared with the variation of Eqs. (9), (16), and (41) for heat transfer of liquids in short tubes.

© 1983 Hemisphere Publishing Corporation

II. Concentric annular ducts

Experimental data for the heat transfer coefficients for the flow of air in concentric circular annuli heating on the inner wall of the tube while the outer wall was insulated are shown in Fig. 12 in comparison to the values predicted by Eq. (41). For the same boundary condition of Fig. la, experimental data for water are shown in Fig. 13. The experimental Nusselt numbers

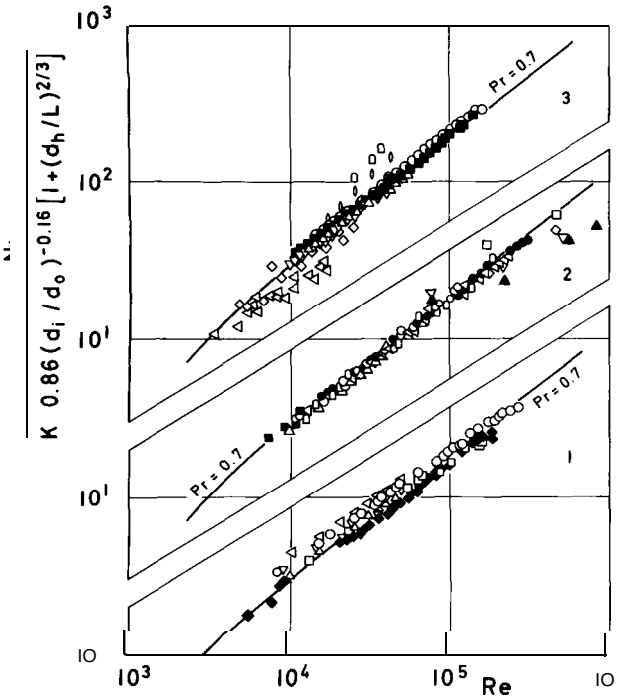

	Author		d_i/d_o	d_h/L	
1	Lee and Barrow	[56]	0.613	0.01	△
			0.374	0.016	▽
			0.258	0.019	◁
	Quarmby	[57]	0.109	0.016	○
			0.174	0.021	□
			0.347	0.022	◇
2	Petukhov and Roizen	[58]	0.072	0.001	●
			0.143	0.001	◁
			0.244	0.001	□
			0.546	0.001	○
			0.692	0.081	△
	Mueller	[59]	0.0016	0.116	▲
			0.0017	0.052	▽
			0.0008	0.109	□
			0.0013	0.089	◇
	Kirschbaum	[60]	0.79	0.001	■
3	Leung et al.	[61]	0.50	0.001	▽
			0.375	0.001	△
			0.255	0.001	□
			0.192	0.001	○
	Zerban	[62]	0.84	0.003	◁
			0.70	0.007	◇
			0.518	0.016	◊
			0.366	0.030	□

Figure 12 Comparison of Eq. (41) with the data of several authors for heat transfer of gases in concentric circular annuli. Heating from the inner tube (boundary condition of Fig. la).

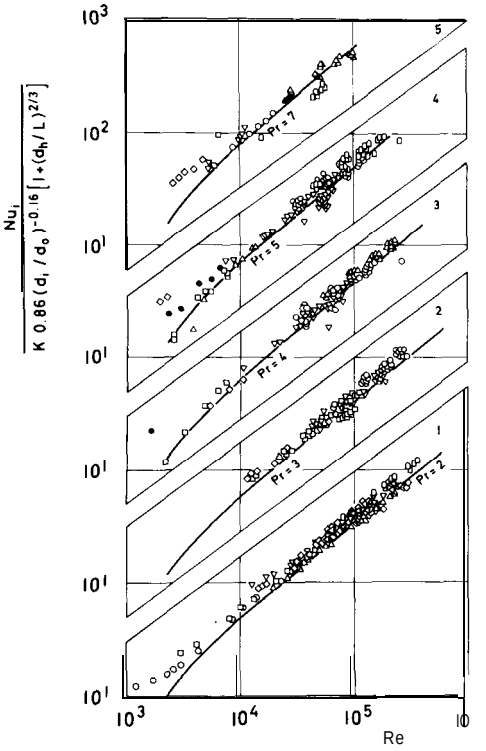

	Author		d_i/d_o	d_h/L	Pr	
1	Mc Millen and Larson	[63]	0.770	0.002	2.4÷3.1	○
			0.625	0.004	2.3÷2.7	□
	Monrad and Pelton	[64]	0.625	0.010	2.2	△
			0.417	0.022	2.2÷2.4	▽
	Stein and Begell	[65]	0.810	0.001	1.9÷3.0	◇
			0.681	0.001	2.3÷3.0	◁
			0.590	0.001	2÷3	□
2	Miller et al.	[66]	0.745	0.044	3.5	△
	Monrad,Pelton	[64]	0.417	0.022	3.0÷3.2	◇
	Stein and Begell	[65]	0.810	0.001	3÷4	□
			0.681	0.001	3÷4	▽
			0.590	0.001	3÷4	○
3	Carpenter et al.	[67]	0.750	0.002	4.6÷4.8	◇
	Mc Millen,Larson	[63]	0.770	0.002	4.6	●
	Krischer	[42]	0.876	0.001	4.3÷4.4	□
	Stein and Begell	[65]	0.810	0.001	4÷5	▽
			0.681	0.001	4÷5	○
			0.590	0.001	4÷5	△
4	Mc Millen and Larson	[63]	0.770	0.002	5÷6	●
			0.652	0.004	5÷6	◇
	Krischer	[42]	0.857	0.001	5÷6	□
			0.842	0.001	5÷6	△
	Stein and Begell	[65]	0.810	0.001	5÷6	▽
			0.681	0.001	5÷6	○
			0.590	0.001	5÷6	□
5	Mc Millen and Larson	[63]	0.770	0.002	6÷7	○
			0.652	0.004	6÷7	◇
	Miller et al.	[66]	0.722	0.03	6÷7	□
			0.745	0.044	6÷7	▽
	Stein and Begell	[65]	0.810	0.001	6÷7	□
			0.681	0.001	6÷7	△

Figure 13 Comparison of Eq. (41) with the data of several authors for heat transfer of liquids in concentric circular annuli. Heating from the inner tube (boundary condition of Fig. la).

© 1983 Hemisphere Publishing Corporation

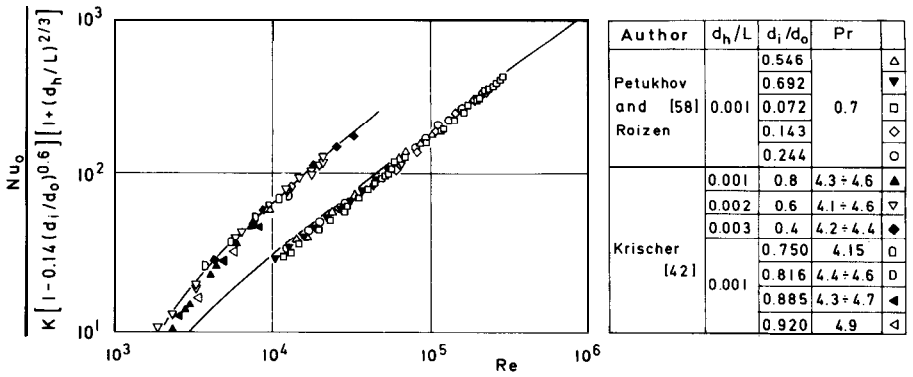

Author	d_h/L	d_i/d_o	Pr	
Petukhov and Roizen [58]	0.001	0.546	0.7	△
		0.692		▼
		0.072		□
		0.143		◇
		0.244		○
Krischer [42]	0.001	0.8	4.3÷4.6	▲
	0.002	0.6	4.1÷4.6	▽
	0.003	0.4	4.2÷4.4	◆
	0.001	0.750	4.15	▯
		0.816	4.4÷4.6	▯
		0.885	4.3÷4.7	◀
		0.920	4.9	◁

Figure 14 Comparison of Eq. (41) with the data of several authors for heat transfer of gases and liquids in concentric annuli. Heating from the outer tube (boundary condition of Fig. lb).

are divided by the factor K according to Eq. (51) or Eq. (52) to take into account the temperature-dependent physical properties; by the factor $[1+(d_h/L)]^{2/3}$ to take into account the dependence of the heat transfer coefficient from the length of the tube; and by the factor $0.86(d_i/d_o)^{-0.16}$ to take into account the annular flow.

The experimental data of several authors for boundary condition of Fig. lb (heating from the outer tube, inner tube insulated) are collected in Fig. 14. To take into account the annular flow and this boundary condition, the Nu, numbers are divided by $1-0.1\,4(d_i/d_o)^{0.6}$.

Nomenclature** for **Section 2.5.1 appears at the beginning** of **Part 2.

REFERENCES FOR SECTION 2.5.1

1. Shah R. K., and London, A. L., ***Laminar Flow Forced Convection in Ducts,*** Academic, New York, 1978.
2. Schlünder, E. U., *Einführung in die Wiirme- und Stoffübertragung*, p. 52, Verlag Vieweg, Braunschweig, 1972.
3. Hausen, H., Neue Gleichungen fur die Wärmeübertragung bei freier oder erzwungener Stromung, *Allg. Waermetech., vol. 9,* pp. 75-79, 1959.
4. Pohlhausen, E., Der Wärmeaustausch zwischen festen Körpern und Fliissigkeiten mit kleiner Reibung und kleiner Wärmeleitung, ***Z. Angew. Math. Mech.***, vol. 1, pp. 115-121, 1921.
5. Stephan, K., Wärmeübergang und Druckabfall bei nichtausgebildeter Laminarströmung in Rohren und ebenen Spalten, ***Chem. Ing. Tech.,*** vol. 31, pp. 773-778, 1959.
6. Stephan, K., Wärmeübergang bei turbulenter und bei laminarer Strömung in Ringspalten, ***Chem. Ing. Tech.,*** vol. 34, pp. 207-212, 1962.
7. Martin, H., Private correspondence, 1979.
8. Kays, W. M., and Nicoll, W. B., Laminar Flow Heat Transfer to a Gas with Large Temperature Differences, ***J. Heat Transfer,*** vol. 85, pp. 329-338, 1963.
9. Davenport, M. E., and Leppert, G., The Effect of Transverse Temperature Gradients on the Heat Transfer and Friction for Laminar Flow of Gases, ***J. Heat Transfer,*** vol. 87, pp. 191-196, 1965.
10. Bankston, C. A., Sibbit, W. L., and Skoglund, V. J., Stability of Gas Flow Distribution Among Parallel Heated Channels, 2d Propulsion Joint Specialist Conf., Colorado Springs, AIAA Paper No. 66-589, 1966.
11. Sieder, E. N., and Tate, G. E., Heat Transfer and Pressure Drop of Liquids in Tubes, ***Ind. Eng. Chem.,*** vol. 8, pp. 1429-1435, 1936.
12. Martinelli, R. C., Southwell, C. J., Alves, G., Craig, H. L., Weinberg, E. B., Lansing, N. F., and Boelter, L. M. K., Heat Transfer and Pressure Drop for a Fluid Flowing in the Viscous Region Through a Vertical Pipe, ***Trans. AIChE, vol. 38,*** pp. 493-530, 1942.
13. McAdams, W. H., ***Heat Transmission,*** McGraw-Hill Series in Chemical Engineering, McGraw-Hill, New York, 1954.
14. Gnielinski, V., New Equations for Heat and Mass Transfer in Turbulent Pipe and Channel Flow, ***Znt. Chem. Eng.,*** vol. 16, pp. 359-368, 1976.
15. Prandtl, L., *Führer durch die Strömungslehre*, Verlag Vieweg, Braunschweig, 1944.
16. Petukhov, B. S., and Popov, V. N., Theoretical Calculation of Heat Exchange and Frictional Resistance in Turbulent Flow in Tubes of an Incompressible Fluid with Variable Physical Properties, ***High Temp. (USSR),*** vol. 1, pp. 69-83, 1963.
17. Hausen, H., Darstellung des Wärmeüberganges in Rohren durch verallgemeinerte Potenzbeziehungen, Z. ***Ver. Dtsch. Ing., Beiheft Verfahrenstech.,*** no. 4, pp. 91-134, 1943.
18. Filonenko, G. K., Hydraulic Resistance in Pipes, ***Tepfoenergetika,*** vol. 1, pp. 40-44, 1954 (in Russian).

© 1983 Hemisphere Publishing Corporation

19. Petukhov, B. S., and Roizen, L. I., Generalized Relationship for Heat Transfer in a Turbulent Flow of Gas in Tubes of Annular Section, ***High Temp. (USSR),*** vol. 2, pp. 65-68, 1964.
20. Gregorig, R., *Wärmeaustausch und Wärmeaustauscher*, p. 171, Verlag Sauerländer, Frankfurt/Main, 1973.
21. Grass, G., Wärmeübergang an turbulent strömende Gase im Rohreinlauf, ***Allg. Waermetech.,*** vol. 7, pp. 58-64, 1956.
22. Boelter, L. M. K., Young, G., and Iversen, H. W., An Investigation of Aircraft Heaters, XXVII-Distribution of Heat Transfer Rate in the Entrance Section of a Circular Tube, NACA Tech. Note TN 1451, 1948.
23. Nusselt, W., ***Der Wärmeübergang in Rohrleitungen,*** Forsch.-Arb.-Ing.-Wes. No. 89, Verlag des Vereins Deutscher Ingenieure, Berlin, 1909.
24. Cholette, A., Local and Average Coefficients for Air Flowing Inside Tubes, ***Chem. Eng. Prog., vol. 44,*** pp. 81-88, 1948.
25. Bialokoz, J. E., and Saunders, 0. A., Heat Transfer in Pipe Flow at High Speeds, *Proc. **Inst. Mech. Eng.,*** vol. 170, pp. 389-399, 1956.
26. Kolar, V., Heat Transfer in Turbulent Flow of Fluids Through Smooth and Rough Tubes, ***Int. J. Heat Mass Transfer, vol. 8,*** pp. 639-653, 1965.
27. Delpont, J. P., Influence du Flux Chaleur et de la Nature du Gaz sur les Coefficients d'Échange dans un Tube Cylindrique Lisse, ***Int. J. Heat Mass Transfer, vol. 7,*** pp. 517-526, 1964.
28. Kirillov, V. N., and Malyugin, Y. S., Heat Transfer during the Flow of a Gas in a Pipe at High Temperature Differences, ***High Temp. (USSR), vol.*** 1, pp. 227-231, 1963.
29. Ruppert, K. A., Druckverlust und Wärmeübergang bei der Verdampfung in durchströmten glatten und rauhen Rohren in Gegenwart von Inertgasen, Dr.-Ing. dissertation, Universität Karlsruhe (TH), 1975.
30. Sleicher, C. A., Experimental Velocity and Temperature Profiles for Air in Turbulent Pipe Flow, ***Trans. ASME, vol. 80,*** pp. 693-704, 1958.
31. Humble, L. V., Lowdermilk, W. H., and Desmon, L. G., Measurement of Average Heat Transfer and Friction Coefficients for Subsonic Flow of Air in Smooth Tubes at High Surface and Fluid Temperatures, NACA Rept. 1020, 195 1.
32. Taylor, M. F., and Kirchgessner, T. A., Measurements of Heat Transfer and Friction Coefficients for Helium Flowing in a Tube at Surface Temperatures up to ***5900*** R, ***Am. Rocket Soc. J., vol. 30,*** pp. 830-832, 889-892, 1960.
33. Mikheyev, M. A., ***Mean*** Heat Transfer of Fluids Flowing in Tubes, Rept. MCL-222, Technical Information Center, Foreign Technology Division, Wright-Patterson Air Force Base, Ohio, pp. 159-179.
34. McEligott, D. M., Magee, P. M., and Leppert, G., Effect of Large Temperature Gradients on Convective Heat Transfer: The Downstream Region, ***J. Heat Transfer,*** vol. 87, pp. 67-76, 1965.
35. Dalle-Donne, M., and Bowditch, F. W., Experimental Local Heat Transfer and Friction Coefficients for Subsonic Laminar Transitional and Turbulent Flow of Air or Helium in a Tube at High Temperatures, Dragon Project Rept. 184, Winfrith, Dorchester, Dorset, U.K., 1963.
36. Evans, S. J., and Sarjant, R. J., Heat Transfer and Turbulence in Gases Flowing Inside Tubes, ***J. Inst. Fuel, vol. 24,*** pp. 216-227, 1951.
37. Barnes, J. F., and Jackson, J. D., Heat Transfer to Air, Carbon Dioxide and Helium Flowing Through Smooth Circular Tubes under Conditions of Large Surface/Gas Temperature Ratio, *J. Mech. Eng. Sci.*, vol. 3, pp. 303-314, 1961.
38. Perkins, H. C., and Worsoe-Schmidt, P., Turbulent Heat and Momentum Transfer for Gases in a Circular Tube at Wall to Bulk Temperature Ratios to ***Seven, ht. J. Heat Mass Transfer,*** vol. 8, pp. 1011-1031, 1965.
39. Lel'chuk, V. L., and Dyadyakin, B. V., Heat Transfer from a Wall to a Turbulent Current of Air Inside a Tube and the Hydraulic Resistance at Large Temperature Differences, AEC-TR-45 11, pp. 114-183, 1962.
40. Sherwood, T. K., and Petrie, J. M., Heat Transmission to Liquids Flowing in Pipes, ***Ind. Eng. Chem.,*** vol. 24, pp. 736-745, 1932.
41. Hufschmidt, W. E., Burck, E., and Riebold, W., Die Bestimmung örtlicher und mittlerer Wärmeübergangszahlen in Rohren bei hohen Wärmestromdichten, *Int. J. **Heat Mass Tmnsfer,*** vol. 9, pp. 539-565, 1966.
42. Krischer, O., Wärmeaustausch in Ringspalten bei laminarer und turbulenter Strömung, ***Chem. Ing. Tech.,*** vol. 33, pp. 13-19, 1961.
43. Alad jev, I. T., Vel tischev, N. A., and Konrat jev, N. S., Heat Transfer by Convection at High Pressure, Rept. MCL-222, Technical Information Center, Foreign Technology Division, Wright-Patterson Air Force Base, Ohio, pp. 206-214.
44. Clapp, M. H., and Fitzsimmons, O. F., The Effect of Heat Transfer on Friction Factors in Fannings Equations, M.S. Thesis, Massachusetts Institute of Technology, Cambridge, Mass., 1928.
45. Morris, E. H., and Whitman, W. G., Heat Transfer for Oils and Water in Pipes, ***Ind. Eng. Chem., vol. 20,*** pp. 234-240, 1928.
46. Stone, J. P., Ewing, C. T., and Miller, P. R., Heat Transfer Studies on Some Stable Organic Fluids in a Forced Convection Loop, ***J. Chem. Eng. Data,*** vol. 7, pp. 519-525, 1962.
47. Lawrence, A. E., and Sherwood, T. K., Heat Transmission to Water Flowing in Pipes, *Ind. **Eng. Chem,*** vol. 23, pp. 301-309, 1931.
48. Allen, R. W., and Eckert, E. R. G., Friction and Heat Transfer Measurements to Turbulent Pipe Flow of Water (Pr = 7 and 8) at Uniform Wall Heat Flux, ***J. Heat Transfer, vol. 86,*** pp. 301-310, 1964.
49. Eagle, A., and Ferguson, R. M., On the Coefficient of Heat Transfer from the Internal Surface of Tube Walls, *Proc. **R. Soc. London Ser. A, vol.*** 127, pp. 540-552, 1930.
50. Keevil, C. S., Heat Transfer and Friction for Heating and Cooling of Fluids in Pipes, Ph.D. thesis, Massachusetts Institute of Technology, Cambridge, Mass., 1930.
51. Ivanovskii, M. N., Rapid Method for Measuring the Average Heat Transfer Coefficient in a Tube, AEC-TR-4511, pp. 90-103, 1962.
52. Kraussold, H., Wärmeübertragung bei zähen Flüssigkeiten in Rohren, VDI-Forschungsheft 351, VDI-Verlag, Berlin, 1931.
53. Sherwood, T. K., Kiley, D. D., and Mangsen, G. E., Heat Transmission to Oil Flowing in Pipes, *Ind. **Eng. Chem.,*** vol. 24, pp. 273-277, 1932.

© 1983 Hemisphere publishing Corporation

54. Hufschmidt, W., and Burck, E., Der Einfluss temperaturabhlngiger Stoffwerte auf den Wärmeübergang bei turbulenter Strömung von Fliissigkeiten in Rohren bci hohen Wärmestromdichten und Prandtlzahlen, ht. *J. Heat* Mass Transfer, vol. 11, pp. 1041-1048, 1968.
55. Reinicke, H., Über den Wärmeübergang von kurzen durchströmten Rohren und querumströmten Zylindern verschiedener Anordnung an zähen Fliissigkeiten verschiedener Prandtlzahl bei kleinen Temperaturdifferenzen, Dr.-Ing. dissertation, Technische Hochschule Darmstadt, 1969.
56. Lee, Y., and Barrow, H., Turbulent Flow and Heat Transfer in Concentric and Eccentric Annuli, *Proc. Inst. Mech. Eng., vol.* 178, Paper 12, pp. I-16, 1964.
57. Quarmby, A., Some Measurements of Turbulent Heat Transfer in the Thermal Entrance Region of Concentric Annuli, *Int. J. Heat Mass Tmnsfer, vol.* 10, pp. 267-276, 1967.
58. Petukhov, B. S., and Roizen, L. I., An Experimental Investigation of Heat Transfer in a Turbulent Flow of Gas in Tubes of Annular Section, *High Temp. (USSR),* vol. 1, pp. 373-380, 1963.
59. Mueller, A. C., Heat Transfer from Wires to Air in Parallel *Flow, Trans. AIChE,* vol. 38, pp. 613-629, 1942.
60. Kirschbaum, E., Neues zum Wärmeübergang mit und ohne Änderung des Aggregatzustandes, *Chem. Ing. Tech., vol. 24,* pp. 393-400, 1952.
61. Leung, E. Y., Kays, W. M., and Reynolds, W. C., Heat Transfer with Turbulent Flow in Concentric and Eccentric Annuli with Constant and Variable Heat Flux, Rept. AHT-4, Thermosciences Division, Department of Mechanical Engineering, Stanford University, Stanford, Calif., 1962.
62. Zerban, A. H., Clarification of the Heat Transfer Characteristics of Fluids in Annular Passages, Ph.D. thesis, University of Michigan, Ann Arbor, 1940.
63. McMillen, E. L., and Larson, R. E., Annular Heat Transfer Coefficients for Turbulent Flow, *Trans. AIChE, vol. 40,* pp. 177-202, 1944.
64. Monrad, C. C., and Pelton, J. F., Heat Transfer by Convection in Annular Spaces, *Trans. AIChE,* vol. 38, pp. 593-611, 1942.
65. Stein, R. P., and Begell, W., Heat Transfer to Water in Turbulent Flow in Internally Heated Annuli, *AIChE J., vol. 4,* pp. 127-131, 1958.
66. Miller, P., Byrnes, J. J., and Benforado, D. M., Heat Transfer to Water in an Annulus, *AIChE J., vol. 1,* pp. 501-504, 1955.
67. Carpenter, F. G., Colburn, A. P., and Schoenborn, E. M., Heat Transfer and Friction of Water in an Annular Space, *Trans. AIChE,* vol. 42, pp. 165-187, 1946.

© 1983 Hemisphere Publishing Corporation

2.5.2

Forced convection around immersed bodies

V. Gnielinski

A. Smooth flat plate

When a fluid of uniform velocity flows over a plate with a streamlined leading edge, the stream adjacent to the plate is retarded, thus forming a laminar boundary layer. The thickness of the laminar boundary layer increases with increasing distance x from the leading edge until a critical length x_{crit} is reached, where transition to a turbulent boundary layer starts. The critical length is determined by the critical Reynolds number $Re_{crit} = ux_{crit}/\nu$, which depends on, among other factors, the degree of turbulence of the stream and the roughness of the plate. In this work $Re_{crit} = 5 \times 10^5$ is assumed. It may be higher if the degree of turbulence in the stream is low, whereas much lower values have been observed when the stream has a high degree of turbulence.

For a flat plate with a streamlined leading edge both types of boundary layers exist, whereas for flow over a flat plate with an obtuse-angled or blunt leading edge only a turbulent boundary layer starting from the leading edge develops. Presser [I] has investigated the influence of the shape of the leading edge.

(a) Laminar boundary layer

I. Entire surface at uniform temperature

Equations for the local and the average value of the Nusselt number were derived by Pohlhausen [2] and Kroujiline [3].

The local *value* of the Nusselt number $Nu_{x,lam}$ at a position x distance from the leading edge of the plate can be calculated from

$$Nu_{x,lam} = 0.332 \sqrt{Re_x} \sqrt[3]{Pr} \quad (1)$$

where

$$Nu_{x,lam} = \frac{\alpha x}{\lambda}$$

and

$$Re_x = \frac{ux}{\nu}$$

The ***average value*** of the Nusselt number $Nu_{l,lam}$ for a plate of length l results from integrating Eq. (1)

$$Nu_{l,lam} = 0.664 \sqrt{Re_l} \sqrt[3]{Pr} \quad (2)$$

with

$$Nu_{l,lam} = \frac{\alpha l}{\lambda}$$

and

$$Re_l = \frac{ul}{\nu}$$

A weak dependence of the factors 0.332 in Eq. (1) and 0.664 in Eq. (2) on Pr is ignored. According to Presser [1], the factor 0.664 increases to 0.703 for Pr = 1 000.

II. Uniform heat flux on the surface of the plate

According to Gauler [4], the local value of the Nusselt number at a position x distance from the leading edge

© 1983 Hemisphere Publishing Corporation

is calculated from

$$Nu_{x,lam} = 0.460 \sqrt{Re_x} \sqrt[3]{Pr} \quad (3)$$

The range of validity of Eqs. (1) and (2) is Re, $< 10^5$, $Re_l < 10^5$, and $0.6 < Pr < 2\ 000$. Physical properties are evaluated at the bulk temperature T_b of the fluid.

(b) Turbulent boundary layer

According to Petukhov and Popov [5], the value of the Nusselt number for a plate at constant wall temperature with the physical properties evaluated at the bulk temperature T_b of the fluid can be calculated using

$$Nu_{turb} = \frac{(\xi/8)\, Re\, Pr}{1 + 12.7 \sqrt{\xi/8}\,(Pr^{2/3} - 1)} \quad (4)$$

For the ***local*** Nusselt number $Nu_{x,turb}$, the drag coefficient ξ presented by Schlichting [6] for a plate with turbulent boundary layer, to be used in Eq. (4) is

$$\frac{\xi}{8} = 0.029\ 6\ Re_x^{-0.2} \quad (5)$$

and results in

$$Nu_{x,turb} = \frac{0.029\ 6\ Re_x^{0.8}\, Pr}{1 + 2.185\ Re_x^{-0.1}\,(Pr^{2/3} - 1)} \quad (6)$$

The range of validity of Eq. (6) is $5 \times 10^5 < Re, < 10$ and $0.5 < Pr < 2\ 000$.

For the ***average*** Nusselt number $Nu_{l,turb}$, the average friction factor given by Schlichting [6] for a plate with a turbulent boundary layer to be used in Eq. (4) is

$$\frac{\xi}{8} = 0.037\ Re_l^{-0.2} \quad (7)$$

yielding

$$Nu_{l,turb} = \frac{0.037\ Re_l^{0.8}\, Pr}{1 + 2.443\ Re_l^{-0.1}\,(Pr^{2/3} - 1)} \quad (8)$$

The range of validity of Eq. (8) is $5 \times 10^5 < Re_l < 10$ and $0.5 < Pr < 2\ 000$.

(c) Combined correlation for average coefficients on a flat plate parallel to the flow

A blunt leading edge and higher degrees of turbulence predominate in practical applications of heat transfer from flat plates. Because of this, no laminar boundary layer will exist along the whole length of a plate at intermediate Reynolds numbers $5 \times 10^3 < Re_l < 5 \times 10^5$, and no sudden change of the Nusselt numbers given by Eq. (2) to those resulting from Eq. (8) is observed, Krischer [7] has presented a graph correlating collected experimental data of heat transfer for air at a flat plate from $10^1 < Re_l < 10^6$. As shown by Gnielinski [8], the following equation represents not only the graph of Krischer but also measured heat transfer coefficients in a wide range of Prandtl numbers.

$$Nu_{l,0} = \sqrt{Nu_{l,lam}^2 + Nu_{l,\ turb}^2} \quad (9)$$

with $Nu_{l,lam}$ from Eq. (2) and $Nu_{l,turb}$, from Eq. (8). Eq. (9) holds for average Nusselt numbers from $10 < Re_l < 10^7$ and $0.5 < Pr < 2\ 000$. Physical properties of the fluid are evaluated at the bulk temperature T_b.

(d) Dependence of the heat transfer on the length of a nonheated initial portion of the plate

The heat transfer from a plate depends not only on the length of the heated plate but will be influenced by the presence of an unheated segment preceding the heated section.

After Brauer [9], the effect of a nonheated initial portion of a plate in the case of a ***laminar*** boundary layer can be calculated by extending Eq. (2) to

$$Nu_{l,lam} = 0.664 \sqrt{Re_l} \sqrt[3]{Pr} \frac{[1 - (1 - l_0/l)^{3/4}]^{2/3}}{l_0/l} \quad (10)$$

and computing $Nu_{l,lam}$ and Re_l with the total length l of the plate, where l_0 denotes the heated length of the plate. According to Zukauskas and Ambrazyavichyus [10], however, this effect may be neglected in the case of a ***turbulent*** boundary layer if $Nu_{l,turb}$ and Re_l in Eq. (8) are calculated with the heated length l_0 and if the ratio l_0/l is between 1 and 0.1.

(e) Effect of the direction of heat flux

The direction of heat flux-that is, heating or cooling the plate-affects the heat transfer in case of temperature-dependent fluid properties. For liquids this effect can be taken into account, according to Zukauskas and Ambrazyavichyus [IO], by introducing a factor

$$K = K_l = \left(\frac{Pr}{Pr_w}\right)^{0.25} \quad (11)$$

Pr and Pr_w are the Prandtl numbers of the liquid at bulk temperature and at wall temperature, respectively.

© 1983 Hemisphere Publishing Corporation

For gases this effect may be allowed for, according to Churchill and Brier [1 1] , by using the factor

$$K = K_g = \left(\frac{T_b}{T_w}\right)^{0.12} \tag{12}$$

T_b and T_w are the absolute temperatures of the gas in the bulk of the flow and of the wall of the plate, respectively. As K is introduced in Eq. (9), the consideration of the direction of the heat flux gives

$$\mathrm{Nu}_l = K\,\mathrm{Nu}_{l,0} \tag{13}$$

(f) Comparison with experimental data

The comparison of Eq. (9) with the data of a number of investigators [1,12-18] who measured heat and mass transfer coefficients for flat plates in tangential flow of air and liquids is shown in Fig. 1. Because of the analogy between heat and mass transfer, Sherwood numbers Sh_l resulting from mass transfer experiments can also be used to test Eq. (9).

In the transition region between laminar and turbulent boundary layer, the data of Žukauskas and Ziugzda [17] and Žukauskas and Slanciauskas [18] show the influence of a low degree of turbulence in the main fluid stream. The mass transfer data of Presser [19] in Figs. 2 and 3 verify Eq. (9) in correlating the data in the case of a blunt leading edge.

B. Single bodies of various shapes

Gnielinski [8] has shown that the Nusselt numbers for single bodies of various shapes, such as cylinders, wires, or spheres, can be calculated from the same correlation as that for a flat plate if the characteristic length used in the calculation of the Reynolds and Nusselt numbers is the streamed length proposed by Krischer

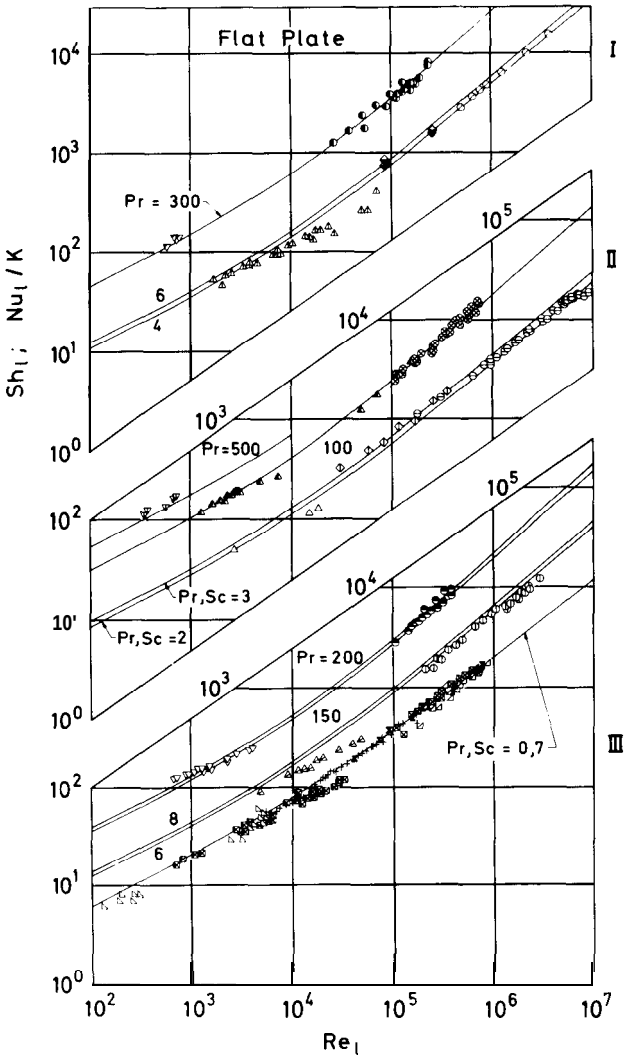

Author	Pr, SC	Part
Jürges [12]	0.7	III
Elias [13]	0.7	III
Edwards and Furber [14]	0.7	III
Loos [15]	0.7	III
Presser [1]	2.5	II
Lemmert [16]	4.2-4.4	I
iukauskas and Ziugzda [171	0.7	III
Žukauskas and Ziugzda [17]	2.9-3.0	I
Žukauskas and Ziugzda [171	4.3-5.4	I
iukauskas and Ziugzda [171	7-6.5	III
Žukauskas and Ziugzda [171	99-107	II
iukauskas and Ziugzda [171	170-180	III
iukauskas and Ziugzda [171	300-400	I
iukauskas and Ziugzda [17]	490-510	II
Žukauskas and Slanciauskas [18]	0.7	III
Žukauskas and Slanciauskas [18]	2.0-3.0	II
Žukauskas and Slanciauskas [18]	5.5-5.7	I
Žukauskas and Slanciauskas [18]	6-7.6	III
iukauskas and Slanciauskas [181	99-105	II
Žukauskas and Slanciauskas [18]	160-176	III
Žukauskas and Slanciauskas [18]	280-320	I

Figure 1 Comparison of Eq. (9) with the data of several authors.

© 1983 Hemisphere Publishing Corporation

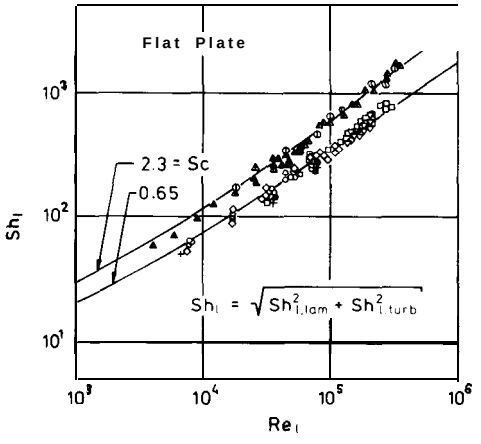

Figure 2 Comparison of Eq. (9) with the data of Presser [19] from a plate with a stumbling leading edge.

[7] . The streamed length I is defined by Pasternak and Gauvin [20] as the total surface area A of the body divided by the maximum perimeter ***1,*** perpendicular to the flow:

$$l = \frac{A}{l_c} \tag{14}$$

Since a minimum value of the Nusselt number exists for any body of three dimensions when the Reynolds number goes to zero, Eq. (9) should be written:

$$Nu_{l,0} = Nu_{l,min} + \sqrt{Nu^2_{l,lam} + Nu^2_{l,turb}} \tag{15}$$

where

$$Nu_{l,lam} = 0.664 \sqrt{Re_l} \sqrt[3]{Pr_l} \tag{2}$$

and

$$Nu_{l,turb} = \frac{0.037\ Re_l^{0.8}\ Pr}{1 + 2.443\, Re_l^{-0.1}(Pr^{2/3} - 1)} \tag{8}$$

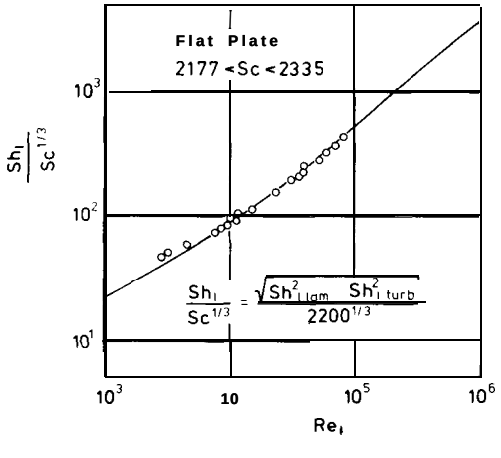

Figure 3 Comparison of Eq. (9) with the data of Presser [19] from a plate with a stumbling leading edge.

(a) Wires, cylinders, tubes of various profiles

I. Combined correlation

The streamed length l is shown in Fig. 4. For the long cylinder one gets according to Eq. (14)

$$l = \frac{A}{l_c} = \frac{\pi dL/2}{L} = \frac{\pi}{2} d \tag{16}$$

The value of $Nu_{l,min}$ for long but finite cylinders is approximately $Nu_{l,min} = 0.3$. The expression for the cylinder becomes

$$Nu_{l,0} = 0.3 + \sqrt{Nu^2_{l,lam} + Nu^2_{l,turb}} \tag{17}$$

$Nu_{l,lam}$ has to be calculated from Eq. (2) and $Nu_{l,turb}$ from Eq. (8). Equation (17) is recommended for $1 < Re_l < 10$ and $0.6 < Pr < 10^3$. In the region of very low Reynolds numbers ($Re_l < 1$), Eq. (2) cannot be used since the thickness of the boundary layer is not small when compared with the dimension of the object. In this region of Stokes flow it is recommended that the following equation be used:

$$Nu_{l,0} = 0.75 \sqrt[3]{Re_l\, Pr} \tag{18}$$

II. Cylinder in a restricted channel

According to Žukauskas [21], the characteristic velocity of the flow for a tube in cross flow in a restricted channel is the average velocity evaluated by integrating the velocity over the channel cross section. This is equal to the velocity in the empty cross section of the channel divided by the void fraction of the channel at the position of the cylinder:

$$u = \frac{u_0}{\psi} \tag{19}$$

wherein ψ is-the void fraction at the location of the cylinder. If the channel has the height l_h, one gets

$$\psi = \left(1 - \frac{\pi d}{4 l_h}\right) \tag{20}$$

III. Effect of an inclined flow to the cylinder

If the flow is inclined to the axis of the cylinder, Nu_l becomes smaller with decreasing angle φ as shown in the following table given by Vornehm [22]:

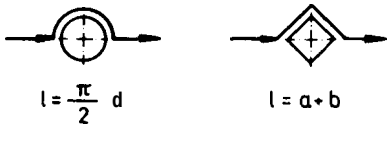

Figure 4 Definition of the streamed length l.

© 1983 Hemisphere Publishing Corporation

ϑ	90	80	70	60	50°	40	30	20
$Nu_{l,\varphi}/Nu_l$	1.0	1.0	0.99	0.95	0.86	0.75	0.63	0.50

IV. Comparison with experimental data

Figures 5 and 6 show a comparison of Eq. (17) with the data of a number of investigators [23-35] who collected or measured heat and mass transfer coefficients for single circular cylinders in cross flow of air and liquids. The data of several authors in the region $5 \times 10^4 < Re_l < 10^6$ show the effect of a low degree of turbulence. To demonstrate this effect, assembled in Fig. 7 are the data of Dyban et al. [32] and of Galloway and Sage [33], who measured heat transfer coefficients for cylinders in air having varying degrees of turbulence Tu in the flow. Equation (17) represents the data with Tu = 6-10%, which should be the degree of turbulence in a technical apparatus. As can be seen from Fig. 8, the roughness of the surface of the cylinder causes a similar effect on the heat transfer coefficients in the transition regime and in the regime of fully developed turbulent flow.

(b) Spheres

I. Combined correlation

The streamed length l of a single sphere calculated from Eq. (14) is

$$l = \frac{\pi d^2}{\pi d} = d \tag{21}$$

The value of $Nu_{l,min}$ for the single sphere is

$$Nu_{l,min} = 2$$

Then one gets, according to Eq. (15),

$$Nu_{l,0} = 2 + \sqrt{Nu^2_{l,lam} + Nu^2_{l\,turb}} \tag{22}$$

$Nu_{l,lam}$ has to be calculated from Eq. (2) and $Nu_{l,turb}$ from Eq. (8). Equation (22) is recommended for $1 < Re_l < 10^5$ and $0.6 < Pr < 10^5$.

In the region of very low Reynolds numbers ($Re_l < 1$), Eq. (2) cannot be used because the thickness of the boundary layer is not small compared to the diameter of the sphere. In this region of Stokes flow one gets for the sphere

$$Nu_{l,0} = 1.01 \sqrt[3]{Re_l\,Pr} \tag{23}$$

II. Sphere in a restricted channel

According to Kast et al. [36] and Vliet and Leppert [37], the characteristic velocity of the flow for a sphere in a restricted channel is the velocity in the empty cross section of the channel u_0 divided by the void fraction of the channel at the position of the sphere:

$$u = \frac{u_0}{\psi} \tag{19}$$

where ψ is the void fraction at the location of the sphere. If the channel has diameter D, one gets

$$\psi = \left(1 - \frac{2d^2}{3D^3}\right) \tag{24}$$

III. Comparison with experimental data

Comparison of Eq. (22) with the data of a number of investigators [37-43] who measured heat and mass transfer coefficients for a single sphere in cross flow of

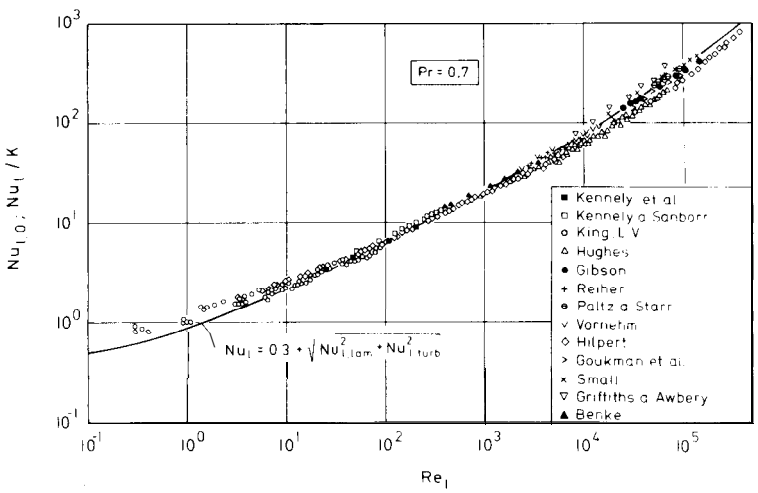

Figure 5 Comparison of Eq. (17) with data of several authors for cylinder in cross flow as collected by McAdams[23]. Symbols according to McAdams[23].

©1983 Hemisphere Publishing Corporation

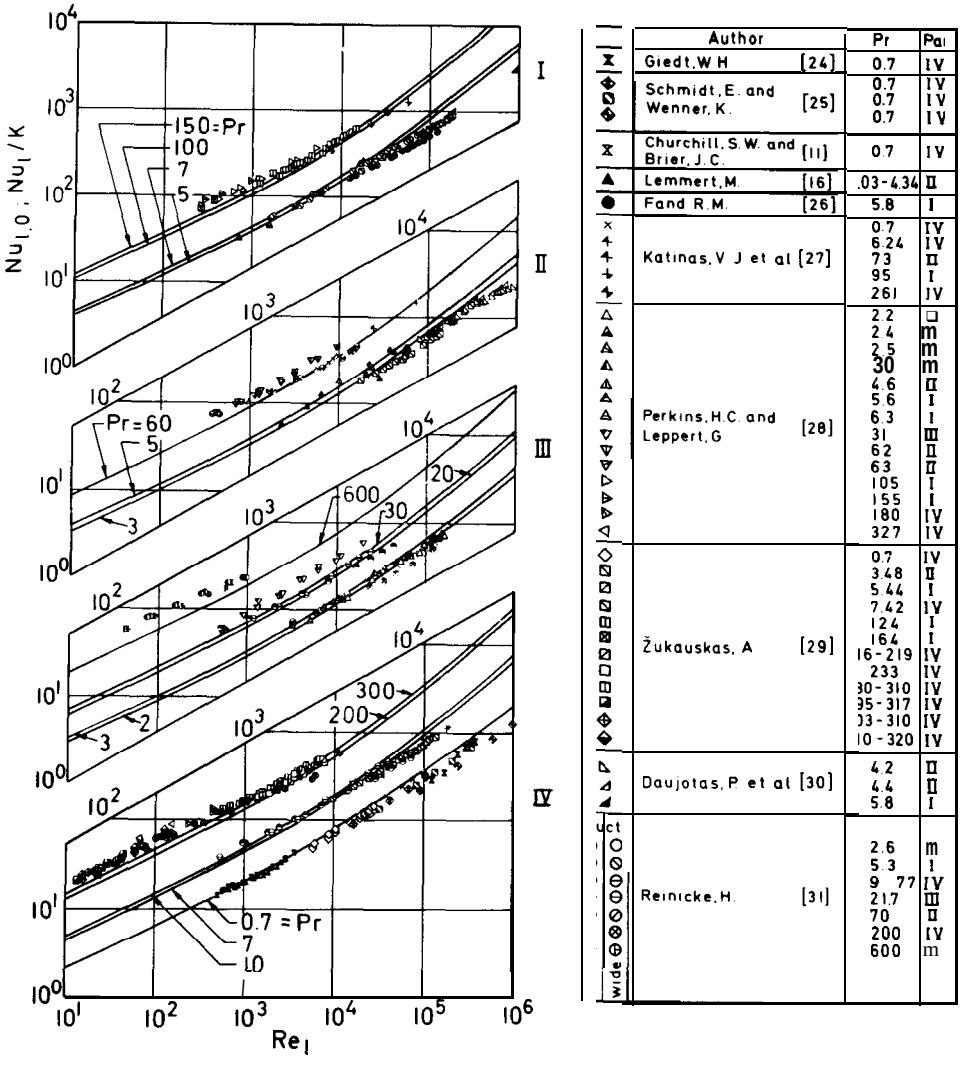

Figure 6 Comparison of Eq. (17) with the data of several authors for cylinder in cross flow.

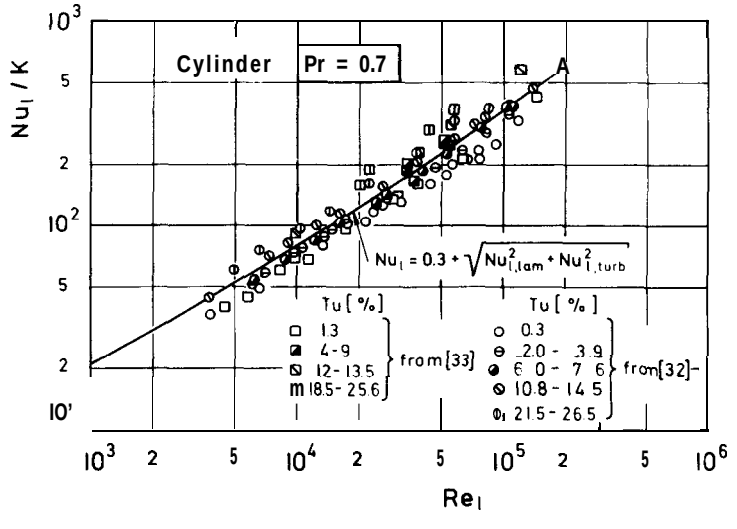

Figure 7 Effect of the degree of turbulence on the heat transfer coefficient of cylinders in cross flow of air.

© 1983 Hemisphere Publishing Corporation

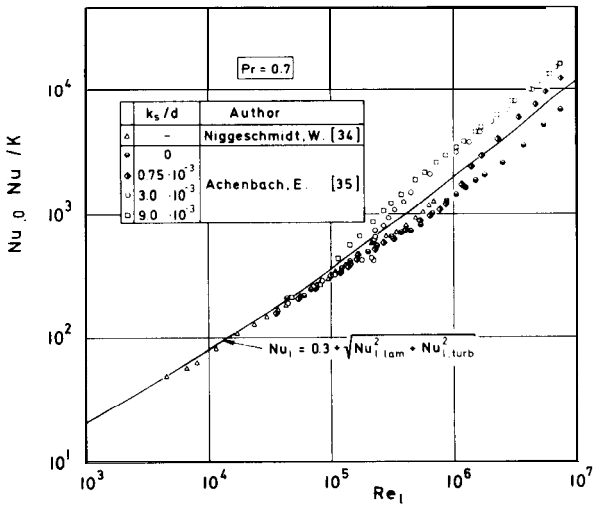

Figure8 Effect of the surface roughness on the heat transfer from a cylinder to the cross flow of air.

air and liquids is shown in Fig. 9. The data of several authors in the region $5 \times 10^4 < Re_l < 10^5$ show the **effect of a low degree of turbulence. Figure 10 shows** the data of Lavender and Pei [39], who measured the heat transfer coefficients of spheres and air varying the degree of turbulence.

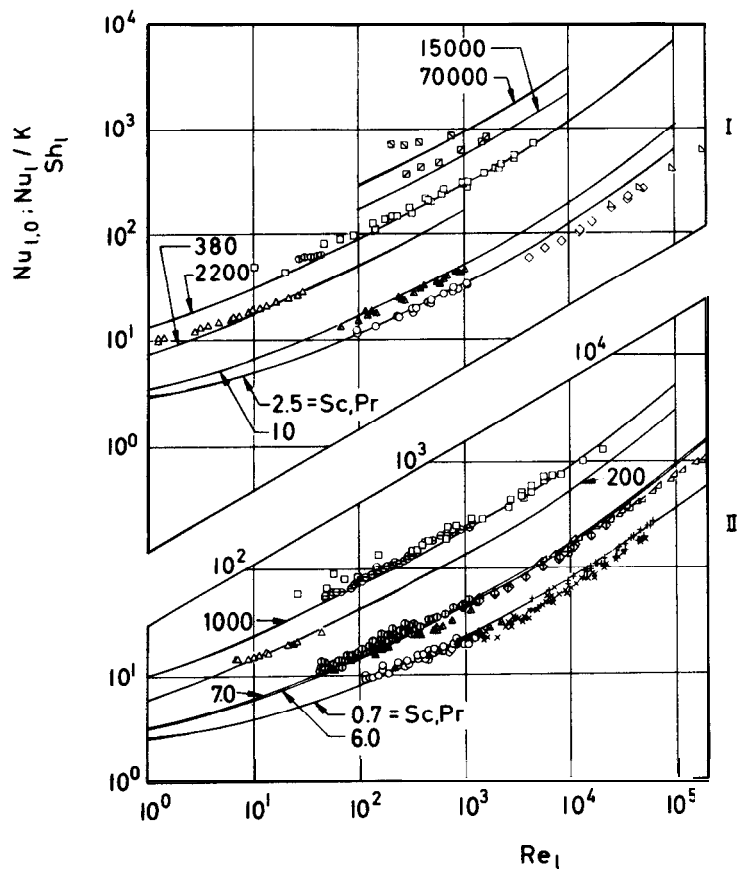

	Author		Pr, Sc	Part
×	Börner, H.	[38]	0.7	II
+	Lavender, W.J. and Pei, D.C.	[39]	0.7	II
○	Rowe, P. N. Claxton, K.T and Lewis, J. B.	[40]	2.55	I
○			2000-2700	I
○			0.7	II
○			6.2-7.3	II
○			1200-1260	II
△	Brown, W.S.	[41]	2.13	I
△			6.74	II
◇	Vliet, G C. and Leppert G	[37]	2.7	I
◇			6.7-7.2	II
△	Kramers, H.	[42]	380	I
△			10.7	I
△			Ii.6	II
△			7.87	II
△			213	II
△			7.3	II
□	Steinberger, R.L. and Treybal, R.E.	[43]	2200	I
□			14970	I
□			69680	I
□			987	II

Figure 9 Comparison of Eq. **(22) with the data of severd authors for a sphere.**

© 1983 Hemisphere Publishing Corporation

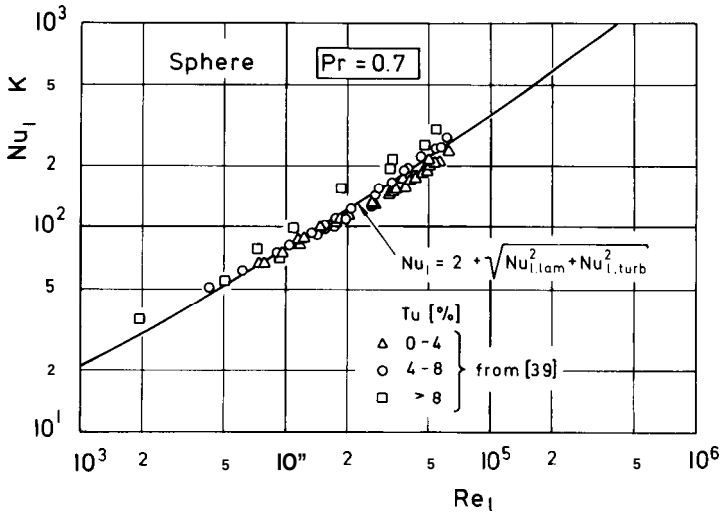

Figure 10 Effect of the degree of turbulence on the heat transfer coefficient of a sphere.

Nomenclature for Section 2.5.2 appears at the beginning of Part 2.

REFERENCES FOR SECTION 2.5.2

1. Presser, K. H., Experimentelle Prüfung der Analogie zwischen konvektiver Wärme- und Stoffiibertragung bei nichtabgeliister Striimung, *Wärme Stoffübertrag.*, vol. 1, pp. 225-235, 1968.
2. Pohlhausen, E., Der Warmeaustausch zwischen festen Körpern und Fliissigkeiten mit kleiner Reibung und kleiner Wärmeleitung, Z. *Angew. Math Mech.*, vol. 1, pp. 115-121, 1921.
3. Kroujiline, G., Investigation de la Couche-limite Thermique, ***Tech. Phys. USSR,*** vol. 3, p. 311, 1936.
4. Gauler, K., Wärme- und Stofftibertragung an eine mitbewegte ebene Grenzfläche bei Grenzschichtströmung, Dr.-Ing., University of Karlsruhe, 1972.
5. Petukhov, B. S., and Popov, V. N., Theoretical Calculation of Heat Exchange and Frictional Resistance in Turbulent Flow in Tubes of an Incompressible Fluid with Variable Physical Properties, ***High Temp. Thermophys,*** vol. 1, pp. 69-83, 1963.
6. Schlichting, H., *Grenzschicht-Theorie*, 3d ed., G. Braun, Karlsruhe, 1958.
7. Krischer, ***O., Die wissenschaftlichen Grundlagen der Trocknungstechnik,*** vol. 1, Springer-Verlag, Berlin, 1956.
8. Gnielinski, V., Berechnung mittlerer Wärme- und Stofftibergangskoeffizienten an laminar und turbulent überströmten Einzelkörpern mit Hilfe einer einheitlichen Gleichung, *Forsch. Zngenieurwes,* vol. 41, pp. 145-153, 1975.
9. Brauer, H., ***Stoffaustausch einschliesslich chemischer Reaktionen,*** Verlag Sauerländer, Frankfurt/Main, 1971.
10. Žukauskas, A., and Ambrazyavichyus, A. B., Heat Transfer of a Plate in a Liquid Flow, *Int. J. Heat Mass Transfer,* vol. 3, pp. 305-309, 1961.
11. Churchill, S. W., and Brier, J. C., Convective Heat Transfer from a Gas Stream at High Temperature to a Circular Cylinder Normal to the Flow, ***Chem. Eng. Frog. Symp. Ser.,*** vol. 5 1, no. 17, pp. 57-65, 1955.
12. Jürges, W., Der Wärmeübergang an einer ebenen Wand, *Beih. Zentralbl. Gesundh. Ing.,* Series 1, no. 19, 1924.
13. Elias, F., Wärmeübertragung einer geheizten Platte an strömende Luft, Z. ***Angew. Math. Mech.***, vol. 10, pp. 1-14, 1930.
14. Edwards, A., and Furber, B. N., The Influence of Free-Stream Turbulence on Heat Transfer by Convection from an Isolated Region of a Plane Surface in Parallel Air Flow, *Proc. Inst. Mech. Eng. London,* vol. 170, pp. 941-954, 1956.
15. Loos, G., Beitrag zur Frage des Wärme- und Stoffaustausches bei erzwungener Striimung an Körpern verschiedener Form, Dr.-Ing., Technische Hochschule Darmstadt, 1957.
16. Lemmert, M., Einfluss der Strömungsgeschwindigkeit auf den Wärmeübergang beim Blasensieden an einzelüberströmten Körpern, Dr.-Ing., University of Karlsruhe, 1975.
17. Žukauskas, A., and Ziugzda, J., Heat Transfer in Laminar Flow of Fluid, ***in Thermophysics,*** vol. 2, Academy of Science of Lithuanian SSR, Vilnius, 1969.
18. Žukauskas, A., and Slanciauskas, A., Heat Transfer in Turbulent Flow of Fluid, in ***Thermophysics,*** vol. 5, Academy of Science of Lithuanian SSR, Vilnius, 1973.
19. Presser, K. H., Stofftibertragung an der längsangeströmten ebenen Platte im Kanal bei Schmidt-Zahlen von 2000, 2 und 0.7. *Wärme Stoffübertrag.*, vol. 5, pp. 153-167, 1972.
20. Pastemak, I. S., and Gauvin, W. H., Turbulent Heat and Mass Transfer from Stationary Particles, ***Can J. Chem. Eng.,*** vol. 38, pp. 35-42, 1960.
21. Žukauskas, A., Heat Transfer from Tubes in Cross Flow, ***Adv. Heat Transfer,*** vol. 8, pp. 93-160, 1972.
22. Vornehm, L., Einfluss der Anströmrichtung auf den Wärmeübergang, Z. ***Ver. Dtsch. Int.,*** vol. 80, pp. 702-703, 1936.
23. McAdams, W., ***Heat Transmission,*** 3d ed, McGraw-Hill Series in Chemical Engineering, McGraw-Hill, New York, 1959.

© 1983 Hemisphere Publishing Corporation

24. Giedt, W. H., Investigation of Variation of Point Unit Heat Transfer Coefficient Around a Cylinder Normal to an Air Stream, *J. Heat Transfer,* vol. 71, pp. 375-381, 1949.
25. Schmidt, E., and Wenner, K., Wärmeabgabe über den Umfang eines angeblasenen geheizten Zylinders, *Forsch. Ingenieurwes.*, vol. 12, pp. 65-73, 1941.
26. Fand, R. M., Heat Transfer by Forced Convection from a Cylinder to Water in *Cross* Flow, *Int. J. Heat Mass Transfer,* vol. 8, pp. 995-1010, 1965.
27. Katinas, V. J., Ziugzda, J., and Žukauskas, A., The Investigation of Heat Transfer for Viscous Flow Past Curved Lined Bodies, *Liet. TSR Mokslu Akad. Darb,, Ser. B.,* vol. 4, no. 63, pp. 209-233, 1970.
28. Perkins, H. C., and Leppert, G., Forced Convection Heat Transfer from a Uniformly Heated Cylinder, *J. Heat Transfer, vol. 84,* pp. 257-263, 1962.
29. Žukauskas, A., Heat Transfer of Cylinders in Cross-Flow, Heat Transfer and Heat Simulation, *Izv. Acad. Nauk USSR,* pp. 201-212, 1959.
30. Daujotas, P., Ziugzda, J., and Žukauskas, A., Heat Transfer of a Single Cylinder in Cross Flow of Water at Critical Re, *Liet. TSR Mokslu Akad Darb., Ser. B,* vol. 3, no. 76, pp. 99-109, 1973.
31. Reinicke, H., Über den Wärmeübergang von kurzen durchströmten Rohren und querangeströmten Zylindern verschiedener Anordnung an zähe Fliissigkeiten verschiedener Prandtl-Zahlen bei kleinen Temperaturdifferenzen, Dr.-Ing., Technische Hochschule Darmstadt, 1969.
32. Dyban, E. P., Epick, E. Y., and Kozlova, L. G., Combined Influence of Turbulence Intensity and Longitudinal Scale and Air Flow Acceleration on Heat Transfer of Circular Cylinder, Jpn. Soc. Mech. Eng, 5th Int. Heat Transfer Conf., Tokyo, Paper FC 8.4, 1974.
33. Galloway, T. R., and Sage, B. H., Local and Macroscopic Transport from a 1.5 in Cylinder in a Turbulent Air Stream, *AIChE J.*, vol. 13, pp. 563-570, 1967.
34. Niggeschmidt, W., Druckverlust und Wärmeübergang bei fluchtenden, versetzten und teilversetzten querangestrijmten Rohrbündeln, Dr.-Ing., Technische Hochschule Darmstadt, 1975.
35. Achenbach, E., The Effect of Surface Roughness on the Heat Transfer from a Circular Cylinder to the Cross Flow of Air, *Int. J. Heat Mass Transfer,* vol. 20, pp. 359-369, 1971.
36. Kast, W., Krischer, O., Reinicke, H., and Wintermantel, K., *Konvektive Wärme- und Stoffübertragung*, Springer-Verlag, Berlin, 1974.
37. Vliet, G. C., and Leppert, G., Forced Convection Heat Transfer from an Isothermal Sphere to Water, *J. Heat Transfer,* vol. 83, pp. 163-175, 1961.
38. Börner, H., Über den Wärme- und Stoffaustausch an umspiilten Einzelkorpern bei Uberlagerung von freier und erzwungener Strömung, Dr.-Ing., Technische Hochschule Darmstadt, 1964.
39. Lavender, W. J., and Pei, D. C. T., The Effect of Fluid Turbulence on the Rate of Heat Transfer from Spheres, *Int. J. Heat Mass Transfer,* vol. 10, pp. 5 29-539, 1967.
40. Rowe, P. N., Claxton, K. T., and Lewis, J. B., Heat and Mass Transfer from a Single Sphere in an Extensive Flowing Fluid, *Trans. Inst. Chem. Eng.,* vol. 43, pp. T14-T31, 1965.
41. Brown, W. S., Forced Convection Heat Transfer from a Uniformly Heated Sphere to Water, Ph.D. thesis, Stanford University. Stanford, Calif., 1960.
42. Kramers, H., Heat Transfer from Spheres to Flowing Media, *Physica*, vol. 12, pp. 61-81, 1946.
43. Steinberger, R. L., and Treybal, R. E., Mass Transfer from a Solid Soluble Sphere to a Flowing Liquid Stream, *AIChE J.*, vol. 6, pp. 227-232, 1960.

© 1983 Hemisphere Publishing Corporation

2.5.3

Banks of plain and finned tubes

V. Gnielinski, A. Žukauskas, and A. Skrinska

A. Single rows and tube banks in cross flow

(a) Definition of heat transfer coefficient

The average heat transfer coefficient α of a single row of tubes or a tube bank is defined by

$$\dot{q} = \alpha \, \Delta T_{LM} \tag{1}$$

in which the logarithmic mean temperature difference ΔT_{LM} is

$$\Delta T_{LM} = \frac{T_{out} - T_{in}}{\ln [(T_w - T_{in})/(T_w - T_{out})]} \tag{2}$$

(b) Heat transfer coefficient of a single row of tubes

The average Nusselt number of a single row of smooth tubes in cross flow can be calculated using Eq. 2.5.2(15) for the Nusselt number for a single tube in cross flow, but with the Reynolds number defined as

$$\mathrm{Re}_{\psi,L} = \frac{wL}{\psi \nu} \tag{3}$$

where w is the velocity of the fluid in the empty cross section of the channel.

The characteristic velocity w/ψ is the average velocity in the space between two adjacent tubes in the row. The void fraction ψ depends only on the dimensionless transverse pitch a = s_1/d, Fig. 1, and is defined as

$$\psi \equiv 1 - \frac{\pi}{4a} \tag{4}$$

The characteristic length ***L,*** which is defined by $d\pi/2$, is the stream length of a single tube. The fluid properties are evaluated at the average temperature of the fluid,

$$T_b = \frac{Tin + Tout}{2} \tag{5}$$

From Eq. 2.5.2(15) $\mathrm{Nu}_{0,\mathrm{row}}$ is given by

$$\mathrm{Nu}_{0,\mathrm{row}} = 0.3 + \sqrt{\mathrm{Nu}^2_{L,\mathrm{lam}} + \mathrm{Nu}^2_{L,\mathrm{turb}}} \tag{6}$$

where

$$\mathrm{Nu}_{L,\mathrm{lam}} = 0.664 \sqrt{\mathrm{Re}_{\psi,L}} \, \mathrm{Pr}^{1/3} \tag{7}$$

$$\mathrm{Nu}_{L,\mathrm{turb}} = \frac{0.037 \, \mathrm{Re}^{0.8}_{\psi,L} \, \mathrm{Pr}}{1 + 2.443 \, \mathrm{Re}^{-0.1}_{\psi,L} (\mathrm{Pr}^{2/3} - 1)} \tag{8}$$

The Nusselt number is defined by

$$\mathrm{Nu}_{L,\mathrm{row}} = \frac{\alpha L}{\lambda} \tag{9}$$

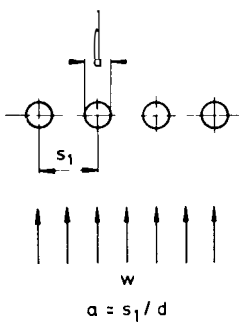

Figure 1 Tube arrangement of a single row.

© 1983 Hemisphere Publishing Corporation

where

$$Nu_{L,row} = Nu_{0,row} K \quad (10)$$

K takes into account the temperature dependence of the fluid properties as described in Sec. (c)II.

These expressions are valid in the following range :

$$10 < Re_{\psi,L} < 10^5$$
$$0.6 < Pr < 10^3 \quad (11)$$

In the region $10^4 < Re_{\psi,L} < 10^6$, the Nusselt numbers may be as much as 40% lower than those given by Eq. (6). This discrepancy is caused by the low degree of turbulence of the fluid, which results from flow acceleration at the entrance of the row or from calming sections in the channel upstream of the tube row.

(c) Heat transfer coefficient of tube banks

The average Nusselt number for banks of smooth tubes in cross flow can be calculated from the average Nusselt number for a single tube row [1] . However, at the same fluid velocity the Nusselt number for a tube row in a tube bank is greater than that of a single tube row and depends on the transverse and longitudinal pitch of the bank. For a tube bank with 10 or more rows of tubes,

$$Nu_{0,bank} = f_A Nu_{0,row} \quad (12)$$

where $Nu_{0,row}$ is given by Eq. (6) and $Nu_{0,bank}$ is defined as

$$Nu_{0,bank} = \frac{\alpha L}{\lambda} \quad (13)$$

The characteristic fluid velocity used to calculate $Re_{\psi,L}$ is again the average velocity in the void fraction of one row in the tube bank at the length of one tube diameter. The void fraction ψ and the arrangement factor f_A depend on the dimensionless transverse pitch $a = s_1/d$ and on the dimensionless longitudinal pitch $b = s_2/d$ of the tube bank. The dimensionless pitches a and b of in-line and regularly staggered tube banks are shown in Fig. 2. The void fraction is

$$\psi = 1 - \frac{\pi}{4a} \quad \text{if } b \geq 1 \quad (14)$$

$$\psi = 1 - \frac{\pi}{4ab} \quad \text{if } b < 1 \quad (15)$$

The arrangement factor f_A for an in-line tube bank is

$$f_{A,\text{in-line}} = 1 + \frac{0.7}{\psi^{1.5}} \frac{b/a - 0.3}{(b/a + 0.7)^2} \quad (16)$$

and for a staggered tube bank,

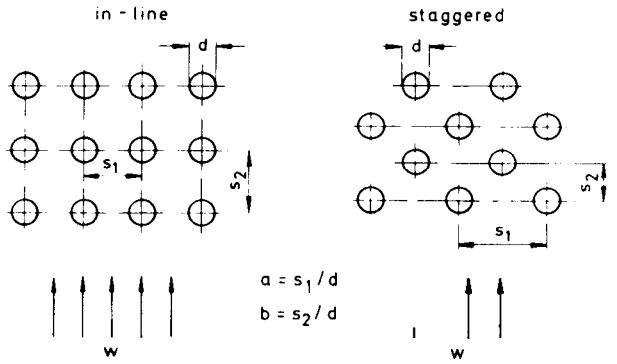

Figure 2 Tube arrangement of in-line and staggered banks.

$$f_{A,stag} = 1 + \frac{2}{3b} \quad (17)$$

Figure 3 shows how $f_{A,\text{in-line}}$ depends on a and b, and Fig. 4 shows how $f_{A,stag}$ depends on b.

The arrangement of partly staggered tube banks and the pitch $c = s_3/d$ are shown in Fig. 5. The arrangement factor f_A for partly staggered tube banks is given by

$$f_{A,\text{ partly stag}} = f_{A,\text{in-line}} \quad \text{if } c < \tfrac{1}{4}a \quad (18)$$

$$f_{A,\text{partly stag}} = f_{A,stag} \quad \text{if } c \geq \tfrac{1}{4}a \quad (19)$$

I. Effect of the number of tube rows

The heat transfer coefficient increases from the first to about the fifth row of a tube bank and remains the same in the following tube rows. In calculating the average Nusselt number of a bank of 10 or more tube rows, the lower heat transfer coefficient of the first tube rows need not be considered. For tube banks containing fewer than 10 tube rows, this effect should be taken into account, as shown by the following equation:

$$Nu_{0,bank} = \frac{1 + (n-1)f_A}{n} Nu_{0,row} \quad (20)$$

where n is the number of tube rows.

II. Effect of the direction of heat flux

The direction of heat flux, that is, whether heating or cooling the fluid, affects the heat transfer in the case of temperature-dependent fluid properties for a tube bank in the same way as for a single row of tubes; see Eq. (10). According to Žukauskas and Ambrazyavičius [2] and Petukhov [3], this effect can be taken into account for liquids by putting

© 1983 Hemisphere Publishing corporation

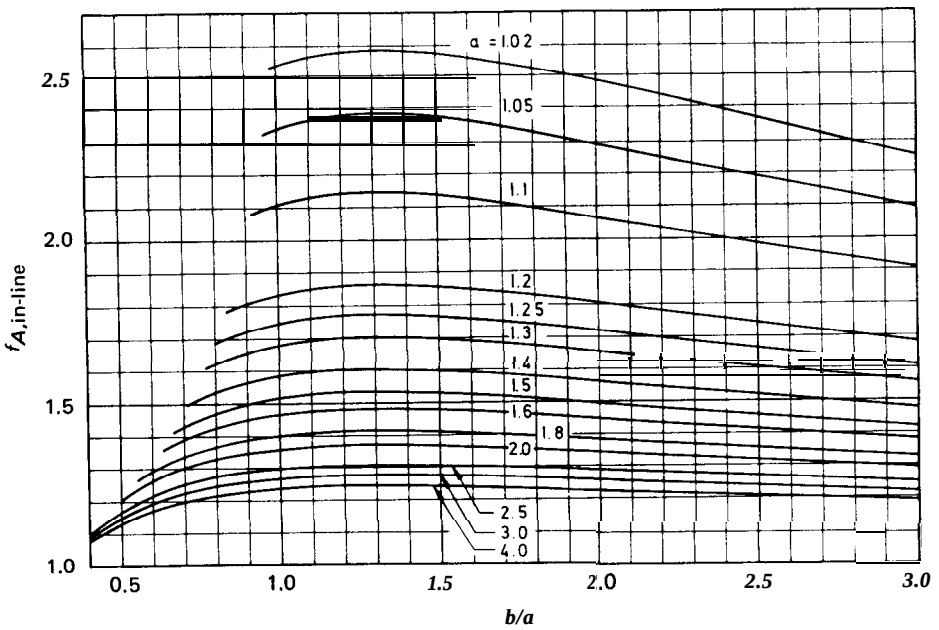

Figure 3 Arrangement factor $f_{A,\text{in-line}}$ versus b/a for an in-line tube bank.

$$K = K_L = \left(\frac{\text{Pr}}{\text{Pr}_w}\right)^{0.25}$$

$$\text{if } \frac{\text{Pr}}{\text{Pr}_w} > 1 \text{ (heating of the liquid)} \tag{21}$$

$$K = K_L = \left(\frac{\text{Pr}}{\text{Pr}_w}\right)^{0.11}$$

$$\text{if } \frac{\text{Pr}}{\text{Pr}_w} < 1 \text{ (cooling of the liquid)} \tag{22}$$

Pr is the Prandtl number at temperature T_b, Eq. (5), and Pr, the Prandtl number at wall temperature T_w.

For gases this effect may be accounted for, according to Churchill and Brier [4], by using the factor

$$K = K_G = \left(\frac{T_b}{T_w}\right)^{0.12} \tag{23}$$

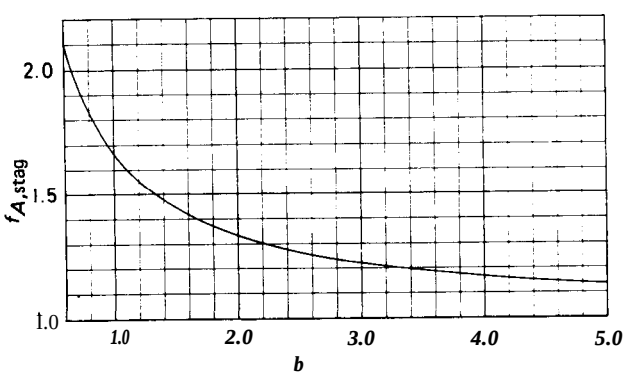

Figure 4 Arrangement factor $f_{A,\text{stag}}$ versus b for a staggered tube bank.

(d) Comparison with experimental data

I. Single row of tubes

In Fig. 6 Eq. (6) is compared with experimental data for heat transfer coefficients for single rows of tubes or for the first row of a tube bank [5-10]. In the region $10^3 < \text{Re}_{\psi,L} < 5 \times 10^4$, nearly all experimental data agree very well with the calculated Nusselt numbers. In the transition region at $\text{Re}_{\psi,L} > 5 \times 10^4$, the degree of turbulence of the fluid affects the heat transfer coefficient. Because these data were obtained in equipment having a low degree of turbulence, the experimental data deviate from Eq. (6) in the transition region by as much as -40%.

II. Tube banks

In Figs. 7 through 10 Eq. (6) is compared with experimental data obtained for in-line, staggered, and partly staggered tube banks with a cross flow of gases and liquids.

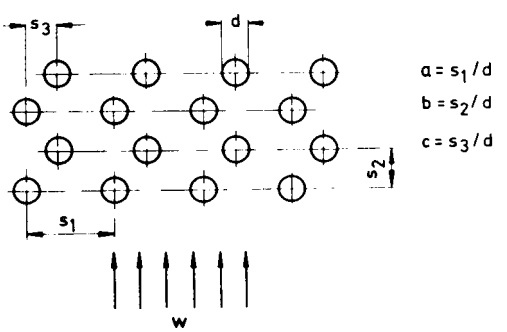

Figure 5 Arrangement of a partly staggered tube bank.

© 1983 Hemisphere I blishing Corporation

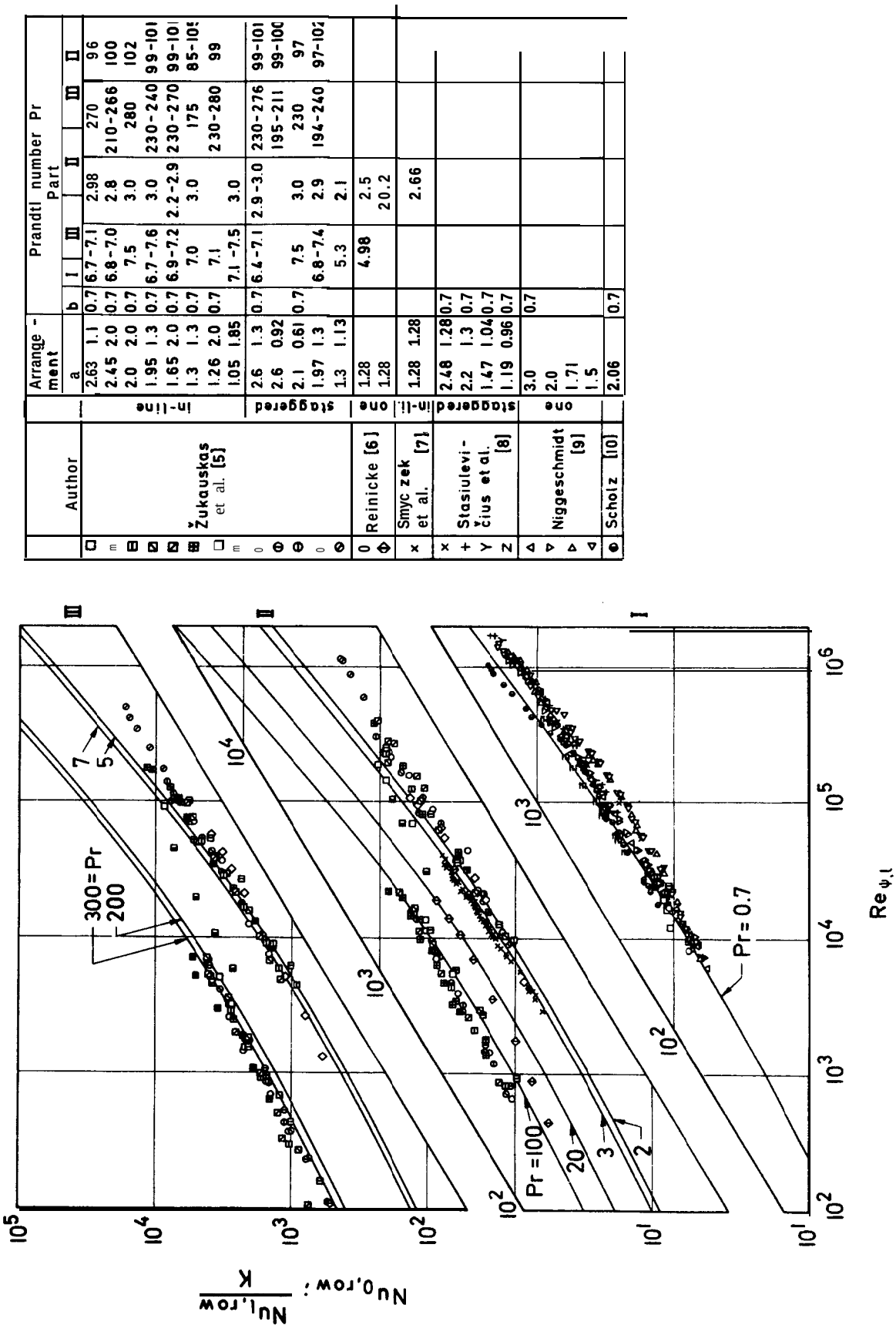

Figure 6 Heat transfer coefficients for fluid flow across a single row of tubes or for the first row of tube banks.

© 1983 Hemisphere Publishing Corporation

2.5.4
Fixed beds

V. Gnielinski

A. Introduction

Heat transfer coefficients between particles and fluid in packed beds are one of the basic pieces of information needed for unit operations and chemical reactor design. Heat transfer is of interest, for example, in chemical reactors with fixed beds of catalysts in which large amounts of heat are absorbed or released, or in fixed beds employed as regenerative heat exchangers. Particles of very different shapes, such as spheres, cylinders, Raschig rings, or Berl saddles, are used as packing material. Because of its great importance, many papers in the literature deal with this problem. Review papers [1, 2] show that there are great differences in the correlating equations. This chapter deals only with packings of spheres of equal size.

B. The calculation process

The measurements of Gillespie et al. [3] show that the Nusselt number during flow in a packing increases markedly in the first two layers of spheres, and finally reaches a fixed value. Ranz [4] found that the Nusselt numbers measured in packings are significantly larger than for single spheres at the same approach velocity, and that they fall along a line parallel to that for single spheres when plotted against the Reynolds number.

From these findings, the mean Nusselt numbers for flow through stationary spherical packings with any void fraction can be calculated [5] from the equation

$$\mathrm{Nu} = f_\psi \, \mathrm{Nu}_{\text{single sphere}} \tag{1}$$

The expression for $\mathrm{Nu}_{\text{single sphere}}$ is given by Eq. 2.5.2(21):

$$\mathrm{Nu}_{\text{single sphere}} = 2 + \sqrt{\mathrm{Nu}_{\text{lam}}^2 + \mathrm{Nu}_{\text{turb}}^2} \tag{2}$$

where

$$\mathrm{Nu}_{\text{lam}} = 0.664 \sqrt{\mathrm{Re}_\psi} \sqrt[3]{\mathrm{Pr}} \tag{3}$$

$$\mathrm{Nu}_{\text{turb}} = \frac{0.037 \, \mathrm{Re}_\psi^{0.8} \, \mathrm{Pr}}{1 + 2.443 \, \mathrm{Re}_\psi^{-0.1} (\mathrm{Pr}^{2/3} - 1)} \tag{4}$$

In these equations, $\mathrm{Nu} = \alpha d/\lambda$ denotes the Nusselt number, $\mathrm{Re}_\psi = w_{\text{free}} d/(\nu\psi)$ the Reynolds number, and $\mathrm{Pr} = \nu/\kappa$ the Prandtl number, where d is the diameter of the sphere and w_{free} is the velocity of the flowing medium in the empty cross section of the packed vessel.

The thermal conductivity λ, the kinematic viscosity ν, and the thermal diffusivity κ of the flowing medium are determined at the mean temperature.

$$T_m = \frac{T_{\text{in}} + T_{\text{out}}}{2} \tag{5}$$

The heat transfer coefficient α is defined in terms of the heat flux $\dot{q}$ that is being transferred by means of the equation

$$\dot{q} = \alpha \, \Delta T_{,,} \tag{6}$$

where the logarithmic mean temperature difference

$$\Delta T_{,,} = \frac{T_{\text{out}} - T_{\text{in}}}{\ln (T_w - T_{\text{in}})/(T_w - T_{\text{out}})} \tag{7}$$

is defined in terms of the wall temperature T_w of the spheres.

The void fraction ψ of the spherical packing is

© 1983 Hemisphere Publishing Corporation

determined from the total volume V_{total} of the packed vessel and the volume V_s of the spheres contained in it, using the equation

$$\psi = \frac{V_{total} - V_s}{V_{total}} \quad (8)$$

For the shape factor f_ψ, the following expression was found [5]:

$$f_\psi = 1 + 1.5(1-\psi) \quad (9)$$

Equation (9) is applicable for spherical packings of equal particle size with void fractions $0.26 < \psi < 1$.

C. Remarks

In the range of Peclet numbers $Pe = Re_\psi Pr$ below 500 to 1 000, the experimentally obtained particle-to-fluid heat transfer coefficients in packed beds are found to be some orders of magnitude below the values predicted from Eq. (2). A large number of those experimental results are summarized by Kunii and Suzuki [6]. Martin [7] has explained the discrepancy between theory and experiment by a simple model accounting for a non-uniform distribution of the void fraction. The model consists of a packed bed of uniformly sized particles with the average void fraction ψ, where a small part of the total cross-sectional area is assumed to have a larger void fraction. Since the same pressure drop applies to both parts of the bed, the superficial velocity will be much larger in the section with larger void fraction, especially in the range of low Reynolds numbers. Even though in both parts of the packed bed the individual transfer coefficients are taken from Eq. (2), the apparent overall transfer coefficients for the nonuniform system become much lower and show the same characteristic variation with Peclet number and the ratio of particle diameter to bed height as the majority of the experimental data in [6].

D. Comparison with experimental data

Figure 1 shows the reduced measured values of the heat transfer coefficient Nu/f_ψ and the mass transfer coefficient Sh/f_ψ, respectively, plotted against Re_ψ. These values have been presented in the literature by a number of authors. The figure contains the results of heat transfer measurements on heated spheres with onflowing streams of air, N_2, H_2, or CO_2, as well as mass transfer measurements on the evaporation of water from porous spheres into onflowing air. The void fraction ψ of the packings studied varied between 0.26 and 0.935. For comparison with these measured values, Fig. 1 also shows as solid lines the plots of the mean Nusselt or Sherwood numbers for flow past a single sphere at $Pr = Sc = 0.7$ and 0.6, which were calculated from Eq. (2) with $f_\psi = 1$. It can be seen that most of the measured values deviate from the values calculated by Eq. (2) by no more than ±15%.

Figure 2 contains, in addition to a repetition of the measured values shown in Fig. 1, the reduced Sherwood

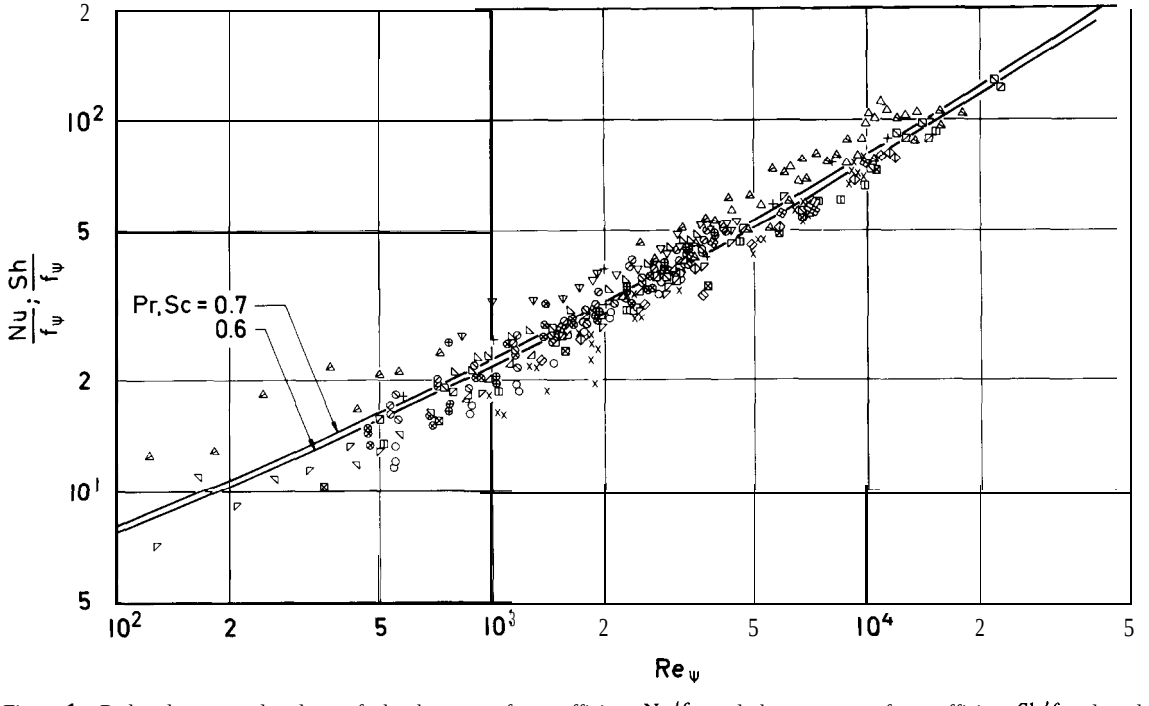

Figure 1 Reduced measured values of the heat transfer coefficient Nu/f_ψ and the mass transfer coefficient Sh/f_ψ plotted against Re_ψ. See Table 1 for explanation of data.

© 1983 Hemisphere Publishing Corporation

Table 1 Data for Figures 1 to 3

Symbol	Authors	Sphere diameter *d*, mm	ψ	Pr; Sc
		Figures 1 and 2, part I		
	Hobson and Thodos [8]	9.4	0.475	0.61
	Gupta and Thodos [9]	15.9	0.444	0.61
		15.9	0.576	0.61
	Rowe and Claxton [10]	38.1	0.26	0.73
		38.1	0.365	0.73
		38.1	0.488	0.73
		38.1	0.632	0.73
		38.1	0.476	0.73
	Glaser and Thodos [11]	7.9	0.453	0.7
	Malling and Thodos [12]	15.9	0.366	0.6
		15.9	0.545	0.6
		15.9	0.788	0.6
		15.9	0.386	0.6
	Gupta [13]	15.9	9.778	0.6
		16.1	0.444	0.6
		15.9	0.576	0.6
+	Thoenes and Kramers [14]	15.0	0.260	0.84
	Glaser [1.5]	12.1	0.42	0.72
		10.3	0.392	0.72
	Jaeschke [16]	22.5	0.668	0.56
		22.5	0.779	0.56
		22.5	0.935	0.56
		22.5	0.476	0.56
×	Bradshaw and Myers [17]	8.7	0.400	0.6
	Gaffney and Drew [18]	12.2	0.519	160
		9.4	0.504	170
		6.3	0.513	160-180
		Figure 2, part II		
	Thoenes and Kramers [14]	15.0	0.260	1.24
		15.0	0.476	1.24
		15.0	0.320	1.24
		15.0	0.480	1.24
		15.0	0.480	1.14
	Gaffney and Drew [18]	12.9	0.504	340-430
		9.5	0.497	420
		9.6	0.5	380
		6.3	0.5 24	370-420
	Venkateswaran and Laddha [19]	10.0	0.47	640-680
		10.0	0.555	670
	Thoenes and Kramers [18]	15.0	0.26	450-605
		Figure 3, part I		
	Thoenes and Kramers [14]	15.0	0.26	2.06
		15.0	0.476	2.06
		13.8	0.32	2.06
		15.0	0.48	2.06
		15.0	0.26	2.8
		15.0	0.476	2.8
		13.8	0.32	2.8
		15.0	0.48	2.8
	Wilkins and Thodos [20]	2.6	0.423	3.72
		3.1	0.421	3.72

© 1983 Hemisphere Publishing Corporation

Table 1 Data for Figures 1 to 3 (*Continued*)

Symbol	Authors	Sphere diameter *d*, mm	ψ	Pr; Sc
		Figure 3, Part I (Continued)		
◇	v. d. Decken et al. [21]	30.0	0.380	2.57
△	Hobson and Thodos [8]	9.4	0.475	1.87
▲		9.4	0.475	1.7
▽		9.4	0.475	1.76
⊕	Rowe and Claxton [10]	38.1	0.26	2.54
○		38.1	0.476	2.54
⊘		38.1	0.365	2.54
⊘		38.1	0.488	2.54
⊗		38.1	0.632	2.54
⊞	Thoenes and Kramers [14]	15.0	0.26	780-1070
⊠		15.0	0.395	910-l 060
□		15.0	0.476	800-l 090
⊡		13.8	0.320	880-l 040
▽	Wilson and Ceankopolis [22]	6.2	0.436	876-l 107
▼		6.3	0.401	760-l 000
▽		6.3	0.441	950-l 070
◸	Bhattacharya and Raja Rao [23]	23.4	0.53	794
◥		23.4	0.49	794
◺		1.9	0.39	794
◭		17.6	0.53	930
△	Evans and Gerald [24]	2.0	0.51	1 050-l 104
◇	Venkateswaran and Laddha [19]	19.0	0.483	867-892
		Figure 3, part II		
⊕	Rowe and Claxton [10]	38.1	0.260	6.0-7.2
⊗		38.1	0.365	6.7-7.0
⊘		38.1	0.488	6.7-7.0
⊘		38.1	0.632	6.6-7.0
○		38.1	0.476	6.4-7.0
◥	Thoenes and Kramers	15.0	0.26	1175-1840
◸		15.0	0.395	1 100-l 320
◭		15.0	0.476	1 100-l 430
◺	Wilson and Geankopolis [22]	6.3	0.403	1171-l 231
▽	Williamson et al. [25]	6.1	0.431	1 103-l 140
⊠	McCune and Wilhelm [26]	6.4	0.375	1 200-l 450
⊞		4.8	0.369	1 240-l 405
⊟		3.2	0.355	1 330-l 350
⊠		6.4	0.375	1 340
□		1.3	0.445	1 340
⊠		2.1	0.433	1 300
△	Karabelas et al. [27]	12.7; 25.4; 76.2	0.26	1 600
⊕	Rowe and Claxton [10]	15.9	0.26	1 360-I 670
⊕		6.4; 12.7	0.37	1 380-l 440
⊗		38.1	0.26	1 360-l 400
○		38.1	0.365	1310-l 410
⊘		38.1	0.488	1280-l 410
⊘		38.1	0.632	1 320-l 370
+	Jolls and Hanratty [28]	25.4	0.410	1 695
✚		25.4	0.410	1 740
×		25.4	0.410	1780

© 1983 Hemisphere Publishing Corporation

Table 1 Data for Figures 1 to 3 (Continued)

Symbol	Authors	Sphere diameter *d*, mm	ψ	Pr; Sc
		Figure 3, part III		
▼	Thoenes and Kramers [14]	15.0	0.26	1960-2 300
▲		15.0	0.26	3 300-3 650
◢		15.0	0.395	2 400-2 800
▽		15.0	0.476	1 960-2 800
△		15 .o	0.476	2 870-3 540
▲		13.8	0.32	3 380-3 530
○	Gaffney and Drew [18]	12.2	0.52	10100-11000
△		9.2	0.497	10400-11000
▽		6.0	0.507	10 700-11500

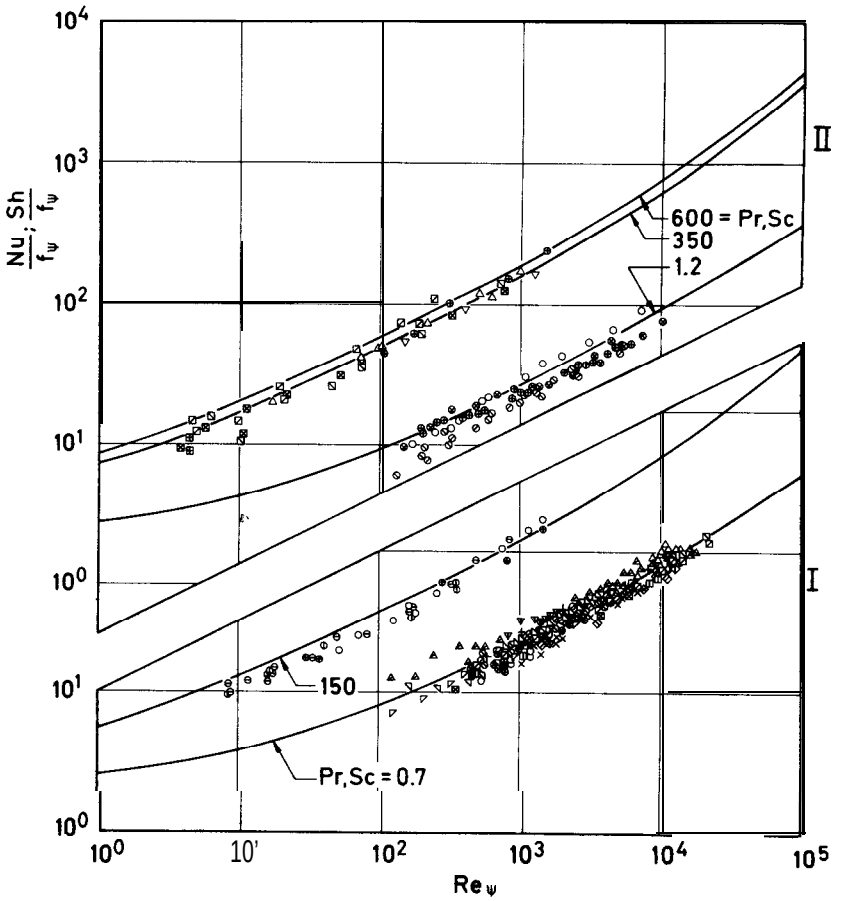

Figure 2 Measured values of $Nu/f_\psi, Sh/f_\psi$, and reduced Sherwood numbers for a series of mass transfer studies with Schmidt numbers between 1.2 and 680. See Table 1 for explanation of data.

© 1983 Hemisphere Publishing Corporation

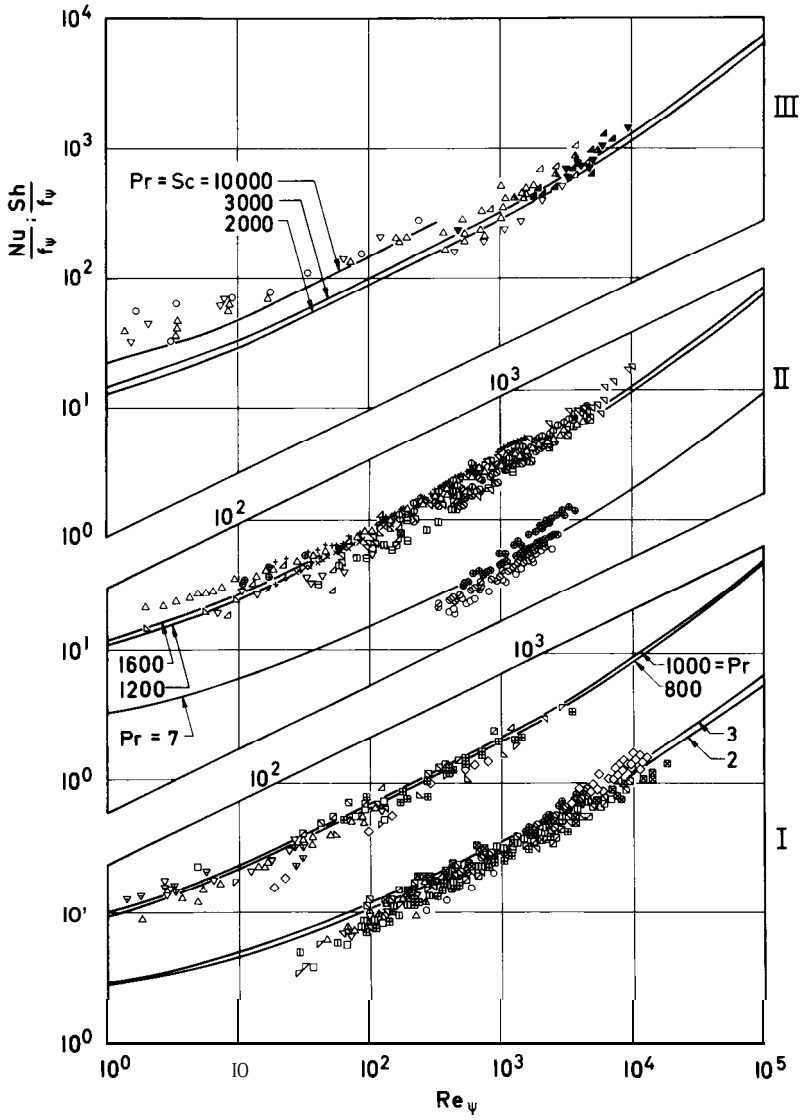

Figure 3 Measured values taken from the literature. See Table 1 for explanation of data.

numbers for a series of mass transfer studies with Schmidt numbers between 1.2 and 680.

Figure 3 shows further measured values from the literature. Here the Prandtl and Schmidt numbers vary between 2 and 10^4, and the void fractions of the packings between 0.26 and 0.63. The solid lines are calculated for the values of Pr or Sc specified on the lines using Eq. (2) with $f_\psi = 1$. This figure also shows that most of the measured values can be reproduced by Eq. (2) with deviations not exceeding ±15%.

Nomenclature for Section 2.5.4 appears at the beginning of Part 2.

REFERENCES FOR SECTION 2.5.4

1. Balakrishnan, A. R., and Pei, D. C. T., Heat Transfer in Gas-Solid Packed Bed Systems. 1. A Critical Review, *Ind. Eng. Chem. Process Des. Dev.*, vol. 18, pp. 30-40, 1979.
2. Barker, J. J., Heat Transfer in Packed Beds, *Ind. Eng. Chem., vol. 5 7,* pp. 43-5 1, 1965.
3. Gillespie, B. M., Crandall, E. D., and Carberry, J. J., Local and Average Interphase Heat Transfer Coefficients in a Randomly Packed Bed of Spheres, *AIChE J.*, vol. 14, pp. 483-490, 1968.
4. Ranz, W. E., Friction and Transfer Coefficients for Single Particles and Packed Beds, *Chem. Eng. Progr.*, vol. 48, pp. 247-253, 1952.

© 1983 Hemisphere Publishing Corporation

5. Gnielinski, V., Equations for the Calculation of Heat and Mass Transfer During Flow Through Stationary Spherical Packings at Moderate and High Peclet Numbers, *Int. Chem. Eng.*, vol. 21, pp. 378-383, 1981.
6. Kunii, D., and Suzuki, M., Particle-to-Fluid Heat and Mass Transfer in Packed Beds of Fine Particles, ***Int. J. Heat Mass Transfer,*** vol. 10, pp. 845–852, 1967.
7. Martin, H., Low Peclet Number Particle-to-Fluid Heat and Mass Transfer in Packed Beds, ***Chem. Eng. Sci.,*** vol. 33, pp. 913-919, 1978.
8. Hobson, M., and Thodos, G., Mass Transfer, Larninar Flow of Gases Through Granular Beds, ***Chem. Eng.*** *Progr.*, vol. 47, pp. 370–375, 1951.
9. Gupta, A. S., and Thodos, G., Direct Analogy Between Mass and Heat Transfer to Beds of Spheres, *AIChE J.*, vol. 9, pp. 751-754, 1963.
10. Rowe, P. N., and Claxton, K. T., Heat and Mass Transfer from a Single Sphere to Fluid Flowing Through an Array, ***Trans. Inst. Chem.*** Eng., vol. 43, pp. T321–T331, 1965.
11. Glaser, M. B., and Thodos, G., Heat and Momentum Transfer in the Flow of Gases Through Packed Beds, *AIChE J.,* vol. 4, pp. 63-68, 1958.
12. Malling, G. F., and Thodos, G., Analogy Between Mass and Heat Transfer in Beds of Spheres: Contributions Due to End-Effects, *Int. J. Heat Mass Transfer,* vol. 10, pp. 489-498, 1967.
13. Gupta, A. S., Evaporation of Water from the Surface of Beds of Cellite Spheres into a Stream of Air Passing Through Voids of Each Bed, Ph.D. thesis, Northwestern University, Evanston, Ill., 1963.
14. Thoenes, D., and Kramers, H., Mass Transfer from Spheres in Various Regular Packings to a Flowing Fluid, ***Chem.*** *Eng. Sci.,* ***vol. 8,*** pp. 271–283, 1958.
15. Glaser, H., Wärmeübergang an Kugelschiittungen, ***Chem. Zng. Tech.,*** vol. 34, pp. 468472, 1962.
16. Jaeschke, L., Über den Wärme- und Stoffaustausch und das Trocknungsverhalten ruhender, luftdurchströmter Haufwerke aus Körpern verschiedener geometrischer Form in geordneter und ungeordneter Verteilung, Diss. TH Darmstadt, 1960.
17. Bradshaw, R. D., and Myers, J. E., Heat and Mass Transfer in Fixed and Fluidized Beds of Large Particles, *AIChE J.,* vol. 5, pp. 590-595, 1963.
18. Gaffney, B. J., and Drew, T. B., Mass Transfer from Packing to Organic Solvents in Single Phase Flow Through a Column, ***Ind. Eng. Chem.,*** vol. 42, pp. 1120–1127, 1950.
19. Venkateswaran, S. D., and Laddha, G. S., Dissolution of Solid Solutes in Moving Liquid Systems in Packed Beds, ***Indian Chem. Eng.,*** vol. 8, pp. T33–T38, 1966.
20. Wilkins, G. S., and Thodos, G., Mass Transfer Driving Forces in Packed and Fluidized Beds, *AIChE J.,* vol. 15, pp. 47-50, 1965.
21. v. d. Decken, C. B., Hantke, H. J., Binckebanck, J., and Bachus, K. P., Bestimmung des Wärmeübergangs von Kugelschiittungen an durchströmendes Gas mit Hilfe der Stoffiibergangs-Analogie, ***Chem. Zng. Tech.,*** vol. 32, pp. 591-594, 1960.
22. Wilson, E. J., and Geankopolis, C. J., Liquid Mass Transfer at Very Low Reynolds Numbers in Packed Beds, ***Znd. Eng. Chem. Fund.,*** vol. 5, pp. 9-14, 1966.
23. Bhattacharya, S. N., and Raja Rao, M., Mass Transfer to Liquids in Fixed Beds, ***Indian Chem. Eng., vol. 9,*** pp. T65-T74, 1967.
24. Evans, G. C., and Gerald, C. F., Mass Transfer from Benzoic Acid Granules to Water in Fixed and Fluidized Beds at Low Reynolds Numbers. ***Chem.*** *Eng. Progr.*, vol. 49, pp. 135-149, 1953.
25. Williamson, J. E., Bazaire, K. E., and Geankopolis, C. J., Liquid Phase Mass Transfer at Low Reynolds Numbers, *Ind. Eng. Chem. Fund.,* vol. 2, pp. 126-129, 1963.
26. McCune, L. K., and Wilhelm, R. H., Mass and Momentum Transfer in Solid Liquid Systems, Fixed and Fluidized Beds, *Ind. Eng. Chem.,* vol. 41, pp. 1124–1134, 1949.
27. Karabelas, A. J., Wegner, T. H., and Hanratty, T. J., Use of Asymptotic Relations to Correlate Mass Transfer Data in Packed Beds, ***Chem.*** *Eng. Sci., vol.* 26, pp. 1581–1589, 1971.
28. Jolls, K. R., and Hanratty, T. J., Use of Electrochemical Techniques to Study Mass Transfer Rates and Local Skin Friction to a Sphere in a Dumped Bed, *AIChE J.,* vol. 15, pp. 199–205, 1969.

© 1983 Hemisphere Publishing Corporation

2.5.5

Fluid-to-particle heat transfer in fluidized beds

S. S. Zabrodsky with revisions by H. Martin

A. Introduction, range of fluidization, bed expansion

Fluidization of solid particles by a streaming gas or liquid requires a fluid velocity u in the range

$$u_{mf} < u < u_t \tag{1}$$

where u_{mf} is the so-called minimum fluidization velocity and u_t is the terminal velocity. The minimum fluidization velocity u_{mf} can be found from a force balance equating the pressure drop of a fixed bed to the weight of the particle (- buoyancy force) per cross-sectional area. Using Ergun s equation [I] for the pressure drop of the fixed bed, one obtains the Reynolds number $\mathrm{Re}_{mf} \equiv \rho_f u_{mf} d/\eta_f$ as a function of Archimedes number $\mathrm{Ar} \equiv g d^3 \rho_f (\rho_p - \rho_f)/\eta_f^2$ and void fraction at minimum fluidization ψ_{mf} (see Sec. 2.2.6):

$$\mathrm{Re}_{mf} = 42.9(1-\psi_{mf}) \left[\sqrt{1 + \frac{\psi_{mf}^3}{(1-\psi_{mf})^2} \frac{\mathrm{Ar}}{3\ 214}} - 1 \right] \tag{2}$$

In the case of particulate (or homogeneous) fluidization, the terminal velocity u_t is equal to the terminal free-fall velocity of a single particle. The corresponding Reynolds number Re, = $\rho_f u_t d/\eta_f$ may be found from a force balance for a single particle:

$$\mathrm{Ar} = \tfrac{3}{4} \mathrm{Re}_t^2 C_D(\mathrm{Re}_t) \tag{3}$$

where $C_D(\mathrm{Re}_t)$ is the drag coefficient.

The simple equation

$$C_D(\mathrm{Re}_t) \cong \frac{1}{3} \left(\sqrt{\frac{72}{\mathrm{Re}}} + 1 \right)^2 \tag{4}$$

which represents the standard drag curve with a reasonable degree of approximation for $0 < \mathrm{Re} < 3 \times 10^5$, provides an explicit formula for $\mathrm{Re}_t(\mathrm{Ar})$ covering the whole range of Reynolds numbers [2]:

$$\mathrm{Re}_{t(\text{single sphere})} \cong 18 \left(\sqrt{1 + \tfrac{1}{9}\sqrt{\mathrm{Ar}}} - 1 \right)^2 \qquad (\mathrm{Ar} < 2 \times 10^{10}) \tag{5}$$

For aggregative or heterogeneous fluidization the terminal velocity, that is, the boundary between fluidization and pneumatic transport, can be higher than u_t for a single sphere. According to Reh (see [2]), $u_{t(\text{hetero})}$ may be estimated (with $C_D \cong 1$) from

$$\mathrm{Re}_{t(\text{hetero})} \cong \sqrt{\tfrac{4}{3}\mathrm{Ar}} \tag{6}$$

For gas-fluidized beds, Re, may be found from $\mathrm{Re}, = \max(\mathrm{Re}_{t(\text{single sphere})}, \mathrm{Re}_{t(\text{hetero})})$. Liquid-fluidized beds may be regarded to be in the range of particulate or homogeneous fluidization [Eq. (5)].

Increasing the fluid velocity u within the range of fluidization [Eq. (1)] simultaneously increases the void fraction ψ or the bed height L. A mass balance for the solid gives

$$(1-\psi)L = (1-\psi_{mf})L_{mf} \tag{7}$$

Bed expansion behavior, that is, the functional relationship between gas velocity u and void fraction ψ, can be most conveniently estimated from the simple

© 1983 Hemisphere Publishing Corporation

empirical equation [3]

$$\frac{u}{u_t} = \psi^n \tag{8}$$

The exponent n in Eq. (8) can be determined from any pair of corresponding values of gas velocity and void fraction (other than $u = u_t; \psi = 1$). Using the set (u_{mf}, ψ_{mf}), the exponent n becomes

$$n = \frac{\ln (\mathrm{Re}_{mf}/\mathrm{Re}_t)}{\ln \psi_{mf}} \tag{9}$$

which is a function of Ar and ψ_{mf}.

B. Recommended equations for fluid-to-particle heat transfer coefficients in fluidized beds

To calculate heat transfer coefficients between the fluid and the surface of the particles in a fluidized bed, the same equations can be used as have been given in Sec. *2.5.4* for fixed beds [4] [Eqs. 2.5.4(1) to 2.5.4(9)]. One has to keep in mind, however, that gas velocity (or Reynolds number) and void fraction cannot be varied independently in a fluidized bed with a given size, shape, and density of the particles.

Figure 1 shows some curves Nu versus Re calculated from the fixed-bed equations 2.5.4(1) to 2.5.4(9) for four specified values of Re, [or Ar; see Eq. (5)] using Eq. (8) with Eqs. (9), (2), and (5), Pr = 0.7, and ψ_{mf} = 0.4. For fluidization of glass spheres or sand in air (p = l-bar, T = 20°C), the values of Re_t (and Ar) correspond to particle diameters between ~7 mm and ~150 μm:

Re_t	10^4	10^3	10	10
Ar	2.9 × 10	4 × 10^5	8.5 × 10^3	3.4 × 10^2
d, mm	6.86	1.64	0.455	0.156

ρ_p = 2 500 kg/m³, ρ_f = 1.188 kg/m³, η_f = 17.98 Pa.

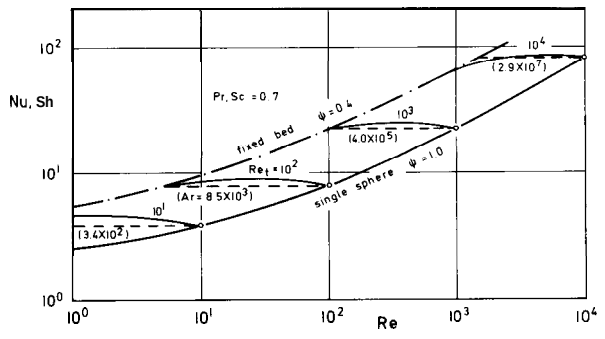

Figure 1 Fluid-to-particle heat and mass transfer coefficients in fluidized beds. Nu, Sh plotted versus Re for Pr, Sc = 0.7. Curves calculated from the equations given in Secs. 2.5.4 and 2.5.5(B).

Within the range of fluidization (Re_{mf} < Re < Re,), the heat (or mass) transfer coefficients remain almost constant, being only slightly higher than the values at $\mathrm{Re}_t(\psi = 1)$ for intermediate Reynolds numbers. Therefore it might be sufficient to calculate the fluid-to-particle heat transfer coefficients in fluidized beds from the simple relation

$$\mathrm{Nu} = \mathrm{Nu}_{\text{single sphere}}(\mathrm{Re}_t, \mathrm{Pr}) \tag{10}$$

(broken horizontal straight lines in Fig. 1) with Re_t from Eq. (5) and $\mathrm{Nu}_{\text{single sphere}}(\mathrm{Re}_t, \mathrm{Pr})$ from Eq. 2.5.2(21):

$$\mathrm{Nu}_{\text{single sphere}} = 2 + \sqrt{\mathrm{Nu}_{\text{lam}}^2 + \mathrm{Nu}_{\text{turb}}^2} \tag{11}$$

where

$$\mathrm{Nu}_{\text{lam}} = 0.664\sqrt{\mathrm{Re}_t}\sqrt[3]{\mathrm{Pr}} \tag{12}$$

$$\mathrm{Nu}_{\text{turb}} = \frac{0.037\,\mathrm{Re}_t^{0.8}\,\mathrm{Pr}}{1 + 2.443\,\mathrm{Re}_t^{-0.1}(\mathrm{Pr}^{2/3} - 1)} \tag{13}$$

C. Comparison with experimental data

It is very difficult to obtain reliable experimental data on fluid-to-particle heat (or mass) transfer in the region of low Peclet numbers Pe = Re Pr (or Re Sc). In an experiment with constant temperature (or concentration) at the surface of the particles, the temperature difference at the outlet of a (packed or fluidized) bed is related to the inlet temperature difference by

$$(T_{F,\text{out}} - T_s) = (T_{F,\text{in}} - T_s)e^{-\mathrm{NTU}} \tag{14}$$

if the fluid is assumed to pass through the bed in perfect plug flow. The number of transfer units NTU is given by

$$\mathrm{NTU} = \frac{\alpha A}{\dot{M}_F c_{p,F}} = \frac{6(1-\psi)L}{d}\,\frac{\mathrm{Nu}}{\mathrm{Re\ Pr}} \tag{15}$$

With Nu ⩾ 2 [see Eq. (11)], NTU becomes relatively large for low values of Pe = Re Pr, or the fluid outlet temperature $T_{F,\text{out}}$ comes very close to its thermal equilibrium value T_s [see Eq. (14)].

So, in order to check whether the heat or mass transfer coefficients in fluidlzed beds actually do come out as predicted by Eqs. (11) to (13) and Eq. (5), one has to look at experimental data at high Peclet numbers (and consequently low NTUs) first. With the low Pr or Sc values of gases, this means high Reynolds numbers, or relatively large particle diameters.

Heat transfer data in this range have been reported by Chang and Wen [5]. Their data with metal spheres (diameters 4.76 and 6.35 mm) fluidized with air actually show that the heat transfer coefficients are independent of the gas flow rate in the range of fluidization [as predicted by Eqs. (10) to (13)].

Figure 2 shows their data (as the shaded narrow

© 1983 Hemisphere Publishing Corporation

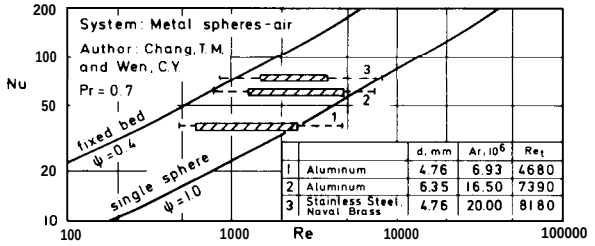

Figure 2 Heat transfer from metal spheres fluidized with air. Experimental data by Chang and Wen shown as shaded rectangular regions. Broken lines mark the range of fluidization as calculated from Eqs. (2) and (5).

rectangles) in a Nu versus Re plot. The broken horizontal lines through the data mark the range of fluidization ($Re_{mf} < Re < Re_t$). Similar results have been obtained with evaporation of water from porous ceramic spheres in air-fluidized beds by Bradshaw and Myers [6], Mosberger [7], and Petrovic and Thodos [8].

Mosberger s data are shown in Fig. 3 in a Sh versus Re plot. Again the mass transfer coefficients were found to be independent of the flow rate in the range of fluidization. The absolute values tend to be lower by about 20 to 30% than predicted by Eqs. (10) to (13). In these experiments there might be an influence of additional internal mass transfer resistance [local drying out of the porous concrete (Siporex) particles], or an influence of backmixing or other deviations from ideal plug flow in the gas phase.

Mass transfer data with solid benzoic acid spheres fluidized in water ($Sc \cong 1700$) obtained by Damronglerd [9] show the same behavior; see Fig. 4. In this case the absolute values are about 20 to 30% ***higher*** than predicted by Eqs. (10) to (13).

Using the same system-dissolution of benzoic acid spheres in water-Tournie et al. [10] continued the measurements of Damronglerd [9] with smaller particles (4.2 mm $\geqslant d \geqslant$ 0.7 mm) covering a range of Reynolds numbers from $1.6 \leqslant Re \leqslant 9\,1$. Their data, with particle diameters changing from run to run, have been plotted

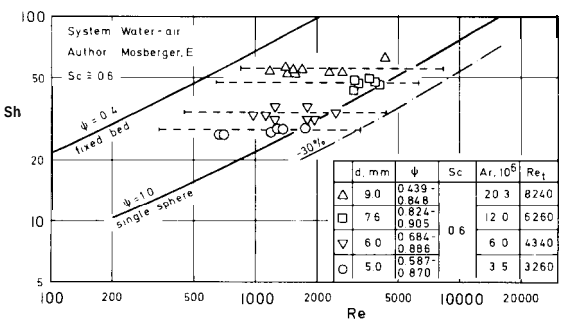

Figure 3 Mass transfer from wet porous concrete (Siporex) spheres fluidized in air. Experimental data by Mosberger. Broken lines mark the range of fluidization (see Fig. 2).

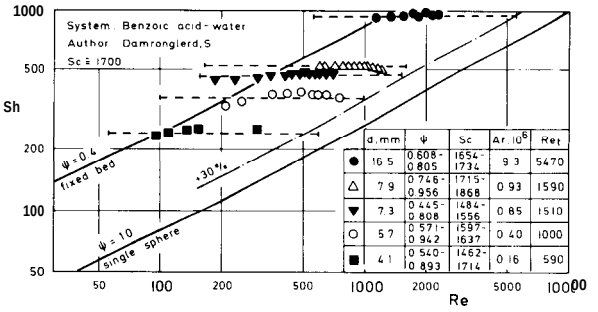

Figure 4 Mass transfer from benzoic acid spheres fluidized in water. Experimental data by Damronglerd. Broken lines as in the previous figures.

in Fig. 5 using different symbols for each half-decade of Archimedes numbers. In contrast to Damronglerd s data, they cover only a narrow range of void fractions $0.49 < \psi < 0.62$. Again these dissolution data show a tendency to be about 20 to 30% higher than predicted by Eqs. (10) to (13).

D. Some remarks on heat and mass transfer coefficients in the range of low Peclet numbers

In the range of low Peclet numbers ($Pe \lesssim 500$), most of the experimentally obtained fluid-to-particle heat and mass transfer coefficients in packed as well as in fluidized beds are found to be some orders of magnitude below the values predicted from Eq. (11) [11 to 15]. There seems to be agreement among the majority of heat and mass transfer specialists that these low values of transfer coefficients, corresponding to Nusselt or Sherwood numbers far below 2, do not represent real or true heat transfer coefficients, but only effective or apparent ones.

The reason for these low apparent heat and mass transfer coefficients may be seen in the fact that they

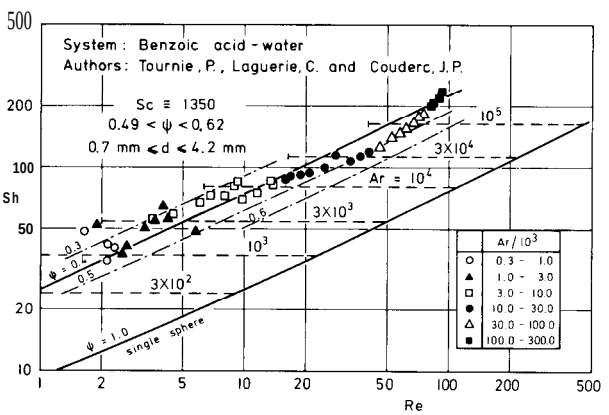

Figure 5 Mass transfer from benzoic acid spheres fluidized in water. Experimental data by Tournie et al. Broken lines calculated from Eqs. (10) to (13).

© 1983 Hemisphere Publishing Corporation

usually have been determined from measured inlet and outlet temperatures assuming the fluid to pass through the bed in perfect plug flow. Actually, in a flow through randomly packed and fluidized beds there is always a certain degree of backmixing and/or flow maldistribution, which can cause a kind of a bypassing effect [14 to 16]. In the range of high Peclet numbers, and consequently low NTUs, these deviations from ideal plug flow do not greatly influence the overall performance. For low Peclet numbers, however, even a very small maldistribution of flow rates over the cross section of a bed may cause the overall, apparent transfer coefficients to drop by several orders of magnitude [see Sec. 2.1.4 and Fig. 2.1.4(5)].

A number of models have been proposed by different authors to account for these effects: Zabrodsky s micro break-through model [11, p204], Kunii and Levenspiel s bubbling bed mode[12, p. 219], or Schlünder's maldistribution model [14]. All these models contain one or more adjustable parameters that may be used to fit the resulting equations to any set of experimental data.

The simplest and most conveniently applicable one-parameter model seems to be the bypass model, which has been used by Zabeschek [16] and by Subramanian et al. [17] for fluidized beds and, in a modified way, by the author [15] for packed beds.

In this model the total flow rate through the bed is subdivided in a mainstream and a bypass stream. The bypass stream is assumed to pass the bed without taking part in the transfer of heat or mass, that is, leaving the bed with its entrance temperature or concentration. With this assumption the outlet fluid temperature (concentration) is just the mixing temperature of both streams:

$$\frac{T_{F,\text{out}} - T_s}{T_{F,\text{in}} - T_s} = (1 - \upsilon)e^{-\text{NTU}_M} + \upsilon \qquad (16)$$

where

$$\upsilon \equiv \frac{M_{\text{bypass}}}{\dot{M}_{\text{total}}} \quad \text{(bypass flow rate ratio)} \qquad (17)$$

and

$$\text{NTU}_M = \frac{6(1-\psi)L\ \text{Nu}}{\text{d}(1-\upsilon)\ \text{Re Pr}} \quad \text{(mainstream NTU)} \qquad (18)$$

The Nusselt number in Eq. (18) is to be calculated from Eqs. (10) to (13) as before. An experimentalist determining heat transfer coefficients from measured fluid inlet, fluid outlet, and solid temperatures, assuming ideal plug flow of the fluid [see Eq. (14)], will obtain apparent heat transfer coefficients:

$$\text{Nu}_{(\text{app})} = -\frac{\text{Re Pr}\ d}{6(1-\psi)L}\ln\left[(1-\upsilon)e^{-\text{NTU}_M} + \upsilon\right] \qquad (19)$$

With a bypass flow rate ratio of 5% ($\upsilon = 0.05$), Eq. (19), with $\psi_{mf} = 0.5$, $L_{mf}/d = 10$, Pr = 0.7 (air), and Re = Re_t gives

Re	1	10	100	1 000	10 000
Nu	2.59	3.88	8.06	22.6	80.4
$\text{Nu}_{(\text{app})}$	0.070	0.699	6.05	21.8	79.6

These apparent Nusselt numbers may be compared with the experimental data of various authors presented in Fig. 6, Chapter 7, of Kunii and Levenspiel s book[12, p. 218].

To compare measured heat or mass transfer data in the range of low Peclet numbers with Eqs. (18) and (19), it is necessary to know the bed height L and the volume-specific surface area:

$$a_v = \frac{6(1-\psi)}{d} \qquad (20)$$

One of the few papers containing all the necessary information about the experimental data-Resnick and White [18] -has been used here to show that the bypass model is able to explain the observed phenomena in the range of low Peclet numbers.

These authors [18] have tabulated the values of NTU, obtained directly from their measured naphthalene partial pressures at the exit of the bed ($p_{1,\text{in}} = 0$):

$$\text{NTU}_{(\text{app})} = \ln\frac{p_1^* - p_{1,\text{in}}}{p_1^* - p_{1,\text{out}}} \qquad (21)$$

Equation (21), which is the mass transfer equivalent to Eq. (14), is based on the assumption of perfect plug

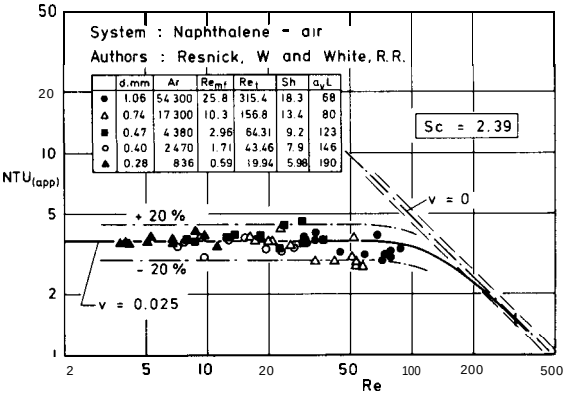

Figure 6 Mass transfer from naphthalene particles fluidized in air. NTU plotted versus Re. Experimental data by Resnick and White compared with a curve calculated from the bypass model with a constant bypass flow rate ratio of $\upsilon = 0.025$.

© 1983 Hemisphere Publishing Corporation

flow of the gas. From the bypass model [Eqs. (16) to (19)], we get

$$NTU_{(app)} = -\ln [(1-\upsilon)e^{-NTU_M} + \upsilon] \quad (22)$$

with NTU_M for mass transfer being

$$NTU_M = \frac{a_v L\ Sh}{(1-\upsilon)\ Re\ Sc} \quad (23)$$

The Sherwood number is obtained from Eqs. (10) to (13) with Nu replaced by Sh and Pr replaced by Sc. It is obvious from Eq. (22) that $NTU_{(app)}$ comes very close to NTU_M if υ is small compared to 1 and if the Peclet number Pe = Re Sc is large, so that NTU_M is low. For low Peclet numbers, that is, when NTU_M becomes greater than about 5, the apparent NTU becomes independent from any property that normally has some influence on heat or mass transfer:

$$\lim_{Pe \to 0} NTU_{(app)} = -\ln \upsilon \quad (24)$$

Figure 6 shows the apparent NTU values measured by Resnick and White [18] with naphthalene particles ($0.28 < d < 1.06$ mm) fluidized by air in a NTU versus Re plot. As predicted by Eq. (24), the apparent NTUs become constant for low Peclet (or Reynolds) numbers. The curves are calculated from Eqs. (22) and (23) and Eqs. (10) to (13) with a bypass flow rate ratio of 2.5% ($\upsilon = 0.025$). (The same data are shown in a Sh versus Re plot in Fig. 2, Chapter 7, of Kunii and Levenspiel [12], compared with curves from the bubbling bed model.)

Without bypass stream NTU is inversely proportional to Re [see Eq. (23) and the dotted line with $\upsilon = 0$ in Fig. 6].

Figure 7 shows similar data, now with one particle diameter (d = 0.4 mm) and three different gases as fluidizing media. Despite the considerable differences in the diffusivity of naphthalene in hydrogen, air, and carbon dioxide, the measured apparent NTUs are the same within less than ±15%. Again the curve is calculated from Eq. (22) with a bypass flow rate ratio of 2.5%. Without bypassing, the NTUs would have been in the ratio 1:2.1:3.8 for H_2, air, and CO_2, respectively (see calculated curves with $\upsilon = 0$ in Fig. 7).

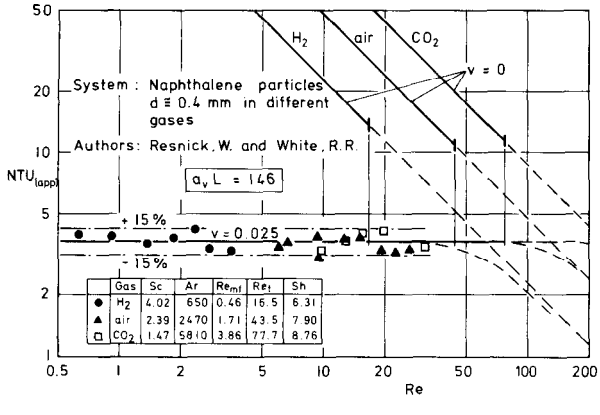

Figure 7 Mass transfer from naphthalene particles fluidized in hydrogen, air, and carbon dioxide. NTU plotted versus Re. Experimental data by Resnick and White compared with a curve calculated from the bypass model with a constant bypass flow rate ratio of υ = 0.025.

It is difficult, if not impossible, to predict the numerical value of the bypass flow rate ratio υ. For Resnick and White s experiments, υ = 0.025 was found to be the best value. Zabeschek [16], using evaporation of water from porous aluminum silicate and molecular sieve particles ($0.92 < d < 4.12$ mm), found a value of υ = 0.05 appropriate to fit his data to the bypass model equations. Subramanian et al. [17], using Zabeschek s apparatus, found that υ should increase linearly with the particle diameter. For particle diameters of 0.92, 2.76, and 4.30 mm, the bypass flow rate ratio υ was determined from measured NTUs (or apparent Sherwood numbers) to be 0.033, 0.098, and 0.152, respectively.

So, if no direct measurement of $NTU_{(app)}$ is available, it is suggested that a value of 5% be used for a first approximation:

$$\upsilon \cong 0.05 \quad (25)$$

This corresponds to a limiting apparent NTU [see Eq. (24)] of $NTU_{(app)} = 3$.

E. Illustrative example

Batchwise cooling of roasted coffee beans in a fluidized-bed cooler (see Fig. 8) will be used as an example.

Coffee is roasted batchwise in a venturi-type fluidized bed. The time to roast one charge is 150 s. During this time the previous charge is to be cooled down in a cylindrical fluidized bed with atmospheric air. The question is whether this time is sufficient to cool the coffee beans from their initial temperature of $T_{s,I} = 300°C$ to less than 30°C. The following data may be given:

Solid (subscript s): Coffee beans

Initial temperature $T_{s,I} = 300°C$
Density $\rho_s = 630$ kg/m^3
Heat capacity c_s = 1.70 kJ/kg K
Conductivity λ_s = 0.10 W/m K
Solid mass per cross-sectional area $M_s/S = m_s$ = 60 kg/m^2
Average particle diameter $d = 6$ mm

Gas (subscript g): Atmospheric air

Inlet temperature $T_{g,in} = 20°C$
Mass velocity $\dot{m}_g$ = 3 kg/m^2 s

© 1983 Hemisphere I blishing Corporation

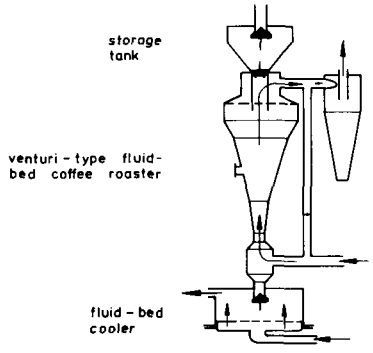

Figure 8 Fluid-bed coffee roaster with storage tank and fluid-bed cooler.

Density $\rho_g = 1\ \text{kg/m}^3$
Heat capacity $c_{p,g} = 1\ \text{kJ/kg K}$
Conductivity $\lambda_g = 0.029\ \text{W/m K}$
Kinematic viscosity $\nu_g = 20 \times 10^{-6}\ \text{m}^2/\text{s}$

It may be assumed that the solid is perfectly mixed, so that T_s is a function of time but not of position.

Neglecting the local change of enthalpy of the gas against that of the solid gives

$$m_s c_s \frac{d\bar{T}_s}{dt} = \dot{m}_g c_{pg} [T_{g,\text{in}} - T_{g,\text{out}}(t)] \tag{26}$$

and

$$\frac{T_{g,\text{out}}(t) - \bar{T}_s(t)}{T_{g,\text{in}} - \bar{T}_s(t)} = (1-\upsilon)e^{-\text{NTU}_M} + \upsilon$$

[from Eq. (16)] (27)

From these two equations (26, 27) for the two unknown functions of time, $T_{g,\text{out}}(t)$ and $\bar{T}_s(t)$, we can eliminate first $T_{g,\text{out}}(t)$, then integrate over the time t to obtain

$$\theta_s \equiv \frac{\bar{T}_s(\tau) - T_{g,\text{in}}}{T_{s,I} - T_{g,\text{in}}} = \exp[-(1-\upsilon)(1-e^{-\text{NTU}_M})\tau] \tag{28}$$

where

$$\tau \equiv \frac{\dot{m}_g c_{pg}}{m_s c_s} t \tag{29}$$

and

$$\text{NTU}_M = \frac{6Um_s/\rho_s}{d\dot{m}_g c_{pg}(1-\upsilon)} \tag{30}$$

Since $\bar{T}_s$ is not the surface temperature of the coffee beans, but the average temperature, α in NTU_M has to be replaced by the overall heat transfer coefficient U, including the internal conduction resistance [see Sec. 2.4.3A(b)]:

$$\frac{1}{U} = \frac{1}{\alpha_{(\text{outside})}} + \frac{1}{\alpha_{(\text{internal})}} \tag{31}$$

The outside heat transfer coefficient is calculated from Eq. (5) and Eqs. (10) to (13):

$$\text{Ar} = \frac{gd^3}{\nu^2}\frac{\rho_s - \rho_g}{\rho_g} = 3.34 \times 10^6$$

$\text{Re}_{mf}(\psi_{mf} = 0.4) = 326$ $\text{Re}_t = 3\,180$ [Eq. (5)]

$\text{Re} = 900 \rightarrow \frac{u}{u_{mf}} = 2.76$ $\text{Pr} = \rho_g c_{pg}\frac{\nu_g}{\lambda_g}$ Pr = 0.69

$\text{Nu}_{\text{lam}} = 33.1$ [Eq. (12)] $\text{Nu}_{\text{turb}} = 21.3$ [Eq. (13)] Nu = 41.32 [Eq. (11)]

$$\alpha_{(\text{outside})} = \frac{\lambda_g}{d}\text{Nu} = 200\ \text{W/m}^2\ \text{K}$$

$$\text{Bi} = \frac{\alpha_{(\text{outside})} d/2}{\lambda_s} = 5.99$$

$$\kappa_s = \frac{\lambda_s}{\rho_s c_s} = 9.34 \times 10^{-8}\ \text{m}^2/\text{s}$$

$\text{Nu}_{i\infty} = 3.90$ [Eq. 2.4.3(62)]

$$t^+ = \frac{\kappa_s t}{(d/2)^2} = 1.556$$

$\text{Nu}_i(t^+) = 4.004$ [Eq. 2.4.3(60)]

$$\alpha_{(\text{internal})} = \frac{\lambda_s}{d/2}\text{Nu}_i = 133\ \text{W/m}^2\ \text{K}$$

$U = 80.0\ \text{W/(m}^2\ \text{K)}$ [Eq. (31)]

$\text{NTU}_M = \frac{2.54}{1-\upsilon}$ $\tau = 4.41$

υ	0.00	0.05	0.10	0.20
θ_s	0.017 2	0.020 2	0.023 9	0.034 0
$\bar{T}_s$, °C	24.8	25.7	26.7	29.5

From this calculation it can be seen that the time of 150 s will be sufficient to cool the coffee beans to less than 30° C even if the bypass flow rate ratio is assumed to be 20%!

Nomenclature for Section 2.5.5 appears at the beginning of Part 2.

© 1983 Hemisphere Publishing Corporation

REFERENCES FOR SECTION 2.5.5

1. Ergun, S., Fluid Flow Through Packed Columns, *Chem. Eng.* ***Prog.,*** vol. 48, pp. 89-94, 1952.
2. Martin, H., Wärme- und Stoffiibertragung in der Wirbelschicht, *Chem.* ***Zng. Tech.,*** vol. 52, pp. 199-209, 1980.
3. Richardson, J. F., Incipient Fluidization and Particulate Systems, in ***Fluidization,*** ed. J. F. Davidson and D. Harrison, p. 52, Academic Press, London and New York, 1971.
4. Gnielinski, V., Gleichungen zur Berechnung des Wärme- und Stoffaustausches in durchströmten ruhenden Kugelschüttungen . . . , ***Verfahrenstechnik*** (Mainz), vol. 12, pp. 363-366, 1978.
5. Chang, T. M., and Wen, C. Y., Fluid-to-Particle Heat Transfer in Air-Fluidized Beds, *Chem.* ***Eng. Prog.*** *Symp.* ***Ser.,*** no. 67, vol. 62, pp. 111-117, 1966.
6. Bradshaw, R. D., and Myers, J. E., Heat and Mass Transfer in Fixed and Fluidized Beds of Large Particles, *AIChE J.*, vol. 9, pp. 590–595, 1963.
7. Mosberper, E., Über den Wärme- und Stoffaustausch zwischen Partikel und Luft in Wirbelschichten sowie über deren Ausdehnungsverhalten, Dissertation, Technische Hochschule, Darmstadt, 1964.
8. Petrovic, L. J., and Thodos, G., Effectiveness Factors for Mass Transfer in Fluidized Systems, *Proc.* ***Znt. Symp. Fluidization,*** *Eindhoven*, cd. A. A. H. Drinkenburg, pp. 586-598, 1967.
9. Damronglerd, S., Transfert de matière en fluidisation homogène, These, Université Paul Sabatier de Toulouse, Toulouse, 1973.
10. Tournie, P., Laguerie, C., and Couderc, J. P., Mass Transfer in a Liquid Fluidized Bed at Low Reynolds Numbers, *Chem.* ***Eng. Sci.,*** vol. 22. pp. 1259-1261, 1977.
11. Zabrodsky, S. S., ***Hydrodynamics and Heat Transfer in*** *Fluidized* ***Beds,*** M.I.T. Press, Cambridge, Mass., 1966 (see Chapter 8 and Fig. 8-l 1).
12. Kunii, D.. and Levenspiel, ***O., Fluidization Engineering,*** Wiley, New York, 1969.
13. Gelperin, N. I., and Einstein, V. G., Heat Transfer in Fluidized Beds, in ***Fluidization,*** ed. J. F. Davidson and D. Harrison, pp. 517-532, Academic Press, London and New York, 1971.
14. Schlünder, E. U., On the Mechanism of Mass Transfer in Heterogeneous Systems, ***Chem. Eng.*** *Sci.*, vol. 32, pp. 845-851, 1977.
15. Martin, H., Low Peclet Number Particle-to-Fluid Heat and Mass Transfer in Packed Beds, *Chem.* ***Eng.*** *Sci.*, ***vol. 33,*** pp. 913-919, 1978.
16. Zabeschek, G., Experimentelle Bestimmung und analytische Beschreibung der Trocknungsgeschwindigkeit rieselfahiger, kapillarporöser Güter in der Wirbelschicht, Dissertation, Universitat Fridericiana Karlsruhe (TH), Karslsruhe, 1977.
17. Subramanian, D., Martin. H., and Schlünder, E. U., Stoffiibertragung zwischen Gas und Feststoff in Wirbelschichten, *Verfahrenstechnik* (Mainz), vol. 11, pp. 748-750, 1977.
18. Resnick, W., and White, R. R., Mass Transfer in Systems of Gas and Fluidized Solids, ***Chem. Eng. Prog., vol. 45,*** pp. 377-390, 1949.

© 1983 Hemisphere **Publishing Corporation**

2.5.6
Impinging jets

H. Martin

A. Introduction

Heating or cooling of large-surface-area products is often carried out in devices consisting of arrays of round or slot nozzles, through which air (or another gaseous medium) impinges vertically upon the product surface. Such impinging flow devices allow for short flow paths on the surface and therefore relatively high heat transfer rates. The annealing of metal and plastic sheets, the tempering of glass, and the drying of textiles, veneer, paper, and film material are some of their more important industrial applications. The gas flow rate, the diameter (or slot width) of the nozzles, their spacing, and their distance to the product surface are the main variables, which can be chosen to solve a given heat or mass transfer problem.

As shown by Schrader [1], Glaser [2,3], and other authors [4–7], the flow pattern of impinging jets from single round and slot nozzles can be subdivided into three characteristic regions: the free ***jet*** region, the ***stagnation flow*** region, and the region of lateral (or radial) flow outside the stagnation zone, also called the ***wall jet*** region after the basic theoretical work of Glauert [8]. The velocity field of an impinging jet is shown schematically in Fig. 1.

Under technically realistic conditions the free jet, developing from the exit of the nozzle ***(a)*** with diameter ***D*** or slot width ***B,*** in general will be turbulent. By an intensive exchange of momentum with the surrounding gas over the free boundaries ***(b)***, the jet broadens linearly with its length z' up to a limiting distance z_g from the solid surface (c). The velocity profile ***(d)***, being nearly rectangular at the nozzle exit,

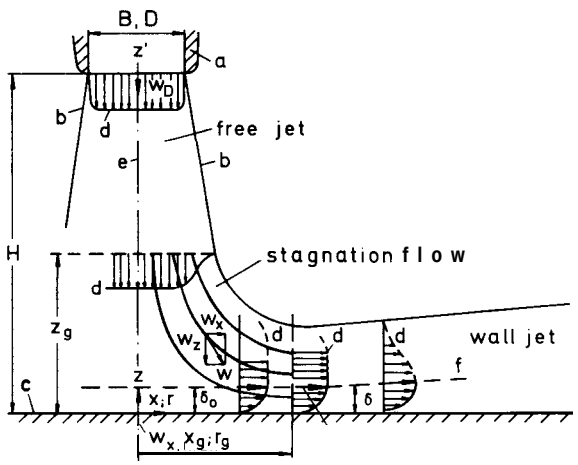

Figure **1** Velocity field of impinging flow.

spreads toward the free boundaries and, for sufficient length of the free jet, approaches a bell shape.

Stagnation flow begins relatively close to the surface (according to Schrader [1], the limiting distance z_g is about 1.2 times the nozzle diameter). Here the vertical velocity component is decelerated and transformed into an accelerated horizontal one. Analytic solutions of the Navier-Stokes equations are known for the idealized limiting case of the infinitely extended plane and axisymmetric laminar stagnation flows (see Schlichting [9], pp. 76-81).

Because of the infinite breadth of the jet and the exchange of momentum with its quiescent surroundings, the accelerated stagnation flow finally must transform to a decelerated wall jet flow. Thus the wall parallel velocity component w_x (w,) initially increasing

© 1983 Hemisphere 1 ıblishing Corporation

linearly from zero must reach a maximum value at a certain distance $x_g(r_g)$ from the stagnation point and finally tends to zero with $x^{-n}(r^{-n})$ in the fully developed wall jet. The exponent n is about 0.5 for the plane [8, 10, 1 1] and about 1 for the axisymmetric [8, 1 I, 12] turbulent wall jet. Whereas the stabilizing effect of acceleration keeps the boundary layer laminar in the stagnation zone, transition to turbulence generally will occur immediately after x_g (or r_g) in the decelerating flow region. Wall boundary layer and free jet boundary grow together, forming the typical wall jet profile where the boundary layer δ is defined as the locus of the maxima of the velocity $[z(w_{x,\max})]$ [see (f) in Fig. 1].

The impinging flow from arrays of nozzles generally shows the same three flow regions-free jet, stagnation zone, wall jet-but in addition there are secondary stagnation zones where the wall jets of adjacent nozzles impinge upon each other. Like the wake zones in the rear of cylinders or spheres in cross flow, these secondary stagnation zones are characterized by boundary layer separation and eddying of the flow.

B. Local variation of the transfer coefficients

(a) Single round and slot nozzles

The local heat transfer coefficient α is defined as the local heat flux per nozzle-exit-to-surface temperature difference:

$$\alpha = \frac{4}{T_{\text{surf ace}} - T_{\text{nozzle exit}}} \qquad (1)$$

In Fig. 2 the local variation of the transfer coefficients is shown in dimensionless form as $(\mathrm{Nu}/\mathrm{Pr}^{0.42})$ versus the relative radial distance ***(r/D)*** from the stagnation point for different relative nozzle exit-to-plate distances ***H/D.*** The figure was plotted from Pötke's [13] naphthalene sublimation data with a single round nozzle for a nozzle exit Reynolds number (Re = wD/ν) of Re = 54 000. The Nusselt number is defined as

$$\mathrm{Nu} = \frac{\alpha D}{\lambda} \qquad (2)$$

that is, with the nozzle diameter ***D*** as the characteristic length.

Similar experimental results may be found for single round nozzles (SRN) as well as for single slot nozzles (SSN), including:

Evaporation of water from porous plates to air jets (Sc = 0.59): [14] SRN, [IS] SSN, see also [16], pp. 8-11.

Heat transfer to air jets (Pr = 0.7): [5, 17, 18] SRN, [19, 20] SSN.

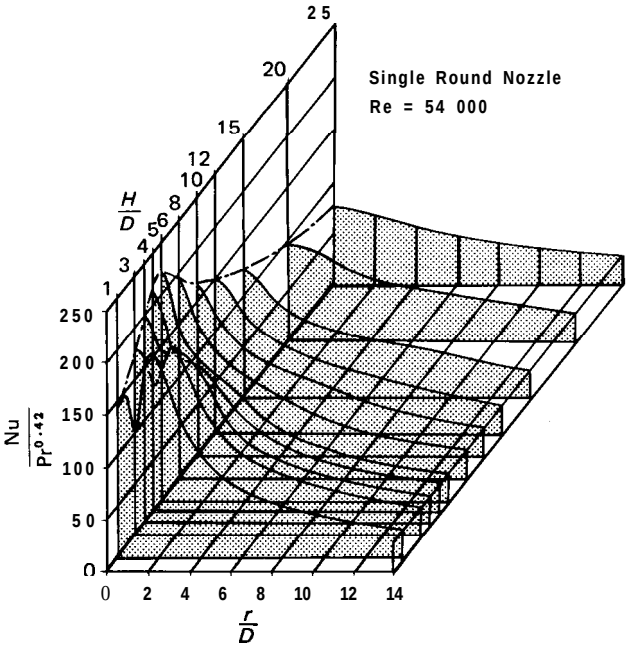

Figure 2 Local variation of heat transfer under a single round nozzle.

Mass transfer naphthalene-air (Sc = 2.5): [13, 21] ***SRN,*** [6, ***22,*** 23] ***SSN.***

Mass transfer *trans*-cinnamic acid-water (Sc ≈ 900): [24] ***SRN.***

For both round and slot nozzles,.the local variation of the transfer coefficients is qualitatively the same: monotonically decreasing bell-shaped curves for large relative nozzle-to-plate distances ***(H/D*** or ***H/B*** $\gtrsim 8$) and curves with a more or less distinct hump or second maximum for smaller ***H/D*** (or ***H/B).*** The sharp increase of the transfer coefficients begins immediately after the end of the accelerated flow region, where the disappearance of the stabilizing streamwise pressure gradient leads to a sudden steep rise in turbulence level [14, 19].

In general, the agreement between experimental results of different authors is quite satisfactory in the wall jet region, whereas larger discrepancies occur in the stagnation zone, probably because of different turbulence levels at the nozzle exit. These discrepancies are of minor importance for the integral average transfer coefficients, which are of predominant technical interest.

Several theoretical or semiempirical approaches combining previously existing stagnation flow [9] and wall jet [8, 10-12, 25] analyses or directly applying boundary layer theory were carried out for single axisymmetric [26-29] and plane [6, 30-32] impinging jets. They did not succeed, however, in predicting the

© 1983 Hemisphere Publishing Corporation

observed nonmonotonic variation of the transfer coefficients for smaller nozzle-to-plate distances. Only for laminar impinging jets could relatively good agreement between theoretical and some experimental results [6, 33, 34] be achieved.

Wolfshtein [35] applied a numerical method [36] to solve systems of elliptic partial differential equations for the problem of impinging flow from a single slot nozzle. The system of equations must be closed by more or less arbitrary hypotheses on the interrelation between the time averaged products of turbulent fluctuating components ($v'v', v'p', v'T'$, for example) and the mean values of velocities, pressure, temperatures, and so on. The method yields plenty of detailed information on the whole flow field: streamlines, lines of equal vorticity, isotherms, and lines of equal turbulence energy. Unfortunately, the computations were carried out only for one fixed relative nozzle-to-plate distance, $H/B = 8$. Nusselt numbers are in reasonable agreement with those measured by Gardon and Akfirat [20]. Their lateral variation, however, deviates significantly from the measured curves, especially for the lower Reynolds numbers.

Recently a group of researchers at McGill University, Montreal, Canada, has tried to improve these numerical prediction methods. including the effects of suction through the impingement surface and temperature-dependent physical properties [37–40].

(b) Arrays of round and slot nozzles

Local measurements of heat and mass transfer coefficients for impinging flow from regular arrays of round nozzles (ARN) [18], single rows of round nozzles [41], and arrays of parallel slot nozzles [20, 22] show qualitatively similar results as from single nozzles. Additionally, there may occur further peaks in the lateral variation of the transfer coefficients where the wall jets of adjacent nozzles impinge upon each other to form secondary stagnation zones.

In many cases the local variation of the transfer coefficients will depend not only on the lateral coordinate x (or the radial r) but also on the transverse coordinate y (see Fig. 3), namely, when the gas cannot be led off directly upward between the nozzles but flows symmetrically to both sides (parallel to the slots in the $\pm y$ directions) over the width of the material. Clearly this outlet stream will influence the whole flow field. The smaller the ratio of the outlet flow area F_A (hatched area in Fig. 3) to the nozzle exit cross section $B\ell$ (for slot nozzles), the larger the outlet flow velocity u and the less uniformly the heat transfer coefficients will be distributed over the width of the material. This influence of the outlet flow conditions is treated in detail in [16 (pp. 27–40)].

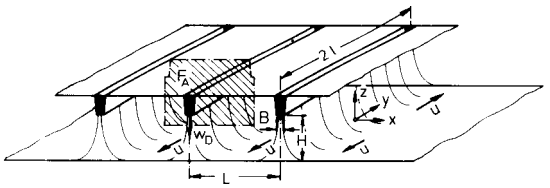

Figure 3 Array of slot nozzles with the outlet flow laterally over the edges of the sheet.

C. Average transfer coefficients

For practical engineering calculations, integral mean heat and mass transfer coefficients are needed:

$$\bar{\alpha} = \frac{1}{A}\iint_{(A)} \alpha dA;\ \bar{\beta} = \frac{1}{A}\iint_{(A)} \beta dA \qquad (3)$$

Equation (3) can be specified for the SRN,

$$\bar{\alpha} = \frac{2}{r^2}\int_0^r \alpha(r')\, r'\, dr' \qquad (4)$$

and for the SSN,

$$\bar{\alpha} = \frac{1}{x}\int_0^x \alpha(x')\, dx' \qquad (5)$$

For single round and slot nozzles, the average heat transfer coefficients, Eqs. (4) and (5), and the corresponding average mass transfer coefficients may be described in the following dimensionless form:

$$\overline{Nu} = F\left(\mathrm{Re}, \mathrm{Pr}, \frac{r}{D}, \frac{H}{D}\right) \qquad (6)$$

$$\overline{Sh} = F\left(\mathrm{Re}, \mathrm{Sc}, \frac{r}{D}, \frac{H}{D}\right) \qquad (7)$$

(for slot nozzles with x/S, H/S instead of r/D, H/D). The characteristic length in Nu, Sh, and Re is chosen to be the diameter D for round nozzles, or the hydraulic diameter S = 2B for slot nozzles.

For arrays of nozzles, the averaging in Eq. (3) must be carried out over those parts of the surface area attributed to one nozzle. For regularly spaced ARNs, these parts are squares with edge lengths L or regular hexagons with edge lengths $L/2$ (see Fig. 4). The relative nozzle area f is given by the ratio of the nozzle exit cross section to the area of the square or the hexagon attached to it:

$$f = \frac{(\pi/4)D^2}{A_{\text{square (hexagon)}}} \qquad (8)$$

© 1983 Hemisphere Publishing Corporation

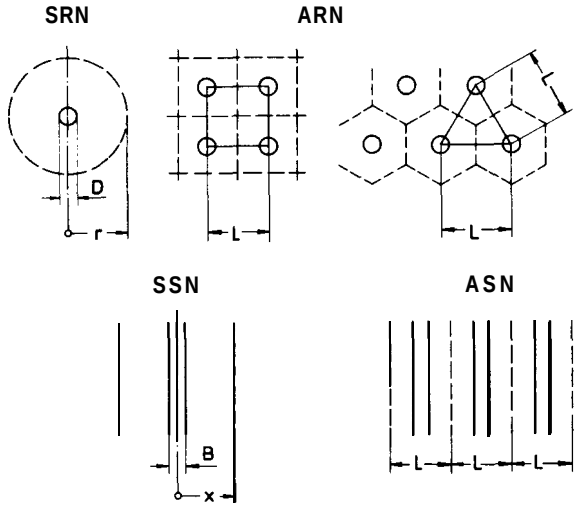

Figure 4 The spatial arrangement of nozzles in regularly spaced arrays.

The radius r in Eqs. (6) and (7) may be replaced by the radius R_T of a circle enclosing the same area as the square or the hexagon: $R_T = D/\sqrt{4f}$.

For ASNs, the integration in Eq. (5) is from x = 0 to x = X with $X = L/2$. This can also be expressed in terms of the relative nozzle area,

$$f = \frac{B\ell}{(L\ell)} = \frac{S}{(2L)} \tag{9}$$

In this case $X = S/4f$.

Thus, for arrays of nozzles, the relative distance from the stagnation point may be replaced by a function of the relative nozzle area:

$$\left(\frac{r}{D}\right)_{\text{ARN}} \triangleq \frac{1}{(4f)^{1/2}} \tag{10}$$

$$\left(\frac{x}{S}\right)_{\text{ASN}} \triangleq \frac{1}{4f} \tag{11}$$

In Table 1 the various expressions for the relative nozzle area f are listed for single nozzles and regularly spaced arrays of nozzles.

(a) Single nozzles

I. Single round nozzles

Heat and mass transfer data for impinging jets from single round nozzles (SRNs) [14, 17, 18, 42, 43] (see Fig. 5) have been correlated by Schlünder and Gnielinski [14] by the empirical equation

$$\left(\frac{\overline{\text{Nu}}}{\text{Pr}^{0.42}}\right)_{\text{SRN}} = \left(\frac{\overline{\text{Sh}}}{\text{Sc}^{0.42}}\right)_{\text{SRN}} = G\left(\frac{r}{D}, \frac{H}{D}\right) F(\text{Re}) \tag{12}$$

Table 1 The relative nozzle area in terms of geometric dimensions of nozzle and plate arrangements

	SRN	$\text{ARN}_\triangle$	$\text{ARN}_\square$	SSN	ASN
f	$\frac{1}{4}\left(\frac{D}{r}\right)^2$	$\frac{\pi}{2\sqrt{3}}\left(\frac{D}{L}\right)^2$	$\frac{\pi}{4}\left(\frac{D}{L}\right)^2$	$\frac{1}{4}\frac{S}{x}$	$\frac{B}{L}$

with

$$G\left(\frac{r}{D}, \frac{H}{D}\right) = \frac{D}{r}\frac{1 - 1.1D/r}{1 + 0.1(H/D - 6)D/r} \tag{12a}$$

The function $F(\text{Re})$, which has been given graphically by the authors [14], may be calculated from

$$F(\text{Re}) = 2\left[\text{Re}\left(1 + \frac{\text{Re}^{0.55}}{200}\right)\right]^{1/2} \tag{12b}$$

The range of validity of Eq. (12) is

$2\,000 \leqslant \text{Re} \leqslant 400\,000$

$2.5 \leqslant \frac{r}{D} \leqslant 7.5 \qquad (0.04 \geqslant f \geqslant 0.004)$

$2 \leqslant \frac{H}{D} \leqslant 12$

II. Single slot nozzles

The mass transfer data for single slot nozzles (SSNs) of Schlünder et al. [15] were correlated by the following empirical equation:

$$\left(\frac{\overline{\text{Sh}}}{\text{Sc}^{0.42}}\right)_{\text{SSN}} = \left(\frac{\overline{\text{Nu}}}{\text{Pr}^{0.42}}\right)_{\text{SSN}} = \frac{1.53\,\text{Re}^{m}(x/S, H/S)}{x/S + H/S + 1.39}$$

$$m = 0.695 - \left[\frac{x}{S} + \left(\frac{H}{S}\right)^{1.33} + 3.06\right]^{-1} \tag{13}$$

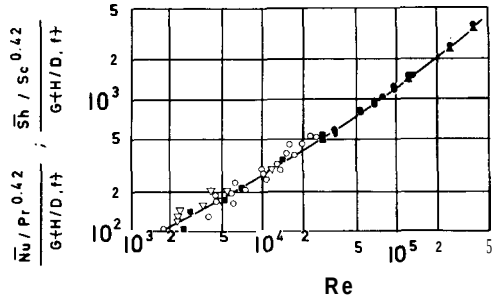

Figure 5 Heat and mass transfer between a circular plate and an impinging jet from a single round nozzle [14]. • Schliinder and Gnielinski, ▲ Petzold, • Gardon and Cobonpue, ▽ Brdlick and Savin, ○ Smirnov et al.

© 1983 Hemisphere Publishing Corporation

The range of validity is

$3\,000 \leqslant \mathrm{Re} \leqslant 90\,000$

$2 \leqslant \frac{x}{S} \leqslant 25 \qquad (0.125 \geqslant f \geqslant 0.01)$

$2 \leqslant \frac{H}{S} \leqslant 10$

The exponent of Re is dependent on the geometric variables and varies from 0.56 to 0.68 in the given range of validity. Equation (13) fits nearly all data of Schlünder et al. [15] within ±15%, as shown in Fig. 6.

(b) Arrays of nozzles

1. Arrays of round nozzles

The average heat and mass transfer coefficients for impinging flow from regular (square or hexagonal) arrays of round nozzles (ARNs) may be calculated from [16, 44]

$$\left(\frac{\overline{\mathrm{Sh}}}{\mathrm{Sc}^{0.42}}\right)_{\mathrm{ARN}} = \left(\frac{\overline{\mathrm{Nu}}}{\mathrm{Pr}^{0.42}}\right)_{\mathrm{ARN}}$$

$$= K\left(\frac{H}{D}, f\right) \frac{\sqrt{f}\,(1 - 2.2\sqrt{f})}{1 + 0.2\,(H/D - 6)\sqrt{f}}\,\mathrm{Re}^{2/3} \qquad (14)$$

with $K(H/D, f)$ from

$$K\left(\frac{H}{D}, f\right) = \left[1 + \left(\frac{H/D}{0.6}\sqrt{f}\right)^6\right]^{-0.05}$$

The range of validity is

$2\,000 \leqslant \mathrm{Re} \leqslant 100\,000$

$0.004 \leqslant f \leqslant 0.04$

$2 \leqslant \frac{H}{D} \leqslant 12$

Figure 7 shows a comparison with experimental data from [2, 44 to 47].

II. Arrays of slot nozzles

Average heat or mass transfer coefficients for impinging flow from arrays of slot nozzles (ASNs) may be found from [16, 48]:

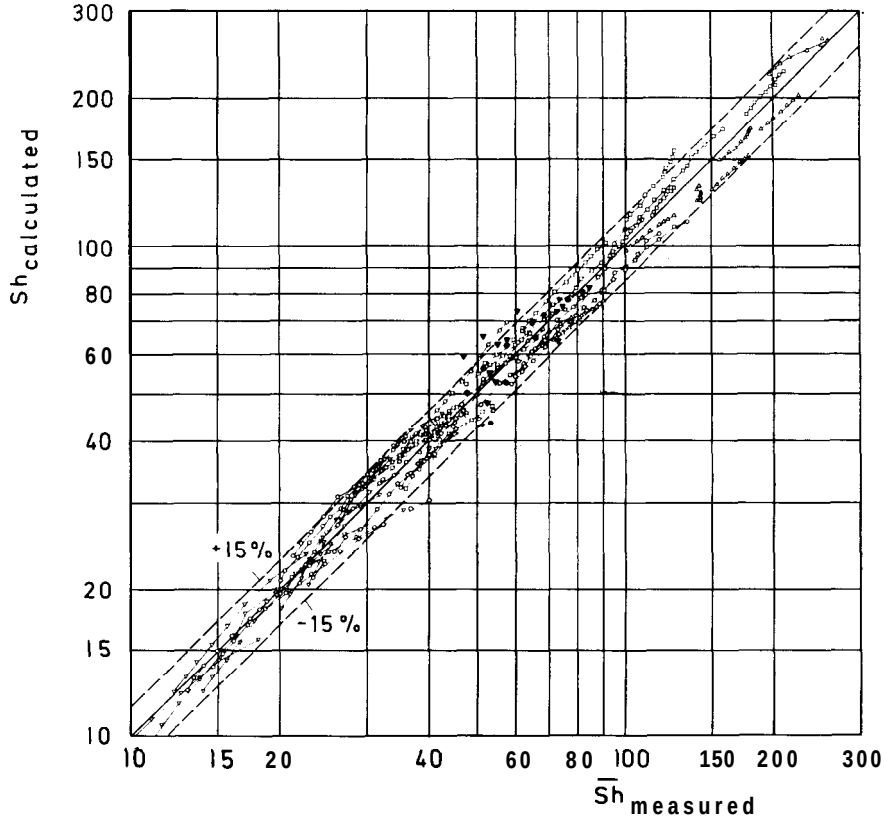

Figure 6 Mass transfer for impinging flow from single slot nozzles [15]. Comparison between measured Sherwood numbers and those calculated from Eq. (13). △ B = 20 mm, □ 10 mm, ○ 5 mm, ▽ 2 mm; Gardon and Akfirat ▼ $B = 3.2$ mm, Korger and Krizek ● $B = 5$ mm.

© 1983 Hemisphere Publishing Corporation

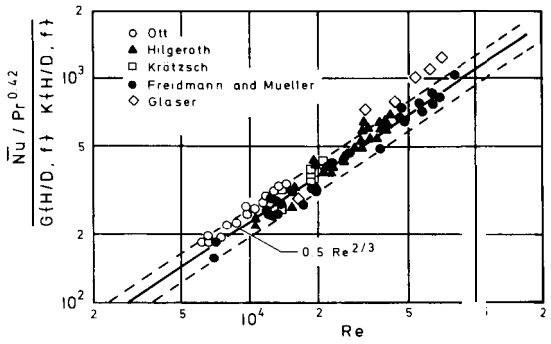

Figure 7 Heat transfer for impinging flow from arrays of round nozzles [16, 44]. Comparison of experimental data with Eq. (14).

$$\left(\frac{\overline{Sh}}{Sc^{0.42}}\right)_{ASN} = \left(\frac{\overline{Nu}}{Pr^{0.42}}\right)_{ASN} = \frac{2}{3} f_0^{3/4} \left(\frac{2\,Re}{f/f_0 + f_0/f}\right)^{2/3} \tag{15}$$

with $f_0\ (H/S) = [60 + 4(H/S-2)^2]^{-1/2}$.

The range of validity is

$1\,500 \leqslant Re \leqslant 40\,000$

$0.008 \leqslant f \leqslant 2.5 f_0\ \left(\frac{H}{S}\right)$

$1 \leqslant \frac{H}{S} \leqslant 40$

As shown by Fig. 8, this equation represents the author s own data within about ±15%. Most of the data available from other investigators [20, 22, 47, 49, 50] are also in reasonable agreement with this correlation (see Fig. 9).

D. Optimal spatial arrangements of nozzles

Here and in the following, the term optimal spatial arrangement means a combination of the geometric variables that yields the highest average transfer coefficient for a given blower rating per unit area of transfer surface. For uniformly spaced arrays of nozzles with good outlet flow conditions, there are always three independent geometric variables: (1) nozzle diameter ***D*** (or slot width ***B***), (2) nozzle-to-nozzle spacing ***L*** (see Table 1 and Fig. 4), (3) nozzle-to-plate distance ***H.***

The mean nozzle exit velocity $\bar{w}$ is to be expressed as a function of the blower rating per unit area of transfer surface ***P:***

$$P = \Delta p \frac{V}{A}$$

$$\Delta p = \xi \left(\frac{\rho}{2}\right) \bar{w}^2 \qquad \bar{w} = \left(\frac{2P}{\xi \rho f}\right)^{1/3} \tag{16}$$

$$\dot{V} = \bar{w} f A$$

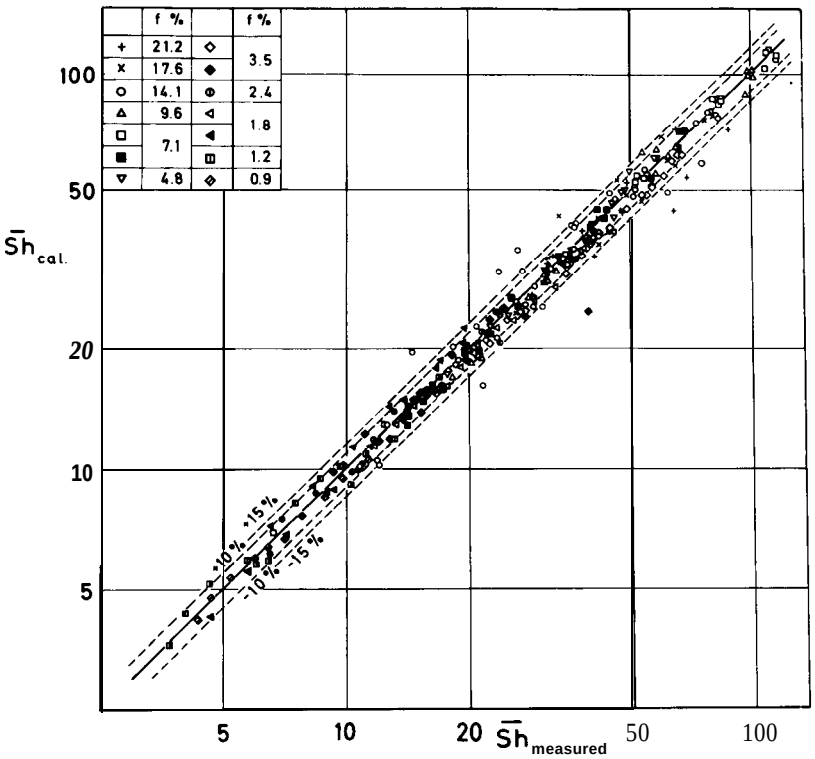

Figure 8 Mass transfer data from [48] for arrays of slot nozzles compared with Eq. (15).

© 1983 Hemisphere I blishing Corporation

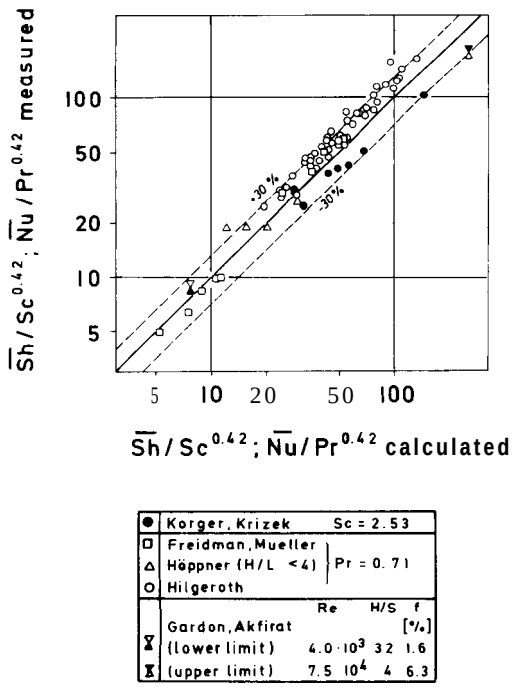

Figure 9 Heat and mass transfer data from various authors compared with Eq. (15). Arrays of slot nozzles.

The pressure loss coefficient ξ is considered to be the sum of all the flow resistances between the blower and the nozzle exit,

$$\xi = \sum_i \xi_i \left(\frac{fA}{a_i}\right)^2 \tag{17}$$

where fA is the total nozzle exit cross-sectional area, and the a_i are the cross-sectional areas of the ducts connecting the blower with the array of nozzles. Most of the flow resistances will be independent of the flow velocity, so their sum may be considered to be a constant.

One of the three lengths involved in the problem must be preset, otherwise one will find that scaling down all three lengths simultaneously results in monotonically increasing transfer coefficients. To determine the optimal spatial arrangement, in the equations for the mean heat and mass transfer coefficients to impinging flow from arrays of nozzles [Eqs. (14) and (15)], the nozzle exit velocity (in the Reynolds number) is replaced by the $\bar{w}$ from Eq. (16). As a result, the mean transfer coefficients are described in terms of the relative blower rating P and the three lengths. According to the choice of the preset length, the optimization problem is solved under three different secondary conditions [D (or B) = const; L = const; H = const], consequently yielding different optimal spatial arrangements [48]. The most important of these three possible secondary conditions to preset is the nozzle-to-plate distance H. A certain minimum distance H will often be imposed by constructional considerations, for example to avoid any contact with the nozzles when the sag of the material varies. Only this secondary condition

$$H = \text{const}$$

will be treated in the following discussion.

Equations (14) and (15), with $\bar{w}$ replaced by Eq. (16), will be reorganized such that the left-hand side, besides the mean transfer coefficient $\bar{\alpha}$ (or $\bar{\beta}$), contains only those parameters that may be considered constant (P, H, ξ, and physical properties):

$$\frac{(\bar{\alpha}H/\lambda)/\mathrm{Pr}^{0.42}}{\{[2P/(\xi\rho)]^{1/3}H/\nu\}^{2/3}} = G_H\left(f, \frac{H}{S}\right) \tag{18}$$

On the right-hand side there will remain a function of the geometric variables alone. This function, G_H, of course can be represented in terms of other sets of two geometric ratios, for example,

$$G_H\left(\frac{D}{H}, \frac{L}{H}\right)_{\mathrm{ARN}} \qquad G_H\left(\frac{B}{H}, \frac{L}{H}\right)_{\mathrm{ASN}}$$

For the ARN one obtains from Eq. (14)

$$G_H\left(f, \frac{H}{D}\right)_{\mathrm{ARN}} = \frac{(H/D)^{1/3}}{f^{2/9}} K\left(f, \frac{H}{D}\right) \sqrt{f}\,\frac{1-2.2\sqrt{f}}{1+0.2(H/D-6)\sqrt{f}}$$

$$K\left(f, \frac{H}{D}\right) = \left[1+\left(\frac{H/D}{0.6/\sqrt{f}}\right)^6\right]^{-0.05} \tag{19}$$

and for the ASN from Eq. (15)

$$G_H\left(f, \frac{H}{S}\right)_{\mathrm{ASN}} = \frac{(H/S)^{1/3}}{f^{2/9}}\frac{2}{3} f_0^{3/4}\left(\frac{2}{f/f_0 + f_0/f}\right)^{2/3}$$

$$f_0\left(\frac{H}{S}\right) = \left[60 + 4\left(\frac{H}{S}-2\right)^2\right]^{-1/2} \tag{20}$$

The functions in Eqs. (19) and (20) each possess an absolute maximum, the position of which may be determined by setting their first derivatives equal to zero [16, 48]. From this the optimal spatial arrangement for an array of round nozzles was found to be

$$f_{\mathrm{opt}} = 0{,}015\,2$$

$$\left(\frac{H}{D}\right)_{\mathrm{opt}} = 5.43$$

$$\max G_H = G_H\left[\left(\frac{H}{D}\right)_{\mathrm{opt}}, f_{\mathrm{opt}}\right] = 0.385 \qquad \text{(ARN)}$$

© 1983 Hemisphere Publishing Corporation

and for an array of slot nozzles the optimal arrangement becomes

$f_{opt} = 0.071\ 8$

$\left(\frac{H}{S}\right)_{opt} = 5.037$

$$\max\ G_H = G_H\left[\left(\frac{H}{S}\right)_{opt}, f_{opt}\right] = 0.355 \qquad \text{(ASN)}$$

The transfer coefficients that are obtained with the optimal ARN are about 8% higher than those for the optimal ASN, provided that the blower ratings, the pressure loss coefficients, and the nozzle-to-plate distances are equal in both cases. The nozzle exit velocities ratio is

$$\frac{\bar{w}_{\text{ARN, opt}}}{\bar{w}_{\text{ASN, opt}}} = \left(\frac{f_{\text{opt, ASN}}}{f_{\text{opt, ARN}}}\right)^{1/3} = \frac{1.68}{1}$$

and the required volumetric flow rates are related to each other by

$$\frac{\dot{V}_{\text{ARN, opt}}}{\dot{V}_{\text{ASN, opt}}} = \left(\frac{f_{\text{opt, ARN}}}{f_{\text{opt, ASN}}}\right)^{2/3} = \frac{1}{2.82}$$

As a result, slot nozzles should be used preferentially if the material does not allow for high impact velocities, as for example in film drying.

Since the optimal spatial arrangements were derived for preset nozzle-to-plate distance ***H,*** it would be much more convenient to give the optimal dimensions in multiples of ***H.*** Rewriting the previous expressions in this way yields for the **ARN:**

Optimal nozzle diamter $D_{opt} = 0.184H$

Optimal spacing

(Hexagonal array) $L_{opt} = 1.4238$

(Orthogonal array) $L_{opt} = 1.324H$

and for the ASN

Optimal (hydraulic) nozzle diameter $S_{opt} = 0.199H$

$(= 2B_{opt})$

Optimal spacing $L_{opt} = 1.383H$

Expressed in these terms, the optimal arrangements are described by nearly the same ratios for both round and slot nozzles. With a reasonable degree of approximation one may use the following rule of thumb for an optimal arrangement valid for both types of nozzles:

$$S_{opt} \approx \tfrac{1}{5}H \qquad (21)$$

$$L_{opt} \approx \tfrac{7}{5}H \qquad (22)$$

(with S = ***D*** for round and S = ***2B*** for slot nozzles).

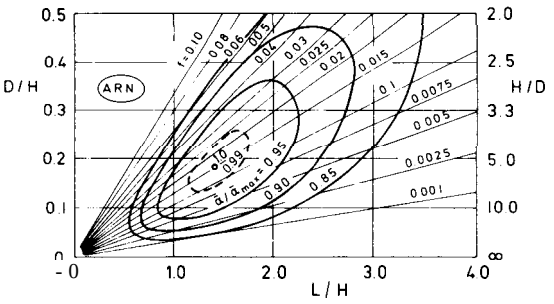

Figure 10 Positions of the optimal spatial arrangements for arrays of round nozzles [**16**].

Using these optimal relations, the transfer coefficients may be calculated from the following simple equations:

$$\left(\frac{\bar{\alpha}H}{\lambda}\,\mathrm{Pr}^{-0.42}\right)_{\text{ARN, max}} = \left(\frac{\bar{\beta}H}{\delta}\,\mathrm{Sc}^{-0.42}\right)_{\text{ARN, max}}$$

$$= 0.16\left(\frac{\bar{w}H}{\nu}\right)^{2/3} \qquad \left(D = \frac{H}{5},\ L = \frac{7H}{5}\right) \qquad (23)$$

$$\left(\frac{\bar{\alpha}H}{\lambda}\,\mathrm{Pr}^{-0.42}\right)_{\text{ASN, max}} = \left(\frac{\bar{\beta}H}{\delta}\,\mathrm{Sc}^{-0.42}\right)_{\text{ASN, max}}$$

$$= 0.20\left(\frac{\bar{w}H}{\nu}\right)^{2/3} \qquad \left(B = \frac{H}{10},\ L = \frac{7H}{5}\right) \qquad (24)$$

Choosing diameters and spacings different from the optimal diminishes the transfer coefficients by the ratio

$$\frac{\bar{\alpha}}{\bar{\alpha}_{max}} = \frac{\bar{\beta}}{\bar{\beta}_{max}} = \frac{G_H(S/H,\ L/H)}{G_H(S_{opt}/H;\ L_{opt}/H)} \qquad (25)$$

The functions in Eq. (25) are plotted in the form of contour lines in Figs. 10 and 11 to give a map showing the position, the extent, and the slopes of the transfer coefficient hill. For convenience, the coordinates f and ***H/S*** (or ***H/D)*** are also shown in these figures.

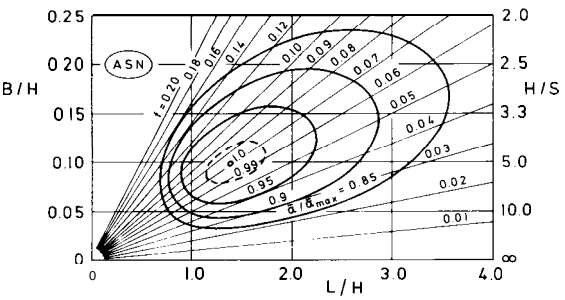

Figure 11 Positions of the optimal spatial arrangements for arrays of slot nozzles [**16**].

© 1983 Hemisphere I blishing Corporation

One may also consider these maps to show a blower rating trough for a given transfer coefficient. The point $\bar{\alpha}/\bar{\alpha}_{max} = 1$ then becomes $P/P_{min} = 1$, and the lines $\bar{\alpha}/\bar{\alpha}_{max} = \text{const}$ have to be marked in values of P/P_{min}, which may be calculated from $(P/P_{min}) = (\bar{\alpha}/\bar{\alpha}_{max})^{-9/2}$ [see Eq. (18)]:

$\bar{\alpha}/\bar{\alpha}_{max}$	1	0.99	0.95	*0.90*	*0.85*
P/P_{min}	1	1.05	1.26	1.61	*2.08*

Thus, with an array of nozzles, the geometric data of which lie outside the contour line $\bar{\alpha}/\bar{\alpha}_{max} = 0.85$, more than twice the blower rating would be required to reach the same transfer coefficient attainable with the optimal arrangement.

Nomenclature for Section 2.5.6 appears at the beginning of Part 2.

REFERENCES FOR SECTION 2.6.5

1. Schrader, H., ***Trocknung feuchter Oberflächen mittels Warmluftstrahlen,*** VDI-Forschungsh. 484, VDI-Verlag, Diisseldorf, 1961.
2. Glaser, H., Untersuchungen an Schlitz- und Mehrdüsenanordnungen bei der Trocknung feuchter Oberflächen durch Warmluftstrahlen, ***Chem. Ing. Tech.,*** vol. 34, pp. 200-207, 1962.
3. Glaser, H., Strömung und Stoffiibertragung bei der Diisentrocknung, ***Melliand Textilber.,*** vol. 44, pp. 292-295, 400-404, 1963.
4. Lohe, H., Wärme- und Stofftransport beim Aufblasen von Gasstrahlen auf Fliissigkeiten, ***Fortschr.*** Ber. ***VDI-Z.,*** Reihe 3, No. 15, 1967.
5. Petzold, K., Experimentelle Untersuchung zum brtlichen Wärmeübergang -an der senkrecht angeströmten Platte, Dissertation, Technische Universität Dresden, 1968.
6. Kumada, M., and Mabuchi, I., Studies on the Heat Transfer of Impinging Jet, ***Bull. JSME, vol. 13,*** pp. 77-85, 1970.
7. Romanenko, P. N., and Davidzon, M. I., Heat Transfer in the Zone of Accelerated Flow During the Normal Impingement of a System of Two-Dimensional Jets onto a Flat Surface, ***Znt. Chem. Eng., vol.*** 10, pp. 223-228, 1970.
8. Glauert, M. B., The Wall Jet, ***J. Fluid Mech.,*** vol. 1, pp. 625-643, 1956.
9. Schlichting, H., ***Grenzschichttheorie,*** 3d ed., G. Braun, Karlsruhe, 1958.
10. Seban, R. A., and Back, L. H., Velocity and Temperature Profiles in a Wall Jet, ***Znt. J. Heat Mass Transfer, vol. 3,*** pp. 255-265, 1961.
11. Schwartz, W. H., and Cosart, W. P., The Two-Dimensional Turbulent Wall Jet, ***J. Fluid Mech., vol. 10,*** pp. 481–495, 1961.
12. Bakke, P., An Experimental Investigation of a Wall Jet, ***J. Fluid Mech.,*** vol. 2, pp. 467-472, 1957.
13. Pötke, W., Wärme- und Stoffiibergang bei der Prallströmung von Freistrahlen mit und ohne Drall, Dissertation, Technische Universität Clausthal, 1974.
14. Schliinder, E. U., and Gnielinski, V., Wärme- und Stoffiibertragung zwischen Gut und aufprallendem Düsenstrahl, ***Chem. Zng. Tech., vol. 39,*** pp. 578-584, 1967.
15. Schliinder, E. U., Krötzsch, P., and Hennecke, F. W., Gesetzmässigkeiten der Wärme- und Stoffiibertragung bei der Prallströmung aus Rund- und Schlitzdüsen, ***Chem. Ing. Tech.,*** vol. 42, pp. 333-338, 1970.
16. Martin, H., Heat and Mass Transfer Between Impinging Gas Jets and Solid Surfaces, ***in Advances in Heat Transfer,*** ed. J. P. Hartnett and Th. F. Irvine, vol. 13, pp. l-60, Academic Press, New York, 1977.
17. Petzold, K., Experimentelle Untersuchung zum örtlichen Wärmeübergang an der senkrecht angeströmten Platte, ***Luft- Kältetech.,*** vol. 5, pp. 175-180, 1969.
18. Gardon, R., and Cobonpue, J., Heat Transfer Between a Flat Plate and Jets of Air Impinging on It, ***in International Developments in Heat Transfer,*** pp. 454–460, ASME, New York, 1962.
19. Gardon, R., and Akfirat, J. C., The Role of Turbulence in Determining the Heat-Transfer Characteristics of Impinging Jets, ***Znt. J. Heat Mass Transfer,*** vol. 8, pp. 1261-1272, 1965.
20. Gardon, R., and Akfirat, J. C., Heat Transfer Characteristics of Impinging Two-Dimensional Air Jets, ***J. Heat Transfer,*** vol. 88, pp. 101-108, 1966.
21. Korger, M., and Křížek, F., Heat and Mass Transfer during Impingement of a Jet of Air from a Single Round Nozzle onto a Plate (in German), ***Verfahrenstechnik, vol. 7,*** pp. 376-381, 1973.
22. Korger, M., and Křížek, F., Mass Transfer Coefficient in Impingment Flow from Slotted Nozzles, ***Znt. J. Heat Mass Transfer,*** vol. 9, pp. 337-344, 1966.
23. Korger, M., and Křížek, F., Die Stoffiibergangszahlen beim Aufprall schräger Flachstrahlen auf eine Platte, ***Verfahrenstechnik,*** vol. 6, pp. 223-228, 1972.
24. Rao, V. V., and Trass, O., Mass Transfer from a Flat Surface to an Impinging Turbulent Jet, Can. ***J. Chem. Eng., vol. 42,*** pp. 95-99, 1964.
25. Myers, G. E., Schauer, J. J., and Eustis, R. H., Heat Transfer to Plane Turbulent Wall Jets, ***J. Heat Transfer,*** vol. 85, pp. 209-214, 1963.
26. Kezios, S. P., Heat Transfer in the Flow of a Cylindrical Air Jet Normal to an Infinite Plane, Ph.D. thesis, Illinois Institute of Technology, Chicago, 1956.
27. Kim, T. S., Analysis of Flow Characteristics in Circular, Submerged, Impinging Jets, Ph.D. thesis, Illinois Institute of Technology, Chicago, 1967.

© 1983 Hemisphere Publishing Corporation

28. Nakatogawa, T., Nishiwaki, H., Hirata, M., and Torii, K., Heat Transfer of Round Turbulent Jet Impinging Normally on Flat Plate, *Proc. 4th Int. Heat Transfer Conf., Paris-Versailles,* vol. II, FC 5.2.
29. Sparrow, E. M., and Lee, L., Analysis of Flow Field and Impingement Heat/Mass Transfer Due to a Nonuniform Slot Jet, *J. Heat Transfer, vol.* 97, pp. 191-197, 1975.
30. Schauer, J. J., and Eustis, R. H., The Flow Development and Heat Transfer Characteristics of Plane Turbulent Impinging Jets, Tech. Rept. No. 3, Dept. Mech. Eng., Stanford University, Stanford, Calif., 1963.
31. Andreev, A. A., Dakhno, V. N., Savin, V. K., and Yudaev, B. N., Investigations *on* Heat Transfer in the Region of Accelerated Flow for Turbulent Normally Impinging Flow from a Slot Nozzle to a Plate (in Russian), *Inzh.-Fiz. Zh.,* vol. 18, pp. 631637, 1970.
32. Miyazaki, H., and Silberman, E., Flow and Heat Transfer on a Flat Plate Normal to a Two-Dimensional Laminar Jet Issuing from a Nozzle of Finite Height, *Znt. J. Heat Mass Transfer,* vol. 15, pp. 2097-2107, 1972.
33. Scholz, M. T., and Trass, O., Mass Transfer in a Nonuniform Impinging Jet, *AIChE J.,* vol. 15, pp. 82-96, 1970.
34. Sparrow, E. M., and Wong, T. C., Impingement Transfer Coefficients Due to Initially Laminar Slot Jets, *Znt. J. Heat Mass Transfer,* vol. 18, pp. 597-605, 1975.
35. Wolfshtein, M., Convection Processes in Turbulent Impinging Jets, Ph.D. thesis, Imperial College, London, 1968.
36. Gosman, A. D., Pun, W. M., Runchal, A, K., Spalding, D. B., and Wolfshtein, M., *Heat and Mass Transfer in Recirculating Flows,* Academic Press, New York, 1969.
37. Van Heiningen, A. R. P., Mujumdar, A. S., and Douglas, W. J. M., Numerical Prediction of Flow Field and Impingement Heat Transfer Under a Laminar Slot Jet, *J. Heat Transfer,* vol. 98, pp. 654-658, 1976.
38. Van Heiningen, A. R. P., Mujumdar, A. S., and Douglas, W. J. M., Flow and Heat Transfer Characteristics of a Turbulent Slot Jet Impinging on a Moving Permeable Wall, Symp. Turbulent Shear Flows, Penn State University, April 1977.
39. Obot, N. T., Mujumdar, A. S., and Douglas, W. J. M., Design Correlations for Heat and Mass Transfer Under Various Turbulent Impinging Jet Configurations, in *Dying* 80, ed. A. S. Mujumdar, vol. 1, sec. VI, Hemisphere, Washington, D.C., 1980.
40. Saad, N. R., Mujumdar, A. S., and Douglas, W. J. M., Heat Transfer Under Multiple Turbulent Slot Jets Impinging on a Flat Plate, in *Dying* 80 ed. A. S. Mujumdar, vol. 1, sec. VI, Hemisphere, Washington, D.C., 1980.
41. Koopman, R. N., and Sparrow, E. M., Local and Average Transfer Coefficients Due to an Impinging Row of Jets, *Znt. J. Heat Mass Transfer, vol. 19,* pp. 673-683, 1976.
42. Brdlick, P. M., and Savin, V. K., Heat Transfer Between an Axisymmetric Jet and a Plate Normal to the Flow (in Russian), *Inzh.-Fiz. Zh.,* vol. 8, pp. 146-155, 1965.
43. Smirnov, V. A., Verevochkin, G. E., and Brdlick, P. M., Heat Transfer Between a Jet and a Plate Held Normal *to* Flow, *Znt. J. Heat Mass Transfer,* vol. 2, pp. 1-7, 1961.
44. Krötzsch, P., Warms und Stoffiibergang bei Prallströmung aus Düsen- und Blendenfeldern, *Chem. Zng. Tech.,* vol. 40, pp. 339-344, 1968.
45. Ott, H. H., Warmeiibergang an einer durch Luftstrahlen gekiihlten Platte, *Schweiz. Bauzeitung,* vol. 79, pp. 834-840, 1961.
46. Hilgeroth, E., Warmeiibergang bei Düsenströmung senkrecht zur Austauschflache, *Chem. Ing. Tech.,* vol. 37, pp. 1264-1272, 1965.
47. Freidman, S. J., and Mueller, A. C., Heat Transfer to Flat Surfaces, *Proc. Gen. Discuss. Heat Transfer,* pp. 138-142, Inst. Mech. Eng., London, 1951.
48. Martin, H., and Schlünder, E. U., Optimierung von Scblitzdiisentrocknern auf Grund neuer Versuchsergebnisse über den Wärme- und Stoffiibergang in solchen Apparaten, *Chem. Ing. Tech., vol. 45,* pp. 290-294, 1973.
49. Höppner, G., Der mittlere Wärme- und Stoffiibergang bei der senkrechten Anblasung ebener isothermer Flächen mit turbulenten Einzelstrahlen und Strahlduschen, *Luft- Kältetech.,* vol. 6, pp. 283-289, 1970.
50. Hilgeroth, E., Warmeiibergang bei Schlitzdüsenströmung, *Chem. Ing. Tech.,* vol. 41, pp. 731-735, 1969.

© 1983 Hemisphere Publishing Corporation

2.5.7

Free convection around immersed bodies

S. W. Churchill

■ A difference in temperature between the surface of a body and the surrounding, unconfined fluid produces a gradient in density, which in turn generates fluid motion. This motion increases the rate of heat transfer between the body and the fluid over that corresponding to pure thermal conduction. The process of motion and heat transfer due to such motion is called free convection.

A difference in composition between the surface of the body and the surrounding fluid may also produce a gradient in density, hence fluid motion and enhanced transfer of species (mass transfer). Insofar as the net transfer of mass from the surface is small relative to the mass rate of flow, the rate of transfer of species can be inferred from the results herein for heat transfer. When a difference in temperature and a difference in composition both occur, the rates of heat and species transfer are affected by both differences.

Free convection may also occur as a result of other potential differences, such as surface tension and magnetic fields, but such special processes will not be considered here. Combined free and forced convection is discussed in Secs. 2.5.9 and 2.5.10.

A well-established theory has been developed for free convection in the laminar boundary-layer regime. It provides a priori predictions and a fundamental structure for the correlation of experimental results. The development of computing facilities and techniques has led to numerical solutions for even a wider range of flow and conditions within the laminar regime. Even so, many problems of intrinsic and practical interest remain unresolved.

The theory of turbulent free convection is less well established. Numerical solutions based on eddy diffusivities for momentum and heat transfer are currently at a critical stage of development, and results of increasing reliability and extent are to be expected.

Experimental data for free convection are generally less precise and accurate than for forced convection, owing to the slower rates of heat transfer and the associated difficulty of making measurements without disturbing the process.

Most theoretical models for free convection invoke the Boussinesq approximations of negligible viscous dissipation, negligible variation in pressure due to motion, and negligible variation in physical properties except for the density in the gravitational force, which is postulated to vary as

$$\rho = \frac{\rho_\infty}{1 + \zeta(T - T_\infty)} \tag{1}$$

where ρ = density, kg/m^3
T = temperature, K
ζ = coefficient of expansion with temperature, K^{-1}

The subscript ∞ indicates the free fluid. These idealizations have been examined, as noted subsequently, and found to be generally justifiable.

Boundary-layer theory additionally postulates that the velocity and temperature gradients are confined to a narrow band of fluid adjacent to the surface of the immersed body, and that diffusion of momentum and energy is negligible in the direction of flow. The conditions under which these assumptions are valid are examined herein.

Free convection from an isothermal or uniformly

© 1983 Hemisphere I blishing Corporation

heated vertical plate has received extensive theoretical and experimental attention because of its simplicity as well as because of its practical importance. The theoretical solutions for this geometry are generally based on the postulate of a plate of infinite width and semi-infinite length upward, immersed in a fluid of infinite extent, with no motion below the bottom edge of the plate. Despite these idealizations, the solutions are found to provide a useful structure for the correlation of experimental data. The same structure also proves useful for other geometries and conditions. Hence the theoretical solutions are examined first, then the experimental data.

A heated plate and upward flow are implied throughout for simplicity. Obviously, the results are applicable for a cooled plate and downward flow. Convection from inclined and horizontal plates is compared and contrasted with that from vertical plates. Finally, induced flow through heated channels with open ends is examined.

Free convection from bluff bodies is more complicated because of the separation of the streamlines and the formation of a wake or plume at the rear. Even so, boundary-layer theory is found to have an appreciable range of validity. Theoretical solutions for very weak convection have proved to be more successful for spheres and cylinders than for flat plates.

Several general reviews of free convection may be mentioned at the outset. Ostrach [1], in 1954, considered free convection within a more general survey. Schmidt [2], in 1961, reviewed free and natural convection with emphasis on recent advances. In 1965, Bansal [3] surveyed the work on steady free and natural convection. Churchill [4], in 1966, described progress in numerical methods for free and natural convection. Ede [5], in 1967, thoroughly reviewed the results for free convection from vertical plates. Morgan [6] has included free convection in a recent review of convection from cylinders.

A. Vertical plates

(a) Dimensionless groupings

For steady laminar free convection subject to the Boussinesq idealizations, it can readily be shown that

$$\mathrm{Nu} = \phi(\mathrm{Gr}, \mathrm{Pr}) \tag{2}$$

where the variables not previously mentioned are

$\mathrm{Nu} = \alpha x/\lambda$ = local Nusselt number at x

$\mathrm{Gr} = g\rho^2\zeta(T_w - T_\infty)x^3/\eta^2$ = Grashof number based on x

$\mathrm{Pr} = c_p\eta/\lambda$ = Prandtl number

$\phi(z)$ = function of z

α = local heat transfer coefficient, $\mathrm{W/m^2\ K}$

x = distance upward from bottom edge of plate, m

λ = thermal conductivity, W/m K

g = acceleration due to gravity, $\mathrm{m/s^2}$

T_w = temperature of surface, K

η = dynamic viscosity, Pa s

c_p = specific heat capacity at constant pressure, J/kg K

Any independent grouping such as

$$\mathrm{Nu} = \phi(\mathrm{Ra}, \mathrm{Pr}) \tag{3}$$

where $\mathrm{Ra} = \mathrm{Gr\ Pr} = g\rho^2 c_p\zeta(T_w - T_\infty)x^3/\eta\lambda$ = Rayleigh number based on x

is equally valid. The constraints imposed by the laminar-boundary model permit (see, for example, Hellums and Churchill [7]) reduction of Eqs. (1) and (2) to

$$\mathrm{Nu} = \mathrm{Gr}^{1/4}\phi(\mathrm{Pr}) \tag{4}$$

or

$$\mathrm{Nu} = \mathrm{Ra}^{1/4}\phi(\mathrm{Pr}) \tag{5}$$

Furthermore, it can be shown that in the limit as $\mathrm{Pr} \to 0$,

$$\mathrm{Nu} \to A\,\mathrm{Gr}^{1/4}\mathrm{Pr}^{1/2} = A(\mathrm{Ra\ Pr})^{1/4} = A\ \mathrm{Bq}^{1/4} \tag{6}$$

where A = a dimensionless constant dependent on the boundary conditions

$\mathrm{Bq} = \mathrm{Gr\ Pr}^2 = \mathrm{Ra\ Pr} = g\rho^2 c_p^2\zeta(T_w - T_\infty)x^3/\lambda^2$ = Boussinesq number based on x

Also, in the limit as $\mathrm{Pr} \to \infty$,

$$\mathrm{Nu} \to B(\mathrm{Gr\ Pr})^{1/4} = B\ \mathrm{Ra}^{1/4} \tag{7}$$

where B is a dimensionless constant dependent on the boundary conditions. Historically the forms involving the Grashof number have usually been chosen for correlation. However, as will be shown, all fluids except liquid metals are represented reasonably well by Eq. (7). The Rayleigh number is therefore more convenient for working correlations than the Grashof number, since the Prandtl number is then only a weak parameter.

Equation (7) can also be written in the more explicit form

$$\alpha\left[\frac{x\eta}{g\rho^2 c_p\lambda^3\zeta(T_w - T_\infty)}\right]^{1/4} = B \tag{8}$$

as suggested by Hellums and Churchill [7]. The unnamed group on the left side of Eq. (8) is obviously the characteristic one for laminar free convection of a large Prandtl number fluid. Equation (8) also has the advantage of revealing the relationship between α and the other individual variables.

If uniform heating rather than uniform surface temperature is specified, it is better to replace one or the other of the then dependent variables α and T_w by

© 1983 Hemisphere publishing Corporation

the heat flux $\dot{q}$ (in W/m^2) through the relationship defining the local heat transfer coefficient:

$$\alpha \equiv \frac{\dot{q}}{T_w - T_\infty} \tag{9}$$

If $T_w - T_\infty$ is replaced, Eq. (8) becomes, after rearrangement,

$$\alpha\left(\frac{x\eta}{g\rho^2 c_p \lambda^3 \zeta \dot{q}}\right)^{1/5} = B^{4/5} \tag{10}$$

and if α is replaced,

$$(T_w - T_\infty)\left(\frac{g\rho^2 c_p \lambda^3 \zeta}{\dot{q}^4 x\eta}\right)^{1/5} = \text{B-415} \tag{11}$$

The form corresponding to Eq. (7) is

$$\mathrm{Nu} = B^{4/5}\,\mathrm{Ra}^{*1/5} \tag{12}$$

where Ra* = Ra Nu = $g\rho^2 c_p \zeta \dot{q} x^4/\eta\lambda^2$
= modified Rayleigh number for uniform heating

This grouping has frequently been used to represent results for uniform heating but has the disadvantage of disguising the near equivalency of the results for uniform wall temperature (UWT) and uniform heat **flux (UHF)** when expressed in the form of Eq. (7) or (8).

As discussed by Ede [5] and Churchill [8], dimensional analysis is applicable to turbulent motion provided that one or more postulates are made with respect to the limiting behavior. Thus Jakob and Linke [9] asserted that α should be independent of x for large Ra, requiring Eq. (2) to reduce to

$$\mathrm{Nu} = \mathrm{Ra}^{1/3}\phi(\mathrm{Pr}) \qquad \text{for Ra} \to \infty \tag{13}$$

which can also be written as

$$\alpha\left[\frac{\eta}{g\rho^2 c_p \lambda^2 \zeta (T_w - T_\infty)}\right]^{1/3} = \phi\left(\frac{\eta c_p}{\lambda}\right) \qquad \text{for } x \to \infty \tag{14}$$

The further postulate that viscous and inertial forces are negligible for Pr → 0 and Pr → ∞ reduces Eq. (13) to

$$\mathrm{Nu} = \mathrm{C}\,\mathrm{Bq}^{1/3} \qquad \text{for Pr} \to 0,\ \mathrm{Bq} \to \infty \tag{15}$$

and

$$\mathrm{Nu} = \boldsymbol{E}\,\mathrm{Ra}^{1/3} \qquad \text{for Pr} \to \infty,\ \mathrm{Ra} \to \infty \tag{16}$$

where C and ***E*** are dimensionless constants dependent on the boundary conditions.

(b) Solutions and correlating equations for uniform wall temperature

I. Laminar regime

The following asymptotic solutions were derived by LeFevre [10] for the laminar boundary-layer regime:

$$\mathrm{Nu} = 0.600\,4\,\mathrm{Bq}^{1/4} \qquad \text{for Pr} \to 0 \tag{17}$$

and

$$\mathrm{Nu} = 0.502\,7\,\mathrm{Ra}^{1/4} \qquad \text{for Pr} \to \infty \tag{18}$$

The value of the constant A in Eq. (6) is thus 0.600 4 and that of ***B*** in Eqs. (6) and (7) is 0.502 7.

Ostrach [11] and others have obtained numerical solutions for intermediate Pr. These values are represented within 0.7% by the following empirical equation of Churchill and Usagi [12]

$$\mathrm{Nu} = 0.503(\mathrm{Ra}\,\psi(\mathrm{Pr}))^{1/4} \tag{19}$$

where

$$\psi(\mathrm{Pr}) = \left[1 + \left(\frac{0.492}{\mathrm{Pr}}\right)^{9/16}\right]^{-16/9} \tag{20}$$

Equations (19) and (20) provide a smooth interpolation between Eqs. (17) and (18). The coefficient 0.492 = (0.502 745/0.600 408) represents the central value of the Prandtl number for this system, and provides an explanation for the successful correlation of the data for most liquids and even air by Eq. (7), or the equivalent, with only slightly differing coefficients. As shown in the succeeding paragraphs, Eq. (20) proves to be a universal function for the dependence on Pr in natural convection in all boundary layers.

The integrated mean Nusselt number over x from 0 to L corresponding to Eq. (19) is

$$\overline{\mathrm{Nu}} = 0.670(\mathrm{Ra}_L\,\psi(\mathrm{Pr}))^{1/4} \tag{21}$$

Churchill and Chu [13] proposed this relationship for the thin laminar boundary-layer regime ($10^4 < \mathrm{Ra} < 10^9$). Failure for higher Ra_L would be expected because of the initiation of turbulence, and for lower Ra_L because of the invalidity of the postulates of boundary-layer theory near the starting edge. A generally accepted solution has not been developed for lower Ra_L, but the experimental data of Saunders [14] indicate a limiting value of 0.68 for Nu as $\mathrm{Ra}_L \to 0$. Churchill and Chu [13] used this result to construct the following correlating equation for all $\mathrm{Ra}_L < 10^9$:

$$\overline{\mathrm{Nu}} = 0.68 + 0.67(\mathrm{Ra}_L\,\psi(\mathrm{Pr}))^{1/4} \tag{22}$$

The corresponding expression for the local value is

$$\mathrm{Nu} = 0.68 + 0.503(\mathrm{Ra}\,\psi(\mathrm{Pr}))^{1/4} \tag{23}$$

© 1983 Hemisphere I blishing Corporation

Equation (22) is compared with experimental data in Fig. 1. A reasonable representation is demonstrated for $Ra_L < 10^9$ for all Pr including 0.025 (mercury). The data for mass transfer (large Sc) follow this expression even up to Ra = 4 X 10^{11}, suggesting that transition from laminar to turbulent motion is characterized by Gr_L rather than Ra_L. It should be noted that the data for free convection, particularly for low Ra_L, characteristically show more scatter than for forced convection, owing to stray fluid currents, and so on. Equation (21) is included in the figure to indicate the lower limit of applicability of thin-laminar bounday-layer theory.

Equations (19) and (23) are similarly compared with data for the local rate in Fig. 2. The band of values of Gryzagonidis [15] for Ra < 4 X 10^{-4} represents the effect of different configurations of the leading edge. The agreement is otherwise good for Ra < 10^9, above which transition to turbulent motion appears to occur.

II. Turbulent regime

A number of investigators, including Cebeci and Khattah [16], Plumb and Kennedy [17], and Lin and Churchill [18], have integrated the partial differential equations of conservation with arbitrary expressions for the eddy diffusivities for momentum and heat transfer to obtain theoretical expressions for the turbulent regime. Their results all indicate a dependence on Ra slightly greater than the 1/3 power and perhaps decreasing to the 1/3 power as Ra increases. The dependence on Pr is not yet resolved by such calculations. Bayley [19], Kutateladze [20], and others used Eq. (16) to correlate experimental data for the turbulent regime (Ra > 10^{12}). Churchill and Chu [13] utilized Eqs. (15) and (16) and the same central value of Pr as in (20) to obtain

$$\mathrm{Nu} = 0.15(\mathrm{Ra}\,\psi(\mathrm{Pr}))^{1/3} \tag{24}$$

The coefficient 0.15 was determined from experimental data.

III. Transition regime

Considerable uncertainty seems to exist regarding the transition from laminar to turbulent convection, even to the extent of the controlling dimensionless group. Sparrow et al. [21] computed the critical Grashof number for the onset of instability from the Orr-Sommerfeld equation and found it to increase with Pr. Their values, however, are far below those observed for

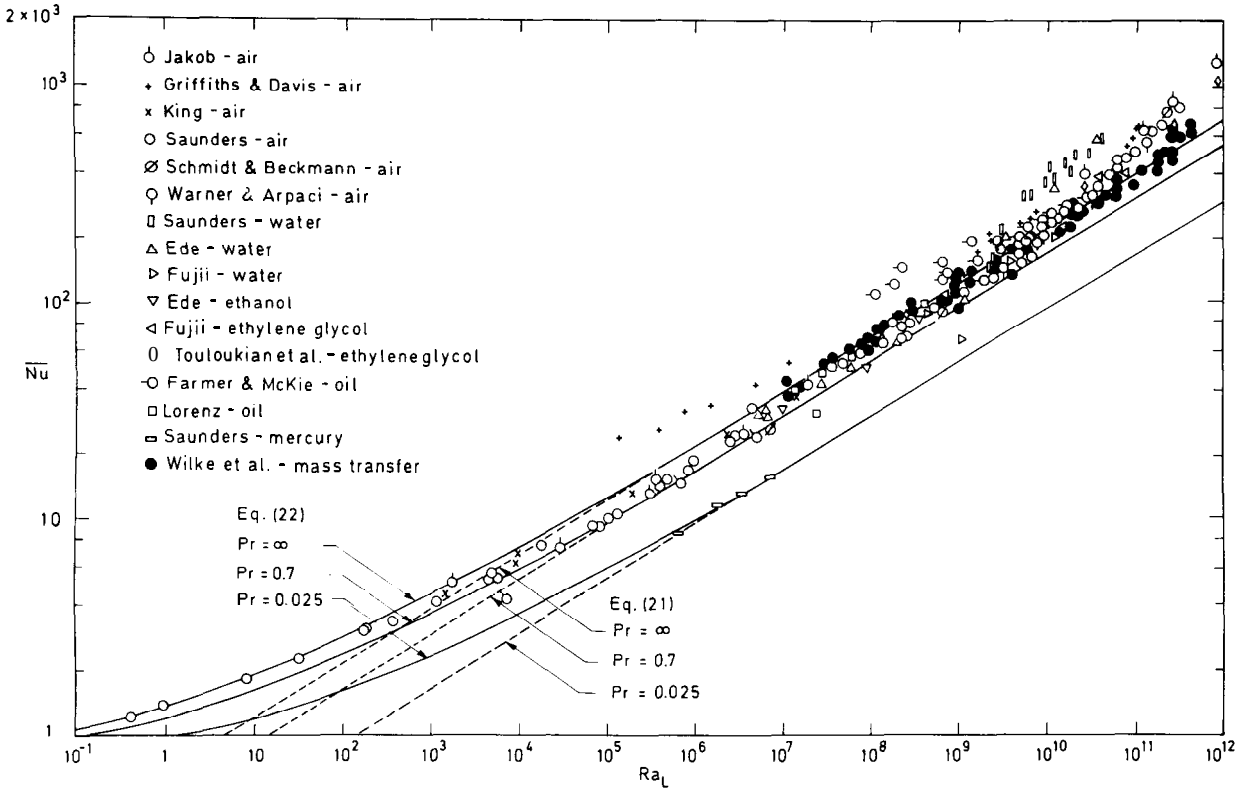

Figure 1 Comparison of Eq. (22) with experimental data for the mean Nusselt and Sherwood numbers in laminar free convection from isothermal, vertical plates.

© 1983 Hemisphere Publishing Corporation

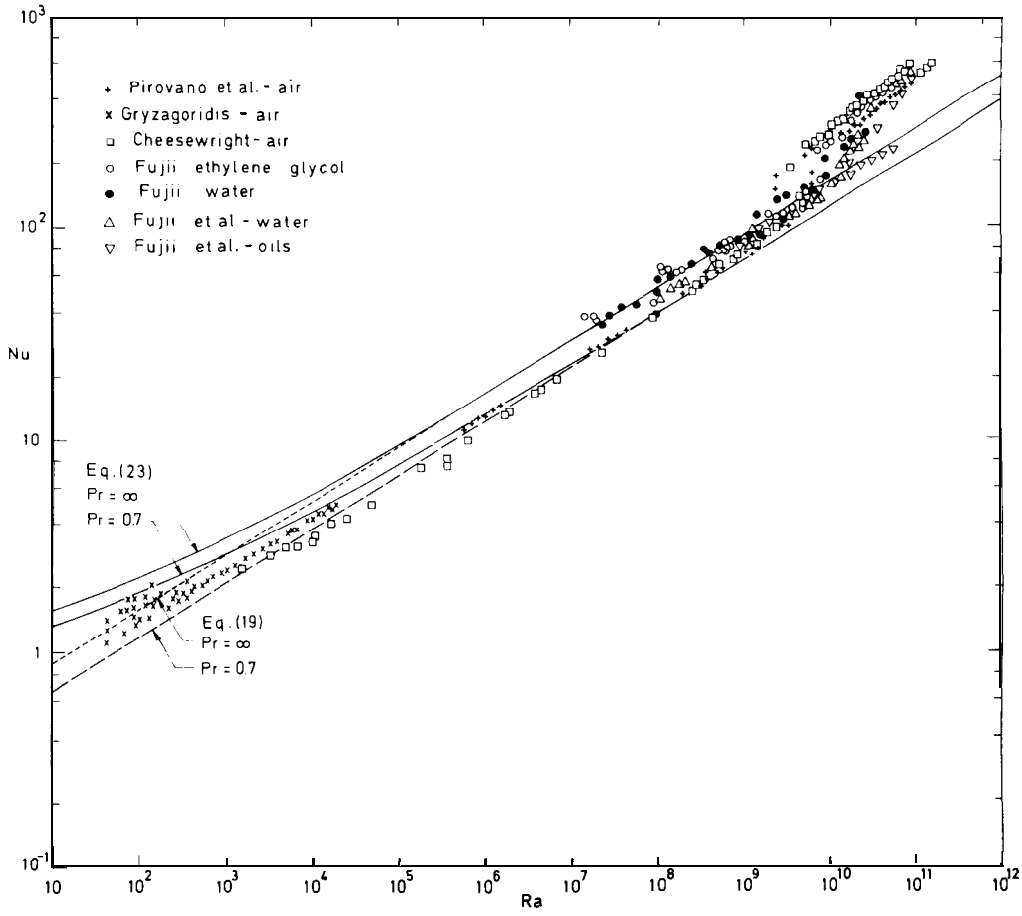

Figure 2 Comparison of Eq. (23) with experimental data for the local **Nusselt** number in laminar free convection from isothermal, vertical plates.

the transition in Nu. This result was confirmed by Fujii [22], who observed the formation of instabilities at a lower value of Ra than the transition in Nu. Klyacho [23] proposed Ra = 2 X 10^8 as the criterion based on the intersection of a particular pair of equations for $\overline{Nu}$ for laminar and turbulent flow. As indicated in the prior and subsequent figures, the bulk of the experimental data indicate that the transition in Nu begins about Gr = 10^9 and is complete by about Gr = 10^{10}.

If the transition is postulated to begin at Gr = 10^9, Eqs. (19) and (22) can be combined to obtain the following expression for both the transition and the turbulent regime:

$$Nu = 89.4\ Pr^{1/4}\psi^{1/4}(Pr) + 0.15(Ra^{1/3} - 1000\ Pr^{1/3})\psi^{1/3}(Pr) \quad (25)$$

Integration of these same equations yields the corresponding expression for the mean value:

$$\overline{Nu} = 119.3\ Pr^{1/4}\psi^{1/4}(Pr) + 0.15(Ra_L^{1/3} - 1\,000\ Pr^{1/3})\psi^{1/3}(Pr) \quad (26)$$

Equations (25) and (26) are compared with experimental data in Figs. 3 and 4, respectively. Equations (19) and (24) are included in Fig. 3 as asymptotes, and similarly, Eqs. (21) and (24) in Fig. 4. The discrepancies in the transition regime are not unexpected, since transition depends on secondary variables, such as free-stream turbulence and surface roughness. The local values of Fujii et al. [24] for spindle oil (Pr = 77-170) and for Mobiltherm oil (Pr = 260-2 600) fall below those of water (Pr = 5.8). Hence, the discrepancies between these data and Eqs. (24) and (26) are presumed to be due to experimental error.

IV. Combined regimes

A single correlating equation for $\overline{Nu}$ for all Ra_L and Pr can be constructed by combining Eqs. (22) and (24) as

$$\overline{Nu} = 0.68 + 0.67(Ra_L\psi(Pr))^{1/4}\ (1 + 1.6 \times 10^{-8}\,Ra\,\psi(Pr))^{1/12} \quad (27)$$

This expression is compared with experimental data in terms of the composite variable Ra ψ(Pr) in Fig. 5.

© 1983 Hemisphere Publishing Corporation

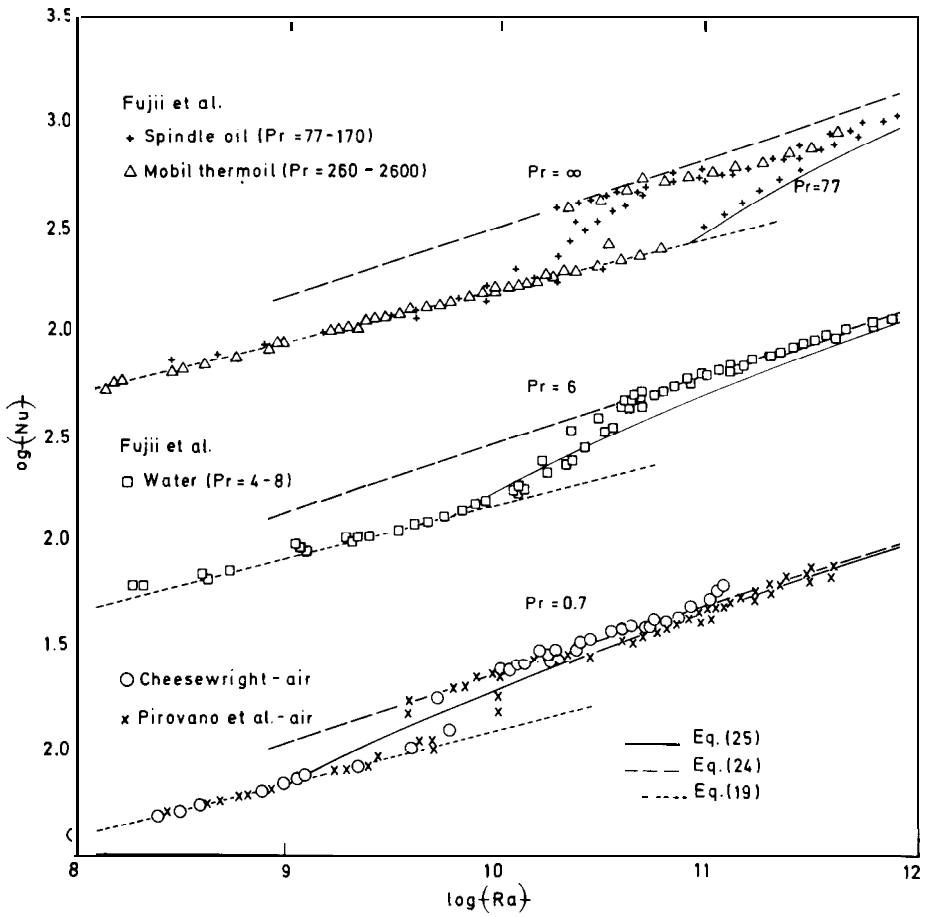

Figure 3 Comparison of Eq. (25) with experimental data for the local **Nusselt** number in the transition regime of free convection from isothermal, vertical plates.

The agreement is good for those data that have a transition to turbulent motion at $Ra_L \cong 10^9$. The values for large Pr or Sc are better represented by Eq. (22) than Eq. (26) because of their delayed transition to turbulent motion in terms of $Ra_L \psi(Pr)$.

(c) Solutions and correlating equations for uniform heating

Theoretical solutions have also been derived for a uniform heat flux density on the plate in the thin laminar boundary-layer regime. These results are very similar to those for uniform wall temperature. According to Churchill and Ozoe [25], the asymptotic expressions are

$$Nu = 0.692\ 2\ Bq^{1/4} \quad \text{for } Pr \to 0 \tag{28}$$

and

$$Nu = 0.562\ 7\ Ra^{1/4} \quad \text{for } Pr \to \infty \tag{29}$$

(Here the local value of $T_w - T_\infty$ is used in Bq and Ra.) They correlated computed values of their own and others for intermediate Pr within 2% with the expression

$$Nu = 0.563(Ra\,\phi(Pr))^{1/4} \tag{30}$$

where

$$\phi(Pr) = \left[1 + \left(\frac{0.437}{Pr}\right)^{9/16}\right]^{-16/9} \tag{31}$$

This latter expression corresponds to Eq. (20) for uniform surface temperature. $\psi(Pr)$ and $\phi(Pr)$ differ a maximum of 12.5% (for $Pr \to 0$) but their 1/4 power and 1/3 power differ by only 3% and 4%, respectively. This difference is less than the experimental uncertainty in most instances, and indeed a rounded-off value of 0.5 may be used in place of 0.492 and 0.437 for practical purposes. The surface temperature profile corresponding to Eq. (30) is

$$T_w = T_\infty + 1.584\left(\frac{\dot{q}^4 \eta x}{g\rho^2 c_p \lambda^3 \zeta}\right)^{1/5} \phi^{1/5}(Pr) \tag{32}$$

In the absence of definitive theoretical or experimental results for $Ra \to 0$, the same limiting value as

© 1983 Hemisphere Publishing Corporation

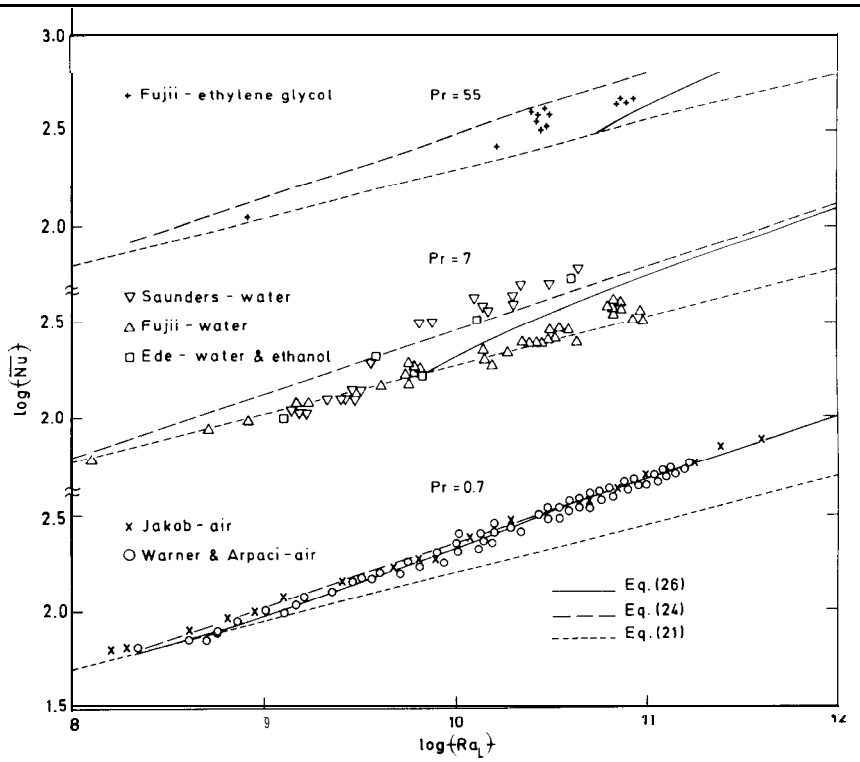

Figure 4 Comparison of Eq. (26) with experimental data for the mean Nusselt number in the transition regime of free convection from isothermal, vertical plates.

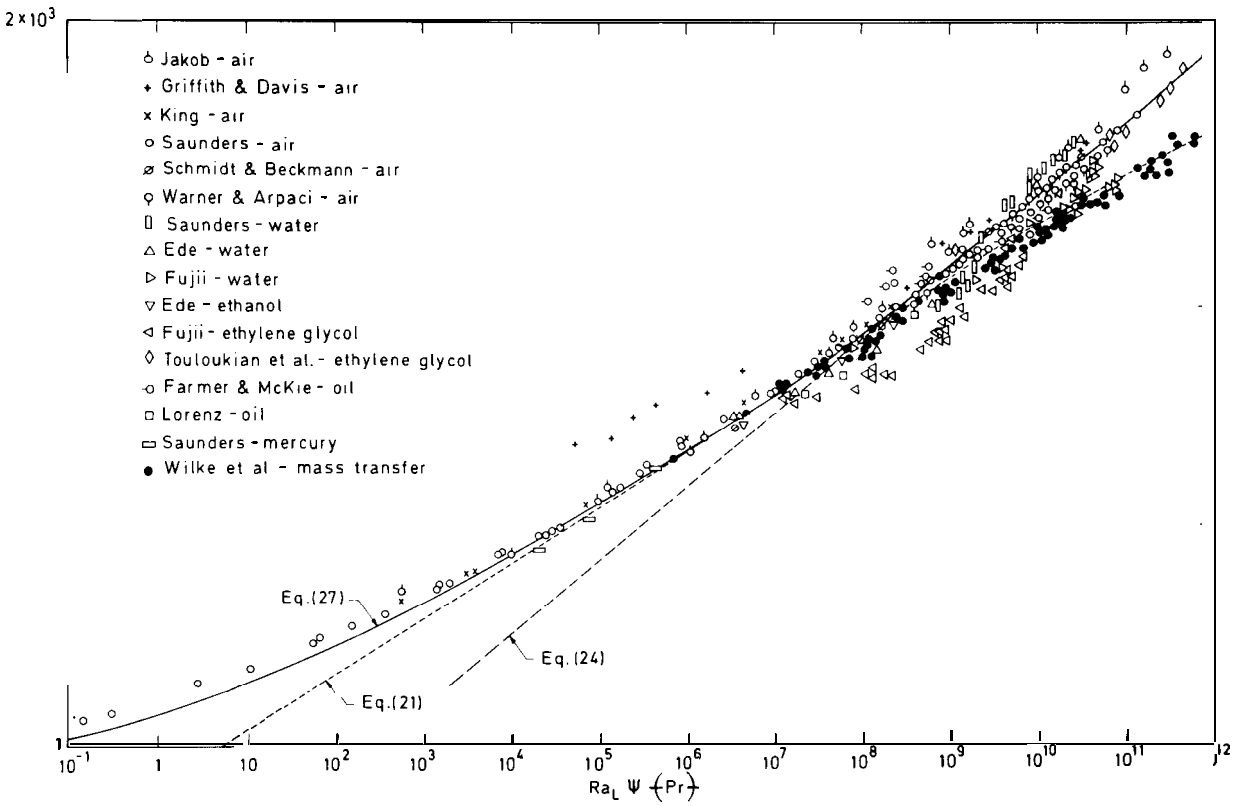

Figure 5 Comparison of Eq. (27) with experimental data for the mean Nusselt and Sherwood numbers in all regimes of free convection from isothermal, vertical plates.

© 1983 Hemisphere Publishing Corporation

for uniform wall temperature may be postulated, yielding

$$\mathrm{Nu} = 0.68 + 0.563(\mathrm{Ra}\,\phi(\mathrm{Pr}))^{1/4} \tag{33}$$

Insofar as Nu is proportional to $\mathrm{Ra}^{1/3}$ in turbulent flow, the surface temperature is uniform for uniform heating. Hence Eq. (24) should be a reasonable approximation for uniform heating in the turbulent regime. A slight improvement might be obtained by replacing 0.492 with 0.437, giving

$$\mathrm{Nu} = 0.15(\mathrm{Ra}\,\phi(\mathrm{Pr}))^{1/3} \tag{34}$$

The counterpart of Eq. (25) is then

$$\mathrm{Nu} = 100\ \mathrm{Pr}^{1/4}\phi^{1/4}(\mathrm{Pr}) + 0.15(\mathrm{Ra}^{1/3} - 1000\ \mathrm{Pr}^{1/3})\phi^{1/3}(\mathrm{Pr}) \tag{35}$$

The definition of $\overline{\mathrm{Nu}}$ for uniform heating is somewhat arbitrary. However, Sparrow and Gregg [26] have shown that for the thin laminar boundary-layer regime the use of the surface temperature at the midpoint of the region (L/2) yields values of $\overline{\mathrm{Nu}}$ in better agreement with those for an isothermal plate than the integrated mean temperature difference or the integrated mean heat transfer coefficient. With this definition Eq. (30) yields

$$\overline{\mathrm{Nu}} = 0.670(\mathrm{Ra}_L\,\phi(\mathrm{Pr}))^{1/4} \tag{36}$$

Equation (36) can be converted to one for the integrated mean temperature by multiplying the coefficient 0.670 by $(6/5)^{5/4}/2^{1/4}$, giving 0.708, and to one for the integrated mean heat transfer coefficient by multiplying 0.670 by $(5/4)^{5/4}/2^{1/4}$, giving 0.745.

Since Eqs. (34), (35), and (36) differ negligibly from Eqs. (24), (25), and (21), respectively, either set should be satisfactory for any temperature distribution between uniformity and that given by Eq. (32) in which $(T_w - T_\infty) \approx x^{1/5}$.

Equations (30), (36), and (34) can be put in the following explicit forms, as discussed earlier. For the thin laminar boundary-layer regime, Eq. (30) becomes

$$\mathrm{Nu} = 0.631(\mathrm{Ra}^*\phi(\mathrm{Pr}))^{1/5} \tag{37}$$

and Eq. (36) becomes

$$\overline{\mathrm{Nu}} = 0.726(\mathrm{Ra}_L^*\phi(\mathrm{Pr}))^{1/5} \tag{38}$$

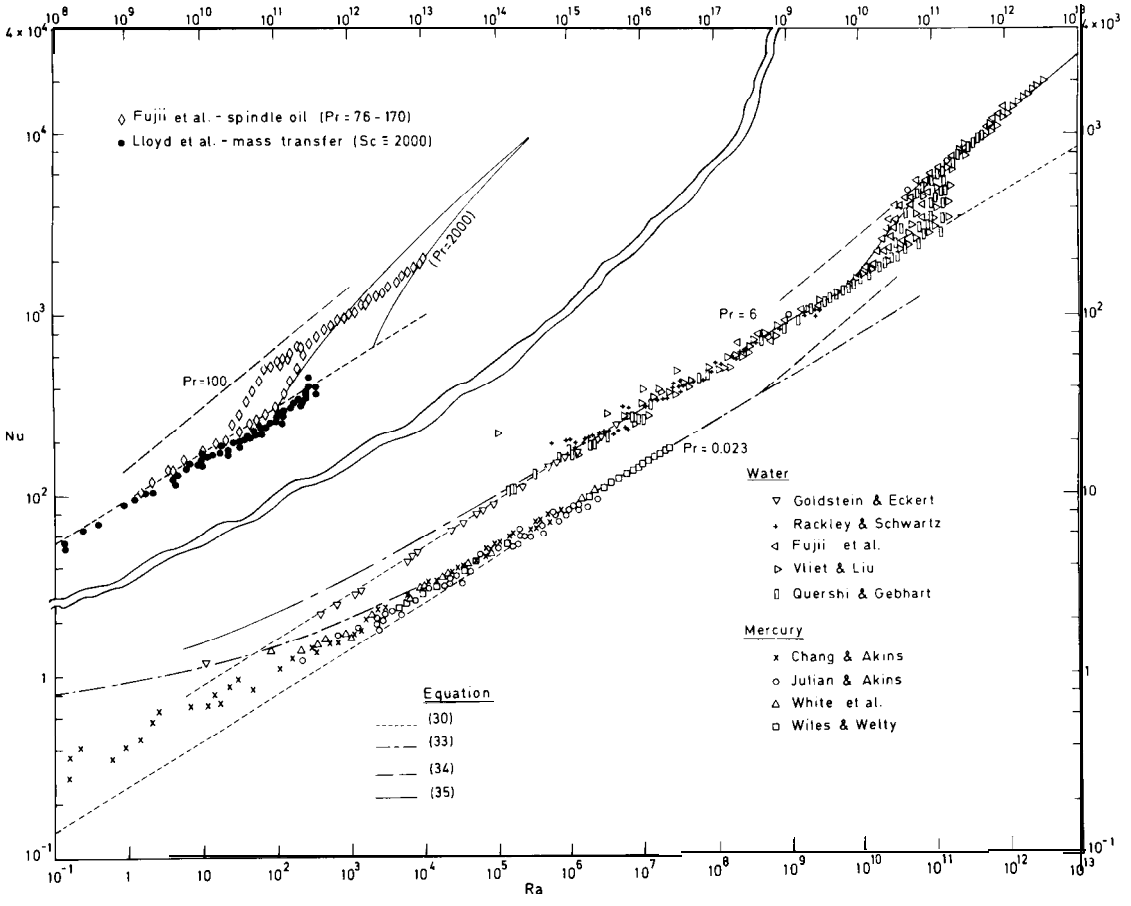

Figure 6 Comparison of Eqs. (33), (34), and (35) with experimental data for the local Nusselt number in free convection from uniformly heated, vertical plates.

© 1983 Hemisphere Publishing Corporation

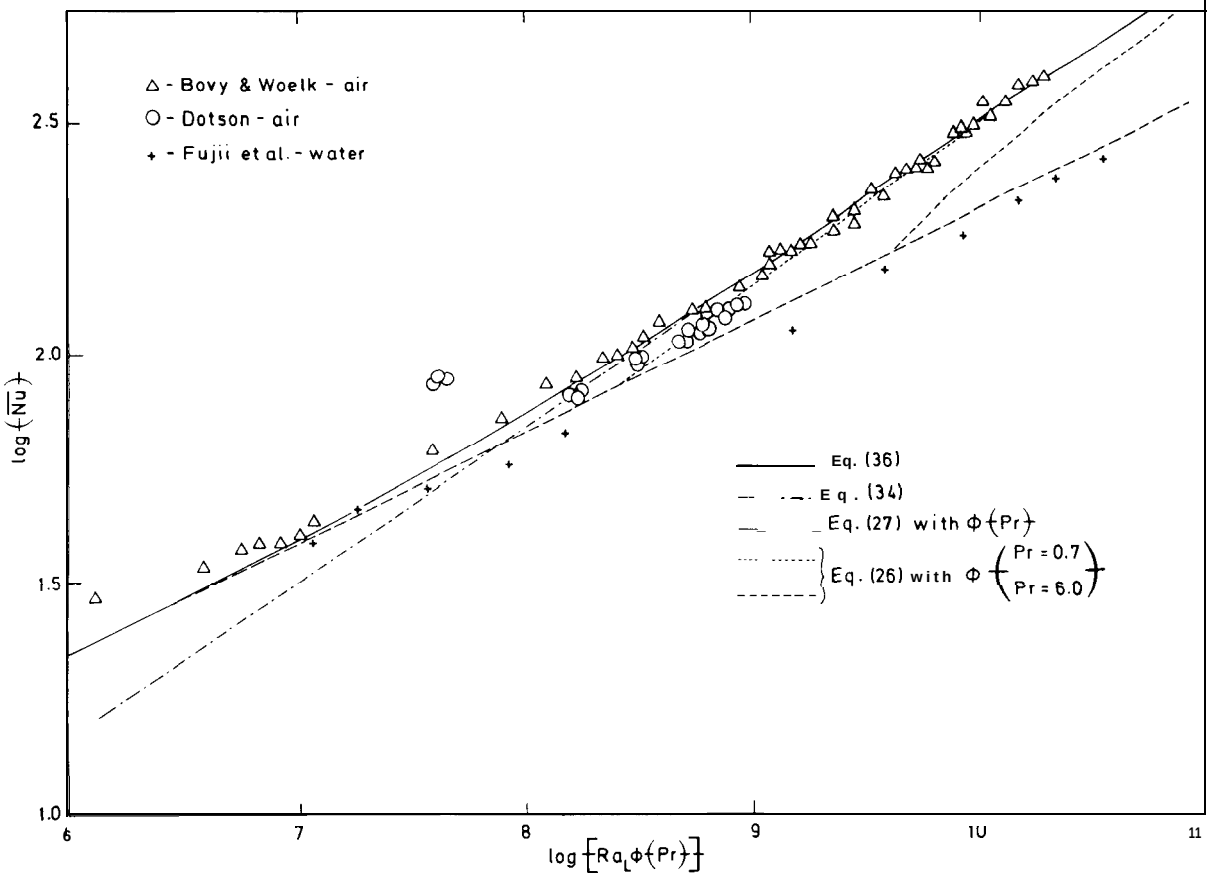

Figure 7 Comparison of Eqs. (27), (34), and (36) with experimental data for the mean Nusselt number in free convection from uniformly heated, vertical plates.

For the turbulent regime,

$$\mathrm{Nu} = 0.241(\mathrm{Ra}^* \phi(\mathrm{Pr}))^{1/4} \tag{39}$$

Equations (30), (33), (34), and (35) are compared with local values of Nu for uniform heating in Fig. 6. Excellent agreement may be noted for both the laminar and turbulent regimes except for very low Ra, where the data suggest a lower limiting value than 0.68, and for the data of Fujii et al. [24] for spindle oil at large Ra. These latter data are for a boundary condition intermediate between uniform heating and uniform temperature, and hence are included here as well as in Fig. 3. A more abrupt transition than predicted by Eq. (35) is observed in all cases.

Equations (34) and (36), and Eqs. (26) and (27) with $\phi(\mathrm{Pr})$ substituted for $\psi(\mathrm{Pr})$ are similarly compared with mean values in Fig. 7. Except for the delayed transition with water, the agreement is good.

(d) Transient behavior

When the surface of a vertical plate is subjected to a step rise in temperature, the temperature field in the fluid at first rises in accordance with the solution for pure conduction to a semi-infinite region. Inertia delays the development of fluid motion, resulting in an oscillatory approach to the steady state. The rate of heat transfer also approaches the steady state in an oscillatory manner. Churchill and Usagi [27] correlated the gross behavior (the first overshoot and recovery) given by the numerical solution of Hellums and Churchill [28] with an empirical equation which can be generalized for all Pr as

$$\frac{\mathrm{Nu}^{20}}{\mathrm{Ra}^5} = \left(\frac{1}{\pi t}\right)^{10}\left[\frac{c_p \mu x}{g\lambda\zeta(T_w - T_\infty)}\right]^5 + \left\{\frac{0.502\,6/[\,1 + (0.492/\mathrm{Pr})^{9/16}\,]^{4/9}}{1 + (2.3/t)^8\,[c_p\mu x/g\lambda\zeta(T_w - T_\infty)]^4}\right\}^{20} \tag{40}$$

where t = time (s). Ingham [29] has recently questioned the convergence of the numerical solution, but his results do not appear to invalidate the genera1 behavior indicated by Eq. (40). Qualitative agreement may be noted in Fig. 8 with the very scattered experimental data of Klei [30] for air.

© 1983 Hemisphere Publishing Corporation

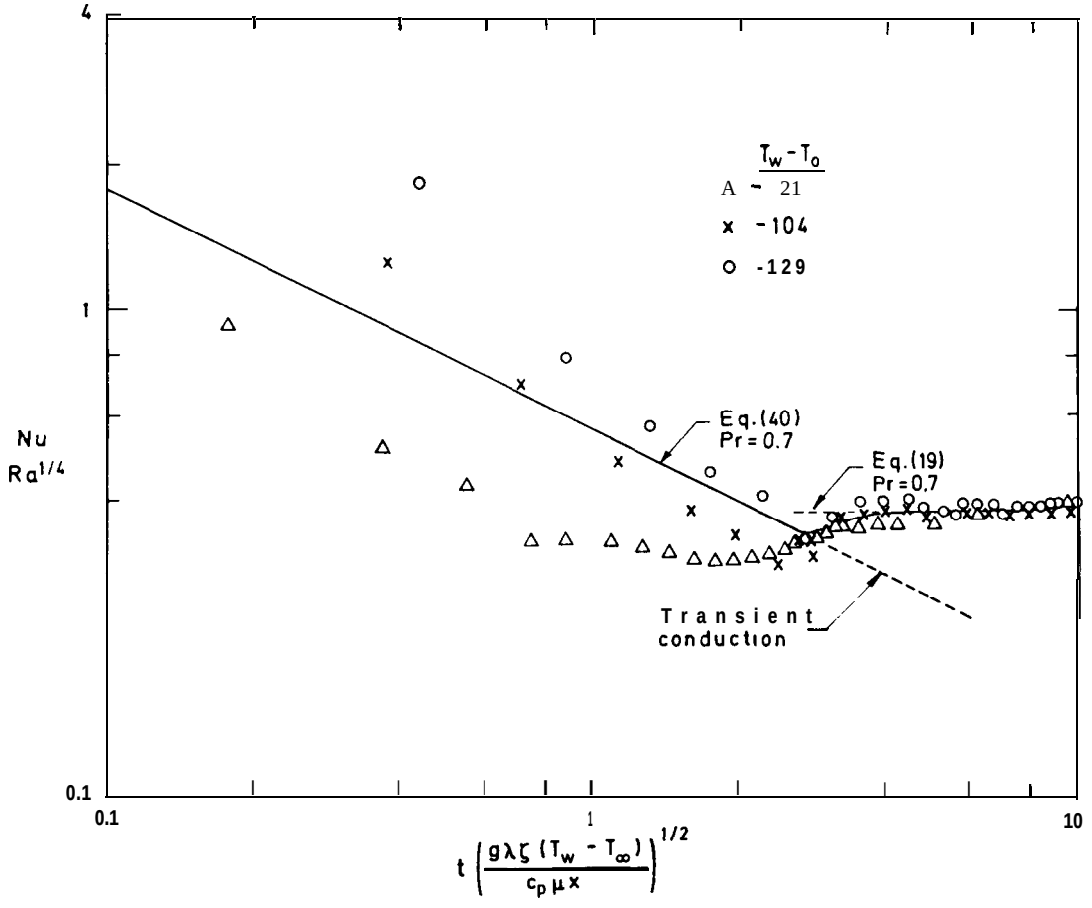

Figure 8 Comparison of Eq. (40) with the experimental data of Klei [30] for the local Nusselt number in transient, laminar, free convection from an isothermal, vertical plate to air.

A step in heat flux does not appear to generate significant overshoot or oscillations, at least for Pr > 0.01, and Churchill [31] developed the following expression for interpolation between the solutions for pure conduction and steady-state convection:

$$\mathrm{Nu}^6 = \left(\frac{\pi \rho c_p x^2}{4kt}\right)^3 + 0.100\ 5\ \mathrm{Ra}\ \phi(\mathrm{Pr})^{3/2} \qquad (41)$$

The exponent 6 was chosen to represent the experimental data of Goldstein and Eckert [32] for water and the approximate numerical solution of Gebhart [33]. The resulting impression is compared in Fig. 9 with the (uncoded) experimental data for four locations and two heat flux densities.

(e) Non-Newtonian behavior

Acrivos [34] has derived a solution for a non-Newtonian fluid with Pr $\to\infty$ and an effective viscosity that follows the power law model:

$$\eta = M \left|\frac{d\bar{u}}{dy}\right|^{n-1} \qquad (42)$$

where M = coefficient, kg $s^{n-2} m^{-1}$
u = velocity in x direction, m/s
y = distance from wall, m
n = dimensionless exponent

The solutions above for Newtonian fluids were found to be applicable with the substitution $\phi(n)\,\mathrm{Ra}''^{1/3n+1}$ for $\mathrm{Ra}^{1/4}$. Here

$$\mathrm{Ra}'' = \frac{g\rho^{n+1} c_p^n \zeta (T_w - T_\infty) x^{2n+1}}{M\lambda^n} \qquad (43)$$

$\phi(n)$ is the weak function given in Table 1. As indicated by Figs. 10 and 11 from Agarwal et al. [35], this solution provides a good representation for a number of fluids with $0.68 \leqslant n \leqslant 1.0$ but not for $n < 0.4$.

Chen and Wollersheim [36] derived the analogous solution for a uniformly heated plate and showed that the Acrivos solution was applicable for $\overline{\mathrm{Nu}}$ if the temperature difference was evaluated at $L/2$. As indicated in Fig. 12, the agreement of this solution with the experimental work of Dale [37] for $0.4 \leqslant n \leqslant 1.0$ is very good.

Fujii et al. [38] have obtained numerical solutions

© 1983 Hemisphere 1 blishing Corporation

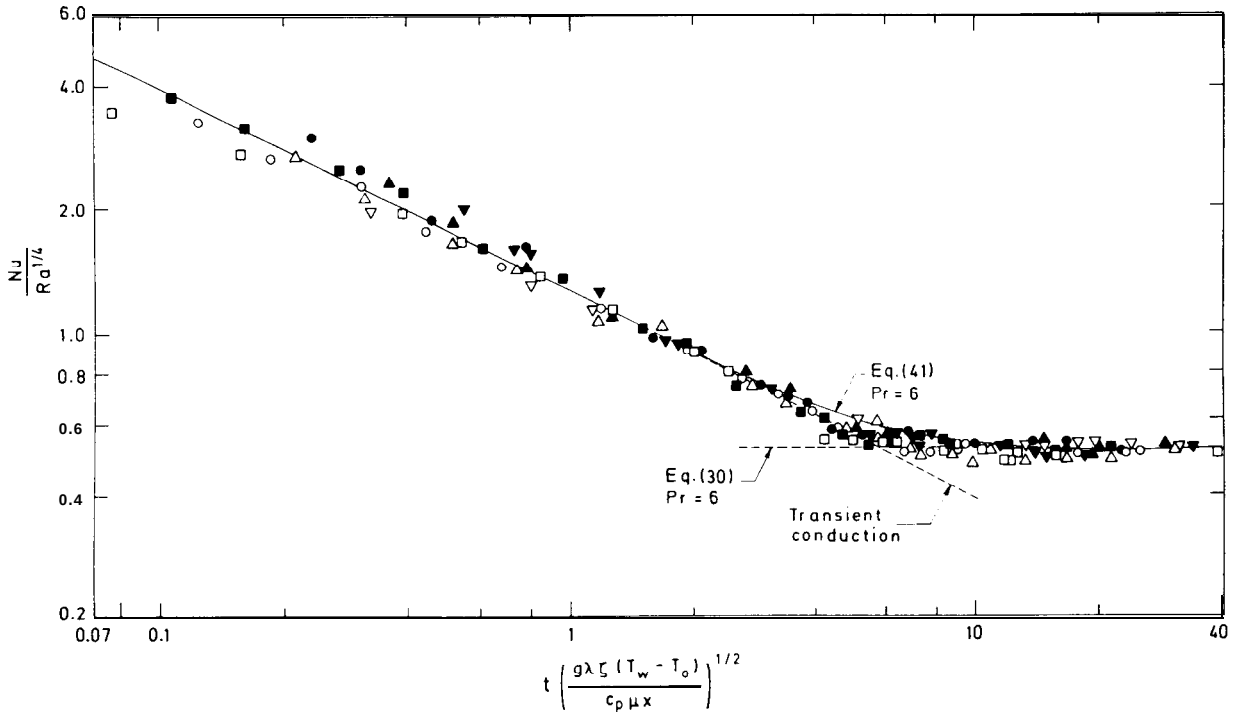

Figure 9 Comparison of Eq. (41) with the experimental data of Goldstein and Eckert [32] for the local Nusselt number in transient, laminar, free convection from a uniformly heated, vertical plate to water.

for a Sutterby fluid at finite Pr, and experimental results for aqueous solutions of polyethylene oxide for both uniform wall temperature and uniform heating. As illustrated in Fig. 13 for uniform wall temperature, their results indicate that the Acrivos solution, as represented by Eq. (19) in terms of Ra from Eq. (43), is a reasonable approximation for Nu if M and n are evaluated for the shear stress at the midpoint (L/2) of the heated plate. Similar agreement was demonstrated for uniform heating using the equivalent of Eq. (37).

(f) Evaluation of idealizations

Gray and Georgini [39] showed that the Boussinesq model is satisfactory for air and water under most circumstances. Brown [40], on the other hand, showed that the temperature dependence of the volumetric coefficient of expansion can lead to serious errors. Eshghy and Morrison [41] concluded that the effect of compressibility is negligible for all but very unusual circumstances. Wylie [42] has shown that no choice of a reference temperature can account for the complex variation of properties of all gases and liquids. However, the analysis of Sparrow and Gregg [43] suggests that evaluation of the properties at $(T_w + T_\infty)/2$ will result in an acceptable result for most practical purposes.

Bonilla and Sigel [44] concluded that the standard correlations for turbulent free convection are applicable near the critical point if the logarithmic mean temperature is used for $1/\zeta$. Schechter and Isbin [45] provide an involved solution for free convection in water in the region of maximum density (0-4° C).

Gebhart [46] and others have derived expressions for the effect of viscous dissipation in the laminar boundary-layer regime. However, Brown [47] concludes that such effects are negligible in all practical circumstances except possibly in the high effective force field produced by rotating machinery.

Table 1 Coefficient $\phi(n)$ in free convection solutions of Acrivos [34] for power law fluids

n	0.1	0.5	1.0	1.5
Vertical plate	0.90	0.94	1.0	1.06
Cylinder	0.86	0.90	1.0	1.07
Sphere	0.90	0.92	1.0	1.06

(g) Transfer of species

As shown in Fig. 14, the experimental data of Wilke et al. [48] for the transfer of species by laminar convection for a number of materials with Sc ranging from 500 to 80 000 were correlated by the expression

$$\overline{\mathrm{Sh}} = 0.66\ \mathrm{Ra}_L'^{1/4} \qquad (44)$$

© 1983 Hemisphere 1 ublishing Corporation

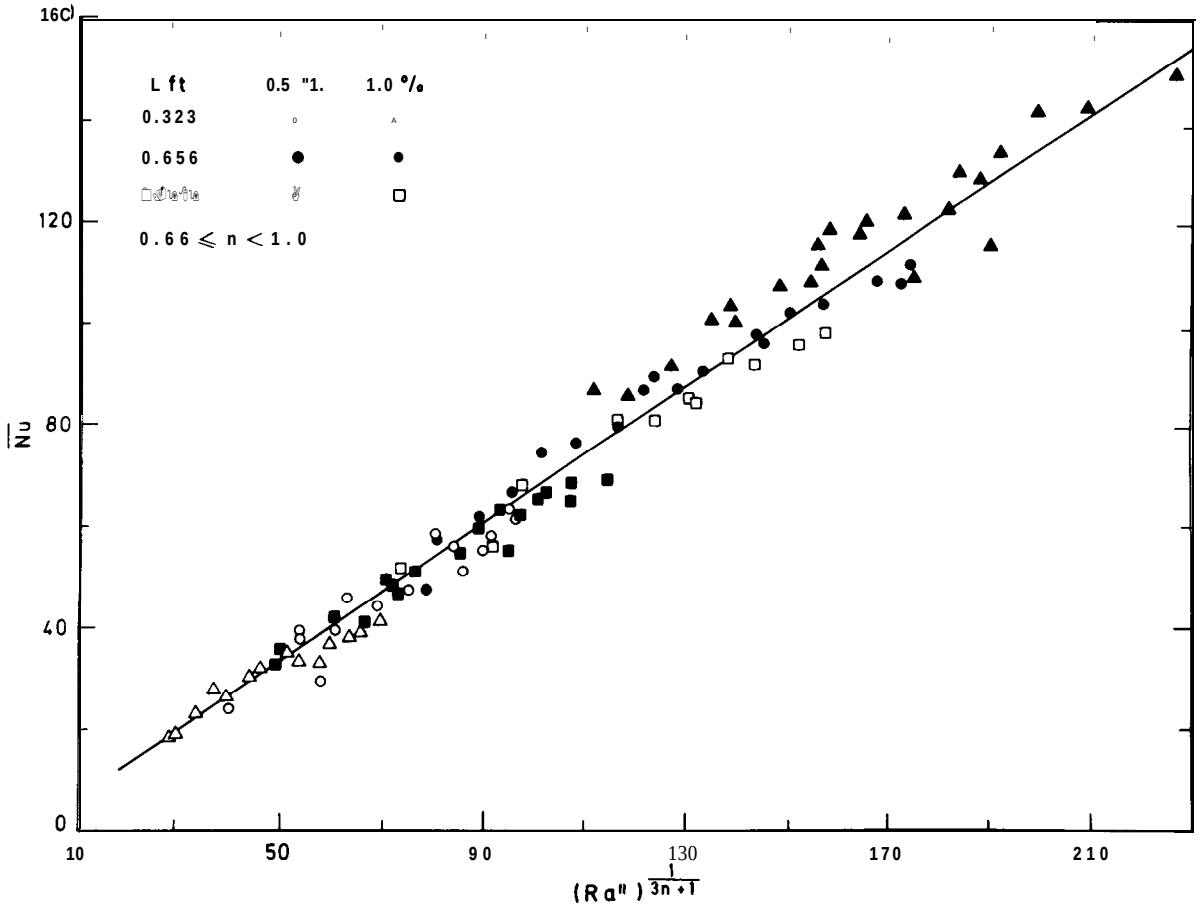

Figure 10 Comparison of Eq. (21) with experimental data for the mean Nusselt number in laminar free convection from isothermal, vertical plates to non-Newtonian fluids (Carbopol solutions), power law indices n greater than 0.68. From Agarwal et al. [35].

where $Sc = \eta/\rho\delta$ = Schmidt number

$Sh = \beta x/\delta$ = Sherwood number

$Ra = g\rho\gamma_i \Delta w_i L^3/\delta\eta$ = Rayleigh number for species transfer

δ = diffusivity, m^2/s

β = species transfer coefficient, m/s

γ_i = dimensionless coefficient of expansion due to weight fraction of ith species

w_i = weight fraction of ith species

Equation (44) can be seen to be equivalent to Eq. (21), thus confirming the analogy between heat and species transfer for this case. Transition did not occur because $Gr'_L = Ra'_L/Sc$ was less than 10^9 even for $Ra'_L = 4 \times 10$.

(h) Simultaneous heat and species transfer

Saville and Churchill [49] have shown theoretically that for thin laminar boundary layers with Pr = Sc, the density changes due to temperature and composition are simply additive if imposed in the same direction. Therefore, Ra in all of the above equations for the laminar regime can simply be replaced by Ra + Ra . The reasonable postulate that the turbulent Prandtl and Schmidt numbers are also essentially equal suggests that the equations for turbulent flow are similarly adaptable.

For $Sc \neq Pr$, the situation is quite complex and not completely resolved. For the special case of a thin laminar boundary layer with $Sc \gg Pr \to \infty$ and $Gr'/Gr \to 0$, Lightfoot [50], as well as Saville and Churchill, have shown that Eq. (18) is applicable for Nu but that

$$Sh = 0.502\ 7\ Ra^{1/}\left(\frac{Sc}{Pr}\right)^{1/3} \tag{45}$$

The 1/3 power dependence on Sc results from species transfer in a linear velocity field driven wholly by temperature. The related expressions for $\overline{Nu}$ and $\overline{Sh}$ follow directly. These latter predictions have not yet been confirmed experimentally.

© 1983 Hemisphere Publishing Corporation

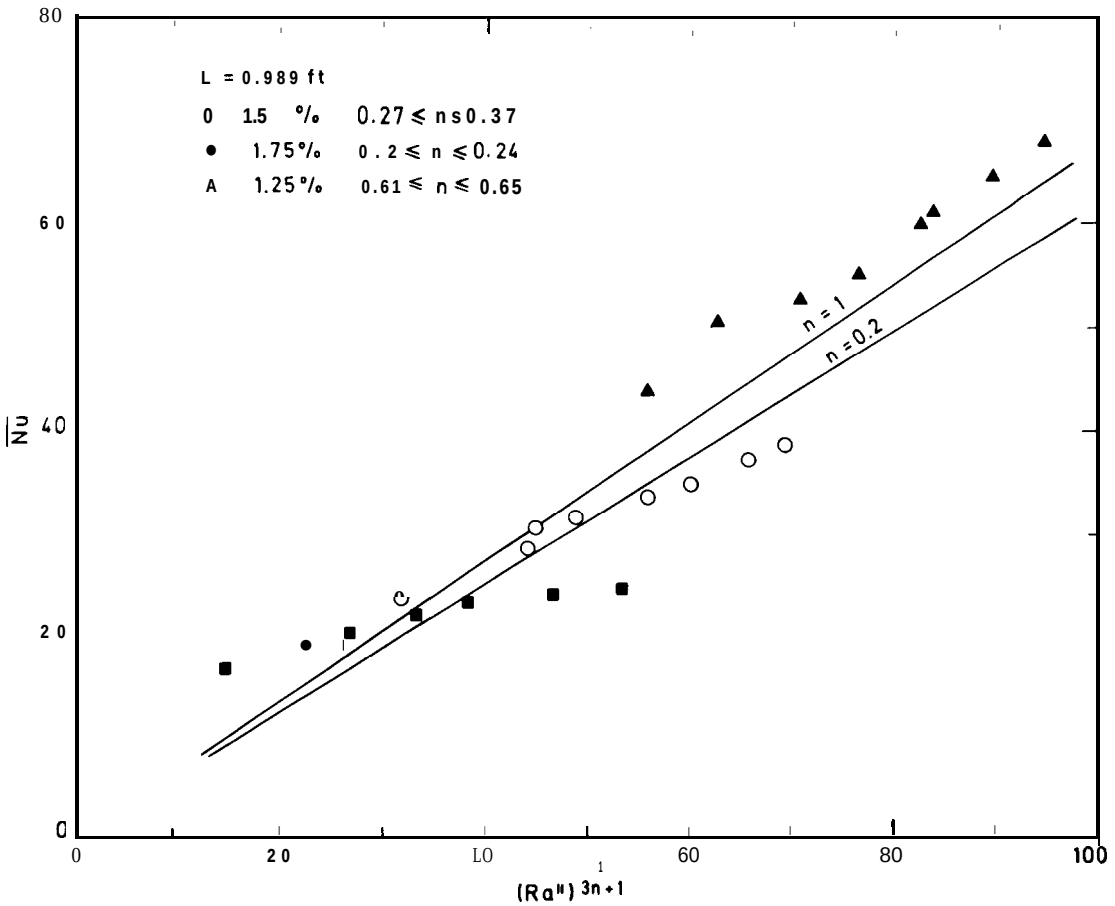

Figure 11 Comparison of theoretical solution of Acrivos [34] with experimental data for the mean Nusselt number in laminar free convection from isothermal, vertical plates (Carbopol solutions) to non-Newtonian fluids with power law indices n less than 0.68. From Agarwal et al. [35].

B. Inclined and horizontal surfaces

Experimental data for inclined surfaces have generally been correlated in terms of the expressions for vertical and horizontal plates, with g replaced by the effective component of gravity. Downward-facing and upward-facing heated surfaces differ somewhat in behavior and are examined separately. Herein, θ represents the upward angle of inclination of the heated surface from the vertical.

(a) Downward-facing heated surfaces

I. Uniform surface temperature

The experimental data of Moran and Lloyd [51] for the local rate of transfer of species ($Sc \cong 2\,000$) are

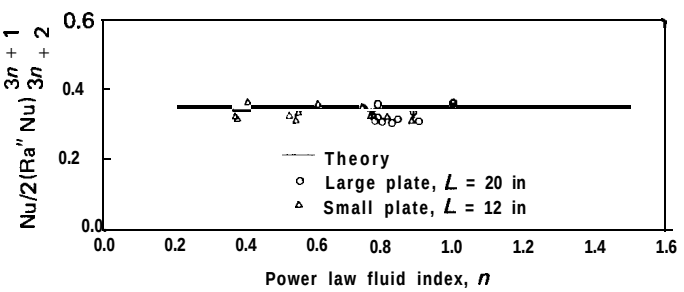

Figure 12 Comparison of theoretical solution with experimental data of Dale [37] for the mean Nusselt number in laminar free convection from a uniformly heated, vertical plate to non-Newtonian liquids. From Chen and Wollersheim 1361.

© 1983 Hemisphere Publishing Corporation

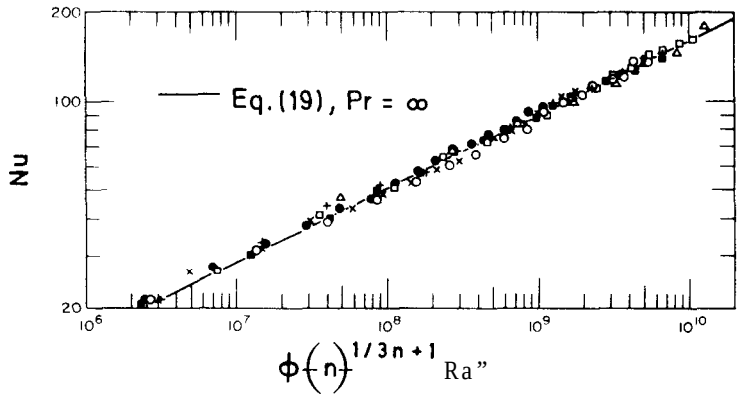

Figure 13 Comparison of Eq. (19) with experimental data for the local Nusselt number in laminar free convection from an isothermal, vertical plate to a Sutterby fluid. From Fuiii et al. [38]. Reprinted with permission. Copyright 1973, Pergamon Press, Ltd.

plotted in Figs. 15 and 16 for the laminar and turbulent regimes, respectively. In these plots Ra'_θ signifies the Rayleigh number for the transfer of species, with g cos θ, the component of gravity parallel to the surface, replacing g. The data in Fig. 15 are in good agreement with the prediction of Eq. (19), as represented by an ordinate value of 1.003. The prediction of the effect of inclination is also satisfactory in Fig. 16, but the measured values of $Sh/Ra'^{1/3}_\theta$ at all angles, including the vertical case ($\theta = 0$), fall significantly below the value of 0.149 predicted by Eq. (24), presumably because the transition to turbulent motion

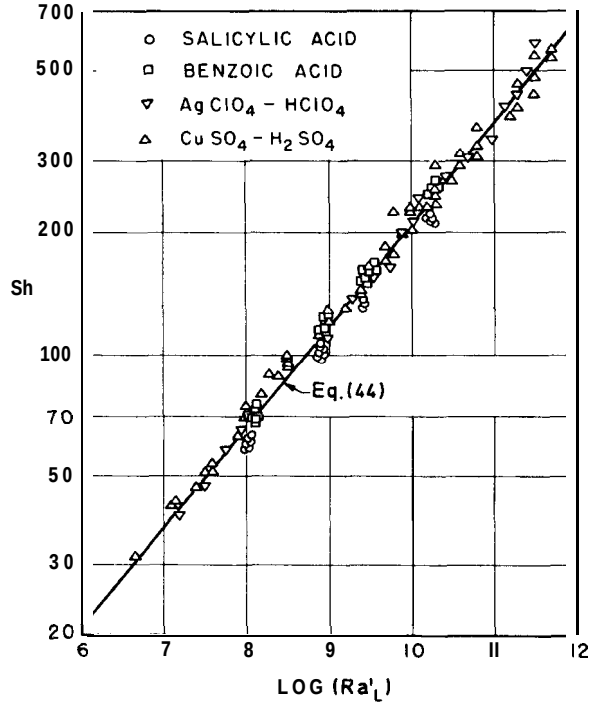

Figure 14 Comparison of Eq. (44) with experimental data for the mean Sherwood number in laminar free convection for vertical plates. From Wilke et al. [48].

is incomplete at the maximum experimental values of Ra'_θ of $\sim 1.2 \times 10^{13}$ ($Gr'_\theta \cong 6 \times 10^9$).

The line drawn by Hassan and Mohamed [52] through their local data and that of Kierkus [53] for air in Fig. 17 is equivalent to Eq. (19) with a coefficient of 0.509 instead of 0.503, and hence is in good agreement with the theoretical prediction for the laminar regime. The data of Fujii and Imura [54] for $\overline{Nu}$ for water in Fig. 18 are in fair agreement with Eq. (21), since their coefficient of 0.56 corresponds to a coefficient of 0.623 instead of 0.67.

Infinite, isothermal, horizontal plates with the heated surfaces facing downward ($\theta = -\pi/2$) do not generate convection, but species with one or more finite dimensions do. For a gravitational force normal to a plane surface, dimensional analysis indicates that

$$\overline{Nu} = \boldsymbol{B}\, Ra^{1/5} \tag{46}$$

where $\boldsymbol{B}$ is a function of shape and Pr. In the absence of sufficient information to derive an expression for the dependence on Pr, Eq. (20) can be postulated as an approximation. Goldstein et al. [55] showed that for upward-facing, heated surfaces, $\boldsymbol{B}$ was essentially constant for all geometries when the area divided by the perimeter was used as the characteristic length in Nu and Ra. Then Eq. (46) becomes

$$\overline{Nu}_A = G(Ra_A\, \psi(Pr))^{1/5} \tag{47}$$

where the subscript A indicates the above characteristic length.

Values of Nu for several geometries have been derived by integral boundary-layer theory. Some of the corresponding coefficients for Eq. (47) are listed in Table 2. These values are all subject to considerable uncertainty because of idealizations in the derivations. Experimental values of several investigators are plotted in Fig. 19. The agreement with Eq. (47) with a representative value of 0.6 for the coefficient G is

© 1983 Hemisphere Publishing Corporation

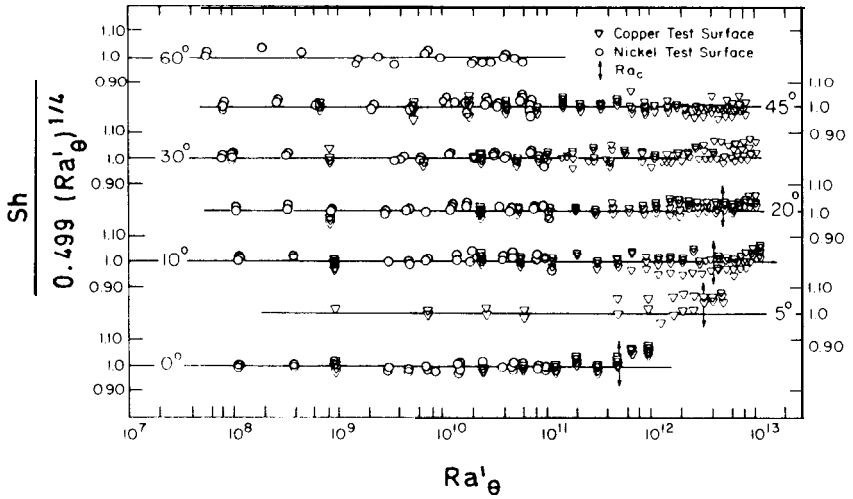

Figure 15 Comparison of Eq. (19) (as represented by an ordinate of 1.003) with experimental data for the local Sherwood number in laminar free convection from downward-facing, inclined plates. From Moran and Lloyd [51].

generally good. The data of Fujii and Imura [54] for water fall consistently lower, as also noted with regard to Fig. 18.

Local values of $Nu_A/(Ra_A \psi (Pr))^{1/5}$ for two-dimensional convection from rectangular plates are compared in Fig. 20 with a curve representing the solution of Singh and Birkebak [57]. The agreement is reasonably good.

II. Uniform heating

Data for the uniform-heating boundary condition have generally been reported in the form of Nu versus $Ra_\theta^* = Nu\ Rae$. The data of Fussey and Warneford [60] for water, as plotted in this form in Fig. 21, are seen to be in reasonable agreement with Eqs. (30) and (34), when g cos θ is substituted for g. Fussey and Wameford also developed the following empirical expression for the onset of transition:

$$Ra_c^* = 6.31 \times 10^{12} e^{-4.04\theta} \quad (48)$$

which is consistent with the transitions indicated in Fig. 21.

(b) Upward-facing heated surfaces

I. Uniform surface temperature

As contrasted with downward-facing and vertical surfaces, transition to turbulent motion occurs because of separation as Ra increases beyond a critical value, Ra_s. Fujii and Imura [54] give the following empirical prediction of this value for an isothermal surface:

$$Ra_s = 1 \times 10^5 e^{11.5 \cos\theta} \quad (49)$$

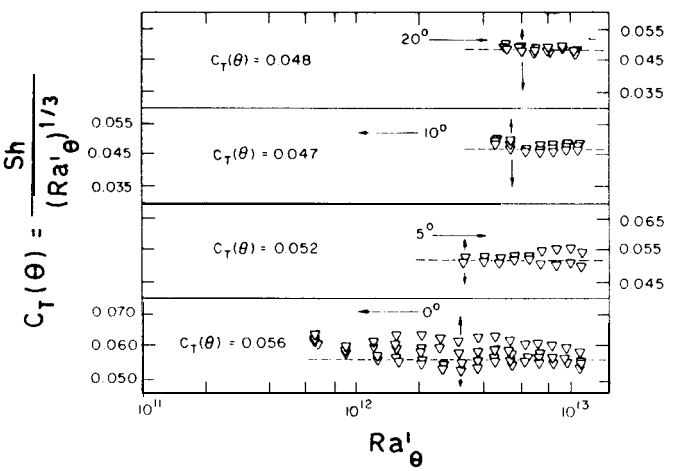

Figure 16 Comparison of Eq. (24) (as represented by an ordinate of 0.149) with experimental data for the local Sherwood number in free convection from downward-facing, inclined plates. From Moran and Lloyd [51].

© 1983 Hemisphere I blishing Corporation

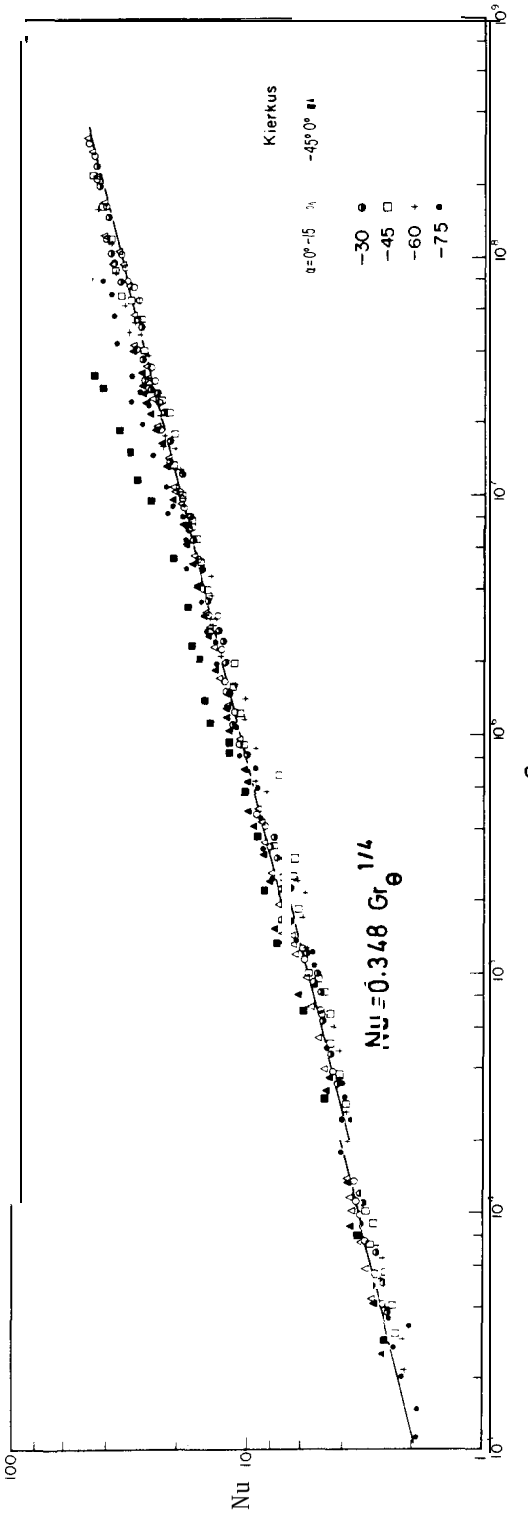

Figure 17 Comparison of Eq. (18) (with a coefficient of 0.059) with experimental data for the local Nusselt number in laminar free convection from downward-facing, inclined, isothermal plates in air. From Hassan and Mohamed [52].
Copyright 1970, Pergamon Press, Ltd. Reprinted with permission.

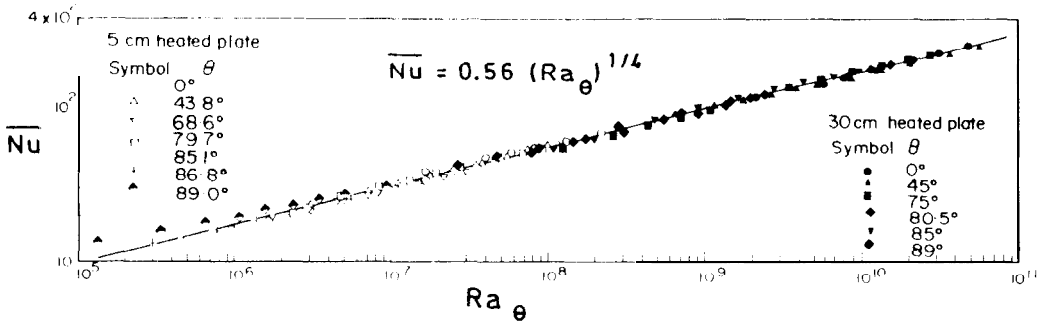

Figure 18 Comparison of Eq. (21) (with a coefficient of 0.623) with experimental data for the mean Nnsselt number in laminar free convection from isothermal, downward-facing, inclined plates to water. From Fujii and Imura [54]. Copyright 1972, Pergamon Press, Ltd. Reprinted with permission.

Table 2 Coefficients for Eq. (47) for heated, downward-facing surfaces (characteristic length = area/perimeter)

Source	Square	Circle	Long strip
Singh et al. [56]	0.748	0.667	0.600
Singh and Birkebak [57]			0.55 1
Wagner [58]			0.600
Faw and Dullforce [59]	0.689		

For the laminar regime, and for the turbulent regime at small angles of inclination, the same expressions as for downward-facing plates are applicable, as indicated by the extensive data for Nu in Fig. 22. The first point in each .set of data that appears to indicate the onset of turbulent motion is circled. These circled values are consistent in trend with the prediction of Eq. (49). For the turbulent regime at large angles of inclination, Raithby and Hollands [61] suggest that the component of gravity perpendicular to rather than parallel to the surface is effective and hence that Nu is proportional to $(\sin \theta)^{1/3}$. The corresponding expression is then

$$\mathrm{Nu} = 0.15(\mathrm{Ra}\,\psi\,\mathrm{Pr})\sin\theta)^{1/3} \tag{50}$$

The data plotted in Fig. 23 appear to confirm this conjecture. Both $\overline{\mathrm{Nu}}$ and Nu are included, since the distinction is negligible in this regime. Rotem and Claassen [62] derived an exact solution for the boundary-layer regime of convection from an infinite horizontal strip facing upward, and carried out the required numerical calculations for a series of values of Pr. Churchill [63] correlated these values of $\overline{\mathrm{Nu}}$ within 0.6% using the expression

$$\overline{\mathrm{Nu}}_A = \frac{0.766\ \mathrm{Ra}_A^{1/5}}{[\,1+(0.322/\mathrm{Pr})^{11/20}\,]^{4/11}} \tag{51}$$

For the turbulent regime, Eq. (34) can be rewritten in corresponding form as

$$\overline{\mathrm{Nu}}_A = \frac{0.15\ \mathrm{Ra}_A^{1/3}}{[\,1+(0.322/\mathrm{Pr})^{11/20}\,]^{20/33}} \tag{52}$$

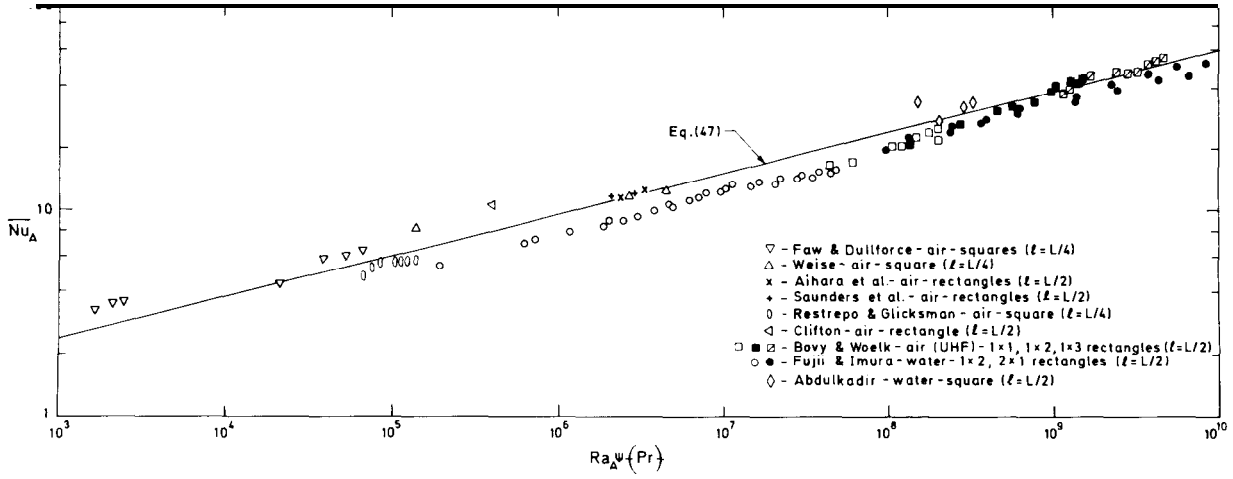

Figure 19 Comparison of Eq. (47) with experimental data for the mean Nusselt number in laminar free convection from isothermal, downward-facing, horizontal plates.

© 1983 Hemisphere Publishing Corporation

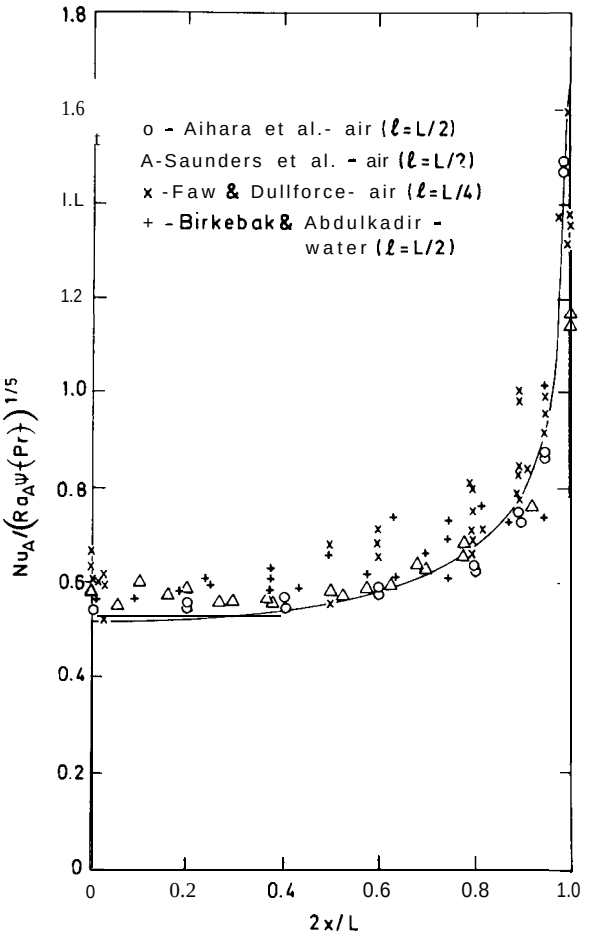

Figure 20 Comparison of theoretical solution of Singh and Birkebak [57] with experimental data for the local Nusselt number in laminar free convection from isothermal, downward-facing, horizontal plates.

The experimental data of a number of investigators are compared with Eqs. (51) and (52) in Fig. 24. Based on the previously mentioned conjecture of Goldstein et al. [55], data for a variety of shapes are included in terms of Nu_A and Ra_A. The predicted dependence on Pr, Ra, and shape appears to be represented within the scatter of the data. However, the data fall predominately above the equations, suggesting that, the theoretical coefficients should be interpreted as lower boundary values.

II. Uniform heating

According to Fussey and Warneford [60, transition for a uniformly heated, upward-facing surface occurs at

$$Ra_c^* = 6.31 \times 10^{12} e^{-11\theta} \qquad (53)$$

Equation (30) for the laminar regime and Eq. (34) for the turbulent regime for small inclinations, both with g cos θ substituted for g, and Eq. (50) for large inclinations, would be expected to be applicable here. The data of Shaukatullah and Gebhart [64] for $\theta = 29\pi/180$ and the laminar-only data of Vliet [65] for θ from $15\pi/180$ to $60\pi/180$ rad, both for water, are seen in Fig. 25 to agree well with Eqs. (30) and (34). However, the indicated transition in the data of Shaukatullah and Gebhart is delayed somewhat beyond the prediction of $\log [Ra\,\phi(Pr)] = 10.22$ by Eq. (53). Vliet and Ross [66], as well as Vliet [65], assert that their turbulent data for air, and air and water, respectively, are better correlated with Ra than with Ra_θ. Data to test Eq. (50) do not appear to be available, other than those of Fujii and Imura [54], which have already been examined in this sense in Fig. 23.

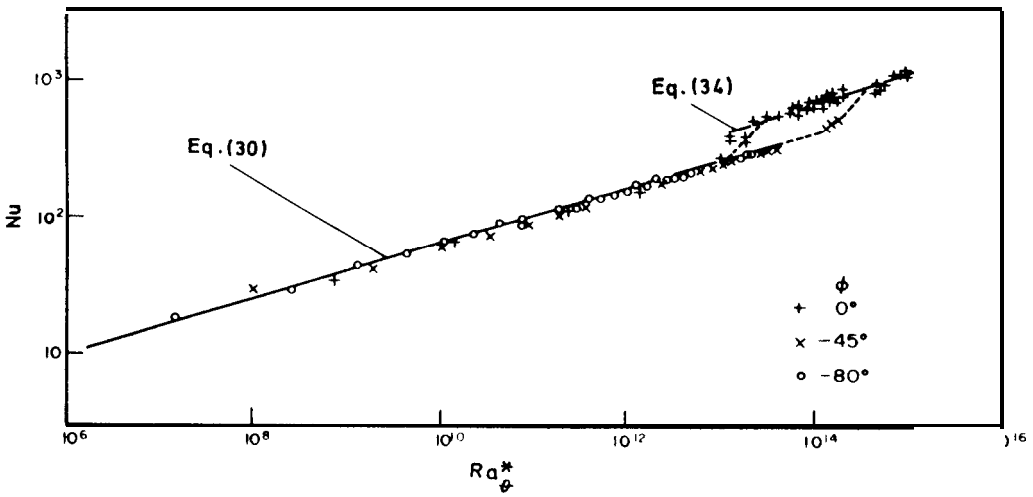

Figure 21 Comparison of Eqs. (30) and (34) with experimental data for the local Nusselt number in free convection from a uniformly heated, downward-facing inclined plate to water. From Fussey and Warneford [60]. Copyright 1978, Pergamon Press, Ltd. Reprinted with permission.

© 1983 Hemisphere Publishing Corporation

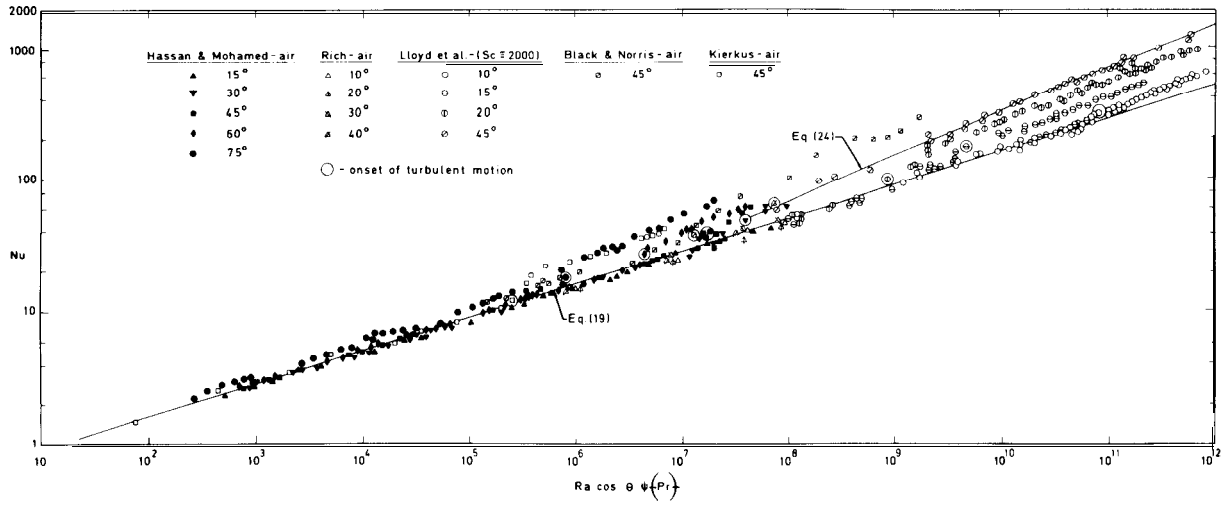

Figure 22 Comparison of Eqs. (19) and (24) with experimental data for the local Nusselt and Sherwood numbers in free convection from isothermal, upward-facing, inclined plates.

C. Buoyancy-induced flow in channels

Heating the walls of an open-ended vertical channel induces a convective flow. Churchill [67] has correlated the experimental and computed values for uniform wall temperature and uniformly heated walls in cylindrical tubes and between parallel plates with the expression

$$\overline{\mathrm{Nu}} = \frac{A\ \mathrm{Ra}^{\#}}{\{1 + (4A/3)^{3/2}\,[1 + (C/\mathrm{Pr})^{9/16}]^{2/3}(\mathrm{Ra}^{\#})^{9/8}\}^{2/3}} \qquad (54)$$

The constants are summarized in Table 3. The modified Rayleigh number for induced flow is here defined as

$$\mathrm{Ra}^{\#} = \frac{g\rho^2 c_p \zeta (T_w - T_\infty)\ell^4}{L\lambda\eta} \qquad (55)$$

where ℓ is the characteristic length in Table 3 and L is the length of the channel. Equation (54) is based on boundary-layer theory in the inlet (with the coefficient adjusted to account for entrance effects per Aihara [68] and for curvature) and on fully developed convection at the outlet. Excellent agreement with the experimental data is indicated in Fig. 26. The data of

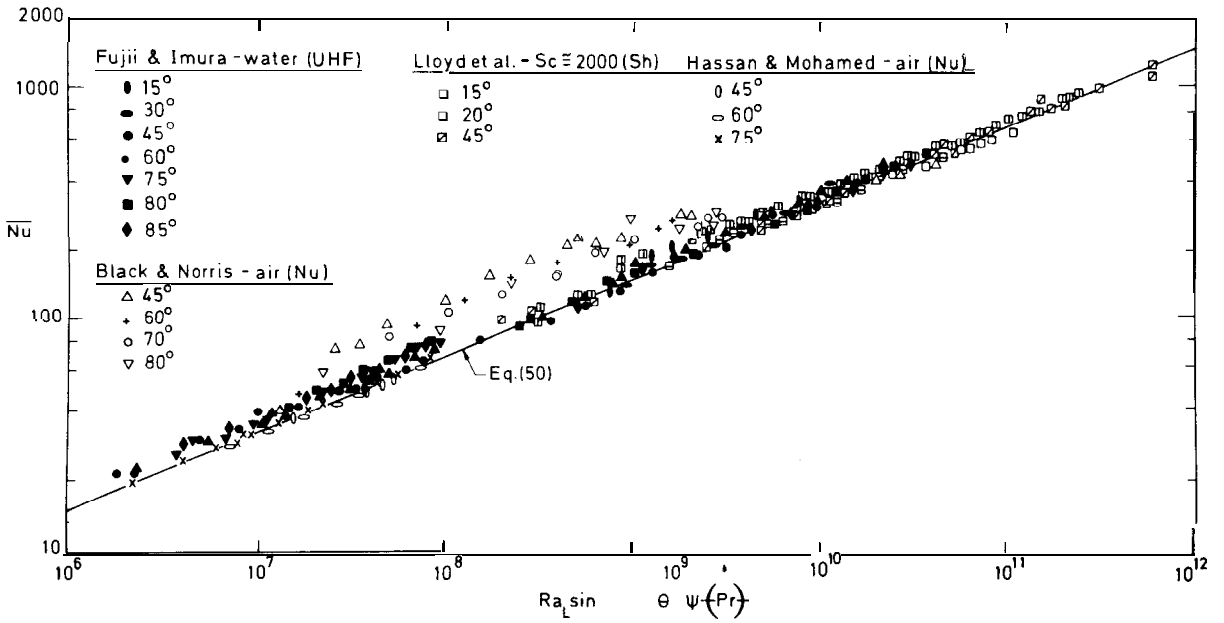

Figure 23 Comparison of Eq. (50) with experimental data for the local and mean Nusselt and Sherwood numbers in turbulent free convection from upward-facing plates inclined at large angles from the vertical.

© 1983 Hemisphere Publishing Corporation

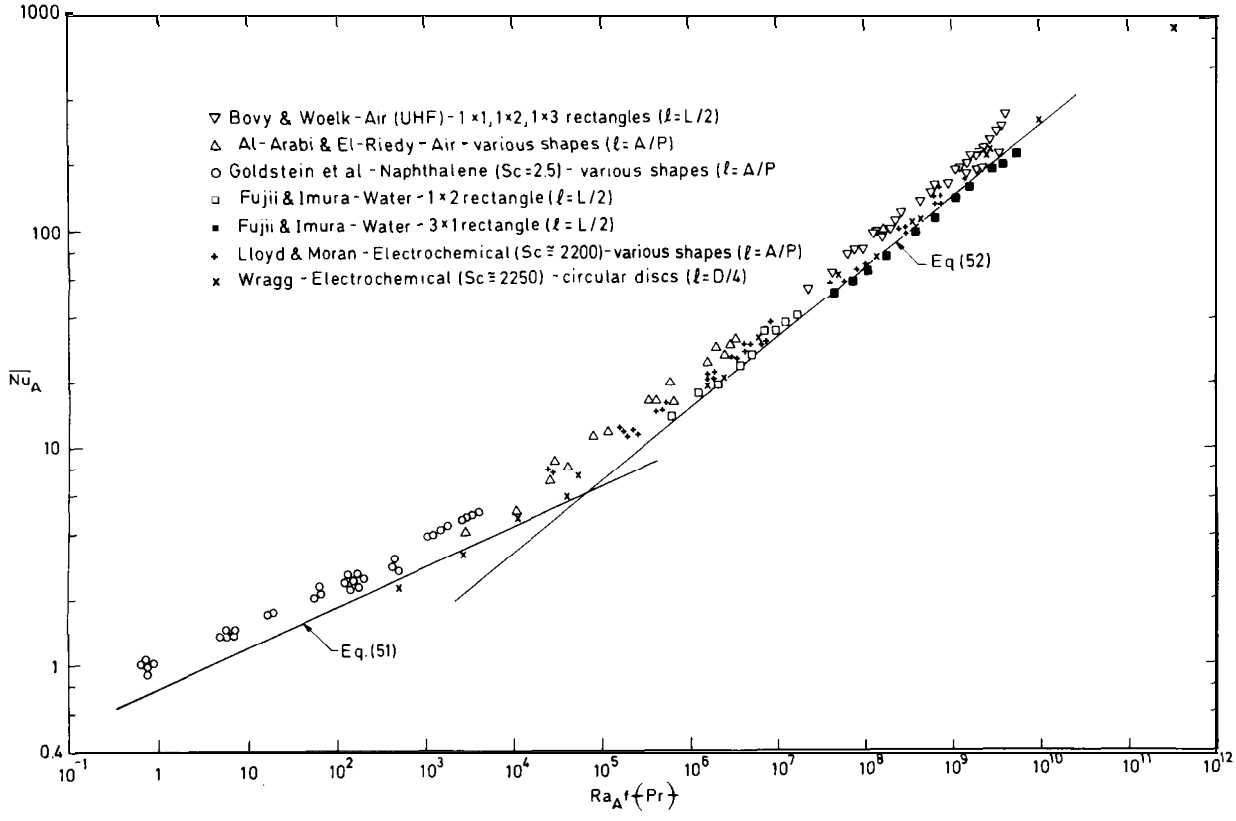

Figure 24 Comparison of Eqs. (51) and (52) with experimental data for the mean Nusselt and Sherwood numbers in free convection from upward-facing isothermal horizontal plates.

Aung et al. [69] for unsymmetrical heating are included in terms of the average temperature difference at the mid-height.

D. Horizqntal cylinders

Thin, laminar boundary-layer theory is of less direct utility in correlating data for horizontal cylinders than for flat plates because of the formation of a plume or wake at the rear of the cylinder at moderate Ra and the curvature of the boundary layer itself. Even so, it proves to be indispensable in constructing a correlation.

Churchill and Chu [70] combined the asymptotic solutions from the thin boundary-layer solutions of LeFevre [10] for $Pr \to \infty$ and of Saville and Churchill [71] for $Pr \to 0$ to obtain the following correlating equation for UWT:

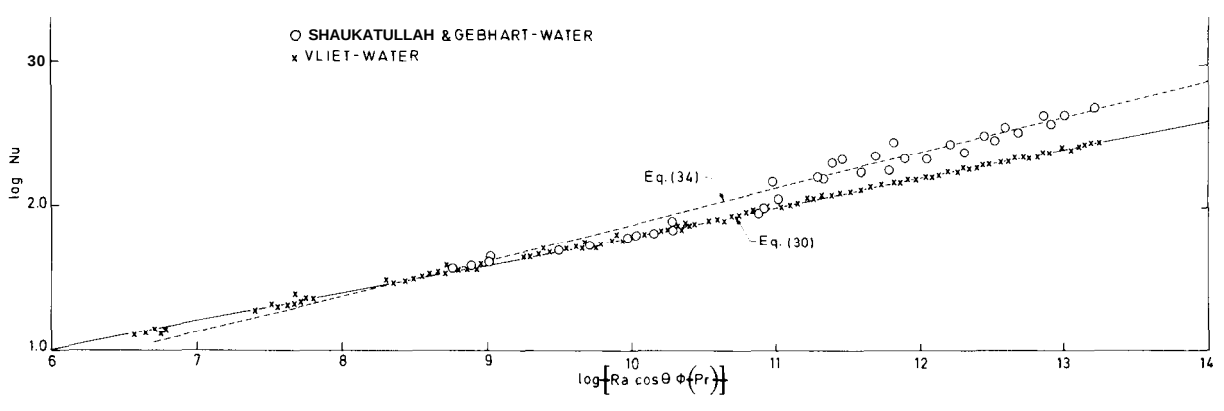

Figure 25 Comparison of Eqs. (30) and (34) with experimental data for the local Nusselt number in free convection from uniformly heated, upward-facing, inclined plates to water.

© 1983 Hemisphere Publishing Corporation

Table 3 Characteristic lengths and coefficients for Eq. (54) for buoyancy-induced convection[a]

Channel	Condition	Characteristic length[b]	A	c
Cylinder	UWT	D	1/128	0.492
Parallel plates	UWT	b	1/24	0.492
Cylinder	UHF	D	1/64	0.437
Parallel plates	UHF	b	1/12	0.437

[a] From Churchill [67].
[b] b = distance between plates.

$$\overline{\mathrm{Nu}} = \frac{0.518\ \mathrm{Ra}^{1/4}}{[\,1 + (0.559/\mathrm{Pr})^{9/16}\,]^{4/9}} \tag{56}$$

The characteristic length in Eq. (56) and all subsequent expressions in this section is the diameter ***D.***

Equation (24) is found to be applicable for the turbulent regime for horizontal cylinders as well as vertical plates, and the following combination, analogous to Eq. (27), provides an overall correlation for the two, thin boundary-layer regimes:

$$\overline{\mathrm{Nu}}_f = \frac{0.518\ \mathrm{Ra}^{1/4}}{[\,1 + 0.559/\mathrm{Pr})^{9/16}\,]^{4/9}}$$

$$\times \left(1 + \frac{3.47\ \mathrm{X}\ 10^{-7}\ \mathrm{Ra}}{[\,1 + (0.559/\mathrm{Pr})^{9/16}\,]^{16/9}}\right)^{1/12} \tag{57}$$

Langmuir [72] derived the following expression for the effect of the curved thickness of the curved boundary layer on a cylinder:

$$\overline{\mathrm{Nu}} = 2\ \ln\ \left(1 + \frac{2}{\overline{\mathrm{Nu}}_f}\right) \tag{58}$$

Equation (58) can be combined with Eq. (56) to provide a predictive expression for the entire laminar regime, with Eq. (24) for the turbulent regime, and with (57) for all Ra.

A number of solutions for creeping flow (Ra → 0) have been derived by the method of matched asymptotic expansions. The most accurate appears to be that of Nakai and Okazaki [73], which can be written as

$$\overline{\mathrm{Nu}} = 6/\ln\ \left(\frac{49.8\ (\mathrm{Pr} + 9.4)^{1/2}}{\mathrm{Nu\ Pr\ Ra}}\right) \tag{59}$$

Equation (57) was asserted by the authors to be valid only for Pr Ra < 10^{-3}.

These several expressions are compared in Fig. 27

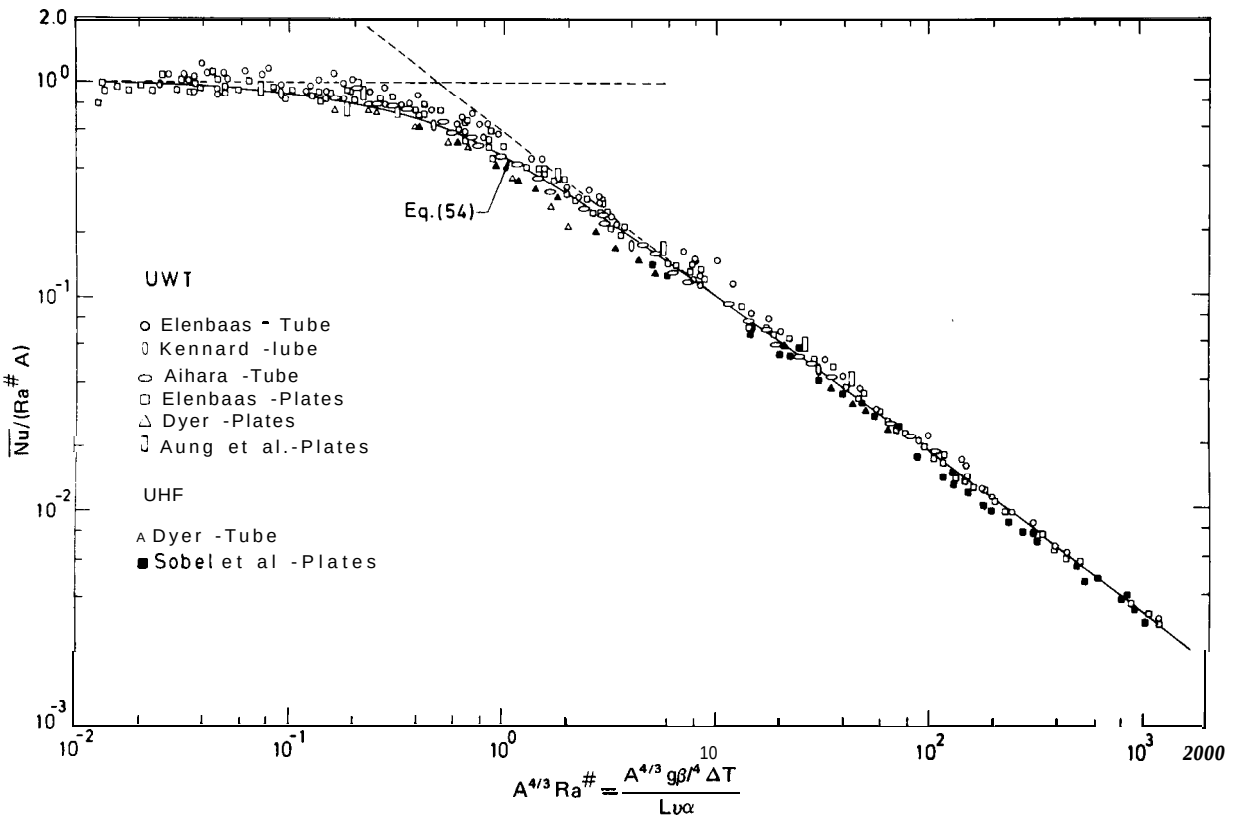

Figure 26 Comparison of Eq. (54) with experimental data for the mean Nusselt number in laminar, buoyancy-induced flow in open-ended, vertical channels. From Churchill [67]. Copyright 1977, Pergamon Press, Ltd. Reprinted with permission.

© 1983 Hemisphere Publishing Corporation

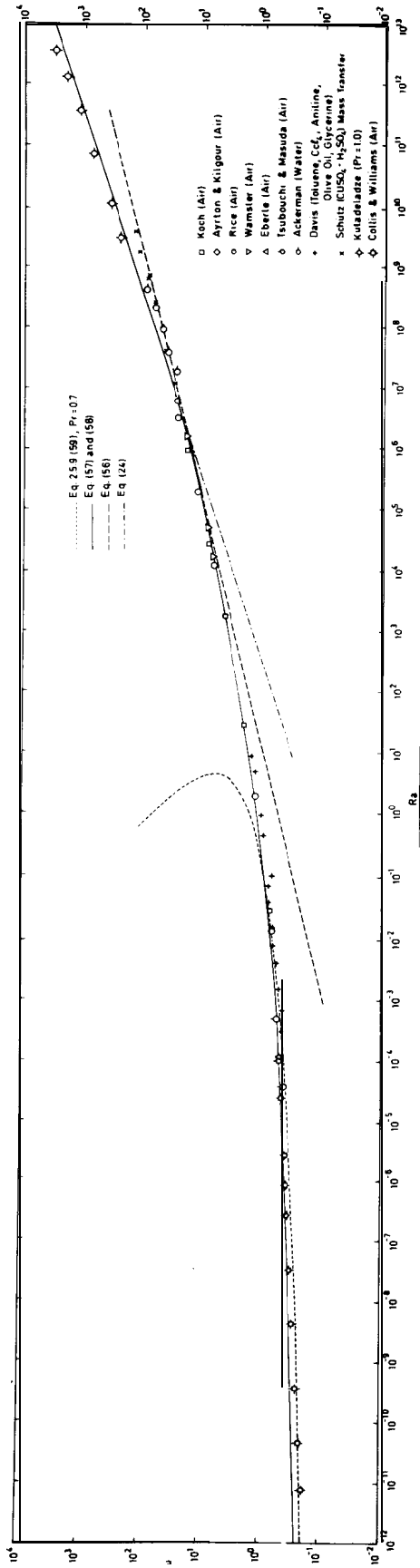

Figure 27 Comparison of Eqs. (56),(57),(58), and (59) with experimental data for the mean Nusselt and Sherwood numbers in free convection from isothermal, horizontal cylinders.

© 1983 Hemisphere Publishing Corporation

with experimental data of a number of investigators for a wide range of Ra and Pr. The combination of Eqs. (57) and (58) is seen to provide a good overall prediction, except for the data for large Sc that follow Eq. (56), owing to the persistence of laminar flow. Equation (59) is in better agreement with the data than the combination of Eqs. (59) [or (56)] and (58) only for $Ra < 10^{-8}$. However, the values of $\overline{Nu}$ observed experimentally for very low Ra are undoubtedly somewhat high, as a result of stray air currents and end effects.

The many sets of experimental data and the various other correlations that have been proposed are analyzed by Morgan [6]. The appropriate modifications of the above expressions for uniform heating, physical property variation, simultaneous transfer of species, and non-Newtonian behavior are the same as for the vertical plate. The correction factors for the latter case are included in Table 1. For uniform heating the central value of Pr is 0.442 rather than 0.559, but this difference is negligible except for liquid metals. Goldstein and Aung [74] showed that the equivalent of Eq. (59) is applicable even near the critical point, provided that the properties are properly evaluated.

E. Vertical and inclined cylinders

Fujii and Uehara [75] derived the following expression for a vertical cylinder with any arbitrary, specified temperature distribution:

$$\overline{Nu} = \overline{Nu}_p + 0.97\,\frac{x}{D} \tag{60}$$

where $\overline{Nu}_p$ = local Nusselt number for a flat plate at the same distance x and with the same temperature profile
x = distance up cylinder
D = diameter

The characteristic distance is here taken as x.

The following expression for inclined cylinders (with insulated end surfaces) in the thin boundary-layer regime ($10^5 < Ra < 10^9$) is based on Eq. (56) for horizontal cylinders and Eq. (21) for vertical flat plates as asymptotes, with g cos θ substituted for g in both and 0.559 for 0.492 in the latter:

$$\overline{Nu} = \frac{0.518(Ra\cos\theta)^{1/4}\,[\,1 + (2.80\,\tan\theta/x)^{3/2}\,]^{1/6}}{[\,1 + (0.559)/Pr^{9/16}\,]^{4/9}} \tag{61}$$

Here θ is the angle of inclination of the axis of the cylinder from the vertical and D is the characteristic length in $\overline{Nu}$ and Ra. It is implied that x/D is sufficiently short so that the correction given by Eq. (60) is negligible. The exponent 6 is based on the theoretical calculations of Raithby and Hollands [76] for intermediate inclinations and $Pr = \infty$.

The computed values of Raithby and Hollands are seen in Fig. 28 to be closely represented by Eq. (61), but the experimental values of Oosthuizen [77] for air fall consistently and significantly higher. They are, however, well represented by the following expression developed by Oosthuizen:

$$\overline{Nu} = 0.42(Gr\cos\theta)^{1/4}\left\{1 + \left[1.31\left(\frac{D\tan\theta}{L}\right)^{1/4}\right]^8\right\}^{1/8} \tag{62}$$

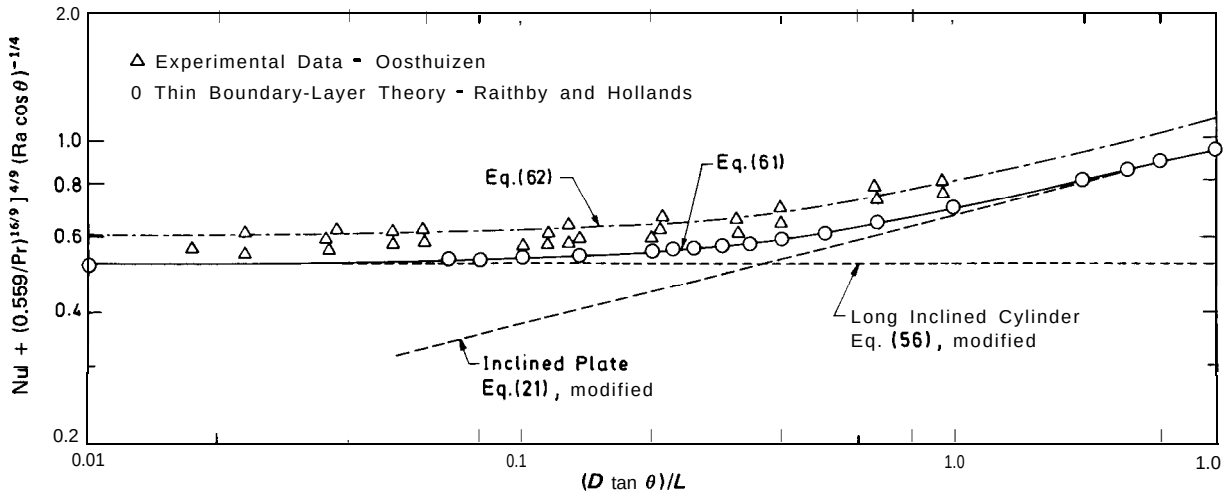

Figure. 28 Comparison of Eqs. (61) and (62) with the experimental data of Oosthuizen [77] for the mean Nusselt number in laminar free convection from isothermal, inclined cylinders to air.

© 1983 Hemisphere Publishing Corporation

Equation (62) is analogous to Eq. (61), but with empirically determined coefficients equivalent to 0.6 and 0.55 in place of the theoretical values of 0.518 and 0.67. The difference due to the exponents of. 2 and 1/8 instead of 3/2 and 1/6 is not significant.

The data are not given in a form that permits the use of Eq. (58), but test calculations suggest that it would represent the data. Hence, the combination of Eqs. (61) and (58) is recommended for prediction, because of presumed greater generality.

Morgan [6] has compiled and discussed various other sets of data and proposed alternative correlations.

F. Vertical cones

The theoretical value of 0.709 8 derived by Stewart [78] for $\overline{Nu}/(Ra \cos\theta)^{1/4}$ as $Pr \to \infty$ can be used with the values computed by Hering [79] for low Pr to construct the following generalized correlating equation for the thin boundary layer for all Pr:

$$\overline{Nu} = \frac{0.710(Ra_L \cos\theta)^{1/4}}{[1 + (0.352/Pr)^{9/16}]^{4/9}} \quad (63)$$

Here the characteristic distance in $\overline{Nu}$ and Ra_L is the slant height of the cone, and θ is the angle between the generating lines and the axis. Kuiken [80] derived an expression for the effect of boundary-layer thickening, the first two terms of which can be generalized as

$$\overline{Nu} = \overline{Nu}_f + \frac{0.412}{\tan\theta} \quad (64)$$

where Nu_f is represented by Eq. (63).

Oosthuizen and Donaldson [81] correlated their own experimental data for air, as shown in Fig. 29, by the analogous expression

$$\overline{Nu} = 0.63(Gr_L \cos 2\theta)^{1/4} + \frac{0.907}{\tan\theta} \quad (65)$$

The coefficients in Eq. (65) were chosen empirically to fit these data. The use of cos 2θ rather than cos θ was not explained, but does not account for the discrepancy relative to Eq. (64) since the maximum angle in the experiments was $5.85\pi/180$ rad.

G. Spheres

Churchill [82] utilized the theoretical solutions of Chiang et al. [83] for Pr = 0.7, Mori et al. [84] for Sc = 1, 100, 500, and 650, and Stewart [76] for $Sc \to \infty$ to construct the following correlating equation for the local and mean Nusselt numbers in the thin laminar boundary-layer regime:

$$\overline{Nu} = \frac{0.770(1 - 0.071\,6\,\theta^2)Ra^{1/4}}{[1 + (0.469/Pr)^{9/16}]^{4/9}} \quad (65)$$

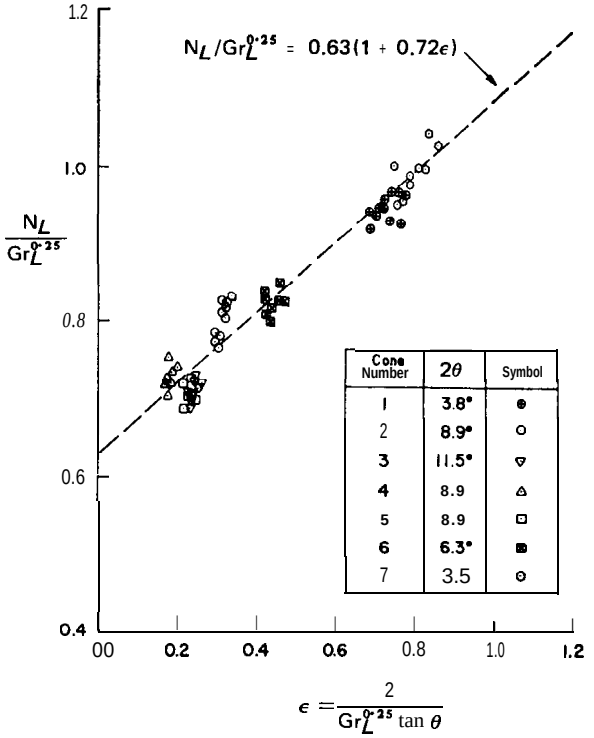

Figure 29 Comparison of Eq. (65) with experimental data for the mean Nusselt number in laminar free convection from isothermal, vertical cones to air. From Oosthuizen and Donaldson [81].

and

$$\overline{Nu} = \frac{0.589\ Ra^{1/4}}{[1 + (0.469/Pr)^{9/16}]^{4/9}} \quad (67)$$

where the diameter is used as the characteristic length, and

θ = angle from forward stagnation point, rad

The correction for the curved, finite thickness of the boundary layer, per Langmuir [72], corresponds to adding the limiting solution of 2.0 for pure conduction to the right side of Eqs. (66) and (67). Thus, for the mean value,

$$\overline{Nu} = 2 + \frac{0.589\ Ra^{1/4}}{[1 + (0.469/Pr)^{9/16}]^{4/9}} \quad (68)$$

The turbulent regimes were encompassed as well by combining Eq. (68) with a slightly modified Eq. (24) as

$$\overline{Nu} - 2 = \frac{0.589\ Ra^{1/4}}{[1 + (0.469/Pr)^{9/16}]^{4/9}} \times \left\{1 + \frac{7.44 \times 10^{-8}\ Ra}{[1 + (0.469/Pr)^{9/16}]^{16/9}}\right\}^{1/12} \quad (69)$$

© 1983 Hemisphere Publishing Corporation

The data of many investigators for $\overline{Nu}$ (and $\overline{Sh}$) for a wide range of conditions are compared with Eq. (69) in Fig. 30. The representation is generally satisfactory, although those sets of data for large Pr and Sc have a delayed transition in terms of Ra[1 + $(0.469/Pr)^{9/16}]^{-4/9}$ and hence are better represented by Eq. (68) for all Ra.

The experimental data of a number of investigators for the local Nusselt number at moderate values of Ra are compared with Eq. (66) in Fig. 31. The data are in reasonable agreement with the prediction, although they generally fall somewhat below for small angles. As Ra increases, separation occurs. Beyond the point of separation, the rate of heat transfer increases with angle. The contribution of the wake to the overall heat transfer is seen from the data of Schütz [85] to increase with Ra. The use of Nu — 2 rather than Nu as the ordinate of Fig. 31 would presumably improve the representation, particularly for lower Ra, but separate values of Nu and Ra were not available in all cases.

Hossain and Gebhart [86] derived the following expression for creeping flow (Gr → 0):

$$\overline{Nu} = 2 + Gr + Gr^2(0.139 - 0.419\ Pr + 1.1\ 902\ Pr^2) \quad (70)$$

Equation (70) presumably gives a more reliable dependence on Gr and Pr for Gr → 0 than Eq. (68). However, owing to the dominance of the limiting value of 2, the difference in $\overline{Nu}$ is not of practical importance.

Equation (68), with the special Rayleigh number defined by Eq. (43), is applicable for spheres in power law fluids with the coefficients given in Table 1. Acrivos [34] gives theoretical results graphically for the local Nusselt number for power law indices of 1/2 and 3/2. As shown in Fig. 32, the data of Amato and Tien [87] for $\overline{Nu}$ fall below Eq. (68) for small Ra but are in good agreement for large Ra . Their local data (not shown) closely follow the theoretical prediction of Acrivos.

H. Other immersed shapes

Theoretical results have been obtained for a few geometries in addition to those already mentioned. Experimental results have been obtained for many more shapes, particularly those involving fins and radiators. Only a few of these results of particular generality will be noted here.

Raithby et al. [88] obtained data for one prolate and two oblate spheroids and developed correlations in the Churchill-Usagi form covering the regimes of creeping, boundary-layer, and turbulent flow. Merkin [89] obtained solutions for horizontal, elliptical cylinders by numerical integration. Lin and Chao [90] derived series solutions for the same conditions as Merkin, ysing the Merk [91] method. Lock [92] formulated a generalized boundary-layer solution for $\overline{Nu}$ for inclined, arbitrarily shaped, plane surfaces and used it to obtain results for an m-sided pyramid. Stewart [78] derived and compiled laminar boundary-layer solutions for Pr → ∞ for a number of surfaces, including inclined disks and square and circular fins on horizontal tubes, in addition to the surfaces already mentioned.

I. Generalized solutions and correlations

Considerable progress has been achieved in generalizing the solutions and correlations for free convection. Stewart [78] has shown that the solutions for three-dimensional free convection in the thin laminar boundary-layer regime of all geometries for Pr → ∞ and an isothermal surface can be generalized as

$$\overline{Nu} = IA\ Ra''|^{1/4} \quad (71)$$

where A is a function of geometry only and the absolute value sign indicates the same A for heating and cooling. He further showed that for power law fluids,

$$\overline{Nu} = A\phi(n)|Ra''|^{1/1+3n} \quad (72)$$

with Ra and $\phi(n)$ defined as before. The values of $\phi(n)$ for vertical plates, horizontal cylinders, and spheres are given in Table 1.

Saville and Churchill [93] showed that Görtler-type transformations of variable could be utilized to generalize the thin boundary-layer equations for any given class of body shape such as round-nosed cylinders, sharp-nosed cylinders, and round-nosed axisymmetric bodies. Results for any specified body contour are then obtained by using the appropriate coefficients for a general series solution for that class of body and a specific Prandtl number. They asserted that these Gbrtler-type series converged more rapidly than Blasius-type series. Lin and Chao [90] contend that the Merk-type series is accurate to larger distances or angles.

Stewart [78] developed a general formulation for the thin laminar boundary-layer solution for $\overline{Nu}$ in the limit of Pr → ∞ for most three-dimensional surfaces in terms of a simple integral involving geometry only. Raithby and Hollands [76] generalized this solution by incorporating the universal function of Churchill and Usagi [14] for the dependence on Pr. They also derived a correction factor for small Ra.

Leinhard [94] noted that as a first-order approximation for laminar free convection in air with all geometries,

$$\overline{Nu} \cong 0.5\ Ra^{1/4} \quad (73)$$

© 1983 Hemisphere Publishing Corporation

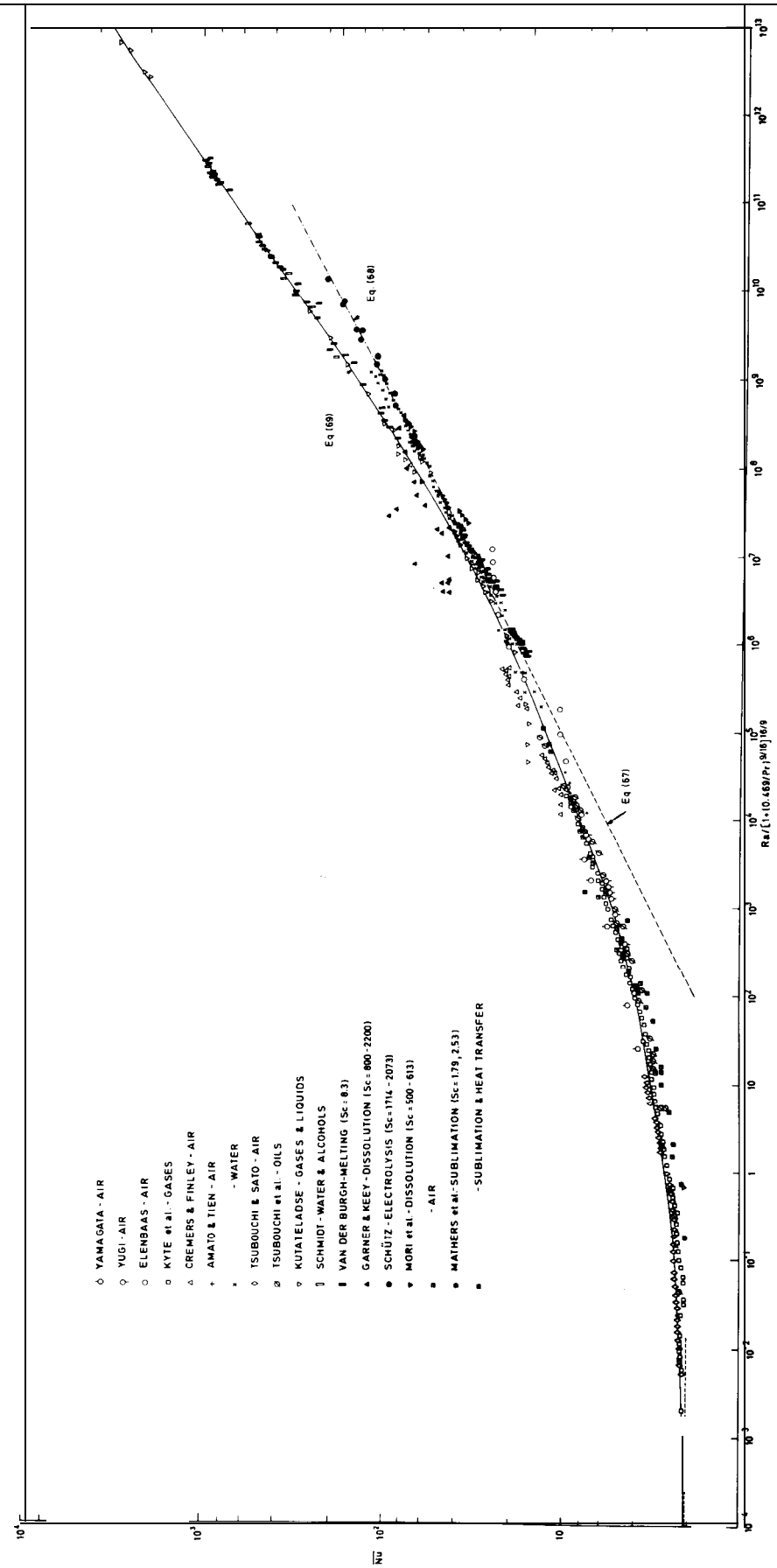

Figure 30 Comparison of Eqs. (68) and (69) with experimental data for the mean Nusselt and Sherwood numbers in free convection from isothermal plates. From Churchill [82].

© 1983 Hemisphere Publishing Corporation

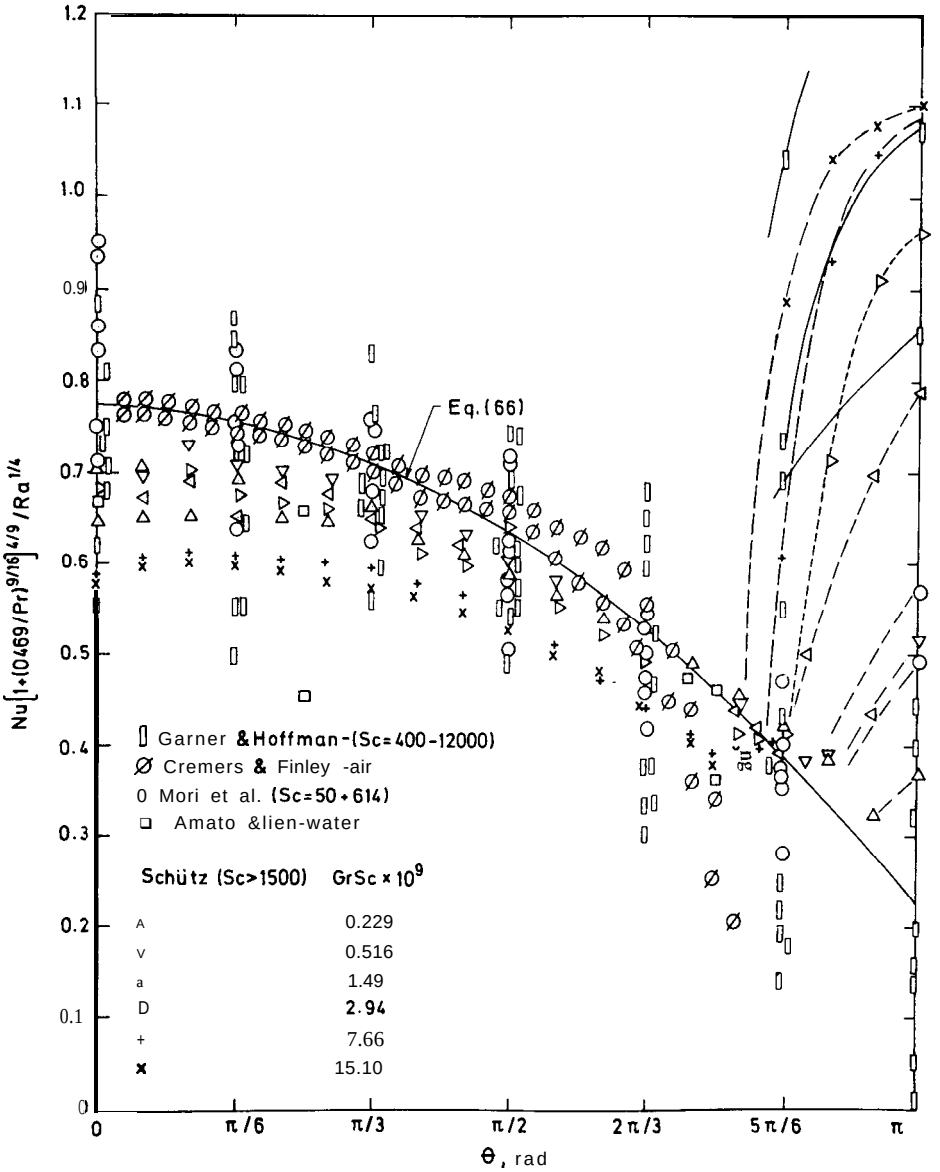

Figure 31 Comparison of Eq. (66) with experimental data for the local Nusselt and Sherwood numbers in free convection from isothermal spheres. From Churchill [82].

if the length of the boundary layer is used as the characteristic dimension. Tsubouchi and Satō [95] generalized the experimental data for horizontal cylinders, spheres, and spheroids by using $2V/A$ as the characteristic length, where

V = volume, m^3

A = surface area, m^2

Churchill and Thelen [96] and Churchill and Churchill [97] noted that the thin laminar boundary-layer solutions for all geometries and all Prandtl numbers have the form

$$\overline{Nu} = A\,(Ra\, f(Pr))^{1/4} \tag{74}$$

This expression can be extended to small Ra by adding a limiting value Nu_0 to account for boundary-layer thickening, yielding

$$\overline{Nu} = Nu_0 + A\,(Ra\, f(Pr))^{1/4} \tag{75}$$

They demonstrated that

$$f(Pr) = \left[1 + \left(\frac{0.5}{Pr}\right)^{9/16}\right]^{-16/9} \tag{76}$$

is a good approximation for all geometries and forced the coefficient A into conformity with that for a vertical plate by arbitrarily defining the characteristic length as in Table 4. The corresponding values of Nu_0 are included in the table. Their general correlation for

© 1983 Hemisphere publishing Corporation

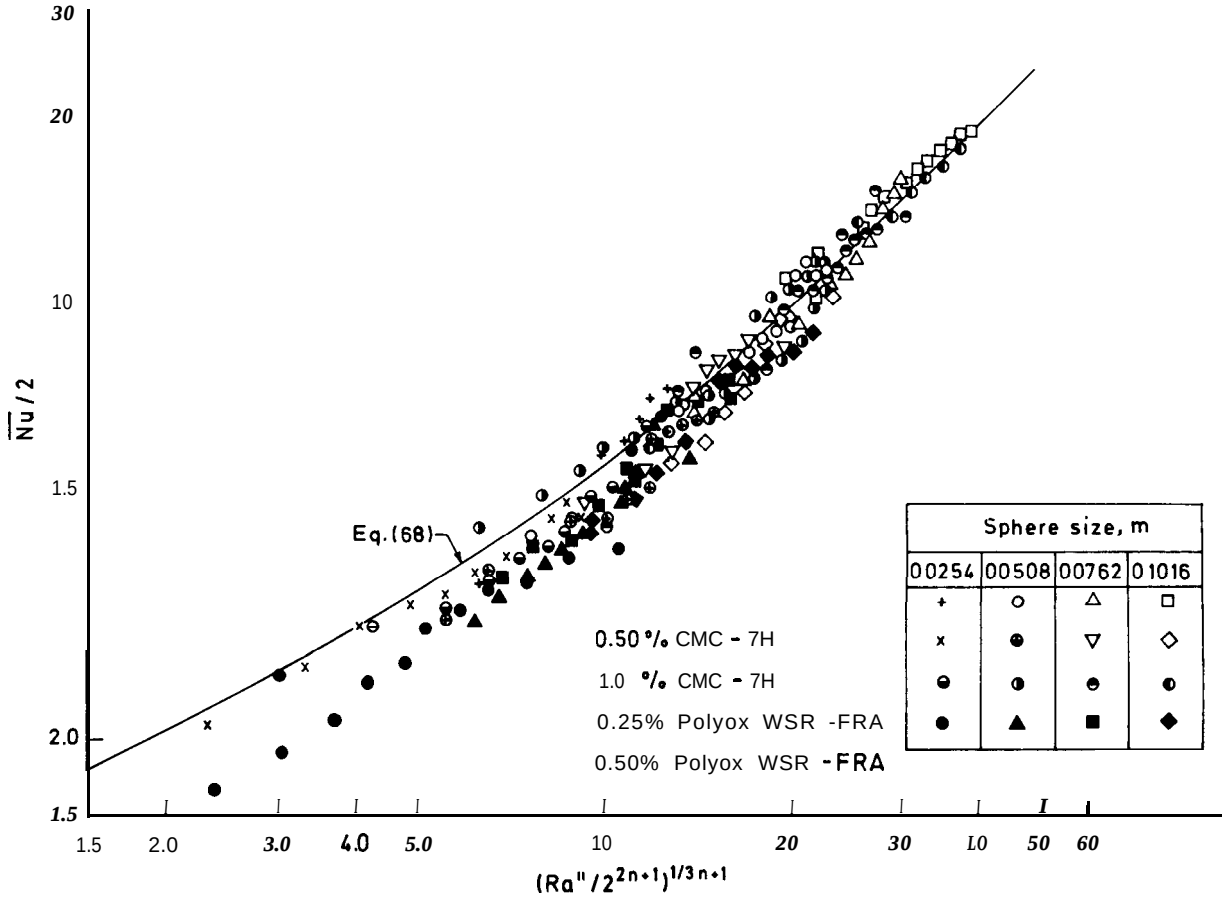

Figure 32 Comparison of Eq. (68) with experimental data for the mean Nusselt number in laminar free convection from isothermal spheres to polymer solutions. From Amato and Tien [87]. Copyright 1976, Pergamon Press. Reprinted with permission.

all geometries, all Pr, and all Ra in the laminar regime is then

$$\overline{Nu} = Nu_0 + \left(\frac{Ra\, f(Pr)}{5}\right)^{1/4} \tag{77}$$

They similarly proposed for the turbulent regime the general expression

Table 4 Characteristic lengths and Nu_0 for generalized correlations[a]

	Length[b]	N u ,
Inclined plate	x	*0.68*
Inclined disk	$9D/11$	*0.56*
Vertical cylinder	x	*0.68*
Cone	$4x/5$	*0.54*
Horizontal cylinder	πD	0.36π
Sphere	$\pi D/2$	π
Spheroids	$3\pi V/A$	$A^3/36V^2$

[a] From Churchill and Churchill [97].
[b] x is the slant distance.

$$\overline{Nu} = \left(\frac{Ra\, f(Pr)}{300}\right)^{1/3} \tag{78}$$

and for the entire range of Ra,

$$\overline{Nu}^{1/2} = Nu_0^{1/2} + \left(\frac{Ra\, f(Pr)}{300}\right)^{1/6} \tag{79}$$

A somewhat better overall correlation is provided by

$$\overline{Nu} = Nu_0 + \left(\frac{Ra\, f(Pr)}{5}\right)^{1/4} \times (1 + 1.6 \times 10^{-8}\, Ra\, f(Pr))^{1/12} \tag{80}$$

The characteristic lengths and values of Nu_0 in Table 4 are also appropriate for Eqs. (78)-(80). Equations (75)-(80) are applicable for uniform heating with the temperature difference evaluated at the midpoint of the surface. They are adaptable for power law fluids and for transfer of species as above.

© 1983 Hemisphere l ublishing Corporation

Nomenclature for Section 2.5.7 appears at the beginning of Part 2.

REFERENCES FOR SECTION 2.5.7

1. Ostrach, S., Laminar Flow with Body Forces, in *Theory* of *Laminar* Flows, ed. F. K. Moore, pp. 528-718, Princeton University Press, Princeton, N.J., 1964.
2. Schmidt, E., Heat Transfer by Natural Convection, ***Int. Div. Heat Transfer,*** ASME, New York, 1962.
3. Bansal, T. D., Steady State Free Convection Phenomena, ***J. Sci. Ind. Res.,*** vol. 12, pp. 271-281, 1965.
4. Churchill, S. W., The Prediction of Natural Convection, ***Proc. 3d Int. Heat Transfer Conf., Chicago,*** vol. 6, pp. 15-30, 1967.
5. Ede, A. J., Advances in Free Convection, in ***Advances in Heat Transfer,*** vol. 4, pp. l-64, Academic, New York, 1967.
6. Morgan, V. T., The Overall Convective Heat Transfer from Smooth Cylinders, in ***Advances in Heat Transfer,*** vol. 11, pp. 199-264, Academic, New York, 1975.
7. Hellums, J. D., and Churchill, S. W., Dimensional Analysis and Natural Convection, ***Chem. Eng. Prog. Symp. Ser.,*** no. 32, vol. 57, pp. 75-80, 1961.
8. Churchill, S. W., An Analysis of Heat and Component Transfer by Turbulent Free Convection from a Vertical Plate, ***Proc. Chemeca*** 70, session 6A, pp. 1-16, Butterworths, Sydney, Australia, 1970.
9. Jakob, M., and Linke, W., Der Wärmeübergang von einer waagerechten Platte an siedenders Wasser, *Forsch. Ingenieurwes.,* vol. 4, pp. 75-81, 1933.
10. LeFevre, E. J., Laminar Free Convection from a Vertical Plane Surface, ***Proc. 9th Int. Congr.*** *Appl. Mech., Brussels,* vol. 4, pp. 168-174, 1956.
11. Ostrach, S., An Analysis of Laminar Free-Convection Flow and Heat Transfer About a Flat Plate Parallel to the Direction of the Generating Body Force, NACA Rept. 1111, Washington, D.C., 1953.
12. Churchill, S. W., and Usagi, R., A General Expression for the Correlation of Rates of Transfer and Other Phenomena, *AIChE J.,* vol. 18, pp. 1121-1128, 1972.
13. Churchill, S. W., and Chu, H. H.-S., Correlating Equations for Laminar and Turbulent Free Convection from a Vertical Plate, *Int. J. Heat Mass Transfer,* vol. 18, pp. 1323-1329, 1975.
14. Saunders, 0. A., Effect of Pressure Upon Natural Convection in Air, ***Proc. Roy Soc. London,*** vol. A157, pp. 278-291, 1936.
15. Gryzagoridis, J., Leading Edge Geometry Effects on Natural Convection from an Isothermal Vertical Plate, *Lett. Heat Mass Transfer, vol. 5,* pp. 203-213, 1978.
16. Cebeci, T., and Khattab, A., Prediction of Turbulent Free Convection Heat Transfer from a Vertical Flat Plate, ***J. Heat Transfer,*** vol. 97, pp. 469-471, 1975.
17. Plumb, 0. A., and Kennedy, L. A., Application of K-E Turbulence Model to Natural Convection from a Vertical Isothermal Surface, ***J. Heat Transfer,*** vol. 99, pp. 79-85, 1977.
18. Lin, S.-J., and Churchill, S. W., Turbulent Free Convection from a Vertical, Isothermal Plate, ***Num. Heat Transfer, vol.*** 1, pp. 129-145, 1978.
19. Bayley, F.-J., An Analysis of Turbulent Free Convection Heat Transfer, *Proc. Inst. Mech. Eng. London, vol.* 169, pp. 361-370, 1955.
20. Kutateladze, ***S.*** E., ***Fundamentals of Heat Transfer,*** pp. 293-294, Edward Arnold, London, 1963.
21. Sparrow, E. M., Trow, F. K., and Kurtz, E. K., Jr., Stability of Laminar Free Convection Flow on a Vertical Plate, ***Phys.*** *Fluids,* vol. 8, pp. 1559-1561, 1965.
22. Fujii, T., Experimental Studies of Free Convection Heat Transfer, ***Bull. Jpn. Soc. Mech. Eng.,*** vol. 2, pp. 551-555, 1959.
23. Klyacho, L. S., Relations for the Critical State Describing Transition from Laminar to Turbulent Flow in Free Convection, *Int. J. Heat Mass Transfer, vol. 5,* pp. 763-764, 1962.
24. Fujii, T., Takeuchi, M., Fujii, M., Suzaki, K., and Uehara, H., Experiments on Natural Convection Heat Transfer from the Outer Surface of a Vertical Cylinder to Liquids, ***Int. J. Heat Mass Transfer,*** vol. 13, pp. 753-785, 1970.
25. Churchill, S. W., and Ozoe, H., A Correlation for Laminar Free Convection, ***J. Heat Transfer, vol. 95,*** pp. 540-541, 1973.
26. Sparrow, E. M., and Gregg, J. L., Laminar Free Convection from a Vertical Plate with Uniform Surface Heat Flux, ***Trans.*** *ASME,* vol. 78, pp. 435-440, 1956.
27. Churchill, S. W., and Usagi, R., A Standardized Procedure for the Production of Correlations in the Form of a Common Empirical Equation, *Ind. Eng. Chem. Fundam.,* vol. 13, pp. 39-44, 1974.
28. Hellums, J. D., and Churchill, S. W., Transient and Steady, Free and Natural Convection, Numerical Solutions, Part I, The Isothermal Plate, *AIChE J.,* vol. 8, pp. 690–692, 719, 1962.
29. Ingham, D. B., Transient Free Convection on an Isothermal Vertical Flat Plate, ***Int. J. Heat Mass Transfer,*** vol. 21, pp. 6769, 1978.
30. Klei, H., Transient Free Convection from a Vertical Flat Plate, S.B. thesis in chemical engineering, Massachusetts Institute of Technology, Cambridge, Mass., 19.5 7.
31. Churchill, S. W., Transient, Laminar Free Convection from a Uniformly Heated Vertical Plate, *Lett. Heat Mass Transfer,* vol. 2, pp. 311-314, 1975.
32. Goldstein, R. J., and Eckert, E. R. G., The Steady and Transient Free Convection Boundary Layer on a Uniformly Heated Vertical Plate, ***Znt. J. Heat Mass Transfer, vol. 1,*** pp. 208-218, 1960.
33. Gebhart, B., Transient Natural Convection from Vertical Elements, ***J. Heat Transfer,*** vol. 83C, pp. 61-70, 1961.
34. Acrivos, A., A Theoretical Analysis of Laminar Natural Convection Heat Transfer to Non-Newtonian Fluids, *AIChE J.,* vol. 6, pp. 584-590, 1960.
35. Agarwal, B. K. D., Lieu, K. S., and Adelman, M., Experimental Verification of Acrivos Equation for Laminar Natural Heat Convection to Non-Newtonian Fluids, private communication.

© 1983 Hemisphere Publishing Corporation

36. Chen, T. Y. W., and Wollersheim, D. E., Free Convection at a Vertical Plate with Uniform Flux Condition in Non-Newtonian Power Law Fluids, *J. Heat Transfer,* vol. 95C, pp. 123-124, 1973.
37. Dale, J. D., Laminar Free Convection of Non-Newtonian Fluids from a Vertical Plate with Uniform Surface Heat Flux, Ph.D. thesis, University of Washington, Seattle, 1969; see also Dale, J. D., and Emery, A. F., The Free Convection of Heat from a Vertical Plate to Several Non-Newtonian Pseudoplastic Fluids *J. Heat Transfer,* vol. 94C, pp. 64-72, 1972.
38. Fujii, T., Miyatake, O., Fujii, M., Tanaka, H., and Murokami, K., Natural Convective Heat Transfer from a Vertical Isothermal Surface to a Non-Newtonian Sutterby Fluid, *Int. J. Heat Mass Transfer,* vol. 16, pp. 2177-2187, 1973; Natural Convective Heat Transfer from a Vertical Surface of Uniform Heat Flux to a Non-Newtonian Sutterby Fluid, ibid., vol. 17, pp. 149-154, 1974.
39. Gray, D. B., and Georgini, A., The Validity of the Boussinesq Approximation for Liquids and Gases, *Int. J. Heat Mass Transfer,* vol. 19, pp. 545-551, 1976.
40. Brown, A., The Effect on Laminar Free Convection Heat Transfer of the Temperature Dependence of the Coefficient of Volumetric Expansion, *J. Heat Transfer,* vol. 97, pp. 133-135, 1975.
41. Eshghy, S., and Morrison, F. A., Jr., Compressibility and Free Convection, *Proc.* Roy. *Soc. London,* vol. A293, pp. 395-407, 1966.
42. Wylie, R. G., The Transfer Coefficients of a Laminar Boundary Layer with Variable Fluid Properties, *Chem. Eng. J.,* vol. 6, pp. 1-14, 1973.
43. Sparrow, E. M., and Gregg, J. L., The Variable Fluid-Property Problem in Free Convection, in *Recent Advances in Heat and Mass Transfer,* pp. 353-371, McGraw-Hill, New York, 1961.
44. Bonilla, C. F., and Sigel, L. A., High Intensity Natural Convection Heat Transfer Near the Critical Point, *Chem. Eng. Prog. Symp.* Ser., no. 32, vol. 51, pp. 87-95, 1961.
45. Schechter, R. S., and Isbin, H. S., Natural Convection Heat Transfer in Regions of Maximum Fluid Density, *AIChE J.,* vol. 4, pp. 81-89, 1958.
46. Gebhart, B., Effects of Dissipation in Natural Convection, *J. Fluid Mech.,* vol. 14, pp. 225-232, 1962.
47. Brown, A., Relative Importance of Viscous Dissipation and Pressure Stress Effects on Laminar Free Convection, *Trans. Inst. Chem. Eng., vol. 56,* pp. 77-80, 1978.
48. Wilkie, C. R., Tobias, C. W., and Eisenberg, M., Free-Convection Mass Transfer at Vertical Plates, *Chem. Eng. Prog.,* vol. 49, pp. *663-674,* 1953.
49. Saville, D. A., and Churchill, S. W., Simultaneous Heat and Mass Transfer in Free Convection Boundary Layers, *AIChE J., vol.* 16, pp. 268-273, 1970.
50. Lightfoot, E. N., Free Convection Heat Transfer: The Limiting Case of $Gr_{AB}/Gr \rightarrow 0$ and $Pr/Sc \rightarrow 0$, *Chem. Eng. Sci.,* vol. 23, p. 931, 1968.
51. Moran, W. R., and Lloyd, J. R., Natural Convection Mass Transfer Adjacent to Vertical Downward-Facing Inclined Surfaces, *J. Heat Transfer, vol.* 97C, pp. 472-474, 1975.
52., Hassan, K. E., and Mohamed, S. A., Natural Convection from Isothermal Flat Surfaces, *Int. J. Heat Mass Transfer, vol.* 13, pp. 1873-1886, 1970.
53. Kierkus, W. T., An Analysis of Laminar Free Convection about an Inclined Isothermal Plate, *Int. J. Heat Mass Transfer,* vol. 11, pp. 241-253, 1968.
54. Fujii, T., and Imura, H., Natural Convection Heat Transfer from a Plate with Arbitrary Inclination, *Int. J. Heat Transfer,* vol. 15, pp. 755-767, 1972.
55. Goldstein, R. J., Sparrow, E. M., and Jones, D. C., Natural Convection Mass Transfer Adjacent to Horizontal Plates, *Int. J. Heat Mass Transfer,* vol. 15, pp. 2293-2308, 1912.
56. Singh, S. N., Birkebak, R. C., and Drake, R. M., Jr., Laminar Free Convection from Downward-Facing Horizontal Surfaces of Finite Dimensions, in *Progress in Heat Transfer,* vol. 2, pp. 87-98, Pergamon, Oxford, 1969.
57. Singh, S. N., and Birkebak, R. C., Laminar Free Convection from a Horizontal Infinite Strip Facing Downwards, Z. *Angew. Math. Phys.,* vol. 20, pp. 454-461, 1969.
58. Wagner, C., Discussion on Integral Methods in Natural Convection Flow, *J. Appl. Mech.,* vol. 23, pp. 320-321, 1956.
59. Faw, R. E., and Dullforce, T. A., Holographic Interferometry Measurement of Convective Heat Transport Beneath a Heated Horizontal Plate *in* Air, *Znt. J. Heat Mass Transfer,* vol. 24, pp. 859-869, 1981.
60. Fussey, D. E., and Warneford, I. P., Free Convection from a Downward Facing Inclined Flat Plate, *Int. J. Heat Mass Transfer,* vol. 21, pp. 119-126, 1978.
61. Raithby, G. D., and Hollands, K. G. T., A General Method of Obtaining Approximate Solutions to Laminar and Turbulent Free Convection Problems, *Advances in Heat Transfer,* vol. 12, pp. 265-315, Academic, New York, 1974.
62. Rotem, Z., and Claassen, L., Natural Convection Above Unconfined Horizontal Surfaces, *J. Fluid Mech.,* pp. 173-192, 1969.
63. Churchill, S. W., *A Correlating Equation for Almost Evetything,* Etaner Press, Thornton, Pa., 1982.
64. Shaukatullah, H., and Gebhart, B., An Experimental Investigation of Natural Convection Flow on an Inclined Surface, *Int. J. Heat Mass Transfer,* vol. 21, pp. 1481-1490, 1978.
65. Vliet, G. C., Natural Convection Local Heat Transfer on Constant-Heat-Flux Inclined Surfaces, *J. Heat Transfer,* vol. 91C, pp. 511-516, 1969.
66. Vliet, G. C., and Ross, D. C., Turbulent Natural Convection on Upward and Downward Facing Inclined Constant Heat Flux Surfaces, *J. Heat Transfer,* vol. 97C, pp. 549-555, 1975.
67. Churchill, S. W., A Comprehensive Correlating Equation for Buoyancy Induced Flow in Channels, *Lett. Heat Mass Transfer, vol. 4,* pp. 193-199, 1977.
68. Aihara, T., Effects of Inlet Boundary-Conditions on Numerical Solutions of Free Convection Between Vertical Parallel Plates, *Repts. Inst. High Speed Mech., Jpn., vol. 28,* pp. I-27, 1973.
69. Aung, W., Fletcher, L. S., and Sernas, V., Developing Laminar Free Convection Between Vertical Flat Plates with Asymmetric Heating, *Int. J. Heat Mass Transfer,* vol. 15, pp. 2293-2308, 1972.

© 1983 Hemisphere Publishing Corporation

70. Churchill, S. W., and Chu, H. H.-S., Correlating Equations for Laminar and Turbulent Free Convection from a Horizontal Cylinder, *Int. J. Heat Mass Transfer, vol.* 18, pp. 1049-1053, 1975.
71. Saville, D. A., and Churchill, S. W., Free Convection at Low Prandtl Numbers in Laminar Boundary Layers, *Ind. Eng. Chem. Fun&m.,* vol. 8, pp. 829-832, 1969.
72. Langmuir, I., Convection and Conduction of Heat in Gases, *Phys. Rev.,* vol. 34, pp. 401422, 1912.
73. Nakai, S., and Okazaki, T., Heat Transfer from a Circular Wire at Small Reynolds and Grashof Numbers-I. Pure Convection, *Int. J. Heat Mass Transfer,* vol. 18, pp. 387-396, 1975.
74. Goldstein, R. J., and Aung, W., Heat Transfer by Free Convection from a Horizontal Wire to Carbon Dioxide in the Critical Region, *J. Heat Transfer,* vol. 90, pp. 51-55, 1968.
75. Fujii, T., and Uehara, H., Laminar Natural-Convective Heat Transfer from the Outer Surface of a Vertical Cylinder, *Int. J. Heat Mass Transfer,* vol. 13, pp. 607–615, 1970.
76. Raithby, G. D., and Hollands, K. G. T., Analysis of Heat Transfer by Natural Convection (or Film Condensation) for Three Dimensional Flows, *Proc. 6th Int. Heat Transfer Conf., Toronto,* vol. 2, pp. 187-192, 1978.
77. Oosthuizen, P. A., Experimental Study of Free Convective Heat Transfer from Inclined Cylinders, *J. Heat Transfer,* vol. 98, pp. 672-674, 1976.
78. Stewart, W. E., Asymptotic Calculation of Free Convection in Laminar Three-Dimensional Systems, *Int. J. Heat Mass Transfer,* vol. 14, pp. 1013-1031, 1971.
79. Hering, R. G., Laminar Free Convection from a Non-isothermal Cone at Low Prandtl Numbers, *Int. J. Heat Mass Transfer,* vol. 8, pp. 1333-1337, 1965.
80. Kuiken, H. K., Axisymmetric Free Convection Boundarv-Laver Flow Past Slender Bodies. *Int. J. Heat Mass Transfer,* vol. 11, pp. 1141–1153, 1968.
81. Oosthuizen, P. A., and Donaldson, E., Free Convective Heat Transfer from Vertical Cones, *J. Heat Transfer, vol. 94,* pp. 330-331, 1972.
82. Churchill, S. W., Correlating Equations for Natural Convection from Spheres, in review.
83. Chiang, T., Ossin, A., and Tien, C. L., Laminar Free Convection from a Sphere, *J. Heat Transfer,* vol. 86, pp. 537-542, 1962.
84. Mori, S., Tanimoto, A., Yamashita, M. Aoki, M., and Kazuhiko, Y., Mass Transfer by Laminar Free Convection from a Solid Sphere, *Kagaku Kogaku Ronbunshu,* vol. 2, pp. 214-215, 1976.
85. Schütz, G., Natural Convection Mass-Transfer, Measurements on Spheres and Horizontal Cylinders by an Electrochemical Methods, *Int. J. Heat Mass Transfer, vol. 6,* pp. 873-879, 1963.
86. Hussain, M. A., and Gebhart, B., Natural Convection About a Sphere at Low Grashof Number, *Heat Transfer 1970,* vol. 4, NC 1.6, pp. 1-12, Elsevier, Amsterdam, 1970.
87. Amato, W. S., and Tien, C., Free Convection Heat Transfer from Isothermal Spheres in Polymer Solutions, *Int. J. Heat Mass Transfer,* vol. 19, pp. 1257-1266, 1976.
88. Raithby, G. D., Pollard, A., Hollands, K. T. G., and Yovanovich, M. M., Free Convection from Spheroids, *J. Heat Transfer,* vol. 98, pp. 452-458, 1976.
89. Merkin, J. H., Free Convection Boundary Layers on Cylinders of Elliptic Cross Section, *J. Heat Transfer,* vol. 99, pp. 455-457, 1977.
90. Lin, F. N., and Chao, B. T. Predictive Capabilities of Series Solutions for Laminar Free Convection Boundary Layer Heat Transfer, *J. Heat Transfer,* vol. 100, pp. 160-163, 1978.
91. Merk, H. J., Rapid Calculations for Boundary Layer Transfer Using Wedge Solutions and Asymptotic Expansions, *J. Fluid Mech.,* vol. 5, pp. 460–480, 1959.
92. Lock, G. S. H., Steady Laminar Free Convection from Inclined Arbitrarily Shaped Plane Surfaces, *Znt. J. Heat Mass Transfer,* vol. 7, pp. 669673, 1964.
93. Saville, D. A., and Churchill, S. W., Laminar Free Convection in Boundary Layers Near Horizontal Cylinders and Axisymmetric Bodies, J. *Fluid Mech.,* vol. 29, pp. 391-399, 1967.
94. Leinhard, J. H., On the Commonality of Equations for Natural Convection from Immersed Bodies, *Znt. J. Heat Mass Transfer,* vol. 16, pp. 2121-2123, 1973.
95. Tsubouchi, T., and Satō, S., Heat Transfer from Fine Wires and Particles by Natural Convection, *Chem. Eng. Prog. Symp. Ser.,* no. 30, vol. 56, pp 269-284, 1960.
96. Churchill, S. W., and Thelen, H.-J., Eine Allgemeine Korrelationsgleichung für den Wärme- und Stoffubergang bei Freier Konvection, *Chem. Eng. Tech.,* vol. 47, p. 453, 1975.
97. Churchill, S. W., and Churchill, R. U., A Comprehensive Correlating Equation for Heat and Component Transfer by Free Convection, *AIChE J., vol.* 21, pp. 604-606, 1975.

© 1983 Hemisphere Publishing Corporation

2.5.8

Free convection in layers and enclosures

S. W. Churchill

Natural convection occurs in enclosures as a result of gradients in density, which are in turn due to variations in temperature or concentration. The rate of heat transfer is usually characterized by a Nusselt number as a function of a Rayleigh number, the Prandtl number, the geometry, and the boundary and initial conditions. The Nusselt and Rayleigh numbers are ordinarily based on the external temperature difference and the dimension of the enclosure in the direction of heat transfer, with some exceptions as noted below. The other variables in these groups are defined as in Sec. 2.5.7.

Catton [1] provides a recent, comprehensive, and interpretive review of natural convection in enclosures. Ostrach [2,3] discusses cylindrical and rectangular enclosures in somewhat greater detail. Koschmieder [4] has reviewed Bénard-type convection and Buchberg et al. [5] applications of natural convection in solar collectors. Churchill and Ozoe [6] have utilized theoretical and experimental results for asymptotic conditions to develop correlating equations for heat transfer in rectangular and cylindrical enclosures for a wide range of conditions with special attention to the effect of the angles of inclination and rotation.

In this section a description of the fluid motion is provided and correlations are recommended for heat transfer for conditions of primary practical importance. Referral to the references cited herein and in the above reviews is suggested for derivations and further details.

Experimental results for natural convection in enclosures are generally less accurate than for forced convection owing to difficulty in repressing and evaluating the heat fluxes through and along the nonisothermal walls. As a consequence, discrepancies between various sets of data are not completely resolved. Also, the time scale of experiments, particularly with liquids, is sometimes insufficient to attain the true stationary state.

Theoretical results are limited in accuracy and scope owing to the inherent three dimensionality of the velocity and temperature fields in all enclosures with two or three finite dimensions. This three dimensionality affects the transitions from one mode of circulation to another. If one or the other aspect ratio is near unity, the three dlmensionality affects the rates of circulation and heat transfer significantly. Even so, the many two-dimensional and the few three-dimensional solutions provide a useful basis for the interpretation, correlation, and extrapolation of the experimental values.

For a horizontal layer of fluid with a uniform temperature on the upper surface and a higher uniform temperature on the lower surface, a quiescent fluid is the stable state below a critical value of the Rayleigh number, Ra_c. For the reverse boundary conditions, a quiescent fluid is the stable steady state for all Ra. A fluid motion occurs for all other thermal boundary conditions.

A. Infinite horizontal layers of fluid heated from below

Natural convection in this geometry has received extensive attention since 1900, when Bénard [7] observed hexagonal roll cells upon the onset of convection in molten spermaceti with a free upper surface. The motion observed by Bénard has since been attributed to surface tension rather than gravity. Hexagonal roll cells have

© 1983 Hemisphere Publishing corporation

been observed for gravitational convection with a rigid upper surface, as illustrated in Fig. 1 by Quinn [8], but the incipient motion for truly isothermal surfaces is believed to be either longitudinal or circular roll cells, depending on the configuration of the side walls. All three motions are sketched in Fig. 2.

Rayleigh [9] was the first to compute a critical value, Ra_c, for the onset of convection. The accepted theoretical value of this dimensionless group, as defined below Eq. 2.5.7(3), is 1 708 for rigid upper and lower surfaces. This value is independent of the postulated mode of convection.

For *free* convection from an immersed surface, as discussed in Sec. 2.5.7, a gradual transition occurs from no flow to a thin laminar boundary layer, followed by a rapid transition to a turbulent boundary layer as the Rayleigh number increases. For a confined fluid, by contrast, a series of discrete transitions occurs, associated with Rayleigh-like modes of instability of increasing order. Such transitions in the rate of circulation and rate of heat transfer have been observed experimentally by Malkus [10], Garon and Goldstein [11], and others. Malkus and Veronis [12] derived the following expression for the rate of heat transfer based on this concept:

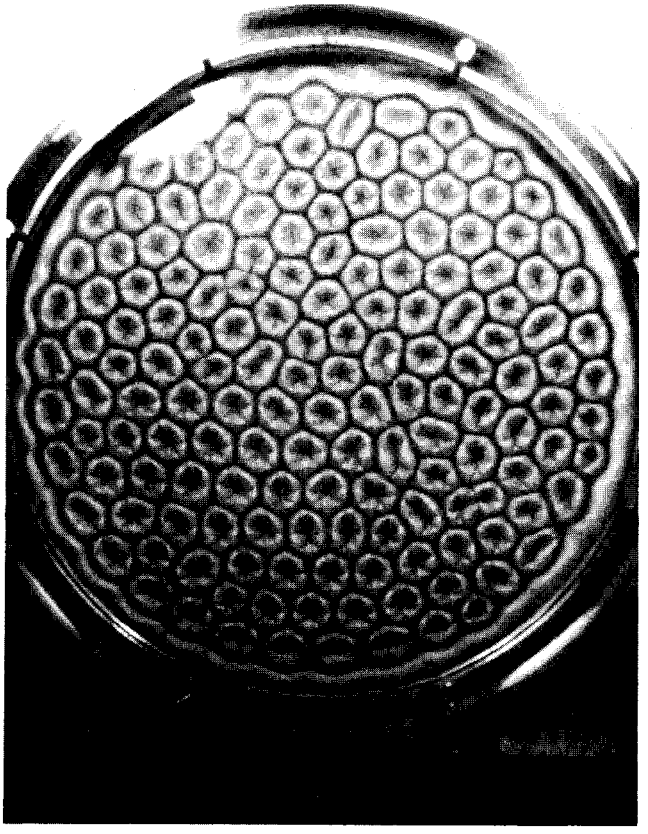

Figure 1 Hexagonal roll cells in a horizontal layer of silicone oil heated from below with rigid upper surface. Courtesy of J. A. Quinn [8].

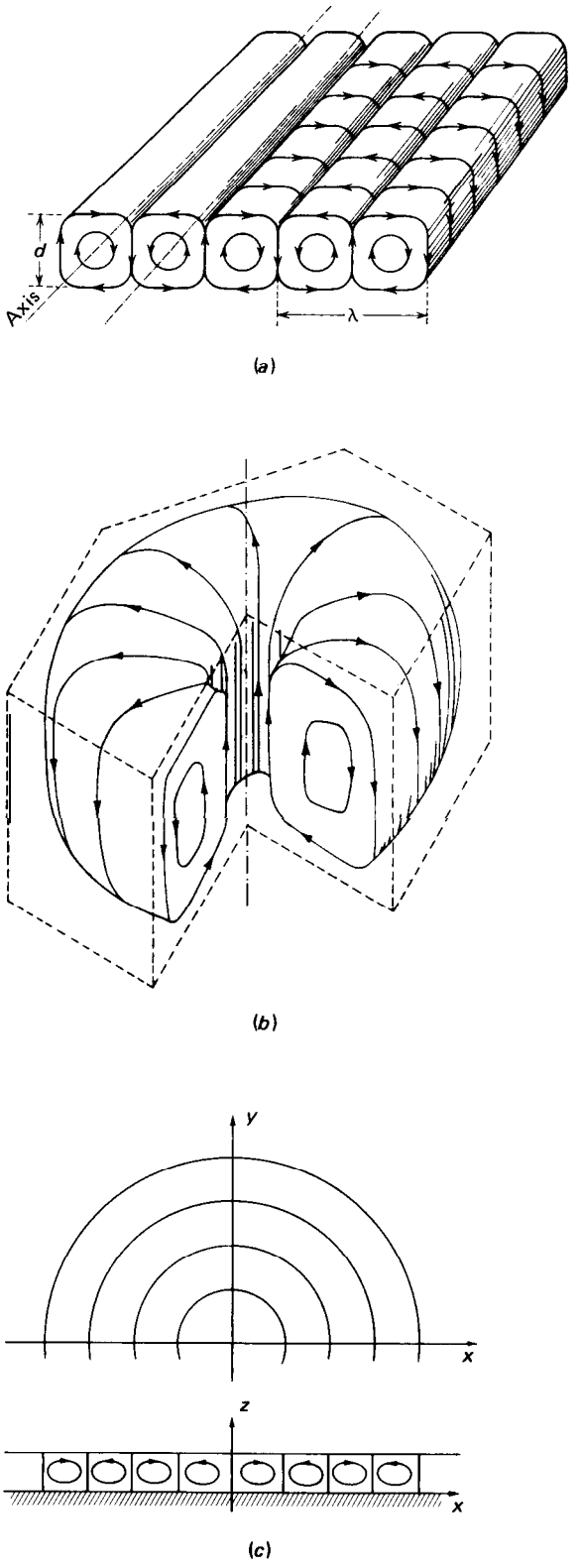

Figure 2 Sketches of roll cells in horizontal layers of liquid heated from below. (a) Longitudinal cells. (b) Hexagonal cell. (c) Circular (ring) cells. From Koschmieder [4].

© 1983 Hemisphere Publishing Corporation

$$\mathrm{Nu} = 1 + \sum_{i=1}^{\infty} \mathrm{Nu}_i \left(1 - \frac{\mathrm{Ra}_{ci}}{\mathrm{Ra}}\right) U(\mathrm{Ra} - \mathrm{Ra}_{ci}) \qquad (1)$$

where Nu_i = Nusselt number for ith mode
Ra_{ci} = critical Rayleigh number for ith mode
$U(\mathrm{Ra} - \mathrm{Ra}_{ci})$ = unit step function; 0 for $\mathrm{Ra} < \mathrm{Ra}_{ci}$, 1 for $\mathrm{Ra} > \mathrm{Ra}_{ci}$

The improved values of Nu_i and Ra_{ci} computed by Catton [13] are given in Table 1. The results are presumably for the asymptotic case of $\mathrm{Pr} \to \infty$. Nevertheless, values of Nu computed from the values in the table are seen in Fig. 3 to be in good agreement with experimental data for a variety of fluids.

Churchill and Ozoe [6] used the first two terms of the series above, the mixing length solution of Kraichnan [14] for large Ra and Pr, and the universal dependence on Pr of Churchill and Usagi [15], as given by Eq. 2.5.7(76), to develop the following correlating equation:

$$\mathrm{Nu} = \left\{ \left[1 + 1.446 \left(1 - \frac{\mathrm{Ra}_c}{\mathrm{Ra}}\right)\right]^{15} + \left(\frac{\mathrm{Ra}\, f(\mathrm{Pr})}{1\,420}\right)^5 \right\}^{1/15} \qquad (2)$$

Equation (2) with Ra_c = 1 708 is compared withseveral sets of experimental data in Fig. 4. The data for air and water fall somewhat above the prediction for $10^4 < \mathrm{Ra} < 1\,0^8$, and the data for water somewhat below for $\mathrm{Ra} > 10^8$ as well. If complete confidence were placed on the data in Fig. 4 rather than on the asymptote of Kraichnan, $0.109\ \mathrm{Ra}^{0.313}$ could be substituted for $(\mathrm{Ra}\, f(\mathrm{Pr})/1420)^{1/3}$ in Eq. (2). Hollands et al. [16] have proposed alternative correlating equations for selected sets of data for air and water.

Table 1 Critical Rayleigh numbers and heat transport coefficients for heating from below as computed by Catton [13]

Mode	Ra_{ci}	Nu_i
1	1 101.162	1.446
2	17 610	1.664
3	75 709	1.761
4	219 885	1.822
5	509 657	1.865
6	1 202 509	1.901
7	1 843 582	1.932
8	3 085 828	1.960
9	4 870 124	1.990
10	7 334 779	2.000

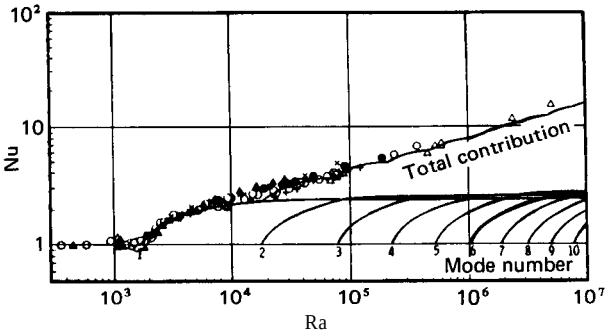

Figure 3 Comparison of Eq. (1) with experimental data for heat transfer between horizontal plates heated from below. ○, water; +, heptane; ×, ethylene glycol; ●, silicone oil AK3; ▲, silicone oil AK350; △, air. From Catton [13].

B. Enclosures heated from below

(a) Critical Rayleigh number

The drag of side walls increases Ra_c. The prediction of this value for different geometries and enclosures is important, since it serves as a criterion for the design of enclosures with negligible circulation and minimal heat transfer.

Davis [17] used linear stability theory to calculate Ra_c as a function of the two aspect ratios of a rectangular enclosure with infinitely conducting side walls. Catton [20, 21] also carried out calculations for the more practical cases of nonconducting and partially conducting side walls. His tabulated results for infinitely conducting and nonconducting side walls are reproduced as Tables 2 and 3. Comparison of the values in these two tables reveals that conducting walls increase the critical Rayleigh number.

Churchill and Ozoe [6] correlated the computed values of Ra_c for nonconducting walls and integral values of the two aspect ratios $H_1 \geqslant H_2 \geqslant 1$ within 0.8% using the empirical expression

$$\mathrm{Ra}_c = 1\,708 \left(1 + \frac{0.425}{H_1^{3/2}}\right)\left(1 + \frac{3}{H_2^2}\right)^{1/4} \qquad (3)$$

For a long channel, $H_1 \to \infty$ and

$$\mathrm{Ra}_c = 1\,708 \left(1 + \frac{3}{H_2^2}\right)^{1/4} \qquad (4)$$

where $H_1 = b/d$
$H_2 = w/d$
b = breadth (major horizontal dimension), m
w = width (minor horizontal dimension), m
d = thickness of fluid layer, m

Catton and Edwards [22] suggested the following general expression for the critical Rayleigh number of an enclosure of any shape:

© 1983 Hemisphere Publishing Corporation

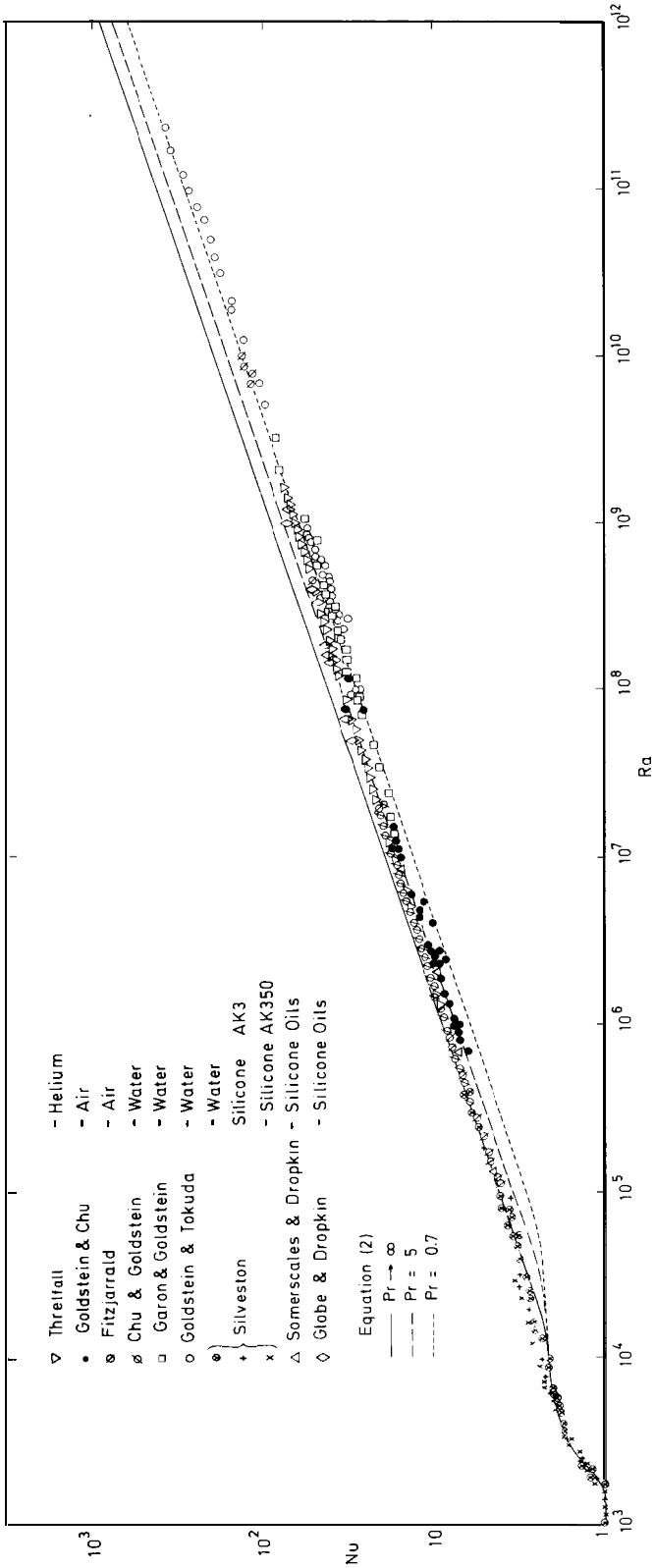

Figure 4 Comparison of Eq. (2) with experimental data for heat transfer between horizontal plates heated from below. From Churchill and Ozoe [6].

© 1983 Hemisphere Publishing Corporation

Table 2 Critical Rayleigh number for onset of motion in rectangular enclosures with infinitely conducting side walls as computed by Catton [20]

	H_2								
H_1	0.125	0.25	0.5	1.0	2.0	3.0	4.0	5.0	6.0
0.125	9 802 960.0	1 554 480.0	606 001.0	469 377.0	444 995.0	444 363.0	4.57 007.0	473 725.0	494 742.0
0.25	1 554 480.0	638 754.0	115 596.0	64 270.8	53 529.7	50 816.4	50 136.1	50 088.6	50 410.1
0.50	606 001.0	115 596.0	48 178.9	14 615.3	11 374.5	9 831.6	9 311.9	9 099.4	8 980.2
1.00	469 377.0	64 270.8	14 615.3	6 974.0	5 137.9	3 906.0	3 633.6	3 446.2	3 357.9
2.00	444 995.0	53 529.7	11 374.5	5 138.2	3 773.6	2 753.6	2 530.5	2 359.5	2 285.7
3.00	444 363.0	50 816.4	9 831.6	3 906.0	2 753.6	2 557.4	2 337.2	2 174.4	2 100.9
4.00	457 007.0	50 136.1	9 312.0	3 633.6	2 530.5	2 337.2	2 270.2	2 110.9	2 037.2
5.00	473 725.0	50 088.7	9 099.4	3 446.2	2 359.5	2 174.44	2 110.9	2 081.7	2 007.8
6.00	494 741.0	50 410.1	8 980.2	3 358.0	2 285.7	2 101.0	2 037.2	2 007.8	1991.9

$$\mathrm{Ra}_c = \frac{(a^2 + 16)^3}{a^2} \tag{5}$$

Here a is a horizontal wave number which depends on the shape and aspect ratio or ratios. Catton [21] proposed the following (herein corrected) expression for a for rectangular boxes with $\frac{2}{3}H_1 < H_2 < 1$:

$$a^2 = \pi^2 \left(\frac{4}{H_1^2} + \frac{1}{H_2^2}\right) \tag{6}$$

Churchill and Ozoe [6] also correlated the computed values of Catton [18] for infinitely conducting walls, but not so precisely as for nonconducting walls, perhaps owing to greater error in the values themselves. For integral aspect ratios with $H_1 \geqslant H_2 \geqslant 1$, their empirical expression is

$$\mathrm{Ra}_c = 1\ 708 \left(1 + \frac{0.116}{H_1}\right)^8 \left(1 + \frac{22}{H_2^2}\right)^{1/6} \tag{7}$$

For a long channel, $H_1 \to \infty$ and Eq. (7) simplifies to

$$Ra_c = 1\ 708 \left(1 + \frac{22}{H_2^2}\right)^{1/6} \tag{8}$$

For a square enclosure ($H = H_1 = H_2$), a simpler and more accurate approximation for $H \geqslant 1$ is

$$\mathrm{Ra}_c = 1\ 708 \left(1 + \frac{3.083}{H^{1.63}}\right) \tag{9}$$

As an approximation for round cylindrical enclosures with insulated side walls, Catton and Edwards [22] proposed that a in Eq. (5) be taken as the larger of 2.8.22 and $5.75d/D$, and for an ipfinitely conducting

Table 3 Critical Rayleigh numbers for onset of motion in rectangular enclosures with nonconducting side walls as computed by Catton [21]

	H_2									
H_1	0.125	0.25	0.50	1.00	2.00	3.00	4.00	5.00	6.00	12.00
0.125	3 011 718(1)									
0.25	333 013(1)	203 163(1)								
0.50	70 040(1)	28 452(1)	17 307(1)							
1.00	37 689(1)	11 962(1)	5 262(1)	3 446(1)						
1.50	39 798(2)	12 540(2)	5 341(1)	3 270(1)						
2.00	36 262(2)	11 020(2)	4 524(2)	2 789(2)	2 276(2)					
2.50	37 058(3)	11 251(3)	4 567(2)	2 754(2)	2 222(2)					
3.00	35 875(3)	10 757(3)	4 330(3)	2 622(3)	3 121(3)	2 004(3)				
3.50	36 209(4)	10 858(4)	4 355(3)	2 609(3)	2 098(3)	1 978(3)				
4.00	35 664(4)	10 635(4)	4 245(4)	2 552(4)	2 057(4)	1 941(4)	1 894(4)			
4.50	35 794(5)	10 666(5)	4 261(4)	2 545(4)	2 044(4)	1 927(4)	1 878(4)			
5.00	35 486(5)	10 544(5)	4 186(5)	2 502(5)	2 009(5)	1 897(5)	1 852(5)			
5.50	35 556(6)	10 571(6)	4 196(5)	2 498(5)	2 001(5)	1 888(5)	1 842(5)			
6.00	35 380(6)	10 499(6)	4 158(6)	2 480(6)	1 989(6)	1 879(6)	1 833(6)	1 810(6)	1 797(6)	
6.50	35 45 l(7)	10 518(7)	4 165(6)	2 447(6)	1 984(6)	1 871(6)	1 826(6)	1 803(6)	1 789(6)	
12.00	35 193(12)	10 426(12)	4 118(12)	2 453(12)	1 967(12)	1 855(12)	1 808(12)	1 783(12)	1 768(12)	1 741(12)

© 1983 Hemisphere I blishing Corporation

side wall as the larger of 2.822 and $7.66d/D$. These same expressions were also proposed for hexagonal cylinders with the distance between opposing vertical flats taken as D.

An experimental test by Stork and Müller [23] of the theoretical results of Davis [17] and Catton [18] for infinitely conducting enclosures with $H_1 = 4$ and varying H_2 is shown in Fig. 5. Similar results were obtained for other values of H_1, and similar agreement would be expected for partially or negligibly conducting walls. Oertel and Kirchartz [24] also confirmed the theoretical values for rectangular enclosures with infinitely conducting walls experimentally but found some evidence of a dependence on Pr. However, Verhoeven [25] found experimental values for mercury (Pr = 0.025) in a tall cylinder with insulated side walls to be in agreement with the prediction of Eq. (5) for a = $5.75d/D$.

(b) Modes of circulation

For integral values of $H_1 \geqslant H_2 \geqslant 1$ in rectangular enclosures, the fluid motion in the laminar regime consists of roll cells, such as those in Fig. 2*a*, of essentially square cross section with their axes horizontal and parallel to the shorter side wall of the enclosure. These roll cells increase in strength but persist in form up to the onset of turbulent motion at Ra $\cong 10^6$. Ozoe et al. [26] have demonstrated both theoretically and experimentally, as illustrated in Fig. 6, that all particle paths in the laminar regime are double helices and are confined to one or the other half of a roll cell. The circulation pattern following a change in boundary conditions may initially consist of roll cells of some other number and/or orientation. The transition to the stable state may require a very long time, particularly for nonintegral aspect ratios, since the entropy production for other quasistable configurations differs only slightly.

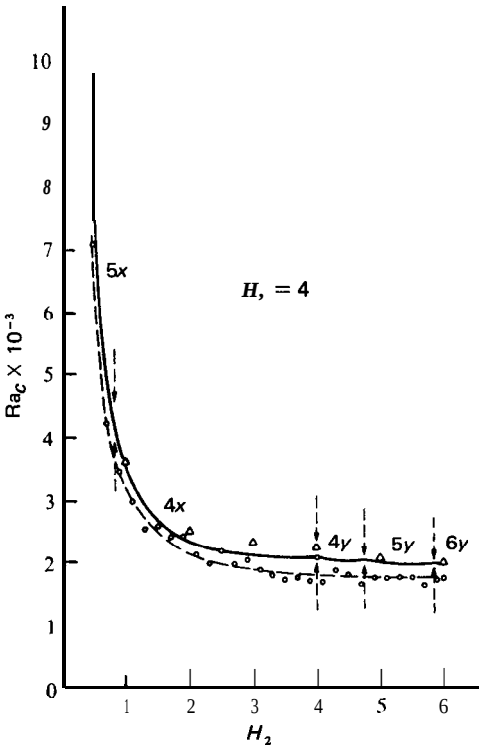

Figure 5 Comparison of the predictions of Davis [17] and Catton [18] with experimental data for the critical Rayleigh number in rectangular enclosures heated from below. —— Davis; △, Catton; —— ○ ——, experimental. From Stork and Müller [23].

The laminar mode of circulation in the annulus between two concentric vertical cylinders heated on the lower horizontal surface has been shown experimentally by Stork and Müller [27] and both experimentally and theoretically by Ozoe et al. [28] to consist of roll cells with horizontal, radial axes as shown in Fig. 7. An even number of cells occur, approximately equal to the mean circumference divided by the depth. The particle paths are oblique double helices confined to one-half of a roll cell as illustrated in Fig. 8.

(c) Heat transfer rates

Churchill and Ozoe [6] proposed the use of Eq. (2) for finite rectangular enclosures as well, using the appropriate values of Ra, as given in the previous section. The experimental results of Catton and Edwards [22] for various liquids in hexagonal-sided enclosures with conducting walls are shown in Fig. 9 and with nonconducting walls in Fig. 10. The curves in these plots represent the theoretical values corresponding to Eq. (1). However, these curves differ negligibly from Eq. (2) for Pr $\geqslant$ 6. Other sets of data are in general agreement. Unfortunately, extensive and precise results for low Pr to test that dependence do not appear to be available.

Equation (2), with an experimental value of Ra, = 3 200, is seen in Fig. 11 to be in agreement with the experimental values of Ozoe et al. [28] for a circular annulus between heated and cooled horizontal plates. [For Ra < 5 000, Eq. (1) with Ra_{ci} = 3 200 was used instead of Eq. (2), owing to a second intersection of the component equations.] The values they obtained by three-dimensional finite difference calculations are higher, but in qualitative agreement.

C. Rectangular enclosures heated and cooled on the sides

The flow pattern and rate of heat transfer in a rectangular enclosure heated and cooled on the side walls depend strongly on the aspect ratio or ratios as well as on the Rayleigh and Prandtl numbers. The majority of

© 1983 Hemisphere Publishing Corporation

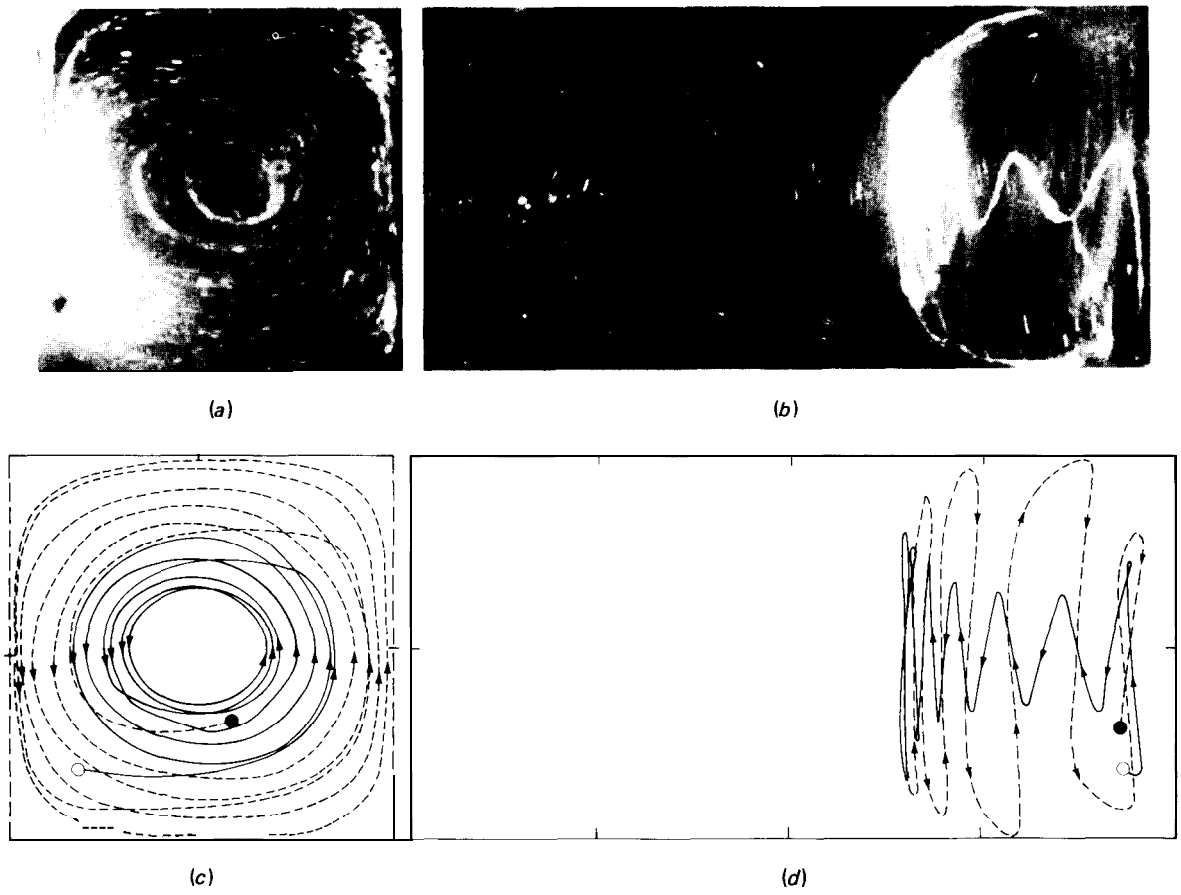

Figure 6 Experimental particle paths and computed streaklines for a 1 X 1 X 2 rectangular enclosure heated from below. Experimental: Ra = 14 400, Pr = 4 300. (a) Front view. (*b*) Side view. Computed: Ra = 4 000, Pr = 10, Ax = Δy = Az = 0.125. (c) Front view. (*d*) Side view. From Ozoe et al. [26].

experimental and theoretical results are for long channels, such that the aspect ratio for breadth is very large and can be ignored. The choice of the characteristic length in the Nusselt and Rayleigh numbers is not clear cut, since the rate of heat transfer for the conductive regime depends primarily on the distance d in the direction of heating; for the laminar boundary-layer regime primarily on the vertical distance h perpendicular to the direction of heating; and in the turbulent region on neither. To avoid confusion, the characteristic length in both Nu and Ra will be designated by subscripts. Unless otherwise noted, one aspect ratio is assumed to be sufficiently large so as to be negligible.

In 1963, Wilkes and Churchill [29,30] derived

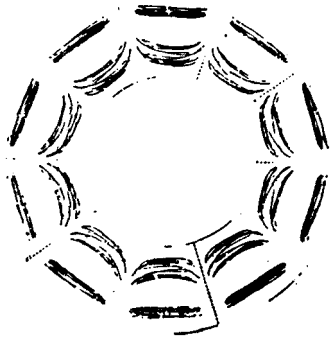

Figure 7 Top view of computed streaklines for a vertical annulus heated from below with r_1/d = 1, r_2/d = 2, Ra = 6 000, and Pr = 10. From Ozoe et al. [28].

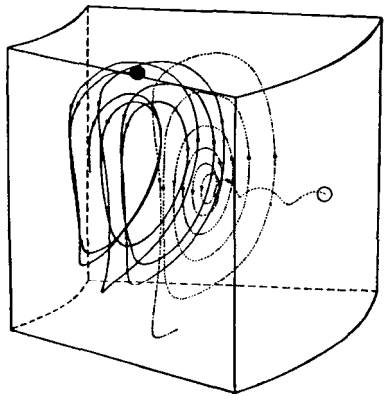

Figure 8 Perspective view of computed streaklines for a vertical annulus heated from below with r_1/d = 1, r_2/d = 2, Ra = 6 000, and Pr = 10. From Ozoe et al. [28].

© 1983 Hemisphere Publishing Corporation

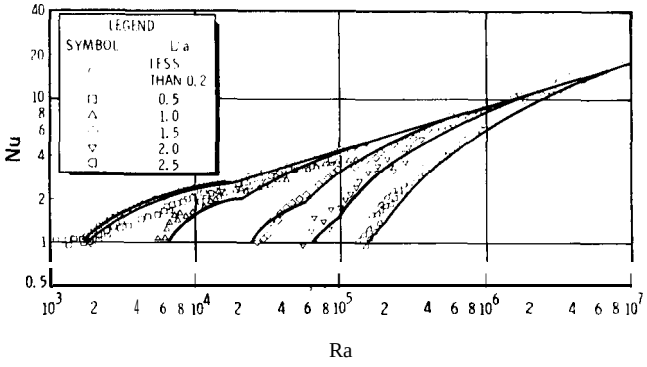

Figure 9 Comparison of Eq. (1) with experimental data for heating from below in hexagonal enclosures with conducting side walls. From Catton and Edwards [22].

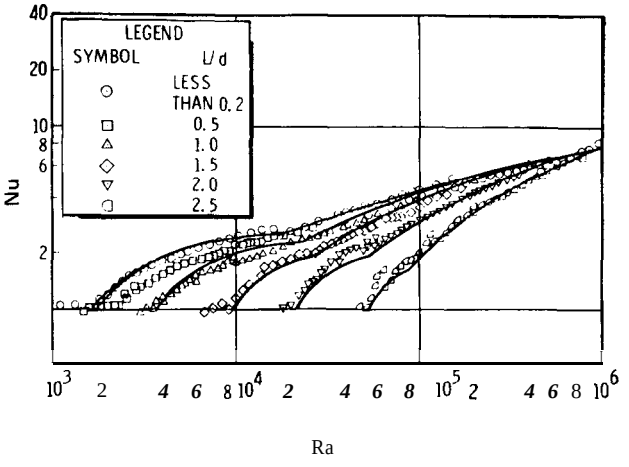

Figure 10 Comparison of Eq. (1) with experimental data for heating from below in hexagonal enclosures with nonconducting side walls. From Catton and Edwards [22].

a solution by finite-difference methods for two-dimensional laminar natural convection in a rectangular channel heated and cooled on the vertical sides, and insulated or perfectly conducting on the horizontal walls. The results of this and the many subsequent numerical solutions by both finite-difference and weighted-residual methods have proven to be reliable over an ever-increasing range of conditions. Hence, they are used herein, along with experimental data, to evaluate correlating equations.

The behavior in enclosures of very high, moderate, and very low aspect ratios differs in character, and therefore these three regimes will be treated separately.

(a) Enclosures with very large aspect ratios

Batchelor [31] analyzed the behavior for a channel made up-of vertical walls at different uniform temperatures and insulated horizontal end plates. He showed that for $Ra_d < 500h/d$, the fluid moves up in the half-width near the heated wall, across the top, down the half-width near the cooled wall, and across the bottom, with the parabolic velocity distribution shown in Fig. 12*a*. The rate of heat transfer increases linearly with Ra_d over that for pure conduction owing to the energy carried from one side to the other by the circulation. His

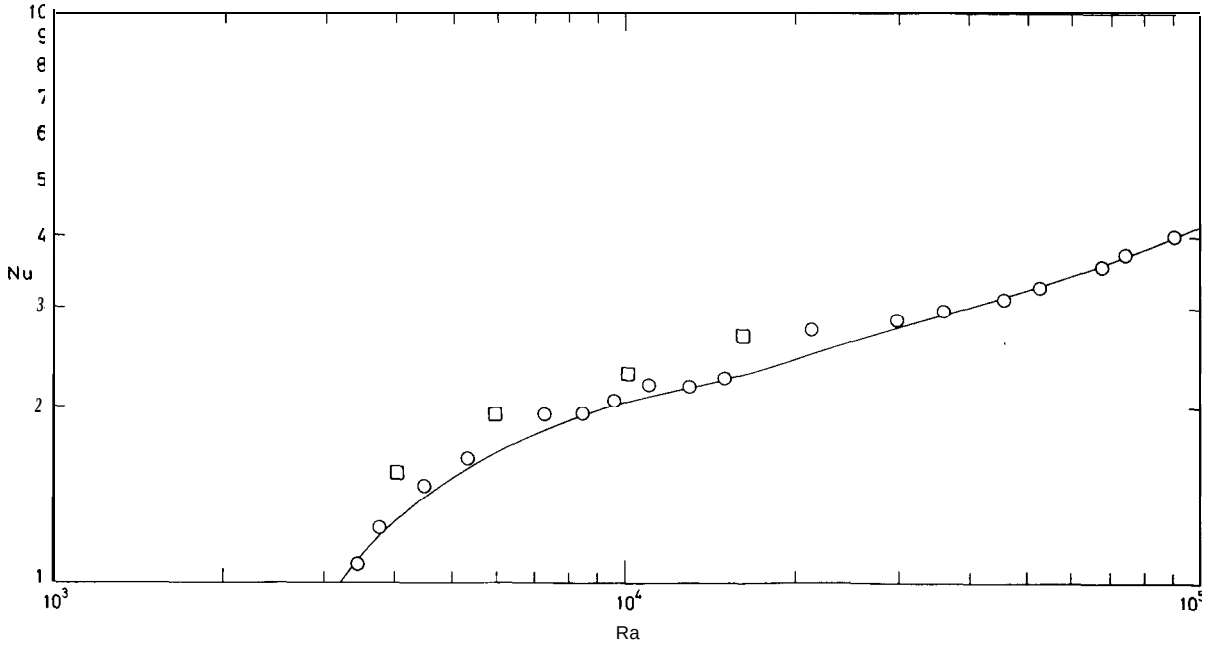

Figure 11 Comparison of experimental and theoretical rates of heat transfer for silicone oil in a circular annulus heated and cooled on the ends with r_1/d = 0.96 and r_2 = 2. ○, experimental values; □, computed values (both by Ozoe et al. [22]). —— Eq. (2).

© 1983 Hemisphere Publishing Corporation

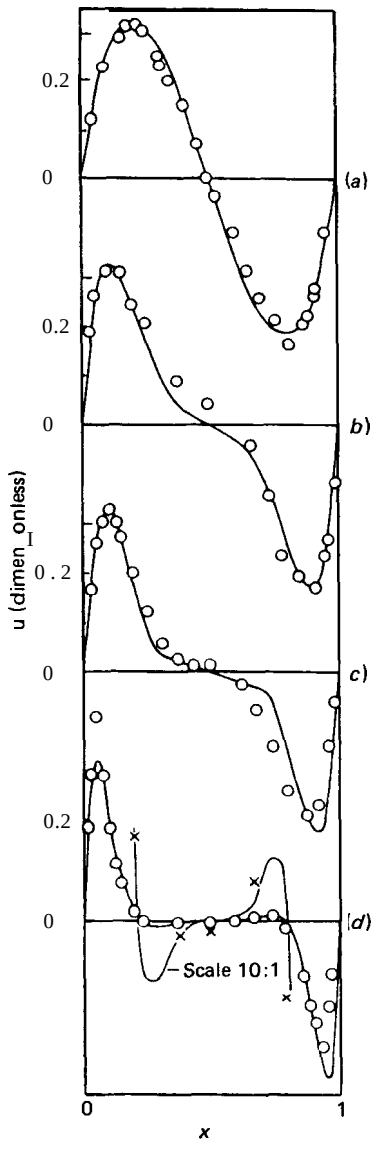

Figure 12 Velocity profiles at mid-height of tall rectangular channels heated and cooled on the vertical sides, as measured by Elder [32].

Ra_d	h/d	Re_d d/h
(a) 3.08 x 10^4	19.40	1.587 X 10
(b) 2.95 x 10^5	13.73	2.149 X 10^4
(c) 6.56 X 10^5	13.85	4.736 X 10^4
(d) 3.61 X 10^6	7.18	5.028 X 10^5

solution for this ***asymptotic regime*** can be expressed as

$$Nu_d = 1 + \frac{Ra_d}{720}\frac{d}{h} \tag{10}$$

Setting the derivative of the heat transfer coefficient with respect to d to zero reveals that a minimum value of 4/3 occurs for Nu_d at

$$\frac{d}{h} = \frac{240}{Ra_d} = \left(\frac{240}{Ra_h}\right)^{1/4} \tag{11}$$

This is an important criterion for design in certain applications such as double windows.

As Ra_h increases, the circulation eventually undergoes a transition to a thin laminar boundary layer along the walls or directly to a turbulent boundary layer. In either event (and contrary to Batchelor), the central core becomes quasistagnant with a vertical temperature gradient as illustrated in Fig. 13. Batchelor s criterion for the transition to turbulent motion is

$$Ra_{dc} \geqslant \left(18\,700\,Pr,\ 10^9\left(\frac{d}{h}\right)^3\right)_{max} \tag{12}$$

[The notation of Eq. (12) implies the larger of the two functions set apart by the comma.] The boundaries of the asymptotic, laminar boundary layer and turbulent regimes, as provided by this and the previous criterion, are indicated in Fig. 14. A laminar boundary-layer regime apparently cannot exist for $h/d > 42$.

The experimental measurements by Elder [32] of the velocity profile at the mid-height of cavities are reproduced in Fig. 12. They appear to confirm the analysis of Batchelor qualitatively, although the para-

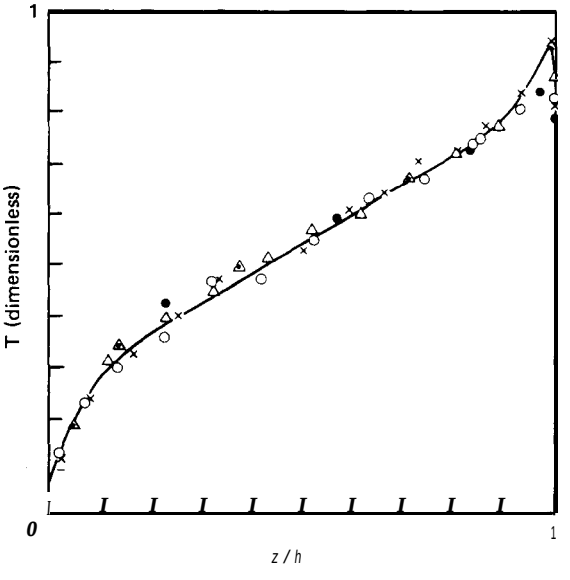

Figure 13 Vertical dimensionless temperature profile in central plane of rectangular channels for Ra = 1.2 X 10^6. From Elder [32].

h/d	Symbol
4.7	0
2.5	X
1.25	△
0.025	●

© 1983 Hemisphere publishing Corporation

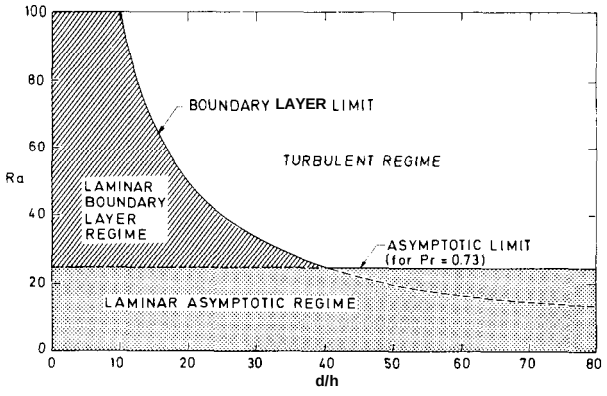

Figure 14 Regimes of natural convection for air in tall rectangular channels heated and cooled on the vertical sides. After Batchelor [31].

bolic velocity profile is seen to persist to at least Ra_d $d/h = 1\,587$.

Bejan [33] derived an asymptotic expansion and a correction factor for the laminar boundary layer, which Churchill and Ozoe [6] generalized as

$$Nu_h = \frac{0.364(Ra_h f(Pr))^{1/4}}{\phi(Ra_h, h/d)} \tag{13}$$

where

$$\phi\left(Ra_h, \frac{h}{d}\right) = \left\{1 + \frac{0.231}{[Ra_h(h/d)^4]^{1/4}}\right\}^2 \tag{14}$$

For the turbulent regime, Churchill and Ozoe proposed

$$Nu_h = 0.05(f(Pr)\,Ra_h)^{1/3} \tag{15}$$

In both Eqs. (13) and (15), $f(Pr)$ is the universal dependence given by Eq. 2.5.7(76). Equation (15) implies that the heat transfer coefficient is independent of the width of the channel and hence of the drag of the horizontal walls. This independence is also implied by Eq. (13) for large $Ra_h(h/d)^4$ such that the correction factor ϕ approaches unity, Equations (10), (13), and (14) are compared with representative experimental data and computed values for large h/d in Fig. 15. The general prediction of the dependence on Ra, Pr, and h/d appears to be satisfactory considering the scatter of the values themselves. Except for one set of data for mercury, the transition to turbulent motion appears to occur in the range $10 < Ra_d(d/h) < 10^7$. These and other sets of data have generally been correlated as powers of Pr, h/d, and Ra_d or Ra_h, with the power evaluated by least squares. The odd powers obtained in this manner by various investigators undoubtedly reflect the correlation of data extending over two or more regimes, as well as experimental error. On the other hand, the independence of Eq. (13), in the limiting case of large Ra $(h/d)^4$, from the width d indicates some idealization with respect to the dependence on the aspect ratio as implied by the odd powers in purely empirical expressions.

(b) Enclosures with aspect ratios near unity

For the asymptotic regime of flow at low Ra_d, Batchelor [31] derived

$$Nu_d = 1 + A\,Ra_d^2 \frac{d}{h} \tag{16}$$

He postulated that the constant $A = O(10^{-8})$ and that Eq. (16) was valid for $Ra_d < 10^3$. Poots [34] subsequently determined a value for A of 5×10^{-8} from a series solution. Churchill and Ozoe [6] combined Eq. (16) with Eqs. (13) and (15), which are still applicable, to obtain

$$Nu_d = \left(\left\{\left[1 + \left(\frac{Ra_d}{4\,472}\right)^2 \frac{d}{h}\right]^{-8} + \left[\frac{Ra_d(d/h)f(Pr)}{57\phi}\right]^{-2}\right\}^{-3/8} + \frac{Ra_d f(Pr)}{8\,000}\right)^{1/3} \tag{17}$$

This expression is compared with the limited experimental data but extensive computed values in Fig. 16. The prediction is generally satisfactory, but is relatively untested for Pr other than 0.7. Also, none of the computed or experimental values extend into the completely turbulent regime $(Ra_d > 10^{10})$.

(c) Enclosures of very low aspect ratio

Bejan and Tien [35] derived for $h/d \to 0$ and small Ra, or $Ra \to 0$ and small h/d,

$$Nu_d = 1 + \frac{(Ra_h\, h/d)^2}{362\,880} \tag{18}$$

and for the laminar boundary-layer regime,

$$Nu_h = 0.623\,Ra_h^{1/5} \tag{19}$$

Since they omitted the inertial terms in the equation for the conservation of momentum, Eq. (19) is actually an asymptotic expression for $Pr \to \infty$. It can therefore be generalized as

$$Nu_h = 0.623(Ra_h f(Pr))^{1/5} \tag{20}$$

where $f(Pr)$ is again given by Eq. 2.5.7(72). As contrasted with Eq. (10), Eq. (18) indicates a decreasing contribution of convection to the heat transfer coefficient as the width of the channel increases, but Eq. (18) again indicates independence from width in the boundary layer regime.

The combination of Eq. (18) with Eq. (20) per the Churchill-Usagi model gives the following expression for

©1983 Hemisphere Publishing Corporation

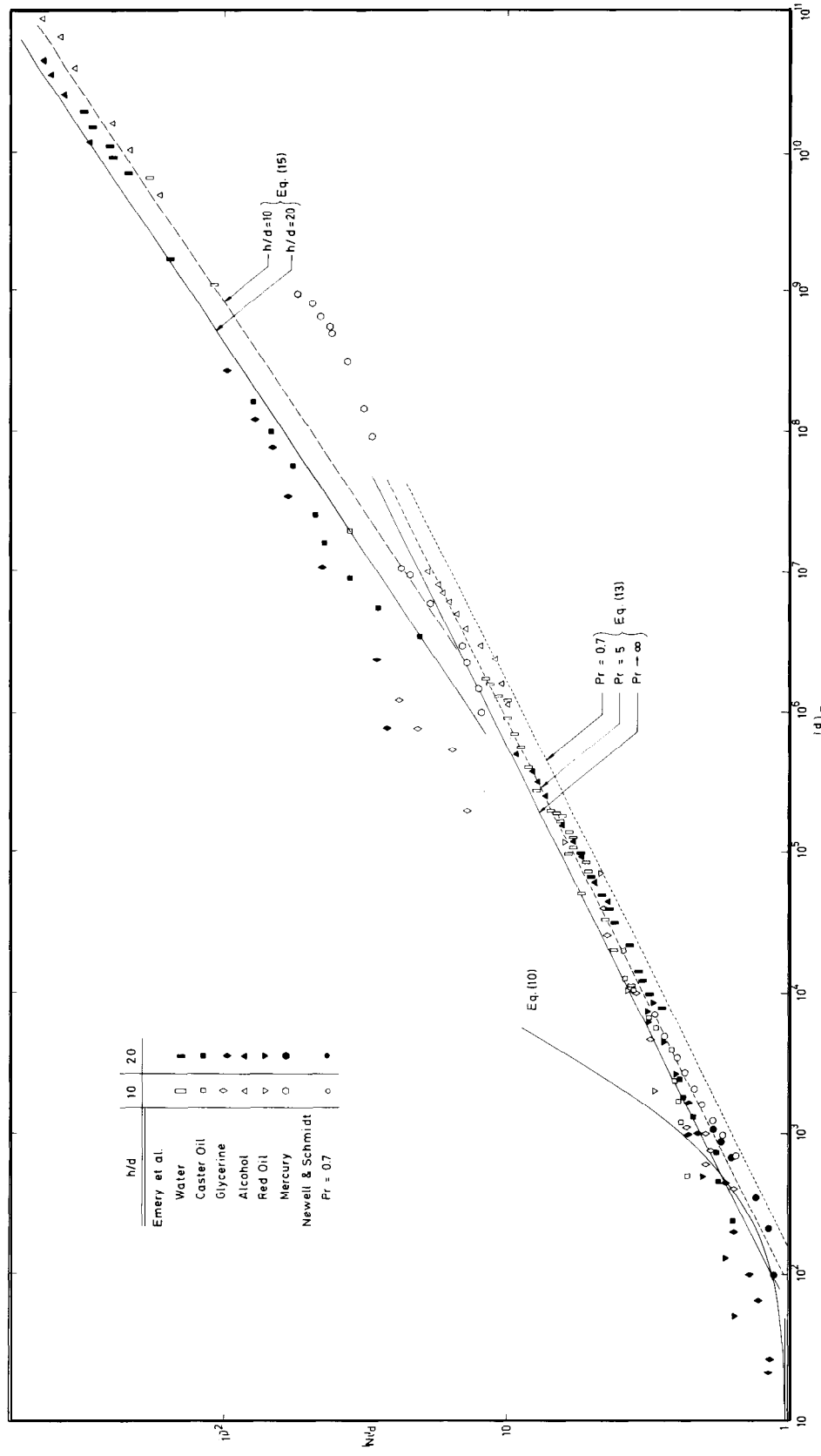

Figure 15 Comparison of Eqs. (10), (13), and (15) with experimental data and computed values for Nu in rectangular channels of large aspect ratio heated and cooled on the vertical sides.

© 1983 Hemisphere Publishing Corporation

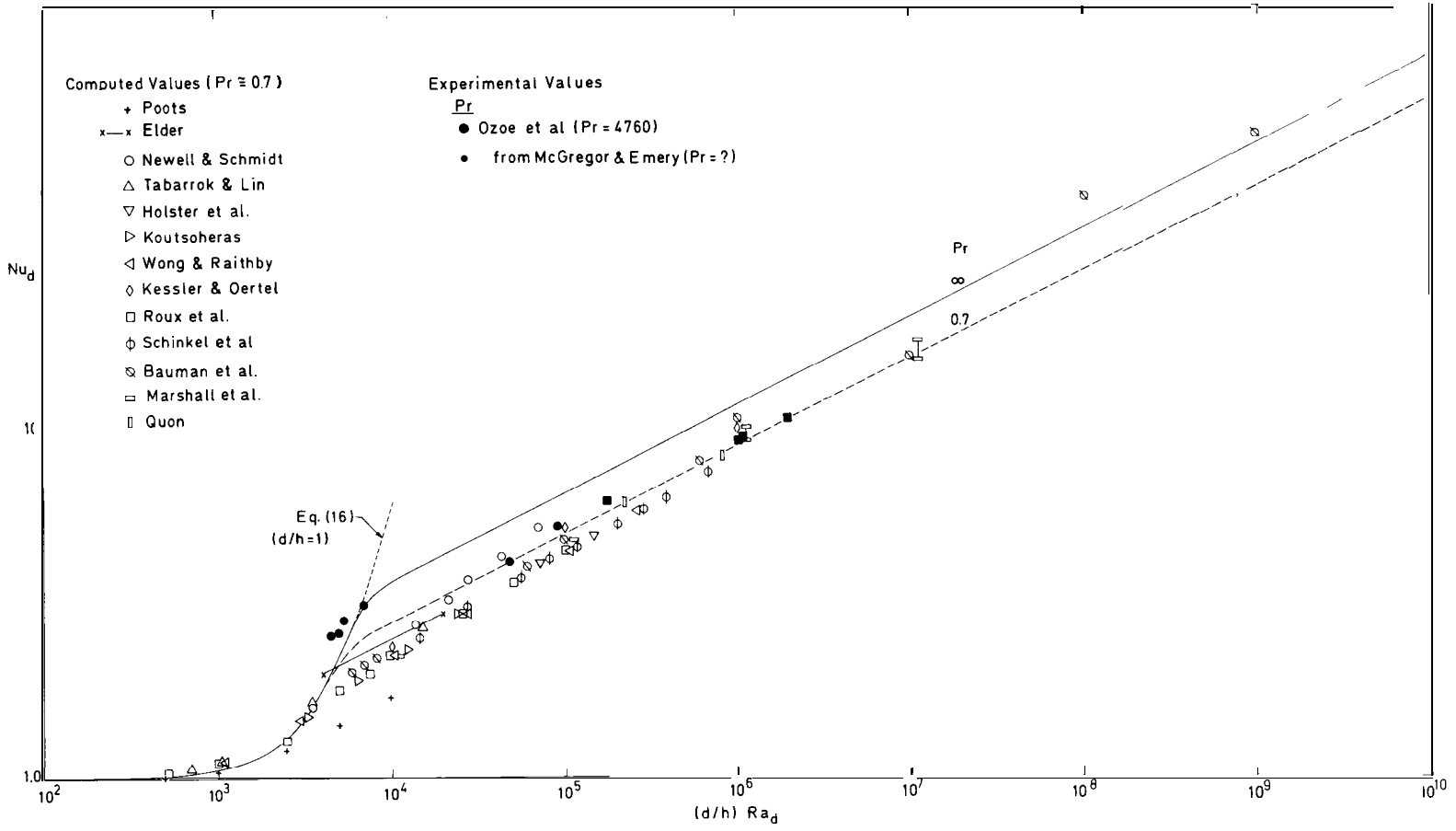

Figure 16 Comparison of Eqs. (13, (15), (16), and (17) with experimental data and computed values of Nu for rectangular channels of aspect ratio near unity, heated and cooled on the vertical sides.

© 1983 Hemisphere Publishing Corporation

the full laminar regime:

$$\mathrm{Nu} = 1 + \left\{\left(\frac{\mathrm{Ra}_h\, h/d}{602.4}\right)^{-0.8} + \left[\left(\frac{\mathrm{Ra}_h f(\mathrm{Pr})}{10.66}\right)^{1/5} \frac{d}{h}\right]^{-0.4}\right\}^{-2.5} \qquad (21)$$

Equation (21) agrees even better with the experimental data plotted in Fig. 17 than the curves calculated by Bejan and Tien using integral boundary-layer theory.

Equation (20) differs in form from Eq. (13) and hence is presumably invalid for h/d of the order of magnitude of unity or greater. The greater deviation of the data for $h/d = 1$ therefore is not surprising.

(d) Local heating

Chu and Churchill [36,37] investigated the effect of local heating by a horizontal strip on one vertical wall of a rectangular channel experimentally and by finite-difference computations. The measurements of the heat transfer rate were in general agreement with the calculations but were not of sufficient precision to provide a critical test. However, their observed and computed flow patterns are in excellent agreement as illustrated in Fig. 18. The computed effects of heater size and location are illustrated in Figs. 19 and 20. The optimum location of a heating strip for maximum heat transfer is seen to be a function of Ra rather than fixed at mid-height. Also, increasing the size of the heater produces a diminishing increase in the total heat transfer. Most significant, Fig. 21, in which Nu is plotted versus the rate of circulation (as characterized by the maximum value of the stream function), reveals that the same rate of heat transfer can be attained for two different rates of circulation, or vice versa, by varying the location of the heating strip.

D. Circular annuli heated and cooled on the vertical curved surfaces

de Vahl Davis and Thomas [38] obtained a finite-difference solution for isothermal vertical walls with the inner temperature higher. Churchill and Ozoe [6] showed that these computed values for $10^4 \leqslant \mathrm{Ra}_d \leqslant 10^5$, Pr = 1, h/d = 5, 10, 15, and $r_o/r_i = 1$, 2, where $d = r_o - r_i$, can be correlated by the following modified version of Eq. (13):

$$\mathrm{Nu}_h = 0.364(\mathrm{Ra}_h f(\mathrm{Pr}))^{1/4} \left(\frac{r_o}{r_i}\right)^{1/2} \qquad (22)$$

as demonstrated in Fig. 22. The predominance of deviations on the high side is presumed to be due to discretization error in the numerical solution. Caution is suggested for r_o/r_i outside the indicated range.

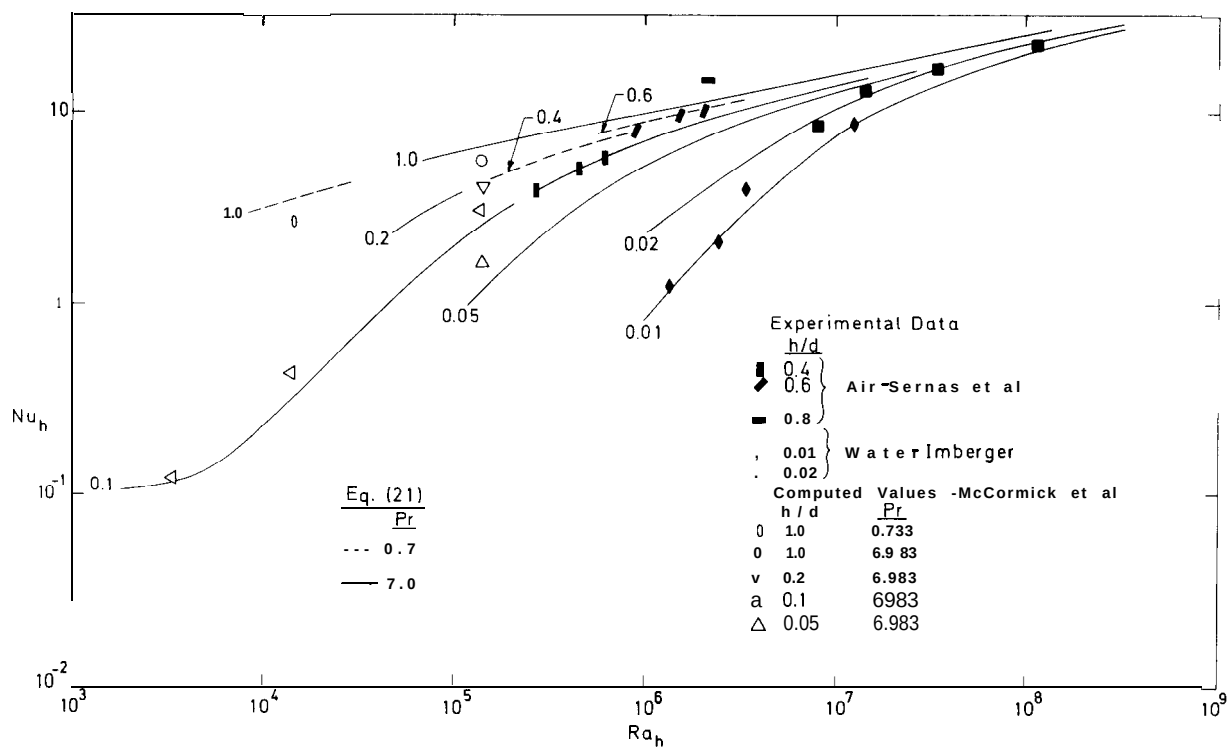

Figure 17 Comparison of Eqs. (18), (20), and (21) with experimental data and computed values for Nu for rectangular channels of low aspect ratio heated and cooled on the vertical sides.

© 1983 Hemisphere Publishing Corporation

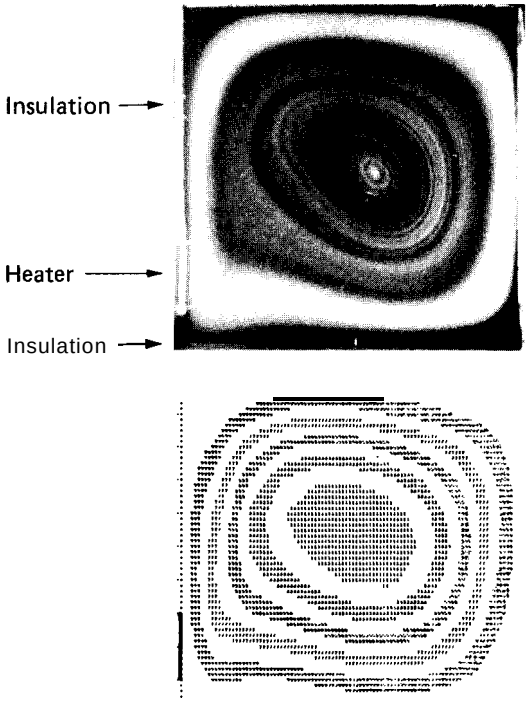

Figure 18 Comparison of photographed and computed streamlines for heating along a horizontal strip of a vertical wall of a square channel at Ra = 10^5. From Chu and Churchill [36].

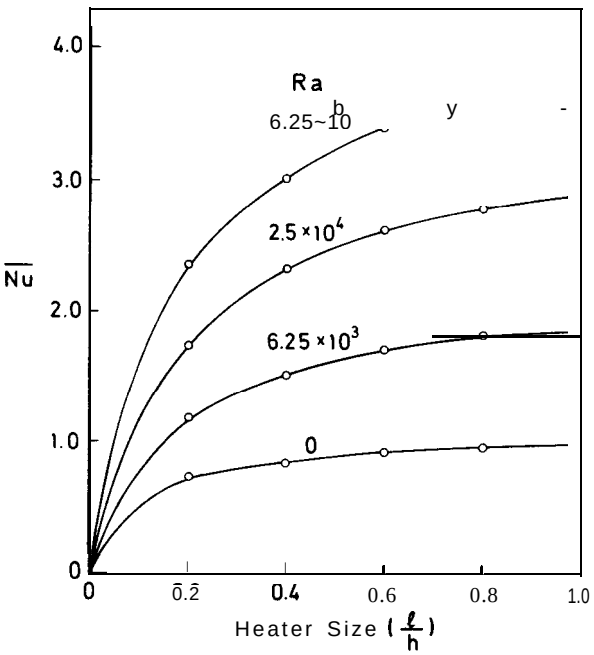

Figure 19 Effect of heater size in the vertical wall of a square channel with insulated horizontal walls on Nu. From Chu and Churchill [36].

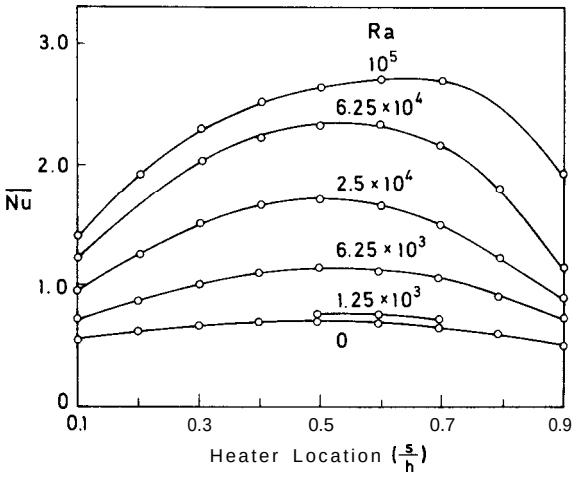

Figure 20 Effect of heater location in the vertical wall of a square channel with insulated horizontal walls on Nu. From Chu and Churchill [36].

E. Horizontal cylinders

The behavior of the fluid in a horizontal cylinder heated and cooled on different portions of the curved surface is qualitatively similar to that in a rectangular channel (see, for example, Ostrach [2]). The heat transfer rates computed by Hellums and Churchill [39] are in fair agreement with the measured values of Martini and Churchill [40] and, as indicated in Fig. 23, correspond to Eq. (13) with a coefficient of 0.28. The indicated range of the experimental values represents Ra evaluated at the extreme temperatures rather than irreproducibility.

Bejan and Tien [41] developed an asymptotic solution for small Ra and large length-to-diameter ratio for a horizontal cylinder heated on the ends, similar to that represented by Eq. (18) for a rectangular channel. However, their solution involves unevaluated coefficients and hence is not reproduced here.

F. Horizontal annuli

Kuehn and Goldstein [42] developed the following correlating equation for the convective component of heat transfer between concentric or eccentric cylinders at different uniform temperatures

$$(\mathrm{Nu}_{D_i})_{\mathrm{conv}} = 2/\ln\{1 + 2/(\{0.518\,\mathrm{Ra}_{D_i}^{1/4}[1 + (0.559/\mathrm{Pr})^{3/5}]^{-5/12}\}^{15} + (0.1\,\mathrm{Ra}_{D_i}^{1/3})^{15})^{1/15}/1 \times 2/[(\{[2/(1 - e^{-0.25})]^{5/3} + (0.587G\,\mathrm{Ra}_{D_o}^{1/4})^{5/3}\}^{3/5})^{15} + (0.1\,\mathrm{Ra}_{D_o}^{1/3})^{15}]^{1/15}\} \quad (23)$$

© 1983 Hemisphere Publishing Corporation

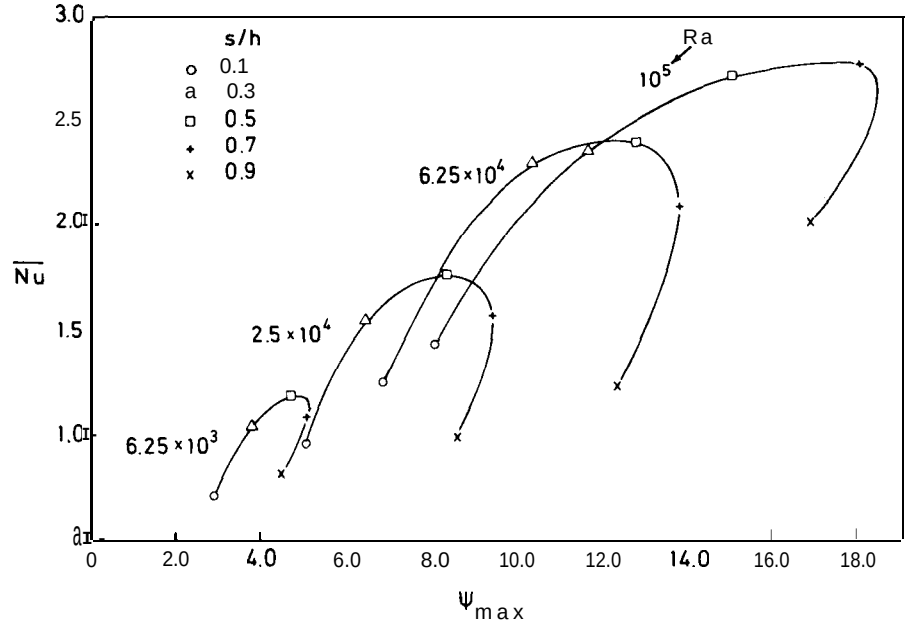

Figure 21 Relationship between Nu and rate of circulation (ψ_{max}) in a square channel heated along a horizontal strip in the vertical wall. From Chu and Churchill [36].

where

$$G = \left[\left(1 + \frac{0.6}{\mathrm{Pr}^{0.7}}\right)^5 + (0.4 + 2.6\,\mathrm{Pr}^{0.7})^5\right]^{-1/5} \tag{24}$$

Here D_i = inner diameter, m

D_o = outer diameter, m

The corresponding expression for pure conduction is

$$(\mathrm{Nu}_{D_i})_{\mathrm{cond}} = -\frac{2}{\cosh^{-1}[(D_i^2 + D_o^2 + 4\epsilon^2)/2D_iD_o]} \tag{25}$$

where ϵ = distance the inner cylinder is moved from the concentric position, m.

The total rate of heat transfer is

$$\mathrm{Nu}_{D_i} = [(\mathrm{Nu}_{D_i})_{\mathrm{conv}}^{15} + (\mathrm{Nu}_{D_i})_{\mathrm{cond}}^{15}]^{1/15} \tag{26}$$

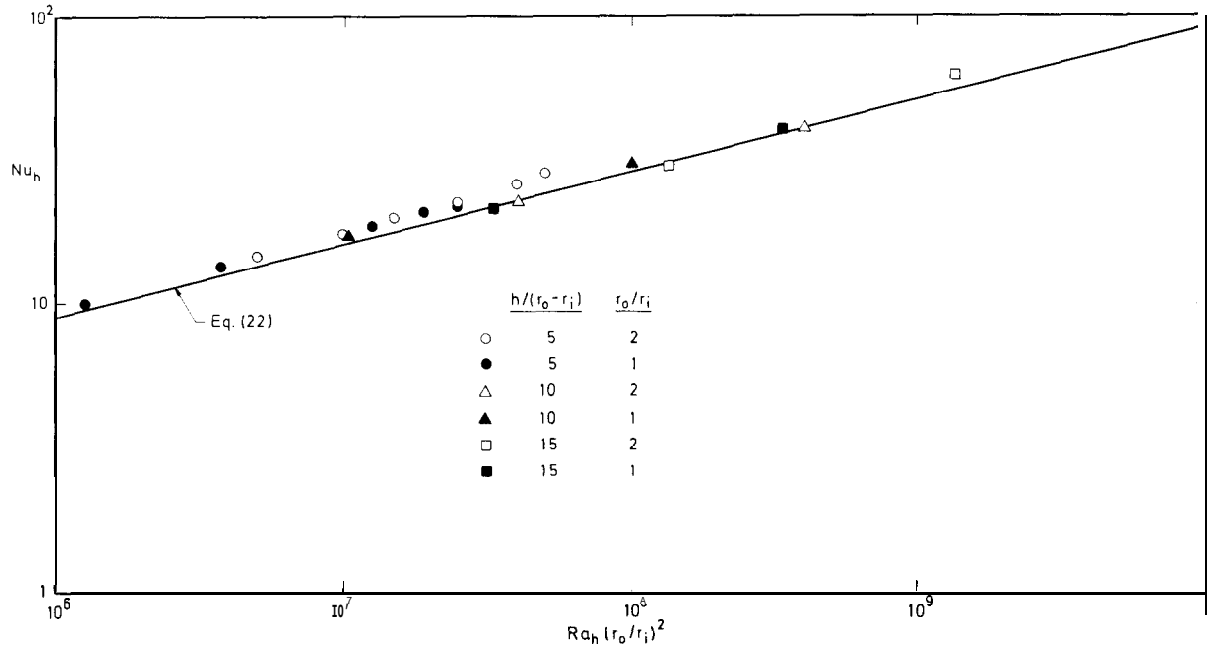

Figure 22 Comparison of Eq. (22) with computed values of de Vahl Davis and Thomas [38] for Nu in circular annuli heated and cooled on the vertical curved surfaces. Pr = 1.0. From Churchill and Ozoe [6].

© 1983 Hemisphere Publishing Corporation

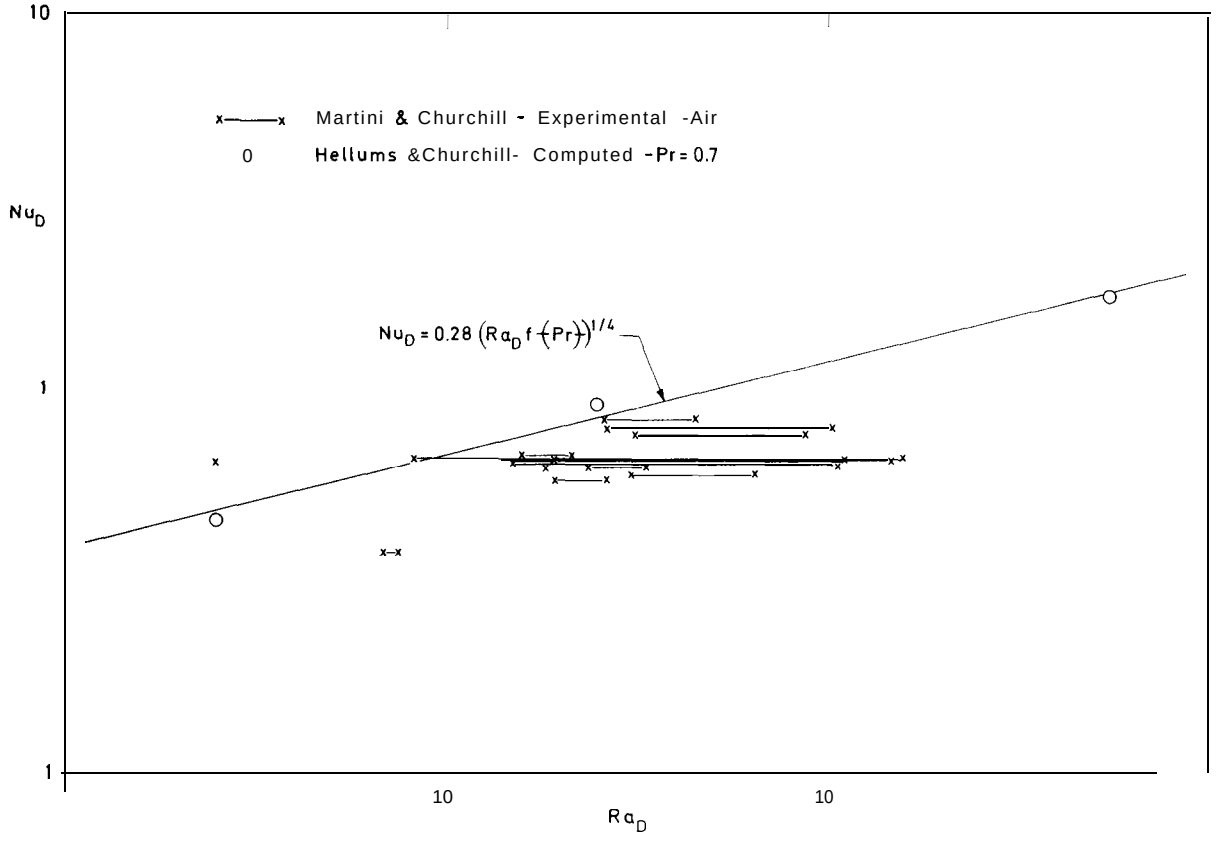

Figure 23 Comparison of Eq. (13) (with a coefficient of 0.28) with the experimental data of Martini and Churchill [40] and the computed values of Hellums and Churchill [39] for Nu_D in a long horizontal cylinder heated on one curved vertical side and cooled on the other.

This expression is compared with experimental results for concentric cylinders in Fig. 24 and with those for eccentric cylinders Fig. 25.

Equation (23) can be degenerated to yield the following expression for quasisteady convection inside a horizontal cylinder:

$$Nu_{D_o} = 2/(-\ln\{1-2/[(\{[2/(1-e^{-1/4})]^{5/3} + (0.5876\ Ra_{D_o}^{1/4})^{5/3}\}^{3/5})^{15} + (0.1\ Ra_{D_o}^{1/3})^{15}]^{1/15}\}) \quad (27)$$

This expression is compared with experimental data in Fig. 26.

Huetz and Petit [43] correlated later data for a liquid metal alloy of 56% K and 44% Na (Pr = 0.02) in a concentric cylindrical annulus with the expression

$$Nu_{D_e} = \frac{2.45 \times 10^{-2}}{\ln(D_o/D_i)} (Ra_{D_e} Pr)^{0.536} \quad (28)$$

where $D_e = D_o - D_i$ = hydraulic diameter, rn.

The success of their correlation for large Ra_{D_e} Pr is indicated in Fig. 27.

G. Concentric spheres

Bishop et al. [44] correlated data for convective heat transfer in air between isothermal concentric spheres with the expression

$$Nu_d^* = 0.16\ Gr_d^{0.276} \quad (29)$$

where

$$Nu_d^* = \frac{Qd}{\pi\lambda D_i D_o\ \Delta T}$$

and

$$d = \frac{D_o - D_i}{2}, \text{ m}$$

Good agreement is demonstrated in Fig. 28. Equation (29) can be tentatively generalized per Eq. (13) as

$$Nu_d^* = 0.21(Ra_d\ f(Pr))^{1/4} \quad (30)$$

where $f(Pr)$ is given by Eq. 2.5.7(72).

© 1983 Hemisphere Publishing Corporation

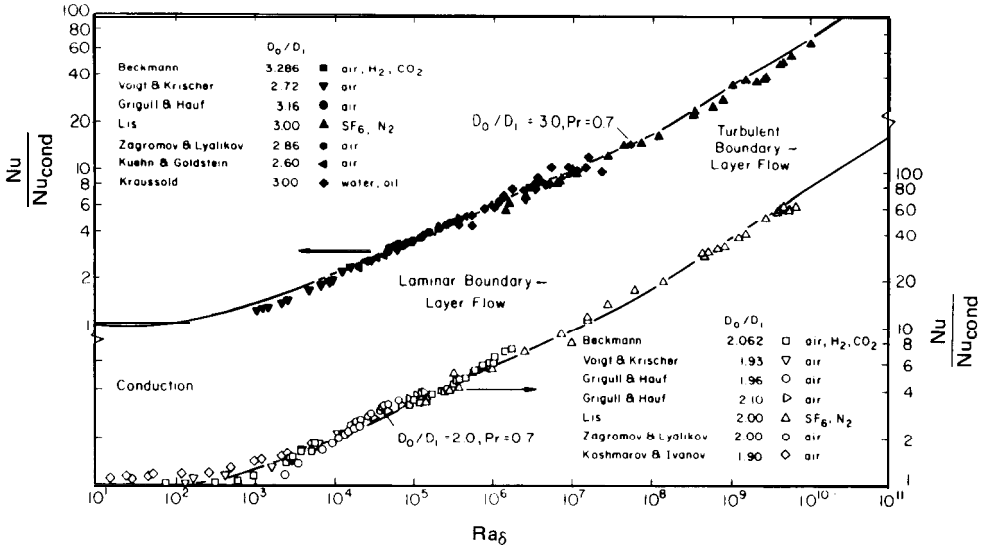

Figure 24 Comparison of Eq. (26) with experimental data for convection between concentric horizontal cylinders at different uniform temperatures. $\delta = (D_o - D_i)/2$. From Kuehn and Goldstein [42].

H. Inclined enclosures

Inclined rectangular enclosures are widely used for solar collectors and hence have been studied extensively. However, owing to the dependence on the angle of inclination and the angle of rotation as well as on two aspect ratios and the Rayleigh and Prandtl numbers, the behavior is not wholly documented. Inclined hexagonal, cylindrical, and annular enclosures have been studied somewhat more briefly.

(a) Very large aspect ratios

Fluid motion occurs for all inclinations of the heated surface from the horizontal. For $\mathrm{Ra}_d \cos\theta < 1\,708$, the fluid moves slowly up along the heated surface and down along the cooled surface and contributes negligibly to the rate of heat transfer. Here θ is the angle of inclination of the heated surface from the lower, horizontal position. For $\mathrm{Ra}_d \cos\theta > 1\,708$, a series of roll cells occurs, and as Ra_d continues to increase, the motion

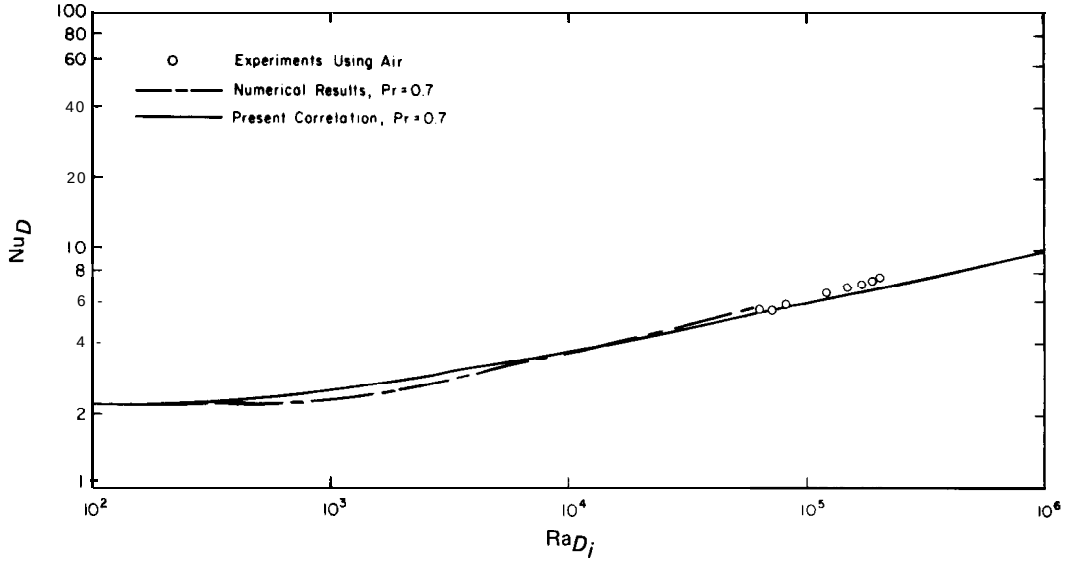

Figure 25 Comparison of Eq. (26) with experimental data for convection between eccentric horizontal cylinders. From Kuehn and Goldstein [42].

© 1983 Hemisphere Publishing Corporation

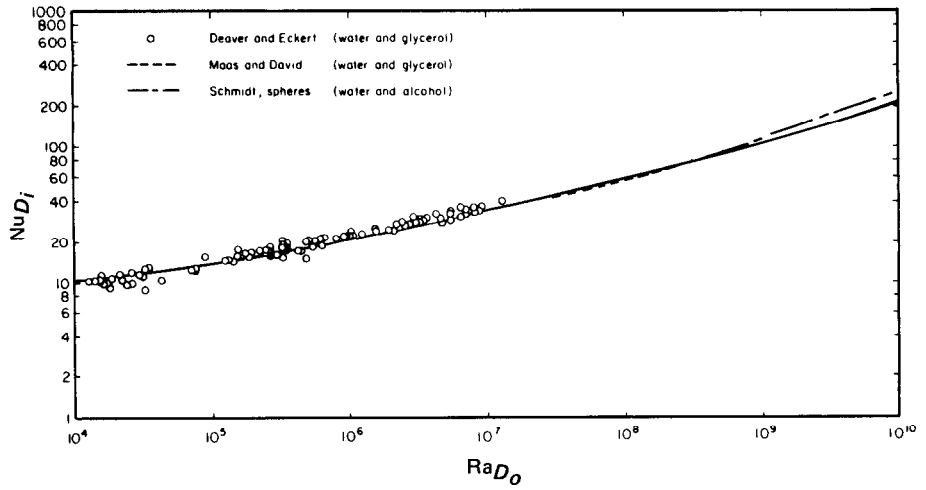

Figure 26 Comparison of Eq. (27) with experimental data for quasisteady-state convection in heated horizontal cylinders and spheres. From Kuehn and Goldstein [42].

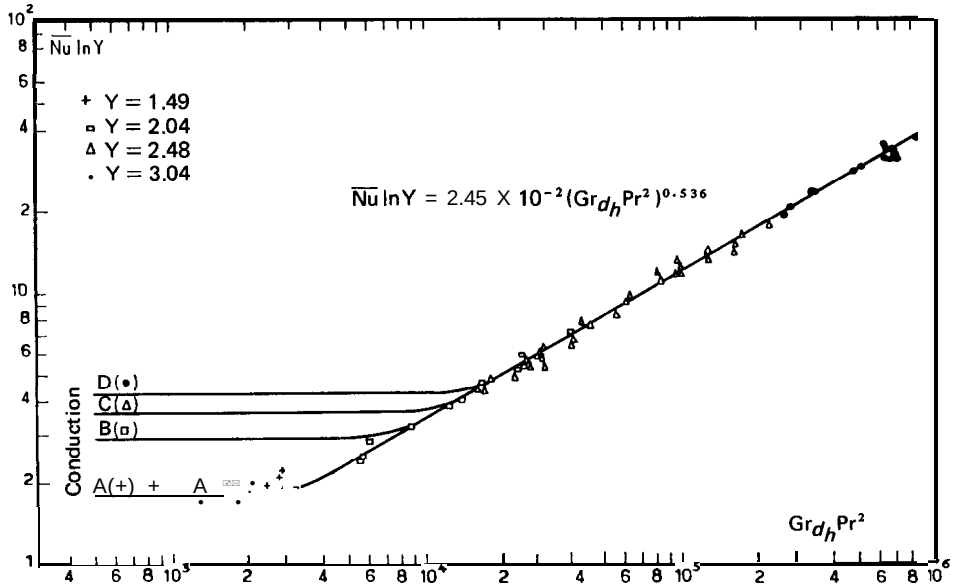

Figure 27 Comparison of Eq. (28) for convection in horizontal annuli for NaK. Y = D_o/D_i, $Gr_{d_h}Pr^2 = Ra_{D_e}$ Pr. From Huetz and Petit [43].

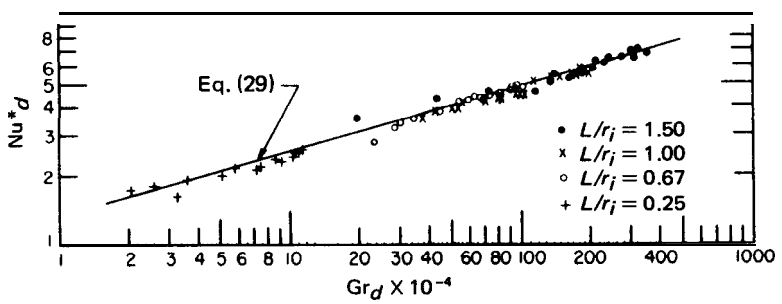

Figure 28 Comparison of Eq. (29) with experimental data for air between concentric spheres From Bishop et al. [44].

© 1983 Hemisphere Publishing Corporation

becomes three-dimensional and unsteady. The motion is somewhat more complex for $\theta \gtrsim 5\pi/12$, as described by Hart [45] and Hollands and Konicek [46].

Churchill and Ozoe [6] modified Eq. (2) by replacing Ra_d with $\mathrm{Ra}_d \cos\theta$, eliminating $f(\mathrm{Pr})$, introducing a factor from the correlating equation of Holland et al. [47], and changing the exponent 15 to 3 to obtain the following expression for $0 \leqslant \theta \leqslant 4\pi/9$:

$$\mathrm{Nu}_d = \left(\left\{ 1 + 1.446 \left(1 - \frac{1\,708}{\mathrm{Ra}_d \cos\theta} \right) \times \left[1 - \frac{1\,708\,(\sin 1.8\theta)^{1.6}}{\mathrm{Ra}_d \cos\theta} \right] \right\}^3 + \frac{\mathrm{Ra}_d \cos\theta}{1\,420} \right)^{1/3} \tag{31}$$

For $4\pi/9 \leqslant \theta \leqslant$ n/2, they suggested

$$\mathrm{Nu}_d = \left[(\mathrm{Nu}_{80}^3 - 1) \frac{\sin\theta}{0.985} + 1 \right]^{1/3} \tag{32}$$

and for $\pi/2 \leqslant \theta \leqslant \pi$, following Arnold et al. [48],

$$\mathrm{Nu}_d = 1 + \left\{ \left[(\mathrm{Nu}_{80}^{1/3} - 1) \frac{\sin\theta}{0.985} + 1 \right]^{1/3} - 1 \right\} \sin\theta \tag{33}$$

Here Nu_{80} is the value of Nu_d given by Eq. (31) for $\theta = 4\pi/9$. These expressions are compared with experimental values for large but finite ***h/d*** in Fig. 29. The prediction is within the disparity of the different sets of data, except for large θ, for which it is generally low.

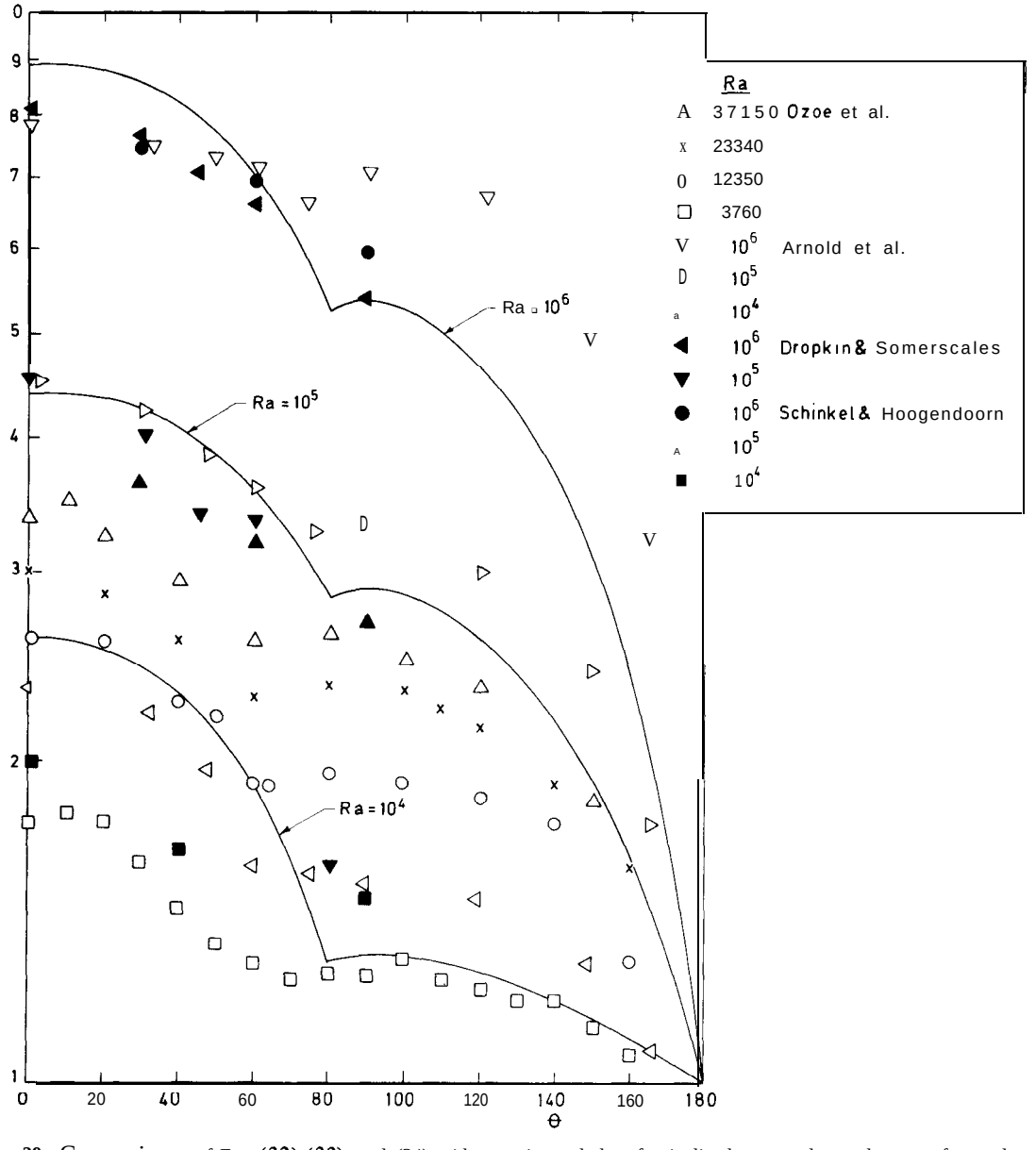

Figure 29 Comparison of Eqs. (32),(33), and (34) with experimental data for inclined rectangular enclosures of very large aspect ratio. From Churchill and Ozoe [6].

© 1983 Hemisphere Publishing Corporation

(b) Moderate aspect ratios

Ozoe and co-workers (26, 49-53] have shown experimentally and through numerical solutions that three dimensionality has a critical effect on the behavior of inclined enclosures with one or both aspect ratio near unity. The motion in a long horizontal channel, heated on the lower surface consists of a series of roll cells of nearly square cross section with their axes parallel to the shorter horizontal dimension. As illustrated by the particle paths in Fig. 30, these roll cells become oblique and distorted as the heated surface is inclined about the long dimension. When the inclination becomes sufficient so that these roll cells cross the diagonal plane of the enclosure, a sudden transition occurs to a single circulation up the heated surface and down the cooled one. On the other hand, when the shorter horizontal dimension of a 1 X 1 X 2 box is inclined, the two initial roll cells rotate until their axes become coincident, resulting in a single circulation up the heated surface and down the cooled surface as illustrated in Fig. 3 1. Qualitatively similar behavior occurs for other Ra_d, Pr, aspect ratios, and rotations of the enclosure.

As contrasted with the case of large aspect ratio, for which Nu_d decreases almost continuously as θ increases from 0 to π, Nu_d decreases to a minimum value coincident with the transition described above, then increases to a maximum and thereafter decreases to unity for heating from above ($\theta = \pi$). Churchill and Ozoe [6] predicted that the maximum value of Nu_d would occur at

$$(\theta_1)_{max} = \tan^{-1}\left(\left[\left(\frac{h_1}{d}\right)^2 + \left(\frac{h_2}{d}\right)^2\right]^{1/2}\right) \quad (34)$$

and

$$(\theta_2)_{max} = \tan^{-1}\left(\frac{h_2}{h_1}\right) \quad (35)$$

where θ_1 = angle of inclination of plane of heated surface, rad
θ_2 = angle of rotation of shorter side of enclosure from a horizontal line in the heated surface, rad
h_1 = longer side, m
h_2 = shorter side, m

The predicted inclination of $(\theta_1)_{max} = \tan^{-1}(\sqrt{2}) = 55$ and rotation of $(\theta_2)_{max} = \tan^{-1}(1) = 45°$ for a cubical enclosure has been confirmed by the finite-difference calculations of Churchill and Ozoe [6]. The constrained maximum Nu_d for $\theta_2 = 0$, corresponding to inclination of the longer side only, occurs at

$$(\theta_1)_{max} = \tan^{-1}\left(\frac{h_1}{d}\right) \quad (36)$$

and for $\theta_2 = n/2$ corresponding to inclination of the shorter side only, at

$$(\theta_1)_{max} = \tan^{-1}\left(\frac{h_2}{d}\right) \quad (37)$$

The angles of inclination for the minimum and maximum values of Nu_d, as determined experimentally by Ozoe et al. [54] and from their three-dimensional numerical solutions, are plotted in Fig. 32 versus d/h_2. This plot is for $\theta_2 = n/2$, that is, for inclination of the shorter side. Equation (37) is seen to provide a reasonable prediction for $(\theta_1)_{max}$. The discrepancy for aspect ratios approaching unity may be due to difficulty in determining the maximum of a flat curve for Nu versus θ_1 for the theoretical as well as the experimental results. The curve for $(\theta_1)_{min}$ is completely empirical.

Churchill and Ozoe [6] proposed the following expressions for Nu_d for inclination of the shorter dimension.

For $0 \leq \theta_1 < (\theta_1)_{min}$:

$$Nu_d = Nu_0 - (Nu_0 - Nu_{min})\frac{\theta_1}{(\theta_1)_{min}} \quad (38)$$

For $(\theta_1)_{min} \leq \theta_1 \leq (\theta_1)_{max}$:

$$Nu_d = 1 + (Nu_{max} - 1)\sin\left(\theta + \frac{\pi}{2} - (\theta_1)_{max}\right) \quad (39)$$

For $(\theta_1)_{max} \leq \theta_1 \leq \pi$:

$$Nu_d = 1 + (Nu_{max} - 1)\sin^2\left(\frac{\pi}{2}\left(\frac{\pi - \theta_1}{\pi - (\theta_1)_{max}}\right)\right) \quad (40)$$

From Eq. (39),

$$Nu_{min} = 1 + (Nu_{max} - 1)\sin\left((\theta_1)_{min} + \frac{\pi}{2} - (\theta_1)_{max}\right) \quad (41)$$

Nu_0, for $\theta_1 = 0$, can be estimated from Eq. (2). A correlation has not yet been developed for Nu_{max}, but a value can be estimated from Eq. (17). Equations (38)-(40), using experimental values of Nu_{max} and Nu_{min}, are compared with several sets of data in Fig. 33.

I. Honeycombs

Partitions of poorly conducting material perpendicular to the heated and cooled surfaces are sometimes utilized to suppress heat transfer by convection. Such partitions, usually forming hexagonal or rectangular cells, are often called honeycombs. Experimental measurements such as those by Sun and Edwards [55] and Hollands [56] for

© 1983 Hemisphere Publishing Corporation

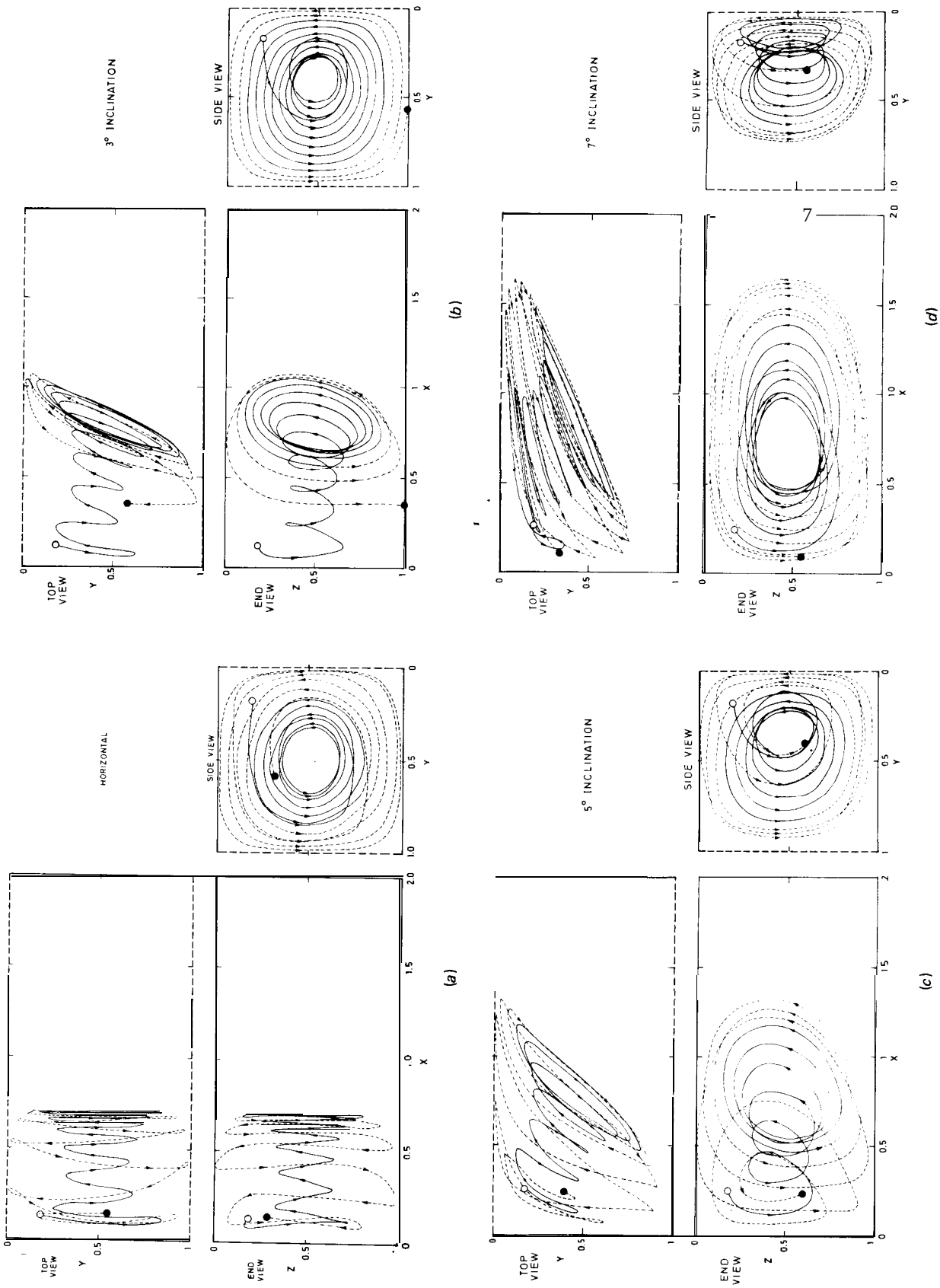

Figure 30 Computed streaklines for a 1 × 2 rectangular channel heated from below with Ra = 4 000 and Pr = 10, and inclined about the longer (infinite) dimension. Dashed boundaries indicate planes of symmetry. From Ozoe et al. [51].

© 1983 Hemisphere Publishing Corporation

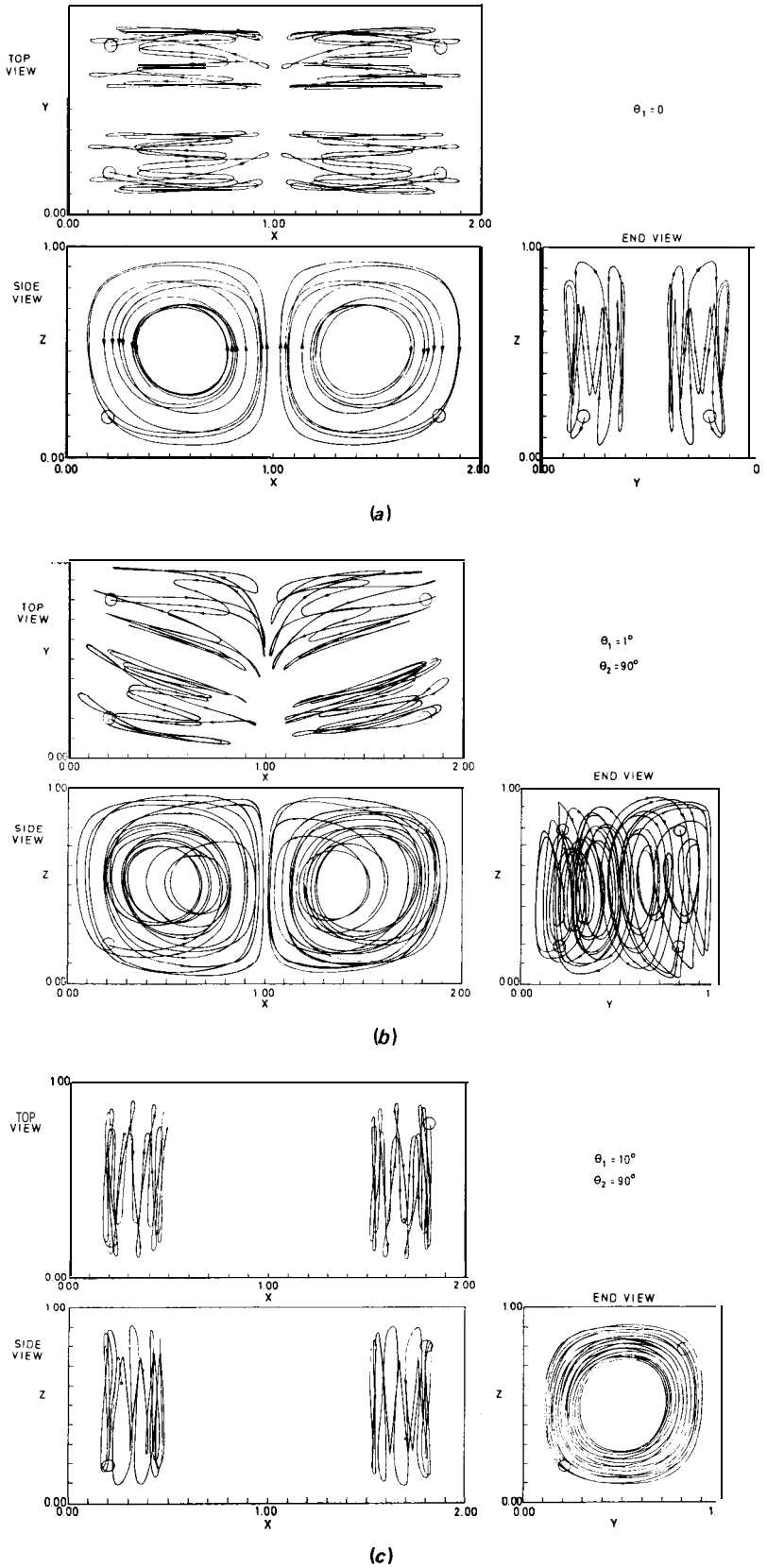

Figure 31 Computed streaklines for a 1 X 1 X 2 rectangular enclosure heated from below with Ra = 6 000 and **Pr** = 10, and inclined about the longer horizontal dimension. From Ozoe et al. [53].

© 1983 Hemisphere Publishing Corporation

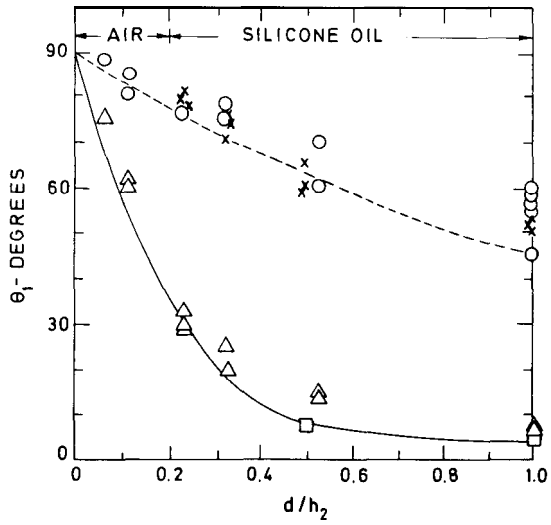

Figure 32 Experimental and computed values of angles of inclination for minimum and maximum rates of heat transfer in inclined rectangular channels.

Nu_{max} { ○ experimental; x computed } Nu_{min} { △ experimental; □ computed }

—— Eq. (38)

From Ozoe et al. [54].

heating from below, and by Cane et al. [57] and Arnold et al. [58] for inclined enclosures, indicate that the correlations for single enclosures of very low aspect ratio are applicable for honeycombs, although conduction along the partitions and radiant interchange may be significant.

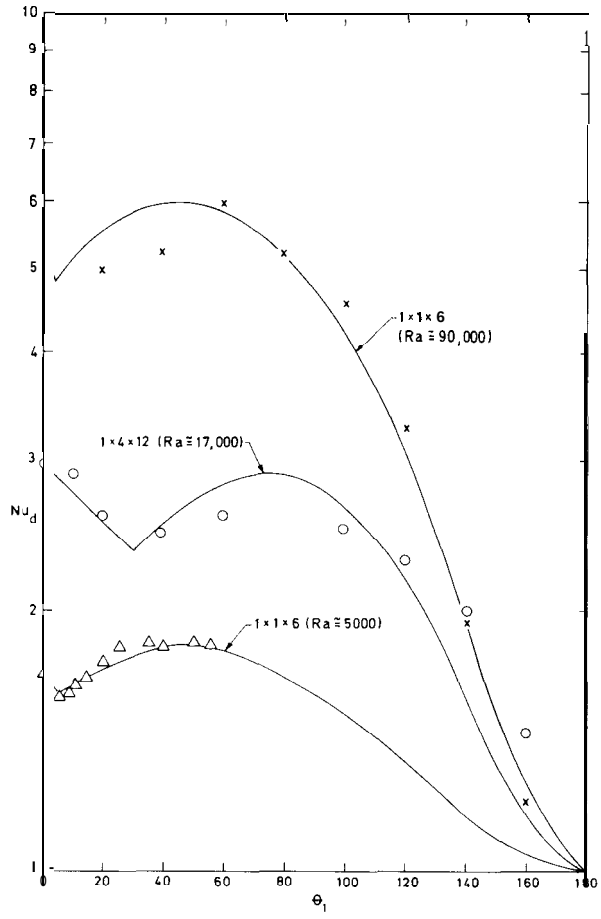

Figure 33 Comparison of Eqs. (39), (40), and (41) with experimental data and computed values of Ozoe et al. [50, 54] for rectangular enclosures with the shorter dimension inclined.

Nomenclature for Section 2.5.8 appears at the beginning of ***Part 2.***

REFERENCES FOR SECTION 2.5.8

1. Catton, I., Natural Convection in Enclosures, *Proc. 6th Int. Heat Transfer Conf., Toronto,* vol. 6, pp. 13-31, 1978.
2. Ostrach, S., Natural Convection in Enclosures, ***Advances in Heat Transfer,*** vol. 8, pp. 161-227, 1972.
3. Ostrach, S., Stable and Unstable Confined Natural Convection, unpublished review presented at First Mech. Eng. Congr., Pahlavi University, Shiraz, Iran, May 1975.
4. Koschmieder, E. L., Bénard Convection, ***Advan. Chem. Phys.,*** vol. 26, pp. 177-212, 1974.
5. Buchberg, H., Catton, I., and Edwards, D. K., Natural Convection in Enclosed Spaces: A Review of Application to Solar Energy Collection, ***J. Heat Transfer, 98,*** 1976.
6. Churchill, S. W., and Ozoe, H., The Prediction of Natural Convection in Rectangular Enclosures, in preparation.
7. Binard, H., Les tourbillons cellulaires dans une nappe liquide transportant de la chaleur par convection en regime permenant, Rev. *gén. Sci. pur. appl.*, vol. 11, pp. 1261-1271, 1309-1328, ***1900; Ann. Chim. Phys.***, vol. 23, 62–144, 1901.
8. Quinn, J. A., private communication.
9. Rayleigh, Lord (J. W. Strutt), On Convection Currents in a Horizontal Layer of Fluid When the Higher Temperature is on the Underside, ***Phil. Mug.,*** ser. 6, vol. 32, pp. 833-844, 1926.
10. Malkus, W. V. R., Discrete Transitions in Turbulent Convection, ***Proc. R. Soc. (London) Ser. A,*** vol. 225, pp. 185-195, 1954.
11. Garon, A. M., and Goldstein, R. J., Velocity and Heat Transfer Measurements in Thermal Convection, ***Phys. Fluids,*** vol. 16, pp. 1818–1825, 1973.
12. Malkus, W. V. R., and Veronis, G., Finite Amplitude Cellular Convection, ***J. Fluid Mech.***, vol. 4, pp. 225-260, 1958.
13. Catton, I., Natural Convection in Horizontal Liquid Layers, ***Phys. Fluids,*** vol. 9, pp. 2521-2522, 1966.
14. Kraichnan, R. H., Turbulent Thermal Convection at Arbitrary Prandtl Number, ***Phys. Fluids,*** vol. 5, pp. 1374-1389, 1962.

© 1983 Hemisphere Publishing Corporation

15. Churchill, S. W., and Usagi, R., A General Expression for the Correlation of Rates of Transfer and Other Phenomena, *AIChE J.*, vol. 18, pp. 1121-1128, 1972.
16. Hollands, K. G. T., Raithby, G. D., and Konicek, M., Correlation Equations for Free Convection Heat Transfer in Horizontal Layers of Air and Water, ***Znt. J. Heat Mass Transfer,*** vol. 18, pp. 879-884, 1975.
17. Davis, S. H., Convection ***in*** a Box: Linear Theory, *J. Fluid Mech.*, vol. 30, pp. 465-478, 1967.
18. Catton, I., Convection in a Closed Region: The Onset of Motion, ***J. Heat Transfer, vol. 92,*** pp. 186-188, 1970.
19. Oertel, H., Jr., Steady and Time Dependent Convection in a Rectangular Box, *Proc.* 6th *Int. Heat Transfer Conf.*, ***Toronto. vol. 2,*** pp. 281-286, 1978.
20. Catton, I., The Effect of Insulating Vertical Walls on the Onset of Motion in a Fluid Heated from Below, ***Int. J. Heat Mass Transfer,*** vol. 15, pp. 665-672, 1972.
21. Catton, I., Effect of Wall Conduction on the Stability of a Fluid in a Rectangular Region Heated from Below, ***J. Heat Transfer,*** vol. 94, pp. 446-452, 1972.
22. Catton, I., and Edwards, D. K., Effect of Side Walls on Natural Convection between Horizontal Plates Heated from Below, ***J. Heat Transfer,*** vol. 89, pp. 295-299, 1967.
23. Stork, K., and Mtiller, U., Convection in Boxes: Experiments, ***J. Fluid Mech., vol. 34,*** pp. 599-611, 1972.
24. Oertel, H., Jr., and Kirchartz, K. R., Influence of Initial and Boundary Conditions on Bénard Convection, in ***Recent Developments in Experimental and Fluid Mechanics,*** ed. U. Mtiller, K. G. Roesner, and B. Schmidt, pp. 355-366, Springer-Verlag, Berlin, 1979.
25. Verhoeven, J. D., Experimental Study of Thermal Convection in a Vertical Cylinder of Mercury Heated from Below, *Phys.* ***Fluids,*** vol. 9, pp. 1733-1740, 1969.
26. Ozoe, H., Sato, N., and Churchill, S. W., Experimental Confirmation of the Three-Dimensional Helical Streaklines Previously Computed for Natural Convection in Inclined Rectangular Enclosures (in Japanese), ***Kagaku Kogaku Ronbunshu, vol. 5,*** pp. 19-25, 1979; English transl., ***Znt. Chem. Eng.,*** vol. 19, pp. 454-462, 1979.
27. Stork, K., and Mtiller, U., Convection in Boxes: An Experimental Investigation in Vertical Cylinders and Annuli, ***J. Fluid Mech., vol.*** 71, pp. 231-240, 1975.
28. Ozoe, H., Okamoto, T., and Churchill, S. W., Natural Convection in a Vertical Annular Space Heated from Below (in Japanese), ***Kagaku Koguku Ronbunshu,*** vol. 5, pp. 457-463, 1979, English transl., ***Heat Transfer Jpn. Res.,*** vol. 8, pp. 82-93, 1979.
29. Wilkes, J. O., The Finite Difference Computation of Natural Convection in an Enclosed Rectangular Cavity, Ph.D. thesis, University of Michigan, Ann Arbor, 1963.
30. Wilkes, J. O., and Churchill, S. W., The Finite-Difference Computation of Natural Convection in a Rectangular Enclosure, ***AZChE J.,*** vol. 12, pp. 161-166, 1966.
31. Batchelor, G. K., Heat Transfer by Free Convection Across a Closed Cavity Between Vertical Boundaries at Different Temperatures, *Q. Appl.* ***Math.,*** vol. 12, pp. 209-233, 1954.
32. Elder, J. W., Laminar Free Convection in a Vertical Slot, ***J.*** Fluid *Mech.*, vol. 23, pp. 77-98, 1965.
33. Bejan, A., Note on Gill s Solution for Free Convection in a Vertical Enclosure, ***J. Fluid Mech., vol. 90,*** pp. 561-568, 1979.
34. Poots, G., Heat Transfer by Laminar Free Convection in Enclosed Plane Gas Layers, *Q. J. Mech. Appl.* ***Math.,*** vol. 11, pp. 257-273, 1958.
35. Bejan, A., and Tien, C.-L., Natural Convection in Horizontal Space Bounded by Two Concentric Cylinders with Different End Temperatures, ***Znt. J. Heat Mass Transfer,*** vol. 22, pp. 919-927, 1979.
36. Chu, H.-H. S., and Churchill, S. W., The Effect of Heater Size, Location, Aspect Ratio, and Boundary Conditions on Two-Dimensional, Laminar, Natural Convection in Rectangular Channels, ***J. Heat Transfer, vol. 98,*** pp. 194-201, 513, 1976.
37. Chu, H.-H. S., and Churchill, S. W., The Development and Testing of a Numerical Method for Computation of Laminar Natural Convection in Enclosures, ***Computers Chem. Eng.,*** vol. 1, pp. 103-108, 1977.
38. de Vahl Davis, G., and Thomas, R. W., Natural Convection Between Concentric Vertical Cylinders, *Phys.* ***Fluids,*** vol. 12, suppl. II, pp. 198-207, 1969.
39. Hellums, J. D., and Churchill, S. W., Transient and Steady-State, Free and Natural Convection, Numerical Solutions: Part II. The Region Inside a Horizontal Cylinder, ***AZChE J.,*** vol. 8, pp. 692-719, 1962.
40. Martini, W. R., and Churchill, S. W., Natural Convection Inside a Horizontal Cylinder, ***AZChE J., vol. 6,*** pp. 25 l-257, 1960.
41. Bejan, A., and Tien, C.-L., Laminar Natural Convection Heat Transfer in a Horizontal Cavity with Different End Temperatures, ***J. Heat Transfer,*** vol. 100, pp. 641-647, 1978.
42. Kuehn, T. H., and Goldstein, R. J., Correlating Equations for Natural Convection Heat Transfer between Horizontal Circular Cylinders, ***Znt. J. Heat Mass Transfer,*** vol. 19, pp. 1127-1134, 1976.
43. Huetz, J., and Petit, J. P., Etude expérimentale de la convection naturelle dans un espace annulaire horizontal, *Proc.* ***6th Znt. Heat Transfer*** *Conf.*, ***Toronto, vol. 2,*** pp. 245-249, 1978.
44. Bishop, E. H., Mack, L. R., and Scanlan, J. A., Heat Transfer by Natural Convection Between Concentric Spheres, ***Znt. J. Heat Mass Transfer,*** vol. 9, pp. 649-662, 1966.
45. Hart, J. E., Stability of the Flow in a Differentially Heated Inclined Box, ***J. Fluid Mech., vol. 47,*** pp. 547-576, 1971.
46. Hollands, K. G. T., and Konicek, L., Experimental Study of the Stability of Differentially Heated Inclined Air Layers, ***Znt. J. Heat Mass Transfer,*** vol. 16, pp. 1467-1476, 1973.
47. Hollands, K. G. T., Unny, T. E., Raithby, G. D., and Konicek, L., Free Convective Heat Transfer Across Inclined Air Layers, ***J. Heat Transfer,*** vol. 98, pp. 189-193, 1976.
48. Arnold, J. N., Bonaparte, P. N., Catton, I., and Edwards, D. K., Experimental Investigation of Natural Convection in a Finite Rectangular Region Inclined at Various Angles from 0 to 180°, *Proc. 1974* ***Heat Transfer Fluid*** *Mech.* ***Inst.,*** pp. 321-329.
49. Ozoe, N., Yamamoto, K., Churchill, S. W., and Sayama, H., Three-Dimensional, Numerical Analysis of Laminar Natural Convection in a Confined Fluid Heated from Below, ***J. Heat Transfer,*** vol. 98, pp. 202-207, 5 19, 1976.
50. Ozoe, H., Yamamoto, K., and Churchill, S. W., Three-Dimensional Numerical Analysis of Natural Convection in an Inclined Channel with a Square Cross Section, ***AZChE J.,*** vol. 25, pp. 709-716, 1979.

© 1983 Hemisphere Publishing Corporation

51. Ozoe, H., Yamamoto, K., Sayama, H., and Churchill, S. W., Natural Convection Patterns in a Long Inclined Rectangular Box Heated from Below, Part II. Three-Dimensional Numerical Results, ***Znt. J. Heat Mass Transfer***, vol. 20, pp. 131-139, 1977.
52. Ozoe, H., Churchill, S. W., Okamoto, T., and Sayama, H., Natural Convection in Doubly Inclined Rectangular Boxes, *Proc.* ***6th*** *Int.* ***Heat Transfer*** *Conf.*, ***Toronto,*** vol. 2, pp. 293-298, 1978.
53. Ozoe, H., Churchill, S. W., Okamoto, T., and Sayama, H., Three-Dimensional Natural Convection in Inclined Rectangular Enclosures, *Proc.* ***PACHEC'77,*** vol. 1, pp. 24-31, 1977.
54. Ozoe, H., Sayama, H., and Churchill, S. W., Natural Convection in an Inclined Rectangular Channel at Various Aspect Ratios and Angles-Experimental Measurements, *Int. J.* ***Heat Mass Transfer,*** vol. 18, pp. 1425-1431, 1975.
55. Sun, W. M., and Edwards, D. K., Natural Convection in Cells with Finite Conducting Side Walls Heated from Below, *Proc.* ***4th Znt. Heat Transfer*** *Conf.*, ***Paris- Versailles,*** vol. 4, paper NC23, 1970.
56. Hollands, K. G. T., Natural Convection in HorizontalThin-Walled Honeycomb Panels, ***J. Heat Transfer,*** vol. 95, pp. 439-444, 1973.
57. Cane, R. L. D., Hollands, K. G. T., Raithby, G. D., and Unny, T. E., Free Convection Heat Transfer across Inclined Honeycomb Panels, ***J. Heat Transfer,*** vol. 99, pp. 86-91, 1977.
58. Arnold, J. N., Edwards, D. K., and Catton, J., Effect of Tilt and Horizontal Aspect Ratio on Natural Convection in a Rectangular Honeycomb, ***J. Heat Transfer,*** vol. 99, pp. 120-122, 1977.

© 1983 Hemisphere publishing Corporation

2.5.9

Combined free and forced convection around immersed bodies

S. W. Churchill

■ Heat transfer by forced convection between a fluid and an immersed body implies a temperature difference and hence a density difference. The density difference gives rise to free convection. The effect of buoyant motion in the direction of the forced flow is to increase the velocity in the boundary layer and thereby the rate of heat transfer over that for pure forced convection. Buoyant motion in opposition to the forced motion reduces the velocity and the rate of heat transfer relative to pure forced or free convection. Also, assisting flows retard and opposing flows advance the point of separation of the boundary layer on immersed bodies. Hall and Price [1] found that the rate of heat transfer in a turbulent free convection was at first decreased and then increased by a superimposed forced flow in the same direction. They attributed the decrease to the suppression of turbulence. In view of these complexities, it is apparent that the suggestion of McAdams [2], that the higher of the rates of heat transfer for the two pure processes be used for the combined process, can be considered only as a first-order approximation. More accurate correlating equations for various regimes are recommended below.

A. Assisting convection

(a) Thin laminar boundary-layer regime

Extensive theoretical and experimental results have been obtained for aiding free and forced convection in the laminar boundary-layer regime, and many expressions have been proposed for their correlation, generally in the form

$$Nu'' = \mathrm{Nu}_F^n + \mathrm{Nu}_N^n \tag{1}$$

where $\mathrm{Nu} = \alpha l/\lambda$ = Nusselt number
α = heat transfer coefficient, $\mathrm{W/m^2\ K}$
λ = thermal conductivity, W/m K
l = characteristic length, m
and the subscripts F and N designate forced and free (natural) convection, respectively. A value of 2 for the exponent n has been rationalized by many investigators, based on the vector sum of the imposed free-stream velocity and a somewhat arbitrary, equivalent velocity for free convection. A value of 4 has been rationalized by others on the basis of the additivity of the work of forced and free convection. The approximation of McAdams corresponds to $n \to \infty$. Churchill [3] examined the various sets of experimental and theoretical values for isothermal and uniformly heated, vertical plates and concluded that n = 3 results in a better representation than 2 or 4. Ruckenstein [4] has since provided theoretical support for this choice. Churchill also demonstrated that Eq. (1) with n = 3 is a good approximation for immersed bodies as well as vertical plates. Substitution of the general theoretical expressions for laminar boundary layers then yields

$$\mathrm{Nu}^3 = (A_F\,\mathrm{Re}^{1/2}\,\mathrm{Pr}^{1/3}\,f_F(\mathrm{Pr}))^3 + [A_N(\mathrm{Ra}\,f_N(\mathrm{Pr}))^{1/4}]^3 \tag{2}$$

where $\mathrm{Re} = u_\infty l\rho/\eta$ = Reynolds number
$\mathrm{Pr} = \eta c_p/\lambda$ = Prandtl number
$\mathrm{Ra} = g\rho^2 c_p \zeta (T_w - T_\infty) l^3/\eta\lambda$ = Rayleigh number

$$f_F(\mathrm{Pr}) = [\,1 + (C_F/\mathrm{Pr})^{2/3}\,]^{-1/4} \tag{3}$$

$$f_N(\mathrm{Pr}) = [1 + (C_N/\mathrm{Pr})^{9/16}\,]^{-16/9} \tag{4}$$

and u_∞ = free-stream velocity, m/s

© 1983 Hemisphere Publishing Corporation

HEDH

Table 1 Recommended constants and characteristic lengths for mixed convection per Churchill [3]

	l	A_F	A_N	C_F	C_N	Nu_0
Vertical plate						
Local						
Uniform T	x	0.339	0.503	0.0468	0.492	0.5^a
Uniform $\dot{q}$	x	0.464	0.563	0.0205	0.437	0.5^a
Mean						
Uniform T	x	0.677	0.670	0.0468	0.492	0.5^a
Uniform $\dot{q}$	$x/2$	0.656	0.669	0.0205	0.437	0.5^a
Horizontal cylinder						
Mean						
Uniform T	πD	1.08^a	0.690	0.412	0.559	1.0^b
Uniform $\dot{q}$	πD		0.694	0.442		
Sphere						
Mean						
Uniform T	$\pi D/2$	0.69^a	0.659			π^c
General approximate values		0.67^d	0.67^e	0.45^f	0.45	

[a] Experimental.
[b] From the solution of King [5] for potential flow.
[c] From solution for pure conduction.
[d] Except for Nu on plates and $\overline{Nu}$ on cylinders
[e] Except for Nu on plates.
[f] Except for plates.

The other symbols are defined as in Sec. 2.5.7. Values of A_F, C_F, A_N, and C_N for various bodies and the two above-mentioned boundary conditions are given in Table 1. The values of these coefficients were determined from boundary-layer theory, except as noted. Local values of Nu for all bodies are obtained by using x, the distance from the leading edge or forward stagnation point, as the characteristic length in Nu, Re, and Ra. Mean values of Nu are obtained using the indicated characteristic lengths.

Equations (2), (3), and (4) indicate that the dimensionless groups that determine the relative importance of free and forced convection are $Ra/Re^2\,Pr^{4/3} = Gr/Re^2\,Pr^{1/3}$ in the limit as $Pr \to \infty$ and $Ra/Re^2\,Pr = Gr/Re^2$ in the limit as $Pr \to 0$. Here

$$Gr = \frac{g\rho^2\zeta(T_w - T_\infty)l^3}{\eta^2} = \text{Grashof number}$$

These two asymptotic groupings were identified as early as 1966 by Acrivos [6], but erroneous groupings, and in particular Gr/Re^2 for large Pr, have frequently been utilized or recommended.

Equation (2) is compared with experimental data for a number of shapes and fluids in Fig. 1. Theoretically computed values are not included because with the exception of a few values of doubtful accuracy, they fall essentially on the curve representing the correlating equation.

The computed values of Chen and Mucoglu [7] for the local rate of heat transfer in combined convection to a vertical cylinder are represented approximately by Eq. (2) if Nu is replaced by $Nu - 0.88(x/D)$ and the characteristic length chosen as x. However, these results have not been tested experimentally, and their range of validity is not certain.

Laminar boundary-layer theory becomes invalid as Re and Ra approach zero. This breakdown occurs as the thickness of the boundary layer approaches the magnitude of the characteristic length of the surface. The regime of lower Re and Ra is not of great practical importance for flat surfaces but may be for small horizontal cylinders (wires) and particles. The correlating equation of Churchill and Bernstein [8] for forced

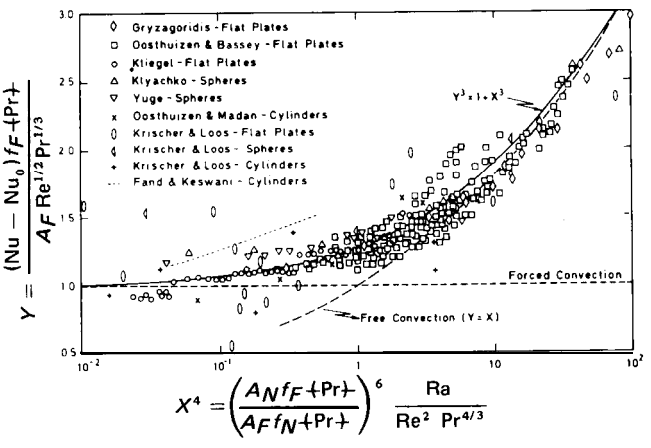

Figure 1 Test of Eq. (2) for assisting forced and free convection to immersed bodies. From Churchill [3].

© 1983 Hemisphere Publishing Corporation

convection to cylinders indicates that laminar boundary-layer theory may be used with less than a 10% error down to Re $Pr^{2/3}$ = 50 for Pr → ∞ and to Re Pr = 36 for Pr → 0. The corresponding limits for free convection, as given by the correlating equation of Churchill and Chu [9], are Ra = 7 200 for Pr → ∞ and Ra Pr = 40 000 for Pr → 0. These limits are presumed to apply approximately for other bodies and hence to Eq. (2). Results for lower Re and Ra are considered below.

(b) Regime of creeping flow (Re and Ra → 0)

Churchill (3) developed a correlation for horizontal cylinders in this regime by combining the separate analytical solutions of Nakai and Okazaki [IO] for creeping flow *in* pure free and forced convection as

$$\frac{2}{\overline{Nu}} = -\ln\left\{\frac{Re\ Pr}{5.20} + \left[\frac{\overline{Nu}\ Ra\ Pr}{49.6\ (Pr + 9.4)^{1/2}}\right]^{1/3}\right\} \qquad (5)$$

Here ***D*** is used as the characteristic length in $\overline{Nu}$, Re, and Ra. Equation (5), which is presumed to be valid only for both Re Pr and $(Ra\ Pr)^{1/3}$ less than 0.2, is compared in Fig. 2 with experimental data for air. The agreement of the prediction with the data of Nakai and Okazaki for 10 000 < ***L/D*** < 12 500 is excellent. The data of Gebhart and Pera [11] for ***L/D*** = 8 000 fall somewhat below. Additional data of Gebhart and Pera indicate that ***L/D*** may be a parameter for values less than 16 000 for small wires. This remarkable sensitivity is apparently due to perturbations in the flow. The data of Gebhart and Pera for silicone oils (Pr = 6.3 and 63) fall far below the prediction of Eq. (5), but also are generally above the indicated limits of Re Pr and Ra Pr for the correlation.

(c) Regime of slightly inertial flow

A considerable gap exists between the upper limit of validity of the regime of creeping flow and the lower limit of validity of the regime of a thin laminar boundary layer. Interpolation between Eqs. (2) and (5) is possible, but the singularity in Eq. (5) is an impediment to the development of a correlating equation for that purpose. Churchill [3] instead suggested approximation of the limiting behavior in the regime of creeping flow by a constant, Nu_0, and hence the following expression for interpolation:

$$(Nu - Nu_0)^3 = [A_F\ Re^{1/2}\ Pr^{1/3}\ f_F(Pr)]^3 + [(A_N\ (Ra\ f(Pr))^{1/4}]^3 \qquad (6)$$

His recommended values of Nu_0 (corresponding to the indicated characteristic lengths) are included in Table 1. Experimental data for the creeping and intermediate ranges of flow are included in Fig. 1. The value of Nu, for spheres has a firm theoretical basis, that for cylinders has some theoretical basis, and that for vertical plates is purely empirical.

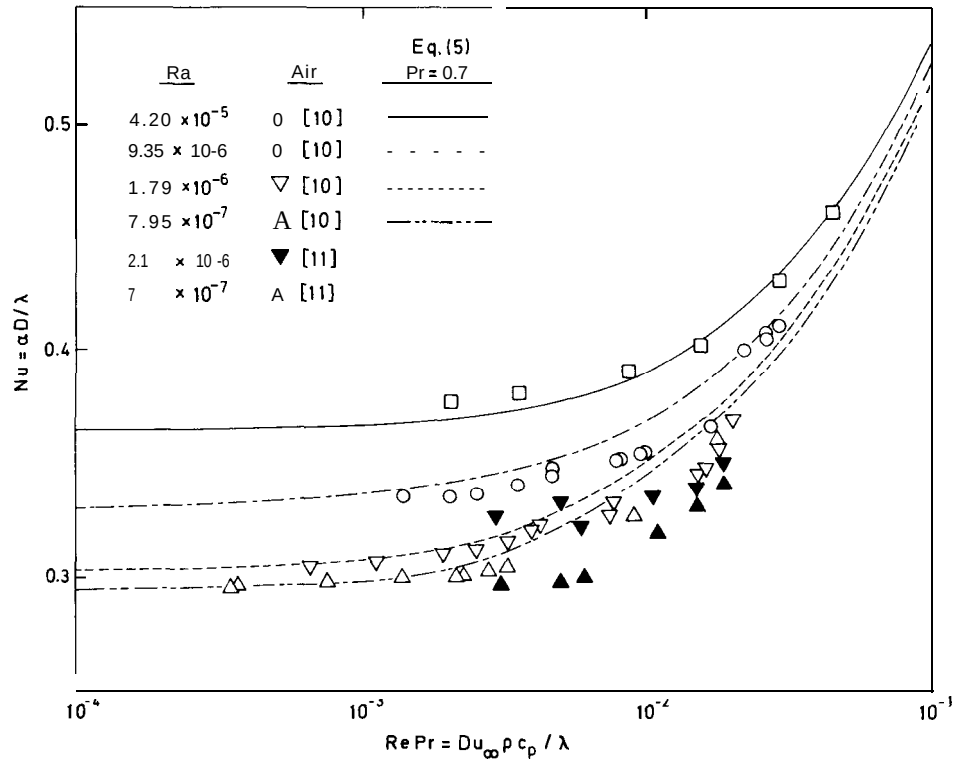

Figure 2 Test of Eq. (5) for assisting forced and free convection to horizontal cylinders in regime of creeping flow.

© 1983 Hemisphere Publishing Corporation

(d) Turbulent regime

Sufficient experimental data to support construction of a correlating equation for the completely turbulent regime do not appear to exist. In the absence of such data, Eq. (1) is tentatively recommended with $n = 3$ and Nu_F and Nu_N from correlating equations for pure forced and free convection in the respective turbulent regimes. Buoyant flow may suppress the onset of turbulence in forced flow and hence at first decrease Nu as mentioned above.

B. Opposing convection

The experimental and theoretical results are less extensive than for assisting convection. The following correlating equation is recommended by Churchill [12]:

$$Nu = |Nu_F^3 - Nu_N^3|^{1/3} \tag{7}$$

with Nu_F and Nu_D chosen as for assisting convection. As indicated in Fig. 3, Eq. (7) yields a value of zero for $Nu_F = Nu_N$, whereas the experimental data indicate a finite value, but otherwise Eq. (7) appears to predict the correct trends.

C. Transverse convection

Free convection is superimposed at a right angle to forced convection in horizontal flow over a flat surface or an immersed body. Chen et al. [13] and others have shown that the upward buoyant motion above a heated (or downward below a cooled) flat surface is analogous to a favorable pressure gradient and thereby increases the rate of heat transfer, whereas the downward buoyant motion above a cooled (or upward below a heated) plate is analogous to an adverse pressure gradient and thereby decreases the rate of heat transfer. The former case is stabilizing, but the latter is destabilizing and leads to separation.

(a) Horizontal plates

Churchill [12] proposed the following correlating equation for both the local and mean rates of heat transfer in laminar forced flow along horizontal plates:

$$(Nu - Nu_0)^{7/2} = [A_F Re^{1/2} Pr^{1/3} f_F(Pr)]^{7/2} \pm [A_N (Ra\, f_N(Pr))^{1/5}]^{7/2} \tag{8}$$

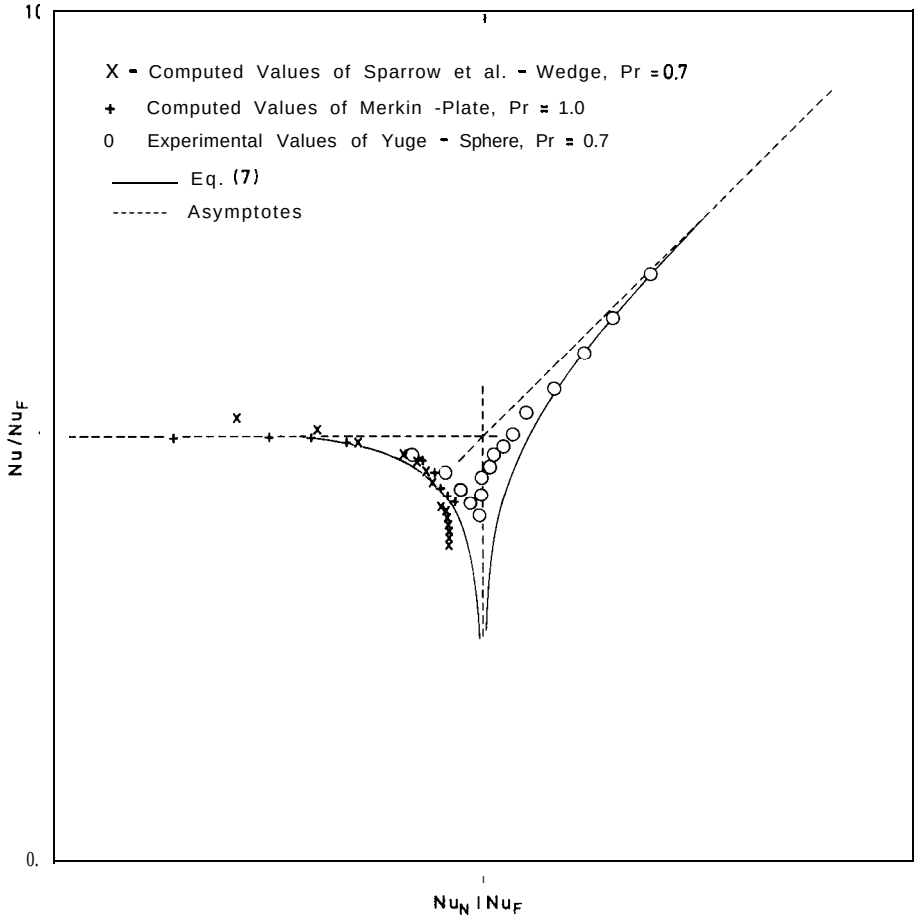

Figure 3 Test of Eq. (7) for opposing convection per Churchill [12].

© 1983 Hemisphere Publishing Corporation

Table 2 Recommended constants for free convection from a horizontal plate per Churchill [12]

	A_N	C_N
Local coefficient		
Uniform T	0.456	0.312
Uniform $\dot{q}$	0.625[b]	(0.309
Mean coefficient		
Uniform T	0.760[a]	0.312
Uniform $\dot{q}$	0.760	(0.309

[a] From boundary-layer theory per Hieber [14].
[b] Estimated from boundary-layer calculations of Mucoglu and Chen [15].
[c] Postulated for $T_w - T_\infty$ at $x/2$.
[d] Postulated value.

Equation (8) is applicable for $f_F(\mathrm{Pr})$ and the values in Table 1 for Nu_0, A_F, and C_F. Values of A_N are given in Table 2, together with the special values of C_N to be used with Eq. (4). The coefficients in this latter table are based on the theoretical values for a thin laminar boundary layer.

The positive sign in Eq. (8) is applicable when the fluid on the upper side is heated or on the lower side is cooled. The negative sign is applicable for the two reverse situations, Separation occurs before the buoyant term in Eq. (8) exceeds the forced convective term. Hence a zero value on the right side represents the limit of applicability of this expression. The coefficients in Table 2 for the local coefficient with an isothermal surface thus give $\mathrm{Ra}\, f_N(\mathrm{Pr})/(\mathrm{Re}^{1/2}\mathrm{Pr}^{1/3} f_F(\mathrm{Pr}))^5 = 0.226$ as a criterion for separation. For Pr = 0.7 this gives $\mathrm{Gr}/\mathrm{Re}^{5/2} = 0.35$, which is somewhat higher than the estimate of 0.1 by Chen et al. [13] based on the velocity field.

Experimental data to test Eq. (8) do not appear to be available, but computed values are compared with this expression in Fig. 4. The prediction is excellent for the values in the thin boundary-layer regime but seriously overpredicts $\mathrm{Nu}/\mathrm{Nu}_F$ for the two values at Re = 40. The expressions utilized for Nu_F and NUN in Eq. (5) are apparently inadequate in this regime. Equations (1) and (7) may be satisfactory both above and below the thin boundary-layer regime if appropriate values are used for Nu_F and NUN.

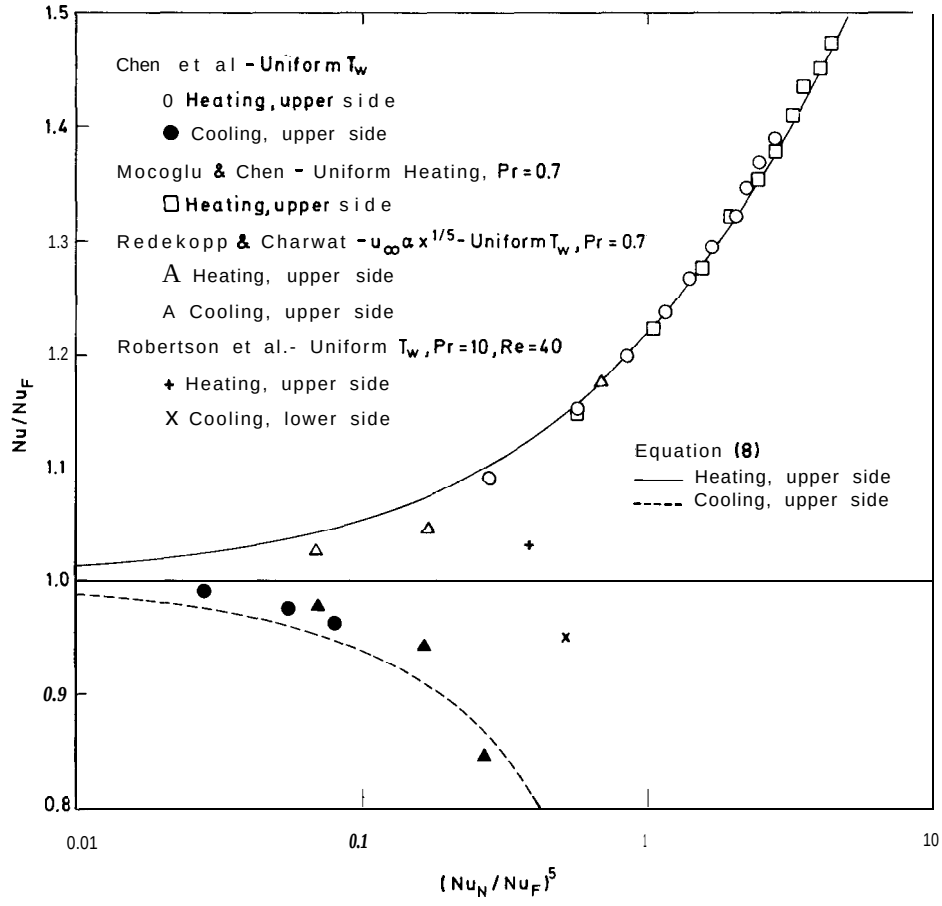

Figure 4 Comparison of Eq. (8) with computed values for mixed convection from horizontal plates per Churchill [12].

© 1983 Hemisphere Publishing Corporation

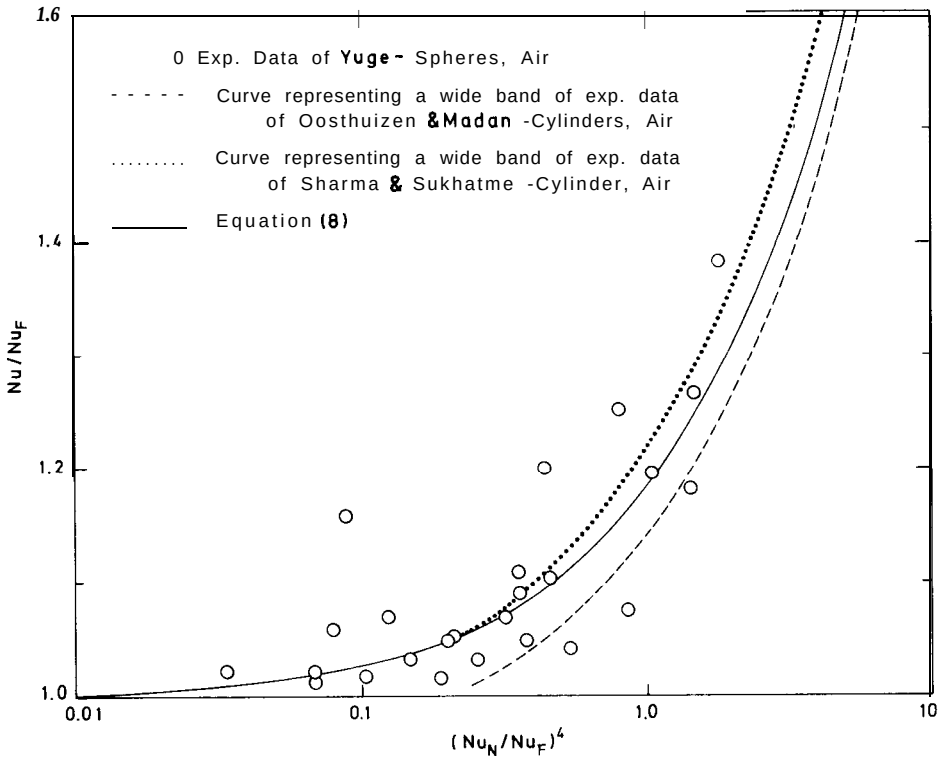

Figure 5 Test of Eq. (9) for cross flow over spheres and cylinders per Churchill [12].

(b) Immersed bodies

Churchill [12] correlated experimental data for spheres and cylinders in cross flow (normal to the buoyant force) with the expression

$$(\mathrm{Nu} - \mathrm{Nu}_0)^4 = \mathrm{Nu}_F^4 + \mathrm{Nu}_N^4 \qquad (9)$$

The success of this representation is demonstrated in Fig. 5. The agreement is fair, considering the scatter of the three sets of data. The data of Nakai and Okazaki [10] for creeping flow demonstrate a minimum in Nu as Re increases and hence are not represented by Eq. (9).

Nomenclature for Section 2.5.9 appears at the beginning of Part 2.

REFERENCES FOR SECTION 2.5.9

1. Hall, W. B., and Price, P. H., Mixed Forced and Free Convection from a Vertical Heated Plate to Air, *Proc. 4th Int. Heat Transfer Conf., Paris-Versailles,* vol. 4, paper NC3.3, 1970.
2. McAdams, W. H., ***Heat Transmission, 3d ed.,*** p. 258. McGraw-Hill, New York, 1954.
3. Churchill, S. W., A Comprehensive Correlating Equation for Laminar, Assisting, Forced and Free Convection, *AIChE J.,* vol. 10, pp. 10-16, 1977.
4. Ruckenstein, E., Interpolating Equations between Two Limiting Cases for the Heat Transfer Coefficient, *AIChE J.,* vol. 24, pp. 940-941, 1978.
5. King, L. V., On Convection of Heat from Small Cylinders in a Stream of Fluid, ***Phil. Trans. R. Soc. London Ser. A,*** vol. 274, pp. 373-432, 1914.
6. Acrivos, A., On the Combined Effect of Forced and Free Convection Heat Transfer in Laminar Boundary Layer Flows, *Chem. Eng. Sci.,* vol. 21, pp. 343-352, 1966.
7. Chen, T. S., and Mucoglu, A., Buoyancy Effects on Free Convection Along a Vertical Cylinder, ***J. Heat Transfer,*** vol. 97, pp. 198-203, 1975.
8. Churchill, S. W., and Bernstein, M., A Correlating Equation for Forced Convection from Gases and Liquids to a Circular Cylinder in Crossflow, ***J. Heat Transfer,*** vol. 99, pp. 300-306, 1977.
9. Churchill, S. W., and Chu, H. H.-S., Correlating Equations for Laminar and Turbulent Free Convection from a Horizontal Cylinder, ***Znt. J. Heat Mass Transfer,*** vol. 18, pp. 1049-1053, 1975.
10. Nakai, S., and Okazaki, T., Heat Transfer from a Horizontal Circular Wire at Small Reynolds and Grashof Numbers, I. Pure Convection; II. Mixed Convection, ***Znt. J. Heat Mass Transfer,*** vol. 18, pp. 387-396, 397-413, 1975.

© 1983 Hemisphere Publishing Corporation

11. Gebhart, B., and Pera, L., Mixed Convection from Long Cylinders, *J. Fluid Mech.*, vol. 45, pp. 49-64, 1970.
12. Churchill, S. W., Correlating Equations for Free and Forced Convection in Opposing and Horizontal Flow, in preparation.
13. Chen, T. S., Sparrow, E. M., and Mucoglu, A., Mixed Convection in Boundary Layer Flow on a Horizontal Plate, *J. Heat Transfer*, vol. 99, pp. 66-71, 1977.
14. Hieber, C. A., Mixed Convection Above a Heated Horizontal Surface, *Int. J. Heat Mass Transfer*, vol. 16, pp. 769-785, 1973.
15. Mucoglu, A., and Chen, T. S., Mixed Convection on a Horizontal Plate with Uniform Surface Heat Flux, *Proc. 6th ht. Heat Transfer Conf., Toronto, vol.* 1, pp. 85-90, 1978.

© 1983 Hemisphere Publishing Corporation

2.5.10

Combined free and forced convection in channels

S. W. Churchill

■ The temperature difference associated with heat transfer by forced convection in channels generates a density gradient. The effect of the resulting buoyant motion on the rate of heat transfer has been studied very extensively because of its obvious industrial importance. Even so, the results are less well correlated than those for external combined convection, as described in Sec. 2.5.9, because of a number of additional complexities.

In flow through a channel, the increased or decreased velocity near the wall due to buoyancy is necessarily compensated by a decrease or increase, respectively, in the central region of the channel, and in the extreme may actually produce a reversal in the direction of flow. The effect of the variation of viscosity with temperature is correspondingly more complex and may be of the same order of magnitude as that of the buoyancy. Furthermore, for a uniform surface temperature, the temperature difference varies along the length of the channel and the choice of an effective mean value in the Nusselt and Rayleigh numbers is arbitrary.

Heating a fluid in upward laminar flow through a channel (or cooling in downward flow) results in an increased velocity gradient near the surface, thereby increasing the rate of heat transfer. On the other hand, the compensating decrease in the velocity near the center of the channel results in a decrease in the rate of transfer in the turbulent regime. Heating a fluid in downward flow (or cooling in upward flow) has the reverse effect on the velocity, thereby producing an increase in the rate of heat transfer in the laminar regime and a decrease in the turbulent regime.

Heating a fluid in horizontal flow through a round channel produces a secondary motion in the form of a circulation upward along the two vertical tube walls and downward in the central region, thereby increasing the rate of heat transfer. Cooling a fluid in horizontal flow produces the same two circulations, but in the opposite direction, and the same increase in the rate of heat transfer.

Metais and Eckert [1] prepared a graph, reproduced as Fig. 1, which indicates the regimes of Re and Ra D/L in which the motion in a vertical round tube with a uniform wall temperature is laminar or turbulent and primarily free, mixed, or forced. The mixed regime is defined as one in which the heat flux deviates 10% or more from that for pure free or forced convection. Here

$$\mathrm{Re} = \frac{Du_b\rho}{\eta}$$

$$\mathrm{Ra}_{LM} = \frac{g\rho^2 c_p \zeta (T_w - T_b)_{LM} D^3}{\eta\lambda}$$

D = tube diameter, m

u_b = mixed mean velocity, m/s

ρ = density, $\mathrm{kg/m^3}$

η = dynamic viscosity, Pa s

g = acceleration due to gravity, $\mathrm{m/s^2}$

c_p = specific heat capacity at constant pressure, J/kg K

ζ = volumetric coefficient of expansion with temperature, $\mathrm{K^{-1}}$

T_w = temperature of wall, K

© 1983 Hemisphere Publishing Corporation

HEDH

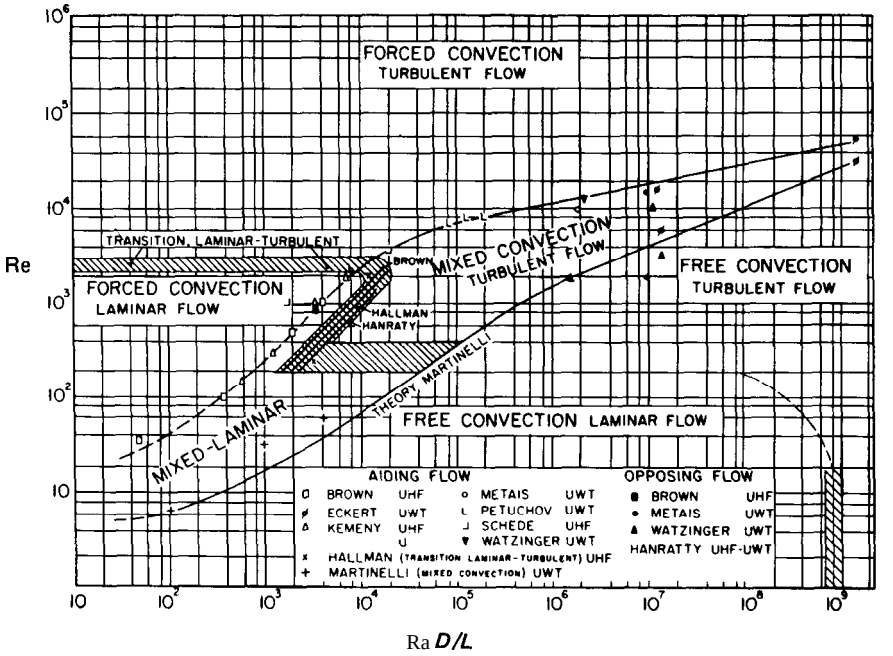

Figure 1 Regimes of laminar and turbulent, free, forced, and mixed convection in vertical tubes. $10^{-2} < \mathrm{Pr}\ D/L < 1$. From Metais and Eckert [1].

T_b = mixed mean temperature, K

λ = thermal conductivity, W/m K

L = length of tube, m

LM = logarithmic mean

Their corresponding plot for horizontal tubes is reproduced as Fig, 2. They considered the boundary between mixed and free convection to be too uncertain to draw. As indicated, both Figs. 1 and 2 are limited in applicability to $10^{-2} < \mathrm{Pr}\ D/L < 1$.

A. Vertical channels

(a) Laminar assisting convection

Many correlating equations have been proposed for assisting convection. Equation 2.5.9(1) with $n = 3$, that is,

$$\mathrm{Nu}^3 = \mathrm{Nu}_F^3 + \mathrm{Nu}_N^3 \qquad (1)$$

appears to be a satisfactory expression for both the local and the mean value for many cases. Here

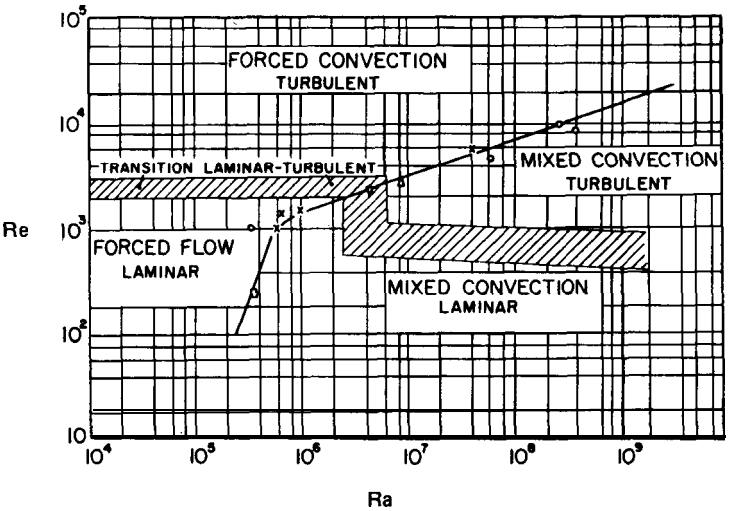

Figure 2 Regimes of laminar and turbulent, free, forced, and mixed convection in horizontal tubes. $10^{-2} < \mathrm{Pr}\ D/L < 1$.

© 1983 Hemisphere Publishing Corporation

$\mathrm{Nu} = \dfrac{\alpha D}{\lambda}$ = Nusselt member

α = heat transfer coefficient, $\mathrm{W/m^2\,K}$

and the subscripts F and N designate individual expressions for pure forced and pure free convection, respectively.

I. Uniform wall temperature

For a laminar fully developed thermal boundary layer, Nu_F is a constant independent of Re, Pr, and L/D. For a round tube with a uniform wall temperature,

$$\mathrm{Nu}_F = \overline{\mathrm{Nu}}_F = 3.657 \tag{2}$$

where the bar indicates the length-mean value. For free (induced) laminar convection in a vertical tube with a uniform wall temperature, Churchill [2] proposed the semitheoretical expression

$$\mathrm{Nu}_N = \frac{0.75\,(\mathrm{Ra}\,D/L)^{1/4}}{[1 + (0.492/\mathrm{Pr})^{9/16}]^{4/9}} \tag{3}$$

Throughout Sec. 2.5.10, the logarithmic mean temperature difference is implied in Nu_N and Ra in the absence of some specific designation. Equation (1), together with Eqs. (2) and (3), is compared in Fig. 3 with selected experimental data of Martinelli et al. [3] for small Gz. The agreement is reasonable considering the large physical property variations and the undoubted persistence of thermal development.

For the entrance region of a round tube, Martinelli and Boelter [4] proposed the use of Eq. (1) for $(\mathrm{Nu})_{AM}$, using for forced convection the Lévêque [5] solution

$$(\mathrm{Nu}_F)_{AM} = 1.75 F_1\,\mathrm{Gz}^{1/3} \tag{4}$$

and for free convection the empirical expression

$$(\mathrm{Nu}_N)_{AM} = 0.729 F_1 F_2^{1/3} \left(\mathrm{Ra}\,\frac{D}{L}\right)^{0.28} \tag{5}$$

The subscript AM indicates that the arithmetic mean temperature difference $(2T_w - T_i - T_o)/2$, is to be used in Nu. Also,

$\mathrm{Gz} = \dfrac{\dot{M} c_p}{\lambda L}$ = Graetz number

M = mass flow rate, kg/s

$$F_1 = \frac{Z}{\ln\left(\dfrac{2+Z}{2-Z}\right)} = \frac{\mathrm{Nu}_{AM}}{\mathrm{Nu}_{LM}} \tag{6}$$

$$Z = \frac{2(T_o - T_i)}{(2T_w - T_o - T_i)} = \frac{\pi \mathrm{Nu}_{AM}}{\mathrm{Gz}} \tag{7}$$

T_w = tube wall temperature, K

T_o = fluid outlet temperature, K

T_i = fluid inlet temperature, K

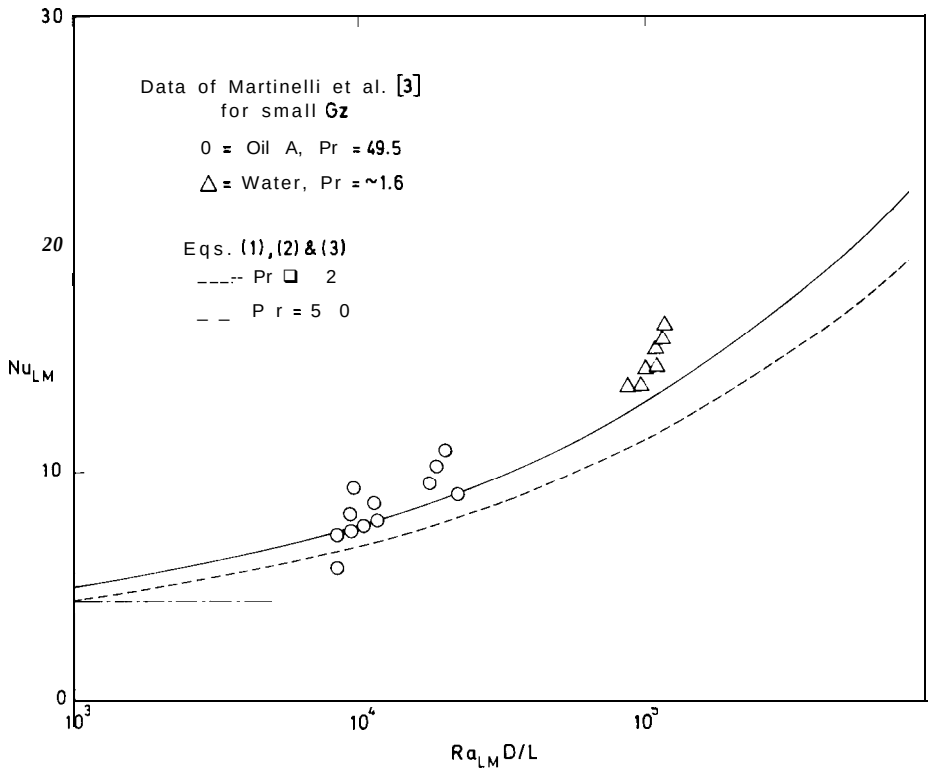

Figure 3 Comparison of Eq. (1) using component Eqs. (2) and (3) with experimental data for fully developed, assisting, laminar convection in an isothermal, vertical tube.

© 1983 Hemisphere Publishing Corporation

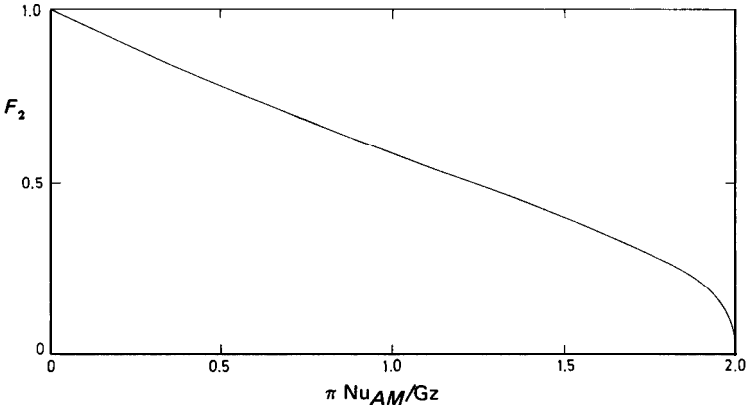

Figure 4 Correction factor in Eq. (5) for use of inlet rather than integrated mean temperature difference in Rayleigh number.

Ra_i = Rayleigh number based on temperature difference at inlet, $T_w - T_i$

F_2 = correction factor for use of inlet rather than integrated mean temperature difference in Rayleigh number

$$= \frac{5}{4} \int_0^1 \xi^{1/4} e^{-\phi \xi^{2/3}}\, d\xi \qquad (8)$$

and

$$\phi = \frac{3\pi Nu_{AM}}{4F_1\, Gz} \qquad (9)$$

The absence of a subscript N or F implies the value for the combined process. It is recommended that the properties in Gz be evaluated at the arithmetic mean fluid temperature $(T_2 + T_o)/2$, and those in Nu and Ra_i at the tube wall temperature. F_2, as calculated from Eq. (8), using Eqs. 2.5.8(6) and 2.5.8(9), is plotted versus $\pi Nu_{AM}/Gz$ in Fig. 4. Equation (1) with Eqs. (4) and (5), and so on, is seen in Fig. 5 to agree well with all of the experimental data of Martinelli et al. [3] for heating oil and water in upward flow. This complex correlation necessarily requires trial and error.

Pigford [6] developed analytical solutions for assisting flow taking into account the variation in viscosity as well as density with temperature. His results are plotted in Fig. 6. The influence of viscosity is seen to be significant although somewhat less than that of buoyancy. Experimental data are compared with the predicted values in Fig. 7.

II. Uniform longitudinal heating

The behavior for uniform longitudinal heating is somewhat simpler than for a uniform wall temperature since dT_b/dx is constant, and for fully developed heat transfer $T_w - T_b$ and dT_w/dx are also constant. The heat flux density and temperature are uniform about the circumference of a round vertical tube as a result of symmetry.

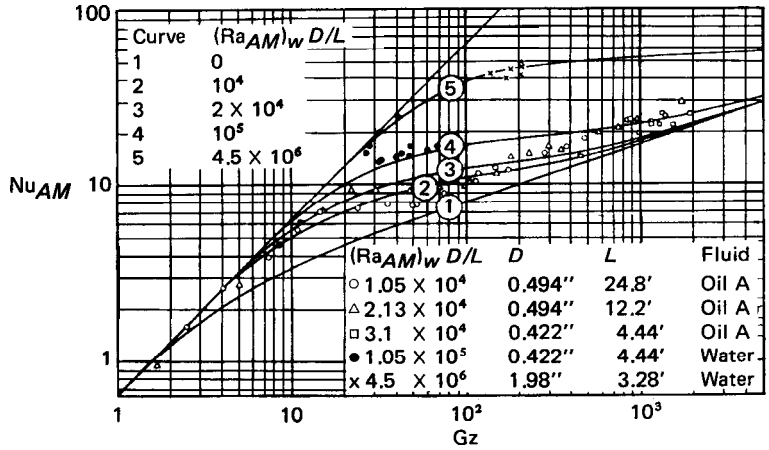

Figure 5 Comparison of Eq. (1) using Eqs. (4) and (5) with experimental data of Martinelli et al. [3] for heating oil and water in upward laminar flow. From Martinelli and Boelter [4].

© 1983 Hemisphere Publishing Corporation

For nonround channels, one or both of these quantities varies around the perimeter. Theoretical results are generally for two extreme conditions: (1) uniform peripheral temperature, corresponding to infinite peripheral conduction in the wall; and (2) uniform peripheral heating, corresponding to negligible peripheral conduction in the wall. Boundary conditions 1 and 2 provide lower and upper bounds, respectively, for Nu.

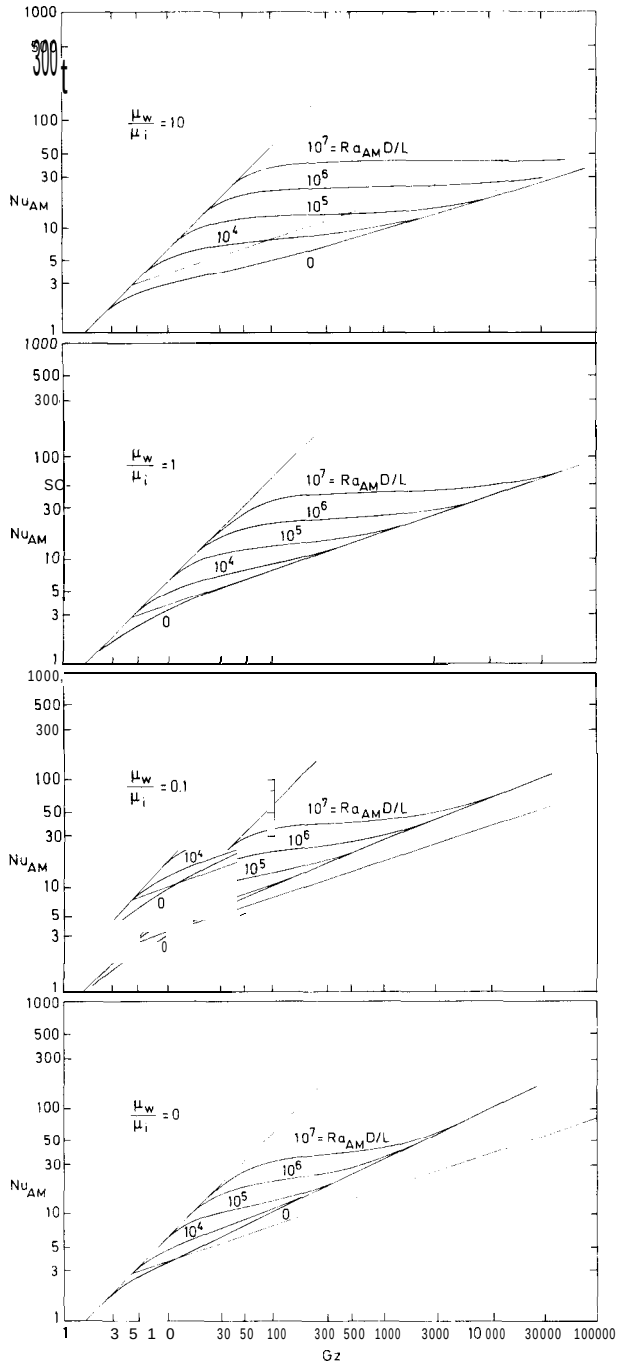

Figure 6 Theoretical solution for effect of variable viscosity and density on developing laminar assisting convection in a vertical, isothermal tube. From **Pigford [6].**

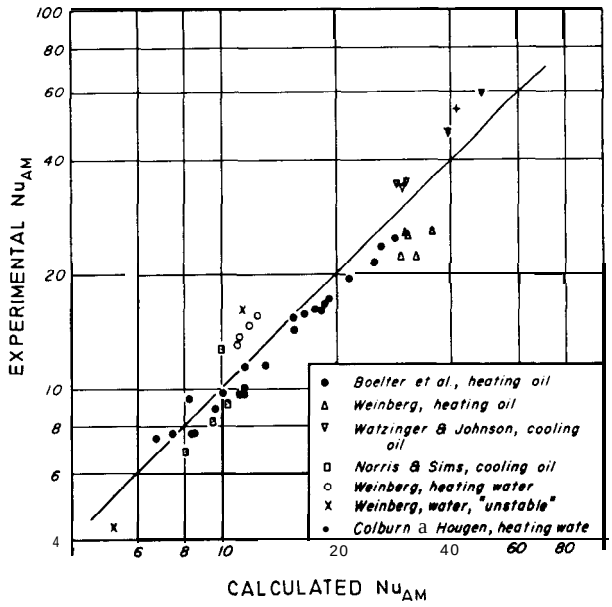

Figure 7 Comparison of theoretical solution for assisting laminar flow with experimental data. From **Pigford [6].**

Experimental results for finite peripheral conduction in the wall fall between, but generally near condition 1.

Neither experimental nor theoretical results appear to be available for the inlet region. For fully developed heat transfer in pure free convection in a round tube, the exact solution obtained by Tao [7] and others is

$$Nu_N = 0.846(Ra^*)^{1/4} \tag{10}$$

where

$$Ra^* = \frac{g\zeta\rho^2 c_p D^4}{\eta\lambda}\left(\frac{dT_b}{dx}\right) \tag{11}$$

and for pure fully developed forced convection,

$$Nu_F = \frac{48}{11} \tag{12}$$

The experimental data of Hallman [8] and values computed from the series solutions of Tao [7] and Brown [9] are compared in Fig. 8 with the prediction of Eq. (1) using Eqs. (10) and (12). The upward deviation of the theoretical values for large Ra* may be due to numerical error in computing the series, or possibly to a low coefficient in Eq. (10). In any event, it is apparent that a large value of n, such as 6, fits these values, and particularly the experimental data, far better than $n = 3$. The recommended equation for uniform heating is therefore

$$Nu = Nu_F^6 + Nu_N^6 \tag{13}$$

rather than Eq. (1).

Numerical solutions have been derived for uniform heating in a number of other geometries and for both

© 1983 Hemisphere Pu lishing Corporation

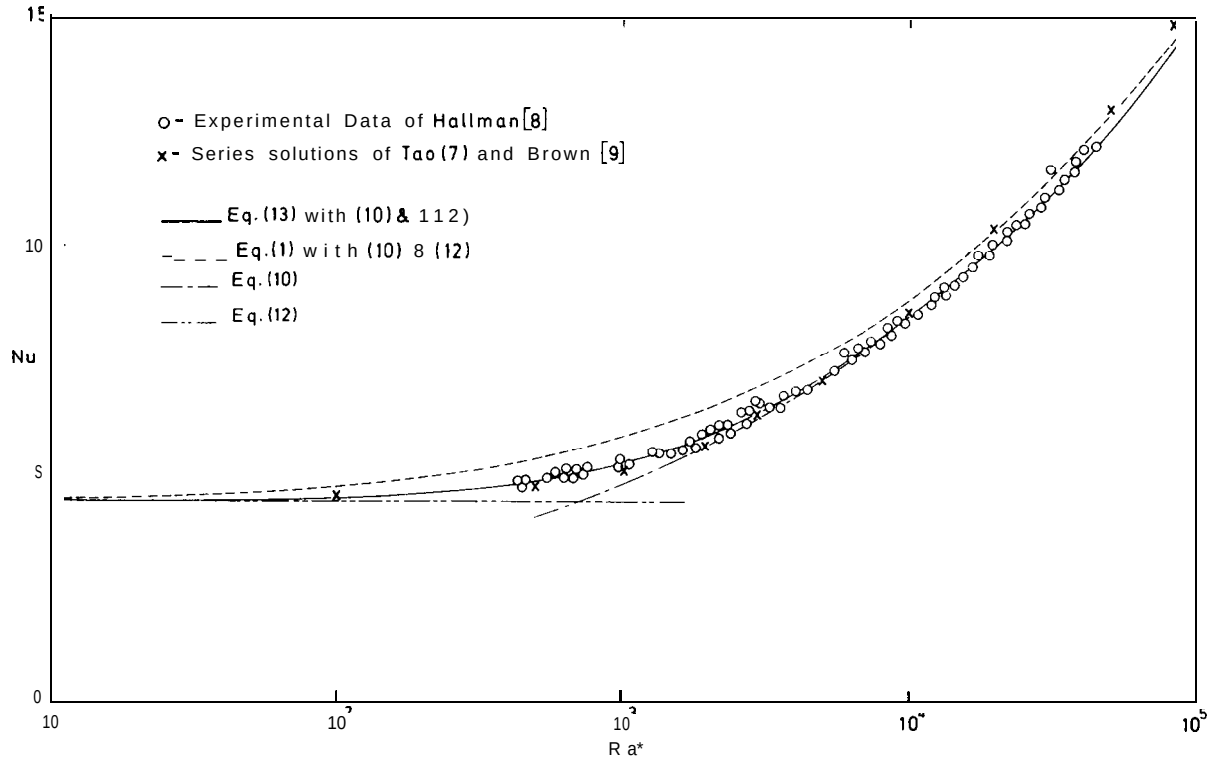

Figure 8 Comparison of Eqs. (1) and (13) using component Eqs. (10) and (12) for fully developed, laminar assisting convection in a uniformly heated, vertical tube.

boundary conditions 1 and 2. Some of these computed values are compared with Eq. (12) in Fig. 9 using the values of Nu_F and $Nu_N/(Ra^*)^{1/4}$ listed in Table 1. The overall agreement is excellent, confirming again the choice of $n = 6$. It is possible that the deviations on the low side are due to numerical error in the theoretical solutions or the values of the Nu_F and Nu_N in Table 1.

The hydraulic diameter

$$D_h = \frac{4S}{P_w}, \text{ m} \qquad (14)$$

where S = cross-sectional area of channel, m^2

P_w = perimeter of channel, m

is used as the characteristic length in the values of Nu and Ra* in Fig. 9 and Table 1.

(b) Laminar opposing convection

Martinelli and Boelter [4] suggested that laminar opposing convection could be represented simply by inserting a negative sign in Eq. (1). The corresponding generalized model is

$$Nu = |Nu_F^3 - Nu_N^3|^{1/3} \qquad (15)$$

with Nu_F and Nu_N from Eqs. (4) and (5). Equation (15) gives too low values for $Nu_F \simeq Nu_N$, but does provide a lower bound and a reasonable approximation if either forced or free convection is dominant. An upper bound is provided by the higher of Nu_N and Nu_F. A more precise correlation has not yet been established. The data of Brown [9] for uniform heating of water in down flow in a round tube do not cover a sufficient range in Fig. 10 to provide a critical test of Eq. (15).

(c) Turbulent convection

As discussed by Hall [13] and others, the onset of assisting free convection actually decreases the rate of heat transfer in the turbulent regime as a result of the decreased velocity and thereby the shear stress and the turbulence in the core. The opposite effect occurs for opposing convection; that is, the rate of heat transfer is increased. This behavior is illustrated in Fig. 11 by the data of Herbert and Sterns [14] for water heated in upward and downward flow over a range of Re from 5 800 to 71 000. Ra was approximately 4 X 10 for all of the runs.

For opposing convection (downward flow), these data are seen to conform reasonably well to Eq. (1) using the following expressions of Churchill [15] for turbulent forced convection and Churchill and Chu [16] for turbulent free convection:

$$Nu_F = \frac{0.035\ 7\ \text{Re}\ Pr^{1/3}\,(1 + Pr^{-4/5})^{-5/6}}{\ln (\text{Re}/7)} \qquad (16)$$

© 1983 Hemisphere Publishing Corporation

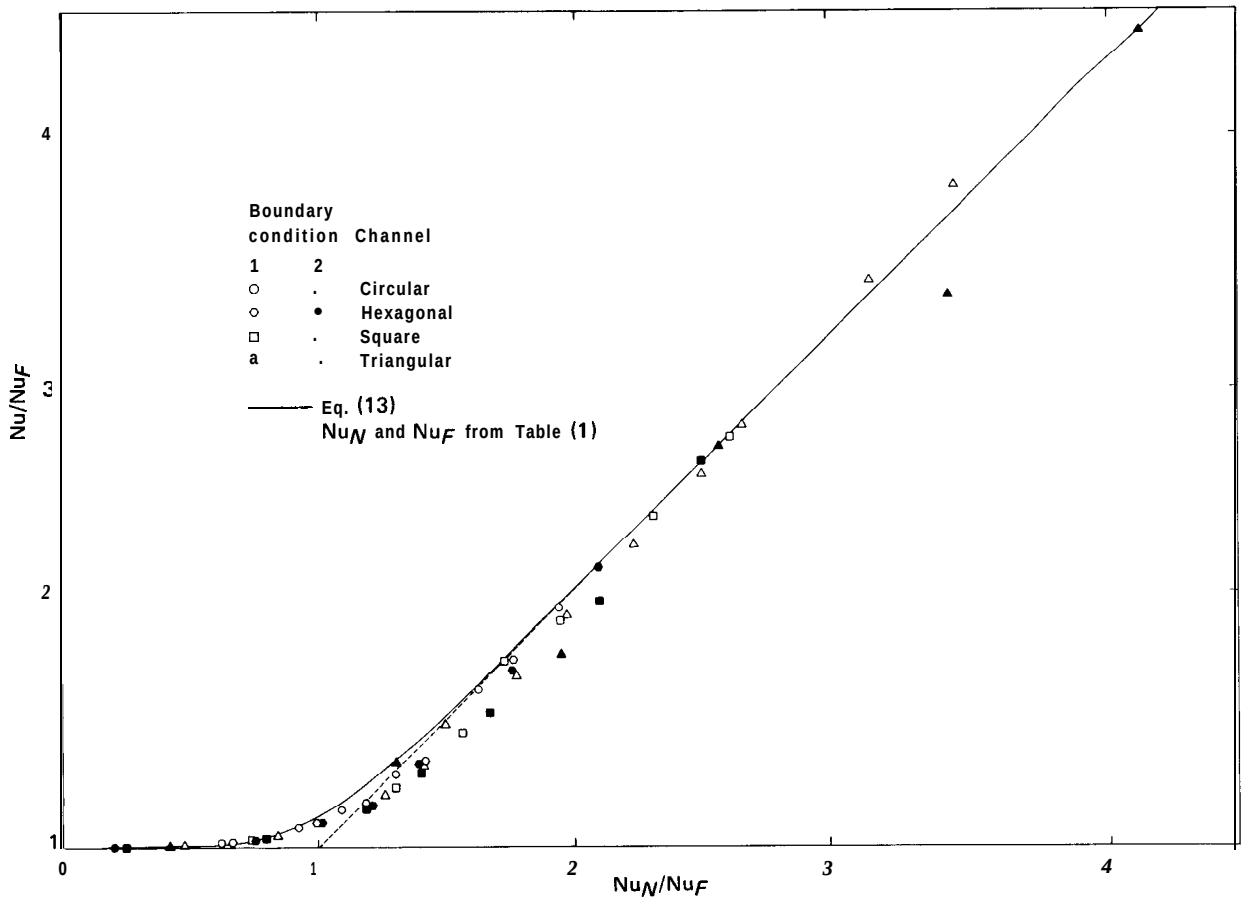

Figure 9 Comparison of Eq. (13) using component Eqs. (11) and (12) with numerical solutions for fully developed, laminar assisting convection in vertical, uniformly heated channels.

and

$$Nu_N = 0.15\ Ra^{1/3}\left[1+\left(\frac{0.492}{Pr}\right)^{9/16}\right]^{-16/27} \qquad (17)$$

For assisting convection (upward flow), the data appear to follow Eq. (15). These trends are the opposite of those for laminar flow.

B. Horizontal channels

(a) Uniform wall temperature

Jackson et al. [17] proposed for air in the inlet region of a round tube with a uniform wall temperature a correlating equation equivalent to

$$Nu_{LM} = [362\,Gz^2 + 0.027\ 7\ (Ra_{LM})^{3/2}]^{1/6} \qquad (18)$$

It may be noted that the empirical constant 362 in Eq. (18) corresponds to a coefficient 2.67 for $Gz^{1/3}$ as compared to a theoretical value of 1.75. This discrepancy is attributed by the authors to incomplete development of the velocity profile. They recommend that the properties in Gz be evaluated at the average fluid temperature, and those in Nu and Ra at the wall temperature. For convenience, the logarithmic mean temperature difference in Ra can be replaced by the temperature difference at the inlet through the following relationship, which is obtainable from an overall energy balance:

$$\frac{(T_w - T)_{LM}}{T_w - T_i} = \frac{Gz}{\pi\, Nu_{LM}}\left(1 - e^{-\pi\, Nu_{LM}/Gz}\right) \qquad (19)$$

Also, Nu_{LM} can be replaced by $Nu_{AM}/F_1(Z)$, as indicated above for vertical channels. However, in any form, trial and error is required if T_2 is unknown.

Equation (18), expressed in terms of Nu_{AM}, and with a mean value of Ra = 1.65 X 10^6, is compared in Fig. 12 with the experimental data of Jackson et al. for air with 1.1 X $10^6 < Ra < 2.2 \times 10^6$. The agreement is good. Equation (18) can be generalized for other Pr, per Churchill and Usagi [18], by replacing the coefficient 0.027 7 by 0.090 5 $[1+(0.492/Pr)^{9/16}]^{-8/3}$.

(b) Uniform heating along the tube

Just as for vertical tubes, more extensive results are available for uniform heating than for uniform wall

© 1983 Hemisphere Publishing Corporation

Table 1 Solutions for fully developed forced and free convection in uniformly heated channels

	Boundary condition 1		Boundary condition 2	
	Nu_F	$Nu_N/(Ra^*)^{1/4}$	Nu_F	$Nu_N/(Ra^*)^{1/4}$
Polygonal [10] sides				
3	3.111 1	0.827	1.90	0.784
4	3.607 8	0.839	3.23	0.809
5	3.87	0.842	3.65	0.816
6	4.01	0.844	3.88	0.815
7	4.10	0.845	4.02	0.824
8	4.16	0.846	4.13	0.829
12	4.21	0.846	4.28	0.845
Circular [7]	4.363 6	0.846	4.363 6	0.846
Rhombic [11] α				
20	2.451 4	0.823		
30	2.718 2	0.825		
40	2.969 2	0.826		
50	3.186 7	0.828		
60	3.365 0	0.829		
70	3.488 4	0.830		
80	3.565 9	0.831		
90	3.61	0.831		
Triangular [12]				
60-60-60	3.111 1	0.8 29		
30-60-90	2.887 5	0.824		
4545-90	2.981 9	0.827		

temperature because of the greater buoyant effect, and more extensive theoretical results because of greater susceptibility to analysis.

Equation (13) appears to be applicable for horizontal as well as for vertical flow. Churchill and Ozoe [19] developed the following expression for the local coefficient for forced convection in the inlet region of a round tube :

$$Nu_F = 5.364\left[1 + \left(\frac{Gz}{55}\right)^{10/9}\right]^{3/10} - 1 \qquad (20)$$

Hong et al. [20] developed an empirical correlation for their data for fully developed, pure natural convection in air in a horizontal tube. This expression, generalized, per Churchill and Usagi [18], for any fluid is

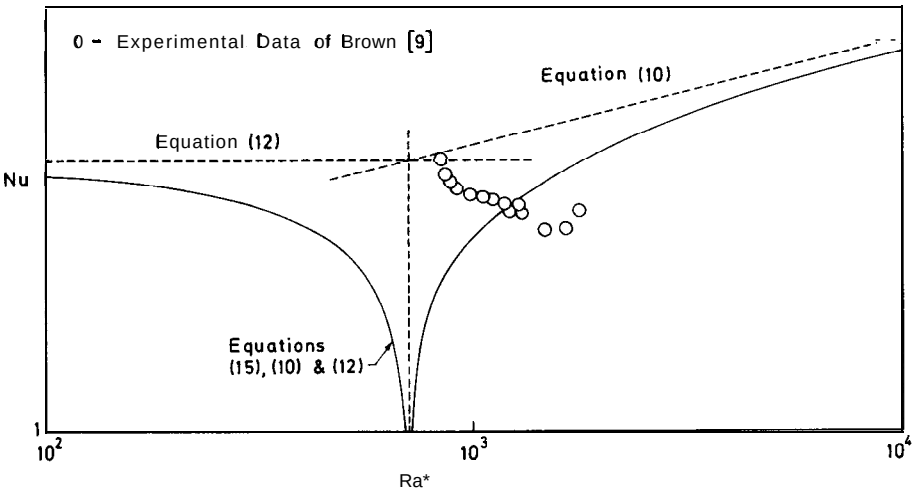

Figure 10 Comparison of Eqs. (10), (12), and (15) with experimental data for fully developed laminar, opposing convection in a uniformly heated, vertical tube.

© 1983 Hemisphere Publishing Corporation

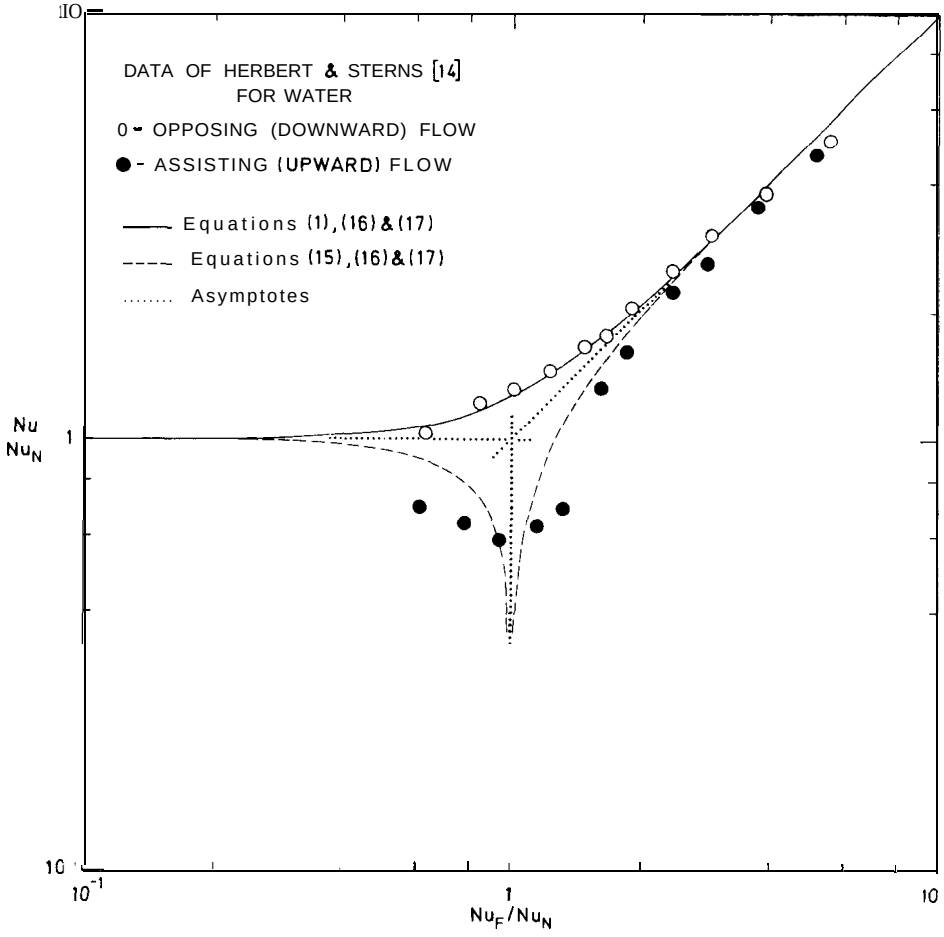

Figure 11 Comparison of Eqs. (1) and (15), using component Eqs. (16) and (17), with experimental data for turbulent assisting and opposing convection in isothermal vertical tubes.

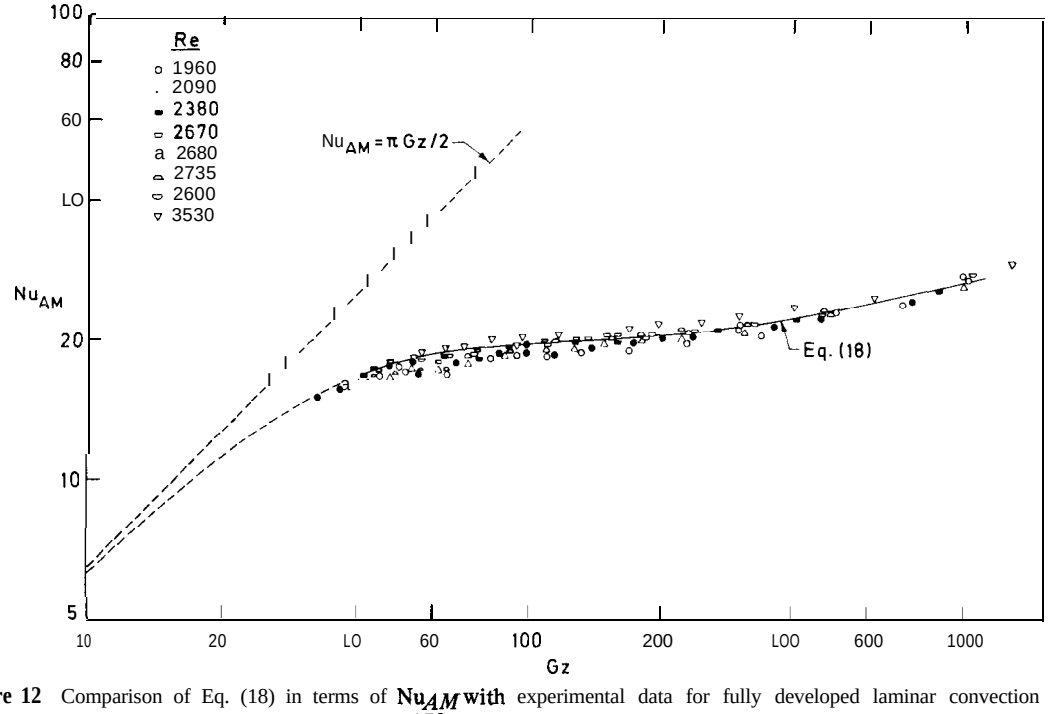

Figure 12 Comparison of Eq. (18) in terms of Nu_{AM} with experimental data for fully developed laminar convection in an isothermal horizontal tube. From Jackson et al. [17].

© 1983 Hemisphere Publishing Corporation

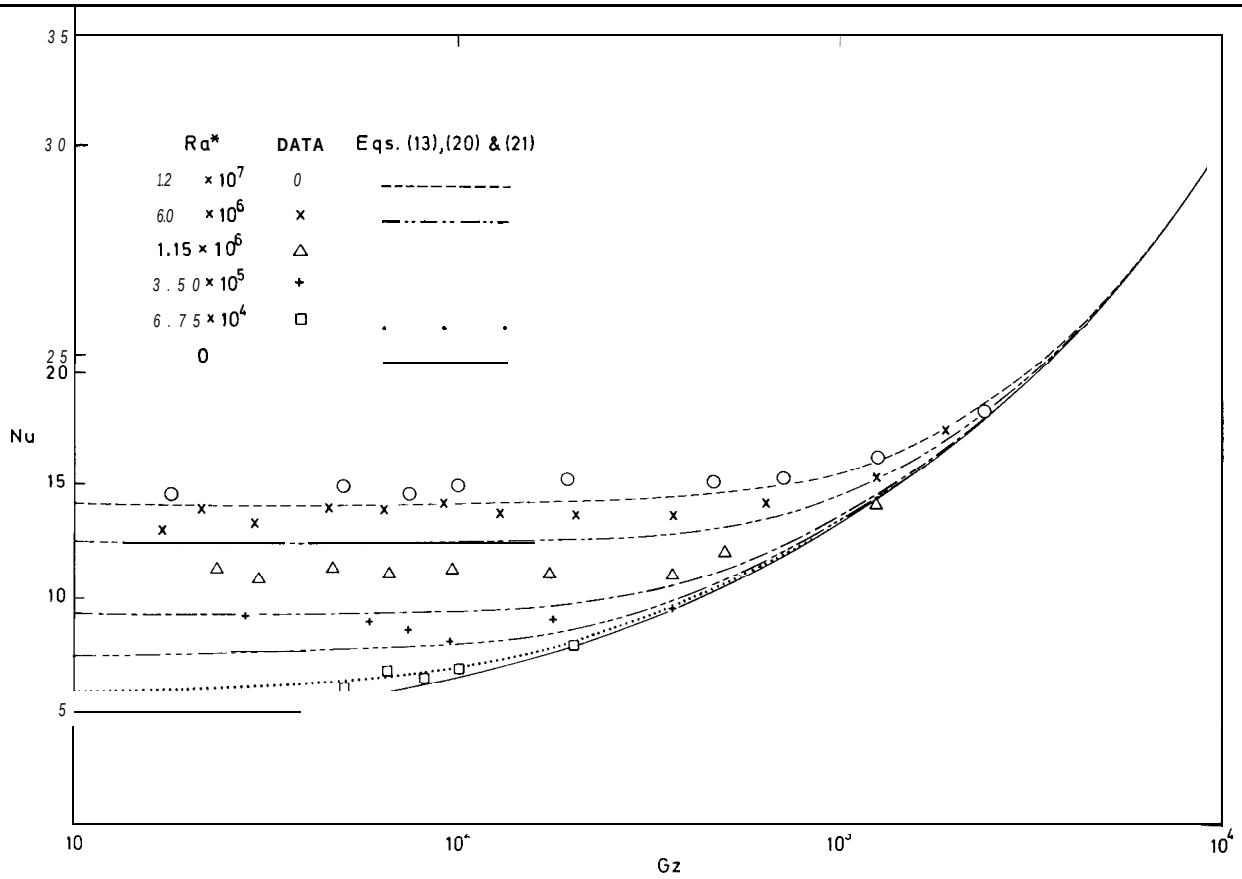

Figure 13 Comparison of Eq. (18) using component Eqs. (20) and (21) with experimental data of Petukov and Polyakov [21] for developing laminar convection in water in a uniformly heated, horizontal tube.

$$Nu_N = 0.847\,(Ra^*)^{0.177}\left[1 + \left(\frac{0.492}{Pr}\right)^{9/16}\right]^{-0.315} \quad (21)$$

where $Ra^* = Ra\ Nu_N = g\rho^2 c_p \zeta \dot{q} D^4/\eta\lambda^2$

Equation (21) may be reexpressed in terms of Ra as

$$Nu_N = 0.817\ Ra^{0.215}\left[1 + \left(\frac{0.492}{Pr}\right)^{9/16}\right]^{-0.382} \quad (22)$$

Equation (13), using Eqs. (20) and (21), is tested with the data of Petukhov and Polyakov [21] for water in Fig. 13. The agreement is reasonably good. This correlation and these data are in good accord with the theoretical calculations of Cheng and Ou [22] and of Bergles and Simonds [23]. Hong et al. [20] also proposed the following modified expression for finite peripheral conduction:

$$\frac{Nu_F^{0.12}}{pp.33} = \frac{8\ Ra^{0.28}\ Pr^{0.05}}{f^{0.12}} \quad (23)$$

where

$$f = \frac{hD^2}{\delta\lambda_w} \quad (24)$$

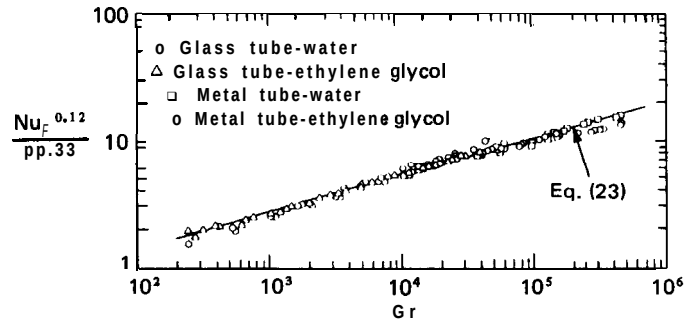

Figure 14 Comparison of Eq. (23) with experimental data for fully developed laminar convection in a uniformly heated, horizontal tube with appreciable peripheral conduction in the tube wall. From Hong et al. [20].

© 1983 Hemisphere Publishing Corporation

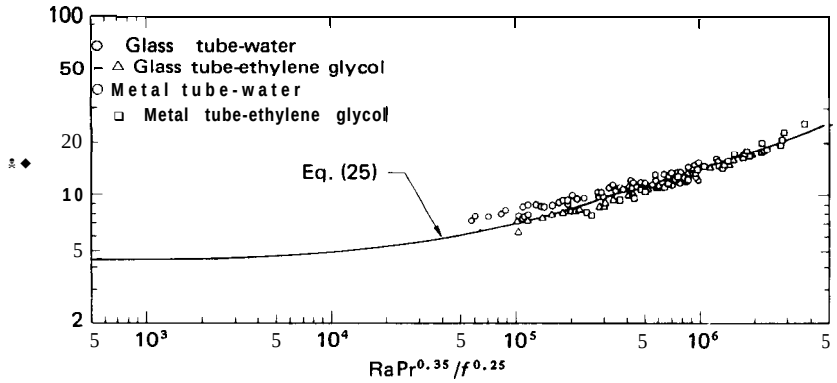

Figure 15 Comparison of Eq. (25) with experimental data for fully developed laminar convection in a uniformly heated, horizontal tube with appreciable peripheral conduction in the tube wall. From Morcos and Bergles [24].

and

δ = thickness of tube wall, m

λ_w = thermal conductivity of tube wall, W/m K

They recommended evaluation of the physical properties at $(\bar{T}_w + T)/2$, where $\bar{T}_w$ is the circumferential average wall temperature. Their test of Eq. (23) for glass and metal tubes is reproduced in Fig. 14.

For fully developed heat transfer with finite peripheral conduction, Morcos and Bergles [24] proposed the correlating equation

$$Nu = \left\{(4.36)^2 + \left[0.05\left(\frac{Ra\ Pr^{0.35}}{f^{1/4}}\right) - 0.4\right]^2\right\}^{1/2} \qquad (25)$$

with all properties evaluated at $(\bar{T}_w + T)/2$. The discrepancy between the exponents of 6 and 2 in Eqs. (13) and (25) arises from the different powers of Ra. The 0.4 power of Eq. (25) was chosen to represent data extending to higher Ra and possibly into the turbulent regime. Equation (25) is compared with their own experimental data in Fig. (15).

Hwang and Cheng [25] have developed theoretical solutions for laminar flow in the entrance of uniformly heated rectangular channels. As contrasted with a round tube, the secondary motion consists of a series of circulations of approximately square cross section as illustrated by the sketch and photograph in Fig. 16. Their computed Nusselt numbers have the same qualitative dependence on Gz and Ra as for a round tube, with the aspect ratio as an additional parameter. These results have not yet been represented by a correlating equation or confirmed experimentally.

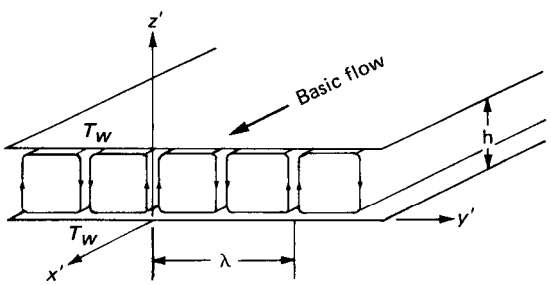

Figure 16 Photograph and sketch of circulation pattern for fully developed laminar convection in a uniformly heated, horizontal, rectangular channel. From Hwang and Cheng [25]. Reprinted with permission. Copyright 1972, Pergamon Press, Ltd.

© 1983 Hemisphere Publishing Corporation

Nomenclature for Section 2.5.10 appears at the beginning of Part 2.

REFERENCES FOR SECTION 2.5.10

1. Metais, B. and Eckert, E. R. G., Forced, Mixed and Free Convection Regimes, *J. Heat Transfer,* vol. 86, pp. 295-296, 1964.
2. Churchill, S. W., A Comprehensive Correlating Equation for Buoyancy-Induced Flow in Channels, *Lett. Heat Mass Transfer,* vol. 4, pp. 193–199, 1977.
3. Martinelli, R. C., Southwell, J. C., Alves, G., Craig, H. L., Weinburg, E. B., Lansing, N. F., and Boelter, L. M. K., Heat Transfer and Pressure Drop for a Fluid Flowing in the Viscous Region Through a Vertical Pipe, *Trans. AIChE,* vol. 38, pp. 493-530, 1942.
4. Martinelli, R. C., and Boelter, L. M. K., An Analytical Prediction of Superimposed Free and Forced Viscous Convection in a Vertical Pipe, *Univ. Calif. Publ. in Eng.,* vol. 5, no. 2, pp. 23–58, 1942.
5. Lévêque, M. A., Transmission de chaleur par convection,Ann. *Mines,* vol. 13, pp. 201–300, 1928.
6. Pigford, R. L., Non-isothermal Flow and Heat Transfer Inside Vertical Tubes, *Chem. Eng. Prog. Symp. Ser., vol. 5* 1, no. 17, pp. 79–92, 1955.
7. Tao, L. N., Heat Transfer of Combined Free and Forced Convection in Circular and Sector Tubes, *Appl. Sci. Res., Sec. A.,* vol. 9, pp. 357–368, 1960.
8. Hallman, T. M., Experimental Study of Combined Forced and Free Convection in a Vertical Tube, NASA TN D-1104, December 1961.
9. Brown, W. G., Die Überlagerung von erzwungener und natürlicher konvektion bei niedrigen Durchsätzen in einem lotrechten Rohr, *VDI Forschungsch. 480,* vol. 26, pp. l-31,1960.
10. Iqbal, M., Ansari, S. A., and Aggarwala, B. D., Effect of Buoyancy on Forced Convection in Vertical Polygonal Ducts, *J. Heat Transfer,* vol. 92, pp. 237-244, 1970.
11. Iqbal, M., Aggarwala, B. D., and Fowler, A. G., Laminar Combined Free and Forced Convection in Vertical Non-circular Ducts Under Uniform Heat Flux, *Int. J. Heat Mass Tmnsfer,* vol. 12, pp. 1123-1139, 1969.
12. Aggarwala, B. D., and Iqbal, M., On Limiting Nusselt Numbers from Membrane Analogy for Combined Free and Forced Convection Through Vertical Ducts, *Znt. J. Heat Mass Transfer,* vol. 12, pp. 737–748, 1969.
13. Hall, W. B., Heat Transfer Near the Critical Point, *Advan. Heat Transfer, vol. 7,* pp. l-86, 1971.
14. Herbert, L. S., and Stems, U. J., Heat Transfer in Vertical Tubes-Interaction of Forced and Free Convection, *Chem. Eng. J.,* vol. 4, pp. 46–52, 1972.
15. Churchill, S. W., Comprehensive Correlating Equations for Heat, Mass and Momentum Transfer in Fully Developed Flow in Smooth Tubes, *Ind. Eng. Chem., Fundam.,* vol. 15, pp. 789–800, 1972.
16. Churchill, S. W., and Chu, H. H.-S., Correlating Equations for Laminar and Turbulent Free Convection from a Vertical Plate, *Znt. J. Heat Mass Transfer, vol.* 18, pp. 1823–1829, 1975.
17. Jackson, T. W., Spurlock, J. M., and Purdy, K. R., Combined Free and Forced Convection in a Constant Temperature Horizontal Tube, *AIChE J., vol.* 7, pp. 38–41, 1961.
18. Churchill, S. W., and Usagi, R., A General Expression for the Correlation of Rates of Transfer and Other Phenomena, *AIChE J., vol.* 18, pp. 1121–1128, 1972.
19. Churchill, S. W., and Ozoe, H., Correlations for Laminar Forced Convection with Uniform Heating in Flow Over a plate in Developing and Fully Developed *Flow in* a Tube, *J. Heat Transfer,* vol. 95, pp. 78-84, 1973.
20. Hong, S. W., Morcos, S. M., and Bergles, A. E., Analytical and Experimental Results for Combined Forced and Free Laminar Convection in Horizontal Tubes, *Proc. 5th Znt. Heat Transfer Conf., Tokyo,* vol. 3, NC4.6, pp. 154-158, 1974.
21. Petukhov, B. S., and Polyakov, A. F., Experimental Investigation of Viscogravitational Fluid Flow in a Horizontal Tube, *High Temp.,* vol. 5, pp. 75–81, 1967.
22. Cheng, K. C., and Ou, J.-W., Free Convection Effects on Graetz Problem for Large Prandtl Number Fluids in Horizontal Tubes with Uniform Wall Heat Flux, *Proc. 5th Znt. Heat Transfer Conf., Tokyo,* vol. 3, NC4.7, pp. 159–163, 1974.
23. Bergles, A. E., and Simonds, R. R., Combined Forced and Free Convection for Laminar Flow in Horizontal Tubes with Uniform Heat Flux, *Int. J. Heat Mass Transfer, vol.* 14, pp. 1989-2000, 1971.
24. Morcos, S. M., and Bergles, A. E., Experimental Investigation of Combined Forced and Free Laminar Convection in Horizontal Tubes, *J. Heat Transfer,* vol. 95, pp. 212–218, 1975.
25. Hwang, G. J., and Cheng, K. C., Finite Amplitude Convection with Longitudinal Vortices in plane Poiseuille Flow-The Effect of Uniform Axial Temperature Gradient, *Znt. J. Heat Mass Transfer,* vol. 15, pp. 789-800, 1972.

© 1983 Hemisphere Publishing Corporation

2.5.11

Augmentation of heat transfer

Arthur E. Bergles

A. Introduction

Energy and materials saving considerations, as well as economic incentives, have led recently to expanded efforts to produce more efficient heat exchange equipment. Common thermo-hydraulic goals are to reduce the size of a heat exchanger required for a specified heat duty, to upgrade the capacity of an existing heat exchanger, to reduce the approach temperature difference for the process streams, or to reduce the pumping power.

The study of improved heat transfer performance is referred to as heat transfer augmentation, enhancement, or intensification. In general, this means an increase in heat transfer coefficient. Attempts to increase normal heat transfer coefficients have been recorded for more than a century, and there is a large store of information. A recent report [1] cites 1967 technical publications, excluding patents and manufacturers literature. The recent growth of activity in this area is clearly evident from the yearly distribution of the publications presented in Fig. 1.

Augmentation techniques can be classified either as passive methods, which require no direct application of external power (Fig. 2), or as active methods, which require external power. The effectiveness of both types of techniques is strongly dependent on the mode of heat transfer, which may range from single-phase free convection to dispersed-flow film boiling. Brief descriptions of these methods follow.

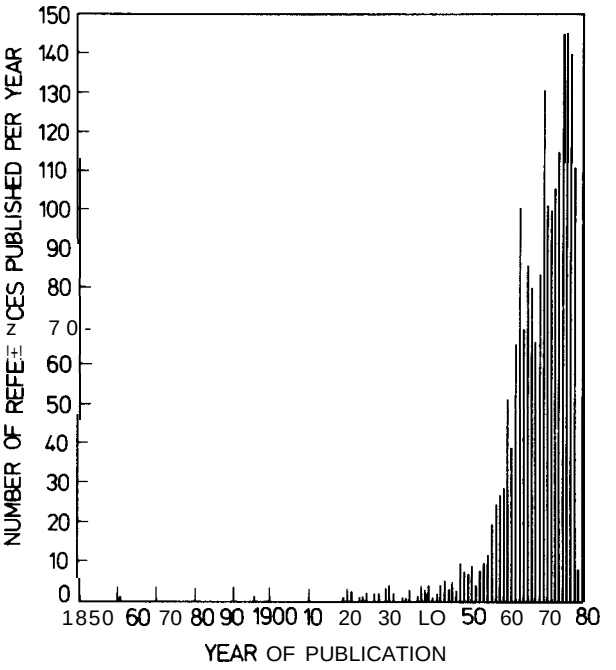

Figure 1 References on heat transfer augmentation versus year of publication (to early 1979) [1].

(a) Passive methods

1. Treated surfaces involve fine-scale alternation of the surface finish or coating (continuous or discontinuous). They are used for boiling and condensing; the roughness height is below that which affects single-phase heat transfer.

© 1983 Hemisphere I blishing Corporation

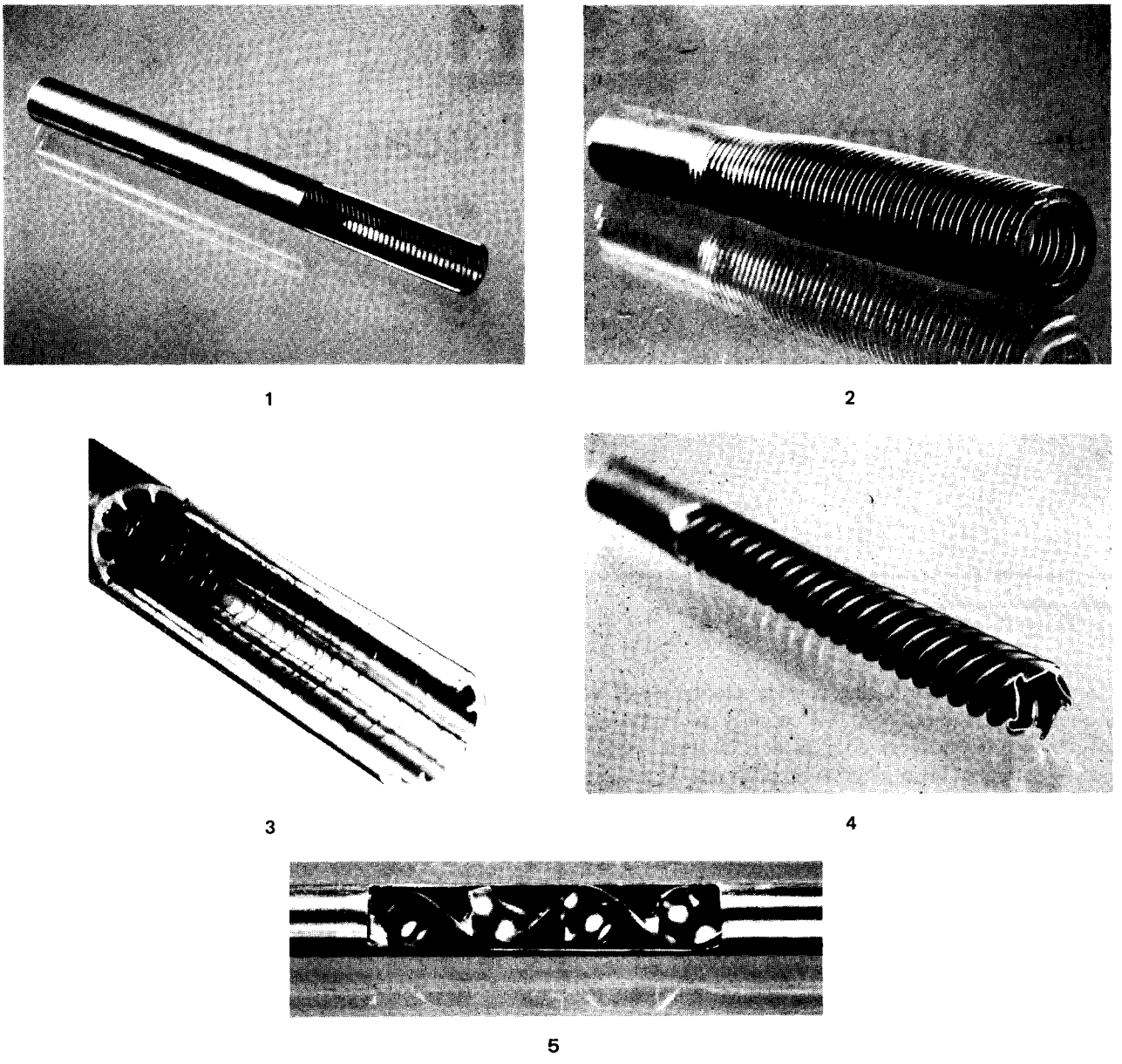

Figure 2 Enhanced tubes for augmentation of single-phase heat transfer. (1) Internal helical repeated rib-roughness. (2) Integral external fins. (3) Integral internal fins. (4) Spirally fluted tube. (5) Static mixer insert.

2. Rough surfaces are produced in many configurations ranging from random sand-grain-type roughness to discrete protuberances. The configuration is generally chosen to disturb the viscous sublayer rather than to increase the heat transfer surface area. Application of rough surfaces is directed primarily toward single-phase flow.

3. Extended surfaces are routinely employed in many heat exchangers. Current work of interest in this review is directed toward development of new types of extended surfaces, such as integral inner-fin tubing, and improvement of heat transfer coefficients on extended surfaces by shaping or perforating the surfaces.

4. Displaced enhancement devices are inserted into the flow channel so as indirectly to improve energy transport at the heated surface. They are used with forced flow.

5. Swirl-flow devices include a number of geometric arrangements or tube inserts for forced flow that create rotating and/or secondary flow: coiled tubes, inlet vortex generators, twisted-tape inserts, and axial core inserts with a screw-type winding.

6. Surface tension devices consist of wicking or grooved surfaces to direct the flow of liquid in boiling and condensing.

7. Additives for liquids include solid particles and

© 1983 Hemisphere Publishing Corporation

gas bubbles in single-phase flows and liquid trace additives for boiling systems.

8. Additives for gases are liquid droplets or solid particles, either dilute phase (gas-solid suspensions) or dense phase (fluidized beds).

(b) Active methods

1. Mechanical aids involve stirring the fluid by mechanical means or by rotating the surface. Surface scraping, widely used for batch processing of viscous liquids in the chemical process industry, is being applied to the flow of such diverse fluids as high-viscosity plastics and air. Equipment with rotating heat exchanger ducts is found in commercial practice.

2. Surface vibration at either low or high frequency has been used primarily to improve single-phase heat transfer.

3. Fluid vibration is the more practical type of vibration enhancement because of the mass of most heat exchangers. The vibrations range from pulsations of about 1 Hz to ultrasound. Single-phase fluids are of primary concern.

4. Electrostatic fields (DC or AC) are applied in many different ways to dielectric fluids. Generally speaking, electrostatic fields can be directed to cause greater bulk mixing of fluid in the vicinity of the heat transfer surface.

5. Injection is utilized by supplying gas to a flowing liquid through a porous heat transfer surface or by injecting similar fluid upstream of the heat transfer section. Surface degassing of liquids can produce augmentation similar to gas injection. Only single-phase flow is of interest.

6. Suction involves vapor removal, in nucleate or film boiling, or fluid withdrawal, in single-phase flow, through a porous heated surface.

Two or more of the above techniques may be utilized simultaneously to produce an enhancement that is larger than either of the techniques operating separately. This is termed compound augmentation.

It should be emphasized that one of the motivations for studying enhanced heat transfer is to assess the effect of an inherent condition on heat transfer. Some practical examples include roughness produced by standard manufacturing, degassing of liquids with high gas content, surface vibration resulting from rotating machinery or flow oscillations, fluid vibration resulting from pumping pulsation, and electrical fields present in electrical equipment.

The preceding is a general introduction to the present section on augmentation of single-phase heat transfer as well as subsequent sections on augmentation of condensation (Sec. 2.6.6) and boiling (Sec. 2.7.9). The emphasis is on effective and cost-competitive (proved or potential) techniques that have made the transition from the laboratory to commercial heat exchangers. Broad reviews of developments in augmented heat transfer are available [2 to 4].

B. Free convection

(a) Passive techniques

With the exception of the familiar technique of providing extended surfaces, the passive techniques have little to offer in the way of augmented heat transfer. This is because the velocities are usually too low to cause flow separation or secondary flow. A recent review [5] of the limited data for free convection from machined or formed rough surfaces, with air, water, and oil, concludes that increases in heat transfer coefficient up to 100% can be obtained with air, but that the increases with liquids are very small.

Design procedures for single fins and fin arrays are well established (see Sec. 2.5.3B); however, little attention has been given to interrupted extended surfaces. The restarting of thermal boundary layers is expected to increase coefficients so as to more than compensate for the lost area. The effectiveness of this concept has been demonstrated in the wire-loop fins used for baseboard hot water heaters or convectors [6]. This problem is also of interest in electronic cooling, where the heat sinks are often discontinuous fins, and in natural draft cooling of finned tube banks necessitated by loss of fan power. Of considerable interest recently has been the heat transfer performance of medium integral fin tubes for use in hot water heaters and solar thermal storage. The established equations for large fins in air, as found in baseboard convectors, are not applicable. The single-tube correlations of Gorenflo [7] are recommended as a starting point in design:

$$\mathrm{Nu}_o = 0.6(\mathrm{Ra}_o)^{0.25} \quad \text{for } \mathrm{Ra}_o < 2 \times 10 \qquad (1a)$$

$$\mathrm{Nu}_o = 0.155(\mathrm{Ra}_o)^{1/3} \quad \text{for } \mathrm{Ra}_o > 2 \times 10^7 \qquad (1b)$$

Caution should be exercised when using these equations for coils and other vertical arrays found in storage tanks. Manufacturers data should be consulted for the performance of specific coils.

The only clear-cut example of a beneficial fluid additive appears to be injection of vapor bubbles at the bottom of a heated surface. Tomari and Nishikoma [8] observed increases in average heat transfer coefficients when air was injected into water or ethylene glycol. The improvement is due primarily to the circulation induced by the rising bubbles.

© 1983 Hemisphere I blishing Corporation

(b) Active techniques

Mechanically aided heat transfer is a standard technique in the chemical and food industries when viscous liquids are involved. Refer to Sec. 3.14 for data and design procedures. Data are also available for a heated cylinder rotating about its own axis in a bulk stagnant fluid. At large rotational Reynolds numbers, where rotation dominates, Tang and McDonald [9] correlated data for several liquids by the following equation:

$$\mathrm{Nu} = 0.12 \left(\frac{d^2\omega}{2\nu}\right)^{2/3} \mathrm{Pr}^{1/3} \qquad (2)$$

Surface vibration has been extensively studied in the laboratory. The predominant geometry has been the horizontal cylinder vibrated either horizontally or vertically. Heat transfer coefficients can be increased lo-fold for both low-frequency/high-amplitude and high-frequency/low-amplitude situations. Although the improvements can be dramatic, it must be recognized that natural convection is inherently an inefficient mode of heat transfer. Since at maximum enhancement, the average velocity of the surface over a cycle is less than 1 m/s, it is more practical to provide steady forced flow. The mechanical designer is also concerned that such intense vibrations could result in equipment failure.

Several studies examined the effects of vibrating an entire enclosure containing a heated section immersed in liquid. Smith and Forbes [10] observed improvements in free convection heat transfer coefficients of up to 33% with a heated sidewall, and Pak et al. [11] recorded improvements of up to 200% with a small-diameter wire.

Since it is usually difficult to apply surface vibrations to practical equipment, an alternative technique is utilized whereby vibrations are applied to the fluid and focused toward the heated surface. Generators employed range from flow interrupters to piezoelectric transducers, thus covering the range from pulsation of 1 Hz to ultrasound of 10^6 Hz. Much research has been reported on the effects of acoustic vibrations on heat transfer to gases from horizontal cylinders. Increases in average coefficients are observed only above an intensity of about 140 db, which is far in excess of human ear tolerance. The maximum increases reported are usually 100 to 200%. With proper ultrasonic transducer design, it is also possible to improve heat transfer to simple heaters immersed in liquids by several hundred percent. Cavitation is generally the dominant enhancement, mechanism. As an example, a vibration study of the effect of ultrasonic vibration on heat transfer to water was presented by Yukawa et al. [12]. The maximum improvement reported was a 500% increase in coefficient; however, little improvement was noted with degassed water. In general, with liquids there is considerable difficulty in designing systems to transmit vibrational energy to large surfaces.

The extensive literature on both surface and fluid vibrations is discussed in [2–4]. Few studies have been reported in recent years, probably in recognition of practical limitations. It does not appear that any commercial equipment utilizes vibration as an augmentation technique. For most systems it is more convenient and economical to provide steady forced flow to achieve the desired Increase in heat transfer coefficient.

Electric fields can be utilized to increase heat transfer coefficients in free convection. The configuration may be a heated wire in a concentric tube maintained at a high voltage relative to the wire, or a fine wire electrode may be utilized with a horizontal plate. Dielectrophoretic or electrophoretic (especially with ionization of gases) forces cause greater bulk mixing in the vicinity of the heat transfer surface. Reference [2] cites studies that report heat transfer coefficients improved by as much as a factor of 40. The paper by Yabe et al. [13] provides a good example of the large local improvements that can be expected in heat transfer coefficient.

Recent activity has centered on the application of corona discharge cooling to practical problems. Cooling of cutting tools by point electrodes was proposed by Blomgren and Blomgren [14], whereas Reynolds and Holmes [15] have used parallel-wire electrodes to improve the heat dissipation of a standard, horizontal finned tube. Heat transfer coefficients can be increased by several hundred percent when sufficient electrical power is supplied. It would appear, however, that the equivalent effect could be produced at lower capital cost and without the hazards of 10,000–100,000 V by simply providing forced convection with a blower or fan.

Gas injection into a liquid through a porous heated plate, which has been used to similate nucleate boiling, can be regarded as an augmentative technique. Although coefficients can be increased several hundred percent [16], the practical applications of injection would appear to be rather limited because of the difficulty of supplying and removing the gas.

C. Forced convection

(a) Passive techniques

The present discussion is restricted to augmentation of heat transfer ***inside*** ducts that are primarily of circular cross section. Relevant information on external flow normal to or parallel to augmented tubes is given in Secs. 2.5.3B and 2.8.4.

Surface roughness has been used extensively to aug-

© 1983 Hemisphere Publishiig Corporation

ment forced convection heat transfer. Integral roughness may be produced by the traditional manufacturing processes of machining, forming, casting, or welding. Various inserts can also provide surface protuberances. In view of the infinite number of possible geometric variations, it is not surprising that, even after more than 200 studies [1], no unified treatment is available.

Laminar flow data for tubes are provided by studies that considered convoluted tubes [17,18] and transverse fins in an annular passage [19]. Improvements of as much as 100% are observed. Augmentation is widely utilized in plate heat exchangers. Pescod [20] reported on a study of the improvements obtained by using spikes and ripples to enhance nominally laminar flow of air in parallel-plate channels of large aspect ratios. Most plate heat exchangers utilize corrugated surfaces, for structural reasons as well as augmentation. It is generally agreed that the heat transfer and pressure drop characteristics of commercial corrugated surfaces used in plate exchangers are quite similar.

It has been demonstrated that the analogy between heat transfer and friction for rough surfaces in turbulent flow is dependent on the type of roughness. An analogy solution for a sand-grain-type roughness was developed by Dipprey and Sabersky [21]. Recent work has considered surfaces that can be produced commercially. Webb et al. [22] have correlated heat transfer coefficients for tubes with square repeated-rib roughness by first correlating the friction factor using Nikuradse s similarity function U_e^+, the roughness Reynolds number e^+, and p/e. By application of the heat transfer-momentum transfer analogy, the Stanton number is given by

$$\mathrm{St} = \frac{f/2}{1 + (f/2)^{0.5}[\bar{g}(e^+)F(\mathrm{Pr}) - U_e^+(e^+, p/e)]} \tag{3}$$

Excellent correlation of their data was achieved, as shown in Fig. 3. Equation (3) also successfully predicted air data of other investigations, even for other rib profiles [23]. Turbulent flow data for many types of rough tubes are summarized in [24]; the improvements in heat transfer coefficient (based on nominal surface area) are as much as 250%.

Extended surfaces can be considered old technology as far as most applications are concerned. The real interest is in increasing heat transfer coefficients on the extended surface. Compact heat exchangers of the plate-fin or tube-and-center variety use several augmentation techniques: offset strip fins, louvered fins, perforated fins, or corrugated fins [25]. Coefficients are several hundred percent above the smooth-tube values; however, the pressure drop is also substantially increased, and there may be vibration and noise problems [26]. For more details on the current status of air-side (external) heat transfer in finned-tube heat exchangers, the review of Webb [74] should be consulted.

Internally finned circular tubes are available in aluminum and copper (or copper alloys). The following correlations of Watkinson et al. [27] are available for laminar flow:

Spiral-fin tubes:

$$\frac{\mathrm{Nu}_e}{\mathrm{Pr}^{1/3}(d_e/L)^{1/3}(\eta_b/\eta_w)^{0.14}\phi_e} = 19.2\left(\frac{b}{p}\right)^{0.5}\mathrm{Re}_e^{0.26} \tag{4a}$$

where

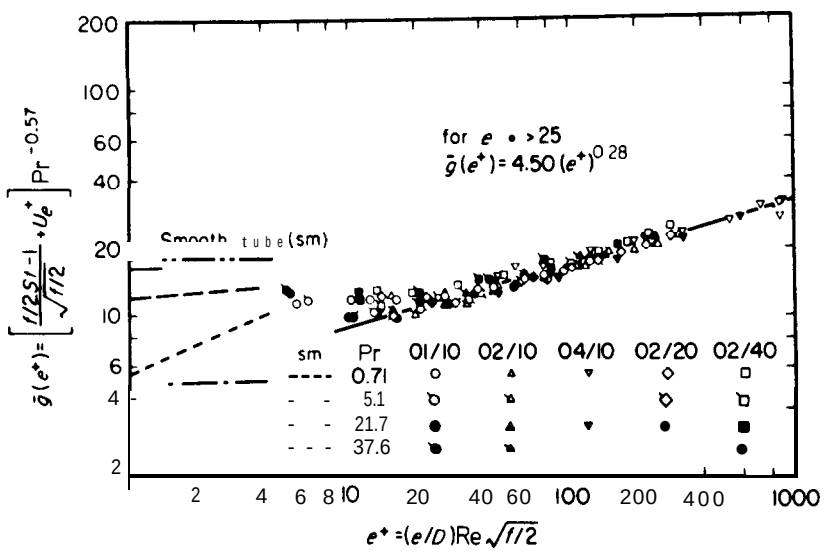

Figure 3 Correlation of heat transfer data for tubes with internal repeated-rib roughness [22].

© 1983 Hemisphere Publishing Corporation

$$\phi_e = \frac{2.25(1 + 0.01\ \mathrm{Gr}_e^{1/3})}{\log \mathrm{Re},} \tag{4b}$$

Straight-fin tubes:

$$\frac{\mathrm{Nu}_e}{\mathrm{Pr}^{1/3}(d_e/L)^{1/3}(\eta_b/\eta_w)^{0.14}\phi_e} = 2.43\left(\frac{1}{n}\right)^{0.5} \mathrm{Re}_e^{0.46} \tag{5}$$

Isothermal friction factors for all tubes:

$$f_e = \frac{16.4(d_e/d)^{1.4}}{\mathrm{Re}_e} \tag{6}$$

These correlations are based on data for oil in horizontal tubes having approximately uniform temperature (steam heating). Other data for both water and ethylene glycol, in both steam-heated and electrically heated tubes, are in approximate agreement with the correlations [28].

Several studies have assessed the thermal-hydraulic performance of internally finned tubes (all from one manufacturer) in turbulent flow. In the latest report of this work, Carnavos [29] recommends the following equations:

$$\mathrm{Nu}_e = 0.023\ \mathrm{Pr}^{0.4}\ \mathrm{Re}_e^{0.8}\left(\frac{A_{fa}}{A_{fc}}\right)^{0.1}\left(\frac{A_n}{A_a}\right)^{0.5}(\sec\psi)^3 \tag{7}$$

$$f = 0.046\ \mathrm{Re}_e^{-0.2}\left(\frac{A_{fa}}{A_{fn}}\right)^{0.5}(\sec\psi)^{0.75} \tag{8}$$

It is noted that tin inefficiency corrections must be incorporated when applying these equations. These correlations provide a reasonable description of the available data for air, water, and ethylene glycol/water; however, there are significant differences among data from different investigations for essentially the same tube [4].

A numerical analysis of turbulent flow in tubes with idealized straight fins was reported by Patankar et al. [30]. The necessary constant for the turbulence model was obtained from experimental data for air. Further improvements in numerical techniques are expected so that a wider range of geometries and fluids can be handled without resort to extensive experimental programs.

internally finned tubes can be stacked to provide multiple internal passages of small hydraulic diameter. Carnavos [31] demonstrated the large increases in heat transfer coefficient (based on outer tube nominal area) that can be obtained in these tubes with air flow. Of course, pressure drop is also increased with these tubes.

Many proprietary surface configurations have been produced by deforming the basic tube. The convoluted, corrugated, spiral, or spirally fluted tubes have multiple-start spiral corrugations along the tube length. A systematic survey of the single-tube performance of 11 commercially available tubes in surface steam condenser service (condensing steam outside, water inside) is given by Marto et al. [32]. Up to 400% increase in the nominal inside heat transfer coefficient (based on diameter of smooth tube of same maximum inside diameter) was noted; however, pressure drops on the water side were about 20 times higher.

Displaced enhancement devices are typically in the form of inserts, with elements arranged to promote transverse mixing (static mixers). They are used primarily for viscous liquids, to promote either heat transfer or mass transfer. Figure 4 illustrates typical improvements that can be gained from the use of static mixers [33]. There are no broad-based correlations available because of the many geometric arrangements and the strong influence of fluid properties and heating conditions. In general, the higher the heat transfer coefficient, the higher the pressure drop; the percentage increase in heat transfer is generally greater than the heat transfer increase. For example, the SMX Standard mixer exhibits a 7-fold increase in heat transfer and a nearly 70-fold increase in pressure drop. Additional data for the Kenics mixer are given in [28] and [34]. Similar inserts or packings have been used for turbulent flow; however, this application is recommended only for short sections with high heat fluxes, since the pressure drop is so high [35].

Heat transfer coefficients can be substantially higher in coiled tubes than in straight tubes because of the secondary flow generated by the curvature. The correlation of Schmidt [36] is recommended for the peripherally averaged Nusselt number for fully developed laminar flow in tubes with uniform wall temperature:

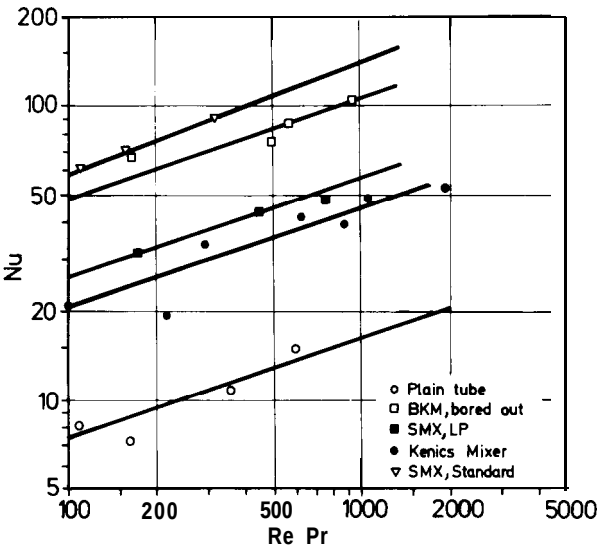

Figure 4 Heat transfer data for typical static mixer inserts in laminar flow [33].

© 1983 Hemisphere Publishing Corporation

$$\mathrm{Nu} = 3.65 + 0.08\left[1 + 0.08\left(\frac{d}{d_c}\right)^{0.9}\right](\mathrm{Re})^{\phi}(\mathrm{Pr})^{1/3} \tag{9a}$$

where

$$\phi = 0.5\ t0.290\ 3\left(\frac{d}{d_c}\right)^{0.914} \tag{9b}$$

The recent correlation of Abul-Hamayel and Bell [37] can be used for uniformly heated tubes:

$$\mathrm{Nu} = \left[4.36 + 2.84\left(\frac{\mathrm{Gr}}{\mathrm{Re}^2}\right)^{3.94}\right] \times (1 + 0.027\ 6\ \mathrm{De}^{0.75}\mathrm{Pr}^{0.197}) \times \left[1 + 0.934\ 8\left(\frac{\mathrm{Gr}}{\mathrm{De}^2}\right)^{2.78}\exp\left(-1.33\frac{\mathrm{Gr}}{\mathrm{De}^2}\right)\right] \times \left(\frac{\eta_b}{\eta_w}\right)^{0.14} \tag{10}$$

Note that since these investigators found free convection to be important in their vertical-axis coil, a similar factor would be expected in Eq. (9a).

Schmidt s correlation for isothermal friction factor is [36]

$$f = \left[1 + 0.14\left(\frac{d}{d_c}\right)^{0.97}(\mathrm{Re})^{\gamma}\right]\left(\frac{16}{\mathrm{Re}}\right) \tag{11a}$$

where

$$\gamma = 1 - 0.644\left(\frac{d}{d_c}\right)^{0.312} \tag{11b}$$

Schmidt s correlations for heat transfer and isothermal friction factor in the transition and turbulent regions are as follows [36]:

For $\mathrm{Re}_{,,} < \mathrm{Re} < 2.2 \times 10^4$:

$$\mathrm{Nu} = 0.023\left[1 + 14.8\left(1 + \frac{d}{d_c}\right)\right]\left(\frac{d}{d_c}\right)^{1/3}(\mathrm{Re})^{\chi}(\mathrm{Pr})^{1/3} \tag{12a}$$

where

$$\chi = 0.8 - 0.22\left(\frac{d}{d_c}\right)^{0.1} \tag{12b}$$

For $2 \times 10^4 < \mathrm{Re} < 1.5 \times 10^5$:

$$\mathrm{Nu} = 0.023\left[1 + 3.6\left(1 + \frac{d}{d_c}\right)\right]\left(\frac{d}{d_c}\right)^{0.8}(\mathrm{Re})^{0.8}(\mathrm{Pr})^{1/3} \tag{13}$$

For $\mathrm{Re}_{cr} < \mathrm{Re} < 2.2 \times 10^4$:

$$f = \left[1 + 2.88 \times 10^4(\mathrm{Re})^{-\left(\frac{d}{d_c}\right)^{0.5}}\right] \times [0.0791(\mathrm{Re})^{-0.25}] \tag{14}$$

For $2 \times 10^4 < \mathrm{Re} < 1.5 \times 10^5$:

$$f = \left[1 + 0.082\ 3\left(1 + \frac{d}{d_c}\right)\right]\left(\frac{d}{d_c}\right)^{0.53}(\mathrm{Re})^{0.25} \times [0.0791(\mathrm{Re})^{-0.25}] \tag{15}$$

In applying the above.formulas, the transition Reynolds number is given by Ito's formula [38]:

$$\mathrm{Re}_{cr} = 2 \times 10^4\left(\frac{d}{d_e}\right)^{0.32} \tag{16}$$

Twisted-tape inserts have been widely used to improve heat transfer in both laminar and turbulent flow. The following correlation is recommended for fully developed laminar flow in a uniformly heated tube [39]:

$$\mathrm{Nu} = 5.172[1 + 5.484 \times 10^{-3}(\mathrm{Pr})^{0.7}(\mathrm{Re})(y)^{-1.25}]^{0.5} \tag{17}$$

Note that the correlation was established for a tape with no heat transfer. The correlation does not seem to be applicable to heating or cooling with a constant wall temperature [28]. At $\mathrm{Re} < 100$, the isothermal friction factors can be approximated by the expression for a semicircular tube,

$$f = 42.2(\mathrm{Re})^{-1} \tag{18}$$

Turbulent flow heat transfer in tubes with twisted-tape inserts has been correlated by [40]:

$$\mathrm{Nu}_e = F\ 0.02\left[1 + \left(\frac{\pi}{2y}\right)^2\right]^{0.4}(\mathrm{Re}_e)^{0.8}(\mathrm{Pr})^{0.4} + 0.193\left[(\mathrm{Re}_e)^2(y)^{-1}\left(\frac{d_e}{d}\right)\left(\frac{\Delta\rho}{\rho}\right)(\mathrm{Pr})\right]^{1/3} \tag{19}$$

The fin factor F, which represents the ratio of total heat transfer to the heat transferred by the walls alone, can be estimated from conduction calculations. Isothermal friction factors are given by the following expression [40]:

$$f_e = 0.046(y)^{-0.046}(\mathrm{Re}_e)^{-0.2} \tag{20}$$

Modest improvements in heat transfer are observed when gas bubbles or solid particles are added to liquids. Kenning and Kao [41] found heat transfer increases up to 50% when nitrogen bubbles were injected into turbulent water flow. Watkins et al. [42] studied suspensions of polystyrene spheres in oil to determine the mechanism of enhancement for addition of solid particles to laminar flows. Maximum improvements of 40% were observed.

Gas-side heat transfer can be enhanced by adding a small volumetric fraction of solid particles. The particles are carried along with the stream and separated for reuse, in the case of a once-through system, or circu-

© 1983 Hemisphere Publishing Corporation

lated, in the case of a closed system. The enhancements of up to four times the pure gas heat transfer coefficients, shown in Fig. 5, are attributed to thinning of the viscous sublayer and higher thermal conductivity in that layer. Design information and a guide to the extensive literature are given in [44]. It does not appear that any practical applications of dilute-phase gas-solid heat transfer are currently being considered.

Fluidized beds are being considered for many industrial applications. Heat transfer coefficients to tubes within a bed can be enhanced by a factor of 20, compared to pure gas flow at the same flow rate. Fluidized-bed heat transfer is treated in Sec. 2.5.5.

When liquid droplets are added to a flowing gas stream, heat transfer is enhanced by sensible heating of the two-phase mixture, evaporation of the liquid, and disturbance of the boundary layer. Thomas and Sunderland [45] demonstrated that heat transfer coefficients can be increased as much as a factor of 30 if a continuous liquid film is formed on the heated surface. A more realistic indication of practical enhancement was provided by Yang and Clark [46], who applied spray cooling to a compact heat exchanger core. The maximum improvement of 40% was attributed to formation of a partial liquid film and sensible heating of that film. In general, the large volume of liquid required tends to limit practical application of this technique.

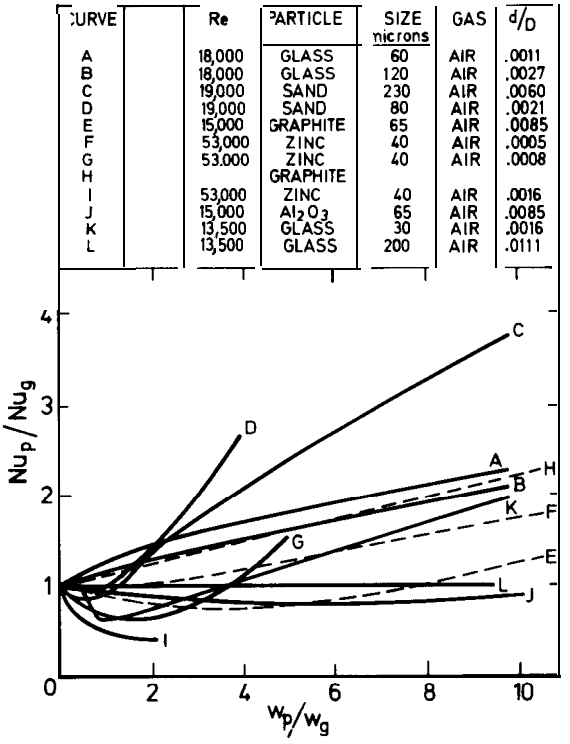

Figure 5 Composite heat transfer data for gas-solid suspensions [43].

(b) Active techniques

Mechanically aided heat transfer in the form of surface scraping can increase forced convection heat transfer. Unfortunately, the necessary hardware is not particularly compatible with most heat exchangers. A recent application of scraped-surface heat transfer to air flows is reported by Hagge and Junkhan [47]; a lo-fold improvement in heat transfer coefficient was reported for laminar flow over a flat plate.

The other aspect of this technique is rotating surfaces. Moderate increases in heat transfer coefficients have been reported for laminar flow in (1) a straight tube rotating about its own axis [48], (2) a straight tube rotating around a parallel axis [49], (3) a rotating circular tube [50], and (4) the rotating, curved, circular tube [51]. Increases in turbulent flow are less; for example, in [50] maximum improvements of 350% were recorded for laminar flow, but for turbulent flow the maximum increase was 25%. In general, these are examples of naturally occurring phenomena that result in enhancement: cooling windings of rotating electrical machinery, cooling of gas turbine rotor blades, and so on.

Surface vibration has been demonstrated to improve heat transfer to both laminar and turbulent duct flow of liquids [2]. The largest improvements (up to 200%) are observed with laminar or transitional flow utilizing a concentric-tube heat exchanger with the inner tube vibrated transversely or a rectangular channel with a flexible, vibrating side. The complexity of the vibrational equipment and the relatively large power expenditure would seem to rule out this technique for practical application.

Fluid vibration has been extensively studied for both air (loudspeakers and sirens) and liquids (flow interruptors, pulsators, and ultrasonic transducers) [2]. The gas results are not encouraging, as intensities above 120 db are required and the effect is largely one of triggering fully turbulent flow at transitional Reynolds numbers. The experiments of Moissis and Maroti [52] are important in that they demonstrate practical limitations. Even with high-intensity acoustic vibrations, the gas-side heat transfer coefficient was improved by only 30% for a compact heat exchanger core.

Pulsations are relatively simple to apply to low-velocity liquid flows, and improvements of several hundred percent can be realized [2]. Turbulence trig gering and cavitation appear to be important enhancement mechanisms. Application of high-frequency vibrations is difficult, and only modest improvements in heat transfer coefficients are recorded.

Some very impressive enhancements have been recorded with electrical fields, particularly in the laminar

© 1983 Hemisphere Publishing Corporation

flow region [2]. The recent studies of Porter and Poulter [53], Savkar [54], and Newton and Allen [55] demonstrated improvements of at least 100% when voltages in the 10-kV range were applied to transformer oil. Although it is desirable to take advantage of any naturally occurring electrical fields in electrical equipment, it would appear to be quite difficult to introduce this augmentation in practical equipment.

Mizushina et al. [56] found that even with intense fields, the enhancement disappears as turbulent flow is approached in a circular tube with a concentric inner electrode. Reynolds and Holmes [15] found little effect of corona wind even at low air velocities, with the exception of tests with three electrodes under a finned tube. In this case, a 60% increase in heat transfer coefficient was noted.

Single-phase heat transfer can be enhanced by injecting gas into a liquid through a porous heated surface [2]. Tauscher et al. [57] have demonstrated up to fivefold increases in local heat transfer coefficients by injecting similar fluid into a turbulent tube flow. The effects are similar to that produced by an orifice plate; in both cases the effect has died out after about $10L/d$.

Large increases in heat transfer coefficient are predicted for laminar [58] and turbulent flow [59] with surface suction. The general characteristics of the latter predictions were confirmed by experiments conducted by Aggarwal and Hollingsworth [60]. However, suction is difficult to incorporate into practical heat exchange equipment.

(c) Compound techniques

Compound techniques are a slowly emerging area of enhancement that hold promise for practical applications, since heat transfer coefficients can usually be increased above each of the several techniques acting alone. Some examples are as follows:

1. Rough tube wall with twisted-tape insert [61]
2. Rough cylinder with acoustic vibrations [62]
3. Internally finned tube with twisted-tape insert [63]
4. Finned tubes in fluidized beds [64]
5. Externally finned tubes subjected to vibrations [65]
6. Gas-solid suspension with an electrical field [66]
7. Fluidized bed with pulsations of air [67]

It is interesting to note that some compound attempts are unsuccessful. Masliyah and Nandakumar [68], for example, found analytically that average Nusselt numbers for internally finned, coiled tubes were lower than for plain coiled tubes.

D. Performance evaluation criteria

One may consider the use of augmentation techniques to satisfy any of the following thermal-hydraulic objectives: (1) to reduce prime surface area, (2) to increase heat transfer capacity, (3) to reduce the approach temperature difference for the process streams, or (4) to reduce pumping power. Having defined a basic objective, the designer will establish the parameters that are fixed and the basic constraints that must be satisfied. Through manipulation of the data or correlations for heat transfer coefficients and friction factors, performance ratios can be calculated, for example, the ratio of the prime surface area of the enhanced heat exchanger to that of the normal or reference exchanger at constant pumping power. Design objectives and performance ratios are discussed in detail in [69 to 72].

Augmentation usually will not be attractive unless the augmented heat exchanger offers a cost advantage relative to the use of conventional heat transfer configurations. Additional factors entering into the ultimate decision to use an augmentation technique are materials limitations, fouling potential, safety, and reliability. The current status and prospects for commercial development and use of augmentation techniques are discussed in [73].

NOMENCLATURE FOR SECTION 2.5.11

A_{fa}	actual free-flow area in duct
A_{fn}	nominal free-flow area based on inside diameter
b	average distance between tins
c_p	specific heat at constant pressure
De	Dean number, $\mathrm{Re}(d/d_c)^{1/2}$
d	inside diameter of tube or outside diameter of cylinder, unless otherwise noted
d_c	coil diameter
e	rib height
e+	roughness Reynolds number [22], see Fig. 2
F	Prandtl number function [22], $F = \mathrm{Pr}^{0.57}$ in Fig. 2; fin factor for twisted tape [40]
f	Fanning friction factor
Gr	Grashof number, $g_n d^3 \Delta\rho/\rho\nu^2$
$\bar{g}$	heat transfer roughness function [22], see Fig. 2
g_n	gravitational acceleration
L	heated length
Nu	Nusselt number, $\alpha d/\lambda$
n	number of fins in a tube
Pr	Prandtl number, $\eta c_p/\lambda$

© 1983 Hemisphere Publishing Corporation

P	rib spacing or fin pitch
Ra	Rayleigh number, Gr Pr
Re	Reynolds number, $\rho ud/\eta$
Re_{cr}	critical Reynolds number for transition to turbulence
St	Stanton number, $\alpha/\rho uc_p$
U_e^+	Nikuradse similarity function [22]
U	average flow velocity
w_g	mass flow rate of gas
WP	mass flow rate of particles
Y	tube diameters per 180° turn of twisted tape
α	heat transfer coefficient, based on actual surface area
γ	exponent, Eq. (11*b*)
λ	thermal conductivity
η	dynamic viscosity
ν	kinematic viscosity
ρ	density
$\Delta\rho$	density difference between liquid and vapor
ϕ	exponent, Eq. *(9b)*
ϕ_e	free convection factor, Eq. *(4b)*
χ	exponent, Eq. (12*b*)
ψ	helix angle of internal spiral fins
ω	rotational velocity

Subscripts

b	evaluated at bulk fluid temperature
e	based on hydraulic diameter
0	based on outside diameter of finned tube
W	evaluated at wall temperature

REFERENCES FOR SECTION 2.5.11

1. Bergles, A. E., Webb, R. L., Junkhan, G. H., and Jensen, M. K., Bibliography on Augmentation of Convective Heat and Mass Transfer, HTL-19, ISU-ERI-Ames-79206, Iowa State University, 1979.
2. Bergles, A. E., Survey and Evaluation of Techniques to Augment Convective Heat and Mass Transfer, ***in Progress in Heat and Mass*** Transfer, ed. U. Grigull and E. Hahne, vol. 1, pp. 331-424, Pergamon Press, Oxford, 1969.
3. Bergles, A. E., Recent Developments in Convective Heat Transfer Augmentation, ***Appl. Mech. Rev.,*** vol. 26, pp. 675-682, 1973.
4. Bergles, A. E., Enhancement of Heat Transfer, ***in Heat Transfer 1978,*** vol. 6, pp. 89-108, Hemisphere, Washington, D.C., 1978.
5. Bergles, A. E., Junkhan, G. H., and Webb, R. L., Energy Conservation via Heat Transfer Enhancement, C00-4649-5, Iowa State University, 1979.
6. Benforado, D. M., and Palmer, J., Wire Loop Finned Surface-A New Application (Heat Sink for Silicon Rectifiers), *Chem. Eng. Prog. Symp. Ser.,* vol. 61, pp. 315-321, 1965.
7. Gorenflo, D., Zum Waermeuebergang bei Bhsenverdampfung an Rippenrohren, Dissertation, Technische Hochschule, Karlsruhe, 1966.
8. Tamuri, M., and Nishikawa, K., The Stirring Effect of Bubbles upon the Heat Transfer to Liquids, ***Heat Transfer Jpn. Res.,*** vol. 5, pp. 31-44, 1976,
9. Tang, I., and McDonald, T. W., A Study of Boiling Heat Transfer from a Rotating Horizontal Cylinder, *Int. J. Heat Mass Transfer,* vol. 14, pp. 1643-1658, 1971.
10. Smith, G. V., and Forbes, R. E., The Effect of Random Vibration.on Natural Convective Heat Transfer in Rectangular Enclosures, ***in Augmentation of Convective Heat Transfer,*** pp. 158-162, ASME, New York, 1970,
11. Pak, H. Y., Winter, E. R. F., and Schoenhals, R. J., Convection Heat Transfer in a Contained Fluid Subjected to Vibration, in *Augmentation of Convective Heat Transfer,* pp. 148-157, ASME, New York, 1970.
12. Yukawa, H., Hoshino, T., and Saito, H., Effect of Ultrasonic Vibration on Free Convective Heat Transfer from an Inclined Plate in Water, ***Heat Transfer Jpn. Res.,*** vol. 5, pp. 1-16, 1976.
13. Yabe, A., Mori, Y ., and Hijikata, K., Heat Transfer Augmentation Around a Downward-Facing Flat Plate by Non-Uniform Electric Fields, ***Heat Transfer 1978,*** vol. 3, pp. 171-176, Hemisphere, Washington, D.C., 1978.
14. Blomgren, 0. C., Sr., and Blomgren, 0. C., Jr., Method and Apparatus for Cooling the Workpiece and/or the Cutting Tools of a Machining Apparatus, U.S. Patent No. 3,670,606, 1972.
15. Reynolds, B. L., and Holmes, R. E., Heat Transfer in a Corona Discharge, *Mech. Eng.,* pp. 44-49, October 1976.
16. Sims, G. E., Akturk, U., and Evans-Lutterodt, K. O., Simulation of Pool Boiling Heat Transfer by Gas Injection at the Interface, *Int. J. Heat Mass Transfer,* vol. 6, pp. 531-535, 1963.
17. Blumenkrantz, A. R., and Taborek, J., Heat Transfer and Pressure Drop Characteristics of Turbotec Spirally Grooved Tubes in the Turbulent Regime, Heat Transfer Research, Inc., Report 2439-300-7, 1970.
18. Rozalowski, G. R., and Gater, R. A., Pressure Loss and Heat Transfer Characteristics for High Viscous Flow in Convoluted Tubing, ASME Paper 75-HT-40, 1975.
19. Zappa, R. F., and Geiger, G. E., Effect of Artificial Surface Roughness on Heat Transfer and Pressure Drop for a High Prandtl Number Fluid in Laminar Flow, ASME Paper 71-HT-36, 1971.
20. Pescod, D., The Effects of Turbulence Promoters on the Performance of Plate Heat Exchangers, ***in Heat Exchangers: Design and Theory*** *Sourcebook*, eds. N. H. Afgan and E. U. S&hinder, pp. 601-616, Hemisphere, Washington, D.C., 1974.
21. Dipprey, D. F., and Sabersky, R. H., Heat and Momentum Transfer in Smooth and Rough Tubes at Various Prandtl Numbers, *Znt. J. Heat Mass Transfer,* vol. 6, pp. 329-353, 1963.
22. Webb, R. L., Eckert, E. R. G., and Goldstein, R. J., Heat Transfer and Friction in Tubes with Repeated Rib Roughness, *Znt. J. Heat Mass Transfer, vol.* 14, pp. 601-618, 1971.
23. Webb, R. L., Eckert, E. R. G., and Goldstein, R. J., Generalized Heat Transfer and Friction Correlations for Tubes with Repeated-Rib Roughness, *Int. J. Heat Mass Transfer, vol.* 15, pp. 180-184, 1972.

© 1983 Hemisphere Publishing Corporation

24. Bergles, A. E., and Jensen, M. K., Enhanced Single-Phase Heat Transfer for OTEC Systems, *Proc. Fourth Annual Conference on Ocean Thermal Energy Conversion, New Orleans, Louisiana, March 1977,* pp. VI-41–VI-54.
25. Kays, W. M., and London, A. L., ***Compact Heat Exchangers,*** 2d ed., McGraw-Hill, New York, 1964.
26. Shah, R. K., Perforated Heat Exchanger Surfaces, Part 1, Flow Phenomena, Noise and Vibration Characteristics, ASME Paper 75-WA/HT-8, 1975.
27. Watkinson, A. P., Miletti, D. C., and Kubanek, G. R., Heat Transfer and Pressure Drop of Internally Finned Tubes in Laminar Oil Flow, ASME Paper 75-HT-41, 1975.
28. Marner, W. J., and Bergles, A. E., Augmentation of Tubeside Laminar Flow Heat Transfer by Means of Twisted-Tape Inserts, Static-Mixer Inserts, and Internally Finned Tubes, ***Heat Transfer*** 1978, vol. 2, pp. 583-588, Hemisphere, Washington, D.C., 1978.
29. Carnavos, T. C., Heat Transfer Performance of Internally Finned Tubes in Turbulent Flow, ***in Advances in Enhanced Heat Transfer,*** pp. 61–67, ASME, New York, 1979.
30. Patankar, S. V., Ivanovic, M., and Sparrow, E. M., Analysis of Turbulent Flow and Heat Transfer in Internally Finned Tubes and Annuli, ***J. Heat Transfer,*** vol. 101, pp. 29-37, 1979.
31. Carnavos, T. C., Cooling Air in Turbulent Flow with Multipassage Internally Finned Tubes, ASME Paper 78-WA/HT-52, 1978.
32. Marto, P. J., Reilly, D. J., and Fenner, J. H., An Experimental Comparison of Enhanced Heat Transfer Condenser Tubing, in *Advances in Enhanced Heat Transfer,* pp. l-9, ASME, New York, 1979.
33. Pahl, M. H., and Muschelknautz, E., Einsatz and Auslegung Statischer Mischer, ***Chem. Ing. Tech.,*** vol. 5 1, pp. 347-364, 1979.
34. Lin, S. T., Fan, L. T., and Azer, N. Z., Augmentation of Single Phase Convective Heat Transfer with in-Line Static Mixers, *Proc. 1978 Heat Transfer and Fluid Mechanics Institute,* Stanford University Press, Stanford, Calif., 1978.
35. Megerlin, F. E., Murphy, R. W., and Bergles, A. E., Augmentation of Heat Transfer in Tubes by Means of Mesh and Brush Inserts, ***J. Heat Transfer,*** vol. 96, pp. 145-151, 1974.
36. Schmidt, E. F., Waermeuebergang and Druckverlust in Rohrschlangen, ***Chem. Ing. Tech.,*** vol. 39, pp. 781-789, 1967.
37. Abul-Hamayel, M. A., and Bell, K. J., Heat Transfer in Helically-Coiled Tubes with Laminar Flow, ASME Paper 79-WA/HT-11, 1979.
38. Ito, H., Friction Factor for Turbulent Flow in Curved Pipes, ***J. Basic Eng.,*** vol. 81, pp. 123-134, 1959.
39. Hong, S. W., and Bergles, A. E., Augmentation of Laminar Flow Heat Transfer by Means of Twisted-Tape Inserts, ***J. Heat Transfer,*** vol. 98, pp. 251-256, 1976.
40. Lopina, R. F., and Bergles, A. E., Heat Transfer and Pressure Drop in Tape Generated Swirl Flow of Single-Phase Water, ***J. Heat Transfer,*** vol. 91, pp. 434–442, 1969.
41. Kenning, D. B. R., and Kao, Y. S., Convective Heat Transfer to Water Containing Bubbles: Enhancement Not Dependent on Capillarity, *Int. J. Heat Mass Transfer,* vol. 15, pp. 1709-1718, 1972.
42. Watkins, R. W., Robertson, C. R., and Acrivos, A., Entrance Region Heat Transfer in Flowing Suspensions, *Int. J. Heat Mass Transfer, vol.* 19, pp. 693-695, 1976.
43. Bergles, A. E., Junkhan, G. H., and Hagge, J. K., Advanced Cooling Systems for Agricultural and Industrial Machines, SAE Paper 751183, 1976.
44. Depew, C. A., and Kramer, T. J., Heat Transfer to Flowing Gas-Solid Mixtures, ***Adv. Heat Transfer,*** vol. 9, pp. 113-180, 1973.
45. Thomas, W. C., and Sunderland, J. E., Heat Transfer Between a Plane Surface and Air Containing Water Droplets, *Ind. Eng. Chem. Fundamentals,* vol. 9, pp. 368-374, 1970.
46. Yang, W.-J., and Clark, D. W., Spray Cooling of Air-Cooled Compact Heat Exchangers, *Int. J. Heat Mass Transfer,* vol. 18, pp. 311-317, 1975.
47. Hagge, J. K., and Junkhan, G. H., Mechanical Augmentation of Convective Heat Transfer in Air, ***J. Heat Transfer,*** vol. 97, pp. 5 16-520, 1975.
48. McElhiney, J. E., and Preckshot, G. W., Heat Transfer in the Entrance Length of a Horizontal Rotating Tube, ***Znt. J. Heat Mass Transfer,*** vol. 20. pp. 847-854, 1977.
49. Mori, Y ., and Nakayama, W., Forced Convection Heat Transfer in a Straight Pipe Rotating Around a Parallel Axis, *Int. J. Heat Mass Transfer,* vol. 10, pp. 1179-1194, 1967.
50. Mori, Y., Fukada, T., and Nakayama, W., Convective Heat Transfer in a Rotating Radial Circular Pipe (2nd Report), *Int. J. Heat Mass Transfer,* vol. 14, pp. 1807-1824, 1971.
5 1. Miyazaki, H., Combined Free and Forced Convective Heat Transfer and Fluid Flow in a Rotating Curved Circular Tube, ***Znt. J. Heat Mass Transfer,*** vol. 14, pp. 1295-1309, 1971.
52. Moissis, R., and Maroti, L. A., The Effect of Sonic Vibrations on Convective Heat Transfer in an Automotive Type Radiator Section, Dynatech Corporation Report 322, July 1962.
53. Porter, J. E., and Poulter, R., Electra-Thermal Convection Effects with Laminar Flow Heat Transfer in an Annulus, ***Hear Transfer*** 1970, vol. 2, Paper FC3.7, Elsevier, Amsterdam, 1970.
54. Savkar, S. D., Dielectrophoretic Effects in Laminar Forced Convection Between Two Parallel Plates, ***Phys. Fluids, vol.*** 14, pp. 2670-2679, 1971.
55. Newton, D. C., and Allen, P. H. G., Senftleben Effect in Insulating Oil Under Uniform Electric Stress, ***Lett. Heat Mass Transfer,*** vol. 4, pp. 9-16, 1977.
56. Mizushina, T., Ueda, H., and Matsumoto, T., Effect of Electrically Induced Convection on Heat Transfer of Air Flow in an Annulus, ***J. Chem. Eng. Jpn.,*** vol. 9, pp. 97-102, 1976.
57. Tauscher, W. A., Sparrow, E. M., and Lloyd, J. R., Amplification of Heat Transfer by Local Injection of Fluid Into a Turbulent Tube Flow, *Int. J. Heat Mass Transfer,* vol. 13, pp. 681–688, 1970.
58. Kinney, R. B., Fully Developed Frictional and Heat Transfer Characteristics of Laminar Flow in Porous Tubes, *Int. J. Heat Mass Transfer,* vol. 11, pp. 1393–1401, 1968.
59. Kinney, R. B., and Sparrow, E. M., Turbulent Flow, Heat Transfer, and Mass Transfer in a Tube with Surface Suction, ***J. Heat Transfer,*** vol. 92, pp. 117-125, 1970.

© 1983 Hemisphere Publishing Corporation

60. Aggarwal, J. K., and Hollingsworth, M. A., Heat Transfer for Turbulent Flow with Suction in a Porous Tube, *Int. J. Heat Mass Transfer,* vol. 16, pp. 591–609, 1973.
61. Bergles, A. E., Lee, R. A., and Mikic, B. B., Heat Transfer in Rough Tubes with Tape-Generated Swirl Flow, *J. Heat Transfer,* vol. 91, pp. 443-445, 1969.
62. Kryukov, Y. V., and Boykov, G. P., Augmentation of Heat Transfer in an Acoustic Field, *Heat Trans. Soviet Res.,* vol. 5, no. 1, pp. 26-28, 1973.
63. Van Rooyen, R. S., and Kröger, D. G., Laminar Flow Heat Transfer in Internally Finned Tubes with Twisted-Tape Inserts, *Heat Transfer 1978,* vol. 2, pp. 577-581, Hemisphere, Washington, D.C., 1978.
64. Bartel, W. J., and Genetti, W. E., Heat Transfer from a Horizontal Bundle of Bare and Finned Tubes in an Air Fluidized Bed, *AIChE Symp. Ser. No. 128,* vol. 69, pp. 85-93, 1973.
65. Zozulya, N. V., and Khorunzhii, Y., Heat Transfer from Finned Tubes Moving Back and Forth in Liquid, *Chem. Petroleum Eng.,* no. 9-10, pp. 830–832, 1968.
66. Mm, K., and Chao, B. T., Particle Transport and Heat Transfer in Gas-Solid Suspension Flow Under the Influence of an Electric Field, *Nuclear Sci. Eng.,* vol. 26, pp. 534-546, 1966.
67. Bhattacharya, S. C., and Harrison, D., Heat Transfer in a Pulsed Fluidized Bed, *Trans. Inst. Chem. Eng.,* vol. 54, pp. 281-286, 1976.
68. Masliyah, J. H., and Nandakumar, K., Fluid Flow and Heat Transfer in Internally Finned Helical Coils, *Can. J. Chem. Eng.,* vol. 55, pp. 27–36, 1977.
69. Webb, R. L., and Eckert, E. R. G., Application of Rough Surfaces to Heat Exchanger Design, *Znt. J. Heat Mass Transfer,* vol. 15, pp. 1647–1658, 1972.
70. Bergles, A. E., Blumenkrantz, A. R., and Taborek, J., Performance Evaluation Criteria for Enhanced Heat Transfer Surfaces, *Heat Transfer 1974,* vol. 2, pp. 239-243, Japan Society of Mechanical Engineers, Tokyo, 1974.
71. Bergles, A. E., Junkhan, G. H., and Bunn, R. L., Performance Criteria for Cooling Systems on Agricultural and Industrial Machines, *SAE Trans.,* vol. 85, pp. 38–48, 1976.
72. Shah, R. K., Compact Heat Exchanger Surface Selection Methods, *Heat Transfer* 1978, vol. 4, pp. 193-201, Hemisphere, Washington, D.C., 1978.
73. Bergles, A. E., Webb, R. L., and Junkhan, G. H., Energy Conservation Via Heat Transfer Enhancement, *Energy, vol. 4,* pp. 193-200, 1979.
74. Webb, R. L., Air-Side Heat Transfer in Finned Tube Heat Exchangers, *Heat Transfer Eng.,* vol. 1, no. 3, pp. 33-49, 1980.

© 1983 Hemisphere Publishing Corporation

2.5.12

Heat transfer for non-Newtonian fluids

Robert C. Armstrong and H. H. Winter

A. Introduction

Section 2.5.12 describes ways in which heat transfer in non-Newtonian fluids is different from that in Newtonian fluids. As polymers constitute the largest class of non-Newtonian fluids, we shall focus our attention on them. Moreover, we shall focus on differences in heat transfer characteristics between Newtonian and polymeric fluids that can be attributed to differences in viscous behavior between these two classes of fluids. These distinctions involve both the shear rate dependence that is commonly observed in non-Newtonian fluids and also the different magnitude of the viscosity in polymers as opposed to low-molecular-weight fluids. In addition to these viscous effects, it is clearly possible that many interesting changes in heat transfer problems could result from the elastic character of polymeric fluids. For example, in duct flows involving noncircular cross sections, certain non-Newtonian fluids show qualitatively different secondary velocity patterns than Newtonian fluids. These clearly have some effect on heat transfer. Very little can yet be said quantitatively about these elastic effects, however?

In addition to these differences in heat transfer between Newtonian and non-Newtonian fluids, there are differences in the kinds of information that we are generally interested in for nonisothermal flows of these two classes of fluids. Let us break the possible calculations into two categories: global and local. For Newtonian fluids it is the global result, the evaluation of a heat transfer coefficient to relate bulk temperature differences to heat fluxes, that is of most interest. This heat transfer coefficient, which is used for sizing heat exchange equipment and estimating bulk temperature changes, is not as useful for non-Newtonian fluids for two reasons: first, in problems with significant viscous heating, which are common for molten polymers, the heat transfer coefficient cannot be defined meaningfully; and second, because of the peculiar physical properties of polymers, heat transfer between a flowing polymer and its surroundings is generally ignored. There are, of course, exceptions to this last statement, such as cooling extruders for low-temperature extrusion of foamed polymers and cooling of polymerization reactors.

For polymeric fluids, evaluation of the local temperature field is usually of primary interest. Because of the sensitivity of the physical properties to temperature, the temperature field can have a pronounced effect on the flow field and therefore on the process itself. In addition, many polymers are temperature sensitive and will degrade at high temperatures, say, at T_{degrad}. It is important to be sure that the local temperature never exceeds T_{degrad}. Finally, relaxation phenomena in polymers are strongly temperature sensitive, and the amount and location of residual stress or strain in a polymeric product will depend on the local temperature history of the polymer.

In conjunction with the interest in temperature fields in molten polymers there are many important heat

†H. H. Winter (unpublished research) has performed experiments on heating molten polyethylene flowing through a coiled tube. Although in such flows a secondary flow is known to occur, no effect on the radial temperature distribution was found relative to corresponding heating in a straight tube.

© 1983 Hemisphere 1 blishing Corporation

transfer problems that involve phase change. In almost all polymer processing operations, polymer is introduced as a solid, melted, formed, and finally frozen into the final product shape. The melting and freezing calculations required to model these processes can involve large property changes, phase changes, crystallization, moving interfaces, frictional heating between solid surfaces, and thermoelasticity (stresses produced by density changes on cooling).

In order to give perspective to the subsequent discussion, a brief survey of typical values of physical properties of polymers relevant to heat transfer problems is given in Sec. B. Following this, the important dimensionless groups that determine the qualitative nature of the heat transfer problem are enumerated. Then in Secs. D and E, specific solutions to heat transfer problems are given, with and without viscous heating, respectively. The problems looked at are mostly confined channel flows. Finally, in Sec. F the influence of small amounts of polymer additives on heat transfer in turbulent tube flow is described.

B. Physical properties

The two most important physical properties to be considered in this section are the thermal conductivity and the non-Newtonian viscosity. The thermal conductivity, of course, enters heat transfer calculations directly and is of particular interest here because of its low value for polymers. The viscosity is important in this context because of its temperature sensitivity, which couples the fluid flow problem with the heat transfer problem. The following discussion treats undiluted molten polymers.

(a) Thermal conductivity

Polymer melts, like their solid counterparts, are typically poor conductors. Sample values of the thermal conductivity λ are given in Table 1. The key feature to note in Table 1 is that the values of λ are several orders of magnitude lower than those for low-molecular-weight (Newtonian) liquids. As a result of these small sizes, heat transfer to polymers is effective only over very small distances in most processes. Thus heat removal limitations govern cycle time in forming thermoplastic parts and control part thickness in thermosetting plastics with exothermic reactions.

Table 1 Thermal conductivity and heat capacity of some molten polymers at temperatures T_0 (tabulated in [2])

Polymer	T_0, °C	c_p, 10^3 J/kg K	λ, W/m K
LDPE	150	2.57	0.241
HDPE	150	2.65	0.255
PP	180	2.80	
PVC	100	1.53	0.166
PS	150	2.04	0.167
PMMA	150		0.195

Molten polymers appear to be isotropic with respect to heat conduction, so that the values in Table 1 apply to conduction in all directions. Experiments on strained solid polymer samples [1] show higher conductivities in the direction of strain than transverse to the strain. These differences are quite dramatic in crystallizable polymers, where order-of-magnitude differences are possible in the two directions. However, in glassy polymers, the effect of orientation on λ is not nearly as dramatic, and this should be more indicative of conduction in polymer melts. Thus it is possible that in flows where the magnitude of the strain rate exceeds the reciprocal of the longest relaxation time of the polymer, λ_p,

$$\lambda_p \|\dot{\gamma}\| \gg 1$$

that the conductivity will depend somewhat on direction, However, no data are available to verify this, and in any event, the directional differences in conductivity for the glassy solids are at most factors of two to three.

It is important to note that λ is insensitive to the chemical nature of the polymer, molecular weight, temperature, and pressure [1]. For many typical polymers, λ is between 3 and 12 X 10^{-4} W/m K, irrespective of these variables. Conductivity data are frequently given as the thermal diffusivity κ,

$$\kappa = \frac{\lambda}{\rho c_p} \tag{1}$$

where ρ is the density and c_p is the heat capacity per unit mass. Shoulberg [3] has shown that κ for polymers is nearly independent of T, p, and chemical characteristics. It should be kept in mind that there are fewer data available for A and κ than for viscosity, so there may well be exceptions to trends indicated here.

Because of the insensitivity of λ or κ to temperature, accurate representations, which are useful for design calculations, can be given for λ, ρ, and c_p by low-order polynomials. Examples of such fits for low-density polyethylene (LDPE), high-density polyethylene (HDPE), and polyvinyl chloride (PVC) as obtained by Kleindienst [4] are presented in Tables 2-4.

(b) Temperature-dependent viscosity

The viscosity of non-Newtonian fluids depends on temperature and pressure. This influence can be described by the method of reduced variables [5]. In this method, viscosity data at a variety of temperatures and pressures

© 1983 Hemisphere Publishing Corporation

Table 2 Dependence of thermal conductivity λ on temperature [4]
$\lambda\,(\mathrm{W/m\,K}) = a\times10^{-1} + b\times10^{-4}(T-273.2) + c\times10^{-6}(T-273.2)^2 + d\times10^{-8}(T-273.2)^3 + e\times10^{-10}(T-273.2)^4$
(T in K)

Polymer	Temperature range, °C	a	b	c	d	e
HDPE	10-143	4.53	-8.59	-5.29	4.12	-1.98
	143-200	2.6	0	0	0	0
LDPE	10-126	3.65	-4.07	-7.34	8.28	-5.5 3
	126-200	2.23	0	0	0	0
PVC	O-200	1.68	0	0	0	0

can be reduced to a single master curve at a reference temperature T_0 and a reference pressure p_0 by plotting $\log\,(\eta(\dot\gamma, T, p)\eta_0(T_0, p_0)/\eta_0(T, p))$ versus $\log\,(a_T\dot\gamma)$, where $a_T(T,p)$ is a material-dependent ***shift factor.*** The small amount of available data on pressure dependence of η show that the temperature dependence is much stronger than the pressure dependence. As a result, pressure dependence will be neglected in the following and we assume that $\eta = \eta(\dot\gamma, T)$ and $a_T = a_T(T)$.

From molecular theories of dilute polymer solutions [6], it is predicted that

$$a_T = \frac{(\eta_0 - \eta_s)_T T_0 \rho(T_0)}{(\eta_0 - \eta_s)_{T_0} T\rho(T)} \tag{2}$$

where η_s is the solvent viscosity. If we assume that this result can be applied for large concentrations or undiluted polymers, then $\eta_s \ll \eta_0$, and the above reduces to

Table 3 Temperature dependence of density ρ [4]
$\rho^{-1}\,(\mathrm{cm^3/g}) = a + 10^{-4}b(T-273.2) + 10^{-5}c(T-273.2)^2 + 10^{-7}d(T-273.2)^3 + 10^{-9}e(T-273.2)^4 + 10^{-11}f(T-273.2)^5$
(*Tin* K)

Polymer	Temperature range, °C	a	b	c	d	e	f
HDPE	10-133	1.033	17.87	-7.19	16.11	-15.45	5.58
	133-200	1.158	8.09				
LDPE	10-113.5	1.078	1.24	2.68	-3.95	2.35	
	113.5-200	1.158	8.09				
PVC	10-110	0.715 4	1.02	0.078 1	-0.016 7	0.052 4	
	11 O-200	0.679 1	5.67				

Table 4 Temperature dependence of heat capacity c_p [4]
$c_p\,(\mathrm{kJ/kg\,K}) = a + b(T-273.2) + c(T-273.2)^2 + d(T-273.2)^3 + e(T-273.2)^4$
(*Tin* K)

Polymer	Temperature range, °C	a	b	c	d	e
HDPE	10-88	1.597	3.61×10^{-3}	5.96×10^{-5}	-3.44×10^{-8}	9.77×10^{-9}
	88-121	-1.983×10	6.17	-6.34×10^{-2}	2.19×10^{-4}	
	121-130	-2.837×10^{2}	2.41			
	130-133	1.208×10^{3}	-9.07			
	133-200	1.984	3.88×10^{-3}			
LDPE	10-90	1.943	5.39×10^{-3}	2.56×10^{-2}	-3.23×10^{-6}	3.53×10^{-8}
	90-105	8.497×10	-1.84	1.04×10^{-2}		
	105-110	-1.29×10^{2}	1.3			
	110-113.5	3.786×10^{2}	-3.31			
	113.5-200	1.98	3.70×10^{-3}			
PVC	IO-67	0.75	4.66×10^{-3}			
	67-96	1.361×10^{2}	-6.64	1.21×10^{-1}	-9.71×10^{-4}	2.90×10^{-6}
	96-200	1.208	2.96×10^{-3}			

© 1983 Hemisphere Publishing Corporation

$$a_T = \frac{\eta_0(T)T_0\rho(T_0)}{\eta_0(T_0)T\rho(T)} \tag{3}$$

The ratio $T_0\rho(T_0)/T\rho(T)$ is about unity and changes very little over ordinary temperature ranges. For example, this ratio is 0.92 for LDPE at 150°C relative to 200°C. However, the complete shift factor has a value of 0.32 for these same two temperatures.

If zero-shear-rate viscosity data are not available, then Eq. (3) cannot be used to compute a_T. In this case a_T must be determined empirically in the process of shifting data to construct a master curve for viscosity. One particularly convenient way to do this is to use the fact that from Eq. (3) a shear stress τ at temperature T can be reduced to a reference temperature T_0 by

$$\tau_r = \frac{T_0\rho_0}{T\rho}\tau \tag{4}$$

where τ_r is the reduced shear stress. Thus τ is fairly insensitive to temperature; moreover, it can be shifted without knowing a_T. Construction of a master curve of τ_r versus $a_T\dot{\gamma}$ will involve arbitrary shifting along the shear rate axis only. Typical values of the shift factor are shown in Figs. 1 and 2.

Two types of exponential functions have been used for describing the temperature dependence. For some materials and in some temperature ranges, the logarithm of a_T is linear in $(1/T)$ [see data for LDPE, HDPE, and PP (polypropylene) in Fig. 1]. Then the temperature dependence is given by an Arrhenius function

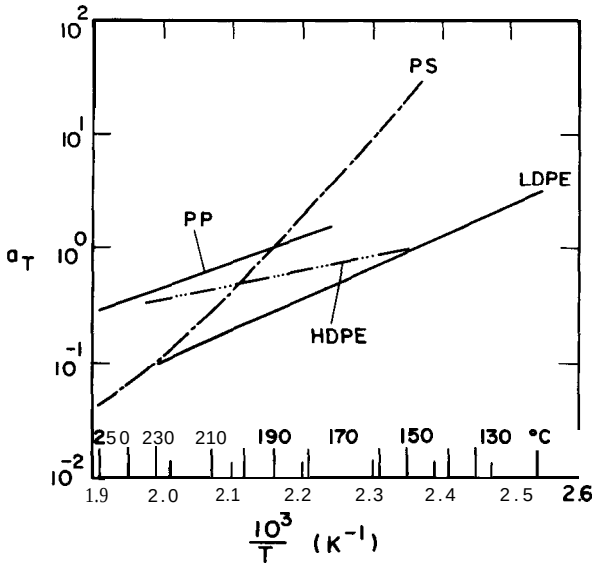

Figure 1 Shift factors a_T for several molten polymers as determined by Miinstedt [7]. The reference temperature T_0 is 150° C for LDPE and HDPE and 190° C for PP and PS.

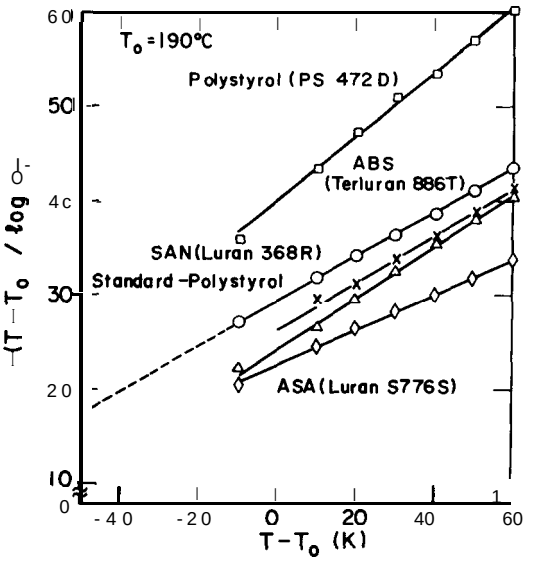

Figure 2 Shift factor a_T for molten polystyrenes as determined by Miinstedt [7]. The reference temperature T_0 is 190° C.

$$a_T = \exp\left[\frac{E}{R}\left(\frac{1}{T}-\frac{1}{T_0}\right)\right] \tag{5}$$

This behavior is observed with low-molecular-weight fluids and with molten polymers 100 K or more above their glass transition temperatures. Typical values of E/R are 4.50 X 10^3 K (LDPE), 2.83 X 10^3 K (HDPE), and 5.14 X 10^3 K (PP). These values, of course, depend on molecular parameters of the polymer and therefore may change considerably within each class of polymer. For LDPE, a linear correlation with the density ρ_{20} (density at room temperature) has been observed [7]:

$$\frac{E}{R} = a_0 + a_1\rho_{20} \tag{6}$$

with a_0 = 8.277 X 10^4 K and a_1 = -8.330 X 10^4 K cm^3/g.

For temperatures between the glass transition temperature T_g and T_g + 100, the WLF equation for a_T has been found to hold for a wide variety of polymers [8]:

$$\log a_T = \frac{-C_1^0(T-T_0)}{C_2^0+(T-T_0)} \tag{7}$$

If T_0 is taken to be the glass transition temperature, then C_1^0 = 17.44 and C_2^0 = 5 1.6 K. These constants are useful when specific data on a polymer are not available. When some data are available, then it is better to take C_1^0 = 8.86 and C_2^0 = 101.6 K, and then to choose T_0 to give a best fit with the data.

Styrene polymers are usually well described by the WLF equation. The agreement of a_T data with the WLF equation is shown best by plotting $(T-T_0)/\log a_T$

© 1983 Hemisphere Publishing Corporation

versus $(T - T_0)$, as shown in Fig. 2 for a variety of polystyrenes (PS).

It is helpful to give some examples of introducing the temperature shift into empirical viscosity functions [see Table 2.2.8(4)]. Two of these are the following.

1. Power law (shifted):

$$\eta(\dot\gamma, T) = \eta^0\left(\frac{\dot\gamma}{\dot\gamma^0}\right)^{n-1} a_T^n \tag{8}$$

with $\eta^0 = \eta(\dot\gamma^0, T_0)$.

2. Carreau (shifted):

$$\eta(\dot\gamma, T) = \eta_0(T_0)[1 + (\lambda_p(T_0)a_T\dot\gamma)^2]^{(n-1)/2} a_T \tag{9}$$

In Eq. (8), $\dot\gamma^0$ is a reference shear rate characteristic of the process (see following subsection). Also, in Eq. (9), $\lambda_p(T_0)$ is the characteristic time for the fluid at temperature T_0. Note that η^0 is the reference viscosity and η_0 is the zero-shear-rate viscosity.

C. Governing equations and dimensionless groups

Most quantitative studies of heat transfer to non-Newtonian fluids have taken the constitutive equation to be the generalized Newtonian fluid model, either for the purpose of calculation or for presenting results. For this reason we restrict the discussion here to this model. A discussion of flows in which this model might not be sufficient is given by Pearson and McIntire [9].

When the constitutive equation for the generalized Newtonian fluid (see Sec. 2.2.8) is combined with the conservation equations for momentum and energy, the resulting equations that govern heat transfer and flow in this class of non-Newtonian fluids (assumed also to be incompressible and to have constant thermal conductivity λ here) are

$$\rho\frac{D\mathbf{v}}{Dt} = -\nabla p + (\nabla\cdot\eta\dot\gamma) + \rho\mathbf{g} \tag{10}$$

$$\rho c_p\frac{DT}{Dt} = \lambda\nabla^2 T + \frac{1}{2}\eta(\dot\gamma:\dot\gamma) \tag{11}$$

In these equations $\dot\gamma[= \nabla\mathbf{v} + (\nabla\mathbf{v})^\dagger]$ is the rate of strain tensor. It is assumed in obtaining Eq. (11) that the internal energy of an element of fluid depends only on the instantaneous temperature and pressure in that element, and not on, say, the strain history of the element. Although there have been no experimental tests of this assumption, it has been used universally in heat transfer calculations.

In order to use Eqs. (10)-(11), it is necessary to specify the temperature and shear rate dependence of viscosity. Various empiricisms for $\eta(\dot\gamma)$ have been given in Table 2.2.8(4). The temperature dependence of η has been discussed in the preceding section.

Before solutions to these equations are presented for specific heat transfer problems, it is worthwhile to consider the important dimensionless groups that will govern their solution.

Putting Eq. (10) into dimensionless form is much the same as for isothermal flows [see 10]. Here we assume that the density is constant and that a characteristic value for viscosity is $\eta^0 = \eta(\dot\gamma^0, T^0)$, where $\dot\gamma^0$ and T^0 are a characteristic shear rate and temperature, respectively. We further suppose that p_0 is a reference pressure, H is a characteristic length scale (e.g., a pipe radius or channel gap), V is a characteristic velocity (wall velocity or mean velocity, for example), and t_p is a characteristic time for the process (e.g., a residence time). The assumption that we have available a reference velocity means that we focus our attention on forced, rather than free, convection problems. With these reference values we see that a characteristic shear rate is

$$\dot\gamma^0 = \frac{V}{H} \tag{12}$$

and a dimensionless pressure P can be defined as

$$P = \frac{p - p_0}{\eta^0 V/H} \tag{13}$$

Note that pressure is scaled by viscous stress rather than by inertia, since most polymer fluid flows are creeping flows. Finally, the equation of motion can be written

$$\mathrm{Re}\left(\frac{H}{Vt_p}\right)\frac{D^*\mathbf{v}^*}{Dt^*} = -\nabla^* P + \nabla^*\cdot\left(\frac{\eta}{\eta^0}\right)\dot\gamma^* + \frac{\mathrm{Re}}{\mathrm{Fr}}\left(\frac{\mathbf{g}}{g}\right) \tag{14}$$

where $D^*/Dt^* = t_p D/Dt$ is a dimensionless substantial derivative, $\nabla^* = H\nabla$ is a dimensionless spatial derivative, and $\dot\gamma^* = \dot\gamma/(V/H)$. The Reynolds number Re and Froude number Fr are given by

$$\mathrm{Re} = \frac{\rho VH}{\eta^0} \qquad \mathrm{Fr} = \frac{V^2}{gH} \tag{15}$$

The Froude number is generally necessary only for free surface flows. The inertial terms on the left side of Eq. (14) are scaled by the product of Re and a ratio of characteristic times, the reciprocal characteristic shear rate $1/\dot\gamma^0$, and the process time t_p. If the only choice for t_p is $1/\dot\gamma^0$, then only the Reynolds number will appear on the left. However, if we consider flow through a channel of length L, then t_p could be taken to be the residence time L/V. In this case the inertial terms would be scaled by Re H/L. These distinctions arising from

© 1983 Hemisphere Publishing Corporation

different choices of t_p are not usually important in connection with the momentum equation, since for most polymer flows Re $\ll 1$ and the inertial terms are negligible in any case. The use of t_p is more important for the energy equation.

In order to cast the energy equation into dimensionless form, we must first select a characteristic temperature difference ΔT^0 with which temperature changes can be scaled. There are numerous possibilities for this choice, and the proper one depends on the particular problem; these choices have been discussed by Pearson [11] and are listed below:

$$\Delta T_{\text{process}} = |T_w - T_i| \tag{16}$$

$$\Delta T_{\text{rheol}} = \left| \frac{\eta}{\partial \eta / \partial T} \right|_{\substack{T = T^0 \\ \dot{\gamma} = V/H}} \tag{17}$$

$$\Delta T_{\text{ad}} = \frac{\Delta p}{\rho c_p} \tag{18}$$

$$\Delta T_{\text{gen}} = \frac{\eta^0 V^2}{\lambda} \tag{19}$$

The process temperature difference $\Delta T_{\text{process}}$ is based on a AT defined by operating conditions, for example, a wall temperature T_w and inlet temperature T_i. The importance of nonisothermal effects on the rheology is given by ΔT_{rheol}, which gives a characteristic temperature difference that will produce appreciable changes in the viscosity. ΔT_{ad} gives the adiabatic temperature rise that could be produced by the overall pressure drop Δp. An order-of-magnitude balance between viscous heat generation and conduction gives a characteristic temperature difference ΔT_{gen} that can be attributed to viscous heating.

We now make the energy equation dimensionless as we did for the equation of motion; for the moment we leave the temperature scale unspecified and define a dimensionless temperature Θ by

$$\Theta = \frac{T - T^0}{\Delta T^0} \tag{20}$$

Equation (11) then becomes

$$\text{Pe} \left(\frac{H}{V t_p} \right) \frac{D^* \Theta}{D t^*} = \nabla^{*2} \Theta + \frac{1}{2} \text{Gn} \left(\frac{\eta}{\eta^0} \right) (\dot{\gamma}^* : \dot{\gamma}^*) \tag{21}$$

The two groups that arise here are the Peclet number Pe, which gives the relative importance of convection and conduction, and a heat-generation number Gn, defined by Pearson [11]:

$$\text{Pe} = \frac{\rho c_p V H}{\lambda} \tag{22}$$

$$\text{Gn} = \frac{\eta^0 V^2}{A \Delta T^0} \tag{23}$$

For steady-state problems in which t_p is taken to be $1/\dot{\gamma}^0$, the Peclet number adequately scales the convection term. However, if we are concerned with heat transfer in flow through a channel of length L, then the residence time L/V is a better choice for t_p. In this case the convection term is scaled by the Graetz number Gz, defined by

$$Gz = \frac{\rho c_p V H^2}{AL} = \text{Pe} \left(\frac{H}{L} \right) \tag{24}$$

Note that Gz and Pe will differ only when the aspect ratio of the channel is much different from unity. In this event the Graetz number is preferred inasmuch as it compares axial convection with conduction to the wall.

The generation number Gn will take on one of two standard forms depending on the choice of ΔT^0. If we take $\Delta T^0 = \Delta T_{\text{process}}$, then Gn becomes the Brinkman number, Br :

$$\text{Br} = \frac{\eta^0 V^2}{\lambda \Delta T_{\text{process}}} \tag{25}$$

This is a reasonable choice for ΔT^0 (and Gn) provided that $\Delta T_{\text{process}}$ is not large enough to alter the viscosity substantially, that is, provided that the Pearson number Pn is small:

$$\text{Pn} \equiv \frac{\Delta T_{\text{process}}}{\Delta T_{\text{rheol}}} \ll 1 \tag{26}$$

For large Pn, ΔT^0 should be chosen to be ΔT_{rheol}. Therefore we take Gn to be the Nahme-Griffith number, Na:

$$\text{Na} = \frac{\eta^0 V^2}{\lambda \Delta T_{\text{rheol}}} = \text{Br Pn} \tag{27}$$

A detailed discussion of the forms of the temperature profiles that can result for various combination of values of these dimensionless groups is given by Pearson [11]. For our purposes it is sufficient to note that most nonisothermal polymer processing flows are high-Gz processes. This means that we are generally interested in developing temperature profiles rather than fully developed values. In the next two sections we consider solutions to the energy equation for large and small Br and also large and small Pn.

D. Heat transfer in steady confined channel flows without viscous heating

In this section we present steady-state solutions to nonisothermal flows through tubes and slits with either constant wall temperature or constant heat flux. In

© 1983 Hemisphere Publishing Corporation

these problems we shall assume that viscous heating is unimportant, that is,

$$\mathrm{Gn} \ll 1$$

so that we can neglect the last term on the right side of Eq. (21). In addition, since most polymer flows are creeping, we take Re = *0;* we also absorb gravity into the pressure term, and take $t_p = L/V$, where L is the tube or slit length. The equations of interest in this subsection are then

$$0 = -\nabla^* P + \nabla^* \cdot \left(\frac{\eta}{\eta^0}\right) \dot{\gamma}^* \tag{28}$$

$$\mathrm{Gz}\, \mathbf{v} \cdot \nabla^* \Theta = \nabla^{*2} \Theta \tag{29}$$

Once solutions to Eqs. (28) and (29) have been obtained, the results can be presented in terms of the Nusselt number, Nu:

$$\mathrm{Nu} = \frac{2\alpha H}{\lambda} \tag{30}$$

where α is a local heat transfer coefficient based on the difference in local wall temperature and bulk temperature,

$$\alpha = \frac{q_{\mathrm{wall}}}{(T_{\mathrm{bulk}} - T_{\mathrm{wall}})} \tag{31}$$

and H is the channel thickness for slit flow or the radius R for pipe flow.

(a) Constant physical properties (Pn = 0)

In order to see the effects of the non-Newtonian character of the fluid on the Nusselt number, we first present results for a temperature-independent viscosity, that is, we take Pn = 0. We suppose that fluid is flowing through a slit or tube with uniform temperature T_0 prior to a position z = 0; for z ⩾ 0, either the wall temperature is raised to T_w or a constant heat flux q_1 is removed at the wall (see Fig. 3). For these two types of boundary conditions it is possible to obtain analytical solutions for the temperature field for both the thermal entrance region (small z) and the thermally fully developed region (large z). Tables 5 and 6 contain these solutions presented in terms of the local Nusselt number. Derivations of many of these entries can be found in [12].

In the sense used in Tables 5 and 6, large and small z refer to the importance of the convective term in Eq. (29). Consistent with taking $t_p = L/V$, here we take the dimensionless axial coordinate z^* to be

$$z^* = \frac{z}{L} \tag{32}$$

Then in the thermal entrance region z^* will be less than the axial distance required for significant heat transfer from the wall to take place. Since the latter is given by Gz, we have

Thermal entrance region:

$$\frac{z^*}{\mathrm{Gz}} \ll 1 \quad \text{or} \quad \frac{\lambda z}{\rho c_p V H^2} \ll 1 \tag{33}$$

Similarly the thermally fully developed region is

Thermally fully developed flow:

$$\frac{z^*}{\mathrm{Gz}} \gg 1 \quad \text{or} \quad \frac{\lambda z}{\rho c_p V H^2} \gg 1 \tag{34}$$

As the following example shows, the thermal entrance region is often the more important one in heat transfer to polymers.

Example. A molten polystyrene is to be formed into a rectangular shape by injecting it into a cold mold that is 30 cm long, 7.5 cm wide, and 0.2 cm thick [13]. The time required to fill the mold is 2.5 s (= t_p) with a pressure gradient of 1.33 X 10^6 Pa/m. The temperature of the molten polymer entering the mold is 250°C and the mold walls are at 50°C. For polystyrene, A = 1.295 X 10^{-1} J/K m s and κ = 7.05 X 10^{-8} m^2/s [14]. Find the local Nusselt number to describe the heat transfer between the polymer and mold.

Solution. We begin by calculating the Graetz number to determine which formula in Table 6 to use. From the data above we know that the average velocity $\langle v_z \rangle$ = ***Vis***

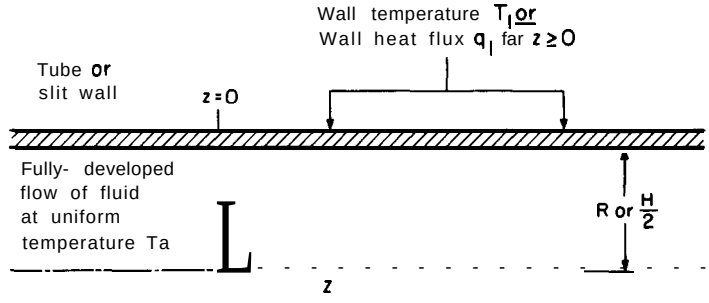

Figure 3 Heat transfer to non-Newtonian fluids in tubes and slits.

© 1983 Hemisphere Publishing Corporation

Table 5 Asymptotic results for local Nusselt numbers in tube flow [12]; $Nu = \alpha D/\lambda$

	Fluid flow	Boundary conditions, Fig. 3: Constant wall temperature		Constant wall heat flux	
Thermal entrance region, $z^* \ll Gz$	Plug flow	$Nu = \frac{1}{\sqrt{\pi}}\left(\frac{Gz}{z^*}\right)^{1/2}$	(A)	$Nu = \frac{\sqrt{\pi}}{2}\left(\frac{Gz}{z^*}\right)^{1/2}$	(G)
	Laminar non-Newtonian flow	$Nu = \frac{2}{9^{1/3}\Gamma(\frac{4}{3})}\left[\frac{Gz}{z^*}\left(-\frac{1}{4}\frac{dv_z^*}{dr^*}\Big\|_{r^*=1}\right)\right]^{1/3}$	(B)	$Nu = \frac{2\Gamma(\frac{2}{3})}{9^{1/3}}\left[\frac{Gz}{z^*}\left(-\frac{1}{4}\frac{dv_z^*}{dr^*}\Big\|_{r^*=1}\right)\right]^{1/3}$	(H)
	Laminar Newtonian flow	$Nu = \frac{2}{9^{1/3}\Gamma(\frac{4}{3})}\left(\frac{Gz}{z^*}\right)^{1/3}$	(C)	$Nu = \frac{2\Gamma(\frac{2}{3})}{9^{1/3}}\left(\frac{Gz}{z^*}\right)^{1/3}$	(I)
Thermally fully developed flow, $z^* \gg Gz$	Plug flow	$Nu = 5.772$	(D)	$Nu = 8$	(J)
	Laminar non-Newtonian flow	$Nu = \beta_1^2$, where β_1 is the lowest eigenvalue of $\frac{1}{r^*}\frac{d}{dr^*}\left(r^*\frac{dX_n}{dr^*}\right) + \beta_n^2 v_z^*(r^*)X_n = 0$; $X_n'(0) = 0$	(E)	$Nu = \left\{2\int_0^1 \frac{1}{r^*}\left[\int_0^{r^*} \bar{r}^* v_z^*(\bar{r}^*)\,d\bar{r}^*\right]^2 dr^*\right\}^{-1}$	(K)
	Laminar Newtonian flow	$Nu = 3.657$	(F)	$Nu = \frac{48}{11}$	(L)

Note: $v_z^* = v_z/\langle v_z\rangle$, $r^* = r/R$, $z^* = z/L$, and $Gz = \langle v_z\rangle R^2/\kappa L$.

Hemisphere Publishing Corpora
HEMISPHERE

Table 6 Asymptotic results for local Nusselt numbers in thin slit flow [12]; $Nu = 2\alpha H/\lambda$

	Fluid flow	Boundary conditions, Fig. 3: Constant wall temperature	Constant wall heat flux	
Thermal entrance region, $z^* \ll Gz$	Plug flow	$Nu = \frac{2}{\sqrt{\pi}}\left(\frac{Gz}{z^*}\right)^{1/2}$	(A) $Nu = \sqrt{\pi}\left(\frac{Gz}{6}\right)^{1/2}$	
	Laminar non-Newtonian flow	$Nu = \frac{2^{5/3}}{9^{1/3}\Gamma(\frac{4}{3})}\left[\frac{Gz}{z^*}\left(-\frac{dv_z^*}{dy^*}\Big\|_{y^*=1/2}\right)\right]^{1/3}$	(B) $Nu = \frac{2^{5/3}}{9^{1/3}(H)}\left[\frac{Gz}{z^*}\left(-\frac{dv_z^*}{dy^*}\Big\|_{y}\right)\right]^{1/3}$	
	Laminar Newtonian flow	$Nu = \frac{2^{4/3}}{3^{1/3}\Gamma(\frac{4}{3})}\left(\frac{Gz}{z^*}\right)^{1/3}$	(C) $Nu = \frac{2^{4/3}\Gamma(\frac{2}{3})}{3^{1/3}}\frac{Gz}{0z^*}^{1/3}$	(I)
Thermally fully developed flow, $z^* \gg Gz$	Plug flow	$Nu = 9.86$	(D) $Nu = 12$	(J)
	Laminar non-Newtonian flow	$N = 4\beta_1^2$, where β_1 is the lowest eigenvalue of the equation $\frac{d^2X_n}{dy^{*2}} + 4\beta_n^2 v_z^*(y^*)X_n = 0; X_n(\pm\frac{1}{2}) = 0$ (E)	$Nu = \left[2\int_0^{1/2}\left(\int_0^{y^*} v_z^*(\bar{y}^*)\,d\bar{y}^*\right)^2 dy^*\right]$	(K)
	Laminar Newtonian flow	$Nu = 1.54$	(F) $Nu = \frac{140}{17}$	(L)

Note: $v_z^* = v_z/\langle v_z\rangle$, $y^* = y/H$, $z^* = z/L$, and $Gz = \langle v_z\rangle H^2/\kappa L$

emisphere Publishing Corp

$$V = \frac{L}{t_p} = \frac{30}{2.5} = 12.0 \text{ cm/s}$$

The Graetz number is then

$$\text{Gz} = \frac{VH^2}{\kappa L} = \frac{(0.12)(0.002)^2}{(7.05 \times 10^{-8})(0.30)} = 22.7$$

Since $z^* = z/L$ clearly lies between 0 and 1.0, we see that

$$z^* \ll \text{Gz}$$

to a good approximation throughout the mold. Thus the polymer is in the thermal entrance region.

In the absence of any detailed rheological information from which we can calculate the velocity gradient at the wall, we use Eq. (C) in Table 6 to estimate Nu:

$$\text{Nu} = \frac{2^{4/3}}{3^{1/3}\Gamma(\frac{4}{3})}\left(\frac{\text{Gz}}{z^*}\right)^{1/3} = 5.54 z^{*-1/3} \tag{35}$$

where $\Gamma(x)$ is the gamma function.

This result is clearly to be regarded as a rough estimate inasmuch as we have neglected shear rate and temperature dependence of viscosity, the formation of a solid polymer skin next to the mold surface, and the influence of the free surface at the front on the velocity patterns. Nonetheless, it illustrates how the entries in Tables 5 and 6 can be used, and shows the importance of the thermal entry region. A more detailed treatment of heat transfer in injection molding is given by Janeschitz-Kriegl [15].

(b) Variable physical properties (Pn > I)

Here we consider the effect of temperature-dependent viscosity on the heat transfer, that is, problems in which Pn is of order unity. For problems of this type, Eqs. (28) and (29) must be solved simultaneously because of the coupling that occurs through the viscosity and velocity. Solution to these equations must generally be done numerically for each situation of interest. To illustrate the resulting influence of $\eta(T)$ on Nu, we describe below results computed by Christiansen and Craig [16].

Christiansen and Craig [16] considered heat transfer to a power law fluid in tube flow with constant wall temperature (see Fig. 3). The temperature dependence of viscosity was given by an Arrhenius form similar to Eq. (5):

$$\eta(\dot{\gamma}, T) = m\dot{\gamma}^{n-1} e^{nE/RT} \tag{36}$$

If we take AT,,,, to be $(T_1 - T_0)$ and evaluate ΔT_{rheol} at a mean temperature $T_m = \sqrt{T_0 T_1}$,

$$\Delta T_{\text{rheol}} = \left|\frac{\eta}{\partial\eta/\partial T}\right|_{T_m} = \frac{RT_0T_1}{nE} \tag{37}$$

then the Pearson number is given by [cf. Eq. (26)]

$$\text{Pn} = \frac{nE}{R}\left(\frac{1}{T_0} - \frac{1}{T_1}\right) \tag{38}$$

Average Nusselt numbers Nu, were calculated as functions of Gz for a range of values of n and (l/n) Pn (denoted by Ψ in [16]). Nu, is defined as in Eq. (30) except that an average heat transfer coefficient α_a is used based on an arithmetic average temperature difference over a length L of heated section:

$$q = \alpha_a\left(T_1 - \frac{T_0 + T_L}{2}\right) \tag{39}$$

where T_L is the bulk temperature at z = L.

In Figs. 4 and 5, typical results from these calculations are shown. Figure 4 is for temperature-independent viscosity, Pn = 0, and shows the effect of shear thinning alone on Nu,. Figure 5 shows the effect of Pn on Nu_a for $n = \frac{1}{3}$, which is typical of many molten polymers. It is seen that Nu, is affected in similar ways by increasing shear rate sensitivity ($n \to 0$) and increasing temperature sensitivity ($\text{Pn} \to \infty$). In fact, the limiting curves in these two figures appear to be identical. Christiansen and Craig compared these results with experimental data for aqueous polymer solutions and found excellent agreement (better than 7%), provided that natural convection was negligible [16].

E. Influence of viscous heating on heat transfer

As mentioned in the introduction, one of the important distinctions between nonisothermal flows of polymeric fluids and Newtonian fluids is the importance of viscous heating in the former. Because of the high viscosities of these fluids, Gn [Eq. (23)] is not small and the last term on the right side of Eq. (21), the energy equation, must be retained. In this section we consider the effect of this viscous heating term on the temperature field in two types of flows. First we re-examine the steady confined channel flows from the last section; then we discuss transient, circular Couette flow; and finally we look at the implications of these results for the definition of the Nusselt number. The channel flow (both slit and tube) and Couette flow examples treated here are illustrations of a variety of heat transfer problems that can be analyzed as limiting cases of helical flow [2].

(a) Viscous dissipation in steady confined channel flow

With viscous dissipation included, Eq. (21) has been solved analytically only for a few limiting cases of channel flow (see, for example, [17] and [18]). These solutions have incorporated a temperature-independent

© 1983 Hemisphere Publishing Corporation

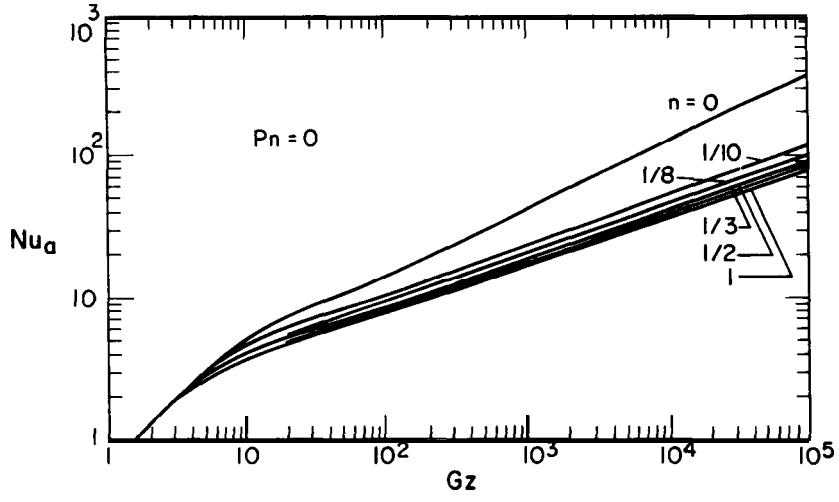

Figure 4 Average Nusselt number [Eq. (39)] as a function of Graetz number for laminar tube flow of power law and Newtonian fluids. The viscosity is assumed to be temperature independent in these calculations (Pn = 0). Results are shown with the power law slope n as a parameter. From Christiansen and Craig [16].

viscosity and relatively simple boundary conditions. Moreover, the analytical solutions have a complicated structure that requires computer calculations to obtain numerical values for the temperature field. For this reason it seems to us to be most reasonable to obtain the temperature field by direct numerical solution to Eq. (21). In this way temperature dependence of the viscosity can be included with little extra effort and also solutions can easily be generated for a variety of boundary conditions.

Here we give an example of a numerical solution to Eq. (21) for a specific example. In particular, we consider pipe flow of a power law fluid with $n = 0.4$ (see Fig. 3). The reference temperature T^0 is taken to be the uniform entrance temperature T_0, and the temperature dependence of viscosity is given by an exponential factor

$$e^{-\beta(T-T_0)}$$

so that

$$\Delta T_{\text{rheol}} = \frac{1}{\beta} = \frac{RT_0^2}{nE} \tag{40}$$

The dimensionless temperature we use is

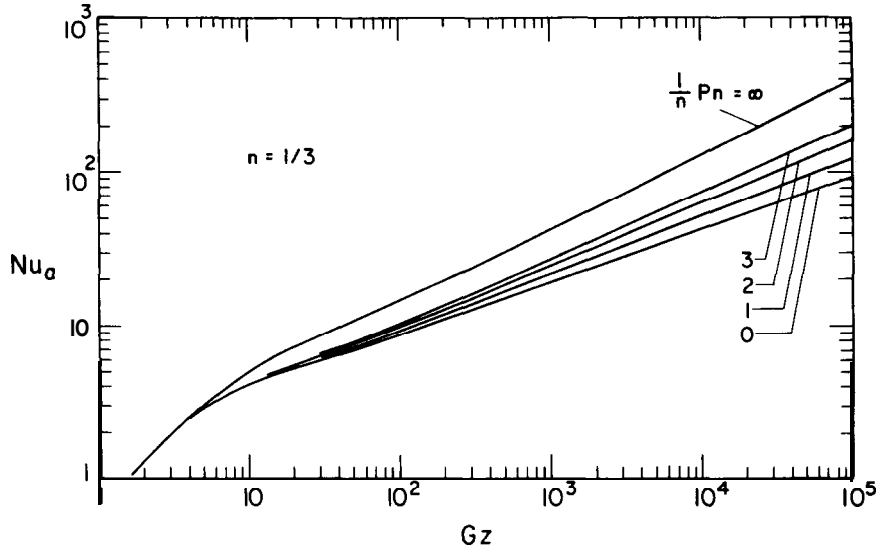

Figure 5 Average Nusselt number [Eq. (39)] as a function of Graetz number for heat transfer to power law fluids with $n = \frac{1}{3}$ in laminar tube flow. Results were obtained numerically by Christiansen and Craig [16] for each of the Pearson numbers [defined in Eq. (38)] shown. From Christiansen and Craig [16].

© 1983 Hemisphere Publishing Corporation

$$\Theta = \frac{T - T_0}{\Delta T_{\text{rheol}}} = \beta(T - T_0) \tag{41}$$

consistent with the assumption that viscosity will vary significantly with temperature. In addition, we take the viscous heating to be significant, with

$$\text{Na} = 5 \tag{42}$$

Instead of the two limiting boundary conditions given in Fig. 3, we use the more general relation between the heat flux in the fluid at the wall and the temperature difference between the wall Θ_w and the surroundings Θ_s:

$$\left(\frac{\partial \Theta}{\partial r^*}\right)_{w,f} = \text{Bi}\,(\Theta_w - \Theta_s) \tag{43}$$

In the above, $r^* = r/R$ is scaled by the pipe radius, the temperature gradient is taken in the fluid layer at the wall, and Bi is the Biot number.

The developing temperature profile is shown in Fig. 6 for three typical Bi values. In these calculations we have taken the inlet and surroundings temperature to be identical, $\Theta_s = 0$. The temperature of course increases with increasing distance downstream from the inlet. The amount of increase depends on r^*, however, inasmuch as viscous dissipation is nonuniform with maximum value at the wall and zero magnitude at the center of the pipe. Thus radial temperature differences build up and radial conduction becomes important. The axial heat flux due to conduction is negligible compared to the convective flux.

Far from the entry region $(z^* = z/L \gg \text{Gz}^{-1})$, the temperature distribution becomes fully developed. Then the radial heat flux to the wall is balanced by heat generation in the flow. For very small Biot numbers (nearly adiabatic wall), the fully developed temperature is not reached until the temperature-dependent viscosity becomes so small that viscous dissipation is negligible. For large Bi values a large radial temperature gradient ***in the fluid*** is generated, whereas for small Bi values a large temperature difference ***in the wall,*** $\Theta_w - \Theta_s$, is created. Both limiting cases are shown in Fig. 6.

Note that the average temperature increase in the pipe is larger with intensive cooling (Bi = 100) than with intermediate cooling (Bi = 10). This is a phenomenon that has been observed experimentally in polymer processing. Presumably the intensive cooling produces this effect by increasing the viscosity near the wall. This in turn will decrease shear rates near the wall and shift the maximum shear rate nearer the center of the tube. Thus extra viscous heating is produced in the interior, and the increased layer of slowly moving polymer near the wall acts as an insulator.

It is found that the magnitude of the temperature increase depends significantly on Na, that is, on the magnitude of viscous heat generation. However, the shape of the temperature profile is relatively insensitive to Na. An example is given in Fig. 7, where the developing temperature profiles scaled by the fully developed bulk temperature $\Theta_{b\infty}$ are shown for slit flow of a power law fluid for two different values of Na. Although $\Theta_{b\infty}$ increases by a factor of almost 10 when Na is increased from 1 to 10, the shapes of $\Theta/\Theta_{b\infty}$ are virtually unaffected.

In modeling viscous heating in two-component pipe flow [20] a rather interesting, but not surprising phenomenon has been noted. The flow region was divided

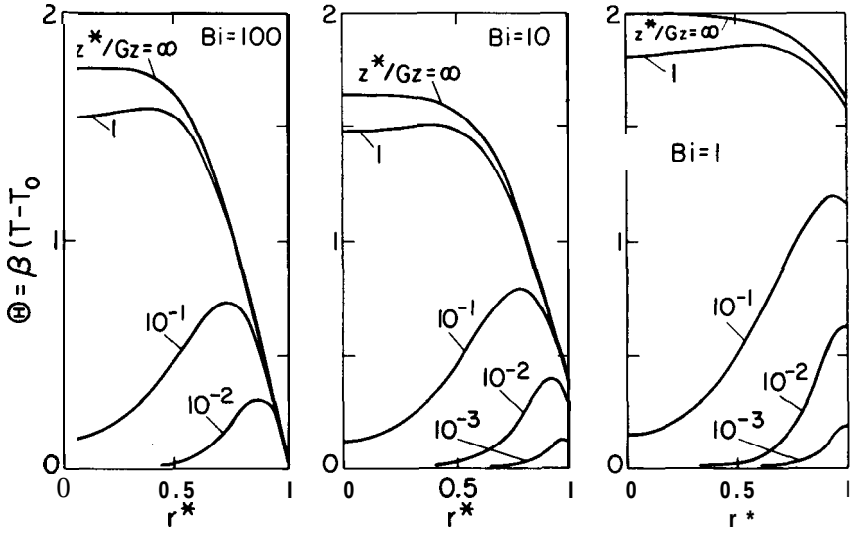

Figure 6 Developing temperature profiles in a power law fluid $(n = 0.4)$ flowing in pipes with uniform thermal boundary conditions [Eq. (43)]. The dimensionless axial and radial positions are $z^* = z/L$ and $r^* = r/R$. Results for three different Biot numbers are shown. In all cases Na = 5 and $\Theta_s = 0$. From Winter [2].

© 1983 Hemisphere Publishing Corporation

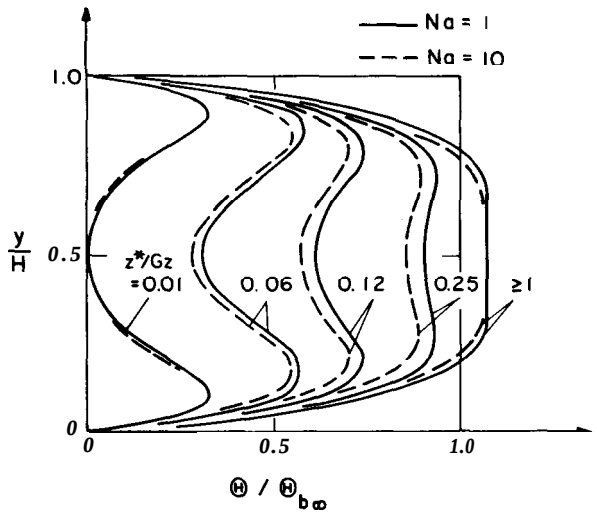

Figure 7 Developing temperature profiles for a power law fluid ($n = 0.4$) flowing in a slit with walls at a constant temperature equal to the entrance temperature T_0. The local dimensionless temperature is scaled by the fully developed bulk temperature $\Theta_{b\infty}$ and is given at a variety of axial positions $z^* = z/L$. For the two Nahme-Griffith numbers considered, it is found that $\Theta_{b\infty} = 0.5$ (Na = 1) and $\Theta_{b\infty} = 4.6$ (Na = 10). From Winter [19].

into a core of high-viscosity fluid and a thin layer of low-viscosity fluid near the wall. From the calculations it was found that the rate of viscous heating can be orders of magnitude higher in the low-viscosity fluid than in the high-viscosity fluid core. This is accounted for, of course, by the extraordinarily high shear rates that would occur in the low-viscosity lubrication layer next to the wall.

(b) Viscous dissipation in circular Couette flow

Here we consider the flow generated in the annular gap between two concentric cylinders in relative rotation about their common axis. The development of the temperature profile is given by the energy equation Eq. (21), where the characteristic process time t_p could be chosen to be the duration of an experiment. The degree of thermal development is described by the Fourier number,

$$\mathrm{Fo} = \frac{t_p \kappa}{H^2} \tag{44}$$

which is equivalent to Gz^{-1} for confined channel flow. Note that for dimensionless time $t^* = t/t_p$ small compared to Fo^{-1}, the temperature distribution is still developing, whereas for $t^* \gg \mathrm{Fo}^{-1}$, steady-state conditions will have been reached.

There are relatively few applications of viscous heating calculations in circular Couette flow. One interesting one is in rotational viscometry, where viscous heating sometimes limits the largest shear rates that can be used in an instrument.

The fully developed temperature and velocity fields have drawn much attention because of the existence of a double-valued solution found in 1940 by Nahme [21]. The shear stress cannot exceed a certain value, even if the shear rates are increased indefinitely. At high shear rates the decrease in the temperature-dependent viscosity overcompensates the increase in stress due to the increase in shear rate. The shear rate V_0/H (relative velocity between the surfaces divided by the gap) as a function of the shear stress is shown in Fig. 8 for a power law fluid [22]. For a given shear stress, there are two modes to run an experiment: one at high shear rates and one at low shear rates.

(c) Definition of *Nu with viscous heating*

In many flow applications, viscous heating is greatest in the fluid near a wall, as for example in pressure-driven channel flows. Small velocities (no slip condition) make convection a minor factor in this region, so that the local temperature is determined by a balance between dissipation and conduction. Because of the low thermal conductivity, large temperature gradients build up, with the result that the temperature distribution near the wall is only weakly dependent on the bulk temperature of the fluid. Therefore the use of a heat transfer coefficient [Eq. (31)] or a Nusselt number [Eq. (30)] based on the bulk temperature can result in physically unreasonable values for these quantities. We next illustrate this with an example and then redefine the Nusselt number to make it applicable to flows with significant viscous heating.

Figure 9 shows the developing temperature profiles in pipe flow with negligible viscous heating (Na = 0.001) and with appreciable viscous heating (Na = 1.0). For flow without significant dissipation (left graph), the temperature of the fluid gradually approaches the wall temperature, and the heat flux at the wall can be described by a Nusselt number using a mean temperature difference between the wall and fluid. However, if viscous dissipation significantly changes the developing temperature (right graph), the heat flux at the wall has to be described by the temperature gradient at the wall and not by an average temperature difference. It can clearly be seen that the temperature gradient at the wall changes its sign at an axial position where the average fluid temperature is still much below the wall temperature. An unusual situation is generated, where the fluid heats the wall even if its mean temperature is much below the wall temperature. For these conditions, the Nusselt number in its classical definition can become negative .

A more useful definition of the Nusselt number

© 1983 Hemisphere I blishing Corporation

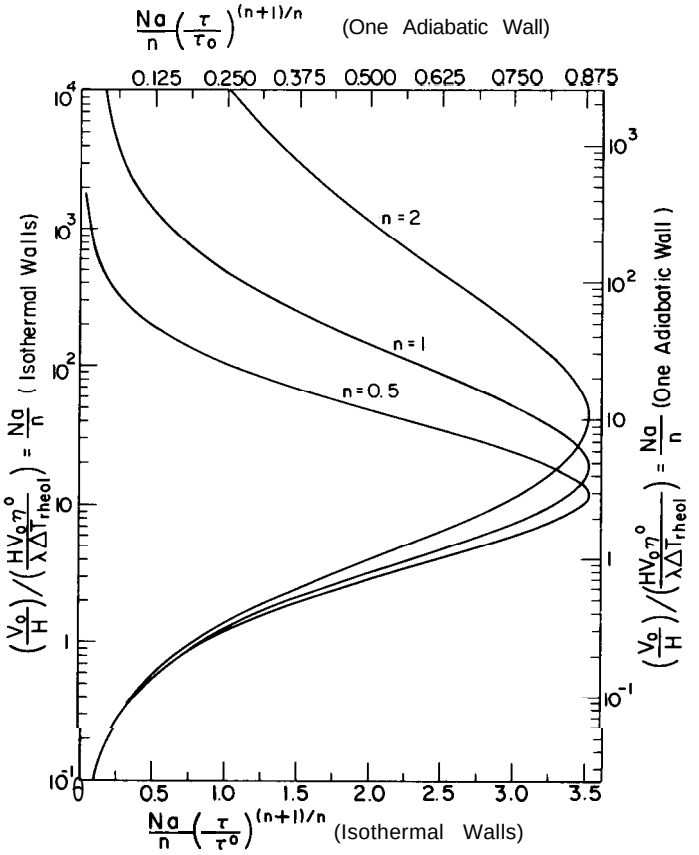

Figure 8 Dimensionless shear rate Na/n as a function of dimensionless shear stress $(\mathrm{Na}/n)(\tau/\tau^0)^{(n+1)/n}$ for steady-state shear flow of a power law fluid between parallel plates. One plate slides relative to the other with velocity V_0, and the separation between them is H. Two sets of thermal boundary conditions are included: both walls isothermal at temperature T_w, and one wall at T_w with the other wall adiabatic. In the figure the reference viscosity is $\eta^0 = \eta(V_0/H, T_w)$, the reference-shear stress is $\tau^0 = \eta^0 V_0/H$, n is the power law slope, $\Delta T_{\mathrm{rheol}} = (E/RT_w^2)^{-1}$, and $\mathrm{Na} = V_0^2 \eta^0/\lambda \Delta T_{\mathrm{rheol}}$. From Gavis and Laurence [22].

has been suggested [2] that returns to the original meaning of the Nusselt number as a dimensionless temperature gradient in the fluid at the wall:

$$\mathrm{Nu} = \frac{H}{\Delta T^0}\left(\frac{\partial T}{\partial r}\right)_{w,f} = \left.\frac{\partial \Theta}{\partial r^*}\right|_{w,f} \tag{45}$$

Here ΔT^0 has to be chosen to be the same characteristic temperature difference that has been used to make the energy equation dimensionless.

F. Heat transfer in turbulent flows of dilute polymer solutions

It is well known (see Sec. 2.2.8) that addition of small amounts of high-molecular-weight polymer additives to turbulent pipe flow can result in substantial reduction in the friction factor at a given Reynolds number. It is not surprising that the same mechanism that yields this drag reduction might also affect heat (and mass) transfer to the wall in turbulent flows.

In Fig. 10, data of Debrule and Sabersky [23] are shown that illustrate this. In Fig. 10*a* the friction factor is shown for water with and without 50 ppm polyethylene oxide (PEO); it is seen that the addition of the polymer produces drag reduction (f decreases by about 75% at Re = 10^5) and that the Prandtl (Pr = $c_p\mu/\lambda$) has no effect on f as expected. In Fig. 10*b* the heat transfer coefficient is presented in terms of the Stanton number,

$$\mathrm{St} = \frac{q_0}{(T_w - T_b)c_pG} = \frac{\alpha}{c_pG} \tag{46}$$

in which q_0 is the uniform heat flux applied to the tube wall, $T_w - T_b$ is the local difference between the wall and bulk temperature, α is the local heat transfer coefficient, and G is the mass velocity. It is clear that there is a substantial reduction in heat transfer upon addition of the polymer. Even though St clearly depends on Pr, the change in St produced by the polymer is approximately the same at each Pr. At Re = 10^5, for example, St is reduced by about 82% at all three Prandtl numbers.

© 1983 Hemisphere Publishing Corporation

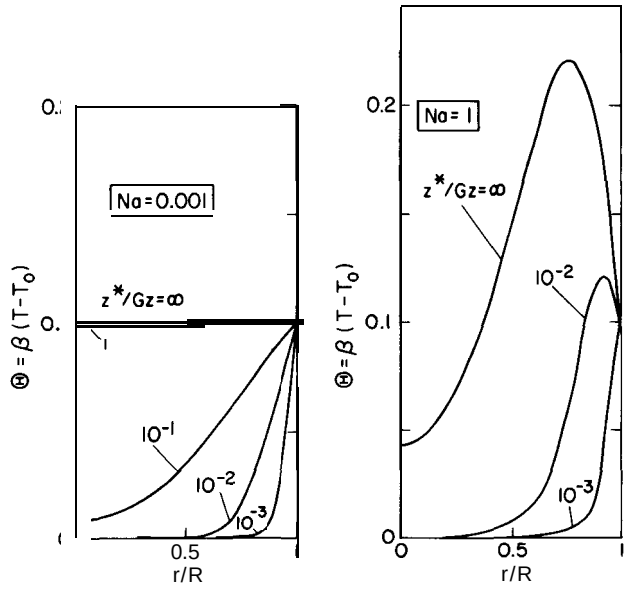

Figure 9 Developing temperature profiles in pipe flow of a power law fluid (n = 0.4) with viscous heating (Na = 1) and without (Na = 0.001). Axial locations are given by $z^* = z/L$. The pipe wall is slightly hotter than the entrance temperature, $\Theta_w = 0.1$. From Winter [2].

Other data on the effect of polymer additives on St at high Re can be found elsewhere [24-29]. These data agree on the decrease in heat transfer with addition of drag-reducing polymer, but there is disagreement on the relative size of the effects on St and f. It is thus necessary to be cautious in generalizing the results of Fig. 10.

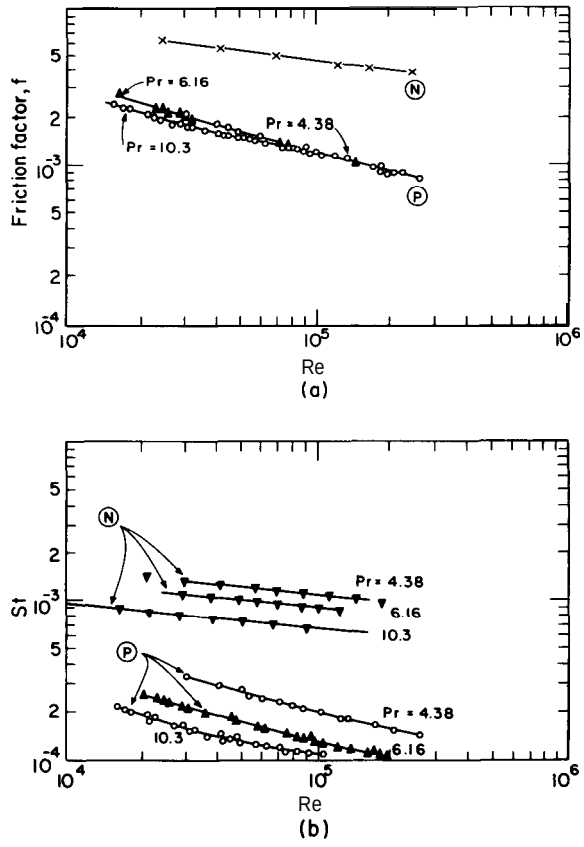

Figure 10 Friction factor and Stanton number for turbulent pipe flow of water (N) and 50 ppm poly(ethylene oxide) in water (P) at three different Prandtl numbers. (*a*) The friction factor for the polymer solution shows a slight dependence on Pr; the water curve is for all three Pr. (b) The decrease in St upon addition of the polymer is similar for each Pr. From Bird et al. [12].

NOMENCLATURE FOR SECTION 2.5.12

ABS acrylonitrile, butadiene, styrene terpolymer
ASA acrylonitrile, styrene, acrylester terpolymer
HDPE high-density polyethylene
LDPE low-density polyethylene
PEO poly(ethylene oxide)
PMMA polymethylmethacrylate
PP polypropylene
PS polystyrene
PVC polyvinyl chloride
SAN styrene-acrylonitrile copolymer

REFERENCES FOR SECTION 2.5.12

1. Tadmor, Z., and ***Gogos, C. G., Principles of Polymer Processing,*** Wiley-Interscience, New York, 1979.
2. Winter, H. H., Viscous Dissipation in Shear Flows of Molten Polymers, *Adv. **Heat Transfer,*** vol. 13, pp. 205-267, 1977.
3. Shoulberg, R. H., The Thermal Diffusivity of Polymer Melts, *J. Appl. **Polymer** Sci.*, vol. 7, pp. 1597-1611, 1963.
4. Kleindienst, U., Untessuchung des Abkuhlungs vorganges und dessen Einfluss auf das Eigenspannungsfeld in der want extrudiertes Kunststoffrohre, Doctoral thesis, University of Stuttgart, 1976.
5. Ferry, J. D., ***Viscoelastic Properties of Polymers,*** 2d ed., Wiley, New York, 1970.
6. Bird, R. B., Hassager, O., Armstrong, R. C., and Curtiss, ***C.*** F., ***Dynamics** of Polymeric **Liquids, Vol. 2, Kinetic Theory,*** Wiley, New York, 1977.
7. Münstedt, H., Viskositabdaten von Kunststoffschmelzen, ***Kunststoffe,*** vol. 68, pp. 92-98, 1978.
8. Williams, M. L., Landel, R. F., and Ferry, J. D., The Temperature Dependence of Relaxation Mechanisms in Amorphous Polymers and Other Glass-Forming Liquids, *J. Am. Chem. Soc.*, vol. 77, pp. 3701-3707, 1955.
9. Pearson, J. R. A., and McIntire, L. V., Non-isothermal Rheology of Polymers and Its Significance in Polymer Processing, *J. Non-**Newtonian** Fluid Mech.*, vol. 6, pp. 81-95, 1979.

© 1983 Hemisphere Publishing Corporation

10. Bird, R. B., Stewart, W. E., and Lightfoot, E. N., ***Transport Phenomena,*** Wiley, New York, 1960.
11. Pearson, J. R. A., Polymer Flows Dominated by High Heat Generation and Low Heat Transfer, ***Poly. Eng. Sci.***, vol. 18, pp. 222-229, 1978.
12. Bird, R. B., Armstrong, R. C., and Hassager, O., ***Dynamics of Polymeric Liquids, Vol. 1, Fluid Mechanics***, Wiley, New York, 1977.
13. Wales, J. L. S., van Leeuwen, J., and van der Vijgh, R., Some Aspects of Orientation in Injection Molded Objects, *Poly. Eng. Sci.*, vol. 12, pp. 359-363, 1972.
14. Brandrup, J., and Immergut, E. H., ***Polymer Handbook,*** Interscience, New York, 1966.
15. Janeschitz-Kriegl, H., Injection Moulding of Plastics, II. Analytical Solution of Heat Transfer Problem, *Rheol. Acta*, vol. 18, pp. 693-701, 1979.
16. Christiansen, E. B., and Craig, S. E., Jr., Heat Transfer to Pseudoplastic Fluids in Laminar Flow, ***AIChE J.,*** vol. 8, pp. 154-160, 1962.
17. Bird, R. B., Viscous Heat Effects in Extrusion of Molten Plastics, *Soc. Plast. Eng. J.*, vol. 11, pp. 35-41, 1955.
18. Dinh, S. M., and Armstrong, R. C., Non-isothermal Channel Flows of Non-Newtonian Fluids with Viscous Heating, ***AIChE J., vol.*** 28, 1982.
19. Winter, H. H., Temperature Fields in Extruder Dies with Circular, Annular, or Slit Cross-Section, ***Poly. Eng. Sci.,*** vol.15, pp. 84-96, 1975.
20. Uhland, E., Stratified Two-Phase Flow of Molten Polymers in Circular Dies, *Poly. Eng. Sci.*, vol. 17, pp. 671-681, 1977.
21. Nahme, R., Beitrage zur hydrodynamischen Theorie der lagerreibung, *Ing.-Archiv*, vol. 11, pp. 191-209, 1940.
22. Gavis, J., and Laurence, R. L., Viscous Heating of a Power-Law Liquid in Plane Flow, ***Znd. Eng. Chem. Fund.,*** vol. 7, pp. 525-527, 1968.
23. Debrule, R. M., and Sabersky, R. H., Heat Transfer and Friction Coefficients in Smooth and Rough Tubes with Dilute Polymer Solutions, *Int. J. Heat Mass Transfer,* vol. 17, pp. 529540, 1974.
24. Smith, K. A., Keuroghlian, G. H., Virk, P. S., and Merrill, E. W., Heat Transfer to Drag-Reducing Polymer Solutions, ***AIChE J.,*** vol. 15, pp. 294-297, 1969.
25. Poreh, M., and Paz, U., Turbulent Heat Transfer to Dilute Polymer Solutions, ***Znt. J. Heat Mass Transfer,*** vol. 11, pp. 805-818, 1968.
26. Dimant, Y., and Poreh, M., Heat Transfer in Flows with Drag Reduction, ***Adv. Heat Transfer,*** vol. 12, pp. 77-113, 1976.
27. Wells, C. S., Jr., Turbulent Heat Transfer in Drag Reducing Fluids, ***AIChE J., vol. 14,*** pp. 406-410, 1968.
28. Marrucci, G., and Astarita, G., Turbulent Heat Transfer in Viscoelastic Liquids, ***Znd. Eng. Chem. Fund.,*** vol. 6, pp. 470-471, 1967.
29. Gupta, M. K., Metzner, A. B., and Hartnett, J. P., Turbulent Heat Transfer Characteristics of Viscoelastic Fluids, ***Znt. J. Heat Mass Transfer,*** vol. 10, pp.1211-1224, 1967.

© 1983 Hemisphere Publishing Corporation

2.5.13

Heat transfer in liquid metals

V. M. Borishanski and E. V. Firsova

■ Liquid metals differ from gases and other liquids in that their thermal diffusivity is considerably greater than their kinematic viscosity, that is, Pr ≪ 1. Molecular heat transfer in the laminar or turbulent flow of a liquid metal plays a significant part in both the boundary layer and turbulent core. The Nusselt number is a function of the Péclet number, Nu = f(Pe).

A. Flow in channels

(a) Tubes

The Nusselt number ($0.007 \leqslant \mathrm{Pr} \leqslant 0.03$) for liquid metals flowing in tubes with $l/d \geq 30$ is given by

$$\mathrm{Nu} = 7.5 + 0.005\,\mathrm{Pe} \qquad (300 \leqslant \mathrm{Pe} \leqslant 10^4) \tag{1}$$

when q_w = const [1,2], and

$$\mathrm{Nu} = 5 + 0.025\,\mathrm{Pe}^{0.8} \qquad (100 \leqslant \mathrm{Pe} \leqslant 2.10^4) \tag{2}$$

when t_w = const [3, 4]. In the range $30 \leqslant \mathrm{Pe} \leqslant 300$, the following formula is recommended for q_w = const :

$$\mathrm{Nu} = 4.36 + 0.016\,\mathrm{Pe} \tag{3}$$

This formula provides a limiting transition to the calculated value of the Nusselt number for fully developed laminar flow.

These formulas are valid for both the heating and cooling of a tube under the condition that the impurity (oxygen, nitrogen, etc.) content in the liquid metal is less than the oxide solubility limit at the operating temperature. If this is not true, the heat transfer coefficient is greatly decreased because of the increased resistance to heat transfer at the wall-fluid boundary. The minimum value of the Nusselt number when heating a liquid metal contaminated with impurities may be found [1],

$$\mathrm{Nu} = 4.3 + 0.002\,1\,\mathrm{Pe} \qquad \text{when } 100 \leqslant \mathrm{Pe} \leqslant 10^4 \tag{4}$$

The thermal resistance at the wall-boundary interface may have various values depending on the physicochemical properties of the coolant. Several cases taking into account the thermal junction resistance effect on the Nusselt number are given in [5].

(b) Annular channels

The Nusselt number for the turbulent flow of liquid metals ($0.007 \leqslant \mathrm{Pr} \leqslant 0.03$) in annular channels, in contrast to flow in pipes, depends on the diameter ratio of the pipes forming the channel, as well as on the nature of heat input (outside, inside, or both).

With unequal heat fluxes it is necessary to check the calculated wall temperature, since under certain heat flux conditions the concept of the heat transfer coefficient loses its meaning (wall temperature T_1 or T_2 becomes equal to the mean mixed temperature of liquid T_b). There is also a possibility that heat will be transferred from one wall to another. As shown by a special analysis [6], even at equal heat fluxes or equal temperatures, annular channels with $d_2/d_1 \geqslant 3$ are not recommended for practical uses.

The Nusselt number for the turbulent flow of pure liquid metal in an annular channel for an outside wall (Nu_2) and an inside wall (Nu_1) with one-sided or two-

© 1983 Hemisphere I blishing Corporation

sided heating or cooling is given by [6]

$$\mathrm{Nu} = a + b(\bar{\epsilon}\ \mathrm{X}\ \mathrm{Pe})^c \quad (5)$$

where a, b, c are functions of the ratio of the channel s outside diameter to inside diameter and of the nature of the heat input or output. Numerical values of the coefficients a, b, c are given in Table 1. The characteristic dimension used in the Nusselt number is the hydraulic diameter. Equation (5) is valid for $\bar{\epsilon} \geqslant 0$ [7], where

$$\bar{\epsilon} = 1 - \frac{1.82}{\mathrm{Pr}\,(\nu_T/\nu)_{\max}^{1.4}} \quad (6)$$

The ratio $(\nu_T/\nu)_{\max}$ for an annular gap is expressed by the relationship

$$\frac{\nu_T}{0\,\nu}_{max} = 4.0 + 0.002\,897\,\mathrm{Re}^{0.919} \quad (7)$$

$$\mathrm{Re} = \frac{w(d_2 - d_1)}{\nu}$$

(c) Cross flow

The Nusselt number for the cross flow of a liquid metal past staggered and in-line tube bundles for $0.007 \leqslant \mathrm{Pr} \leqslant 0.03$ and $10 \leqslant \mathrm{Pe} \leqslant 1\,300$ can be calculated using [8]

$$Nu = 2\,\mathrm{Pe}^{0.5} \quad (8)$$

where Pe is defined using the velocity of the stream approaching the bundle. The characteristic dimension is the outside diameter of the tubes of the bundle. The thermophysical properties of coolants are evaluated at the mean bulk temperature.

The Nusselt number for liquid metal flow past plain tube bundles when the angle ψ (the acute angle between flow direction and tube axis) is in the range of 30-90 for $0.007 \leqslant \mathrm{Pr} \leqslant 0.03$ and $10 \leqslant \mathrm{Pe} \leqslant 700$ is [9]

$$\mathrm{Nu}_\psi = \mathrm{Nu}\ (\sin\psi)^{0.4} \quad (9)$$

where Nu is the Nusselt number for cross flow, Eq. (8). The characteristic dimension used for the Nusselt and Péclet numbers is the outside tube diameter.

The thermophysical properties are evaluated at the mean flow temperature.

(d) In-line flow through rod bundles

The Nusselt number for cross liquid metal flow past bundles of tubes arranged in an equilateral triangle for $0.007 \leqslant \mathrm{Pr} \leqslant 0.03$ and $1.1 < P/d \leqslant 1.5$ may be calculated from the formula [10]

Laminar flow $30 < \mathrm{Pe} \leqslant 200$:

$$\mathrm{Nu}_{mc} = 24.15 \log\left[-8.12 + 12.76\,\frac{P}{d} - 3.65\left(\frac{P}{d}\right)^2\right] \quad (10)$$

Turbulent flow $200 < \mathrm{Pe} \leqslant 2\,000$:

$$\mathrm{Nu} = \mathrm{Nu}_{,} + 0.017\,4\left\{1 - \exp\left[-6\left(\frac{P}{d} - 1\right)\right]\right\} X\ (\mathrm{Pe} - 200)^{0.9} \quad (11)$$

where $\mathrm{Nu}_{,}$ is calculated from Eq. (10). The charac-

Table 1 Empirical constants in Eq. (5) for heat transfer to liquid metals flowing in concentric annuli under conditions of uniform heat fluxes and fully developed velocity and temperature profiles (turbulent flow)

Conditions of heat transfer	Nusselt $\frac{d}{d_1} = y$	a		b	c
Heat transfer from inner wall only	Nu_1	1-7	$4.82 + 0.697y$	0.022 2	$0.758y^{0.053}$
Heat transfer from outer wall only	Nu_2	1-7	$5.54 - 0.023y$	$0.018\,9 + 0.003\,16y + 0.000\,086\,7y^2$	$0.758y^{-0.020\,4}$
Equal heat fluxes from both walls	Nu_1	1.0	9.49	0.059 6	0.688
		1.25	10.53	0.066 2	0.698
		1.50	11.81	0.072 6	0.701
		2.0	15.30	0.085 5	0.704
		3.00	27.0	0.109 5	0.707
		4.00	50.0	0.127 8	0.708
Equal heat fluxes from both walls	Nu_2	1.00	9.49	0.059 6	0.688
		1.25	8.72	0.049 0	0.707
		1.50	8.24	0.042 0	0.723
		2.0	7.60	0.037 9	0.735
		3.0	6.94	0.036 0	0.741
		4.0	6.64	0.355	0.743
Heat transfer from both walls, with $T_1 = T_2$ at any axial position	Nu_1	1-7	$7.82 + 1.72y - 0.051y^2$	$0.059\,2 - 0.000\,342y + 0.000\,723\,y^2$	$0.655 + 0.363y - 0.003\,7y^2$
	Nu,	1-7	$7.11 + 3.22/y - 0.842/y^2$	$0.039\,6 + 0.020\,0/y$	$0.746 - 0.086\,4/y + 0.028\,2/y=$

© 1983 Hemisphere Publishing Corporation

teristic dimension used in Nu and Pe is the equivalent diameter of the bundle with an infinite number of tubes arranged in an equilateral triangle,

$$D_h = d\left[1.1\left(\frac{P}{d}\right)^2 - 1\right] \quad (12)$$

where P/d is the relative pitch of an equilateral tube bundle. The thermophysical properties of coolants are evaluated at the mean flow temperature.

For relative pitches $P/d < 1.1$, the mean Nusselt number depends on the thermal boundary condition [1, 11].

B. Liquid metal heat exchangers

Liquid metal heat exchangers differ substantially from those with conventional coolants because the coolants have small heat capacities and large thermal conductivities and the conduction of heat in the direction of flow may be much larger than that between the coolants (if values of Pe are not very large). As a result, temperature irregularities across the heat exchanger play an important part and lead to a decrease in the exchanger s effectiveness [I] .

The use of the conventional formula

$$Q = UA\ \mathrm{AT},, \quad (13)$$

for calculating the heat transfer in liquid metal heat exchangers requires that the coefficient U be defined empirically for the specific device. As a consequence, this value is substantially less than the calculated value obtained from the formula.

For example, the respective values of U for the sodium-sodium heat exchanger for the Enrico Fermi reactor are 3 700 and 8 200 W/m^2 K [12], and for the heat exchanger for the Phenix reactor are 8 600 and 11 200 W/m^2 K [13, 14] (in the latter case values were calculated using the recommendations [5]).

Inefficient utilization of the heat transferring surface is caused by the fact that local coolant rates are nonuniformly distributed across the bundle. Among the factors causing this nonuniformity is the deformation of tubes in the bundle resulting from their different thermal expansions. It changes the tube packing in the bundle and causes the formation of regions having more or less of a tight packing when compared with the mean tightness across the bundle. Additional effects are caused by the side inlet and outlet of coolant on the shell side, by the nonuniform inlet of coolant along the bundle perimeter, by leakages along the shell, and by nonuniform coolant distribution in the tubes. In [11, 15, 16] an approach is outlined for taking into account the effect of the complicated nature of coolant flow on the heat transfer in tube bundles. A semiempirical method is also suggested for defining the correction factor presented in Eq. (13) that is directly applicable for engineering calculations [15, 16]. The heat exchanger nonuniformity parameter is introduced representing the quantitative characteristic of the mentioned factors influence on the decrease of heat transfer efficiency [16]. The following formulas are used for calculating:

$$\dot{Q} = UA\ \Delta Tm \quad (14)$$

$$Q = Cp_2 M_2 (T_{2,\mathrm{out}} - T_{2,\mathrm{in}}) = \eta_2 Cp_2 \dot{M}_2 (T_{1,\mathrm{in}} - T_{2,\mathrm{in}}) \quad (15)$$

where

$$\mathrm{AT},, = \psi\ \mathrm{AT},,$$

$\psi < 1$ is a correction function, $\psi = \psi(\eta_2, m, \epsilon)$

$$\psi = \frac{m-\epsilon}{m-1} \frac{\ln\left[(m-\eta_2)/m(1-\eta_2)\right]}{\ln\left[\epsilon(m-\eta_2)/m(\epsilon-\eta_2)\right]} \quad \text{for } \eta_2 < m \quad (16)$$

$$\psi = \frac{\epsilon-\eta_2}{1-\eta_2} \quad \text{for } \eta_2 = m \quad (17)$$

$$\psi = \frac{\epsilon(\epsilon-\eta_2)}{\eta_2(1-\epsilon)} \ln\frac{\epsilon(1-\eta_2)}{\epsilon-\eta_2} \quad \text{for } m = \epsilon \quad (18)$$

$$\psi = \frac{\eta_2(1-\epsilon)}{1-\eta_2} \frac{1}{\ln\left[\epsilon(1-\eta_2)/(\epsilon-\eta_2)\right]} \quad \text{form} = \mathrm{I} \quad (19)$$

$$m = \frac{Cp_1 M_1}{Cp_2 \dot{M}_2}$$

is the water equivalents ratio of heating and heated coolants.

η_2 is the heat exchanger efficiency defined as a temperature excess of cold coolant, Eq. (15). The nonuniformity factor ϵ is defined empirically [15]. Its recommended value is $\epsilon = 0.85$ [17]. For counterflow heat exchangers, $\eta_2 < \epsilon < 1$.

Nomenclature** for **Section 2.5.13 appears at the beginning** of **Part 2.

REFERENCES FOR SECTION 2.5 .13

1. Borishanski, V. M., Kutateladze, S. S., Novikov, I. I., and Fedinski, 0. S., ***Liquid Metal Coolant Media,*** Atomizdat, MOSCOW, 1976.
2. Nuclear Reactor Heat Exchanger Code: Heat Transfer and Hydraulic Resistance, pp. 36-41, RTM 24.031.05-72, MOSCOW, 1972.

© 1983 Hemisphere Publishing Corporation

3. Seban, R. A., and Shimazaki, T. T., Heat Transfer to a Fluid Flowing Turbulently in Smooth Pipe with Wall at Constant Temperature, *Trans. ASME*, vol. 72, no. 6, p. 789, 1950.
4. Kirillov, P. L., Generalization of Experimental Data on Heat Transfer in Molten Metals, *At. Energy,* vol. 13, no. 5, p. 481, 1962.
5. Andreev, P. A., Borishanski, V. M., and Firsova, E. V., Heat Transfer in Liquid Metals, *Energomachinostroenie,* no. 8, pp. 37-38, 1972.
6. Dwyer, 0. E., and Tu, P. S., Bilateral Heat Transfer to Liquid Metals Flowing Turbulently through Annuli. *Nucl. Sci. Eng.,* vol. 21, p. 90, 1965.
7. Dwyer, 0. E., and Tu, P. S., Unilateral Heat Transfer to Liquid Metals Flowing in Annuli. *Nucl. Sci. Eng.,* vol. 15, pp. 58-68, 1963.
8. Borishanski, V. M., Zhinkina, V. B., and Firsova, E. V., Convective Heat Transfer in Steam Generator and Heat Exchanger Components. *Trudi CKTI,* no. 86, pp. 58-64, 1968.
9. Borishanski, V. M., Gotovski, M. A., Zhinkina, V. B., Shneiderman, L. L., and Firsova, E. V., Heat Transfer to Liquid Metals Flowing through Tube Bundles Being Inclined, *Eng. Phys. J.*, vol. 19, no. 6, pp. 977-982, 1970.
10. Borishanski, V. M., Gotovski, M. A., and Firsova, E. V., Heat Transfer to Liquid Metals Flowing in-Line through a Rod Bundle, *At. Energy,* vol. 27, no. 6, pp. 549-552, 1967.
11. Subbotin, V. I., Ibragimov, M. H., Ushakov, P. A., Bobkov, V. P., Zhukov, A. V., and Jurjev, J. *S., Hydrodynamics and Heat Transfer in Atomic Power Plants Design,* Atomizdat, Moscow, 1975.
12. Zaman, S. U., Ford, J. A., and Wilber, H. A., Sodium Hydraulic and Thermal Performance of the Enrico Fermi Reactor through *200* MW, *Trans. ANS,* vol. 14, suppl. 2, pp. 16-17, 1971.
13. Befre, I. L., Delishe, I. P., and Robin, M. G., La Centrale Phenix: Circuits et Composants Principaux, *Nucl. Eng. Int.*, vol. 16, no. 182, pp. 567-570, 1971.
14. Robin, M. G., Performances de Générateur de Vapeur du Phenix. Comparées du Prévisions, *Communication francaise*, no. 1, pp. 1-6, Dimitrovgrad, 1975.
15. Andreev, P. A., Borishanski, V. M., Gotovski, M. A., Firsova, E. V., Lebedev, M. E., and Mizonov, N. V., Contribution to Design of the Countercurrent Liquid Metal Heat Exchangers, *Trudi CKTI,* no. 131, pp. 3-20, 1975.
16. Gotovski, M. A., Lebedev, M. E., Mizonov, N. V., and Firsova, E. V., Thermohydraulic Irregularities Influence on the Effectiveness of Shell and Tube Counter Flow Heat Exchangers, *Proc. 6th Int. Heat Transfer Conf., Toronto, August 7-11, 1978,* vol. 4, pp. 213-217, 1978.
17. Borishanski, V. M., Gotovski, M. A., Lebedev, M. E., Mizonov, N. V., and Firsova, E. V., Mean Temperature Difference and Effectiveness of Liquid-Metal Heat Exchangers, *in Single-Phase Flow Heat Exchange nnd Hydrodynamics in Rod Bundles,* Nauka, Leningrad, pp. 68-78, 1979.

© 1983 Hemisphere Publishing Corporation

2 . 7

Boiling and evaporation

Contents

2.7.1
BOILING OF SINGLE-COMPONENT LIQUIDS: BASIC PROCESSES, J. G. Collier 2.7.1-1

A. Vapor formation **2.7.1-1**
B. Evaporation 2.7.1-2
C. Homogeneous nucleation **2.7.1-2**
D. Heterogeneous nucleation **2.7.1-3**
E. Sizing of active nucleation sites **2.7.1-5**
F. Bubble growth **2.7.1-6**
G. Bubble detachment and frequency **2.7.1-7**

References for Section 2.7.1 **2.7.1-8**

2.7.2
POOL BOILING, J. G. Collier 2.7.2-1

A. The onset of nucleate boiling **2.7.2-2**
B. Nucleate boiling **2.7.2-3**
C. Critical heat flux **2.7.2-9**
D. Transition boiling **2.7.2-13**
E. Minimum heat flux **2.7.2-13**
F. Film boiling **2.7.2-14**

References for Section 2.7.2 **2.7.2-15**

2.7.3
BOILING WITHIN VERTICAL TUBES, J. G. Collier 2.7.3-1

A. Introduction **2.7.3-1**
B. Subcooled boiling **2.7.3-5**
C. Saturated boiling **2.7.3-9**
D. Critical heat flux **2.7.3-12**
E. Heat transfer in areas where the critical heat flux has been exceeded **2.7.3-30**

References for Section 2.7.3 **2.7.3-34**

2.7.4
CONVECTIVE BOILING INSIDE HORIZONTAL TUBES, J. G. Collier 2.7.4-1

A. Dryout in horizontal tubes, bends, and coils 2.7.4-1
B. Heat transfer rates in horizontal tubes, bends, and coils **2.7.4-4**

References for Section 2.7.4 **2.7.4-6**

2.7.5
BOILING OUTSIDE TUBES AND TUBE BUNDLES, J. G. Collier 2.7.5-1

A. Boiling outside single tubes in cross flow 2.7.5-1
B. Critical heat flux outside single tubes in cross flow **2.7.5-2**
C. Film boiling **2.7.5-3**
D. Boiling on the outside of tubes within a horizontal tube bundle **2.7.5-4**
E. Heat transfer rates outside horizontal tubes in tube bundles **2.7.5-4**
F. Critical heat flux outside horizontal tubes in tube bundles **2.7.5-5**

References for Section 2.7.5 **2.7.5-7**

© 1983 Hemisphere Publishing Corporation

2.7.6
BOILING OF BINARY AND MULTICOMPONENT MIXTURES: BASIC PROCESSES, J. G. Collier 2.7.6-1

A. Elementary phase equilibrium 2.7.6-1

References for Section 2.7.6 2.7.6-7

2.7.7
BOILING OF BINARY AND MULTICOMPONENT MIXTURES: POOL BOILING, J. G. Collier 2.7.7-1

A. Nucleate boiling 2.7.7-1
B. Critical heat flux 2.7.7-4
C. Transition boiling 2.7.7-5
D. Minimum heat flux 2.7.7-5
E. Film boiling 2.7.7-6

References for Section 2.7.7 2.7.7-7

2.7.8
BOILING OF BINARY AND MULTICOMPONENT MIXTURES: FORCED CONVECTION BOILING, J. G. Collier 2.7.8-1

A. Saturated nucleate boiling 2.7.8-1
B. Two-phase forced convection region 2.7.8-2
C. Simplified treatment for binary and multicomponent evaporation 2.7.8-3
D. Interfacial mass transfer during evaporation of binary and multicomponent mixtures 2.7.8-4
E. Critical heat flux in forced convection boiling 2.7.8-6

Nomenclature for Sections 2.7.1-2.7.8 2.7.8-8
References for Section 2.7.8 2.7.8-10

2.7.9
AUGMENTATION OF BOILING AND EVAPORATION, Arthur E. Bergles 2.7.9-1

A. Pool boiling 2.7.9-1
B. Boiling within tubes 2.7.9-3

References for Section 2.7.9 2.7.9-4

© 1983 Hemisphere Publishing Corporation

2.7.1

Boiling of single-component liquids: Basic processes

J. G. Collier

A. Vapor formation

Figure 1 shows diagramatically the pressure-volume isotherms for a pure single-component substance. For a constant temperature ***T,*** the pressure and volume vary along a line such as ***ABFG.*** Liquid only exists along the line ***AB,*** and vapor only exists along the line ***FG.*** Liquid and vapor coexist along the line ***BDF. The*** saturation curve is the locus of points such as ***B*** and ***F.*** Corresponding values of the pressure and temperature taken from the curve ***BDF are*** known as the ***saturation pressure*** (p_{sat}) and ***saturation temperature*** (T_{sat}), respectively. So far, only ***stable*** equilibrium phase states have been considered. Other ***metasatable*** or ***unstable*** states can occur. For example, it is possible with care to reduce the pressure imposed on a liquid at constant temperature along a line ***AB*** without the formation of vapor at point ***B.*** Likewise, it is possible to increase the pressure imposed on a vapor along a line ***G F*** without the formation of liquid at ***F.*** The coordinates of these metastable states he along an extrapolation of ***AB*** to C or ***GF*** to ***E.*** Points in the metastable region may also be reached by carefully increasing the liquid temperature above the saturation temperature corresponding to the imposed static pressure; this process is referred to as ***superheating*** and the metastable liquid state is referred to as ***superheated liquid.***

The author thanks the United Kingdom Atomic Energy Authority (UKAEA) for permission to use Figs. 2.7.1(1), 2.7.1(3), 2.7.1(4), 2.7.2(1), 2.7.3(1), 2.7.3(2), 2.7.3(3), 2.7.3(4), 2.7.3(5), 2.7.3(6), 2.7.3(8), 2.7.3(10), 2.7.3(13), 2.7.3(14), 2.7.3(15), 2.7.3(16), 2.7.3(17), 2.7.3(18), 2.7.3(19), 2.7.3(20), 2.7.3(21), 2.7.3(22), 2.7.3(23), 2.7.3(26), 2.7.3(29), 2.7.3(31), 2.7.4(3), 2.7.5(2), and 2.7.5(7), and Table 2.7.6(1), which remain UKAEA copyright material.

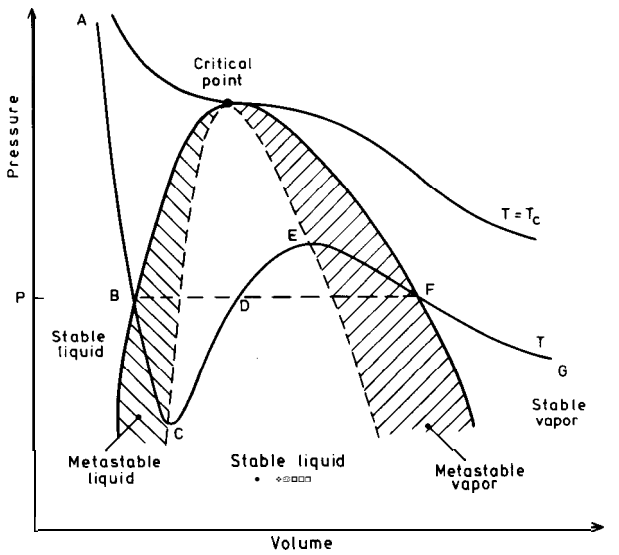

Figure **1** Pressure-volume surface for a pure substance.

Vapor and liquid phases can coexist in unstable equilibrium states along lines such as ***BC*** or ***FE.*** In this instance the pressures in the liquid and vapor in the vicinity of the interface are no longer equal at equilibrium. If the interface is concave with the center of curvature in the vapor phase, then the vapor pressure (p_g) will be greater than the liquid pressure (p_ℓ) by an amount given by the relationship

$$p_g - p_\ell = \sigma\left(\frac{1}{r_1} + \frac{1}{r_2}\right) \tag{1}$$

© 1983 Hemisphere F blishing Corporation

where σ is the surface tension and r_1 and r_2 are the respective radii of curvature of the interface. Because of the increased vapor pressure, the number of molecules striking and being absorbed by the interface from the vapor phase is greater than when the interface was planar. To maintain equilibrium, the number of molecules emitted through the interface from the liquid must increase correspondingly. This increase can be accomplished only by increasing the temperature of the system (liquid and vapor) above that necessary for equilibrium with a planar interface, i.e., the saturation temperature (T_{sat}) corresponding to the liquid pressure (p_ℓ). Therefore the liquid adajcent to the curved interface is superheated with respect to the imposed liquid pressure. This latter equilibrium state is unstable, since any change in the curvature of the interface in either sense will result in a divergent departure from the equilibrium state.

To summarize, vapor may form in one of three ways, each corresponding to departure from an equilibrium liquid-vapor state:

1. Formation of vapor at a planar interface corresponds to departure from a stable equilibrium state and occurs when the liquid temperature is increased above or the local vapor pressure is reduced below the corresponding saturation condition. ***The*** term ***evaporation*** will be reserved for this process.

2. Formation of vapor nuclei within a liquid held at a temperature above or at a static pressure below the saturation condition corresponds to departure from a metastable equilibrium state. The term ***homogeneous nucleation*** is reserved to describe this situation.

3. Formation of vapor at a preexisting vapor nucleus within a liquid corresponds to departure from an unstable equilibrium state. The term ***heterogeneous nucleation*** will be used to describe this process.

B. Evaporation

Phase change at a planar interface can be viewed from the standpoint of kinetic theory as the difference between two molecular fluxes-a rate of arrival of molecules from the vapor space toward the interface and a rate of departure of molecules from the surface of the liquid into the vapor space. During evaporation the departure rate exceeds the arrival rate, during condensation the reverse occurs, and at equilibrium the two rates are equal. On this simple basis, the net flux $(\dot{m})$ is given by

$$\dot{m} = \left(\frac{\tilde{M}}{2\pi\tilde{R}T}\right)^{1/2} \Delta p \tag{2}$$

For evaporation to take place, the vapor pressure must be less than the liquid pressure or, alternatively, the liquid must be at a temperature ΔT above the thermostatic saturation temperature corresponding to the prevailing vapor pressure. An interfacial heat transfer coefficient (α_i) can be defined as

$$\alpha_i = \frac{\dot{q}}{\Delta T} = \frac{\dot{m}\Delta h_v}{\Delta T} \tag{3}$$

From Eqs. (2) and (3) and using the Clausius-Clapeyron relationship,

$$\alpha_i = \left(\frac{\tilde{M}}{2\pi\tilde{R}}\right)^{1/2} \frac{\Delta h_v^2}{T^{3/2}(v_g - v_\ell)} \tag{4}$$

Whether liquids evaporate at the maximum rate calculated by Eq. (2) has been hotly debated for many years. Various experimental studies seem to lead to the conclusion that polar liquids vaporize at rates significantly less than the maximum rate, whereas nonpolar liquids vaporize at the maximum rate. For water, for example, it is commonly reported that the evaporation rate and therefore the interfacial heat transfer coefficient is 0.03-0.05 of the maximum value given by Eqs. (2) and (4), respectively. However, more recent experiments have indicated that for both nonpolar and polar liquids [1], even water [2, 3], the maximum rate is achieved and that experimental uncertainty about the liquid surface temperature is responsible for the reported very low values in the literature. It has been established that the rate of evaporation falls rapidly as the time of exposure of the evaporating interface is increased. Temperature gradients are set up in the liquid phase adjacent to the interface in order to supply the latent heat of the net vapor flux. A simple transient conduction analysis [4] based on the Plesset-Zwick approach (see Sec. F) will yield the following equation for the effective interface heat transfer coefficient after an exposure time (t):

$$\alpha_i = \frac{\sqrt{3}\lambda_\ell}{\sqrt{\pi\kappa t}} \tag{5}$$

For water, the interfacial heat transfer coefficient falls from the maximum value given by Eq. (4) to the much lower values given by Eq. (5) within a few milliseconds (see Fig. 2).

C. Homogeneous nucleation

Initial considerations relating to the formation of vapor from a metastable liquid or an unstable equilibrium state invariably start from the equation defining the mechanical equilibrium of a spherical vapor nucleus (radius r^*) in a liquid at a constant temperature (T_g) and pressure (p_ℓ). Thus

© 1983 Hemisphere Publishing Corporation

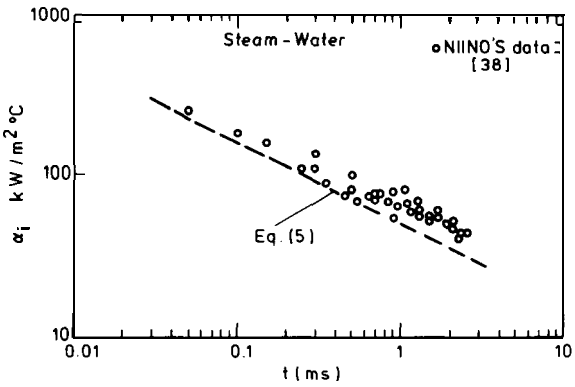

Figure 2 Interfacial heat transfer coefficient for water as a function of exposure time.

$$p_g - p_\ell = \frac{2\sigma}{r^*} \tag{6}$$

where p_g is the vapor pressure inside the nucleus and p_ℓ is the imposed liquid pressure corresponding to a saturation temperature T_{sat}. To calculate the liquid superheat $(T_g - T_{sat})$ corresponding to the pressure difference $(p_g - p_\ell)$, use can be made of the Clausius-Clapeyron equation and the perfect gas law. The resulting equation is

$$T_g - T_{sat} = \frac{\tilde{R} T_{sat} T_g}{\Delta h_v \tilde{M}} \ln\left(1 + \frac{2\sigma}{p_\ell r^*}\right) \tag{7}$$

If $(2\sigma/p_\ell r^*) \ll 1$, then Eq. (7) simplifies to

$$T_g - T_{sat} = \frac{\tilde{R} T_{sat}^2}{\Delta h_v \tilde{M}} \frac{2\sigma}{p_\ell r^*} \tag{8}$$

It will be observed from this equation that the size of the equilibrium vapor nucleus (r*) becomes smaller as the superheat is increased, i.e., as a result of a decrease in system pressure (p_ℓ) along a line ***BC*** (Fig. 1). Close to C the size of the equilibrium nucleus approaches molecular dimensions. Thermal fluctuations occur in the metastable liquid, and there is a small but finite probability of a cluster of molecules with vaporlike energies coming together to form a vapor embryo of the size of the equilibrium nucleus. This probability is given in terms of the number of nuclei of radius ***(r*)*** formed per unit volume per unit time:

$$\frac{dn}{dt} = N\left(\frac{2\sigma}{\pi m}\right)^{1/2} \exp\left[\frac{-16\pi\sigma^3}{3kT_g(p_g - p_\ell)^2}\right] \tag{9}$$

The rate of homogeneous nucleation (dn/dt) is an extremely sensitive function of the superheated liquid temperature (T_g). At low superheats the rate is insignificantly small, but it increases very rapidly as the superheat is increased. Significant nucleation occurs for values of dn/dt between 10^9 and $10^{13}\,m^{-3}s^{-1}$. For benzene these values correspond to a very narrow range of temperature from 224 to 225.2°C, respectively. Table 1 gives similar values of limiting superheat for other organics both calculated from Eq. (9) (with $dn/dt \cong 10^{12}\,m^{-3}s^{-1}$) and measured experimentally.

Equation (9) is in a rather awkward form to evaluate T_g, and a rather simple expression sufficiently accurate for most purposes has been proposed by Lienhard [5] on the basis of the measurements of Skripov [6]:

$$T_{r,g} - T_{r,sat} = 0.905 - T_{r,sat} + 0.095 T_{r,sat}^8 \tag{10}$$

where the subscript ***r*** refers to a reduced quantity, i.e., an absolute temperature divided by the critical temperature.

For water at atmospheric pressure, the liquid temperature corresponding to a dn/dt of $10^{13}\,m^{-3}s^{-1}$ is 320.7°C, i.e., a superheat of 220.7°C. This value is much higher than any experimental measurement for water, even under very carefully controlled conditions. For water, at least, homogeneous nucleation from a metastable liquid state can be discounted as a mechanism for vapor formation. However, homogeneous nucleation can and does occur in organic liquids. The reader is referred to the review by Blander and Katz [7] for further details.

D. Heterogeneous nucleation

Noncondensable gas bubbles or foreign bodies held in suspension in the liquid, together with gas- or vapor-filled cracks or cavities in container surfaces (known as ***nucleation sites),*** normally provide ample nuclei to act as centers of vapor formation. The presence of a dissolved gas in the liquid necessitates the gas partial pressure being taken into account when considering the mechanical equilibrium of the vapor nucleus. Thus Eq. (6) is modified to

$$p_g + p_a - p_\ell = \frac{2\sigma}{r^*} \tag{11}$$

and Eq. (7) to

$$T_g - T_{sat} = \frac{\tilde{R} T_{sat} T_g}{\Delta h_v \tilde{M}} \ln\left[1 + \left(\frac{2\sigma}{p_\ell r^*} - \frac{p_a}{p_\ell}\right)\right] \tag{12}$$

The presence of dissolved gas reduces the superheat required to maintain a bubble of radius ***r**** in unstable equilibrium. In practice, the evaluation of the gas partial pressure may be complicated by the presence of temperature gradients and finite rates of diffusion of gas through the liquid.

On any container surface there will be pits or cavities having relatively small included angles (Fig. 3). Consideration of the successive positions of the inter-

© 1983 Hemisphere Publishing Corporation

Table 1 Homogeneous nucleation: limits of superheat at 1 atm[a,b]

Substance	T_{sat}, °C	T_g, °C Meas.	T_g, °C Calc.	Meas. T_g/T_c, K/K	References
Normal alkanes					
Methane	-161.5	–	-107.5	–	[33]
Ethane	-88.6	–4	-3.5	0.881	[33]
Propane	-42.1	53.0	55.3	0.882	[33, 34]
Butane	–0.5	105.0	105.2	0.890	[31, 34]
Pentane	36.0	147.8	148.3	0.896	[6, 29, 35, 36]
Hexane	68.7	184	184.3	0.901	[6, 28, 29, 36]
Heptane	98.0	214	214.5	0.902	[6, 28, 31, 36]
Octane	125.7	239.8	242.7	0.902	[6]
Nonane	150.8	265.3	262.0	0.906	[31]
Decane	174.1	285.1	282.8	0.904	[31]
Branched alkanes					
2-Methylpropane	-11.8	87.8	87.7	0.884	[33]
2,2-Dimethylpropane	9.5	113.4	–	0.891	[31]
2-Methylbutane	27.9	139		0.895	[6, 36, 37]
2,3-Dimethylbutane	58.0	173.2	175.9	0.893	[31]
2,2,4-Trimethylpentane	99.2	215.3	214.9	0.898	[31]
Cyclic hydrocarbons					
Cyclopropane	-32.9	17.5	–	0.882	[33]
Cyclopentane	49.3	183.8	173.2	0.893	[31]
Cyclohexane	80.7	219.6	216.3	0.890	[6, 31, 361
Cyclooctane	148.5	287.5	–	–	[31]
Methylcyclopentane	71.8	202.9	–	0.894	[31]
Methylcyclohexane	100.9	237.2	232.0	0.892	[31]
Benzene	80.1	225.3	–	0.887	[6, 32, 35]
1,3-Dimethylbenzene	139.1	235	–	0.824	[32] (c)
Alkenes and Alkynes					
Propene	-47.7	52.4	50.3	0.882	[33]
Propadiene	-34.5	73.0	–	0.881	[33]
Propyne	-23.2	83.6	88.2	0.887	[33]
1-Butene	-6.3	97.8	100.2	0.884	[33]
cis-2-Butene	3.7	112.2	–	0.885	[33]
trans-2-Butene	0.9	106.5		0.886	[33]
2-Methylpropene	-6.9	96.4	i-9.3	0.884	[33]
1,3-Butadiene	–4.4	104.1		0.888	[33]
1-Pentene	30.0	144	141.9	0.898	[31]
1-Octene	121.3	237.1	–	0.901	[31]
1-Hexyne	71.3	192	–		[31]
Cyclopentene	44.2	178.2	–	0.892	[31]
Halocarbons					
Chloromethane	-24.2	93.0	–	0.880	[33]
1,1-Difluoroethane	-24.7	70.4	–	0.889	[33]
Chloroethene	13.9	100.9	–	0.867	[33]
Fluoroethene	-72.2	16.9	–	0.885	[33]
Ethyl chloride	12.3	126	–	0.867	[37]
Chloroform	61.7	173	–	0.832	[32] (c)
Chlorobenzene	132	250	–	0.827	[32] (c)
Bromobenzene	156	261		0.197	[32] (c)
Hexafluorobenzene	74.5	194.7	195.4	0.905	[6, 34]
Perfluoropentane	27.0	108.3	108.9	0.904	[6]
Perfluorohexane	50.9	136.6	137.4	0.915	[6]
Perfluoroheptane	70.9	161.6	161.2	0.916	[6]
Perfluorooctane	94.8	183.8	185.2	0.910	[6]
Perfluorononane	114.5	205.3	205.7	0.913	[6]
Perfluorodecane	133.0	223.9	223.1	0.917	[6]
Methanol	65.0	186.0	186.5	0.896	[6, 30, 32] (c)
Ethanol	78.5	189.5	191.8	0.896	[6, 30, 32] (c)
Acetone	56.2	174	–	0.879	[32] (c)
Carbon disulfide	46.3	168	–	0.803	[32] (c)
Sulfur dioxide	-10	50	–	0.750	[32] (c)
Aniline	184.1	262	–	0.766	[32] (c)
Diethyl ether	34.5	147	145	0.901	[6, 32, 36, 37]

[a] From Blander and Katz [7].
[b] All measurements were by the droplet technique unless noted by a (c) in the last column.

© 1983 Hemisphere publishing Corporation

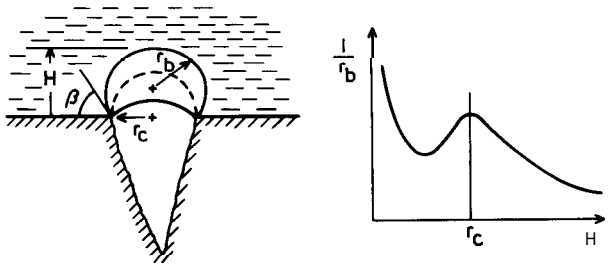

Figure 3 Interfacial curvature vs. bubble volume for nucleation site.

face within such a narrow crevice shows that the radius of curvature (r_b) increases until the interface reaches the lip of the crevice. As the bubble volume increases further, the radius of curvature temporarily decreases to that determined by the dimensions of the mouth of the crevice (r_c) before increasing again. The significant feature is that whereas the complete curve is both a function of cavity geometry and contact angle β, the minimum radius of curvature, which in turn dictates the superheat for a vapor bubble to form at this cavity, is always that determined by the mouth of the crevice provided that $\beta \leqslant 90^\circ$, i.e., the liquid wets the surface. This fact was verified experimentally by Griffith and Wallis [8].

E. Sizing of active nucleation sites

Only a very small fraction of the crevices and cavities in a surface are able to act as effective nucleation sites. To explain this it is necessary to consider what happens when an initially dry surface is flooded with liquid (Fig. 4). The advancing liquid will trap a mixture of air and vapor in the crevice (Fig. 4*a*). The air will rapidly dissolve and, if the liquid wets the cavity walls $(\beta < 90^\circ)$, then the remaining vapor pressure will be insufficient to balance the surface tension forces, leading to complete penetration of the liquid to the base of the crevice (Fig. 4b). A cavity that is completely filed with liquid cannot act as a nucleation site. If, however, the walls of the cavity are poorly wetted or irregular in shape, the curvature of the interface may reverse so that surface tension forces now resist further penetration even when the vapor

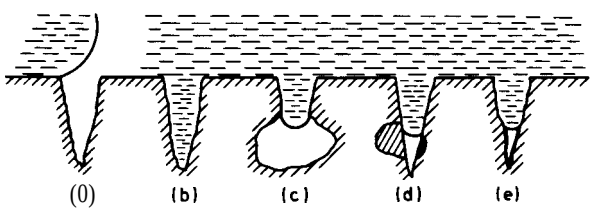

Figure 4 Formation of an active site. (a) Before filling. (b) Wetting cavity. (*c*) Reentrant cavity. (*d*) Nonwetting inclusion. (e) Nonwetting deposit.

pressure in the cavity is negligible. During subsequent heating the vapor pressure rises sharply, driving the interface back up to the mouth of the crevice. Stabilization of the interface within the crevice may occur as a result of an internal enlargement (Fig. 4*c*), as a result of a nonwetting inclusion in, say, a metal surface (Fig. 4*d*), or as a result of a nonwetting surface film or deposit (Fig. 4e). In this latter case the entire surface may be covered by such a film or deposit. When the surface is flooded, liquid is forced into the cavity by the imposed liquid pressure. If heat is applied to the surface subsequently, wetting may occur as a result of the dissolution of grease films in a solvent liquid or, in the case of liquid metals, a chemical reaction between a nonwetting surface oxide and the liquid metal. Nucleation is then initiated from the size of vapor embryo given by the minimum radius to which the liquid has penetrated into the cavity. Thus,

$$r = \frac{2\sigma}{p_\ell - (p_g + p_a)} \tag{13}$$

This relationship also gives the minimum neck radius of an active reentrant cavity for the case where $\beta \leqslant 90$. A number of experimental confirmations of this method of characterizing the size of active sites have been attempted [9–11], with varying amounts of success.

More recently, Lorentz et al. [12] have developed a model that takes into account both the wettability of the surface, in terms of the contact angle β, and the geometric shape of the cavity, in terms of the included angle ψ. The model assumes a conical cavity being inundated by an advancing liquid front (Fig. 5*a*). Once

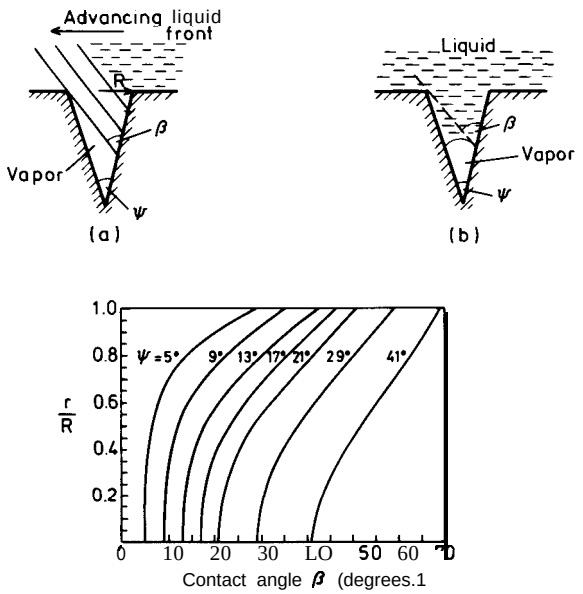

Figure 5 Vapor trapping model of Lorentz et al. [12] for sizing active cavities.

© 1983 Hemisphere I blishing Corporation

the vapor is trapped by the liquid, the interface readjusts to form a vapor embryo of radius r (Figure 5b). Conservation of vapor volume requires that r is a function of β and ψ (Fig. 5c). This model is useful in that if the size of active sites on a surface is known for one liquid, then the equivalent value of r for other liquids with different contact angles can be derived.

F. Bubble growth

Once the vapor nucleus in the superheated liquid has attained a size greater than that for unstable equilibrium, it will grow spontaneously. The growth rate is limited in the early stages by the inertia of the surrounding liquid and in the later stages by the rate at which the latent heat of vaporization can diffuse to the vapor-liquid interface. Mikic et al. [13] have examined vapor bubble growth close to a surface and within a liquid analytically. For a bubble growing in an initially uniformly superheated liquid from an initial radius greater than the critical radius (r*) given by Eq. (7), they give the following expression:

$$R^+ = \tfrac{2}{3}[(t^+ + 1)^{3/2} - (t^+)^{3/2} - 1] \qquad (14)$$

where

$$R^+ = \frac{RA}{B^2} \qquad t^+ = \frac{tA^2}{B^2}$$

$$A = \left(b\,\frac{\Delta T_{sat}\Delta h_v \rho_g}{T_{sat}\rho_\ell}\right)^{1/2} \qquad B = \left(\frac{12}{\pi}\,\mathrm{Ja}^2\kappa_\ell\right)^{1/2}$$

For bubble growth in an infinite medium $b = \frac{2}{3}$ and $\Delta T_{sat} = T_g - T_{sat}$. In the inertia-controlled region $t^+ \ll 1$, Eq. (14) becomes

$$R^+ = t^+ \qquad (15)$$

which is the well-known Rayleigh [14] solution. For the diffusion-controlled region $t^+ \gg 1$, Eq. (14) becomes

$$R^+ = (t^+)^{1/2} \qquad (16)$$

which is the asymptotic solution derived by Plesset and Zwick [15] and others. The validity of Eq. (14) was confirmed experimentally by Lien and Griffith [16], who measured the growth of vapor bubbles in superheated water over the pressure range 1.22 X 10^3 to 3.8 X 10^4 N/m^2, superheats in the range 8.3-15.5°C and 58 < Ja < 2 690. The excellent agreement is shown in Fig. 6.

Mikic et al. [13] extended their analysis to the case of vapor bubbles growing in nonuniform temperature fields adjacent to a heated surface. For this case b = n/7 and AT,,, = $T_w - T_{sat}$. For the inertia-controlled region Eq. (15) remains valid, whereas for the diffusion-controlled region the following expression is given:

$$R^+ = (t^+)^{1/2} - \theta\,[(t^+ + t_w^+)^{1/2} - (t_w^+)^{1/2}] \qquad (17)$$

t_w^+ is the dimensionless time (the *waiting time)* measured from the moment that the liquid at a uniform temperature T_ℓ comes into contact with the surface at a temperature T_w to the point of initiation of bubble

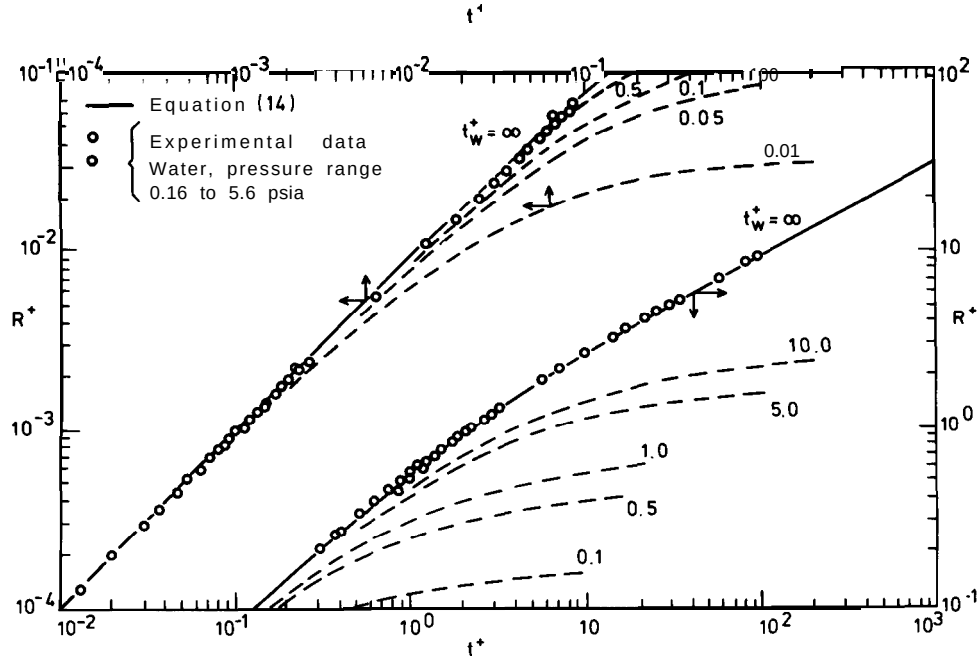

Figure 6 Bubble growth correlation of Mikic et al.[13] compared with the experimental results of Lien and Griffith [16].

© 1983 Hemisphere Publishing Corporation

growth; $\theta = (T_w - T_\ell)/(T_w - T_{sat})$. The effect of waiting time (t_w^+) on bubble growth rate is seen in Fig. 6. Experimental information for vapor bubble growth in nonuniform temperature fields under conditions where the waiting time t_w was measured are limited, but what data there are indicate lower growth rates than predicted by Eq. (14) by up to a factor of 2. This observation is qualitatively consistent with that predicted from the modified expression, Eq. (17).

The above relationships are valid only for situations where $\rho_g \ll \rho_\ell$. Corrections are necessary for situations where ρ_g/ρ_ℓ is significant [17]. The reader is referred to the review by Plesset and Prosperetti [18] for a more detailed discussion of bubble dynamics.

G. Bubble detachment and frequency

The size and shape of vapor bubbles departing from a heated surface are a strong function of the way in which they are formed. The prime forces acting on a vapor bubble during the later phases of its growth are buoyancy and hydrodynamic drag forces attempting to detach it from the surface, and surface tension and liquid inertia forces acting to prevent detachment. The growth velocity of a bubble and hence the inertial force is a strong function of the liquid superheat, which, in turn, is inversely proportional to the size of the active cavity. A small cavity thus forms a bubble with a faster growth rate than from a large cavity. Hatton and Hall [19] have considered all the forces acting on a growing bubble and have concluded that for small cavity sizes (I, < 10 μm for water at atmospheric pressure), the bubble size at departure is dictated mainly by a balance between buoyancy and liquid inertia forces. For larger cavity sizes, the growth rate decreases, the dynamic forces become small, and the bubble size at departure is set by a balance between buoyancy and surface tension forces [20]. Fritz [21] first considered this latter case and proposed the equation

$$D_b = 0.0208\beta \left[\frac{\sigma}{g_n(\rho_\ell - \rho_g)} \right]^{1/2} \tag{18}$$

When surface tension forces are dominant, the departing bubbles tend to be spherical. When inertial forces dominate, the bubble tends to be hemispherical; and when both forces are significant, the bubble has an oblate shape [22].

Equation (18) does not satisfactorily predict experimentally observed bubble departure diameters. However, a useful correlation of the data for various fluids $(p/p_c < 0.2)$ has been given by Cole and Rohsenow [23] (Fig. 7) as follows:

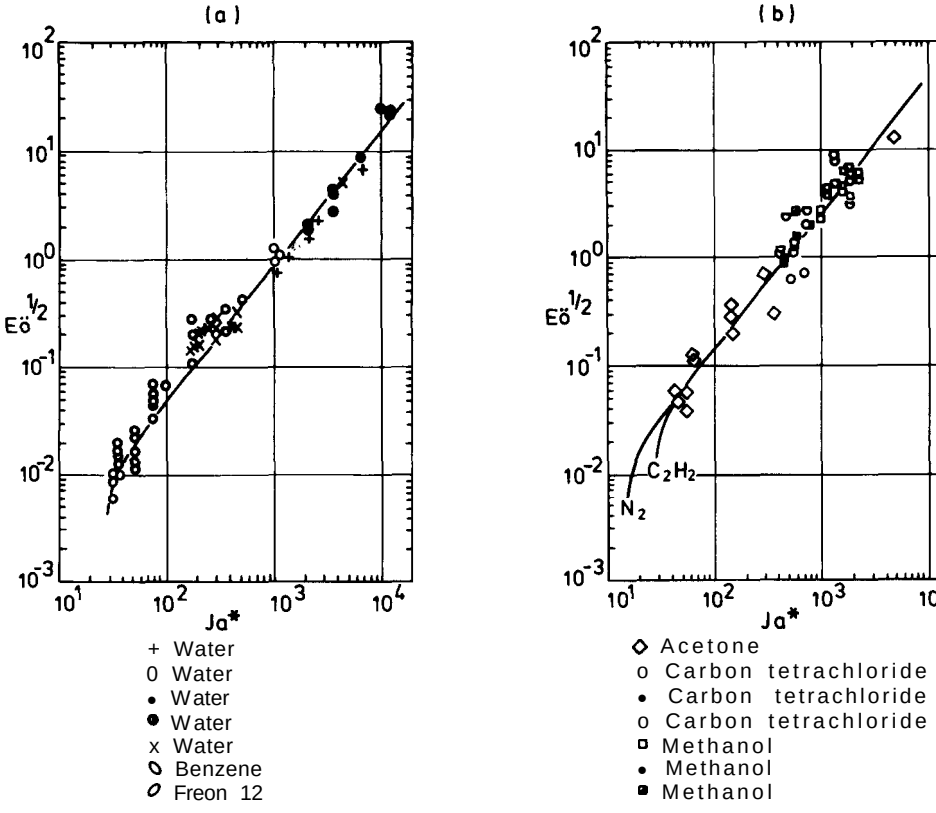

Figure 7 Bubble departure diameter correlation [23] (a) for water and (*b*) for other liquids.

© 1983 Hemisphere Publishing Corporation

For water: $Eö^{1/2} = 1.5 \times 10^{-4}(Ja^*)^{5/4}$

For other fluids: $Eö^{1/2} = 4.65 \times 10^{-4}(Ja^*)^{5/4}$ (19)

where

$$Eö = \frac{g_n(\rho_\ell - \rho_g)D_b^2}{\sigma} \qquad Ja^* = \frac{\rho_\ell c_{p\ell} T_{sat}}{\rho_g \Delta h_v}$$

Cooper et al. [24] have recently examined the behavior of vapor bubbles growing at a plane wall into a stagnant uniformly superheated liquid under both gravity and gravity-free conditions. Expressions are given for the shape and departure time of the bubble and for the thickness of the liquid microlayer between the growing bubble and the wall. Contrary to current theories, it is reported that surface tension can assist departure of the bubble in certain circumstances and delay departure in other situations.

Individual nucleation sites emit bubbles with a constant frequency, the value of which varies from site to site. Jakob [25] observed that the product of bubble frequency f and departure diameter D_b was a constant. More recently, Ivey [26] has shown that this is an approximation and that the form of the product depends on whether the bubble growth is inertia- or diffusion-controlled. Under conditions where the bubble departure process is governed by dynamic forces, the relationship becomes $D_b f^2 =$ const. Cole [27] suggested the following relation:

$$D_b f^2 = \frac{4}{3}\frac{g_n(\rho_\ell - \rho_g)}{C_{drag}\,\rho_\ell} \tag{20}$$

which for steam bubbles in water at atmospheric pressure ($C_{drag} \cong 1$, $\rho_g \ll \rho_\ell$) reduces to

$$D_b f^2 = 1.32 g_n \tag{21}$$

For the region where bubble growth is limited by diffusion of heat to the interface, the relationship becomes $D_b f^{1/2} =$ const. Rohsenow, using the bubble growth analysis of Mikic et al. [13], has derived the following expression for this region:

$$D_b f^{1/2} = \tfrac{3}{4}(\pi \kappa_\ell)^{1/2}\,Ja \tag{22}$$

The above equations have not been extensively verified by comparison with experimental data and therefore should be considered as approximate. For water at atmospheric pressure, bubble departure diameters are in the range I-2.5 mm, and bubble frequencies are in the range $20\text{–}40\ s^{-1}$.

Nomenclature** for **Section 2.7.1 appears at the end** of Section **2.7.8.

REFERENCES FOR SECTION 2.7.1

1. Lednovick, S. L., and Fenn, J. B., Absolute Evaporation Rates for Some Polar and Non-polar liquids, *AIChE J.*, vol. 23, no. 4, pp. 454–459, 1977.
2. Bonacci, J. C., Myers, A. L., Nongbri, G., and Eagleton, L. C., The Evaporation and Condensation Coefficient of Water, Ice and Carbon Tetrachloride, *Chem. Eng. Sci.*, vol. 31, pp. 609-617, 1976.
3. Maa, J. R., Rates of Evaporation and Condensation Between Pure Liquids and Their Own Vapours, *Znd. Eng. Chem.*, vol. 9, no. 2, pp. 283–287, 1970.
4. Saha, P., Development of Constitutive Relations-Effect of Pressure Change, Reactor Safety Research Program QPR (April lst-June 30th 1977), BNL-NUREG50683, 1977.
5. Lienhard, J. H., Correlation for the Limiting Liquid Superheat, *Chem. Eng. Sci.*, vol. 31, pp. 847-849, 1976.
6. Skripov, V. P., *Metastable Liquids*, transl. R. Kondor, Wiley, New York, 1974.
7. Blander, M., and Katz, J. L., Bubble Nucleation in Liquids, *AIChE J.*, vol. 21, no. 5, pp. 833-848, 1975.
8. Griffith, P., and Wallis, J. D., The Role of Surface Conditions in Nucleate Boiling, *Chem. Eng. Prog. Symp. Ser.*, no. 30, vol. 56, pp. 49–63, 1960.
9. Holtz, R. E., The Effect of the Pressure-Temperature History upon Incipient Boiling Superheats in Liquid Metals, Argonne Natl. Laboratory Rept. ANL-7184, 1966.
10. Griffith, P., and Snyder, G., The Mechanism of Void Formation in Initially Subcooled Systems, Massachusetts Institute of Technology Mechanical Engineering Department Rept. 9041-26, 1964.
11. Dwyer, 0. E., On Incipient Boiling Wall Superheats *in* Liquid Metals, *Znt. J. Heat Mass Transfer*, vol. 12, pp. 1403-1419, 1969.
12. Lorentz, J. J., Mikic, B. B., and Rohsenow, W. M., The Effect of Surface Conditions on Boiling Characteristics, *Heat Transfer 1974*, vol. *4, Proc. 5th Znt. Heat Transfer Conf. Tokyo, September* 3-7, 1974, Paper, 1974.
13. Mikic, B. B., Rohsenow, W. M., and Griffith, P., On Bubble Growth Rates. *Znt. J. Heat Mass Transfer*, vol. 13, pp. 657-665, 1970.
14. Rayleigh, L., Pressure Due to Collapse of Bubbles, *Phil. Mag.*, vol. 34, pp. 94-98, 1917.
15. Plesset, M. A., and Zwick, S. A., The Growth of Vapor Bubbles in Superheated Liquids, *J. Appl. Phys.*, vol. 25, no. 4, pp. 493–500, 1954.
16. Lien, Y., and Griffith, P., Bubble Growth Rates at Reduced Pressure. Sc.D. thesis, Massachusetts Institute of Technology, Cambridge, Mass., 1969.
17. Scriven, L. E., On the Dynamics of Phase Growth, *Chem. Eng. Sci.*, vol. 10, pp. 1-13, 1959.
18. Plesset, M. S., and Prosperetti, A., Bubble Dynamics and Cavitation, *Annu. Rev. Fluid Mech.*, vol. 9, pp. 145-185, 1977.

© 1983 Hemisphere I blishing Corporation

19. Hatton, A. P., and Hall, I. S., Photographic Study of Boiling on Prepared Surfaces. *3d Int. Heat Transfer Conf., Chicago, August 1966.* vol. 4, pp. 24–37.
20. Howell, J. R., and Siegel, R., Incipience, Growth and Detachment of Boiling Bubbles in Saturated Water from Artificial Nucleation Sites of Known Geometry and *Size, 3d Znt. Heat Transfer Conf., Chicago, August 1966,* vol. 4, pp. 12-23.
21. Fritz, W., Berechnung des Maximal Volume von Dampf blasen. *Phys. Z.,* vol. 36, p. 379, 1935.
22. Johnson, M. A., de la Pera, J., and Mesler, R. B., Bubble Shapes in Nucleate Boiling, *AIChE J.,* vol. 12, no. 2, pp. 344-348, 1966.
23. Cole, R., and Rohsenow, W. M., Correlation of Bubble Departure Diameters for Boiling of Saturated Liquids, *Chem. Eng. Prog. Symp. Ser.,* vol. 65, no. 92, p. 211, 1969.
24. Cooper, M. G., Judd, A. M., and Pike, R. A., Shape and Departure of Single Bubbles Growing at a Wall, *Proc. 6th Znt. Heat Transfer Conf., Toronto, August 7-11, 1978,* vol. 1, pp. 115-120, 1978.
25. Jakob, M., *Heat Transfer, vol.* 1, Wiley, New York, 1958.
26. Ivey, H. J., Relationship Between Bubble Frequency, Departure Diameter and Rise Velocity in Nucleate Boiling, *Znt. J. Heat Mass Transfer,* vol. 10, no. 8, p. 1023, 1967.
27. Cole, R., *AIChE J.,* vol. 6, no. 4, p. 533, 1960.
28. Basu, D. K., and Sinha, D. B., A Study of Superheat Property of Liquids, *Znd. J. Phys.,* vol. 42, p. 198, 1968.
29. Blander, M., Hengstenberg, D., and Katz, J. K., Bubble Nucleation in n-Pentane, *n*-Hexane, n-Pentane + Hexadecane Mixtures and Water, *J. Phys. Chem.,* vol. 75, p. 3613, 1971.
30. Eberhart, J. G., Hathaway, E. J., and Blander, M., The Limit of Superheat of Methanol and Ethanol, *J. Colloid Interface Sci.,* vol. 44, p. 389, 1973.
31. Eberhart, J. G., Kremsner, W., and Blander, M., Metastability Limits of Superheated Liquids: Bubble Nucleation Temperatures of Hydrocarbons and Their Mixtures, *J. Colloid Interface Sci.,* vol. 50, p. 369, 1975.
32. Kenrick, F. B., Gilbert, C. S., and Wismer, K. L., The Superheating of Liquids, *J. Phys. Chem.,* vol. 28, p. 1297, 1924.
33. Porteous, W., and Blander, M., Limits of Superheat and Explosive Boiling of Light Hydrocarbons, Halocarbons and Hydrocarbon Mixtures, *AIChE J.,* vol. 21, no. 3, pp. 560-566, 1975.
34. Renner, T., Kucera, G. H., and Blander, M., Measurements of the Limit of Superheat of Liquids, Physical Inorganic Chemistry Annual Report, July 1973–June 1974, Chem. Eng. Div., Argonne Natl. Laboratory, ANL-8123, p. 13, 1974.
35. Sinha, D. B., and Jalaluddin, A. K., On the Superheat of Liquids, *Znd. J. Phys.,* vol. 35, p. 311, 1961.
36. Wakeshima, H., and Takata, K., On the Limit of Superheat, *J. Phys. Soc. Jpn.,* vol. 13, p. 1398, 1958.
37. Wismer, K. L., The Pressure Volume Relation of Superheated Liquids, *J. Phys. Chem.,* vol. 26, p. 301, 1922.
38. Niino, M., Study of Single Bubble Generation and Growth by Laser Beam, Ph.D. thesis, University of Tohoku, Japan, 1975.

© 1983 Hemisphere Publishing Corporation

2.7.2
Pool boiling

J. G. Collier

■ Pool boiling is defined as boiling from a heated surface submerged in a large volume of stagnant liquid. This liquid may be at its boiling point, in which case the term ***saturated pool boiling*** is employed, or below its boiling point, when the term ***subcooled pool boiling*** is used. The results of investigations into heat transfer rates in pool boiling are usually plotted on a graph of surface heat flux $(\dot{q})$ against heater wall surface temperature (T_w)—the ***boiling*** curve. Such a curve for water boiling at atmospheric pressure is shown diagrammatically in Fig. 1. An alternative presentation might use the wall superheat $(T_w - T_{sat})$ rather than the wall temperature itself.

The component parts of the boiling curve are as follows:

1. The natural convection region ***AB,*** where temperature gradients are set up in the pool and heat is removed by natural convection to the free surface and thence by evaporation to the vapor space.

2. The onset of nucleate boiling ***(ONB)***, where the wall superheat becomes sufficient to cause vapor nucleation at the heating surface. This may occur close to the point where the curves ***AB*** and ***B'C*** meet, as is usually the case for water at atmospheric pressure and above. Alternatively, it may occur at much larger superheats than those required to support fully developed nucleate boiling, resulting in a sharp drop in surface temperature from ***B*** to ***B'*** for the case of a constant surface heat flux. This latter behavior is associated with fluids at very low reduced pressures, e.g., water below atmospheric pressure and liquid metals in particular.

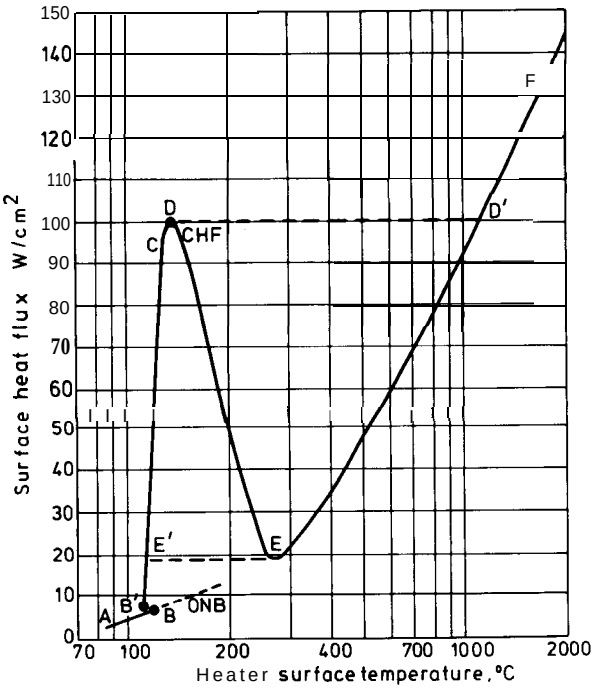

Figure 1 Pool boiling curve for water at atmospheric pressure.

© 1983 Hemisphere Publishing Corporation

3. The nucleate boiling region ($B'C$), where vapor nucleation occurs at the heating surface. Starting with a few individual sites at low heat fluxes, the vapor structure changes as the heat flux is increased as a result of bubble coalescence, and finally, at high heat fluxes, vapor patches and columns are formed close to the surface.

4. The critical heat flux (CHF or point D) marks the upper limit of nucleate boiling where the interaction of the liquid and vapor streams causes a restriction of the liquid supply to the heating surface.

5. The transition boiling region (DE) is characterized by the existence of an unstable vapor blanket over the heating surface that releases large patches of vapor at more or less regular intervals. Intermittent wetting of the surface is believed to occur. This region can be studied only under conditions approximating a constant surface temperature.

6. The film boiling region (EF), where a stable vapor film covers the entire heating surface and vapor is released from the film periodically in the form of regularly spaced bubbles. Heat transfer is accomplished principally by conduction and convection through the vapor film, with radiation becoming significant as the surface temperature is increased.

In the natural convection region (1), the liquid may be at or below the saturation temperature. The temperature gradient away from the surface may be established from work on single-phase natural convection (see Sec. 2.5.7). The remaining regions of the boiling curve will now be considered in more detail.

A. The onset of nucleate boiling

As the surface heat flux is increased, so the surface temperature exceeds the saturation temperature. Establishing the onset of nucleate boiling requires a criterion for bubble nucleation within the nonuniform liquid temperature field adjacent to the heating surface. Consider Fig. 2, which shows a conical active nucleation site with a hemispherical vapor nucleus radius r_c (corresponding to a contact angle β of 90°), sitting at the mouth of the cavity. For other contact angles simple geometric relationships exist for the height of the bubble,

$$y_b = C_1 r_c = (H \cos \beta) r_c \tag{1}$$

and the radius of curvature of the bubble,

$$r_b = C_2 r_c = \frac{1}{\sin \beta} r_c \tag{2}$$

Also shown is the liquid temperature profile away from the surface. The liquid temperature well away from the surface is $T_{\ell\infty}$, and the wall temperature is T_w. The temperature gradient is assumed to be essentially linear through the thermal boundary layer, thickness 6. If the heat transfer coefficient in single-phase natural convection is α, then δ is given approximately by the expression

$$\delta = \frac{\lambda_\ell}{\alpha} \tag{3}$$

Typically, δ may be of the order 0.1-0.5 mm for water.

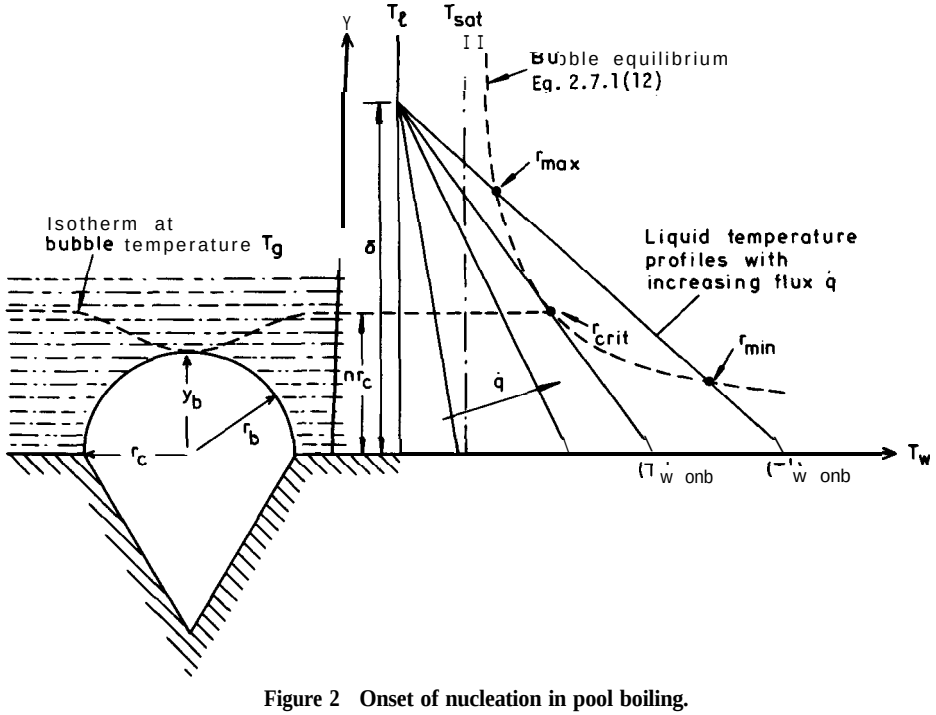

Figure 2 Onset of nucleation in pool boiling.

© 1983 Hemisphere Publishing Corporation

Hsu [1] postulated that the criterion for nucleation from this site is that the temperature of the liquid surrounding the top of the bubble should exceed that necessary for the nucleus to remain in equilibrium [Eq. 2.7.1(12)] . A convenient way of representing this criterion diagramatically is shown in Fig. 2, taking into account distortion of the temperature isotherm as a result of the presence of the bubble. If the line representing the liquid temperature profile intersects the equilibrium bubble curve, then nucleation occurs. The first nucleation site to be activated corresponds to the point of tangency between the equilibrium bubble curve and the liquid temperature profile. The wall temperature corresponding to this condition will be $(T_w)_{onb}$. The remaining variable is the relation of the location of the liquid temperature isotherm for T_g to the critical bubble radius. Hsu [1] chose this distance to be $2r_c$, but Han and Griffith [2] suggested $1.5r_c$ from potential flow theory. The equation for the critical size of nucleation site derived by Han and Griffith based on this assumption was

$$r_c = \frac{\delta(T_w - T_{sat})}{3(T_w - T_{\ell\infty})}\left[1 \pm \sqrt{1 - \frac{12(T_w - T_{\ell\infty})T_{sat}\sigma}{(T_w - T_{sat})^2\delta\rho_g\Delta h_v}}\right] \quad (4)$$

It is often convenient to assume that no distortion of the isotherm occurs and the distance is then y_b. With this latter assumption, if $\beta = 90$ and the liquid pool is at the saturation temperature, i.e., $TQ, = T_{sat}$, then the size of cavity satisfying the condition of tangency will be $r_c = \delta/2$, i.e., approximately 50-250 μm for water at atmospheric pressure. The superheat corresponding to this range of cavity size is less than 1° C for water. In practice, some10-15°C of superheat is normally required to initiate boiling of water from a flat metallic surface at atmospheric pressure.

The discrepancy lies in the fact that cavities of radius 50-250 μm are not normally active nucleation sites (that is, they do not contain a vapor embryo). Returning to Fig. 2, if an active site of size r_c does not exist on the heating surface, then the wall temperature must be increased until the liquid temperature profile intersects the equilibrium bubble curve at a point where active cavities do exist, e.g., to $(T'_w)_{onb}$. Brown [3] has measured the active site distribution on various surfaces, and reasonable populations of active sites (greater than 1 site/cm*) occur only for cavity radii below 10 μm.

The size of active nucleation sites may be estimated from the methods given in Sec. 2.7.1E, particularly Eq. 2.7.1(13). Alternatively, as a rough guide, the following figures may be taken for the maximum size of active nucleation sites on smooth metallic surfaces: for water, ~5 μm; for organics and refrigerants, -0.5 μm; for cryogenic fluids on aluminum or copper, -0.1-0.3 μm. These figures may be considerably increased on rough surfaces, specially prepared porous surfaces, or porous deposits caused by fouling.

B. Nucleate boiling

In the nucleate boiling region the surface temperature increases only slowly for relatively large changes in the surface heat flux (Fig. 1). The surface temperature variation can be expressed in the form of a simple power law relationship,

$$T_w = T_{sat} + \Psi\dot{q}^m \quad (5)$$

where Ψ and m are constants depending on the physical properties of the liquid and vapor and on the nucleation properties of the surface; m will normally be in the range 0.25-0.5, with a most probable value around 0.3-0.33.

The important effect that surface condition has on nucleate pool boiling must be stressed immediately. As an example, Fig. 3 shows experimental data taken by Berenson [4] for n-pentane boiling on copper. Different surface finishes cause the wall superheat ΔT_{sat} $(= T_w - T_{sat})$ for a given heat flux to vary by nearly a factor of 5.

It is usual to express heat transfer rates in terms of a heat transfer coefficient (α). In convective processes this represents the ratio between the heat flux $(\dot{q})$ and the temperature difference between surface and fluid (ΔT). Rearranging Eq. (5) to give an explicit expression for α, it is noted that in pool boiling the heat transfer coefficient is itself a function of the heat flux $(\dot{q})$. Thus

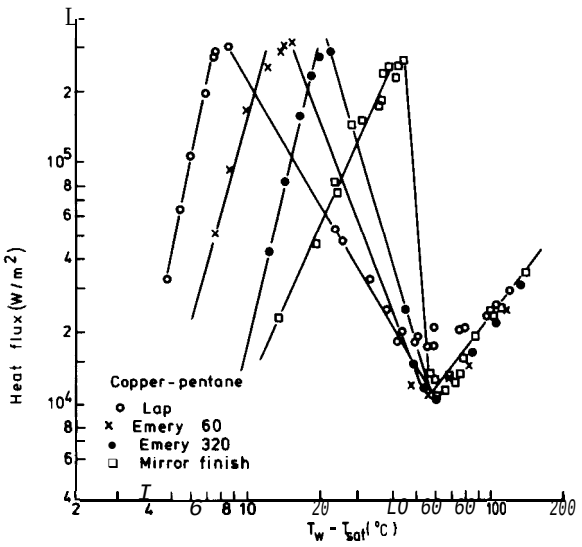

Figure 3 Effect of surface finish on boiling curve. From Berenson [4].

© 1983 Hemisphere Publishing Corporation

$$\alpha = \frac{1}{\Psi}\dot{q}^{(1-m)} = A\dot{q}^{n} \tag{6}$$

where $n \cong 0.7$ and A is a function of liquid and vapor physical properties and of surface condition.

Many of the available correlations for nucleate pool boiling heat transfer start from a simplified model of the boiling process and are expressed in terms of a number of dimensionless groups. Appropriate characteristic dimensions and velocities, such as the bubble departure diameter or the bubble growth velocity, are used in the formulation of these dimensionless groupings. One such well-known correlation is that proposed by Rohsenow [5]:

$$\frac{c_{p\ell}\Delta T_{sat}}{\Delta h_v} = C_{sf}\left\{\frac{\dot{q}}{\eta_\ell \Delta h_v}\left[\frac{\sigma}{g_n(\rho_\ell - \rho_g)}\right]^{1/2}\right\}^{r}\left(\frac{c_p\eta}{\lambda}\right)_\ell^{s} \tag{7}$$

The original equation had a value of $r = 0.33$ and $s = 1.7$. More recently, however, Rohsenow has recommended that, for water only, the value of s be changed to unity. C_{sf} is an arbitrary constant included to account for the differing nucleation properties of any particular liquid-surface combination. Values of C_{sf} for various liquid-surface combinations are given in Table 1. A detailed study of the values of C_{sf} and r for various liquid-surface combinations and various surface preparation techniques has been reported by Vachon et al. [6, 7].

Another well-tried correlation based on similar precepts is that of Forster and Zuber [8]:

$$\frac{\dot{q}}{\rho_g \Delta h_v}\left(\frac{\pi}{\kappa_\ell}\right)^{1/2}\left(\frac{\rho_\ell r^{*3}}{2\sigma}\right)^{1/4} = 0.001\,5\left[\frac{\rho_\ell}{\eta_\ell}\left(\frac{\Delta T_{sat}\lambda_\ell}{\rho_g \Delta h_v}\right)^2\frac{\pi}{\kappa_\ell}\right]^{5/8}\left(\frac{c_p\eta}{\lambda}\right)_\ell^{1/3} \tag{8}$$

where r^* is the equilibrium bubble radius given by Eq. 2.7.1(8). The coefficient (0.001 5) was evaluated from data for water at 1 and 50 bar† pressure, n-butyl alcohol at 3.4 bar, aniline at 2.4 bar, and mercury at 1 and 3 bar. It is presumably influenced by surface condition in the same way as C_{sf}, but there has been no systematic examination so far published.

Although the Rohsenow [Eq. (7)] and Forster/Zuber [Eq. (8)] correlations first appeared more than 20 yr ago, they are still in widespread use and form the basis of convective boiling design methods, as indicated in Sec. 2.7.3.

Various research workers in the U.S.S.R. have suggested correlations of the following form [9]:

†1 bar = 10^5 Pa.

Table 1 Values of C_{sf} for the Rohsenow equation for various liquid surface combinations ($r = 0.33$) (see [6])[a]

	Liquid-surface combination	C_{sf}	s
Water	on polished copper	0.0128	1.0
	on lapped copper	0.0147	1.0
	on scored copper	0.0068	1.0
	on ground and polished stainless steel	0.0080	1.0
	on Teflon-pitted stainless steel	0.005 8	1.0
	on chemically etched stainless steel	0.0133	1.0
	on mechanically polished stainless steel	0.0132	1.0
	on nickel	0.006	1.0
	on platinum	0.013	1.0
	on brass	0.006	1.0
n-Pentane	on polished copper	0.0154	1.7
	on polished nickel	0.0127	1.7
	on lapped copper	0.0049	1.7
	on emery-rubbed copper	0.0074	1.7
	on chromium	0.015	1.7
Carbon tetrachloride on polished copper		0.007 0	1.7
Benzene on chromium		0.101	1.7
Ethyl alcohol on chromium		0.0027	1.7
Isopropyl alcohol on copper		0.0025	1.7
n-Butyl alcohol on copper		0.003 0	1.7
35% K_2 CO, on copper		0.005 4	1.7
50% K_2 CO, on copper		0.0027	1.7

Whenever possible it is recommended that a pool boiling experiment be carried out to determine the value of C_{sf} applicable to the particular conditions of interest. In the absence of such information, a value of C_{sf} of 0.013 may be used as a fust approximation.

$$\mathrm{Nu}^* = A\,\mathrm{Pr}^{n_1}\,\mathrm{Pe}^{*n_2}\,K_p^{n_3}\,K_t^{n_4}\,\mathrm{Ar}^{*n_5} \tag{9}$$

with the coefficients and exponents given in Table 2. Again, the coefficient A is not really a constant but a function of the surface-liquid interaction.

Mikic and Rohsenow [10] and Ratiani and Shekriladze [11] have shown that the cavity size distribution for the surface greatly influences the position of the boiling curve. Provided that this cavity size distribution can be established for the particular fluid-surface combination at one pressure, it is then possible to predict the boiling curve at some other pressure. Alas, it is not practical to make measurements of cavity size distribution for the great variety of industrial fluids and heating surfaces in use.

Ratiani and Shekriladze [11] found the following correlation represented a wide range of pool boiling data for water, organics, refrigerants, and liquid metals:

$$\frac{\alpha r_c}{\lambda_\ell} = 0.07\left(\frac{\dot{q}r_c^2\Delta h_v\rho_g}{\sigma T_{sat}\lambda_\ell}\right)^{0.7}\left[\frac{\rho_\ell\sigma T_{sat}c_{p\ell}}{(\Delta h_v\rho_g)^2 r_c}\right]^{0.25} \times \left\{\frac{r_c[p(v_g - v_\ell)]^{1/2}}{\nu_\ell}\right\}^{0.25} \tag{10}$$

© 1983 Hemisphere Publishing Corporation

Table 2 Coefficients and exponents for use in the various U.S.S.R. correlations of nucleate pool boiling, Eq. (9)[a]

Author	A	n_1	n_2	n_3	n_4	n_5
Kichigan and Tobilevich	1.04×10^{-4}	0	0.7	0.7	0	0.125
Kutaleladze	7.0×10^{-4}	-0.35	0.7	0.7	0	0
Borishanski and Minchenko	8.7×10^{-4}	0	0.7	0.7	0	0
Kruzhilin and Averin	0.082	-0.5	0.7	0	0.377	0
Labuntsov	0.125	-0.32	0.65	0	0.35	0
Volsoshko (Freons)	$1.14\text{-}2.74 \times 10^{-2}$	0	0.706	0	0.588	0

[a] $\mathrm{Nu}^* = A\,\mathrm{Pr}^{n_1}\mathrm{Pe}^{*n_2}K_p^{n_3}K_t^{n_4}\mathrm{Ar}^{*n_5}$.

$$\mathrm{Nu}^* = \frac{\alpha}{\lambda_\ell}\left[\frac{\sigma}{g_n(\rho_\ell - \rho_g)}\right]^{1/2} \qquad \mathrm{Pe}^* = \frac{\dot{q}}{\kappa_\ell \rho_g \Delta h_v}\left[\frac{\sigma}{g_n(\rho_\ell - \rho_g)}\right]^{1/2}$$

$$K_p = \frac{p}{[g\sigma(\rho_\ell - \rho_g)]^{1/2}} \qquad K_t = \frac{(\rho_g \Delta h_v)^2}{Jc_{p\ell}T_{\mathrm{sat}}\rho_\ell[g\sigma(\rho_\ell - \rho_g)]^{1/2}}$$

$$\mathrm{Ar}^* = \frac{g_n}{\nu^2}\left[\frac{\sigma}{g_n(\rho_\ell - \rho_g)}\right]^{3/2}\left(1 - \frac{\rho_g}{\rho_\ell}\right)$$

This correlation takes the surface condition into account through the radius of the active nucleation sites (r_c). Where information of the size of the mean active nucleation site is not available, a value of r_c equal to 20 μm is recommended.

The dimensionless correlations discussed so far have a number of disadvantages: They require accurate physical properties, they are complicated to evaluate, and the inherent uncertainty induced by the condition of the surface is considerable. As an alternative, simple dimensional equations can be prescribed for individual fluids using data from experimental studies. One basis for such equations is the work of Borishanski [12], which makes use of the law of corresponding states. The heat transfer coefficient is evaluated from

$$\alpha = A^* \dot{q}^{0.7} F(p) \tag{11}$$

where $F(p)$ is a function of reduced pressure p_r as shown in Fig. 4 and A* is a constant evaluated at the reference reduced pressure $p_r^* = 0.029\,4$.

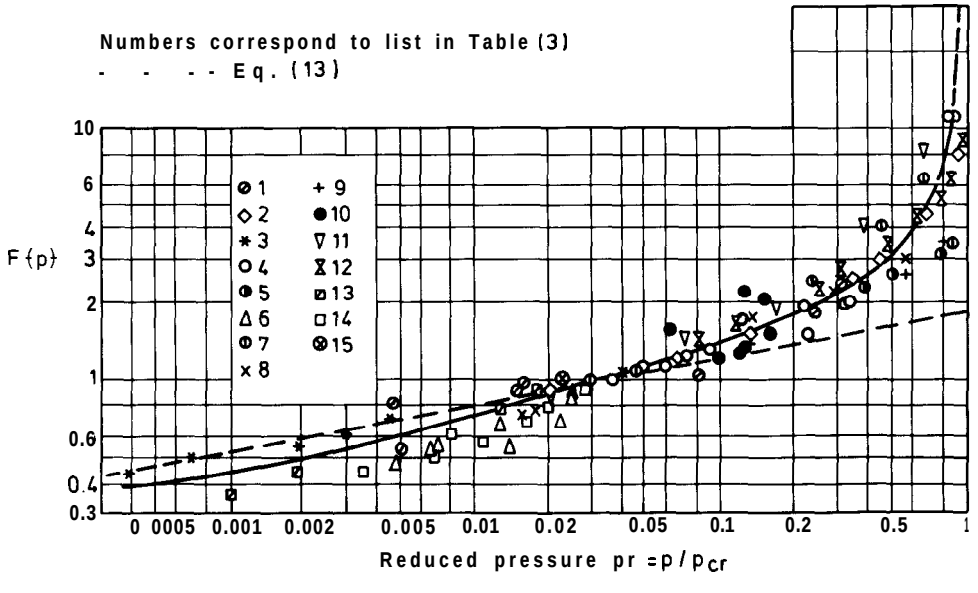

Figure 4 Effect of pressure on nucleate pool boiling. From Borishanski [12].

© 1983 Hemisphere Publishing Corporation

A variation of this method has been given by Mostinski [13], who has proposed the following expression for A * and $F(p)$:

$$A = 0.10111 p_{cr}^{0.69}$$
$$F(p)_1 = 1.8p_r^{0.17} + 4p_r^{1.2} + 10p_r^{10} \quad (12)$$

Values of A* evaluated from Eq. (12) at $p_r^* = 0.029\ 4$ are given in Table 3 for comparison with values derived from experimental measurements by Borishanski and others. Palen et al. [14] report that the Mostinski correlation was superior to any of the physical property-based correlations that they had tested. However, for application to pool boiling-type reboilers (Sec. 3.3.4), a safe design curve is recommended that is obtained by dropping the last two terms in the poly nomial of Eq. (12):

$$F(p)_2 = 1.8p_r^{0.17} \quad (13)$$

This recommendation is due to the great scatter and generally increasing uncertainty in the boiling behavior as the critical point is approached.

German workers at the University of Karlsruhe [15] have found that for the refrigerants (RI 1, R12, R113, R115, etc.) the function $F(p)$ is somewhat different than that given by Eq. (12) and proposed by Borishanski. They propose a relationship for $F(p)$ such that

$$F(p) = 0.7 + 2p_r \left(4 + \frac{1}{1 - p_r}\right) \quad (14)$$

This function is compared with that proposed by Mostinski in Fig. 5 and in Table 4. It is recommended that for refrigerants $F(p)$, together with the values of A* within braces in Table 3, be used in Eq. (11). A comparison between measured values of α and those predicted from this recommended method is given in Fig. 6.

Table 3 Simple dimensional equations for nucleate pool boiling heat transfer[a,b]

Liquid	Pressure range, bar	Reference pressure p^* A^* (p_r = 0.0294), bar	A^* from exp. study	A^* from Eq. (12)	Critical pressure p_{cr}, bar	Reference	No. in Fig. 4
Water	1-70	6.50	4.09	4.21	221.2	1441	1
	1-196	6.50	4.02	4.21	221.2	[45, 46]	2
	0.09-1	6.50	5.80	4.21	221.2	[47]	3
	1-72.5	6.50	4.47	4.21	221.2	[45]	4
	1-170	6.50	4.44	4.21	221.2	[47 1	5
	1-5.25	6.50	5.74	4.21	221.2	[48]	6
Pentane	1-28.6	0.98	1.09	1.14	33.4	[44]	7
Heptane (80%)	0.45-14.8	0.78	1.18	0.967	26.4	[44 1	8
n-Heptane	0.45-21.7	0.78	1.63	0.967	26.4	[44]	9
Benzene	1-44.4	1.44	1.06	1.48	49.0	[44]	11
	0.9-20.7	1.44	1.32	1.48	49.0	[49]	
Diphenyl	0.9-8	0.91	1.12	1.08	31.0	[49]	
Methanol	0.08-1 .39	2.33	(0.69)	2.07	79.5	[50]	13
Ethanol	1-7.9	1.87	1.83	1.78	63.8	[44]	10
	1-59	1.87	2.59	1.78	63.8	[45, 46]	12
Butanol	0.17-1.38	1.31	(0.44)	1.39	44.7	[50]	14
R11 ($CFCl_3$)	1-3	1.28	1.95 (1.73)	1.37	43.7	[52]	
R12 (CF_2Cl_2)	1-4.87	1.21	2.43	1.31	41.1	[51]	15
	6-40.5	1.21	3.49 (2.57)	1.31	41.1	[54]	
R13 (CF_3 Cl)	2.8-10.5	1.13	(1.79)	1.26	38.6	[15]	
R13B1 (CF_3Br)	17-39	1.17	4.43 (2.48)	1.29	39.9	[54]	
R22 (CHF_2 Cl)	0.4-2.15	1.45	(2.39)	1.49	49.36	[15]	
R113 ($C_2Cl_3F_3$)	1-3	1.00	1.24	1.15	34.1	[55]	
R115 (C_2F_5Cl)	8-31	0.92	3.79 (2.38)	1.08	31.2	[54]	
RC318 (C_4F_8)	3.6-27	0.82	3.13 (2.50)	1.00	27.8	[54]	
Methylene Chloride	1-4.5	1.79	(1.91)	1.72	60.8	[52]	
Ammonia	1-8	3.32	3.90	2.64	113	[52]	
Methane	1-42	1.37	2.68	1.43	46.5	1531	

Adapted from Borishanski[46].

[b] $\alpha = A\dot{q}^{0.7}$; α in W/m K; q in W/m . Values shown in parentheses ( ) are uncertain; values shown within braces { } relate to the use of Eq. (14) for $F(p)$.

© 1983 Hemisphere Publishing Corporation

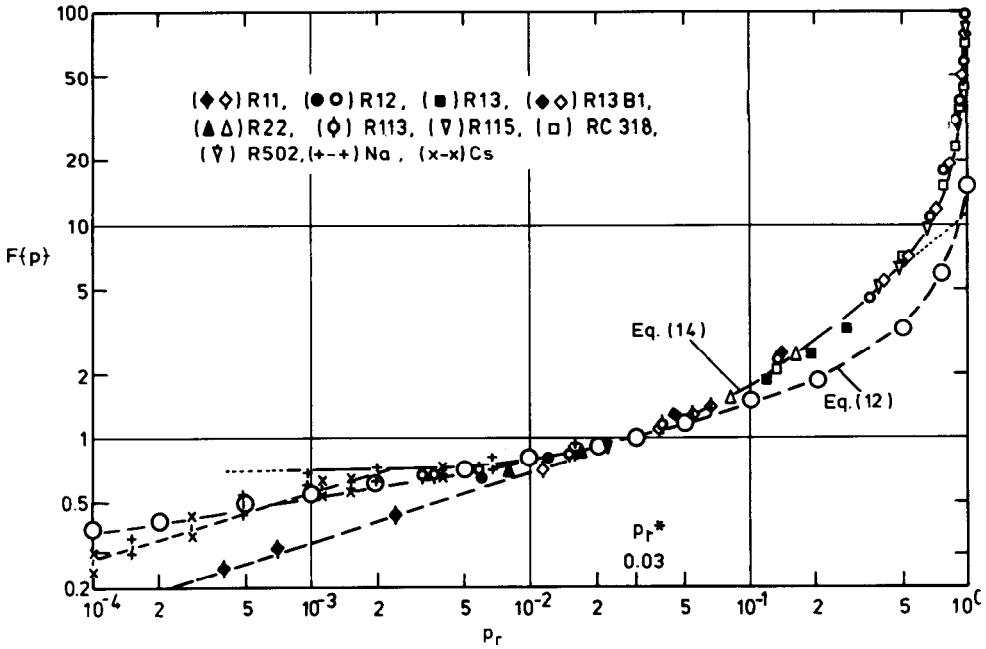

Figure 5 Comparison of $F(p)$ by Eq. (12) with that given by Eq. (14).

(a) Independent variables influencing heat transfer rates in nucleate boiling

In this section the influence of various independent factors on nucleate boiling heat transfer rates is summarized.

I. Influence of system pressure

In all instances an increase in system pressure shifts the curve of surface heat flux $(\dot{q})$ versus wall superheat (ΔT_{sat}) to the left (Fig. 7). At very low values of reduced pressure $(p_r$ <O.OOO 1), the extent of the nucleate boiling region may become restricted. Nucleate boiling will not be initiated until relatively large wall superheats are reached, corresponding to moderate levels of heat flux. At the same time, the critical heat flux reduces with decreasing system pressure. At some very low pressure, the first generation of vapor is sufficient to induce the critical heat flux and the nucleate boiling region disappears altogether. (Fig. 8).

Table 4 Values of $F(p)$ as a function of reduced pressure

p_r	$Ffp)$ from Eq. (12)	$F(p)$ from Eq. (13)	$Ffp)$ from Eq. (14)
0.000 1	0.376 0	0.376 0	0.701 0
0.000 2	0.423 1	0.423 1	0.702 0
0.000 5	0.494 8	0.494 4	0.705 0
0.001	0.557 2	0.556 2	0.710 0
0.002	0.628 1	0.625 8	0.720 0
0.005	0.738 2	0.731 3	0.750 0
0.01	0.838 6	0.822 7	0.800 0
0.02	0.962 2	0.925 6	0.900 8
0.029 4	1.046 4	0.988 3	0.995 8
0.05	1.191 5	1.081 7	1.205 3
0.1	1.469 3	1.216 9	1.722
0.2	1.948 9	1.369 1	2.800
0.5	3.350 8	1.599 9	6.700
0.8	5.867 0	1.733 0	15.100
1.0	15.800 0	1.800 0	

II. Influence of surface condition

As already emphasized, surface condition has a considerable influence on the heat transfer rates in nucleate boiling (Fig. 3). Mechanical roughening of the surface, by scoring or grooving, or alternatively by emery clothing or sandblasting, initially shifts the boiling curve to lower wall superheats. The roughening process appears to provide both an increased number of active nucleation sites and an increase in their effective size. However, in many instances of prolonged boiling on such surfaces, much of the gain in heat transfer coefficient due to roughness disappears, indicating that many of the new larger sites are not stable.

Surfaces can, however, be prepared where stable reentrant shaped cavities are provided. Such surfaces include porous welds and porous metallic coatings. Tubing with a bonded porous metallic coating is now available commercially-see Sec. 2.7.9.

Whereas under conditions of single-phase heat transfer, fouling of the heat transfer surface always reduces the effective heat transfer coefficient, this is

© 1983 Hemisphere I blishing Corporation
HDH

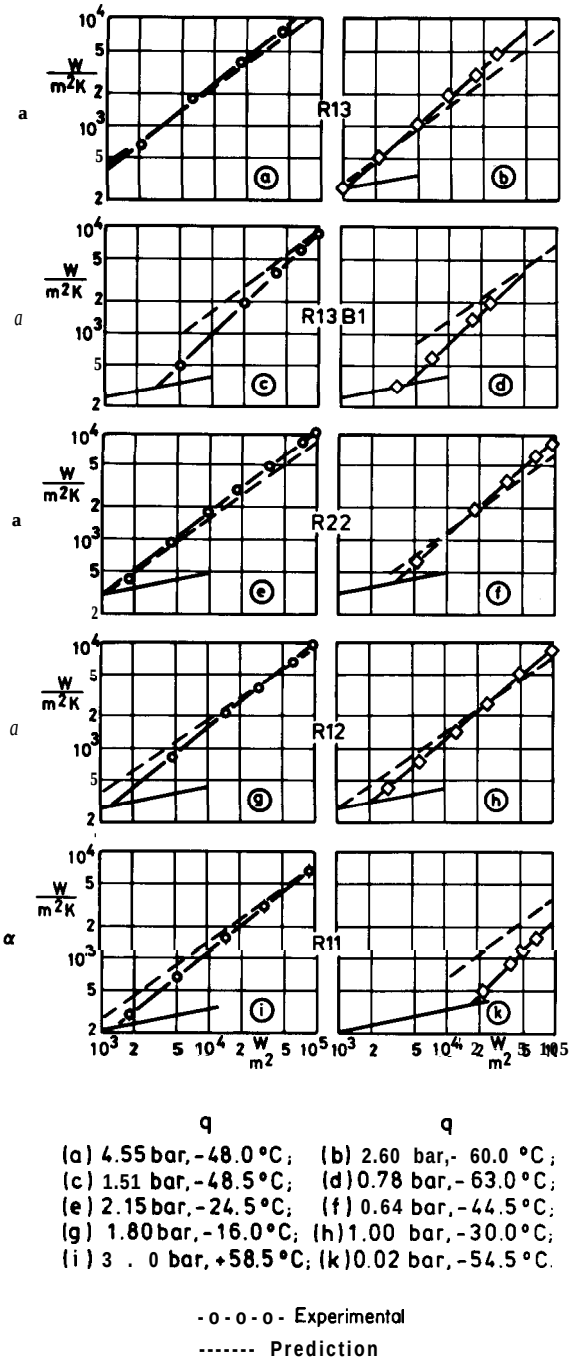

Figure 6 Comparison of experimental and predicted values of heat transfer coefficient. Predicted values from Eq. (11) with A * values in square brackets in Table (3) and $F(p)$ evaluated from Eq. (14).

not always the case with nucleate boiling. If the fouling layer is porous in nature, it may act to provide large, stable nucleation sites that will promote boiling at a reduced wall superheat [16]. However, the effect is often short-lived [17], and in many other cases, essentially organic fouling, there are no promotion effects at all.

III. Influence of noncondensable gas

The presence of noncondensable gases dissolved in the liquid influences the boiling curve in the vicinity of the initiation of the nucleate boiling region. Gas bubbles may appear at the heating surface well below the normal saturation temperature. This influence on the point of initiation of vapor formation can be allowed for by including in the analysis described in Sec. A the partial pressure of the noncondensable gas. At low heat fluxes just after the onset of degassing, additional convection induced by the gas bubbles increases heat transfer rates compared to the situation with no gas present. This effect, however, dies out at higher heat fluxes once fully developed nucleate boiling is achieved.

IV. Hysteresis in the boiling curve

For liquids that tend to wet the heating surface particularly well, there may be a difference in the boiling curve measured during an increase or a decrease in heat flux. As the heat flux is increased, the onset of nucleate boiling may be delayed, with a consequent overshoot in wall temperature.

V. Influence of size and orientation of surface

For fully developed nucleate pool boiling, the wall superheat is independent of the linear dimensions and orientation of the heating surface. Provided that the only movement of the liquid is that induced by the boiling process itself, similar rates of heat transfer will be achieved on horizontal flat plates, tubes, and on short vertical plates and tubes. At low heat fluxes near the point of onset of nucleate boiling, natural convec-

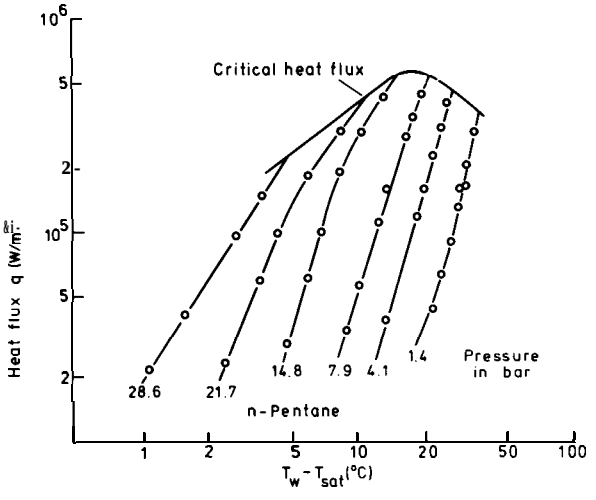

Figure 7 Effect of pressure on nucleate boiling. From Cichelli and Bonilla [44].

© 1983 Hemisphere Publishing Corporation

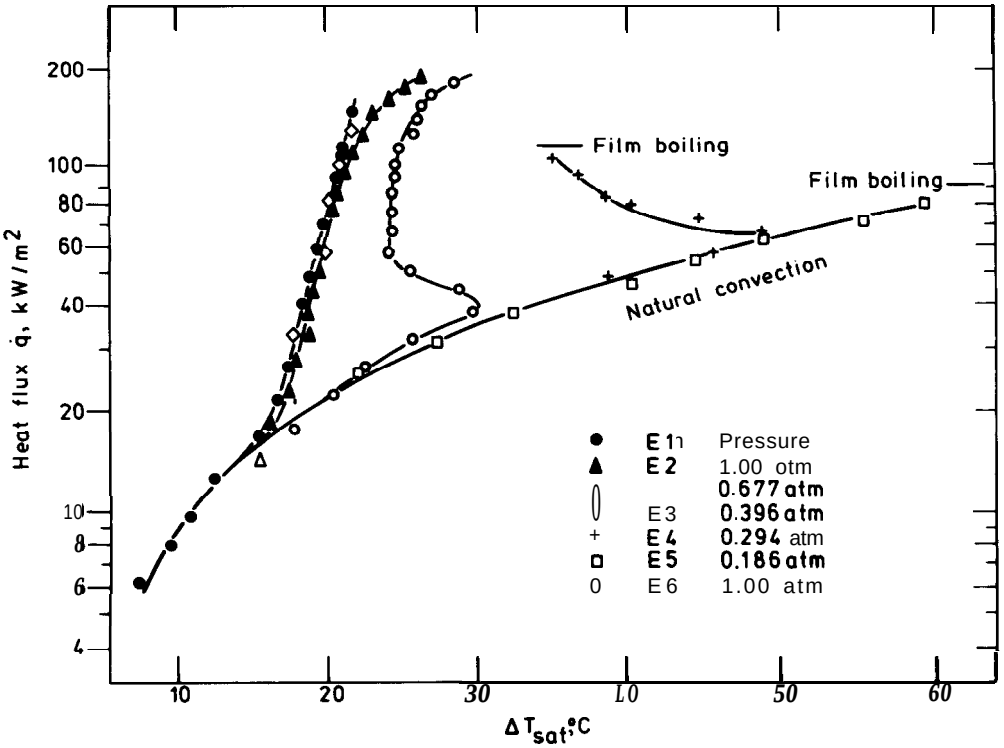

Figure 8 Boiling curves for ethanol showing decreasing nucleate boiling region and its **final** disappearance at low pressure. From Rallis and Jawurek [57].

tion accounts for a significant fraction of the heat removed, and this process is, of course, geometry dependent.

VI. Influence of liquid subcooling

The position of the boiling curve in terms of the surface heat flux ($\dot{q}$) and the wall superheat (AT,,,) is not greatly influenced by the level of subcooling of the liquid pool (ΔT_{sub}). Individual curves of heat flux versus wall superheat will be observed somewhat displaced from one another. Their relative position will be related to the heater geometry to the extent that convection influences the boiling curve. To a first approximation the influence of subcooling on fully developed nucleate boiling may be neglected [18].

VII. Influence of wettability of surface

The nucleate boiling region may be seriously curtailed in situations where the liquid does not wet the heating surface. In particular, the critical heat flux is seriously reduced at large contact angles (see Fig. 12).

VIII. Influence of gravitational acceleration

Increases above the normal gravitational acceleration appear to have little influence in the fully developed nucleate boiling region, and few correlations explicitly include an effect of gravitational acceleration. Increases in acceleration do, however, enhance the rate of natural convection and therefore there is some increase of heat transfer rates at low heat fluxes where bubble-enhanced natural convection is important.

C. Critical heat flux

The curve shown in Fig. 1 can be obtained in its entirety under circumstances where the temperature of the heating surface is controlled to a specified value. In many practical cases, however, the surface heat flux is the independently controlled variable. In this case the boiling curve in the natural convection (AB) and nucleate boiling ($B'C$) regions remains basically unaltered. However, if an attempt is made to increase the value of the surface heat flux above ***D,*** the surface temperature will jump from that corresponding to $D(\sim 1150^{\circ}C)$, the next stable operating point in the film boiling region. In many practical cases this large temperature jump is sufficient to cause failure of the heating surface. Hence, the colloquial name ***burnout,*** which is often used to refer to this phenomenon.

It is now generally accepted that the critical heat flux in pool boiling occurs as a result of a hydro-

© 1983 Hemisphere Publishing Corporation

dynamic flow pattern transition close to the heating surface. The mechanism is one in which insufficient liquid is able to reach the heating surface because of the rate at which vapor is leaving the surface. Zuber [19] idealized the flow pattern as a square array of vapor jets leaving the heated surface with a spacing corresponding to the most rapidly growing Taylor instability wavelength λ_d. Interaction of adjacent vapor jets due to Helmholtz instability limits the vapor volumetric flux from the surface to

$$(j_g)_{max} = \frac{\pi}{24}\left[\frac{\sigma g_n(\rho_\ell - \rho_g)}{\rho_g^2}\right]^{1/4} \tag{15}$$

For the case where the liquid is at the saturation temperature and all the vapor is produced at the heating surface (for liquid metals and also for certain two-component systems this latter assumption may not be valid),

$$j_g = \frac{\dot{q}}{\rho_g \Delta h_v} \tag{16}$$

and thus

$$\dot{q}_{cr} = K\Delta h_v \rho_g^{1/2} \quad [\sigma g_n(\rho_\ell - \rho_g)]^{1/4} \tag{17}$$

where according to Zuber, K = n/24. This theory thus confirmed the earlier correlation proposed by Kutateladze [20], in which K was 0.16 ± 0.03. More recently, Lienhard and Dhir [21] have reexamined the Zuber theory in the light of up-to-date experimental evidence and have concluded that the constant K given by Zuber should be increased by a factor 1.14, i.e., K should be 0.149. It is, however, useful to use the value predicted from Eq. (17) with the original value of K given by Zuber, i.e., n/24, as a reference critical heat flux, denoted by $\dot{q}_{cr,z}$.

Accurate physical properties may not always be available, and Lienhard and Schrock [22] have given a useful reformulation of Eq. (17) in terms of the law of corresponding states, thus:

$$q_{cr} = g_n^{1/4} p_c \frac{P}{\tilde{M}}\left(\frac{\tilde{M}p_c}{\tilde{R}T_c}\right)^{3/4} f(p_r) \tag{18}$$

In this expression P is the parachor, tables of which are given by Partington [23], and $f(p_r)$ is a function of reduced pressure p_r, which is given in Table 5. Geometric, liquid viscosity, subcooling, and surface effects may modify the value from that given by Eq. (17).

(a) Geometric effects

The Zuber analysis is strictly valid only for boiling of pure liquid on large, thick, well wetted horizontal surfaces facing upward. Thus,

$$\frac{q_{cr,F}}{\dot{q}_{cr,z}} = 1.14 \tag{19}$$

For small plates where the width is less than $3\lambda_d$, the number of vapor jets that can be accommodated on the heater surface is limited. In the region where the heater width is between 2 and $3\lambda_d$, there appears to be a considerable reduction in $\dot{q}_{cr}$ (Fig. 9). In this region Lienhard and Dhir [21] give the equation

$$\dot{q}_{cr} = \frac{N_j \lambda_d^2}{A_h} 1.14 \dot{q}_{cr,z} \tag{20}$$

where N_j is the number of vapor jets that can be accommodated on the heating surface; λ_d is the most rapidly growing Taylor instability wavelength, given by

$$\lambda_d = 2\pi\sqrt{3}\left[\frac{\sigma}{g_n(\rho_\ell - \rho_g)}\right]^{1/2} \tag{21}$$

and A_h is the surface area of the heater plate. In the limit only one vapor jet can be accommodated on the plate, and the critical heat flux increases rapidly as further reductions in heater width occur.

Lienhard and Dhir [21] have given expressions for q_{cr} corresponding to other heater geometries. A nondimensional heater size L' is used:

$$L' = \frac{L}{[\sigma/g_n(\rho_\ell - \rho_g)]^{1/2}} \tag{22}$$

Details are given in Table 6 and Fig. 10. It will be observed that the critical heat flux for large vertical heaters is less than for large horizontal heaters by the ratio 0.904/1.14, i.e., 0.79. This is consistent with the experimental values examined by Bernath [24].

Table 5 Values of $f(p_r)$ for use with Eq. (18)[a, b]

Reduced pressure p_r	*0.004*	0.01	*0.02*	*0.06*	*0.2*	*0.35*	*0.6*	*0.8*	1.0
$F(p_r)$	1.0	1.56	*2.05*	*3.0*	*3.75*	*4.0*	*3.4*	*2.0*	*0*

[a] Adapted from Lienhard and Schrock [22].

[b] Note that $f(p_r)$ is the *value* for a large, flat, horizontal, upward-facing plate. The value for other geometries will also be a function of L' (see Lienhard and Watanabe [56]).

© 1983 Hemisphere Publishing Corporation

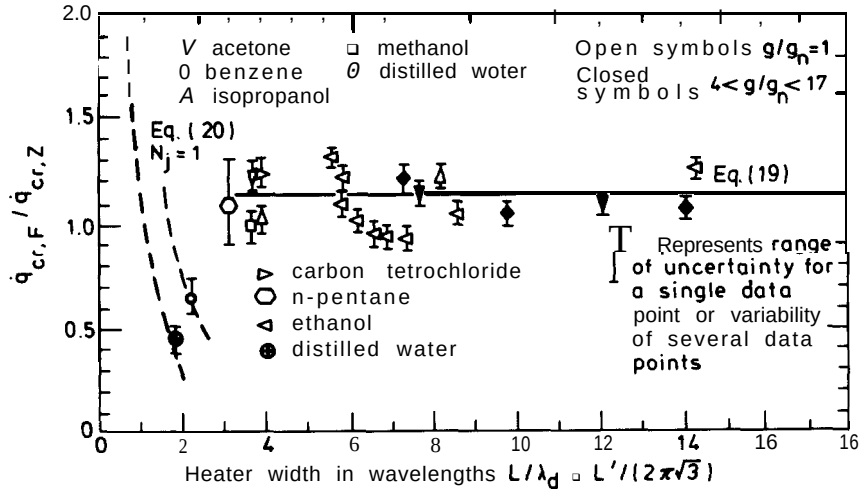

Figure 9 Critical heat flux for a horizontal flat plate. From Lienhard and Dhir [21].

Table 6 Modifications to the hydrodynamic theory of pool boiling critical heat flux to account for different heater geometries[a]

Heater geometry	Reference dimension	Applicability limit	Equation for $\dot{q}_{cr}$
Large horizontal flat plate	L = diameter of plate or length of side if square	$3 < \frac{L}{\lambda_d}$ $\left(\text{or } \frac{L'}{2\pi\sqrt{3}}\right)$	$\frac{q_{cr,F}}{q_{cr,z}} = 1.14$
Small horizontal flat plate	L = diameter of plate or width of rectangular pkte.	$0.5 \leq \frac{L}{\lambda_d} \leq 2$	$\dot{q}_{cr} = \frac{N_j \lambda_d^2}{A_h} 1.14 \dot{q}_{cr,z}$
Large horizontal cylinder	L = radius of cylinder	$1.17 \leq R'$	$\frac{\dot{q}_{cr}}{\dot{q}_{cr,z}} = 0.904$
Small horizontal cylinder	L = radius of cylinder	$0.12 < R' < 1.17$	$\frac{q_{cr}}{\dot{q}_{cr,z}} = 0.94(R')^{-1/4}$
Large spheres	L = radius of sphere	$4.36 \leq R'$	$\frac{q_{cr}}{q_{cr,z}} = 0.84$
Small spheres	L = radius of sphere	$0.18 < R' < 4.36$	$\frac{q_{cr}}{\dot{q}_{cr,z}} = 1.754(R')^{-1/2}$
Small horizontal ribbons aligned vertically	L = height of ribbon	$H' \leq 2.6$	$\frac{q_{cr}}{\dot{q}_{cr,z}} = 1.18(H')^{-1/4}$
Small horizontal ribbons aligned vertically (one side insulated)	L = height of ribbon	$H' \leq 6$	$\frac{q_{cr}}{\dot{q}_{cr.z}} = 1.4(H')^{-1/4}$

From Lienhard and Dhir [21].

$$\dot{q}_{cr,z} = \frac{\pi}{24} \rho_g^{1/2} \Delta h_v [\sigma g_n (\rho_\ell - \rho_g)]^{1/4}$$

$$L' = L \left[\frac{g_n(\rho_\ell - \rho_g)}{\sigma}\right]^{1/2}$$

$$\lambda_d = 2\pi\sqrt{3} \left[\frac{\sigma}{g_n(\rho_\ell - \rho_g)}\right]^{1/2}$$

N_j = no. of vapor jets on square array with spacing λ_d that can be accommodated on plate

A_h = surface area of heater plate

© 1983 Hemisphere Publishing Corporation

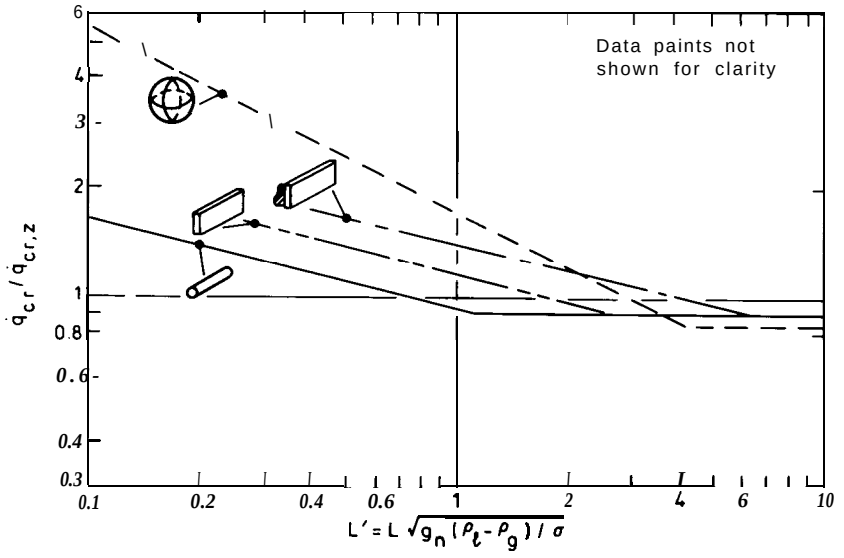

Figure 10 Influence of heater geometry on critical heat flux. From Lienhard and Dhir [21].

None of the expressions in Table 6 should be used when $L' < 0.15$. For very small heaters or for very low gravity situations, surface tension forces are much greater than inertial forces and the hydrodynamic theory for pool boiling critical heat flux breaks down. Indeed, at very low values of $L' \leqslant 0.01$, both nucleate boiling and the maxima and minima in the boiling curve are absent. The boiling curve then consists of a region of natural convection leading directly into a region of film boiling (Fig. 8).

(b) Liquid viscosity

Borishanski [25] extended the Kutateladze correlation to include the effect of liquid viscosity. For large, flat, horizontal heaters, he proposed

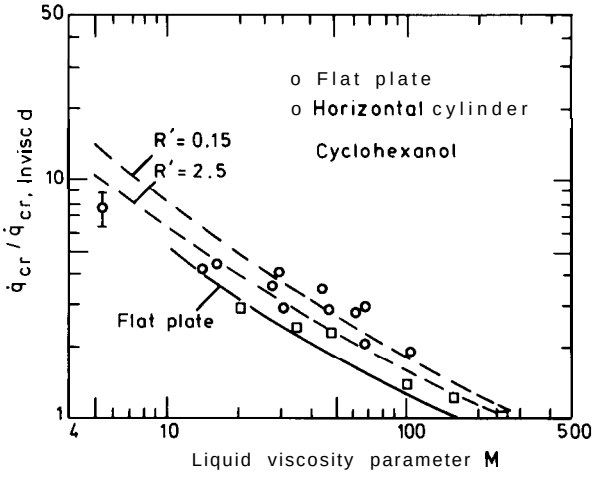

Figure 11 Effect of liquid viscosity on pool boiling critical heat flux. From Dhir and Lienhard [26].

$$\dot{q}_{cr} = \left(\frac{1 + 30.5}{N^{2/5}}\right) q_{cr,F} \tag{23}$$

where N is given by

$$N = \frac{\rho_\ell \sigma}{\eta_\ell^2}\left[\frac{\sigma}{g(\rho_\ell - \rho_g)}\right]^{1/2} \tag{24}$$

Dhir and Lienhard [26], in reexamining this effect, used the parameter *M:*

$$M = \frac{\rho_\ell \sigma^{3/4}}{\eta_\ell g_n^{1/4}(\rho_\ell - \rho_g)^{3/4}} \tag{25}$$

For values of M less than about 400, the critical heat flux is increased over that for the inviscid case. Figure 11 shows the magnitude of the effect for horizontal flat plates or cylindrical heaters.

(c) Subcooling

In the case of a liquid subcooled below its saturation temperature, the critical heat flux is increased

$$q_{cr,sub} = \dot{q}_{cr,sat}(1 + B\Delta T_{sub}) \tag{26}$$

For B, Zuber [19] proposes

$$B = 5.3\,\frac{(\lambda_\ell \rho_\ell c_{p\ell})^{0.5}}{\rho_g \Delta h_v}\left[\frac{\rho_g^2}{\sigma g_n(\rho_\ell - \rho_g)}\right]^{1/8}\left[\frac{g_n(\rho_\ell - \rho_g)}{\sigma}\right]^{1/4} \tag{27}$$

Equation (26), using this value of B, agreed with experimental data for water and ethyl alcohol at pressures up to $10^6\ N/m^2$. Simpler expressions have been proposed by Kutateladze [27],

© 1983 Hemisphere Publishing Corporation

$$B = 0.065\left(\frac{\rho_\ell}{\rho_g}\right)^{0.8}\frac{c_{p\ell}}{\Delta h_v} \tag{28}$$

and by Ivey and Morris [28],

$$B = 0.1\left(\frac{\rho_\ell}{\rho_g}\right)^{0.75}\frac{c_{p\ell}}{\Delta h_v} \tag{29}$$

Equation (26), using this value of ***B,*** agreed with experimental data for water, ethyl alcohol, ammonia, carbon tetrachloride, and isooctane over a wide pressure range, and Eq. (29) is therefore recommended for ***B.***

(d) Surface condition

The influence of surface condition on $\dot{q}_{cr}$ has not been clearly established. The hydrodynamic theory would predict that there is little or no effect, and this appears to be borne out by the results of Berenson [29] (Fig. 2). In particular, mechanical preparation of the surface in various ways, e.g., scoring, roughening, sandblasting, does not appear to greatly influence $\dot{q}_{cr}$. On the other hand, surfaces that have oxidized or had deposits formed on them appear to have higher values of $\dot{q}_{cr}$. This effect appears to be due to the increased wettability of the surface. Thus, Ivey and Morris [30] and Bernath [24] both report higher values of $\dot{q}_{cr}$ on oxidized aluminum surfaces than on clean aluminum surfaces, whereas Costello and Frea [31] and Owens [32] found that deposits formed from tap water considerably increased the value of $\dot{q}_{cr}$ compared with that measured for distilled water. The critical heat flux on essentially nonwetting surfaces, e.g., covered with grease or having a fluorocarbon coating, will be markedly reduced [32a], possibly even down to the heat flux corresponding to the initiation of nucleate boiling (Fig. 12).

D. Transition boiling

In this little-studied region of the boiling curve, liquid periodically contacts the heating surface with the result that the formation of large amounts of vapor forces the liquid away from the surface and an unstable vapor film or blanket is formed. This in turn collapses, allowing the liquid to contact the surface once more. The region is normally obtainable only by controlling the surface temperature to a predetermined value. From Fig. 1 it will be seen that for water at atmospheric pressure this temperature range is about 140-250° C. One such study, by Sakurai and Shiotsu [33], has revealed the existence of hysteresis effects in the transition boiling region near the critical heat flux point. The maximum heat flux reached at point ***D***

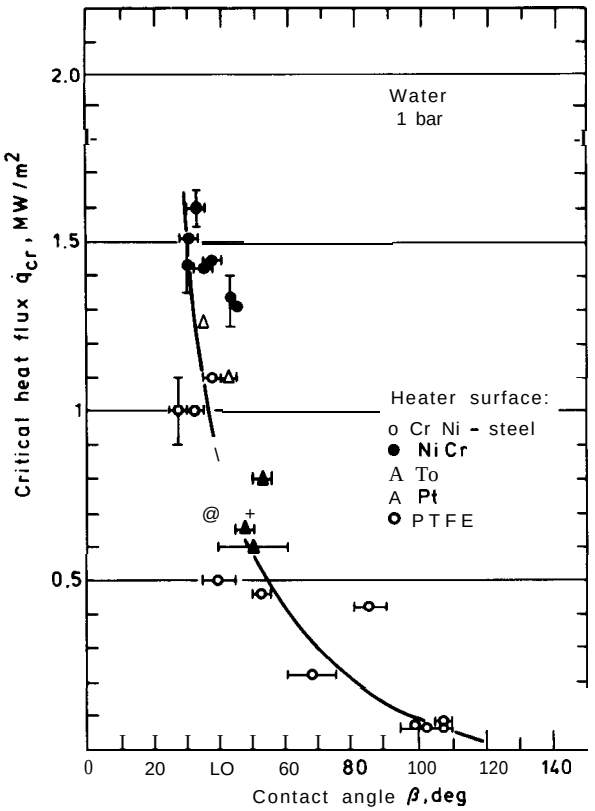

Figure 12 Influence of contact angle on the pool boiling critical heat flux of water at atmospheric pressure. From Diesselhorst et al. [32a].

when the surface temperature is reduced through the transition boiling region was found to be less than the maximum (critical) heat flux reached when the surface temperature was increased through the nucleate boiling region. Because of the periodic nature of the process, the surface heat flux and temperature undergo large variations with both time and position on the heater. However, the average heat flux decreases as the temperature increases, because the proportion of the time and heater surface that the liquid spends in contact with the surface continually decreases. A discussion of some of the factors that are important in transition boiling was given by Bankoff and Mehra [34]. No adequate theory or model of this region exists at this time. However, it is usually reasonable to interpolate linearly on log-log paper between the critical and minimum heat flux points on a curve of heat flux versus temperature difference (Fig. 3).

E. Minimum heat flux

The minimum heat flux $\dot{q}_{min}$ is reached when the heat flux matches the minimum rate of vapor formation that will sustain a stable vapor film over the heating surface. Vapor is released from this film in the

© 1983 Hemisphere I blishing Corporation

form of bubbles produced regularly in both time and space. If the heat flux is less than $\dot{q}_{\min}$, the interface will collapse onto the heating surface, cooling it and reestablishing nucleate boiling. Thus, the surface temp erature would move from ***E*** to ***E'*** on Fig. 1. The vapor release rate can be considered as the product of the volume of a released bubble, the number of bubbles per cycle per unit area, and a minimum wave frequency. This leads to the expression for $\dot{q}_{\min}$ on a flat plate first derived by Zuber [19] and subsequently modified by Berenson [35]:

$$\dot{q}_{\min,F} = \text{const}\ \rho_g \Delta h_v \left[\frac{\sigma g_n(\rho_\ell - \rho_g)}{(\rho_\ell + \rho_g)^2}\right]^{1/4} \quad (30)$$

Because of uncertainty in the minimum wave frequency, the constant in Eq. (30) must really be determined experimentally. Zuber proposed various values for the constant that are mostly too high, and Berenson s later experiments resulted in 0.09, which remains the best current estimate for a flat plate surface. Berenson also gave the following expression for the wall superheat $(T_w - T_{\text{sat}})$ at the minimum heat flux point:

$$T_w - T_{\text{sat}} = 0.127 \frac{\rho_g \Delta h_v}{\lambda_g}\left[\frac{g_n(\rho_\ell - \rho_g)}{\rho_\ell + \rho_g}\right]^{2/3} \times \left[\frac{\sigma}{g_n(\rho_\ell - \rho_g)}\right]^{1/2}\left[\frac{\eta_g}{g_n(\rho_\ell - \rho_g)}\right]^{1/3} \quad (31)$$

For horizontal cylinders $\dot{q}_{\min}$ increases above that given by Eq. (30) as the diameter is reduced, and Lienhard and Wong [36] have proposed the following expression with the constant evaluated from experiments with isopropanol and benzene:

$$\dot{q}_{\min} = 0.057 \frac{\rho_g \Delta h_v}{R}\left[\frac{2g_n(\rho_\ell - \rho_g)}{\rho_\ell + \rho_g} + \frac{\sigma}{R^2(\rho_\ell + \rho_g)}\right]^{1/2} \times \left[\frac{g_n(\rho_\ell - \rho_v)}{\sigma}\right]^{-3/4}\frac{1}{2R^2} \quad (32)$$

The experimental determination of $\dot{q}_{\min}$ for cylinders is made difficult by the presence of the end mountings, which tend to induce the transition from film boiling to nucleate boiling at heat fluxes above the true $\dot{q}_{\min}$. Kovalev [37] overcame this difficulty in his experiments with water at various pressures and reported results about 40% lower than given by Eq. (32). Likewise, experimental data have been reported [22, 33] that are up to a factor 5 higher than given by Eq. (32). The value of $q_{\min}$ for a vertically oriented heater is lower than for a horizontally mounted heater in a similar ratio to that found for the critical heat flux, i.e., -0.75.

F. Film boiling

At large temperature differences a continuous vapor film blankets the heater surface. The major resistance to heat transfer is confined to this vapor film, and because there is lack of liquid-solid contact, this region is the most tractable to analyze. The relationships for the heat transfer coefficient in laminar or turbulent film boiling in various geometric situations can be established by direct analogy with the identical relationships derived for filmwise condensation (see Sec. ***2.6.2).***

Berenson [38] analyzed film boiling on a large horizontal plate and produced the following equation, which was compared with data for pentane (Fig. 3), carbon tetrachloride, benzene, and ethyl alcohol:

$$\alpha = 0.425\left[\frac{\lambda_g^3 \rho_g(\rho_\ell - \rho_g) g_n \Delta h_v'}{\eta_g \Delta T(\lambda_c/2\pi)}\right]^{1/4} \quad (33)$$

where λ_c is the critical (or shortest unstable) wavelength for Taylor instability, given by

$$\lambda_c = 2\pi\left[\frac{\sigma}{g_n(\rho_\ell - \rho_g)}\right]^{1/2} \quad (34)$$

and $\Delta h_v'$ is an effective latent heat of vaporization allowing for the effect of superheat,

$$\Delta h_v' = \Delta h_v\left[1 + \xi\left(\frac{c_{pg}\Delta T}{\Delta h_v}\right)\right] \quad (35)$$

For use in Eq. (35), ξ should be taken as 0.4.

For laminar film boiling from a horizontal tube, Bromley [39] gives

$$\alpha = 0.62\left[\frac{\lambda_g^3 \rho_g(\rho_\ell - \rho_g) g_n \Delta h_v'}{\eta_g \Delta T D}\right]^{1/4} \quad (36)$$

where ξ in Eq. (35) should be taken as 0.68.

For very large tubes, horizontal flat surfaces, and very thin wires, Eq. (36) is inaccurate. For large-diameter tubes and flat horizontal surfaces, the characteristic length is more correctly λ_c than the tube diameter ***D.*** Thus, Breen and Westwater [40] modified Eq. (36):

$$\alpha = \left(0.59 + 0.069\frac{\lambda_c}{D}\right)\left[\frac{\lambda_g^3 \rho_g(\rho_\ell - \rho_g) g_n \Delta h_v'}{\eta_g \Delta T \lambda_c}\right]^{1/4} \quad (37)$$

where $\Delta h_v'$ is now given by

$$\text{Ah:} = \text{Ah,}\left(1 + 0.34\frac{c_{pg}\Delta T}{\Delta h_v}\right)^2 \quad (38)$$

Equation (37) is valid for $0.8 < (\lambda_c/D) < 8$, whereas

© 1983 Hemisphere Publishing corporation
HEDH

Eqs. (36) and (37) become essentially identical when $D \gg \lambda_c$.

For a vertical flat surface, a laminar flow analysis for the situation of zero interfacial stress gives for the local heat transfer coefficient $\alpha(z)$ at a distance z up the surface from the start of film boiling,

$$a(z) = 0.707 \left[\frac{\lambda_g^3 \rho_g (\rho_\ell - \rho_g) g_n \Delta h_v'}{\eta_g \Delta T z} \right]^{1/4} \quad (39)$$

The average coefficient $\bar{\alpha}(z)$ over the region up to a distance z is given by

$$\bar{\alpha}(z) = \tfrac{4}{3} \alpha(z) \quad (40)$$

For the boundary condition of zero interfacial velocity, the coefficient 0.707 in Eq. (39) should be replaced by 0.5. In practice this latter condition is true only at very low values of $\rho_g \eta_g / \rho_\ell \eta_\ell$ [41], and it is common to take a mean between the two values.

On vertical heated surfaces, it is clear that the classical laminar film boiling equations are valid only for a very short distance from the start of film boiling. Beyond this region, vapor is released in large globular voids, which ensures a time-varying but thinner vapor film. Typically, heat transfer coefficients may be up to twice those estimated from Eq. (39).

On a vertical cylinder, Bailey [42] suggested that these globular voids are formed by a process of varicose instability. The wavelength for maximum growth for a surface tension-governed instability of this type is

$$\lambda_c = 2.07 \pi D \quad (41)$$

Substitution of λ_c from this equation for z in Eq. (39) leads to

$$\alpha = 0.47 \left[\frac{\lambda_g^3 \rho_g (\rho_\ell - \rho_g) g_n \Delta h_v'}{\eta_g \Delta T D} \right]^{1/4} \quad (42)$$

An alternative that predicts heat transfer coefficients about 33% higher than Eq. (42) is the application of Eq. (36) that was derived for film boiling on the outside of horizontal cylinders.

The effect of liquid subcooling on film boiling coefficients can be considerable. As an example, for organic liquids such as *n*-hexane, benzene, methanol, carbon tetrachloride, and ethyl alcohol, coefficients will be increased fourfold by subcooling the liquid 40°C.

Surface temperatures are usually high in film boiling, and heat may be transferred by radiation. Bromley [39] proposes the following approximation for combining the effects of convection and radiation:

$$\alpha = a, + 0.75 \alpha_r \quad (43)$$

where α_c is the convective coefficient [for example, Eq. (36) or (42)] and α_r is the radiation coefficient. For simplicity the radiation coefficient α_r can be calculated by assuming radiation between infinite parallel planar surfaces with the liquid acting as a perfect black body,

$$\alpha_r = C_s \epsilon \left(\frac{T_w^4 - T_\ell^4}{T_w - T_\ell} \right) \quad (44)$$

where C_s is the Stefan-Boltzmann constant and ϵ is the emissivity of the heating surface.

Comparisons of the equations given in this section for film boiling with experimental data sets covering a wide range of fluids, viz., nitrogen, oxygen, water, methane, ethane, ethylene, ethylene mixtures, propane, n-butane, methanol, ethyl alcohol, benzene, carbon tetrachloride, suggest an average standard deviation of between 30 and 40%. For fuller details the reader is referred to the reviews by Clements and Colver [43].

Nomenclature** for **Section 2.7.2 appears at the end of Section 2.7.8.

REFERENCES FOR SECTION 2.7.2

1. Hsu, Y. Y., On the Size Range of Active Nucleation Cavities on a Heating Surface, *J.* Heat Transfer, vol. 1, no. 84C(3), pp. 207-216, 1962.
2. Han, C. Y., and Griffith, P., The Mechanism of Heat Transfer in Nucleate Pool Boiling, Pt. I, Bubble Initiation, Growth and Departure, ***Int. J. Heat Mass Transfer, vol. 8,*** no. 6, pp. 887-904, 1965.
3. Brown, W. T., A Study of Flow Surface Boiling, Ph.D. thesis, Massachusetts Institute of Technology, Cambridge, Mass., 1967.
4. Berenson, P. J., Experiments on Pool Boiling Heat Transfer, ***Int. J. Heat Mass Transfer,*** vol. 5, p. 958, 1962.
5. Rohsenow, W. M., A Method of Correlating Heat Transfer Data for Surface Boiling of Liquids. ***Pans. ASME,*** vol. 74, p. 969, 1952.
6. Vachon, R. I., Nix, G. H., and Tanger, G. E., Evaluation of Constants for the Rohsenow Pool Boiling Correlation, ***J. Heat Tyansfer,*** vol. 90C, no. 2, pp. 239-247, May 1968.
7. Vachon, R. I., Tanger, G. E., Davis, D. L., and Nix, G. H., Pool Boiling on Polished and Chemically Etched Stainless Steel Surfaces, ***J. Heat Transfer,*** vol. 90C, no. 2, pp. 231-238, 1968.
8. Forster, H. K., and Zuber, N., Dynamics of Vapour Bubble Growth and Boiling Heat Transfer, ***AIChE J.,*** vol. 1, no. 4, pp. 531-535, 1955.

© 1983 Hemisphere Publishing Corporation

9. Kutateladze, ***S. S., Fundamentals of Heat Transfer,*** Academic, New York, 1963.
10. Mikic, B. B., and Rohsenow, W. M., A New Correlation of Pool Boiling Data Including the Effect of Heating Surface Characteristics, ***J. Heat Transfer,*** vol. 91, pp. 245-250, 1969.
11. Ratiani, G. V., and Shekriladze, I. G., Study of the Process of Fully Developed Boiling of Liquids, ***Heat Transfer Sov. Res., vol.*** 4, no. 4, pp. 126-141, 1972.
12. Borishanski, V. M., Correlation of the Effect of Pressure on the Critical Heat Flux and Heat Transfer Rates Using the Theory of Thermodynamic Similarity, ***in Problems of Heat Transfer and Hydraulics of Two-Phase Media,*** ed. S. S. Kutateladze, pp. 16-37, Pergamon, Oxford, 1969.
13. Mostinskii, ***Teploenergetika,*** Calculation of Heat Transfer and Internal Heat Fluxes in Boiling Liquid Based on Law of Corresponding States, vol. 4, p. 66, 1963; English Abstract,&. ***Chem. Eng.,*** vol. 8, no. 8, p. 580, 1963.
14. Palen, J. W., Yarden, A., and Taborek, J., Characteristics of Boiling Outside Large-Scale Horizontal Multi-Tube Bundles, Heat Transfer-Tulsa, ***AIChE Symp. Ser.,*** vol. 68, no. 118, pp. 50–62, 1972.
15. Bier, K., Engelhorn, H., and Gorenflo, D., Wärmeübergang an tiefsiedende Halogenkältemittel, ***Klima Kälte Ing.,*** vol. 11, pp. 399406, 1976.
16. Cohen, P., and Taylor, G. R., Discussion of Boiling Heat Transfer at Low Heat Flux, by W. ***C.*** Elrod et ***al., J. Heat Transfer,*** vol. 89C, p. 242, 1967.
17. Palen, J., and Westwater, J. W., Heat Transfer and Fouling Rates during Pool Boiling of Calcium Sulphate Solutions, ***Chem. Eng. Prog. Symp. Ser.,*** vol. 62,no. 64, pp. 77-86. 1966.
18. Fand, R. M., and Keswani, K. K., The Influence of Subcooling on Pool Boiling Heat Transfer from a Horizontal Cylinder in Water, ***Heat Transfer 1974,*** vol. 4, ***Proc. 5th Znt. Heat Transfer Conf., Tokyo, Sept.*** 3-7, ***1974,*** Paper B1.3, pp. 11-14, 1974.
19. Zuber, N., On the Stability of Boiling Heat Transfer. ***Trans. ASME,*** vol. 80, p. 711, 1958; see also Zuber, N., Tribus, M., and Westwater, J. W., The Hydrodynamic Crisis in Pool Boiling of Saturated and Subcooled Liquids, ***Znt. Dev. Heat Transfer,*** vol. 2, p. 230, 1961.
20. Kutateladze, S. S., A Hydrodynamic Theory of Changes in the Boiling Process Under Free Convection Conditions, ***Izv. Akad. Nauk SSR Otd. Tekh. Nauk,*** no. 4, pp. 529-536, 1951.
21. Lienhard, J. H., and Dhir, V. K., Extended Hydrodynamic Theory of the Peak and Minimum Pool Boiling Heat Fluxes, NASA Rept. NASA-CR-2270, July 1973.
22. Lienhard, J. H., and Schrock, V. E., The Effect of Pressure, Geometry and the Equation of State upon the Peak and Minimum Boiling Heat Flux, ***J. Heat Transfer, vol.*** 85C, pp. 261-272, 1963.
23. Partington, J. R., ***An Advanced Treatise on Physical Chemistry, vol.*** II ***The Properties of Liquids,*** p. 144, Longmans, Green, New York, 1951.
24. Bernath, L., A Theory of Local Burnout and Its Application to Existing Data, ***Chem. Eng. Prog. Symp. Ser.,*** vol. 56, no. 30, p. 95, 1960.
25. Borishanski, V. M., An Equation Generalising Experimental Data on the Cessation of Bubble Boiling in a Large Volume of Liquid, ***Zhum Tekh. Fiz., vol. 26,*** p. 452, 1956 (tr. in Sov. ***Phys. Tech. Phys.,*** vol. 1, p. 438).
26. Dhir, V. K., and Lienhard, J. H., Peak Pool Boiling Heat Flux in Viscous Liquids, ***J. Heat Transfer,*** vol. 96C, no. 1, pp. 71-78, 1974.
27. Kutateladze, ***S. S., Fundamentals of Heat Transfer,*** Academic, New York, 1963.
28. Ivey, H. J., and Morris, D. J., On the Relevance of the Vapour-Liquid Exchange Mechanism for Sub-cooled Boiling Heat Transfer at High Pressures, UKAEA Rept. AEEW-R137, Winfrith Heath, Dorset, England, 1961.
29. Berenson, P. J., Experiments on Pool Boiling Heat Transfer, ***Int. J. Heat Mass Transfer,*** vol. 5, pp. 985-999, 1962.
30. Ivey, H. J., and Morris, D. J., The Effect of Test Section Parameters on Saturation Pool Boiling Burnout at Atmospheric Pressure, UKAEA Rept. AEEW-R176, Winfrith Heath, Dorset, England, 1962.
31. Costello, C. P., and Frea, W. J., A Salient Non-hydrodynamic Effect on Pool Boiling Burnout of Small Semi-cylindrical Heaters, ***Chem. Eng. Prog. Symp. Ser., vol. 61, no. 57, p. 258, 1965.***
32. Owens, W. L., An Analytical and Experimental Study of Pool Boiling with Particular Reference to Additives, UKAEA Rept. AEEW-R180, Winfrith Heath, Dorset, England, 1963.

32a. Diesselhorst, T., Grigull, U., and Hahne, E., Hydrodynamic and Surface Effects on the Peak Heat Flux ***in*** Pool Boiling, ***in Heat Transfer in Boiling,*** eds. E. Hahne and U. Grigull, ch. 6, p. 124, Hemisphere, Washington, D.C., 1977.

33. Sakurai, A., and Shiotsu, M., Temperature Controlled Pool Boiling Heat Transfer, ***Heat Transfer 1974,*** vol. 4, ***Proc. 5th Znt. Heat Transfer Conf., Tokyo Sept. 3-7, 1974,*** pp. 81-85, 1974.
34. Bankoff, S. G., and Mehra, V. S., A Quenching Theory for Transition Boiling, ***Znd. Eng. Chem. Fundam.,*** vol. 1, pp. 3840, 1962.
35. Berenson, P. J., Transition Boiling Heat Transfer from a Horizontal Surface, Massachusetts Institute of Technology Heat Transfer Laboratory Technical Rept. 17, 1960.
36. Lienhard, J. H., and Wong, P. T. Y., The Dominant Unstable Wavelength and Minimum Heat Flux During Film Boiling on a Horizontal Cylinder, ASME/AIChE 6th Natl. Heat Transfer Conf., Boston, Paper 63-HT-3, 1963.
37. Kovalev, S. A., An Investigation of Minimum Heat Fluxes in Pool Boiling of Water, ***Znt. J. Heat Mass Transfer,*** vol. 19, pp. 1219-1226, 1966.
38. Berenson, P. J., Film Boiling Heat Transfer from a Horizontal Surface, ***J. Heat Transfer, vol. 83,*** pp. 351-358, 1961.
39. Bromley, L. A., Heat Transfer in Stable Film Boiling, ***Chem. Eng. Prog.,*** vol. 46, no. 5, pp. 221-227, 1950.
40. Breen, B. P., and Westwater, J. W., Effect of Diameter of Horizontal Tubes on Film Boiling Heat Transfer, AIChE/ASME 5th Natl. Heat Transfer Conf., Houston, AIChE Preprint 19, 1962.
41. Koh, J. C. Y., Analysis of Film Boiling on Vertical Surfaces, ***J. Heat Transfer,*** vol. 84, p. 55, 1962.
42. Bailey, N. A., Film Boiling on Submerged Vertical Cylinders, UKAEA Rept. AEEW-M1051, Winfrith Heath, Dorset, England, 1971.

© 1983 Hemisphere Publishing Corporation

43. Clements, L. D., and Colver, C. P., Natural Convection Fihn Boiling Heat Transfer, ***Znd. Eng. Chem.,*** vol. 62, no. 9, pp. 2646, 1970.
44. Cichelli, M., and Bonilla, C., Heat Transfer to Boiling Liquids under Pressure, ***Trans.*** *AIChE,* vol. 41, p. 75.5, 1945.
45. Borishanski, V. M., (a) ***Energomaschinostroyeniye,*** no. *7,* **1958; (b) *Zh. Tekh. Fiz.,*** no. 2, 1956; ***(c)*** *Kotloturbostroyeniye,* no. 4, 1952.
46. Borishanski, V. M., Bobrovich, G. I., and Minchenko, F. P., Heat Transfer from a Tube to Water and to Ethanol in Nucleate Pool Boiling, ***in Problems of Heat*** *Transfer* ***and Hydraulics of Two-Phase Media,*** ed. S. S. Kutateladze, pp. 85-106, Pergamon, Oxford, 1969.
47. McAdams, W., ***Heat Transmission,*** McGraw-Hill, New York, 1954.
48. Kutateladze, ***S. S., Trud. ZKTZ,*** Book 2, Mashig, 1947.
49. Huber, D. A., and Hoehne, J. C., Pool Boiling of Benzene, Diphenyl and Benzene-Diphenyl Mixtures under Pressure, ***J. Heat Transfer,*** pp. 215-220, 1963.
50. Cryder, D. S., and Finalborgo, ***Trans.*** *AIChE,* vol. 33, p. 346, 1937.
51. Myers, J., and Katz, D., Boiling Coefficients outside Horizontal Tubes, ***Chem. Eng. Prog. Symp. Ser.,*** no. 5, p. 49, 1953.
52. Danilova, G. N., Heat Transfer to Boiling Refrigerants, ***in Problems of Heat Transfer and Hydraulics of Two-Phase Media,*** ed. S. S. Kutateladze, pp. 107-130, Pergamon, Oxford, 1969.
53. Sciance, C. T., Colver, C. P., and Sliepcevich, C. M., ***Adv. C'ryog. Eng.,*** vol. 12, pp. 395-409, 1967.
54. Bier, K., Gorenflo, D., and Wickenhäuser, G., Pool Boiling Heat Transfer at Saturation Pressures up to Critical, in ***Heat Transfer in Boiling,*** eds. E. Hahne and U. Grigull, ch. 7, Hemisphere, Washington, D.C., 1977.
55. Gorenflo, D., Influence of Pressure on Heat Transfer from Horizontal Tubes to Boiling Refrigerants, *Proc. 12th* ***Znt. Congr. Refrigeration, Madrid,*** vol. 2, pp. 587-599, 1969.
56. Lienhard, J. H., and Watanabe, K., On Correlating the Peak and Minimum Boiling Heat Fluxes with Pressure and Heater Configuration, ***J. Heat Transfer,*** pp. 94-100, 1966.
57. Rallis, C. J., and Jawurek, H. H., Latent Heat Transport in Saturated Nucleate Boiling, ***Znt. J. Heat Mass Transfer,*** vol. 7, pp. 1051-1068. 1964.

© 1983 Hemisphere Publishing Corporation

2.7.3

Boiling within vertical tubes

J. G. Collier

A. Introduction

In this section it is proposed to describe boiling under steady-state conditions in a vertical, uniformly heated tube. Each of the various heat transfer regions present will be described briefly, together with simple correlations for the estimation of heat transfer coefficients in each region and for the transition from one region to another.

(a) Regions of heat transfer in a vertical heated tube

Consider a vertical tube heated uniformly over its length with a low heat flux and fed with subcooled liquid at its base. At such a rate the liquid is totally evaporated over the length of the tube. Figure 1 shows in diagramatic form the various flow patterns encountered over the length of the tube, together with the corresponding heat transfer regions.

While the liquid is being heated up to the saturation temperature and the wall temperature remains below that necessary for nucleation, the process of heat transfer is ***single-phase convective heat transfer to the liquid phase*** (region **A).** At some point along the tube, the conditions adjacent to the wall are such that the formation of vapor from nucleation sites can occur. Initially, vapor formation takes place in the presence of subcooled liquid (region B), and this heat transfer mechanism is known as ***subcooled nucleate boiling.*** In the subcooled boiling region, B, the wall temperature remains essentially constant a few degrees above the saturation temperature, while the mean bulk fluid temperature is increasing to the saturation temperature. The amount by which the wall temperature exceeds the saturation temperature is known as the ***degree of superheat,*** ΔT_{sat}, and the difference between the saturation and the bulk fluid temperature is known as the ***degree of subcooling,*** ΔT_{sub}.

The transition between regions B and C, the ***subcooled nucleate boiling region*** and the ***saturated nucleate boiling region,*** is clearly defined from the thermodynamic viewpoint. It is the point at which the liquid reaches the saturation temperature ($x = 0$) found on the basis of simple heat balance calculations. However, subcooled liquid can persist in the liquid core, even in the region defined as saturated nucleate boiling. Vapor generated in the subcooled region is present at the transition between regions B and C ($x = 0$); thus, some of the liquid must be subcooled to ensure that the liquid mixed mean (mixing cup) enthalpy equals that of saturated liquid ***(hp).*** This effect occurs as a result of the radial temperature profile in the liquid, and the subcooled liquid flowing in the center of the channel will reach the saturation temperature only at some distance downstream of the point x = 0.

In the regions C to G, the variable characterizing the heat transfer mechanism is the thermodynamic mass quality (x) of the fluid. The quality of the liquid-vapor mixture at a distance, z, is given on a thermodynamic basis as

$$x(z) = \frac{h(z) - h_\ell}{\Delta h_v} \tag{1}$$

In the region $0 < x < 1$ and for complete thermodynamic equilibrium, x represents the ratio of the

© 1983 Hemisphere Publishing Corporation

HEDH

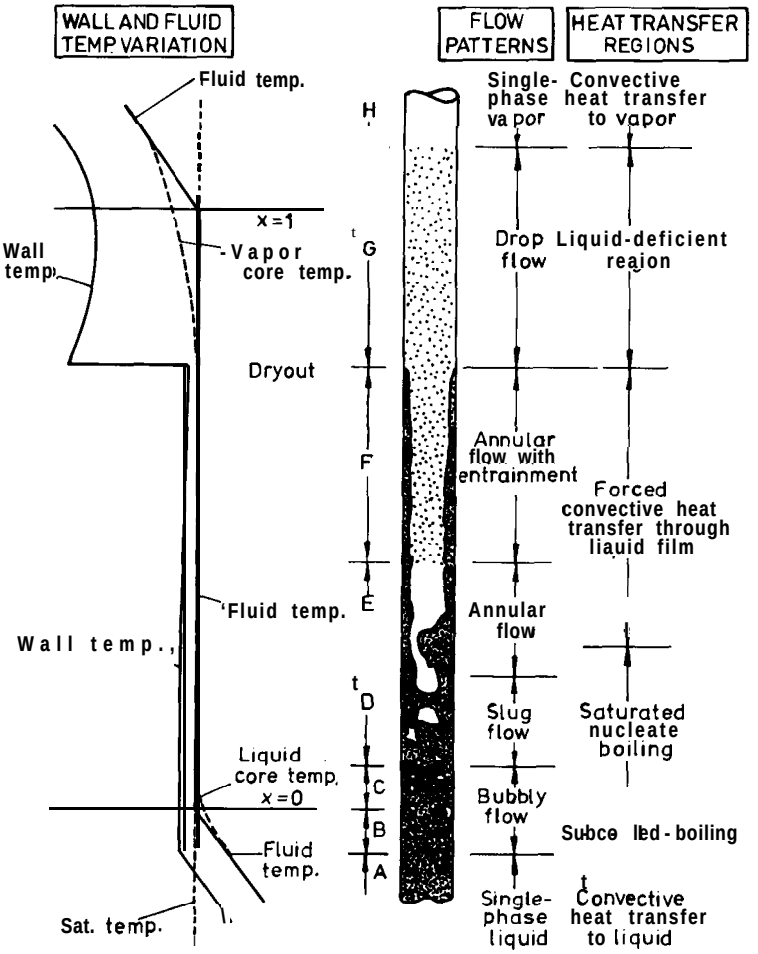

Figure 1 Regions of heat t nsfer in convective boiling.

vapor mass flow rate to the total mass flow rate. From the thermodynamic definition, Eq. (1), x may have both negative values and values greater than unity. Although these are sometimes used for convenience, negative values or values greater than unity have no practical significance other than to signify that, in the former case, the condition is that of a subcooled liquid and, in the latter case, that of a superheated vapor. The variable x is also often referred to as the ***vapor mass fraction.***

As the quality increases through the saturated nucleate boiling region, a point may be reached where a fundamental transition in the mechanism of heat transfer takes place. The process of boiling is replaced by the process of evaporation. This transition is preceded by a change in the flow pattern from bubbly or slug flow to annular flow (regions E and F). In the latter regions the thickness of the thin liquid film on the heating surface is often such that the effective thermal conductivity is sufficient to prevent the liquid in contact with the wall being superheated to a temperature that would allow bubble nucleation. Heat is carried away from the wall by forced convection in the film to the liquid film-vapor core interface, where evaporation occurs. Since nucleation is completely suppressed, the heat transfer process can no longer be called boiling. The region beyond the transition has been referred to as the ***two-phase forced convective region*** of heat transfer (regions E and F).

At some critical value of quality, the complete evaporation of the liquid film occurs. This transition is known as *dryout,* and is accompanied by a rise in the wall temperature for channels operating with a controlled surface heat flux. The area between the dryout point and the transition to ***saturated vapor*** (region H) has been termed the ***liquid-deficient region*** (corresponding to the drop flow pattern) (region G). This dryout condition often puts an effective limit on the amount of evaporation that can be allowed to take place in a channel at a particular value of heat flux.

© 1983 Hemisphere Publishing Corporation

(b) Variation of heat transfer coefficient with quality

It is useful at this stage to describe, at least qualitatively, the progressive variation of the local surface temperature (or local heat transfer coefficient) along the length of the tube as evaporation proceeds. The local heat transfer coefficient can be established by dividing the surface heat flux (constant over the tube length) by the difference between the wall temperature and the bulk fluid temperature. Typical variations of these two temperatures with length along the tube are shown in Fig. 1. The variation of heat transfer coefficient with length along the tube for the conditions represented in Fig. 1 is given in Fig. 2 [curve i, solid line]. In the single-phase convective heat transfer region, the wall temperature is displaced above the bulk fluid temperature by a relatively constant amount (the heat transfer coefficient is approximately constant) and is modified only slightly by the influence of temperature on the liquid physical properties. In the subcooled nucleate boiling region, the temperature difference between the wall and the bulk fluid decreases linearly with length up to the point where x = 0. The heat transfer coefficient therefore increases linearly with length in this region. In the saturated nucleate boiling region, the temperature difference, and therefore the heat transfer coefficient, remains constant. Because of the reducing thickness of the liquid film in the two-phase forced convective region, the difference in temperature between the surface and the saturation temperature is reduced and the heat transfer coefficient is increased with increasing length or mass quality. At the dryout point the heat transfer coefficient is suddenly reduced from a very high value in the forced convective region to a value near that expected for heat transfer by forced convection to saturated steam. As the quality increases through the liquid-deficient region, so the vapor velocity increases and the difference in temperature between the surface and the saturation value decreases with the corresponding rise in heat transfer coefficient. Finally, in the single-phase vapor region (x > 1), the wall temperature is once again displaced by a constant amount above the bulk fluid temperature and the heat transfer coefficient levels out to that corresponding to convective heat transfer to a single-phase vapor flow.

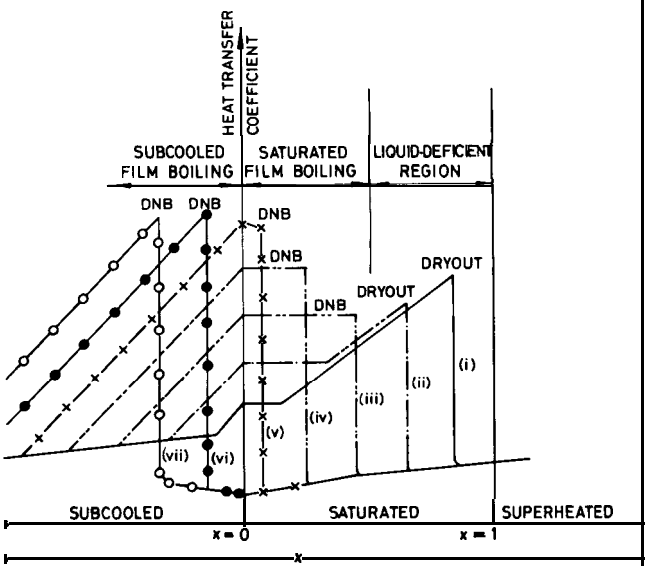

Figure 2 Variation of heat transfer coefficient with quality with increasing heat flux as parameter.

The above comments have been restricted to the case where a relatively low heat flux is supplied to the walls of the tube. The effect of progressively increasing the surface heat flux while keeping the inlet flow rate constant will now be considered with reference to Figs. 2-4. Figure 2 shows the heat transfer coefficient plotted against mass quality with increasing flux as parameter (curves i to vii). Figure 3 shows the various regions of two-phase heat transfer in forced convective boiling on a three-dimensional diagram with heat flux, mass quality, and temperature as coordinates- the boiling surface. Figure 4 shows the regions of two-phase forced convective heat transfer as a function of quality with increasing heat flux as ordinate (an elevation view of Fig. 3 taken in the direction of the arrow). Curve i of Fig. 2 relates to the conditions shown in Fig. 1 for a low heat flux being supplied to the walls of a tube. The temperature pattern shown in Fig. 1 will be recognized as the projection in plan view (temperature-quality coordinates) of Fig. 3. Curve ii shows the influence of increasing the heat flux. Subcooled boiling is initiated sooner; the heat transfer coefficient in the nucleate boiling region is higher but is unaffected in the two-phase forced convective region. Dryout occurs at a lower mass quality. Curve iii shows the influence of a further increase in the heat flux. Again, subcooled boiling is initiated earlier and the heat transfer is again higher in the nucleate boiling region. As the mass quality increases, before the two-phase forced convective region is initiated, and while bubble nucleation is still occurring, an abrupt deterioration in the cooling process takes place. This transition is essentially similar to the critical heat flux phenomenon in saturated pool boiling and will be termed departure from nucleate boiling (DNB).

The mechanism of heat transfer under conditions where the critical heat flux (DNB or dryout) has been exceeded is dependent on whether the initial condition

© 1983 Hemisphere F blishing Corporation

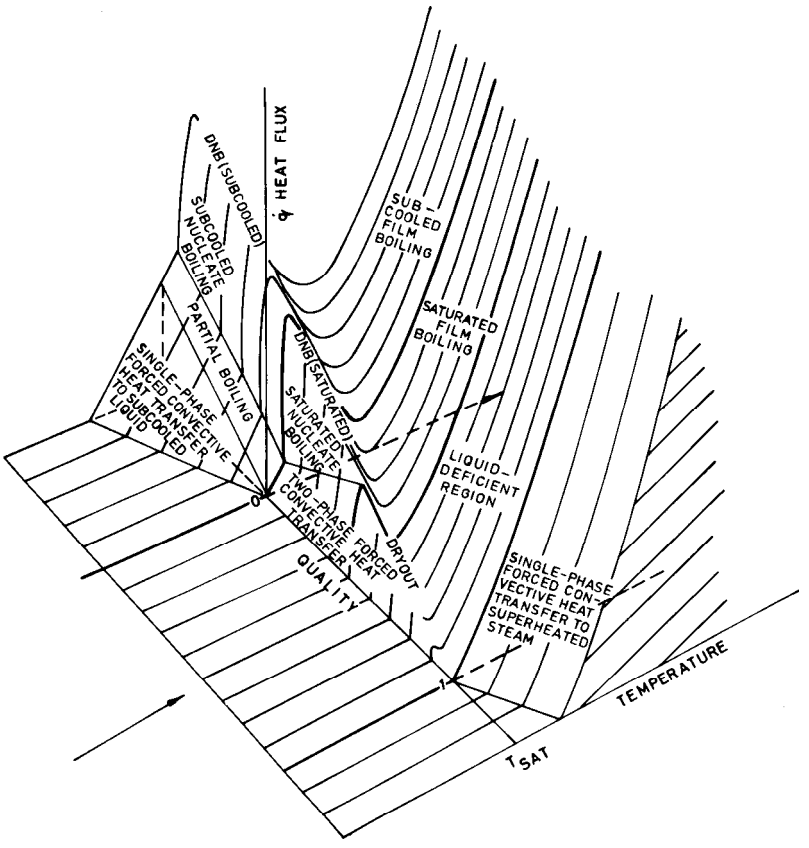

Figure 3 Forced convection boiling surface (T, x, $\dot{q}$ coordinates).

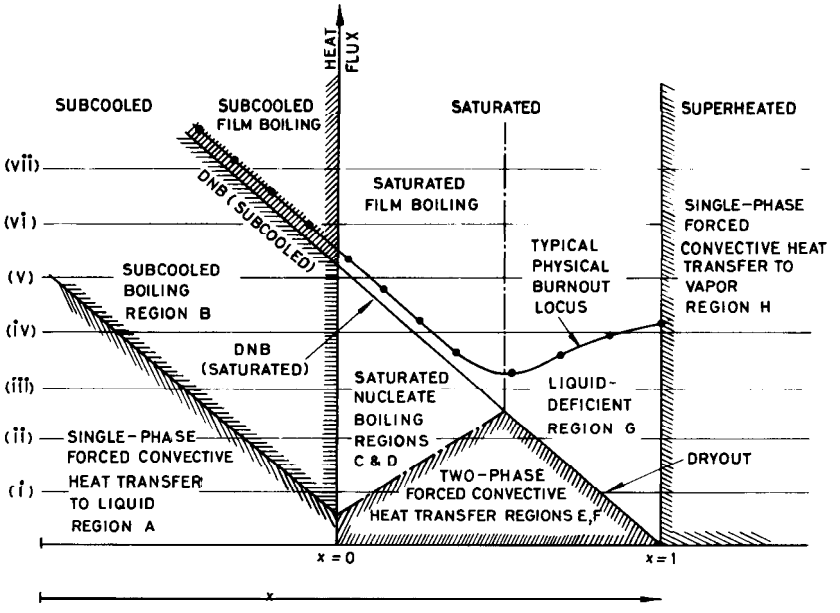

Figure 4 Regions of two-phase forced convective heat transfer as a function of quality with increasing heat flux as ordinate.

© 1983 Hemisphere Publishing Corporation

was the process of boiling (i.e., bubble nucleation in the subcooled or low mass quality regions) or the process of evaporation (i.e., evaporation at the liquid film-vapor core interface in the higher mass quality areas). In the latter case, the liquid-deficient region is initiated; in the former case the resulting mechanism is one of film boiling (Figs. 3 and 4).

By returning to Fig. 2, it can be seen that further increases in heat flux (curves vi and vii) cause the condition of DNB to occur in the subcooled region with the whole of the saturated or quality region being occupied by, first, film boiling and, in the latter stages, the liquid-deficient region-both relatively inefficient modes of heat transfer. In Fig. 3 and Fig. 4 the film boiling surface has been arbitrarily divided into two regions: subcooled film boiling and saturated film boiling. Film boiling in forced convective flow is essentially similar to that observed in pool boiling. An insulating vapor film covers the heating surface through which the heat must pass. The heat transfer coefficient is orders of magnitude lower than in the corresponding region before the critical heat flux was exceeded, mainly because of the lower thermal conductivity of the vapor adjacent to the surface.

In the following sections, criteria will be given whereby the boundaries delineated in Figs. 3 and 4-the boiling surface-can be established. In addition, methods for calculating heat transfer rates in each heat transfer region will be given.

B. Subcooled boiling

(a) Single-phase liquid heat transfer

Figure 5 shows, in an idealized form, the flow pattern and the variation of the surface and liquid temperatures in the regions designated by A, B, and C. The tube surface temperature in region A, convective heat transfer to single-phase liquid, is given by

$$T_w = T_\ell(z) + \Delta T_\ell \tag{2}$$

and

$$\Delta T_\ell = \frac{q}{\alpha_{\ell o}} \tag{3}$$

where ΔT_ℓ is the temperature difference between the tube inside surface and the mean bulk liquid temperature at a length z from the tube inlet, and $\alpha_{\ell o}$ is the heat transfer coefficient to single-phase liquid under forced convection. The liquid in the channel may be in laminar or turbulent flow; in either case the laws governing the heat transfer are well established and the reader is referred to Sec. 2.5.1 for details. For turbulent flow the well-known Dittus-Boelter equation has been found satisfactory:

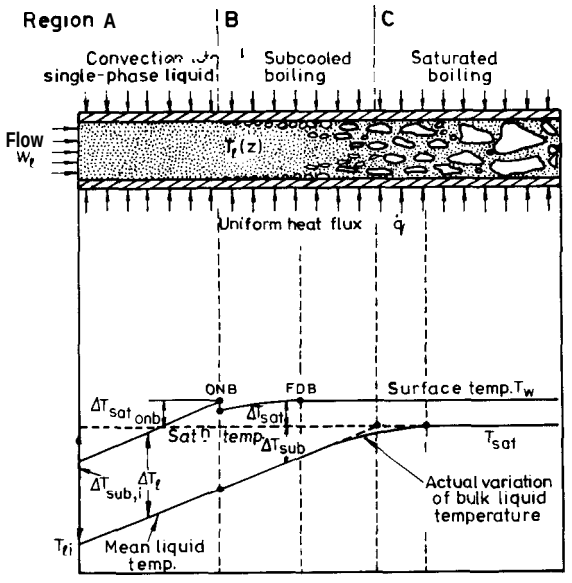

Figure 5 Surface and liquid temperature distributions in subcooled boiling.

$$\frac{\alpha_{\ell o} D}{\lambda_\ell} = 0.023 \left(\frac{\dot{m} D}{\eta_\ell}\right)^{0.8} \left(\frac{c_p \eta}{\lambda}\right)_\ell^{1/3} \tag{4}$$

This relation is valid for heating in vertical up flow with $z/D > 50$ and $\dot{m}D/\eta_\ell > 10\ 000$.

(b) The onset of subcooled nucleate boiling

Figure 6 shows, in qualitative form, the variation of tube inside surface temperature at a point z as the heat flux is steadily increased at a given inlet subcooling and mass velocity. Three regions are shown as the single-phase region ***AB***, the partial boiling region ***BCDE***, and the fully developed subcooled boiling region ***EF***.

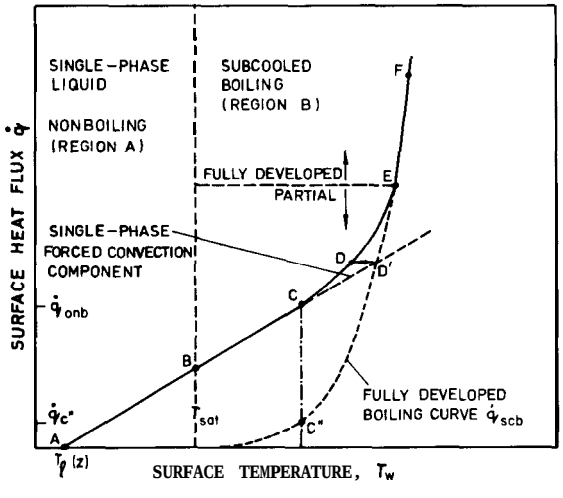

Figure 6 Subcooled boiling curve.

© 1983 Hemisphere Publishing Corporation

As the heat flux is increased, the surface temperature will follow the line ***ABD'*** until the first bubbles nucleate. A higher degree of superheat is necessary to initiate the first bubble nucleation sites at a given heat flux than indicated by the curve ***ABCDE.*** When nucleation first occurs, the surface temperature drops from ***D'*** to ***D*** and, for further increases in heat flux, follows ***the line DEF.*** The criterion for the onset of boiling can be crudely established as the intersection of line ***ABD'*** and the fully developed boiling curve, $C''EF$.

A more refined treatment of the onset of nucleation can be derived by considering the temperature profile in the region adjacent to the heated wall (see Sec. 2.7.2A). Using this approach, Bergles and Rohsenow [1] obtained an equation for the wall superheat required for the onset of subcooled boiling. Their equation is ***valid for water only*** and is

$$(T_w - T_{sat})_{onb} = 0.556 \left(\frac{\dot{q}}{1\,082p^{1.156}}\right)^{0.463p^{0.0234}} \tag{5}$$

where $\dot{q}$ is the surface heat flux (W/m^2) and p is the system pressure (bar). An alternative expression by Davis and Anderson [2] ***valid for all fluids*** is

$$(T_w - T_{sat})_{onb} = \left(\frac{8\sigma\dot{q}T_{sat}}{\lambda_\ell \Delta h_v \rho_g}\right)^{0.5} \tag{6}$$

Equations (5) and (6) are in good agreement with each other for the case of high-pressure water flows. Frost and Dzakowic [3] have extended this treatment to cover other liquids. In their study, nucleation was assumed to occur when the liquid temperature, $T_\ell(y)$ was matched to the temperature for bubble equilibrium T_g at a distance nr_c, where $n = (c_p\eta/\lambda)^2_\ell$ rather than r_c [see Fig. 2.7.2(2)]. Thus Eq. (6) becomes

$$(T_w - T_{sat})_{onb} = \left(\frac{8\sigma\dot{q}T_{sat}}{\lambda_\ell \Delta h_v \rho_g}\right)^{0.5} \mathrm{Pr}_\ell \tag{7}$$

This equation was compared with experimental data for the onset of boiling for a variety of different fluids. A parameter X can be defined as

$$X = \frac{(T_w - T_{sat})_{onb}}{\dot{q}^{0.5}\mathrm{Pr}_\ell} = \left(\frac{8\sigma T_{sat}}{\lambda_\ell \Delta h_v \rho_g}\right)^{0.5} \tag{8}$$

Figure 7 shows values of X_{exp}/X_{ref} plotted against reduced pressure. X_{exp} was calculated from reported values of $(T_w - T_{sat})_{onb}$ and $\dot{q}_{onb}$; X_{ref} was evaluated from fluid physical properties at a constant reduced pressure of 0.05. Values of X_{ref} for various fluids are given in Table 1.

The above treatments can only predict the onset of nucleate boiling accurately if there is a sufficiently wide range of active cavity sizes available on the heating surface. This is not always the case, and for this reason Eq. (8) represents the lower bound of the experimental results shown in Fig. 7; i.e., boiling in many instances was not initiated until higher values of surface temperature than estimated from Eq. (8) were reached. The optimum size of active cavity r_c (see Sec. 2.7.2A) may be evaluated from

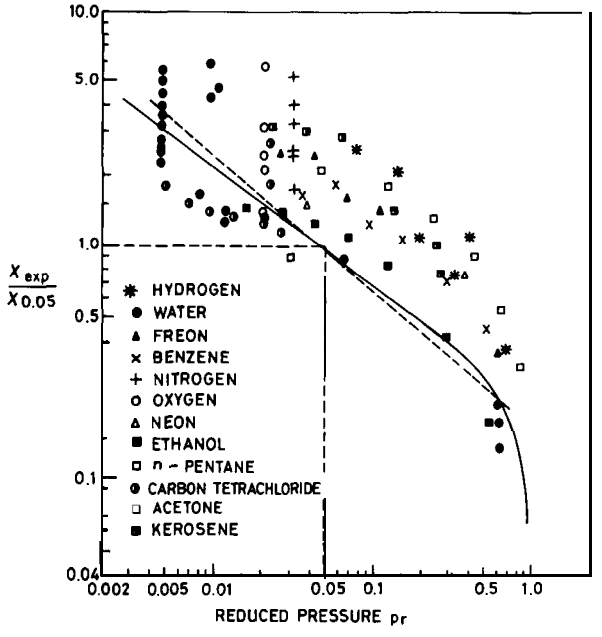

Figure 7 Experimental data for the onset of boiling compared with Eq. (8). From Frost and Dzakowic [3].

$$r_c = \left(\frac{2\sigma T_{sat}\lambda_\ell}{\dot{q}\Delta h_v \rho_g}\right)^{0.5} \tag{9}$$

The size of active nucleation sites actually present on the heated surface may be estimated by the methods given in Sec. 2.7.1E. Alternatively, some guidance is also given at the end of Sec. 2.7.2A. If r_c ***exceeds*** these typical values, then evaluate the wall superheat for the onset of boiling from

$$(T_w - T_{sat})_{onb} = \frac{2\sigma T_{sat}}{r_{max}\Delta h_v \rho_g} + \frac{\dot{q}r_{max}}{\lambda_\ell} \tag{10}$$

where r_{max} is the estimated maximum size of active nucleation site on the surface.

For the subcooled boiling region, Eq. (6) or (7) must be solved simultaneously with the heat transfer equation,

$$\dot{q} = \alpha_{\ell o}(T_w - T_\ell(z)) = \alpha_{\ell o}[(T_w - T_{sat})_{onb} + (T_{sat} - T_\ell(z))] \tag{11}$$

to give the heat flux $\dot{q}$ and $(T_w - T_{sat})_{onb}$ required for the onset of boiling. The boundary between region A and region B shown in Fig. 4 can be derived

© 1983 Hemisphere Publishing Corporation

Table 1 Reference values of X for eq. (8) evaluated at a reduced pressure of 0.05

Fluid	X_{ref}, $K/(Wm^{-2})^{0.5}$
Ammonia	0.004 32
Carbon dioxide	0.011 86
Carbon tetrachloride	0.013 64
Mercury	0.003 97
Neon	0.002 41
n-Pentane	0.012 14
p-Hydrogen	0.003 38
Nitrogen	0.005 19
Propane	0.009 60
Oxygen	0.005 07
Benzene	0.013 39
Water	0.004 4 1
Freon 12	0.014 17
Ethanol	0.008 91
Acetone	0.011 20
Kerosene (JP-4)	0.012 67
Helium4	0.002 31
Argon	0.006 01

from such a simultaneous solution, and it is noted that at the condition $T_{sat} - T_\ell(z) = 0$,

$$(\dot{q}_{onb})_{\Delta T_{sub}(z)=0} = \frac{8\alpha_{\ell o}^2 \sigma T_{sat}}{\lambda_\ell \Delta h_v \rho_g} \qquad (12)$$

For heat fluxes ***below*** that given by Eq. (12), the bulk liquid must be superheated before vapor generation can take place at the heating surface; i.e., there is no subcooled boiling region. Such conditions often lead to unstable operation of heat transfer equipment and should be avoided. The above treatment may also be extended to cover the influence of dissolved gases upon nucleation.

(c) Fully developed subcooled boiling

When boiling is first initiated, only a limited number of nucleation sites are operating, so a proportion of the heat will continue to be transferred by normal single-phase processes between patches of bubbles. This transition region is referred to as ***partial boiling.*** As the surface temperature increases, so the number of bubble sites also increases and the area for single-phase heat transfer decreases. Finally, the whole surface is covered by bubble sites, boiling becomes ***fully developed,*** and the single-phase component reduces to zero. In the fully developed boiling region, velocity and subcooling, both of which have a strong influence on single-phase heat transfer, have little or no effect on the surface temperature. In subcooled boiling the surface temperature is primarily a function of the surface heat flux and the system pressure for a given fluid. The influence of surface condition should be less for forced convective boiling than for pool boiling, because the higher heat fluxes and wall superheats shift the range of active nucleation sites to the smaller sizes that should be readily available on most surfaces. However, there is little direct experimental evidence to support this contention.

It would appear that the form of the equations found suitable for the correlation of pool boiling data (Sec. 2.7.2) is also suitable for the representation of forced convective, fully developed, subcooled boiling data. The values of the slope and intercept [***n*** and ***A*** of Eq. 2.7.2(6)] may, however, need to be adjusted from the values found appropriate for pool boiling.

One such correlation is due to Rohsenow [4] [see Sec. 2.7.2, Eq. 2.7.2(7)]. Values of C_{sf} derived specifically from forced [1, 5, 6] (and natural [7]) convection inside tubes (rather than pool boiling data) are given in Table 2.

Table 2 Values of C_{sf} in eq. 2.7.2(7) obtained in the reduction of the forced (and natural) convection subcooled boiling data of various investigators[a]

Reference	Heating surface	C_{sf}	Fluid surface
Rohsenow and Clark [5]	Vertical tube (4.56 mm ID)	0.006	Water-nickel
Krieth and Summerfield [6]	Horizontal tube (14.9 mm ID)	0.015	Water-stainless steel
Piret and Isbin [7]	Vertical tube (27.1 mm ID)	0.013	Water-copper
		0.013	Carbon tetrachloride-copper
		0.002 2	Isopropyl alcohol-copper
		0.003 0	*n*-Butyl alcohol-copper
		0.002 75	50% K_2 CO, -copper
		0.005 4	35% K_2 CO, -copper
Bergles and Rohsenow [1]	Horizontal tube (2.39 mm ID)	0.020	Water-stainless steel

[a] Further guidance is provided in Table 2.7.2(1).

© 1983 Hemisphere Publishing Corporation

Jens and Lottes [8] summarized experiments on subcooled boiling of water flowing upward in vertical, electrically heated stainless steel or nickel tubes, having inside diameters ranging from 3.63 to 5.74 mm. System pressures ranged from 7 to 172 bar, water temperatures from 115 to 340°C, mass velocities from 11 to 1.05 X 10^4 kg/m^2 s, and heat fluxes up to 12.5 MW/m^2. These data were correlated by a dimensional equation valid for water only,

$$\Delta T_{sat} = 25\dot{q}^{0.25}\, e^{-p/62} \tag{13}$$

where p is the absolute pressure in bar, $\Delta T_{sat}(=T_w - T_{sat})$ is in °C, and $\dot{q}$ is in MW/m^2. More recently, Thorn [9] reported that the values of AT,,, estimated from Eq. (13) were consistently low over the range of his experiments. A modified equation of the same form and valid only for water was suggested:

$$\Delta T_{sat} = 22.65\dot{q}^{0.5}\, e^{-p/87} \tag{14}$$

The values of $AT,,,$ and α calculated from these equations are not markedly different from those obtained using Eqs. 2.7.2(11), 2.7.2(12), and Table 2.7.2(3). In the absence of other information, use may be made of the procedure described in Sec. 2.7.2B to evaluate fully developed subcooled boiling curves for fluids other than water.

(d) Partial boiling

In the partial boiling region, nucleation and single-phase convection processes occur simultaneously. Rohsenow [IO] proposed the superposition of a single-phase forced convection component and a subcooled boiling component :

$$\dot{q} = \dot{q}_{\ell o} + \dot{q}_{scb} \tag{15}$$

The single-phase convection heat flux is evaluated from

$$\dot{q}_{\ell o} = \alpha_{\ell o}[T_w - T_\ell(z)] \tag{16}$$

and the nucleate boiling heat flux $\dot{q}_{scb}$ from Eq. 2.7.2(7). An alternative proposal by Bowring [I I] is discussed in detail by Collier [12]. A simple method of constructing the transition between the single-phase convective region and the fully developed boiling region has been suggested by Bergles and Rohsenow [I]. The procedure can be summarized by reference to Fig. 6. The fully developed subcooled boiling curve, $\dot{q}_{scb}$, ***FED'C"*** is established from experimental data at high values of $T_w - T_{sat}$ or constructed using empirical equations of the form of Eq. (13). The single-phase forced convection curve ***ABCD'*** is constructed from Eq. (16).

The flux $\dot{q}_{onb}$ for the onset of nucleation (point C on Fig. 6) can be calculated from the methods given previously. The fixing of point C enables a point C to be found on the extrapolated fully developed boiling curve at the same surface temperature as point C. A simple interpolation formula is given that satisfies the characteristics of the boiling curve between C and ***E:***

$$\dot{q} = \dot{q}_{\ell o}\left\{1 + \left[\frac{\dot{q}_{scb}}{\dot{q}_{\ell o}}\left(1 - \frac{\dot{q}_{c''}}{\dot{q}_{scb}}\right)\right]^2\right\}^{1/2} \tag{17}$$

Equation (17) is then applied by picking off values of $\dot{q}_{\ell o}$ and $\dot{q}_{scb}$ at various values of T_w to fill in the section ***CE.*** This method is recommended for rapid calculation of the complete forced convective subcooled boiling curve.

(e) Void fraction and pressure drop in subcooled boiling

A knowledge of the amount of vapor present in the channel during subcooled boiling is needed to establish the influence on the pressure gradient (see Sec. 2.3.2). In the representation of subcooled boiling shown in Fig. 8, it will be seen that, for high subcoolings, just after the onset of nucleation, the vapor generated remains as discrete bubbles attached to the surface while growing and collapsing; voidage in this region is essentially a wall effect. At somewhat lower subcoolings, bubbles detach from the surface, condensing only slowly as they move through the slightly subcooled liquid; voidage in this region is a bulk fluid effect.

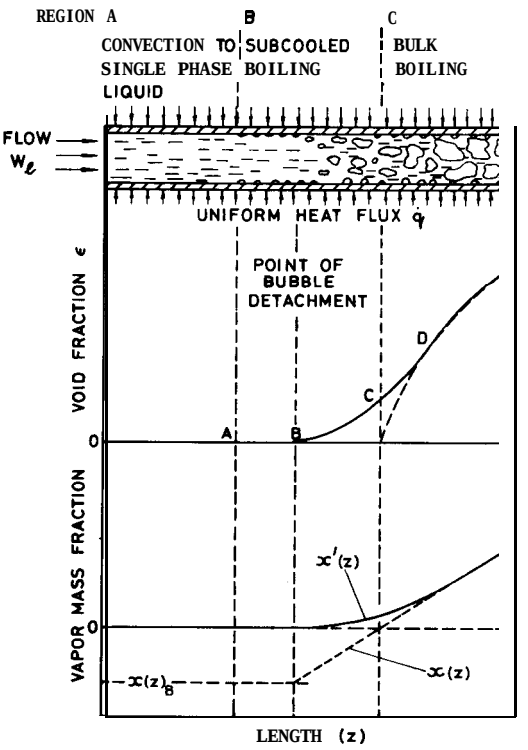

Figure 8 Void fraction in subcooled boiling.

© 1983 Hemisphere Publishing Corporation

Over the region ***AB,*** the void fraction usually remains low and can be neglected. If it is necessary to calculate a value at point ***B,*** the approximate expression due to Levy [13] can be used:

$$\epsilon_{gB} \cong \frac{\pi}{6} \frac{Y_B}{D_h} \tag{18}$$

where Y_B is the distance from the heated wall to the tip of the vapor bubble, and D_h is the heated equivalent diameter of the channel. Y_B is given by

$$Y_B = 0.015\left(\frac{\sigma D_e}{\tau_w}\right)^{0.5} \tag{19}$$

where τ_w is the wall shear stress and D_e is the hydraulic equivalent diameter. The wall shear stress can be evaluated from

$$\tau_w = \frac{f_{\ell o} G^2}{2\rho_\ell} \tag{20}$$

where $f_{\ell o}$ is the single-phase Fanning fraction factor corresponding to a relative roughness of $\epsilon/D_e = 10^{-4}$ (smooth drawn tubing).

Saha and Zuber [14] have proposed a simple method of calculating the point of net vapor generation, which can be assumed to be coincident with point ***B,*** the point of bubble detachment, shown in Fig. 8. At low flow rates the bubble detachment is assumed to be thermally controlled, occurring at a fixed value of the Nusselt number $[\dot{q}D/\lambda_\ell(T_{sat} - T_\ell(z)_B)]$. At high flow rates bubble departure is hydrodynamically induced and occurs at a fixed Stanton number $[\dot{q}/\dot{m}c_{p\ell}(T_{sat} - T_\ell(z)_B)]$. Figure 9 shows experimental data from three fluids plotted as Stanton number versus Peclet number $(\dot{m}Dc_{p\ell}/\lambda_\ell)$. Two regions can be distinguished. Below a Pe value of 70 000, the data fall on a line of slope -1. Above this value St is a constant.

If Pe < 70 000, the value of $\Delta T_{sub}(z)_B$ $(= T_{sat} - T_\ell(z)_B)$ at point ***B*** is given by

$$\Delta T_{sub}(z)_B = 0.002\,2\,\frac{\dot{q}D}{\lambda_\ell} \tag{21}$$

for Pe > 70 000, the value of $\Delta T_{sub}(z)_B$ at ***B*** is given by

$$\Delta T_{sub}(z)_B = 153.8\,\frac{q}{\dot{m}c_{p\ell}} \tag{22}$$

For the region ***BCD,*** both the void fraction and the pressure drop can be evaluated using the relationships given in Sec. 2.3.2, provided that the actual vapor quality can be established. A suitable empirical method has been suggested by Levy [13]. It is assumed that the actual or true vapor mass fraction $x'(z)$, is

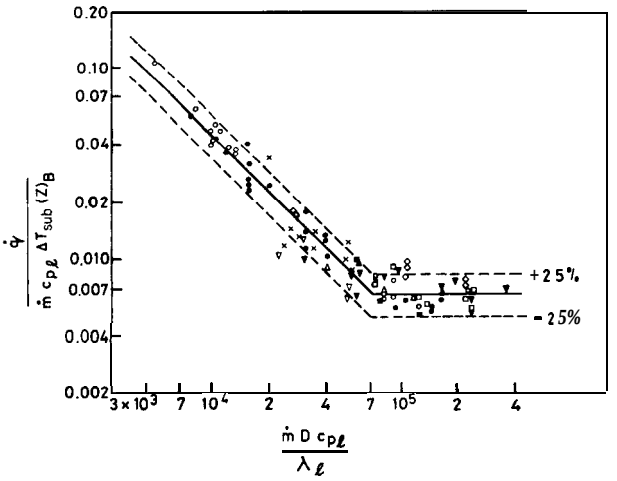

Figure 9 Conditions for point of bubble detachment (point B). From Saha and Zuber [14].

related to the thermodynamic vapor mass fraction, $x(z)$, by the relationship

$$x'(z) = x(z) - x(z)_B \exp\left(\frac{x(z)}{x(z)_B} - 1\right) \tag{23}$$

where $x(z)_B$ is the (negative) thermodynamic vapor mass fraction at the point of bubble detachment, given by

$$x(z)_B = -\frac{c_{p\ell}\Delta T_{sub}(z)_B}{\Delta h_v} \tag{24}$$

Equation (23) is a simple relationship that satisfies the following boundary conditions:

1. At $x(z) = x(z)_B$, then $x'(z) = 0$.
2. $(d/dz)(x'(z))$ at point ***B*** must be zero.
3. $x'(z) \to x(z)$ for $x(z) \gg |x(z)_B|$.

Other methods are available, but Levy s method is recommended as being simple to use for a wide range of fluids.

C. Saturated boiling

(a) Saturated nucleate boiling region

The mechanism of heat transfer in the saturated nucleate boiling region is essentially identical to that in the subcooled region. A thin layer of liquid near the heated surface is superheated to a degree sufficient to allow nucleation. The heat transfer coefficient and heater surface temperature variation is smooth and continuous through the thermodynamic boundary $(x = 0)$ marking the onset of saturated boiling. The methods and equations used to correlate experimental data in the subcooled region remain valid for this

© 1983 Hemisphere I blishing Corporation

region with the proviso that $T_\ell(z) = T_{sat}$. Just as the heat transfer mechanism in the subcooled region is independent of the subcooling and, to a large degree, the mass velocity, so it may be inferred that the heat transfer process in this region is independent of the mass quality $x(z)$ and the mass velocity $(\dot{m})$. This, indeed, is found to be the case for experimental studies of fully developed nucleate boiling. Because the bulk temperature is constant in this region, the heat transfer coefficient is also constant, since ΔT_{sat} is fixed for a given heat flux and system pressure.

(b) Suppression of saturated nucleate boiling

To maintain nucleate boiling on the heater surface, it is necessary that the wall temperature exceeds the critical value for a specified heat flux. If the wall superheat is less than that given by Eq. (6) for the imposed surface heat flux, then nucleation does not take place; the value of ΔT_{sat} $(= T_w - T_{sat})$ for comparison with this equation is calculated from the ratio $(\dot{q}/\alpha_{tp})$, where α_{tp} is the two-phase heat transfer coefficient in the absence of nucleation:

$$q_{onb} = \frac{8\alpha_{tp}^2 \sigma T_{sat}}{\lambda_\ell \Delta h_v \rho_g} \tag{25}$$

Equation (25) represents an equation for the boundary between the saturated nucleate boiling and the two-phase forced convective region (Fig. 4). As for the case of subcooled nucleate boiling, this relationship is valid only on the basis of a complete range of sizes of active cavities on the heating surface. By analogy with the subcooled region, there is a similar partial boiling transition between fully developed saturated nucleate boiling and the two-phase forced convective regions. In this transition region, both the forced convective and nucleate boiling mechanisms are significant.

Direct observations of nucleation in annular flow have been reported by Hewitt et al. [15]. The geometry used was an internally heated annulus with a climbing film on the inner heated surface only. The results obtained are shown in Fig. 10 and qualitatively confirm the expected trends. However, the values of $\dot{q}_{onb}$ calculated from Eq. (25) are very much lower than measured. This is because of the restricted range of active cavity sizes available on the stainless steel surface employed as the heater. For such circumstances, Eq. (10) should be used to evaluate $(T_w - T_{sat})_{onb}$, together with the recommendations given in Sec. 2.7.2A regarding the evaluation of r_c. For the experimental conditions shown in Fig. 10, a maximum size of active cavity present might be ~1 μm radius.

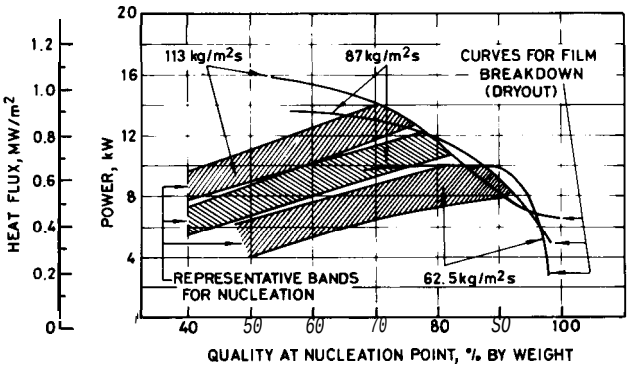

Figure 10 Suppression of nucleation in annular flow.

(c) The two-phase forced convection region

The two-phase forced convective region is most likely to be associated with the annular flow pattern. Heat is transferred by conduction or convection through the liquid film, and vapor is generated continuously at the liquid film/vapor core interface. Extremely high heat transfer coefficients are possible in this region; values can be so high as to make accurate assessment difficult. Typical figures for water of up to 200 kW/m²°C have been reported.

Following the suggestion of Martinelli, many workers [16-22] have correlated their experimental results for heat transfer rates in the two-phase forced convective region in the form

$$\frac{\alpha_{tp}}{\alpha_{\ell o}} \left(\text{or } \frac{\alpha_{tp}}{\alpha_\ell} \right) = fn\left(\frac{1}{X_{tt}}\right) \tag{26}$$

where $\alpha_{\ell o}$ (and α_ℓ) is the value of the single-phase liquid heat transfer coefficient based on the total (or liquid component) flow and X_{tt} is the Martinelli parameter $[= (\Delta p_\ell / \Delta p_g)^{1/2}]$ for turbulent-turbulent flow (see Sec. 2.3.2). A number of relationships of the form of Eq. (26) have been proposed, and in some cases these have also been extended to cover the saturated nucleate boiling region. Table 3 summarizes some of the correlations proposed. These correlations do, however, have a high mean error (530%).

It can be shown that

$$\frac{\alpha_{tp}}{\alpha_\ell} = \frac{D}{46} = \frac{1}{1 - \epsilon_g} \tag{27}$$

where δ is the liquid film thickness on the heating surface and $1 - \epsilon_g$ is the liquid hold-up. Martinelli successfully correlated the liquid hold-up $1 - \epsilon_g$ using the parameter X (see Sec. 2.3.2). Thus, it might be expected that an approach such as that implied by Eq. (26) might also be successful. However, the use of Eq. (27), together with actual or predicted void fraction

© 1983 Hemisphere Publishing Corporation

Table 3 Various correlations for heat transfer in the two-phase forced convection and nucleate boiling regions

Reference	Two-phase system fluid	Equation for two-phase forced convective region	Criterion for initiation of nucleation	Modification for nucleate boiling in liquid film
Dengler and Addoms [16]	2.54 cm X 6.1 m vertical steam-heated tube (water)	$\frac{\alpha_{tp}}{\alpha_{\ell o}} = 3.5\left(\frac{1}{X_{tt}}\right)^{0.5}$	$(\Delta T_{sat})_{onb} = 7.9 u_\ell^{0.5}$ where u_ℓ is the local liquid velocity (m/s), given by $u_\ell = \frac{\dot{m}(1-x)}{\rho_\ell(1-\epsilon_g)}$	$\frac{\alpha_{tp}}{\alpha_{\ell o}} = F 3.5\left(\frac{1}{X_{tt}}\right)^{0.5}$ $F = 0.67\left\{[\Delta T_{sat} - (\Delta T_{sat})_{onb}] \times \left(\frac{dp}{dT_{sat}}\frac{D}{\sigma}\right)_w\right\}^{0.1}$
Guerrieri and Talty [17]	1.9 cm X 1.83 m vertical tube (various organics)	$\frac{\alpha_{tp}}{\alpha_{\ell o}} = 3.4\left(\frac{1}{X_{tt}}\right)^{0.45}$	$\frac{r^*}{\delta} > 0.049$ r^* is the radius of an equilibrium bubble corresponding to the wall superheat [Eq. 2.7.1(7)]. δ is the thickness of the laminar fii given by $\delta = \frac{10\eta_\ell}{\rho_\ell}\left[\frac{4\rho_\ell}{(dp/dz)D}\right]^{0.5}$	$\frac{\alpha_{tp}}{\alpha_\ell} = E 3.4\left(\frac{1}{X_{tt}}\right)^{0.45}$ $E = 0.187\left(\frac{r^*}{\delta}\right)^{-5/9}$
Bennett et al. [18]	Internally heated vertical annulus (water)	$\frac{\alpha_{tp}}{\alpha_\ell} = 0.564\left(\frac{1}{X_{tt}}\right)^{0.74} \dot{q}^{0.11}$ $\dot{q}$ in W/m²		Used Rohsenow Eq. 2.7.2(7) for nucleate boiling
Schrock and Grossman [19, 20]	Vertical tubes heated electrically (water)	These authors proposed one equation for both regions of heat transfer: $\frac{\alpha_{tp}}{\alpha_\ell} = \gamma\left[\frac{\dot{q}}{\dot{m}\Delta h_v} + m\left(\frac{1}{X_{tt}}\right)^n\right]$ where $\gamma = 7.39 \times 10^3$, $m = 1.5 \times 10^{-4}$, and $n = 0.66$ However, Collier et al. [22] found better agreement with their data when the modified values given by Wright [21] ($\gamma = 6.70 \times 10^3$, $m = 3.5 \times 10^{-4}$, $n = 0.66$) were used.		

data, yields estimates of α_{tp} that are about 50% higher than values measured experimentally.

Chen [23] has proposed a correlation that has been generally accepted as one of the best available. The correlation covers both the saturated nucleate boiling region and the two-phase forced convective region. It is assumed that both nucleation and convective mechanisms occur to some degree over the entire range of the correlation and that the contributions made by the two mechanisms are additive:

$$\alpha_{tp} = \alpha_{nb} + \alpha_c \tag{28}$$

where α_{nb} is the contribution from nucleate boiling and α_c the contribution from convection through the liquid film.

An earlier, very similar approach that has been used successfully for design in the process industries over a number of years was given by Fair [24].

In the Chen correlation α_c, the convective contribution, is given by

$$\alpha_c = 0.023\left(\frac{\dot{m}(1-x)D}{\eta_\ell}\right)^{0.8}\left(\frac{\eta c_p}{\lambda}\right)_\ell^{0.4}\frac{\lambda_\ell}{D}F \tag{29a}$$

The parameter F is a function of the Martinelli parameter X_{tt} (Fig. 11). The equation of Forster and Zuber [25] was taken as the basis for the evaluation of the nucleate boiling component α_{nb}. Their pool boiling analysis [see Eq. 2.7.2(8)] was modified to account for the thinner boundary layer in forced convective boiling and the lower effective superheat that the growing vapor bubble sees The modified Forster-Zuber equation becomes

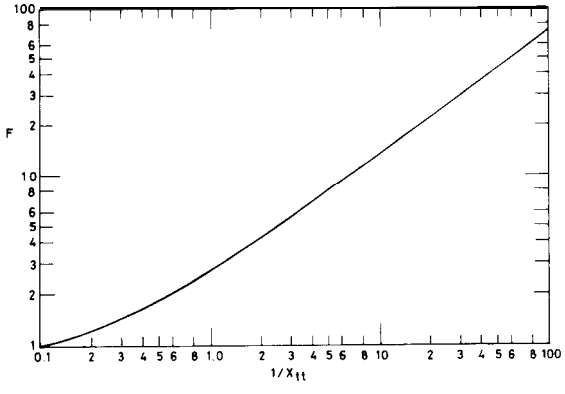

Figure 11 Convective boiling factor F.

© 1983 Hemisphere Publishing Corporation

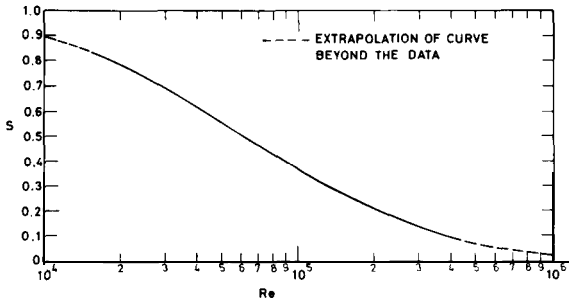

Figure 12 Nucleate boiling suppression factor S.

$$\alpha_{nb} = 0.00122 \left(\frac{\lambda_\ell^{0.79} c_{p\ell}^{0.45} \rho_\ell^{0.49}}{\sigma^{0.5} \eta_\ell^{0.29} \Delta h_v^{0.24} \rho_g^{0.24}} \right) \Delta T_{sat}^{0.24} \Delta p_{sat}^{0.75} S \qquad (29b)$$

where S is a suppression factor defined as the ratio of the mean superheat seen by the growing bubble to the wall superheat ΔT_{sat}. S is represented as a function of the local two-phase Reynolds number Re_{tp} $(=\mathrm{Re}_\ell F^{1.25})$ (Fig. 12).

Curve fits to the functions shown in Figs. 11 and 12 for F and S, respectively, are

$$F = 1 \quad \text{for} \quad \frac{1}{X_{tt}} \leqslant 0.1$$

$$F = 2.35 \left(\frac{1}{X_{tt}} + 0.213 \right)^{0.736} \quad \text{for} \quad \frac{1}{X_{tt}} > 0.1 \qquad (30)$$

$$S = \frac{1}{1 + 2.53 \times 10^{-6} \mathrm{Re}_{tp}^{1.17}} \qquad (31)$$

This correlation fits the available experimental data remarkably well (with a standard deviation of 11% on heat transfer coefficient).

To calculate the heat transfer coefficient α_{tp} at a known heat flux $\dot{q}$, mass velocity, and quality, the steps are as follows:

1. Calculate $1/X_{tt}$ (see Sec. 2.3.2) or use

$$X_{tt} \cong \left(\frac{1-x}{x} \right)^{0.9} \left(\frac{\rho_g}{\rho_\ell} \right)^{0.5} \left(\frac{\eta_\ell}{\eta_g} \right)^{0.1}$$

2. Evaluate F from Fig. 11.
3. Calculate α_c from Eq. (29a).
4. Calculate Re_{tp} from Re_ℓ $[= \dot{m}(1-x)D/\eta_\ell]$ and F $(\mathrm{Re}_{tp} = \mathrm{Re}_\ell F^{1.25})$.
5. Evaluate S from Fig. 12 using the calculated value of Re_{tp}.
6. Calculate α_{nb} for a range of values of ΔT_{sat}.
7. Calculate α_{tp} from Eq. (28) for the range of ΔT_{sat} values.
8. Plot $\dot{q}(=\alpha_{tp} \Delta T_{sat})$ for the ΔT_{sat} range against α_{tp} and interpolate α_{tp} at $\dot{q}$.

The correlation developed by Chen is the best available for the saturated forced convective boiling region in vertical ducts and is recommended for use with all single component nonmetallic fluids. An alternative correlation, which is also valid for saturated forced convective boiling in horizontal ducts, is discussed in Sec. **2.7.4.**

Ananiev et al. [26] proposed a particularly simple relationship to correlate their data for condensation of steam in a horizontal tube at elevated pressure. It originates from the analogy between liquid film flow and single-phase flow in a pipe and may be used to get a quick estimate of the heat transfer coefficient in evaporation as well as for condensation.

$$\alpha_{tp} = \alpha_{\ell o} \sqrt{\frac{\rho_\ell}{\bar{\rho}}} \qquad (32)$$

where $\alpha_{\ell o}$ is the heat transfer coefficient to liquid flowing at the same total flow rate as the vapor-liquid mixture in the tube and $\bar{\rho}$ is the homogeneous mean density of the vapor-liquid mixture, given by

$$\frac{1}{\bar{\rho}} = \left(\frac{x}{\rho_g} + \frac{1-x}{\rho_\ell} \right) \qquad (33)$$

The average coefficient $\bar{\alpha}_{tp}$ for complete evaporation of a liquid is given (approximately) by

$$\bar{\alpha}_{tp} = \frac{\alpha_{\ell o}}{2} \left[1 + \left(\frac{\rho_\ell}{\rho_g} \right)^{1/2} \right] \qquad (34)$$

These relationships will give only very approximate values of heat transfer coefficient and should not be used when (ρ_ℓ/ρ_g) is greater than 50.

D. Critical heat flux

The critical heat flux (CHF) condition forms a most important boundary when considering the performance of heat exchange equipment in which boiling or evaporation occurs. It is characterized by a sharp reduction of the local heat transfer coefficient that results from the replacement of liquid by vapor adjacent to the heat transfer surface. For the case where the surface heat flux is the independent variable, such as in a radiantly heated furnace or a nuclear reactor fuel element, the condition manifests itself as a sharp increase in surface temperature as the critical heat flux value is reached.

The vast majority of experimental studies of the critical heat flux condition relate to water as the evaporating fluid. Fluids other than water are dealt with in a separate subsection toward the end of Sec. (j).

© 1983 Hemisphere publishing Corporation

(a) Nomenclature

There is considerable disparity in nomenclature for the CHF condition. The most common name is burnout, but this implies a physical destruction of the heated surface. The alternative forms DNB (departure from nucleate boiling) and dryout are equally unsatisfactory for a *general* description of the phenomenon, although they correctly describe specific mechanisms. The term critical heat flux condition has therefore been chosen to denote the state of the system when the characteristic reduction in heat transfer coefficient has just occurred, and the term critical heat flux (CHF) to describe the value of heat flux at which, and local to the point at which, this state of the system first occurs. The main difficulty in using the chosen nomenclature is that it implies an approach to the critical condition by increasing the heat flux, whereas, in fact, the critical condition may also be approached for a given system by varying any of the other independent variables: pressure, inlet temperature (or mass quality), and mass velocity.

Considerable differences also exist in the practical methods used to define and measure the critical condition. Thus, before attempting to compare data from different sources, it is always necessary to ensure that the definition and methods used in the different works are the same or, at least, are likely to give similar results.

(b) Critical heat flux in uniformly heated vertical tubes

For the present, the discussion will be restricted to the case of a stable subcooled water flow evaporating in vertical uniformly heated tubes. In general, for uniformly heated channels, the onset of the CHF condition occurs first at the exit end of the channel. For nonuniform axial heat flux distribution, overheating may occur first either at the exit or upstream of the exit.

There are certainly five major variables that can influence the critical heat flux: the inlet flow rate, the inlet temperature, the system pressure, the tube internal diameter, and the tube length,

$$\dot{q}_{cr} = fn(\dot{m}, \Delta T_{sub,i}, p, D, z) \tag{35}$$

Since overheating of the tube surface at the critical condition almost invariably begins at the exit of the heated section, it can be argued that display and correlation should be in terms of the exit condition. The thermodynamic state of the fluid at the tube exit may be either subcooled or saturated. Either the fluid enthalpy $h(z)$ or the thermodynamic mass quality $x(z)$ may be chosen to characterize the exit condition. Each of these dependent variables is related to the inlet subcooling via the heat balance equation:

$$h(z) = h_\ell + \frac{4\dot{q}z}{D\dot{m}} - \Delta h_{sub,i} \tag{36}$$

$$x(z) = \frac{1}{\Delta h_v}\left(\frac{4\dot{q}z}{D\dot{m}} - \Delta T_{sub,i} c_{p\ell}\right) \tag{37}$$

Thus, as alternatives to Eq. (35), it is possible to write

$$\dot{q}_{cr} = fn(\dot{m}, h(z), p, D, z) \tag{38}$$

$$= fn(\dot{m}, x(z), p, D, z) \tag{39}$$

It is helpful to examine briefly the manner in which the CHF varies with some of the independent variables. Examples of such relationships are shown in Figs. 13-19. The following conclusions can be drawn from these examples.

1. When the influence of one particular variable on the critical heat flux is considered, it is essential to specify which of the other independent (or dependent) variables is held constant.

2. When the pressure, tube diameter, and tube length are held constant, the critical heat flux increases linearly with inlet subcooling for fixed mass velocity and increases with mass velocity at fixed inlet subcooling (Fig. 13).

3. When the pressure, tube diameter, and tube length are held constant, the critical heat flux decreases linearly with increasing exit mass quality (xfz) for a fixed mass velocity (Fig. 14). In the subcooled region (negative values of $x(z$ j), the critical heat flux increases with increased mass velocity at

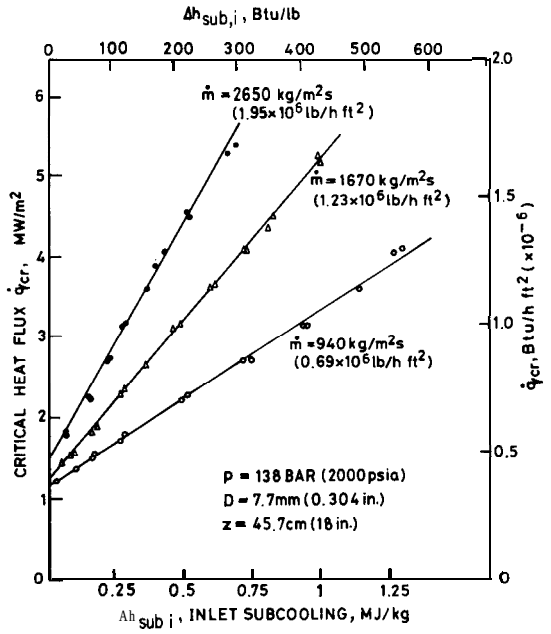

Figure 13 The effect of inlet subcooling on critical heat flux.

© 1983 Hemisphere Publishing Corporation

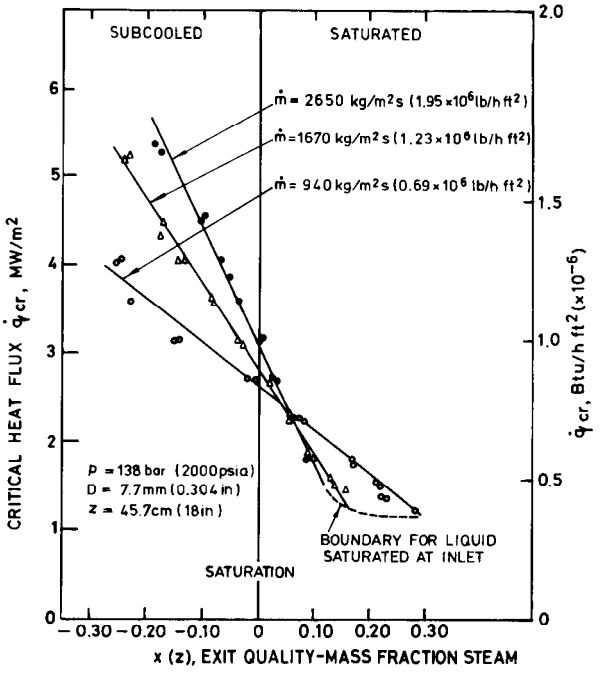

Figure 14 The influence of exit quality on critical heat flux.

constant exit conditions. In the saturated region (positive values of xfz), there is a crossover, and at high values of exit quality the critical heat flux decreases with increasing mass velocity.

4. For fixed values of pressure, tube diameter, and mass velocity, the critical heat flux decreases with increasing tube length (z) at fixed inlet subcooling (Fig. 15). The linear variation between critical heat flux and inlet subcooling breaks down at low values of z/D.

5. At fixed values of pressure, tube diameter, and mass velocity, the effect of tube length (z) on the critical heat flux for fixed exit quality is small (Fig. 16).

6. At fixed pressure, tube length, and mass velocity, an increase in the tube diameter (D) increases the critical heat flux value for a fixed inlet subcooling (Fig. 17).

7. At fixed pressure, tube length, and mass velocity, the critical heat flux decreases as the tube diameter (D) is increased for fixed values of exit quality (Fig. 18).

8. For fixed tube diameter, tube length, and mass velocity, the critical heat flux falls rapidly as the pressure is increased for fixed exit mass quality (xfz) = 0) (Fig. 19). At mass velocities below 2 700 kg/m² s, the value of CHF at xfz) = 0 will be increased for pressures below 100 bar and decreased at higher pressures. For higher mass velocities the converse is true. For the condition where the inlet subcooling is held constant, the CHF passes through a

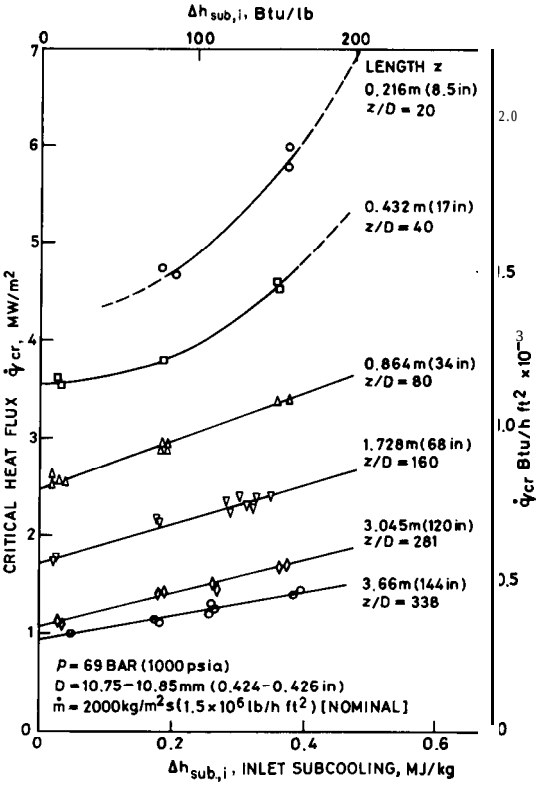

Figure 15 The effect of tube length on critical heat flux at fixed inlet conditions.

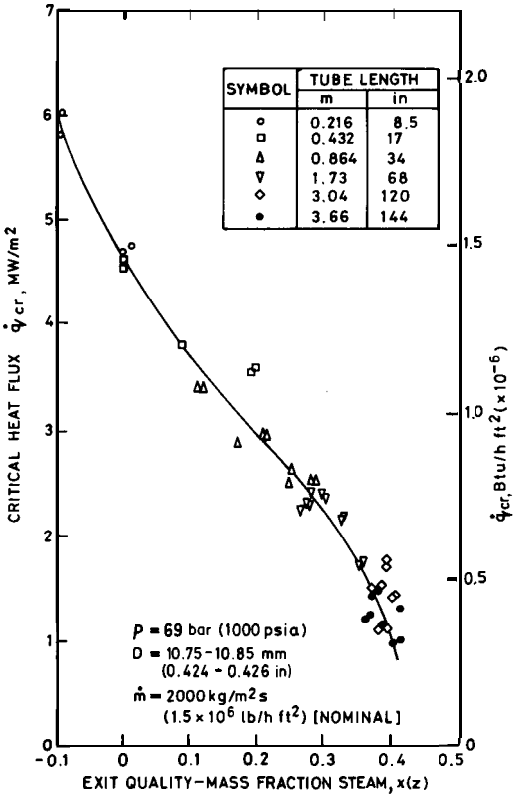

Figure 16 The effect of tube length on critical heat flux at fixed exit conditions.

© 1983 Hemisphere Publishing Corporation

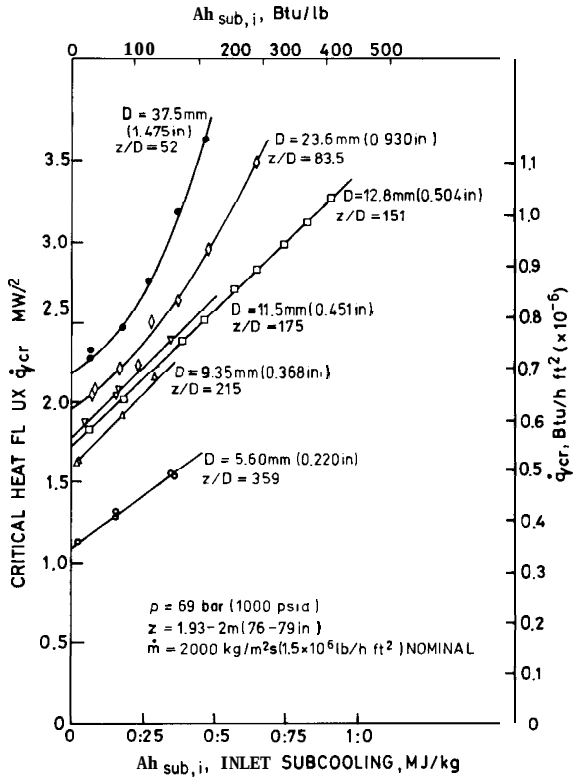

Figure 17 The influence of tube diameter on critical heat flux at fixed inlet conditions.

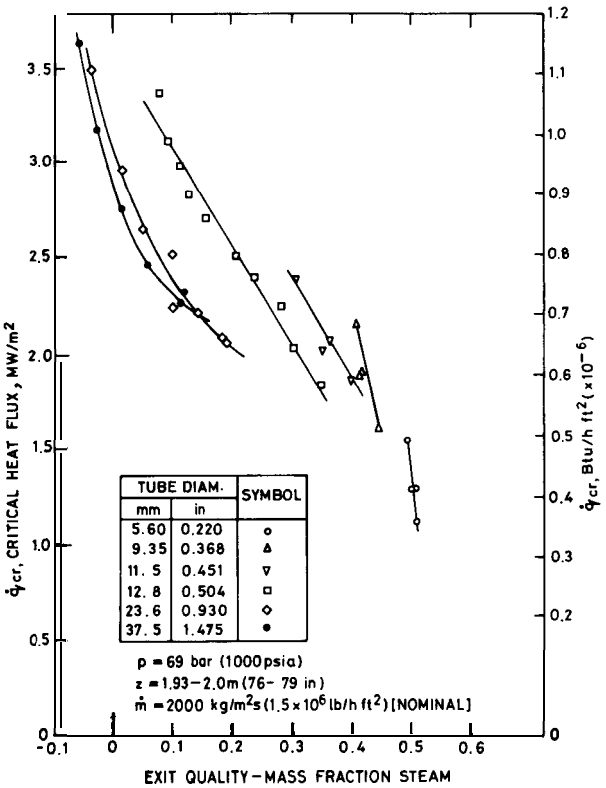

Figure 18 The influence of tube diameter on critical heat flux at fixed exit conditions.

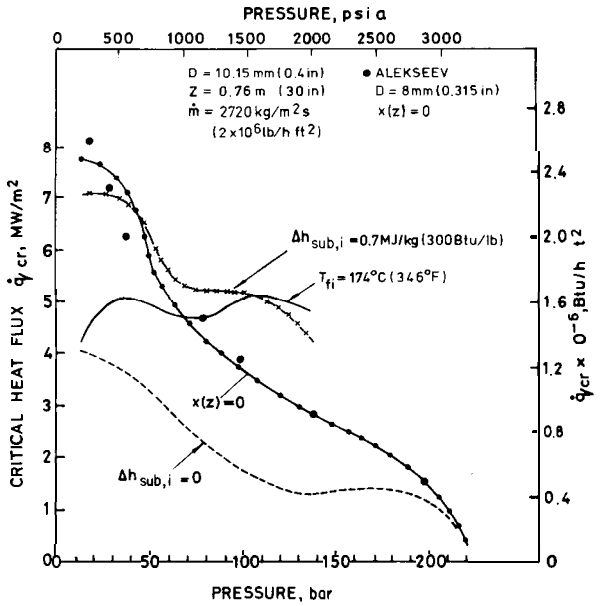

Figure 19 The influence of system pressure on the critical heat flux.

maximum at low pressures and then falls as the pressure is increased. A secondary maximum may be found in the pressure range 100-200 bar that is enhanced by increasing the subcooling and mass velocity and by reducing the z/D ratio. If the inlet water temperature $T_{\ell i}$ is held constant, then the inlet subcooling increases as the pressure is raised and the influence of system pressure on CHF is much reduced over the entire pressure range.

The observation that the critical heat flux is independent of tube length for a given exit quality can be used to simplify Eq. (39), which now becomes

$$\dot{q}_{cr} = fn(x(z), \dot{m}, p, D) \tag{40}$$

From this it follows that these further equations hold:

$$\dot{q}_{cr} = fn(z_{sat}, \dot{m}, p, D) \tag{41}$$

$$x_{cr} = fn(z_{sat}, \dot{m}, p, D) \tag{42}$$

where z_{sat} is the length of the tube over which the mass quality is raised from zero to x_{cr}, the mass quality at the CHF condition. Figure 16 suggests there is a general relationship between $\dot{q}_{cr}$ and the local quality, whereas Eq. (42) suggests that the mass fraction of the liquid that can be evaporated (x_{cr}) in the channel before the onset of the critical condition is a function of the length over which the evaporation takes place (z_{sat}). Neither of these two views of the critical phenomenon is completely correct, and neither, as it turns out, can be used as a general basis for the prediction of more complex cases. Figure 20 shows the data of Fig. 16 replotted in the form suggested by Eq. (42).

© 1983 Hemisphere Publishing Corporation

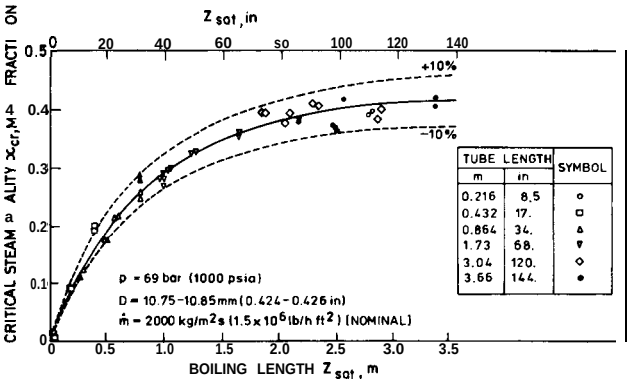

Figure 20 Critical steam quality as a function of boiling length.

(c) Availability of *experimental information*

Experiments to determine the critical heat flux for water in vertical uniformly heated round tubes have been carried out in many countries over the past 20 years or so. A compilation of much of this data was published by Thompson and Macbeth [27] in 1964. A total of 4 389 separate experimental results are recorded, covering a very wide range of independent variables. None of the wide range of experimental data from the U.S.S.R. is included in this compilation. However, the Soviet data is generally in good agreement with the data in the compilation. Moreover, the U.S.S.R. Academy of Sciences [28] has produced a series of standard tables of critical heat flux as a function of the local bulk mean water condition and for various pressures and mass velocities for a fixed tube diameter of 8 mm. These tables are reproduced as Table 4 and are valid for $z/D \geqslant 20$. For tube diameters other than 8 mm, the critical heat flux is given by the approximate relationship

$$q_{cr} = q_{cr,8\,mm}\left(\frac{8}{D}\right)^{0.5} \quad \text{or } 4 \leqslant D \leqslant 16 \text{ mm} \qquad (43)$$

(d) Limits of *critical heat flux*

The critical heat flux condition cannot exist if the heating surface temperature lies below the saturation temperature. Thus, the minimum possible CHF is given by

$$(\dot{q}_{cr})_{min} \quad \frac{\Delta T_{sub,i}}{4\bar{z}/\dot{m}c_{p\ell}D + 1/\alpha_{fo}} \qquad (44)$$

The critical heat flux condition must occur at or before all the liquid fed to the channel is evaporated $[x(z) = 1]$. Thus the maximum possible CHF is given by

$$(\dot{q}_{cr})_{max} = \frac{\dot{m}D\Delta h_v}{4z}\left(1 + \frac{c_{p\ell}\Delta T_{sub,i}}{\Delta h_v}\right) \qquad (45)$$

(e) Empirical correlation of experimental data for water

The technical importance of the CHF condition has led to the development of a bewildering variety of correlations. One well-known empirical correlation is that of Thompson and Macbeth [27], and is based on the local conditions hypothesis, which suggests that the critical heat flux is solely a function of the ***local*** mass quality at the point of overheating [as implied by Eq. (40)]. A more recent correlation that retains the basis and accuracy of the Thompson/Macbeth correlation but is more convenient to use has been provided by Bowring [29]. The assumption is made that $\dot{q}_{cr}$ is a linear function of local quality $x(z)$, leading to a correlation of the form

$$\dot{q}_{cr} = \frac{A + B\,\Delta h_{sub,i}}{C + z} \qquad (46)$$

where $\dot{q}_{cr}$ is the critical heat flux in W/m^2; $\Delta h_{sub,i}$ is the inlet subcooling in J/kg; z is the tube length in m; and ***A, B,*** and C are functions given by

$$A = 2.317\,\frac{(0.25\,\Delta h_v D\dot{m})F_1}{1.0 + 0.0143F_2D^{1/2}\dot{m}}$$

$$B = 0.25D\dot{m} \qquad (47)$$

$$C = \frac{0.077F_3D\dot{m}}{1.0 + 0.347F_4(\dot{m}/1356)^n}$$

where D is the internal tube diameter in m, $\dot{m}$ is the total mass velocity in kg/m^2 s, and Ah, is the latent heat of vaporization in J/kg. The exponent n is given by

$$n = 2.0 - 0.00725p \qquad (48)$$

where p is the system pressure in bar. F_1, F_2, F_3, and F_4 are functions of system pressure and are tabulated in Table 5. The correlation was derived from data covering the following parameter ranges:

Pressure (p):	2-190 bar
Tube diameter (D):	0.002-0.045 m
Tube length (z):	0.15-3.7 m
Mass velocity ($\dot{m}$):	136-18 600 kg/m^2 s

The root-mean-square (rms) error of the correlation is 7% and the 95% confidence level is ±14%.

© 1983 Hemisphere Publishing Corporation

Table 4 U.S.S.R. Academy of Sciences [28] standard tables for CHF for water in upward flow with uniform heat flux[a]

Mass velocity, kg/m² s	Local bulk mean water conditions: Subcooling, °C					Quality														
	75	50	25	10	0	0.05	0.1	0.15	0.2	0.25	0.3	0.35	0.4	0.45	0.5	0.55	0.6	0.65	0.7	0.75
										***p* = 29.5** bar										
750		–	–	–	–	7.95	7.50	7.10	6.75	6.45	6.15	5.80	5.50	5.25	5.00	4.80	4.20	3.75	3.20	–
1 000	–	–	8.80	8.40	8.20	7.70	7.25	6.75	6.35	5.95	5.60	5.25	4.95	4.65	4.30	4.00	3.70	3.35	–	–
1500	–	9.50	8.75	8.20	8.00	7.25	6.55	6.00	5.40	4.90	4.60	4.15	3.80	3.40	3.00	2.60	–	–	–	–
2 000	10.53	9.65	8.60	8.00	7.75	6.70	5.90	5.55	4.75	4.25	3.80	3.35	2.90	2.50	–	–	–	–	–	–
2 500	10.80	9.90	8.65	7.90	7.60	6.35	5.50	4.80	4.25	3.70	3.25	2.80	2.35	–	–	–	–	–	–	–
3 000	11.25	10.05	8.65	7.85	7.40	6.05	5.20	4.55	3.95	3.25	3.05	2.65	–	–	–	–	–	–	–	–
4 000	12.10	10.35	8.75	7.75	7.20	5.75	4.80	4.05	3.50	3.05	2.65	–	–	–	–	–	–	–	–	–
5 000	12.60	10.65	8.85	7.70	7.05	5.25	4.30	3.80	3.30	2.90	2.50	–	–	–	–	–	–	–	–	–
										***p* = 49** bar										
750	–	–	–	–	7.40	6.75	6.25	5.80	5.40	5.10	4.85	4.60	4.35	4.15	3.95	3.75	3.55	3.40	3.20	3.00
1000	–	8.55	8.00	7.60	7.40	6.50	5.95	5.55	5.20	4.90	4.60	4.30	4.05	3.85	3.60	3.40	3.20	2.95	–	–
1500	**9.40**	8.75	8.10	7.60	7.25	6.25	5.50	5.00	4.60	4.30	4.05	4.80	3.55	3.30	3.05	2.85	–	–	–	–
2 000	**9.75**	9.00	8.15	7.60	7.10	5.90	5.10	4.50	4.05	3.70	3.40	3.15	2.90	2.65	–	–	–	–	–	–
2 500	10.05	9.20	8.20	7.45	7.00	5.70	4.75	4.15	3.70	3.35	3.05	2.75	2.35	–	–	–	–	–	–	–
3 000	10.40	9.40	8.25	7.35	6.90	5.55	4.60	3.95	3.50	3.10	2.75	2.45	–	–	–	–	–	–	–	–
4 000	11.20	9.75	8.30	7.20	6.60	5.30	4.30	3.65	3.15	2.60	2.10	–	–	–	–	–	–	–	–	–
5 000	11.65	10.15	8.40	7.10	6.35	5.05	4.05	3.35	2.85	2.30	1.75	–	–	–	–	–	–	–	–	–
										***p* = 69** bar										
750	–	7.40	6.85	6.45	6.20	5.45	4.90	4.50	4.20	3.95	3.75	3.55	3.35	3.20	3.00	2.85	2.65	2.45	2.25	–
1000	8.15	7.60	6.85	6.45	6.15	5.30	4.70	4.30	4.00	3.75	3.50	3.30	3.05	2.80	2.60	2.35	2.10	–	–	–
1500	8.50	7.80	6.95	6.45	5.95	5.10	4.35	3.95	3.60	3.25	2.95	2.75	2.55	2.35	–	–	–	–	–	–
2 000	8.85	8.00	7.00	6.40	5.90	4.80	4.05	3.55	3.20	2.85	2.55	2.30	2.05	–	–	–	–	–	–	–
2500	9.20	8.25	7.00	6.35	5.70	4.50	3.75	3.25	2.90	2.55	2.25	1.95	–	–	–	–	–	–	–	–
3 000	9.75	8.45	7.15	6.25	5.55	4.30	3.60	3.10	2.65	2.25	1.90	–	–	–	–	–	–	–	–	–
4 000	10.20	8.90	7.25	6.10	5.35	4.10	3.30	2.75	2.25	1.90	–	–	–	–	–	–	–	–	–	–
5 000	11.40	9.60	7.40	6.30	5.65	4.25	3.10	2.45	1.95	1.50	–	–	–	–	–	–	–	–	–	–
										***p* = 98** bar										
500	–	–	4.95	4.65	–	–	–	–	–	–	–	–	–	–	–	–	–	–	–	–
750	6.30	5.80	5.20	4.90	4.55	3.90	3.55	3.30	3.05	2.80	2.60	2.40	2.25	2.10	1.95	1.75	1.55	–	–	–
1000	6.55	5.95	5.05	4.80	4.55	3.90	3.45	3.10	3.10	2.85	2.40	2.20	2.00	1.75	1.60	–	–	–	–	–
1 500	7.05	6.25	5.25	4.80	4.50	3.85	3.30	2.90	2.60	2.30	2.05	1.80	1.55	–	–	–	–	–	–	–
2 000	7.65	6.50	5.40	4.85	4.45	3.60	2.95	2.50	2.20	1.90	1.65	–	–	–	–	–	–	–	–	–
2 500	8.25	7.00	5.65	5.00	4.30	3.40	2.80	2.40	2.05	1.70	1.40	–	–	–	–	–	–	–	–	–
3 000	8.75	7.50	6.00	5.15	4.30	3.35	2.60	2.10	1.75	1.45	1.20	–	–	–	–	–	–	–	–	–
4 000	10.00	8.25	6.40	5.25	4.50	3.25	2.40	1.95	1.55	1.25	0.95	0.75	0.55	0.45	0.35	–	–	–	–	–
5 000	11.40	9.40	6.90	5.80	4.65	3.30	2.25	1.70	1.35	1.10	0.90	0.75	0.60	0.50	0.40	–	–	–	–	–
										***p* = 118** bar										
500	**4.90**	4.40	3.90	3.70	–	–	–	–	–	–	–	–	–	–	–	–	–	–	–	–
750	5.20	4.60	4.00	3.70	3.40	2.95	2.60	2.40	2.25	2.05	1.90	1.75	1.60	1.45	1.30	1.20	–	–	–	–
1 000	5.55	4.80	4.20	3.75	3.45	2.95	2.65	2.40	2.20	1.95	1.60	1.45	1.30	–	–	–	–	–	–	–
1 500	6.15	5.40	4.45	3.90	3.45	2.90	2.50	2.20	1.90	1.65	1.45	1.25	–	–	–	–	–	–	–	–
2 000	7.20	6.15	4.85	4.10	3.55	2.90	2.40	2.05	1.75	1.45	1.15	–	–	–	–	–	–	–	–	–
2 500	7.80	6.60	5.20	4.20	3.60	2.90	2.35	1.90	1.50	1.25	1.05	–	–	–	–	–	–	–	–	–
3 000	8.75	7.15	5.55	4.45	3.70	2.95	2.15	1.70	1.30	1.00	0.80	0.65	0.55	–	–	–	–	–	–	–
4 000	9.60	7.85	6.20	5.00	3.90	3.00	2.15	1.70	1.30	1.00	0.80	0.65	0.55	0.45	0.40	–	–	–	–	–
5 000	11.10	8.80	6.75	5.55	4.45	3.05	2.15	1.70	1.35	1.10	0.90	0.75	0.60	0.50	0.45	–	–	–	–	–
										***p* = 137** bar										
500	**3.90**	3.45	3.00	2.70	2.55	–	–	–	–	–	–	–	–	–	–	–	–	–	–	–
750	4.10	3.65	3.15	2.80	2.50	2.25	2.05	1.85	1.70	1.55	1.40	1.30	1.20	1.10	–	–	–	–	–	–
1000	4.50	3.95	3.40	3.05	2.80	2.25	2.00	1.80	1.60	1.40	1.30	1.15	–	–	–	–	–	–	–	–
1500	5.30	4.50	3.80	3.25	2.95	2.30	1.95	1.70	1.45	1.20	0.90	–	–	–	–	–	–	–	–	–
2 000	6.15	5.15	4.15	3.50	3.10	2.40	1.95	1.60	1.30	1.00	0.80	–	–	–	–	–	–	–	–	–

© 1983 Hemisphere Publishing Corporation

Table 4 (*Continued*) U.S.S.R. Academy of Sciences [28] standard tables for CHF for water in upward flow with uniform heat flux[a]

Mass velocity, kg/m² s	Local bulk meanwater conditions: Subcooling, °C 7	5	50	25	10	0	Quality 0.05	0.1	0.15	0.2	0.25	0.3	0.35	0.4	0.45	0.5	0.55	0.6	0.65	0.7	0.75
								$p = 137$ bar													
2500	6.75	5.70	4.50	3.75	3.25	2.50	1.95	1.45	1.10	0.90	0.75	0.60	0.50	0.40	0.30	–	–	–	–	
3000	7.55	6.30	4.90	4.00	3.40	2.55	1.90	1.45	1.15	0.90	0.80	0.60	0.55	0.40	0.35	–	–	–	–	
4000	9.25	7.40	5.70	4.65	3.80	2.75	2.05	1.55	1.30	1.05	0.90	0.75	0.65	0.55	0.45	–	–	–	–	
5000	10.60	8.45	6.40	5.30	4.30	3.05	2.20	1.80	1.50	1.25	1.05	0.90	0.75	0.60	0.50	–	–	–	–	
								$p = 157$ bar													
500	2.95	2.55	2.20	1.85	–	–	–	–	–	–	–	–	–	–	–	–	–	–	–	
750	3.30	2.90	2.45	2.15	2.00	1.75	1.50	1.35	1.20	1.05	0.95	0.85	–	–	–	–	–	–	–	
1000	3.75	3.25	2.70	2.35	2.10	1.80	1.55	1.35	1.20	1.05	0.90	–	–	–	–	–	–	–	–	
1500	4.55	3.80	3.25	2.75	2.30	1.95	1.60	1.35	1.15	0.95	0.80	0.60	–	–	–	–	–	–	–	
2000	5.40	4.50	3.65	3.00	2.45	2.10	1.75	1.45	1.25	1.05	0.85	0.60	0.45	0.35	0.30	–	–	–	–	
2500	6.10	5.05	4.05	3.35	2.65	2.20	1.80	1.55	1.25	1.00	0.80	0.65	0.50	0.45	0.40	–	–	–	–	
3000	6.80	5.65	4.45	3.60	2.85	2.25	1.85	1.55	1.30	1.05	0.85	0.65	0.55	0.45	0.40	–	–	–	–	
4000	8.30	6.70	5.25	4.25	3.15	2.60	2.10	1.75	1.45	1.20	1.00	0.85	0.70	0.55	0.45	–	–	–	–	
5000	9.80	7.85	5.90	4.70	3.75	3.00	2.40	2.00	1.65	1.40	1.20	1.00	0.80	0.65	0.55	–	–	–	–	
								$p = 176$ bar													
500	2.20	1.90	1.65	1.50	1.40	–	–	–	–	–	–	–	–	–	–	–	–	–	–	
750	2.95	2.50	2.10	1.75	1.50	1.30	1.10	0.95	0.80	0.70	0.60	0.50	–	–	–	–	–	–	–	
1000	3.45	2.85	2.25	1.90	1.60	1.35	1.15	1.00	0.85	0.75	0.65	0.50	0.40	0.30	0.20	–	–	–	–	
1500	3.70	3.20	2.55	2.25	1.80	1.55	1.30	1.10	0.90	0.80	0.65	0.55	0.45	0.35	0.30	–	–	–	–	
2000	4.60	3.75	3.00	2.50	2.10	1.75	1.45	1.25	1.10	0.95	0.75	0.60	0.45	0.35	0.30	–	–	–	–	
2500	5.05	4.35	3.30	2.80	2.15	1.90	1.65	1.45	1.20	1.00	0.80	0.65	0.55	0.45	0.35	–	–	–	–	
3000	5.70	4.70	3.55	3.00	2.35	2.05	1.80	1.55	1.35	1.15	0.95	0.80	0.65	0.50	0.40	–	–	–	–	
4000	7.25	5.75	4.40	3.55	2.85	2.45	2.05	1.80	1.55	1.35	1.15	1.00	0.80	0.65	0.50	–	–	–	–	
5000	8.70	6.85	4.95	3.85	3.05	2.75	2.40	2.05	1.70	1.45	1.20	1.00	0.85	0.70	0.60	–	–	–	–	
								$p =$ 196bar													
500	1.70	1.55	1.45	1.35	1.30	–	–	–	–	–	–	–	–	–	–	–	–	–	–	
750	2.05	1.80	1.60	1.40	1.35	1.00	0.80	0.70	0.65	0.50	0.45	0.45	–	–	–	–	–	–	–	
1000	2.30	2.05	1.75	1.55	1.35	1.10	0.95	0.80	0.70	0.60	0.50	0.40	0.30	–	–	–	–	–	–	
1500	2.95	2.55	2.00	1.80	1.50	1.30	1.15	1.00	0.85	0.70	0.55	0.45	0.40	0.35	0.25	–	–	–	–	
2000	3.55	2.85	2.40	2.00	1.65	1.45	1.30	1.15	1.00	0.85	0.70	0.55	0.45	0.35	0.30	–	–	–	–	
2500	4.05	3.45	2.65	2.20	1.75	1.60	1.45	1.25	1.10	0.95	0.80	0.65	0.55	0.45	0.35	–	–	–	–	
3000	4.95	3.75	3.00	2.35	1.90	1.75	1.55	1.35	1.20	1.05	0.90	0.75	0.65	0.50	0.40	–	–	–	–	
4000	6.25	4.85	3.55	2.65	2.00	1.85	1.70	1.55	1.40	1.25	1.10	0.90	0.75	0.60	0.50	–	–	–	–	
5000	7.55	5.80	4.05	3.00	2.30	2.30	2.10	1.90	1.70	1.45	1.25	1.05	0.90	0.75	0.60	–	–	–	–	

'Tube diameter 8 mm bore; figures in MW/m².

(f) Critical heat flux for water in vertical round tubes with nonuniform heating

Various methods have been proposed to deal with a nonuniform axial heat flux profile.

I. The local conditions hypothesis

If it is assumed that there is a unique relationship between critical heat flux and local mass quality, for example, of the form Eq. (40), then the case of a nonuniformly heated tube can be dealt with in a straightforward manner. The distance along the tube is denoted by z, the functional form of the heat flux profile by $f(z)$, the local heat flux by $\dot{q}(z)$, and the peak heat flux by $\dot{q}_{max}$.

$$\dot{q}(z) = f(z)\dot{q}_{max} \tag{49}$$

If $(\dot{q}_{max})_{cr,z}$ is the value of the peak heat flux when the CHF is exceeded at z, then it can be shown that

$$(\dot{q}_{max})_{cr,z} = \frac{A + B\Delta h_{sub,i}}{Cf(z) + \int_0^z f(z)dz} \tag{50}$$

© 1983 Hemisphere Publishing Corporation

Table 5 The Bowring [29] critical heat flux correlation

Pressure, bar	F_1	F_2	F_3	F_4
1	0.418	1.782	0.400	0.000 4
5	0.478	1.019	0.400	0.005 3
10	0.478	0.662	0.400	0.016 6
15	0.418	0.514	0.400	0.0324
20	0.478	0.441	0.400	0.052 1
25	0.480	0.403	0.401	0.075 3
30	0.488	0.390	0.405	0.102 9
35	0.519	0.406	0.422	0.138 0
40	0.590	0.462	0.462	0.188 5
45	0.707	0.564	0.538	0.266 3
50	0.848	0.698	0.647	0.381 2
60	1.043	0.934	0.890	0.708 4
68.9	1.000	1 .000	1.000	1.000
70	0.984	0.995	1.003	1.030
80	0.853	0.948	1.033	1.322
90	0.743	0.903	1.060	1.647
100	0.651	0.859	1.085	2.005
110	0.572	0.816	1.108	2.396
120	0.504	0.115	1.129	2.819
130	0.446	0.736	1.149	3.274
140	0.395	0.698	1.168	3.760
150	0.350	0.662	1.186	4.277
160	0.311	0.628	1.203	4.825
170	0.277	0.595	1.219	5.404
180	0.247	0.564	1.234	6.013
190	0.220	0.534	1.249	6.651
200	0.197	0.506	1.263	7.320

Tabulation of functions F_1, F_2, F_3, and F_4 for water only.

The minimum value of $(\dot{q}_{max})_{cr,z}$, i.e., the predicted first occurrence of the CHF condition, occurs when

$$\frac{d}{dz}\left(Cf(z) + \int_0^z f(z)\, dz\right) = 0 \tag{51}$$

Using values of A, **B,** and C derived from CHF data taken from uniformly heated tubes, Barnett [30] compared the predictions of Eq. (50) with experimental data from two sources [31, 32]. Predicted values of $(\dot{q}_{max})_{cr}$ were consistently higher than experimental values. The method did, however, appear satisfactorily to predict the area of the tube over which the CHF condition would occur. This comparison showed that the local conditions hypothesis is not generally valid.

II. The "overall power" hypothesis

The overall power hypothesis suggests that the total power that can be fed to the tube with nonuniform heating before the CHF condition is reached will be the same as that for a uniformly heated tube of the same dimensions with the same inlet conditions. No prediction of the location of CHF is made with this method. It was found that the method predicted the critical power for a number of sine-wave-profile tubes reasonably well. Barnett [30], however, showed that the hypothesis was not generally valid for different heat flux profiles when he compared the data of Swenson et al. [32].

III. The quality/boiling length approach (x_{cr} versus z_{sat})

An improvement over the overall power hypothesis is to use the critical quality/boiling length form of correlation suggested by Eq. (42) and Fig. 16. CHF data for nonuniform heat flux tend to fall on the same line as those for uniform heat flux conditions when plotted on these coordinates. An example is given in Fig. 21. Although the x_{cr}/z_{sat} method is an improvement, it is still not fundamentally correct, because in some instances it is possible to insert an unheated (cold) patch into a uniformly heated tube, which reduces the value of z_{sat} but increases the critical quality x_{cr}.

IV. The *F*-factor method

An empirical method has been derived by Tong and co-workers [33-35] that enables the effect of the upstream flux profile on the local CHF value to be taken into account. A factor **F** is defined such that

$$F = \frac{(\dot{q}_{cr}(z))_u}{(\dot{q}_{cr}(z))_{nu}} \tag{52}$$

where $(\dot{q}_{cr}(z))_u$ is the value of the CHF at any given local enthalpy for the uniform heat flux profile case and $(\dot{q}_{cr}(z))_{nu}$ is the corresponding value for the particular nonuniform heat flux profile. The form of the correction factor **F** was obtained from an energy balance and is

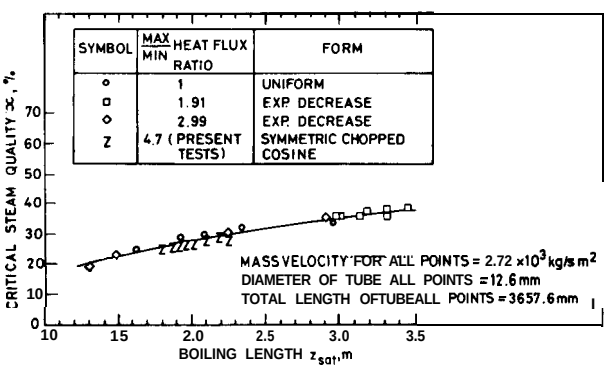

Figure 21 Example of nonuniform CHF data x_{cr} plotted against z_{sat}. From Keeys et al. [101].

© 1983 Hemisphere Publishing Corporation

$$F = \frac{\Omega}{1 - \exp(-\Omega z_{cr})} \int_0^{z_{cr}} \frac{\dot{q}(z)}{\dot{q}(z_{cr})} \times \exp[-\Omega(z_{cr} - z)]\, dz \quad (53)$$

From the definition of F,

$$(\dot{q}_{cr}(z))_{nu} = \frac{A + B\Delta h_{sub,i}}{(F/C) + \int_0^{z_{cr}} (\dot{q}(z)/\dot{q}(z_{cr}))\, dz} \quad (54)$$

The ratio $\dot{q}(z)/\dot{q}(z_{cr})$ in Eqs. (53) and (54) may be replaced by $f(z)/f(z_{cr})$ and thus both integrals are functions of the flux profile only and can be evaluated directly as a function of z,,. The value of the factor Ω has been determined by fitting the method to experimental data. Values of Ω are given by Tong et al. [33] and Lee [36], and further details of the method are given by Collier [12].

To summarize, no completely general analytic method is available at present for the prediction of CHF in tubes with a nonuniform axial heat flux profile. Studies of heat flux distributions other than a sine wave profile have confirmed that the critical power that can be applied to a tube is seldom greater than that for a uniform heat flux profile and may be up to 30% lower if the peak heat flux occurs near the tube exit. The one exception to this finding is the case of a linear or hyperbolic decreasing heat flux profile, for which improvements of up to 10% in critical power above the uniform profile case have been observed. If a simple method is needed for design purposes, then that based on the critical quality/boiling length (x_{cr} versus z_{sat}) approach is recommended.

(g) Critical heat flux in noncircular geometries

A considerable amount of work has been carried out to determine CHF values in a variety of noncircular ducts. Many of these geometries are representative of the fuel channels for different types of nuclear reactors cooled by water. The three most common geometries, rectangular channels, annuli, and multirod cluster assemblies, will be considered briefly.

I. Rectangular channels

In many studies only the two longer sides of the rectangle were heated. The CHF appears to vary with the individual independent variables in the same general manner as for round tubes. Macbeth [37] has correlated much of the CHF data available for rectangular channels, and these correlations are reproduced in the book by Collier [12]. Macbeth showed that the substitution of the heated equivalent diameter into round-tube CHF correlations did not accurately predict the rectangular channel case. For situations where the whole perimeter of the rectangular channel is heated, overheating occurs in the corner near the exit of the channel, with a considerably reduced average heat flux.

II. Annuli

Several extensive compilations of data [38-40] exist for the CHF in vertical annular channels with uniform heating on the internal surface. The CHF in internally heated annuli can be correlated in terms of the equation

$$\dot{q}_{cr} = f(\dot{m}, x(z), p, D_i, D_o) \quad (55)$$

Barnett [40] has correlated much of the CHF for steam-water flow in internally heated annuli using a Macbeth-type equation [Eq. (46)]. For a pressure of 69 bar (1 000 psia),

$$A = 67.4 D_h^{0.68} (\dot{m} \times 10^{-6})^{0.192} \times \{1 - 0.744 \exp[-6.512 D_e (\dot{m} \times 10^{-6})]\}$$

$$B = 0.2587 D_h^{1.261} (\dot{m} \times 10^{-6})^{0.817} \quad (56)$$

$$C = 185.0 D_e^{1.415} (\dot{m} \times 10^{-6})^{0.212}$$

D_e is the hydraulic equivalent diameter, given by $D_o - D_i$.

D_h is the heated equivalent diameter, given by $(D_o^2 - D_i^2)/D_i$.

The correlation is in British engineering units and covers the following range of parameters:

D_i: 0.375-3.798 in (0.952-9.65 cm)
D_o: 0.551-4.006 in (1.4-10.16 cm)
z: 24.0-108 in (0.61-2.74 m)
$\dot{m}$: 0.140-6.20 lb/h/ft^2 ($\times 10^{-6}$) (190-8 430 kg/m^2 s)
$Ah_{sub,i}$: O-412 Btu/lb (O-O.958 MJ/kg)

The rms error of this correlation is 5.9%. For pressures other than 69 bar (1 000 psia), Eq. (46) may be used with a slight modification in that A should be replaced by $A(\Delta h_v/649)$, where A, B, and C have the values given above, and Ah, is the latent heat of vaporization at the pressure considered in Btu/lb. This procedure appears satisfactory over the pressure range 41.5-96.5 bar (600-l 400 psia).

CHF experiments have been undertaken with both the internal and external surfaces of the annulus heated. Under these circumstances the critical quality (x_{cr}) passes through a maximum depending on the fraction of the total power input that is applied to the outer tube (Fig. 22).

© 1983 Hemisphere Publishing Corporation

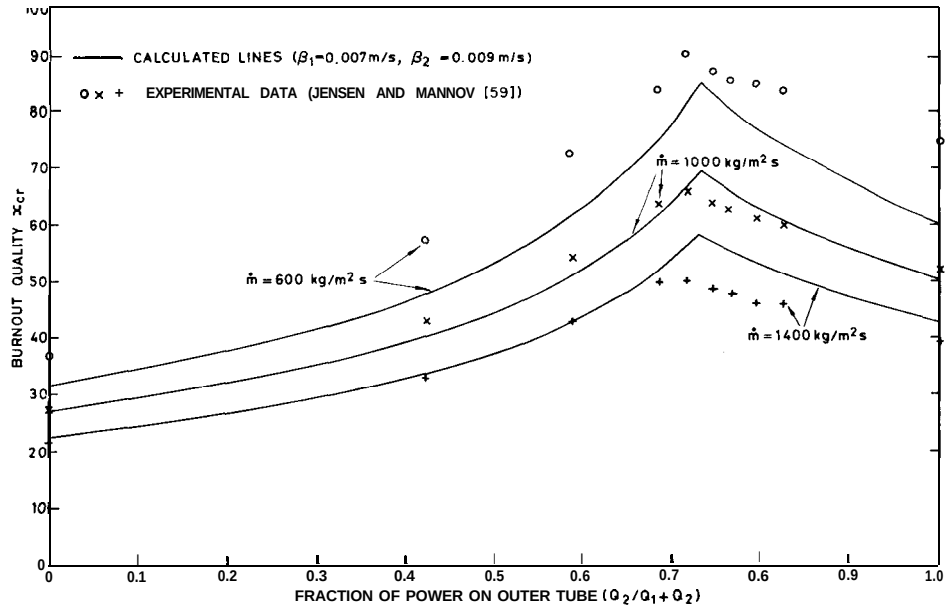

Figure 22 Variation of dryout quality with power distribution within annular channels.

III. Multirod cluster assemblies

Analysis of thermohydraulic conditions within a multirod cluster can be handled in various levels of detail.

(i) Mixed-flow analyses. In the mixed-flow approach the entire channel is assumed to behave in a one-dimensional manner, with average properties being ascribed to the variables such as mass flow rate, quality, and heat flux. No attempt is made to consider any two-dimensional fine structure within the channel. An early attempt at such a correlation was that of Macbeth [41], who applied the local conditions hypothesis to a selection of data from uniformly heated vertical rod clusters. Barnett [40, 42] showed that his annulus correlation, Eq. (56), predicts a wide range of rod cluster data with remarkable accuracy. For rod clusters the values of D_i and D_o are defmed as follows for use in Eqs. (46)-(56):

Equivalent $D_i = D_R$, the rod diameter (in)

Equivalent $D_o = [D_R(D_R + D_h^*)]^{1/2}$ *(in)*

where

$$D_h^* = \frac{4 \text{ X flow area}}{S \text{ X heated perimeter}} \qquad (57)$$

and

$$S = \sum_{\text{rods}} \xi$$

ξ is the ratio of heat flux on a rod to the maximum heat flux in the cluster. If all the rods carry the same heat flux, $D_h^* = D_h$; the defmition of D_h^* ensures that the rod cluster and the equivalent annulus have the same exit quality for the same critical heat flux. One of the most recent mixed-flow correlations is that of Bowring [43], which can be applied to all types of nuclear fuel elements and has corrections for both nonuniform axial and radial (rod-to-rod) heating.

(ii) Subchannel analyses. With the subchannel approach the flow channel is considered to be subdivided into a number of parallel, interacting flow subchannels between rods. The equations of mass, momentum, and energy conservation are solved to give radial and axial variations in quality (or fluid enthalpy) and mass flow rate. Interchange of mass, heat, and momentum is allowed between neighboring subchannels, the amounts being governed by the conservation equations. Once the *local* enthalpy and flow conditions at each subchannel node have been established, suitable constitutive relations in the form of empirical correlations are used to defme the heat transfer regime, including the CHF, to provide the local temperature of the rod surface. Details of such calculations have been given by Weisman and Bowring [44].

(iii) Phenomenological analyses. Under the general heading of phenomenological analyses, an attempt is made to model the kinetics of the various physical processes that occur. Clearly, such analyses must relate to the actual flow patterns present and, more important, they must be able to handle departures from hydrodynamic equilibrium (i.e., not "fully developed flows). To illustrate these points, an example of the

© 1983 Hemisphere Publishing Corporation

phenomenological model developed at Harwell for two-phase flow in a vertical rod cluster is given in the next section.

(h) Mechanisms for the critical heat flux condition

There is, at present, no complete understanding of the mechanisms leading to the CHF condition despite the very large amount of research work that has been performed. Although relatively little is known about the mechanism of the CHF condition corresponding to departure from nucleate boiling, considerably more is known about the mechanism of dryout in the higher-quality regions.

I. Subcooled and low-quality region

Tong and Hewitt [45] have identified at least three separate mechanisms for initiating the CHF condition (Fig. 23).

(i) Dryout under a vapor clot. As a result of evaporation of the microlayer, a dry patch tends to form under a growing vapor bubble. When the bubble departs from the surface, this dry patch is rewetted and a stable situation results from the alternate heating and quenching of the surface at the dry spot. Fiori and Bergles [46] and Kirby et al. [47] found that if the heat flux is high, the temperature rise of the dry patch is such that it cannot easily be rewetted following bubble departure and there is a progressive increase in the surface temperature leading to the CHF condition.

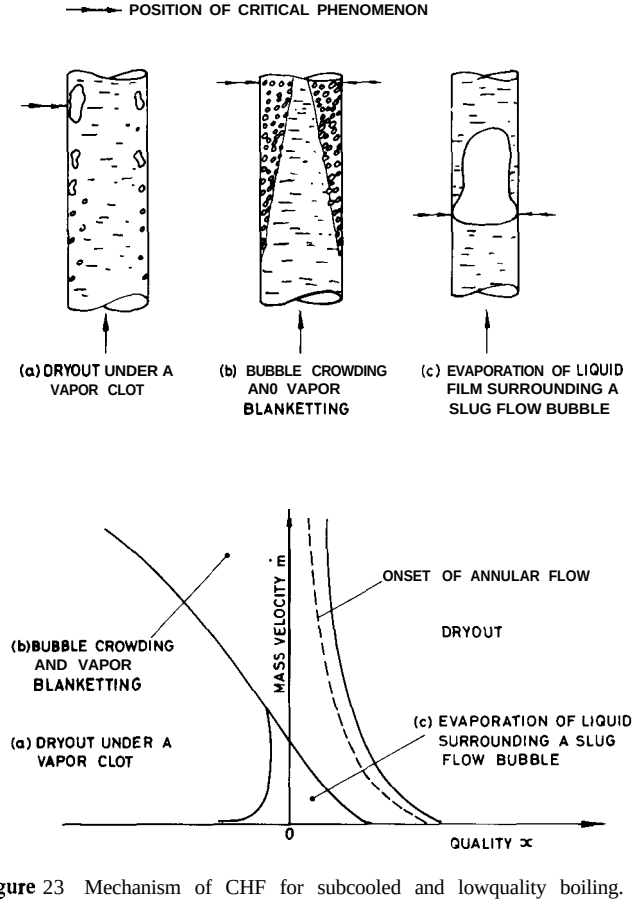

Figure 23 Mechanism of CHF for subcooled and lowquality boiling.

(ii) Bubble crowding and vapor blanketing. At moderate subcoolings, a boundary layer of bubbles may grow to the point where it restricts the access of liquid to the heated surface. At some point, if access is seriously affected, overheating occurs, with the formation of a continuous vapor layer adjacent to the wall. Kutateladze and Lenont ev[48] and later Tong [49] suggest that the critical phenomenon is separation of the hydrodynamic boundary layer. An analogy is suggested between the phenomenon of boundary layer separation induced by the injection of gas into a flowing liquid through a porous wall and the CHF condition in subcooled boiling. The flow stagnation that occurs in the separated boundary layer could result in vapor blanketing.

(iii) Evaporation of liquid surrounding a slug flow bubble. At low mass velocities the slug flow pattern may occur with a liquid film initially remaining between the vapor bubble and the heated wall. If, however, the heat flux is high, this film may be completely evaporated and a form of dryout with consequent overheating of the tube wall may occur.

A tentative map with mass velocity and subcooling as ordinates, showing where these various mechanisms might be expected to occur, has been. published by Semeria and Hewitt [50].

II. High-quality region (annular flow)

By making measurements of the annular liquid film flow rate at the exit of a heated tube as a function of the tube length and applied power, Hewitt et al. [51, 52] were able to build up a complete picture of the conditions occurring along the heated tube and were able to demonstrate that the CHF condition occurred when the flow rate of the liquid film on the heated surface fell to zero; hence the name dryout. These experiments also revealed that the distribution of the liquid phase between entrained droplets and the liquid film at a particular quality and mass velocity in a heated tube is significantly different from that observed at the same quality and mass velocity at the end of a long unheated tube, i.e., under fully developed equilibrium conditions.

The departures from hydrodynamic equilibrium in

© 1983 Hemisphere Publishing Corporation

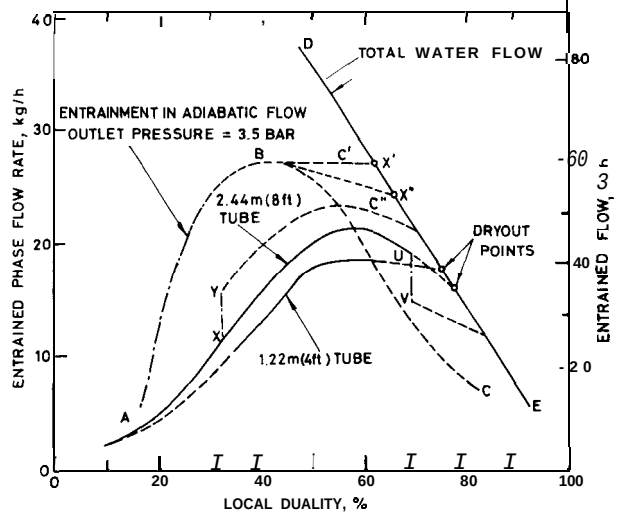

Figure 24 Entrained phase flow rate as a function of local quality. From Hewitt et al. [52].

an evaporating flow are illustrated in Fig. 24, which shows the flow rate of the liquid phase entrained as droplets versus the vapor quality. The equilibrium flow rate of liquid entrained in the vapor core is plotted (as curve ABC). Also shown is the total liquid flow rate in the tube ***(DE);*** the difference between curves ***ABC*** and ***DE*** is the flow rate in the liquid film.

Now consider an evaporating flow in a heated tube. If the conditions at every axial location in the heated tube correspond to the fully developed equilibrium state at the corresponding quality in the unheated tube, then the amount of liquid entrained in the vapor core will increase up to an axial location corresponding to the maximum (point ***B).*** Deposition of droplets onto the film would take place in the downstream parts of the tube (region ***BC***), and dryout would occur at approximately 100% quality. Clearly this is not the true picture. Hewitt et al. [51] initially postulated that entrainment was fairly rapid but that deposition was a rather slow process. In this instance the entrained liquid flow in the lower parts of the tube would follow curve ***AB*** closely until the maximum at ***B. Since*** deposition was regarded as a slow process, the entrained liquid flow rate tended to remain constant (curve ***ABC')*** or decrease only slowly (curve ***ABC")*** with further increase in quality; dryout (i.e., liquid film flow rate → 0) would now occur at x' or x''. It was found in the later series of measurements [52] that the measured entrained liquid flow rates in the lower part of the tube were considerably lower than the equilibrium value. Clearly neither entrainment nor deposition occurs rapidly. The measured relationships for tube lengths 2.44 and 1.22 m are shown in Fig. 24. The observed approximately constant exit quality at dryout is the result of two effects-the longer tube having the higher entrainment flow rate but also the higher deposition rate.

Many of the different effects observed with nonuniform heating mentioned earlier can be quantitatively explained [53] using Fig. 24. For example, the introduction of a short, unheated length into the heated section will produce a different effect depending on whether it is placed in a location before or after that corresponding to point ***B*** in the tube. If it is placed before ***B,*** then, although the quality remains constant across the cold patch, liquid entrainment will continue as the flow attempts to become fully developed. Thus the effect of the cold patch can be shown in Fig. 24 by the vertical line XY. Likewise, if it is placed after ***B,*** then deposition occurs at constant quality and the effect is illustrated by the vertical line ***UV.*** Another example is the heating profile that involves an exponential decrease in heat flux versus length. This profile has a short length over which entrainment may occur and a long length for deposition to take place giving a higher quality at dryout than a uniform heat flux profile.

This qualitative description has been developed into a quantitative closed form theory for dryout in annular flow. Figure 25 shows the mass balance on an elemental length of tube δz. A mass balance on the liquid film gives

$$\underbrace{M_{lf} + \pi D \dot{m}_d \delta z}_{\text{Inflow}} = \underbrace{\dot{M}_{lf} + \frac{\partial M_{lf}}{\partial z}\delta z + \pi D E \delta z + \pi D \frac{\dot{q}}{\Delta h_v}\delta z}_{\text{Outflow}} + \underbrace{\frac{M_{lf}}{\partial t}\delta z}_{\text{Accumulation}} \tag{58}$$

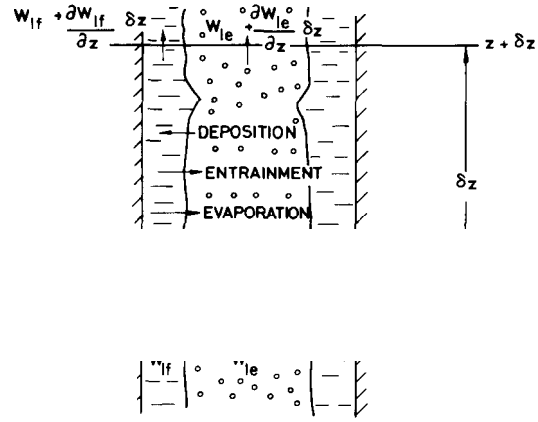

Figure 25 Mass balance in annular flow on elemental length of channel. From Whalley et al. [57].

© 1983 Hemisphere. Publishing Corporation

where $\dot{M}_{lf}$ = liquid film flow rate
D = tube diameter
$\dot{m}_d$ = deposition rate of droplets onto the film
E = entrainment rate of droplets from the film
$\dot{q}$ = local heat flux
Δh_v = latent heat of vaporization of the liquid
M_{lf} = mass of liquid contained in the film per unit length

so

$$M_{lf} = \pi D \delta \rho_\ell \tag{59}$$

where δ is the average liquid film thickness and ρ_ℓ is the liquid density. Hence

$$\frac{\partial \dot{M}_{lf}}{\partial z} = \pi D \left(\dot{m}_d - E - \frac{4}{\Delta h_v} - \rho_\ell \frac{\partial \delta}{\partial t} \right) \tag{60}$$

Similarly, a mass balance over the liquid entrained in the gas core gives

$$\frac{\partial M_{le}}{\partial z} = \pi D (E - \dot{m}_d) - \frac{\pi D^2}{4} \frac{\partial C}{\partial t} \tag{61}$$

where C is the concentration (mass per unit volume) of droplets in the core. Methods of calculating the entrainment and deposition rates and also the liquid film thickness are needed.

The deposition rate for droplets can be calculated from the mass transfer coefficient β

$$\dot{m}_d = \beta C \tag{62}$$

β was found to be a function of the physical properties of the system being considered and to a first approximation was related to the surface tension of the fluid (see Fig. 26.) The entrainment rate E was assumed to be given by

$$E = \beta C_E \tag{63}$$

where β is again the mass transfer coefficient and C_E is the concentration of droplets that would be in equilibrium with the liquid film. E was shown [54] to be a function of the dimensionless group $\delta\tau/\sigma$, where τ is the interfacial shear stress and σ is the surface tension (Fig. 27). Thus the problem of calculating the entrainment rate reduces to that of calculating τ and 6. These qualities can be evaluated because, if the film flow rate is known, there are two relationships between them:

1. A triangular relationship among τ, δ, and $\dot{M}_{lf}$,

$$\frac{4\delta}{D} = \sqrt{\frac{(dp/dz)_{lf}}{dp/dz}} \tag{64}$$

where $(dp/dz)_{lf}$ is the pressure gradient that would occur in a single-phase liquid flow where the mass flow was identical to that in the liquid film (calculated by the method given by Hewitt and Hall-Taylor [55]) and dp/dz is the pressure gradient in the two-phase flow.

2. An interfacial roughness correlation based on the assumption that the roughness presented by the liquid film interface is only a function of the liquid film thickness. The particular form of the interfacial roughness correlation used was that due to Wallis [56], in which the interfacial friction factor (defined in terms of a homogeneous gas core) can be expressed as $(1 + 360\delta/D)$ times the friction factor for the gas core flowing alone in the absence of a liquid film.

By using these relationships, Eq. (58) (with the time derivatives set equal to zero) can be integrated

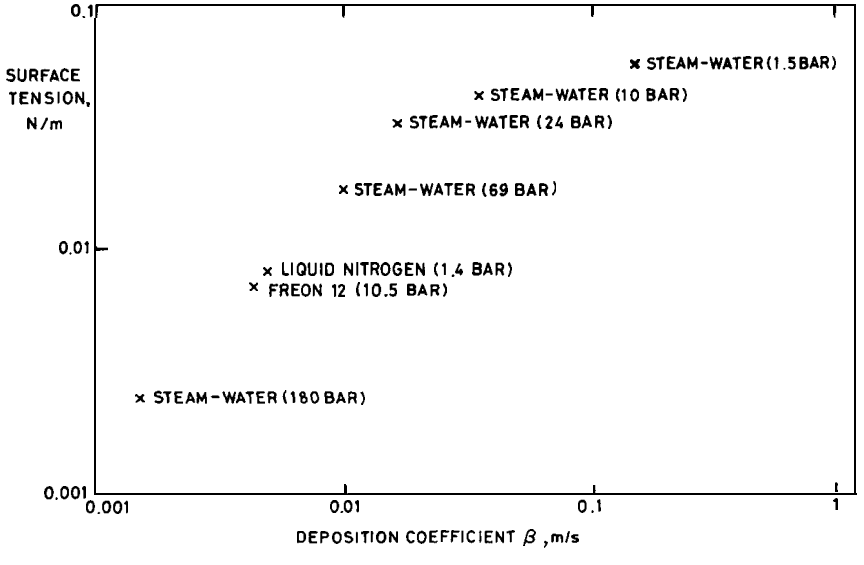

Figure 26 Variation of deposition coefficient with surface tension.

© 1983 Hemisphere Publishing Corporation

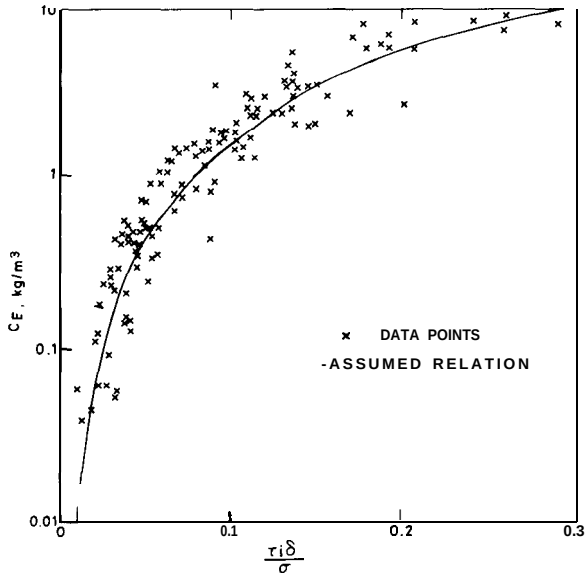

Figure 27 Entrainment correlation.

from the point of onset of annular flow (assumed arbitrarily to start at 1% quality with 99% of the liquid entrained at this point) and the integration is continued along the channel until $\dot{M}_{lf}$ becomes zero, indicating dryout. Some examples [57] of calculated CHF values for uniformly heated tubes for steam-water mixtures at 1.5, 69, and 180 bar pressure are given in Fig. 28 for comparison with experimental data. A further comparison with experimental data for Freon 12 is also shown.

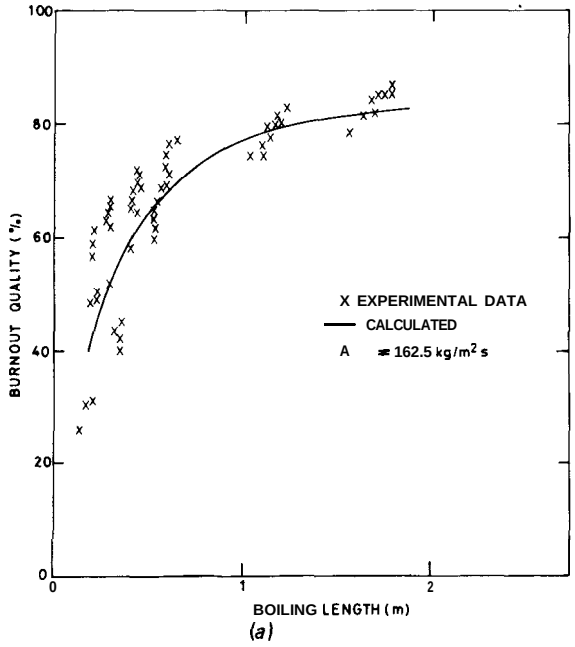

Figure 28(*a*) Burnout in steam-water flow at 1.5 bar. $D = 9.3$ mm, $k \simeq$ 0.15 m/s. Data from Hewitt et al. [57].

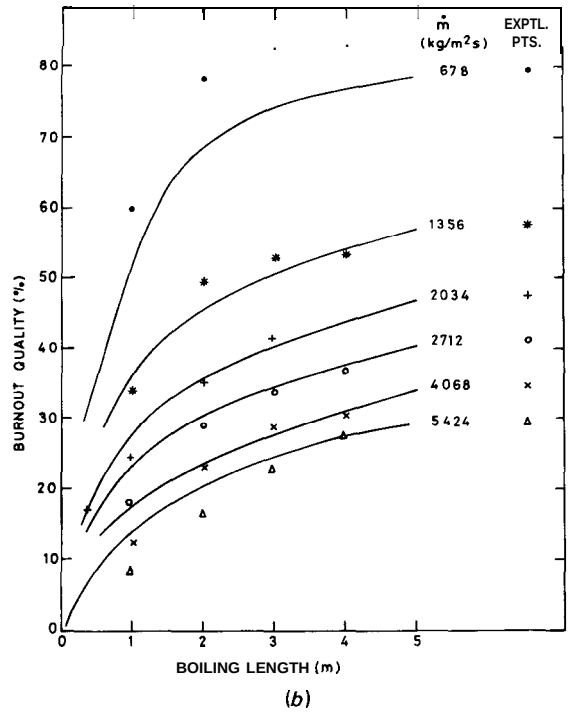

Figure 28(*b*) Burnout in steam-water flow at 69 bar. D = 12.6 mm, k = 0.01 m/s. Data from Bennett et al. [18].

More recently, the theoretical model has been extended to an annular geometry [58] in which both the inside and outside surface may be heated and to multirod clusters [60,61]. Figure 22 shows a comparison of the predicted CHF for comparison with the experimental CHF value of Jensen and Mannov [59] for an annulus with independent heating of the inner and outer surfaces. Also shown are predictions for a

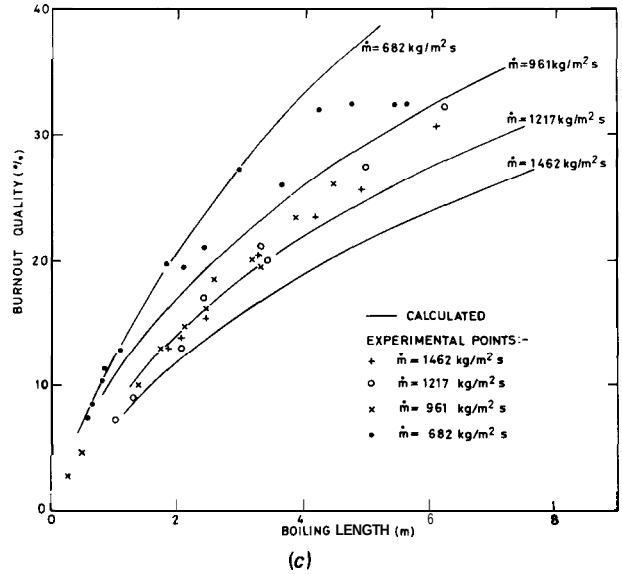

Figure 28(c) Burnout in steam-water flow at 180 bar. D = 32 mm, k = 0.001 5 m/s. Data from Chojnowski and Wilson [57].

© 1983 Hemisphere Publishing Corporation

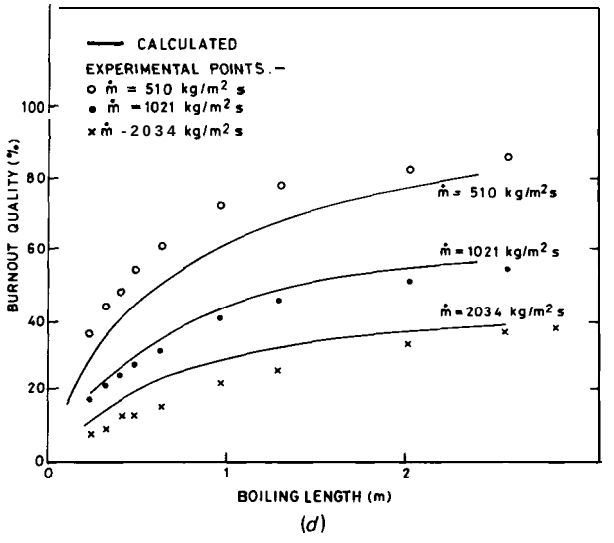

Figure 28(d) Burnout in Freon 12 at 10.5 bar. $D = 8.5$ mm, k = 0.004 3 m/s. Data from Stevens et al. [63, 64].

seven-rod cluster cooled by Freon 12 at 10.7 bar. The geometry of the bundle was varied so that the gap between the rods was altered, the outer six rods always being at the vertices of a regular hexagon with the seventh rod at the center of the hexagon. In one set of tests the outer rods touched the center rod; in another they touched the outer containing tube; positions intermediate between these extremes were also studied. Experimental and predicted dryout powers as a function of the gap between the rods are shown in Fig. 29.

(i) Critical heat flux in counter-current flow

It is well known that for the case of a vertical channel with a reservoir of fluid above the channel the CHF does not approach zero as the flow to the bottom of the channel ceases. Liquid can run back from the reservoir into the channel to provide cooling. However, there will be some limiting vapor flow rate at the tube upper exit above which no liquid can run back. The heat flux corresponding to this condition can be thought of as the CHF. Nejat [62] has carried out experiments for a range of fluids (carbon tetrachloride, n-hexane, and water) and tube diameters (8, 10, and 14 mm ID) and has produced the following correlation in terms of dimensionless groups:

$$\dot{q}^* = 3.2^{-1} \frac{\dot{q}_{cr}}{\rho_g^{1/2} \Delta h_v} [g_n \sigma(\rho_\ell - \rho_g)]^{-1/4}$$

$$D^* = D \left[\frac{\sigma}{g_n(\rho_\ell - \rho_g)} \right]^{-1/2} \tag{65}$$

$$q^* \left(\frac{z}{D} \right)^{-0.1} = 1 - 1.5 D^{*(-1/2)}$$

(j) Critical heat flux in forced flow of fluids other than water

Table 6 gives a selection of the available sources of experimental data on the critical heat flux taken under forced convection conditions for various organic

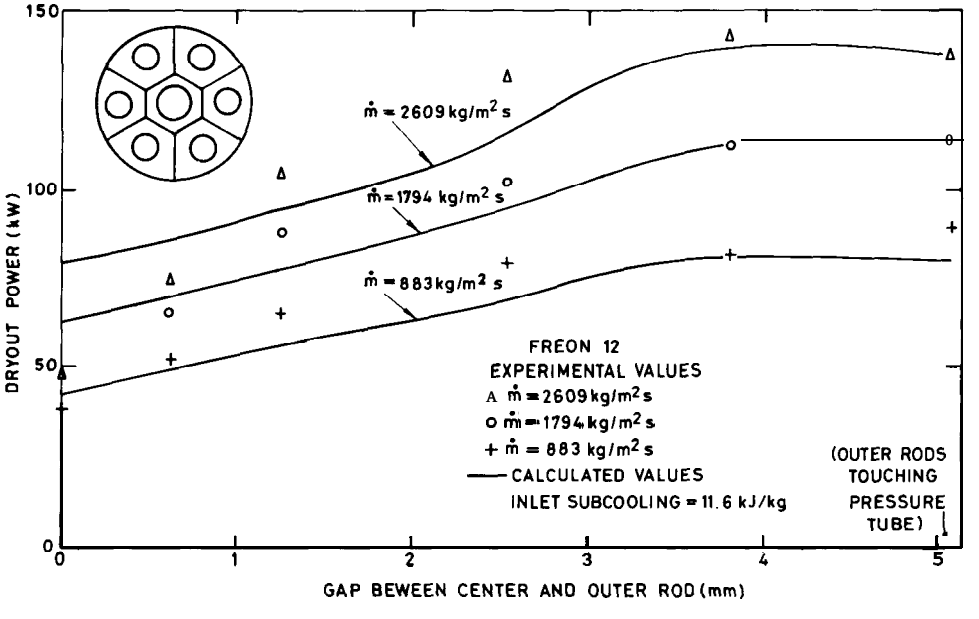

Figure 29 Comparison between experimental and predicted value of CHF for annulus and multirod cluster (prediction using Hewitt/Whalley/Hutchinson annular-flow model).

© 1983 Hemisphere Publishing Corporation

Table 6 Available experimental data for critical heat flux in forced flow of fluids other than water

Reference	Fluid	Geometry	Experimental ranges: Pressure, bar	Subcooling, °C	Velocity, m/s	Critical heat flux, kW/m²	No. of tests
Noel [86]	Hydrazine	Tube	6.9-83	55-281	0.3-28.4	2 330-44 500	62
Hines [87]	Hydrazine	Tube	13.2-71	57-263	4.02-36.8	4 450-43 300	22
Noel [88]	Ammonia	Tube	11.7-126	1.6-115	0.947.6	2 840-23 400	45
Dimmock [89]	Ammonia	Tube	11.4-88	0.5-l 12	3.79-25	2 460-16 350	111
Core and Sato [90]	Diphenyl	Annulus	1.6-28	O-183	0.15-5.2	220-2 800	48
	Santowax R		6.9	–	0.15-4.6		10
	Polyphenyl mixture		4.4-22	5-213	0.15-4.6		25
	Monoisopropyl-biphenyl (MIPB)		26.6-27.6	88-179	0.15-4.6	1230-3 000	6
Robinson and Lurie [91]	Santowax R and other polyphenyls	Tube	1.52–10.35	19-157	1.25-7.7	1005-3 720	94
Birdseye [92]	Nitrogen tetroxide	Tube	10.35–42.5	o-111	3.11-18.2	1730-11 300	73
Gambill and Bundy [93]	Ethylene glycol	Tube	1.38-6.1	86-147	5.3-27	6 500-19 700	5
Povamin [94]	Ethyl alcohol	Tube	2.062	O-210	0.49-50	567-21 600	163
Lewis et al. [95]	Nitrogen	Tube	3.45	1.6	0.027	50-177	11
	Hydrogen	Tube	3.45	o-3.3	0.10	19-66	44
Stevens et al. [63]	Freon 12	Tube	10.7	O-28 kJ/kg		22-284	Large number
Stevens et al. [64]	Freon 12	Tube (non-uniform heating)	10.7	O-28 kJ/kg		93.5-315	81
Barnett and Wood [96]	Freon 12	Tube	7.3-13.8	O-60.5 kJ/kg		79–440	Large number
Hoffman and Krakoviak [97]	Potassium	Tube				101-l 100	6
Lurie [98]	Sodium	Annulus	0.35-0.55	o-34		945-2 520	11
Aladyev et al. [99]	Potassium	Tube (uniform and nonuniform heating)	1.1-1.3	100-390	Low	252-l 890	
Tippets et al. [100]	Potassium	Tube	2.1-3.8		Low	252-l 320	

liquids, cryogenic fluids, and liquid metals. Apart from the work of Stevens et al. [63,64], the studies have been somewhat limited in scope. The very comprehensive set of experiments on Freon have shown that this fluid, at least, behaves qualitatively in a way identical to that of water. The data for both the cryogenic fluids and the liquid metals clearly show that as the mass velocity and diameter are reduced or the tube length increased, the critical heat flux approaches that needed for complete evaporation of the fluid.

A number of attempts have been made to produce empirical correlations applicable to both water and other fluids. None of these correlations can be proposed for general use. In the absence of an extensive bank of experimental CHF data for fluids other than water, no completely comprehensive method can be presented. Two different approaches are possible:

1. The derivation and use of a set of scaling laws relating the critical heat flux in water to the value in the nonaqueous fluid

2. The application of the phenomenological dry-out model described in previous sections to fluids other than water

An attempt to determine the relevant physical properties and a set of scaling laws for the critical heat flux condition was made at U.K. Atomic Energy Establishment Winfrith [65,66]. Barnett [65] discusses which of the numerous physical property terms are likely to be important and goes on to develop appropriate dimensionless property groupings. A number of hypothetical relationships between these groupings have been examined using the experimental data for water and Freon [66,67]. None of the relationships tested was entirely satisfactory, although one set of laws, Eq. (66), does appear to be near the truth:

$$\frac{\dot{q}_{cr}\gamma^{0.5}}{\Delta h_v \rho_\ell^{0.5}} = fn\left(\frac{z}{D}, \frac{}{\lambda_\ell \gamma^{0.5}}^{0.5}, \frac{\dot{m}\gamma^{0.5}{}_{p\ell}\rho_\ell^{v}}{\rho_\ell^{0.5}}, \rho_g, \frac{\Delta h_{sub,i}}{\Delta h_v}\right)_3 \quad (66)$$

© 1983 Hemisphere I blishing Corporation

where

$$\gamma = \frac{d(\rho_\ell/\rho_g)_{sat}}{dp}$$

Using scaling factors obtained empirically [68] from round-tube critical heat flux data for water and Freon 12, Stevens and Wood [69] were able directly to relate CHF data for the two fluids taken in other more complex geometries, including a rod cluster. One of the more successful approaches to the problem of scaling is that of Ahmad [70]. Using classical dimensional analysis, he deduced that the critical heat flux (expressed in terms of the boiling number $\dot{q}_{cr}/\dot{m}\Delta h_v$) would depend on 12 dimensionless groups, of which 6 were eliminated by inductive arguments. Three dimensionless groups are commonly matched in scaling of the critical heat flux: $\Delta h_{sub,i}/\Delta h_v$, ρ_ℓ/ρ_g, z/D [see Eq. (66)]. This left three dimensionless groups, which were combined into a single modeling parameter ψ_{cr} as follows:

$$\psi_{cr} = \frac{\dot{m}D}{\eta_\ell}\left(\frac{\eta_\ell}{\sigma D \rho_\ell}\right)^{2/3}\left(\frac{\eta_\ell}{\eta_g}\right)^{1/8} \tag{67}$$

or, alternatively, as

$$\psi_{cr} = \frac{\dot{m}D}{\eta_\ell}\left(\frac{\gamma^{0.5}\eta_\ell}{D\rho_\ell^{0.5}}\right)^{2/3}\left(\frac{\eta_\ell}{\eta_g}\right)^{1/8} \tag{68}$$

Equation (67) is the more basic version, but Eq. (68) gives nearly identical results over wide ranges of pressure and temperature. The usefulness of this scaling law may be judged from Fig. 30, where data for water, Freon 12, and carbon dioxide are compared [17].

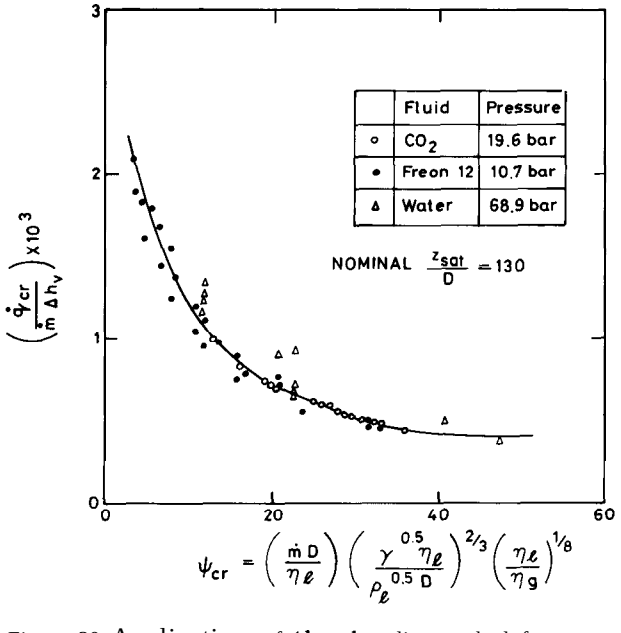

Figure 30 Application of Ahmad scaling method for water, Freon 12, and carbon dioxide. From Hauptmann et al. [71].

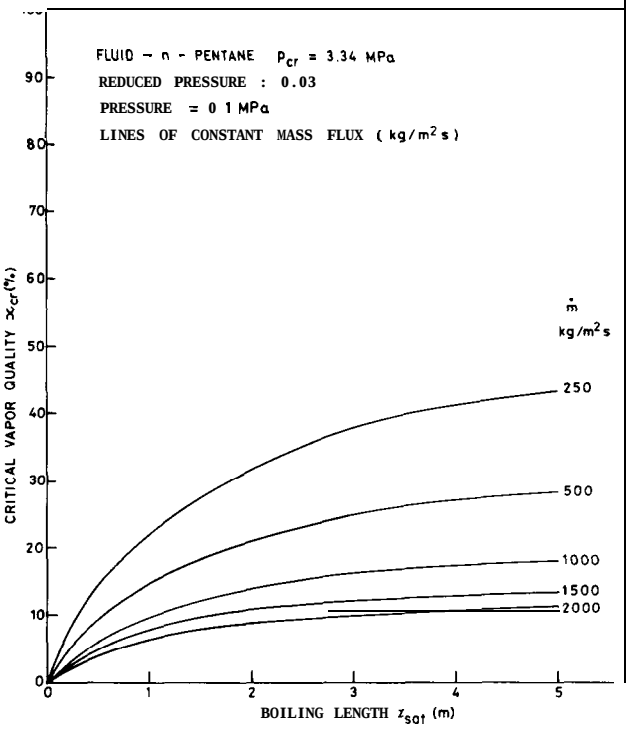

Figure 31 Critical vapor quality x_q as a function of boiling length z_{sat} for a reduced pressure of 0.03 with mass velocity as parameter.

The phenomenological model described in the previous section can be used to generate critical vapor quality (x_{cr}) versus saturated boiling length (z_{sat}) curves for any fluid [72]. Where limited experimental data are available, these may be used to check the estimates that have been prepared. As examples, four fluids have been considered:

Refrigerant (Freon) 12 (p_{cr} = 41.1 bar)
Nitrogen (p_{cr} = 34.0 bar)
C-5 Hydrocarbon (pentane) (p_{cr} = 33.4 bar)
Ethanol (p_{cr} = 63.8 bar)

A constant tube diameter of 20 mm was adopted together with a maximum boiling length (z_{sat}) of 5 m. Four pressures were chosen, corresponding to reduced pressures (p/p_{cr}) of 0.03, 0.1, 0.2, and 0.5. Five mass velocity levels were examined, viz., 250, 500, 1 000, 1 500, and 2 000 kg/m² s.

The curve of critical vapor quality versus boiling length for pentane for a reduced pressure of 0.03 is shown in Fig. 31 as an example. Values of x_{cr} for pentane and the other fluids are also tabulated in Table 7 so that similar graphs can be prepared for any other situation.

This information may be easily converted to a critical heat flux by the use of the relationship

© 1983 Hemisphere P ublishing Corporation

Table 7 Values of x_{cr} for fluids other than water as a function of pressure, mass velocity, and boiling length

	z_{sat}, m				
$\dot{m}$, kg/m s	1	2	3	4	5
	Refrigerant 12				
	$p/p_{cr} = 0.03$ p = 1.23 bar				
250	0.375	0.515	0.595	0.655	0.695
500	0.260	0.360	0.425	0.465	0.490
1000	0.175	0.245	0.285	0.305	0.315
1500	0.140	0.190	0.220	0.230	0.240
2000	0.115	0.160	0.180	0.190	0.200
	$p/p_{cr} = 0.1$ p = 4.11 bar				
250	0.51	0.685	0.775	0.825	0.860
500	0.36	0.50	0.58	0.625	0.645
1000	0.25	0.34	0.385	0.410	0.425
1500	0.195	0.265	0.295	0.315	0.335
2000	0.165	0.220	0.245	0.265	0.285
	p/p_{cr} = 0.2 p = 8.22 bar				
250	0.55	0.73	0.82	0.875	0.90
500	*0.39*	0.535	0.62	0.665	0.69
1000	0.265	0.370	0.415	0.445	0.465
1500	0.205	0.280	0.320	0.345	0.380
2000	0.170	0.235	0.265	*0.295*	0.315
	$p/p_{cr} = 0.5$ p = *20.55* bar				
250	0.46	0.65	0.76	0.82	0.865
500	0.31	0.46	0.545	0.595	0.630
1000	0.20	0.30	0.360	0.395	0.420
1500	0.15	0.23	0.215	0.310	0.335
2000	0.12	0.19	0.225	0.260	0.280
	Nitrogen				
	$p/p_{cr} = 0.03$ p = 1.02 bar				
250	0.22	0.315	0.370	0.415	0.450
500	0.15	0.215	0.255	0.280	0.300
1000	0.10	0.140	0.165	0.180	0.190
1500	0.08	0.110	0.125	0.140	0.145
2000	0.065	0.09	0.105	0.115	0.120
	p/p_{cr} = 0.1 p = *3.40* bar				
250	0.305	0.435	0.510	0.565	0.605
500	0.205	0.300	0.355	0.390	0.415
1000	0.140	0.195	0.230	0.250	0.265
1500	0.105	0.155	0.175	0.190	0.205
2000	0.09	0.130	0.145	0.160	0.170
	p/p_{cr} = 0.2 p = *6.80* bar				
250	0.33	0.465	0.555	0.615	0.660
500	0.22	0.320	0.385	0.425	0.450
1000	0.15	0.215	0.250	0.275	0.290
1500	0.11	0.165	0.190	0.210	0.225
2000	0.09	0.135	0.160	0.175	0.190
	$p/p_{cr} = 0.5$ p = 17.00 bar				
250	0.265	*0.390*	0.485	0.555	0.605
500	0.160	0.250	0.325	0.370	0.405
1000	0.10	0.160	0.205	0.235	0.255
1500	0.07	0.120	0.155	0.175	0.195
2000	0.06	*0.095*	0.125	0.145	0.160

Table 7 *(Continued)* Values of x_{cr} for fluids other than water as a function of pressure, mass velocity, and boiling length

	z_{sat}, m				
$\dot{m}$, kg/m² s	1	2	3	4	5
	n-Pentane				
	p/p_{cr} = 0.03 p = 1.Obar				
250	0.22	0.315	0.38	0.41	0.435
500	0.15	0.21	0.25	0.27	0.285
1000	0.10	0.14	0.16	0.17	0.18
1500	0.08	0.105	0.12	0.13	0.135
2000	0.065	0.085	0.10	0.11	0.115
	p/p_{cr} = 0.1 p = *3.34* bar				
250	0.315	0.435	0.51	0.56	0.595
500	0.215	0.30	0.35	0.38	0.40
1000	0.14	0.20	0.225	0.245	0.255
1500	0.11	0.15	0.175	0.19	0.20
2000	0.09	0.125	0.145	0.16	0.17
	p/p_{cr} = 0.2 p = *6.68* bar				
250	0.34	0.475	0.56	0.615	0.645
500	0.23	0.325	0.38	0.415	0.44
1000	0.15	0.215	0.245	0.265	0.285
1500	0.115	0.165	0.190	0.210	0.225
2000	0.095	0.135	0.155	0.175	0.190
	$p/p_{cr} = 0.5$ p = 16.70 bar				
250	0.30	0.45	0.545	0.605	0.65
500	0.195	0.30	0.365	0.405	0.435
1000	0.12	0.185	0.230	0.260	0.285
1500	0.09	0.14	0.175	0.20	0.22
2000	0.075	0.115	0.14	0.165	0.18
	Ethanol				
	p/p_{cr} = 0.03 p = 1.91 bar				
250	0.24	0.33	0.39	0.425	0.45
500	0.165	0.225	0.26	0.285	0.295
1000	0.105	0.145	0.165	0.180	0.190
1500	0.085	0.115	0.125	0.135	0.145
2000	0.070	0.090	0.105	0.110	0.120
	p/p_{cr} = 0.1 p = *6.38* bar				
250	0.355	0.49	0.565	0.615	0.645
500	0.240	0.335	0.390	0.420	0.435
1000	0.160	0.225	0.255	0.280	0.290
1500	0.125	0.180	0.190	0.210	0.220
2000	0.110	0.140	0.160	0.175	0.185
	p/p_{cr} = 0.2 p = 12.76 bar				
250	0.405	0.555	0.645	0.695	0.730
500	0.275	0.390	0.450	0.485	0.505
1000	0.185	0.255	0.290	0.315	0.335
1500	0.145	0.195	0.225	0.245	0.265
2000	0.120	0.160	'0.190	0.210	0.220
	$p/p_{cr} = 0.5$ p = 31.90 bar				
250	0.36	0.52	0.62	0.685	0.725
500	0.235	0.35	0.425	0.465	0.495
1000	0.145	0.225	0.270	0.305	0.335
1500	0.105	0.165	0.205	0.235	0.255
2000	0.085	0.135	0.170	0.190	0.215

© 1983 Hemisphere Publishing Corporation

$$\dot{q}_{cr} = \frac{x_{(z)cr} D \dot{m} \Delta h_v}{4 z_{sat}} \quad (69)$$

Thus, for *n*-pentane at a pressure of 1 bar (p/p_{cr} = 0.03), a mass velocity of 1 000 kg/m^2 s, and a boiling length of 5 *m*, *x(z)*,, from Fig. 31 is 0.18. The corresponding value of $\dot{q}_{cr}$ from Eq. (69) is then 64.62 kW/m^2.

E. Heat transfer in areas where the critical heat flux has been exceeded

The critical heat flux condition (shown as a ridge in the three-dimensional representation of the boiling surface in Fig. 3) represents a situation at which there is a more or less sudden decrease in the value of the heat transfer coefficient by one or two orders of magnitude as compared with the values obtained in the nucleate boiling or two-phase forced convective regions. This decrease is a consequence of the fact that the heat transfer surface is no longer completely wetted by the liquid phase. Vapor now completely or partially blankets the surface, and heat transfer is no longer to a highly conducting liquid but to a poorly conducting gas.

By referring to Figs. 3 and 4, it will be noted that such a condition can occur for both the subcooled and saturated liquid states. Four separate areas can be identified, and it is convenient to consider the heat transfer mechanisms in terms of these four regions-transition boiling, subcooled film boiling, saturated film boiling, and the liquid-deficient (postdryout) region-although there would appear to be no well-defined boundaries between the regions. The transition boiling region occupies the reverse slope (partly obscured) in Fig. 3, whereas the other regions-subcooled film boiling, saturated film boiling, and the liquid-deficient (postdryout) region all occupy parts of the slope on the other side of the valley representing the minimum heat flux.

(a) Transition boiling

The use of experimental techniques where the surface temperature rather than the surface heat flux is the controlling variable has established the existence of a transition boiling region in the forced convection condition as well as for pool boiling. A comprehensive review of published information for this heat transfer region has been prepared by Groeneveld and Fung [73].

Various attempts have been made to produce correlations for heat transfer in the transition boiling region. Probably the most useful currently available for water is that by Tong and Young [74], which is given in terms of the heat flux in the transition boiling region ($\dot{q}_{tb}$),

$$\dot{q}_{tb} = \dot{q}_{nb} \exp\left[-0.001 \frac{x^{2/3}}{dx/dz} \left(\frac{\Delta T}{55} \right)^{(1+0.0029 \Delta T)} \right] \quad (70)$$

where $\dot{q}_{nb}$ is the nucleate boiling heat flux (presumably equated with the critical heat flux) in W/m^2 and *AT* is the temperature difference between the surface and the saturation condition in C. A transition boiling correlation having a wider range of application may be developed if the heat flux and wall temperature difference at the points of maximum and minimum in the boiling surface can be predicted with confidence. The present state of the art allows an accurate prediction of $\dot{q}_{cr}$ and also *AT*,,, but the conditions at the minimum point are still subject to a large degree of uncertainty. The experimental data of Iloeje et al. [75] show that the conditions at the minimum point are a complex function of the mass quality and flow rate in the channel.

(b) Film boiling

Visual studies in film boiling inside vertical tubes indicate that at low qualities the flow regime would appear to be an inverted annular one with the liquid in the center and a thin vapor film adjacent to the heating surface. The vapor-liquid interface is not smooth but irregular, with the irregularities occurring at random locations but appearing to retain their identity to some degree as they pass up the tube with velocities of the same order as the liquid core.

Because the liquid is displaced from the heating surface by a vapor film and the uncertainties associated with bubble nucleation are removed, film boiling is amenable to analytic solution. In general, the problem may be treated as an analog of filmwise condensation, and solutions are available for horizontal and vertical flat surfaces and also inside tubes under both laminar and turbulent conditions with and without interfacial shear.

I. Vertical flat surface

For laminar flow and zero interfacial shear stress (τ_i = 0), the local heat transfer $\alpha_{(z)}$ at a distance z up the surface from the start of film boiling is given by

$$\frac{\alpha_{(z)} z}{\lambda_g} = \left[\frac{z^3 g_n \rho_g (\rho_\ell - \rho_g) \Delta h_v}{4 \lambda_g \eta_g \Delta T} \right]^{1/4} \quad (71)$$

The average coefficient $\bar{\alpha}_{(z)}$ over the region z is $\frac{4}{3}$

© 1983 Hemisphere Publishing Corporation

times the local coefficient at the position z. A similar analysis can be carried out for the assumption of turbulent flow in the vapor film. In this case,

$$\frac{\bar{\alpha}(z)z}{\lambda_g} = 0.056\ \mathrm{Re}_g^{0.2}\ (\mathrm{Gr}^*\ \mathrm{Pr})^{1/3} \qquad (72)$$

where Re, is the Reynolds number in the tube based on the vapor flow rate, and Gr* is given by

$$\mathrm{Gr}^* = \frac{z^3 g_n \rho_g (\rho_\ell - \rho_g)}{\eta_g^2} \qquad (73)$$

Note that in this equation $\bar{\alpha}(z)$ is independent of distance z. Because of neglect of the resistance between the vapor film and the interface and the effect of interfacial drag, the heat transfer coefficients computed from Eq. (73) may be somewhat higher than measured.

II. Vertical rod

As mentioned previously, the vapor film appears to break away from the wall in large globular voids, and various attempts have been made to produce models more consistent with this physical behavior than Eq. (71). Bailey [76] suggested that, for a vertical rod, the globular voids are formed by a process of varicose instability of a hollow gas cylinder within a denser liquid. The wavelength for maximum growth for a surface tension governed instability of this type is

$$\frac{\lambda_c}{2\pi} = \frac{r}{0.484}$$

which leads to the following expression for the heat transfer coefficient:

$$\alpha = \left[\frac{\lambda_g^3 g_n \rho_g (\rho_\ell - \rho_g)\Delta h_v}{\eta_g \Delta T r}\right]^{1/4} \qquad (74)$$

where r is the radius of the rod on which film boiling is taking place. An alternative for vertical rods that predicts heat transfer coefficients about 33% higher is to use the original Bromley equation [Eq. 2.7.2(36)] for film boiling outside horizontal tubes in stagnant pools.

To summarize, the evidence at the present time is that classical laminar film boiling occurs only over a relatively short distance (~5 cm) downstream of the dryout or rewet front. Beyond this region, vapor is released in large globular voids, which ensures a time-varying but thinner film. The coefficient becomes independent of distance and takes on a value considerably (approximately twice) higher than the laminar solution would indicate. In addition, there is evidence that film boiling heat transfer coefficients in down flow may be lower than for up flow, particularly under conditions where the down flow velocity is equal to the bubble rise velocity. Bjornard and Griffith [77] have therefore rewritten the post-CHF heat transfer correlations in terms of the drift flux model to account for the directional influence at low velocities.

(c) Heat transfer in the postdryout (liquid-deficient) region

In the film boiling region the flow pattern was that of an annular vapor film with a central liquid core. As the vapor quality is increased, the flow pattern changes to one in which liquid droplets are dispersed in a high-velocity vapor core. This latter drop flow pattern is characteristic of the postdryout or liquid-deficient region of heat transfer. Heat transfer coefficients in this region are considerably higher than in film boiling. This fact, coupled with the reduced critical heat flux values in the higher-quality region, means that the liquid-deficient region is often quite extensive.

I. Postdryout correlations

Three general approaches to estimating heat transfer rates in this region have been adopted:

1. Empirical correlations that make no attempt to take into account the physical processes occurring in postdryout heat transfer.
2. Correlations that recognize that a departure from thermodynamic equilibrium can occur and attempt to calculate the true vapor quality and vapor temperature. A conventional single-phase heat transfer correlation is then used to calculate the heating wall temperature.
3. Semitheoretical models where attempts have been made to look at and write down equations for the various individual hydrodynamic and heat transfer processes occurring and relate these to the heating wall temperature. One example of each of these approaches will be discussed briefly.

(i) Empirical correlations. Probably the most accurate of these purely empirical correlations is that proposed by Groeneveld [78]. This has the form

$$\mathrm{Nu}_g = a\left\{\mathrm{Re}_g\left[x + \frac{\rho_g}{\rho_\ell}(1-x)\right]\right\}^b \mathrm{Pr}_{g,w}^c Y^d \qquad (75)$$

where

$$Y = 1 - 0.1\left(\frac{\rho_\ell}{\rho_g} - 1\right)^{0.4}(1-x)^{0.4}$$

and the coefficients a, $b, c,$ and d are given in Table 8 together with the range of independent variables on which the correlations are based. A number of

© 1983 Hemisphere Publishing Corporation

Table 8 Empirical postdryout correlations

Groeneveld						
Geometry	a	b	c	d	No. of points	rms error
Tubes	1.09×10^{-3}	0.989	1.41	-1.15	438	11.5%
Annuli	5.20×10^{-2}	0.688	1.26	-1.06	266	6.9%
Tubes and annuli	3.27×10^{-3}	0.901	1.32	-1.50	704	12.4%

Range of data on which correlations are based

Geometry	Tube	Annulus
Flow direction	Vertical and horizontal	Vertical
D_ℓ, mm	2.5-25	1.5-6.3
p, MPa	6.8-21.5	3.4-10.0
$\dot{m}$, kg/m² s	700-S 300	800-4 100
x, fraction by weight	0.10-0.90	0.10-0.90
q, kW/m²	120-2 100	450-2250
Nu_g	95-1770	160-640
$Re_g[x + (1-x)\rho_g/\rho_\ell]$	6.6×10^4-1.3×10^6	1.0×10^5-3.9×10^5
Pr_w	0.88-2.21	0.91-1.22
Y	0.706-0.976	0.610-0.963

improvements in the Groeneveld correlations have been made by Slaughterback [79]. The use of the above correlations outside the range of variables for the respective geometries given in Table 8 is strongly discouraged.

(ii) Correlations allowing for departure from thermodynamic equilibrium. Wall temperatures in the postdryout region are bounded by two limiting situations.

1. Complete departure from equilibrium: The rate of heat transfer from the vapor phase to the entrained droplets is so slow that their presence is simply ignored and the vapor temperature $T_g(z)$ downstream of the dryout point is calculated on the basis that all the heat added to the fluid goes into superheating the vapor. The wall temperature $T_w(z)$ is calculated using a conventional heat transfer correlation of the Dittus-Boelter type.

2. Complete thermodynamic equilibrium: The rate of liquid droplets is so fast that the vapor-phase temperature $T_g(z)$ remains at the saturation temperature until the energy balance indicates that all the droplets have evaporated. The wall temperature $T_w(z)$ is again calculated using a conventional single-phase heat transfer correlation, this time with allowance made for the increasing vapor velocity resulting from droplet evaporation.

Postdryout heat transfer behavior tends toward situation 1 at low pressures and low velocity, whereas at high pressure (approaching the critical condition) and high flow rates (> 2-3 000 kg/m² s) situation 2 pertains.

Groeneveld and Delorme [SO] have expressed their correlation in terms of the difference between the equilibrium quality xfz) and the true non-equilibrium vapor quality $x^*(z)$. The difference $x(z) - x^*(z)$ is expressed as a function of a number of independent variables,

$$x(z) - x^*(z) = \exp(-\tan\psi) \tag{76}$$

where

$$\psi = a_1 \, Re_{tp}^{a_2} \sum_{i=0}^{i=2} b_i \left(\frac{p}{p_{cr}}\right)^i \sum_{i=0}^{i=2} c_i x_e(z)^i \tag{77}$$

$x_e(z)$ is the thermodynamic quality that can have a value greater than unity, but for conditions where xfz) is less than unity, xfz) = $x_e(z)$.

If $\psi < 0$, then $\psi = 0$

If $\psi > \frac{\pi}{2}$, then $\psi = \frac{\pi}{2}$

and

$$Re_{tp} = \frac{\dot{m}D}{\eta_g}\left[x(z) + \left(\frac{\rho_g}{\rho_\ell}\right)(1 - x(z))\right]$$

The coefficients to be inserted into Eq. (77), the ranges of the experimental data points used, and the accuracy of the correlation are given in Table 9.

The Groeneveld/Delorme [SO] method is a significant improvement over the empirical correlation discussed earlier but does appear to suffer from the disadvantage of discontinuities in the slope of the

© 1983 Hemisphere I blishing Corporation

quality versus length relationship at both the dryout point and the point where the thermodynamic quality xfz) = 1.

(iii) Semitheoretical models. A comprehensive theoretical model of heat transfer in the postdryout region must take into account the various paths by which heat is transferred from the heating surface to the bulk vapor phase. Six separate mechanisms can be identified:

1. Heat transfer from the surface to liquid droplets that impact with the wall (wet collisions)
2. Heat transfer from the surface to liquid droplets that enter the thermal boundary layer but that do not wet the surface (dry collisions)
3. Convective heat transfer from the surface to the bulk vapor
4. Convective heat transfer from the bulk vapor to suspended droplets in the vapor core
5. Radiation heat transfer from the surface to the liquid droplets
6. Radiation heat transfer from the surface to the bulk vapor

One of the first semitheoretical models proposed was that of Bennett et al. [81] and is a one-dimensional model starting from known equilibrium conditions at the dryout point. It is assumed that there is negligible pressure drop along the channel, that the wall surface temperature increases to such an extent that the droplets no longer wet the surface, and that the heat transfer coefficient between the wall and the fluid is given by one of the well-known single-phase relationships. These assumptions mean that mechanisms 1 and 2 above were not considered.

Table 9 Groeneveld and Delorme correlation of nonequilibrium vapor quality

Coefficient	Value
a_1	0.138 64
a_2	0.203 1
a_3	0.200 06
a_4	-0.092 32
b_0	1.307 2
b_1	-1.083 3
b_2	0.845 5

Range of data for correlation	
Water	
p:	4.1-20.5 MPa
$\dot{m}$:	270-S 150 kg/m² s
$\dot{q}$:	150-2 700 kW/m²
x_E	0.1-1.50
T_w	400-845°C
No. of points:	1402

The position of the dryout point must be known or calculated. At this point it is assumed that liquid and vapor are in equilibrium and therefore the quality $x(z_{cr})$ is known and the vapor is at the saturation temperature. To obtain the bulk vapor temperature downstream of the dryout point, four simultaneous differential equations are solved in a stepwise manner using the Runge-Kutta method. The first of these equations is a mass balance, which assumes that the number of droplets passing through unit cross section per unit time (N) does not change:

$$\frac{dx}{dz} = -\frac{NW?}{2\dot{m}} d^2 \frac{dd}{dz} \tag{78}$$

where

$$N = \frac{6\dot{m}(1 - x(z_{cr}))}{\pi d_{cr}^3 \rho_\ell}$$

and

x = vapor quality (vapor mass flow/total mass flow)
d = droplet diameter

The second equation is a heat balance giving the bulk vapor temperature $T_g(z)$:

$$\frac{dT_g}{dz} = \frac{\dot{q}\pi D - (A\dot{m}\Delta h_v dx/dz)}{A\dot{m}xc_{pg}} \tag{79}$$

The third equation describes the acceleration of the droplets in the vapor stream using Ingebo s[82] drag coefficient:

$$\frac{du_d}{dz} = \frac{K_1(u_g - u_d)^{1.16} - g_n(1 - \rho_g/\rho_\ell)}{u_d} \tag{80}$$

where u_d is the droplet velocity, u_g is the vapor velocity, and

$$K_1 = 20.25\left(\frac{\eta_g^{0.84}\rho_g^{0.16}}{\rho_\ell d^{1.84}}\right) \tag{81}$$

Equation (81) describes the evaporation of the droplets using Ryley s[83] method:

$$\frac{dd}{dz} = \frac{2}{d}\frac{dr^2}{dt}\frac{1}{u_d} \tag{82}$$

$$\frac{dr^2}{dt} = -\frac{2FMK_g(p_g - p_\infty)}{\rho_\ell R T_g} = -\frac{2\lambda_g F(T_g - T_{sat})}{\rho_\ell \Delta h_v} \tag{83}$$

where p_g = pressure in the droplet
T_{sat} = saturation temperature at p_g
$\tilde{R}$ = universal gas constant
K_g = self-diffusion coefficient in the vapor = $M\lambda_g(\gamma - 1)/\rho_g\tilde{R}$
$r = d/2$

© 1983 Hemisphere I blishing Corporation

F = ventilation factor

$$= 1 + 0.276\left[\frac{\rho_g(u_g - u_d)d}{\eta_g}\right]^{0.5}\left(\frac{\eta_g}{K_g\rho_g}\right)^{1/3} \qquad (84)$$

Bennett et al. [81] compared estimates of surface temperature made using this method with experimental data in the liquid-deficient region for water evaporating at 69 bar in a vertical, 5.8 m long X 12.6 mm ID tube. Figure 32 shows this comparison for three different values of mass velocity. The equations proposed by Heineman [84] were taken for the heat transfer coefficient to superheated steam. It was found that a reasonable fit was obtained with an assumed droplet size at the dryout point (d_{cr}) of about 0.3 mm.

Other, more recent models have been proposed by Iloeje et al. [75] and by Chen et al. [85]. Because of the way in which these models are formulated, they should apply equally well to both the steam-water system and to other fluid systems.

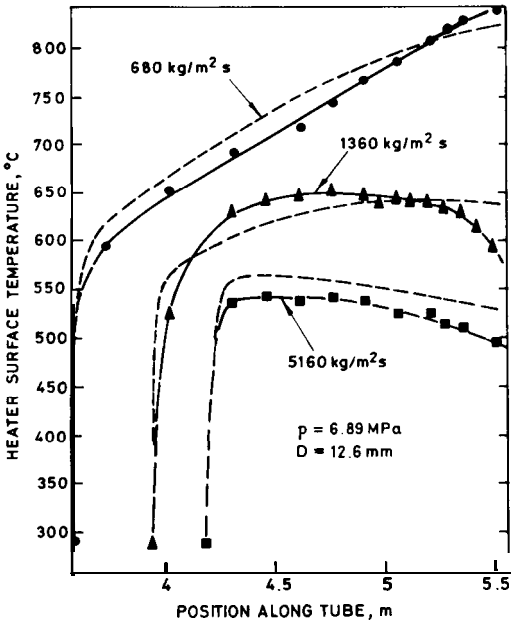

Figure 32 Experimental and calculated temperature profiles for heat transfer to steam-water mixtures in the liquid-deficient condition. From Bennett et al. [81].

Nomenclature for Section 2.7.3 appears at the end of Section 2.7.8.

REFERENCES FOR SECTION 2.7.3

1. Bergles, A. E., and Rohsenow, W. M., The Determination of Forced Convection Surface Boiling Heat Transfer, *J. Heat Transfer,* vol. 86C, p. 365, 1964.
2. Davis, E. J., and Anderson, G. H., The Incipience of Nucleate Boiling in Forced Convection Flow, *AIChE J.,* vol. 12, no. 4, pp. 774-780, 1966.
3. Frost, W., and Dzakowic, G. S., An Extension of the Method of Predicting Incipient Boiling on Commercially Finished Surfaces, ASME/AIChE Heat Transfer Conf., Seattle, Paper 67-HT-61, 1967.
4. Rohsenow, W. M., A Method of Correlating Heat Transfer Data for Surface Boiling of Liquids, *Trans. ASME, vol. 74,* p. 969, 1952.
5. Rohsenow, W. M., and Clark, J. A., Heat Transfer and Pressure Drop Data for High Heat Flux Densities to Water at High Sub-critical Pressure, *in 1951 Heat Transfer and Fluid Mechanics Institute,* Stanford University Press, Stanford, Calif., 1951.
6. Kreith, F., and Summerfield, M., Heat Transfer to Water and High Flux Densities with and without Surface Boiling, *Trans. ASME,* vol. 71, no. 7, pp. 805-815, 1949.
7. Piret, E. L., and Isbin, H. S., Two-Phase Heat Transfer in Natural Circulation Evaporators, *Chem. Eng. Prog. Symp. Ser.,* vol. 50, no. 6, p. 305, 1953.
8. Jens, W. H., and Lottes, P. A., Analysis of Heat Transfer Burnout, Pressure Drop and Density Data for High Pressure Water, Rept. ANL-4627, May 1951.
9. Thorn, J. R. S., Walker, W. M., Fallon, T. A., and Reising, G. F. S., Boiling in Subcooled Water During Flow up Heated Tubes or Annuli, Symp. Boiling Heat Transfer Steam Generating Units Heat Exchangers, Manchester, September 15-16, 1965, Institution of Mechanical Engineers, London, Paper 6.
10. Rohsenow, W. M., Heat Transfer with Evaporation, *Heat Transfer,* Symp. University of Michigan, 1952, University of Michigan Press, pp. 101-150, 1952.
11. Bowring, R. W., Physical Model Based on Bubble Detachment and Calculation of Steam Voidage in the Subcooled Region of a Heated Channel, OECD Halden Reactor Project Rept. HPR-10, 1962.
12. *Collier,* J. G., *Convective Boiling and Condensation,* McGraw-Hill, London, 1972.
13. Levy, S., Forced Convection Subcooled Boiling Prediction of Vapour Volumetric Fraction, *Znt. J. Heat Mass Transfer,* vol. 10, pp. 951-965, 1967.
14. Saha, P., and Zuber, N., Point of Net Vapour Generation and Vapour Void Fraction in Subcooled Boiling, *Proc. 5th Znt. Heat Transfer Conf., Tokyo, September* 3-7, 1974, Paper B4.7, 1974.
15. Hewitt, G. F., Kearsey, H. A., Lacey, P. M. C., and Pulling, D. J., Burnout and Nucleation in Climbing Film Flow, Rept. AERE-R4374, 1963.
16. Dengler, C. E., and Addoms, J. N., Heat Transfer Mechanism for Vaporization of Water in a Vertical Tube, *Chem. Eng. Prog. Symp. Ser.,* vol. 52, no. 18, pp. 95-103, 1956.

© 1983 Hemisphere F blishing Corporation

17. Guerrieri, S. A., and Talty, R. D., A Study of Heat Transfer to Organic Liquids in Single Tube Natural Circulation Vertical Tube Boilers, *Chem. Eng. Prog. Symp. Ser.,* vol. 52, no. 18, pp. 69–77, 1956.
18. Bennett, J. A. R., Collier, J. G., Pratt, H. R. C., and Thornton, J. D., Heat Transfer to Two-Phase Gas-Liquid Systems, pt I, Steam-Water Mixtures in the Liquid Dispersed Region in an Annulus, Trans. *Inst. Chem. Eng.,* vol. 39, p. 113, 1961; also Rept. AERE-R-3519, 1959.
19. Schrock, V. E., and Grossman, L. M., Forced Convection Boiling in Tubes, *Nuclear Sci. Eng.,* vol. 12, pp. 474–480, 1962.
20. Schrock, V. E., and Grossman, L. M., Forced Convection Boiling Studies, Forced Convection Vaporization Project, Final Rept. 73307-UCZ21821, November 1952, University of California, Berkeley, Calif., 1959.
21. Wright, R. M., Downward Forced Convection Boiling of Water in Uniformly Heated Tubes, Rept. UCRL-9744, 1961.
22. Collier, J. G., and Pulling, D. J., Heat Transfer to Two-Phase Gas-Liquid Systems, pt. II, Further Data on Steam/Water Mixtures in the Liquid Dispersed Region in an Annulus, Rept. AERE-R3809, 1962.
23. Chen, J. C., Correlation for Boiling Heat Transfer to Saturated Liquids in Convective Flow, *Ind. Eng. Chem. Process Des. Dev.,* vol. 5, p. 322, 1966.
24. Fair, J. R., What You Need to Design Thermosyphon Reboilers, *Pet. Refiner,* vol. 39, no. 2, pp. 105-124, 1960.
25. Forster, H. K., and Zuber, N., Dynamics of Vapour Bubbles and Boiling Heat Transfer, *AIChE J.,* vol. 1, no. 4, pp. 531-535, 1955.
26. Ananiev, E. P., Boyko, L. D., and Kruzhilin, G. N., Heat Transfer in the Presence of Steam Condensation in a Horizontal Tube, *International Developments in Heat Transfer,* Int. Heat Transfer Conf., Boulder, Colo., pt. II, Paper 34, pp. 290-295, August 1961.
27. Thompson, B., and Macbeth, R. V., Boiling Water Heat Transfer-Burnout in Uniformly Heated Round Tubes: A Compilation of World Data with Accurate Correlations, Rept. AEEW-R-356, 1964.
28. Tabular Data for Calculating Burnout When Boiling Water in Uniformly Heated Round Tubes, Working Party of the Heat and Mass Transfer Section of the Scientific Council of the U.S.S.R. Academy of Sciences, *Teploenergetika, vol. 23,* no. 9, pp. 90-92, 1976; *Thermal Eng.,* pp. 77-79, September 1971.
29. Bowring, R. W., A Simple but Accurate Round Tube Uniform Heat Flux, Dryout Correlation over the Pressure Range 0.7-17 MN/m^2 (100-2 500 psia), Rept. AEEW-R789, 1972.
30. Barnett, P. G., The Prediction of Burnout in Non-uniformly Heated Rod Clusters from Burnout Data for Uniformly Heated Round Tubes, Rept. AEEW-R362, 1964.
31. Lee, D. H., and Obertelli, J. D., An Experimental Investigation of Forced Convection Burnout in High Pressure Water-pt. II, Rept. AEEW-R309, 1963.
32. Swenson, H. S., Carver, J. R., and Kakarala, C. R., The Influence of Axial Heat Flux Distribution on the Departure from Nucleate Boiling in a Water-cooled Tube, ASME Winter Amm. Meet., New York, November 1962, Paper 62-WA-297, 1962.
33. Tong, L. S., Currin, H. B., Larsen, P. S., and Smith, 0. G., Influence of Axially Non-uniform Heat Flux on DNB, *Chem. Eng.* Prog. *Symp. Ser.,* vol. 62, no. 64, pp. 35-40, 1966; also Rept. WCAP-2767, 1965.
34. Smith, 0. G., Tong, L. S., and Rohner, W. M., Burnout in Steam-Water Flows with Axially Non-uniform Heat Flux, ASME Paper 65-WA/HT-33, 1965.
35. Tong, L. S., Prediction of Departure from Nucleate Boiling for an Axially Non-uniform Heat Flux Distribution, Rept. WCAP-5584, *rev. 1,* 1966; *see* also *J. Nucl. Energy,* vol. 21, no. 3, pp. 241-248, 1967.
36. Lee, D. H., An Experimental Investigation of Forced Convection Burnout in High Pressure Water-pt. IV, Rept. AEEW-R479, 1966.
37. Macbeth, R. V., Burnout Analysis, pt. 4, Application of a Local Condition Hypothesis to World Data for Uniformly Heated Round Tubes and Rectangular Channels, Rept. AEEW-R267, 1963.
38. Becker, K. M., and Hernborg, G., Measurements of Burnout Conditions for Flow of Boiling Water in an Annulus, ASME/AIChE 6th Natl. Heat Transfer Conf., Boston, Paper 63-HT-25, August 1963.
39. Janssen, E., Levy, S., and Kervinen, J. A., Investigations of Burnout in an Internally Heated Annulus Cooled by Water at 600 to 1400 psia, ASME Winter Annu. Meet., Philadelphia, Paper 63-WA-149, November, 1963; see also Rept. GEAP 3899, 1963.
40. Barnett, P. G. A Correlation of Burnout Data for Uniformly Heated Annuli and Its Use for Predicting Burnout in Uniformly Heated Rod Bundles, Rept. AEEW-R-463, 1966.
41. Macbeth, R. V., Burnout Analysis-pt. 5, Examination of Published World Data for Rod Bundles, Rept. AEEW-R358, 1964.
42. Barnett, P. G., A Comparison of the Accuracy of Some Correlations for Burnout in Annuli and Rod Bundles, Rept. AEEW-R558, 1968.
43. Bowring, R. W., A New Mixed Flow Cluster Dryout Correlation for Pressures in the Range 0.6-15.5 MN/m* (90-2 250 psia)–for Use In a Transient Blowdown Code, Conf. Heat Fluid Flow Water Reactor Safety, September 13-15, 1977, Institution of Mechanical Engineers, Manchester, Paper C217/77.
44. Weisman, J., and Bowring, R. W., Methods for Detailed Thermal and Hydraulic Analysis of Water-cooled Reactors, *Nucl. Sci. Eng.,* vol. 57, pp. 255-276, 1975.
45. Tong, L. S., and Hewitt, G. F., Overall Viewpoint of Flow Boiling CHF Mechanisms, ASME Paper 72-HT-54, 1972.
46. Fiori, M. P., and Bergles, A. E., Model of Critical Heat Flux in Subcooled Flow Boiling, in *Heat Transfer* 1970, vol. 6, Paper B6.3, Elsevier, Amsterdam, 1970.
47. Kirby, G. J., Staniforth, R., and Kinneir, J. H., A Visual Study of Forced Convection Boiling, pt. I, Rept. AEEW-R281, 1965, and pt. II, Rept. AEEW-R506, 1967.
48. Kutateladze, S. S., and Lenont ev, A. I., Some Applications of the Asymptotic Theory of the Turbulent Boundary Layer, *Proc. 3d Int. Heat Transfer Conf., Chicago, August 7-12,* vol. 3, pp. 1-6, 1966.
49. Tong, L. S., Boundary Layer Analysis of the Flow Boiling Crisis, *Int. J. Heat Mass Transfer,* vol. 11, no. 7, pp. 1208-1211, 1968.

© 1983 Hemisphere Publishing Corporation

50. Semeria, R., and Hewitt, G. F., Aspects of Heat Transfer in Two-Phase One-Component Flows, Seminar Recent Developments Heat Exchangers, Int. Centre Heat Mass Transfer, Trogir, Yugoslavia, Lecture Session H53, September 1972.
51. Hewitt, G. F., Kearsey, H. A., Lacey, P. M. C., and Pulling, D. J., Burnout and Nucleation in Climbing Film Flow, Rept. AERE-R4374, 1963.
52. Hewitt, G. F., Kearsey, H. A., Lacey, P. M. C., and Pulling, D. J., Burnout and Film Flow in the Evaporation of Water in Tubes, Rept. AERE-R4864, 1965.
53. Hewitt, G. F., Kearsey, H. A., Keeys, R. K. F., and Pulling, D. J., Studies of Burnout in Boiling Heat Transfer to Water in Round Tubes with Non-uniform Heating, Rept. AERE-R5076, 1966.
54. Hutchinson, P., and Whalley, P. B., A Possible Characterization of Entrainment in Annular Flow, ***Chem. Eng. Sci.,*** vol. 28, pp. 974-975, 1973.
55. Hewitt, G. F., and Hall-Taylor, ***N., Annular Two-Phase*** Flow, Pergamon, Oxford, 1970.
56. Wallis, ***G.*** B., ***One Dimensional Two-Phase Flow,*** McGraw-Hill, New York, 1969.
57. Whalley, P. B., Hutchinson, P., and Hewitt, G. F., The Calculation of Critical Heat Flux in Forced Convection Boiling, ***Proc. 5th Int. Heat Transfer Conf., Tokyo, September*** 3-7, 1974, Paper B6.11, 1974.
58. Whalley, P. B., Hutchinson, P., and Hewitt, G. F., Prediction of Annular Flow Parameters for Transient Conditions and for Complex Geometries, European Two-Phase Flow Group Meet., Haifa, 1975; see also Rept. AERE-M2661, 1974.
59. Jensen, A., and Mannov, G., Measurements of Burnout, Film Flow, Film Thickness and Pressure Drop in a Concentric Annulus 3 500 X 26 X 17 mm with Heated Rod and Tube, European Two-Phase Flow Group Meet., Harwell, Paper A.5, June 1974.
60. Whalley, P. B., The Calculation of Dryout in a Rod Bundle, Rept. AERE-R8319, 1976.
61. Whalley, P. B., The Calculation of Dryout in a Rod Bundle-A Comparison of Experimental and Calculated Results, Rept. AERE-R8977, 1978.
62. Nejat, Z., Maximum Heat Flux for Countercurrent Two Phase Flow in a Closed End Vertical Tube, ***Proc. 6th Znt. Heat Transfer Conf., Toronto, August 7-11, 1978,*** vol. 1, pp. 441–444, 1978.
63. Stevens, G. F., Elliott, D. F., and Wood, R. W., An Experimental Investigation into Forced Convection Burnout in Freon, with Reference to Burnout in Water, Rept. AEEW-R321, 1964.
64. Stevens, G. F., Elliott, D. F., and Wood, R. W., An Experimental Comparison Between Forced Convection Burnout in Freon 12 Flowing Vertically Upwards Through Uniformly and Non-uniformly Heated Round Tubes, Rept. AEEW-R426, 1965.
65. Barnett, P. G., The Scaling of Forced Convection Boiling Heat Transfer, Rept. AEEW-R134, 1963.
66. Bamett, P. G., An Experimental Investigation to Determine the Scaling Laws of Forced Convection Boiling Heat Transfer, pt. I, Rept. AEEW-R363, 1964.
67. Bamett, P. G., and Wood, R. W., An Experimental Investigation to Determine the Scaling Laws of Forced Convection Boiling Heat Transfer, pt. II, Rept. AEEW-R443, 1965.
68. Stevens, G. F., and Kirby, G. J., A Quantitative Comparison Between Burnout Data for Water at 1 000 lb/in² (abs) and Freon 12 at 155 lb/in in Uniformly Heated Round Tubes, Rept. AEEW-R327, 1964.
69. Stevens, G. F., and Wood, R. W., A Comparison Between Burnout Data for 19 Rod-Cluster Test Sections Cooled by Freon 12 at 155 lb/in² (abs) and by Water at 1 000 lb/in in Vertical Upflow, Rept. AEEW-R468, 1966.
70. Ahmad, S. Y., Fluid to Fluid Modelling of Critical Heat Flux: A Compensated Distortion Model, ***Int. J. Heat Mass Transfer,*** vol. 16, pp. 641–661, 1973.
71. Hauptmann, E. G., Lee, V., and McAdam, D., Two-Phase Fluid Modelling of the Critical Heat Flux, ***Proc. Int. Meet. Reactor Heat Transfer, Karlsruhe,*** October 9-11, 1973, pp. 557-576.
72. Whalley, P. B., Personal communication, 1978.
73. Groeneveld, D. C., and Fung, K. K., Forced Convection Transition Boiling-A Review of Literature and Comparison of Prediction Methods, Rept. AECL-5543, 1976.
74. Tong, L. S., and Young, J. D., A Phenomenological Transition and Film Boiling Heat Transfer Correlation, ***Proc. 5th Int. Heat Transfer Conf., Tokyo, September 3-7,*** vol. 4, 1974.
75. Iloeje, 0. C., Plummer, D. N., Rohsenow, W. M., and Griffith, P., A Study of Wall Rewet and Heat Transfer in Dispersed Vertical Flow, Massachusetts Institute of Technology Department of Mechanical Engineering Rept. 7278-92, September 1974.
76. Bailey, N. A., Film Boiling on Submerged Vertical Cylinders, Rept. AEEW-M1051, 1971.
77. Bjornard, T. A., and Griffith, P., PWR Blowdown Heat Transfer, ASME Symp. Thermal Hydraulic Aspects Nuclear Reactor Safety, Atlanta, Ga., November 27-December ***2,*** 1977, vol. 1, ***Light Water Reactors,*** pp. 17-11, ASME, New York.
78. Groeneveld, D. C., Post-Dryout Heat Transfer at Reactor Operating Conditions, Natl. Topical Meet. Water Reactor Safety, Salt Lake City, Utah, March 26-28, 1973, ANS Paper AECL-4513.
79. Slaughterback, D. C., Ybarrondo, L. J., and Obenchain, C. F., Flow Film Boiling Heat Transfer Correlations-Parametric Study with Data Comparisons, ASME/AIChE Heat Transfer Conf., Atlanta, Ga., August 1973. ASME Preprint No. 73-HT-50.
80. Groeneveld, D. C., and Delorme, G. G. J., Prediction of the Thermal Non-equilibrium in the Postdryout Regime, ***Nucl. Eng. Design,*** vol. 36, pp. 17-26, 1976.
81. Bennett, A. W., Hewitt, G. F., Kearsey, H. A., and Keeys, R. K. F., Heat Transfer to Steam-Water Mixtures Flowing in Uniformly Heated Tubes in Which the Critical Heat Flux Has Been Exceeded, Thermodynamics and Fluid Mechanics Conv., Bristol, March 27-29, 1968, IME Paper 27; see also Rept. AERE-R5373, 1967.
82. lngebo, R. D., Drag Coefficients for Droplets and Solid Spheres and Clouds Accelerating in Air Streams, Rept. NACA-TN 3762, 1956.
83. Ryley, D. J., The Evaporation of Small Liquid Drops with Special Reference to Water Drops in Steam, ***J. Liverpool Eng. Soc.,*** vol. 7, no. 1, p. 1, 1961/1962.
84. Heineman, J. B., An Experimental Investigation of Heat Transfer to Superheated Steam in Round and Rectangular Channels, Rept. ANL-6213, 1960.

© 1983 Hemisphere Publishing Corporation

85. Chen, J. C., Sundaram, R. K., and Ozkayrak, F. T., A Phenomenological Correlation for Post-CHF Heat Transfer, Lehigh University Rept. NUREG-0237, 1977.
86. Noel, M. B. Experimental Investigation of Heat-Transfer Characteristics of Hydrazine and a Mixture of 90% Hydrazine and 10% Ethylenediamine, JPL Tech. Rept. 32-109, June 1961.
87. Hines, W. S., Forced Convection and Peak Nucleate Boiling Heat Transfer Characteristics for Hydrazine Flowing Turbulently in a Round Tube at Pressures to 1 000 psia, Rocketdyne Rept. R2059, August 1959.
88. Noel, M. B. Experimental Investigation of the Forced Convection and Nucleate Boiling Heat Transfer Characteristics of Liquid Ammonia, JPL Tech. Rept. 32-125, July 1961.
89. Dimmock, T. H. Heat Transfer Properties of Anhydrous Ammonia, Reaction Motors Rept. RMI-124-S1, July 1957.
90. Core, T. C., and Sato, K. Determination of Burnout Limits of Polyphenyl Coolants, Rept. IDO-28007, 1958.
91. Robinson, J. M., and Lurie, H., Critical Heat Flux for Some Polyphenyl Coolants, 55th Annu. Meet., Chicago, December 1962, AIChE Preprint 156.
92. Birdseye, D. E., Experimental Investigation of Heat Transfer Characteristics of Liquid Nitrogen Tetroxide, JPL Tech. Rept. 32-37, October 1962.
93. Gambill, W. R., and Bundy, R. D., High Flux Heat Transfer Characteristics of Pure Ethylene Glycol, AIChE Natl. Meet., Los Angeles, Calif., Paper 2, February 1962.
94. Povarnin, P. I., Critical Boiling Point in the Flow of 96% Ethyl Alcohol Under Low Heating Conditions, *Teploenergetihz,* vol. 9, no. 12, pp. 57-63, 1962; Rept. ORNL-tr-108, 1964.
95. Lewis, J. P., et al., Boiling Heat Transfer to Liquid Hydrogen and Nitrogen in Forced Flow, Rept. NASA-TN-D-1314, 1962.
96. Bamett, P. G., and Wood, R. W., An Experimental Investigation to Determine the Scaling Laws of Forced Convection Boiling Heat Transfer, pt. 2, Rept. AEEW-R443, 1965.
97. Hoffman, H. W., and Krakoviak, A. I., Convective Boiling with Liquid Potassium, 1964 Heat Transfer Fluid Mechanics Inst., Stanford University, Stanford, Calif., 1964.
98. Lurie, H., Atomics International Progress Repts. NAA-SR-10501 and NAA-SR-10850, 1964; see also report to 1966 Int. Heat Transfer Conf., Chicago, Paper 160.
99. Aladyev, I. T., et al., Heat Transfer to Boiling Potassium in Tubes, 3d Int. Heat Transfer Conf., Chicago, 1966, vol. III, no. 93, pp. 123-128, 1966.
100. Tippets, F., Alkali Metals Boiling and Condensing Investigations, Rept. QPRs 2-12, Contract NAS 3-2528, General Electric Co., April 1963.
101. Keeys, R. K. F., Ralph, J. C., and Roberts, D. N., Post Burnout Heat Transfer in High Pressure Steam-Water Mixtures in a Tube with Cosine Heat Flux Distribution, Prog. *Heat Mass Transfer, vol. 6,* pp. 99-118, 1971.

© 1983 Hemisphere publishing Corporation

2.7.4

Convective boiling inside horizontal tubes

J. G. Collier

■ Horizontal tubes are often used in waste heat boilers, refrigerant evaporators, and a number of other types of heat exchange equipment. For the sake of compactness, the horizontal sections are often relatively short in length and connected by return bends to form so-called serpentines; alternatively, the tube may be formed into a helical coil. It is therefore convenient to consider the influence of bends and coils on heat transfer rates in this section.

Heat transfer rates in horizontal tubes differ from those in vertical tubes to the extent that the gravitational forces cause an asymmetric flow pattern. A useful review has been given by Butterworth and Robertson [1] . Because the differences in behavior from that in a vertical tube are associated directly with the occurrence of dry portions of the tube perimeter, we shall consider this aspect first.

A. Dryout in horizontal tubes, bends, and coils

Dryout in a horizontal tube differs from that in a vertical tube in two ways:

1. Stratification of the flow can occur at low velocities for both low-quality and subcooled conditions. Such conditions can lead to overheating of steam boiler tubes at quite modest heat fluxes.

2. Dryout of the tube at high vapor qualities occurs over a relatively long tube length, starting at the top of the tube where the liquid film thickness and flow rate are lowest and ending up with the final evaporation of the rivulet running along the bottom of the tube. Under these conditions the vapor in the upper parts of the tube may become superheated before dryout occurs at the bottom of the tube.

Styrikovich and Miropolskii [2] reported the effects of stratification of a high-pressure steam-water mixture in a horizontal pipe. These caused wide temperature differences between the top and bottom of the boiler tube. Experiments were carried out on a single, 7.5-m, 56-mm-ID tube at pressures between 10 and 220 bar with heat fluxes in the range 22-135 kW/m^2 and inlet velocities between 0.24 and 1 m/s. There was a critical two-phase velocity v, below which stratification occurred and above which it did not. This critical velocity v increased with heat flux up to 60 kW/m^2 and decreased with increase in pressure (Fig. 1). An investigation into the effect of the angle of slope θ showed that overheating occurred only if the angle of slope was less than 9.5 to the horizontal.

Using an alcohol-water analog for steam-water flow, Gardner and Kubie [3] established the following expression for the critical velocity v:

$$v = 2.57 \left\{ \frac{[\sigma g_n \cos\theta(\rho_\ell - \rho_g)]^{0.5}}{\rho_\ell f K^2} \right\}^{0.5} \quad (1)$$

Here θ is the angle of inclination of the tube to the horizontal and cos θ is introduced to give the appropriate component of the gravitational field normal to the interface; f is the Fanning friction factor; and K is an empirical constant found by Gardner and Kubie [3] to be 2.17. Substituting for f and K leads to the following equation for v:

$$v = 6.67 \left\{ \frac{D^{0.2}[\sigma g_n(\rho_\ell - \rho_g)]^{0.5}}{\rho_\ell^{0.8}\eta_\ell^{0.2}} \right\}^{0.555} \quad (2)$$

© 1983 Hemisphere Publishing Corporation

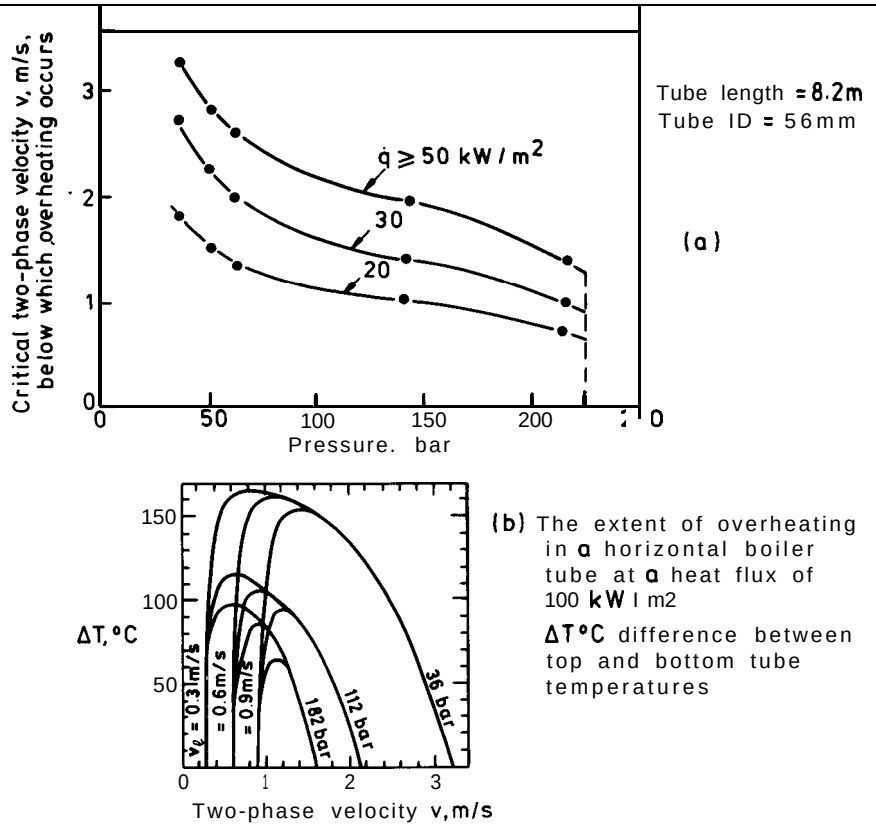

Figure 1 Stratification and overheating of horizontal boiler tubes. From Styrikovich and Miropolskii [2].

Table 1 gives the values of v calculated from Eq. (2) for steam-water flows over a range of pressures and tube diameters. Excellent agreement is seen with the data in Fig. 1, and Eq. (2) is recommended as giving the minimum single or two-phase velocity below which stratification will occur in a horizontal tube.

At higher qualities a dryout condition analogous to that for vertical flow is seen. However, the heat flux at which it occurs in horizontal tubes can be much lower than in vertical tubes, as illustrated by the results of Robertson [4] in Fig. 2. Although no general rule is available to relate the dryout heat fluxes in horizontal and vertical tubes, it is possible to state that the difference between the two situations becomes less as the tube diameter decreases, the phase density difference becomes less (pressure becomes greater), and the mass velocity increases.

Another factor influencing dryout in horizontal tubes is the 180 return bend. Work by Lis and Strickland [5] has shown that the bend produces severe flow disturbances over a wide range of operating conditions. The disturbances cause large amplitude oscillations of wall temperature at up to 70 diameters downstream of the bend. At low heat fluxes (≅100 kW/m²), these disturbances appear to reach a maximum in the wavy or low-velocity annular-flow region (i.e., void fractions in the range 0.6-0.65) and for water are confined to low mass velocities, below 1 200-l 000 kg/m² s.

Stratification may also occur in vertical bends and in helical coils (Fig. 3). For the case of a vertical bend, Bailey [6] showed that the gravitational force maintaining stratified flow is supplemented by centrifugal forces so that $g_n \cos\theta$ in Eq. (1) is replaced by $g_n + v^2/r$. Incorporating this modification into Eq. (2),

$$v = 6.67 \left\{ \frac{D^{0.2}\,[\sigma(g_n + v^2/r)(\rho_\ell - \rho_g)]^{0.5}}{\rho_\ell^{0.8}\,\eta_\ell^{0.2}} \right\}^{0.555} \qquad (3)$$

The derivation of Eq. (3) neglects the secondary flow that is known to exist in both bends and coils (see Sec. 2.2.2). This secondary flow tends to enhance the

Table 1 Values of critical velocity v (m/s) to prevent stratification [Eq. (2)] for steam-water flow in horizontal tubes

	p, bar					
D, mm	33.5	64.2	112.9	146	165	186.7
20	2.71	2.47	2.11	1.82	1.63	1.37
40	2.92	2.67	2.28	1.97	1.77	1.48
60	3.06	2.80	2.38	2.06	1.85	1.55

© 1983 Hemisphere Publishing Corporation

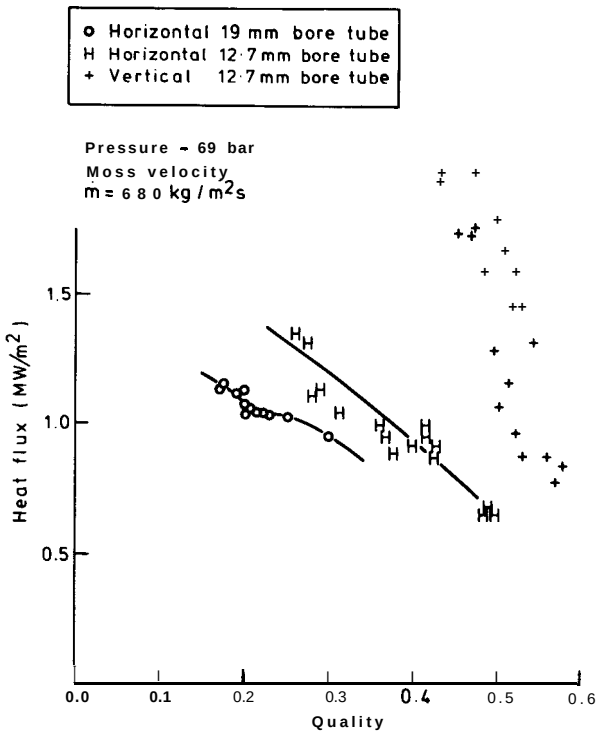

Figure 2 Dryout heat flux versus quality for vertical and horizontal tubes. From Robertson [4].

stratification and increase the value of v. For the example examined experimentally by Bailey, a tube of 19 mm ID with a bend radius (r) of 0.45 m, the constant in Eq. (3) is increased to 7.48 and the critical velocity v by 17-20%. Experimental results confirmed that the secondary flow effect should be taken into account at low void fractions ($\epsilon_g < 0.5$) but was not appropriate for high void fractions ($\epsilon_g > 0.8$).

For the case of a helical coil, since the gravitational and centrifugal forces do not act in the same direction, so $g_n \cos\theta$ in Eq. (1) must be replaced by $[(g_n \cos\theta)^2 + (v^2/r)^2]^{0.5}$, the resultant force, where θ now is the angle of inclination of the coiled tube.

Miropolskii et al. [7,8], Carver et al. [9], and Ruffell [10] have reported critical heat flux data for coiled tubes. Miropolskii et al. [7,8] found that in subcooled regions the critical heat flux was reduced from that in a straight vertical tube because of stratification of the type discussed earlier. All three sets of workers agree that at higher vapor qualities the transition to the liquid-deficient condition in the helical coil occurs at a higher average vapor quality than the corresponding condition in a straight vertical tube (Fig. 4). In most cases the vapor quality for the transition at all parts of the tube circumference is higher than the straight-tube value. Dryout occurs first at locations on the tube wall between the point closest to the center of curvature (D) and the top of the tube (A). At low pressures it is possible for the centrifugal forces acting on the vapor phase to be higher than on the liquid phase because of the differing phase velocities, i.e., $(\rho_g u_g^2/r) > \rho_\ell u_\ell^2/r$. The liquid can then flow on the inside rather than on the outside parts of the coil. Experiments at low pressure with boiling in a helical coil reported by Owhadi and Bell [11] support this picture, and dryout occurs first near 100% quality at the top (A) and bottom positions (C) around the tube circumference rather than at the point nearest the center of gravity.

Ruffell [10] has given a correlation that may be used to estimate the dryout quality for the circumferential positions nearest (D) and farthest (B) from the center of curvature for steam-water flow over a limited range of conditions, namely, pressures between 60 and 180 bar, mass fluxes $(\dot{m})$ between 300 and 1 800 kg/m² s, tube diameter (D) between 10.7 and 18.6 mm, and coil-to-tube diameter ratios (d/D) between 6.25 and 185.

The steam quality at dryout for the point on the tube circumference closest to the center of curvature of the coil (D) is given by

$$x_{cr,D} = 1 - 0.53 \frac{\rho_g}{\rho_\ell} \frac{d/100D}{(\dot{m}/10^3)^{1.5}} \left(\frac{\dot{q}}{100}\right)^n \qquad (4)$$

where

$$n = 0.75 \left(\frac{\dot{m}}{10^3}\right)^{0.5}$$

The steam quality at dryout for the point on the tube circumference farthest from the center of curvature of the coil (D) is given by

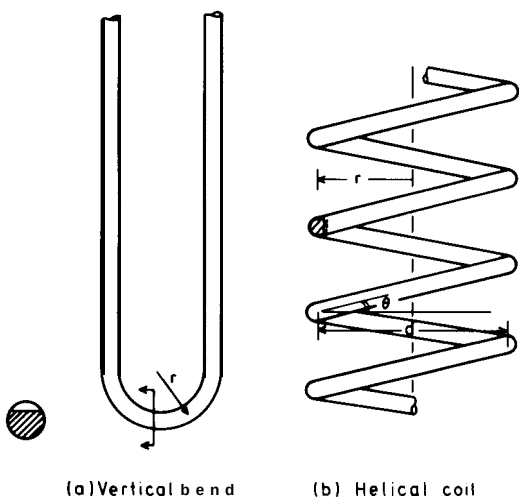

Figure 3 Stratification in bends and coils.

© 1983 Hemisphere Publishing Corporation

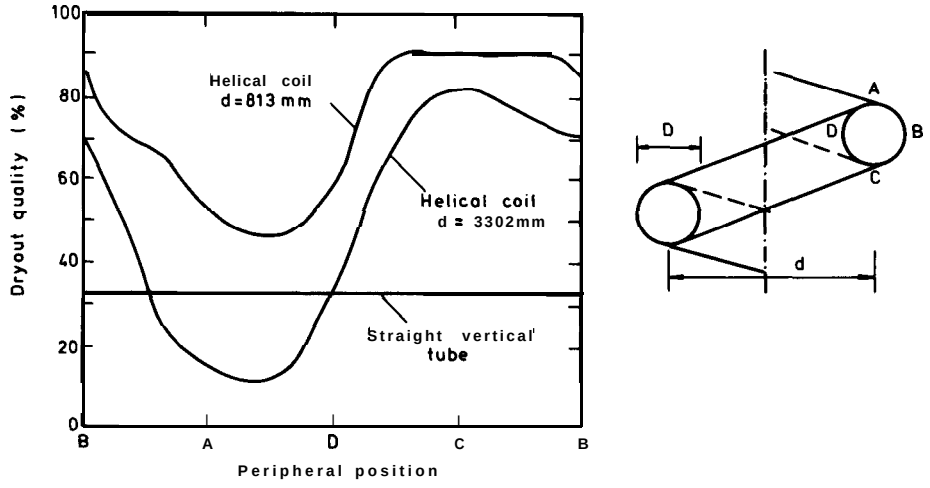

Figure 4 **Dryout** in a helical coil. Fluid: steam-water; pressure: 179 bar; core diameter d = 813 and 3 302 mm; tube diameter D = 10.7 mm; mass flux $\dot{m}$ = 678 kg/m² s; heat flux $\dot{q}$ = 394 kW/m² . From Carver, J. R., Kakarala, C. R., and Slotnik, J. S., Heat Transfer in Coiled Tubes with Two-Phase Flow, Babcock and Wilcox Rept. 4438, 1964.

$$x_{cr,B} = 1 - 1.163 \frac{\rho_g}{\rho_\ell} \frac{\dot{q}}{10^3} - 0.044\,6 \frac{\rho_g}{\rho_\ell} \left(\frac{\dot{m}}{10^3}\right)^2 \left(\frac{d}{D}\right)^{0.5} \quad (5)$$

B. Heat transfer rates in horizontal tubes, bends, and coils

As already mentioned, the heat exchanger designer forced to use horizontal tubes in which boiling occurs should choose a small tube diameter and as high a liquid inlet velocity as permitted by pressure drop considerations. As an initial step, the range of flow patterns expected over the entire evaporator tube should be established using the methods outlined in Sec. 2.3.2. The location of any seriously stratified regions and of the dryout quality should be established using the guidance given in the preceding section. For regions where the complete perimeter of the tube remains fully wetted, as is the case for dispersed bubbly flow and high-velocity annular flow, the heat transfer rates may be calculated using the methods discussed in Sec. 2.7.3. At low velocities, however, asymmetric flow patterns such as stratified, wavy, or slug flow occur, and the mean heat transfer rate will be reduced because the upper parts of the tube run dry some or all of the time. This influence of flow pattern is clearly seen in Fig. 5, which shows data taken by **Bandel** and Schlunder [12] for the evaporation of refrigerant 11 in a 14-mm-diameter tube. These authors propose the following equation for the annular-flow region:

$$\frac{\alpha_{tp}}{\alpha_\ell} = C(\phi_f^2)^{(n-1)/n} \quad (6)$$

where n is the exponent in the relationship $dp/dz \propto \dot{m}^n$ and ϕ_f^2 is the Martinelli factor $[= (dp/dz)_{tp}/(dp/dz)_\ell]$. The constant C was dependent on the fluid used:

C = 1.45 for refrigerant 11 (T_{sat} = 10° C)

C = 1.85 for refrigerant 12 (T_{sat} = 0°C)

C = 1.95 for refrigerant 22 (T_{sat} = — 10° C)

In the stratified-flow region, incomplete wetting reduced the average value of heat transfer coefficient

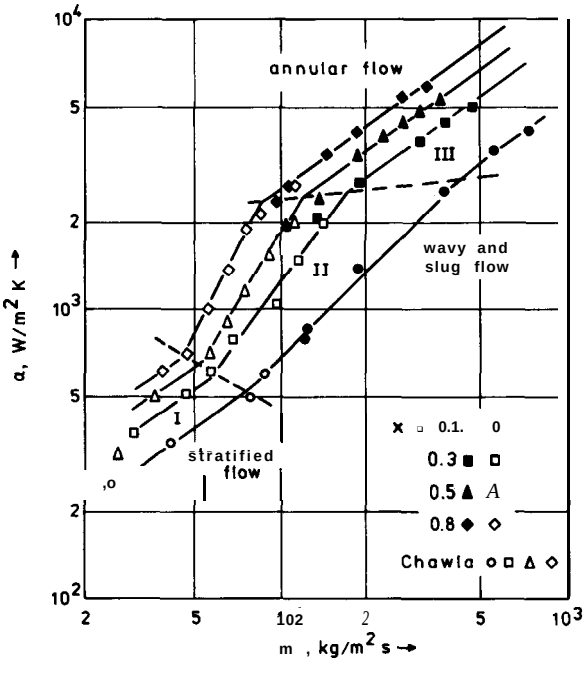

Figure 5 Convective boiling in horizontal tubes: influence of flow pattern (refrigerant 11). T_{sat} = 10°C, D = 14 mm. From Bandel and Schlunder [12].

© 1983 Hemisphere Publishing Corporation

and the constant C is given by the above values divided by $(1 + x)^{0.5}$. For the intermediate wavy/slug-flow pattern a logarithmic interpolation was proposed.

An alternative is to use the correlation proposed recently by Shah [13]. This correlation is similar to that of Chen (see Sec. 2.7.3) but has the advantage that it can be applied to partially stratified flows in horizontal channels. The correlation is given in the form of a graph (Fig. 6). The ordinate is the ratio α_{tp}/α_ℓ and the abscissa C_o is

$$\left(\frac{1-x}{x}\right)^{0.8}\left(\frac{\rho_g}{\rho_\ell}\right)^{0.5}$$

Two other parameters are used:

$$B_o = \text{the boiling number} = \frac{q}{\dot{m}\Delta h_v}$$
$$\mathrm{Fr}_\ell = \text{the Froude number} = \frac{\dot{m}^2}{\rho_\ell^2 g_n D} \qquad (7)$$

Figure 7 illustrates the use of the chart. Values of the abscissa C_o, of B_o, and of Fr_ℓ are calculated for the specified conditions.

Example I: Vertical tube C_o = 0.10, B_o = ***20 X*** 10^{-4}, Fr_ℓ = 0.002. Since the tube is vertical, ignore Fr_ℓ. Draw a vertical line at C_o = 0.10 to intersect the curve for B_o = *20* X 10^{-4}. From this point of intersection, draw a horizontal line to the left and read α_{tp}/α_ℓ at the ordinate (= 20).

Example 2: Vertical tube C_o = 0.10, B_o = ***2 X*** 10^{-4}, Fr_ℓ = 0.002. Since the tube is vertical, ignore Fr_ℓ. Draw a vertical line at C_o = 0.10 until it intersects line ***AB.*** Curves for values of B_o less than 4.5 X 10^{-4} all merge into line ***AB;*** therefore the boiling number has no influence in this example. Draw a horizontal line from the point of intersection to the ordinate and read α_{tp}/α_ℓ (= 11).

Example 3: Horizontal tube C_o = 0.10, B_o = 20 X 10^{-4}, Fr_ℓ = 0.002. Draw a vertical line at C_o = 0.10. From the point it intersects the line for Fr_ℓ = 2 X 10^{-3}, draw a horizontal line to the right to intersect the line ***AB.*** From this intersection draw a vertical line to intersect the curve for B_o = ***20 X*** 10^{-4}. Then draw a horizontal line from this last intersection to the left to the ordinate and read α_{tp}/α_ℓ (= 14).

Example 4: Horizontal tube C_o = 0.10, B_o = ***2 X*** 10^{-4}, Fr_ℓ = 0.002. Draw a vertical line at C_o = 0.10. From the point it intersects the line Fr_ℓ = 2 X 10^{-3}, draw a horizontal line to the right to intersect the line ***AB.*** Curves for values of B_o less than 2.0 X 10^{-4} all merge into line ***AB,*** so the boiling number has no

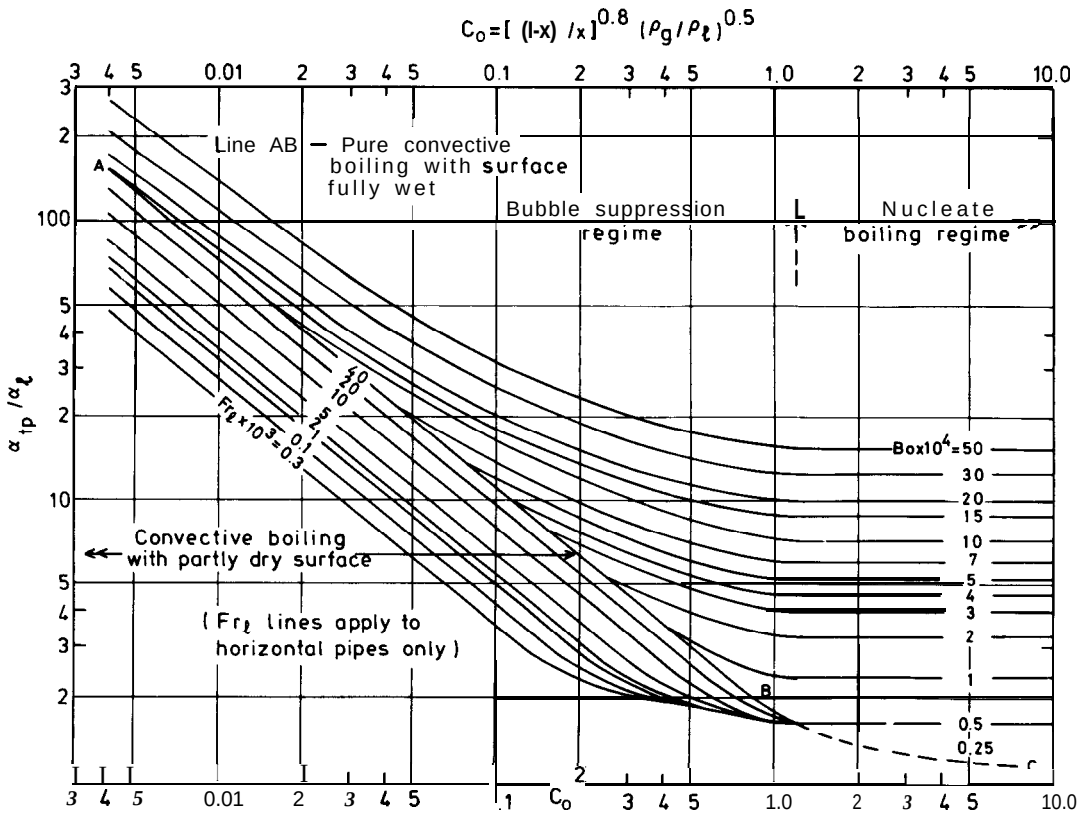

Figure 6 The Shah [13] correlation.

© 1983 Hemisphere Publishing Corporation

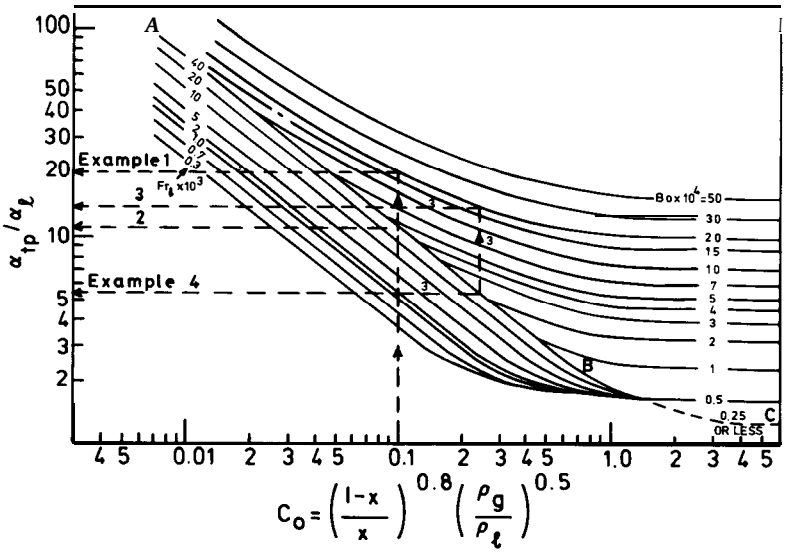

Figure 7 Solution of examples l-4, explaining the use of Fig. 6.

influence in this example. Extend the horizontal line to the left and read α_{tp}/α_ℓ at the ordinate (= 5.4).

The correlation is valid over the reduced pressure range 0.004 to 0.8. The rms error on 780 data points is 14%, somewhat higher than for the Chen correlation. About 10% of the data points show deviations greater than ±30%. It will be noted that when the correlation is used for a horizontal tube, the value of $\bar{\alpha}_{tp}$ is the mean coefficient over the tube perimeter. The Shah correlation agrees well with the experimental data of Bandel and Schlunder [12] for heat transfer coefficients to refrigerant 11 evaporating in a 14-mm horizontal tube.

In bends and helical coils the heat transfer coefficient in annular flow varies somewhat around the circumference of the tube. This effect was clearly seen in the experiments of Owhadi and Bell [11]. However, the nucleate boiling coefficient is not influenced by the centrifugal forces, and from a design viewpoint the heat transfer coefficient should be assumed to be unaltered from the straight vertical tube situation except for those situations where stratification or dryout ensure that part of the tube circumference is running dry.

Finally, it should be noted that overheating of the upper tube surfaces and local drying out of the liquid film after a bend when combined with deposition of particulate material may contribute to tube failures in boilers by the process of on-load corrosion. Stratification and premature dryout should thus be avoided in waste heat boilers or in situations where the heat flux is the independent variable. In other types of evaporator where the heat source is temperature controlled, such as by condensing steam, stratification or premature dryout, while reducing the mean heat transfer coefficient, may not be expected to have other serious consequences, provided that the process fluid is clean.

Nomenclature** for **Section 2.7.4 appears at the end** of **Section 2.7.8.

REFERENCES FOR SECTION 2.7.4

1. Butterworth, D., and Robertson, J. M., Boiling and Flow in Horizontal Tubes, ***in Two-Phase Flow and Heat Transfer,*** eds. D. Butterworth and G. F. Hewitt, chap. 11, Oxford University Press, London, 1977.
2. Styrikovich, M. A., and Miropolskii, Z. L., ***Dokl. Akad. Nauk SSSR,*** **vol. 71,** no. 2, 1950.
3. Gardner, G. C., and Kubie, J., Flow of Two Liquids in Sloping Tubes: An Analogue of High Pressure Steam and Water, ***Int. J. Multiphase Flow,*** **vol. 2,** pp. 435451, 1976.
4. Robertson, J. M., Dryout in Horizontal Hairpin Waste-Heat Boiler Tubes, ***AIChE Symp. Ser.,*** vol. 69, no. 131, pp. 55-62, 1973.
5. Lis, J., and Strickland, J. A., Local Variations of Heat Transfer in a Horizontal Steam Evaporator Tube, 4th Int. Heat Transfer Conf. paper B4 Vol. 5, Paris, August 1970.
6. Bailey, N. A., Dryout in the Bend of a Vertical U-Tube Evaporator, Personal communication, 1977.
7. Miropolskii, Z. L., Picus, V. Yu., and Shitsman, M. E., Regimes of Deteriorated Heat Transfer at Forced Flow of Fluids in Curvilinear Channels, 3d Int. Heat Transfer Conf., Chicago, August 1976, vol. II, pp. 95-101, Paper 50, 1966.

© 1983 Hemisphere I blishing Corporation

8. Miropolskii, Z. L., and Picus, V. Yu., Critical Boiling Heat Fluxes *in* Curved Channels, ***Heat Transfer Sov. Res.,*** vol. 1, no. 1, pp. 74-79, 1969.
9. Carver, J. R., Kakarala, C. R., and Slotnik, J. S., Heat Transfer in Coiled Tubes with Two-Phase Flow, Rept. TID 20983, 1964; see also Babcock and Wilcox Co. Rept. 4438, 1964.
10. Ruffell, E. E., The Application of Heat Transfer and Pressure Drop Data to the Design of Helical Coil Once-Through Boilers, Symp. Multi-Phase Flow Systems, University of Strathclyde, ***Inst. Chem. Eng. Symp. Ser.,*** no. 38, Paper 15, 1974.
11. Owhadi, A., and Bell, K. J., Forced Convection Boiling inside Helically-Coiled Tubes, ***Znt. J. Heat Mass Transfer,*** vol. 10, pp. 397401, 1967.
12. Bandel, J., and Schlünder, E. U., Frictional Pressure Drop and Convective Heat Transfer of Gas-Liquid Flow in Horizontal Tubes, ***Proc. 5th Znt. Heat Transfer Conf., Tokyo, September*** 3-7, 1974, Paper B.5.2, 1974; see also Bandel, J., and Schlünder, E. U., Druckverlust und Wärmeübengang bei der Vendampfung seidender Kaltemittel im durchstromten Rohr, ***Chem. Zng. Tech.,*** vol. 45, no. 6, pp. 345-349, 1973; and Bandel, J., Doktor-Ingenieur dissertation, University of Karlsruhe, 1973.
13. Shah, M., A New Correlation for Heat Transfer During Boiling Flow through Pipes, ***ASHRAE Trans., vol. 82,*** no. 2, pp. 66-86, 1976.

© 1983 Hemisphere Publishing Corporation

2.7.5

Boiling outside tubes and tube bundles

J. G. Collier

A. Boiling outside single tubes in cross flow

This section deals with the case where the flow past the tube or cylinder is by forced rather than by natural convection. This latter situation is dealt with in Sec. 2.7.2. Photographs presented by Vliet and Leppert [1] show very clearly the flow patterns that occur when nearly saturated water flows upward across a uniformly heated cylindrical tube. At moderate heat fluxes, typically around 20% of the critical heat flux, a vapor cavity forms in the cylinder s wake. Initially this cavity is not continuous along the length of the cylinder, but as the heat flux is increased, the increase in the length of the cavity in the direction of flow results in the formation of a very uniform vapor sheet. An increase of velocity from 0.4 to 1.5 m/s or of tube diameter from 0.254 to 4.8 mm also results in a large stable vapor cavity behind the cylinder. Under these circumstances the only liquid reaching the top half of the cylinder is that which is supplied between the vapor bubbles and the heater surface as the bubbles enter the cavity wake near the horizontal diameter. For low heat fluxes, more liquid is supplied than evaporated and the excess is removed by entrainment in the cavity. The critical heat flux is reached when the liquid supplied in this manner becomes insufficient to cool the upper half of the cylinder.

In a parallel study, Vliet and Leppert [2] extended their work to include the effect of subcooled water flowing across the heated rod. For low subcoolings ($<16°C$), the flow pattern observed was similar to that for water at the saturation temperature. For greater subcoolings there is insufficient vapor to form a cavity in the wake of the cylinder because of the rapid condensation.

Experimental information on boiling of liquids in cross flow on heated cylinders has been reported by Vliet and Leppert [1,2], Beecher [3], McKee and Bell [4], Cochran and Andracchio [5], and Min [6] for water; by Cochran and Andracchio [5] for Freon 113; by Mm [6] for methanol; and by Lienhard and Eichhorn [7] for isopropanol.

Figure 1 shows experimental data taken by

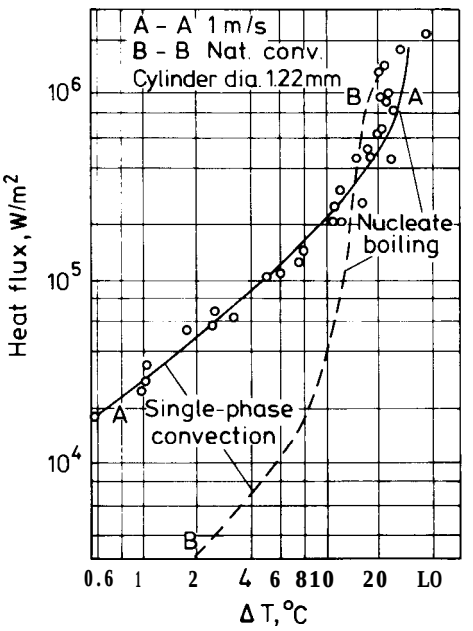

Figure 1 Effect of cross flow on nucleate boiling curve for water (1 bar). From Beecher [3].

© 1983 Hemisphere Publishing Corporation

Beecher [3] for saturated water flowing at 1 m/s normal to an electrically heated stainless steel cylinder 1.22 mm in diameter. The data are compared with a curve for water boiling from a similar cylinder under natural convection pool boiling conditions. In the region of high heat flux the two curves are nearly coincident, whereas at low temperature differences the individual curves are in agreement with the respective single-phase forced convection and natural convection predictions. The forced convective boiling curve may therefore be established by an interpolation procedure (Fig. 2).

This method is based on that proposed by Bergles and Rohsenow [8]. A fully developed nucleate boiling heat flux ($\dot{q}_n$) versus wall superheat (AT,,,) curve is established using the methods given in Sec. 2.7.2. Similarly, a single-phase forced convection heat flux ($\dot{q}_c$) is calculated as a function of wall temperature (T_w) using the methods given in Sec. 2.5.2. This heat flux ($\dot{q}_c$) is then plotted, together with $\dot{q}_n$, against wall superheat, AT,,, . The wall superheat corresponding to the onset of nucleation ($\Delta T_{\text{sat},i}$) is estimated using the methods given in Sec. 2.7.3. The corresponding heat flux $\dot{q}_i$, is read off the fully developed nucleate boiling curve. The forced convective boiling curve is then given by the curve $\dot{q}_c$ up to a wall superheat $\Delta T_{\text{sat},i}$ and then using the following interpolation formula at higher wall superheats by picking off corresponding values of $\dot{q}_n$ and $\dot{q}_c$ to substitute into the equation

$$\dot{q} = \dot{q}_c \left\{ 1 + \left[\frac{\dot{q}_n}{\dot{q}_c} \left(1 - \frac{\dot{q}_i}{\dot{q}_n} \right) \right]^2 \right\}^{1/2} \tag{1}$$

If $\dot{q}_i \ll \dot{q}_n$, as it often is for saturated conditions, Eq. (1) reduces to the form suggested by Kutateladze [9]:

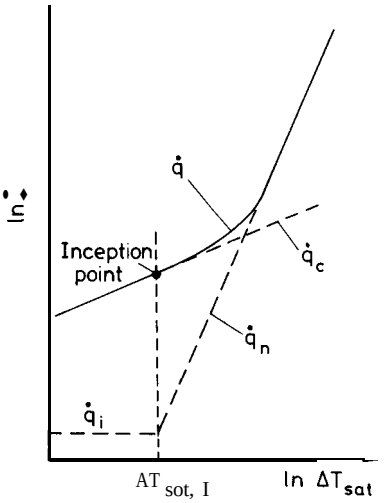

Figure 2 Interpolation procedure for construction of forced convection nucleate boiling curve.

$$\dot{q} = \dot{q}_c \left[1 + \frac{\left(\frac{\dot{q}_n}{\dot{q}_c} \right)^2}{\dot{q}_c} \right]^2 \dot{q}_n^{1/2} \tag{2}$$

Variations up to 30% in the wall superheat occur around the circumference of a heated cylinder in an upward cross flow [4]. As might be expected, the lowest rates of heat transfer usually occur on the upper half of the cylinder in the region of the separated wake. In this region, nucleate boiling provides the main heat transfer mechanism, with little contribution from convection, which enhances the heat transfer rates at the sides and particularly the bottom of the cylinder.

B. Critical heat flux outside single tubes in cross flow

Lienhard and Eichhorn [7] have correlated the available experimental critical heat flux data for cross flow of liquids upward over single cylinders and tubes in relation to the various hydrodynamic flow patterns. Three separate regions were identified.

1. ***Very-low-velocity region:*** Up to the point at which a two-dimensional wake is formed, the equations for the critical heat flux ($\dot{q}_{cr}$) are those valid for natural convection pool boiling. Thus,

$$\frac{4_{cr,p}}{4_{cr,z}} = \begin{cases} 0.94(R')^{-1/4} & \text{for } 0.12 < R' < 1.17 \\ 0.904 & \text{for } R' \geqslant 1.17 \end{cases} \tag{3}$$

where $\dot{q}_{cr,z}$ is Zuber s expression for the critical heat flux on an infmite horizontal plate,

$$q_{cr,z} = \frac{\pi}{24} \rho_g^{1/2} \Delta h_v [\sigma g_n (\rho_\ell - \rho_g)]^{1/4} \tag{4}$$

and R' is the dimensionless heater radius,

$$R' = R \left[\frac{\sigma}{g_n(\rho_\ell - \rho_g)} \right]^{-1/2} \tag{5}$$

2. Low-velocity region: The transition to a two-dimensional wake occurs at a velocity (u,) given by†

$$We_g \cong 0.1 \frac{\rho_g}{\rho_\ell} R'^2 \qquad (= 6.3 \times 10^{-5} R'^2 \text{ for water}) \tag{6}$$

where

$$We_g = \frac{2R\rho_g u_\infty^2}{\sigma}$$

†Equation (6) was given incorrectly in the original paper by Lienhard and Eichhorn and was subsequently corrected.

© 1983 Hemisphere Publishing Corporation

At liquid velocities greater than those given by Eq. (6), the critical heat flux is given by

$$\frac{\pi \dot{q}_{cr}}{\rho_g \Delta h_v u_\infty} = 1 + \left(\frac{4}{We_g}\right)^{1/3} \tag{7}$$

3. High-velocity region: A second transition occurs at a higher liquid velocity when u_∞ is given by

$$\frac{\pi \dot{q}_{cr}}{\rho_g \Delta h_v u_\infty} = 0.275 \left(\frac{\rho_\ell}{\rho_g}\right)^{1/2} + 1 \tag{8}$$

At liquid velocities greater than those given by Eq. (8), the critical heat flux is given by

$$\frac{\pi \dot{q}_{cr}}{\rho_g \Delta h_v u_\infty} = 0.005\,92 \left(\frac{\rho_\ell}{\rho_g}\right)^{0.75} + 0.052\,1 \left(\frac{\rho_\ell}{\rho_g}\right)^{0.5} \tag{9}$$

This latter equation represents 85% of the data for water, Freon 113, methanol, and isopropanol with a ±20% accuracy. These equations show that, for cross flow of saturated liquid over a cylinder, $\dot{q}_{cr}$ increases as $(u_\infty)^{1/3}$ and decreases as $D^{-1/3}$. These trends are illustrated in Fig. 3, which shows the critical heat flux for water plotted against cylinder diameter with velocity as parameter. The experimental results of McKee and Bell [4] for water were taken with relatively large-diameter cylinders of 6.35 and 18.0 mm. Visual observation suggested that the critical heat flux measurements were made in region (1), that is, before a two-dimensional wake was formed.

The critical heat flux values measured with the 18-mm-diameter cylinder at cross-flow velocities up to 1.66 m/s were approximately equal to those measured for pool boiling. The criterion developed by Lienhard and Eichhorn, Eq. (6), predicts the transition to a two-dimensional wake at a much lower velocity. However, comparison is made difficult by the short length of the test specimen ($L/D \approx 2.5$) and by the design of the mountings used.

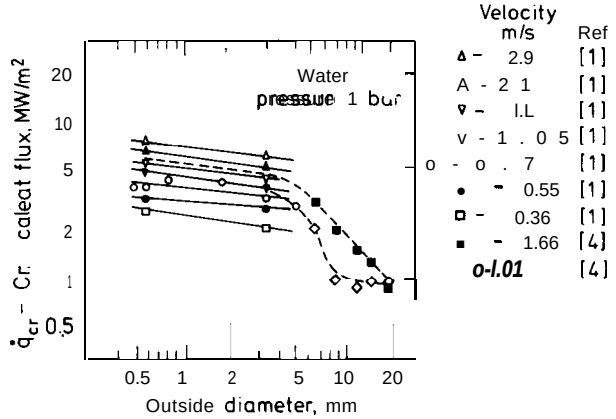

Figure 3 Critical heat flux in cross flow-effect of diameter and velocity. From McKee and Bell [4].

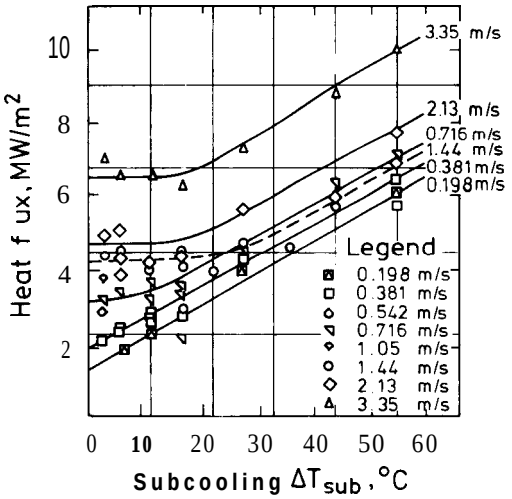

Figure 4 Effect of subcooling on $\dot{q}_{cr}$ for cross flow of water over a 3.17-mm-OD tube. From Vliet and Leppert [2].

Information on the effect of subcooling on $\dot{q}_{cr}$ for cylinders in cross flow is limited. Figure 4 shows data for water taken by Vliet and Leppert [2]. Except at high velocities, the lines for each velocity appear parallel, suggesting a constant incremental increase in $\dot{q}_{cr}$ with subcooling, irrespective of velocity. Conservatively basing this increment on that for subcooled pool boiling,

$$\dot{q}_{cr,sub} = \dot{q}_{cr,sat} + \dot{q}_{cr,p} B \Delta T_{sub} \tag{10}$$

where $\dot{q}_{cr,sat}$ is that for cross flow of saturated liquid evaluated by the procedure described above and $\dot{q}_{cr,p}$ is the saturated pool boiling critical heat flux given by Eq. 2.7.2(17). Any of the expressions for B given in Sec. 2.7.2C might be used [Eq. 2.7.2(27), 2.7.2(28), or 2.7.2(29)]. Choosing the expression given by Eq. 2.7.2(28),

$$q_{cr,sub} = q_{cr,sat} + 0.065 \left(\frac{\rho_\ell}{\rho_g}\right)^{0.8} \frac{c_{p\ell} \Delta T_{sub}}{\Delta h_v} \dot{q}_{cr,p} \tag{11}$$

At high velocities, $\dot{q}_{cr,sub}$ becomes independent of subcooling at temperatures near saturation (Fig. 4). Therefore, for $0.03 > (c_{p\ell} \Delta T_{sub}/\Delta h_v)$,

$$q_{cr,sub} = q_{cr,sat} \tag{12}$$

and for $(c_{p\ell} \Delta T_{sub}/\Delta h_v) \geq 0.03$,

$$q_{cr,sub} = q_{cr,sat} + 0.065 \left(\frac{\rho_\ell}{\rho_g}\right)^{0.8} \left(\frac{c_{p\ell} \Delta T_{sub}}{\Delta h_v} - 0.03\right) \dot{q}_{cr,p} \tag{13}$$

C. Film boiling

Film boiling during upward cross flow over a horizontal cylinder has been studied by Bromley et al.

© 1983 Hemisphere Publishing Corporation

[10]. The experimental data taken using an electrically heated graphite tube and for a variety of liquids including n-hexane, carbon tetrachloride, benzene, and ethyl alcohol were correlated in two regions. At low cross-flow velocity,

$$\frac{u_\infty}{\sqrt{g_n D}} < 1.0$$

$$\alpha = a, + 0.75\alpha_r \quad (14)$$

where α_r is the radiation heat transfer coefficient given by Eq. 2.7.2(44), α_c is that value suggested by Bromley for natural convection [Eq. 2.7.2(36)], D is the outside diameter, and u_∞ is the free-stream velocity.

For higher velocities,

$$\frac{u_\infty}{\sqrt{g_n D}} > 2.0$$

$$\alpha = a, + 0.875\alpha_r \quad (15)$$

where α_c is now given by

$$\alpha_c = 2.7 \left(\frac{u_\infty \lambda_g \rho_g \Delta h_v'}{D \Delta T_{sat}} \right)^{1/2} \quad (16)$$

where $\Delta h_v'$ is defined by Eq. 2.7.2(35). The heat transfer coefficient increases with higher velocities and decreased tube diameters. Typical values of α_c for n-hexane, benzene, and ethyl alcohol vary from 230 W/m^2 K for no flow to 625-800 W/m^2 K at a velocity of 4 m/s. The values for carbon tetrachloride were approximately one-half these figures.

This work was extended to upward cross flow of subcooled liquids over a horizontal cylinder by Motte and Bromley [11]. At velocities (u_∞) above about 2.5 m/s, the heat transfer coefficients (α_c) are increased approximately fourfold by subcooling the liquid approximately 45° C. These values, thus, numerically approach the values expected for nucleate boiling for organic liquids (2 000-3 000 W/m^2 K).

D. Boiling on the outside of tubes within a horizontal tube bundle

Although it is known that the rate of heat transfer from a heated tube within an evaporator tube bundle is different from that for an isolated single tube, there have been few published studies quantifying the differences. Horizontal tube bundles are used in refinery kettle reboilers and in water chillers, and this lack of published information is surprising. Nevertheless, the available published studies, particularly those of Palen et al. [12-14], do provide much useful information. Figure 5 shows schematically the essential differences between the boiling curve for boiling outside a horizontal tube and for a tube within a horizontal tube bundle. Agitation, particularly because of vapor within

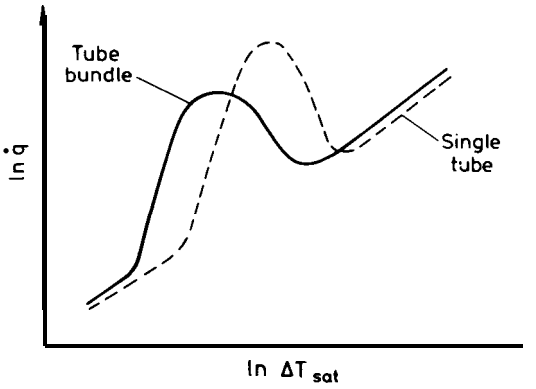

Figure 5 Boiling curve for tube bundle compared with that for a single tube (based on [12]).

the bundle, Increases the heat transfer coefficient in the nucleate boiling region, particularly at low heat fluxes [15]. At higher values of wall superheat AT,,,, the presence of large amounts of vapor within the bundle causes vapor blanketing of the heat transfer surfaces to occur at heat fluxes below the critical heat flux for an isolated single tube. This reduction is greater the larger the physical size of the tube bundle and the closer the packing density of the tubes. The variation of heat flux with wall superheat in the region of the critical heat flux also tends to be much flatter than for a single tube. Finally, the heat transfer coefficient in the film boiling region may also be enhanced by the increased levels of turbulence in the tube bundle, although to a somewhat lesser extent than in the nucleate boiling.

Based on limited industrial experience, Kern [16] suggested that the maximum heat transfer coefficient for boiling within a tube bundle should be taken as 1 700 W/m^2 K for organic liquids and 5 700 W/m^2 K for water. It was also recommended that the maximum heat flux within the bundle should not exceed 38 000 W/m^2 for units operating with organics in a natural circulation mode and 63 000 W/m^2 for units operating with organics in a forced circulation mode. The maximum allowable heat flux for the evaporation of water or an aqueous solution within a tube bundle operating in either mode was 95 000 W/m^2. This very general guidance usually produces very conservative designs except under vacuum conditions or where pressures are close to the critical point. In general, the methods identified in Secs. E and F are to be preferred for design purposes.

E. Heat transfer rates outside horizontal tubes in tube bundles

Heat transfer rates under evaporating conditions in a tube bundle are considerably enhanced over those for a

© 1983 Hemisphere Publishing Corporation

single tube because of the influence of vapor passing through the bundle. Detailed studies of this phenomenon have been reported by Robinson and Katz [17], by Nakajima and Morimoto [18], and by Montgomery [19]. These studies have shown that:

1. There is little or no change in the boiling heat transfer rate for a heated tube within a bundle compared with an isolated single tube under similar conditions where the heated tube is located in a single-phase liquid cross flow.

2. There is a considerable enhancement in the heat transfer rate for any particular tube within the tube bundle for locations where that tube is bathed by vapor generated from upstream tubes.

3. This enhancement is greatest at low values of wall superheat or surface heat flux and is proportional to the volumetric flow of the vapor. This is demonstrated most clearly in Fig. 6, which shows results obtained by Robinson and Katz [17] for the injection of vapor under a heated tube within a tube bundle evaporating Freon 12.

Because the enhancement is greatest at low wall superheats, it is clear that the mechanism of enhancement is related to the convective component of the total heat flux. If it is assumed that the presence of the vapor serves only to increase the liquid-phase velocity, then the enhancement of the convective heat flux is given by

$$\frac{\alpha_{c,\,tp}}{\alpha_c}\,\frac{q_{c,\,tp}}{\dot{q}_c} = \left(\frac{1}{1-\epsilon_g}\right)^n \tag{17}$$

where the subscript c relates to the single-phase liquid heat transfer rate calculated for tube bundles using the method given in Sec. 2.5.3 and the subscript c, *tp* relates to the expected two-phase heat transfer rate corresponding to a local vapor void fraction of ϵ_g. If the liquid is in laminar flow, $n = \frac{1}{3}$; in turbulent flow, $n = 0.8$.

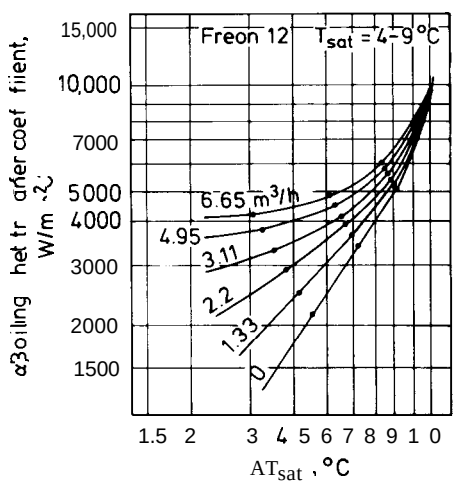

Figure 6 Effect of vapor injection on heat transfer rates in a rod bundle. From Robinson and Katz [17].

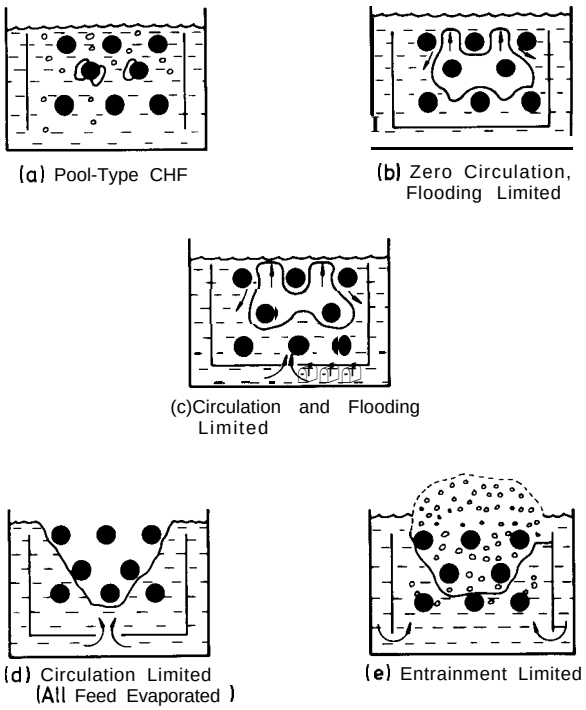

Figure 7 Sketches of possible dryout mechanisms inside tube bundles.

In order to estimate the total heat transfer rate for a heated tube within a bundle, use is made of Eq. (2) with $\dot{q}_{c,\,tp}$ substituted for $\dot{q}_c$. In order to use this type of approach, it is necessary to know the liquid and vapor velocities within the bundle. These may be estimated from tube-to-tube calculations and the methods given in Sec. 2.3.2 to estimate the void fraction. Alternative methods, valid only for refrigerants, have been given by Bier et al. [15] and by Leong and Cornwell [20]. It should be noted that the heat transfer rates in an actual tube bundle will be sensitive to the amount of liquid that bypasses the gap between the tube bundle and the shell wall. With large quantities of vapor corresponding to high bundle void fractions, vapor blanketing will occur, reducing the heat transfer coefficient. This reduction will occur earlier at high surface heat fluxes and should be expected when the void fraction (ϵ_g) exceeds ~0.85.

F. Critical heat flux outside horizontal tubes in tube bundles

A number of mechanisms are possible whereby a limiting heat flux is reached within a tube bundle. They may be briefly described as follows (Fig. 7).

© 1983 Hemisphere Publishing Corporation

1. ***Pool boiling-type critical heat flux:*** This mechanism will occur in small bundles with widely spaced tubes. In this case the flow passages within the bundle are essentially filled with liquid and the limiting process is the same as that for an isolated single tube.

2. Zero circulation and flooding limited: This mechanism occurs when there is no net circulation through the tube bundle. Liquid entering the bundle can do so only from above and is hindered in doing so by the vapor being released from the bundle. A flooding condition is reached where the vapor release is such as to prevent sufficient down flow of liquid to reach all the heating surfaces within the bundle. This mechanism is more likely to occur in large bundles with closely spaced tubes. Down flow can occur in some lanes and with up flow in others, giving an apparent internal circulation.

3. Circulation and flooding limited: This mechanism is similar to mechanism 2 except that some small circulation into the bundle from the sides and base occurs. This low in flow of liquid is evaporated within the bundle and the resulting vapor passes upward to join that generated from liquid passing into the bundle from above. Again, the limiting condition is reached when this total vapor flow is such as to prevent a sufficient liquid in flow from above. As with mechanism 2, this mechanism occurs in large bundles with closely spaced tubes.

4. Circulation limited: As the circulation through the bundle increases, a condition is reached where the vapor flow produced from this circulation alone is sufficient to prevent any liquid entering the bundle from above. The limiting condition is then complete evaporation of the liquid feed, starving the upper tubes in the bundle of liquid. Such a condition might occur in narrow but tall tube bundles.

In practice it is difficult to distinguish among mechanisms 2, 3, and 4 in actual tube bundle geometries.

5. Entrainment limited: As the circulation through the bundle is further increased, a substantial amount of liquid may be entrained as droplets within the vapor flow and thus dryout will occur on the upper tubes on the bundle at vapor qualities considerably less than 100%.

It is possible to derive a simple analytical expression for condition 2 on the assumption that for a bundle of circular cross section located within a blind-ended rectangular channel, flooding will occur first at the horizontal diameter of the bundle. By using the critical vapor velocity for flooding given in Sec. 2.3.2, the following expression can be derived by analogy with the equation for the critical heat flux in a blind-ended heated tube (see Sec. 2.7.3):

$$\dot{q}_{cr} = \left[\frac{D_b(P-D)^{3/2}}{PN\pi D}\right] \frac{\Delta h_v [g_n \rho_g(\rho_\ell - \rho_g)]^{1/2}}{[1 + (\rho_g/\rho_\ell)^{0.25}]^2} \qquad (18)$$

where D_b is the bundle diameter, N is the total number of tubes, P is the tube pitch, and D is the tube outside diameter. It will be seen that this expression for the critical heat flux in a tube bundle can be considered the product of two terms: a bundle geometry-characterizing parameter and a liquid physical property group. As might be expected, $\dot{q}_{cr}$ increases as the bundle decreases in size (D_b/N increases) and as the pitch (P) to tube diameter (D) ratio increases. Should $\dot{q}_{cr}$ predicted from Eq. (18) exceed the value calculated for an isolated single tube, then the latter value should be used. The situation is then that corresponding to condition 1 described above. In some cases it is the total bundle power per unit length of bundle, $\dot{Q}_{cr}$, that is of interest. Rearranging Eq. (15) gives

$$\dot{Q}_{cr} = \frac{D_b}{P}(P-D)^{3/2} \frac{\Delta h_v [g_n \rho_g(\rho_\ell - \rho_g)]^{1/2}}{[1 + (\rho_g/\rho_\ell)^{0.25}]^2} \qquad (19)$$

Palen and Small [14] have given a correlation for the critical heat flux within a tube bundle under conditions where the liquid circulation is limited. It was arrived at by modifying the isolated single-tube value given by Zuber, $q_{cr,z}$ given by Eq. (4). As discussed above, the critical heat flux was found to be a function of a dimensionless tube density factor Φ and a dimensional physical property factor Ψ

$$\Phi = \frac{D_b L}{A} \cong \frac{2P\sqrt{N(\sin\theta)/\pi}}{\pi DN} = 0.359\,\frac{P}{D}\sqrt{\frac{(\sin\theta)/\pi}{N}} \qquad (20)$$

where L is the bundle length, A is the tube bundle surface area, and θ is the tube layout angle.

$$\Psi = \Delta h_v \rho_g^{1/2} [g_n \sigma(\rho_\ell - \rho_g)]^{1/4} \qquad (21)$$

Values of Ψ for a range of hydrocarbons are given in Table 1.

$$q_{cr} = K(\Phi)(\Psi) \qquad (22)$$

The variation of bundle maximum heat flux as a function of these two parameters is shown in Fig. 8. The curves were faired into the single-tube value calculated by the Zuber correlation at the single-tube value of $\Phi = 1/\pi$. The empirical constant K in Eq. (22) for the condition where $0.06 < \Phi$ was given by Palen and Small as 1.23.

Available experimental evidence suggests that the predictions of both Eqs. (18) and (22) are conservative. These equations given the onset of vapor blanketing within a bundle. As the average wall superheat is increased, more tubes become dry, but the decrease in

© 1983 Hemisphere F blishing Corporation

Table 1 Values of Ψ ($\times 10^{-6}$), W/m^2

	Pressure, bar		
Liquid	1	**3.45**	**20.1**
Ethane	–	–	**4.50**
Propane	–	3.12	**3.44**
Propylene	–	**3.08**	**3.89**
n-Butane	2.14	**2.83**	**3.00**
i-Butane	1.91	**2.68**	**2.54**
Butene-1	1.92	**2.82**	**2.92**
n-Pentane	1.76	**2.67**	**2.58**
i-Pentane	1.78	**2.70**	**2.62**
n-Hexane	1.80	**2.57**	**2.10**
Cyclohexane	**2.06**	**2.78**	**2.75**
Benzene	**2.40**	**3.72**	**4.87**
n-Heptane	1.70	1.64	–

heat transfer for these tubes is partially balanced by the increase in coefficient for those tubes that are still adequately supplied with liquid. This results in a rather flat maximum in the heat flux-versus-wall superheat ***curve.***

Experimental data for $\dot{q}_{cr}$ where there is an imposed forced circulation through the bundle, condition 5 above, are sparse. Kezios et al. [21] measured values of $\dot{q}_{cr}$ for water flowing through various crossed-rod matrices of 0.3-cm rods. Each matrix was composed of 12 rows of rods, rods in adjacent rows being oriented at right angles to one another. The pitch in any one row was varied; assemblies with pitches of 0.475, 0.635, and 0.950 cm were tested. The values of critical heat flux obtained for these assemblies were higher than for a **single** rod but fell as the rod pitch was increased. It would appear that increased blockage significantly increases the critical heat flux over and above that expected due to the local increase in linear velocity. The method of testing was such that this conclusion is valid only for subcooled boiling conditions. Jansson and Strandberg [22] presented information of $\dot{q}_{cr}$ in a tube bank consisting of two rows of 1.23-cm-diameter tubes, on a 1.97-cm pitch arranged so that the individual rods were in line with one another and the rod spacing between rows was 0.5 cm. Water at atmospheric pressure was the test fluid, and the results were consistent with those for an isolated single tube. Coffield et al. [23], and later Jaikrischnan and Rohner [24], investigated subcooled critical heat flux with Freon 113 flowing normal to a matrix of 27 tubes, one or more of which was steam heated. A variety of correlations were suggested, but none with any generality.

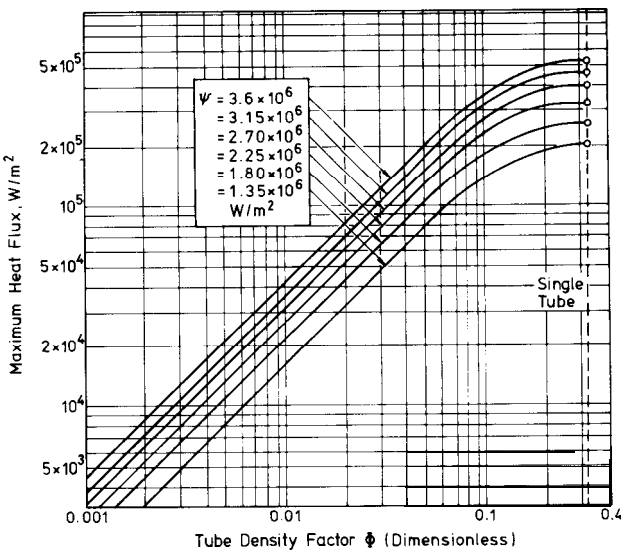

Figure 8 Maximum heat flux in horizontal tube bundles. From **Palen** and Small [**14**].

Nomenclature for Section 2.7.5 appears at the end of Section 2.7.8

REFERENCES FOR SECTION 2.7.5

1. Vliet, G. C., and Leppert, G., Critical Heat Flux for Nearly Saturated Water Flowing Normal to a Cylinder, **ASME** Winter Annu. Meet., New York, November 25-30, 1962, Paper **62-WA-173,** 1962.
2. Vliet, G. C., and Leppert, G., Critical Heat Flux for Subcooled Water Flowing Normal to a Cylinder, **ASME** Winter **Annu.** Meet., New York, November 25-30, 1962, Paper 62-WA-174, 1962.
3. Beeches, N., M.S. thesis, Massachusetts Institute of Technology, Cambridge, Mass., 1948.
4. McKee, H. R., and Bell, K. J., Forced Convection Boiling from a Cylinder Normal to the Flow, ***Chem. Eng. Prog. Symp. Ser.,*** vol. 65, no. 92, pp. 222-230, 1969; see also H. R. McKee, Forced Convection Boiling from a Cylinder Normal to the Flow, Ph.D. thesis, Oklahoma State University, April 1967.
5. **Cochran,** T. H., and **Andracchio,** C. R., Forced Convection Peak Heat Flux on Cylindrical Heaters and Refrigerant 113, NASA Rept. D-7553, February 1974.
6. **Min,** T. K., Masters thesis, University of Kentucky, Lexington, 1975.
7. Lienhard, J. H., and Eichhorn, R., Peak Boiling Heat Flux on Cylinders ***in*** a Cross Flow, ***Int. J. Heat Mass Transfer,*** vol. 19, pp. 1135-1142, 1976.
8. Beagles, A. E., and Rohsenow, W. M., The Determination of Forced Convection Surface Boiling Heat Transfer, ***J. Heat Transfer,*** vol. 86, pp. 365-371, 1964.

© 1983 Hemisphere Publishing Corporation

9. Kutateladze, S. S., Boiling Heat Transfer, *Int. J. Heat Mass Transfer,* vol. 4, pp. 31–45, 1961.
10. Bromley, L. A., Le Roy, N. R., and Robbers, J. A., Heat Transfer in Forced Convection Fihn Boiling, *Znd. Eng. Chem.,* vol. 45, no. 12, pp. 2639-2646, 1953.
11. Motte, E. I., and Bromley, L. A., Film Boiling of Flowing Subcooled Liquids, *Znd. Eng. Chem.,* vol. 49, no. 11, pp. 1921-1928, 1957.
12. Palen, J. W., Yarden, A., and Taborek, J., Characteristics of Boiling outside Large-scale Horizontal Multi-Tube Bundles, *AIChE Symp. Ser., vol. 68,* no. 118, pp. 50-61, 1972.
13. Palen, J. W., and Taborek, J. J., Refinery Kettle Reboilers-Proposed Method for Design and Optimization, *Chem. Eng. Prog.,* vol. 58, no. 7, pp. 37–46, 1962.
14. Palen, J. W., and Small, W. M., A New Way to Design Kettle and Internal Reboilers, *Hydrocarbon Process.,* vol. 43, no. 11, pp. 199-208, 1964.
15. Bier, K., Engelhorn, H. R., and Gorenflo, D., Heat Transfer to Low-boiling Halogen Refrigerants, Measurements Taken with Single Tubes and Transmission in Tube Bundles, *Klima Kälte Zng.,* no. 11, pp. 399–406, 1976.
16. Kern, D. *Q., Process Heat Transfer,* McGraw-Hill, New York, 1950.
17. Robinson, D. B., and Katz, D. L., Effect of Vapour Agitation on Boiling Coefficients, *Chem. Eng. Prog.,* vol. 47, no. 6, pp. 317-324, 1951.
18. Nakajima, K., and Morimoto, K., Boiling Heat Transfer on Outside Walls of Refrigerant Filled Horizontal Tube Bundles, *Reito,* vol. 44, no. 495, pp. 3-15, 1969 (UKAEA Trans. LB/G/211/4, January 1973).
19. Montgomery, R. T., A Study of the Effect of Tube Bundle Geometry on the Nucleate Boiling Region of a Series of Hydrocarbon Liquids, Ph.D. thesis, University of Missouri, Rolla, 1969.
20. Leong, L. S., and Cornwell, K., Heat Transfer Coefficients in a Reboiler Tube Bundle, *Chem. Eng.,* no. 343, pp. 219-221, April 1979.
21. Kezios, S. P., Kim, Tong-Soo, and Rafchiek, F. M., Burnout in Crossed-Rod Matrices Under Forced Convection Flow of Water, *1961 Znt. Heat Transfer Conf., International Developments in Heat Transfer, Boulder, Colorado,* vol. II, pp. 262-269, 1961.
22. Jansson, J. E., and Strandberg, O., Burnout Conditions for Cross Flow of Water Through a Tube Bundle, EAEC Symp. Heat Transfer Problems Nuclear Reactors, Karlsruhe, March 8-10, 1960.
23. Coftield, R. D., Jr., Rohner, W. M., and Tong, S., An Investigation of DNB in a Crossed-Rod Matrix with Normal Flow of Freon-113 Coolant, *Nucl. Eng. Design,* vol. 6, pp. 147-154, 1967.
24. Jaikrishnan, K. R., and Rohner, W. M. Study of the Effect of Pressure on the DNB in a Crossed-Rod Matrix with R-113 Coolant, *Nucl. Eng. Design,* vol. 22, pp. 244-251, 1972.

© 1983 Hemisphere Publishing Corporation

2.7.6

Boiling of binary and multicomponent mixtures: Basic processes

J. G. Collier

■ Sections 2.7.1-2.7.5 discuss the behavior of pure single-component fluids during evaporation. However, in the petrochemical industries in particular, many processes involve the evaporation (and condensation) of binary (n = 2) and multicomponent (n > 2) mixtures, where n is the number of components. In the boiling of binary and multicomponent mixtures, the heat- transfer and the mass transfer processes are closely linked, with the evaporation rate usually being limited by the mass transfer processes. This is significantly different from single-component systems, where interfacial mass transfer rates are normally very high.

In this section the differences to be expected in the basic physical processes will be considered. This will lead to a presentation of the available information on pool boiling of mixtures (Sec. 2.7.7). Finally, the problems of predicting heat transfer rates in forced convective evaporation of mixtures will be examined (Sec. 2.7.8). Starting with the early work of Bonilla and Perry [1] and Cichelli and Bonilla [2], a considerable body of published information on pool boiling of binary mixtures has been built up. However, very little has been published relating to forced convection evaporation of mixtures. The evaporation of multicomponent mixtures is largely unexplored.

A. Elementary phase equilibrium

(a) Binary systems

In a mixture of vapors the partial pressure p_A of component A is that pressure which would be exerted by A alone in a volume appropriate to the concentration of A in the mixture at the same temperature. Since $p = \Sigma p_A$, for an ideal mixture the partial pressure p_A is proportional to the mole fraction of A in the vapor phase:

$$p_A = \tilde{y}_A p \tag{1}$$

Two laws relate the partial pressure in the vapor phase to the concentration of component A in the liquid phase.

1. Henry s*law* states that the partial pressure p_A is directly proportional to the mole fraction $\tilde{x}_A$ of component A in the liquid phase:

$$p_A = \text{const}\ \tilde{x}_A \tag{2}$$

This holds for dilute solutions only, where $\tilde{x}_A$ is small.

2. *Raoult's* law states that the partial pressure p_A is related to the mole fraction $\tilde{x}_A$ and the vapor pressure of pure component A at the same temperature:

$$p_A = p_A^0 \tilde{x}_A \tag{3}$$

where p_A^0 is the vapor pressure of pure component A at the same temperature. This holds for high values of $\tilde{x}_A$ only.

If a mixture follows Raoult s law, it is said to be ideal, and values of $\tilde{y}$ can be calculated for various values of $\tilde{x}$ from a knowledge of the vapor pressures of the two pure components at various temperatures.

Few mixtures behave in an ideal manner. If the ratio of the partial pressure p_A to the mole fraction in the liquid phase $\tilde{x}_A$ is defined as the ***volatility,*** then for a binary mixture of components A and B,

© 1983 Hemisphere Publishing Corporation

Volatility of A = $\frac{p_A}{\tilde{x}_A}$ Volatility of B = $\frac{p_B}{\tilde{x}_B}$

The ratio of these two volatilities is known as the ***relative volatility*** α, given by

$$\alpha = \frac{p_A \tilde{x}_B}{p_B \tilde{x}_A} \tag{4}$$

Substituting Eq. (1),

$$\alpha = \frac{\tilde{y}_A \tilde{x}_B}{\tilde{y}_B \tilde{x}_A} \quad \text{or} \quad \frac{\tilde{y}_A}{\tilde{y}_B} = \alpha \frac{\tilde{x}_A}{\tilde{x}_B} \tag{5}$$

Clearly, from Eq. (3), for an ideal mixture the relative volatility is just the ratio of the vapor pressures of the pure components A and B at the chosen temperature. Values of α vary somewhat with temperature, and tables for different binary systems are available in chemical engineering handbooks.

Consider a container initially filled with a binary liquid mixture having a mole fraction $\tilde{x}_0$ of the more volatile component and held at constant pressure p and temperature T_1 (Fig. la). What happens when the liquid mixture is heated at constant pressure can be shown conveniently on a ***temperature-composition diagram*** (Fig. lb). In this diagram the mole fraction of the more volatile component in the liquid is plotted as the abscissa and the temperature at which the mixture boils as the ordinate.

The initial conditions in the container are denoted by point Q. The container is now heated at constant pressure. When the temperature reaches T_2, the liquid will start to boil, as shown by point R. Some vapor is formed of composition $\tilde{y}_0$, as shown by point S. This initial vapor is rich in the more volatile component. If the experiment is repeated for the complete range of values of $\tilde{x}_0$, then a series of points such as R and S can be determined. The locus of points like R is a curve $AXZRB$, which is known as the ***bubble-point*** or ***boiling-point*** curve. The locus of points like S is a curve $AWVSB$, which is known as the ***dew-point*** curve.

If the container is heated further, the composition of the liquid will change because of the loss of the more volatile component to the vapor. The boiling point will therefore rise to some temperature T_3. Both the liquid and vapor phases become richer in the less volatile component, with the liquid having a composition represented by point Z and the vapor having a composition represented by point V. Since no material is lost from the container, the proportion of liquid to vapor must be given by

$$\frac{L}{V} = \frac{UV}{ZU} = \frac{\tilde{y} - \tilde{x}_0}{\tilde{x}_0 - \tilde{x}} \tag{6}$$

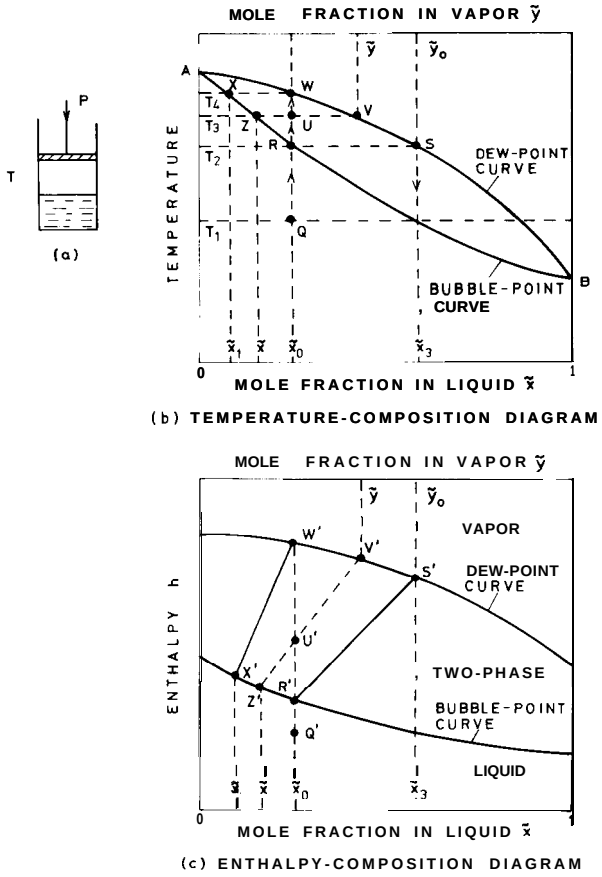

Figure **1** Elementary phase equilibria for binary mixtures.

The ratio $\tilde{y}/\tilde{x}$ at constant temperature is referred to as the ***equilibrium ratio K:***

$$K = \frac{y}{\tilde{x}} \tag{7}$$

Combining Eqs. (6) and (7), we have

$$\tilde{x} = \frac{\tilde{x}_0(L/V + 1)}{K + L/V} \tag{8}$$

Upon further heating to a temperature T_4, all the liquid is vaporized to give a vapor of the same composition as the original liquid (point W). The last drop of liquid to disappear is very rich in the less volatile component ($\tilde{x}_1$) (point X). During this hypothetical experiment, the mass fraction vaporized, the specific volume, and the heat added to the system to bring it to each temperature condition would also have been recorded. Note the analogy between this experiment and the once-through vaporization of a liquid mixture fed to the bottom of a tube.

In the design of evaporation equipment for liquid mixtures, thermodynamic equilibrium is usually assumed. However, this clearly must be an approximation, since temperature and concentration differences must exist for evaporation to occur. Equilibrium is

© 1983 Hemisphere Publishing Corporation

invariably assumed to exist at vapor-liquid interfaces, i.e., where the phases remain in intimate contact with one another. However, it is possible to conceive a situation where the vapor bubbles formed rise to the surface and into a vapor space such that there is no longer any close contact with the liquid phase. Further evaporation of the liquid must occur with a heavier (less volatile) liquid than originally designed for. There will be a corresponding rise in the boiling point, the effective temperature driving force for evaporation will be reduced, and the available surface area may become insufficient to accomplish the required duty. Such a separation of the vapor from the liquid may occur when evaporating a mixture on the shell side of a kettle reboiler, especially at low circulation rates. Alternatively, it could also occur within tubes where there is stratification or poor distribution of the flows.

Temperature-composition diagrams such as Fig. 1 ***b*** are helpful in interpreting different physical situations. For example, consider the case where subcooled boiling of a binary liquid mixture of composition $\tilde{x}_0$ and temperature T_1 occurs (point Q). The vapor formed at the heat transfer surface will have a composition $\tilde{y}_0$. If the vapor bubble detaches from the surface, passes through the liquid, and condenses, the condensed liquid will have a composition $\tilde{x}_3$ corresponding to $\tilde{y}_0$. Thus the liquid adjacent to the heating surface will tend toward a composition $\tilde{x}_1$, whereas the liquid some way away from the heating surface will tend toward $\tilde{x}_3$. These composition changes will be accompanied by changes in physical properties of the liquid.

In considering energy flows, particularly for nonideal mixtures where the molar latent heat is not constant and there is a substantial heat of mixing, an ***enthalpy-composition chart*** is useful (Fig. lc). The upper curve represents the dew point and the lower curve the bubble point. The enthalpies of liquid and vapor mixtures in equilibrium occur on the bubble-point or dew-point curves, respectively, at either end of a tie line, e.g., ***R'S'.*** Points corresponding to those on Fig. **lb** are shown with a prime.

Some temperature-composition curves look like those shown in Fig. 2. For these binary systems there are critical compositions $\tilde{x}_a$ where the vapor has the same composition as the liquid such that there is no change of composition upon evaporation. It will be seen later that for these special mixtures, called ***azeotropes,*** mass transfer limitations are absent and the mixture behaves when it is boiled like a pure component having mean mixture physical properties.

(b) Multicomponent mixtures

The above concepts can readily be extended to multicomponent mixtures. If Raoult s law applies, then Eq.

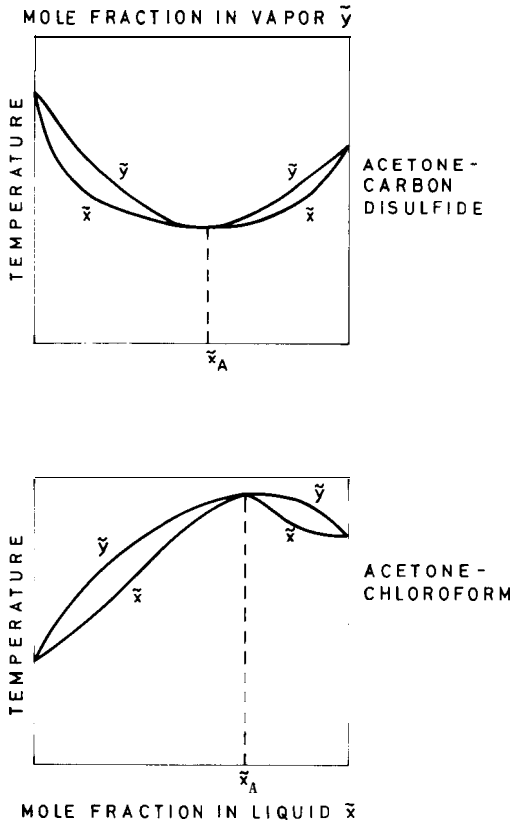

Figure 2 Temperature-composition diagrams for binary mixtures forming azeotropes.

(8) can be used with the appropriate $\tilde{x}_0$ and ***K*** values. Various values of ***L/V*** are assumed for a known liquid composition at a given pressure and temperature. The correct ***L/V*** ratio is that which satisfies the constraint

$$\Sigma\tilde{x} = 1 \tag{9}$$

The application of Eq. (8) to multicomponent nonideal mixtures is more difficult and involves a further constraint,

$$\Sigma K\tilde{x} = 1 \tag{10}$$

The calculations can be carried out in terms of the number of moles of each component in each phase instead of using mole fractions as above. ***K*** values have been measured for a wide range of hydrocarbons at various pressures, and some values are shown in Fig. 3. The methods used to measure or predict phase equilibrium data are, however, outside the scope of this section.

The evaporation of any binary or multicomponent liquid can be expressed in terms of a curve of the equilibrium temperature (T) against an amount of heat (Q)—the conventional cooling or condensation curve. It is a unique curve provided that the pressure ***p*** throughout the evaporator is constant. Another, and in some

© 1983 Hemisphere. I blishing Corporation

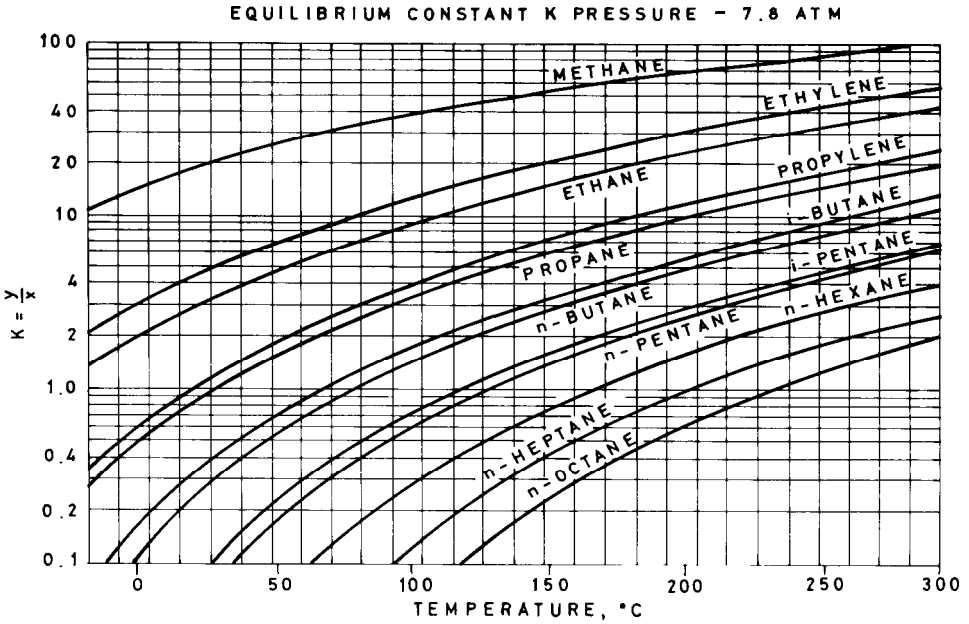

Figure 3 Vapor-liquid equilibrium data for hydrocarbons.

ways more convenient, way of expressing this curve is in terms of the temperature against the specific enthalpy $\tilde{h}$ (Fig. 4). Transferring one curve to another is quite straightforward and can be done by

$$\tilde{h} = \frac{Q - Q_r}{\mathrm{N}} \tag{11}$$

where Q_r is a reference value of Q that could conveniently be either the value at the lowest temperature reached in the system or the bubble-point value at the lowest pressure p; N is the total number of moles of fluid.

The condensation curve must always be provided to the heat exchanger designer. Typical information will be in a tabular form for a series of pressures spanning the range of interest for each mixture. Since the heat exchanger designer has to work with local conditions within the exchanger, the local pressure will always be known at any point in the calculation, and it is therefore possible to allow for the effect of pressure on the equilibrium temperature by interpolation between tables at given pressures. For the sake of clarity, however, the effect of pressure is omitted from the rest of this discussion.

In addition to there being a unique T-$\tilde{h}$ relationship at each pressure level, there is also a unique x-$\tilde{h}$ relationship, where x is the quality or the vapor phase mass fraction. When the condensation curve $(T\text{-}\tilde{h})$ is specified, the corresponding values of x must also be given (Fig. 4).

It is possible to consider the change in enthalpy of a binary or multicomponent fluid with temperature as made up of three terms:

$$d\tilde{h} = (1 - x)dT\tilde{c}_{p\ell} + xdT\tilde{c}_{pg} + \mathbf{ah\text{-}},\ dx \tag{12}$$

These are (1) the sensible heat change in the liquid phase $(1 - x)$; (2) the sensible heat change in the vapor phase (x); and (3) the heat of vaporization of an amount of liquid (dx). This concept differs from that for a single component system since, in that case, enthalpy changes are either sensible heat changes or latent heat changes (at constant temperature).

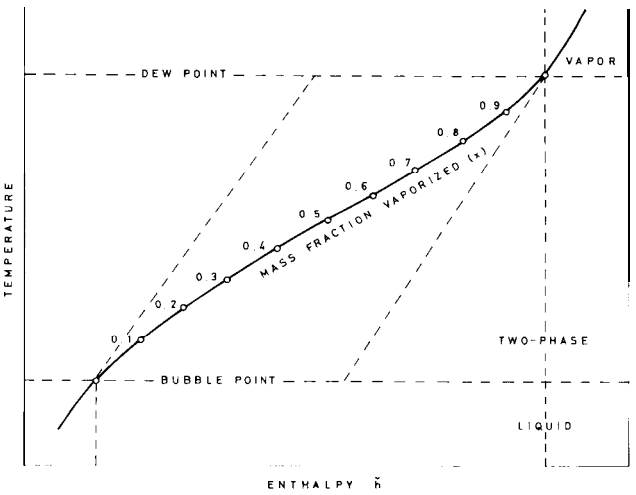

Figure 4 Temperature-enthalpy curve.

© 1983 Hemisphere Publishing Corporation

(c) Nucleation in a binary system

As with a single component system (Sec. 2.7.1), vapor may be formed from a binary liquid mixture at either a planar (stable equilibrium) or curved interface (unstable equilibrium). The superheat $(T_g - T_{sat})$ required to maintain a bubble embryo of radius r^* in equilibrium is given by

$$T_g - T_{sat} = \frac{2\sigma}{(\partial p_{sat}/\partial T)r^*} \tag{13}$$

For mixtures, both $\partial p_{sat}/\partial T$ and the surface tension σ depend on the composition as well as the temperature. The extended Clapeyron equation is given by [3, 4]

$$\frac{\partial p_{sat}}{\partial T} = \left(\frac{\partial p}{\partial T}\right)_{\tilde{x}} + \frac{p}{\tilde{R}T}\left(\frac{\partial \tilde{x}}{\partial T}\right)_p (K-1)\,\tilde{x}\left(\frac{\partial^2 g}{\partial \tilde{x}^2}\right)_{T,p} \tag{14}$$

where K is the equilibrium constant and g is the Gibbs free energy. For ideal systems, $(\partial^2 g/\partial \tilde{x}^2)_{T,p}$ is given by

$$\left(\frac{\partial^2 g}{\partial \tilde{x}^2}\right)_{T,p} = \frac{\tilde{R}T}{\tilde{x}(1-\tilde{x})} > 0 \tag{15}$$

The slope of the boiling-point curve on an equilibrium diagram at constant pressure can be evaluated by rearranging Eq. (14) and noting that $\partial p_{sat}/\partial T = 0$ at constant pressure and $(\partial p/\partial T)_{\tilde{x}} = p\Delta\tilde{h}_v/\tilde{R}T^2 = \rho_g \Delta h_v/T$. Rearranging Eq. (14) with these constraints,

$$\left(\frac{\partial T}{\partial \tilde{x}}\right)_p = -\frac{T}{\Delta\tilde{h}_v}(K-1)\,\tilde{x}\left(\frac{\partial^2 g}{\partial \tilde{x}^2}\right)_{T,p} \tag{16}$$

Alternatively, substituting for $(\partial^2 g/\partial \tilde{x}^2)_{T,p}$ from Eq. (15),

$$\left(\frac{\partial T}{\partial \tilde{x}}\right)_p = -\frac{pT}{\rho_g \Delta h_v}\frac{K-1}{1-\tilde{x}} \leqslant 0 \tag{17}$$

This expression can be seen to be almost independent of pressure.

The second term on the right-hand side of Eq. (14) is always negative. This means that the value of $\partial p_{sat}/\partial T$ is always somewhat less than the value for an equivalent pure liquid. Nevertheless, Shock [5] has shown that $\partial p_{sat}/\partial T$ for a binary mixture can be higher than the value for the pure components alone. If Eq. (13) is considered, the influence of this change in $\partial p_{sat}/\partial T$ is usually small compared with changes in both the surface tension σ and the size of the active nucleation sites on the heated surface r^*.

The addition of relatively small quantities of a second component to water often greatly reduces the surface tension. Figure 5 shows the changes in bubble-/dew-point temperature and in surface tension σ for two systems, ethanol-water and ethanol-benzene. This figure also shows the calculated superheat values as a function of r^* for these same two systems. For the ethanol-water system, the reduction in surface tension as the mole fraction of ethanol is increased causes a sharp drop in the superheat required to maintain a given size bubble embryo in equilibrium. Conversely, for the ethanol-benzene system, the variation of surface tension and also of superheat with composition is small.

(d) Size of nucleation sites

Before Eq. (13) can be used to estimate the superheat required of a mixture on a heated surface, it is necessary to know how the maximum size of nucleation site on the surface varies with composition. This maximum size is determined by the penetration of the liquid into preexisting cracks and flaws in the surface.

This penetration is influenced by changes in both surface tension and contact angle. Experimental evidence from Shock [5] suggests that these changes in the maximum size of nucleation site with composition can be profound. Table 1 shows the variation of the computed size of nucleation site at the onset of boiling on a nickel-plated surface for the ethanol-water system. On this evidence it would appear that changes in mixture composition, particularly when one of the components is water, may produce significant increases in the superheat required to initiate and sustain nucleation primarily as a result of a reduction in the contact angle and hence the maximum active nucleation site.

(e) Bubble growth in a binary system

Bubble growth in a single-component system is limited very rapidly by the rate at which heat can diffuse to the interface to provide the latent heat of vaporization. In a binary liquid mixture, however, a limitation also occurs as a result of the liquid close to the bubble interface becoming depleted in the more volatile component [6]. For vaporization and bubble growth to continue, the more volatile component must now diffuse from the bulk liquid through the depleted region. This is shown diagramatically in Fig. 6. The initial bulk liquid contains a mass fraction (x_0) of the more volatile liquid and is superheated by an amount $AT_{,,,}$ (to point E) above the boiling point corresponding to the initial liquid composition $T(\tilde{x}_0)$ (point D). At the bubble interface the mass concentration of the more volatile component in the liquid phase has fallen to x (point A), whereas the composition of the vapor within the bubble is y (point B). The corresponding

© 1983 Hemisphere publishing Corporation

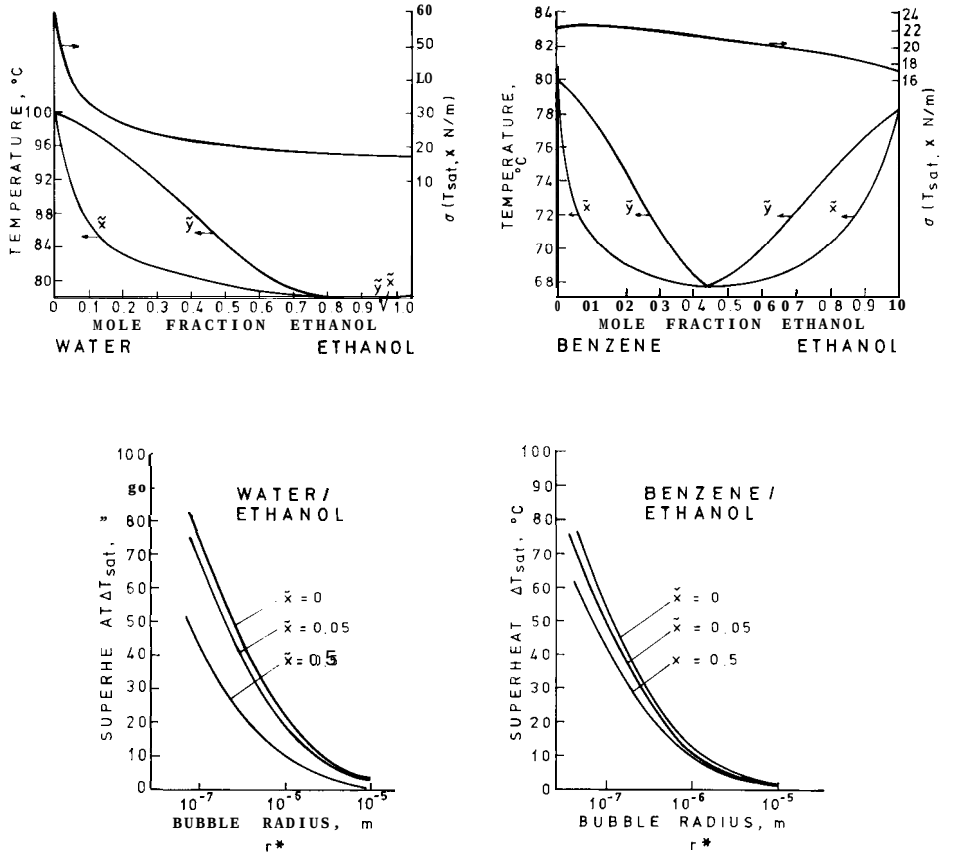

Figure 5 Nucleation in binary mixtures.

rise in the saturation temperature at the bubble wall $[T(x)-T(x_0)]$ is denoted by AT

Van Stralen [7,8] has given the theory for bubble growth in binary liquid mixtures. A mass balance at the interface for the more volatile component is

$$\rho_g(y-x)\dot{R} = \rho_\ell \delta \left(\frac{\partial x}{\partial r}\right)_{r=R} \tag{18}$$

If $(\partial x/\partial r)_{r=R}$ is approximated by assuming that the concentration falls from x_0 to x across a diffusion shell thickness of z_M, the bubble growth rate can be given as

$$\dot{R} = \frac{\rho_\ell}{P}\frac{(x_0-x)}{g(y-x)}\frac{\delta}{z_M} = \frac{\rho_\ell}{\rho_g}\frac{x\,(x_0-x)}{(y-x)}\frac{\delta}{(\pi/3)^{1/2}(Dt)^{1/2}} \tag{19}$$

Van Stralen has termed $(x_0-x)/(y-x)$ the ***vaporized mass diffusion fraction*** G_d.

It will also be seen from Fig. 6 that the effective superheat conducting heat to the bubble wall is not AT,,, but $AT_{,,,} - AT$. Thus the bubble growth rate is also given by

$$\dot{R} = \frac{\rho_\ell}{\rho_g}\frac{(\Delta T_{sat}-\Delta T)c_{p\ell}}{\Delta h_v}\frac{\kappa_\ell}{(\pi/3)^{1/2}(\kappa_\ell t)^{1/2}} \tag{20}$$

Equating Eqs. (19) and (20), substituting for G_d, and rearranging give

$$\frac{\Delta T}{G_d} = \left(\frac{\delta}{\kappa_\ell}\right)^{1/2}\frac{\Delta h_v}{c_{p\ell}}\left(\frac{\Delta T_{sat}}{\Delta T}-1\right) \tag{21}$$

Table 1 Variation of size of active nucleation site with composition for boiling of ethanol-water on a nickel-plated surface[a,b]

Composition mole fraction ethanol- $\tilde{x}$	Wall temperature at ONB,[c] °C	$T_g - T_{sat}$ at ONB, °C	$r_{max} \times 10^6$, m
0	138.2	9.9	1.05
0.058	**143.5**	**26.6**	**0.23**
0.058	**143.0**	**26.7**	**0.24**
0.058	**146.5**	**29.3**	**0.20**
0.058	**145.4**	**28.6**	**0.21**
0.197	145.2	**36.8**	**0.095**
0.197	145.0	**36.7**	**0.095**

From Shock[5]. (The author thanks the United Kingdom

[b] p = 2.5-2.6 bar.

[c] ONB, onset of nucleate boiling.

© 1983 Hemisphere Publishing Corporation

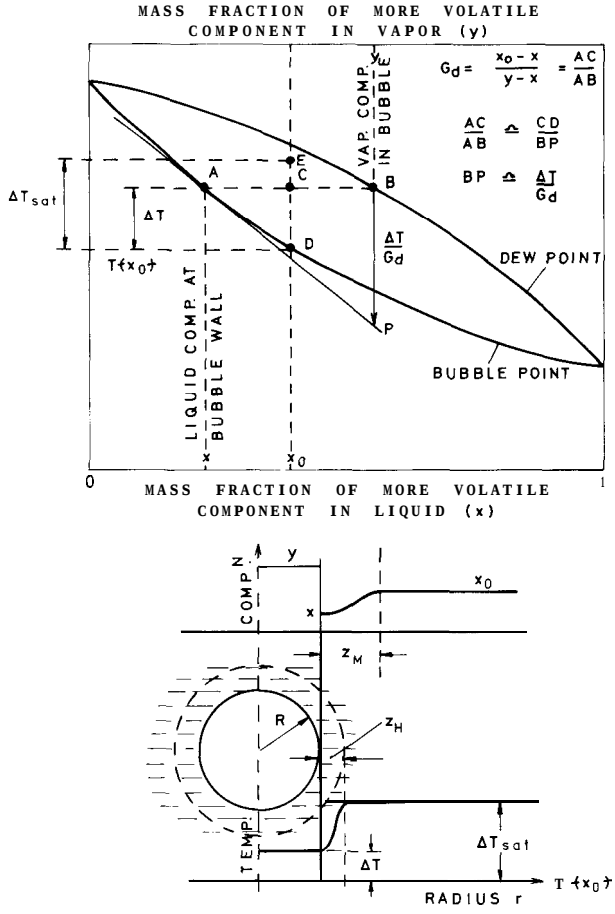

Figure 6 The gowth of vapor **bubbles in binary systems.**

It may be assumed that $\Delta T_{sat}/\Delta T$ and therefore $\Delta T/G_d$ are independent of the actual value of ΔT_{sat}:

$$\frac{\Delta T}{G_d}(x_0) = -(K-1)\, x_0 \left(\frac{\partial T}{\partial x}\right)_p \tag{22}$$

It may be estimated at x = x_0 using Eq. (17) for $(\partial T/\partial x)_p$ or evaluated graphically from equilibrium data as shown in Fig. 6.

The asymptotic bubble growth equation for binary fluid mixtures is obtained by substituting Eq. (21) in Eq. (20):

$$R = \frac{\Delta T_{sat}}{(\rho_g/\rho_\ell)[\Delta h_v/c_{p\ell} + (\kappa_\ell/\delta)^{1/2}(\Delta T/G_d)]} \left(\frac{3}{\pi}\frac{\kappa_\ell}{t}\right)^{1/2} \tag{23}$$

It can be seen that a minimum value of $\dot{R}$ for a binary mixture corresponds to a maximum value of $\Delta T/G_d$. This was confirmed by van Stralen using experimental observations.

The bubble growth rate in a binary system is sharply reduced from that for a single-component system, since the mass diffusivity δ of the more volatile component is an order of magnitude smaller than the thermal diffusivity κ_ℓ.

The much lower growth rate also results in much smaller bubbles at the point of departure from the surface. A further important point is that the proportion of the heat transferred to the bubble while still attached to the heating surface is greatly reduced in the case of mixtures, and in the case of binary mixtures the bubbles continue to growth significantly after their departure from the surface.

Zeugin et al. [9] have studied the behavior of the microlayer underneath a bubble formed from a binary liquid mixture and growing at a heated surface. As the bubble grows, initially, the surface temperature under the bubble falls sharply from the initial superheat to just above the bubble point of the liquid mixture. The surface temperature then recovers more slowly than in the case of pure liquids with the temperature rise following the increase in bubble point of the microlayer as the more volatile component is depleted. Evidently, vapor produced from evaporation of the microlayer will be less rich in the more volatile component than that produced from the rest of the bubble wall. If the microlayer evaporates completely, then the composition of the vapor produced will be that of the original liquid.

In summary, the addition of a second component to a pure liquid has a profound effect on such basic processes as the initiation of nucleation, bubble growth, and bubble departure from the heating surface. For the case where water is one of the components, these effects manifest themselves as a sharp increase in the surface superheat needed to initiate boiling, a corresponding reduced bubble growth rate leading to much reduced bubble departure diameters. Although the effects for mixtures of organic fluids are less pronounced, they still nevertheless greatly influence the mechanism of nucleate boiling and result in significantly reduced heat transfer coefficients compared with the pure fluid.

Nomenclature for ***Section 2.7.6 appears at the end*** of ***Section 2.7.8***

REFERENCES FOR SECTION 2.7.6

1. Bonilla, C. F., and Perry, C. W., Heat Transmission to Boiling Binary Mixtures, *Trans. AIChE.* vol. 37, pp. 685-705, 1941.
2. Cichelli, M. T., and Bonilla, C. F., Heat Transfer to Liquids Boiling Under Pressure, ***Trans. AIChE,*** vol. 40, pp. 755-787, 1944.

© 1983 Hemisphere Publishing Corporation

3. Stein, H. N., Some Thermodynamic Relations for Binary Liquid-Gas Equilibria, in ***Boiling*** Phenomena, S. van Stralen and R. Cole, vol. 2, pp. 535-553, Hemisphere, Washington, D.C., 1979.
4. Malesinsky, W., ***Azeotrophy and Other Theoretical Problems of Vapour-Liquid Equilibrium,*** Wiley-Interscience, London, 1965.
5. Shock, R. A. W., Nucleate Boiling in Binary Mixtures, ***Int. J. Heat Mass Transfer,*** vol 20, pp. 701-709, 1977.
6. Scriven, L. E., On the Dynamics of Phase Growth, ***Chem. Eng. Sci,*** vol. 10, no 1/2, pp. l-l 3, 1959.
7. Van Stralen, S. J. D., and Zijl, W., Fundamental Developments in Bubble Dynamics, ***Proc. 6th Int. Heat Transfer Conf., Toronto, August 7-11, 1978,*** vol. 6, pp. 429449, 1978.
8. Van Stralen, S. J. D., Bubble Growth Rates in Boiling Binary Mixtures, ***Br. Chem. Eng.,*** vol. 12, no. 3, pp. 390-394, 1967.
9. Zeugin, L., Donovan, J., and Mesler, R., A Study of Microlayer Evaporation for Three Binary Mixtures during Nucleate Boiling, ***Chem Eng. Sci.,*** vol. 30, pp. 679-683, 1975.

© 1983 Hemisphere Publishing Corporation

2.7.7

Boiling of binary and multicomponent mixtures: Pool boiling

J. G. Collier

■ The pool boiling curve is considerably altered when the fluid being evaporated is a binary mixture rather than a pure single-component liquid. The principal changes are shown diagramatically in Fig. 1. First, the onset of boiling is delayed to higher wall superheats as a result of the temperature gradients set up in the pool to accommodate the corresponding gradients in liquid composition. Heat transfer coefficients in the nucleate boiling region are sharply reduced. The critical heat flux may be increased or reduced depending on the extent of the contribution from convection in the pool. The minimum heat flux and the corresponding wall superheat are increased. Finally, heat transfer rates in the film boiling region are also somewhat higher.

A. Nucleate boiling

Even small amounts of a second component cause considerable reductions in the heat transfer rate under nucleate pool boiling conditions compared with that measured for the pure liquid. The reason for this reduction can be traced back to the influence of the second component on the bubble growth rate. The minimum bubble growth rate, the minimum heat transfer coefficient, and the occurrence of a maximum critical heat flux all occur at the same liquid composition corresponding to a maximum value of $|\tilde{y}-\tilde{x}|$. Starting with the early work of Bonilla and Perry [1] and Cichelli and Bonilla [2], many experimental studies of pool boiling of binary mixtures have been published. A good deal of useful experimental data for nucleate pool boiling of binary liquids have been presented by Sternling and Tichacek [3]. They used

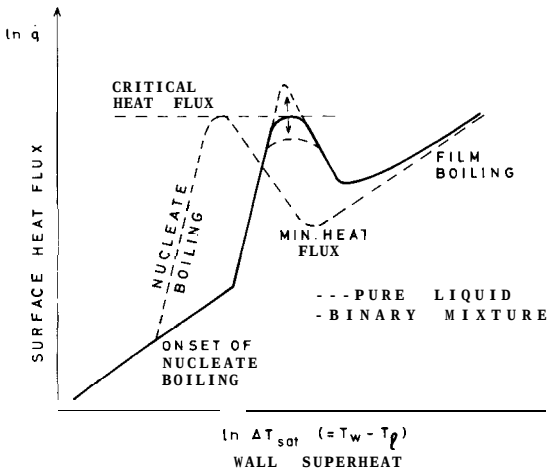

Figure 1 Schematic diagram showing principal changes to pool boiling curve for binary mixtures.

14 binary systems with components ranging from water to light alcohols to heavy oils. AU the mixtures had a wide boiling range, at least 90°C. For all the systems the heat transfer coefficient for a given heat flux was less than would be expected for an ideal single-component fluid with the same physical properties.

Stephan and Körner [4] have suggested a simple method whereby heat transfer coefficients in binary systems may be computed from data for the pure components. The method is illustrated in Fig. 2. The upper part of this diagram represents an equilibrium diagram for the system A-B and shows the mole fraction of component B in the vapor phase $(\tilde{y})$ plotted against the mole fraction of component B in

© 1983 Hemisphere Publishing Corporation

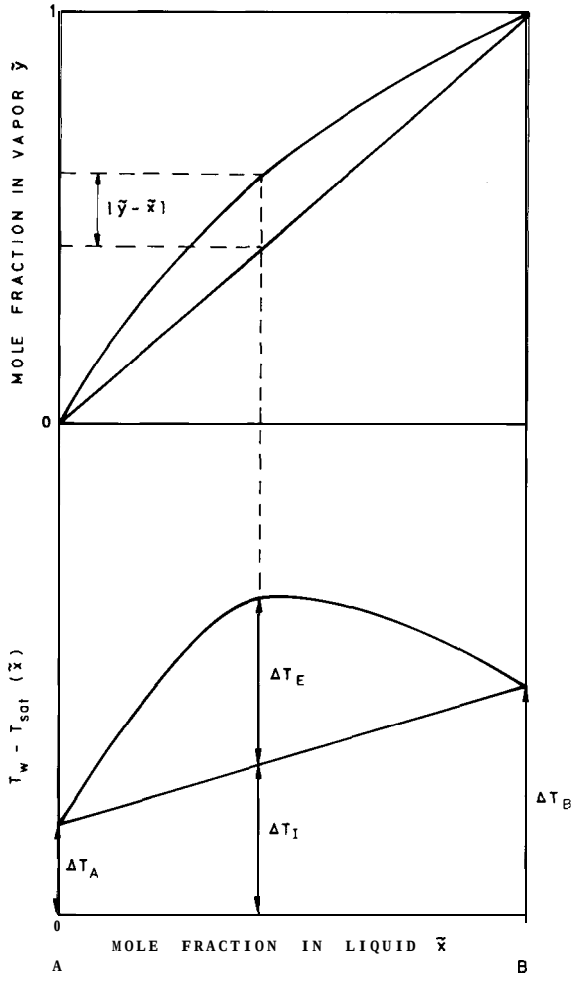

Figure 2 The evaluation of nucleate boiling heat transfer coefficients for binary systems. From Stephan and Körner[4].

the liquid phase $(\tilde{x})$ for a constant pressure. The lower part of the diagram shows the difference in temperature between the heating surface T_w and the bubble point $T_{sat}(\tilde{x})$ corresponding to a liquid composition $(\tilde{x})$. The curve of $(T_w - T_{sat}(\tilde{x}))$ passes through a maximum corresponding to the maximum value of $|\tilde{y} - \tilde{x}|$. The value of $(T_w - T_{sat}(\tilde{x}))$ may be expressed as

$$(T_w - T_{sat}(\tilde{x})) = \Delta T_I + \Delta T_E = \Delta T_I\ (1 + \Theta) \qquad (1)$$

ΔT_I is the ideal value of the temperature difference and is evaluated from the values of ΔT_{sat} for the two pure components A and B calculated for the same pressure and heat flux as the mixture. These wall superheat values will be denoted ΔT_A and ΔT_B, respectively. Then ΔT_I is given by

$$\Delta T_I = (1 - \tilde{x})\Delta T_A + \tilde{x}\Delta T_B \qquad (2)$$

Stephan and Körner found that Θ in Eq. (1) could be correlated against the value of $|\tilde{y} - \tilde{x}|$. Thus,

$$\Theta = \Lambda|\tilde{y} - \tilde{x}| \qquad (3)$$

A was found to vary with pressure, and over the pressure range l-10 bar the following expression was used :

$$A = Ae(0.88 + 0.12p) \qquad (4)$$

where p is the system pressure in bar and Λ_0 is a constant dependent on the particular binary system studied. Values of Λ_0 are given in Table 1 for 17 common systems. A value of Λ_0 of 1.53 was recommended when no experimental data for the system under consideration are available. This method is not reliable if one of the components is strongly surface active.

Happel and Stephan [5] have reported the results of pool boiling experiments with benzene-toluene, ethanol-benzene, and water-isobutanol mixtures over the entire range of compositions and at pressures of 0.5, 1, and 2.0 bar. The results were presented in terms of heat transfer coefficient rather than temperature difference. If there was no influence of mass transfer on the boiling process the heat transfer coefficient (ideal value) at any liquid composition $(\tilde{x})$ would be related to the coefficients of the pure components at the same condition (α_A, α_B):

$$\alpha_I = \alpha_A(1 - \tilde{x}) + \alpha_B\tilde{x} \qquad (5)$$

This differs from Eq. (2) in that now

$$\frac{1}{\Delta T_I} = \frac{1 - \tilde{x}}{\Delta T_A} + \frac{\tilde{x}}{\Delta T_B} \qquad (6)$$

Table 1 Value of Λ_0 for use in Eqs. (3) and (4) for the estimation of nucleate boiling heat transfer coefficients for binary mixtures[a]

System	Λ_0
Acetone-ethanol	0.75
Acetone-butanol	1.18
Acetone-water	1.40
Ethanol-benzene	0.42
Ethanol-cyclohexane	1.31
Ethanol-water	1.21
Benzene-toluene	1.44
Heptane-methyl cyclohexane	1.95
Isopropanol-water	2.04
Methanol-benzene	1.08
Methanol-amyl alcohol	0.8
Methyl ethyl ketone-toluene	1.32
Methyl ethyl ketone-water	1.21
Propanol-water	3.29
Water-glycol	1.47
Water-glycerine	1.50
Water-pyridin	3.56

[a] From Stephan and Körner [4].

© 1983 Hemisphere Publishing Corporation

Figure 3 shows results for benzene-toluene mixtures and confirms that the minimum coefficient does occur at the maximum value of $|\tilde{y}-\tilde{x}|$. For mixtures that form azeotropes (where the liquid and the vapor phases in equilibrium have the same composition; $|\tilde{y}-\tilde{x}| = 0$), however, such as ethanol-benzene, one might expect the heat transfer coefficient to approach the ideal value at the azeotropic composition, and this also is confirmed. The ratio of the actual to the ideal coefficient was correlated as a function of $|\tilde{y}-\tilde{x}|$.

$$\frac{\alpha}{\alpha_I} = \frac{\Delta T_I}{\mathrm{AT}} = 1 - B(\tilde{y}-\tilde{x})^n \tag{7}$$

where $\boldsymbol{B}$ depends on the mixture and the pressure. For benzene-toluene mixtures at 1 bar, $\boldsymbol{B}$ = 1.5 and n = 1.4; for ethanol-benzene mixtures, $\boldsymbol{B}$ = 1.25 and n = 1.0; and for water-isobutanol mixtures over their range of miscibility, $\boldsymbol{B}$ = **0.9** and n = 0.7.

One of the few correlations to attempt to relate quantitatively the reduction in bubble growth rate to the reduction in heat transfer coefficient is that of Calus and Rice [6]. The correlation reduces to a form

$$\alpha = \frac{\alpha_I}{[1 + |\tilde{y}-\tilde{x}|(\kappa_\ell/\delta)^{0.5}]^{0.7}} \tag{8}$$

where α_I is the ideal coefficient evaluated for the equivalent pure fluid using the modified Borishanski-Minchenko correlation described in Table 2.7.2(2); $|y-x|$ is based on the mass rather than mole fraction. Atlhough it is interesting to compare the form of this relationship with Eqs. (1) and (7), it should be noted that $(\kappa_\ell/\delta)^{0.5}$ does vary considerably with changes in mixture composition.

To extend these concepts to multicomponent mixtures ($n > 2$), Stephan and Preusser [7] have again made use of ΔT_I, the ideal value of the temperature difference, now defined as [cf. Eq. (2)]

$$\boldsymbol{AT,} = \sum_1^n \tilde{x}_i \Delta T_{\mathrm{sat},i} \tag{9}$$

also

$$\Theta = \sum_1^n \Lambda_i^{(n)}(\tilde{y}_i - \tilde{x}_i) \tag{10}$$

For a ternary mixture (n = 3), we therefore obtain

$$\Theta = \Lambda_1^{(3)}(\tilde{y}_1 - \tilde{x}_1) + \Lambda_2^{(3)}(\tilde{y}_2 - \tilde{x}_2) \tag{11}$$

Since a ternary mixture includes as limiting cases the three- binary mixtures, for a binary mixture consisting of components 1 and 3 ($\tilde{y}_2 = \tilde{x}_2 = 0$) and for another mixture consisting only of components 2 and 3 ($\tilde{y}_1 = \tilde{x}_1 = 0$),

$\Lambda_1^{(3)} = \Lambda_{13}$ and $\Lambda_2^{(3)} = \Lambda_{23}$

In a similar manner, for a mixture of n components,

$\Lambda_i^{(n)} = \Lambda_{in}$ $(i = 1, 2, \ldots, n-1)$

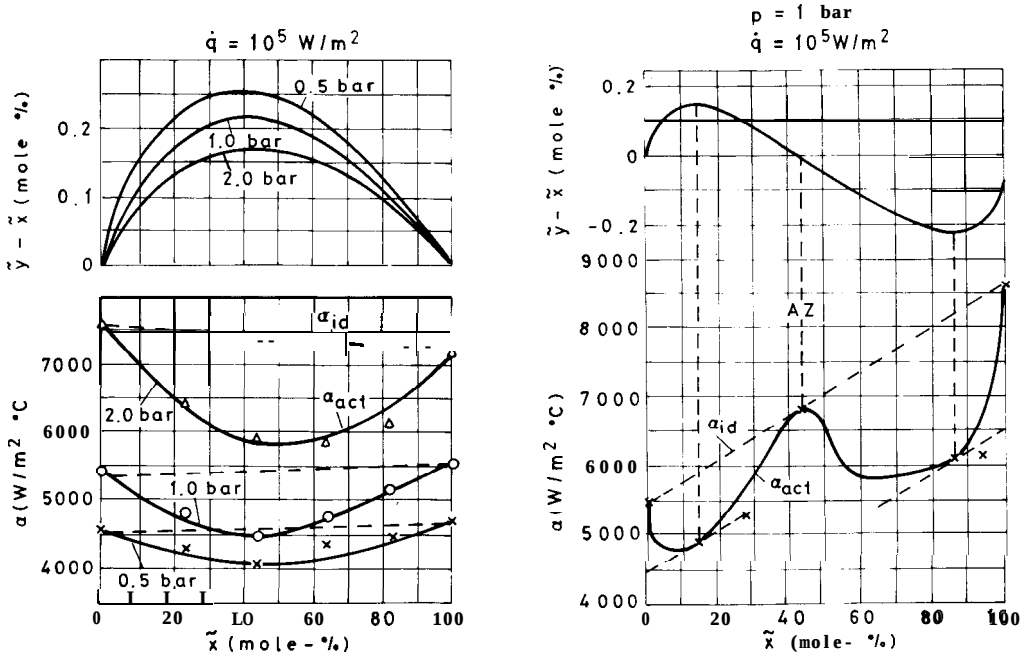

Figure 3 Variation of heat transfer coefficient for binary mixtures with composition and pressure. From Happel and Stephan [5].

© 1983 Hemisphere Publishing Corporation

In this way the unknown value of $\Lambda_i^{(n)}$ can be determined from the known values of A measured for the separate binary mixtures. In one example quoted by Stephan and Preusser, satisfactory agreement was achieved between this method and experimental results for an acetone-methanol-water ternary mixture.

B. Critical heat flux

Changes in the pool boiling critical heat flux occur when small amounts of a second component are added to a pure liquid. The critical heat flux may be higher or lower than the value for either component alone. As with the heat transfer coefficient in nucleate boiling, the change induced by the second component would appear to be large compared with the small changes in physical properties (surface tension; viscosity and density) attributed to the second component. It is, therefore, not possible to predict, a priori, the influence a second component might have on the critical heat flux simply by substituting the altered physical properties into an equation of the type proposed for pool boiling critical heat flux by Kutateladze [8] or Zuber et al. [9] *(see Sec.* 2.7.2C).

The experimental and theoretical understanding of the critical heat flux phenomenon for binary mixtures has been increased very considerably by the work of van Stralen [10]. The early investigations suggested the action of several conflicting mechanisms regarding such variables as the volatility, the molecular weight of the second component, and the geometry of the heating section. Some of this early work and the resulting explanations are reviewed briefly below.

Lowry and Westwater [11] suggested that their observed increases in the critical heat flux for methanol were due to the second component providing particles that acted as nucleation sites within the superheated boundary layer. Van Stralen [12] concluded that the increases he observed in the critical heat flux for water with the addition of a more volatile component were due to the formation of smaller bubbles (see Sec. 2.7.6). Dunkus and Westwater [13] obtained data on the effects of various additives on the heat transfer characteristics of boiling isopropanol. They concluded that when the second component came from the same homologous series, the magnitude of the increase was greater the higher the molecular weight. A decreased volatility of the second component also increased the critical heat flux. These authors suggested that the increases could be attributed to a depletion of the solvent with respect to the nonvolatile second component at the bubble wall leaving the bubble surrounded by a fluid of high viscosity, which tended to reduce coalescence between bubbles, promote foaming, and also reduce the motion of eddies.

An effect of geometry was observed by Kutateladze [14] for boiling on a wire and a plate. In this instance, butanol was used to influence the critical heat flux for water at a pressure of 10 bar. For a wire heater the critical heat flux had a maximum at about 10% butanol of 2.5 times the value for pure water. For a plate heater the critical heat flux had a minimum at about 6% butanol of 0.56 times the value for pure water. A similar discrepancy was found by Owens [15] when he compared his results for the boiling on a stainless steel tube of water containing various additives with the results obtained by van Stralen [12] for similar binary systems using a thin wire heater.

The more recent work of van Stralen [10] has presented an explanation for many of the phenomena reported above. Van Stralen has shown that the maximum often observed in the critical heat flux with binary mixtures corresponds to the minimum bubble growth rate and to the maximum value of $|\tilde{y} - \tilde{x}|$. The lower bubble growth rate considerably reduces the heat transfer coefficient from the heating surface to the boiling fluid, with the result that the wall superheat is considerably increased. The critical heat flux can be considered as the sum of two terms, one resulting from direct vaporization at the heating surface and the second from convection of hot liquid away from the heating surface coupled with indirect vaporization into the bubble away from the heating surface. The work of Costello et al. [16] and of Lienhard and Keeling [17] suggests that even for pure liquids the second term is important. These latter workers examined the influence of a parameter I, which was termed an induced convection scale parameter and which represented a balance among inertia, surface tension, and viscous forces:

$$I = \left(\frac{\rho_\ell \, Lo}{\eta_\ell^2} \right)^{1/2} \tag{12}$$

where L is the characteristic dimension of the surface (width, diameter, etc). At large values of the parameter I, the critical heat flux $\dot{q}_{cr}$ dropped considerably below that predicted from the Zuber equation, $\dot{q}_{cr,z}$ [Eq. 2.7.2(17)] and approached a value approximately $0.5\dot{q}_{cr,z}$ when $I > 1\,500$ and $L' \cong 50$. L' is the dimensionless heater size, given by

$$L' = L \left[\frac{g_n(\rho_\ell - \rho_g)}{\sigma} \right]^{1/2}$$

Figure 4 shows the influence of the parameter I on the ratio $\dot{q}_{cr}/\dot{q}_{cr,z}$ for a narrow range of values of L'.

Van Stralen [10] was able to show that for binary

© 1983 Hemisphere Publishing Corporation

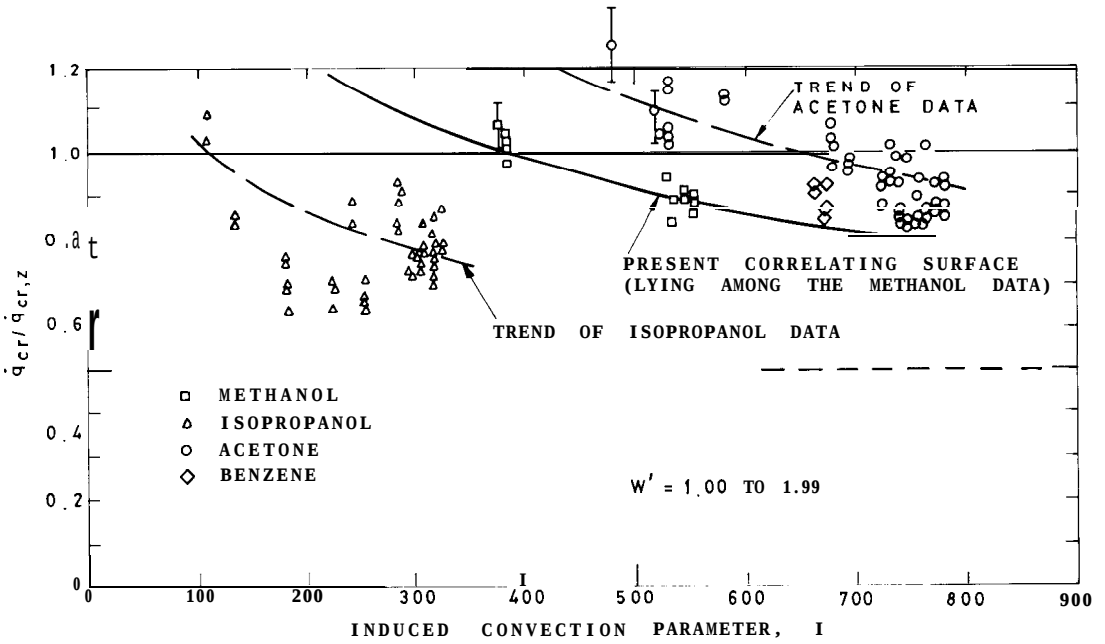

Figure 4 Influence of induced convection on pool boiling critical heat flux. From Lienhard and Keeling [17].

systems also the induced convective component of the critical heat flux can be large. The work of Lienhard and Keeling offers a possible explanation for the observations of Owens [15] and Kutateladze [14] concerning the effect of heater geometry. Clearly the increases of critical heat flux observed with thin wires relate to situations where both I and L' are small, i.e., where capillary and viscous forces outweigh buoyancy forces. For the larger heaters associated with process equipment, it is doubtful if such increases in critical heat flux will occur. Indeed, van Stralen points out that the first component of the critical heat flux, that attributable to direct vaporization, is, in fact, decreased by going to a binary system. This is also consistent with Lienhard and Keeling s analysis and with the reduced fraction of the heat transferred to the bubble while it is still attached to the heater surface.

Therefore, to estimate the critical heat flux for a binary mixture, it is recommended that the influence of heater size and induced convection be characterized by evaluating L' and I. For low values of $L'(< 1)$ and $I(< 500)$, an increase in the critical heat flux above that for the pure components may be anticipated. A maximum value will occur at $|\tilde{y} - \tilde{x}|$. For intermediate values of L' and I, the critical heat flux is likely to be close to that arrived at by substituting the mixture physical properties into the expression given in Sec. 2.7.2C. For large values of $L'(\cong 50)$ and $I(\cong 1\,500)$, the critical heat flux for the mixture may fall below that for the pure components. However, it will not fall to less than $0.5\dot{q}_{cr,z}$.

C. Transition boiling

Little has been published on transition boiling of binary mixtures. Happel and Stephan [5] report that qualitatively the composition of the mixture has a similar influence as in the nucleate boiling region.

D. Minimum heat flux

The additional diffusional resistance in the liquid phase due to the mass transfer of the more volatile component into the vapor film at the heating surface results in the interface being at a higher temperature (T_i) than the rest of the liquid (T_∞). A significant proportion of the total heat flux passing through the vapor film is therefore conducted from the interface into the bulk liquid rather than forming vapor directly. As a consequence, the vapor film is thinner. Van Stralen et al. [18], studying film boiling of water-2-butanone mixtures on a thin wire, observed that direct vapor production at the heating surface corresponded to only 53% of the applied heat flux compared with a figure of 95% for pure fluids. The remaining component of the heat flux is convected into the liquid phase and thence indirectly into the vapor bubbles. Thus the minimum heat flux may be expected to be greater for a binary mixture compared with an equivalent pure fluid.

Yue and Weber [19] have examined the minimum heat flux for horizontal cylinders. The minimum AT is given by

© 1983 Hemisphere Publishing Corporation

$$\Delta T_{\min} = (T_w - T_i) + (T_i - T_\infty) \quad (13)$$

where $T_w - T_i$ is the temperature drop across the vapor film and $T_i - T_\infty$ is that through the liquid. The latter is, as just noted, essentially zero for a pure liquid.

The first term is calculated from a semiempirical relationship that Yue and Weber developed from Berenson s correlation, Eq2.7.2(31):

$$T_w - T_i = 0.42 \left(\frac{D}{\lambda_d}\right)^{1/3} \frac{\rho_g \Delta h_v}{\lambda_g} \left[\frac{g_n(\rho_\ell - \rho_g)}{\rho_\ell + \rho_g}\right]^{2/3} \times \left[\frac{\sigma}{g_n(\rho_\ell - \rho_g)}\right]^{1/2} \left[\frac{\eta_g}{g_n(\rho_\ell - \rho_g)}\right]^{1/3} \quad (14)$$

where λ_d is the most rapidly growing Taylor instability wavelength given by Eq. 2.7.2(34). Equation (14) is valid for $0.2\lambda_d < D < \lambda_d$.

The second term is correlated as a function of $T^* - T_\infty$, where T^* is the dew point of a vapor mixture having the same composition as the liquid (Fig. 5).

$$T_i - T_\infty = \frac{y - x}{(y - x)_{\max}} (T^* - T_\infty) \quad (15)$$

Experiments were conducted on mixtures of acetone-hexanol, benzene-cumene, isopropanol-toluene, *n*-hexane-toluene, and ethanol-ethylbenzene on a horizontal cylinder 7.9 mm is diameter.

E. Film boiling

Yue and Weber [20] have carried out a theoretical and experimental study of film boiling of binary mixtures on a vertical plate. The analysis assumes a two-phase boundary layer and involves vapor formation by evaporation at an approximately planar interface with no vapor removal by bubble formation. The heat flux, for a given wall superheat, is increased as a result of the heat convected from the interface into the bulk liquid. Contrast this with the situation in the nucleate boiling region where, for a given wall superheat, heat fluxes are reduced by the addition of a second component. A point is reached, however, where the heat flux is sufficiently high to reduce the concentration of the more volatile component at the interface to zero. The heat flux through the liquid phase is then at its maximum and as the overall heat flux is increased, thus becomes a smaller fraction of the total. The effect of the second phase is predicted to disappear at values of wall superheat above that given by

$$T_w - T_\infty = \frac{3\Delta h_v}{c_{pg}} \mathrm{Pr}_g \quad (16)$$

where T_∞ is the bulk liquid temperature remote from the vapor film. Experimental results generally confirm the analytic predictions. For acetone-cyclohexanol mixtures with a relative volatility of up to 80, the simple Bromley relationship [Eq. 2.7.2(36)] yields heat fluxes as much as 30% too low. The contribution from radiation evaluated from Eq. 2.7.2(44) must also be included.

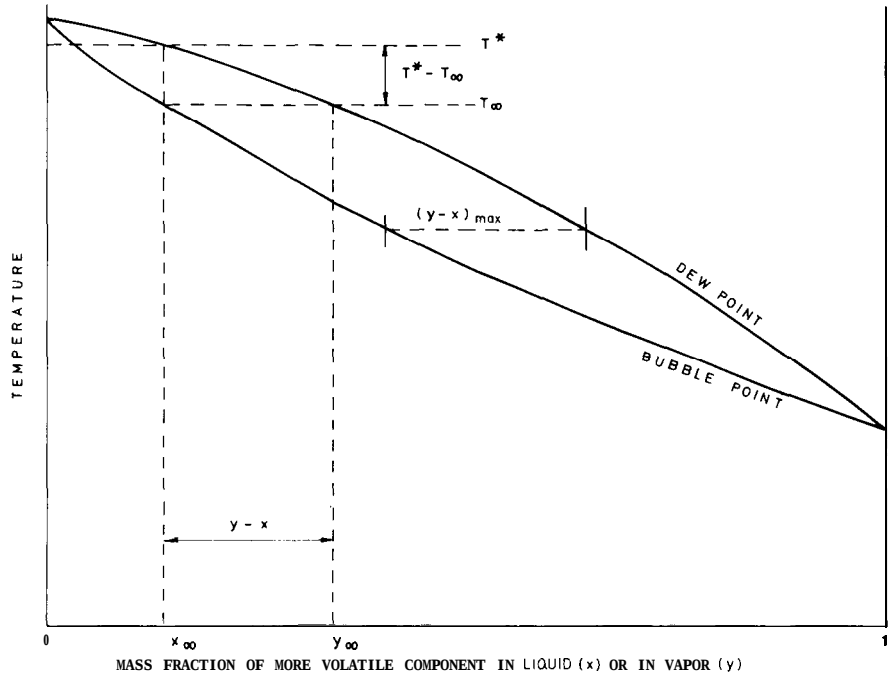

Figure 5 Definition of terms for Yue and Weber minimum heat flux correlation. From Yue and Weber [19].

© 1983 Hemisphere Publishing Corporation

Nomenclature for *Section 2.7.7 appears at the end* of *Section 2.7.8.*

REFERENCES FOR SECTION 2.7.7

1. Bonilla, C. F., and Perry, C. W., Heat Transmission to Boiling Binary Mixtures, *Trans. AIChE,* ***vol. 37,*** pp. 685-705, 1941.
2. Cichelli, M. T., and Bonilla, C. F., Heat Transfer to Liquids Boiling under ***Pressure, Trans.*** *AIChE,* vol. 40, pp. 755-787, 1944.
3. Sternling, C. V., and Tichacek, L. J., Heat Transfer Coefficients for Boiling Mixtures, *Chem.* ***Eng. Sci.***, vol. 16, no. 4, pp. 297-337, 1961.
4. Stephan, K., and Körner, M., Calculation of Heat Transfer in Evaporating Binary Liquid Mixtures, *Chem.* Zng. ***Tech.,*** vol. 41, no. ***7,*** pp. 409-717, 1969.
5. Happel, O., and Stephan, K., Heat Transfer from Nucleate Boiling to the Beginning of Film Boiling in Binary Mixtures, *Proc.* ***5th Znt. Heat Transfer Conf., Tokyo, September*** 3-7, 1974, Paper B7.8, 1974.
6. Calus, W. F., and Rice, P., Pool Boiling-Binary Liquid Mixtures, ***Chem. Eng. Sci.,*** vol. 27, pp. 1687-1697, 1972.
7. Stephan, K., and Preusser, P., Heat Transfer in Natural Convection Boiling of Polynary Mixtures, *Proc.* ***6th Znt. Heat Transfer Conf., Toronto, August 7-11, 1978, vol.*** 1, pp. 187-192, 1978.
8. Kutateladze, S. S., A Hydrodynamic Theory of Changes in the Boiling Process Under Free Convection, ***Zzv. Akad. Nauk SSR Otd. Tekh.*** *Nauk,* no. 4, p. 529, 1951.
9. Zuber, N., Tribus, M., and Westwater, J. W., The Hydrodynamic Crisis in Pool Boiling of Saturated and Subcooled Liquids, *Proc.* ***Znt. Heat Transfer*** *Conf.,* Boulder, Colo., Paper 27, August 1961.
10. Van Stralen, S. J. D., The Mechanism of Nucleate Boiling in Pure Liquids and in Binary Mixtures, pt. I and pt. ***II,*** *Int. J.* ***Heat Mass Transfer,*** vol. 9, pp. 995-1046, 1966.
11. Lowry, A. J., Jr., and Westwater, J. W., Heat Transfer to Boiling Methanol-Effect of Added Agents, ***Znd. Eng. Chem.,*** vol. 49, pp. 1445-1448, 1957.
12. Van Stralen, S. J. D., Heat Transfer to Boiling Binary Liquid Mixtures, pt. I and pt. II, ***Br. Chem. Eng.,*** vol. 4, no. 1, pp. 8-17, 1959, and vol. 4, no. 2, pp. 78-82, 1959.
13. Dunkus, T., and Westwater, J. W., The Effect of Trace Additions on the Heat Transfer to Boiling Isopropanol, *AIChE/ASME* ***Natl. Heat Transfer*** *Conf.,* Buffalo, N.Y. AIChE Preprint 30, August 1960.
14. Kutateladze, S. S., Boiling Heat Transfer, ***Znt. J. Heat Mass Transfer, vol.*** 1, pp. 31-45, 1961.
15. Owens, W. L., Jr., An Analytical and Experimental Study of Pool Boiling with Particular Reference to Additions, ***UKAEA Rept.*** AEEW-180, 1964.
16. Costello, C. P., Bock, C. O., and Nichols, C. C., A Study of Induced Convective Effects on Pool Boiling Burnout, ***Chem. Eng.*** *Prog.* ***Symp. Ser.,*** vol. 61, pp. 271-280, 1965.
17. Lienhard, J. H., and Keeling, K. B., An Induced-Convection Effect upon the Peak Boiling Heat Flux, ***J. Heat Transfer,*** vol. 92, pp. 1-5, 1970.
18. Van Stralen, S. J. D., Joosen, C. J. J., and Sluyter, W. M., Film Boiling of Water and an Aqueous Binary Mixture, *Int. J.* ***Heat Mass Transfer,*** vol. 15, pp. 2427-2445, 1972.
19. Yue, P. L., and Weber, M. E., Minimum Film Boiling Flux of Binary Mixtures, ***Trans. Inst. Chem. Eng.,*** vol. 52, pp. 217-221, 1974.
20. Yue, P. L., and Weber, M. E., Film Boiling of Saturated Binary Mixtures, *Int. J.* ***Heat Mass Transfer,*** vol. 16, pp. 1877-1887, 1973.

© 1983 Hemisphere Publishing Corporation

2.7.8

Boiling of binary and multicomponent mixtures: Forced convection boiling

J. G. Collier

■ The published literature on forced convection vaporization of mixtures is very limited. One of the earliest published studies is that of McAdams et al. [1], who in 1940 carried out experiments using a four-pass horizontal-tube evaporator heated by steam. Each pass had three separate steam jackets to allow the local heat flux to be measured. The fluid was a benzene-oil mixture. Bulk fluid temperatures were found to increase throughout the saturated boiling length as the liquid became richer in oil. Thus, some of the heat transferred to the liquid was retained in the form of sensible heat to maintain the fluid at saturation conditions and was not available for evaporation. Average boiling heat transfer coefficients were calculated for each pass where boiling occurred in all three jackets. At a given vapor mass quality, the coefficient decreased as the oil content of the feed increased.

A number of workers [2, 3] have studied the performance of complete reboilers, but such studies cannot provide information on the local conditions in the evaporating stream.

A. Saturated nucleate boiling

Saturated nucleate boiling will be influenced by the addition of a second component in the same qualitative manner as nucleate pool boiling (Sec. 2.7.7). The well-known Chen correlation (see Sec. 2.7.3) is formed by adding together a nucleate boiling (α_{nb}) and a convective heat transfer (a,) contribution. The nucleate boiling contribution may be modified in the manner proposed by Stephan and Körner [4] for pool boiling and then becomes

$$\frac{1}{\alpha_{nb}} = \left(\frac{1-\tilde{x}}{S\alpha_A} + \frac{\tilde{x}}{S\alpha_B}\right)(1 + \Lambda|\tilde{y} - \tilde{x}|) \qquad (1)$$

where $\tilde{x}$ is the mole fraction of the more volatile component B in the liquid phase, $\tilde{y}$ is the mole fraction in the vapor phase, α_A and α_B are the nucleate pool boiling coefficients for the pure components A and B at the same heat flux, and S is the suppression factor introduced by Chen to allow for temperature gradient effects.

The convective heat transfer coefficient α_c may be computed from the mixture physical properties in the manner for a pure fluid. However, this term also may be influenced by the second component, particularly at low qualities where bubbly flow occurs. The stripping of the more volatile component into the bubble cavity leaves around each bubble a shell of more viscous, nonvolatile liquid. This tends to inhibit bubbie coalescence because of the increased time needed for drainage of the fii between colliding bubbles. The consequence usually is the formation of a foam that is stable to higher void fractions than is normal for pure liquids. In bubbly flow any increase in the convective heat transfer results primarily from the increased liquid velocity as a consequence of the increased liquid-vapor volumetric flow:

$$\frac{\alpha_{tp}}{\alpha_{\ell}} = \left(\frac{1}{1-\epsilon_g}\right)^{0.8} \qquad (2)$$

where ϵ_g is the void fraction.

© 1983 Hemisphere 1 ıblishing Corporation

The presence of vapor may also induce turbulence in an otherwise laminar liquid flow but, in any case, the increase over the single-phase heat transfer coefficient predicted by Eq. (2) is relatively small (<2). In some instances, the two-phase convective heat transfer coefficient (α_{tp}) may turn out to be lower than the single-phase value (α_ℓ). This is because the correct fluid properties for the calculation of α_ℓ in Eq. (2) are those of the more viscous, nonvolatile liquid surrounding the bubble cavity. The composition in this liquid may be estimated using the concept of G_d, the ***vaporized mass diffusion fraction,*** introduced by van Stralen and discussed in Sec. 2.7.6.

B. Two-phase forced convection region

Farther up the evaporator tube, annular flow is formed and this flow pattern will occupy most of the channel length. The liquid is displaced to the heating wall and it is necessary to evaluate mass transfer effects, first within the liquid film and subsequently within the vapor core. Shock [5] has considered these effects in some detail.

Consider first the liquid film, Fig. 1. If the molar concentration of component A is represented by $\tilde{c}$, then the conservation equation in the liquid film is given by

$$u_x \frac{\partial \tilde{c}}{\partial x} + u_y \frac{\partial \tilde{c}}{\partial y} + u_z \frac{\partial \tilde{c}}{\partial z} = \delta_{\text{eff}} \left(\frac{\partial^2 \tilde{c}}{\partial x^2} + \frac{\partial^2 \tilde{c}}{\partial y^2} + \frac{\partial^2 \tilde{c}}{\partial z^2} \right) \tag{3}$$

There is no net convection in the x and y directions, and assuming that the concentration profile in the y direction is fully developed,

$$u_z \frac{\partial \tilde{c}}{\partial z} = \delta_{\text{eff}} \left(\frac{\partial^2 c}{\partial y^2} \right) \tag{4}$$

This equation must be integrated using an expression for the mass diffusivity δ_{eff}:

$$J = -(\delta + \epsilon_M) \frac{\partial \tilde{c}}{\partial y} = -\delta_{\text{eff}} \left(\frac{\partial \tilde{c}}{\partial y} \right) \tag{5}$$

For a laminar film, $\delta_{\text{eff}} = 6$, and

$$\int_0^m u_z \frac{\partial \tilde{c}}{\partial c} dy = \delta \int_0^m \frac{\partial^2 \tilde{c}}{\partial y^2} dy \tag{6}$$

Define a mean bulk molar concentration $\tilde{c}_A$ at any location z such that

$$\tilde{c}_A = \frac{1}{\dot{V}} \int_0^m u_z \tilde{c} \, dy \tag{7}$$

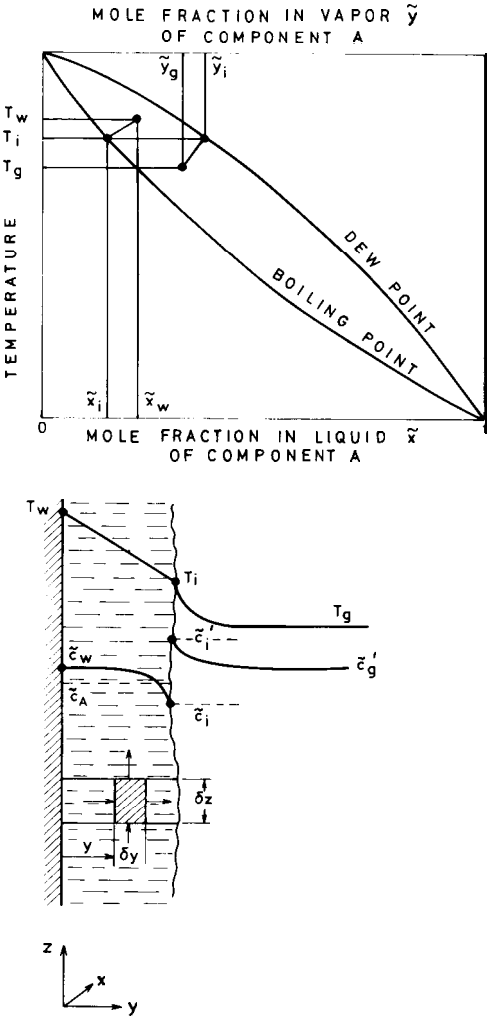

Figure 1 Mass transfer from a thin liquid film. Data from Shock [5].

where $\dot{V}$ is the volumetric flow rate per unit wetted perimeter :

$$\dot{V} = \int_0^m u_z \, dy \tag{8}$$

Also,

$$\dot{V} \frac{\partial \tilde{c}_A}{\partial z} = -J_i \tag{9}$$

where J_i is the molar flux at the interface:

$$\frac{\partial \tilde{c}}{\partial z} = \frac{\partial \tilde{c}_A}{\partial z} = -\frac{J_i}{\dot{V}} \tag{10}$$

Substituting for $\partial \tilde{c}/\partial z$ in Eq. (4) leads to

$$\frac{\partial^2 \tilde{c}}{\partial y^2} = -\frac{J_i u_z}{\dot{V} \delta} \tag{11}$$

© 1983 Hemisphere Publishing Corporation

or

$$\frac{\partial \tilde{c}}{\partial y} = -\frac{J_i}{\dot{V}\delta}\int_0^y u_z\, dy \tag{12}$$

Define a molar mass transfer coefficient ***kp:***

$$k_\ell = \frac{J_i}{\tilde{c}_A - \tilde{c}_i} \tag{13}$$

1. ***For a laminar falling film,*** the Sherwood number is given by

$$\mathrm{Sh}_\ell = \frac{k_\ell m}{\delta} = \frac{70}{17} \tag{14}$$

or, combining it with the relevant expression for film thickness to give an explicit relationship for the mass transfer coefficient k_ℓ,

$$m = \left[\frac{3\dot{V}\eta_\ell}{(\rho_\ell - \rho_g)g_n}\right]^{1/3} \qquad k_\ell = \frac{70}{17}\left[\frac{(\rho_\ell - \rho_g)g_n\delta^3}{3\dot{V}\eta_\ell}\right]^{1/3} \tag{15}$$

By analogy with the situation for heat transfer, it seems probable that the actual mass transfer coefficient will be higher than that given by Eq. (15) because of the presence of waves.

2. For ***a laminar film with constant shear stress across the film*** (as in upward annular flow at high interfacial shear), the Sherwood number is given by

$$\mathrm{Sh}_\ell = \frac{k_\ell m}{\delta} = 5 \tag{16}$$

or, combining it with the relevant expression for film thickness to give an explicit relationship for the mass transfer coefficient k_ℓ,

$$m = \left(\frac{2\dot{V}\eta_\ell}{\tau_i}\right)^{1/2} \qquad k_\ell = 5\left(\frac{\tau_i\delta^2}{2\dot{V}\eta_\ell}\right)^{1/2} \tag{17}$$

where τ_i is the interfacial shear stress. If the analogy with the heat transfer situation applies, mass transfer coefficients in practice may be lower than estimated from Eq. (17) by about 30%.

3. Turbulence within the liquid *film* will enhance the mass transfer coefficient for a given film thickness. Equation (5) applies, where ϵ_m is the ***eddy mass diffusivity.*** Expressions for turbulent mass transfer in liquid films can be developed by an analogous procedure to that used to establish the hydrodynamic and heat transfer characteristics of the film. Shock [5] assumed that ϵ_m for use in Eq. (5) was identical to the eddy viscosity ϵ and that the expression given by Deissler for ϵ could be used to establish the relationship between a dimensionless concentration C^+ and a dimensionless distance y^+. C^+ is defined as

$$C^+ = \frac{u^*}{J_i}(\tilde{c} - \tilde{c}_i) \tag{18}$$

where u^* is the friction velocity (= $\sqrt{(\tau/\rho_\ell)}$). Mass transfer coefficients were deduced from the dimensionless concentration profile evaluated at the appropriate value of the dimensionless film thickness y_i^+. The molar mass transfer coefficient k_ℓ is defined as

$$k_\ell = \frac{J_i}{\tilde{c}_A - \tilde{c}_i} = \frac{u^*}{C_b^+} \tag{19}$$

where C_b^+ is the bulk value of C^+ evaluated from the profiles of C^+ and y^+. A liquid film Sherwood number can also be defined as

$$\mathrm{Sh}_\ell = \frac{k_\ell m}{\delta} = \frac{\mathrm{SC}\, y_i^+}{C_b^+}$$

For the case of constant shear stress across the film, Shock [5] has produced tables of Sh_ℓ against film Reynolds number Rep with Schmidt number (SC) as parameter. The following equation fits the results of Shock acceptably well:

$$\mathrm{Sh}_\ell = 5 - 0.11\ \mathrm{SC} + 0.01\ \mathrm{Re}_\ell\ \mathrm{SC} \tag{20}$$

C. Simplified treatment for binary and multicomponent evaporation

Consider a simple single-pass evaporator heated by a fluid stream in counter-current flow. The subscripts ***h*** and e stand for the heating and evaporating streams, respectively:

$$\frac{d\dot{Q}}{dz} = \dot{M}_e\frac{dh_e}{dz} = \dot{M}_h\frac{dh_h}{dz} = UA(T_h - T_e) \tag{21}$$

In Eq. (21), ***A*** is the effective heat exchange area per unit length (perimeter), allowing for any secondary surface that may be present, U is the overall heat transfer coefficient, and T_h and T_e are, respectively, the local temperature of the heating stream and the equilibrium (bubble-point) temperature of the evaporating stream.

If the local values of the enthalpies h_h and h_e are known, then the temperatures T_h and T_e are also known, together with the mass fraction vaporized (x_e). This, together with the flow rates, provides sufficient information to calculate the overall coefficient U. Thus Eq. (21) can be progressively integrated along the evaporator starting from known conditions at the evaporator inlet (z = 0).

Define Γ as the flow rate per unit perimeter,

© 1983 Hemisphere Publishing Corporation

$$\Gamma_e = \frac{\dot{M}_e}{A} \tag{22}$$

Likewise, the product $U(T_h - T_e)$ represents the heat flux $(\dot{q}_w)$ passing through the wall separating the two streams:

$$\dot{q}_w = U(T_h - T_e) \tag{23}$$

Substituting Eqs. (22) and (23) into Eq. (21),

$$\dot{q}_w\, dz = \Gamma_e\, dh, \tag{24}$$

Consider Fig. 2, which shows a section of an evaporator heated by a fluid stream in counter-current flow separated from the vaporizing stream by a wall. The heating stream is flowing downward and the evaporating stream upward. It is assumed that the flow pattern on the evaporating side is annular flow and that the evaporating liquid is displaced to the wall as a thin liquid film.

Consider the situation at a position z from the evaporator inlet and over a length dz. There is a change of evaporating fluid bubble-point temperature over this length so that

$$dh = (1 - x_e)dT_e c_{p\ell} + x_e dT_e c_{pg} + dx_e \Delta h_v \tag{25}$$

Now the heat flux through the vapor-liquid interface q_i is less than $\dot{q}_w$ by the amount of the flux absorbed in heating the liquid flow $\Gamma_e(1-x_e)$ through dT_e. Therefore,

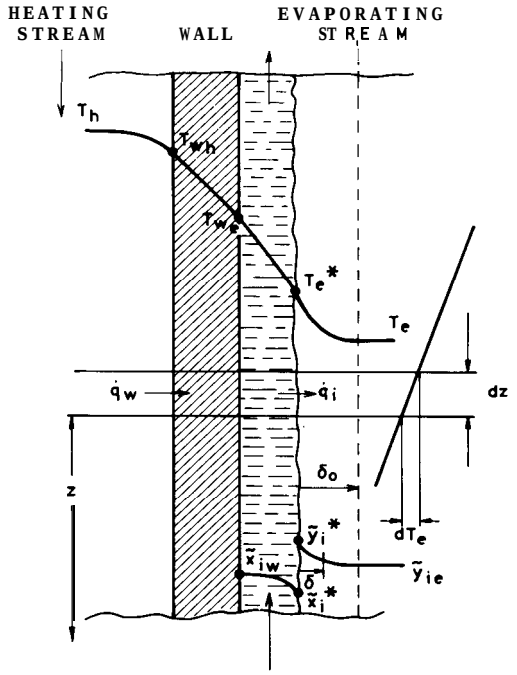

Figure 2 Evaporation **of** a multicomponent **fluid in annular flow.**

$$\dot{q}_i = \dot{q}_w - \Gamma_e(1 - x_e)\frac{dT_e}{dz} c_{p\ell} \tag{26}$$

Of course, in pure single-component vaporization (or condensation), $\dot{q}_w \cong \dot{q}_i$ because there is no axial temperature gradient of any consequence.

The interfacial heat flux $\dot{q}_i$ is, in turn, made up of two terms, an evaporation flux $\dot{q}_V$ at the interface and a sensible heat flux $\dot{q}_g$ required to heat the vapor phase through dT_e.

D. Interfacial mass transfer during evaporation of binary and multicomponent mixtures

At the interface, mass transfer and heat transfer processes occur in parallel, and the resistances to mass and heat transfer must be considered together. To induce these parallel mass and heat transfer processes, there must be parallel concentration and temperature driving forces from the interface to the bulk vapor phase. Shock [5] has shown that mass transfer resistances in the liquid phase are negligible by comparison, and therefore it is assumed that the resistance to heat and mass transfer occurs in the vapor phase across a boundary layer of thickness δ_0.

It is necessary to define some of the variables commonly used in this type of analysis:

The molar concentration $\tilde{c}_i$ of component i is given by

$$\tilde{c}_i = \frac{\rho_i}{M_i}$$

where ρ_i is the density of component i and M_i is its molecular weight.

The total molar concentration of the mixture is given by

$$\tilde{c} = \sum_{i=1}^{n} \tilde{c}_i$$

The ***mole fraction*** in the liquid $\tilde{x}_i$ or the vapor $\tilde{y}_i$ is defined by

$$\tilde{y}_i \text{ (or } \tilde{x}_i) = \frac{\tilde{c}_i}{\tilde{c}}$$

The ***molar flux*** $\dot{n}_i$ is the number of moles of component i passing normally through unit area in unit time.

The diffusive molar flux J_i is the flux of component i relative to the mixture total molar flux $\dot{n}$.

The mixture total molar flux $\dot{n}$ is defined as

$$\dot{n} = \sum_{i=1}^{n} \dot{n}_i$$

© 1983 Hemisphere Publishing Corporation

Thus the basic transport equation for the molar flux of component i from the interface is

$$\dot{n}_i = \dot{n}\tilde{y}_{ie} + J_i \tag{27}$$

where $\tilde{y}_{ie}$ is the mole fraction of component i in the bulk vapor.

These equations were first set down by Colburn and Drew [6] in 1937 for a binary system and have recently been reiterated by Price and Bell [7].

The ***diffusive molar flux*** J_i can be evaluated from

$$J_i = k_{i,\,\mathrm{eff}}(\tilde{y}_i^* - \tilde{y}_{ie}) \tag{28}$$

where $k_{i,\mathrm{eff}}$ is an effective mass transfer coefficient. The sensible heat flux $\dot{q}_g$ from the interface to the vapor core is the sum of the sensible heat flux due to the bulk flow of the vapor from the interface and the heat conducted through the boundary layer:

$$\dot{q}_g = (T - T_e^*)\sum_{i=1}^{n} \dot{n}_i \tilde{c}_{pi} + \alpha_g \frac{dT}{d\delta} \tag{29}$$

By integrating this equation from $\delta = 0$, $T = T_e^*$ to $\delta = \delta_0$, $T = T_e$ gives

$$\dot{q}_g = \frac{a}{1 - e^{-a}}\alpha_g(T_e^* - T_e) = \alpha_g'(T_e^* - T_e) \tag{30}$$

where

$$a = \frac{1}{\alpha_g}\sum_{i=1}^{n} \dot{n}_i \tilde{c}_{pi}$$

The evaporative heat flux required to form the mixture molar vapor flux $\dot{n}$ is

$$\dot{q}_V = \dot{n}\Delta\tilde{h}_v \tag{31}$$

where $\Delta\tilde{h}_v$ is the mixture molar latent heat of vaporization. Thus, the interfacial heat flux is given by

$$\dot{q}_i = \dot{q}_g + \dot{q}_V$$

$$= \frac{a}{1 - e^{-a}}\alpha_g(T_e^* - T_e) + \dot{n}\Delta\tilde{h}_v \tag{32}$$

In general, the solution of such sets of equations is complicated by the fact that the conditions at the interface are not known and must be guessed. An iteration is then necessary to achieve a solution.

A simplifying assumption is to say that for situations where the thickness of the mass transfer and heat transfer boundary layers in the vapor phase are equal,

$$\mathrm{Le} = \frac{\mathrm{Sc}}{\mathrm{Pr}} = \frac{\kappa}{\delta} \cong 1 \tag{33}$$

then the resistance to heat transfer and the resistance to mass transfer will also be about equal. Thus, if we evaluate the resistance to the transfer of the sensible heat component $\dot{q}_g$ in Eq. (30), then it is argued that there will be sufficient mass transfer driving force to provide $\dot{q}_v$ as well. Thus the overall heat transfer coefficient on the evaporating side will be described by the equation

$$T_{we} - T_e = (T_{we} - T^*) + (T^* - T_e)$$

Now, if $\dot{q}_i \cong \dot{q}_w$ [but see Eq. (26)], then the overall local evaporating side coefficient α_e can be given by

$$\frac{q_w}{\alpha_e} = \frac{q_w}{\alpha_{fe}} + \frac{q_g}{\alpha_g'} \tag{34}$$

where α_{fe} is the coefficient for the liquid film and α_g' is the modified single-phase vapor heat transfer coefficient [defined by Eq. (30)]. Dividing both sides of Eq. (34) by $\dot{q}_w$ gives

$$\frac{1}{\alpha_e} = \frac{1}{\alpha_{fe}} + \frac{\dot{q}_g/\dot{q}_w}{\alpha_g'} \tag{35}$$

The term $\dot{q}_g/\dot{q}_w$ was denoted Z by Bell and Ghaley [8] and is given by

$$\frac{q_g}{\dot{q}_w} = z = x_e \frac{dT_e}{dz} c_{pg} \tag{36}$$

This term is easily computed from the known phase equilibrium information, and the approximation can be used for both binary and multicomponent systems. Although the liquid-vapor interface is rough, it is recommended that the smooth-tube value of α_g be used in Eq. (30) to ensure adequate mass transfer driving force.

The more rigorous approach given earlier [Eq. (32)] is strictly correct only for binary mixtures and can be solved using the methods described by Price and Bell [7]. The extension of these methods to multicomponent systems, primarily in relation to condensation (see Sec. 2.6.5), is being pursued by Standart and co-workers [9-12], although the interactions between the diffusive fluxes of the various components makes the solution complex. Krishna and Standart [IO] have pointed out that Eq. (28) is incorrect for multicomponent evaporation. The correct relationship is

$$J_i = \sum_{j=1}^{n} k_{ij}(\tilde{y}_j^* - \tilde{y}_{je}) \quad (i = 1, \ldots, n) \tag{37}$$

Methods of calculating the matrix k_{ij} of mass transfer coefficients have been discussed by Krishna and Standart [10,12]. The energy balance becomes

$$\dot{q}_i = \frac{a}{1 - e^{-a}}[\alpha_g(T_e^* - T_e)] + \sum_{i=1}^{n} \dot{n}_i \Delta\tilde{h}_{v,i} \tag{38}$$

© 1983 Hemisphere I blishing Corporation

Table 1 Experimental studies of DNB for binary mixtures

Reference	Fluids	Geometry	Experimental ranges: Pressure, bar	Subcooling, °C	Velocity, m/s	critical heat flux, MW/m²
Tolubinskiy and Matoriu [13]	Ethanol-water Acetone-water Ethanol-benzene Ethylene glycol-water	Tube 4 mm ID 60 mm long	3.3-13.2	10-110	2.5-10	2-13
Andrews et al. [16]	Acetone-toluene Benzene-toluene	Annulus 6.35 mm ID 2.09 mm OD 76 mm long	1	20-50	1.09-4.36	1-4.5
Sterman et al. [14]	Monoisopropyl-diphenyl-benzene	Annulus 10 mm ID 16 mm OD 110 mm long	2	25-70	4-12	1-4.5
Naboichenko et al. [17]	Monoisopropyl-diphenyl-benzene	Annulus 6 mm ID 10 mm OD 80 mm long	2.94-16.37	25-125	4-8	1-6
Came [18]	Benzene-toluene Acetonetoluene	Internally heated annulus 6.35 mm ID 19.05 mm OD 76.2 mm long	2.05	20-80	2.18-4.36	0.5-3.0

By using vapor-liquid equilibrium data, Eqs. (27) and (37) can be solved to provide T_c^* and $\dot{n}_i$. The heat balance relationships Eqs. (30) and (38) are then used to calculate the bubble point at some point farther down the evaporator. The vapor-phase composition is calculated from

$$\frac{1}{A}\frac{d\dot{N}_i}{dz} = \dot{n}_i$$

from which the vapor-phase mole fractions $\tilde{y}_{ie}$ are readily calculated. No comparisons have been published between this method and the more simplified method given earlier for the case of multicomponent evaporation. Some comparisons are, however, available for the analogous condensation situation and have been given by Price and Bell [7] and by Krishna and Standart [10].

E. Critical heat flux in forced convection boiling

The critical heat flux (CHF) for binary and multicomponent mixtures in forced convection boiling is best considered in terms of the separate mechanisms of departure from nucleate boiling (DNB), which occurs under subcooled and low-quality conditions, and dryout, which occurs at higher vapor qualities (see Sec. 2.7.3D).

(a) Departure from nucleate boiling

Data for the critical heat flux of binary organic mixtures for subcooled and saturated forced convection boiling have been given by a number of workers (Table 1). Maxima in the CHF–versus-composition curves, corresponding to maximum values of $|\tilde{y} - \tilde{x}|$, are seen in these results also (Fig. 3),

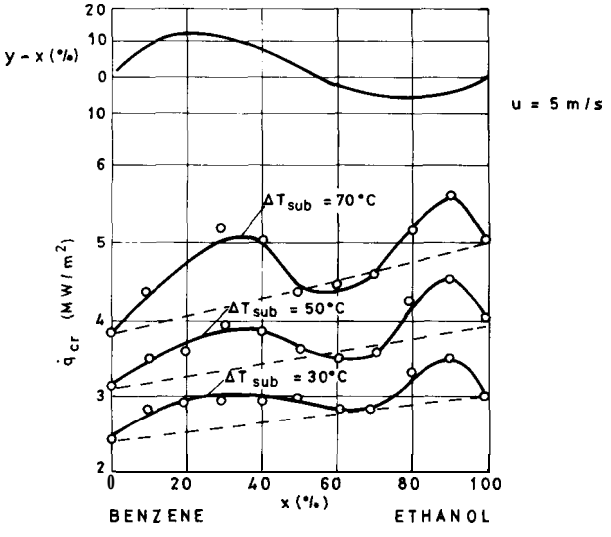

Figure 3 Critical heat flux for forced convection boiling of benzene-ethanol mixtures. From Tolubinskiy and Matorin [13].

© 1983 Hemisphere Publishing Corporation

although not so marked as for the pool boiling case (see Sec. 2.7.7). The CHF for the binary mixture increases with both increased velocity and increased subcooling in a similar manner to that for pure liquids. The value of the critical heat flux for a binary mixture $q_{cr,m}$ may be expressed by analogy of the treatment by Stephan and Körner for pool boiling heat transfer as the sum of two terms: $\dot{q}_{cr,I}$, the ideal value of the critical heat flux evaluated from the values of $\dot{q}_{cr}$ for the two pure components A and B calculated at the same pressure, velocity, and subcooling as the mixture; and $\dot{q}_{cr,E}$, an additional heat flux that allows for the enhancement in CHF brought about by mass transfer effects, etc.:

$$\dot{q}_{cr,m} = \dot{q}_{cr,I} + \dot{q}_{cr,E} = \dot{q}_{cr,I}(1 + \chi) \tag{39}$$

where

$$\dot{q}_{cr,I} = \dot{q}_{cr,A}(1 - \tilde{x}) + \dot{q}_{cr,B}\tilde{x} \tag{40}$$

Tolubinsky and Matorin [13] and Sterman et al. [14] found that χ in Eq. (39) could be expressed as a function

$$\chi = \chi\left(|\tilde{y} - \tilde{x}|, \left(\frac{\dot{m}D}{\eta_\ell}\right)_A, \frac{T_{sat,B}}{T_{sat,m} - T_{sat,B}}\right) \tag{41}$$

The Reynolds number $(\dot{m}D/\eta_\ell)_A$ is based on the properties of the less volatile component, since this component becomes concentrated at the heated surface.

Tolubinskiy and Matorin [13] suggest the following expression for χ:

$$\chi = 1.5(|\tilde{y} - \tilde{x}|)^{1.8} + 6.8(|\tilde{y} - \tilde{x}|)\frac{T_{sat,m} - T_{sat,B}}{T_{sat.B}} \tag{42}$$

This expression correlated CHF data for ethanol-water, acetone-water, ethanol-benzene, and water-ethylene glycol mixtures within ±20%. For mixtures forming an azeotrope, Tolubinskiy and Matorin recommend that $T_{sat,m}$ be set equal to $T_{sat,B}$ at the azeotropic composition, so that $\dot{q}_{cr,m} = \dot{q}_{cr,I}$. This recommendation is confirmed by examination of the results for benzene-ethanol mixtures shown in Fig. 3.

In the experiments of Sterman et al. [14], the values of χ varied from 0 to 0.8 and an alternative expression for χ was given:

$$\chi = 3.2 \times 10^5 \frac{(|\tilde{y} - \tilde{x}|)^3}{(\dot{m}D/\eta_\ell)_A} + 6.9 \frac{(|\tilde{y} - \tilde{x}|)^{1.5}}{(\dot{m}D/\eta_\ell)_A^{0.4}} \times \frac{T_{sat,B}}{T_{sat,m} - T_{sat,B}} \tag{43}$$

(b) Dryout

For higher vapor qualities, associated with the annular flow pattern, dryout is likely to be determined by the point at which the flow rate of the liquid film on the heated surface approaches zero. No experimental data or theoretical models have been published relating to dryout in binary or multicomponent mixtures. However, it is possible to recommend the method proposed by Hewitt and his co-workers (see Sec. 2.7.3D). On the evidence of Shock [5], it is apparent that the flow rates within the liquid film and of entrained liquid within the vapor core are dictated primarily by hydrodynamic effects and that mass transfer effects on the distribution of the phases will be small. In carrying out the step-by-step integration of the equations given in Sec. 2.7.3D, it is recommended that equilibrium be assumed between the liquid and vapor at each axial location. If it is considered important, the small departures from the equilibrium situation can be introduced using the equations given by Shock [5]. Breakdown of the liquid film into rivulets may occur somewhat earlier than for a pure liquid because of surface tension and temperature gradient effects. Figure 4 shows that the minimum wetting rate for a water-n-propanol mixture is a strong function of the composition (Norman and Binns [15]).

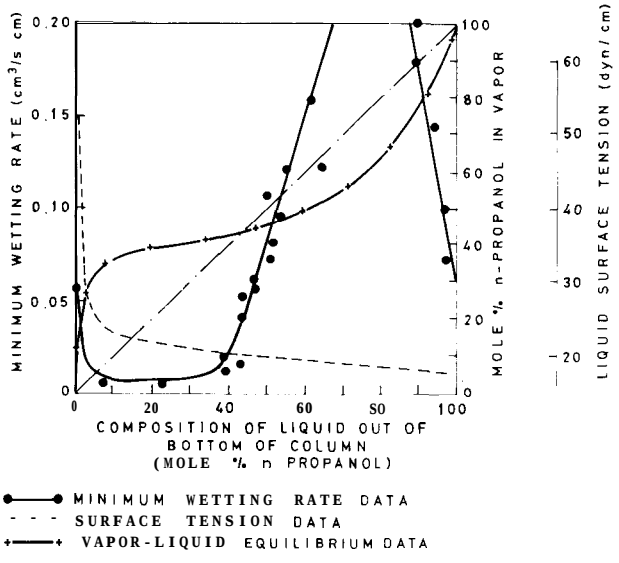

Figure4 Minimum wetting rates for water-n-propanol mixtures. From Norman and Binns [15].

© 1983 Hemisphere Publishing Corporation

NOMENCLATURE FOR SECTIONS 2.7.1-2.7.8

A	parameter defined by Eq. 2.7.1(14); constant; parameter in Eqs. 2.7.3(46) and 2.7.3(47); flow area, m^2
A^*	parameter defined by Eq. 2.7.2(12)
Ar*	dimensionless group $\{=(g_n/\nu^2)[\sigma/g_n(\rho_\ell-\rho_g)]^{3/2}(1-\rho_g/\rho_\ell]\}$
B	parameter defined by Eq. 2.7.1(14); parameter given by Eqs. 2.7.2(27)-2.7.2(29); parameter in Eqs. 2.7.3(46) and 2.7.3(47)
B_o	boiling number $(=\dot{q}/\dot{m}\Delta h_v)$
b	constant $(=\frac{2}{3}$ for bubbles in an infinite sea; $=\pi/7$ for bubbles adjacent to a surface)
C	concentration of droplets, kg/m^3; parameter in Eqs. 2.7.3(46) and 2.7.3(47); constant in Eq. 2.7.4(6)
C_1, C_2	constants in Eqs. 2.7.2(1) and 2.7.2(2)
C_{drag}	drag coefficient
C_s	Stefan-Boltzman constant, 5.6697×10^{-8} $W/m^2 K^4$
C_{sf}	arbitrary constant in Eq. 2.7.2(7) taking account of liquid/surface effect
C_o	dimensionless number $[=(1-x/x)^{0.8}(\rho_g/\rho_\ell)^{0.5}]$
c	concentration of species, kg/m^3
c_p	heat capacity, J/kg K
D	tube diameter, m
D^*	dimensionless diameter in Eq. 2.7.3(65)
D_b	diameter of the tube bundle, m; bubble departure diameter, m
D_e	hydraulic equivalent diameter, m
D_h	heated equivalent diameter, m
d	droplet diameter, m; coil diameter, m
E	entrainment rate, $kg/m^2 s$
Eö	Eötvös number $[=g_n(\rho_\ell-\rho_g)D_b^2/\sigma]$
F	Chen factor given by Eq. 2.7.3(30); ratio of critical heat flux under uniform heating conditions to that under nonuniform heating conditions; ventilation factor in Eq. 2.7.3(84)
F_1-F_4	functions of system pressure given in Table 2.7.3(5)
$F(p)$	function of reduced pressure p_r
Fr	Froude number $(=\dot{m}^2/\rho_\ell^2 g_n D)$
f	bubble frequency, s^{-1}; Fanning friction factor
G_d	vaporized mass diffusion fraction $[=(x_0-x)/(y-x)]$
Gr*	modified Grashof number $[=z^3 g_n \rho_g(\rho_g-\rho_\ell)/\eta_g^2]$
g	Gibbs free energy, J/kg
g_n	acceleration due to gravity, m/s^2
h	specific enthalpy, J/kg
Δh_v	latent heat of vaporization, J/kg
$\Delta h_v'$	modified latent heat of vaporization, J/kg
I	induced convection scale parameter $(=\rho_\ell L\sigma/\eta_\ell^2)$
J	molar flux of specific component, $kmol/m^2 s$
Ja	Jakob number $(=\rho_\ell c_{p\ell}\Delta T/\rho_g \Delta h_v)$
Ja*	modified Jakob number $(=\rho_\ell c_{p\ell} T_{sat}/\rho_g \Delta h_v)$
j	volumetric flux, m/s
K	constant in Eq. 2.7.2(17); empirical constant in Eq. 2.7.4(1); equilibrium ratio
K_1	constant defined by Eq. 2.7.3(81)
K_g	self diffusion coefficient, m^2/s
K_p	dimensionless group $\{=p/[g_n\sigma(\rho_\ell-\rho_g)]^{1/2}\}$
K_t	dimensionless group $\{=(\rho_g\Delta h_v)^2/Jcp_\ell T_{sat}\ \rho_\ell [g\sigma(\rho_\ell-\rho_g)]^{1/2}\}$
k	Boltzman constant, kg m^2/s^2 K
k_ℓ	mass transfer coefficient, m/s
L	heater size, m
L'	nondimensional heater size in Eq. 2.7.2(22)
Le	Lewis number (= K/6)
M	liquid viscosity parameter $[=\rho_\ell\sigma^{3/4}/\eta_\ell g^{1/4}(\rho_\ell-\rho_g)]$
$\tilde{M}$	molecular weight, kg/kmol
$\dot{M}$	mass flow rate, kg/s
m	mass of one molecule, kg; index; film thickness, m
$\dot{m}$	mass velocity, $kg/m^2 s$; mass flux of molecules, $kg/m^2 s$
$\dot{m}_d$	deposition rate for droplets, $kg/m^2 s$
N	number of moles; total number of tubes in a tube bundle; number of molecules per unit volume, m^{-3}; number of droplets passing through unit area per unit time, $m^{-2}s^{-1}$; dimensionless number $\{=(\rho_\ell\sigma/\eta_\ell^2)[\sigma/g_n(\rho_\ell-\rho_g)]^{1/2}\}$
N_j	number of jets
Nu	Nusselt number $\{=\dot{q}D/\lambda_\ell[T_{sat}-T_\ell(z)_B]\}$
Nu*	modified Nusselt number $\{=(\alpha/\lambda_\ell)[\sigma/g_n(\rho_\ell-\rho_g)]^{1/2}\}$
n	number of vapor embryos of critical size formed per unit volume, m^{-3}; exponent
n_1-n_5	constants in Eq. 2.7.2(9) [see Table 2.7.2(2)]
P	parachor; tube pitch, m
Pe	Peclet number $(=\dot{m}Dc\rho_\ell/\lambda_\ell)$
Pe*	modified Peclet number $I=(\dot{q}/\kappa_\ell\rho_g\Delta h_v)[\sigma/g_n(\rho_\ell-\rho_g)]^{1/2}\}$
PI	Prandtl number $(=c_p\eta/\lambda)$
p	partial pressure, N/m^2; pressure, N/m^2
p_r^*	reference reduced pressure, 0.0294
Δp	pressure difference, N/m^2
Q	total amount of heat, J; total power, W
q	heat flux, W/m^2
$\dot{q}^*$	modified heat flux in Eq. 2.7.3(65)
R	radius of bubble cavity, m; radius of cylinder of heater, m
$\tilde{R}$	gas constant, 831 4 J/kmol K
R^+	dimensionless bubble radius in Eq. 2.7.1(14)
$\dot{R}$	rate of bubble growth, m/s

© 1983 Hemisphere Publishing Corporation

R' dimensionless heater radius
Re Reynolds number (= $\dot{m}D/\eta$)
r index; radius of bend or coil, m
r, r_1, r_2 radii of curvature of an interface, m
r^* critical size of vapor nucleus, m
S Chen suppression factor given by Eq. 2.7.3(31)
SC Schmidt number (= ν/δ)
Sh Sherwood number (= $k_\ell m/\delta$)
St Stanton number {$= \dot{q}/\dot{m}c_{p\ell}[T_{sat} - T_\ell(z)_B]$}
s index
T temperature, K, °C
T^* dew point of vapor mixture, K, °C
AT temperature difference, °C
t time, s
t^+ dimensionless bubble growth period in Eq. 2.7.1(14)
t_w^+ dimensionless bubble waiting period
u velocity, m/s
u_∞ free-stream velocity, m/s
$\dot{V}$ volumetric flow rate per unit parameter, m^2/s
v critical velocity given by Eq. 2.7.4(1), m/s; specific volume, m^3/kg
We Weber number (= $2R\rho_g u_\infty^2/\sigma$)
X parameter defined by Eq. 2.7.3(8)
X_{tt} Martinelh parameter [= $(\Delta p_\ell/\Delta p_g)^{1/2}$]
x thermodynamic vapor quality
x' true vapor mass fraction
$\tilde{x}$ mole fraction in liquid phase
Y parameter defined below Eq. 2.7.3(75)
Y distance away from heating surface, m
y_b, Y_b distance from wall to bubble tip, m
$\tilde{y}$ mole fraction in vapor phase
Z parameter used by Bell and Ghaly, Eq. 2.7.8(36)
z distance up heated surface, m
z_H thickness of thermal diffusion shell, m
z_M thickness of mass diffusion shell, m
α relative volatility; heat transfer coefficient, $W/m^2\,°C$
β mass transfer coefficient, m/s; contact angle measured through liquid, deg
Γ mass flow rate per unit parameter, kg/m s
γ parameter defined below Eq. 2.7.3(66), m^2/N
δ thickness of liquid film, m; diffusivity, m^2/s; thickness of boundary layer, m
ϵ surface roughness, m; emissivity of surface
ϵ_g void fraction
η dynamic viscosity, kg/m s
Θ parameter defined by Eq. 2.7.7(1)
θ angle to horizontal, deg; tube layout angle, deg; subcooling factor $[=(T_w - T_\ell)/(T_w - T_{sat})]$
κ thermal diffusivity, m^2/s
Λ parameter defined by Eq. 2.7.7(3)
λ thermal conductivity, W/m K
λ_c, λ_d instability wavelength, m
ν kinematic viscosity, m^2/s
ξ constant; ratio of heat flux on a rod to maximum in rod cluster
ρ density, kg/m^3
σ surface tension, N/m
τ shear stress, N/m^2
Φ dimensionless tube density factor, Eq. 2.7.5(20)
Φ_f Martinelli parameter {$[dp/dz)_{tp}/(dp/dz)_\ell]^{1/2}$}
Ψ dimensionless physical property factor, Eq. 2.7.5(21); constant in Eq. 2.7.2(5)
ψ parameter used in Eq. 2.7.3(76); modeling parameter in Eq. 2.7.3(67); included angle of cavity, deg
Ω parameter in Eq. 2.7.3(53), m^{-1}

Subscripts

A, B components A, B
a noncondensable gas
B point *B*
b bubble
c convection; mouth of cavity; critical point
c'' point c''
cr critical point; critical heat flux
d droplet
E equilibrium; excess
e evaporating
eff effective
exp experimental
F flat plate
fe liquid film
g gas or vapor
h heated; heating
I ideal
i inside; interface; inlet
le liquid entrained
lf liquid film
ℓ liquid
ℓo total flow assumed liquid
max maximum
min minimun
n fully developed nucleate boiling
nb nucleate boiling
o outside
onb onset of nucleate boiling
R rod
r reduced (reference to critical point); radiation
ref reference
sat saturation
scb subcooled boiling
sub subcooled
tb transition boiling

© 1983 Hemisphere Publishing Corporation

tp	two-phase
w	wall
x, y, z	coordinates
Z	Zuber
∞	away from surface

Superscripts

	average property
	molar quantity
0	vapor pressure of pure component

REFERENCES FOR SECTION 2.7.8

1. McAdams, W. H., Wood, W. K., and Herman, L. C., Vaporization inside Horizontal Tubes-II, Benzene-Oil Mixtures, ***Trans. ASME,*** pp. 193-200, 1942.
2. Bonnet, W. E., and Gerster, J. A., Boiling Coefficients of Heat Transfer-C, Hydrocarbon/Furfural Mixtures inside Vertical Tubes, ***Chem Eng. Prog., vol. 17, no. 3,*** pp. 151-158, 1951.
3. Shellene, K. R., Sterling, C. V., and Snyder, N. H., Experimental Study of a Vertical Thermosyphon Reboiler, ***Chem. Eng. Prog. Symp. Ser.,*** vol. 64, no. 82, pp. 102-113, 1968.
4. Stephan, K., and Körner, M., Calculation of Heat Transfer in Evaporating Binary Liquid Mixtures, ***Chem. Zng. Tech.,*** vol. 41, no. 7, pp. 409-417, 1969.
5. Shock, R. A. W., Evaporation of Binary Mixtures in Upward Annular Flow, ***Int. J. Multiphase Flow,*** vol. 2, pp. 411433, 1976.
6. Colburn, A. P., and Drew, T. B., The Condensation of Mixed Vapors, ***Trans. AZChE,*** vol. 33, pp. 197-215, 1937.
7. Price, B. C., and Bell, K. J., Design of Binary Vapor Condensers Using the Colburn-Drew Equations, ***AZChE Symp. Ser.,*** vol. 70, no. 138, pp. 163-171, 1974.
8. Bell, K. J., and Ghaly, M. A., An Approximate Generalized Design Method for Multi-component/Partial Condensers, ***AZChE Symp. Ser.,*** vol. 69, no. 131, pp. 72-79, 1972.
9. Standart, G. L., Krishna, R., and Cullinan, H. T., Multi-component Isothermal Mass Transfer, ***AZChE Conf.,*** Tulsa, Okla., March 1974; see also Krishna, R., Interphase Transport of Mass and Energy in Multi-component Systems, Ph.D. thesis, University of Manchester Institute of Science and Technology, 1975.
10. Krishna, R., and Standart, G. L., Determination of Interfacial Mass and Energy Transfer Rates for Multi-component Vapor-Liquid Systems, ***Lett. Heat Mass Transfer,*** vol. 3, no. 2, pp. 173-182, 1976.
11. Krishna, R., Panchal, C. B., Webb, D. R., and Coward, I., An Ackerman-Colburn and Drew Type Analysis for Condensation of Multi-component Mixtures, ***Lett. Heat Mass Transfer,*** vol. 3, no. 2, pp. 63-172, 1976.
12. Krishna, R., and Standart, G. L. A Multi-component Film Model Incorporating a General Matrix Method of Solution to the Maxwell-Stefan Equation, ***AZChE J.,*** vol. 22, p. 383, 1976.
13. Tolubinskiy, V. I., and Matorin, P. S., Forced Convection Boiling Heat Transfer Crisis with Binary Mixtures, ***Heat Transfer Sov. Res.,*** vol. 5, no. 2, pp. 98-101, 1973.
14. Sterman, L., Abramov, A., and Checketa, G., Investigation of Boiling Crisis at Forced Motion of High Temperature Organic Heat Carriers and Mixtures, Int. Symp. on Research into Co-current Gas-Liquid Flow, University of Waterloo, Waterloo, Ontario, Canada, vol. 2, Paper E2, September 1968.
15. Norman, W. S., and Binns, D. T., The Effect of Surface Tension Changes on Minimum Wetting Rates in a Wetted Rod Distillation Column. ***Trans. Inst. Chem. Eng.,*** vol. 38, pp. 294-300, 1960.
16. Andrews, D. G., Hooper, F. C., and Butt, P., Velocity, Subcooling and Surface Effects in the Departure from Nucleate Boiling of Organic Binaries, ***Can. J. Chem. Eng.,*** vol. 46, no. 3, pp. 194-199, 1968.
17. Naboichenko, K. V., Kiryutin, A, A., and Gribov, B. S., A Study of Critical Heat Flux with Forced Flow of Monoisopropyldiphenyl-Benzene Mixture, ***Teploenergetika, vol. 12,*** no. 11, pp. 81-86, 1965 (tr. Thermal ***Eng.,*** vol. 12, no. 11, pp. 107-114, 1965).
18. Came, M., Studies of the Critical Heat Flux for Some Binary Mixtures and Their Components, ***Can. J. Chem. Eng.,*** vol. 42, No. 6, pp. 235-240, 1963.

© 1983 Hemisphere Publishing Corporation

2.7.9

Augmentation of boiling and evaporation

Arthur E. Bergles

■ Selected passive and active augmentation techniques have been shown to be effective for pool boiling and flow boiling [1-4]. Most techniques apply to nucleate boiling; however, some techniques are applicable to transition and film boiling.

A. Pool boiling

The strong influence of surface treatment on nucleate pool boiling, including the effect of ageing, has been discussed in Sec. 2.7.2. Numerous types of surface treatment and structuring have been utilized to intentionally reduce the wall-minus-saturation temperature difference AT,. Although it is possible to improve nucleate boiling by minor changes in surface finishing procedures [5], special procedures are most effective. For water, the placement of small nonwetting spots (Teflon or epoxy), either splattered on the surface or placed in pits, reduces AT, at constant $\dot{q}$ by a factor of 3-4 [6]. This comparison, as well as others in this section, is based on heat flux evaluated for the surface area of the plain tube.

With nonwetting fluids (refrigerants, cryogens, organics, alkali liquid metals), doubly reentrant cavities are required to ensure vapor trapping. These can be produced by machining and/or forming [7-10]. A magnified view of the Hitachi Thermoexel-E formed surface is shown in Fig. 1. It is possible to minimize ***AT,*** by selecting the optimum pore or groove size for the fluid conditions of interest. An alternative technique involves coating the surface with a porous metallic layer by poor welding [11], sintering or brazing [12,13] (Fig. 2), electrolytic deposition [14], flame spraying [13,15], or metallic coating of a foam substrate [16]. Most examples referred to represent processes that have been patented and, in some cases, commercialized.

Superheat reductions of up to a factor of 10 have been reported with various machined or coated surfaces. It should be noted that the mechanism of vaporization is different for these surfaces than for normal cavity boiling. Here, the liquid flows to the interior, where thin film evaporation occurs over a large surface area; the vapor is then ejected by bubbling [17,18]. Typical data are given in Fig. 3. It should be emphasized, however, that the boiling performance is very sensitive to surface geometry and fluid condition, and that measurements at very low temperature difference are subject to considerable uncertainty.

Limited evidence indicates that the critical or burnout heat flux $\dot{q}_c$ with structured surfaces is usually as high as or higher than that with plain surfaces [12]. In general, these surfaces should be used with clean fluids, as concentrations of impurities or corrosion products in the pores will reduce the augmentation. When used with tube bundles, it may be advisable to use the augmented tubes only in the lower rows, as the upper tubes have such high velocities that the augmented surfaces are not effective.

Low-fin tubes with external, circumferential fins are produced by many manufacturers for heating of organics. Local α and $\dot{q}_c$ are frequently lower than for plain tubes; however, this is more than compensated by the area increase [19,20]. Boiling curves are usually different for tube bundles than for single tubes

© 1983 Hemisphere Publishing Corporation

HEDH

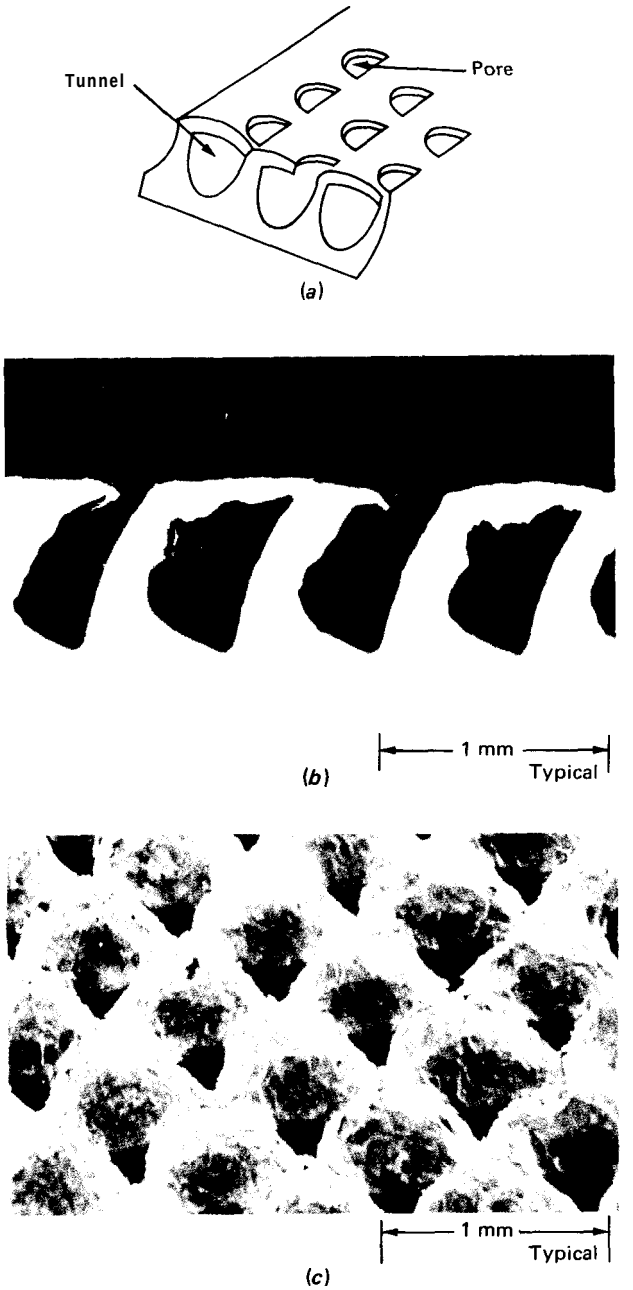

Figure 1 Magnified view of the Hitachi Thermoexcel-E surface. (a) Enlarged sketch. (b) Crosssectional view of tunnels. (c) Plan view of pores. From Nakayama et al. [9].

because of differences in circulation [19]. Large fins properly shaped or insulated promote large heat dissipation rates if the base temperature is in the film boiling range [21].

Additional passive augmentation techniques are discussed in [1–4]. Although the use of displaced egg crate structures, wicking, or trace additives can be very effective in reducing ΔT, or elevating $\dot{q}_c$, the practical applications of these techniques are quite limited.

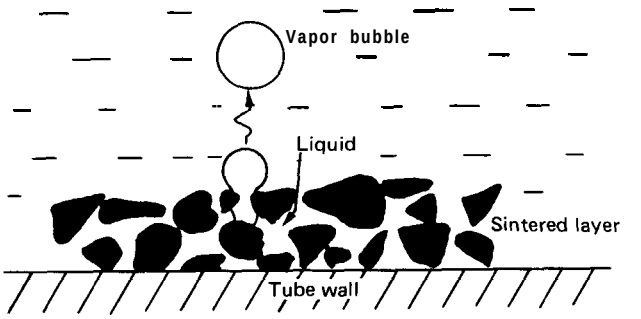

Figure 2 Sintered metallic layer, Linde High Flux surface.

Active augmentation techniques include heated surface rotation, surface wiping, surface vibration, fluid vibration, electrostatic fields, and suction at the heated surface [1–4]. Although active techniques are effective in reducing ΔT, and/or increasing $\dot{q}_c$, the practical applications are very limited, largely because of the difficulty of reliably providing the mechanical or electrical effect. Perhaps the major contribution of the many studies in this area is the information that is available to predict changes in pool boiling when these effects occur naturally in heat transfer equipment.

Compound augmentation, which involves two or more techniques applied simultaneously, has also been studied. The addition of surface roughness to the evaporator side of a rotating evaporator-condenser increased the overall coefficient by 10% [22].

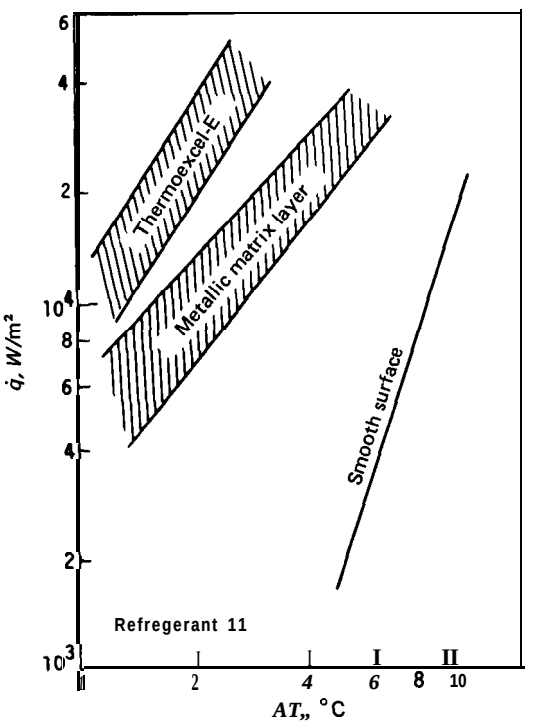

Figure 3 Nucleate pool boiling for smooth and structured surfaces. From Nakayama et al. [9].

© 1983 Hemisphere Publishing Corporation

B. Boiling within tubes

In accordance with the general observation that surface finish has less effect on flow boiling than on pool boiling, the various surface treatments mentioned above have relatively little influence on boiling within tubes. A prime consideration, of course, is that it is difficult to modify internal surfaces. Porous boiling surfaces do not improve high-flux, subcooled flow boiling; however, the annoying boiling curve hysteresis with refrigerants is eliminated [23]. Various types of rough surfaces increase subcooled $\dot{q}_c$ by only 10% [24].

A variety of surface modifications have been proposed to improve forced convection evaporation of water and other power cycle fluids: dual-diameter tubes, slotted helical inserts, helical ribs, machined protuberances, and coiled wire inserts [1]. Most configurations are effective in increasing vaporization $\alpha, \dot{q}_c$, and postdryout α. Few techniques are in commercial service because of manufacturing difficulty and fouling or corrosion potential. Notable exceptions are spirally indented tubes, which increase α for vaporization of R12 by up to 200% [25], and internally ribbed tubes, which suppress pseudo-film boiling with supercritical water, thereby permitting operation at higher $\dot{q}$ than is possible with smooth tubes [26].

Tubes with integral internal fins are available for refrigerant evaporators. Heat transfer rates can be increased by several hundred percent over the smooth-tube values [27,28], as illustrated by the data given in Fig. 4. Enhanced heat transfer surfaces are widely used for vertical-tube evaporators. Although distorted tubes (e.g., doubly fluted and spirally corrugated) have been developed primarily for augmentation of condensation on the outside wall, heat transfer coefficients for the evaporating brine on the inside of the tube are also increased [29]. In

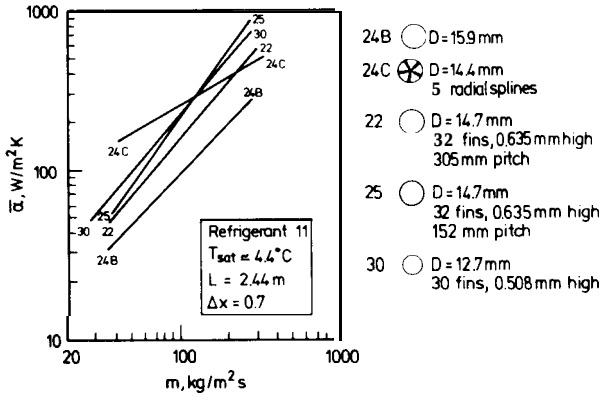

Figure 4 Heat transfer coefficient for internally finned tubes. From Kubanek and Miletti [28].

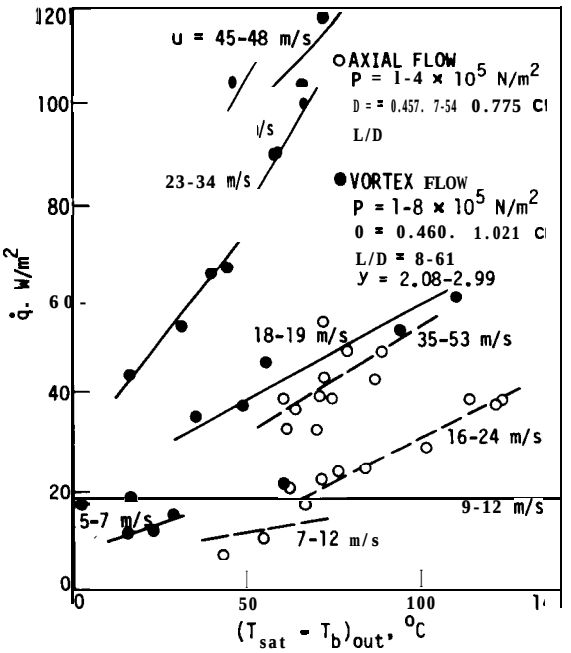

Figure 5 Influence of twisted-tape inserts on critical heat flux for subcooled boiling of water. From Gambill et al. [37].

falling-film evaporation, α can be increased by a factor of more than 10 by use of internally finned tubes [30].

By modifying the spacer configuration or the shroud, $\dot{q}_c$ can be increased for nuclear fuel element rod clusters [31,32]. Strict nuclear codes usually prohibit use of such devices in actual reactors.

A variety of devices have, been proposed to augment flow boiling by imparting a swirling of secondary motion to the flow. Inlet vortex generators of the spiral ramp or tangential slot variety have been used to accommodate very large heat fluxes for subcooled flow boiling of water. One of the highest fluxes on record, $\dot{q}_c = 1.73 \times 10^8 \text{ W/m}^2$, has been obtained with this technique [33]. Inlet swirl is effective in increasing $\dot{q}_c$ for subcooled boiling of water in a tube [34] or in an annulus (inner tube heated) [35].

Twisted tapes are quite popular because of their simplicity and adaptability to existing heat exchange equipment. They are ideal for hotspot applications, since a short tape can cure the thermal problem while having little effect on the overall pressure drop. Boiling curves for subcooled boiling with twisted tapes are similar to those with empty tubes [36]; however, $\dot{q}_c$ can be increased by up to 100% [37], as shown in Fig. 5. The critical heat fluxes for swirl flow are approximately twice those for straight flow at the same test section pumping power.

Loose-fitting tape inserts have been used in down-flow vertical-tube evaporators for seawater

© 1983 Hemisphere Publishing Corporation

desalination [38]. These inserts are also effective for once-through cryogenic vaporizers [39] or steam generators [40,41], since all regimes are beneficially affected. Coiled-tube vapor generators have advantages in terms of packing and generally higher heat transfer performance. The augmentation of boiling is very sensitive to geometrical and flow conditions [42,43]. Modest improvements in α (circumferential average) for forced convection vaporization are obtained, with the improvement increasing as coil diameter is decreased. In the subcooled region, $\dot{q}_c$ is lower than for a comparable straight tube; however, $\dot{q}_c$ or X_c is usually substantially higher than the straight-tube value at outlet qualities of 0.2 and higher. The postdryout α is also increased.

Trace additives are not particularly effective in subcooled nucleate boiling; AT, is reduced with some additives, but increased for others [1]. On the other hand, the overall α was doubled when a surfactant was added to seawater evaporating in vertical tubes (up flow) [44].

Active techniques are difficult to apply to boiling with tubes. The effects of tube vibration [45] or flow pulsation [1] are small. Electric fields also improve boiling heat transfer; for example, increases in $\dot{q}_c$ of more than 100% have been reported. However, the additional equipment complications and potential electrical hazard tend to rule out application of this technique [1].

Little work has been done to develop thermohydraulic performance evaluation criteria for boiling heat transfer. An index for subcooled boiling is developed in [46]; the volumetric heat transfer rate accommodation for the channel is compared with the pumping power per unit volume.

Nomenclature for ***Section 2.7.9 appears at the beginning*** of ***Part 2.***

REFERENCES FOR SECTION 2.7.9

1. Bergles, A. E., Survey and Evaluation of Techniques to Augment Convective Heat and Mass Transfer, in Progress in *Heat and Mass Transfer*, eds. U. Grigull and E. Hahne, vol. 1, pp. 331-334, Pergamon, Oxford, 1969.
2. *Collier,* J. *G., Convective Heat and Mass Transfer,* pp. 348-368, McGraw-Hi& Maidenhead, 1972.
3. Bergles, A. E., Survey of Augmentation of Two-Phase Heat Transfer, *ASHRAE Trans.,* vol. 82, pt. 1, pp. 881-890, 1976.
4. Bergles, A. E., Enhancement of Heat Transfer, *in Heat Transfer* 1978, vol. 6, pp. 89-108, Hemisphere, Washington, D.C., 1978.
5. Berenson, P. J., Experiments on Pool-Boiling Heat Transfer, *Znt. J. Heat Mass Transfer,* vol. 5, pp. 985-999, 1962.
6. Young, R. K., and Hummel, R. L., Improved Nucleate Boiling Heat Transfer, *Chem. Eng. Prog.,* vol. 60, no. 7, pp. 53-58, 1964.
7. Ragi, E., Composite Structure for Boiling Liquids and Its Formation, U.S. Patent 3,684,007, August 15, 1970.
8. Webb, R. L., Heat Transfer Surface Having a High Boiling Heat Transfer Coefficient, U.S. Patent 3,696,861, October 10, 1972.
9. Nakayama, W., Daikoku, T., Kuwahara, H., and Kakizaki, K., High-Flux Heat Transfer Surface THERMOEXCEL, *Hitachi Rev.,* vol. 24, pp. 329-334, 1975.
10. Wieland-Werke AG, Metallwerke, Ulm, F.R. Germany, High-Performance Tubes for Flooded Evaporators, Wieland-Product-Information SAW-15e-06.78, 1978.
11. Marto, P. J., and Rohsenow, W. M., Effects of Surface Conditions on Nucleate Pool Boiling of Sodium, *J. Heat Transfer,* vol. *88,* pp. 196-204, 1966.
12. O'Neill, P. S., Gottzmann, C. F., and Terbot, C. F., Novel Heat Exchanger Increases Cascade Cycle Efficiency for Natural Gas Liquefaction, *Adv. Cryog. Eng.,* vol. 17, pp. 421-437, 1972.
13. Danilova, G. N., Guygo, F. I., Borishanskaya, A. V., Bukin, V. G., Dyundin, V. A., Kozyrev, A. A., Malkov, L. S., and Malyugin, G. I., Enhancement of Heat Transfer during Boiling of Liquid Refrigerants at Low Heat Fluxes, *Heat Transfer Sov. Rex,* vol. 8, no. 4, pp. l-8, 1976.
14. Oktay, S., and Schmeckenbecher, A. F., Preparation and Performance of Dendritic Heat Sinks, *J. Electrochem. Soc.,* vol. 21, pp. 912-918, 1974.
15. Dahl, M. M., and Erb, L. D., Liquid Heat Exchanger Interface Method, U.S. Patent 3,990, 862, November 9, 1976.
16. Janowski, K. R., Shum, M. S., and Bradley, S. A., Heat Transfer Surface, U.S. Patent 4,129,181, December 12, 1978.
17. Czikk, A. M., and O'Neill, P. S., Correlation of Nucleate Boiling from Porous Metal Films, in *Adv. Enhanced Heat Transfer,* ASME, New York, pp. 53-60, 1979.
18. Nakayama, W., Daikoku, T., Kuwahara, H., and Nakajima, T., Dynamic Model of Enhanced Boiling Heat Transfer on Porous Surfaces, in *Adv. Enhanced Heat Transfer,* ASME, New York, pp. 31-43, 1979.
19. Palen, J. W., Yarden, A., and Taborek, J., Characteristics of Boiling Outside Large-Scale Horizontal Multitube Bundles, *AIChE Symp. Ser., vol. 68,* no. 118, pp. 50-61, 1972.
20. Hesse, G., Heat Transfer in Nucleate Boiling, Maximum Heat Flux and Transition Boiling, *Znt. J. Heat Mass Transfer,* vol. 16, pp. 1611-1627, 1973.
21. Westwater, J. W., Development of Extended Surface for Use in Boiling Liquids, *AIChE Symp. Ser.,* vol. 69, no. 131, pp. 1-9, 1973.
22. Bromley, C. A., Humphreys, R. F., and Murray, W., Condensation on and Evaporation from Radially Grooved Rotating Disks, *J. Heat Transfer,* vol. 88, pp. 80-93, 1966.
23. Murphy, R. W., and Bergles, A. E., Subcooled Flow Boiling of Fluorocarbons-Hysteresis and Dissolved Gas Effects on Heat Transfer, *Proc. 1972 Heat Transfer and Fluid Mechanics Inst.,* pp. 400416, Stanford University Press, Stanford, Calif., 1972.

© 1983 Hemisphere Publishing Corporation

24. Burck, E., Hufschmidt, W., and De Clereq, E., Eiiuss Künstlicher Rauigkeit auf die Kritische Wärmestromdichte bei Erzwungener Konvection, *Atomkernenergie,* vol. 14, pp. 305-308, 1969.
25. Withers, J. G., and Habdas, E. P., Heat Transfer Characteristics of Helical Corrugated Tubes for Intube Boiling of Refrigerant R-12, ***AIChE Symp. Ser.,*** vol. 70, no. 138, pp. 98-106, 1974.
26. Ackerman, J. W., Pseudoboiling Heat Transfer to Supercritical Pressure Water in Smooth and Ribbed Tubes, *J. Heat Transfer,* vol. 92, pp. 490-498, 1970.
27. Schlünder, E., and Chwala, J., Local Heat Transfer and Pressure Drop for Refrigerants Evaporating in Horizontal, Internally Finned Tubes, ***Proc. Int. Cong. Refrigeration,*** Paper 2.41, 1967.
28. Kubanek, G. R., and Miletti, D. L., Evaporative Heat Transfer and Pressure Drop Performance of Internally-Finned Tubes with Refrigerant ***22, J. Heat Transfer,*** vol. 101, pp. 447–452, 1979.
29. Johnson, B. M., Jansen, G., and Otwzarski, P. C., Enhanced Evaporating Film Heat Transfer from Corrugated Surfaces, ASME Paper 71-HT-33, 1971.
30. Thomas, D. G., and Young, G., Thin Film Evaporation Enhancement by Finned Surfaces, ***Ind. Eng. Chem. Process Des. Dev.,*** vol. 9, pp. 317-323, 1970.
31. Tong, L. S., Steer, R. W., Wenzel, A. H., Bogaardt, M., and Spigt, C. L., Critical Heat Flux of a Heater Rod in the Center of Smooth and Rough Sleeves, and in Line Contact with an Unheated Wall, ASME Paper 67-WA/HT-29, 1967.
32. Ryabov, A. N., Kamen shchikov, F. T., Filipov, V. N., Chalykh, A. F., Yuagy, T., Stolyarov, Y. V., Blagovestova, T. I., Mandrazhitskiy, V. M., and Yemel yanov, A. I., Boiling Crisis and Pressure Drop in Rod Bundles with Heat Transfer Enhancement Devices, ***Heat Transfer*** Sov. ***Res.,*** vol. 9, no. 1, pp. 112-121, 1977.
33. Gambill, W. R., and Greene, N. D., A Preliminary Study of Boiling Burnout Heat Fluxes for Water in Vortex Flow, ***Chem. Eng.*** Prog., vol. 54, no. 10, pp. 68-76, 1958.
34. Mayinger, F., Schad, O., and Weiss, E., Investigations into the Critical Heat Flux in Boiling, MAN Rept. 09.03.01, 1966.
35. Omatskiy, A. P., Chernobay, V. A., Vail yev, A. F., and Perkov, S. V., A Study of the Heat Transfer Crisis with Swirled Flows Entering an Annular Passage, ***Heat Transfer Sov. Res,*** vol. 5, no. 4, pp. 7-10, 1973.
36. Lopina, R. F., and Bergles, A. E., Subcooled Boiling of Water in Tape-generated Swirl Flow, ***J. Heat Transfer,*** vol. 95, pp. 281-283, 1973.
37. Gambill, W. R., Bundy, R. D., and Wansbrough, R. W., Heat Transfer, Burnout, and Pressure Drop for Water in Swirl Flow Tubes with Internal Twisted Tapes, ***Chem. Eng. Prog. Symp. Ser.,*** vol. 57, no. 31, pp. 127-137, 1961.
38. Sephton, H. H., Interface Enhancement for Vertical Tube Evaporator: A Novel Way of Substantially Augmenting Heat and Mass Transfer. ASME Paper 71-HT-38, 1971.
39. Bergles, A. E., Fuller, W. D., and Hynek, S. J., Dispersed Film Boiling of Nitrogen with Swirl Flow, ***Int. J. Heat Mass Transfer,*** vol. 14, pp. 1343-1354, 1971.
40. Cumo, M., Farello, G., Ferrari, G., and Palazzi, G., The Influence of Twisted Tapes in Subcritical, Once-Through Vapor Generator in Counter Flow, ***J. Heat Transfer,*** vol. 96, pp. 365-370, 1974.
41. Hunsbedt, A., and Roberts, J. M., Thermal-Hydraulic Performance of a 2MWT Sodium Heated, Forced Recirculation Steam Generator Model, ***J. Eng. Power,*** vol. 96, pp. 66-76, 1974.
42. Hopwood, P. F., Pressure Drop, Heat Transfer and Flow Phenomena for Forced Convection Boiling in Helical Coils-A Literature Review, Rept. AEEW R-157, 1972.
43. Gorlov, I. G., and Rzaev, A. I., Features of Hydrodynamics and Heat Exchanges during the Flow of Liquids in Helically-coiled Tubes, ***Heat Transfer Sov. Res.,*** vol. 5, no. 4, pp. 80-88, 1972.
44. Sephton, H. H., Upflow Vertical Tube Evaporation of Sea Water with Interface Enhancement; Process Development by Pilot Plant Testing, ***Desalination,*** vol. 16, pp. l-13, 1975.
45. Pearce, H. R., The Effect of Vibration on Burnout in Vertical, Two-Phase Flow, Rept. AERE-R 6375, 1970.
46. Megerlin, F. E., Murphy, R. W., and Bergles, A. E., Augmentation of Heat Transfer in Tubes by Means of Mesh and Brush Inserts, ***J. Heat Transfer,*** vol. 96, pp. 145-151, 1974.

© 1983 Hemisphere Publishing Corporation

2.8
Heat transfer to gas-solid systems

Contents

2.8.1
STAGNANT PACKED BEDS,
R. Bauer 2.8.1-1

A. Description of heat transfer situation 2.8.1-l
B. Equation governing the two-dimensional temperature field $T(r,t)$ 2.8.1-1
C. Heat transfer parameters of interest 2.8.1-2
D. Equation governing the one-dimensional temperature field $\bar{T}(t)$ 2.8.1-10
E. The heat quantity Q 2.8.1-12

Nomenclature for Section 2.8.1 2.8.1-14
References for Section 2.8.1 2.8.1-14

2.8.2
PACKED BEDS WITH A GAS FLOWING THROUGH, R. Bauer 2.8.2-l

A. Description of heat transfer situation 2.8.2-l
B. Equation governing the two-dimensional temperature field $T(r,z)$ 2.8.2-l
C. Heat transfer parameters of interest ***2.8.2-2***
D. Equation governing the one-dimensional temperature field $\bar{T}(z)$ ***2.8.2-7***
E. The heat rate Q ***2.8.2-7***
F. Equations governing the temperature field $T_s(r,z)$ of the solid phase and $T_g(r,z)$ of the gas phase ***2.8.2-7***

Nomenclature for Section 2.8.2 ***2.8.2-8***
References for Section 2.8.2 ***2.8.2-8***

2.8.3
HEAT TRANSFER TO PACKED AND AGITATED BEDS,
E. Muchowski 2.8.3-l

A. Heat transfer to packed beds 2.8.3-l
B. Heat transfer to moving and agitated beds ***2.8.3-3***

References for Section 2.8.3 ***2.8.3-9***

2.8.4
FLUIDIZED BEDS, J. S. M. Botterill 2.8.4-l

A. Introduction 2.8.4-l
B. Predictive formulas ***2.8.4-4***
C. Immersed tubes ***2.8.4-6***

Nomenclature for Section 2.8.4 ***2.8.4-7***
References for Section 2.8.4 ***2.8.4-7***

© 1983 Hemisphere I blishing Corporation

HEDH

2.8.1

Stagnant packed beds

R. Bauer

■ In industry, gas-solid systems are used as dryers, coolers, heaters, absorbers, chemical reactors, and so on. Since most of these processes are associated with energy transfers, there are heat fluxes and temperature profiles that must be known for design purposes.

Usually, the heat exchange takes place through an adjacent wall. The heat transfer between this wall and the gas-solid system, as well as within the gas-solid system itself, is a process consisting of different components according to various operating conditions. The simplest case is when both the solid phase and the gas phase are motionless (stagnant packed bed). By this means, the heat passes through gas and solid paths to the interior of the packing. In the second case the gas is flowing through the interspaces of the packing in parallel with the wall while the solid phase is motionless (packed bed with gas flow through). Because of this flow through the interspaces an improvement of the heat transfer in the packing is achieved. In the third case the gas phase as well as the solid phase is in motion because of stirring or vibration in the packing (agitated bed) or by impulse exchange between the flowing gas and the particles (fluidized bed). There is an additional improvement in the heat transfer occurring in the solid phase because of the motion of the particles.

Heat fluxes and temperature profiles in such gas-solid systems are obtained by solving the appropriate energy balance equations, which account for the various modes of energy transport.

A. Description of heat transfer situation

In packed beds the exact mathematical description of heat transfer is quite a complex problem. For this reason, simplified conditions are necessary to solve the problems with acceptable accuracy in an appropriate amount of time.

In order to describe heat transfer in gas-solid systems by an adequate model, the following conditions are generally assumed:

1. The heterogeneous gas-solid system is considered as a quasihomogeneous continuum with an effective thermal conductivity. By this means, there are no temperature differences between the solid and the gas phase.

2. The heat transfer occurring in the packing is disarranged at the adjacent wall and is subdivided into two parts. One part is the region near the wall surface with a thickness of about one particle diameter with the heat transfer described using a wall heat transfer coefficient. The second part is the remaining central core of the packing with the conditions described in 1 above.

B. Equation governing the two-dimensional temperature field $T(r,t)$

In the following, we shall determine the temperature field in a fixed gas-solid system without gas flow. For example, let us consider the nonsteady heating of a

© 1983 Hemisphere I blishing Corporation

tubular packed bed through its cylindrical wall (see Fig. 1).

The equation governing the heat balance at a cylindrical sector of the packed bed with thickness dr under the assumption of bed homogeneity and constant physical properties (see Fig. 2) may be written in cylindrical coordinates as

$$-\frac{1}{r}\frac{\partial(r\dot{q}_r)}{\partial r} = [(1-\psi)\rho_s c_s + \psi\rho c_p]\frac{dT}{dt} \qquad (1)$$

where $\dot{q}_r$ = radial heat flux at position r
ψ = bed porosity
ρ_s, ρ = density of solid phase and gas phase, respectively
c_s, c_p = heat capacity of solid phase and gas phase, respectively

With Fourier s law of heat conduction in homogeneous bodies,

$$\dot{q}_r = -\lambda_{so}\frac{dT}{dr} \qquad (2)$$

and the fact that momentary changes of gas enthalpy are neglected compared with that of the solid, the above equation leads to

$$\lambda_{so}\left(\frac{d^2T}{dr^2} + \frac{1}{r}\frac{dT}{dr}\right) = (1-\psi)\rho_s c_s \frac{dT}{dt} \qquad (3)$$

λ_{so} in this equation is the so-called effective thermal conductivity of the stagnant gas-solid system.

The initial conditions are

$$t = 0: \quad T = T_A \qquad (4)$$

and the boundary conditions are

$$r = \frac{D}{2}; \quad T = T_w = \text{const} \qquad (5)$$

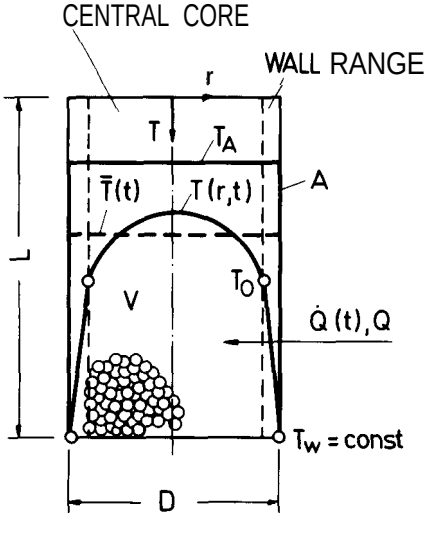

Figure 1 Nonsteady heating of a tubular fixed bed without gas flow.

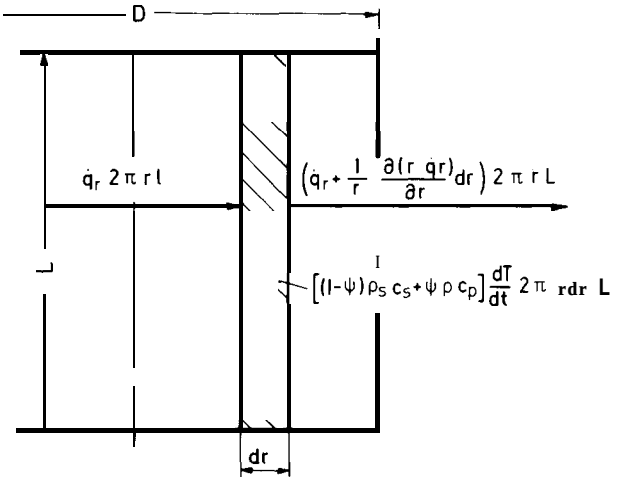

Figure 2 Heat balance on a cylindrical sector of the fixed bed with thickness dr.

$$r = 0: \quad \frac{\partial T}{\partial r} = 0$$

In order to account for the heat transfer at the wall, the following boundary condition is introduced:

$$r = \frac{D}{2}: \quad -\lambda_{so}\frac{dT}{dr}_{D/2} = \alpha_{max}(T_0 - T_w) \qquad (6)$$

with $T_0 - T_w$ as a fictitious temperature rise. In this equation α_{max} is the so-called wall heat transfer coefficient of the stagnant gas-solid system.

The analytic solution of Eq. (3) is discussed in [1].

C. Heat transfer parameter of interest

(a) Effective thermal conductivity λ_{so} of stagnant packed beds

The theoretical and experimental evaluation of the effective thermal conductivity λ_{so} of packed beds with a stagnant gas has a long history with a steady refinement of the theoretical and experimental work. Modern theories provide equations for λ_{so} in terms of system properties and geometry.

Probably one of the most refined theories is that of Hengst [2]. As early as 1933, Hengst introduced a method for calculating λ_{so} by arranging spherical particles in a model so that the direction of heat flow passes through the centers of two contiguous spheres. The effective thermal conductivity of this arrangement can be determined mathematically by assuming differential thermal conductivities above the basis surface of the cell. A simplifying assumption of this model is the existence of parallel heat flux lines. The error introduced by this assumption as well as the one of an arbitrary particle shape is compensated by Zehner

© 1983 Hemisphere Publishing Corporation

[3] by means of a variable contour of the model particle. In 1977 Bauer [4] extended this model to describe beds of nonspherical particles such as cylinders and Raschig rings as well as packed beds with different particle size distributions.

According to the Zehner-Bauer model illustrated in Fig. 3, one portion of the heat is transferred only through the fluid phase with the relative torus $1 - \sqrt{1-\psi}$ by molecular conduction as well as by radiation. The other portion passes through both the fluid and the solid phases; its surface fraction is $\sqrt{1-\psi}$. This separation is necessary in order to describe effective coefficients of diffusion in packings under nonflow conditions. It is further assumed that the solid-solid contact of the adjacent particles has a finite area. The fraction $\sqrt{1-\psi}$ is therefore divided into a surface fraction φ for heat transfer through contact and the remaining surface fraction $1-\varphi$ for transfer through the two particle halves that are separated by a wedge of the fluid.

The conductive and radiative heat transfer as well as the Smoluchowski effect (pressure effect), which depends in each case on the size of this fluid wedge, are included by substituting the equivalent thermal conductivities λ_s^*, λ_R, and λ_D in summing up the individual local thermal conductivities. Finally, the calculation for the total cell yields the following equation for the prediction of λ_{so}:

$$\frac{\lambda_{so}}{\lambda} = (1-\sqrt{1-\psi})\left[\frac{\psi}{(\psi-1)+\lambda/\lambda_D} + \psi\frac{\lambda_R}{\lambda}\right] + \sqrt{1-\psi}\left[\varphi\frac{\lambda_s^*}{\lambda} + (1-\varphi)\frac{\lambda_{so}^*}{\lambda}\right] \tag{7a}$$

where

$$\frac{\lambda_{so}^*}{\lambda} = \frac{2}{P}\left(\frac{B(\lambda_s^*/\lambda + \lambda_R/\lambda - 1)(\lambda/\lambda_D)(\lambda/\lambda_s^*)}{P^2}\right.$$

$$\times \ln\frac{(\lambda_s^*/\lambda + \lambda_R/\lambda)(\lambda/\lambda_D)}{B[1+(\lambda/\lambda_D-1)(\lambda_s^*/\lambda+\lambda_R/\lambda)]} - \frac{B-1}{p}\frac{\lambda}{\lambda_D} + \frac{B+1}{2B}\left\{\frac{\lambda_R}{\lambda}\frac{\lambda}{\lambda_D} - B\left[1+\left(\frac{\lambda}{\lambda_D}-1\right)\frac{\lambda_R}{\lambda}\right]\right\}\Bigg) \tag{7b}$$

with

$$p = \left[1+\left(\frac{\lambda_R}{\lambda} - B\frac{\lambda_D}{\lambda}\right)\frac{\lambda}{\lambda_s^*}\right]\frac{\lambda}{\lambda_D} - B\left(\frac{\lambda}{\lambda_D}-1\right) \times \left(1+\frac{\lambda_R}{\lambda}\frac{\lambda}{\lambda_s^*}\right) \tag{7c}$$

Equation (7b) is not defined for $p = 0$. In the limit the analysis leads to

$$\lim_{p\to 0}\frac{\lambda_{so}^*}{\lambda} = \frac{\lambda_s^*/\lambda}{B(B-1)[1+(\lambda/\lambda_D-1)(\lambda_s^*/\lambda+\lambda_R/\lambda)]} \times\left\{\frac{2}{3}\frac{B^3-1}{(B-1)[1+(\lambda_R/\lambda)(\lambda/\lambda_s^*)]} + (B+1)\times\left(\frac{\lambda_R}{\lambda}-1\right)\right\} \tag{7d}$$

In Eq. (7), λ is the thermal conductivity of the gas phase in an infinitely expanded space.

λ_s^* is a mean thermal conductivity of the solid phase. For nonmetallic particles λ_s^* is equal to the thermal conductivity λ_s of the particles. In the case of metallic particles covered with an oxide layer of thickness s_{ox} and thermal conductivity λ_{ox}, one obtains

$$\frac{\lambda_s^*}{\lambda} = \frac{\lambda_s}{\lambda}\frac{1}{1+\mathrm{Bi}} \tag{8}$$

with

$$\mathrm{Bi} = \frac{s_{ox}}{\lambda_{ox}}\frac{\lambda_s}{\bar{d}} \tag{9}$$

Generally the ratio s_{ox}/λ_{ox} is not known and must be determined experimentally.

$\bar{d}$ in Eq. (9) is the average diameter of an arbitrary particle the reciprocal of which,

$$\frac{1}{\bar{d}} = \sum_{i=1\,n}\frac{\Delta D_i}{d_{V,i}} \tag{10}$$

is to be formed by summing up all particle sizes i with mass fractions ΔD_i divided by the volume-equivalent sphere diameter $d_{V,i}$. Thereby, hollow spaces in the particles such as in Raschig rings are disregarded. In the case of a monodisperse packed bed, $\bar{d}$ is of course equal to the sphere diameter d.

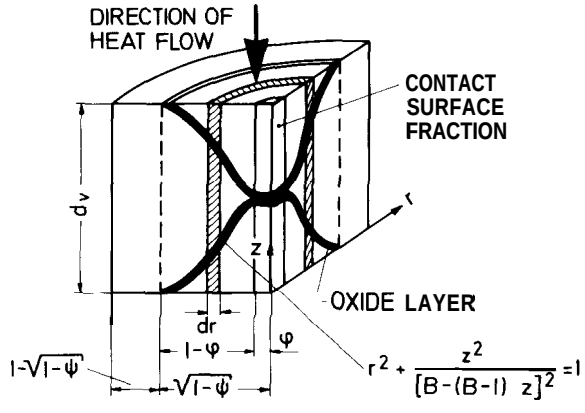

Figure 3 Model for precalculation of effective thermal conductivity λ_{so} according to [4].

© 1983 Hemisphere I blishing Corporation

λ_R is the equivalent thermal conductivity for the energy transfer by radiation as already suggested by Damköhler.

$$\frac{\lambda_R}{\lambda} = \frac{0.04 C_s}{(2/\epsilon - 1)\lambda}\left(\frac{T}{100}\right)^3 x_R \tag{11}$$

with C_s = 5.775 W/m^2K^4, ϵ the emission ratio, and T the absolute temperature of the packing.

x_R is the effective radiation length that characterizes the distance between the particle surfaces of any packing and is calculated by

$$\frac{1}{x_R} = \sum_{i=1,n} \frac{\Delta D_i}{R d_{V,i}} \tag{12}$$

R is a shape factor taking into account that the apparent shape of the particle with respect to radiative energy exchange may be different from its geometric one and must be determined from experiments.

λ_D is the equivalent thermal conductivity between the surfaces of the solid phase due to the Smoluchowski effect. Therefore, in such gaps the normal movement of the gas molecules is so inhibited at the boundary surface that there is an additional heat transfer resistance in this system. Since this resistance is directly proportional to the mean free path length of the gas, the smaller the distance between the solid surfaces, the more important this resistance becomes. In a region around the point of contact of the particles in a packing, the distance between the surfaces of these particles is always on the order of magnitude of this mean free path length. As the heat transfer in the gas is related to the temperature of the solid surfaces, the result is an equivalent thermal conductivity λ_D of the gas,

$$\frac{\lambda}{\lambda_D} = 1 + \frac{2\sigma}{x_D}\left(\frac{2}{\gamma} - 1\right) \tag{13}$$

Here, x_D is the effective gas path that characterizes the size of the space between the particles with respect to the heat conduction in a rarefied gas and is calculated from

$$\frac{1}{x_D} = \sum_{i=1,n} \frac{\Delta D_i}{D d_{V,i}} \tag{14}$$

D is a shape factor taking into account that the apparent shape of the particles with respect to Knudsen diffusion may be different from the geometric one. D is determined from experiments.

γ in Eq. (13) is the accommodation coefficient and σ the mean free path length of the gas molecules. Since σ is inversely proportional to the gas pressure,

$$\sigma = \sigma_0 \frac{T}{T_0}\frac{P_0}{P} \tag{15}$$

with σ_0 the mean free path length at temperature T_0 = 273.15 K and pressure p_0 = 1.01 X 10^5 N/m^2, the effective thermal conductivity λ_{so} of the complete system becomes a function of the gas pressure. Also, under the normalized conditions, σ_0 is a function of the molecule diameter η, m:

$$\sigma_0 = \frac{8.4 \text{ X } 10^{-27}}{\eta^2} \tag{16}$$

The quantity B in Eq. (7) is a deformation parameter by which the real shape of the particles is replaced by an artificial one so that the streamlines of the heat flux remain parallel throughout the packing.

B follows from

$$B = C\left(\frac{1-\psi}{\psi}\right)^{10/9}(1 + 3\xi_1) \tag{17}$$

with ψ the mean porosity of a packing and C a shape factor with respect to particle heat conduction. C has to be determined from experiment.

ξ_1 in Eq. (17) describes the influence of the number of contact points, which changes with the particle size distribution because the majority of the conducted heat is transported in the vicinity of these contact points. It is the standard deviation relative to the mean value of the numerical distribution, also called the coefficient of variation:

$$\xi_1 = \left[\frac{\sum_{i=1,n} \Delta D_i/d_{V,i}^2}{\left(\sum_{i=1,n} \Delta D_i/d_{V,i}\right)^2}\right]^{0.5} \tag{18}$$

In the case of monodisperse packings, ξ_1 becomes zero.

The quantity φ in Eq. (7) describes the additional heat transfer through the solid path between contiguous particles:

$$\varphi = \frac{23\rho_k^2}{1 + 22\rho_k^{4/3}} \tag{19}$$

In this equation ρ_k^2 is the relative contact area of the solid path,

$$\rho_k^2 = \left(\frac{d_k}{\bar{d}}\right)^2 \tag{20}$$

where d_k is the diameter of the contact area. Since this area fraction is a function of many still indeterminable, limiting quantities, such as the elasticity of the material, external mechanical stress, surface state, and so on, ρ_k^2 can only be found experimentally.

In conclusion, effective thermal conductivity ratios

© 1983 Hemisphere Publishing Corporation

X,/X calculated from Eq. (7)-(20) for some special cases are plotted in Fig. 4; they can be used to estimate the most important limiting quantities.

In the following figures the basis equations to calculate effective thermal conductivities λ_{so} are compared with experimental results from packings consisting of spheres, cylinders, hollow cylinders, and broken solids of equal and unequal size. The different shape factors *C*, ***R,*** and ***D*** as derived from experiments are compiled in Table 1.

For example, in Figs. 5-8, according to Bauer [4], and Figs. 9-12, according to Yagi and Kunii [5], measurements are presented to show the influence of thermal conduction and radiation in different packings.

The measurements in Fig. 5 show quite clearly that the radiation fraction of thermal conductivity λ_{so} is very dependent on the conduction transfer of heat in the solid phase. Thus, with steel tubes, which are good conductors, the increase of λ_{so} due to radiation is clearly stronger than in the case of ceramic, which is a poor conductor.

In Fig. 6 the dominant influence of the particle size

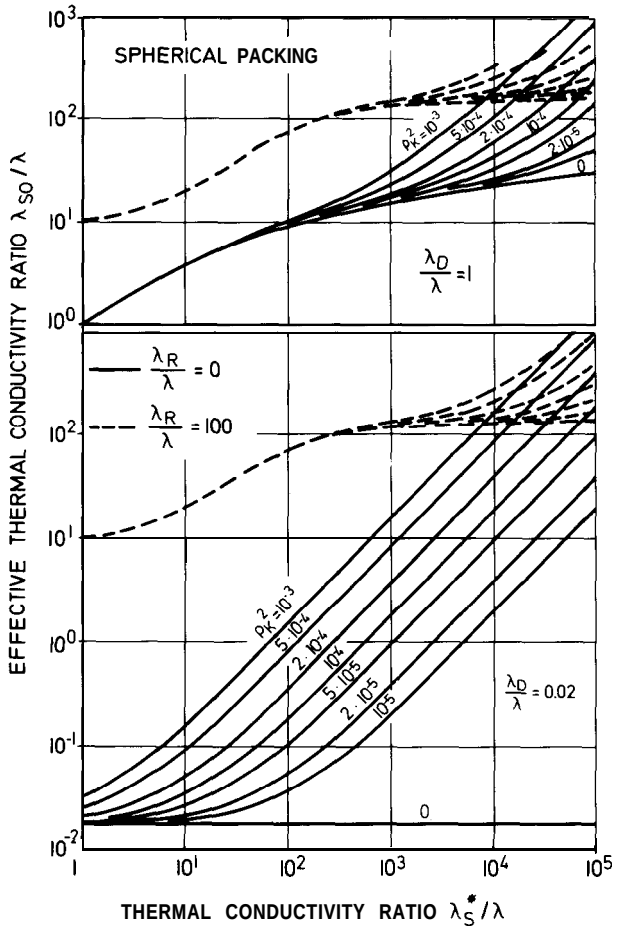

Figure 4 Calculated effective thermal conductivity ratios λ_{so}/λ for packings of uniformly sized spheres according to Eq. (7).

distribution on the conductive heat transfer can be seen clearly. As the diameter ratio d_1/d_2 of the spherical fractions involved increases, there is an increase in the number of points of contact and a consequent increase in the conduction fraction of λ_{so}. Moreover, the number of contact points changes with the composition ΔD_1 of the mixture so that in each case a maximum value is attained.

Recently published comprehensive experimental results of Imura and Takegoshi [6] as well as data from Swift [7] and Kling [8] are shown in Figs. 13-23 to test the theory concerning the influence of pressure. These are especially applicable to the design of the important powder insulations.

If the measured effective thermal conductivities λ_{so} are plotted as a function of the pressure p in logarithmic coordinates, they will show a typical S-shaped curve (see Fig. 13). The constant value at very low pressures is explained by the fraction of conduction through surface contact that can be determined by varying ρ_k^2 until the measured value agrees with the theoretical.

The value $\rho_k^2 = 3.5 \times 10^{-4}$ thus obtained should be independent of the gas content, since at very low pressures the effective thermal conductivity rests practically exclusively on these bridges of solid material. As shown in Figs. 14-18, the experimental values for several gases in spherical ceramic packings with special attention to the different particle sizes as well as size distributions are reproduced equivocally.

To calculate heat transfer accurately in packings with metallic particles at high pressures, it is sometimes necessary to take into account that a poorly conducting oxide layer inhibits heat transfer. In each case, the resistance of such an oxide layer can be well described by $s_{ox}/\lambda_{ox} = 0.15 \times 10^{-3}\,\mathrm{W/m^2\,K}$ (see Figs. 19 and 20).

In contrast, measurements with perfectly clean metal spheres are given in Figs. 21-23.

The unsatisfactory aspect of different contact surface fractions ρ_k^2 found for the various packings is not at all surprising since they depend on many limiting quantities that cannot be determined in advance. The mechanical compression of the particles resulting from the packing process, bed height, and thermal expansion of the particles may be one of the dominant variables.

Some properties of the packings used in the figures above are listed in Table 2.

(b) Heat transfer coefficient α_{max} from walls to stagnant packed beds

When solving the differential equation (3), the heat transfer between the wall and the packing has to be taken into consideration as a boundary condition of

© 1983 Hemisphere publishing Corporation

Table 1 Shape factors *C, R, D,* and volume equivalent sphere diameter $d_{V,i}$ for calculating the effective thermal conductivity λ_{so} of various packings

Form	c	*R*	*D*	$d_{V,i}$
Sphere with diameter ***d***	1.25	1	1	***d***
Cylinder with diameter ***d,*** length *l*	***2.5***	1	1	$d\sqrt[3]{\frac{3l}{2d}}$
Hollow cylinder with outer diameter ***d,*** inner diameter d_i, length I	$2.5\left[1+\left(\frac{d_i}{d}\right)^2\right]$	1	1	$d\sqrt[3]{\frac{3l}{2d}}$
Binary sphere mixture with diameters d_1, d_2 and mass fraction AD, $= \frac{M_1 \text{ (mass of sphere 1)}}{M \text{ (total mass)}}$	***1.25***	*1*	1	d_1, d_2
Broken particle size distribution with mass fraction $\Delta D_i = \frac{M_i \text{ (mass of size fraction } i)}{M \text{ (total mass)}}$ z number of particles in size fraction ***i***	***1.4***	1	1	$\sqrt[3]{\frac{6}{\pi}\frac{M_i}{z\rho_s}}$

the so-called third part. This is necessary to give preference to the fact that heat transfer with respect to short contact times (i.e., less than 0.1 s) is quite different from that at moderate and long contact times (i.e., greater than 1 s). When the contact time approaches zero, the heat transfer tends toward a finite and maximum value contrary to that experienced in a real homogeneous body.

The physical arguments with their mathematical formulation have been derived by Schlünder [9] for spherical packings. He analyzed the heat conduction in the gaseous gap between the wall and the adjacent sphere with the assumption that there is only solid point contact. Adding now the necessary aspect of contact area and the influence of oxide layer resistance (recall Sec. C), we get

$$\alpha_{max} = (1-\varphi)\alpha^*_{max} + 2\varphi\frac{\lambda_s^*}{d} \qquad (21a)$$

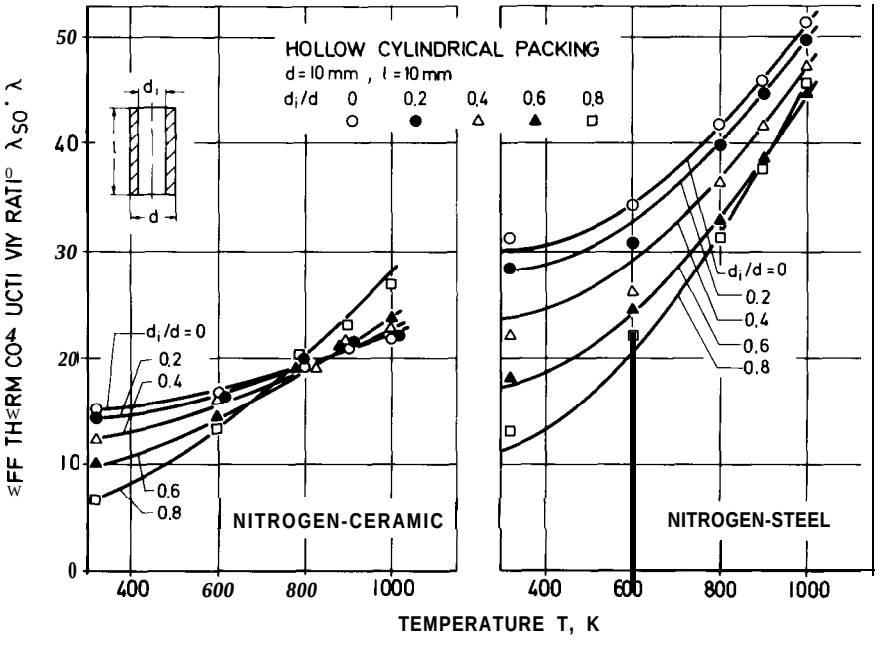

Figure 5 Influence of temperature ***T*** on effective thermal conductivity ratio λ_{so}/λ for packings of uniformly sized hollow cylinders at normal pressure according to [4] and Eq. (7). Various inner-to-outer diameter ratios d_i/d.

© 1983 Hemisphere Publishing Corporation

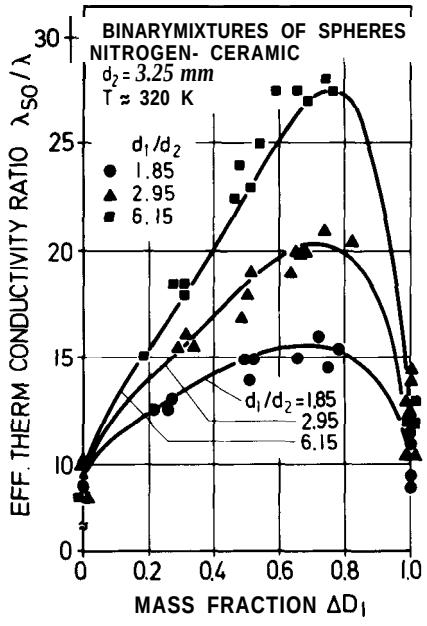

Figure 6 Effective thermal conductivity ratio λ_{so}/λ for packings of binary mixtures of ceramic spheres as a function of the mass fraction ΔD, at normal pressure according to [4] and Eq. (7). Various diameter ratios d_1/d_2.

with

$$\alpha_{\max} = \frac{4\lambda}{d}\left\{\left[\frac{4\sigma}{d}\left(\frac{2-\gamma}{\gamma}\right)+1\right]\ln\left[\frac{d}{4\sigma}\left(\frac{\gamma}{2-\gamma}\right)+1\right]-1\right\}+0.04\epsilon C_s\left(\frac{T_m}{100}\right)^3 \qquad (21b)$$

λ_s^* and φ have to be calculated from Eqs. (8) and (19), respectively. The first term in Eq. (21 ***b)*** represents the

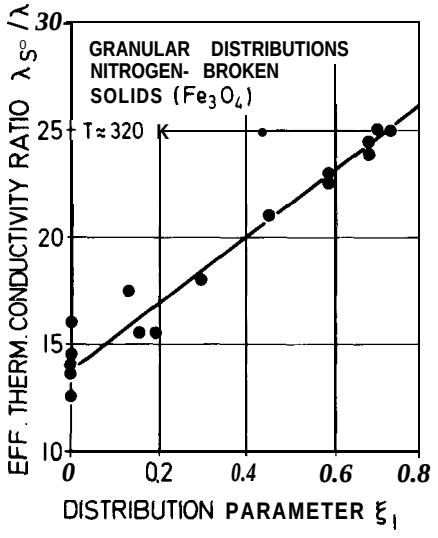

Figure 7 Influence of distribution parameter ξ_1 on effective thermal conductivity ratio λ_{so}/λ for packings of granular distributions of broken solids (Fe_3O_4) at normal pressure according to [4] and Eq. (7).

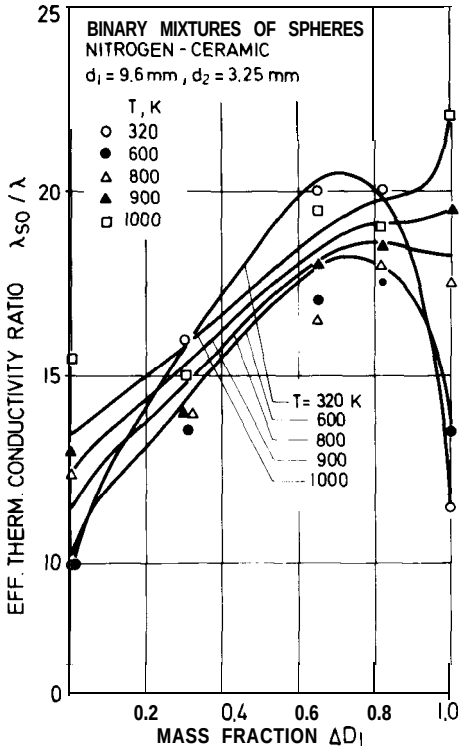

Figure 8 Effective thermal conductivity ratio λ_{so}/λ for packings of binary mixtures of ceramic spheres as a function of the mass fraction ΔD_1 at normal pressure according to [4] and Eq. (7). Various temperatures.

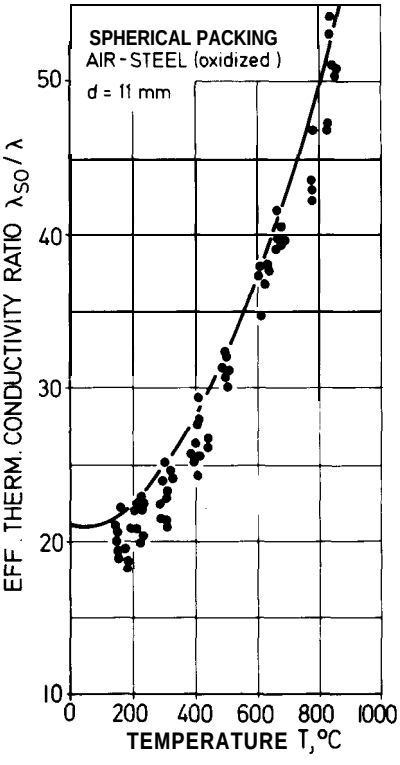

Figure 9 Influence of temperature T on effective thermal conductivity ratio λ_{so}/λ of uniformly sized spheres at normal pressure according to [5] and Eq. (7).

© 1983 Hemisphere I blishing Corporation

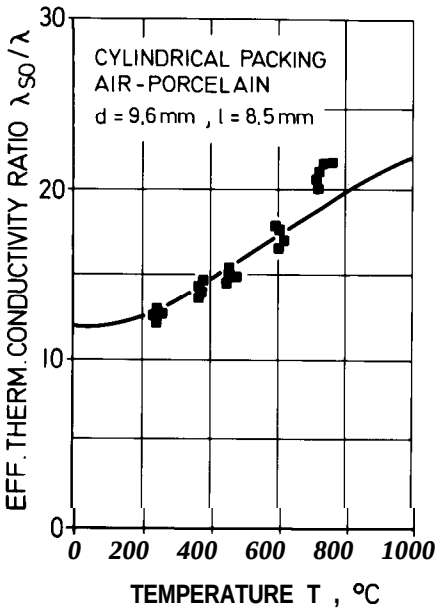

Figure **10** Influence of temperature T on effective thermal conductivity ratio λ_{so}/λ of uniformly sized cylinders at normal pressure according to [5] and Eq. (7).

molecular heat conduction in a rarefied gas, whereas the second accounts for the radiation between wall and packing.

In detail, λ is the thermal conductivity of the gas, d is the diameter of the sphere, σ is the mean free path of the gas molecules and may be derived from Eq. (15), γ is the accommodation coefficient, ϵ is the radiation emissivity, and T_m is the absolute average temperature between the wall and the first particle layer.

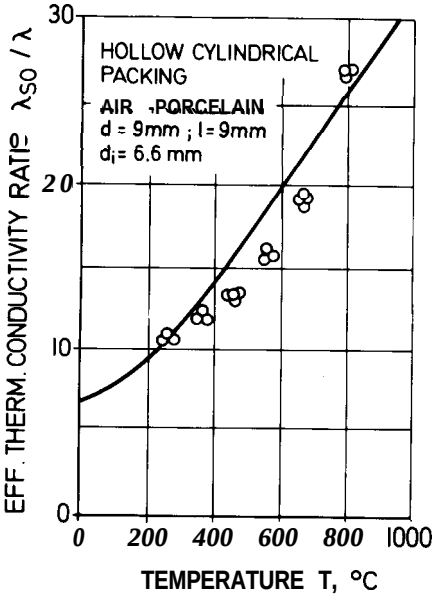

Figure 11 Influence of temperature T on effective thermal conductivity ratio λ_{so}/λ of uniformly sized hollow cylinders at normal pressure according to [5] and Eq. (7).

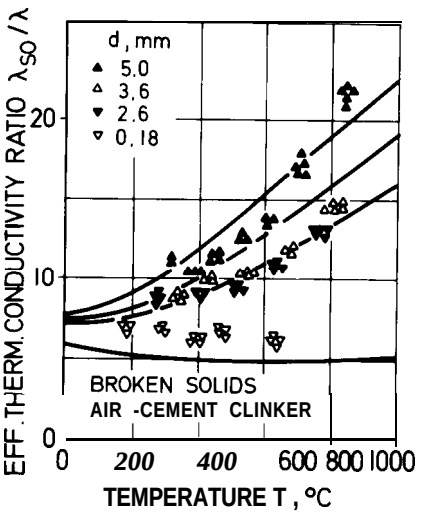

Figure **12** Influence of temperature T on effective thermal conductivity ratio λ_{so}/λ for packings of broken solids at normal pressure according to [5] and Eq. (7). Various mean diameters.

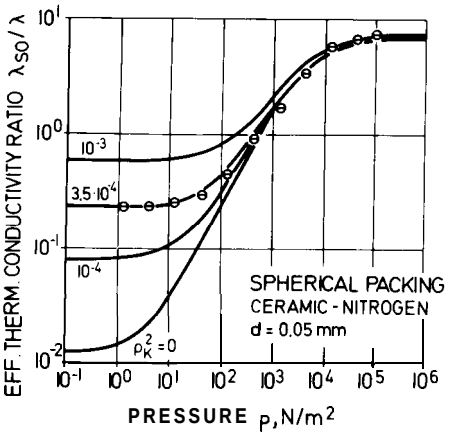

Figure 13 Influence of contact area fraction ρ_k^2 on effective thermal conductivity ratio λ_{so}/λ of uniformly sized spheres at different gas pressures p and room temperature according to [6] and Eq. (7).

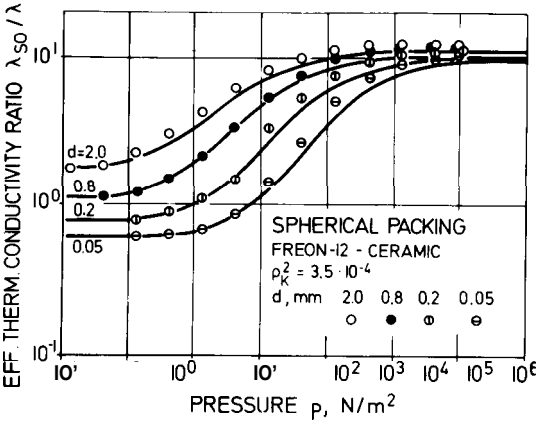

Figure 14 Effective thermal conductivity ratio λ_{so}/λ of uniformly sized spheres at different gas (Freon 12) pressures p and room temperature according to [6] and Eq. (7). Various diameters.

© 1983 Hemisphere Publishing Corporation

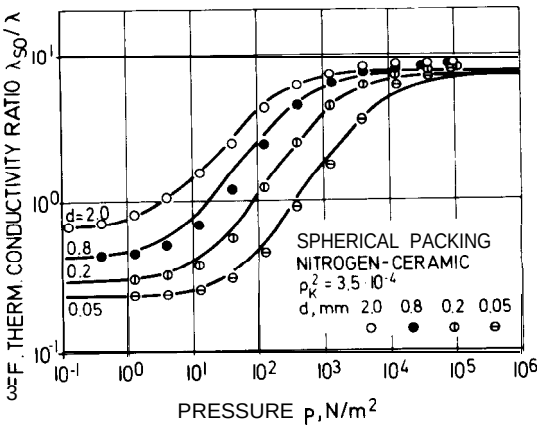

Figure 15 Effective thermal conductivity ratio λ_{so}/λ of uniformly sized spheres at different gas (nitrogen) pressures p and room temperature according to [6] and Eq. (7). Various diameters.

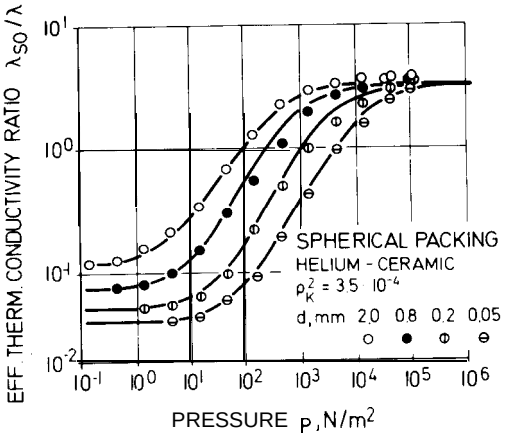

Figure 16 Effective thermal conductivity ratios λ_{so}/λ of uniformly sized spheres at different gas (helium) pressures p and room temperature according to [6] and Eq. (7). Various diameters.

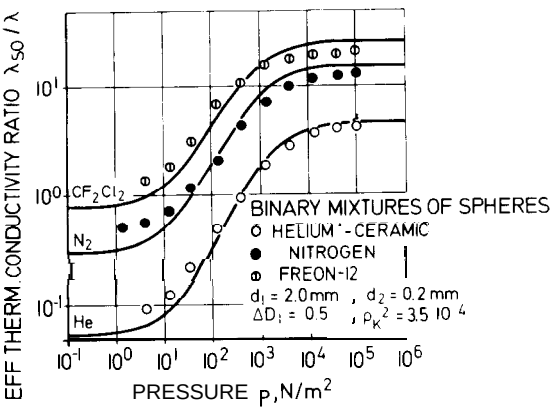

Figure 17 Influence of the gas thermal conductivity on effective thermal conductivity ratio λ_{so}/λ for a binary mixture of spheres at various pressures p and room temperature according to [6] and Eq. (7).

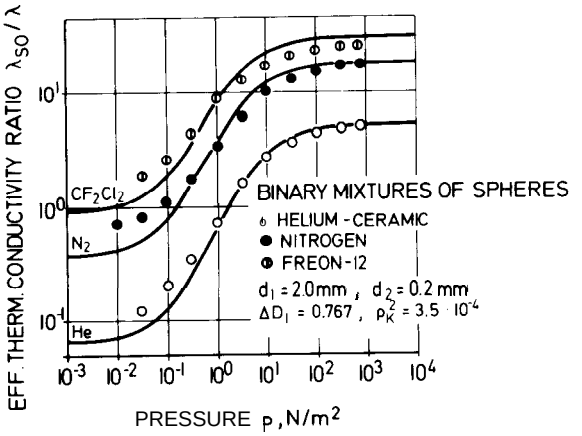

Figure 18 Influence of the gas thermal conductivity on effective thermal conductivity ratio λ_{so}/λ for a binary mixture of spheres at various pressures p and room temperature according to [6] and Eq. (7).

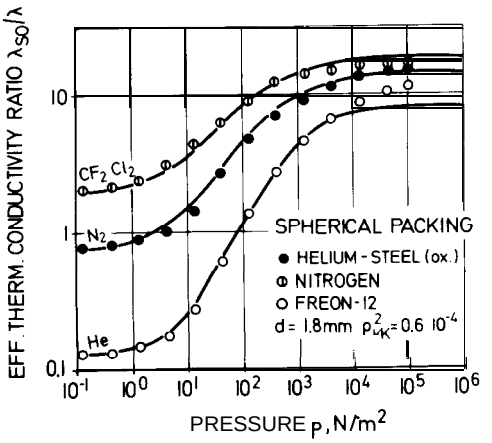

Figure 19 Effective thermal conductivity ratio λ_{so}/λ of oxidized metal spheres of different filling gases at various pressures p and room temperature according to [6] and Eq. (7).

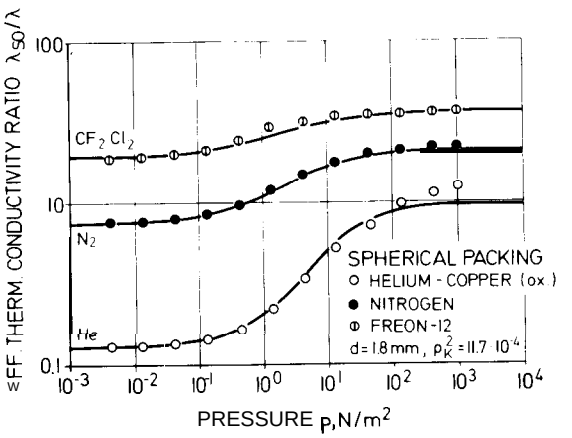

Figure 20 Effective thermal conductivity ratio λ_{so}/λ of oxidized metal spheres of different tilling gases at various pressures p and room temperature according to [6] and Eq. (7).

© 1983 Hemisphere Publishing Corporation

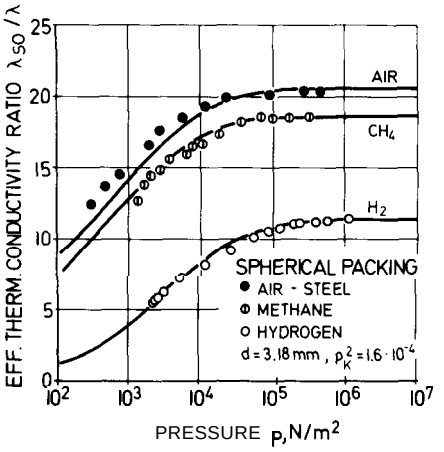

Figure 21 Effective thermal conductivity ratio λ_{so}/λ of non-oxidized spheres for different filling gases at various pressures p and room temperature according to [8] and Eq. (7).

Finally, Wunschmann [10] has confirmed the validity of Eq. (21) by nonsteady-state heat transfer experiments as described in Sec. D.

D. Equation governing the one-dimensional temperature field $\bar{T}(t)$

It is usual and sufficient according to most industrial practices to obtain an answer about the average temperature $\bar{T}(t)$ of the packing (see Fig. 1) with the help of overall heat transfer coefficients. By this means the average temperature $\bar{T}(t)$, the so-called integral coloric mean temperature, is defined by

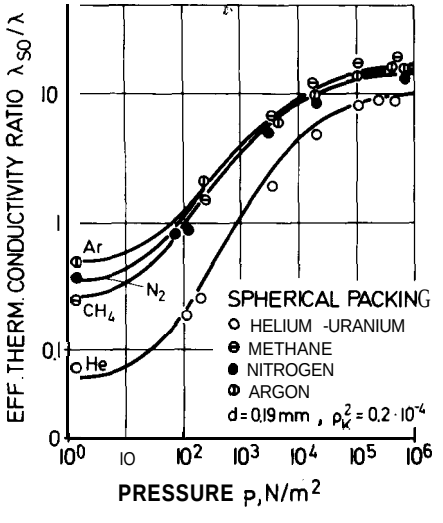

Figure 22 Effective thermal conductivity ratio λ_{so}/λ of non-oxidized spheres for different filling gases at various pressures p and room temperature according to [7] and Eq. (7).

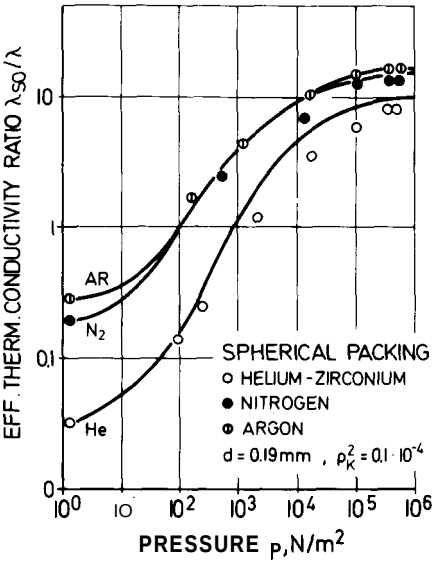

Figure 23 Effective thermal conductivity ratio λ_{so}/λ of non-oxidized spheres for different filling gases at various pressures p and room temperature according to [7] and Eq. (7).

$$\bar{T}(t) = \frac{\int_0^r (1-\psi)\rho_s c_s T(r,t)\, r\, dr}{\int_0^r (1-\psi)\rho_s c_s r\, dr} \tag{22}$$

Then the equation for the heat balance of the whole cylindrical packed bed becomes

$$\dot{Q}(t) = -(1-\psi)V\rho_s c_s \frac{d\bar{T}(t)}{dt} \tag{23}$$

with $\dot{Q}$ the overall heat rate through the wall and V the total volume of the packing. With Newton s law of heat transfer,

$$\dot{Q}(t) = U_t(t)A(\bar{T}(t) - T_w) \tag{24}$$

the above equation leads to

$$\frac{A}{V} U_t(t)(\bar{T}(t) - T_w) = (1-\psi)\rho_s c_s \frac{d\bar{T}(t)}{dt} \tag{25}$$

A is the wall surface according to the heat rate $\dot{Q}(t)$ and $U(t)$ is the momentary overall heat transfer coefficient between the wall and the whole packing.

The integration of Eq. (25) with the help of the time-dependent overall heat transfer coefficient

$$U_0(t) = \frac{1}{t} \int_0^t U_t(t)\, dt \tag{26}$$

results in

$$\frac{\bar{T}(t) - T_w}{T_A - T_w} = \exp\left[-\frac{AU_0(t)t}{V(1-\psi)\rho_s c_s}\right] \tag{27}$$

© 1983 Hemisphere Publishing Corporation

Table 2 Properties of the packings. Comparison of calculations and experimental results

Author	Solid	Gas	ϵ	s_{ox}/λ_{ox} X 10^3/W/m² K	$\rho_k^2 \times 10^4$	σ_0, nm	γ	p, bar	T, °C
Bauer [4]	Styropor	N_2	*0.93*	*0*	3.5	61.8	0.9	1	
	Foam glass								
	Glass								
	Ceramic	N_2	0.85	0	3.5	61.8	0.9	1	
	Steatit	N_2	0.78	0	3.5	61.8	0.9	1	
	Steel (oxidized)	N_2	0.85	0.15	1.5	61.8	0.9	1	
	Steel (nonoxidized)	N_2	0.3	0	1.5	61.8	0.9	1	
	Copper (oxidized)	N_2	0.78	0.15	2.0	61.8	0.9	1	
	Copper (nonoxidized)	N_2	0.2	0	2.0	61.8	0.9	1	
Imura and Takegoshi [6]	Ceramic	He				126.3	0.4		
		N_2	0.9	0	3.5	61.8	0.9		30
		CF, Cl,				31.5	1.0		
	Steel	He				126.3	0.4		
	(oxidized)	N_2	0.85	0.15	0.6	61.8	0.9		30
		CF, Cl,				31.5	1.0		
	Copper	He				126.3	0.4		
	(oxidized)	N_2	0.78	0.15	11.7	61.8	0.9		30
		CF, Cl,				31.5	1.0		
Swift [7]	Uranium	He				126.3	0.4		
	(nonoxidized)	CH_4	0.1	0	*0.2*	57.4	0.8		25
		N_2				61.8	0.9		
		Ar				71.8	0.95		
	Zirconium	He				126.3	0.4		
	(nonoxidized)	N_2	0.1	0	0.1	61.8	0.9		25
		Ar				71.8	0.95		
Kling [8]	Steel	H_2				112.0	0.15		
	(nonoxidized)	CH_4	0.1	0	1.6	57.4	0.8		33
		Air				64.0	0.9		
Yagi and Kunii [5]	Steel (oxidized)	Air	0.8	0.15	1.5	64.0	0.9	1	
	Porcelain	Air	0.93	0	3.5	64.0	0.9	1	
	Cement clinker	Air	0.93	0	3.5	64.0	0.9	1	

the time-dependent course of the average temperature $\bar{T}(t)$ in a packing.

The consequent comparison of Eq. (27) with the exact solution of Eq. (3) gives values for the unknown overall heat transfer parameter $U_0(t)$. Still with regard to practical design, the following manner of approach yields a sufficiently good approximation.

First, the heat transfer resistance of the central core of the packing as well as the heat transfer resistance between the wall and the packing are connected in series:

$$\frac{1}{U_0(t)} = \frac{1}{\alpha_{max}} + \frac{1}{\alpha_{so}(t)} \tag{28}$$

In this relationship the heat transfer coefficient α_{so} of the central core is the suited superposition of two asymptotic solutions:

1. Short-time solution

$$\alpha_{t,0}(t) = \frac{1}{\sqrt{\pi}} \frac{\sqrt{(1-\psi)\rho_s c_s \lambda_{so}}}{\sqrt{t}} \tag{29}$$

with the integral value

$$\alpha_{so,0}(t) = \frac{2}{\sqrt{\pi}} \frac{\sqrt{(1-\psi)\rho_s c_s \lambda_{so}}}{\sqrt{t}} \tag{30}$$

2. Long-time solution and integral value

$$\alpha_{t,\infty}(t) = \alpha_{so,\infty}(t) = \frac{\lambda_{so}}{D} K = \text{const} \tag{31}$$

Superposition of 1. and 2. leads to

$$\alpha_{so}(t) = \sqrt{\alpha_{so,0}^2(t) + \alpha_{so,\infty}^2} \tag{32}$$

© 1983 Hemisphere. Publishing Corporation

Table 3 Values of K [see Eq. (31)] for several shapes of the packing wall

	Plate	Cylinder	Sphere
$\frac{A}{V}D$	2	4	6
K	$\frac{1}{2}\pi^2$	5.78	$\frac{2}{3}\pi^2$
D	Thickness	Diameter	

Values of K are listed in Table 3 for several shapes of packing wall.

Figure 24 shows that with increasing contact time t, the momentary heat transfer coefficient $U_t(t)$ [see Eq. (24)] follows Eq. (21) at the beginning, then Eq. (29), and finally Eq. (31). In addition, the limiting value for very short contact time is independent of the thermal properties of the solid but strongly dependent on the particle diameter. However, in the range of Eq. (29) at longer contact times, the reverse behavior is valid: The heat transfer coefficient depends strongly on the thermal properties of the solid but slightly on the diameter of the particles.

Wunschmann [10] has confirmed the validity of Eq. (21) by nonsteady-state heat transfer experiments. A packed bed resting on a plate was heated from below for a certain time t. Figures 25-27 show the experimental result. The parameter is the gas (air) pressure. On the left $U_t(t)$ according to Eq. (21) and on the right according to Eq. (29) is indicated. During the experiments no fully developed temperature profiles were obtained, so Eq. (3 1) is not reached.

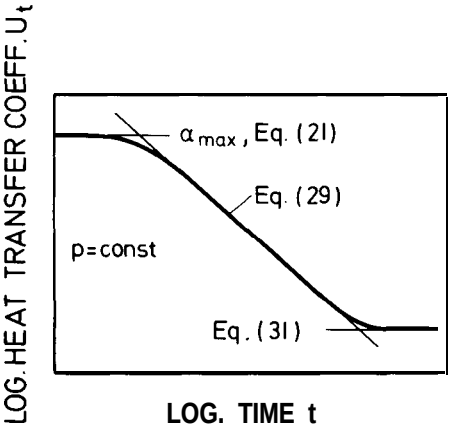

Figure 24 Asymptotic overall heat transfer coefficients describing nonsteady heat transfer in stagnant packings.

E. The heat quantity Q

The total heat rate Q transferred from time zero to time t_1 is

$$Q(t_1) = \int_0^{t_1} \dot{Q}(t)\,dt \tag{33}$$

With the total heat balance on the packing

$$Q(t_1) = (1-\psi)\rho_s c_s V(T_A - \bar{T}(t_1)) \tag{34}$$

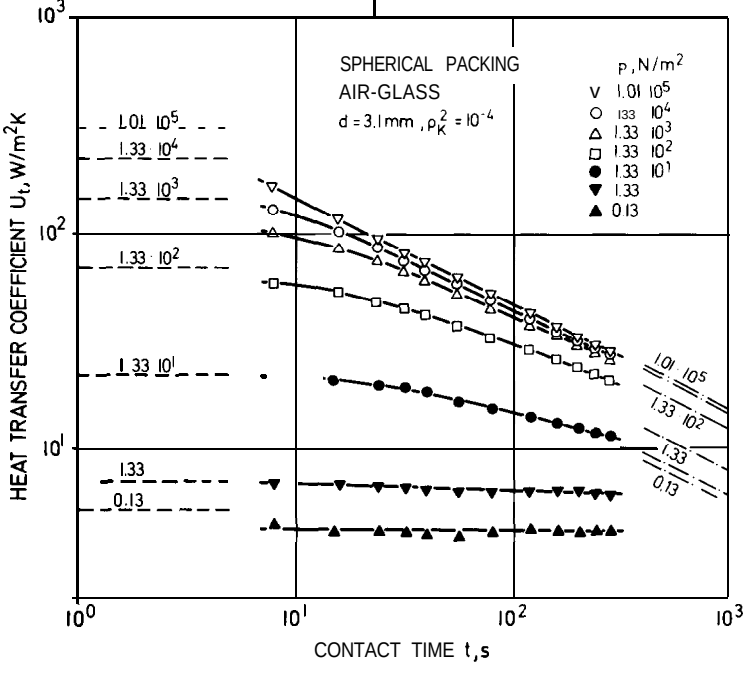

Figure 25 Overall heat transfer coefficients obtained by [10] from nonsteady heat transfer experiments at room temperature and various gas (air) pressures p. Packing with uniformly sized glass spheres.

© 1983 Hemisphere Publishing Corporation

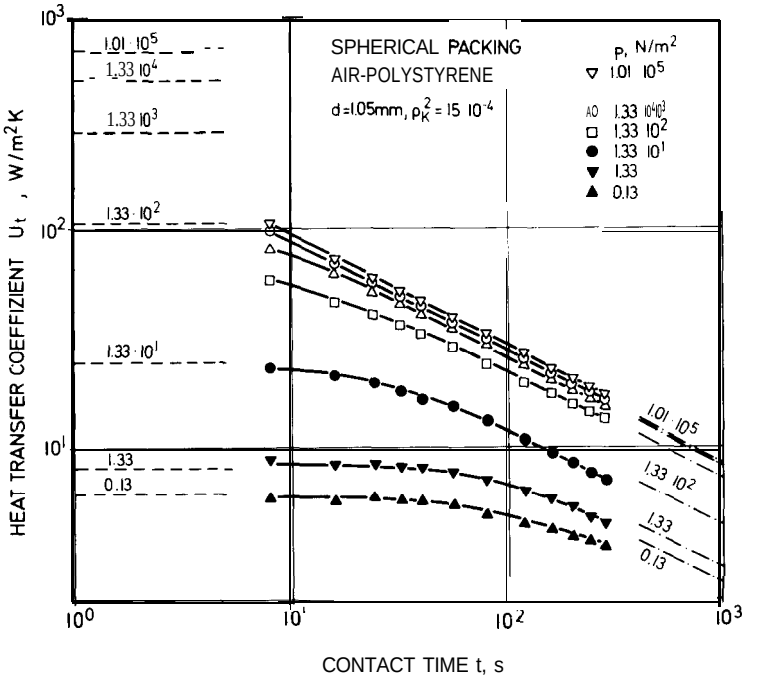

Figure 26 Overall heat transfer coefficients obtained by [10] from nonsteady heat transfer experiments at room temperature and various gas (air) pressures *p.* Packing with uniformly sized polystyrene spheres.

introduced in Eq. (27), this leads to

$$Q(t_1) = U_0(t_1) A \Delta T_m t_1 \tag{35}$$

with

$$\mathrm{AT}_{,,,} = \frac{T_A - \bar{T}(t_1)}{\ln[(T_A - T_w)/(\bar{T}(t_1) - T_w)]}$$

the so-called logarithmic mean temperature difference.

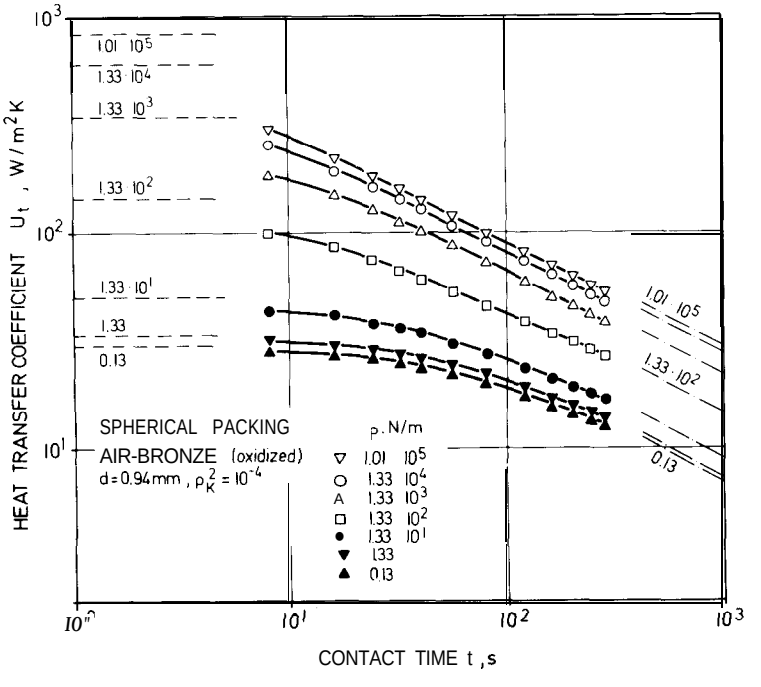

Figure 27 Overall heat transfer coefficients obtained by [10] from nonsteady heat transfer experiments at room temperature and various gas (air) pressures ***p.*** Packing with uniformly sized bronze spheres.

© 1983 Hemisphere Publishing Corporation

NOMENCLATURE FOR SECTION 2.8.1

A	wall surface area
c_p, c_s	heat capacity of gas and solid phases, respectively
C_s	Stefan-Boltzmann constant
D	tube diameter
d	sphere diameter
$d_{V,i}$	volume equivalent sphere diameter
d_k	diameter of contact area
ΔD_i	mass fractions
p	pressure
q	heat flux
Q	heat quantity
$\dot{Q}$	overall heat rate
r	cylindrical coordinate
s_{ox}	thickness of oxide layer
t	time
T	absolute temperature
U_t	instantaneous overall heat transfer coefficient
U_0	overall heat transfer coefficient
V	total volume of packing
α_{max}	heat transfer coefficient from wall to stagnant packed bed
α_{so}	effective heat transfer coefficient of stagnant packed bed
γ	accommodation coefficient
ϵ	emissivity
η	molecule diameter
λ, λ_s	thermal conductivity of gas and solid phases, respectively
λ_{so}	effective thermal conductivity of stagnant packed bed
λ_{ox}	thermal conductivity of oxide layer
ρ, ρ_s	density of gas and solid phases, respectively
ρ_k^2	relative contact area
σ	mean free path length of gas molecules
φ	surface fraction
ψ	bed porosity

REFERENCES FOR SECTION 2.8.1

1. Von Rosenberg, D. U., ***Methods for the Solution of Partial Differential Equations,*** Elsevier, New York, 1969.
2. Hengst, G., Die Wärmeleitfähigkeit pulverförmiger Stoffe bei hohem Gasdruck, Ph.D. thesis, University of Munich, 1934.
3. Zehner, P., Experimentelle und theoretische Bestimmung der effektiven Wärmeleitfähigkeit durchströmter Kugelschüttungen bei mässigen und hohen Temperaturen, Ph.D. thesis, University of Karlsruhe, 1972.
4. Bauer, R., Effektive radiale Wärmeleitfähigkeit gasdurchströmter Schüttungen mit Partikeln unterschiedlicher Form und Grössenverteilung, ***VDI Forschungsh., 582,*** 1977.
5. Yagi, S., and Kunii, D., Studies on Effective Thermal Conductivities in Packed Beds, ***AIChE J.,*** vol. 3, pp. 373-381, 1957.
6. Imura, S., and Takegoshi, E., Effect of Gas Pressure on Effective Thermal Conductivity, ***Nippon Kikai Gakkai Ronlum Shu, Tokyo,*** vol. 40, pp. 489-497, 1974.
7. Swift, D. L., The Thermal Conductivity of Spherical Metal Powders Including the Effect of an Oxide Coating, ***Int. J. Heat Mass Transfer,*** vol. 9, pp. 1061-1074, 1966.
8. Kling, G., Das Wärmeleitvermögen eines Kugelhaufwerks, Ph.D. thesis, University of Munich, 1937.
9. Schlünder, E. U., Wärmeübergang an bewegte Kugelschüttungen bei kurzfristigem Kontakt, ***Chem. Zng. Tech., vol. 43,*** pp. 651-654, 1971.
10. Wunschmann, J., Wärmeübergang von beheizten Flächen an bewegte Schüttungen bei Normaldruck und Vakuum, Ph.D. thesis, University of Karlsruhe, 1974.

© 1983 Hemisphere Publishing Corporation

2.8.2

Packed beds with a gas flowing through

R. Bauer

A. Description of heat transfer situation

The importance of packed beds in a large variety of engineering endeavors is widely appreciated. A frequent and important area of use is flow-through packings of nonadiabatic catalytic reactors in the chemical industry.

Basically, such systems consist of a cylindrical tube packed with catalyst particles through which the reacting fluid passes. The heat of reaction is removed by the cooling medium in the outer shell surroanding the cylinder. One of the questions associated with the design of such reactors is the temperature rise that can be tolerated due to undesirable secondary and follow-up reactions as well as the thermal destruction of the catalyst particles.

The associated question of the maximum diameter of the reactor tube that will allow dissipation of the heat generated without exceeding the prescribed temperature level can be answered only from a knowledge of the heat transfer characteristic of such packed beds.

B. Equation governing the two-dimensional temperature field $T(r,z)$

If a fluid is flowing through a packing, in a strict sense, there is always a difference between the temperature of the solid and the temperature of the fluid. In most cases, however, particularly for chemical reactors, it is advantageous to ignore the temperature difference between the fluid and the solid and take both as approximately equal. As in Sec. 2.8.1, the packed bed can be taken as a quasihomogeneous medium with effective conductivities. Furthermore, the effective conductivities for the radial and axial transport of heat are expected to be different.

In the vicinity of the wall the radial thermal resistance increases drastically. Because of this, and remembering the results of Sec. 2.8.1, the whole packing is subdivided into a central core and the wall region (see Fig. 1).

To describe the temperature field in such a flow-through tubular packing, the differential heat balance has to be carried out on a volume element of the packing (see Fig. 2). With the assumption that the tube wall

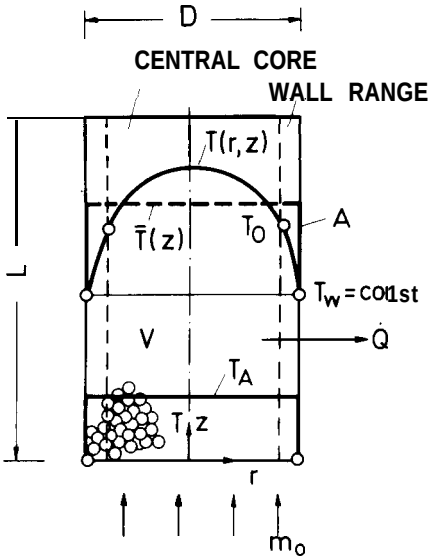

Figure 1 Stationary heat transfer situation in a tubular fiied bed with a gas flowing through.

© 1983 Hemisphere Publishing Corporation

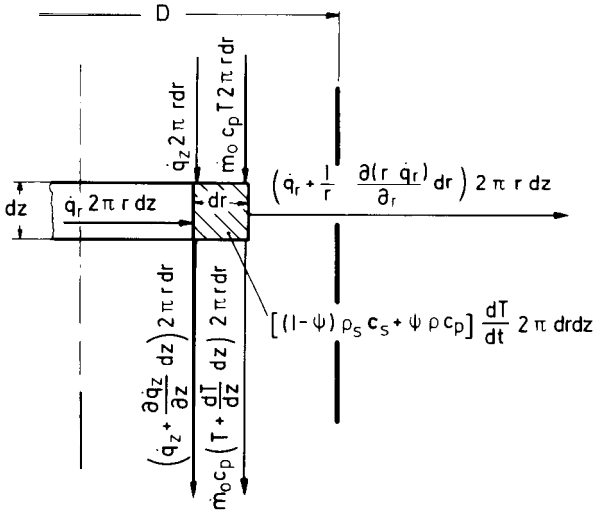

Figure 2 Heat balance on a differential torus of a tubular fixed bed.

is uniformly heated or cooled, rotary symmetric conditions are expected.

The summary of the different heat fluxes in Fig. 2 may be written in the form

$$-\frac{d\dot{q}_z}{dz} - \frac{1}{r}\frac{\partial(r\dot{q}_r)}{\partial r} = \dot{m}_0 c_p \frac{dT}{dz} \tag{1}$$

where $\dot{q}_z, \dot{q}_r$ = axial and radial heat flux
$\dot{m}_0$ = superficial mass flux
c_p = heat capacity of gas

In most applications the effective axial conduction is negligible compared with the enthalpy transport by the flow.

With Fourier s law of heat conduction in a homogeneous medium according to radial heat flux

$$\dot{q}_r = -\Lambda \frac{dT}{dr} \tag{2}$$

the above equation leads to

$$\Lambda\left(\frac{d^2T}{dr^2} + \frac{1}{r}\frac{dT}{dr}\right) = \dot{m}_0 c_p \frac{dT}{dz} \tag{3}$$

A in this equation is the effective radial thermal conductivity of packings with gas flow.

The boundary conditions are

$$z = 0: \quad T = T_A \tag{4}$$

$$r = \frac{D}{2}: \quad T = T_w = \text{const} \tag{5}$$

To account for the changed heat transfer conditions at the wall, a separate thermal resistance existing at the wall is postulated:

$$r = \frac{D}{2}: \quad -\Lambda \left(\frac{dT}{dr}\right)_{D/2} = \alpha_w (T_0 - T_w) \tag{6}$$

with $T_0 - T_w$ as a fictitious temperature rise. In Eq. (6), α_w is the so-called wall heat transfer coefficient of packings with a fluid flowing through.

In connection with the analytic solution of Eq. (3), attention is called to [1].

C. Heat transfer parameters of interest

(a) Effective radial thermal conductivity A of packed beds with a gas flowing through

From detailed analysis of experimental results, Yagi and Kunii [2] proposed a model in which heat was transferred simultaneously by two independent mechanisms. Accordingly, the effective radial thermal conductivity A, made dimensionless with the molecular thermal conductivity λ of the gas flow, yields

$$\frac{A}{\lambda} = \frac{\lambda_{so}}{\lambda} + \frac{\lambda_g}{\lambda} \tag{7}$$

with λ_{so} the effective thermal conductivity of the stagnant bed (see Sec. 2.8.1C) according to the combined conduction and radiation exchange processes, and with λ_g a transport coefficient due to the convective lateral mixing of the gas flow.

According to Eq. (7), the contribution of λ_{so} will be small if the lateral mixing of the flow and the flow velocity respectively are sufficiently large, the usual case in industrial performance. Under these limitations, Schlünder [3] has proposed a model (see Fig. 3) in which the flow separates from the particles and complete mixing occurs in the voids. He derived

$$\frac{\lambda_g}{\lambda} = \frac{\mathrm{Pe}_x}{K} \tag{8}$$

with

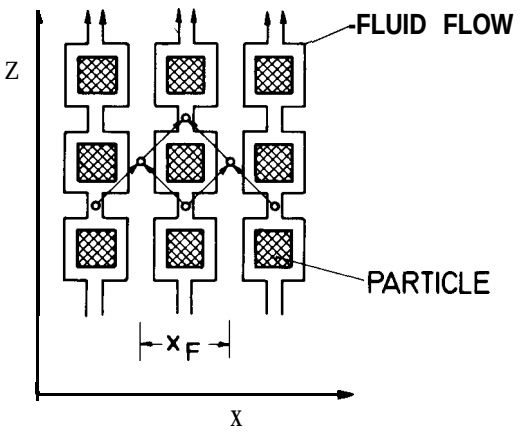

Figure 3 Flow pattern in a flow-through fixed bed according to Schliinder [3].

© 1983 Hemisphere Publishing Corporation

$$\mathrm{Pe}_\infty = \frac{m_0 c_p}{\lambda} x_F \tag{9}$$

the Péclet number formed with the so-called mixing length x_F, which is of the magnitude of the particle diameter.

Bauer [4] has extended this model by taking into consideration the influence of particle form, size, and size distribution along the mixing length x_F. Replacing the complicated overall turbulent flow in a packing by appropriate superposition of individual subflows, he derived

$$x_F = \sum_{j=1,m} \Delta\psi_j \left(\frac{1}{\sum_{i=1,n} \Delta D_i / x_{F,i}} \right)_j \tag{10}$$

with the individual mixing lengths of the subflows

$$x_{F,i} = F_i d_{F,i} \tag{11}$$

where F_i is a shape factor that must be determined experimentally for the various particle forms. The equivalent dimensions $d_{F,i}$ in Eq. (11) correspond to

1. The volume equivalent sphere diameter $d_{V,i}$ for a subflow around the particle
2. The double projected length $d_{H,j}$ of a through-flow channel (e.g., the hollow space of Raschig rings) for a subflow through the particle

The constant K in Eq. (8) has the value 8 for an infinite packed bed. For a finite packed bed, Schlünder [3] recommended

$$K = 8 \left[2 - \left(1 - \frac{2}{D/\bar{d}} \right)^2 \right] \tag{12}$$

which gives best agreement with experimental results (see Fig. 4). $\bar{d}$ is calculated from Eq. 2.8.1(10).

Predictions of effective radial thermal conductivities based on the above concept agree very well with experimental results with packings consisting of spheres, cylinders, hollow cylinders, and broken solids of equal and unequal size (see Figs. 5-l 0).

The shape factors F_i derived from experiments are compiled in Table 1.

Figure 5 shows data for A versus Pe for packed beds of styrene, ceramic, steel, and copper spheres of 10 mm diameter at moderate temperatures. The fluid was nitrogen. The full lines represent Eq. (7). Linear increase of effective thermal conductivity with increase of flow rate was observed in all the measurements, which confirms the separation and additive overlapping of two independent fractions in Eq. (7).

Figure 6 shows the influence of the temperature up to 1 000 K both of poor and good conducting material. The solid lines represent the calculation. To show the

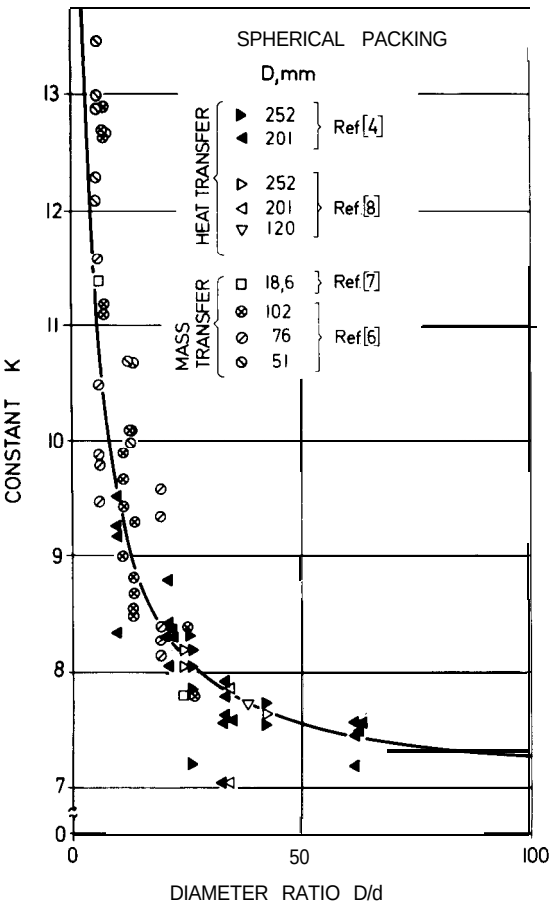

Figure 4 Constant K as a function of bed-to-particle diameter ratio according to Bauer [4] and Eq. (12). Packings of uniformly sized spheres.

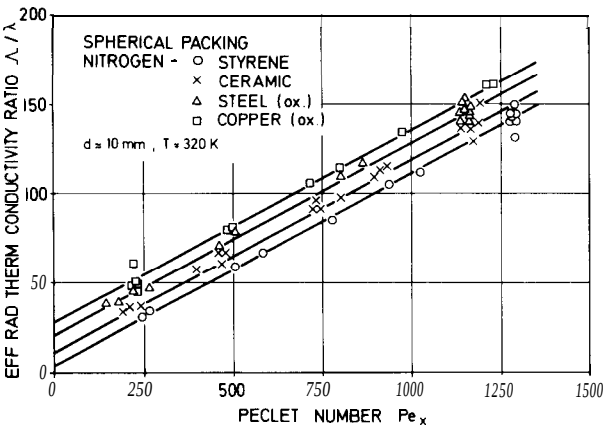

Figure 5 Effective radial thermal conductivity ratio of uniformly sized spheres of different material versus Pe, at normal pressure and room temperature according to Bauer [4] and Eq. (7). Pe, = 0: λ_{so}/λ according to Eq. 2.8.1(7).

© 1983 Hemisphere Publishing Corporation

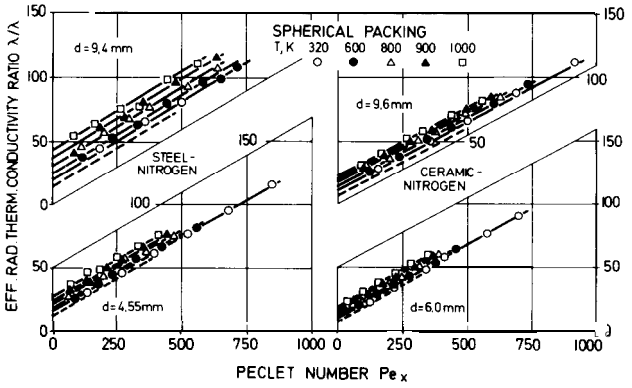

Figure 6 Influence of temperature Ton effective radial thermal conductivity Λ/λ of good and poor conducting uniformly sized spheres versus Pe, at normal pressure and room temperature according to Bauer [4] and Eq. (7). Pe, = 0: λ_{SO}/λ according to Eq. 2.8.1(7). Dashed lines calculated neglecting radiation heat transfer for $T = 1\ 000$ K.

influence of radiation, the dashed lines are calculated neglecting heat transfer by radiation for $T = 1\ 000$ K.

In Figs. 7 and 8 the mixing lengths for cylinders and hollow cylinders are plotted against geometric variables of these particles. Since good mixing is usually a very desirable characteristic that reduces undesirable temperature gradients in the packed bed, the advantage of the hollow cylinders over solid cylinders and spheres lies not only in the increased surface area, the reduced amount of material, and the drop in gas flow pressure, but also sometimes in a very great improvement of the mixing effect. For example, for the long, thin-walled tubules $(d/l = 0.25;\ d_i/d = 0.8)$, there is an improvement in mixing of around 1 000% and an increase in surface

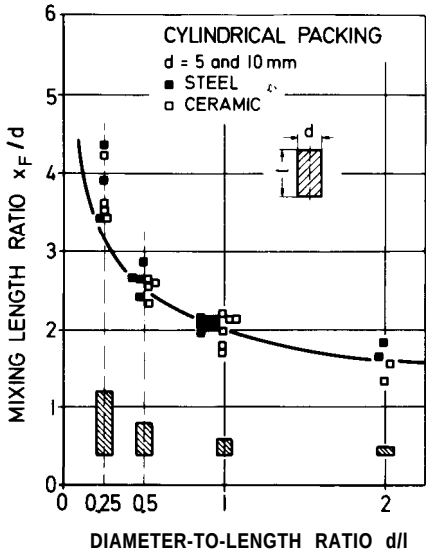

Figure 7 Mixing length x_F for packings of uniformly sized cylinders at different diameter-to-length ratios d/l according to Bauer [4] and Eq. (10).

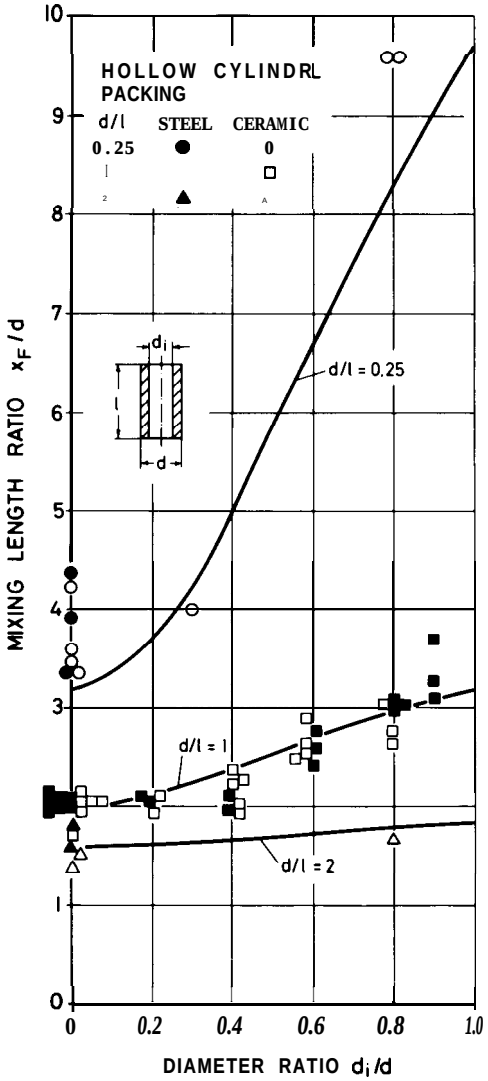

Figure 8 Mixing length x_F for packings of uniformly sized hollow cylinders at different inner-to-outer diameter ratios d_i/d according to Bauer [4] and Eq. (10). Various diameter-to-length ratio d/l.

area of about $50\%/m^3$ of packing in comparison with spheres of the same nominal diameter d.

The mixing lengths of binary mixtures of spheres, made dimensionless with the sphere diameter d_1 of the larger fraction, are plotted in Fig. 9 as a function of the mass fraction ΔD_1 of this larger sphere fraction. In each case the particles with the smaller diameter have the greatest influence on the effective mixing length. In other words, the mixing effect is considerably poorer than might have been expected according to the arithmetically weighted mean (see curve a). For comparison, the mean diameter of the volumeequivalent sphere is also shown (see curve b); it has been proposed as the determining mixing length in the earlier literature.

The mixing lengths x_F for different continuous particle size distributions, made dimensionless with the

© 1983 Hemisphere Publishing Corporation

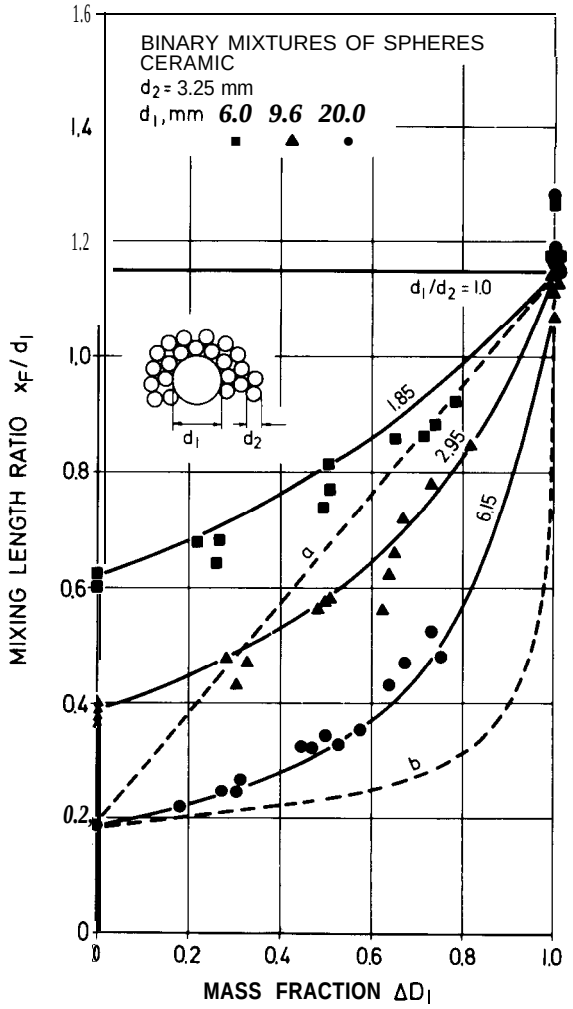

Figure 9 Effective mixing length x_F for packings of binary mixtures of spheres at various mass fractions AD, according to Bauer [4] and Eq. (10). Various diameter ratiosd, $/d_2$.

mean particle size $d_{1,2}$ of these distributions, are plotted in Fig. 10 as a function of the coefficient of variation ξ_1 [see Eq. 2.8.1(18)], a parameter used here to represent mathematically the scope of experiments. The mean particle size $d_{1,2}$, theoretically derived from Eq. (10), is also called the arithmetically weighted mean of the surface area distribution, which includes the mean equivalent particle dimensions $d_{V,i}$ of the fractionated distribution.

Since all of the shape factors F_i found for subflows around the different shaped particles are of the same order of magnitude, it can be assumed that the value found for broken solids is generally applicable for packings with any irregularly shaped solid particles.

(b) Heat transfer coefficient α_w from walls to packed beds with a gas flowing through

For predicting wall heat transfer coefficients α_w, a model has to be developed that is analogous to that outlined for the effective radial thermal conductivity. Accordingly, there are two independent heat fluxes. As in the central core of the packing, there is a heat flux through the fluid and a solid phase on the one hand. On the other, there is a flux only through the fluid phase, that is, through the laminar boundary layer at the wall:

$$\mathrm{Nu}_w = \frac{\alpha_w x_w}{\lambda} = \frac{\alpha_{\max} x_w}{\lambda} + \frac{\alpha_{wg} x_w}{\lambda} \qquad (13)$$

with $\alpha_{\max}$ found by applying Eq. 2.8.1(21) and x_w a particle dimension with regard to the particle shape.

Similar calculations to those for flow over plates with a dependence on the Péclet number have to be expected, especially for the second term on the right-hand side of Eq. (13).

Now, wall heat transfer coefficients in tubular reactors with a fluid passing through can be determined by analyzing overall heat transfer coefficients (see Sec. D). Recently Hennecke [5] has evaluated about 5 000 data points collected from 14 authors who have determined overall heat transfer coefficients. Assuming plug flow, he obtained wall heat transfer coefficients depending not only on the Péclet number but also on the ratio of tube diameter D to length L as shown in Fig. 11.

Accordingly, some of the Nu_w data not only tend

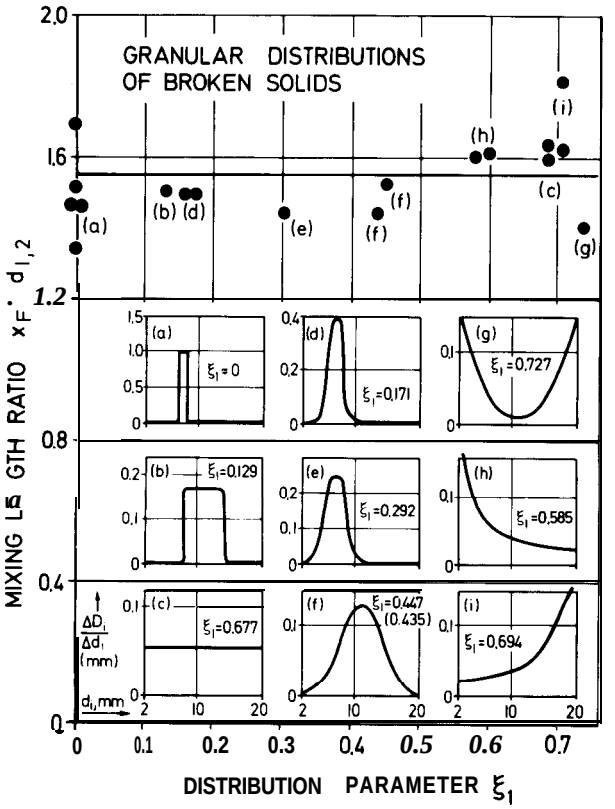

Figure 10 Effect of range and form of distribution of continuous granulations on effective mixing length x_F according to Bauer [4] and Eq. (10).

© 1983 Hemisphere Publishing Corporation

Table 1 Shape factors F for calculating the effective thermal conductivity Λ of various packings

Form	x_F	F
Sphere with diameter d, length l	Fd	1.15
Cylinder with diameter d, length l	$F_1 d \sqrt[3]{\frac{3l}{2d}}$	1.75
Hollow cylinder with outer diameter d, inner diameter d, length l	$\Delta\psi_1 F_1 d \sqrt[3]{\frac{3l}{2d}} + (1-\Delta\psi_1)F_2\sqrt{21}$	1.75
	$\Delta\psi_1 = \left[1 + \frac{1-\psi_1}{\psi_1}\left(\frac{d_i}{d}\right)^2\right]^{-1} \qquad \psi_1 = 0.39 + 0.02\left[\left(\frac{l}{d} - 0.85\right)^2\right]^{2/3}$	2.8
Binary sphere mixture with diameters d_1, d_2 and mass fraction $\mathrm{AD}_i = \frac{M_1 \text{ (mass of sphere 1)}}{\mathrm{M}\ \text{(total mass)}}$	$\frac{1}{(\Delta D_1/Fd_1)(1-\Delta D_1/Fd_2)}$	1.15
Broken particle size distribution with mass fraction $\Delta D_i = \frac{M_i \text{ (mass of size fraction } i)}{M \text{ (total mass)}}$ z = number of particles in size fraction i	$Fd_{1,2} \qquad d_{1,2} = \frac{1}{\sum_{i=1,n} \Delta D_i / \sqrt[3]{(6/\pi)(M_i/z\rho_s)}}$	1.4

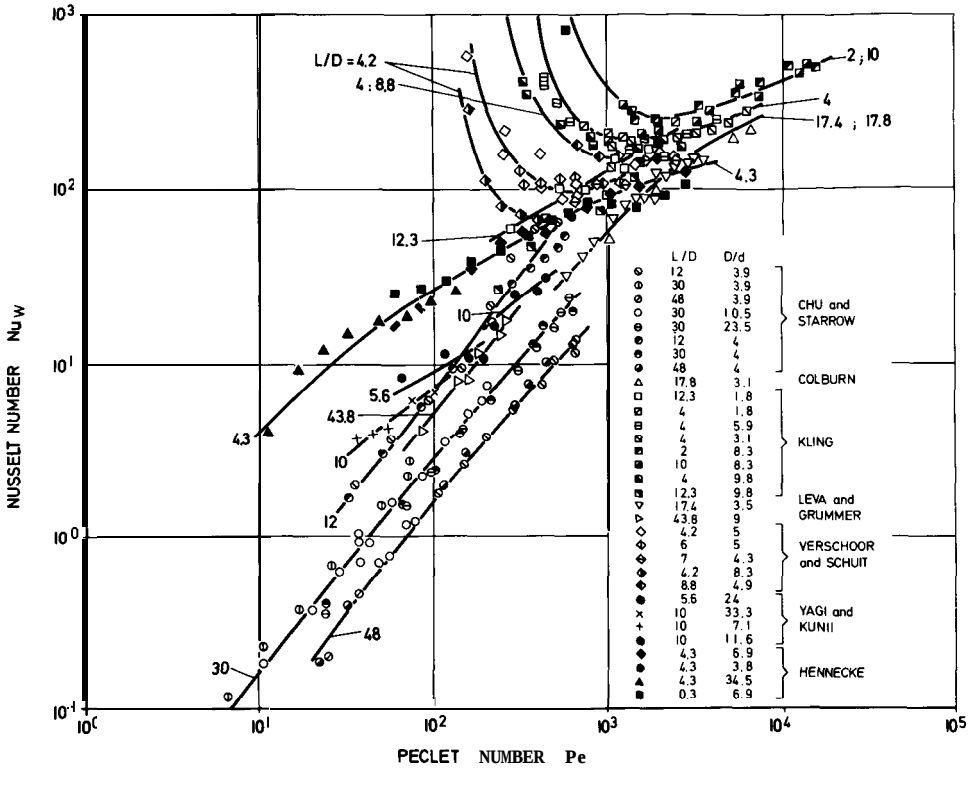

Figure. 11 Wall heat transfer coefficients $\mathrm{Nu}_w = \alpha_w d/\lambda$ versus Péclet number Pe = $\dot{m}_0 c_p d/\lambda$ obtained by evaluation of overall heat transfer coefficients in tubular packed beds according to Hennecke [5]. D = tube diameter, L = tube length.

© 1983 Hemisphere publishing Corporation

toward infinity but also turn out to be negative. For long tubes the wall heat transfer coefficients are still lower by orders of magnitude than those for short tubes. This effect is still not really understood. It may be that this is due to a bypass effect as described in Sec. 2.5.4. However, this is an assumption and is still subject to a reliable calculatior. method.

D. Equation governing the one-dimensional temperature field $\bar{T}(z)$

It is sufficient in many technical applications to calculate the average temperature field $\bar{T}(z)$ in the tubular packing (see Fig. 1) with the help of overall heat transfer coefficients. In the case of chemical reactions, however, the reaction velocity calculated will be too low even if this average temperature is properly described. This fault is all the more important when large radial temperature profiles are present.

The equation governing the heat balance cylindrical disk of the packing with the thickness dz may be written in the form

$$d\dot{Q} = -\dot{m}_0 c_p L \frac{d\bar{T}(z)}{dz} \tag{14}$$

with $d\dot{Q}$ the individual overall heat flux through the wall of length dz.

With Newton s law of heat transfer,

$$d\dot{Q} = U_z(z) A(\bar{T}(z) - T,)\, dz \tag{15}$$

the above equation leads to

$$\frac{A}{L} U_z(z)(\bar{T}(z) - T_w)\, dz = \dot{m}_0 c_p \frac{d\bar{T}(z)}{dz} \tag{16}$$

$U_z(z)$ is the local overall heat transfer coefficient between the wall and the whole packing.

The integration with the help of the overall heat transfer coefficient,

$$U = \frac{1}{z} \int_{Jo}^{z} U_z(z)\, dz \tag{17}$$

results in

$$\frac{\bar{T}(z) - T_w}{T_A - T_w} = \exp\left(-\frac{A}{L}\frac{U}{\dot{m}_0 c_p} z\right) \tag{18}$$

the average temperature field $\bar{T}(z)$ in the tubular packing.

According to the overall heat transfer coefficient U, the heat transfer resistance of the central core of the packing α_s will be connected in series:

$$\frac{1}{U} = \frac{1}{\alpha_w} + \frac{1}{\alpha_s} \tag{19}$$

with α_w according to Eq. (13) and α_s from superposition of the short-time and long-time solutions in good approximation :

$$\alpha_s = \frac{\Lambda}{D}\sqrt{K^2 + \frac{4}{\pi}\frac{\dot{m}_0 c_p}{\Lambda}\frac{D^2}{L}} \tag{20}$$

with A the effective radial thermal conductivity applying Eq. (7) and K from Table 2.8 .1(3).

E. The heat rate $\dot{Q}$

The total heat rate $\dot{Q}$ transferred through the whole wall surface of the reactor is

$$\dot{Q} = \int_0^L d\dot{Q}(z) \tag{21}$$

With the total heat balance on the flow-through packing,

$$\dot{Q} = \dot{m}_0 c_p (T_A - \bar{T}(L)) \tag{22}$$

introduced in Eq. (52), this leads to

$$\dot{Q} = UA\, \mathbf{A}\, \mathbf{T}, \tag{23}$$

with the logarithmic mean temperature difference

$$\mathrm{AT}, = \frac{T_A - \bar{T}(L)}{\ln[(T_A - T_w)/(\bar{T}(L) - T_w)]} \tag{24}$$

F. Equations governing the temperature field $T_s(r,z)$ of the solid phase and $T_g(r,z)$ of the gas phase

In the rare cases of fast-changing temperature profiles in the packing, such as in regenerators, as well as fast reactions with a great amount of heat production, one has to distinguish between the temperature of the solid phase and of the gas phase. These temperature profiles are obtained if an adequate model for the energy transport both in the solid as well as in the gas phase can be predicted and if the parameters in this model are available. In this situation, the following coupled energy balance seems to be suitable:

Solid phase :

$$(1-\psi)\Lambda_s\left(\frac{d^2 T_s}{dr^2} + \frac{1}{r}\frac{dT_s}{dr}\right) = ka^*(T_g - T_s) \tag{25}$$

with the boundary condition

$$r = \frac{D}{2}: \quad -\Lambda_s \left.\frac{dT_s}{dr}\right|_{D/2} = \alpha_{\max}(T_{os} - T_w) \tag{26}$$

© 1983 Hemisphere Publishing Corporation

Gas phase :

$$\psi\Lambda_g\left(\frac{d^2T_g}{dr^2}+\frac{1}{r}\frac{dT_g}{dr}\right)+\dot{m}_0c_p\frac{dT_g}{dz}$$
$$=-ka^*(T_g-T_s) \qquad (27)$$

with the boundary condition

$$r=\frac{D}{2}: \quad -\Lambda_g\frac{dT_g}{dr}_{D/2}=\alpha_{wg}(T_{og}-T_w) \qquad (28)$$

The procurement for the evaluation of the transport parameters of this heterogeneous model can be derived by subdividing the parameters of the homogeneous model in such a way that the static part is joined to the solid phase and the fluid dynamic part is joined to the gas phase. One obtains

$$\frac{\Lambda_s}{\lambda}=\frac{1}{\sqrt{1-\psi}}\left[\varphi\frac{\lambda_s^*}{\lambda}+(1-\varphi)\frac{\lambda_{so}^*}{\lambda}\right] \qquad (29)$$

with λ_{so}^* according to Eq. 2.8.1(76), and

$$\frac{\Lambda_g}{\lambda}=(1-\sqrt{1-\psi})\left(\frac{1}{\psi-1+\lambda/\lambda_D}+\frac{\lambda_R}{\lambda}\right)+\frac{1}{\psi}\frac{\lambda_g}{\lambda} \qquad (30)$$

with λ_g/λ according to Eq. (8).

k in Eqs. (25) and (27) is the heat transfer coefficient connected with the difference of the mean gas temperature T_g and the mean solid temperature T_s, which can be calculated from Sec. 2.5.4. a* is the accompanying specific surface area.

A satisfying theoretical model to calculate the wall heat transfer coefficient α_{wg} in Eq. (28) according to Eq. (13) does not exist at the present time. This is the motivation of further investigation.

NOMENCLATURE FOR SECTION 2.8.2

A	wall surface area
a^*	specific surface area
c_p	heat capacity of gas phase
D	diameter of cylindrical wall
d	sphere diameter
$d_{V,i}$	volume equivalent sphere diameter
ΔD_i	mass fractions
k	heat transfer coefficient between gas and solid phases
L	total length of packing
m_0	superficial mass flux
$\dot{q}$	heat flux
$\dot{Q}$	heat rate
r, z	coordinates
T	absolute temperature
U_z	local overall heat transfer coefficient
U	overall heat transfer coefficient
α_{max}	heat transfer coefficient from wall to stagnant packed bed
α_w	heat transfer coefficient from wall to flow-through packing
λ	thermal conductivity of gas phase
λ_{so}	effective thermal conductivity of stagnant packed bed
A	effective radial thermal conductivity of flow-through packing
A,, Λ_g	effective radial thermal conductivity of the solid and gas phases respectively
φ	surface fraction
ψ	bed porosity

REFERENCES FOR SECTION 2.8.2

1. Von Rosenberg, D. U., ***Methods for the Solution of Partial Differential Equations,*** Elsevier, New York, 1969.
2. Yagi, S., and Kunii, D., Studies on Effective Thermal Conductivities in Packed Beds, ***AIChE J.***, vol. 3, pp. 373-381, 1957.
3. Schliinder, E. U., W&me- und Stoffiibertragung zwischen durchströmten Schtittungen und darin eingebetteten Einzelkörpern, Chem. ***Ing. Tech., vol. 38,*** pp. 967-978, 1966.
4. Bauer, R., Effektive radiale Wärmeleitfähigkeit gasdurchströmter Schiittungen mit Partikeln unterschiedlicher Form und Grössenverteilung, ***VDI Forschungsh., 582,*** 1977.
5. Hennecke, F. W., Über den Wandwiderstand beim Wärmetransport in Schüttungsrohren, Ph.D. thesis, University of Karlsruhe, 1972.
6. Fahien, R. W., and Smith, J. M., Mass Transfer in Packed Beds, ***AIChE J.***, vol. 1, pp. 28-37, 1955.
7. Olbricht, W. E., and Potter, 0. E., Heat Transfer in Small Diameter Packed Beds, ***Chem. Eng. Sci., vol. 27,*** pp. 1723-1732, 1972.
8. Zehner, P., Experimentelle und theoretische Bestimmung der effektiven Wärmeleitfähigkeit durchströmter Kugelschiittungen bei mässigen und hohen Temperaturen, Ph.D. thesis, University of Karlsruhe, 1972.

© 1983 Hemisphere Publishing Corporation

2.8.3

Packed and agitated beds

E. Muchowski

A. Heat transfer to packed beds

(a) The wall heat transfer coefficient α_w

Gas-phase molecular heat conduction between the granules of a packed bed strongly controls the heat transfer in the packed bed as well as the heat transfer from the walls to the bed. Thus, the effective thermal conductivity of a granular bed is orders of magnitude smaller than the conductivity of the solid granules, especially when the bed is at a reduced pressure. When heat is transferred from the walls to a packed bed of granules, a wall resistance appears that depends strongly on the transport properties of the gas phase. In addition, heat will be exchanged by radiation and contact area conduction.

All the transport phenomena mentioned above may be considered to be independent of one another. Therefore the total heat transfer coefficient α_w at the wall is given by

$$\alpha_w = \alpha_g + \alpha_c + \alpha_r \tag{1}$$

where g = molecular gas conduction
c = contact area conduction
r = radiation

Now

$$\alpha_w = \frac{\dot{q}_w}{T_w - T_s} \tag{2}$$

is the ratio of the heat flux $\dot{q}_w$ to the driving force $T_w - T_s$ at the wall (see Fig. 1). The wall resistance and the temperature drop are directly proportional.

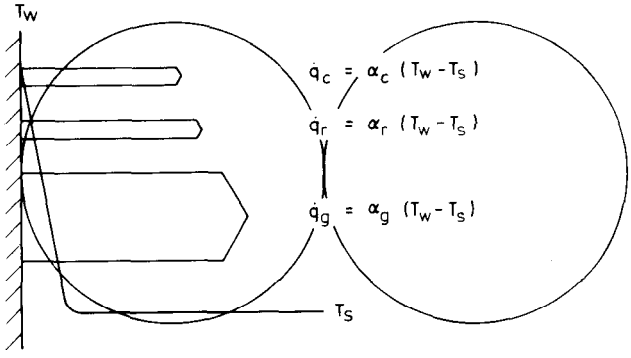

Figure 1 Temperature distribution and heat fluxes near the wall.

This simplified concept is also valid for the case of contact area conduction resistance as demonstrated by Muchowski [1]. Thus, in the case of transient heat transfer from a wall to a packed bed, the overall heat transfer coefficient is limited by the wall resistance when the time approaches zero.

I. The contribution of molecular gas conduction to α_w

For spherical particles α_g can be calculated by Schlünder s[2] formula

$$\alpha_g = \frac{2\lambda_G}{R}\left[(\mathrm{Kn}+1)\ln\left(1+\frac{1}{\mathrm{Kn}}\right)-1\right] \tag{3}$$

where

$$\mathrm{Kn} = \frac{2\Lambda}{R}\frac{2-\gamma}{\gamma} \tag{4}$$

© 1983 Hemisphere Publishing Corporation

is the modified Knudsen number, A is the mean free path of the gas molecules, R is the radius of the particles, and γ is the accommodation coefficient. Equation (3) is based on the fact that the pressure-dependent mean free path of the gas molecules exceeds the gap between the particles and the wall in the neighborhood of the contact zone. In that zone, the conductivity of the gas becomes pressure dependent (see Fig. 2). A can be evaluated from the Sutherland formula,

$$\Lambda(P,T) = \frac{\Lambda_\infty P/P}{1 + T_v/T} \tag{5}$$

where $\Lambda_\infty P$ is a constant for each specific gas and T_v is the Sutherland constant. Values of $\Lambda_\infty P, T_v, \lambda_g$, and γ are listed in Table 1 for a range of gases; the kinetic data were taken from Diels and Jaeckel [3].

The accommodation coefficient γ is a function of both the molecular weight and the temperature (see Sec. 2.8.2). Heat transfer coefficients versus pressure are plotted for air in Fig. 3. Obviously the wall heat transfer coefficient decreases considerably with decreasing pressure. Thus the gas heat transfer in the gap between the wall and the particle is much greater than the contributions by radiation and contact conduction at atmospheric pressure.

II. Heat transfer at the wall by radiation

The contribution of radiation to the heat transfer from the wall to the packed bed can be expressed by a radiation heat transfer coefficient,

$$\alpha_r = 0.04 c_s \epsilon \left(\frac{T_m}{100}\right)^3 \tag{6}$$

where $c_s = 5.76\ \mathrm{W/m^2}$ is the modified Stefan-Boltzmann constant, ϵ is the absorption ratio, and T_m is the mean temperature at the surface. For granules that are rough,

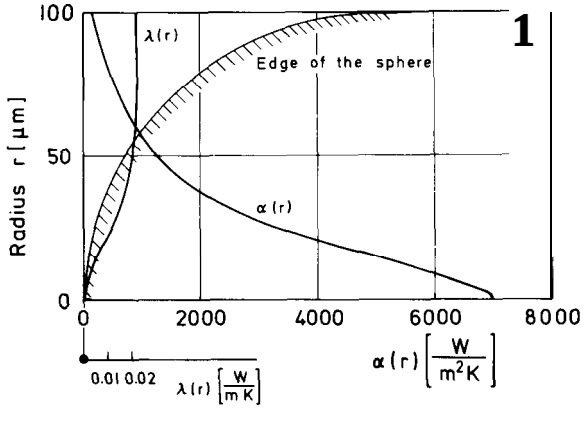

Figure 2 Local heat transfer coefficient $\alpha(r)$ and thermal conductivity h(r) for a sphere of 200 μm diameter at 1 bar gas pressure.

Table 1 Mean free path Λ_∞, Sutherland temperature T_v, thermal conductivity λ_g, and accommodation coefficient γ for various gases at room temperature

Gas	$\Lambda_\infty P$ x 10^3 m Pa	T_v, K	λ_g, W/m K	γ
He	21.35	79	0.148	0.4
H_2	14.09	76	0.189	0.146
Air	8.49	116	0.026	0.9
H_2O	12.67	600	0.023 1	0.82
CO_2	7.6	273	0.016	0.95
C_2H_5OH	6.15	525	0.015	0.95

as found in practice, the value $\epsilon = 0.9$ is in good agreement with the experimental findings. Thus α_r = 5.2 $\mathrm{W/m^2}$ K at room temperature and α_r = 78 $\mathrm{W/m^2}$ K at *450°C.*

III. The contact area resistance

The contribution α_c of the contact area conduction to the wall heat transfer coefficient is strongly dependent on the material, the geometry of the granules, and the structure of the particle surface. α_c is negligible for poorly conducting granules. Values of α_c between 30 and 5.5 $\mathrm{W/m^2}$ K have been measured by Muchowski [1] for bronze spheres of 0.1-1.0 mm diameter. Oxidation of the metal surfaces will decrease the α_c values.

(b) Overall heat transfer coefficient for transient heat transfer to packed beds

The overall heat transfer coefficient from walls to packed beds is defined by

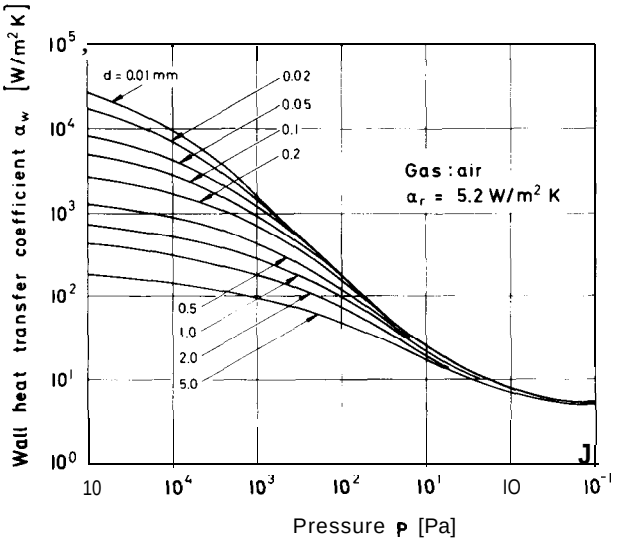

Figure 3 Wall heat transfer coefficient $\alpha_w = \alpha_g + \alpha_r$ for air versus pressure for various particle diameters.

© 1983 Hemisphere Publishing Corporation

$$\alpha_{ov} = \frac{\dot{q}}{T_w - \bar{T}} \tag{7}$$

where $\bar{T}$ is the mean temperature of the bulk. It satisfies the equation

$$\frac{1}{\alpha_{ov}} = \frac{1}{\alpha_w} + \frac{1}{\alpha_i} \tag{8}$$

as the outer and inner heat transfer resistances are in series. α_i is the inner heat transfer coefficient and can be calculated by applying Fourier s theory of heat conduction and depends on the boundary conditions. See [4]. For constant wall temperature the instantaneous transfer coefficient is given by

$$\alpha_i = \sqrt{\frac{1}{\pi}\frac{(\lambda\rho c)_{app}}{t}} = \frac{\lambda_{app}}{s}\frac{1}{\sqrt{\pi}}\frac{1}{\sqrt{Fo}} \tag{9}$$

and for constant heat flux

$$\alpha_i = \frac{\sqrt{\pi}}{2}\sqrt{\frac{(\lambda\rho c)_{app}}{t}} = \frac{\lambda_{app}}{s}\frac{\sqrt{\pi}}{2}\frac{1}{\sqrt{Fo}} \tag{10}$$

λ_{app} is the steady-state apparent heat conductivity of the packed bed (see Sec. 2.8.2), κ_{app} the apparent thermal diffusivity of the porous packing, and

$$Fo = \kappa_{app}\frac{t}{s^2} \tag{11}$$

is the Fourier number formed with the bed height s. Equations (9) and (10) are valid only if the temperature field has not reached the edge of the bulk material, for example, for Fo < 0.1.

For large Fourier numbers the long-time solution of the heat conduction equation for a flat plate leads to

$$\alpha_i = \frac{\pi^2}{4}\frac{\lambda_{app}}{s} \tag{12}$$

for constant wall temperature and to

$$\alpha_i = \frac{3\lambda_{app}}{s} \tag{13}$$

in the case of constant heat flux.

The overall heat transfer coefficient is limited by three asymptotic curves. For very short times the inner heat transfer resistance can be neglected. Then the overall heat transfer coefficient is equal to the wall heat transfer coefficient α_w. For long times α_{ov} becomes constant [Eqs. (12) and (13)]. In the interval between, α_{ov} is time dependent and follows Eqs. (9) and (10) (see Fig. 4).

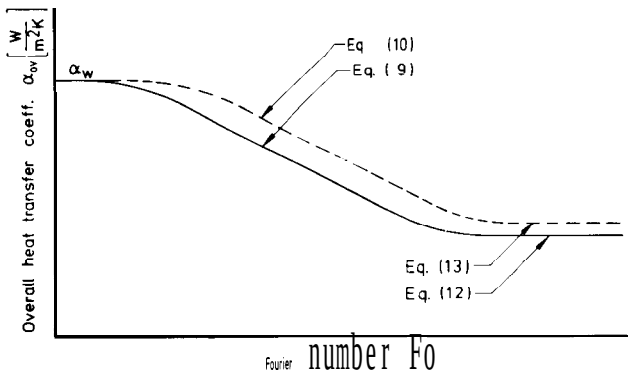

Figure 4 Instantaneous overall heat transfer coefficient α versus Fo for transient heat transfer from walls to packed beds. Solid lines: T_w = const (standard condition); dotted lines: flux $\dot{q}_w$ = const.

B. Heat transfer to moving and agitated beds

(a) Heat transfer to a moving bed

The particle flow in a duct is assumed to have a uniform velocity profile, that is, u = const; see Fig. 5. Each particle has a velocity u when it is in contact with the heated wall in the area $0 < x < L$. The wall is of a uniform temperature T_w. In the steady state, the mean heat transfer coefficient from the wall to the particle flow is given by

$$\bar{\alpha} = \frac{1}{t_s}\int_0^{t_s} \alpha_{ov}(t)\,dt \tag{14}$$

where

$$t_s = \frac{u}{L} \tag{15}$$

is the time that the particle flow is in contact with the heated wall. The local heat transfer coefficient $\alpha_{ov}(t)$

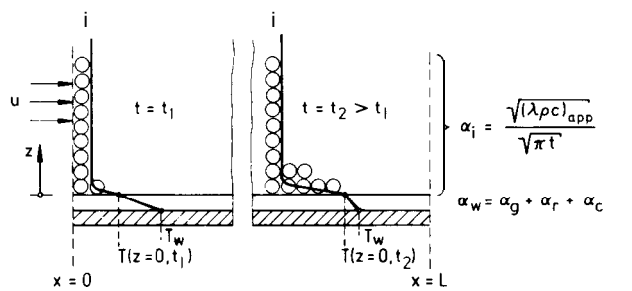

Figure 5 Temperature profiles for heat transfer into a moving bed. The driving potential $T_w - T_s(z = 0)$ decreases with increasing contact time, caused by the time-dependent inner heat resistance. The outer heat transfer coefficient is represented by a gap.

© 1983 Hemisphere Publishing Corporation

can be obtained from Eqs. (8) and (9). Integration of Eq. (14) leads to

$$\frac{\bar{\alpha}}{\alpha_w} = \frac{2}{\sqrt{\pi}\ \mathrm{Bi}\sqrt{\mathrm{Fo}_s}}\left[1 - \frac{1}{\sqrt{\pi}\ \mathrm{Bi}\sqrt{\mathrm{Fo}_s}}\ln\left(1 + \mathrm{Bi}\sqrt{\mathrm{Fo}_s}\right)\right] \tag{16}$$

where the Biot number is defined by

$$\mathrm{Bi} = \frac{\alpha_w s}{\lambda_{app}} \tag{17}$$

and

$$\mathrm{Fo} = \frac{\kappa_{app} t_s}{s^2} \tag{18}$$

The expression (16) is valid for Fo < 0.1. Figure 6 shows that good agreement was obtained between the predictions of Eq. (16) and the experimental values determined by Ernst [5].

(b) Heat transfer to agitated beds

As reported in Sec. A, the overall heat transfer coefficient in a packed bed decreases with increasing particle contact time at the wall. This is because of the drop in the temperature gradient at the wall. Periodic displacement of the particles from the heated surface into the bulk of the bed by agitation will maintain a steeper temperature gradient at the wall and thus improve the heat transfer. See Fig. 7.

The more frequently the particles are removed from the heated surface by the stirrer blades or other means, the greater is the improvement in the heat transfer. If there is a gap between the wall and blades,

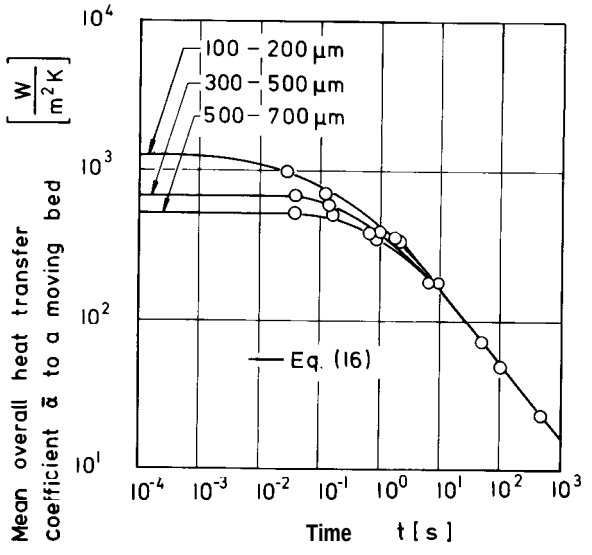

Figure 6 Mean overall transfer coefficient to a moving bed of sand particles. ○ Experimental values reported by Ernst [5].

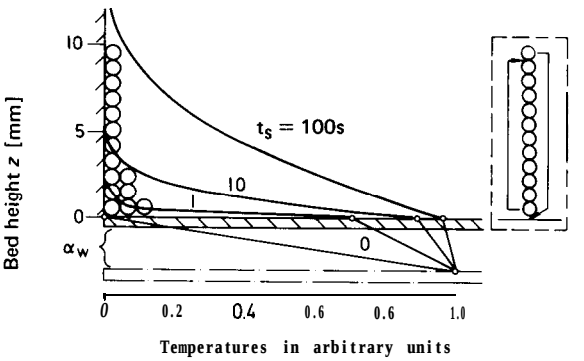

Figure 7 Decrease of the driving potential $T_w - T(z = 0)$. Removal of heated particles from the wall after every t_s seconds leads to a periodic renewal of the driving force.

an additional heat transfer resistance will appear due to the unagitated region of particles in the zone between the blades and the surface. Figure 8 shows measured heat transfer coefficients versus time from walls to stirred beds at various pressures obtained by Wunschmann and Schlünder [6]. After an initial period the value of α approaches a constant. The asymptotic α values increase with increasing stirrer speed.

A model describing the ideal stirred bed starts from the fully developed periodic mixing at each element of the heated wall as the stirrer blade passes it. Between successive passages of the stirrer, the particles rest on the plate. The mean contact time of the particles at the wall is then

$$t_s = (fn)^{-1} \tag{19}$$

where f is the stirrer frequency and n is the number of stirrer blades near the surface.

In the steady state the $\bar{\alpha}$ values can be obtained as the mean α numbers for a packed bed during the contact time t_s (see Fig. 9). When the Fourier number [Eq. (18)] is established with t_s from Eq. (19), the $\bar{\alpha}$ values of the ideal stirred bed can be calculated from Eq. (16).

A comparison of $\bar{\alpha}$ versus Fo, for ideal and real stirred beds is shown in Fig. 10. The observed $\bar{\alpha}$ values are smaller than the calculated ones, and the discrepancy is larger when a gap exists between the stirrer and the wall.

(c) The heat transfer in rotating drums

Lehmberg [7] observed that the particle movement in a rotating drum is caused by the friction stresses between the particles and the wall. The particles move on cyclic paths as shown in Fig. 11. In the case of no particle slip at the wall, the particle velocity at the wall is equal to the drum velocity. The contact time of the particles is then

© 1983 Hemisphere Publishing Corporation

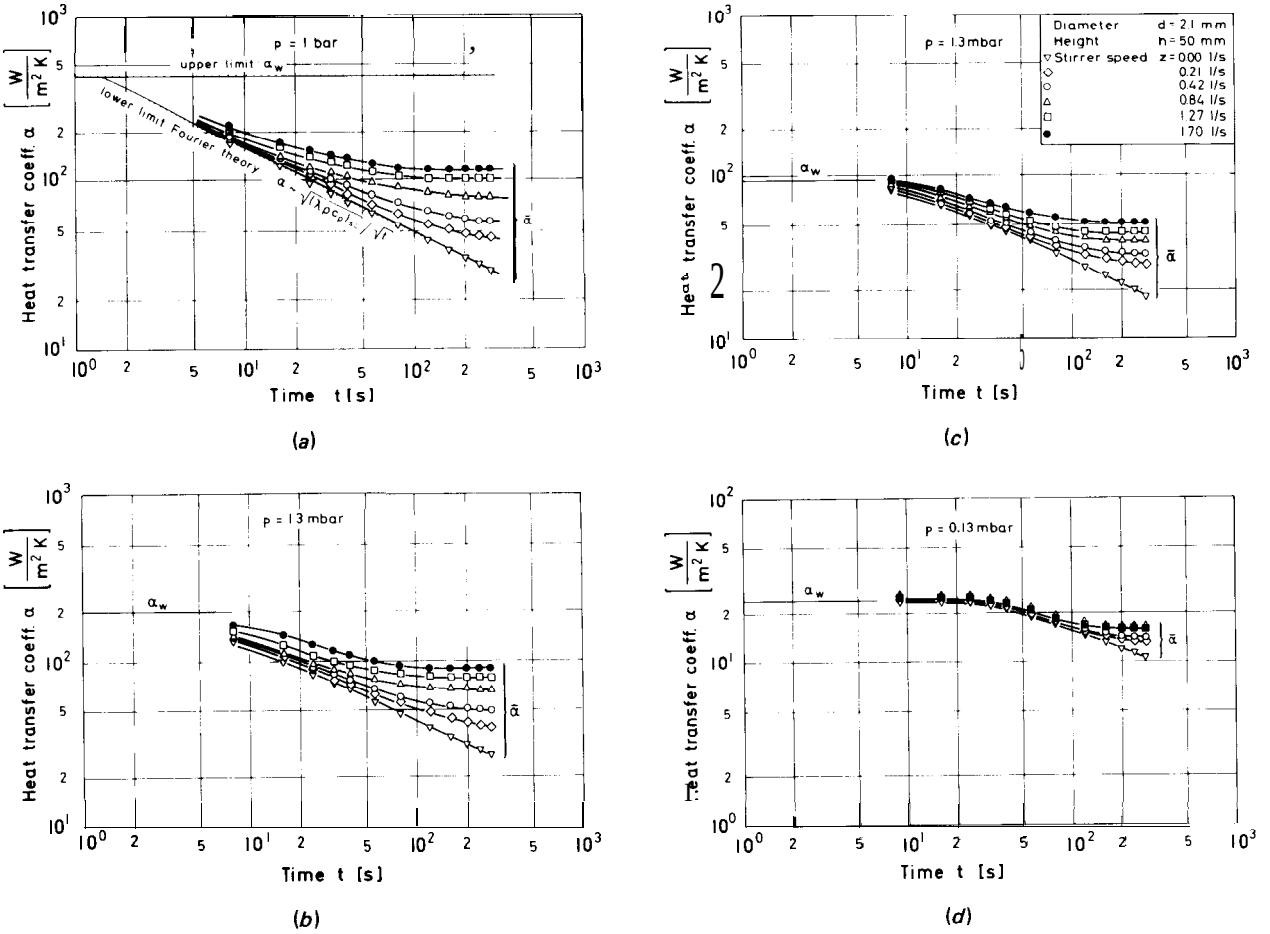

Figure 8 Experimental data for heat transfer coefficients from horizontal walls to stirred beds versus time. From Wunschmann and Schltinder [6]. The solid lines are fitted curves.

$$t_s = \frac{\varphi}{2\pi f} \tag{20}$$

where φ is the angle of filling and f is the rotational frequency of the drum. On applying this model, which only approximates the actual case, $\bar{\alpha}$ values can be obtained from Eq. (16). Figure 12 compares experimental $\bar{\alpha}$ values with calculated $\bar{\alpha}$ numbers from the model above. The calculated $\bar{\alpha}$ values are twice the measured values.

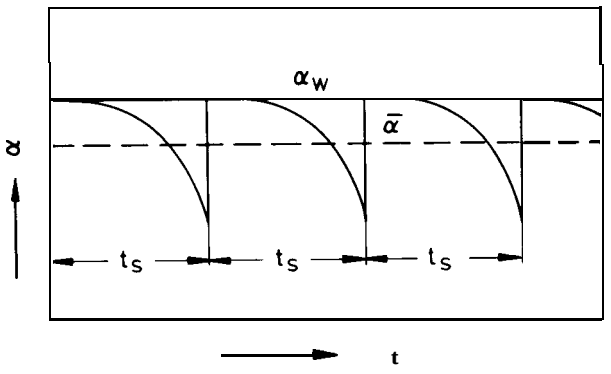

Figure 9 Schematic representation of how the periodic particle renewal affects steady state $\bar{\alpha}$ values for the ideal stirred bed.

(d) The heat transfer to vibrated beds

Particle movement in a vibrated bed is rather complicated. Particles of diameter 0.5 mm and more move circularly in a vibrated vessel, whereas particles of 0.1 mm diameter and less are agitated turbulently under the influence of vibration. Figure 13 shows how the friction stresses between the particles and the vertical walls of a vibrated vessel cause the circular movement. Heat transfer coefficients can be calculated when the particle velocity is known. For a detailed description, see [8]. The heat transfer from the bottom of a vibrated vessel to granular materials implies an additional heat transfer resistance. It is related to the periodic gap between the bottom and the bulk. The gap arises under vibration conditions where the acceleration exceeds the gravitational acceleration. Figure 14 shows experimentally obtained heat transfer coefficients versus acceleration for vibrated glass spheres at 1 bar and

© 1983 Hemisphere I blishing Corporation

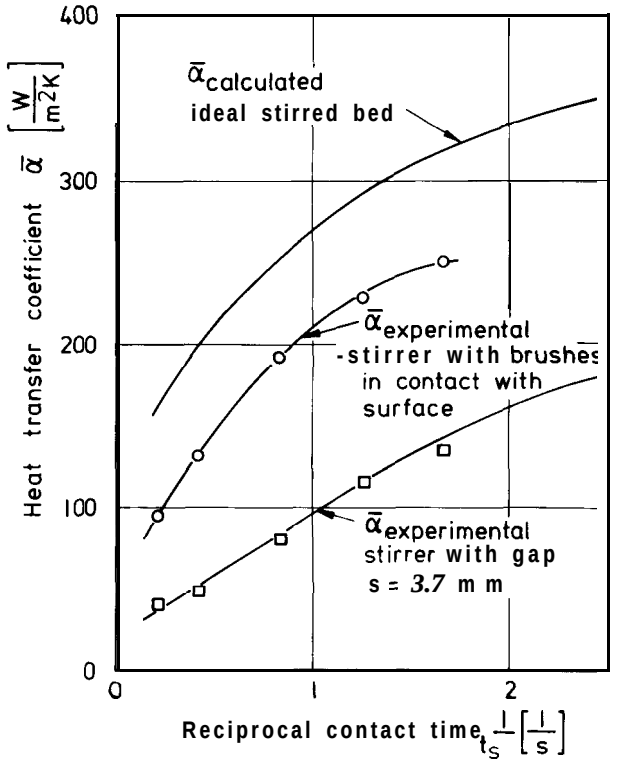

Figure 10 Comparison between measured and calculated $\bar{\alpha}$ numbers for a stirred bed.

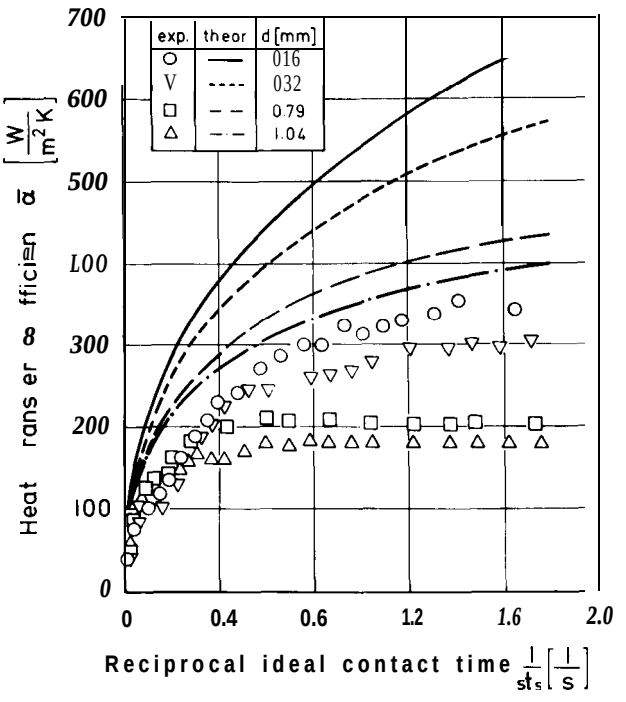

Figure 12 Comparison between calculated $\bar{\alpha}$ numbers for the ideal rotating drum (lines) and experimentally obtained $\bar{\alpha}$ values (symbols).

0.13 mbar pressure. In Fig. 15*b* the $\bar{\alpha}$ values of Fig. 15*a* (glass spheres of 0.1 mm diameter at 1 .O bar) are plotted against the frequency of vibration. After a steep increase with increasing frequency the $\bar{\alpha}$ values reach a maximum in all cases at about 42 Hz.

If the heated wall in the vibrated vessel is vertical, no gap arises between the granules and the wall. That encourages heat transfer. Figure 16 shows experimentally determined $\bar{\alpha}$ values from vertical heaters to vibrated glass spheres obtained from [9].

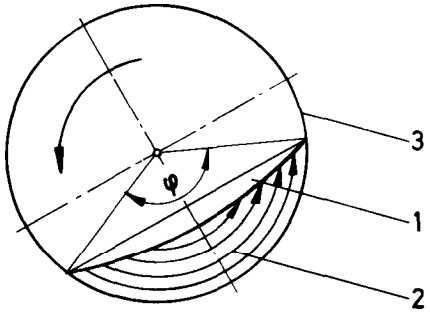

Figure **11** Schematic representation of particle movement in a rotating drum: (1) slope zone; (2) bulk material; (3) drum wall; φ angle of filling.

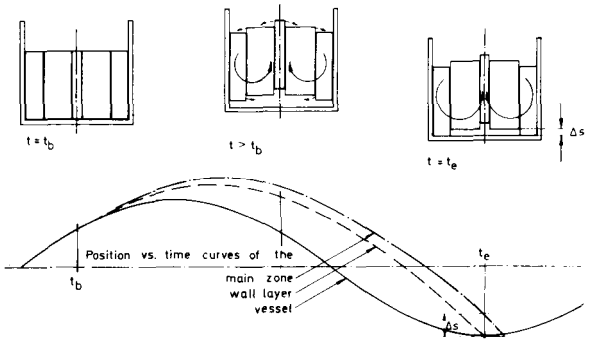

Figure 13 Schematic representation of how the frictional stresses between the particles and the vertical walls of a vibrated vessel influence the particle movement at various distances from the walls. Lower curves: Position versus time diagrams of different zones during sinusoidal movement of the vessel (section of a vibration period).

© 1983 Hemisphere Publishing Corporation

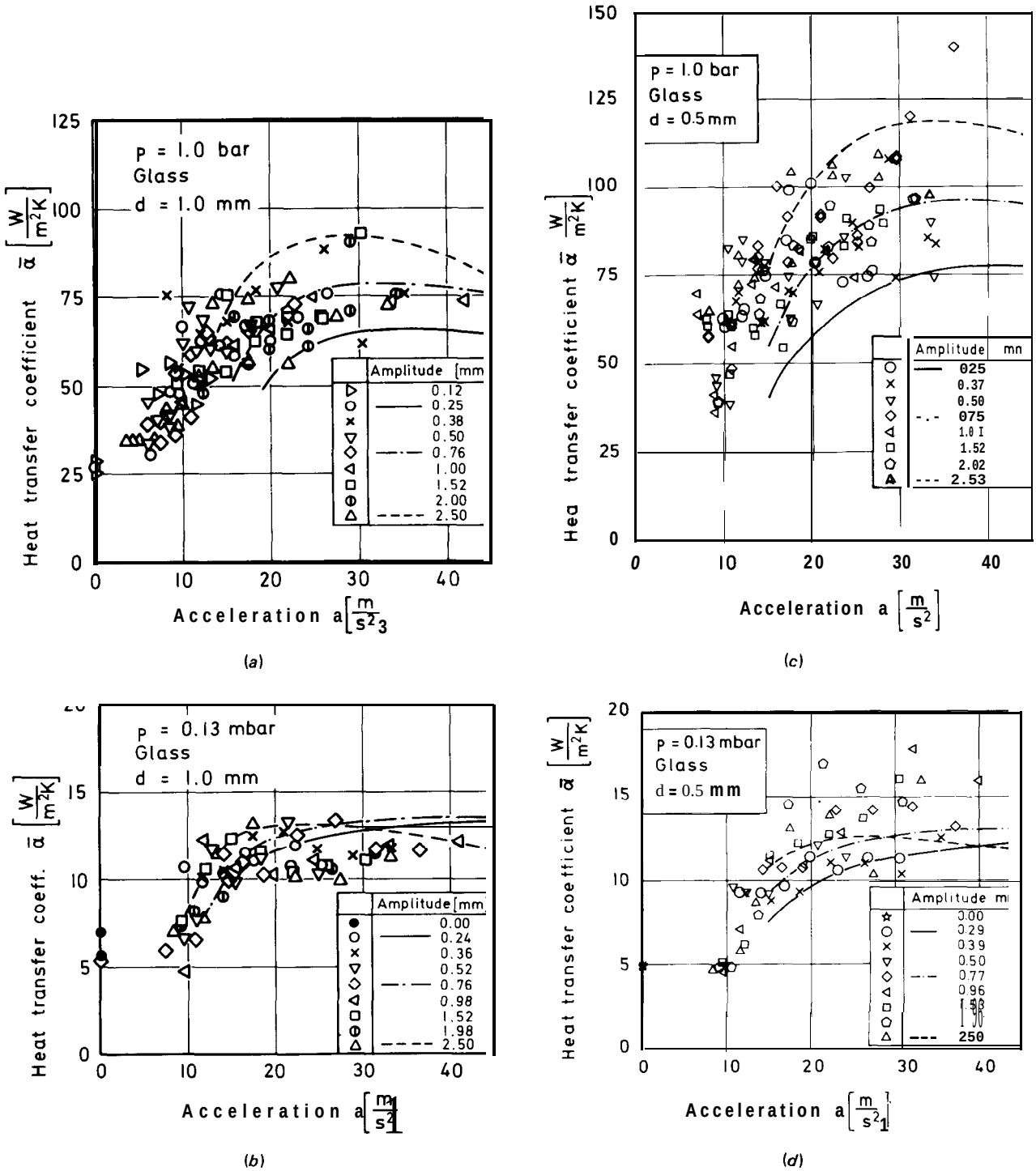

Figure 14 Heat transfer coefficients between the base of a vibrated vessel and a bed of glass spheres versus acceleration The lines represent calculated $\bar{\alpha}$ numbers following the circular flow model derived by Muchowski [8].

© 1983 Hemisphere publishing Corporation

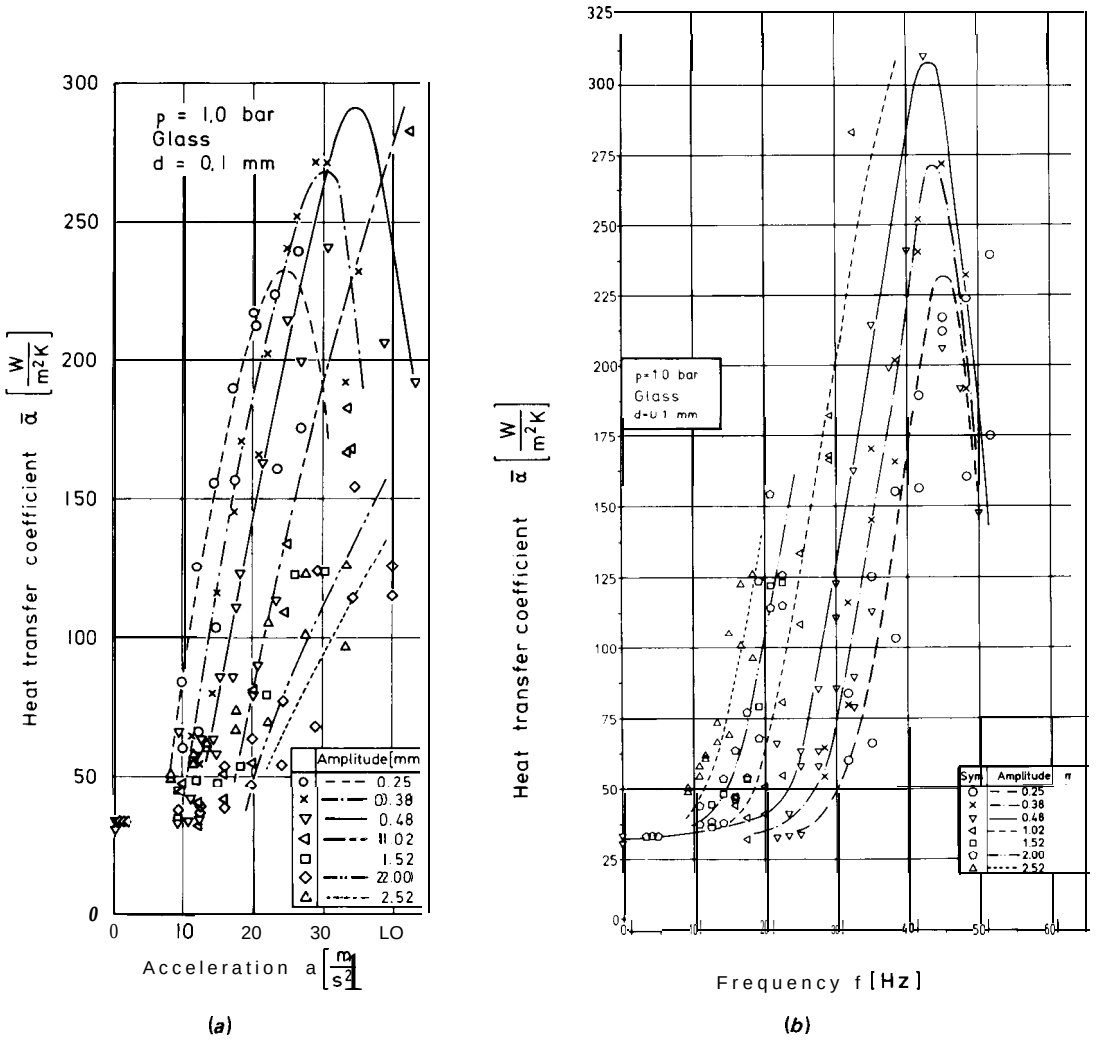

Figure 15 Experimentally obtained heat transfer coefficients $\bar{\alpha}$ from the bottom of a vibrated vessel to glass spheres (d = 0.1 mm). In (a) $\bar{\alpha}$ is plotted against the vibrational acceleration, whereas in (*b*) the $\bar{\alpha}$ numbers are plotted against the vibrational frequency.

© 1983 Hemisphere Publishing Corporation

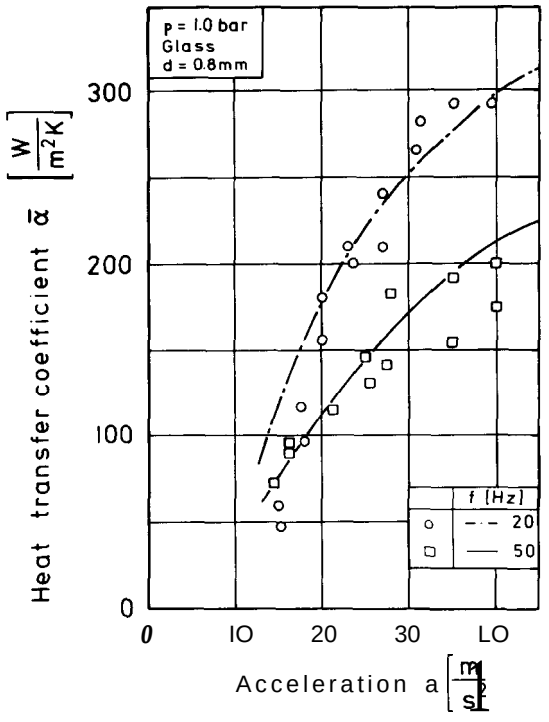

Figure 16 Heat transfer coefficients versus acceleration from a vertical heater to a vibrated bed of spheres. The lines represent calculated α numbers after the circular flow model derived by Muchowski [8]. Symbols: Experimentally obtained $\bar{\alpha}$ numbers from Gutmann [9].

Nomenclature for Section 2.8.3 appears at the beginning of Part 2

REFERENCESFORSECTION2.8.3

1. Muchowski, E., Der Wärmeübergang vom Boden vibrierter Gefässe an Kugelschtittungen bei Atmosphlrendruck und im Vakuum, Dissertation, University of Karlsruhe, 1977.
2. Schlünder, E. U., Wärmeübergang an bewegte Kugelschiittungen bei kurzfristigem Kontakt, *Chem. Ing. Tech.,* vol. 43, pp. 65 l-654, 1971.
3. Diels, K., and Jaeckel, R., *LeyboldVakuumTaschenbuch*, Springer-Verlag, Berlin, 1962.
4. Carlslaw, H. S., and Jaeger, J. C., Conduction ***of Heat in Solids,*** Oxford University Press, London, 1959.
5. Ernst, R., Der Mechanismus des Wärmeüberganges an Wärmeaustauschern in Fliessbetten (Wirbelschichten), *Chem. Ing. Tech.,* vol. 31, pp. 166-173, 1959.
6. Wunschmann, J., and Schlünder, E. U., Wärmeübergang von beheizten Flächen an Kugelschiittungen, *Verfahrenstechnik (Mainz)*, vol. 9, pp. 501-505, 1975.
7. Lehmberg, J., Untersuchungen zum Wärmeübergang zwischen der Wand und der Feststoffschicht eines Drehrohrofens, Dissertation, Technical University of Hannover, 1975.
8. Muchowski, E., Der Warmeiibergang vom Boden vibrierter Gefässe an Kugelschtittungen bei Atmosphärendruck und im Vakuum, ***Verfahrenstechnik*** *(Mainz)*, vol. 12, pp. 217-223, 1978.
9. Gutmann, R. G., Vibrated Beds of Powders: Part I-A, Theoretical Model for the Vibrated Bed, *Trans.* ***Inst. Chem. Eng.,*** vol. 54, pp. 174-183, 1976.

© 1983 Hemisphere Publishing Corporation

2.8.4
Fluidized beds

J. S. M. Botterill

A. Introduction

The general behavior of fluidized systems is outlined in Sec. 2.2.6 and described in detail elsewhere, for example, by Botterill [1], Davidson and Harrison [2], Kunii and Levenspiel [3], and Zabrodsky [4]. Particles in the fluidized condition are supported by the drag force exerted on them by fluid flowing upward through the bed. Gas-fluidized systems are characterized by the vigorous mixing generated within the bulk of the bed by the rising gas bubbles. The volume flow rate of bubbles approximately equals that of the gas in excess of the flow necessary to bring the bed to the fluidized condition, i.e., over the minimum fluidizing velocity u_{mf}. With fine powders of lower-density material (mean diameter 20-100 μm and density $<1\,400$ kg/m^3), there is a region of stable bed expansion with increase in fluidizing gas flow rate before bubbling begins (Geldart group A [5]). With larger, denser particles, bubbling occurs as soon as the minimum fluidizing velocity is exceeded.

Fluidization requires the expenditure of power for fluidization. The pressure drop across the bed equals its weight per unit area, and this can be excessive with deep beds, although its relative importance reduces as the static operating pressure increases. Operating conditions are obviously limited to within the range of gas flows over which the bed may be fluidized. If the gas throughput is too low, segregation may occur with beds of wider particle size distribution, and the bed will defluidize if the flow rate is below that for minimum fluidization. Conversely, if the gas flow rate is too high, there will be excessive carryover of material from the bed. This depends on particle size and the physical properties of the fluid and solid [1-4]. Such considerations influence the choices to be made in design.

Because of the large area of particle surface exposed within a fluidized bed (1 m^3 of 100-μm-diameter particles has a surface area $>30\,000$ m^2), fluid-to-particle heat transfer is rarely a limiting factor, although gas-solid contact is far from uniform throughout the bed. Primarily, it is the heat capacity of the particles and their circulation within the bed that are responsible for the good thermal properties of the gas fluidized bed [1]. At atmospheric pressure, the volumetric heat capacity of the solids is of the order of 1 000 times that of the gas. The particle mixing produces isothermal conditions within the bulk of the bed. The very wide range of possible bed behavior causes a problem. In particular, the fluidization behavior of small-scale beds can be very different from that of larger beds, so that small-scale tests can be quite misleading (see, for example, the study reported by de Groot [6]). This comes about because bubbles are constrained in size by the scale of the equipment in beds of small diameter but can grow very much larger in large-scale equipment according to the characteristic of the bed material. Thus, with finer, less dense powders, the maximum stable bubble size is less than with coarser, denser powders. Large bubbles rise correspondingly faster through the bed than do smaller ones. Accordingly, there is much variation in the overall bed expansion because of varying bubble volume hold-up and the rate of solids circulation will also be affected. The situation is further complicated by the varying degree of the continuous phase expansion as operating temperature

© 1983 Hemisphere Publishing Corporation

and hence the fluidizing gas viscosity change [7]. Immersion of heat transfer surfaces within the bed also affects the bubbling behavior and can have different effects according to operating circumstances [1–4]. Therefore, caution must be exercised in using the published correlations.

To a first approximation, the heat transfer coefficient α between an immersed surface and a gas-fluidized bed can be thought to consist of three additive components:

1. The particle convective component α_{pc}, which is dependent on heat transfer through particle exchange between the bulk of the bed and the region adjacent to the heat transfer surface
2. The interphase gas convective component α_{conv}, by which heat transfer between particle and surface is augmented by interphase gas convective heat transfer
3. The radiant component of heat transfer α_{rad}.

Thus:

$$\underset{\substack{\text{Approximate range of} \rightarrow \\ \text{significance}}}{\alpha} = \underset{40\ \mu\text{m} \rightarrow 1\ \text{mm}}{\alpha_{pc}} + \underset{\substack{>800\ \mu\text{m} \\ \text{and at higher} \\ \text{static pressure}}}{\alpha_{conv}} + \underset{\substack{\text{Higher temperature} \\ (>1\,000\ \text{K}) \text{ and} \\ \text{differences}}}{\alpha_{rad}} \qquad (1)$$

(a) Particle convective component α_{pc}

Particles in the bulk of the bed exchange heat with the fluidizing gas and, by conduction through the gas, with each other. They usually stay within the bulk of the bed long enough to come to the same temperature as their neighbors. Then, while at the bulk bed temperature, some are swept into close proximity to the heat transfer surface by the bubble-induced circulation patterns occurring within the bed. Heat flows from the particles to the surface by conduction through the gas; this is the limiting stage in this mechanism. When the particles first arrive close to the heat transfer surface, there is a high local temperature gradient and heat consequently transfers rapidly. The longer the particles reside close to the transfer surface, the closer the surface and local bed temperatures become. Thus the highest mean transfer coefficients will be obtained under those conditions that generate rapid exchange of material between the vicinity of the transfer surface and the bulk of the bed, that is, with low particle residence times adjacent to the transfer surface. With fine powders (d_s < 20 μm), bed circulation is inhibited by interparticle forces. The strong inverse dependence of coefficient on particle size between ~80 μm and 1 mm (Fig. 1) is a consequence of the decrease in relative area across

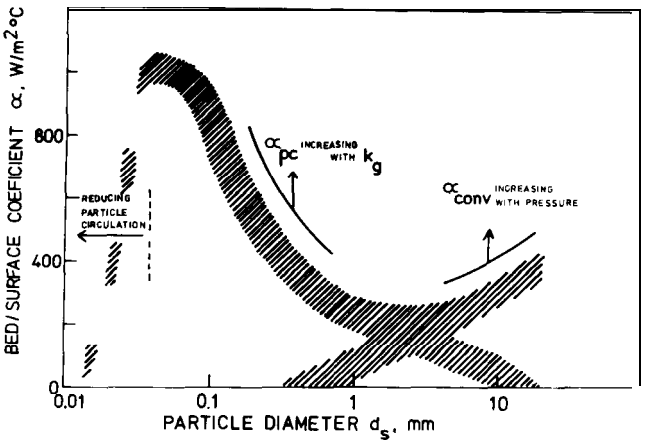

Figure 1 General effect of mean particle diameter on bed/surface heat transfer coefficient.

which the heat can flow through a short gas conduction path between the surface and adjacent particle. It is not until particle size and/or static operating pressure are sufficiently increased for the fluidizing gas flow conditions to enter the transitional or turbulent flow regime that significant interphase convective transfer occurs through the gas [Sec. A(b)] and the bed-to-surface heat transfer increases with further increase in particle size.

The bed-to-surface coefficient increases from that for the unrestrained packed bed condition with increase in gas velocity beyond the point of minimum fluidization because the bed becomes mobile under the influence of the bubble flow (Fig. 2). At higher gas flow rates, a maximum is reached, and the coefficient then decreases with further increase in gas flow rate because of the blanketing effect of the increasing bubble flow across the transfer surface. This maximum occurs at velocities closer to the minimum fluidization velocity as particle size increases. With fine powders of Geldart s

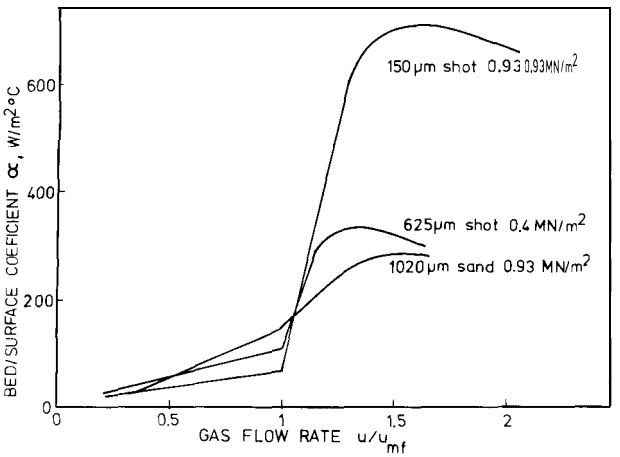

Figure 2 Effect of gas flow rate on bed/surface heat transfer coefficient.

© 1983 Hemisphere Publishing Corporation

group A [5], for which there is stable bed expansion as the gas velocity is first increased beyond the point of minimum fluidization, there is an additional minor peak in the rising portion of the curve when particles begin to circulate by diffusive mixing (Khan et al. [8]). The coefficient then decreases with further bed expansion until the minimum bubbling velocity is exceeded when the bed collapses back and the bubble-generated particle circulation develops.

(b) Interphase gas convective component α_{conv}

Until the gas flow condition through the continuous phase becomes turbulent or at least enters the transitional regime, the interphase heat transfer by convection through the gas is of only secondary importance compared with that transported by the particle convective mechanism. The threshold for significance of this component is therefore dependent on mean particle diameter ($>800\,\mu m$) and static operating pressure (see Fig. I). However, with beds of very large mean particle diameter where the maximum particle size may be several millimeters, the effect of the finer tails in a wide particle size distribution may be dominant because of their influence on the gas flow condition. In effect, larger fractions can be fluidized in the fluid constituted by the fluidized tines and mean particle size then ceases to have importance between systems where the tail fractions are similar (Golan et al. [9]).

(c) Radiative component α_{rad}

The estimation of the radiative component presents the most difficulty. Radiation tends to transfer some heat at the expense of the particle convective mode, and this effect is greater with bigger particles because the heat transfer surface receives radiant energy from the whole of the particle s surface visible to it. Relatively less heat flows by conduction from the particle to the transfer surface through the short gas conduction path close to the point of contact [1]. Although the particles used in high-temperature beds are likely to be of a refractory nature and therefore to be of low emissivity, the effective emissivities of particles in bulk in the bed as seen from the bed surface will differ from that of an individual isolated particle. Pikashov et al. [10] reported the measured emissivities Table I, which Makhorin et al. [11] later suggested, after improving their technique, were probably 10-20% too low.

Even allowing for the variation in emissivity with temperature that Makhorin et al. measured [I I], in practical situations there also remains the influence of an immersed heat transfer surface on the bed temperature directly adjacent to it. Thus, the presence of a cooler surface, for example, modifies the local bed temperature, consequently reducing the local radiant heat flux. Baskakov et al. [12] have attempted to deal with this on the basis of bulk bed temperature in terms of an effective emissivity ϵ_{ef}. This decreases as the temperature difference between the bed and surface increases (Fig. 3). The effective emissivity also decreases with increase in absolute bed temperature.

Apart from increasing with increase in temperature, the radiant heat transfer component, as noted above, also increases relative to the particle convective component as the mean particle diameter increases [12]. In contrast to lower-temperature systems, maximum heat transfer coefficients are to be expected under those conditions of higher gas flow when the bed is bubbling vigorously. In effect, this opens up the bed so that the heat transfer surface can see deeper into the bed where there has been less influence of the transfer surface on local bed temperature and the interior of the bed is behaving more like a blackbody radiator. A reasonable effective emissivity ϵ_{ef} between a surface and bed under ordinary circumstances is -0.7.

Table 1 Measured effective emissivities[a]

Material of bed	d_s, mm	Gas velocity $\times u_{mf}$	Bulk bed temperature, K	Emissivity of particle	Effective bed emissivity
Molten magnesite compound of MgO and SiO_2 (irregularly shaped particles)	1-1.5	1.2-3.0	775-1 475		*0.95*
River sand (rounded particles)	1-1.5	1.2-3.0	115-1 375	*0.60*	*0.85*
Chamotte (irregularly shaped particles)	1-1.5	1.2-3.0	725-1 375	*0.60*	*0.80*
Zirconium dioxide ZrO_2 (rounded particles)	0.25-1	1.2-4.0	875-l 425	*0.23*	*0.59*
Corundum Al, 0, (rounded particles)	1.5-2	1.2-3.0	1075-l 725	*0.21*	*0.59*

[a] From Pikashov et al. [10].

© 1983 Hemisphere I blishing Corporation

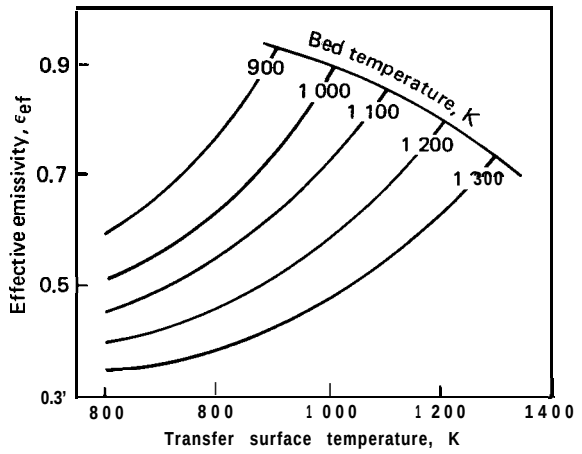

Figure 3 Variation in effective emissivity with the temperature of transfer surface and bed. From Baskakov et al. [12].

B. Predictive formulas

(a) Condition for maximum bed-to-surface heat transfer coefficient

The fluidizing gas velocity for maximum bed-to-surface heat transfer coefficient is a function of mean particle size. It is best expressed in terms of a factor times the minimum fluidizing gas flow rate u_{mf}, and the factor decreases as the mean particle diameter increases. Because of the difficulty in allowing for particle shape and its effect on bed voidage in particular, correlations for the prediction of minimum fluidizing velocity [1-4] are unreliable. Consequently, it is better to measure the minimum fluidization velocity directly, but this is not always feasible at high operating temperatures and pressures. Under these circumstances, the interpolation form of the correlation given by Goroshko et al. [13] is recommended. It has, for example, been found to allow satisfactorily for the effect of the change in gas viscosity and density with temperature [7], provided that the value for the voidage at minimum fluidization E_{mf} is the value that fits the correlation under ambient temperature conditions when u_{mf} can be readily determined. The recommended formula is

$$\mathrm{Re}_{mf} = \frac{\mathrm{Ar}}{150[(1-E_{mf})/E_{mf}^3] + \sqrt{(1.75/E_{mf}^3)\,\mathrm{Ar}}} \qquad (2)$$

Difficulties still remain in using this, however, when the range of physical properties falls consistently within the transitional flow regime, because the correlation is very sensitive to voidage. Apart from the effect of sphericity on voidage, it being smaller for closely sized spherical particles than for angular ones, voidage also tends to be reduced as particle mean size increases. Whereas 0.4 is often cited as the approximate voidage of a packed bed of closely sized, spherical particles, that of a loosely packed bed corresponding to the state at minimum fluidization may readily be 25% higher with angular particles. The voidage also increases with increase in operating temperature whilst the fluidizing gas flow condition remains laminar [7], so that this highly sensitive factor, E_{mf}, is a complicated variable.

Developing from the Goroshko correlation and making assumptions about bed voidage, Todes [14] offers the following correlation for the prediction of the Reynolds number, Re_{opt}, for the gas flow conditions giving maximum bed-to-surface heat transfer coefficient:

$$\mathrm{Re}_{opt} = \frac{\mathrm{Ar}}{18 + 5.22\sqrt{\mathrm{Ar}}} \qquad (3)$$

This is compared with some experimental results derived over a range of conditions with static operating pressure up to 10 atm (Denloye and Botterill [15]) in Fig. 4. Agreement is comparatively good for larger particles where the fluidizing velocity for maximum bed-to-surface heat transfer is close to that for minimum fluidization, but the correlation is not to be recommended for use with powders of mean diameter $<400\,\mu$m where there is increasing difference between these two velocities.

(b) Maximum bed/surface coefficient, α_{pc} dominant (d, $\approx$ *80–800* pm)

The design of the distributor and any internals will obviously have a strong influence on the solids convection patterns within the bed [1-4], and the work reported by de Groot [6], referred to above, illustrates the pronounced change in bed behavior that can occur with change in scale of the equipment. Thus the published correlations reflect the solids circulation patterns obtained within the experimental beds used. These beds have mostly been of small scale, with stable,

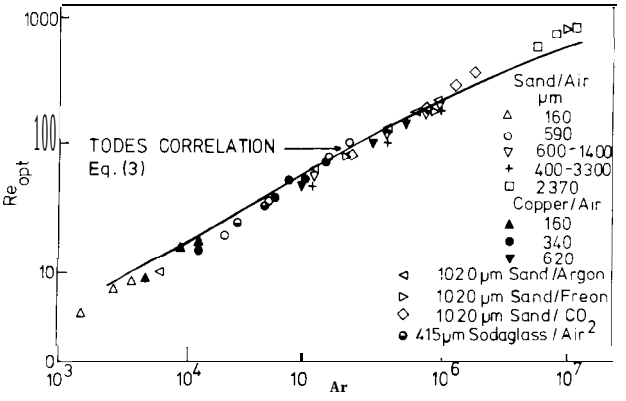

Figure 4 Illustration of the fit between correlation by Todes [14] for optimum gas flow rate and experimental results.

© 1983 Hemisphere Publishing Corporation

definite circulation patterns; bubbles tend to rise in a stream up the center of the bed and with a return flow of solids close to the containing wall. Nevertheless, an approximate correlation has been given by Zabrodsky [4], which can be recommended for the prediction of maximum bed-to-surface heat transfer coefficients omitting the radiation component and for powders for which there is negligible stable bed expansion falling in the size range ~80-800 μm (Geldart s groupB powders [5]). This has the form

$$\alpha_{max} = 35.8\rho_s^{0.2}\lambda_g^{0.6}d_s^{-0.36} \quad (4)$$

the constant being consistent with the use of SI units. This correlation predicts the increase in heat transfer coefficient resulting from a change in gas thermal conductivity as the operating temperature is increased until, beyond 600°C, radiant heat transfer becomes increasingly significant. One might expect to obtain values of 70% of this maximum under reasonable operating conditions. If the continuous phase is capable of a degree of stable expansion, the number of particles adjacent to a unit area of the heat transfer surface will be reduced with consequent reduction in the particle convective component of the heat transfer coefficient (Botterill [1]). For the case of smaller, less dense powders falling within Geldart s group A, Khan et al. [8] give the correlation

$$Nu_{max} = 0.157\ Ar^{0.475} \qquad 2 < Ar < 70 \quad (5)$$

but this has not been tested over a range of operating temperatures.

Many fundamental models of the basically particle convective heat transfer process have been proposed (see Botterill [1]), but these cannot generally be applied for predictive purposes because the condition and thermal properties of the bed directly adjacent to the heat transfer surface are not known.

(c) Maximum bed/surface coefficient, α_{conv} dominant (d, > *800 μm and at higher static pressures)*

Taking the bed-to-surface heat transfer coefficient at the point of fluidization to be a measure of the interphase gas convective component, α_{conv} (there is no particle convective component when the bed is in the quiescent condition), Denloye and Botterill [15] correlated their results covering a range of conditions including static pressures up to 10 atm by the following dimensional equation (Fig. 5) (dimension is $m^{-1/2}$):

$$\frac{\alpha_{conv}d_s^{1/2}}{\lambda_g} = 0.86\ Ar^{0.39} \qquad 10^3 < Ar < 2 \times 10^6 \quad (6)$$

The corresponding maximum particle convective component, $\alpha_{pc,max}$ (assuming the two components to be additive) was correlated against the Archimedes number by the following dimensionless equation:

$$\frac{\alpha_{pc,max}d_s}{\lambda_g} = 0.843\ Ar^{0.15} \quad (7)$$

As noted above [Sec. A(b)], if there is a wide -size distribution the fines may damp out the turbulence in the fluidizing gas, thus reducing the gas convective component. Evidence for this is apparent in the results reported by Golan et al. [9].

Baskakov and Suprun [16] earlier estimated the magnitude of the interphase gas convective component by analogy with mass transfer. Their correlation gives similar predictions at atmospheric pressure, but there is an increasing discrepancy as the static pressure is increased (Fig. 5).

(d) Radiative component of bed/surface heat transfer, α_{rad}

For rule-of-thumb estimates, the radiative component can be estimated using absolute temperatures and an adaptation of the Stefan-Boltzmann equation in the form

$$\alpha_{rad} = \frac{5.67 \times 10^{-8}\epsilon_r(T_{bed}^4 - T_{surface}^4)}{T_{bed} - T_{surface}} \quad (8)$$

where T_{bed} is the absolute temperature of the bulk of the bed and ϵ_r is a reduced emissivity to take into account both the different emissive properties of the surface and bed and the effect of the surface on the temperature of the bed directly adjacent to the transfer surface. As discussed in Sec. A(c), a reasonable value for ϵ_{ef} under ordinary circumstances is ~0.7 (see Fig. 3), but ϵ_r may be readily reduced to as low as 0.1 with a shiny metal transfer tube surface.

Broughton [17] gives a correlation for the maximum bed-to-surface heat transfer coefficient between

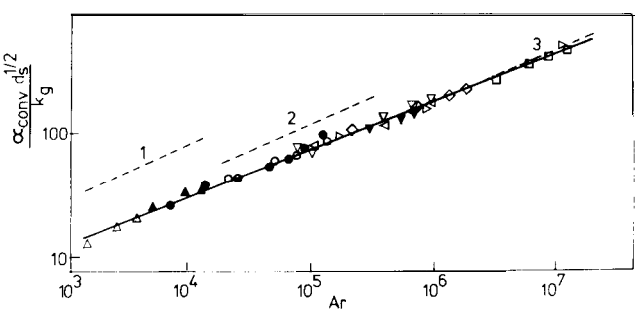

Figure 5 Correlation of quiescent bed (interphase gas convective component) heat transfer coefficients. Identified lines 1, 2, and 3 are predictions of Baskakov Suprun correlation [16] for 160 μm copper, 590 pm sand, and 2 370 μm sand in air, respectively. Other symbols as in Fig. 4.

© 1983 Hemisphere Publishing Corporation

a hot bed of alumina and a water-cooled probe in the form

$$Nu_{max} = 0.043\,4 \left(\frac{T}{273}\right)^2 Ar^{0.271} \quad (9)$$

C. Immersed tubes

Available heat transfer surface can be increased by the immersion of tubes within the bed, but higher fluidizing gas pumping power costs is the penalty to be paid for deeper beds, so this must be borne in mind when considering the tube arrangement. The presence of immersed surfaces will affect the local fluidization conditions and, in turn, will affect the local particle convective component of heat transfer. Thus, when horizontal tubes are immersed within a bed, for example, although much heat transfer surface is exposed to the cross flow of solids, which is advantageous from the point of view of heat transfer, a stagnant layer of defluidized particles will build up on the top of the tube and bubbles may tend to shroud the downward-facing surface. When tubes are mounted on a staggered array there is greater tendency for the rising bubbles to displace the stagnant solids periodically. Although very close spacing seriously affects the particle circulation, McLaren and Williams [18] found that heat transfer coefficients determined in low-temperature tests do not decrease dramatically as the narrowest gap between tubes is progressively reduced. They found a decrease in the coefficient of the order of 25% as the gap was reduced from about 300 mm down to 15 mm in tests with beds of ash of wide size distribution and mean particle size -450 μm but including small fractions of particles greater than 1.7 mm diameter. Vertical arrays may enhance slugging in deep beds, although the use of vertical inserts has also been advocated as a means of controlling bubble growth and so preventing slugging. Because of the influence of the tubes on bed behavior, beds with such inserts will be less sensitive to the overall effects of changing scale (see Sec. A).

Saxena et al. [19] review very fully the published results and correlations for all types and configurations of immersed tubes. It is doubtful, however, if greater inaccuracy would be incurred using estimates based on the simple equations (4) or (6) and (7) as appropriate and (8) if radiant transfer is significant. These should be reliable within ±20%.

In practice, it is prudent to carry out tests on a model of as large a scale as possible. Preferably, when concerned with a multiunit system, this should be a full-sized unit cell of the proposed system, that is, incorporating all the features of one full-scale complete unit of the proposed design. This would be the area of bed fed from one fuel distribution point in the design of a combustor, for example.

Most usually, the limiting coefficient will be on the inside of the tube, but the use of extended surfaces has been advocated in situations where this is not so (e.g., with liquid metal coolants flowing through the tubes). Another application of finned tubes has been in the construction of highly efficient, shallow bed heat exchangers for the recovery of waste heat from exhaust gases [20]. In this latter application, the regions between the fins behave as separate, dilute beds, and bubbles remain restricted in size by the closeness of the fin spacing, which may be as little as 3-5 mm or 15-20 times the particle diameter. In such units, bed expansion can be as high as 400% while still obtaining high bed-to-surface heat transfer coefficients because of the very short particle residence times obtaining at the heat transfer surface. Based on the outside area of the tube, obtainable coefficients are as high as 4 kW/m^2 K. Because the particles in the bed present a very high transfer surface area to the gas, very good heat recovery from the gas can be achieved and it is only necessary to use shallow beds. Such units can thus operate without the pressure drop penalty that is an inherent disadvantage of deeper fluid bed systems. Typically, a unit can be operated with an overall pressure drop as low as 50 mm water gauge using the suction from an exhaust fan to draw the hot fluidizing gases through the bed. Maximum bed-to-surface coefficients based on total area have been correlated by Pillai [21]:

$$Nu_{max} = 0.36\ Ar^{0.22}\left(\frac{T}{273}\right)^{0.82} \quad (10)$$

when operating at temperatures where radiant heat transfer is significant.

Although generally disadvantageous, positioning horizontal tubes close to the distributor can sometimes be advantageous. Thus, gas jetting or bubble development at the distributor may enhance particle exchange at the tubes and hence the particle convective component α_{pc}. Alternatively, however, there may be defluidized zones close to the distributor or gas blanketing, if it occurs, will have a deleterious effect. Gas jetting could also give rise to increased erosion damage to the tubes and attrition damage to the particles. In heat recovery operations, the temperature difference between gas and transfer surface will be highest close to the distributor whereas, with a combustor or other exothermic reactor, the difference will be lowest in that entry region. Hence an advantage could be expected from the heat transfer point of view in the former rather than the latter instance.

© 1983 Hemisphere Publishing Corporation

In applications where it is required to remove more or less heat from a bed that is being used as a heat source, the generally high bed-to-surface transfer coefficient may well pose problems when the heat demand is small. One way to overcome this is to make provision for operating with more or less of the heat transfer surface immersed within the bed. This can be done by varying the fluidizing gas flow rate and thereby the degree of overall bed expansion. However, there is again the danger of increased attrition damage to the particles and erosion damage to the tubes as the bed is operated in a less expanded state with some tubes exposed to the spray of particles from bursting bubbles as the tubes become exposed above the surface of the bed,

NOMENCLATURE FOR SECTION 2.8.4

Ar	Archimedes number $[gd_s^3(\rho_s - \rho_g)\rho_g/\mu_g^2]$
c_s	heat capacity of particle, J/kg K
d_s	surface/volume mean particle diameter, m
E_{mf}	bed voidage at condition of minimum fluidization
Nu_{max}	Nusselt number for maximum bed-to-surface heat transfer, $(\alpha_{max} d_s/\lambda_g)$
Re_{mf}	Reynolds number for minimum fluidization, $(d_s u_{mf}\rho_g/\mu_g)$
Re_{opt}	Reynolds number for maximum bed-to-surface heat transfer, $(d_s u_{max}\rho_g/\mu_g)$
T	absolute temperature, K
u_{max}	gas velocity for maximum bed-to-surface heat transfer, m/s
u_{mf}	minimum fluidization gas velocity, m/s
a!	bed-to-surface heat transfer coefficient, W/m^2 K
$a!_{conv}$	interphase gas convective component of bed-to-surface heat transfer, W/m^2 K
α_{max}	maximum bed-to-surface heat transfer coefficient, W/m^2 K
α_{pc}	particle convective component of bed-to-surface heat transfer coefficient, W/m^2 K
$\alpha_{pc,max}$	maximum particle convective component of bed-to-surface heat transfer coefficient, W/m^2 K
α_{rad}	radiative component of bed-to-surface heat transfer coefficient, W/m^2 K
fef	effective bed emissivity
ϵ_r	reduced emissivity
λ_g	gas thermal conductivity, W/m K
μ_g	viscosity of gas, N s/m^2
ρ_g	density of gas, kg/m^3
PS	density of particle, kg/m^3

REFERENCES FOR SECTION 2.8.4

1. Botterill, J. S. M., ***Fluid-Bed Heat Transfer,*** Academic, London, 1975.
2. Davidson, J. F., and Harrison, D., ***Fluidization,*** Academic, London, 1971.
3. Kunii, D., and Levenspiel, D., ***Fluidization Engineering,*** Wiley, New York, 1969.
4. Zabrodsky, ***S. S., Hydrodynamics and Heat Transfer in Fluidized Beds,*** M.I.T. Press, Cambridge, Mass., 1966.
5. Geldart, D., Types of Gas Fluidization, ***Powder Technol., vol. 6,*** pp. 285-292, 1972.
6. De Groot, J. H., Scaling-up of Gas-fluidized Bed Reactors, *Proc. Int.* ***Symp. Fluidization,*** ed. A. A. H. Drinkenberg, pp. 348-358, Netherlands University Press, Amsterdam, 1967.
7. Botteril, J. S. M., and Teoman, Y., Fluid-Bed Behaviour at Elevated Temperatures, ***Fluidization,*** eds. J. R. Grace and J. M. Matsen, pp. 93-100, Plenum, New York, 1980.
8. Khan, A. R., Richardson, J. F., and Shakiri, K. J., Heat Transfer between a Fluidized Bed and a Small Immersed Surface, ***Fluidization-Proc. 2d Engineering Foundation*** *Conf.*, eds. J. F. Davidson and D. L. Keairns, pp. 351-356, Cambridge University Press, Cambridge, 1978.
9. Golan, L. P., Cherrington, D. C., Diener, R., Scarborough, C. E., and Weiner, S. C., Particle Size Effects in Fluidized Bed Combustion, ***Chem. Eng. Prog.,*** vol. 75, pp. 63-72, July 1979.
10. Pikashov, V. S., Zabrodsky, S. S., Makhorin, K. E., and Il'Chenko, A. I., On the Experimental Study of the Fluidized-Bed Effective Emissivity, ***Heat and Mass Transfer,*** vol. 5, Nauka i Tekhn., Minsk, 1968.
11. Makhorin, K. E., Pikashov, V. S., and Kuchin, G. P., Measuring Particle Temperature and Emissivity in a High Temperature Fluidized Bed, ***Fluidization-Proc. 2d Engineering Foundation*** *Conf.*, eds. J. F. Davidson and D. L. Keairns, pp. 93-97, Cambridge University Press, Cambridge, 1978.
12. Baskakov, A. P., Berg, B. V., Vitt, 0. K., Filippovsky, N. F., Kirakosyan, V. A., Goldobin, J. M., and Maskaev, V. K., Heat Transfer to Objects Immersed in Fluidized Beds, ***Powder Technol.,*** vol. 8, pp. 273-282, 1973.
13. Goroshko, V. D., Rozenbaum, R. B., and Todes, 0. M., Approximate Hydraulic Relationships for Suspended Beds and Hindered Fall, Izv. *Viszov,* ***Neft'e Gas,*** vol. 1, pp. 125-131, 1958.
14. Todes, ***0.*** M., ***Application of Fluidized Beds in the Chemical Industry,*** Part II, pp. 4-27, Izd. Znanie, Leningrad, 1965.
15. Denloye, A. 0. O., and Botterill, J. S. M., Bed to Surface Heat Transfer ***in*** a Fluidized Bed of Large Particles, ***Powder Technol.,*** vol. 19, pp. 197-203, 1978.
16. Baskakov, A. P., and Suprun, V. M., Determination of the Convective Component of the Heat Transfer Coefficient to a Gas in a Fluidized Bed, ***Int. Chem. Eng.,*** vol. 12, pp. 324-326, 1972.
17. Broughton, J., Combustion in Fluidized Beds, Ph.D. thesis, University of Newcastle-upon-Tyne, England, 1972.

© 1983 Hemisphere Publishing Corporation

18. McLaren, J., and Williams, D. F., Combustion Efficiency, Sulphur Retention and Heat Transfer in Pilot Plant Fluidized-Bed Combustors, *J.* Inst. ***Fuel,*** vol. 42, pp. 303-308, 1969.
19. Saxena, S. C., Grewal, N. S., Gabor, J. D., Zabrodsky, S. S., and Galershtein, D. M., Heat Transfer between a Gas Fluidized Bed and Immersed Tubes, ***Adv. Heat Transfer, vol. 14,*** pp. 149-247, 1978.
20. Botterill, J. S. M., and Virr, M. J., The Contribution of Fluid-Bed Technology to Energy Saving and Environmental Protection, *Appl.* ***Energy,*** vol. 3, pp. 139-150, 1977.
21. Pillai, K. K., Some Studies Relating to the Design of Shallow Fluidized-Bed Boilers, Ph.D. thesis, University of Aston in Birmingham, England, 1975.

© 1983 Hemisphere Publishing Corporation

2.9
Heat transfer by radiation

Contents

2.9.1
INTRODUCTION, D. K. Edwards 2.9.1-1

A. Radiation heat transfer in thermal design 2.9.1-1
B. Thermodynamic surfaces and surface systems 2.9.1-1
C. Radiant intensity and flux 2.9.1-2
D. Blackbody radiation 2.9.1-3
E. Fractional functions 2.9.1-4

Bibliography for Section 2.9.1 2.9.1-5

2.9.2
SURFACE RADIATION CHARACTERISTICS, D. K. Edwards 2.9.2-1

A. Introduction to surface characteristics 2.9.2-1
B. Absorption and emission characteristics 2.9.2-1
C. Measurement of absorption and emission characteristics 2.9.2-3
D. Reflection and transmission characteristics 2.9.2-3
E. Measurement of reflection and transmission characteristics 2.9.2-6
F. Electromagnetic theory and the Fresnel relations 2.9.2-7
G. Some useful approximations 2.9.2-10
H. Polarization 2.9.2-12
I. Thermal radiation characteristics in thermal design 2.9.2-15

Bibliography for Section 2.9.2 2.9.2-18

2.9.3
RADIATION TRANSFER BETWEEN PERFECTLY DIFFUSE SURFACES, D. K. Edwards 2.9.3-1

A. Shape factors 2.9.3-1
B. Radiosity-irradiation formulas 2.9.3-4
C. Refractory surfaces 2.9.3-8
D. The radiation network 2.9.3-8
E. Selected working relations 2.9.3-10
F. Diffuse-walled passages 2.9.3-13

Bibliography for Section 2.9.3 2.9.3-16

2.9.4
RADIATION TRANSFER BETWEEN SPECULAR AND IMPERFECTLY DIFFUSE SURFACES, D. K. Edwards 2.9.4-1

A. Specular and imperfectly diffuse surfaces 2.9.4-1
B. The mirror-image concept 2.9.4-1
C. The Monte Carlo algorithm 2.9.4-2
D. Specular-walled passages 2.9.4-5
E. Surface models 2.9.4-7
F. Rough-walled passages 2.9.4-9

Bibliography for Section 2.9.4 2.9.4-10

2.9.5
GAS RADIATION PROPERTIES, D. K. Edwards 2.9.5-1

A. The equation of transfer 2.9.5-1
B. Measurement of gas radiation properties 2.9.5-2

© 1983 Hemisphere Publishing Corporation

HEDH

C. Qualitative remarks on the physics of gas radiation **2.9.5-4**
D. Spectral, band, and total property definitions **2.9.5-4**
E. Molecular gas radiation properties **2.9.5-8**
F. Gas mixtures **2.9.5-11**

Bibliography for Section 2.9.5 **2.9.5-12**

2.9.6
RADIATION TRANSFER WITH AN ISOTHERMAL GAS, D. K. Edwards 2.9.6-l

A. Heat transfer at a black wall **2.9.6-1**
B. The mean-beam-length concept **2.9.6-2**
C. Wall layer transmission **2.9.6-3**
D. Radiosity-irradiation formulation at an isothermal-gas-filled-enclosure wall **2.9.6-3**
E. The radiation network with a gas **2.9.6-4**
F. Some useful results **2.9.6-4**
G. Sample calculation **2.9.6-7**
H. Monte Carlo solution **2.9.6-8**

Bibliography for Section 2.9.6 **2.9.6-9**

2.9.7
NONISOTHERMAL GAS RADIATION, D. K. Edwards 2.9.7-l

A. Solution of the equation of transfer **2.9.7-1**
B. Geometric considerations **2.9.7-2**
C. The slab geometry **2.9.7-3**
D. Differential formulations **2.9.7-5**
E. Spectral considerations and scaling approximations **2.9.7-8**
F. Molecular gas radiation in the slab **2.9.7-10**

Bibliography for Section 2.9.7 **2.9.7-13**

2.9.8
RADIATION ACTING WITH CONDUCTION OR CONVECTION, D. K. Edwards 2.9.8-l

A. Combined phenomena **2.9.8-1**
B. Thermal network analysis **2.9.8-1**
C. Radiation-coupled transient heating or cooling **2.9.8-3**
D. Radiant heat exchanger **2.9.8-4**
E. The radiating fin **2.9.8-4**
F. Linearized radiation and conduction around the hollow cylinder **2.9.8-6**
G. Convection of a radiating molecular gas **2.9.8-7**

Nomenclature for Sections 2.9.1-2.9.8 **2.9.8-10**
Bibliography for Section 2.9.8 **2.9.8-12**

© 1983 Hemisphere Publishing Cmporation

2.9.1
Introduction

D. K. Edwards

A. Radiation heat transfer in thermal design

When does one consider radiation heat transfer, and when does one not? One does not consider radiation inside of a fluid that is highly opaque to the source spectrum. In a fluid such as water, the radiation is merely a contributor to what we know as thermal conductivity. Similarly, one does not consider radiation inside a fluid that is perfectly transparent to the source spectrum. If there is no physical mechanism by which the fluid can absorb energy from radiation passing through it, then it follows from thermodynamics that it cannot emit radiation either, and it cannot be either heated or cooled by radiation. Such a fluid is said to be ***diathermanous.*** The walls surrounding such a fluid, however, may exchange heat radiation, but only if they are not isothermal. Thus one does not ordinarily consider radiation within the passages of a heat exchanger containing oil, water, or air. The first two are opaque. The last is diathermanous.

When two walls at different temperatures are in view of each other or one wall is in view of a participating medium (one neither opaque nor diathermanous), the radiation heat flux (W/m^2) tends to be high when $\Delta C_s T^4$ is high, where C_s is the Stefan-Boltzmann constant, 5.669 7 X 10^{-8} $W/m^2 K^4$. When $\boldsymbol{AT}$ is small compared to the absolute temperature level, $\Delta C_s T^4$ can be written $4C_s T_m^3 \boldsymbol{AT}$, where T_m is the mean temperature level. At 300 K, the value for $4C_s T_m^3$ is slightly over 6 W/m^2 K, on the same order as a naturalconvection heat transfer coefficient. At $T_m = 2\,000$ K, the value is nearly 300 times greater. From such a value, 1 800 W/m^2 K, one can see why radiation contributes to film-boiling heat transfer. Radiation is important when temperatures are high, distances are large (because convective heat transfer coefficients go as passage size $\boldsymbol{D}$ as $D^{-1/5}$ for turbulent flow or D^{-1} for laminar flow), or under vacuum conditions when convective heat transfer coefficients are low because of the low fluid density.

Figures 2.9.1(1-3), 2.9.2(1-3), 2.9.3(1-10), 2.9.4(1-3), 2.9.5(1, 2), 2.9.6(1-4), 2.9.7(1, 2), and 2.9.8(1-3) are from D. K. Edwards, ***Radiation Heat Transfer Notes,*** Hemisphere, Washington, D.C., 1981.

B. Thermodynamic surfaces and surface systems

The thermal designer needs to know surface heat fluxes adjacent to the interface between phases. When one phase is highly opaque and the other is not, the opaque surface system concept is used. Figure 1 depicts a surface system. The s surface lies just outside the highly opaque phase; the u surface lies just within it. The m

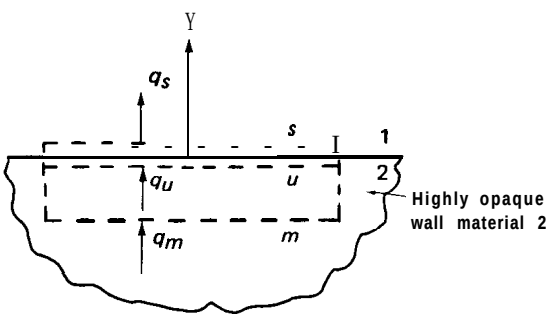

Figure 1 The s, u, and m thermodynamic boundaries for a surface system.

© 1983 Hemisphere Publishing Corporation

surface lies sufficiently below the phase interface so that (1) no radiation crossing the s and u surfaces is transmitted to the m surface. and (2) the radiation flux crossing the m surface is given by the radiation-diffusion equation and is included with the conduction. For no flow through the surfaces and negligible transient heat storage in the mass between the m and u surfaces, one has

$$4s = q_u = q_m = -k_2 \frac{dT_2}{dy}_{m} \tag{1}$$

where q denotes heat flux (W/m^2). In the more transparent medium,

$$q_s = -k_1 \frac{dT_1}{dy}_{s} + q_r \tag{2}$$

where q_r is the net radiant flux across the s surface in medium 1. Note that there is no need to define a radiation heat flux in the opaque medium 2.

C. Radiant intensity and flux

The radiant intensity describes the directional distribution of the radiant flux at an s surface. The radiant flux itself may be separated into two parts, an outgoing flux q^+ away from medium 2 and an incoming flux q^- toward medium 2. Other symbols used for the radiosity q^+ are J and B, and for the irradiation q^-, G, or H. The net flux is

$$q_r = q = q^+ - q^- \tag{3}$$

The outward flux per unit solid angle is the intensity I^+. Solid angle is defined by area dA_s on a sphere of radius R,

$$d^2\Omega \equiv \frac{dA_s}{R^2} \tag{4}$$

In polar-azimuthal coordinates, illustrated in Fig. 2, dA_s is $R\,d\theta\,R\sin\theta\,d\phi$, so that

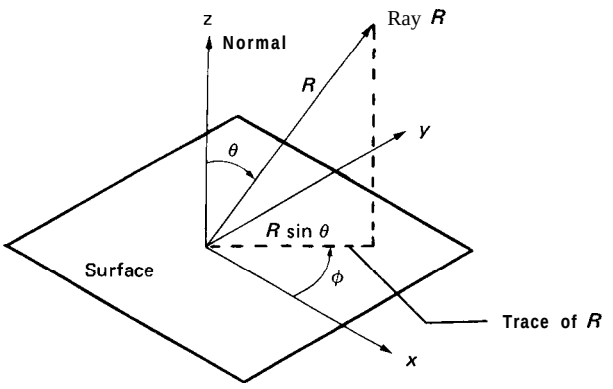

Figure 2 Polar angle θ and azimuthal angle ϕ.

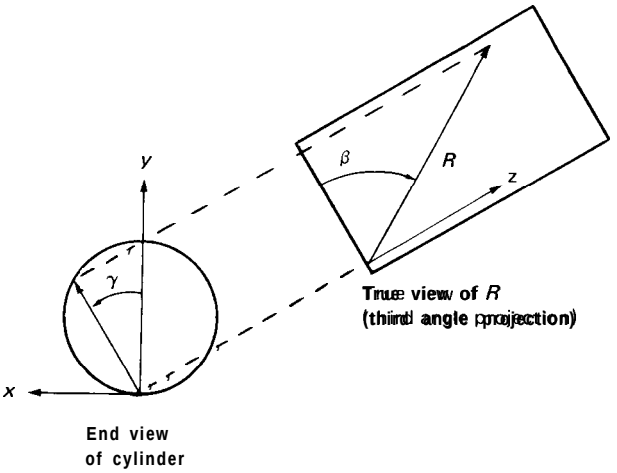

Figure 3 Base angle γ and axial angle β.

$$d^2\Omega = \sin\theta\,d\theta\,d\phi \tag{5}$$

The unitless solid angle is attributed units of steradians, just as a plane angle is said to be measured in radians. The flux per unit solid angle I^+ is power per unit area per unit solid angle, W/m^2 sr, but the normal of the area is understood to be in the direction of I^+. The contribution of $I^+ d^2\Omega$ to the flux across the s surface is

$$d^2q^+ = I^+ \cos\theta\, d^2\Omega \tag{6}$$

Similarly,

$$d^2q^- = I^- \cos\theta\, d^2\Omega \tag{7}$$

Combining Eqs. (5) and (6),

$$q^+ = \int_0^{2\pi}\int_0^{\pi/2} I^+(\theta,\phi)\cos\theta\sin\theta\,d\theta\,d\phi \tag{8}$$

Similarly,

$$q^- = \int_0^{2\pi}\int_0^{\pi/2} I^-(\theta,\phi)\cos\theta\sin\theta\,d\theta\,d\phi \tag{9}$$

When $I^+(\theta,\phi)$ is independent of direction, the radiation is said to be diffuse. For diffuse radiation,

$$q^+ = \pi I^+ \qquad I^+ \neq f(\theta,\phi) \tag{10}$$

$$q^- = \pi I^- \qquad I^- \neq f(\theta,\phi) \tag{11}$$

For heat exchangers where long cylindrical tubes are often employed, Fig. 3 shows base-axial angular coordinates. In these coordinates $dA_s = R\,d\beta\,R\cos\beta\,d\gamma$ and

$$d^2\Omega = \cos\beta\,d\beta\,d\gamma \tag{12}$$

$$\cos e = \cos\beta\cos\gamma \tag{13}$$

$$d^2q^{\pm} = I^{\pm}\cos^2\beta\,d\beta\cos\gamma\,dy \tag{14}$$

© 1983 Hemisphere Publishing Corporation

$$q = \int_{\gamma=-\pi/2}^{+\pi/2} \int_{\beta=-\pi/2}^{+\pi/2} I^{\pm}(\beta,\gamma) \cos^2\beta \, d\beta \cos \gamma \, dy \tag{15}$$

For example, what is the irradiation on the closest element of wall parallel to an infinitely long, 2.5-cm-diameter rod 10 cm away? The rod radiates diffusely 1 850 W/m. If the intensity of the surrounds is negligible compared to that of the rod, Eq. (15) gives

$$q^- = I^- \int_{-\gamma_1}^{+\gamma_1} \int_{-\pi/2}^{+\pi/2} \cos^2\beta \, d\beta \cos\gamma \, d\gamma$$

$$= I^- (2 \sin\gamma_1)\frac{\pi}{2}$$

$$I^-_{\text{wall}} = I^+_{\text{rod}} = \frac{q^+_{\text{rod}}}{\pi} = \frac{\dot{Q}}{\pi DL}\frac{1}{\pi} \quad 2 \quad \sin\gamma_1 = \frac{2.5}{10}$$

$$q^- = \frac{1850}{\pi(0.025)(1)}\frac{1}{\pi}\frac{2.5}{10}\frac{\pi}{2} = 2\,944 \text{ W/m}^2$$

D. Blackbody radiation

A cavity surrounded by an isothermal wall of temperature T is filed with radiation in thermodynamic equilibrium with the wall. Such a cavity is called a *hohlraum.* If one makes a small hole through the cavity wall, the equilibrium is disturbed only slightly. The radiation observed escaping from the hohlraum is blackbody radiation. The word black is used because the hohlraum absorbs all radiation entering the hole in the wall and reflects none, so it appears black when it is cold. The intensity of radiation I_b^+ leaving the hohlraum is isotropic; blackbody radiation is diffuse. Stefan s law relates the blackbody intensity and radiosity to the fourth power of the temperature,

$$q_b^+ = \pi I_b^+ = C_s T^4 \tag{16}$$

where the Stefan-Boltzmann constant C_s is

$$C_s = 5.669\ 7 \times 10^{-8} \text{ W/m}^2\text{K}^4$$

The radiation packets emitted by the random thermal agitations of electrically charged particles in the hohlraum walls travel at the speed of light c as a collapsing electric field builds up a magnetic field that in turn collapses to build up an electric field further along the path of propagation. The energy E, frequency ν_f, wave number ν, and wavelength λ are interrelated through the Einstein photoelectric law,

$$E = h\nu_f = hc\nu = \frac{hc}{\lambda} \tag{17}$$

where h is Planck s constant and c is the velocity of light,

$$h = 6.625\ 6 \times 10^{-34} \text{ J s} \qquad c = 2.997\ 925 \times 10^8 \text{ m/s}$$

The relations among wave number ν, frequency ν_f, and wavelength λ are

$$\nu = \frac{\nu_f}{c} = \frac{1}{\lambda} \tag{18}$$

In dimensional terms,

$$\nu\,(\text{cm}^{-1}) = \frac{10^4}{\lambda\,(\mu\text{m})} \qquad \lambda\,(\mu\text{m}) = \frac{10^4}{\nu\,(\text{cm-}\ )}$$

$$1\ (\mu\text{m}) = 10^{-6}\ (\text{m}) = 1\ 0^4\ (\text{A})\ [25.4\ (\mu\text{m}) = 10^{-3}\ (\text{in})]$$

Very-high-energy photons may be described in terms of their energy in electron volts,

$$E\,(\text{eV}) = \frac{1.240}{\lambda\,(\mu\text{m})}$$

Spectral intensity and spectral flux are, respectively, intensity and flux per unit band width of the spectrum:

$$I_{b\nu} = \frac{dI_b}{d\nu} \qquad I_{b\lambda} = \frac{dI_b}{d\lambda} \tag{19}$$

$$q^+_{b\nu} = \frac{dq^+_b}{d\nu} \qquad q^+_{b\lambda} = \frac{dq^+_b}{d\lambda} \tag{20}$$

$$q^+_{b\nu}\,d\nu = q^+_{b\lambda}\,d\lambda \qquad d\lambda = \frac{1}{\nu^2}\,d\nu$$

$$q^+_{b\lambda} = \nu^2 q^+_{b\nu} \qquad q^+_{b\lambda} = \frac{1}{\lambda^2} q^+_{b\nu} \tag{21}$$

$$d^3 q^{\pm} = I^{\pm}_{\nu} \cos\theta \, d^2\Omega \, d\nu \tag{22}$$

$$q^{\pm} = \int_0^{\infty} q^{\pm}_{\nu}\,d\nu = \int_0^{\infty} q^{\pm}_{\lambda}\,d\lambda \tag{23}$$

$$I^{\pm} = \int_0^{\infty} I^{\pm}_{\nu}\,d\nu = \int_0^{\infty} I^{\pm}_{\lambda}\,d\lambda \tag{24}$$

Planck s law gives the spectral distribution of blackbody radiation as

$$I_{b\nu} = \frac{2hc^2\nu^3}{e^{hc\nu/kT} - 1} \qquad I_{b\lambda} = \frac{2hc^2\lambda^{-5}}{e^{hc/\lambda kT} - 1} \tag{25}$$

$$q^+_{b\nu} = \frac{2\pi hc^2\nu^3}{e^{hc\nu/kT} - 1} \qquad q^+_{b\lambda} = \frac{2\pi hc^2\lambda^{-5}}{e^{hc/\lambda kT} - 1} \tag{26}$$

where k is Boltzmann s constant, the gas constant divided by Avogadro s number,

$$k = 1.380\ 54 \times 10^{-23} \text{ J/K}$$

The first and second radiation constants are

$$c_1 = 2\pi hc^2 = 3.741\ 5 \times 10^{-16} \text{ J m}^2/\text{s}$$

© 1983 Hemisphere P blishing Corporation

$$c_2 = \frac{hc}{k} = 1.438\,8 \times 10^{-2}\ \text{m K}$$

$$= 1.438\,8\ \text{cm K} = 14\,388\ \mu\text{m K}$$

The Stefan-Boltzmann constant is given by

$$q_b^+ = \int_0^\infty \frac{2\pi hc^2 \nu^3}{e^{hc\nu/kT} - 1} d\nu = C_s T^4$$

$$C_s = \frac{2\pi k^4}{h^3 c^2} \int_0^\infty \frac{\zeta^3\, d\zeta}{e^\zeta - 1} = \frac{2\pi^5 k^4}{15 h^3 c^2} \tag{27}$$

Two convenient limits are the Rayleigh-Jeans limit (large T/ν),

$$e^{hc\nu/kT} - 1 \doteq \frac{hc\nu hc}{k\ T\ \lambda kT} \tag{28}$$

and the Wien limit (small T/ν),

$$e^{hc\nu/kT} - 1 \doteq e^{hc\nu/kT} \tag{29}$$

In the Rayleigh-Jeans limit, $q_{b\lambda}^+$ goes as T. In the Wien limit, $q_{b\lambda}^+$ goes as $e^{-c_2/\lambda T}$, like an Arrhenius chemical reaction rate. As the temperature increases, more blackbody radiation is radiated at every wavelength or wave number, but ***relatively,*** more in the short wavelengths and less in the long wavelengths.

E. Fractional functions

The fraction of the total blackbody radiosity between wavelengths 0 and λ is called the fractional function of the first kind or the external fraction f_e:

$$f_e(\lambda, T) = \frac{1}{C_s T^4} \int_0^\lambda q_b^+(\lambda, T)\, d\lambda$$

$$f_e(\lambda T) = \frac{15}{\pi^4} \int_\zeta^\infty \frac{\zeta^3\, d\zeta}{e^\zeta - 1} \qquad \zeta = \frac{c_2}{\lambda T} \tag{30}$$

Wien s displacement law is that $\partial q_b^+(\lambda, T)/\partial\lambda = 0$ occurs at a fixed value of λT,

$$\frac{\partial q_b^+}{\text{a x}} = 0 \quad \text{at} \quad \lambda T = \frac{c_2}{4.965} = 2\,898\ \mu\text{m K}$$

This value of XT corresponds to a value $_{\text{off,}} = 0.25$. But the value has no special sanctity, for on a wave-number basis,

$$\frac{\partial q_b^+}{\partial \nu} = 0 \quad \text{a t} \quad \lambda T = \frac{c_2}{2.821} = 5\,100\ \mu\text{m K}$$

A fractional function of the second kind or the internal fraction f_i is defined by

Table 1 Values of λT at specified values of the external and internal fractions of blackbody radiation

f	Δf	$\Sigma\,\Delta f$	$(\lambda T)_e$, cm K	$(\lambda T)_i$, cm K
0.002 5	0.005	0.005	0.123 0	0.107 3
0.007 5	0.005	0.010	0.139 5	0.120 9
0.012 5	0.005	0.015	0.145 5	0.129 1
0.017 5	0.005	0.02	0.157 3	0.135 2
0.025	0.01	0.03	0.166 2	0.142 3
0.035	0.01	0.04	0.176 2	0.150 1
0.045	0.01	0.05	0.184 8	0.156 5
0.055	0.01	0.06	0.192 2	0.162 5
0.07	0.02	0.08	0.202	0.170 1
0.09	0.02	0.10	0.214	0.179 1
0.11	0.02	0.12	0.225	0.187 4
0.13	0.02	0.14	0.235	0.194 9
0.15	0.02	0.16	0.245	0.202
0.17	0.02	0.18	0.254	0.209
0.19	0.02	0.20	0.263	0.216
0.21	0.02	0.22	0.272	0.222
0.23	0.02	0.24	0.281	0.229
0.25	0.02	0.26	0.290	0.235
0.27	0.02	0.28	0.299	0.242
0.29	0.02	0.30	0.308	0.248
0.31	0.02	0.32	0.317	0.255
0.33	0.02	0.34	0.326	0.261
0.35	0.02	0.36	0.335	0.268
0.37	0.02	0.38	0.344	0.275
0.39	0.02	0.40	0.353	0.281
0.41	0.02	0.42	0.363	0.288
0.43	0.02	0.44	0.373	0.295
0.45	0.02	0.46	0.384	0.303
0.47	0.02	0.48	0.394	0.310
0.49	0.02	0.50	0.405	0.318
0.51	0.02	0.52	0.416	0.326
0.53	0.02	0.54	0.428	0.334
0.55	0.02	0.56	0.440	0.342
0.57	0.02	0.58	0.453	0.351
0.59	0.02	0.60	0.467	0.361
0.61	0.02	0.62	0.482	0.371
0.63	0.02	0.64	0.497	0.382
0.65	0.02	0.66	0.513	0.393
0.67	0.02	0.68	0.531	0.405
0.69	0.02	0.70	0.550	0.417
0.71	0.02	0.72	0.570	0.430
0.73	0.02	0.74	0.593	0.446
0.75	0.02	0.76	0.616	0.462
0.77	0.02	0.78	0.642	0.479
0.79	0.02	0.80	0.671	0.498
0.81	0.02	0.82	0.704	0.521
0.83	0.02	0.84	0.741	0.546
0.85	0.02	0.86	0.783	0.574
0.87	0.02	0.88	0.825	0.609
0.89	0.02	0.90	0.899	0.653
0.91	0.02	0.92	0.982	0.690
0.93	0.02	0.94	1.090	0.774
0.945	0.01	0.95	1.200	0.846
0.955	0.01	0.96	1.298	0.909
0.965	0.01	0.97	1.433	0.997
0.975	0.01	0.98	1.63	1.123
0.982 5	0.005	0.985	1.87	1.28
0.987 5	0.005	0.990	2.22	1.43
0.992 5	0.005	0.995	2.56	1.70
0.997 5	0.005	1.000	7.34	2.49

© 1983 Hemisphere Publishing Corporation

$$f_i(\lambda T) \equiv \frac{1}{4C_s T^3} \int_0^{\lambda} \frac{\partial q_b^+(\lambda, T)}{\partial T}\, d\lambda \qquad (31)$$

Table 1 gives XT values for various values of f_e or f_i. Also shown are Af values for numerical integration based on the trapezoidal rule. Table 2 gives λ values for a few nonblackbody-radiation sources.

For example, consider material being dried by a nearly black electric heater element 10 cm away that is 2.5 cm in diameter and radiates 1 850 W/m. The material absorbs 95% of the irradiation with wavelengths longer than 2.7 μm, but only 30% of that with shorter wavelengths. What is the absorbed flux? Recall that in the previous example with the same geometry we found $q^- = 2\,944\ \mathrm{W/m^2}$. From Stefan s law,

$$C_s T^4 = q_b^+ = \frac{Q}{\pi DL}$$

$$T = \left[\frac{1\,850}{\pi(0.025)(1)(5.669\ 7 \times 10^{-8})}\right]^{1/4} = 803\ \mathrm{K}$$

Accordingly, $\lambda T = (2.7\ \mu\mathrm{m})(803\ \mathrm{K}) = 2\,168\ \mu\mathrm{m\ K}$ and $f_e \doteq 0.095$. Thus the absorbed flux αq^- is

$$\alpha q^- = [(0.095)(0.30) + (0.905)(0.95)]\ 2\,944$$
$$= 2615\ \mathrm{W/m^2}$$

Table 2 Values of wavelength at specified values of the external fraction

			Wavelength λ, pm			
f	Δf	$\Sigma \Delta f$	Extraterrestrial sun	Terrestrial sun	2 900 K tungsten (flat)	2 900 K tungsten (coiled, $P/D = 2$)
0.01	0.02	0.02	0.29	0.35	0.44	0.45
0.03	0.02	0.04	0.33	0.39	0.54	0.55
0.05	0.02	0.06	0.36	0.41	0.58	0.59
0.08	0.04	0.10	0.39	0.44	0.65	0.66
0.15	0.10	0.20	0.45	0.48	0.75	0.76
0.25	0.10	0.30	0.52	0.55	0.88	0.90
0.35	0.10	0.40	0.59	0.62	1.01	1.03
0.45	0.10	0.50	0.68	0.68	1.15	1.17
0.55	0.10	0.60	0.79	0.76	1.30	1.32
0.65	0.10	0.70	0.93	0.84	1.48	1.51
0.75	0.10	0.80	1.11	1.04	1.73	1.78
0.85	0.10	0.90	1.43	1.27	2.15	2.21
0.92	0.04	0.94	1.87	1.64	2.71	2.80
0.95	0.02	0.96	2.23	1.84	3.19	3.30
0.97	0.02	0.98	2.70	2.15	3.73	3.89
0.99	0.02	1.00	3.93	3.10	5.34	5.50

Nomenclature for Section 2.9.1 appears at the end of Section 2.9.8.

BIBLIOGRAPHY FOR SECTION 2.9.1

1. Czerny, M., and Walther, A., ***Tables of Fractional Functions for the Planck Distribution Law,*** Springer-Verlag, Berlin, 1961.
2. Dunkle, R. V., Thermal Radiation Tables and Applications, ***Trans. ASME***, vol. 76, pp. 549-552, 1954.
3. Edwards, D. K., Radiative Transfer Characteristics of Materials, ***J. Heat Transfer,*** vol. 91, pp. l-15, 1969.
4. Knuth, E. L., ***Introduction to Statistical Thermodynamics,*** McGraw-Hill, New York, 1966 (see app. I, Emissions from Surfaces).
5. Planck, M., ***The Theory of Heat Radiation,*** Dover, New York, 1959.
6. Snyder, N. W., A Review of Thermal-Radiation Constants, ***Trans. ASME***, vol. 76, pp. 537-539, 1954.
7. Worthing, A. ***G., Temperature, Its Measurement and Control in Science and Industry,*** pp. 1164-1187, Reinhold, New York, 1941.

© 1983 Hemisphere Publishing Corporation

2.9.2
Surface radiation characteristics

D. K. Edwards

A. Introduction to surface characteristics

To the thermal designer, surface radiation characteristics are numbers that must be entered into a computer in order to get answers to the questions put to the computer about the size, orientation, or spacing of elements; material selection; and so forth. The designer hopes that values of these characteristics can be found in a handbook or data compilation. At times, however, the handbook leaves the designer unsatisfied. It lists no value for a given material or such a large range of values that the designer realizes that a test measurement is in order. Thereupon it becomes apparent that many different kinds of tests can be conducted; many different numbers can be obtained. Which test or set of tests is to be run? How is a single number to be extracted from the test results? What do the numbers that are listed in the handbook mean? Are they really applicable?

It is apparent that two categories of radiation characteristics must be distinguished: (1) model characteristics used to model surface behavior in a computer program or calculation scheme, and (2) real characteristics that describe how the surface really does behave. This section begins with a review of real characteristics and their measurements, reviews the electromagnetic theory of reflection, and concludes by examining the use of surface characteristics in thermal design.

The nomenclature used for surface radiation characteristics varies considerably in the literature. One question that often occurs is the meaning of an ivity ending versus an "ance" ending. Worthing, of the U.S. National Bureau of Standards, at one time suggested using ivity for an intrinsic property of a pure, perfectly polished and annealed specimen, and "ance" for surfaces having roughness, surface oxide layers, or other nonideal features. Various workers have followed the suggestion at one time or another, and others have not. The ivity ending used here has no special meaning and may be regarded as interchangeable with the "ance" ending.

B. Absorption and emission characteristics

Briefly put, the absorptivity of a surface system is a property value between zero and unity that defines what fraction of the irradiation is absorbed. The emissivity is a similar property value between zero and unity that defines what fraction of the blackbody radiosity is actually emitted by a surface system. What are these property values functions of? They clearly depend on the type of surface system, the material it is made of, and its structure as determined by heat treatment, cold work, oxide film thickness, roughness, and so forth. If the structure is in a stable configuration (by no means always the case), one regards the properties as functions of its thermodynamic state, fixed by its temperature T_s. Moreover, the properties depend on the nature of the thermal radiation in question, specifically its direction and wavelength, and at times its state of polarization is a concern.

Accordingly, one distinguishes between directional and directionally averaged values, and spectral and spectrally averaged values. The word hemispherical is reserved for values directionally averaged over the entire 2π steradian hemisphere of solid angle above a surface, and the word total is reserved for values spectrally

© 1983 Hemisphere I blishing Corporation

averaged over the total spectrum, that is, encompassing all wavelengths or wave numbers from zero to infinity. This distinction is by no means universal; one encounters the term total being used in the sense of a totality of directions (i.e., in place of hemispherical) as well as in the sense of a totality of wavelengths.

Let $\alpha(\theta,\phi,\lambda,T_s)$ denote the spectral (λ), directional (θ,ϕ) absorptivity of a surface system at temperature T_s for unpolarized irradiation. Let $\epsilon(\theta,\phi,\lambda, T_s)$ denote the spectral directional emissivity. Then the net flux leaving surface s is

$$q = \int_0^\infty \int_0^{2\pi} \int_0^{\pi/2} [\epsilon(\theta,\phi,\lambda,T_s) I_{b\lambda}(\lambda,T_s) - \alpha(\theta,\phi,\lambda,T_s) I_\lambda^-(\theta,\phi,\lambda)] \cos\theta \sin\theta \, de \, d\phi \, d\lambda \tag{1}$$

Wave number ν and wavelength λ are interchangeable in this and the subsequent relations.

The ***principle of detailed balancing*** requires that at thermodynamic equilibrium there be no net energy transfer between two surfaces at the same temperature, not just in aggregate, but in detail for each direction and wave number. When the surroundings are a hohlraum at temperature T_s, then I_λ^- is $I_{b\lambda}(\lambda,T_s)$ ***in*** Eq. (1), and the principle of detailed balancing requires

$$\epsilon(\theta,\phi,\lambda,T_s) = \alpha(\theta,\phi,\lambda,T_s) \tag{2}$$

This relation is called *Kirchhoff's law.*

Even when the environment, say, a hohlraum at temperature T_e not equal to T_s, is not in equilibrium with the surface, our assumption that the surface system remains in a thermodynamic equilibrium microstate characterized by temperature T_s is sufficient to keep Eq. (2) in force. One may be able to imagine or even contrive to have a nonequilibrium surface state. In such a case Kirchhoff s law would be inoperative.

Let the environment be a hohlraum at temperature T_e. Then $I_\lambda^-(\theta,\phi,\lambda)$ is $I_{b\lambda}(\lambda,T_e)$, and Eq. (1) becomes, with Kirchhoff s law,

$$q = \int_0^\infty \int_0^{2\pi} \int_0^{\pi/2} [\alpha(\theta,\phi,\lambda,T_s) I_{b\lambda}(\lambda,T_s) - \alpha(\theta,\phi,\lambda,T_s) I_{b\lambda}(\lambda,T_e)] \cos\theta \sin\theta \, d\theta \, d\phi \, d\lambda = \epsilon_{TH}(T_s) C_s T_s^4 - \alpha_{TH}(T_s,T_e) C_s T_e^4 \tag{3}$$

This expression defines the total hemispherical emissivity and total hemispherical absorptivity, respectively. These properties are spectrally and directionally averaged. One can, of course, separate the two averaging steps into a hemispherical averaging one denoted by subscript ***H,***

$$\alpha_H(\lambda,T_s) = \frac{1}{\pi} \int_0^{2\pi} \int_0^{n/2} X \, \alpha(\theta,\phi,\lambda,T_s) \cos\theta \sin\theta \, d\theta \, d\phi \tag{4}$$

and a total spectral averaging denoted by subscript ***T,***

$$\epsilon_{TH}(T_s) = \frac{1}{C_s T_s^4} \int_0^\infty \alpha_H(\lambda,T_s) \pi I_{b\lambda}(\lambda,T_s) \, d\lambda \tag{5}$$

$$\alpha_{TH}(T_s,T_e) = \frac{1}{C_s T_e^4} \int_0^\infty \alpha_H(\lambda,T_s) \pi I_{b\lambda}(\lambda,T_e) \, d\lambda \tag{6}$$

Equation 2.9.1(30) shows that

$$\frac{\pi I_{b\lambda}(\lambda,T_s) \, d\lambda}{C_s T_s^4} = df_e(\lambda T_s)$$

Accordingly, Eqs. (5) and (6) can be written as

$$\epsilon_{TH}(T_s) = \int_0^1 \alpha_H(\lambda,T_s) \, df_e(\lambda T_s) \tag{7}$$

$$\alpha_{TH}(T_s,T_e) = \int_0^1 \alpha_H(\lambda,T_s) \, df_e(\lambda T_e) \tag{8}$$

Some have made the observation that as T_e approaches T_s, $\alpha_{TH}(T_s,T_e)$ approaches $\epsilon_{TH}(T_s)$. But this observation is without meaning. When T_e approaches T_s, Eq. (3) may be written as

$$q = \int_0^\infty \alpha_H(\lambda,T_s) [\pi I_{b\lambda}(\lambda,T_s) - \pi I_{b\lambda}(\lambda,T_e)] \, d\lambda = \int_0^\infty \alpha_H(\lambda,T_s) \left[\frac{\partial q_b^+(\lambda,T_s)}{\partial T_s}\right] (T_s - T_e) \, d\lambda = \epsilon_{T_i H}(T_s) 4 C_s T_s^3 (T_s - T_e)$$

where the internal total (hemispherical) emissivity is

$$\epsilon_{T_i H}(T_s) \equiv \frac{1}{4 C_s T_s^3} \int_0^\infty \alpha_H(\lambda,T_s) \left[\frac{\partial q_b^+(\lambda,T_s)}{\partial T_s}\right] d\lambda \tag{9}$$

Comparison with Eq. 2.9.1(3 1) shows that

$$\epsilon_{T_i H} = \int_0^1 \alpha_H(\lambda,T_s) \, df_i(\lambda T_s) \tag{10}$$

Now the observation can be made that internal total

© 1983 Hemisphere Publishing corporation

emissivity $\epsilon_{T_iH}(T_s)$ and internal total absorptivity $\alpha_{T_iH}(T_s)$ are indistinguishable.

Note that Kirchhoffs law as referred to here is understood to be the meaningful Eq. (2) and not the vacuous statement that $\epsilon_{TH}(T_s) = \alpha_{TH}(T_s, T_e = T_s)$.

As a concrete example of the use of Eqs. (7), (8), and (10), assume that a graph of $\alpha_H(\lambda)$ is available for a given material and a value of T_s. For example, stainless steel at 300 K has a graph of $\alpha_H(\lambda)$ that can be approximated by $\alpha_H(\lambda) \doteq 0.44\lambda^{-1/2}$ for the range $1\ \mu m < \lambda < 100\ \mu m$. Suppose that we want the external hemispherical emissivity at 300 K, the internal total hemispherical emissivity at 300 K, and the total hemispherical absorptivity for a 1 000 K blackbody source. Table 1 is constructed from Table 2.9.1(1) and the given $\alpha_H(\lambda)$ data. The results are $\epsilon_{TH} = 0.120$, $\epsilon_{T_iH} = 0.135$, and $\alpha_{TH} = 0.219$.

C. Measurement of absorption and emission characteristics

As can be seen from the foregoing, one can measure spectral or total and/or directional or hemispherical absorptivity or emissivity, and the total quantities can be internal total or external total values.

When one desires spectral values at high values of T_s, one usually measures spectral directional emissivity by placing a heated specimen in a low-temperature hohlraum and comparing the intensity I_λ^+ of the specimen with $I_{b\lambda}$ from a reference cavity emitter at close to the same temperature T_s. When one desires spectral values at moderate or low values of T_s, one usually makes a determination of spectral directional reflectivity $\rho(\theta, \phi, \lambda, T_s)$ (as discussed in Sec. D) and by subtraction obtains (for an opaque specimen)

$$\epsilon(\theta, \phi, \lambda, T) = \alpha(\theta, \phi, \lambda, T) = 1 - \rho(\theta, \phi, \lambda, T) \tag{11}$$

For a transparent specimen, reflectivity and transmissivity can be determined and absorptivity found by subtraction from unity.

For spectral measurements a filter, prism, grating spectrometer, or interferometer is used. The instrument usually views the specimen within a narrow solid angle about θ and ϕ to yield directional quantities, but it is possible to use a hemispherical or masked cylindrical specimen to obtain a hemispherical measurement directly.

For total emissivity measurements one can use a total radiometer having a detector that responds to the total radiant heating effect upon it. One can view a flat or hemispherical specimen, or one can make a calorimetric determination by heating a specimen suspended within a low-temperature evacuated hohlraum. Calorimetric measurements of absorptivity can be similarly made by irradiating such a specimen with high-temperature blackbody radiation.

One should note that a laboratory emissivity determination corresponds exactly to neither the (external) total emissivity defined by Eq. (5) or (7) nor to the internal total emissivity defined by Eq. (9) or (10) when the temperature of the specimen environment T_e is neither far removed from nor very close to the specimen temperature T_s. The laboratory observation is usually one of

$$\alpha_{OH}(T_s, T_e) = \frac{\int_0^\infty \alpha_H(\lambda, T_s)[\pi I_{b\lambda}(\lambda, T_s) - \pi I_{b\lambda}(\lambda, T_e)]\, d\lambda}{C_s T_s^4 - C_s T_e^4} \tag{12}$$

Only when T_e is very small compared to T_s does Eq. (12) approximate Eq. (5); only when T_e is close to T_s does it approximate Eq. (9). For this reason, and for other reasons to be made clear in subsequent sections, spectral data are desirable in addition to (or even instead of) total observations.

D. Reflection and transmission characteristics

One often wants to know what fraction of the irradiation q^- becomes a contribution to the radiosity q^+ on one side or the other of a wall. That fraction pertaining to the irradiated side is termed the ***reflectivity,*** and that pertaining to the other side is the ***transmissivity.*** Clearly these fractions will be properties of the wall material and structure and its thermodynamic state and also the spectral and directional distribution of the irradiation. The terms spectral and total apply to the reflectivity and transmissivity in the same sense as to the absorptivity. The terms directional and hemispherical also apply as before. Accordingly, the spectral directional reflectivity is defined as the reflected portion of the surface radiosity q_R^+ as a fraction of the spectral irradiation $I^- \cos^- \Delta\Omega^-$,

$$\rho_\lambda(\theta^-, \phi^-, \lambda, T_s) = \frac{q_{R\lambda}^+}{I_\lambda^-(\theta^-, \phi^-, \lambda) \cos\theta^- \Delta\Omega^-} \tag{13}$$

Spectral directional transmissivity $\tau(\theta^-, \phi^-, \lambda, T_s)$ is similarly defined, with an additional caveat that the entire wall be near a state of thermodynamic equilibrium characterized by temperature T_s. The idea of an ***m*** surface as shown in Fig. 2.9.1(1) must be abandoned for a transmitting wall. No provision has been made in these definitions for phosphorescence or fluorescence.

Note that these directional characteristics carry no information about the directional distribution of the

© 1983 Hemisphere Publishing Corporation

Table 1 Sample calculation of total emissivity and absorptivity

Fractional function increment	External total emissivity at 300 K				Internal total emissivity at 300 K				Total absorptivity for 1 000 K source			
	λT_s, cm K	λ, μm	α_H	$\alpha_H \Delta f_e$	λT_s, cm K	λ, μm	α_H	$\alpha_H \Delta f_i$	λT_e, cm K	λ, μm	α_H	$\alpha_H \Delta f_e$
0.005	0.123 0	4.10	0.217	0.001 1	0.107 3	3.58	0.233	0.001 2	0.123 0	1.23	***0.397***	0.002 0
0.005	0.139 5	4.65	0.204	0.001 0	0.120 9	4.03	0.219	0.001 1	0.139 5	1.40	0.373	0.001 9
0.005	0.149 5	4.98	0.197	0.001 0	0.129 1	4.30	0.212	0.001 1	0.149 5	1.50	0.360	0.001 8
0.005	0.157 3	5.24	0.192	0.001 0	0.135 2	4.5 1	0.207	0.001 0	0.157 3	1.57	0.35 1	0.001 8
0.01	0.166 2	5.54	0.187	0.001 9	0.142 3	4.74	0.202	0.002 0	0.166 2	1.66	0.341	0.003 4
0.01	0.176 2	5.87	0.182	0.001 8	0.150 1	5.00	0.197	0.002 0	0.176 2	1.76	0.332	0.003 3
0.01	0.184 8	6.16	0.177	0.001 8	0.156 5	5.22	0.193	0.001 9	0.184 8	1.85	0.323	0.003 2
0.01	0.192 2	6.41	0.174	0.001 7	0.162 5	5.42	0.189	0.001 9	0.192 2	1.92	0.317	0.003 2
0.02	0.202	6.73	0.170	0.003 4	0.170 1	5.67	0.185	0.003 7	0.202	2.02	0.310	0.006 2
0.02	0.214	7.13	0.165	0.003 3	0.179 1	5.97	0.180	0.003 6	0.214	2.14	0.301	0.006 0
0.02	0.225	7.50	0.161	0.003 2	0.187 4	6.25	0.176	0.003 5	0.225	2.25	0.293	0.005 9
0.02	0.235	7.83	0.157	0.003 1	0.194 9	6.50	0.173	0.003 5	0.235	2.35	0.287	0.005 7
0.02	0.245	8.17	0.154	0.003 1	0.202	6.73	0.170	0.003 4	0.245	2.45	0.281	0.005 6
0.02	0.254	8.47	0.151	0.003 0	0.209	6.97	0.167	0.003 3	0.254	2.54	0.276	0.005 5
0.02	0.263	8.77	0.149	0.003 0	0.216	7.20	0.164	0.003 3	0.263	2.63	0.271	0.005 4
0.02	0.272	9.07	0.146	0.002 9	0.222	7.40	0.162	0.003 2	0.272	2.72	0.267	0.005 3
0.02	0.28 1	9.37	0.144	0.002 9	0.229	7.63	0.159	0.003 2	0.281	2.81	0.262	0.005 2
0.02	0.290	9.67	0.142	0.002 8	0.235	7.83	0.157	0.003 1	0.290	2.90	0.258	0.005 2
0.02	0.299	9.97	0.139	0.002 8	0.242	8.07	0.155	0.003 1	0.299	2.99	0.255	0.005 1
0.02	0.308	10.3	0.137	0.002 7	0.248	8.27	0.153	0.003 1	0.308	3.08	0.25 1	0.005 0
0.02	0.317	10.6	0.135	0.002 7	0.255	8.50	0.151	0.003 0	0.317	3.17	0.247	0.004 9
0.02	0.326	10.9	0.134	0.002 7	0.261	8.70	0.149	0.003 0	0.326	3.26	0.244	0.004 9
0.02	0.335	11.2	0.132	0.002 6	0.268	8.93	0.147	0.002 9	0.335	3.35	0.240	0.004 8
0.02	0.344	11.5	0.130	0.002 6	0.275	9.17	0.145	0.002 9	0.344	3.44	0.237	0.004 7
0.02	0.353	11.8	0.128	0.002 6	0.281	9.37	0.144	0.002 9	0.353	3.53	0.234	0.004 7
0.02	0.363	12.1	0.127	0.002 5	0.288	9.60	0.142	0.002 8	0.363	3.63	0.231	0.004 6
0.02	0.373	12.4	0.125	0.002 5	0.295	9.83	0.140	0.002 8	0.373	3.73	0.228	0.004 6
0.02	0.384	12.8	0.123	0.002 5	0.303	10.1	0.138	0.002 8	0.384	3.84	0.225	0.004 5
0.02	0.394	13.1	0.121	0.002 4	0.310	10.3	0.137	0.002 7	0.394	3.94	0.222	0.004 4

© 1983 Hemisphere Publishing Corporation

0.02	0.405	13.5	0.120	0.002 4	0.318	10.6	0.135	0.002 7	0.405	4.05	0.219	0.004 4
0.02	0.416	13.9	0.118	0.002 4	0.326	10.9	0.134	0.002 7	0.416	4.16	0.216	0.004 3
0.02	0.428	14.3	0.117	0.002 3	0.334	11.1	0.132	0.002 6	0.428	4.28	0.213	0.004 3
0.02	0.440	14.7	0.115	0.002 3	0.342	11.4	0.130	0.002 6	0.440	4.40	0.210	0.004 2
0.02	0.453	15.1	0.113	0.002 3	0.351	11.7	0.129	0.002 6	0.453	4.53	0.207	0.004 1
0.02	0.467	15.7	0.112	0.002 2	0.361	12.0	0.127	0.002 5	0.467	4.67	0.204	0.004 1
0.02	0.482	16.1	0.110	0.002 2	0.371	12.4	0.125	0.002 5	0.482	4.82	0.200	0.004 0
0.02	0.497	16.6	0.108	0.002 2	0.382	12.7	0.123	0.002 5	0.497	4.97	0.197	0.003 9
0.02	0.513	17.1	0.106	0.002 1	0.393	13.1	0.122	0.002 4	0.513	5.13	0.194	0.003 9
0.02	0.531	17.7	0.105	0.002 1	0.405	13.5	0.120	0.002 4	0.531	5.31	0.191	0.003 8
0.02	0.550	18.3	0.103	0.002 1	0.417	13.9	0.118	0.002 4	0.550	5.50	0.188	0.003 8
0.02	0.570	19.0	0.101	0.002 0	0.430	14.3	0.116	0.002 3	0.570	5.70	0.184	0.003 7
0.02	0.593	19.8	0.099	0.002 0	0.446	14.9	0.114	0.002 3	0.593	5.93	0.181	0.003 6
0.02	0.6 16	20.5	0.097	0.001 9	0.462	15.4	0.112	0.002 2	0.616	6.16	0.177	0.003 5
0.02	0.642	21.4	0.095	0.001 9	0.479	16.0	0.110	0.002 2	0.642	6.42	0.174	0.003 5
0.02	0.671	22.4	0.093	0.001 9	0.498	16.6	0.108	0.002 2	0.671	6.71	0.170	0.003 4
0.02	0.704	23.5	0.091	0.001 8	0.521	17.4	0.106	0.002 1	0.704	7.04	0.166	0.003 3
0.02	0.741	24.7	0.089	0.001 8	0.546	18.2	0.103	0.002 1	0.741	7.41	0.162	0.003 2
0.02	0.783	26.1	0.086	0.001 7	0.574	19.1	0.101	0.002 0	0.783	7.83	0.157	0.003 1
0.02	0.825	27.5	0.084	0.001 7	0.609	20.3	0.098	0.002 0	0.825	8.25	0.153	0.003 1
0.02	0.899	30.0	0.080	0.001 6	0.653	21.8	0.094	0.001 9	0.899	8.99	0.147	0.002 9
0.02	0.982	32.7	0.077	0.001 5	0.690	23.0	0.092	0.001 8	0.982	9.82	0.140	0.002 8
0.02	1.090	36.3	0.073	0.001 5	0.774	25.8	0.087	0.001 7	1.090	10.9	0.133	0.002 7
0.01	1.200	40.0	0.070	0.000 7	0.846	28.2	0.083	0.000 8	1.200	12.0	0.127	0.001 3
0.01	1.298	43.3	0.067	0.000 7	0.909	30.3	0.080	0.000 8	1.298	13.0	0.122	0.001 2
0.01	1.433	47.8	0.064	0.000 6	0.997	33.2	0.076	0.000 8	1.433	14.3	0.116	0.001 2
0.01	1.63	54.3	0.060	0.000 6	1.123	37.4	0.072	0.000 7	1.63	16.3	0.109	0.001 1
0.005	1.87	62.3	0.056	0.000 3	1.28	42.7	0.067	0.000 3	1.87	18.7	0.102	0.000 5
0.005	2.22	74.0	0.05 1	0.000 3	1.43	47.7	0.064	0.000 3	2.22	22.2	0.093	0.000 5
0.005	2.56	85.3	0.048	0.000 2	1.70	56.7	0.059	0.000 3	2.56	25.6	0.087	0.000 4
0.005	7.34	245 .O	0.028	0.000 1	2.49	83.0	0.048	0.000 2	7.34	73.4	0.05 1	0.000 3
				0.120				0.135				0.219

© 1983 Hemisphere Publishing Corporation

HEDH

reflected and transmitted portions of the irradiation. If one wants to know not just the reflected portion of the radiosity q_R^+ but its intensity I_R^+, one requires a characteristic that varies not just with direction of incidence θ^-, ϕ^-, but also with direction of emergence θ^+, ϕ^+. For a perfectly diffuse surface $q_{R\lambda}^+$ is $\pi I_{R\lambda}^+$, of course. Accordingly, a spectral bidirectional reflectivity may be defined as

$$\rho_{B\lambda}(\theta^+, \phi^+, \theta^-, \phi^-, \lambda, T_s) = \frac{\pi I_R^+(\theta^+, \phi^+, \lambda)}{I^-(\theta^-, \phi^-, \lambda)\cos\theta^- \Delta\Omega^-} \tag{14}$$

This quantity finds its main application in thermal engineering in the design of instruments for property determination and in the understanding of the operation of such instruments. It is also of use in problems of thermometry and remote sensing via heat radiation.

If one considers the radiant transfer from, say, a black surface at temperature T_1 to another black one at temperature T_2 via reflection from a nonblack surface at T_s and the transfer from 2 to 1 via the same route, and if one then lets T_1 approach T_2 and invokes the principle of detailed balancing, one is led to the ***Helmholtz reciprocity principle,***

$$\rho_{B\lambda}(\theta_1, \phi_1, \theta_2, \phi_2, \lambda, T_s) = \rho_{B\lambda}(\theta_2, \phi_2, \theta_1, \phi_1, \lambda, T_s) \tag{15}$$

The reciprocity principle has important consequences in instrument design and application and is a constraint on builders of mathematical models for bidirectional reflection behavior of surfaces.

One understands by perfectly diffuse reflection the situation where (as a limiting ideal) the bidirectional reflectivity is independent of direction. For a perfectly diffuse surface there is no distinction among hemispherical, directional, or bidirectional reflectivity. The same numerical value applies to all three characteristics. One understands by imperfectly diffuse reflection the situation where the bidirectional reflectivity defined according to Eq. (14) is finite even in the limit as $\Delta\Omega^-$ goes to zero. In such a case it is clear from Eqs. (13) and (14) and Eq. 2.9.1(8) that the directional reflectivity is

$$\rho_\lambda(\theta^-, \phi^-, \lambda, T_s) = \frac{1}{\pi}\int_0^{2\pi}\int_0^{\pi/2} \rho_{B\lambda}(\theta^+, \phi^+, \theta^-, \phi^-, \lambda, T_s)\cos\theta^+ \sin\theta^+ d\theta^+ d\phi^+ \tag{16}$$

and the hemispherical reflectivity is

$$\rho_{H\lambda}(\lambda, T_s) = \frac{1}{\pi}\int_0^{2\pi}\int_0^{\pi/2} \rho_\lambda(\theta^-, \phi^-, \lambda, T_s)\cos\theta^- \sin\theta^- d\theta^- d\phi^- \tag{17}$$

$$\rho_{H\lambda}(\lambda, T_s) = \frac{1}{\pi}\int_0^{2\pi}\int_0^{\pi/2}\frac{1}{\pi}\int_0^{2\pi}\int_0^{\pi/2} \rho_{B\lambda}(\theta^+, \phi^+, \theta^-, \phi^-, \lambda, T_s)\cos\theta^- \sin\theta^- d\theta^- d\phi^- \times \cos\theta^+ \sin\theta^+ d\theta^+ d\phi^+ \tag{18}$$

Specular reflection gives rise to a reflected intensity that lies entirely within a solid angle $\Delta\Omega^+$ about emergent direction θ^+, ϕ^+ equal to the solid angle $\Delta\Omega^-$ about incident direction θ^-, ϕ^-, where $\theta^+ = \theta^-$, and $\phi^+ = \phi^- + \pi$ [measuring both ϕ^+ and ϕ^- from the same reference x axis as shown in Fig. 2.9 .1(2)] . The reflected intensity I_R^+ is a fraction of the incident I^- fixed by the specular reflectivity,

$$\rho_S(\theta^-, \phi^-, \lambda, T_s) = \frac{I_{R\lambda}^+}{I_\lambda^-} \tag{19}$$

This definition corresponds exactly to Eq. (13) because of the equality in $\cos\theta^+\Delta\Omega^+$ and $\cos\theta^-\Delta\Omega^-$. Equation (17) for the hemispherical reflectivity applies as well.

E. Measurement of reflection and transmission characteristics

A few of the considerations involved in measuring reflection and transmission characteristics are described briefly to give the thermal designer some appreciation for the types of measurements usually employed.

One common consideration is the ability to distinguish reflected or transmitted radiation from emitted radiation. It may be that $I_b(\lambda, T_s)$ is so low by reason of a low temperature T_s that it is negligible compared to the incident or reflected intensities. If it is not, it may be possible to tag the incident radiation by chopping. The irradiation $I^- \cos\theta^-$ AR- is interrupted or modulated in a steady periodic manner, and the signal from the detector is processed to record only the radiation in phase with the irradiation. In this way the thermal emission, which is steady by virtue of the thermal capacity of the specimen, is rejected. The phasing of the source chopper and detection equipment must of course be correct so that the signal recorded is independent of sample temperature, as may be verified by increasing sample temperature with the irradiation shuttered off and observing no change in the zero signal.

In making measurements of directional reflectivity and/or transmittivity, one finds that it is often much

© 1983 Hemisphere 1 blishing Corporation

easier to provide uniform irradiation (I^- independent of θ^-, ϕ^-) than to achieve uniform detection ($I^+ \cos\theta^+ d\Omega^+$ detected equally well independent of direction). One then makes use of the Helmholtz reciprocity principle to interchange the plus- and minus-superscripted angles in Eq. (16), with the result that $I^+_{R\lambda}(\theta^+, \phi^+, \lambda)$ is observed and compared to the uniform I^-_λ. The observed quantity (which may be called the hemispherical-directional reflectivity, following Birkebak and Eckert [27]) is identical to the directional (or hemispherical-directional) quantity defined by Eq. (13). This fact is the basis for the heated cavity reflectometer [12-15], the reciprocal-mode 2π-steradian mirror reflectometer [18-23], and the reciprocal-mode integrating sphere [8-10].

For example, in the heated cavity reflectometer [12,15], a water- or gas-cooled specimen is exposed to a 1 000 K cavity. The irradiation consequently has a uniform intensity $I_{b\lambda}(T_c)$, where T_c is the cavity temperature, except for the small solid angle subtended by the view port. See Fig. 1. The small view port permits the intensity from the specimen to be viewed within a small solid angle AL? about direction θ, ϕ. The signal V_s when the detector views the sample less the signal V_0 when the detector views a cavity at the sample temperature is determined. It is done by having a chopper with a highly reflecting specular blade and directing the reflected line of sight from the detector into a cavity at the sample temperature T_s. When the sample is replaced by a platinum fin at the main cavity temperature T_c, the intensity difference $I_{b\lambda}(T_c) - I_{b\lambda}(T_s)$ gives rise to signal $V_r - V_0$. Accordingly,

$$\frac{V_s - V_0}{V_r - V_0} = \frac{I^+_{s\lambda} - I_{b\lambda}(T_s)}{I_{b\lambda}(T_c) - I_{b\lambda}(T_s)}$$

But

$$\begin{aligned} I^+_{s\lambda} &= \epsilon_\lambda(\theta, \phi, \lambda, T_s) I_{b\lambda}(T_s) \\ &\quad + \rho_\lambda(\theta, \phi, \lambda, T_s) I_{b\lambda}(T_c) \\ &= [1 - \rho_\lambda(\theta, \phi, \lambda, T_s)] I_{b\lambda}(T_s) \\ &\quad + \rho_\lambda(\theta, \phi, \lambda, T_s) I_{b\lambda}(T_c) \end{aligned}$$

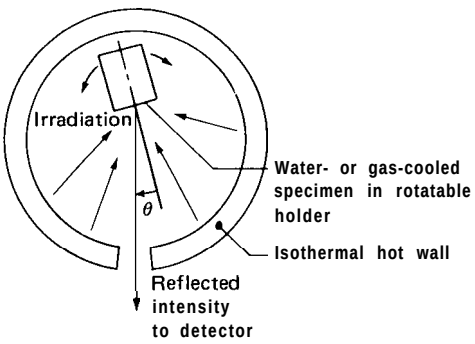

Figure 1 Heated cavity reflectometer.

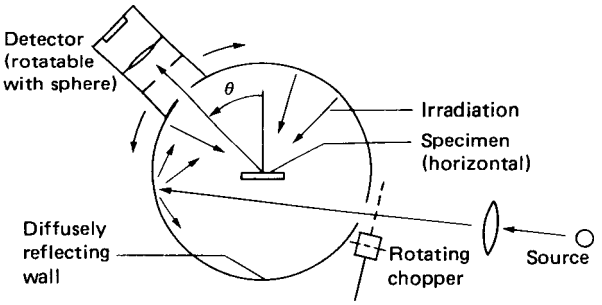

Figure 2 Reciprocal-mode integrating sphere. Note that the source and entrance port are shown rotated 90 from the end and displaced downward for clarity.

The result is

$$\frac{V_s - V_0}{V_r - V_0} = \rho_\lambda(\theta, \phi, \lambda, T_s) \frac{I_{b\lambda}(T_c) - I_{b\lambda}(T_s)}{I_{b\lambda}(T_c) - I_{b\lambda}(T_s)} = \rho_\lambda(\theta, \phi, \lambda, T_s) \quad (20)$$

When a perfectly specular specimen is oriented with $\theta = 0$, the exit port is viewed. If this port leads to an enclosure at temperature T_s, a signal of zero is received for $V_s - V_0$. When a perfectly diffuse specimen is turned toward the exit port by setting $\theta = 0$, no difference is detected. The exit port view factor is changed by the change in $\cos\theta$, which is nearly unity whether θ is zero or a small angle from zero. Thus the small change in the irradiation on a diffuse specimen is not detected.

In the reciprocal-mode 2π-steradian-mirror reflectometer [18-23], the specimen is uniformly irradiated from a cavity (or any continuous-spectrum source) via a mirror. In the reciprocal-mode integrating sphere [8-10], the diffuse irradiation is provided by a highly reflecting diffuse sphere wall that is uniformly irradiated. Interreflections in the sphere serve to smooth out irregularities in the initial irradiation on the sphere wall. In these instruments, source-side chopping is readily achieved, as shown in Fig. 2.

F. Electromagnetic theory and the Fresnel relations

In the classical limit a stream of photons forms a continuous electromagnetic wave with electric field strength E and magnetic field strength H (boldface denotes a vector quantity). Maxwell s equations and the so-called constitutive relations for an isotropic medium govern these quantities. Electromagnetic theory offers a description of the specular reflection from a smooth interface or for a number of such interfaces forming surface films.

The Maxwell equations and constitutive relations [34] are

© 1983 Hemisphere Publishing Corporation

$$\nabla \times \mathbf{E} = -\frac{\partial \mathbf{B}}{\partial t} \tag{21}$$

$$\nabla \times \mathbf{H} = \mathbf{j} + \frac{\partial \mathbf{D}}{\partial t} \tag{22}$$

$$\nabla \cdot \mathbf{D} = \rho_e \tag{23}$$

$$\nabla \cdot \mathbf{B} = 0 \tag{24}$$

$$\mathbf{j} = \sigma_e \mathbf{E} \tag{25}$$

$$\mathbf{D} = \epsilon_e \mathbf{E} \tag{26}$$

$$\mathbf{B} = \mu_m \mathbf{H} \tag{27}$$

where B is the magnetic induction, j is the electric current density, D is the electric induction, ρ_e is the electric charge density, σ_e is the electrical conductivity, ϵ_e is the electric permittivity, and μ_m is the magnetic permeability. The velocity of light in vacuum (denoted by subscript 0) is

$$c_0^2 = \frac{1}{\epsilon_0 \mu_0} \tag{28}$$

Let **E** and H be the real parts of periodic variations,

$$\mathbf{E}(x, y, z, t) = \Re[\tilde{\mathbf{E}}(x, y, z) e^{i\omega t}] \tag{29}$$

$$\mathbf{H}(x, y, z, t) = \Re[\tilde{\mathbf{H}}(x, y, z) e^{i\omega t}] \tag{30}$$

where the super ~ denotes a complex quantity, and

$$\omega = \frac{2\pi c_0}{\lambda_0} \tag{31}$$

Electric neutrality requires that

$$\rho_e = 0 \tag{32}$$

Accordingly, Eqs. (21)-(27) give a time-independent set of equations,

$$\nabla \times \tilde{\mathbf{E}} = -i\omega\mu_m \tilde{\mathbf{H}} \tag{33}$$

$$\nabla \times \tilde{\mathbf{H}} = (\sigma_e + i\omega\epsilon_e)\tilde{\mathbf{E}} \tag{34}$$

$$\nabla \cdot \tilde{\mathbf{E}} = 0 \tag{35}$$

$$\nabla \cdot \tilde{\mathbf{H}} = 0 \tag{36}$$

This set of equations is reduced by taking the curl of Eq. (33) and using Eq. (34) to eliminate $\tilde{H}$.

$$\nabla \times \nabla \times \tilde{\mathbf{E}} = -i\omega\mu_m (\sigma_e + i\omega\epsilon_e)\tilde{\mathbf{E}}$$
$$\nabla \times \nabla \times \tilde{\mathbf{E}} = \omega^2 \mu_m \tilde{\epsilon}_e \tilde{\mathbf{E}} \tag{37}$$

where

$$\tilde{\epsilon}_e = \epsilon_e - \frac{i\sigma_e}{\omega} \tag{38}$$

By virtue of the identity

$$\nabla \times \nabla \times \tilde{\mathbf{E}} = \nabla(\nabla \cdot \tilde{\mathbf{E}}) - \nabla^2 \tilde{\mathbf{E}}$$

and with Eq. (35), one obtains

$$\nabla^2 \tilde{\mathbf{E}} = -\omega^2 \mu_m \tilde{\epsilon}_e \tilde{\mathbf{E}} \tag{39}$$

Let the lengths be made dimensionless by ω/c_0, and denote a dimensionless quantity with subscript *d*. Then Eq. (39) becomes

$$\nabla_d^2 \tilde{\mathbf{E}} = -\tilde{n}^2 \tilde{\mathbf{E}} \tag{40}$$

where $\tilde{n}$ is the complex index of refraction,

$$\tilde{n}^2 = \left(\frac{\mu_m}{\mu_0}\right)\left(\frac{\tilde{\epsilon}_e}{\epsilon_0}\right) = (n - ik)^2 \tag{41}$$

The quantity n is called the refractive index and the quantity k the absorptive index. Collectively they are referred to as the optical constants of the medium. They are in general dependent on wavelength or frequency of the radiation. Note that, in vacuum, $n = 1$ and
A material with a zero value of k
value of σ_e, hence a dielectric.

The governing equation for $\tilde{\mathbf{E}}$ admits a solution periodic in space. Consider a wave in the first quadrant

$$\frac{\partial \tilde{\mathbf{E}}}{\partial x_d} = -i\tilde{a}\tilde{\mathbf{E}} \qquad \frac{\partial \tilde{\mathbf{E}}}{\partial y_d} = 0 \qquad \frac{\partial \mathbf{E}}{\partial z_d} = -i\tilde{b}\tilde{\mathbf{E}}$$

$$\tilde{\mathbf{E}} = \tilde{\mathbf{A}} e^{i(\omega t - \tilde{a}x_d - \tilde{b}z_d)} \tag{42}$$

Equation (40) requires that

$$\tilde{a}^2 + \tilde{b}^2 = \tilde{n}^2 \tag{43}$$

Accordingly, parameter $\tilde{\theta}$ is introduced, where

$$\tilde{a} = \tilde{n} \sin\tilde{\theta} \qquad \tilde{b} = \tilde{n} \cos\tilde{\theta} \tag{44}$$

The result is that the governing electromagnetic equations admit a solution in the form of a wave,

$$\mathbf{E} = \Re[\tilde{\mathbf{A}} e^{i(\omega t - \tilde{n} \sin\tilde{\theta}\, x_d - \tilde{n} \cos\tilde{\theta}\, z_d)}] \tag{45}$$

The magnetic field **H** follows from Eqs. (30) and (34).

To tie this development into our notion of radiant intensity and flux, the power per unit area in direction of unit vector **r** is

$$I\, d\Omega\, \mathbf{r} = \tfrac{1}{4}(\tilde{\mathbf{E}} \times \tilde{\mathbf{H}}^* + \tilde{\mathbf{E}}^* \times \tilde{\mathbf{H}}) = \tfrac{1}{2}\Re(\tilde{\mathbf{E}} \times \tilde{\mathbf{H}}^*) \tag{46}$$

where the super * denotes a complex conjugate; that is, if $\tilde{z} = x + iy$, then $\tilde{z}^* = x - iy$.

To determine the reflectivity of an interface, it is necessary to know the boundary conditions required to be satisfied at an interface. They are continuity of tangential components, continuity of magnetic flux, and conservation of electric charge. Let the interface have normal N, and let subscripts 1 and 2 denote either side :

$$\mathbf{N} \times (\tilde{\mathbf{E}}_2 - \tilde{\mathbf{E}}_1) = 0 \tag{47}$$

© 1983 Hemisphere Publishing Corporation

$$NX\ (\tilde{\mathbf{H}}_2 - \tilde{\mathbf{H}}_1) = 0 \quad (48)$$

$$\mathbf{N} \cdot (\tilde{\mathbf{B}}_2 - \tilde{\mathbf{B}}_1) = 0 \quad (49)$$

$$\mathbf{N} \cdot (\tilde{\mathbf{j}}_2 - \tilde{\mathbf{j}}_1) = -\frac{\partial}{\partial t}\,[\mathbf{N} \cdot (\tilde{\mathbf{D}}_2 - \tilde{\mathbf{D}}_1)] \quad (50)$$

Now consider an approaching wave with amplitude A (see Fig. 3) traveling in vacuum (medium 0) and encountering an interface over medium 1. The vector $\tilde{\mathbf{A}}$ is resolved into components parallel to the plane of incidence (defined by the approaching ray **r** and surface normal N) and perpendicular to the plane of incidence. Subscripts p and s (from the German ***parallel and-senkrecht)*** are used. A reflected ray with amplitude **R** and a transmitted one with amplitude **T** are imagined to exist with parameters θ_0' and θ_1, respectively. The six requirements represented by Eqs. (47)-(50) lead to six required conditions. Two are referred to as Snell s law:

$$n_0 \sin\theta_0 = n_0 \sin\theta_0' = \tilde{n}_1 \sin\tilde{\theta}_1 \quad (51)$$

$$\cos\theta_0 = -\cos\theta_0' \quad (52)$$

The other four lead to the Fresnel relations (subject to the additional assumption that $\mu_1 = \mu_0$).

$$\tilde{r}_{p,0-1} = \frac{\tilde{R}_p}{\tilde{A}_p} = \frac{\tilde{n}_1 \cos\theta_0 - n_0 \cos\tilde{\theta}_1}{\tilde{n}_1 \cos\theta_0 + n_0 \cos\tilde{\theta}_1} \quad (53)$$

$$\tilde{t}_{p,0-1} = \frac{\tilde{T}_p}{\tilde{A}_p} = \frac{2n_0 \cos\theta_0}{\tilde{n}_1 \cos\theta_0 + n_0 \cos\tilde{\theta}_1} \quad (54)$$

$$\tilde{r}_{s,0-1} = \frac{\tilde{R}_s}{\tilde{A}_s} = \frac{n_0 \cos\theta_0 - \tilde{n}_1 \cos\tilde{\theta}_1}{n_0 \cos\theta_0 + \tilde{n}_1 \cos\tilde{\theta}_1} \quad (55)$$

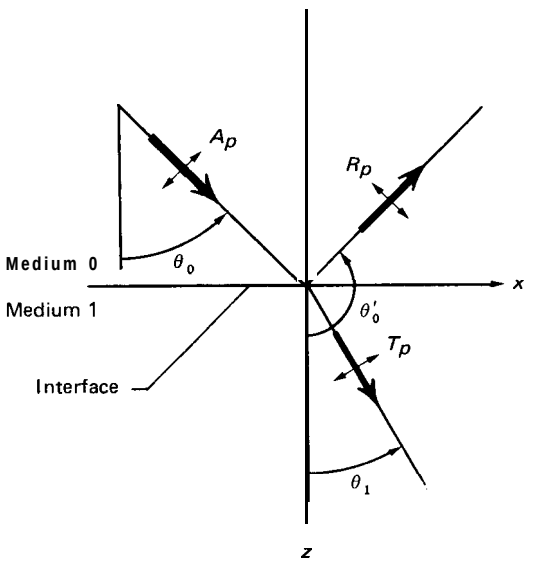

Figure 3 Approaching, transmitted, and reflected waves at an interface.

$$\tilde{t}_{s,0-1} = \frac{\tilde{T}_s}{\tilde{A}_s} = \frac{2n_0 \cos\theta_0}{n_0 \cos\theta_0 + \tilde{n}_1 \cos\tilde{\theta}_1} \quad (56)$$

If a subsequent interface is encountered, another set of relations is obtained by replacing 0 with 1 and 1 with 2 in the subscripts. The quantity n_0 becomes $\tilde{n}_1$, and $\cos\theta_0$ becomes $\cos\tilde{\theta}_1$, in this replacement.

From Eq. (46), one determines that the irradiation in the approaching wave is

$$I^- d\Omega\,\mathbf{r} = (I_p^- + I_s^-)\, d\Omega\mathbf{r} \quad (57)$$

$$I_p^- \cos\theta_0\, d\Omega = \frac{n_0}{\mu_0 c_0} \cos\theta_0 A; \quad (58)$$

$$I_s^- \cos\theta_0\, d\Omega = \frac{n_0}{\mu_0 c_0} \cos\theta_0 A_s^2 \quad (59)$$

The power per unit area in the reflected wave is I_R^+, where similarly,

$$I_R^+ = I_{R,p}^+ + I_{R,s}^+ \quad (60)$$

Reflectivities ρ_p and ρ_s may be defined as follows:

$$\rho_p = \frac{I_{R,p}^+}{I_p^-} = \frac{(n_0/\mu_0 c_0)|\cos\theta_0'|\tilde{R}_p \tilde{R}_p^*}{(n_0/\mu_0 c_0)\cos\theta_0 A_p{}^2} = \tilde{r}_p \tilde{r}_p^* \quad (61a)$$

$$\rho_s = \frac{I_{R,s}^+}{I_s^-} = \tilde{r}_s \tilde{r}_s^* \quad (61b)$$

where the subscripts 0 and 1 have been omitted for simplicity in notation. Similarly, the transmitted to incident power may be found:

$$\tau_p = \Re\left(\frac{\tilde{n}^* \cos\tilde{\theta}\, \tilde{t}_p \tilde{t}_p^*}{n_0 \cos\theta_0}\right) \quad (62a)$$

$$\tau_s = \Re\left(\frac{\tilde{n}^* \cos\tilde{\theta}^*\, \tilde{t}_s \tilde{t}_s^*}{n_0 \cos\theta_0}\right) \quad (62b)$$

Note the difference in the $\cos\tilde{\theta}$ and $\cos\tilde{\theta}^*$ terms.

Since the interface itself is infinitesimally thick, it has no absorptivity, and $\tau_p = 1 - \rho_p$ and $\tau_s = 1 - \rho_s$. However, if the medium 1 is absorbing and infinite in extent, the transmitted radiation is eventually absorbed within the medium; τ_p and τ_s of the interface become α_p and α_s of the surface system.

Edwards [2] developed the Fresnel coefficients $\tilde{r}_{0-2}$, etc., for a surface film made of two interfaces, the O-l and l-2 interfaces a distance δ_1 apart. By repeated application of the formula, $\tilde{r}_{0-n}$ may be constructed by an embedding technique. One begins by obtaining the O-l and l-2 Fresnel coefficients and combines them to obtain the O-2. Then the O-2 values replace O-l, and 2-3 values replace l-2 values in the formula to yield O-3 quantities and so on. The formulas for $\tilde{r}_{p,0-2}$ and $\tilde{t}_{p,0-2}$ are

© 1983 Hemisphere I blishing Corporation

$$\tilde{r}_{p,0-2} = \tilde{r}_{p\,0-1} + \frac{\tilde{m}_1^2 \tilde{t}_{p,0-1} \tilde{r}_{p,1-2} \tilde{t}_{p,1-0}}{1 - \tilde{m}_1^2 \tilde{r}_{p,1-2} \tilde{r}_{p,1-0}} \tag{63a}$$

$$\tilde{t}_{p,0-2} = \frac{\tilde{t}_{p,0-1} \tilde{m}_1 \tilde{t}_{p,1-2}}{1 - \tilde{m}_1^2 \tilde{r}_{p,1-2} \tilde{r}_{p,1-0}} \tag{63b}$$

where

$$\tilde{m}_1^2 = e^{-i4\pi \tilde{n}_1 \cos \tilde{\theta}_1 \delta_1/\lambda_0} \tag{64}$$

The relations for the s-polarized radiation are obtained by replacing p with s in the subscripts above. Reflectivities ρ_p and ρ_s for the O-2 system are obtained by putting Eq. (63a) and the corresponding s relation into Eqs. (61a) and (61b).

An important effect is interference. When δ_1/λ_0 is one value, the reflectivity ρ_p will be a maximum. Excellent mirrors can be made by building up a stack of thin films with appropriate optical properties n and k and thicknesses 6. When δ/λ_0 is another value, the reflectivity will be a minimum. High absorptivity or emissivity surfaces can be made in this way. Absorbing surfaces for solar heat collectors and antireflection coatings for glass are so made.

When the surface film is very thick compared to the wavelength, minor variations in thickness and in wavelength result in high and low values of reflectivity due to the interference phenomenon. The engineer should use the appropriate average value obtained by averaging ρ_p and ρ_s over wavelength or thickness, as shown in [2].

G. Some useful approximations

A number of useful relations can be derived from the foregoing relations when values of optical constants are approximated. For some dielectrics and some semiconductors the refractive index n may be reasonably approximated as a constant over an appreciable portion of the spectrum, and the absorptive index k is small. Furthermore, for normal incidence cos θ_0 is 1 and sin θ_0 is zero. Equations (61a) and (61b), together with Eqs. (53) and (55) reduce to merely

$$\rho_p(\theta = 0) = \rho_s(\theta = 0) = \left(\frac{n-1}{n+1}\right)^2 \tag{65}$$

When k is small, the thickness of the surface system must be sufficiently great to make it opaque. In this case the absorptivity and hence the emissivity is

$$\alpha(\theta = 0) = 1 - \rho(\theta = 0) = \frac{4n}{(n+1)^2} \tag{66}$$

This relation shows that the absorptivity is unity when $n = 1$ and falls with increasing n.

For unpolarized incident radiation (to be explained more fully in Sec. H), $I_p = I_s = Z/2$, and

$$\rho(\theta) = \tfrac{1}{2}[\rho_p(\theta) + \rho_s(\theta)] \tag{67}$$

$$\alpha(\theta) = \tfrac{1}{2}[\alpha_p(\theta) + \alpha_s(\theta)] \tag{68}$$

Equation (4) may be used to obtain the hemispherical absorptance from the directional values fixed by Eqs. (68), (61a) and (61b), (53) and (55), and (51). Figure 4, from Dunkle [36], shows a plot of $\alpha_H/\alpha(\theta = 0)$ for a dielectric.

Figure 4 also shows the ratio for electrical conductors with parameter k/n. Here the approximation is made that cos $\theta_1 \doteq 1$, because n and k are large in Eq. (5 1). The equations reduce to

$$\rho_p(\theta) \doteq \frac{(n \cos\theta_0 - 1)^2 + k^2 \cos^2 \theta_0}{(n \cos\theta_0 + 1)^2 + k^2 \cos^2 \theta_0} \tag{69}$$

$$\rho_s(\theta) \doteq \frac{(\cos\theta_0 - n)^2 + k^2}{(\cos\theta_0 + n)^2 + k^2} \tag{70}$$

For normal incidence,

$$\rho(\theta = 0) = \frac{(n-1)^2 + k^2}{(n+1)^2 + k^2} \tag{71}$$

$$\alpha(\theta = 0) = \frac{4n}{(n+1)^2 + k^2} \tag{72}$$

It is clear how these relations may be used together with Eq. (4) to find the curves in the figure.

The Hagen-Rubens relation is a crude approximation suitable for some metal alloys. It relates electrical resistivity r_e to optical constants n and k [35].

$$n = k = \left(\frac{30\lambda}{r_e}\right)^{1/2} \tag{73}$$

When this relation is substituted into Eq. (72) and $n \gg 1$, one obtains

$$\alpha_\lambda(\theta = 0, \lambda, T_s) = \frac{2}{n} = \left(\frac{2r_e}{15\lambda}\right)^{1/2} \tag{74}$$

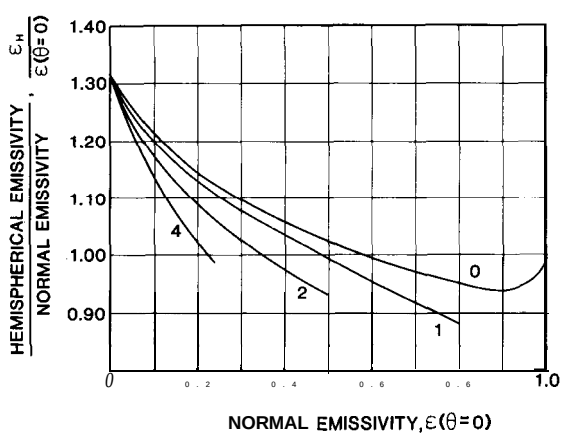

Figure 4 Ratio of hemispherical to normal emissivity as a function of normal emissivity and k/n. From Dunkle [36].

© 1983 Hemisphere Publishing Corporation

The temperature dependency comes about through its effect on r_s. Often r_e increases directly with the absolute temperature, with the result that

$$\alpha_\lambda(\theta = 0, \lambda, T_s) = C\frac{T_s}{\theta\lambda}^{1/2} \tag{75}$$

where

$$c = \left[\frac{2r_e(T_0)}{15T_0}\right]^{1/2} \tag{76}$$

If one now finds the total absorptivity for environmental temperature T_e, one finds

$$\alpha_T(\theta = \theta,\ T_s, T_e) = CT_s^{1/2}\int_0^1 \lambda^{-1/2}\, df_e(\lambda T_e)$$

$$\alpha_T(\theta = 0, T_s, T_e) = CT_s^{1/2}T_e^{1/2}\int_0^1 u^{-1/2}\, df_e(u) \tag{77}$$

where $f_e(u)$ is the external fractional function. The definite integral is simply a constant (times $\sqrt{k/hc}$),

$$A_r = \int_0^1 u^{-1/2}\, df_e(u) = \frac{1}{(\lambda_e T_e)^{1/2}} \tag{78}$$

where

$$f_e(\lambda_e T_e) \doteq 0.49 \qquad \lambda_e T_e \doteq 4\,050\ \mu\text{m K} \tag{79}$$

Therefore

$$\alpha_T(\theta = 0, T_e, T_s) = A_e C(T_s T_e)^{1/2} \tag{80}$$

$$\epsilon_T(\theta = 0, T_e) = A_e C T_s \tag{81}$$

$$\epsilon_{T_i}(\theta = 0, T_s) = A_i C T_s \tag{82}$$

where

$$A_i = \int_0^1 u^{-1/2}\, df_i(u) = \frac{1}{(\lambda_i T_s)^{1/2}} \tag{83}$$

$$f_i(\lambda_i T_s) \doteq 0.49 \qquad \lambda_i T_s \doteq 3\,180\ \mu\text{m K} \tag{84}$$

These results can be restated in words to emphasize their meaning. The total emissivity of a bare (i.e., not heavily oxidized) metal alloy increases directly with absolute temperature. The internal total emissivity of a bare metal alloy is approximately one-eighth greater than its external total emissivity. The total absorptivity of a bare metal alloy can be found from its total emissivity by taking the emissivity at the environmental temperature T_e and multiplying by $(T_s/T_e)^{1/2}$. The total absorptivity or emissivity can be estimated from a spectral curve by taking the spectral value at a wavelength where the appropriate fractional function is 49%.

All these results apply to the normal ($\theta_0 = 0$) total emissivity and absorptivity, but Fig. 4 can be used to correct approximately to hemispherical values using $k/n = 1$ (the curve applies strictly to the spectral values and only approximately to total values).

As has been said, the Hagen-Rubens formula works well only for high-resistivity metals, usually metal alloys. A so-called two-electron model was derived for low-resistivity metals [38]. This model yielded

$$\alpha_\lambda(\theta = 0, \lambda, T_s) = Af\left(\frac{\lambda}{\lambda_{12}}\right) + \frac{B}{C + \lambda^2} \tag{85}$$

where

$$f\left(\frac{\lambda}{\lambda_{12}}\right) = \left[\frac{(1 + \lambda^2/\lambda_{12}^2)^{1/2} - 1}{\lambda^2/2\lambda_{12}^2}\right]^{1/2} \tag{86}$$

and

$$\lambda_{12}(T_s) = \frac{\lambda_0 r_e(T_0)}{r_e(T_s)} \tag{87}$$

$$A(T_s) = \frac{A_0 r_e(T_s)}{r_e(T_0)} \tag{88}$$

$$B(T_s) = B_0 - (C + \lambda_x^2)A(T_s) \tag{89}$$

λ_0, λ_x, C = constants

Table 2 shows parameters for nickel and platinum [2, 37, 38], and Table 3 shows values for a number of other metals when $T_s \doteq 300$ K. In view of Eqs. (77) and (82), the total absorptivity and emissivity values can be obtained approximately from the spectral formula Eq. (85) merely by using a mean wavelength λ_e for absorptivity with surrounds at temperature T_e and λ_s for emissivity at temperature T_s.

$$\alpha_T(\theta = 0, T_s, T_e) \doteq \alpha_\lambda(\theta = 0, \lambda_e, T_s) \tag{90}$$

$$\epsilon_T(\theta = 0, T_s) \doteq \alpha_\lambda(\theta = 0, \lambda_s, T_s) \tag{91}$$

$$\epsilon_{T_i}(\theta = 0, T_s) \doteq \alpha_\lambda(\theta = 0, \lambda_i, T_s) \tag{92}$$

Table 2 Temperature dependence of spectral absorptivity and emissivity for nickel and platinum

(300 K < T < 1 400 K)	(1.5 μm < λ < 25 pm)	
Parameter	Nickel	Platinum
A_0	0.029	0.034
B_0	1.158 μm²	0.577 μm²
C	3.3 μm²	0.0
T_0	306 K	306 K
n	1.7	0.94
λ_0	5.0 pm	7.0 μm
λ_x	1.5 μm	1.7 μm

© 1983 Hemisphere 1 blishing Corporation

Table 3 Spectral absorptivity parameters for metals at room temperature

Metal	A	B	C	λ_{12}
Aluminum foil	0.016 5	0.23	8.9	14
Cadmium, 99.99%, rolled plate	0.054	2.15	3.2	9
Chromium, polished electroplate	0.076	1.58	3.9	3
Columbium, 99.99%, rolled plate	0.15	0.29	- 0	1
Copper, 99.99%, polished	0.018	0.077	3.2	45
Gold, 99.99%, polished	0.020	0.056	1.4	45
Indium, 99.99%, scraped	0.060	0.24	1.3	6
Inconel X, rolled plate	0.44	0.036	- 0	1
Lead, 99.99%, scraped	0.16	0.39	1.1	4
Manganese, 99.99%, polished	0.19	4.8	11	8
Molybdenum, 99.99%	0.033	0.36	- 0	7
Nickel, 99.99%, polished	0.029	0.83	2.4	5
Platinum, 99.99%, cold rolled	0.038	0.42	- 0	4
Rhodium, polished electroplate	0.06	1.27	10	6
Silver, polished electroplate	0.011	0.16	11	70
Stainless steel, 303, lapped	-0.71	- 0	- 0	0.125
Tin, 99.99%, rolled plate	0.052	0.56	0.8	7
Titanium, polished electroplate	0.13	2.9	8.3	12
Titanium, 99%, lapped	0.09	6.5	15	12
Tungsten, 99.99%, lapped	0.05	0.49	0.3	3
Vanadium, 99.99%, rolled plate	0.17	0.66	0.93	1
Zinc, 99.9%	0.036	0.26	- 0	8
Zirconium, 99.99%, rolled plate	0.64	4	35	1

where

$\lambda_e T_e = \lambda_s T_s \doteq 4\,050\ \mu\text{m K}$

$\lambda_i T_s \doteq 3\,180\ \mu\text{m K}$

H. Polarization

The radiant heating of a wall as determined by its absorptivity is seen to be not merely a property of the wall but also the state of polarization of the incident radiation. The engineer can often ignore polarization and still achieve acceptable accuracy in practical situations where the directions of polarization are scrambled in the interreflection process. For example, it was found [41-42] that the transmission of square and circular specular-walled passages could be reasonably well calculated ignoring polarization, but not for the parallel slot. In instruments, such as the integrating-sphere and heated-cavity reflectometers described earlier, polarization in the instrument optics may be a significant source of error, for angles of incidence considerably off normal.

In Sec. 2.9.4C, a Monte Carlo ray-tracing technique is described. If such a computer program is used for radiant heat transfer calculations, one can almost as easily account for polarization as ignore it, thus avoiding having to assess the error in ignoring it. To carry out the ray-tracing calculation, it is necessary for the computer to calculate the fraction of radiation absorbed at a surface from a beam of radiation already polarized by previous reflections or transmissions. The properties of the surface will be calculated from the Fresnel coefficients $\tilde{r}_{p_2}$ and $\tilde{r}_{s_2}$. The subscript 2 denotes the set of p and s directions defined by the ray (unit vector $\mathbf{r}$ directed toward the surface) and the surface normal (vector n).

$$\mathbf{s}_2 = \frac{\mathrm{n} \times (-\mathbf{r})}{|\mathrm{n} \times \mathbf{r}|} \qquad \mathbf{p}_2 = \mathbf{s}_2 \times \mathbf{r} \tag{93}$$

However, the polarization of the beam is known in terms of the p_1, s_1 directions defined by the plane of incidence of the previous surface. To find I_{p_2} and I_{s_2}, it is necessary to resolve the electric vector expressed in the p_1 and s_1 coordinates into the p_2 and s_2 coordinates. With the magnetic vector then fixed from Eq. (34), Eq. (46) gives I_{p_2} and I_{s_2}. It is found that, in general, insufficient information about the electric field vector is carried by I_{p_1} and I_{s_1}. Additional information is needed regarding the temporally and spectrally smoothed averages of the sine and cosine of the phase relation between the p_1 and s_1 components of the electric vector. Hence two more quantities, such as the third and fourth Stokes coefficients, must be introduced.

Consider an approaching wave as described by Eq. (42), where coordinate x is in the p_1 direction, y is in the s_1 direction, and z is along the direction of propagation. Equations (33) and (46) show that the total intensity I is given by

© 1983 Hemisphere Publishing Corporation

$$I\,d\Omega = \frac{1}{4}(\mathbf{k}\cdot\tilde{\mathbf{E}}\times\tilde{\mathbf{H}}^* + \mathbf{k}\cdot\tilde{\mathbf{E}}^*\times\tilde{\mathbf{H}}) = \frac{n}{2\mu_m c_0}(\tilde{A}_p\tilde{A}_p^* + \tilde{A}_s\tilde{A}_s^*) \tag{94}$$

Hence, let

$$\tilde{Z}_p = \left(\frac{n}{2\mu_m c_0\, d\Omega}\right)^{1/2}\tilde{A}_p \qquad \tilde{Z}_s = \left(\frac{n}{2\mu_m c_0\, d\Omega}\right)^{1/2}\tilde{A}_s \tag{95a}$$

In general, there can be an instantaneous phase difference between $\tilde{E}_p$ and $\tilde{E}_s$ or $\tilde{Z}_p$ and $\tilde{Z}_s$, and they can have different instantaneous magnitudes,

$$\tilde{Z}_{p_1} = \tilde{M}_{p_1}e^{i\delta_{p_1}} \qquad \tilde{Z}_{s_1} = \tilde{M}_{s_1}e^{i\delta_{s_1}} \tag{95b}$$

We thus identify I_{p_1} and I_{s_1} as follows:

$$I = I_{p_1} + I_{s_1} \qquad I_{p_1} = \langle\tilde{Z}_{p_1}\tilde{Z}_{p_1}^*\rangle \qquad I_{s_1} = \langle\tilde{Z}_{s_1}\tilde{Z}_{s_1}^*\rangle \tag{96}$$

where the brackets 0 denote temporal and spectral smoothing.

Let p_2 and s_2 be directions twisted from the p_1, s_1 directions by angle β.

$$\cos\beta = \mathbf{p}_2\cdot\mathbf{p}_1 \qquad \sin\beta = \mathbf{p}_2\cdot\mathbf{s}_1 \tag{97}$$

Then

$$\tilde{Z}_{p_2} = \mathbf{p}_2\cdot\mathbf{p}_1\tilde{Z}_{p_1} + \mathbf{p}_2\cdot\mathbf{s}_1\tilde{Z}_{s_1} = \cos\beta\,\tilde{Z}_{p_1} + \sin\beta\,\tilde{Z}_{s_1}$$

$$\tilde{Z}_{s_2} = \mathbf{s}_2\cdot\mathbf{p}_1\tilde{Z}_{p_1} + \mathbf{s}_2\cdot\mathbf{s}_1\tilde{Z}_{s_1} = -\sin\beta\,\tilde{Z}_{p_1} + \cos\beta\,\tilde{Z}_{s_1}$$

Thus

$$\begin{aligned} I_{p_2} &= \langle\tilde{Z}_{p_2}\tilde{Z}_{p_2}^*\rangle \\ &= \langle(\cos\beta\,Z_{p_1} + \sin\beta\,Z_{s_1})(\cos\beta\,Z_{p_1}^* + \sin\beta\,Z_{s_1}^*)\rangle \\ &= \cos^2\beta\,I_{p_1} + \sin^2\beta\,I_{s_1} \\ &\quad + \sin\beta\cos\beta\langle\tilde{Z}_{p_1}\tilde{Z}_{s_1}^* + \tilde{Z}_{p_1}^*\tilde{Z}_{s_1}\rangle \end{aligned}$$

The quantity needed to find I_{p_2} in addition to I_{p_1} and I_{s_1} is the third Stokes coefficient,

$$I_{u_1} = \langle Z_{p_1}Z_{s_1}^* + Z_{p_1}^*Z_{s_1}\rangle = 2\Re\langle\tilde{Z}_{p_1}\tilde{Z}_{s_1}^*\rangle \tag{98}$$

The fourth Stokes coefficient is

$$I_{v_1} = \mathcal{I}\langle\tilde{Z}_{p_1}^*\tilde{Z}_{s_1} - \tilde{Z}_{p_1}\tilde{Z}_{s_1}^*\rangle = 2\mathcal{I}\langle\tilde{Z}_{p_1}\tilde{Z}_{s_1}^*\rangle \tag{99}$$

The twist transformation of the set of $I_{p_1}, I_{s_1}, I_{u_1}, I_{v_1}$ into $I_{p_2}, I_s, I_{u_2}, I_{v_2}$ is compactly represented as matrix multiplication:

$$\begin{vmatrix} I_{p_2} \\ I_{s_2} \\ I_{u_2} \\ I_{v_2} \end{vmatrix} = \begin{vmatrix} \cos^2\beta & \sin^2\beta & \sin\beta\cos\beta & 0 \\ \sin^2\beta & \cos^2\beta & -\sin\beta\cos\beta & 0 \\ -2\sin\beta\cos\beta & 2\sin\beta\cos\beta & \cos^2\beta - \sin^2\beta & 0 \\ 0 & 0 & 0 & 1 \end{vmatrix} \begin{vmatrix} I_{p_1} \\ I_{s_1} \\ I_{u_1} \\ I_{v_1} \end{vmatrix} \tag{100}$$

Because of the random nature of blackbody radiation, one has $\langle M_p\rangle = \langle M_s\rangle$ and $\langle\cos(\delta_p - \delta_s)\rangle = \langle\sin(\delta_p - \delta_s)\rangle = 0$. Thus for blackbody radiation, $\langle\tilde{Z}_p\tilde{Z}_p^*\rangle = \langle Z_s\tilde{Z}_s^*\rangle$ and $\langle Z_pZ_s^*\rangle = \langle Z_sZ_p^*\rangle = 0$; that is,

$$I_{b,p} = I_{b,s} = \frac{I_b}{2} \qquad I_{b,u} = I_{b,v} = 0 \tag{101}$$

A column vector caries the requisite information:

$$|I_b| = |X_b|I_b \tag{102}$$

$$|X_b| = \begin{vmatrix} \frac{1}{2} \\ \frac{1}{2} \\ 0 \\ 0 \end{vmatrix} \tag{103}$$

Finding the intensity I can be represented by multiplying by a row matrix, designated with a super t (for transpose):

$$|E|^t = |1\ \ 1\ \ 0\ \ 0| \tag{104}$$

$$I = |E|^t\cdot|I| \tag{105}$$

With the intensity matrix components known in terms of the principal p_2, s_2 coordinates, the Fresnel coefficients can be used to find the intensity matrix of the reflected ray. Let a prime on the subscript denote the reflected ray and drop the double subscript 2 to simplify the notation. Then

$$\tilde{Z}_{p'} = \tilde{r}_p\tilde{Z}_p \qquad \tilde{Z}_{s'} = \tilde{r}_s\tilde{Z}_s \tag{106}$$

Hence

$$I_{p'} = \langle\tilde{r}_p\tilde{Z}_p\tilde{r}_p^*\tilde{Z}_p^*\rangle = \tilde{r}_p\tilde{r}_p^*\langle\tilde{Z}_p\tilde{Z}_p^*\rangle = \tilde{r}_p\tilde{r}_p^*I_p$$

$$\begin{aligned} I_{u'} &= 2\Re\langle\tilde{r}_p\tilde{Z}_p\tilde{r}_s^*\tilde{Z}_s^*\rangle \\ &= \Re(\tilde{r}_p\tilde{r}_s^*)\Re\langle 2\tilde{Z}_p\tilde{Z}_s^*\rangle - \mathcal{I}(\tilde{r}_p\tilde{r}_s^*)\mathcal{I}\langle 2\tilde{Z}_p\tilde{Z}_s^*\rangle \\ &= \Re(\tilde{r}_p\tilde{r}_s^*)I_u - \mathcal{I}(\tilde{r}_p\tilde{r}_s^*)I_v \end{aligned}$$

Similarly, the $I_{s'}$ and $I_{v'}$ quantities can be found. The column matrix for the reflected intensity is thus

$$\begin{vmatrix} I_{p'} \\ I_{u'} \\ I_{v'} \end{vmatrix} = \begin{vmatrix} \rho_{pp} & 0 & 0 & 0 \\ 0 & \rho_{ss} & 0 & 0 \\ 0 & 0 & \rho_{uu} & \rho_{uv} \\ 0 & 0 & \rho_{vu} & \rho_{vv} \end{vmatrix} \cdot \begin{vmatrix} I_p \\ I_s \\ I_u \\ I_v \end{vmatrix} \tag{107}$$

where

$$\rho_{pp} = \tilde{r}_p\tilde{r}_p^* \qquad \rho_{ss} = \tilde{r}_s\tilde{r}_s^*$$

$$\rho_{uu} = \rho_{vv} = \Re(\tilde{r}_p\tilde{r}_s^*) \qquad \rho_{uv} = -\rho_{vu} = -\mathcal{I}(\tilde{r}_p\tilde{r}_s^*) \tag{108}$$

The fraction of the incident energy reflected is then

$$\rho = \frac{|E|^t\cdot|\rho|\cdot|I|}{|E|^t\cdot|I|} = \frac{|E|^t\cdot|\rho|\cdot|X|}{|E|^t\cdot|X|} \tag{109}$$

© 1983 Hemisphere Publishing Corporation

and the fraction absorbed is $1 - \rho$. It is these fractions that are needed for a ray-tracing calculation.

The state of polarization of the leaving ray is contained in the column matrix IX]:

$$|X'| = \frac{|I'|}{|E^t| \cdot |I'|} = \frac{|\rho| \cdot |X|}{|E^t| \cdot |\rho| \cdot |X|} \tag{110}$$

The p'-s' coordinates and the direction of the reflected ray are also needed. The emergent ray r' maintains its component tangent to the surface in the plane of incidence and reverses its component normal to the surface:

$$\mathbf{r} = -(\mathbf{r} \cdot \mathbf{n})\mathbf{n} + [\mathbf{r} \cdot (\mathbf{n} \times \mathbf{s})](\mathbf{n} \times \mathbf{s}) \tag{111}$$

$$\mathbf{s}' = \mathbf{s} \tag{112}$$

$$\mathbf{p}' = \mathbf{s}' \times \mathbf{r} \tag{113}$$

With this information the ray-tracing procedure of Sec. 2.9.4C can continue to the next wall encounter. Drop the prime on $\mathbf{r}'$, take the normal to the next wall **n**, and use Eq. (93) to find the new p_2-s_2 directions. Taking p'-s' to be p_1-s_1, one finds the twist angle β from Eq. (97) and transforms $|X'|$ to $|X|$ using Eq. (100). Then the reflectivity can be found from Eq. (109), and the ray tracing can be continued by using Eqs. (110)–(113) and repeating the entire process.

As stated at the outset of this section, the designer can often ignore polarization except for special circumstances where several interreflections occur with little or no β twist or where instruments have polarizing optics. In Sec. I, material selection where polarization is not a significant factor is discussed briefly. In the whole of Sec. 2.9.3, where the surfaces are assumed to be perfectly diffuse, and are thus depolarizing by definition, polarization is not a concern. The phenomenon impacts Sec. 2.9.4, where radiant interchange in the presence of specular surfaces is treated. Polarization is also an important feature in scattering from

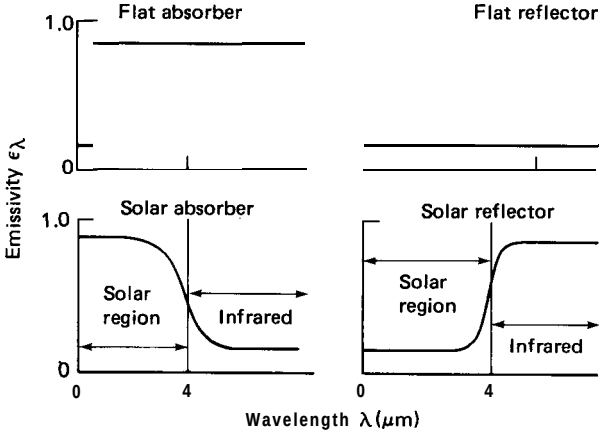

Figure 5 Surface finishes often used in thermal design [43].

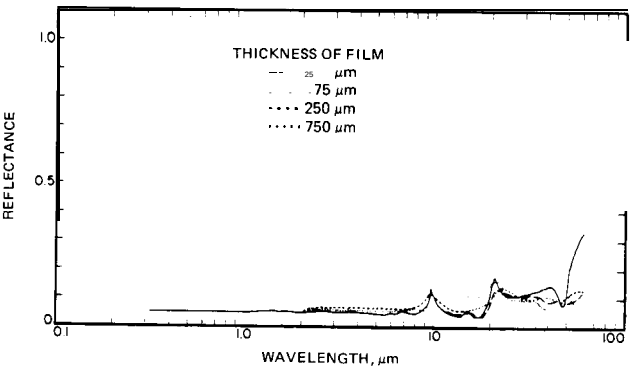

(a)

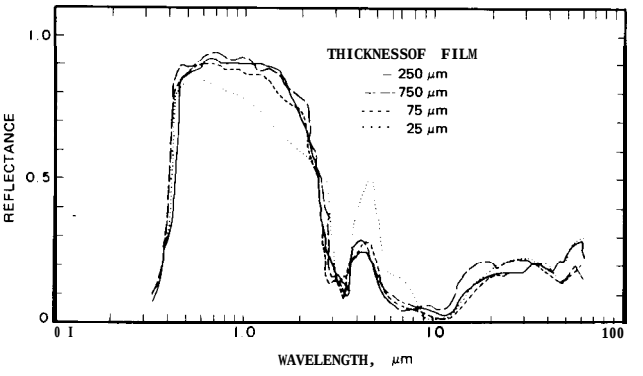

(b)

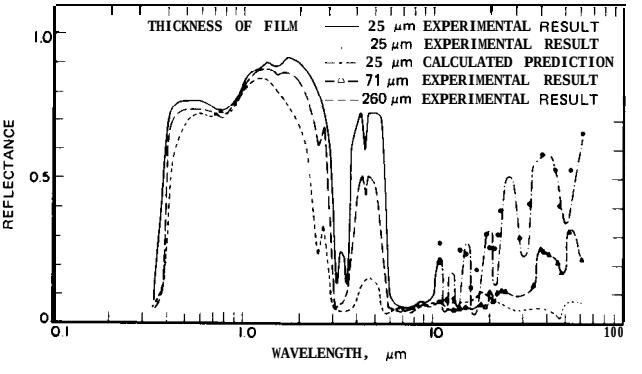

(c)

Figure6 Spectral directional reflectance ($\theta \doteq 0$) for a black, white, and clear paint. (*a*) Reflectance of Cat-a-lac epoxy black paint on aluminum substrate. (b) Reflectance of PV-100 silicone-alkyd white paint on aluminum substrate. (*c*) Reflectance of Laminar X-500 polyurethane clear film on aluminum substrate. From Edwards and Hall [46].

© 1983 Hemisphere Publishing Corporation

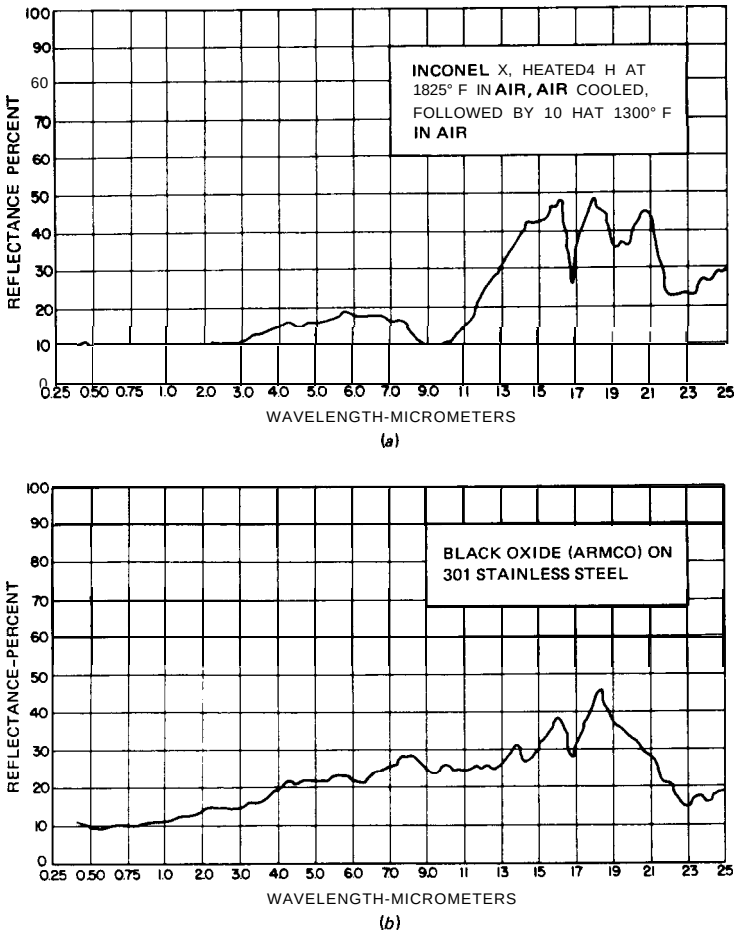

Figure 7 Spectral directional reflectance ($\theta \doteq 0$) of two black oxidized metals. (a) Near-normal spectral reflectance of oxidized Inconel X. (b) Near-normal spectral reflectance of oxidized stainless steel. Note change of wavelength scale at 1 and at 7 μm. From Edwards and Roddick[45].

clouds of particles, one that aids in inferring particle sizes.

I. Thermal radiation characteristics in thermal design

The designer generally wants either to promote or suppress thermal radiation in a given spectral region. The spectral requirements are sometimes different in different spectral regions. If the spectral regions are classified crudely as long wavelengths and short wavelengths, there are four combinations of surface properties, one of which will be often chosen as the main surface finish. Occasionally one of the others will be used in a striped or chessboard pattern to balance the design requirements. The four basic finishes are illustrated in Fig. 5. The flat black absorber is achieved with black paint, black glass enamel, and heavy black oxide or dyed anodized coatings, as shown in Figs. 6*a*, 7, and 8. It is used where high emissivity is desired in the long wavelengths and high solar absorptivity in the short wavelengths is no handicap. The flat reflector is achieved with bare metals and leafing aluminum paint. The metal is at times applied by electroplating or vacuum evaporation. If high specularity is required, a glossy enamel or plastic subcoating may be applied first. For high-temperature applications or corrosive environments, layers to act as barriers to foreign metal and oxygen diffusion may be employed as under and/or over coats. Aluminum foil and aluminized plastic film are used for low temperatures. The flat reflector provides a low emissivity and high reflectivity for both long and short wavelengths. Because the characteristics are the same in the long and short wavelengths, both the flat absorber and flat reflector are said to be nonselective.

The selective black solar absorber has a high absorptivity in the short wavelengths and simultaneously a low emissivity in the long wavelengths. A metal surface with semiconductor coating, particularly a thin one with a gradient in the index of refraction, serves.

© 1983 Hemisphere Publishing Corporation

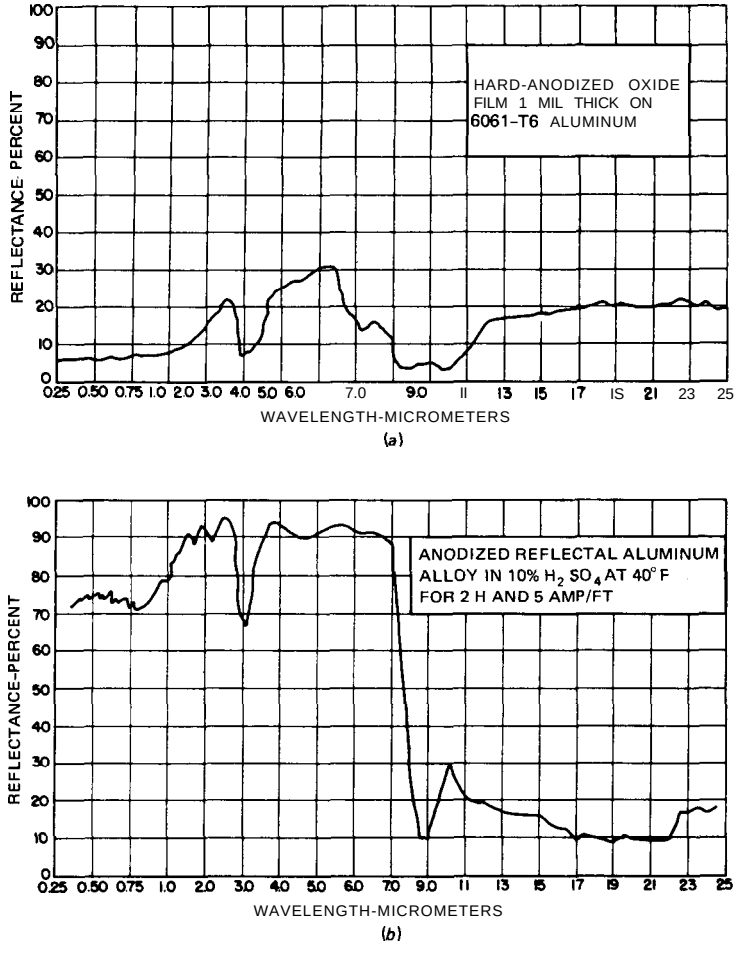

Figure 8 Spectral directional reflectance ($\theta \doteq 0$) of hard and soft anodized aluminum. (a) Near-normal spectral reflectance of hard-anodized aluminum. (b) Near-normal spectral reflectance of soft-anodized aluminum. Note change of wavelength scale at 1 and at 7pm. From Edwards and Roddick [45].

Thin copper or nickel or chrome oxide layers formed by chemical dip or electrochemical finishing are used on copper plated steel, as shown in Fig. 9. Spray-on and baked finishes can be applied to aluminum, and vacuum-deposited films are used. Such surfaces are used for solar heat collectors or to maintain warm temperatures for space vehicles exploring the outer reaches of the solar system.

The solar reflector has a high reflectivity in the short wavelengths and a high emissivity in the long wavelengths. White paint, clear lacquered aluminum, and soft-anodized aluminum, second-surface mirrors, flame or plasma sprayed ceramic coatings, ceramics, and fired enamels are examples in Figs. 6*b*, *c*, 8*b*, 10, and 11. The finish is used to emit unwanted heat and simultaneously reflect unwanted solar energy. The tops of vehicles and structures and instrument cases exposed to solar heating are often painted white.

© 1983 Hemisphere Publishing Corporation

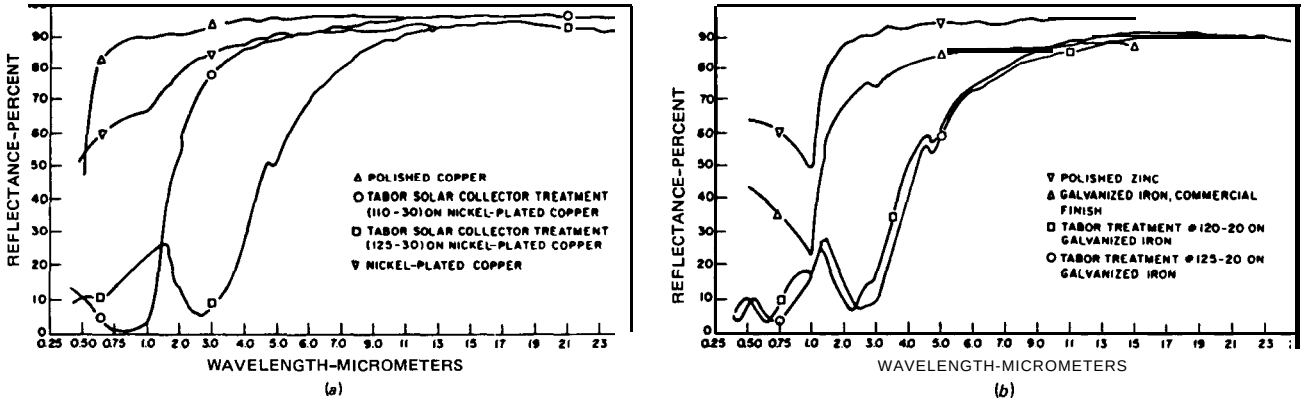

Figure 9 Spectral directional reflectance ($\theta \doteq 0$) of some selective black surfaces. (*a*) Spectral reflectance of Tabor selective blacks on copper. (b) Spectral reflectance of Tabor selective blacks on zinc. Note change of wavelength scale at 1 and at 7 pm. From Edwards [50].

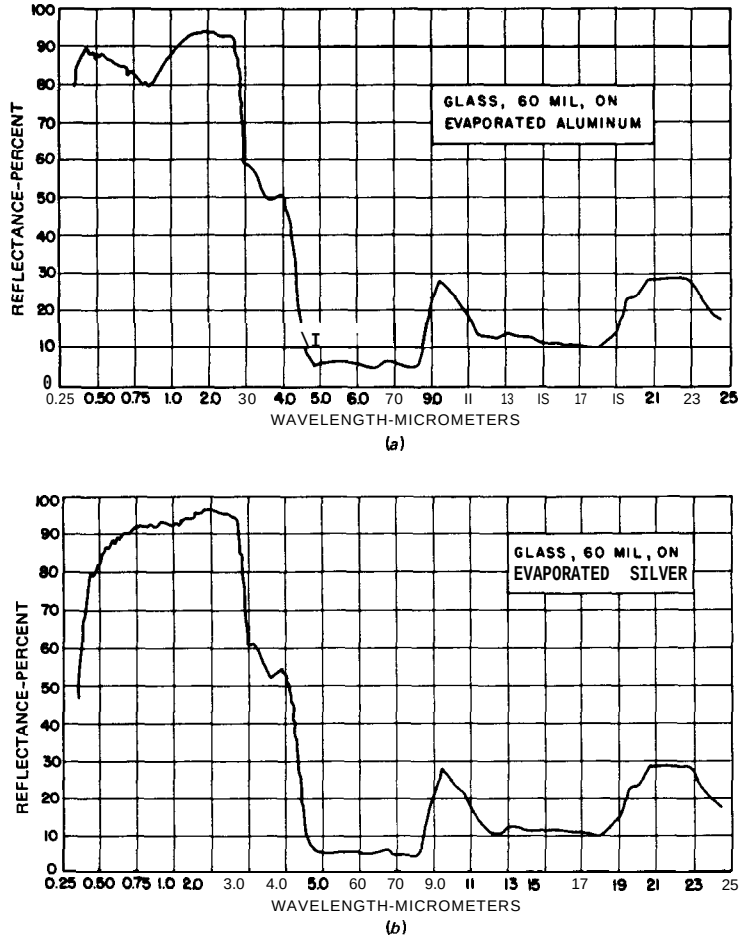

Figure 10 Spectral directional reflectance ($\theta \doteq 0$) of two second-surface mirrors. (*a*) Near-normal spectral reflectance of glass on evaporated aluminum. (*b*) Near-normal spectral reflectance of glass on evaporated silver. Note change of wavelength scale at 1 and at 7 μm. From Edwards and Roddick [45].

© 1983 Hemisphere Publishing Corporation

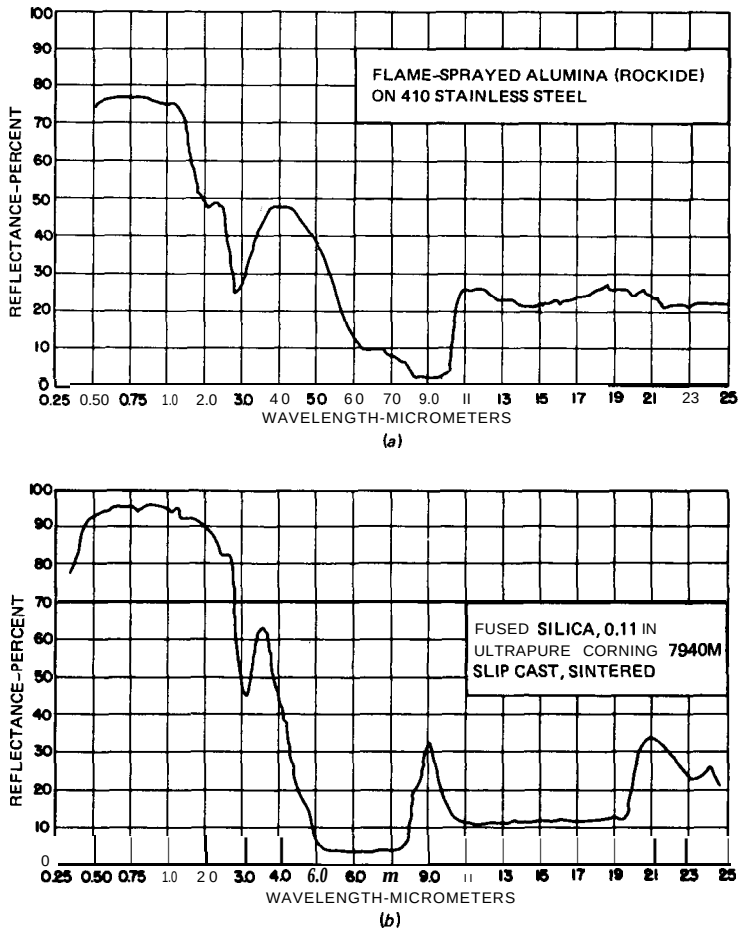

Figure 11 Spectral directional reflectance ($\theta \doteq 0$) of alumina and silica ceramics. (*a*) Near-normal spectral reflectance of flame-sprayed alumina. (b) Near-normal spectral reflectance of fused silica. Note change of wavelength scale at 1 and at 7 μm. From Edwards and Roddick [45].

Nomenclature for Section 2.9.2 appears at the end of Section 2.9.8.

BIBLIOGRAPHY FOR SECTION 2.9.2

Definitions of surface characteristics

1. Dunkle, R. V., Thermal Radiation Characteristics of Surfaces, ***in Fundamental Research in Heat Transfer,*** ed. J. A. Clark, pp. 1-31, Macmillan, New York, 1963.
2. Edwards, D. K., Radiative Transfer Characteristics of Materials, ***J. Heat Transfer,*** vol. 91, pp. 1-15, 1969.
3. Nicodemus, F. E., Directional Reflectance and Emissivity of an Opaque Surface, *Appl. Opt.*, vol. 4, pp. 767-773, 1965.

Measurement techniques

Review papers

4. Dunn, S. T., Richmond, J. C., and Parmer, J. F., Survey of Infrared Measurement Techniques, and Computational Methods in Radiant Heat Transfer, ***J. Spacecraft Rockets, vol. 3,*** pp. 961-975, 1966.
5. Edwards, D. K., Thermal Radiation Measurements, in ***Measurements in Heat Transfer,*** ed. E. R. G. Eckert and R. J. Goldstein, pp. 425-473, Hemisphere, Washington, D.C., 1976.

Total hemispherical emissivity

6. Nelson, K. E., and Bevans, J. T., Errors of the Calorimetric Method of Total Emittance Measurement, in ***Measurement of Thermal Radiation Properties of Solids,*** pp. 55-63, NASA SP-31, 1963.

© 1983 Hemisphere Publishing Corporation

Total directional emissivity

7. Snyder, N. W., Gier, J. T., and Dunkle, R. V., Total Normal Emissivity Measurements on Aircraft Materials Between 100 and 800°F, *Trans., ASME*, vol. 77, pp. 1011–1919, 1955.

Directional reflectance

Integrating spheres

8. McNicholas, H. J., Absolute Methods in Reflectometry, *Natl. Bur. Stds. J. Res.*, vol. 1, pp. 29-73, 1928.
9. Tingwaldt, C. P., Über die Messung von Reflexion, Durchlassigkeit und Absorption an Prufkorpern beliebiger Form in der Ulbrichtschen Kugel, ***Oprik,*** vol. 9, pp. 323-332, 1952.
10. Toporets, A. S., Study of Diffuse Reflection from Powders Under Diffuse Illumination, ***Opt. Spectrosc.,*** vol. 7, pp. 471–473, 1959.
11. Edwards, D. K., Gier, J. T., Nelson, K. E., and Roddick, R. D., Integrating Sphere for Imperfectly Diffuse Samples, ***J. Opt. Soc. Am.***, vol. 51, pp. 1279-1288, 1961.

Heated cavities

12. Gier, J. T., Dunkle, R. V., and Bevans, J. T., Measurement of Absolute Spectral Reflectivity from 1.0 to 15 Microns, ***J. Opt. Soc. Am.,*** vol. 44, pp. 558-562, 1954.
13. Tingwaldt, C. P., Measurement of Spectral Sensitivity in the Infrared, ***Trans. Conf. on the Use of Solar Energy,*** vol. III, pt. 1, sec. A, pp. 57–61, 1955.
14. Dunkle, R. V., Spectral Reflectance Measurements, ***in Surface Effects on Spacecraft Materials,*** ed. F. J. Clauss, pp. 117-137, Wiley, New York, 1960.
15. Dunkle, R. V., Edwards, D. K., Gier, J. T., Nelson, K. E., and Roddick, R. D., Heated Cavity Reflectometer for Angular Reflectance Measurements, Progress ***in International Research on Thermodynamic and Transport Properties,*** pp. 541-562, ASME, New York, 1962.
16. Nelson, K. E., Luedke, E. E., and Bevans, J. T., A Device for the Rapid Measurement of Total Emittance (Reflectance), ***J. Spacecraft Rockets, vol. 3,*** pp. 758-760, 1966.

Hemispherical mirrors

17. Birkebak, R. C., Hartnett, J. P., and Eckert, E. R. G., Measurement of Radiation Properties of Solid Materials, ***Progress in International Research on Thermodynamic and Transport Properties,*** pp. 563-574, ASME, New York, 1962.
18. Janssen, J. E., and Torberg, R. H., Measurement of Spectral Reflectance Using an Integrating Hemisphere, ***Measurement of Thermal Radiation Properties of Solids,*** pp. 169-182, NASA SP-31, 1963.
19. White, J. U., New Method for Measuring Diffuse Reflectance in the Infrared, ***J. Opt. Soc. Am.,*** vol. 54, pp. 1332-1337, 1964.
20. Neher, R. T., and Edwards, D. K., Far Infrared Reflectometer for Imperfectly Diffuse Specimens, ***Appl. Opt.,*** vol. 4, pp. 775-780, 1965.
21. Edwards, D. K., Comments on Reciprocal-Mode 2π-Steradian Reflectometers, *Appl. Opt.,* vol. 5, pp. 175-176, 1966.
22. Dunn, S. T., Richmond, J. C., and Wielbelt, J. A., Ellipsoidal Mirror Reflectometer, ***J. Opt. Soc. Am.,*** vol. 55, p. 604, 1965.
23. Wood, B. E., Pipes, J. G., Smith, A. M., and Roux, J. A,, Hemi-Ellipsoidal Mirror Infrared Reflectometer: Development and Operation, *Appl. Opt.,* vol. 15, pp. 940-950, 1976.

Bidirectional reflectance

Total bidirectional reflectance

24. Schmidt, E., and Eckert, E. R. G., Über die Richtungsverteilung der Warmestrahlung von Oberflachen, ***Forsh. Geb.*** *Ingenieurwes.*, vol. 6, p. 175, 1935.
25. Eckert, E. R. G., Messung der Reflexion von Warmestrahlen an Technischen Oberflachen, ***Forsh. Geb. Zngenieurwes., vol. 7,*** pp. 265–270, 1936.
26. Munch, B., Die Richtungsverteilung bei der Reflexion von Warmestrahlung und ihr Einfluss auf die Warmeubertragung, *Mitteilungen* ***ausder*** *Institut* ***fir*** *Thermodynamik* ***und Verbrennungsmotorenbau,*** no. 16, Verlag Leeman, Zurich, 1955.

Spectral bidirectional reflectance

27. Birkebak, R. C., and Eckert, E. R. G., Effects of Roughness of Metal Surfaces on Angular Distribution of Monochromatic Reflected Radiation, ***J. Heat Transfer,*** vol. 87, pp. 85-94, 1965.
28. Torrance, K. E., and Sparrow, E. M., Off-Specular Peaks in the Directional Distribution of Reflected Thermal Radiation, ***J. Heat Transfer,*** vol. 88, pp. 223-230, 1966.
29. Herold, L. M., and Edwards, D. K., Bidirectional Characteristics of Rough, Sintered-Metals, and Wire-Screen Surface ***Systems, AIAA J.***, vol. 4, pp. 1802–1810, 1966.
30. Birkebak, R. C., Thermal Radiation Properties of Lunar Materials from the Apollo Missions, ***Adv. Heat Transfer,*** vol. 10, pp. l-37, 1974.
3 1. Smith, A. M., Cryofrost Bidirectional Reflectance, *Appl. Cryogenic Tech., vol. 5,* pp. 284-304, 1973.
32. Wood, B. E., and Smith, A. M., An Investigation of Bidirectional Reflection from Infrared Diffuser Surfaces, ***Prog. Astronaut. Aeronaut., vol. 49,*** pp. 67-84, 1976.

© 1983 Hemisphere Publishing Corporation

Specular reflectance

33. Bennett, H. E., and Koehler, W. F., Precision Measurement of Absolute Specular Reflectance with Minimized Systematic Errors, *J. Opt. Soc. Am.,* vol. 50, pp. l-6, 1960.

Electromagnetic theory and polarization

Maxwell equations

34. Stratton, J. A., ***Electromagnetic Theory***, McGraw-Hill, New York, 1941.

Useful approximations

35. Snyder, N. W., Radiation in Metals, ***Trans. ASME***, vol. 76, pp. 541-548, 1954.
36. Dunkle, R. V., Emissivity and Interreflection Relationships for Infinite Parallel Specular Surfaces, ***Symp. Thermal Radiation of*** Solids, pp. 39–44, NASA SP-55, 1965.
37. Seban, R. A., The Emissivity of Transition Metals in the Infrared, *J. Heat Transfer,* vol. 87, pp. 173-176, 1965.
38. Edwards, D. K., and Bayardde-Volo, N., Useful Approximations for the Spectral and Total Emissivity of Smooth Bare Metals, ***Advances in Thermophysical Properties at Extreme Temperatures and*** Pressures, pp. 174-178, ASME, New York, 1965.
39. Toscano, W. M., and Cravalho, E. G., Thermal Radiative Properties of the Noble Metals at Cryogenic Temperatures, *J. Heat Transfer,* vol. 98, pp. 438-445, 1976.

Polarization

40. Edwards, D. K., and Bevans, J. T., Effect of Polarization on Spacecraft Radiation Heat Transfer, ***AIAA J.***, vol. 3, pp. 1323-1329, 1965.
41. Edwards, D. K., and Tobin, R. D., Effect of Polarization on Radiant Heat Transfer through Long Passages, *J. Heat Transfer,* vol. 89, pp. 132-138, 1967.
42. Amar, R. C., and Edwards, D. K., Reflection and Transmission by Rough-Walled Passages, ***Progr. Astronaut. Aeronaut., vol.*** 31, pp. 475–495, 1973.

Thermal design

43. Camack, W. G., and Edwards, D. K., Effect of Surface Thermal Radiation Characteristics on the Temperature-Control Problem in Satellites, in ***Surface Effects on Spacecraft Materials,*** ed. F. J. Clauss, pp. 3-54, Wiley, New York, 1960.
44. Kreith, F., ***Radiation Heat Transfer,*** International Textbook, Scranton, Pa., 1962.
45. Edwards, D. K., and Roddick, R. D., Spectral and Directional Thermal Radiation Characteristics of Surfaces for Heat Rejection by Radiation,Prog. ***Aeronaut. Astronaut.,*** vol. 11, pp. 427–446, 1963.
46. Edwards, D. K., and Hall, W. M., Far Infrared Reflectance of Spacecraft Coatings, ***Prog. Astronaut. Aeronaut.,*** vol. 18, pp. 3–19, 1966.
47. Marshall, K. N., and Breuch, R. A., Optical Solar Reflector: A Highly Stable Low α_S/ϵ Spacecraft Thermal Control Surface, *J. Spacecraft Rockets,* vol. 5, pp. 1051–1056, 1968.
48. Smith, A. M., Theory of Radiative Degradation (an Analytical Study of a Solar Degradation Model for Thermal Control Materials and Some Ramifications for Accelerated Solar Radiation Testing), ***Prog. Astronaut. Aeronaut., vol.*** 21, pp. 639-663, 1969.
49. Kurland, R. M., Brown, G. L., Thomasson, J. F., Bevans, J. T., et al., Properties of Metallized Flexible Materials in the Space Environment, *SAMSO Rept.* TR 78-3 1, 1978.
50. Edwards, D. K., Solar *Collector Design,* rev. ed., Franklin Institute, Philadelphia, 1978.
5 1. Edwards, D. K., Mills, A. F., and Denny, V. E., ***Transfer Processes,*** 2d ed., Hemisphere, Washington, D.C., 1979.

© 1983 Hemisphere Publishing Corporation

2.9.3

Radiation transfer between perfectly diffuse surfaces

D. K. Edwards

A. Shape factors

Recall Eq. 2.9.1(22), which should be remembered as being the most important one in Sec. 2.9.1:

$$d^3 q^{\pm} = I_{\nu}' \cos\theta \, d^2\Omega \, d\nu \tag{1}$$

The equation holds for either the radiosity q^{+} or the irradiation q^{-}, hence the ± notation. This fact has an important result for the shape factor: The shape factor has two equally valid and equally important meanings. (1) The shape factor F_{i-j} is the fraction of the radiated power leaving diffuse surface i that is intercepted by surface j. (2) The shape factor F_{i-j} is the fractional weight to be given the radiosity of diffuse surface j in summing up the irradiation upon surface i, or, put another way, it is the fraction of the surrounds of surface i taken up by surface j.

In what immediately follows, the equations will be written without v or λ subscripts to denote a spectral quantity, but inspection of Eqs. 2.9.1(22) and 2.9.1(23) shows that the same expression holds for either spectral or total quantities.

Consider the first meaning of the shape factor. The power leaving differential surface i is the radiosity times the area,

$$d^4 \dot{Q}_i^{+} = d^2 A_i \, d^2 q_i^{+} = d^2 A_i I_i^{+} \cos\theta_i \, d^2\Omega$$

But for a diffuse surface, $I_i^{+} = q_i^{+}/\pi$ [Eq. 2.9.1(10)]. The power intercepted by finite surface j is then

$$d^2 \dot{Q}_{i-j} = d^2 A_i q_i^{+} \frac{1}{\pi} \iint_{\Omega_{i-j}} \cos\theta_i \, d^2\Omega$$

whereas all the power leaving diffuse surface i is

$$d^2 \dot{Q}_{i-j} = d^2 A_i q_i^{+} \frac{1}{\pi} \iint_{\Omega_{i-j}=0}^{2\pi} \cos\theta_i \, d^2\Omega = d^2 A_i q_i^{+}$$

Hence the fraction of all the power radiated by diffuse, differential surface i and intercepted by surface j is

$$F_{i-j} = \frac{1}{\pi} \iint_{\Omega_{i-j}} \cos\theta_i \, d^2\Omega \tag{2}$$

There are a number of devices described in the literature+ that permit the integral to be obtained graphically or numerically.

The above form of the shape factor definition is particularly convenient when the limits of integration are simple. When the normal to differential surface i coincides with the axis of an axisymmetric surface (such as a disk or sphere), polar-azimuthal angles are used and

$$F_{i-j} = \frac{1}{\pi} \int_0^{2\pi} \int_0^{\theta_{\max}} \cos\theta \sin\theta \, d\theta \, d\phi = \sin^2\theta_{\max} \tag{3}$$

When the normal to differential surface i is perpendicular to infinite cylinder j (circular or not), base-axial angles are used and

†See, for example, R. Farrell, Determination of Configuration Factors of Irregular Shape, *J. Heat Transfer,* vol. 98, pp. 311-313, 1976.

© 1983 Hemisphere 1 blishing Corporation

$$F_{i-j} = \frac{1}{\pi} \int_{\gamma_2}^{\gamma_2} \int_{-\pi/2}^{+\pi/2} \cos^2\beta \, d\beta \cos\gamma \, d\gamma$$

$$= \frac{1}{2} (\sin\gamma_2 - \sin\gamma_1) \tag{4}$$

Introduction of the definition of $d^2\Omega$, Eq. 2.9.1(4), into Eq. (2) gives

$$F_{i-j} = \frac{1}{\pi} \iint_{A_j} \frac{\cos\theta_i \cos\theta_j}{R_{i-j}^2} d^2A_j$$

If area A_i is not infinitesimal, one wants the average shape factor for the finite area. Hence

$$F_{i-j} = \frac{1}{A_i} \iint_{A_i} \iint_{A_j} \frac{\cos\theta_i \cos\theta_j}{\pi R_{i-j}^2} d^2A_j \, d^2A_i \tag{5}$$

This form of the shape factor definition is general.

An important feature of Eq. (5) is shape factor reciprocity,

$$A_i F_{i-j} = A_j F_{j-i} \tag{6}$$

which follows from the symmetry in the double integral. Furthermore, it is clear from the definition that

$$\sum_{j=1}^{N} F_{i-j} = 1 \tag{7}$$

The second meaning of the shape factor can be arrived at by writing Eq. (1)-after integration over ν or with ν subscripts-in the form

$$d^2q_i^- = I_i^- \cos\theta_i \, d^2\Omega$$

But I_i^- is I_j^+ inside of solid angle Ω_{ij} when the fluid is diathermanous. Accordingly,

$$d^2q_i^- = q_j^+ \frac{1}{\pi} \cos\theta_i \, d^2\Omega$$

With the very same definition of the shape factor F_{i-j} appearing in Eq. (2) for differential A_i, or in Eq. (5) for finite A_i, one can write

$$q_i^- = \sum_{j=1}^{N} q_j^+ F_{i-j} \tag{8}$$

Collections of shape factors for elementary geometries have been compiled in a number of works, including [1-4, 7], and a number of computer programs have been written, including [5,6]. In this era of computing machines and programmable calculators, the older graphic representations assume less importance, and those closed-form solutions available, once awkward to use in the past era of mathematical tables and slide rules, are now easily used. Table 1 lists three of the more important ones.

As an example, consider an inert gas-filled furnace with floor 4 by 4 m and ceiling 2 m high. Number the floor 1, the side walls 2, 3, 4, and 5, and the top 6. Sighting into the furnace with a radiometer or pyrometer allows one to observe directly the radiosities of the walls q_1^+, q_2^+, and so on. The radiometer may be calibrated to indicate an apparent temperature $T_{1,ap} = (q_1^+/C_s)^{1/4}$, in which case $q_1^+ = C_s T_{1,ap}^4$, but that is no matter. The following results are observed after many sightings are averaged:

i	$T_{i,ap}$, K	q_i^+, W/m²
1	500	3 544
2	1500	287 000
3	1200	117 600
4	1 200	117 600
5	1 200	117 600
6	1 000	56 700

What is the net radiant heat flux into the floor?

The net ***flux into*** the floor is denoted $-q_1$ to be consistent with the sign convention to be followed later. It is, obviously,

$$-q_1 = q_1^- - q_1^+$$

The quantity q_1^+ is known; the irradiation q_1^- is needed. It is given by Eq. (8):

$$q_1^- = q_1^+F_{1-1} + q_2^+F_{1-2} + q_3^+F_{1-3} + q_4^+F_{1-4} + q_5^+F_{1-5} + q_6^+F_{1-6}$$

All that is needed are the shape factors F_{i-j}. Because no solid angle-cosine product is subtended by surface 1 itself from any point on surface 1, F_{1-1} is clearly zero; the surface cannot see itself. Table 1 gives one relation for F_{i-j} where j = 2, 3, 4, or 5, and another for F_{1-6}. For the former,

$$F_{1-2} = \frac{1}{4\pi X} \left[4X \tan^{-1} \left(\frac{1}{X} \right) + \ldots \right] = 0.146\,19$$

where X = 4/4 = 1 and Y = 2/4 = 1/2. For the latter,

$$F_{1-6} = \frac{2}{\pi XY} \left[\ln \sqrt{\frac{(1+X^2)(1+Y^2)}{1+X^2+Y^2}} + \ldots \right]$$

$$= 0.415\,25$$

where X = 4/2 = 2 and Y = 4/2 = 2. As a check, we note that Eq. (7) is satisfied.

$$F_{1-1} + F_{1-2} + \ldots F_{1-6} = 4(0.146\,19) + 0.415\,25$$

$$= 1.00$$

© 1983 Hemisphere Publishing Corporation

Table 1 Closed-form expressions of selected shape factors

Geometry	Expression
1. Opposite rectangles 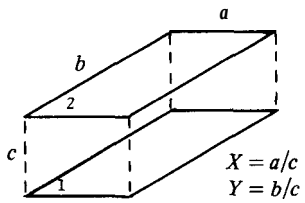	$F_{1-2} = \frac{2}{\pi XY}\left[\ln\sqrt{\frac{(1+X^2)(1+Y^2)}{1+X^2+Y^2}} + X\sqrt{1+Y^2}\tan^{-1}\frac{X}{\sqrt{1+Y^2}} + Y\sqrt{1+X^2}\tan^{-1}\frac{Y}{\sqrt{1+X^2}} - X\tan^{-1}X - Y\tan^{-1}Y\right]$
2. Adjacent rectangles 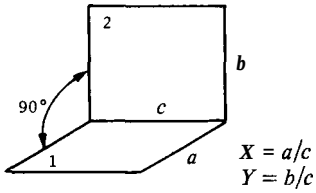	$F_{1-2} = \frac{1}{4\pi X}\left[4X\tan^{-1}\frac{1}{X} + 4Y\tan^{-1}\frac{1}{Y} - 4\sqrt{X^2+Y^2}\tan^{-1}\frac{1}{\sqrt{X^2+Y^2}} + \ln\frac{(1+X^2)(1+Y^2)}{1+X^2+Y^2} + X^2\ln\frac{X^2(1+X^2+Y^2)}{(1+X^2)(X^2+Y^2)} + Y^2\ln\frac{Y^2(1+X^2+Y^2)}{(1+Y^2)(X^2+Y^2)}\right]$
3. Parallel, coaxial circles 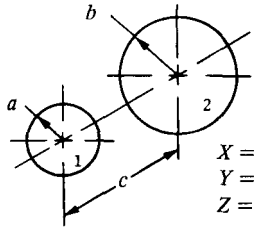	$F_{1-2} = \frac{1}{2}(X - \sqrt{X^2 - 4Y^2Z^2})$

It was not necessary in view of Eq. (7) to have calculated F_{1-2} from the formula in the table; from the value of F_{1-6}, the equation, and the symmetry in the problem, the result could have been obtained; but the check helps guard against errors. To complete the example,

$$q_1^- = (0.146\,19)(287\,000) + (3)(0.14619)(117\,600) + (0.415\,25)(56\,700) = 117\,070\ \text{W/m}^2$$

$$-q_1 = 117\,070 - 3\,540 = 113\,500\ \text{W/m}^2$$

$$-\dot{Q}_1 = -q_1 A_1 = (113\,500)(16) = 1\,816\ \text{kW}$$

The example shows the utility of the shape factor as a weighting factor in Eq. (8) and illustrates the use of Table 1 and Eq. (7).

The value of the relations shown in Table 1 is greatly increased by consideration of shape factor algebra. Denote $A_i F_{i-j}$ in Eqs. (5) and (6) as

$$G_{i-j} = G_{j-i} \equiv A_i F_{i-j} = \iint_{A_i}\iint_{A_j} \frac{\cos\theta_i \cos\theta_j}{\pi R_{i-j}^2} \, dA_j \, dA_i \tag{9}$$

Suppose that area A_j consists of two subareas A_k and A_l. Let the subscript $(k + l)$ denote the total surface j, and let K_{i-j} denote the shape factor kernel,

$$K_{i-j} = \frac{\cos\theta_i \cos\theta_j}{\pi R_{i-j}^2}$$

Then

$$G_{i-(k+l)} = \iint_{A_i}\left(\iint_{A_k} K_{i-k}\, dA_k + \iint_{A_l} K_{i-l}\, dA_l\right) dA_i = G_{i-k} + G_{i-l} \tag{10}$$

This relation makes it possible to find $A_1 F_{1-3}$, illustrated in Fig. 1. A programmable calculator having a

© 1983 Hemisphere Publishing Corporation

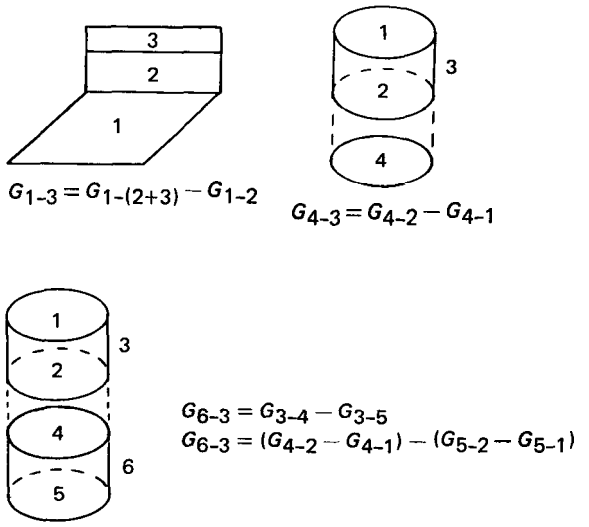

Figure 1 Simple cases of shape factor algebra.

routine to find G_{i-k} can easily be used to find $G_{i-(k+l)}$ and G_{i-k} and then by subtraction G_{i-l}.

Figure 2 shows a somewhat more involved situation. One must recognize from symmetry that $G_{1-3} = G_{4-2}$; then the rest is easy. The fact that G_{1-3} equals G_{4-2} is obvious for the opposed rectangles shown. That G_{1-3} equals G_{4-2} for adjacent unequal rectangles

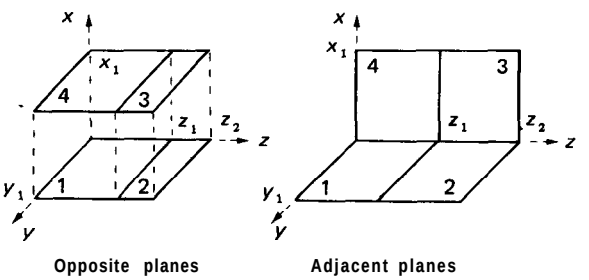

Area Number Notation:

$$G_{1-3} = \tfrac{1}{2}[G_{(1+2)-(3+4)} - G_{1-4} - G_{2-3}\,1$$

x-y-z Limit Notation:

$$G^{(2)}(x_1, y_1, z_1, z_2) = \tfrac{1}{2}[G^{(1)}(x_1, y_1, z_2) - G^{(1)}(x_1, y_1, z_1) - G^{(1)}(x_1, y_1, z_2 - z_1)]$$

where for opposite rectangles, Table 1, item 1,

$$G^{(1)}(c, a, b) = abF_{1-2}(X, Y) \qquad X = \frac{a}{c} \qquad Y = \frac{b}{c}$$

and for adjacent rectangles, Table 1, item 2,

$$G^{(1)}(b, a, c) = acF_{1-2}(X, Y) \qquad X = \frac{a}{c} \qquad Y = \frac{b}{c}$$

Figure 2 Shape factor algebra for offset rectangles with shared z limit.

is not so obvious. However, one way to proceed to show the relation is to divide the rectangles into n equal strips, numbered from left to right, so that the right-hand edge of the mth strip nearly coincides with the line dividing large area, 1 from large area 2. In the limit as n becomes large; the coincidence becomes exact. Starting with an adjacent pair of equal strips and successively adding others allows one to prove a lemma that

$$G_{1-[2'+3'+\ldots+k']} - G_{[2+3+\ldots+k]-1'}$$

where the unprimed numbers here refer to the small strips in one plane and the primed ones to the other. With the aid of this lemma, the theorem

$$G_{[1+2+\ldots+m]-[(m+1)'+\ldots+n']} = G_{[(m+1)+\ldots+n]-[1'+2'+\ldots+m']}$$

is proved by adding $G_{1-[2'+\ldots+n']}$ to $G_{2-[3'+\ldots+n']}$, cancelling the $G_{1-2'}$ and $G_{2'-1}$ terms and continuing the addition until the ***m*th** term is included.

Figure 3 shows two cases of more general interest.

Shape factors between long parallel surfaces such as nuclear fuel rods or boiler tubes are easily obtained via Hottel s string rule[3]. The rule is that the shape factor from (circular or noncircular) cylinder 1 of length $L \to \infty$ and perimeter P_1 to parallel (circular or noncircular) cylinder 2 of length $L \to \infty$ is the sum of the lengths of diagonal strings D_1 and D_2 minus the lateral strings L_1 and L_2 divided by $2P_1$,

$$F_{1-2} = \frac{D_1 + D_2 - L_1 - L_2}{2P_1} \tag{11}$$

The diagonals and laterals are measured in the plane of the cross section as shown in Fig. 4. The diagonals are the crossed strings between the extremities of the two surfaces, and the laterals are the uncrossed ones. The strings are understood to be pulled tight, and may lie along the surface of the body as necessary. For example, if surface 1 is the ***whole*** cylinder ***ABCDEA'*** and surface ***2*** is the ***half*** cylinder ***HIJF,*** then the extremities of 1 are understood to be ***A*** and ***A'*** and those of surface 2 are ***F*** and ***H.*** The diagonals are ***ABCIH*** and ***A'EDJF,*** and the laterals ***ABF*** and ***A'EH.*** The perimeter P_1 is ***ABCDEA',*** and P_2 is ***HIJF.***

B. Radiosity-irradiation formulations

The example in Sec. A illustrating the use of shape factors took values of radiosity to be known from direct measurements. If it is not possible or convenient to make such measurements, or if one wants a model to investigate the results of design changes, it is possible to calculate the radiosity, provided that the wall tem-

© 1983 Hemisphere Publishing Corporation

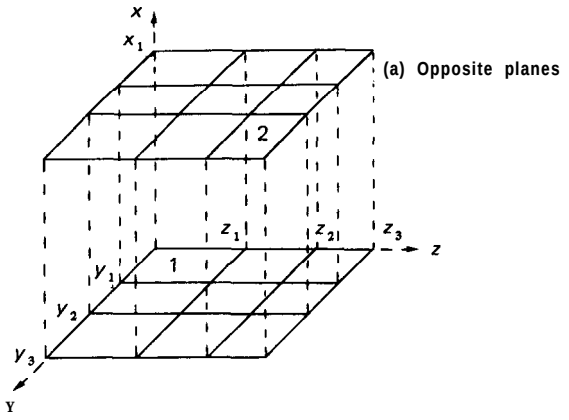

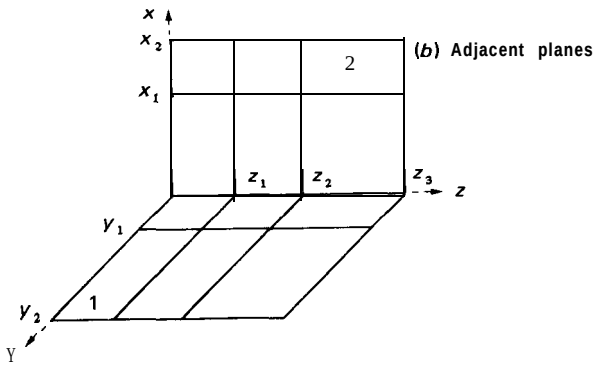

$$G_{1-2} = G^{(5)}(x_1, y_1, y_2, y_3, z_1, z_2, z_3)$$
$$= G^{(4)}(x_1, y_1, y_3, z_1, z_2, z_3) - G^{(4)}(x_1, y_1, y_2, z_1, z_2, z_3)$$
$$G^{(4)}(x_1, y_1, y_2, z_1, z_2, z_3) = G^{(3)}(x_1, y_1, y_2, z_1, z_3) - G^{(3)}(x_1, y_1, y_2, z_1, z_2)$$
$$G^{(3)}(x_1, y_1, y_2, z_1, z_2) = \tfrac{1}{2}[G^{(2)}(x_1, y_2, z_1, z_2) - G^{(2)}(x_1, y_1, z_1, z_2) - G^{(2)}(x_1, y_2 - y_1, z_1, z_2)]$$
$$G^{(2)}(x_1, y_1, z_1, z_2) = \text{See Fig. 2}$$

$$G_{1-2} = G^{(5)}(x_1, x_2, y_1, y_2, z_1, z_2, z_3)$$
$$= G^{(4)}(x_1, x_2, y_1, y_2, z_1, z_3) - G^{(4)}(x_1, x_2, y_1, y_2, z_1, z_2)$$
$$G^{(4)}(x_1, x_2, y_1, y_2, z_1, z_2) = G^{(3)}(x_2, y_1, y_2, z_1, z_2) - G^{(3)}(x_1, y_1, y_2, z_1, z_2)$$
$$G^{(3)}(x_1, y_1, y_2, z_1, z_2) = G^{(2)}(x_1, y_2, z_1, z_2) - G^{(2)}(x_1, y_1, z_1, z_2)$$
$$G^{(2)}(x_1, y_1, z_1, z_2) = \text{See Fig. 2}$$

Figure 3 Shape factor algebra for rectangles in opposite and adjacent planes.

perature or heat flux (or a relation between them) is known. In what follows, the ν or λ subscripts continue to be left off for convenience, with the understanding that the equations hold not only for spectral values in general, but also for total values when the radiation characteristics are approximated as gray. The surfaces are assumed to be perfectly diffuse and opaque.

The engineering radiation transfer problem is formulated for an enclosure of n discrete surfaces; if necessary, an imaginary black surface at ambient temperature is used to complete the enclosure, when the surroundings outside the otherwise incomplete enclosure constitute a hohlraum at the ambient temperature. In some cases (notably the hollow sphere, the hollow cylinder, or infinite parallel plates), a useful exact formulation is achieved by passing from the discrete (and therefore approximate) surface representation with sums of finite terms to a continuous representation with integrals of differential terms. One could commence with the exact integral formulation and pass to the finite one. To be brief, we commence with and confine ourselves to the discrete surface case.

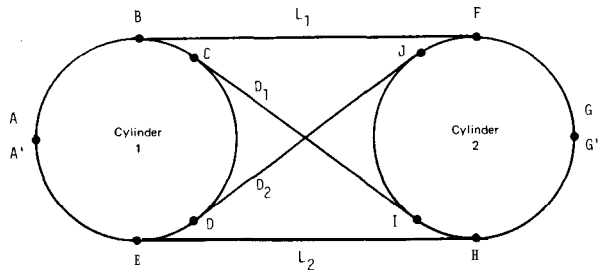

Figure 4 The string rule diagonals and laterals.

The relations necessary to formulate the enclosure problem are few in number. First is simply the net outward flux relation Eq. 2.9.1(3), here rewritten for the ith surface :

$$q_i = q_i^+ - q_i^- \tag{12}$$

Second is the definition of radiosity for a diffuse opaque surface, the sum of emitted plus reflected radiation,

$$q_i^+ = \epsilon_i B_i + \rho_i q_i^- \tag{13}$$

where B_i is used to stand for $q_b^+(T_i) = \pi I_b^+(T_i)$ to simplify notation. Finally, there is the introduction of the shape factor through Eq. (8):

$$q_i^- = \sum_{j=1}^{n} F_{i-j} q_j^+ \tag{14}$$

Of course, with these three equations one has a few auxiliary relations. For the near-equilibrium-state, opaque surface there holds:

$$\rho_i = 1 - \alpha_i = 1 - \epsilon_i \tag{15}$$

The shape factor relations also are pertinent:

$$A_i F_{i-j} = A_j F_{j-i} \tag{16}$$

© 1983 Hemisphere Publishing Corporation

$$\sum_{j=1}^{n} F_{i-j} = 1 \tag{17}$$

Whereas only three equations, Eqs. (12)-(14), describe the enclosure problem, there are more that can be derived from them. Chief among these are those relating the heat flux to the other quantities. From Eqs. (12), (13), and (15), one has

$$q_i = \epsilon_i(B_i - q_i^-) \tag{18}$$

$$q_i^- = B_i - \frac{q_i}{\epsilon_i} \tag{19}$$

$$q_i = \left(\frac{\epsilon_i}{\rho_i}\right)(B_i - q_i^+) \tag{20}$$

$$q_i^+ = B_i - \frac{\rho_i}{0\epsilon_i}\, q_i \tag{21}$$

From Eqs. (12), (14), and (17), one has

$$q_i = q_i^+ - \sum_{j=1}^{n} F_{i-j} q_j^+ = \sum_{j=1}^{n} F_{i-j}(q_i^+ - q_j^+) \tag{22}$$

Returning to the original Eqs. (12)-(14), we see that there are n values of i for each of the three equations, or $3n$ equations in all. There are $3n$ unknowns, n values each of the heat flux q_i, radiosity qf, and irradiation q_i^-. Inspection of the equations shows that only one, Eq. (14), involves n terms; the others relate only to the three quantities for each i. Hence one may easily reduce the 3n equations in $3n$ unknowns to a set of n equations in n unknowns. One has the choice of formulating in q_i^-, qf, or conceivably, some linear combination of them.

If one formulates in q_i^-, one substitutes Eq. (13) into the right-hand side of Eq. (14) to obtain

$$\sum_{j=1}^{n} (\delta_{i,j} - \rho_j F_{i-j}) q_j^- = \sum_{j=1}^{n} F_{i-j}\epsilon_j B_j \tag{23}$$

where $\delta_{i,j}$ is the delta function,

$$\delta_{i,j} = \begin{cases} 1 & j = i \\ 0 & jti \end{cases} \tag{24}$$

If one formulates in q_i^+, one substitutes Eq. (13) into the left-hand side of Eq. (14) to obtain

$$\sum_{j=1}^{n} (\delta_{i,j} - \rho_i F_{i-j}) q_j^+ = \epsilon_i B_i \tag{25}$$

If one formulates in q_i, one substitutes Eqs. (19) and (21) into Eq. (14) to obtain

$$B_i - \frac{q_i}{\epsilon_i} = \sum_{j=1}^{n} F_{i-j}\left[B_j - \left(\frac{\rho_j}{\epsilon_j}\right) q_j\right]$$

Multiplying by A_i, rearranging, and taking the heat flows $\dot{Q}_i = A_i q_i$ instead of the heat fluxes q_i as the unknown quantities gives

$$\sum_{j=1}^{n} \left[\frac{\delta_{i,j}}{\epsilon_i} - \left(\frac{\rho_j}{\epsilon_j A_j}\right) A_i F_{i-j}\right] \dot{Q}_j = \sum_{j=1}^{n} A_i F_{i-j}(B_i - B_j) \tag{26}$$

How one proceeds with the mechanics of obtaining a solution depends on one s goals. If one wants merely a set of heat flows for one particular problem, one might simply use Eqs. (13) and (14) as they stand in an iterative numerical calculation. One might begin by assuming that the irradiation is zero (or that it is $\Sigma \epsilon_j A_j B_j / \Sigma \epsilon_j A_j$ from the exact solution for surfaces on the inside of a sphere), then calculate a set of radiosities q_i^+ from Eq. (13), then calculate a set of irradiations q_i^- from Eq. (14), and then repeat until the solutions converge. Then Eq. (18) or (20) can be used to find the heat fluxes q_i, and those can be multiplied by area to give $\dot{Q}_i$.

More often, one wants not merely a set of heat flows for one particular set of temperatures, but a set of parameters that describe the system behavior for any set of temperatures. The system parameters are the transfer factors $\mathfrak{F}_{i-j}$, where

$$\dot{Q}_i = \sum_{j=1}^{n} A_i \mathfrak{F}_{i-j}(B_i - B_j) \tag{27}$$

An important property of the transfer factor is

$$A_i \mathfrak{F}_{i-j} = A_j \mathfrak{F}_{j-i} \tag{28}$$

That the heat flows are linearly related to the blackbody radiosity differences, as indicated by Eq. (27), derives from the linearity of the governing equations. The linearity permits one, if it is convenient, to use the powerful superposition principle. One may think of $A_i \mathfrak{F}_{i-j}$ as the heat flow into surface j (i.e., $-\dot{Q}_j$) when B_i is set equal to unity and all other B_j are set equal to zero. This concept, for example, shows that one could evaluate $A_i \mathfrak{F}_{i-j}$ numerically via the iterative procedure described after Eq. (26). It follows from this concept that

$$\sum_{j=1}^{n} A_i \mathfrak{F}_{i-j} = \epsilon_i A_i \tag{29}$$

Comparison of Eq. (26) with $\rho_i = 0$ and $\epsilon_i = 1$ with Eq. (27) shows that the transfer factor and shape factor

© 1983 Hemisphere Publishing Corporation

are identical when all the walls are black. When all the walls are black, radiation is emitted by a hot surface i at the full blackbody rate, and only that radiation emitted directly toward surface j is transferred to it. When the walls are not black, the emitted flux at i is only $\epsilon_i B_i$, and surface j does not absorb all of the irradiation received on it, but radiation from i is reflected by other surfaces, and some of this radiation impinges on j. In general, the transfer factor $\mathfrak{F}_{i-j}$ is increased by increasing ϵ_i and ϵ_j (which one can regard as the emissivity and absorptivity, respectively) and by lowering ϵ_k (hence increasing ρ_k) of all other surfaces $k \neq i$ or j.

Matrix inversion and multiplication with the aid of a high-speed, large-storage-capacity computer is the means usually employed to obtain the set of transfer factors. Any of the three equations, Eqs. (23), (25), or (26), may be used. For example, Eq. (23) can be written in matrix form as

$$|m_{i,j}||q_j^-| = |F_{i,j}||b_j| \tag{30}$$

where $|m_{i,j}|$ denotes a matrix,

$$|m_{i,j}| = \begin{vmatrix} m_{1,1} & m_{1,2} \ldots m_{1,n} \\ m_{2,1} & m_{2,2} \ldots m_{2,n} \\ & \\ & \\ m_{n,1} & m_{n,2} \ldots m_{n,n} \end{vmatrix} \tag{31}$$

and an element is, according to Eq. (23),

$$m_{i,j} = \delta_{i,j} - \rho_j F_{i-j} \tag{32}$$

An element of matrix $|F_{i,j}|$ is the shape factor

$$F_{i,j} = F_{i-j} \tag{33}$$

Matrices $|q_j^-|$ and $|b_j|$ are column matrices:

$$|q_j^-| = \begin{vmatrix} q_1^- \\ q_2^- \\ \\ \\ q_n \end{vmatrix} \tag{34}$$

$$|b_j| \equiv \begin{vmatrix} \epsilon_1 B_1 \\ \epsilon_2 B_2 \\ . \\ \\ \epsilon_n B_n \end{vmatrix} \tag{35}$$

The rule for matrix multiplication is as follows: If matrix $|c_{i,j}|$ is the product of two matrices $|a_{i,k}|$ $|b_{k,j}|$,

$$|c_{i,j}| = |a_{i,k}||b_{k,j}| \tag{36}$$

then an element of matrix $|c_{i,j}|$ is

$$c_{i,j} = \sum_{k=1}^{n} a_{i,k} b_{k,j} \tag{37}$$

Standard computer routines exist for obtaining $|M_{i,j}|$, the inverse of $|m_{i,j}|$, so that one can obtain

$$|q_i^-| = |M_{i,k}||F_{k,j}| \cdot |b_j| \tag{38}$$

Now the superposition principle is useful. If the only value of B_j not equal to zero is $B_k = 1$, then

$$q_i^- = M_{i,1} F_{1-k} \epsilon_k + M_{i,2} F_{2-k} \epsilon_k + \ldots + M_{i,n} F_{n-k} \epsilon_k$$

But we understand $\epsilon_i q_i^-$ to be $\mathfrak{F}_{i-k}$ under this circumstance. Accordingly,

$$\mathfrak{F}_{i-k} = \epsilon_i \epsilon_k (M_{i,1} F_{1,k} + M_{i,2} F_{2,k} + \ldots + M_{i,n} F_{n,k}) \tag{39}$$

We see that each element of the transfer factor matrix $|\mathfrak{F}_{i,k}|$ is found by taking the corresponding element from the matrix product,

$$|P_{i,k}| = |M_{i,j}||F_{j,k}| \tag{40}$$

and multiplying it by $\epsilon_i \epsilon_k$,

$$\mathfrak{F}_{i-k} = \epsilon_i \epsilon_k P_{i,k} \tag{41}$$

Alternatively, one may invert the matrix defined by Eq. (25). Equation (20) then indicates that the transfer factors are inverse matrix elements multiplied by $\epsilon_i \epsilon_k / \rho_i$. Although this result is obtained more directly, it is not useful for $\rho_i = 0$. Instead of using Eq. (20), one could use Eq. (22) to avoid the difficulty posed by $\rho_i = 0$, but at the expense of somewhat more complexity.

The matrix inversion technique is needed only when n is large, say, 4 or more. For fewer surfaces, a simpler means of solution, and one that conveys a great deal more physical insight to aid the designer in exercising creativity, is the network method described in the next section. Nevertheless, a matrix example with $n = 2$ is presented. Consider a cubical enclosure with one face being surface 1 at a known temperature and with known emissivity ϵ_1 and the other five faces together being surface 2 with emissivity ϵ_2. Suppose that $\epsilon_1 = \epsilon_2 =$ OS, and $A_1 = 1\ m^2$. To two decimal places, $F_{2-2} =$ 0.80, and $F_{2-1} = 0.20$. The matrix $|m_{i,j}|$ is, from Eq. (32),

$$|m_{i,j}| = \begin{vmatrix} +1.00 & -0.50 \\ -0.10 & +0.60 \end{vmatrix}$$

© 1983 Hemisphere I blishing Corporation

The inverse matrix is

$$|M_{i,j}| = \begin{vmatrix} \frac{0.60}{0.55} & -\frac{0.50}{0.55} \\ -\frac{0.10}{0.55} & \frac{1.00}{0.55} \end{vmatrix}$$

The matrix $|P_{i,k}|$ is, from Eq. (40),

$$|P_{i,k}| = \begin{vmatrix} \frac{12}{11} & \frac{10}{11} \\ \frac{2}{11} & \frac{20}{11} \end{vmatrix} \cdot \begin{vmatrix} 0 & 1 \\ \frac{1}{5} & \frac{4}{5} \end{vmatrix} = \begin{vmatrix} \frac{2}{11} & \frac{20}{11} \\ \frac{4}{11} & \frac{18}{11} \end{vmatrix}$$

The $|\mathfrak{F}_{i-k}|$ matrix is, from Eq. (41),

$$|\mathfrak{F}_{i-k}| = \begin{vmatrix} \frac{1}{22} & \frac{5}{11} \\ \frac{1}{11} & \frac{9}{22} \end{vmatrix}$$

As a check, we observe that $A_1\mathfrak{F}_{1-2} = 5/11 = A_2\mathfrak{F}_{2-1} = 5/1\,1$, satisfying Eq. (28). As a further check, Eq. (29) is verified:

$$A_1\mathfrak{F}_{1-1} + A_1\mathfrak{F}_{1-2} = \frac{1}{22} + \frac{5}{11} = \frac{1}{2} = \epsilon_1 A_1$$

$$A_2\mathfrak{F}_{2-1} + A_2\mathfrak{F}_{2-2} = \frac{5}{11} + \frac{45}{22} = \frac{5}{2} = \epsilon_2 A_2$$

If the surfaces are gray and T_1 = 1 500 K and T_2 = 1 000 K, then, from Eq. (27),

$$\dot{Q}_1 = A_1\mathfrak{F}_{1-2}(C_s T_1^4 - C_s T_2^4)$$

$$= \$5.669\ 7\ \text{X}\ 10^{-8})(1500^4 - 1\ 000^4)$$

$$= 104.7\ \text{kW}$$

C. Refractory surfaces

A perfectly insulated or adiabatic surface is said to be a refractory. For such a surface,

$$q_i = 0 \tag{42}$$

and hence, from Eq. (12),

$$q_i^- = q_i^+ \tag{43}$$

and from Eqs. (12), (13), and (15),

$$B_i = q_i^- = q_i^+ \tag{44}$$

Note that these relations hold regardless of the value of surface emissivity. The refractory surface can be equally well thought of as a perfect reflector or a perfect absorber and reradiator . This statement is made, of course, subject to the assumptions of perfectly diffuse surfaces. Furthermore, if the surface is nongray, it is not adiabatic on a spectral basis even though it may be on a total basis.

If surface k is a refractory surface, the kth column of matrix $|m_{i,j}|$ has elements according to Eqs. (14) and (43) :

$$m_{i,k} = \delta_{i,k} - F_{i,k} \tag{45}$$

and

$$b_k = 0 \tag{46}$$

These changes can be incorporated into Eqs. (38) and (41). However, Eq. (41) applies only to the nonrefractory surfaces; for a refractory surface, $i = k$, $\mathfrak{F}_{k-j}$ is zero.

If surfaces i and j are not refractories, then, if surface is made a refractory, the transfer factor $\mathfrak{F}_{i-j}$ is increased, because the refractory acts as a perfect reflector. As discussed previously, a reflecting surface

faces present in the enclosure.

D. The radiation network

The facts that heat is conserved (just like electrical charge) and that radiant heat flows are proportional to differences in radiosity (just like electrical current being proportional to voltage differences) mean that an electrical analog to the radiation heat transfer problem can be constructed [14,15].

the n surfaces. These n surfaces are regarded as n

The heat flows at each node sum to zero. The heat flow

in m

duction is $\dot{Q}_i$. This heat flow must equal the heat flow

out s control surface.

Equation (22) states that the heat flow out across

$$\dot{Q}_i = q_i A_i = \sum_{j=1}^{n} A_i F_{i-j}(q_i^+ - q_j^+)$$

It is apparent from the equation that radiosity q_i^+ is to be considered the voltage or potential at the *ith* node, and this potential drives heat flows into the other nodes at potentials q_j^+ through internodal conductances $A_i F_{i-j}$, that is, through internodal resistances,

$$R_{i-j} = \frac{1}{A_i F_{i-j}}$$

The relation between surface heat flux and radiosity is given by Eq. (20). Multiplying by area A_i to obtain heat flow gives

$$\dot{Q}_i = \frac{\epsilon_i A_i}{\rho_i}(B_i - q_i^+) \tag{49}$$

© 1983 Hemisphere Publishing Corporation

This equation tells us to regard the heat flow into node i as driven by blackbody radiosity B_i through surface resistance R_i,

$$R_i = \frac{\rho_i}{\epsilon_i A_i} = \frac{1-\epsilon_i}{\epsilon_i A_i} \tag{50}$$

and against the node potential q_i^+.

Figure 5 shows the circuit connections for a single node i. To construct a radiation network for an enclosure, one places the requisite number (n) of nodes on a diagram and draws all interconnections of the R_{i-j} form. One then draws the surface resistances of the form R_i and the requisite potentials B_i. Figure 6 shows a network for $n = 3$.

If $n = 2$, or if $n = 3$ but the surface represented by node $i = 3$ is a refractory so that it is open circuit, the network is readily reduced to a single equivalent resistance between potentials B_1 and B_2. That equivalent resistance is $(1/A_1\mathfrak{F}_{1-2})$. The meaning of the transfer factor is very clear in this context. In reducing the simple series-parallel network, the rules simply are two: (1) Resistances in series add. (2) Conductances in parallel add (conductance is the reciprocal of resistance).

For $n = 3$, the delta-wye and wye-delta transformations may be used to find the transfer factors. Figure 7 shows the transformations.

For example, consider a cubical enclosure with surface 1 the floor at 500 K, surface 2 a side at 1 500 K, and surface 3 the remaining three sides and top at 1 000 K. All surfaces are gray, with an emissivity of 0.50. Area A_1 is taken to be $1\,m^2$, and to two decimal places $F_{1-2} = 0.2$, $F_{1-3} = 0.8$, $F_{2-3} = 0.8$. Figure 2 shows the radiation network. There is found

$$R_{1-2} = \frac{1}{(1)(0.2)} = 5.0$$

$$R_{1-3} = R_{2-3} = \frac{1}{(1)(0.8)} = 1.25$$

$$R_1 = R_2 = \frac{1-0.5}{(1)(0.5)} = 1.0$$

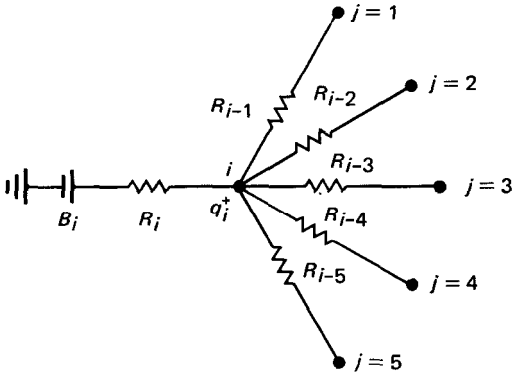

Figure 5 Radiation network connections for node i.

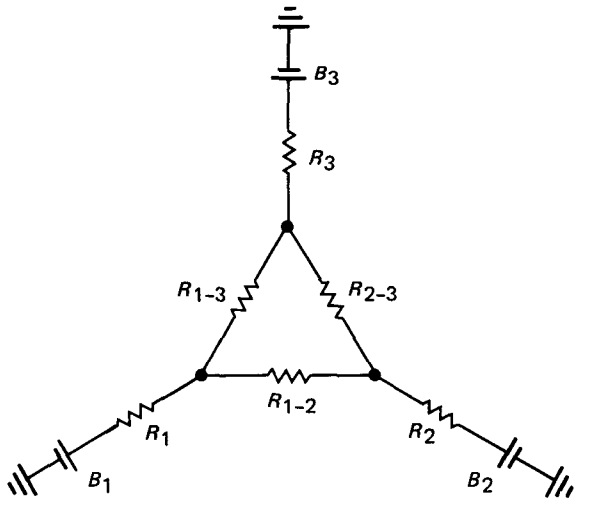

Figure 6 The radiation network for $n = 3$.

$$R_3 = \frac{1-0.5}{(4)(0.5)} = 0.25$$

Following a delta-wye transformation, a wye network is found to exist with each leg of the wye consisting of the surface resistance in series with the resistance found from the transformation. These are added to obtain

$$R_{1,\text{tot}} = R_{2,\text{tot}} = 1.00 + 0.85 = 1.8\overline{3}$$

$$R_{3,\text{tot}} = 0.25 + 0.208\,\overline{3} = 0.458\,\overline{3}$$

Then a wye-delta transformation is made to obtain the transfer factors (in units of m^2)

$$A_1\mathfrak{F}_{1-2} = 0.090\,9 \qquad A_1\mathfrak{F}_{1-3} = 0.363\,6$$

$$A_2\mathfrak{F}_{2-3} = 0.363\,6$$

The heat flows are then found with Eq. (47):

$$\dot{Q}_1 = A_1\mathfrak{F}_{1-2}(B_1 - B_2) + A_1\mathfrak{F}_{1-3}(B_1 - B_3)$$

$$= 0.090\,9(3\,540 - 287\,000) + 0.363\,6(3\,540 - 56\,700) = -45.1\ \text{kW}$$

$$\dot{Q}_2 = A_2\mathfrak{F}_{2-1}(B_2 - B_1) + A_2\mathfrak{F}_{2-3}(B_2 - B_3)$$

$$= 0.090\,9(287\,000 - 3\,500) + 0.363\,6(287\,000 - 56\,700) = +109.5\,\text{kW}$$

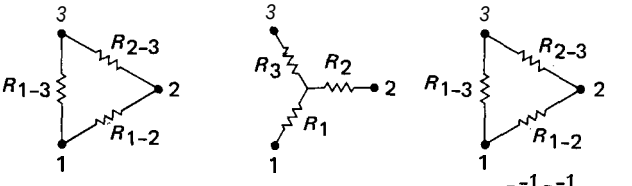

$$R_1 = \frac{R_{1-2}R_{1-3}}{R_{1-2} + R_{2-3} + R_{1-3}} \qquad R_{1-2}^{-1} = \frac{R_1^{-1}R_2^{-1}}{R_1^{-1} + R_2^{-1} + R_3^{-1}}$$

Figure 7 The delta-wye and wye-delta transformations.

© 1983 Hemisphere Publishing Corporation

$$\dot{Q}_3 = A_3\mathfrak{F}_{3-1}(B_3 - B_1) + A_3\mathfrak{F}_{3-2}(B_3 - B_2)$$

$$= 0.363\ 6\ (57\ 600 - 3\ 500)$$

$$+ 0.363\ 6(56\ 700 - 287\ 000) = -64.4\ \text{kW}$$

The radiation network offers the designer a way of conceptualizing the radiation transfer process that is not afforded by the radiosity-irradiation formulation followed by matrix inversion. When the designer views the network representation, he or she is given a grasp of how important various physical quantities such as surface emissivity are. For this reason the designer is urged to draw a network, perhaps with oversimplification to keep n small, to help visualize the transfer problem, even when the matrix inversion algorithm may be employed to obtain numerical values.

E. Selected working relations

With the radiation network as a working tool, it is an easy matter to obtain several useful results. Those reviewed are as follows:

1. A source and a sink
   a. General case
   b. One surface not concave
   c. Parallel walls
   d. Concentric tubes
   e. Effective emissivity of a rough surface
2. A source, a sink, and a refractory
   a. General case
   b. Source and sink not concave
   c. Tube bank over a refractory
3. Radiation shields
   a. General case
   b. Flat shields
   c. Concentric cylindrical shields
   d. Concentric spherical shields

The results here are subject to the assumptions of perfectly diffuse surfaces and uniform radiosity. This latter assumption is exact for some geometries (parallel walls, concentric tubes), but only a rough approximation for others, such as short passages. Long passages, where the approximation of uniform radiosity is clearly inapplicable, are reviewed briefly in the next section.

(a) A source and a sink

The general case of a single source and single sink forming a complete enclosure is represented by a simple series radiation network having merely a potential B_1, a surface resistance $R_1 = (1-\epsilon_1)/\epsilon_1 A_1$, a shape factor resistance $R_{1-2} = 1/A_1F_{1-2}$, a second surface resistance $R_2 = (1-\epsilon_2)/\epsilon_2 A_2$, and potential B_2. Accordingly,

$$\dot{Q}_1 = -\dot{Q}_2$$

$$= \frac{B_1 - B_2}{[(1-\epsilon_1)/\epsilon_1 A_1\ 1 + (1/A_1F_{1-2}) + [(1-\epsilon_2)/\epsilon_2 A_2]} \tag{51}$$

$$A_1\mathfrak{F}_{1-2}$$

$$= \frac{1}{[(1-\epsilon_1)/\epsilon_1 A_1\ \mathrm{I} + (1/A_1F_{1-2}) + (1-\epsilon_2)/\epsilon_2 A_2]} \tag{52}$$

If one surface is not concave (denote it as number 1), then it cannot see itself; so $F_{1-1} = 0$ and $F_{1-2} = 1$. Equation (52) can be rearranged in the form

$$A_1\mathfrak{F}_{1-2} = \frac{A_1}{(1/\epsilon_1) + (A_1/A_2)[(1/\epsilon_2) - 1)]} \tag{53}$$

For infinite parallel plates, in addition $A_1 = A_2$, giving

$$A_1\mathfrak{F}_{1-2} = \frac{A_1}{(1/\epsilon_1) + (1/\epsilon_2) - 1} \tag{54}$$

For infinite concentric tubes, a length L has area $A_1 = \pi D_1 L$, where D_1 is understood to be the outside diameter of the inner tube, and $A_2 = \pi D_2 L$, where D_2 is the inside diameter of the outer tube. Equation (53) gives

$$A_1\mathfrak{F}_{1-2} = \frac{\pi D_1 L}{(1/\epsilon_1) + (D_1/D_2)[(1/\epsilon_2) - 1]} \tag{55}$$

Equation (53) can be rearranged in the form of

$$\mathfrak{F}_{1-2} = \frac{\epsilon_1}{1 + (\epsilon_1 A_1/\epsilon_2 A_2)(1-\epsilon_2)} \tag{56}$$

Whenever $\epsilon_1 A_1(1-\epsilon_2)$ is small compared to $\epsilon_2 A_2$, the transfer factor reduces to simply the emissivity of the small or nonblack surface. This limit shows simply that a large space 2 can be regarded as a hohlraum, that is, as a black body. The presence of a sufficiently small object within it does not alter the blackbody irradiation that falls on a surface that sees only the hohlraum wall.

Consider a rough surface 1 within a large space 2. The surface roughness is gross compared to the wavelengths of concern. The large space is effectively a black body. If the surrounds are black and at isothermal temperature T_2, the area A_2 is of no concern; as shown by Eq. (56), the area A_2 disappears when $\epsilon_2 = 1$. It is convenient to consider A_2 wrapped closely over the envelope of the surface roughness heights. The area A_2 is then the projected area of the surface. If the roughness heights are small compared to the radius of curvature of the mean surface, area A_2 can be regarded as flat, and surface A_1, because of its roughness, is concave. Accordingly, it is F_{2-1} that is to be set to unity in Eq. (52), after substituting A_2F_{2-1} for A_1F_{1-2},

© 1983 Hemisphere Publishing Corporation

and ϵ_2 is set equal to 1. The result is

$$A_1 \mathfrak{F}_{1-2} = A_2 \mathfrak{F}_{2-1} = \frac{1}{[(1-\epsilon_1)/\epsilon_1 A_1] + 1/A_2}$$

$$= \frac{}{(A_2/A_1)[(1/\epsilon_1)-1]+1} \quad -42$$

The quantity $\mathfrak{F}_{2-1}$ is the effective emittance of the rough surface. It is defined so that the transfer factor $A, \mathfrak{F}_{1-2}$ is $A_2\epsilon_{\text{eff}}$ when the surface is within a hohlraum. We have

$$\epsilon_{\text{eff}} = \frac{1}{(A_2/A_1)[(1/\epsilon_1)-11+1} \tag{57}$$

As the surface becomes smooth, and A $_1$ approaches A_2, the effective emittance becomes ϵ_1. As A_1 becomes large compared to A_2, the effective emittance goes to unity. The analysis is exact only for surface roughnesses formed by indentations that are segments of a sphere, because of the assumption of uniform radiosity, and is otherwise approximate. However, the qualitative result is true; the effective emissivity of a rough surface is bounded by ϵ_1 and unity and tends to increase with increasing A_1/A_2.

Occasionally a thermal designer who is unfamiliar with the fundamentals of radiation heat transfer will decide to improve a radiator or heat exchanger by increasing A_1 in some novel manner to increase greatly $A, \mathfrak{F}_{1-2}$, even though subject to a fixed projected area A_2. But $A_1\mathfrak{F}_{1-2} = A_2\mathfrak{F}_{2-1}$ and $\mathfrak{F}_{2-1}$ is bounded by emissivity ϵ_2, which equals unity at most. If A_2 is the projected area of rough surface A_1, there is no way to make $A, \mathfrak{F}_{1-2}$ exceed A_2, that is, to make ϵ_{eff} exceed unity.

(b) A source, a sink, and a refractory

The radiation network for a three-surface enclosure is shown in Fig. 6. If surface 3 is a refractory, no heat crosses the m surface, and this fact is represented by removing the current source shown as battery B_3. Node 3 is free floating, and resistance R_3 is of no concern, because no heat flow (current) flows through it. The equivalent conductance $A, \mathfrak{F}_{1-2}$ is given simply by

$$A_1\mathfrak{F}_{1-2} = 1/\{R_1 + R_2 + 1/[(1/R_{1-2}) + 1/(R_{1-3} + R_{2-3})]\}$$

$$= 1/\{(1-\epsilon_1)/\epsilon_1 A_1 + (1-\epsilon_2)/\epsilon_2 A_2 + 1/[A_1F_{1-2} + 1/(1/A_1F_{1-2} + 1/A_2F_{2-3})]\} \tag{58}$$

This equation is clearly of the form

$$A_1\mathfrak{F}_{1-2} = \frac{1}{[(1-\epsilon_1)/\epsilon_1 A_1] + [(1-\epsilon_2)/\epsilon_2 A_2] + 1/A_1\mathfrak{F}_{1-2,b}} \tag{59}$$

where $\mathfrak{F}_{1-2,b}$ is the transfer factor accounting for the refractory when surfaces 1 and 2 are black,

$$A, \mathfrak{F}_{1-2,b} = A_1F_{1-2} + \frac{1}{(1/A_1F_{1-3}) + (1/A_2F_{2-3})} \tag{60}$$

Equation (59) is true whenever areas A_1 and A_2 can be assumed reasonably to have uniform radiosities, whether the refractory does or not. This point bears upon the long passages considered in the next section.

One often needs to know additionally B_3, in order to specify a refractory material suitable for the temperature T_3. One can proceed by finding the potentials q_1^+ and q_2^+, and the branch current $\dot{Q}_{1-3-2}$. With reference to Fig. 6 (B_3 open),

$$\dot{Q}_1 = A_1\mathfrak{F}_{1-2}(B_1 - B_2) \tag{61a}$$

$$q_1^+ = B_1 - \dot{Q}_1R_1 \tag{61b}$$

$$q_2^+ = B_2 + \dot{Q}_1R_2 \tag{61c}$$

$$\dot{Q}_{1-2} = \frac{1}{R_{1-2}}(q_1^+ - q_2^+) \tag{61d}$$

$$\dot{Q}_{1-3-2} = \dot{Q}_1 - \dot{Q}_{1-2} \tag{61e}$$

$$B_3 = q_1^+ - \dot{Q}_{1-3-2}R_{1-3} \tag{61f}$$

When surfaces A_1 and A_2 are not concave, the simplification results that, since $F_{1-1} = 0$ and $F_{2-2} = 0$,

$$F_{1-3} = 1 - F_{1-2} \qquad F_{2-3} = 1 - F_{2-1} = 1 - \frac{A_1}{A_2}F_{1-2}$$

Thus only the one shape factor F_{1-2} need be evaluated.

For example, consider a cubical enclosure 1 m on a side having one facet being a source at T_1 = 1 500 K, the floor a sink at T_2 = 500 K, and the remaining three walls and ceiling refractory at unknown temperature T_3. Suppose that the surfaces are gray, and $\epsilon_1 = \epsilon_2 =$ 0.5. What is the heat flow and the temperature of the refractory? To two-decimal-place accuracy, $F_{1-2} = 0.2$, so $F_{1-3} = F_{2-3} = 0.8$. From Eq. (60),

$$A_1\mathfrak{F}_{1-2,b} = A_1F_{1-2} + \frac{1}{(1/A_1F_{1-3}) + (1/A_2F_{2-3})}$$

$$\mathfrak{F}_{1-2,b} = 0.2 + \frac{1}{(1/0.8)+(1/0.8)} = 0.60$$

Of the 80% of the radiation leaving 1 and striking 3, half is reradiated back to 1 and the remainder to 2. This half, 40%, exceeds the direct radiation, 20%, by a factor of 2.

To continue, the result for $\mathfrak{F}_{1-2,b}$ is entered into

© 1983 Hemisphere Publishing Corporation

Eq. (59) (with $A_1 = A_2 = 1\,\mathrm{m}^2$) to obtain

$$\mathfrak{F}_{1-2} = \frac{1}{[(1-0.5)/0.5] + [(1-0.5)/0.5] + 1/0.6} = 0.273$$

Heat flow $\dot{Q}_1$ is found from Eq. (27):

$$\dot{Q}_1 = -\dot{Q}_2 = A_1 \mathfrak{F}_{1-2}(C_s T_1^4 - C_s T_2^4)$$
$$= (0.273)(5.669\,7 \times 10^{-8})(1500^4 - 500^4)$$
$$= (0.273)(287\,000 - 3\,500) = 77.3\ \mathrm{kW}$$

To find B_3, we need not use Eq. (61), because of the symmetry in the network. From symmetry in this example we see at once that

$$B_3 = \tfrac{1}{2}(B_1 + B_2) = 145\,300\ \mathrm{W/m^2}$$

$$T_3 = \left(\frac{B_3}{C_s}\right)^{1/4} = 1265\ \mathrm{K}$$

A tube or cylinder bank backed by a refractory wall to act as a reflector-reradiator is a configuration often used by the thermal design engineer. In one common application the cylinders are electrical heaters in rod form. In another, the tubes are filled with flowing fluid to be heated. The tubes are exposed to a furnace enclosure directly on one side. Consider the enclosure to be a hohlraum, and replace it with an imaginary black plane numbered 1. Number the tubes as 2 and the refractory backup wall as 3, as shown in Fig. 8. The distance center to center is the pitch P, and the tube outside diameter is D. The tubes are separated to obtain more uniform heating or cooling of them around their periphery, that is, to make better use of the available heat transfer area to gain a higher heat flow per unit length of tube with specified temperature limits. If P were made equal to D, the back half of the tubes would not be utilized at all. It is desired to know the transfer factor $\mathfrak{F}_{2-1}$ as a function of r = P/D.

If the tubes have a high emissivity (as they usually do) and if they are reasonably isothermal around their circumference, or if r is not too close to unity, their radiosity will be reasonably uniform, and they can be adequately represented by the single node 2. Similarly, if the refractory is spaced reasonably away from the tubes or if it is black and conducts laterally, it too can be represented by a single node. Then Eq. (58) applies directly. All that is necessary is to find the shape factors.

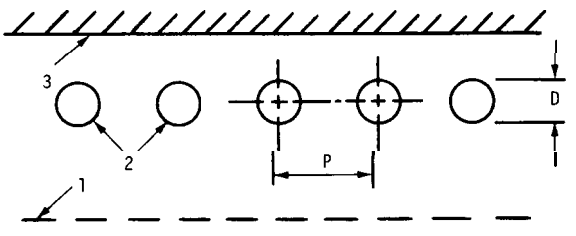

Figure 8 A row of circular cylinders backed by a refractory wall.

The string rule, Eq. (11) and Fig. 4, gives

$$F_{2-2} = \frac{2}{\pi}\left[(r^2 - 1)^{1/2} + \sin^{-1}\left(\frac{1}{r}\right) - r\right] \tag{62a}$$

Shape factor algebra determines the rest:

$$F_{2-1} - F_{2-3} = \frac{1 - F_{2-2}}{2} \tag{62b}$$

$$F_{1-2} = \left(\frac{A_2}{A_1}\right) F_{2-1} = \left(\frac{\pi}{r}\right) F_{2-1} \tag{62c}$$

$$F_{1-3} = 1 - F_{1-2} \tag{62d}$$

For example, if $P = 3D(r = 3)$, then we have the following values:

$F_{2-2} = 0.107\,1$ $\quad F_{2-1} = F_{2-3} = 0.446\,4$

$F_{1-2} = 0.467\,5$ $\quad F_{1-3} = 0.532\,5$

$\mathfrak{F}_{1-2,b} = 0.72$

$\mathfrak{F}_{2-1,b} = 0.68$

The value $\mathfrak{F}_{2-1,b} = 0.68$ is 115% greater than the value $1/\pi$ when the tubes are touching $(r = 1)$, because the backs and sides of the tubes are better utilized. In the limit as r goes to infinity, $\mathfrak{F}_{2-1,b}$ goes to unity, giving a 2 14% increase over the $1/\pi$ value.

The normalized radiosity of the refractory can be obtained via Eq. (61), using values $B_1 = 1$ and $B_2 = 0$. The resulting value of radiosity is the irradiation on the point on the tube nearest the refractory wall, and this value can be compared with the value of unity pertaining to the point farthest from the wall to show the degree of uniformity in tube wall radiant heat flux.

The quantity $\mathfrak{F}_{2-1,b}$ is easily calculated from Eqs. (60) and (62) by hand. Figure 9 shows the behavior versus r. To two decimal places,

$$\mathfrak{F}_{2-1,b} \doteq 1 - \frac{1}{r} \qquad r \geqslant 4$$

Hottel and Sarofim [8] show additional results for double rows of tubes in front of a refractory wall.

(c) Radiation shields

Radiation shields are used by the thermal designer in various forms : aluminized plastic sheet, aluminum foil-paper laminate, thin stainless steel sheet, ceramic tubes, to name a few. The purpose is to reduce unwanted heat transfer. At high temperatures or under vacuum conditions, conduction may be negligible (Sec. 2.9.8 considers combined mode transfer). The radiation shield then can be represented on a radiation

© 1983 Hemisphere I blishing Corporation

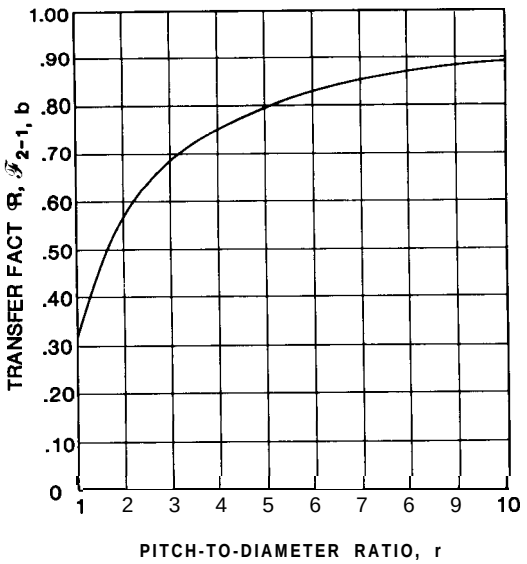

Figure 9 Tube-to-furnace transfer factor for single tube bank over refractory wall.

network as a node with a free-floating radiosity B with a surface resistance on either side. The radiation shield is a two-sided refractory. Consider an array of N shields of the same material between an inner black source area A_1 and a black sink area A_{N+2}. As before, surface resistances to account for nonblack source and sink can be easily added as shown in Eq. (59). Between N shields there are N − 1 spaces, each spacing having resistance

$$R_{s,n} = \frac{1-\epsilon_f}{\epsilon_f A_{f,n}} + \frac{1}{A_{f,n}} + \frac{1-\epsilon_b}{\epsilon_b A_{b,n+1}} \qquad n = 2 \text{ to } N \tag{63}$$

where subscript f refers to the front (or outside) of the smaller shield and b to the back (or inside) of the larger one. In addition to N − 1 of these resistances, there is the surface resistance of the back of the inner shield, the shape factor resistance from the inner surface 1, the surface resistance of the front of the outer shield N + 1, and its shape factor resistance. Therefore,

$$A_1 \mathfrak{F}_{1-(N+2),b} = 1/\{(1/A_1) + [(1-\epsilon_b)/\epsilon_b A_{b,2}] + \Sigma_{n=2}^{N} R_{s,n} + [(1-\epsilon_f)/\epsilon_f A_{f,N+1}\,1 + 1/A_{f,N+1}\} \tag{64}$$

For flat shields $A_1 = A_{,,n} = A_{,,,}$. The areas cancel, and

$$\mathfrak{F}_{1-(N+2),b} = \frac{1}{N[(1/\epsilon_f) + (1/\epsilon_b) - 1] + 1} \tag{65}$$

In this case the transfer factor falls with l/N as N gets large.

For concentric cylindrical shields with constant front-to-front spacing s, thickness δ, and inner source or sink radius r_1, there holds

$$A_1 = 2\pi r_1 L \tag{66a}$$

$$A_{f,n} = 2\pi(r_1 + ns)L \tag{66b}$$

$$A_{b,n} = 2\pi(r_1 + ns - \delta)L \tag{66c}$$

When s/r_1 is small, the summation can be approximated with an integral, and the transfer factor falls as $1/\ln N$ as N gets large.

For concentric spherical shields the following relations pertain :

$$A_1 = 4\pi r_1^2 \tag{67a}$$

$$A_{f,n} = 4\pi(r_1 + ns)^2 \tag{67b}$$

$$A_{b,n} = 4\pi(r_1 + ns - \delta)^2 \tag{67c}$$

When s/r_1 is small, the summation in Eq. (64) can be approximated as an integral, and as N gets large the additional shields produce no added benefit in reducing the transfer factor.

For small s/r_1 the concept of radiation conductivity can be used, and that conductivity can be combined with simultaneous gaseous conduction as explained in Sec. 2.9.8 to obtain an approximate simple closed-form result more convenient than Eqs. (64) and (66) or (67).

F. Diffuse-walled passages

The thermal designer may wish to assess the importance or unimportance of axial radiation, for example, in a regenerative heat exchanger used in a Brayton or Stirling cycle engine or in a combustion air preheater. The leakage of heat radiation through a hole or crack penetrating through thermal insulation is a common concern. In what follows, shape factor algebra is used to formulate the heat flux down a passage. When the side wall radiosity is known, as it is for a black-walled passage with known temperature distribution, or when the side-wall radiosity can be reasonably approximated, as for the refractory-walled passage, the formulation is of direct practical use. When the radiosity is unknown and cannot be readily approximated, the problem is easily formulated using the method illustrated here, and numerical methods of solution can be employed. However, modern practice is to use a direct Monte Carlo calculation. The Monte Carlo technique is described in Sec. 2.9.4.

Consider a passage of length L in the form of a right cylinder with arbitrary cross section. Denote the ends as 1 and 2 and the side walls as 3. Let x run from end 2 toward 1. Consider an imaginary surface 4 located at $x = x_0$. The dimensionless irradiation upon the side of the surface facing end 1 is given by Eq. (14), generalized by passing from the sum to an integral.

© 1983 Hemisphere I blishing Corporation

$$q_4^{*-} = F_{4-1} q_1^{*+} + \int_{x=x_0}^{x=L} q_3^{*+}(x) \frac{dF_{4-3}}{d(x-x_0)} d(x-x_0)$$

The shape factor F_{4-1} is of the same form as $F_{1-2}(L)$, but the length in question is $L-x_0$; that notation is adopted. Shape factor algebra shows that

$$F_{4-3}(x-x_0) = 1 - F_{4-1}(x-x_0)$$
$$= 1 - F_{1-2}(x-x_0)$$

Accordingly, the equation may be written

$$q_4^{*-}(x_0) = F_{1-2}(L-x_0) + \int_{x=x_0}^{x=L} q_3^{*+}(x) \times \frac{d}{d(x-x_0)}(1 - F_{1-2}(x-x_0))\, d(x-x_0) \qquad (68)$$

The dimensionless radiosity, irradiation, and flux are understood to be

$$q_n^{*\pm} \equiv \frac{q_n^{\pm} - q_2^{+}}{q_1^{+} - q_2^{+}} \qquad q^* \equiv \frac{q}{q_1^{+} - q_2^{+}} \qquad (69)$$

Note that q_1^{*+} is unity and q_2^{*} is zero, so that they do not appear explicitly in Eq. (68) or Eq. (70) to follow.

Let surface 5 be the back of surface 4, that is, the side of the cross section at $x = x_0$ facing end 2. Then the irradiation upon 5 is given by an expression similar to that for 4.

$$q_5^{*-} = \int_{x=x_0}^{x=0} q_3^{*+} \frac{d}{d(x_0-x)}(1 - F_{1-2}(x_0-x)) \times d(x_0-x)$$

But the irradiation upon 5 is the radiosity of 4. The net heat ***flux in the negative x direction*** is, from Eq. (12),

$$q^*(x_0) = F_{1-2}(L-x_0) + \int_{x=x_0}^{x=L} q_3^{*+} \frac{d}{d(x-x_0)} \times (1 - F_{1-2}(x-x_0))\, d(x-x_0) - \int_{x=x_0}^{x=0} q_3^{*+} \frac{d}{d(x_0-x)} \times (1 - F_{1-2}(x_0-x))\, d(x_0-x) \qquad (70)$$

Equation (70) is the general expression for the average heat flux at any location x_0 for a diffuse-walled passage having ends with uniform radiosity. Its utility is made more clear by considering the special case when

$$q_3^{*+}(x) = mx + b \qquad (71)$$

The reader recognizes this equation as the intercept-slope representation of a straight-line side-wall radiosity distribution.

Consider the first integral in Eq. (70); denote it as I_1. Let $u = x - x_0$.

$$I_1 = \int_0^{L-x_0} (mx + b + mx_0 - mx_0) \frac{d}{du} \times (1 - F_{1-2}(u))\, du$$
$$= (b + mx_0)(1 - F_{1-2}(L-x_0)) + m \int_0^{L-x_0} u \frac{d}{du}(1 - F_{1-2}(u))\, du$$

Integrate the remaining integral by parts to obtain

$$I_1 = (b + mL)(1 - F_{1-2}(L-x_0)) - m(L-x_0) + m(L-x_0) S(L-x_0)$$

where

$$S(L) \equiv \frac{1}{L} \int_0^L F_{1-2}(x)\, dx \qquad (72)$$

When the same procedure is followed with the second integral, Eqs. (70) and (71) yield

$$q^*(x_0) = [1 - (b + mL)] F_{1-2}(L-x_0) + bF_{1-2}(x_0) + m(L-x_0) S(L-x_0) + mx_0 S(x_0) \qquad (73)$$

When one recalls that q_1^{*+} is unity, q_2^{*+} is zero, $q_3^{*+}(0) = b$, and $q_3^{*+}(L) = b + mL$, then the symmetry in the equation with respect to x_0 and $L - x_0$ may be appreciated.

The cross-sectional geometry fixes the relations for F_{1-2} and S. For the slot with height $H = 1$ (i.e., L is $L/H = 2L/D_H$, where D_H is the hydraulic diameter, and $x = x/H = 2x/D_H$); the string rule shows that

$$F_{1-2}(x) = (1 + x^2)^{1/2} - x \qquad (74a)$$

$$S(x) = \frac{1}{2}[(1+x^2)^{1/2} - x] + \frac{1}{2x} \ln(x + (1+x^2)^{1/2}) \qquad (74b)$$

For the circle with diameter D (i.e., $L = L/D$ and $x = x/D$),

$$F_{1-2}(x) = 1 + 2x^2 - 2x(1+x^2)^{1/2} \qquad (75)$$

$$S(x) = 1 + \frac{2}{3x}[1 + x^3 - (1+x^2)^{3/2}] \qquad (75b)$$

© 1983 Hemisphere Publishing Corporation

For example, suppose that one wanted to estimate the radiant heat flux into the passages of a 5-cm-long regenerator core having approximately circular (D_h = 5 mm) passages of a highemissivity material. Suppose that the inlet to the hot side of the regenerator is approximately a hohlraum at T_1 = 600 K, and the outlet is one at T_2 = 350 K. The wall itself is T_L = 575 K at the inlet and T_0 = 325 K at the outlet. It is agreed approximate the radiosity distribution along the passage wall as a straight line from $C_sT_0^4$ to $C_sT_L^4$. The net heat flux into a passage at its inlet (at $x_0 = L = 5$ cm) is desired.

As a first step, Eq. (73) is written for $x_0 = L$:

$$q^*(L) = 1 - (b + mL) + bF_{1-2}(L) + mLS(L)$$

The values of b and mL are found from Eq. (69):

$$b = q_3^{*+}(0) = \frac{C_sT_0^4 - C_sT_2^4}{C_sT_1^4 - C_sT_2^4} = \frac{325^4 - 350^4}{600^4 - 350^4}$$

$$= -0.034$$

$$mL = q_3^{*+}(L) - q_3^{*+}(0) = \frac{C_sT_L^4 - C_sT_0^4}{C_sT_1^4 - C_sT_2^4}$$

$$= \frac{575^4 - 325^4}{600^4 - 350^4} = 0.857$$

$$b + mL = q_3^{*+}(L) = \frac{C_sT_L^4 - C_sT_2^4}{C_sT_1^4 - C_sT_2^4} = \frac{575^4 - 350^4}{600^4 - 350^4}$$

$$= 0.823$$

Then the values of F_{1-2} and S are found for $L = 5/0.5 = 10$ from Eqs. (75a) and (75b), and $q^*(L)$ is found.

$$F_{1-2}(10) = 0.002\,5$$

$$S(10) = 0.064\,2$$

$$q^* = 1 - 0.823 - 0.034(0.002\,5) + 0.857(0.064\,2) = 0.232$$

The dimensional heat flux follows from Eq. (69):

$$q = (C_sT_1^4 - C_sT_2^4)q^*$$

$$= (5.669\,7 \times 10^{-8})(600^4 - 350^4)(0.232)$$

$$= 1\,507\ \mathrm{W/m^2}$$

When the side-wall radiosity is unknown but the temperature or blackbody radiosity variation with x is known, the problem can be formulated by passing from the sum to the integral in Eq. (14) and using Eq. (13) to eliminate q^+ or q^-. The resulting linear integral equation can be solved numerically. Alternatively, the side wall can be divided into a number of segments, and Eq. (23) or (25) used and solved by matrix inversion as described previously. Shape factor algebra allows all the shape factors to be expressed and calculated in terms of differences of $F_{1-2}(x_i - x_j)$. However, as described in the next section, a Monte Carlo algorithm is more easily applied.

In the case of refractory side walls, the temperature or blackbody radiosity variation with x is unknown. All that is known is that $q_3^+(x) = q_3^-(x)$ regardless of side-wall emissivity. An equivalent statement is simply that

$$\frac{d}{dx_0} q^*(x_0) = 0 \tag{76}$$

where $q^*(x_0)$ is given by Eq. (70). Note that when conduction is absent, no boundary conditions can be imposed. Again the side wall can be divided into a number of zones, the integrals approximated as sums, and matrix inversion applied. Again Monte Carlo calculations are easily programmed for computer execution. What is desired in the end is q^*, which is the $\mathfrak{F}_{1-2,b}$ needed for Eq. (59) to find the transfer factor $\mathfrak{F}_{1-2}$.

An approximate closed-form expression for the refractory-walled-passage transfer factor $\mathfrak{F}_{1-2,b}$ can be found by postulating q_3^{*+} to be a straight line passing through 1/2 at $x = L/2$. The unknown slope m is found, following Hottel and Keller [16], by requiring that Eq. (73) give the same result for $x_0 = 0$ and $x_0 = L/2$ (also, $x_0 = L$ from symmetry). There is found

$$mL = \frac{G(L) - F(L/2)}{(G(L) - F(L/2)) + (S(L/2) - S(L))} \tag{77}$$

where

$$G(L) = \frac{1 + F(L)}{2} \qquad F(L) = F_{1-2}(L) \tag{78}$$

The value of the transfer factor is

$$\mathfrak{F}_{1-2,b} = (1 - mL)G(L) = mLS(L) \tag{79}$$

For the circle cross section, the notion of an extrapolation length E is a good approximation; that is,

$$mL \doteq \frac{L}{L + 2E} \qquad E = 0.5 \text{ for circle}$$

Note that if conduction from the hot source to the end of the passage at $x = L$ and from the end at $x = 0$ to the cold sink is operative, E should be zero and $mL = 1$.

Figure 10 shows values presented versus the length-to-hydraulic-diameter ratio, because transfer factor is independent of cross-sectional shape for small L/D_H. For small L, Eq. (60) or (79) indicates that

$$\mathfrak{F}_{1-2,b} = \frac{1 + F_{1-2}}{2} \qquad \text{as } L \to 0$$

But shape factor algebra shows that

© 1983 Hemisphere 1 blishing Corporation

$$F_{1-2} = 1 - F_{1-3} = 1 - \frac{A_3}{A_1} F_{3-1}$$

Area A_3 is PL, where P is the perimeter of the passage cross section. When L is small, F_{3-3} is small, so that

$$F_{3-1} = F_{3-2} \frac{1 - F_{3-3}}{2} \doteq \frac{1}{2}$$

Accordingly, for small L, but regardless of cross section, one has

$$\mathfrak{F}_{1-2,b} \doteq 1 - \frac{PL}{4A_1} = 1 - \frac{L}{D_H}$$

$$\doteq \frac{1}{1 + (L/D_H)} \qquad L/D_H \text{ small} \tag{80}$$

Figure 10 shows that the insensitivity of the transfer factor persists even to values of L/D_H considerably larger than unity.

For example, suppose that one wanted to know the heat leak per meter $(\dot{Q}/W)$ through a 3-mm crack in a 6-cm-thick insulation layer. Suppose that $T_1 = 600$ K and T_2 = 300 K. One finds the transfer factor from the figure.

$$D_H = \frac{4A}{P} = \frac{4WH}{2W} = 2H = 0.6 \text{ cm}$$

$$\frac{L}{D_H} = \frac{6}{0.6} = 10 \qquad \mathfrak{F}_{1-2,b} \doteq 0.16$$

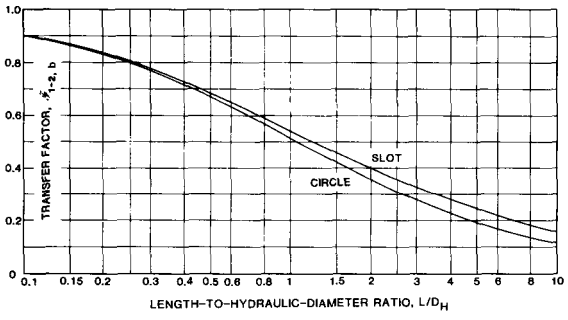

Figure 10 Transfer factor for diffuse-refractory-walled passages [approximate values from Eq. (79)].

Then one uses the definition of the transfer factor, Eq. (27), to evaluate the heat flow.

$$\frac{\dot{Q}}{W} = \frac{qWH}{W} = Hq = H\mathfrak{F}_{1-2,b} C_s (T_1^4 - T_2^4)$$

$$= (0.006)(0.16)(5.669\ 7 \times 10^{-8})(600^4 - 300^4)$$

$$= 6.6 \text{ W/m}$$

Values of $\mathfrak{F}_{1-2,b}$ are available in the literature for a few other cross sections [19] and for tapered passages [18]. Specular-walled passages and passages modeled by the Torrance-Sparrow wall roughness model are discussed in Sec. 2.9.4.

Nomenclature for Section 2.9.3 appears at the end of Section 2.9.8.

BIBLIOGRAPHY FOR SECTION 2.9.3

Shape factors

1. Moon, P., ***The Scientific Basis of Illuminating Engineering,*** McGraw-Hill, New York, 1936.
2. Hamilton, D. C., and Morgan, W. R., Radiant Interchange Configuration Factors, NACA TN 2836, 1952.
3. Hottel, H. C., Radiant Heat Transmission, ***in Heat Transmission,*** ed. W. H. McAdams, 3d ed., chap. 4, McGraw-Hill, New York, 1954.
4. Zijl, H., ***Large-Size Perfect Diffusers,*** 2d rev. ed., Philips Gloeilampenfabrieken, Eindhoven, Netherlands, 1960.
5. Dummer, R. S., and Breckenridge, W. T., Jr., Radiation Configuration Factors Program, Rept. ERR-AN-224, General Dynamics Astronautics, 1963.
6. Toups, K. A., CONFAC II, Technical Documentary Rept. RDL-TDR-64-43, North American Aviation, 1964.
7. Siegel, R., and Howell J. R., ***Thermal Radiation Transfer,*** McGraw-Hill, New York, 1972 (see app. C, Catalog of Selected Configuration Factors).

Radiosityirradiation formulations

8. Hottel, H. C., and Sarofim, A. F., ***Radiative Transfer,*** McGraw-Hill, New York, 1967. See also [3].
9. Gebhart, B., Unified Treatment for Thermal Radiation Transfer Processes-Gray, Diffuse Radiators and Absorbers, AMSE Paper 57-A-34, 1957.
10. O Brien, P. F., Lightning Calculations for Thirty-Five Thousand Rooms, *Illuminating Eng., vol. 55,* pp. 215-226, 1960.
11. Bobco, R. P., Radiation Heat Transfer in Semigray Enclosures with Specularly and Diffusely Reflecting Surfaces, *J. Heat Transfer,* vol. 86, pp. 123-130, 1964.
12. Ishimoto, T., and Bevans, J. T., Method of Evaluating Script F for Radiant Exchange within an Enclosure, *AIAA J.*, vol. 1, pp. 1428-1429, 1963.
13. Wiebelt, J. A., ***Engineering Radiation Heat Transfer,*** Holt, New York, 1966.

© 1983 Hemisphere Publishing Corporation

Radiation network

14. Oppenheim, A. K., Radiation Analysis by the Network Method, *Trans. ASME*, vol. 78, pp. 725–735, 1956.
15. Oppenheim, A. K., The Engineering Radiation Problem-An Example of the Interaction Between Engineering and Mathematics, *Z. Angew. Math. Mech.*, vol. 36, pp. 81-93, 1956.

Diffuse passages

16. Hottel, H. C., and Keller, J. D., Effect of Reradiation on Heat Transmission in Furnaces and Through Openings, *Trans. ASME*, vol. 55, pp. 39-49, 1933.
17. Perlmutter, M., and Siegel, R., Effect of Specularly Reflecting Gray Surface on Thermal Radiation Through a Tube and from Its Heated Wall, *J. Heat Transfer,* vol. 85, pp. 55-62, 1963.
18. Sparrow, E. M., and Jonsson, V. K., The Transport of Radiant Energy Through Tapered Tubes and Gaps, *J. Heat Transfer,* vol. 86, p. 132, 1964.
19. Kezios, S. P., and Wulff, W., Radiative Heat Transfer Through Openings of Various Cross Sections, *Proc. 3d Int. Heat Transfer Conf., Chicago,* vol. 5, pp. 207–218, 1966.

© 1983 Hemisphere Publishing Corporation

2.9.4

Radiation transfer between specular and imperfectly diffuse surfaces

D. K. Edwards

A. Specular and imperfectly diffuse surfaces

The concept of a perfectly diffuse surface was an artifice introduced to simplify formal mathematical analysis of radiant transfer. The concept is widely used in engineering design and analysis for its convenience, and, surprisingly, the answers so obtained are found in many instances to be remarkably close to the answers found with more realistic analytical models. There are situations-for example, in transmission through long passages with specular side walls-where the assumption of perfectly diffuse reflection will lead to serious error, however. Thus the designer or analyst needs to be able to carry out calculations when one or more surfaces are not perfectly diffuse.

Perfectly diffuse reflection is where the bidirectional reflectance is a constant independent of all four angles, the two angles of incidence and the two of emergence. The antithesis of perfectly diffuse reflection is specular reflection, where the bidirectional reflectance is identically zero for all directions of emergence except the specular angle where it has an integrable singularity. Imperfectly diffuse is the term usually used to denote that the bidirectional reflectance is nonzero but not constant with angles of emergence. Mixed specular diffuse reflection occurs when there is a specular component, for example, from the smooth surface of the binder of a glossy enamel paint,. and a (perfectly or imperfectly) diffuse component, for example, from the underlying particles of pigment of such a glossy enamel.

B. The mirror-image concept

The mirror-image concept was introduced formally into thermal radiation transfer analysis by Eckert, Sparrow, and co-workers [1, 2]. The concept is useful primarily when the enclosure in question contains only a few plane specular surfaces arranged so that the number of multiple specular reflections is either limited or forms an easily summed chain. The concept is based on the fact that a ray coming from an element of diffuse surface i and reflected by mirror m to an element of diffuse surface j can be regarded as an uninterrupted straight line from i to the mirror image of j. Thus the shape factor of Eq. 2.9.3(5) can be applied between surface i and the mirror image of j in calculating the transfer between i and j via m. The image of j as seen in m is denoted $j(m)$. The mirror-image shape factor is then written $\tilde{F}_{i-j(m)}$.

If another mirror n is present, the mirror image of j as seen via m may also be viewed via n. Thus there is a mirror image in n of the mirror image in m of surface j. Figure 1 illustrates the single- and multiple-image concept. Use of the mirror-image concept involves assuming that the specular reflectivity of the mirrors does not vary with angle of incidence and thus the absorptivity and emissivity do not either. Directional variations and polarization are neglected in using the concept.

To modify the radiosity-irradiation formulation developed in Sec. 2.9.3, one defines a mirror-image-augmented shape factor

© 1983 Hemisphere Publishing Corporation

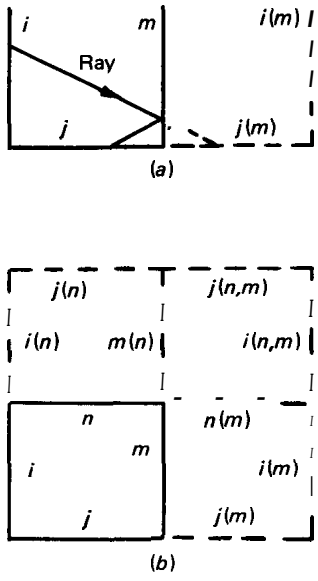

Figure 1 The mirror-image concept. (a) **One** mirror, ***m.*** (*b*) Two mirrors, m and ***n.***

$$F^*_{i-j} = F_{i-j} + \Sigma_m \rho_{S,m} F_{i-j(m)} + \Sigma_n \Sigma_m \rho_{S,n} \rho_{S,m} F_{i-j(m,n)} + \Sigma_n \cdots \Sigma_m \rho_{S,n} \cdots \rho_{S,m} F_{i-j(m,\ldots n)} \quad (1)$$

Only the diffuse -portion of the radiosity of the mirrors appears directly in the formulation. One has

$$q^+_{D,m} = \epsilon_m B_m + \rho_{D,m} q^-_m \quad (2)$$

where $\rho_{D,m}$ and ϵ_m no longer sum to unity, but

$$\rho_{D,m} = 1 - \epsilon_m - \rho_{S,m} \quad (3)$$

The irradiation is no longer given by Eq. 2.9.3(14), but by

$$q^-_m = \sum_{j=1}^{N} F^*_{m-j} q^+_{D,j} \quad (4)$$

Equations (2) and (4) are, as were Eqs. 2.9.3(13) and 2.9.3(14), $2N$ equations in 2N unknowns, and Eq. (2) can be used to reduce the set to N equations in N unknowns by eliminating say $q^+_{D,j}$, leaving

$$q^-_m = \sum_{j=1}^{N} F^*_{m-j} (\epsilon_j B_j + \rho_{D,j} q^-_j) \quad (5)$$

Equation (5) can be solved by matrix inversion or by reiteration. In the latter case one may start with $q^-_j = 0$ and use Eq. (5) to find a better set of values, and repeat the process until the set of q^-_j converges.

Once Eq. (5) is solved, the net heat fluxes and heat flows are found from Eq. 2.9.3(18), which still holds:

$$q_m = \epsilon_m (B_m - q^-_m) \quad (6)$$

$$\dot{Q}_m = \epsilon_m A_m (B_m - q^-_m) \quad (7)$$

As before, the transfer factor $\mathfrak{F}_{i-j}$ can be found by setting $B_i = 1$ and $B_j = 0$ for $j \neq i$. Then one column of the $A_i \mathfrak{F}_{i-j}$ matrix is $-\dot{Q}_j$.

C. The Monte Carlo algorithm

When the engineering designer or analyst wants to consider directional variations, polarization, and other complicating factors, the Monte Carlo algorithm is perhaps the most generally applicable method, and one that is rather easily used. The Monte Carlo technique was applied to radiation heat transfer problems by Howell and co-workers in a number of papers reviewed in [7]. It is a simplified, computerized, statistical sampling approach to ray tracing. According to electromagnetic theory, of the energy flux in an incident wave, definite fractions are reflected, absorbed, and perhaps transmitted in a wall encounter. The Monte Carlo algorithm compares a random number to the theoretical fractions and, based on the comparison, assigns the whole incident flux to the reflected or absorbed or transmitted wave. When the calculational procedure is repeated a large number of times, the net result is correct: Of the total flux of all the rays, certain fractions are reflected, absorbed, and transmitted. The heart of the Monte Carlo algorithm is to avoid branching during a ray-tracing procedure. The energy is not both reflected and transmitted; it is ***either*** reflected or transmitted, and the one result is traced further. The Monte Carlo technique has the great advantage of computing the $\mathfrak{F}$ transfer factor directly without any need to obtain shape factors [8, 9].

The elements of a Monte Carlo program are the following:

1. Choosing a point of emission
2. Choosing a direction of emission
3. Tracing a ray to a wall and determining the wall node number
4. Deciding whether the ray is absorbed, reflected, or transmitted
5. Choosing a direction of reflection or transmission
6. Scoring increments of transfer factor

Each will be briefly discussed.

Consider emitting surface ***i*** with $B_i = 1$ and all $B_j = 0$, $j \neq i$. If N rays are imagined to leave ***i,*** all with energy ϵ_i/N (where ϵ_i is the hemispherical emissivity of surface ***i),*** the sum of the energies of the rays absorbed by surface j is the transfer factor $\mathfrak{F}_{i-j}$. If surface ***i*** has a uniform temperature and finish, it is clear that an

© 1983 Hemisphere Publishing Corporation

area-weighted average should be taken. Thus points of origin on area A_i should be chosen randomly in such a way that a large number of them will be uniformly distributed over the surface. For a simple rectangle located in the domain $0 \leqslant x \leqslant a$ and $0 \leqslant y \leqslant b$, one simply chooses two random numbers between 0 and 1, P_1 and P_2, and lets the point of origin be $x = aP_1$, $y = bP_2$.

More generally, area A_i might be located between $y_1(x)$ and $y_2(x)$ in the domain $x_1 \leqslant x \leqslant x_2$. Then one of two stratagems may be employed. One is hard to program but usually makes efficient use of the computer, and the other is easy to program but often makes inefficient use of the computer. Obviously the one selected will depend on the cost and amount of programming time versus the cost and amount of computing time needed. The computationally efficient stratagem is to compute a fractional function

$$f_A(x) = \frac{\int_{x_1}^{x} (y_2(x) - y_1(x))dx}{\int_{x_1}^{x_2} (y_2(x) - y_1(x))\,dx} \tag{8}$$

Then with two independent random numbers P_1 and P_2,

$$x = x_1 + f_A^{-1}(P_1) \quad \text{and} \quad y = y_1(x) + P_2(y_2(x) - y_1(x)) \tag{9}$$

The simple-to-program method is simply to choose

$$x = x_1 + (x_2 - x_1)P_1 \quad \text{and} \quad y = y_{\min} + (y_{\max} - y_{\min})P_2$$

If $y_1(x) \leqslant y \leqslant y_2(x)$, then the point is used. If not, then another ***pair*** of P_1 and P_2 values is tried. It is essential that both P_1 and P_2 be discarded and two new random values chosen.

Next one needs to choose a direction of origin. Again two approaches are possible. A fractional function may be defined (we suppose that $\epsilon(\theta, \phi) = \epsilon(\theta)$ to illustrate):

$$f_\epsilon = \frac{\int_0^{\theta} \epsilon(\theta) \cos\theta \sin\theta\, d\theta}{\int_0^{\pi/2} \epsilon(\theta) \cos\theta \sin\theta\, d\theta}$$

Then with new random numbers P_1 and P_2,

$$\theta = f_\epsilon^{-1}(P_1) \quad \phi = 2\pi P_2$$

Alternatively, one can merely choose

$$\theta = \sin^{-1}\sqrt{P_1} \quad \phi = 2\pi P_2$$

Here, because of the nature of blackbody radiation, a uniform weighting in $\cos\theta\, d\Omega$ is taken, but the ray for the direction in question is further weighted by $\epsilon_i(\theta, \phi)/\epsilon_i$. If polarization is being considered, the ray in addition to its weight ϵ_i/N or $(\epsilon_i/N)(\epsilon(\theta, \phi)/\epsilon_i)$ is assigned a four component vector; see Amar and Edwards [32].

With the point of origin (x_0, y_0, z_0) known and the direction fixed, the straight-line ray can be represented as

$$x = x_0 + Rr_x$$

$$y = y_0 + Rr_y$$

$$z = z_0 + Rr_z$$

where r_x, r_y, and r_z are the direction cosines; for example, if the z axis and surface normal to i are parallel,

$$r_x = \sin\theta\cos\phi \qquad r_y = \sin\theta\sin\phi \qquad r_z = \cos\theta$$

The intersection of the ray with the plane (or other surface) of each of the other surfaces j can be found, and the intersection tested to see whether it lies within the surface limits. The intersection with the smallest positive ray distance R is the first one hit.

The angle of incidence between the ray and the normal to the wall **n** is found from

$$\cos\theta = -\mathbf{n} \cdot \mathbf{r} = -n_x r_x - n_y r_y - n_z r_z$$

and, when polarization is included, the new s and p directions are found using Eq. 2.9.2(93). The vector components of I are twisted into the new s and p coordinates by the rotation matrix, Eq. 2.9.2(100) with Eq. 2.9.2(97). For the angle of incidence and the state of polarization, the directional absorptivity α and reflectivity ρ are found.

Scorekeeping can be done in either of two ways. One procedure is to record a fraction α of the energy remaining in the ray before it struck the wall as having added to the ***i-j*** transfer factor. The remaining energy is assigned to the reflected ray. (When the reflected ray energy falls below a chosen minimum threshold, all of it may be assigned to a remainder.) Another procedure is to generate a random number P. If it is less than or equal to α, the remaining energy is all absorbed. When it is greater than α, the remaining energy is all reflected.

If a further reflection is traced, the direction of the reflected ray must be found. For specular reflection, Eqs. 2.9.2(111), 2.9.2(112), and 2.9.2(113) apply. For perfectly diffuse reflection, two new random numbers are generated, and θ with respect to the normal **n** is $\sin^{-1}\sqrt{P_1}$ and ϕ with respect to x is $2\pi P_2$. For imperfectly diffuse reflection, θ and ϕ can be found as just described, but the weighting of the

© 1983 Hemisphere Publishing Corporation

ray must be divided by the directional reflectance and multiplied by the bidirectional reflectance for the directions in question. Fractional functions could be used instead, at some expense in analysis and programming time.

When the decided number of rays (usually 4 000 to 10 000) is traced, the totals scored in the j transfer factor registers are normalized and printed, and another i is selected.

A refractory wall is accommodated by causing absorbed radiation to be reemitted, in the case of a total calculation with nonselective surfaces.

Consider, for example, calculating by the Monte Carlo technique the curve in Fig. 2.9.3(10) for the perfectly diffuse, gray, refractory-walled, black-ended, infinitely wide slot. A sample program in FORTRAN is shown in Table 1.

Table 1 A sample Monte Carlo program

```
      PRØGRAM SLØT
C     SLØT COMPUTES SCRIPT F12FØR A DIFFUSE REFRACTORY SLØT
      CØMMØN IX, PI
      READ(5, 11) ZL
   11 FØRMAT(F10.5)
      IX=529814367
      PI=3.1415927
      F12=0.
      DØ 101 I=1,4000
      ZØ=0.
      CALL RANDU(YØ)
      CALL DIRECT (1, RY, RZ)
  100 CONTINUE
      IF(RY.LT.0.) GØ TØ 102
      IF(RY.EQ.0.) GØ TØ 103
      J=2
      R=(1.-YØ)/RY
      Z=ZØ+R*RZ
      ZØ=Z
      YØ=1.
  200 CONTINUE
      IF(Z.LT.0.) GØ TØ 101
      IF(Z.GT.ZL) GØ TØ 201
      CALL DIRECT(J, RY, RZ)
      GØ TØ 100
  102 J=3
      R=-YØ/RY
      Z=ZØ+R*RZ
      ZØ=Z
      YØ=0.
      GØ TØ 200
  103 IF(RZ.LE.0.) GØ TØ 101
  201 F12=F12+1.
  101 CØNTINUE
      F12=F12/4000.
      WRITE(6, 12) ZL,F12
   12 FØRMAT(2X,8HFØR ZL= ,F7.2,2X,5HF12= ,E12.5)
      STØP
      END

      SUBROUTINE DIRECT(J,RY,RZ)
      CØMMØN IX,PI
      CALL RANDU(P)
      S=SQRT(P)
      C=SQRT(1.-P)
      CALL RANDU(P)
      PHI=2. *PI*P
      IF(J.EQ.2) GØ TØ 200
      IF(J.EQ.3) GØ TØ 300
      RZ=C
      RY=S*SIN(PHI)
      RETURN
```

© 1983 Hemisphere Publishing Corporation

Table 1 A sample Monte Carlo program *(Continued)*

```
  200 RY=-C
      RZ=S*CØS(PHI)
      RETURN
  300 RY=+C
      RZ=S*CØS(PHI)
      RETURN
      END

      SUBROUTINE RANDU(P)
C     RANDU GENERATES RANDØM NUMBERS ØN AN IBM360
      CØMMØN IX,PI
      IY=IX*65539
      IF(IY) 5,6,6
    5 IY=IY+2147483847+1
    6 P=IY
      P=P* .4656613E-9
      IX=IY
      RETURN
      END
```

D. Specular-walled passages

Ray tracing, with or without use of the Monte Carlo algorithm, is easily executed for specular-walled passages. Figure 2 shows calculated results from [13] versus length-to-hydraulic-diameter ratio with parameter ρ_N, the normal reflectivity of the side wall. The hydraulic diameter for the square is the side and for the slot is twice the spacing. Full account was taken of polarization and directional variations using absorptive index k equal to refractive index n for ρ_N of 0.50 and greater and $k = 0$ for smaller ρ_N. At small values of L/D, that parameter governs independent of passage cross section; hence the curves for the two cross sections come together for equal values of ρ_N. However, because of polarization in the slot and extra reflections in the square, the curves differ drastically when L/D becomes large.

(a) Isothermal sides

The passage transmissivity τ is directly useful when the side walls are isothermal and the ends open into hohlraums. Denoting the ends as 1 and 2, respectively, and the sides as 3, one recognizes that τ is the transfer factor from 1 to 2, and $1-\tau$ is the transfer factor from 1 to 3 or 2 to 3. Hence,

$$\dot{Q}_1 = \tau A(B_1 - B_2) + (1 - \tau)A(B_1 - B_3) \tag{10}$$

$$\dot{Q}_3 = (1 - \tau)A(B_3 - B_1 + B_3 - B_2) \tag{11}$$

where A is the cross-sectional area. Again B is used to stand for C_sT^4 in the case of gray walls or the Planck function $\pi I_b(\lambda,T)$ when spectral variations in properties are considered.

When the ends are nonblack, a radiosity-irradiation analysis is easily made (alternatively, delta-wye, wye-delta transformations can be made).

$$q_1^+ = \epsilon_1 B_1 + (1 - \epsilon_1)q_1^- \tag{12a}$$

$$q_1^- = (1 - \tau)B_3 + \tau q_2^+ \tag{12b}$$

$$q_2^+ = \epsilon_2 B_2 + (1 - \epsilon_2)q_2^- \tag{12c}$$

$$q_2^- = (1 - \tau)B_3 + \tau q_1^+ \tag{12d}$$

Solving for q_1^-, substituting into $q_1 = \epsilon_1 B_1 - \epsilon_1 q_1^-$, and multiplying by A gives

$$\dot{Q}_1 = A\mathfrak{F}_{1-2}(B_1 - B_2) + A\mathfrak{F}_{1-3}(B_1 - B_3) \tag{13a}$$

where

$$\mathfrak{F}_{1\text{-}2} = \frac{\epsilon_1\epsilon_2\tau}{1 - \tau^2(1-\epsilon_1)(1-\epsilon_2)} \tag{13b}$$

$$\mathfrak{F}_{1\text{-}3} = \frac{\epsilon_1(1-\tau)(1 + \tau - \tau\epsilon_2)}{1 - \tau^2(1-\epsilon_1)(1-\epsilon_2)} \tag{13c}$$

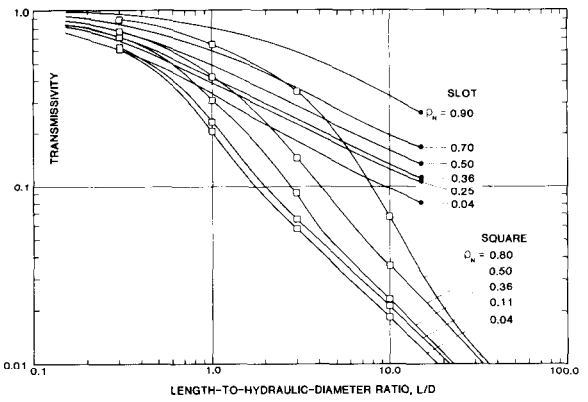

Figure 2 Transmissivity for a passage with indicated cross section and normal wall reflectivity having circular sides.

© 1983 Hemisphere Publishing Corporation

The relations for $\mathfrak{F}_{2-1}$ and $\mathfrak{F}_{2-3}$ can be formed by interchanging the 1 and 2 subscripts.

When the side walls are isothermal due to good lateral conduction but are adiabatic as a whole and are gray, one sets $\dot{Q}_3$ in Eq. (11) equal to zero and solves for B_3. When the result is substituted into Eq. (10), the net heat flow from 1 into 2 is found:

$$\dot{Q}_{1-2} = A\,\frac{1+\tau}{2}(C_s T_1^4 - C_s T_2^4) \qquad (14)$$

(B_3 = constant $\dot{Q}_3 = 0$, gray walls)

(b) Noniso thermal sides

First consider the problem for a number of isothermal segments on the sides. Circumferential variations are assumed absent, or symmetry is assumed for the slot. With black ends and specular sides, no reflected radiation can reverse direction along the x axis of the passage. Thus the transfer factor from end e to side element si between x_i and x_{i+1} is simply

$$A_e \mathfrak{F}_{e-si} = A_{si}\mathfrak{F}_{si-e} = A(\tau(x_i - x_e) - \tau(x_{i+1} - x_e)) \qquad (15)$$

where either side wall properties do not vary with temperature or such variation was accounted for when $\tau(x)$ was computed. By placing imaginary end areas A_{ej} and $A_{e(j+1)}$ at locations x_j and x_{j+1} and realizing that the difference between $\mathfrak{F}_{si-e(j+1)}$ and $\mathfrak{F}_{si-ej}$ is the side-to-side transfer factor $\mathfrak{F}_{si-sj}$, one finds that

$$A_{si}\mathfrak{F}_{si-sj} = A_{sj}\mathfrak{F}_{sj-si} = A(\tau(x_i - x_{j+1}) + \tau(x_{i+1} - x_j) - \tau(x_{i+1} - x_{j+1}) - \tau(x_i - x_j)) \qquad (16)$$

With the general end-to-end, end-to-side, and side-to-side transfer factors known, any desired problem can be readily formulated and solved.

The heat flow at end 1 at x = 0 is found from Eq. (15),

$$\dot{Q}_1 = A\tau(L)(B_1 - B_2) + A\Sigma_i(\tau(x_i) - \tau(x_{i+1}))(B_1 - B_i) \qquad (17)$$

where $x_2 = L$ is the total length of the passage. In the limit as $x_{i+1} - x_i$ goes to zero, the summation passes to an integral so that

$$q_1 = \frac{Q_1}{A} = \tau(L)(B_1 - B_2) + \int_0^L -\frac{d\tau}{dx}(B_1 - B(x))\,dx \qquad (18)$$

Integration by parts presents a form in terms of τ instead of its derivative:

$$q_1 = (B_1 - B(0)) - \tau(L)(B_2 - B(L)) - \int_0^L \tau\frac{dB}{dx}\,dx \qquad (19)$$

For example, if there is no temperature jump at the ends, and a straight-line B gradient exists, one finds from Eq. (19) simply

$$q_1 = (B_1 - B_2)\bar{\tau}(L) \qquad (20)$$

where

$$\bar{\tau}(L) = \frac{1}{L}\int_0^L \tau(x)\,dx \qquad (21)$$

Values of $\bar{\tau}$ may be extracted from the running integrals of τ presented in [13].

(c) Adiabatic sides

If the passage side walls neither conduct longitudinally nor lose or gain heat out of their backs or by convection from their surfaces and are gray, they are said to be in radiative equilibrium. The side-wall blackbody radiosity $B(x) = C_s T(x)^4$ then takes a shape such that

$$\frac{dq_R(x)}{dx} = 0 \qquad (22)$$

where q_R is the net heat flux in the positive x direction at any x cross section. Generalizing Eq. (19) to any position x gives

$$q^*(x) = \frac{q_R(x)}{B_1 - B_2} = \tau(x) + \tau(L - x)\Phi(L) - \tau(x)\Phi(0) - \int_0^x \tau(x - x')\frac{d\Phi}{dx'}\,dx' - \int_x^L \tau(x' - x)\frac{d\Phi}{dx'}\,dx' \qquad (23)$$

where

$$\Phi = \frac{B(x) - B_2}{B_1 - B_2} \qquad (24)$$

If a direct Monte Carlo solution is not available (recall that an adiabatic surface is modeled by requiring absorbed photons to be reemitted in the Monte Carlo algorithm) but calculations of $\tau(x)$ are available, one can employ the same approximate solution by colocation used in Sec. 2.9.3F by assuming that $\Phi(x) = \Phi_0 - (x/L)\,\Delta\Phi$ and requiring $q^*(0) = q^*(L/2) = q^*(L)$. There is found

© 1983 Hemisphere Publishing Corporation

$$\Delta\Phi = \frac{1 + \tau(L) - 2\tau(L/2)}{1 + \tau(L) - 2\tau(L/2) + 2\bar{\tau}(L/2) - 2\bar{\tau}(L)} \tag{25a}$$

$$\Phi_0 = \frac{1 + \Delta\Phi}{2} \tag{25b}$$

$$\mathfrak{F}_{1-2,b} = \tau\left(\frac{L}{2}\right) + \left[\bar{\tau}\left(\frac{L}{2}\right) - \tau\left(\frac{L}{2}\right)\right] \Delta\Phi \tag{25c}$$

Figure 3 shows approximate values [13] found in this manner. This figure may be compared with Fig. 2.9.3(10) for diffuse-refractory-walled passages. The differences are striking. First, Fig. 2.9.3(10) does not depend on side-wall reflectivity at all, because there is no difference between diffusely reflected and diffusely reemitted radiation. Figure 3 depends greatly on side-wall reflectivity because reflected radiation continues in the same x direction. If specular reflectivity is unity, passage transfer factor is 100% regardless of length; the passage becomes a light pipe. Another difference is the sensitivity of the transfer factor to the passage cross section. In Fig. 2.9.3(10) at ***L/D*** = 5, the slot transfer factor is only about 30% greater than that for the circle, whereas in Fig. 3, the difference for $\rho_N = 0.04$ is nearly 50%. The difference arises from high specular reflectivity at grazing angles and, in the slot, polarization to the *s* component for which the reflectivity is still higher.

Recall that for a 3-mm gap in a 6-cm wall between a space at 600 K and 300 K, a heat leak of 6.6 W/m was found at the end of Sec. 2.9.3F for the diffuse side wall. For a specular side wall with 36% normal reflectivity (not atypical of an oxidized metal), Fig. 3 gives a transfer factor of 0.3, and the heat leak is 12.4 W/m.

E. Surface models

The long passage is a geometry for which the transfer factors clearly depend significantly on the type of reflection assumed, specular or diffuse. Other geometries, such as the cubical specular-walled enclosure treated in [5], are not so sensitive to the type of surface reflection. The question of how to model the reflection from a technical surface thus arises mainly in concern with passage transfer factor or with similar elongated configurations.

Two surface effects need to be clearly distinguished, the effect of surface geometry and the effect of surface state. Bennett [15] suggested that differences in emissivity and absorptivity of metals associated with surface roughness were due to surface damage rather than surface geometry. Rolling [16] used platinum, which is easily annealed without surface oxidation, to show that the emissivity of rough but annealed platinum was virtually the same as that of smooth annealed platinum but quite different from that of the roughened unannealed material.

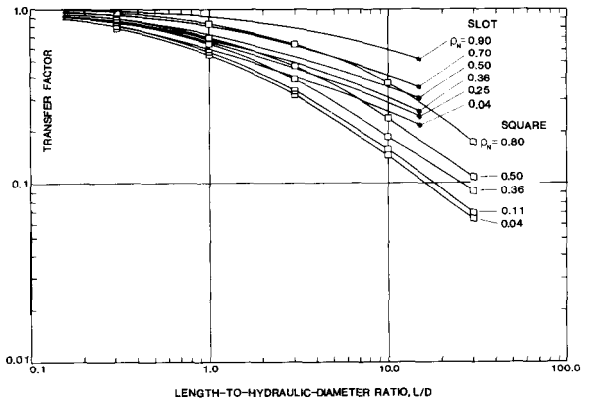

Figure 3 Transfer for a passage with indicated cross section and normal wall reflectivity having specular and adiabatic side *walls*.

Oxidation of a metal tends to create a thin film of metal oxide dielectric or semiconductor on the surface and can be modeled via the thin film optics reviewed in Sec. 2.9.2F. However, the films created by oxidizing a rough or polycrystalline metal are not necessarily even in thickness and homogeneous in depth [17].

Although the surface geometry of metals appears to have a small effect on emissivity and absorptivity (apart from the change in the surface layer from mechanical damage), the surface geometry clearly affects the bidirectional reflection properties. Three types of surface models for modeling bidirectional reflectivity in radiative transfer calculations are briefly reviewed in this section.

(a) Diffraction models

For roughness elements of small height relative to the wavelength and slight slopes, Rice [18], Davies [19], and Beckmann and Spizzichino [20] have proposed models. For root-mean-square (RMS) roughness σ_r and RMS slope σ_r/a and an infinitely conducting metal, the Beckmann equation gives the diffuse bidirectional reflectance as

$$\rho_{B\lambda}(\theta^+, \phi^+, \theta^-, \phi^-, \lambda) = \frac{\pi^2 (a/\lambda)^2}{\cos\theta^+ \cos\theta^-} BFe^{-G} \tag{26a}$$

where

$$B = \frac{1 + \cos\theta^+ \cos\theta^- + \sin\theta^+ \sin\theta^- \cos(\phi^+ - \phi^-)}{\cos\theta^+ + \cos\theta^-} \tag{26b}$$

© 1983 Hemisphere Publishing Corporation

$$G = \left[2\pi \frac{\sigma_r}{\lambda} (\cos \theta^+ + \cos e\text{-})\right]^2 \quad (26c)$$

$$F = \sum_{m=1}^{\infty} \frac{G^m}{mm!} \exp \left\{ -\frac{\pi}{m} \left(\frac{a}{\lambda}\right) [\sin^2 \theta^+ + \sin^2 \theta^- + 2 \sin \theta^+ \sin \theta^- \cos (\phi^+ - \phi^-)] \right\} \quad (26d)$$

The specular reflectance [21,22] is

$$\rho_S(\theta^-, \lambda) = \exp \left\{ -\left(\frac{4\pi\sigma_r \cos \theta^-}{\lambda}\right)^2 \right\} \quad (27)$$

Houchens and Hering [22] found that the Davies relation failed to obey conservation of energy outside of a narrow range of parameters. Beckmann s result above was better in that respect, giving a useful range of σ_r/λ = 0.01-0.20 and a/σ_r = S-75.

It was noted (see [2] of Sec. 2.9.2) that the slightly rough surfaces modeled by the Beckmann equation could be regarded from an engineering point of view as specular. The angles through which the radiation is scattered go as $\lambda/\pi a$ and $\lambda/(\pi a \cos \theta^-)$, whereas the fraction scattered goes as $1 - \exp\{-[(4\pi\sigma_r \cos \theta^-/a)^2 (a/\lambda)^2]\}$. For surfaces with σ_r on the order of 0.5 μm and slopes on the order 0.1 or less, the quantity a is 2.5 μm or more. When a/λ is large, the amount of reflected radiation diffused is large, but the angle through which it is diffused is small. When a/λ is small, the angle through which the reflected radiation is diffused is large, but the amount of diffusely reflected radiation is small. For heat transfer purposes, such surfaces may be modeled as specular.

(b) Geometric optics models

Torrance and Sparrow [23] suggested a simple model to represent the near-field reflection from a surface with large roughness elements compared to the wavelength of the irradiation. A statistical distribution of facet slopes in the form $e^{-\partial \alpha^2}$ was taken. Each facet is one of a pair forming a symmetric V groove whose azimuthal orientation is uniformly random, and the upper edges of all V grooves are in the same plane. The facets were taken to be perfectly specular to the first reflection and perfectly diffuse to interreflections. Edwards and Bertak [24] incorporated the Torrance-Sparrow model into the Monte Carlo method. Look and Love [25] identified the sharp tops of the Torrance-Sparrow model as a matter for concern and suggested rounding them off by introducing another parameter.

The Monte Carlo implementation of the Torrance-Sparrow model is as follows: Each surface is parameterized by optical constants n and k of the facets and a slope distribution angle α_0 = l/c. If one desires, one can fix k = n and compute the hemispherical reflectivity of the rough surface and use a measured value of that parameter to thus fix n and k for a given α_0. Edwards and Bertak [24] suggested using additionally a measured value of slot passage transmittance to fix α_0. When, during the course of a Monte Carlo ray tracing, a wall with fixed optical constants and roughness parameter α_0 is encountered, three more random numbers are taken from the random number generator. One, call it P_1, is used to fix α by a look-up-and-interpolate table previously computed and stored [just as a given value of fractional function is used to fix a wavelength in Table 2.9.1 (1)].

$$P_1 = \frac{\int_0^{\alpha} e^{-\alpha^2/\alpha_0^2} \sin \alpha \cos \alpha \, da}{\int_{I_0}^{\pi/2} e^{-\alpha^2/\alpha_0^2} \sin \alpha \cos \alpha \, d\alpha} \quad (28)$$

The second fixes the azimuthal orientation of the V groove,

$$\beta = 2\pi P_2 \quad (29)$$

and the third fixes the point of entry into the V groove across its top. Then Monte Carlo ray tracing is continued on a microscale, from facet to facet across the groove, until the ray is absorbed or reflected away from the plane of the V-groove upper edge. Upon reflection out of the V-groove system, ray tracing continues on the macro scale.

Amar and Edwards [32] suggested a few of the obvious permutations. The grooves need not be considered symmetric. Once α_{left} is found, another random number can generate α_{right} based on some statistical distribution to simulate the grinding compound or surface finishing tool. The angle β need not be considered to be isotropic when grinding, machining, or rolling introduces a preferred azimuthal orientation of the roughness elements.

(c) Scattering bed models

A coat of paint may be modeled as a cloud of pigment particles suspended in an atmosphere of paint resin or a ceramic as a cloud of voids separated by solid dielectric. Then methods such as those described in Sec. 2.9.6H or 2.9.7D may be used to generate a solution for the directional distribution of the radiation scattered away from the surface. The simplest model, used by Giovanelli [26], is for an infinitely thick cloud in a medium of n = 1. Only a single

© 1983 Hemisphere Publishing Corporation

Table 2 Chandrasekhar s H function and its hemispherical average

	$H(\omega_s, \mu)$										
ω_s	$\mu = 0.05$	0.15	0.25	0.35	0.45	0.55	0.65	0.75	0.85	0.95	$H_H(\omega_s)$
0.2	1.016	1.033	1.044	1.052	1.058	1.064	1.068	1.072	1.075	1.077	1.066
0.4	1.034	1.072	1.098	1.117	1.133	1.145	1.156	1.165	1.173	1.180	1.152
0.6	1.055	1.120	1.167	1.203	1.233	1.258	1.279	1.298	1.314	1.329	1.273
0.8	1.082	1.187	1.266	1.332	1.388	1.437	1.480	1.518	1.553	1.584	1.472
0.9	1.100	1.235	1.343	1.436	1.518	1.592	1.658	1.719	1.775	1.826	1.651
0.95	1.112	1.269	1.401	1.517	1.622	1.719	1.809	1.892	1.970	2.042	1.804
0.975	1.120	1.294	1.443	1.578	1.703	1.820	1.930	2.033	2.132	2.226	1.929
1.000	1.137	1.351	1.547	1.736	1.921	2.104	2.284	2.464	2.642	2.819	2.309

From Chandrasekhar [27].

parameter occurs, ω_s, the albedo for single scatter. The bidirectional reflectance is ϕ independent and given by

$$\rho_B(\theta^+, \theta^-) = \frac{\omega_s}{4} \frac{H(\omega_s, u) H(\omega_s, v)}{u + v} \tag{30}$$

where ω_s (a function of λ and T) is the albedo, and H is given by Chandraskehar [27] as shown in Table 2, and

$$u = \cos\theta^+ \qquad v = \cos\theta^- \tag{31}$$

The directional reflectance is given by

$$\rho(\theta^-) = 1 - (1 - \omega_s)^{1/2} H(\omega_s, v) \tag{32}$$

The hemispherical reflectance is then

$$\rho_H(\theta^-) = 1 - (1 - \omega_s)^{1/2} H_H(\omega_s) \tag{33}$$

where the subscript denotes a hemispherical average as in Eq. 2.9.2(4).

$$H_H(\omega_s) = \int_0^1 H(\omega_s, v) 2v\, dv \tag{34}$$

When the scattering medium is finite (as for a thin coat of paint), additional parameters are the optical constants of the substrate and the optical depth of the bed as well as its albedo for single scatter. If the paint resin has a refractive index different from unity, that becomes another parameter. Finally, the resin surface can be rough [29]. Clearly, a glossy enamel has a smooth resin completely submerging the pigment particles, whereas a flat or matte paint does not.

F. Rough-walled passages

Table 3 shows results [32] calculated using the Torrance-Sparrow model and taking full account of

Table 3 Rough, isothermal-walled passage transmissivity and absorptivity[a,b]

Roughness parameter α_0, deg	Cross section[c]	Passage transmissivity $\mathfrak{T}_{1-2}$				Passage absorptivity $\mathfrak{T}_{1-3}$			
		L/D or $L/H = 1$	2	4	8	L/D or $L/H = 1$	2	4	8
0	Circle	0.922	0.860	0.760	0.620	0.078	0.140	0.240	0.380
	Square	0.921	0.862	0.761	0.624	0.079	0.138	0.239	0.376
	1 x 2	0.941	0.891	0.810	0.683	0.059	0.109	0.190	0.317
10	Circle	0.85 1	0.752	0.594	0.390	0.090	0.168	0.297	0.483
	Square	0.847	0.736	0.581	0.374	0.093	0.180	0.305	0.499
	1 x 2	0.880	0.780	0.65 3	0.457	0.069	0.138	0.245	0.416
20	Circle	0.745	0.588	0.399	0.208	0.098	0.186	0.329	0.479
	Square	0.740	0.589	0.385	0.170	0.101	0.195	0.334	0.518
	1 x 2	0.792	0.652	0.477	0.251	0.076	0.151	0.273	0.448
40	Circle	0.626	0.423	0.227	0.083	0.117	0.222	0.362	0.437
	Square	0.622	0.436	0.228	0.068	0.120	0.217	0.351	0.494
	1 x 2	0.681	0.511	0.309	0.122	0.091	0.176	0.302	0.440

[a] From Amar and Edwards [32].

[b] Facet optical constants: $n = k = 50$, giving $\rho_H = 0.95$.

Cross sections are a circle of diameter D, a square of side D, and a rectangle of $2H$ by H. The hydraulic diameters are respectively D, D, and $4H/3$.

© 1983 Hemisphere Publishing Corporation

polarization. For the passage cross sections and lengths, whether one included polarization or not made essentially no difference for the rough walls and less than 5% difference for the smooth walls. Using a fixed value equal to the normal reflectivity in place of a directionally varying reflectivity gave rise to 10% errors. Using a fixed value of facet reflectivity equal to the hemispherical reflectivity was adequate for the rough surfaces but for the smooth ones caused errors up to 16%. Since the slot was not among the cross sections investigated, the results correlate quite well with the length-to-hydraulic-diameter ratio for a given value of α_0 . Interpreting calculated passage transmissitities using the Torrance and Sparrow model to indicate specularity according to the specular diffuse model (wherein X_S of the reflection is specular and $1 - X_S$ is diffuse) gave the following values [24]:

α_0, deg	X_S
0	1.00
10	**0.94**
20	**0.77**
40	**0.59**

The results suggest that even very rough surfaces behave for heat transfer purposes in a significantly specular manner. However, examination of Table 3 shows that passage transmittance is quite sensitive to α_0, so that complete specularity ($\alpha_0 = 0$) cannot be assumed for very rough surfaces. The idea of using a measured passage transmissivity to fix α_0 or X_S can be made the basis of a specularity- or roughness-measuring instrument.

Nomenclature for Section 2.9.4 appears at the end of Section 2.9.8

BIBLIOGRAPHY FOR SECTION 2.9.4

The mirror-image concept

1. Eckert, E. R. G., and Sparrow, E. M., Radiative Heat Exchange Between Surfaces with Specular Reflection, ***Znt. J. Heat Mass Transfer,*** vol. 3, pp. 42-54, 1961.
2. Sparrow, E. M., Eckert, E. R. G., and Jonsson, V. K., An Enclosure Theory for Radiative Exchange Between Specularly and Diffusely Reflecting Surfaces, ***J. Heat Transfer,*** vol. 84, pp. 294-300, 1964.
3. Bobco, R. P., Radiation Heat Transfer in Semigray Enclosures with Specularly and Diffusely Reflecting Surfaces, ***J. Heat Transfer,*** vol. 86, pp. 123-130, 1964.
4. Sparrow, E. M., and Lin, S. L., Radiation Heat Transfer at a Surface Having Both Specular and Diffuse Reflectance Components, ***Znt. J. Heat Mass Transfer,*** vol. 8, pp. 769-779, 1965.
5. Sarofim, A. F., and Hottel, H. C., Radiative Interchange Among Non-Lambert Surfaces, ***J. Heat Transfer,*** vol. 88, pp. 37-44, 1966.
6. O Brien, P. F., and Bobco, R. P., Interreflections in Mirrored Rooms, ***Illuminating Eng.,*** vol. 59, pp. 337-344, 1964.

The Monte Carlo algorithm

7. Howell, J. R., Applications of Monte Carlo to Heat Transfer Problems, ***Adv. Heat Transfer,*** vol. 5, pp. l-54, 1966.
8. Weiner, M. M., Tindall, J. W., and Candell, L. M., Radiative Interchange Factors by Monte Carlo, ASME Paper 65-WA/HT-51, 1965.
9. Corlett, R. C., Direct Monte Carlo Calculation of Radiative Heat Transfer in Vacuum, ***J. Heat Transfer,*** vol. 88, pp. 376-382, 1966.
10. Toor, J. S., and Viskanta, R., A Numerical Experiment of Radiant Heat Exchange by the Monte Carlo Method, ***Znt. J. Heat Mass Transfer,*** vol. 11, pp. 883-897, 1968.

Smooth-walled passages (see also Fig. 5 of [4])

11. Perlmutter, M., and Siegel, R., Effect of Specularly Reflecting Gray Surface on Thermal Radiation Through a Tube and from Its Heated Wall, ***J. Heat Transfer,*** vol. 85, pp. 55-62, 1963.
12. O Brien, P. F., and Sowell, E. F., Radiant Transfer through Specular Tubes, ***J. Opt. Soc. Am.,*** vol. 57, pp. 28-34, 1967.
13. Edwards, D. K., and Tobin, R. D., Effect of Polarization on Radiant Heat Transfer through Long Passages, ***J. Heat Transfer,*** vol. 89, pp. 132-138, 1967.
14. Felland, J. R., and Edwards, D. K., Solar and Infrared Radiation Properties of Parallel-Plate Honeycomb, ***AZAA J. Energy,*** vol. 2, pp. 309-317, 1978.

Surface models

Surface damage

15. Bennett, H. E., Influence of Surface Roughness, Surface Damage, and Oxide Films on Emittance, pp. 145-152, NASA SP-55, 1965.
16. Rolling, R., Effect of Surface Roughness on the Spectral and Total Emittance of Platinum, ***Prog. Aeronaut. Astronaut.,*** vol. 20, pp. 91-114, 1967.

© 1983 Hemisphere Publishing Corporation

17. Edwards, D. K., and Catton, I., Radiation Characteristics of Rough and Oxidized Metals, ***Advances in Thermophysical Properties at Extreme Temperatures and*** Pressures, pp. 189-199, ASME, New York, 1965.

Diffraction theory

18. Rice, S. O., Reflection of Electromagnetic Waves from Slightly Rough Surfaces, *Commun. **Pure** Appl. **Math.,*** vol. 4, pp. 351-378, 1951.
19. Davies, H., The Reflection of Electromagnetic Waves from a Rough Surface, *Proc. **Inst.** Elec. **Eng.,*** pt. IV, vol. 101, pp. 209-214, 1954.
20. Beckmann, P., and Spizzichino, A., ***The Scattering of Electromagnetic Waves from Rough Surfaces,*** Macmillan, New York, 1963.
21. Bennett, H. E., and Porteus, J. O., Relation Between Surface Roughness and Specular Reflectance at Normal Incidence, ***J. Opt. Soc. Am.,*** vol. 51, pp. 123-129, 1961.
22. Houchens, A. F., and Hering, R. G., Bidirectional Reflectance of Rough Metal Surfaces, ***Prog. Astronaut. Aeronaut.,*** vol. 20, pp. 65-89, 1967.

Geometric optics

23. Torrance, K. E., and Sparrow, E. M., Theory for Off-Specular Reflection from Roughened Surfaces, ***J. Opt.** Soc. **Am.,*** vol. 57, pp. 1105-1114, 1967.
24. Edwards, D. K., and Bertak, I. V., Imperfect Reflections in Thermal Radiation Transfer, *Prog. **Astronaut. Aeronaut.,*** vol. 24, pp. 143-163, 1970.
25. Look, D. C., and Love, T. J., Investigation of the Effects of Surface Roughness upon Reflectance, *Prog. **Astronaut. Aeronaut.,*** vol. 24, pp. 123-142, 1970.

Scattering beds

26. Giovanelli, R. G., Reflection by Semi-Infinite Diffusers, ***Opt.** Acta,* vol. 2, pp. 153-162, 1955.
27. Chandrasekhar, ***S., Radiative Transfer,*** pp. 107, 328, Dover, New York, 1960.
28. Hottel, H. C., and Sarofim, A. F., ***Radiative Transfer,*** pp. 417-418, McGraw-Hill, New York, 1967.
29. Rogers, J. E., and Edwards, D. K., Bidirectional Reflectance and Transmittance of a Scattering-Absorbing Medium with a Rough Surface, ***Prog. Astronaut. Aeronaut.,*** vol. 49, pp. 3-24, 1976.
30. Armaly, B. F., and El-Baz, H. S., Influence of Substrate Properties on the Apparent Emittance of an Isothermal Isotropically Scattering Medium, ***J. Heat Transfer,*** vol. 99, pp. 208-211, 1977.
31. Crosbie, A. L., Apparent Radiative Properties of an Isotropically Scattering Medium on a Diffuse Substrate, ***J. Heat Transfer,*** vol. 101, pp. 68-75, 1979.

Rough-walled passages (see also [4,24])

32. Amar, R. C., and Edwards, D. K., Reflection and Transmission by Rough-Walled Passages, Prog. ***Astronaut. Aeronaut.,*** vol. 31, pp. 475–495, 1913.

© 1983 Hemisphere Publishing Corporation

2.9.5
Gas radiation properties

D. K. Edwards

A. The equation of transfer

Up to this point, a diathermanous medium has been assumed. In such a medium the radiant intensity I of a stream of photons is unaffected by passage through the medium. More generally, the photons and matter interact. Three processes may be distinguished: (1) net absorption (total absorption minus induced emission), (2) spontaneous emission, and (3) scattering. The latter can be broken down into scattering out of the beam and scattering into the beam. The result is that in slant path increment ds there is an incremental change in intensity dI as pictured in Fig. 1. The equation giving dI/ds is named the equation of transfer.

The absorption, emission, and scattering properties of matter are sometimes characterized by cross sections. For example, visualize a spherical oil droplet such as is sprayed into a combustion chamber. The droplet of radius R has a total surface area of $4\pi R^2$, but its projected area is πR^2. The latter is said to be the geometric cross section. If one examines the shadow behind a droplet that is large compared to the wavelength, one finds, due to diffraction, a shadow area of $2\pi R^2$, but a bright halo contains half of the radiant power missing due to the shadow, half of $I\, d\Omega\, 2\pi R^2$. Whether the droplet is large or small, the radiant power missing from the incident beam divided by that incident on an area of πR^2 is termed the extinction efficiency Q,. Thus if one considers the halo radiation as scattered, that is, caused to deviate in direction, the extinction efficiency of a large particle is 2; but, if one considers the halo as undeviated, a more reasonable view for engineering power transfer calculations, then Q_e is 1 for a large particle.

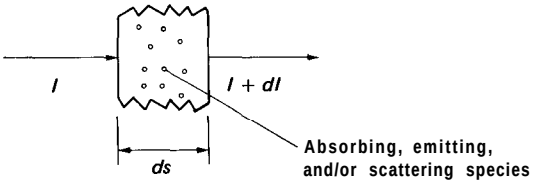

Figure 1 Change of intensity I along incremental path length ds.

The power missing from the shadow may have been absorbed, or it may have been scattered into other directions. The fraction scattered into other directions is called the albedo for single scatter ω_s. The fraction $1-\omega_s$ is sometimes called the particle emissivity. Actually it would be better called the particle absorptivity, but Kirchhoffs law is invoked. The quantity $\omega_s Q_e$ is called the scattering efficiency Q_s, and $(1-\omega_s)Q_e$ is called the absorption efficiency Q_a.

Consider N_V particles per unit volume in a gas. Within volume A ds there are $N_V A\, ds$ particles, each casting a shadow of $Q_e \pi R^2$. The length ds is so short that none of the shadows overlap. Thus the fraction of the radiant power taken out of a beam of cross section A by the particles is the ratio of the shadow area to the total area,

$$k_e\, ds = \frac{N_V A\, ds\, Q_e \pi R^2}{A} = Q_e \pi R^2 N_V\, ds$$

The quantity $k_e(m^{-1})$ is called the extinction coefficient,

© 1983 Hemisphere Pu lishing Corporation

$$k_e = Q_e \pi R^2 N_V \tag{1}$$

The absorption and scattering coefficients follow:

$$k_a = (1 - \omega_s) Q_e \pi R^2 N_V = Q_a \pi R^2 N_V \tag{2}$$

$$k_s = \omega_s Q_e \pi R^2 N_V = Q_s \pi R^2 N_V \tag{3}$$

At times one prefers to think of the radiation-matter interaction in terms of the mass of matter. The density of the absorbing mass present in a sphere is

$$\rho_a = \tfrac{4}{3} \pi R^3 \rho_{\text{solid}} N_V$$

$$\pi R^2 N_V = \frac{3}{4 R \rho_{\text{solid}}} \rho_a \tag{4}$$

Thus Eqs. (1)-(3) can be written (whether the matter is in spherical form or not)

$$k_e = \kappa_e \rho_a \qquad k_a = \kappa_a \rho_a \qquad k_s = \kappa_s \rho_a \tag{5}$$

where κ_e is the mass extinction coefficient, κ_a is the mass absorption coefficient, and κ_s is the mass scattering coefficient.

Although the concepts are presented here for clarity in terms of a cloud of fuel droplets, they are general and are applied equally well (with suitable Q s) to a cloud of gas molecules or soot particles, or other absorbing species.

The first term of the equation of transfer is seen to be simply $-k_e I = -(k_a + k_s) I$, the amount that intensity I is reduced by absorption plus scattering. The emission term is found via Kirchhoffs law for the case of local thermodynamic equilibrium. If the thermodynamic state of the particle or molecule can be characterized by a temperature T, then the emission is $k_a I_b(\nu, T)$. At complete thermodynamic equilibrium when $I = I_b$, the loss of $-k_a I$ is offset exactly by the gain $+ k_a I_b$. The equation of transfer for a nonscattering medium in local thermodynamic equilibrium is thus simply

$$\frac{dI}{ds} = -k_a I + k_a I_b \qquad (k_s = 0) \tag{6}$$

Isotropic scattering is a mathematical concept akin to perfectly diffuse reflection. When the scattering is isotropic, the intensity of the radiation scattered by a single particle is constant regardless of direction. Consider a large opaque specular sphere with reflectivity equal to ω_s, a constant independent of angle of incidence. Consider Fig. 2. Radiation striking the sphere at angle θ_s from its nose is turned through angle θ equal to $2\theta_s$. The power intercepted is $I\, d\Omega \cos\theta\, dA = I_0 d\Omega_0 \cos\theta_s \sin\theta_s R\, d\phi_s R\, d\theta_s$, and a fraction ω_s of this power is scattered in solid angle $d\Omega = \sin\theta\, d\theta\, d\phi = \sin 2\theta_s\, 2\, d\theta_s\, d\phi_s$. The intensity of the scattered radiation is the scattered power per unit projected area and per unit solid angle,

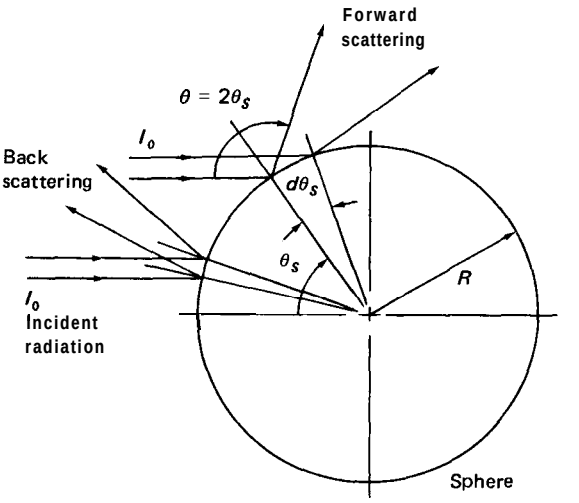

Figure 2 Scattering from a large opaque specular sphere.

$$I_{\text{scattered}} = \frac{\omega_s I_0\, d\Omega_0 \cos\theta_s \sin\theta_s\, R\, d\phi_s\, R\, do,}{\pi R^2 \sin 2\theta_s\, 2\, d\theta_s\, d\phi_s}$$

$$= \omega_s I_0 \frac{d\Omega_0}{4\pi} \tag{7}$$

The value is found to be independent of angle θ_s or θ. For a cloud of particles of thickness ds in a beam of cross-sectional area A, the scattering into the beam is the product of fraction of the area A taken up by particles $k_e\, ds$ times $I_0 d\Omega_0/4\pi$. Recognizing that $\omega_s k_e$ is k_s and integrating over all solid angles of incidence gives the scattering-in source term needed to complete the equation of transfer for isotropic scattering,

$$\frac{dI}{ds} = -(k_a + k_s) I + k_a I_b + \frac{k_s}{4\pi} \int_0^{4\pi} I\, d\Omega \tag{8}$$

If the scattering is anisotropic, for example, if in the case of the-large opaque specular particle the reflectivity ω_s is a function of angle θ_s, the variation with angle is accounted for by a phase function p under the integral. For spherical particles, p is a function merely of $\theta(= 2\theta_s)$. In general, for non-spherical particles lined up by, say, a magnetic field, p would be a bidirectional function. When polarization is included, p becomes a bidirectional 4 X 4 matrix and I a four-element vector.

B. Measurement of gas radiation properties

The execution of a calculation in which an engineer can have confidence is often difficult, because property values are often unknown. In practical situations one is often uncertain about even the composition of the medium. For example, in a burner flame or rocket

© 1983 Hemisphere Publishing Corporation

motor plume, how much soot is present? Even when one thinks he knows, for example, how much ash is present in a pulverized-coal-fired chamber, one may be uncertain as to the size distribution. Ancient Greek-type speculation, that is, calculations in the absence of measurements, does little to supply reliable design figures. What must nearly always be done is to measure the properties needed or otherwise adjust the calculational model to physical reality.

The basic experimental technique used in measuring gas radiation properties is sighting with a radiometer through a length of gas into a cavity or other reference target. The radiometer may be a total device such as a thermopile or thermistor-bridge radiometer, a low-resolution device such as a prism or variable-filter spectrometer, or a high-resolution spectral device such as a precision grating spectrometer or interferometer. The gas may be contained in a cell having windows or uncontained in an open jet. The windows in turn may be either hot or cold. A hybrid gas containment is a cell with open windows. Reviews of experimental measurements are given by Hottel and Sarofim [4] and Edwards [5].

Figure 3 shows an experimental arrangement. A low-resolution detector system at the bottom of the figure is formed by an alkaline halide (NaCl, KBr) salt crystal prism that disperses energy entering the entrance slit into an infrared rainbow. The exit slit picks off the infrared wavelength desired for detection by a thermocouple. The radiation onto the thermocouple is composed of steady heat radiation from the hohlraum formed by the monochromator housing and a fluctuating portion coming through the exit slit. The fluctuation is caused by chopping, interrupting the beam 13 times per second with a rotating blade. When

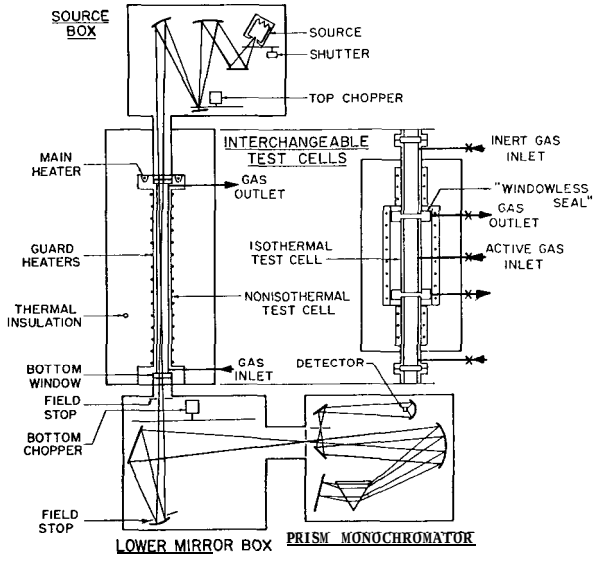

Figure 3 Gas radiation apparatus. From [5].

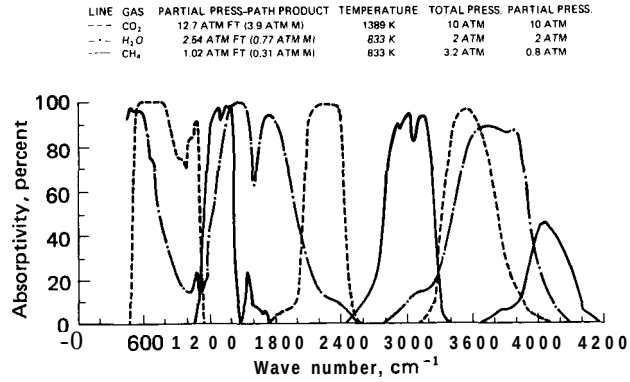

Figure 4 Low-resolution spectra. From [19].

it is desired to measure the transmissivity of the gas, the source radiation is chopped at the top of the gas cell so that emission by the gas arrives upon the detector steadily. The steady irradiation of the detector gives rise to a steady heating which causes a DC signal or bias. The fluctuating radiation gives rise to an AC signal from the detector, and it is the AC component that is amplified and recorded. Thus when the top chopper is used, and the bottom one is off and open, only the transmitted portion of the incident radiation is detected. When the signal from transmitted radiation is divided by the signal obtained with an evacuated cell, the transmissivity is found. Subtraction of the transmissivity from unity gives the experimentally measured absorptivity shown in Fig. 4.

When it is desired to measure the emission from the gas, the source at the top of the figure is made cold, the top chopper is off and open, and the bottom chopper is used. Thus the signal received is $(1 - e^{-\kappa L}) I_b(T_g, \nu)$ when the gas is isothermal. To avoid having the cell windows (also alkaline halide salt crystals) attacked by high temperature or corrosive gases, the isothermal test cell pictured in the figure was used. A heavy, inert and transparent gas supported the test gas, which in turn was capped by a light, inert and transparent gas (helium).

Experimentally it is found that monatomic gases such as He, Ne, and Ar absorb only at wavelengths considerably shorter than 1 μm and then in lines such as those found in the solar spectrum. Much the same is true of symmetric diatomic gases such as N_2 and O_2, except that at very high pressures a pressure-induced dipole is created from molecular collisions. Asymmetric diatomic gases such as CO and NO and polyatomic gases such as CO_2 and H_2O are observed to absorb strongly in certain wave number (or wavelength) regions called absorption bands, as illustrated in Fig. 4. The figure shows, for example, that CO_2 has bands at 15, 4.3, and 2.7 μm. At temperatures well above 300 K, the 9.4- and 10.4-μm bands apparent in the figure in the vicinity of 1 000 cm^{-1} [recall that

© 1983 Hemisphere Publishing Corporation

v (cm-) $=10^4/\lambda\,(\mu m)$] are strongly absorbing, but not at 300 K. Such bands are called hot bands. At high pressure, say, $P > 5$ atm, a 7.5-μm pressure-induced band appears for CO_2.

C. Qualitative remarks on the physics of gas radiation

The quantum mechanical explanation of these observations is that the vibrational energy levels of the molecules are quantized, and only photons with spectrally tuned energies corresponding to the difference in energy levels can interact with the molecules. The interaction can occur only when the mode of vibration has an associated fluctuating electric dipole; hence the lack of absorption by symmetric diatomic molecules. Under high resolution the bands are seen to possess lines; that is, the vibrational energy levels are split. The splitting is due to quantized rotational energy levels, and during absorption or emission vibrational and rotational transitions occur simultaneously. The lines become less intense but broader at high pressures, because the rotational energy levels are perturbed by molecular collisions. If the pressure is high enough, the lines may overlap and not be observable. When pressure increases have an observable effect, the low-resolution absorptivity in Fig. 4 will increase somewhat. More readily apparent is the effect of temperature. As temperature is increased, the bands become wider and less intense at their center. Under high resolution, previously very weak lines are seen to grow with increasing temperature, and the previously strong lines become less intensely absorbing but narrower, the latter effect due to a decreased collision frequency, unless temperatures are so high that Doppler broadening becomes evident from frequency shifts brought about by molecular velocities toward and away from the observer. If weak lines grow between the strong ones, the lines may become overlapped even though the individual collision-broadened lines are narrower.

Temperatures considerably higher than those encountered in furnaces and combustion chambers occur in arcs, in shock-heated gases ahead of hypersonic vehicles such as planetary probes and returning space vehicles, and in nuclear blasts. At these high temperatures electronic energy-level transitions, bound-bound transitions, give rise to lines for monatomic gas and electronic band systems for polyatomic gases. Photoionization, bound-free transitions occur when the photons and thermal excitation are sufficient to ionize the gas species. These transitions give rise to continuum absorption as opposed to line or band absorption because a photon may possess any energy beyond the minimum required for ionization and still interact with the atom or molecule. When the temperatures are high enough to ionize the gases significantly, colliding electrons may emit or absorb photons in so-called free-free transitions or brehmstrahlung.

The minimum energy requirement for photoionization gives rise to an absorption edge such as that evident in Fig. 5, from Chap. 1 of [9], for 10^{17} atoms/cm^3 of nitrogen at a temperature of 10 eV (the electron volt, a unit of energy, is used both to designate temperature through $E = kT$, 1 eV = 11 600 K, and wave number through $E = hcv$, 1 eV = 8 066 cm-). When a gas mixture contains a number of species with different ionization energies, the absorption coefficient log-log plot versus wave number often resembles a sawtooth curve. Notice that the edge is not entirely sharp, due to the thermal distribution of energy states in the high-temperature gas.

D. Spectral, band, and total property definitions

The ideas of spectral and total properties present no problems for continuum radiation; they are the same as discussed previously for the case of surfaces. For example, a cloud containing a distribution of particle sizes gives rise to continuum radiation. By continuum is meant the fact that k_a and k_s and hence Z vary slowly and smoothly with wavelength or wave number. For example, the spectral mass absorption coefficient for soot may be reasonably approximated as

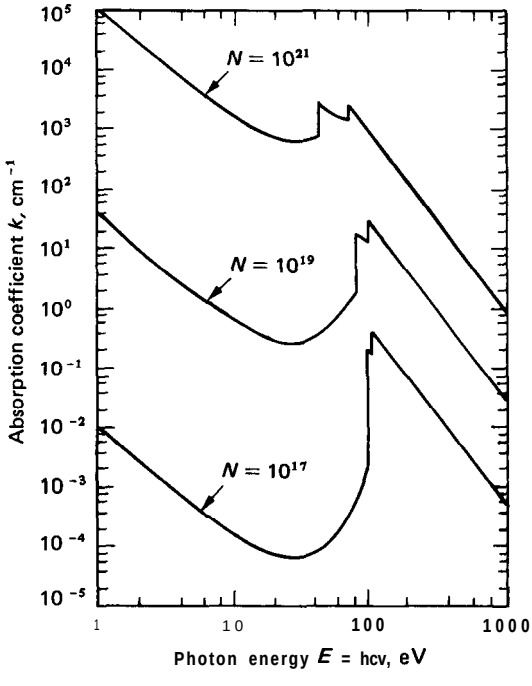

Figure 5 High-energy absorption spectrum of dissociated nitrogen. N = atoms/cm^3, $T_g = 10$ eV. From [9].

© 1983 Hemisphere Publishing Corporation

$$\kappa_a = \kappa_0 \left(\frac{\lambda}{\lambda_0}\right)^{-n} \tag{9}$$

where n is on the order of 1. The spectral emissivity of a beam L long in an isothermal cloud follows from integrating the equation of transfer, Eq. (6), with I_b constant. Introducing Eq. (5) and taking Z = 0 at $s = 0$ gives

$$Z = I_b(1 - e^{-\rho_a \kappa_a L}) \tag{10}$$

One sees that the spectral emissivity (and absorptivity) is

$$\epsilon_\lambda = 1 - e^{-\rho_a \kappa_a L} \tag{11}$$

The total emissivity is then

$$\epsilon = \frac{\int_0^\infty I\, d\lambda}{\int_0^\infty I_b\, d\lambda} = \int_0^1 (1 - e^{-\rho_a \kappa_a L})\, df_e(\lambda T) \tag{12}$$

where f_e is the external fractional function. With slow and smooth spectral variation we have found [e.g., Eq. 2.9.2(79)] that the total property can be approximated by the spectral property at $f_e(\lambda T) \doteq 0.49$. Hence a rough approximation (±7%) to Eq. (12) for soot is

$$\epsilon \doteq 1 - e^{-\rho_a L \kappa_0 (\lambda_m/\lambda_0)^{-n}}$$

$$\lambda_m T = 4\,050\ \mu\text{m K} \qquad \kappa_0 = 5\,600\ \text{m}^2/\text{kg}$$

$$n = 1.086 \tag{13a}$$

A very good approximation (±1%) to Eq. (12) is obtained using three-point Gaussian quadrature:

$$\epsilon \doteq \sum_{i=1}^{3} a_i (1 - e^{-\rho_a L \kappa_0 (\lambda_i/\lambda)^{-n}}) \tag{13b}$$

$$a_1 = 0.28 \qquad a_2 = 0.44 \qquad a_3 = 0.28$$

$$f_e(\lambda_1 T) = 0.11 \qquad f_e(\lambda_2 T) = 0.50 \qquad f_e(\lambda_3 T) = 0.89$$

$$\lambda_1 T = 2260 \qquad \lambda_2 T = 4\,110 \qquad \lambda_3 T = 8900\ \mu\text{m K}$$

The three-point or three-wavelength approximation is equivalent to three gray bands advocated by Hottel [17], the bands here having wavelength limits corresponding to $f(\lambda T) = 0, 0.28, 0.28 + 0.44 = 0.72$, and 1.

In contrast to the case of a cloud with a distribution of particle sizes, a molecular gas absorbs and emits in arrays of lines forming bands. The result is that the absorption coefficient varies very rapidly with wave number or wavelength, and the spectral absorption coefficient is the sum of the contributions of all the lines,

$$\kappa_a(\nu) = \Sigma_i \kappa_i(\nu) \tag{14}$$

where each line has its own shape, intensity, and location. For example, the Lorentz collision-broadened line shape dictates that

$$K\&j = \frac{S_i \gamma_i}{\pi[(\nu - \nu_i)^2 + \gamma_i^2]} \tag{15}$$

The quantity S_i (not to be confused with scattering source intensity; unfortunately, the same symbols are used in the more-or-less separate bodies of literature) is the integrated intensity,

$$S_i = \int_0^\infty \kappa_i(\nu)\, d\nu \doteq \int_{-\infty}^{+\infty} \kappa_i\, d(\nu - \nu_i) \tag{16}$$

The quantity γ_i is called the line half-width, because

$$\kappa_i(\nu - \nu_i = \gamma_i) = \tfrac{1}{2}\kappa_i(\nu - \nu_i = 0) \tag{17}$$

Typical values of γ at room temperature are on the order of 10^{-1} cm- . The line spacings $\nu_i - \nu_{i-1}$ are on the order of 10^0 or 10^1 cm- . The result is that κ_a may vary by several orders of magnitude over a few wave numbers.

Usually the engineer or applied scientist prefers to make calculations with a more smoothly varying function. Hence, the gas emissivity $1 - e^{-\rho_a \kappa_a L}$ or transmissivity $e^{-\rho_a \kappa_a L}$ is usually smoothed by averaging over a few line spacings:

$$\bar{\tau} = \frac{1}{\Delta\nu} \int_{\nu - \Delta\nu/2}^{\nu + \Delta\nu/2} e^{-\rho_a \kappa_a L}\, d\nu \tag{18}$$

Because of the smoothing, the result does not in general obey the Beer-Lambert law; that is,

$$\bar{\tau} \neq e^{-K_a \rho_a L}$$

Instead it is necessary to prescribe an array of lines and carry out the integration prescribed by Eq. (18). The result for $\bar{\tau}$ is called a narrow-band model. For example, the Goody narrow-band model gives

$$\bar{\tau} = \exp\left\{\frac{-(S/d)X}{\sqrt{1 + [(S/d)X/(\pi\gamma/d)]}}\right\} \tag{19}$$

where X is the absorber-partial-density-path-length product $\rho_a L$ and (S/d) and $\eta = \pi\gamma/d$ are narrow-band parameters, the mean line-intensity-to-spacing ratio and mean line-width-to-spacing ratio, respectively.

There are thus seen to be two spectral quantities, (1) the true spectral transmissivity τ, which does obey the Lambert Beer law but which fluctuates so rapidly with wave number that it is useless in practical calculations; and (2) the spectrally smoothed transmissivity $\bar{\tau}$. The smoothed spectral emissivity $1 - \bar{\tau}$ of a gas thus varies with X in the peculiar way prescribed

© 1983 Hemisphere Publishing Corporation

by Eq. (19). When X is very small, the emissivity grows linearly with X. When X is somewhat larger, it may grow as $\sqrt{X}$. Finally, when X is very large, it grows as $1 - e^{-C\sqrt{X}}$ (according to this particular narrow-band model). The line width varies with collision frequency and hence pressure and composition; thus when emissivity varies with $\sqrt{X}$, there is a $\sqrt{P_e}$ dependency as well. At high pressure when $\pi\gamma/d$ is large, the Beer-Lambert law does apply, with (S/d) playing the role of $\bar{\kappa}_a$. The lines are said to be overlapped.

A wide-band model prescribes how (S/d) and η vary with wave number. The model can either be rational, that is, a quantum mechanical-based model, or arbitrary. Among the former is the harmonic oscillator-rigid rotator model, which prescribes, approximately,

$$\frac{S}{d} = \left(\frac{S}{d}\right)_0 (\nu - \nu_0) e^{-(\nu-\nu_0)^2/\omega^2} \tag{20}$$

$$\eta = \beta P_e \tag{21}$$

Among the latter are the Schack model,

$$\frac{S}{d} = \begin{cases} 0 & |\nu - \nu_0| > \dfrac{\omega}{2} \\ \left(\dfrac{S}{d}\right)_0 \left(1 - 2\left|\dfrac{\nu - \nu_0}{\omega}\right|\right) & |\nu - \nu_0| \leqslant \dfrac{\omega}{2} \end{cases} \quad (22)$$

$$\eta = \infty$$

and the exponential-tailed band model,

$$\frac{S}{d} = \left(\frac{S}{d}\right)_0 \exp(-2|\nu - \nu_0|/\omega) \tag{23}$$

$$\eta = \beta P_e \tag{24}$$

Equations (20) and (21) or (23) and (24) give a reasonably accurate model for representing measurements of gas properties, because they make provision for both line and band structures. A wide-band model is thus seen to depend on three parameters, the band width parameter ω, the line width parameter β, and the integrated band intensity α (not to be confused with absorptivity),

$$\alpha = \int_0^\infty \frac{S}{d}\, d\nu \doteq \int_{-\infty}^{+\infty} \frac{S}{d}\, d(\nu - \nu_0) \tag{25}$$

which sets the value of $(S/d)_0$. The band origin ν_0 locates the band spectrally.

For CO_2 bands, ω_k for the kth absorption band is small. Even for H_2O bands it is not unreasonable to make the band approximation based on the idea that the band origins are widely separated compared to the band widths, that is, $\omega_k \ll \Delta\nu_k$. The band approximation is thus

$$\int_0^\infty (1 - e^{-\rho a \kappa a L}) I_b(\nu)\, d\nu \doteq \sum_k I_b(\nu_k) \int_{-\infty}^{+\infty} (1 - e^{-\rho a \kappa a L})\, d(\nu - \nu_k) \tag{26}$$

The quantity with units of wave number is the band absorption,

$$A_k = \int_{-\infty}^{+\infty} (1 - e^{-\rho a \kappa a L})\, d(\nu - \nu_k) \tag{27}$$

$$A_k = \int_{-\infty}^{+\infty} (1 - \bar{\tau})\, d(\nu - \nu_k) \tag{28}$$

When one introduces a wide-band model, one finds

$$A_k^* = \frac{A_k}{\omega} = F(\tau_{H,k}, \eta_k) \tag{29}$$

where $\tau_{H,k}$ is the optical thickness at the band head (for an exponential-tailed band model):

$$\tau_{H,k} = \frac{\alpha_k X}{\omega_k} \tag{30}$$

Section E presents formulas, tabulated physical values, and graphs for finding $\tau_{H,k}$ and η_k for combustion gases H_2O, CO_2, CO, NO, SO_2, and the fuel CH_4. The values there are based on collision-broadened lines. At very high temperatures and low pressure, Doppler broadening would have to be considered for gases (such as HF and HCl) with small values of line width-to-spacing ratio.

The band absorption property is seen to be a spectrally integrated property that is nevertheless not a total property, because it is not integrated over the total spectrum. Total emissivity and absorptivity are defined on the basis of a total-spectrum integration. Consider a gas at temperature T_g exposed to blackbody environment at temperature T_e. The total emissivity is

$$\epsilon_g = \frac{\int_0^\infty (1 - \bar{\tau}) I_b(\nu, T_g)\, d\nu}{\int_0^\infty I_b(\nu, T_g)\, d\nu} \tag{31}$$

$$\epsilon_g \doteq \frac{\Sigma_k A_k I_b(\nu_k, T_g)}{C_s T_g^4/\pi} = \Sigma_k b_k A_k = \Sigma_k b_k \omega_k A_k^* \tag{32}$$

where

$$b_k = \frac{\pi I_b(\nu_k, T_g)}{C_s T_g^4} = \frac{B(\nu_k, T_g)}{C_s T_g^4} \tag{33}$$

© 1983 Hemisphere Publishing Corporation

Similarly, the total absorptivity is

$$\alpha_g = \frac{\int_0^\infty (I - \bar{\tau}) I_b(\nu, T_e)\, d\nu}{\int_0^\infty I_b(\nu, T_e)\, d\nu} \tag{34}$$

$$\alpha_g \doteq \Sigma_k b_k(T_e)\omega_k(T_g) A^*_{k,g} \tag{35}$$

Having a graph of calculated or experimentally measured total emissivity ϵ_g, one often wishes to make a quick estimate of total absorptivity. Approximate rules for finding α_g from ϵ_g follow from Eqs. (32), (33), and (35). The recipe is to find a scaled length L', look up the emissivity at the environmental temperature, and correct it back to the gas temperature:

$$\alpha_g(T_e, T_g, PL, P_e) \doteq \left(\frac{T_g}{T_e}\right)^{1/2} \epsilon_g(T_e, PL', P_e) \tag{36}$$

The rationale of finding ϵ_g at temperature T_e is that the values of $b_k(T_e)$ are correct. The correction of $(T_g/T_e)^{1/2}$ is based on the fact that $\omega_k(T_g)$ varies as $T_g^{1/2}$. The recipe for L' must account for the variation of both $\tau_{H,k}$ and η_k with temperature. At high temperature and pressure the lines are overlapped so that the large values of η_k are no consequence. Thus one wants

$$\tau_{H,k} = \frac{\alpha_k(T_g)\rho_a(T_g)L}{\omega_k(T_g)} = \tau'_{H,k} = \frac{\alpha_k(T_e)\rho_a(T_e)L'}{\omega_k(T_e)} \tag{37}$$

For the important fundamental bands, α_k is constant in T_g; thus we obtain Penner s rule:

$$L' = L \cdot \left(\frac{T_e}{T_g}\right)^{3/2} \qquad (\eta_k > 1) \tag{38}$$

At moderate temperatures and atmospheric pressure, A^*_k depends on $\eta_k \tau_{H,k}$, and η_k goes approximately as $T_g^{1/2}$ ($300 \leqslant T_g \leqslant 1\,200$ K). Thus we obtain Hottel s rule:

$$L' = L \cdot \left(\frac{T_e}{T_g}\right) \qquad \eta_k < 1,\ \tau_{H,k} > \frac{1}{\eta} \tag{39}$$

Figures 6 and 7 present total emissivity charts for gaseous CO_2 and H_2O, respectively. The charts pertain to a dilute mixture of the radiating species in a mixture with nitrogen at a total pressure of one atmosphere. Section E explains how the charts were calculated and how to treat other values of total pressure. In the range where Eq. (38) applies, there is no pressure correction. In the range where Eq. (39) applies, $L \cdot (T_e/T_g)$ is multiplied by P_e; that is,

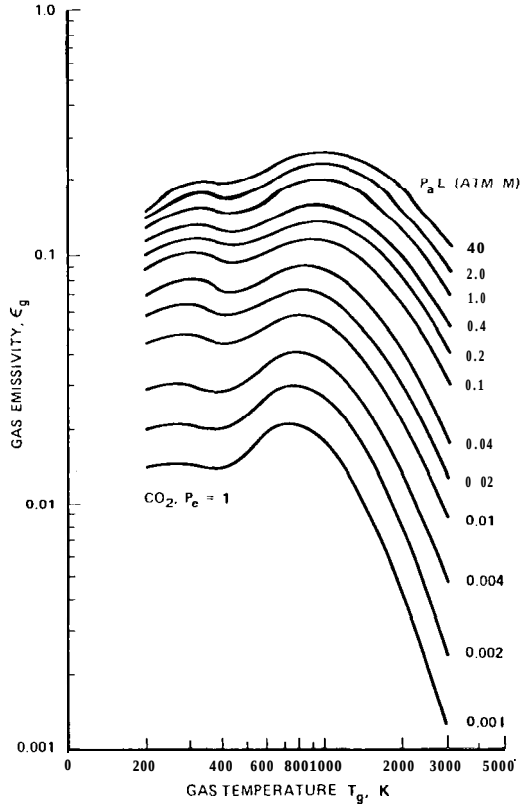

Figure 6 Total emissivity of CO, gas. From [19].

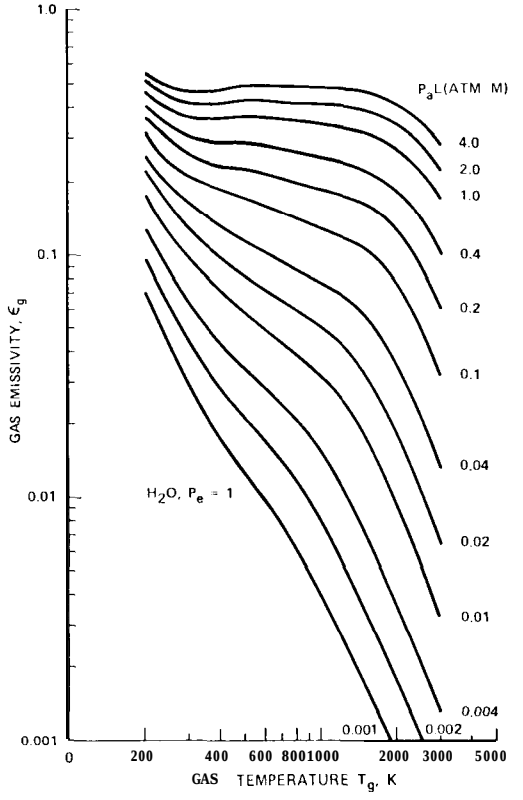

Figure 7 Total emissivity of H_2 0 gas. From [19].

© 1983 Hemisphere Publishing Corporation

$$L' = L \cdot \frac{T_e}{T_g} \cdot P_e \qquad (40)$$

This equation and Eq. (39) with $T_e = T_g$ apply to the emissivity as well. The dimensionless equivalent broadening pressure P_e is found from Eq. (57).

Section F deals briefly with gas mixtures.

E. Molecular gas radiation properties

Given a narrow-band model such as Eq. (19) and a wide-band model such as Eqs. (23), (24), one needs values of band width ω_k, line width-to-spacing parameter β_k, and band intensity α_k or optical thickness $\tau_{H,k} = \alpha_k X/\omega_k$. With these values and Eqs. (19) and (23), (24), one can find spectral properties or one can find band absorption via Eqs. (27)-(29). The determination of ω_k, β_k, and α_k or $\tau_{H,k}$ and the specification of F in Eq. (29) are now described.

Table 1 contains the necessary information. Shown for each gas are the principal radiating bands such as the 6.3-μm H_2O band. Each band is described by a set of vibrational quantum number increments $\pm\delta_1, \pm\delta_2, \pm\delta_3, \ldots$ such as 0, 1, 0 for the 6.3-w H_2O band. The number of vibrational degrees of freedom, $m = 3$ for H_2O, and the wave number ν_i and statistical weight g_i associated with each is shown. A band with a single nonzero positive value of δ_i equal to unity is called a fundamental band, and unless a symmetric vibration is associated with it, is strong. The symmetric band, such as the CO_2 1, 0, 0 has negligible intensity except at high pressure, where it is said to have a pressure-induced (collision-induced) dipole. Thus the symmetric diatomic gases O_2, N_2, H_2, etc., do not appear in the table. A band with a single nonzero value of δ_i equal to 2 or more is called an overtone and is weak, often enough so to be neglected. A band with two or more nonzero values of δ_i is called a combination band, such as the 9.4-w CO_2 band.

The band spectral location is in the vicinity of the sum of the $\pm\delta_i\nu_i$ products. The spectral location recommended for calculation is shown in the table as either a band center ν_c for an approximately symmetric band or as an upper limit ν_u for the 4.3-μm band, which has a head at approximately 2 410 cm^{-1}. Numerical values are shown for pressure parameters n and b and band absorption parameters α_0, p_0, and ω_0.

The band width parameter ω_k for the kth absorption band is readily calculated from the values given in the table. It is simply

$$\omega_k = \omega_0 \left(\frac{T}{T_0}\right)^{1/2} \qquad (41)$$

where ω_0 is related to the rotational constant B (half of the line spacing d) by

$$\omega_0 = 0.90\Gamma^2 \left(\frac{3}{4}\right) \left(\frac{2kT_0}{hcB}\right)^{1/} \qquad (42)$$

where $T_0 = 100$ K has been chosen for the table. Thus for the 6.3-μm H_2O band at 1 000 K, $\omega = 56.4\,(1\,000/100)^{1/2} = 178.4$ cm^{-1}. The quantity α_k is the value α_0 for a fundamental band, but in general for a combination or overtone band,

$$\alpha_k(T) = \alpha_0 \frac{(1 - \exp(-\Sigma_{i=1}^{m} \pm u_i\delta_i))\,\Psi(T)}{1 - \exp(-\Sigma_{i=1}^{m} \pm u_{0,i}\delta_i))\,\Psi(T_0)} \qquad (43)$$

where

$$u_i = \frac{hc\nu_i}{kT} \quad \frac{hc}{k} = 14\,388\ \mu\text{m K} \qquad (44)$$

and

$$\Psi(T) = \frac{\Pi_{i=1}^{m}\Sigma_{v_i=v_{0,i}}^{\infty}[(v_i + g_i + \delta_i - 1)!/(g_i - 1)!v_i!]\,e^{-u_i v_i}}{\Pi_{i-1}^{m}\Sigma_{v_i=0}^{\infty}[(v_i + g_i - 1)!/(g_i - 1)!v_i!]\,e^{-u_i v_i}} \qquad (45)$$

$$v_{0,i} = \begin{cases} 0 & \text{when a positive sign is associated with } \delta_i, \\ & \text{or } \delta_i = 0 \\ \delta_i & \text{when a negative sign is associated with } \delta_i \end{cases} \qquad (46)$$

Note that the values of δ_i shown in the equations are understood to be the absolute values unless preceded by $\pm$; then the appropriate sign is to be associated with δ_i.

The line width-to-spacing parameter β is given by

$$\beta(T) = \beta_0 \left(\frac{T}{T_0}\right)^{-1/2} \frac{\Phi(T)}{\Phi(T_0)} \qquad (47)$$

where

$$\Phi(T) = \frac{(\Pi_{i=1}^{m}\Sigma_{v_i=v_{0,i}}^{\infty}\{[(v_i + g_i + \delta_i - 1)!/(g_i - 1)!v_i!]\,e^{-u_i v_i}\}^{1/2})^2}{\Pi_{i=1}^{m}\Sigma_{v_i=v_{0,i}}^{\infty}[(v_i + g_i + \delta_i - 1)!/(g_i - 1)!v_i]\,e^{-u_i v_i}} \qquad (48)$$

Notice that the 2.7-m H_2O band is composed of three superposed bands, in order of importance, the (0, 0, 1), (1 , 0, 0), and (0, 2, 0) bands. For such a band it is necessary to compute three values of α_j and three values of β_j and then combine them:

© 1983 Hemisphere Publishing Corporation

Table 1 Exponential wide-band-model parameters[a]

Gas	Vibrations ν_k, cm^{-1}	Bands $\delta_1, \delta_2, \ldots$	Pressure parameters n	Pressure parameters b (T_0 = 100 K)	Spectral location ν_c, cm^{-1}	Spectral location ν_u, cm^{-1}	Band absorption parameters α_0, cm^{-1}/gm m^{-2}	Band absorption parameters β_0	Band absorption parameters ω_0, cm^{-1}
(1) H_2O	$m = 3$	(1) Rotational							
	$\nu_1 = 3\,652$		1	$8.6(T_0/T)^{1/2} + 0.5$	140		10 400.0[b]	0.143 11[b]	57.1[b]
	$\nu_2 = 1\,595$	0,0,0							
	$\nu_3 = 3\,756$	(2) 6.3 μm		$8.6(T_0/T)^{1/2} + 0.5$	1600		41.2	0.094 27	56.4
	$g_1 = 1$	0,1,0	1						
	$g_2 = 1$	(3) 2.7 p m							
	$g_3 = 1$	0,2,0					0.19		
		1,0,0	1	$8.6(T_0/T)^{1/2} + 0.5$	3160		2.30	0.073 61	60.0
		0,0,1					22.40		
		(4) 1.87 p m	1	$8.6(T_0/T)^{1/2} + 0.5$	5 350		3.0	0.081 69	43.1
		0,1,1							
		(5) 1.38 μm	1	$8.6(T_0/T)^{1/2} + 0.5$	1250		2.5	0.116 28	32.0
		1,0,1							
(2) CO_2[d]	$m = 3$	(1) 15 μm							
	$\nu_1 = 1351$	0,1,0	0.7	1.3	667		19.0	0.06157	12.7
	$\nu_2 = 667$	(2) 10.4 μm							
	$\nu_3 = 2\,396$	−1,0,1	0.8	1.3	960		2.41×10^{-9}	0.040 17	13.4
	$g_1 = 1$	(3) 9.4 μm							
	$g_2 = 2$	0, −2,1[c]	0.8	1.3	1 060		2.48×10^{-9}[c]	0.118 88[c]	10.1
	$g_3 = 1$	(4) 4.3 pm							
		0,0,1	0.8	1.3		2410	110.0	0.241 23	11.2
		(5) 2.7 μm							
		1,0,1	0.65	1.3	3660		4.0	0.133 41	23.5
		(6) 2.0 p m							
		2,0,1	0.65	1.3	5 200		0.066	0.393 05	34.5
(3) CO	m = 1	(1) 4.7 μm							
	$\nu_1 = 2143$	1	0.8	1.1	2 143		20.9	0.075 06	25.5
	$g_1 = 1$	(2) 2.35 pm							
		2	0.8	1.0	4 260		0.14	0.167 58	20.0
(4) NO	m = 1	(1) 5.34 μm							
	$\nu_1 = 1876$	1	0.65	1.0	1876		9.0	0.180 50	20.0
	$g_1 = 1$								
(5) SO_2	$m = 3$	(1) 19.27 μm							
	$\nu_1 = 1\,151$	0,1,0	0.7	1.28	519		4.22	0.052 91	33.08
	$\nu_2 = 519$	(2) 8.68 μm							
	$\nu_3 = 1361$	1,0,0	0.7	1.28	1151		3.674	0.05952	24.83
	$g_1 = 1$	(3) 7.35 μm							
	$g_2 = 1$	0,0,1	0.65	1.28	1 361		29.97	0.492 99	8.78
	$g_3 = 1$	(4) 4.34 μm							
		2,0,0	0.6	1.28	2 350		0.423	0.475 13	16.45
		(5) 4.0 μm							
		1,0,1	0.6	1.28	2512		0.346	0.589 37	10.91
(6) CH_4	$m = 4$	(1) 7.66 μm							
	$\nu_1 = 2\,914$	0,0,0,1	0.8	1.3	1310		28.0	0.086 98	21.0
	$\nu_2 = 1526$	(2) 3.31 μm							
	$\nu_3 = 3020$	0,0,1,0	0.8	1.3	3020		46.0	0.069 73	56.0
	$\nu_4 = 1\,306$	(3) 2.37 μm							
	$g_1 = 1$	1,0,0,1	0.8	1.3	4220		2.9	0.354 29	60.0
	$g_2 = 2$	(4) 1.71 μm							
	$g_3 = 3$	1,1,0,1	0.8	1.3	5 861		0.42	0.685 98	45.0
	$g_4 = 3$								

[a] From Edwards and Balakrishnan [15], with permission.

[b] For the rotational band of H_2O, $\alpha(T) = \alpha_0 \exp[-5.0(T_0/T)^{1/2}]$ and $\beta(T) = \beta_0(T/T_0)^{-1/2}$. Adapted from Modak (Factory Mutual Res. Rep. OAOE6.8URC78-BT-19).

[c] Because of Fermi resonance between the ν_1 and $2\nu_2$ levels, the Ψ and Φ functions for the 1 060 cm^{-1} band are to be those of the 960 cm^{-1} band; i.e., use the set of δ's for the 960-cm^{-1} band to get Ψ and Φ for either band.

[d] The 1,0,0 band of the linear CO, molecule appears only at high pressures when a dipole is induced by co&ions.

© 1983 Hemisphere Publishing Corporation

$$\alpha_k = \sum_{j=1}^{3} \alpha_{k,j} \tag{49}$$

$$\beta_k = \frac{1}{\alpha_k}\left[\sum_{j=1}^{3} (\alpha_{k,j}\beta_{k,j})^{1/2}\right]^2 \tag{50}$$

Because the formulas for computing Ψ and Φ are rather complex, convenient graphs giving $\tau_{H,k}$ and β_k are presented in Figs. 8-11.

The equivalent broadening pressure P_e is based on a simplified kinetic theory of molecules with optical collision diameters, D_a for the absorbing species, and D_b for the broadening species taken here to be nitrogen. The line width γ results from the natural lines being shifted spectrally during molecular collisions and is proportional to the collision frequency $F_{aa} + F_{ab}$, where

$$F_{ab} = \Delta v \pi D_{ab}^2 \left(\frac{P_b}{kT}\right) \tag{51}$$

where

$$D_{ab} = \tfrac{1}{2}(D_a + D_b) \tag{52}$$

$$\Delta v = \left(\frac{16kT}{\pi}\right)^{1/2}\left(\frac{1}{m_a} + \frac{1}{m_b}\right)^{1/2} \tag{53}$$

Thus one expects that

$$\gamma = \gamma_0 \left(\frac{T}{T_0}\right)^{-1/2}\left(\frac{(P_b + bP_a)}{P_0}\right) \tag{54}$$

where

$$b = \frac{D_{aa}^2}{D_{ab}^2}\left(\frac{2m_b}{m_a + m_b}\right)^{1/2} \tag{55}$$

On empirical grounds the expression is adjusted by exponent n. Thus η is written

$$\eta = \frac{\pi\gamma}{d} = \beta P_e \tag{56}$$

where

$$P_e = \left\{\left(\frac{P}{P_0}\right)[1 + (b-1)x]\right\}^n \tag{57}$$

where x is the mole fraction P_a/P. Table 1 gives recommended values of n and b for $P_0 = 1$ atm. Note the strong temperature dependence of b for the H_2O molecules.

With values of $\tau_{H,k}$ and η_k, one can find A_k^* from the four-region expressions as follows:

1. The linear region for small optical depth and high pressure,

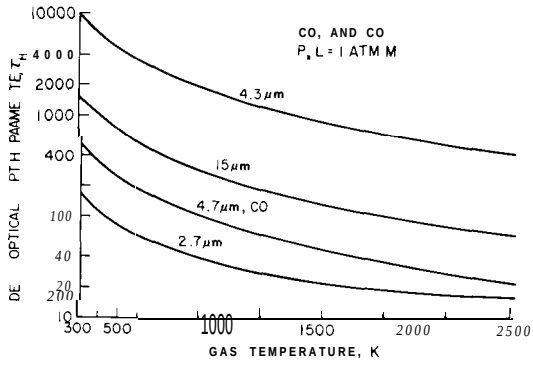

Figure 8 Optical depth at band head, CO and CO_2. From [15].

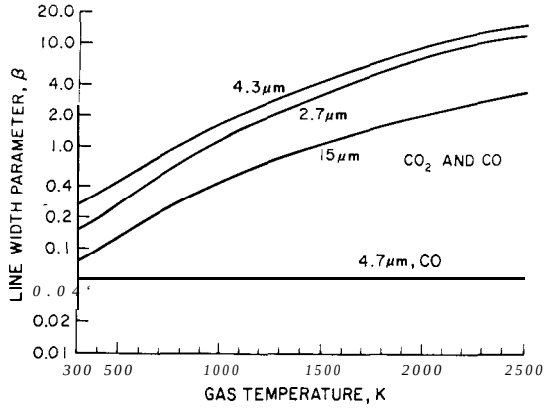

Figure 9 Line width parameter, CO and CO_2. From [15].

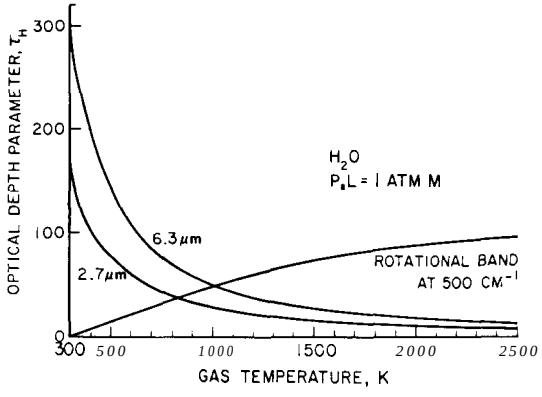

Figure 10 Optical depth at band head, H_2O. From [15].

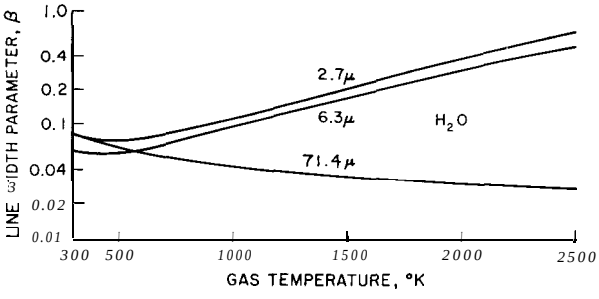

Figure 11 Line width parameter, H_2O.

© 1983 Hemisphere Publishing Corporation

$$\tau_{H,k} \leqslant 1 \qquad \tau_{H,k} \leqslant \eta_k \qquad A_k^* = \tau_{H,k} \tag{58a}$$

2. The square-root region for small to moderate optical depth and low pressure,

$$\eta_k \leqslant \tau_{H,k} \leqslant \frac{1}{\eta_k} \qquad \eta_k \leqslant 1 \qquad A_k^* = (4\eta_k \tau_{H,k})^{1/2} - \eta_k \tag{58b}$$

3. The log-root region for large optical depth and low pressure,

$$\frac{1}{\eta_k} < \tau_{H,k} \qquad \eta_k \leqslant 1 \qquad A_k^* = \ln (\tau_{H,k}\eta_k) + 2 - \eta_k \tag{58c}$$

4. The log region for large optical depth and high pressure,

$$\tau_{H,k} \geqslant 1 \qquad \eta_k \geqslant 1 \qquad A_k^* = \ln \tau_{H,k} + 1 \tag{58d}$$

When the approximate four-region expressions are compared with exact numerical integration of Eq. (28), they are found to be higher. However, the values in Table 1 were found by correlating the approximate four-region expressions to band absorption measurements; thus use of the four-region expressions gives results that agree (±15%) with physical reality. If one wants to employ Eq. (23) for approximate spectral calculations, it is recommended to increase the value of ω_k obtained from the table by 20%.

Even when one intends to use a total emissivity chart, it is well to calculate $\tau_{H,k}$ and η_k of the two or three most important bands in order to know whether to apply Eq. (38) or (39) to obtain total absorptivity and to know whether or not to apply the pressure correction according to Eq. (40). Furthermore, one needs to know where in Table 2.9.6(1) to find the relation between beam length and geometric mean beam length as described in Sec. 2.9.6B.

F. Gas mixtures

For overlapping bands of the ***same species,*** the line structure is similar, and one employs Eqs. (49) and (50). For overlapping bands of different species, one expects that there is no correlation in the line structure so that the product of the individual transmissivities, each given by Eq. (18), applies on a spectral basis.

$$\tau_{\nu,\text{mix}} = \text{II}\ \bar{\tau}_{\nu,i} \qquad (i \text{ is the species}) \tag{59}$$

$$\epsilon_{\nu,\text{mix}} = \alpha_{\nu,\text{mix}} = 1 - \bar{\tau}_{\nu,\text{mix}} \tag{60}$$

If one wants to make a hand calculation and avoid detailed spectral calculations, one uses a block calculation procedure as follows:

1. Determine for each band of each absorbing-emitting species the band absorption A_i.

2. Assign to each band a band transmissivity $\tau_{g,i}$ based on

$$\tau_{g,i} = \frac{\tau_{H,i}}{A_i^*} \frac{dA_i^*}{d\tau_{H,i}} \leqslant 0.90 \tag{61}$$

where A_i^* comes from Eqs. (58*a, b, c,* or ***d).*** If the indicated transmissivity from Eq. (61) is greater than 0.90, the value 0.90 is used.

3. Find the band width:

$$\Delta\nu_i = \frac{A_i}{1 - \tau_{g,i}} \tag{62}$$

4. Following recommended center or upper-limit locations, locate the bands.

Table 2 Band absorptions for a gas mixture[a,b]

Species *i* gas	Band j region	Band absorption $A_{i,j}$, cm-	Band transmissivity $\tau_{g,i,j}$	Band width $\Delta\nu_{i,j}$, cm-	Lower limit $\nu_{\ell,i,j}$, cm^{-1}	Upper limit $\nu_{u,i,j}$, cm^{-1}
1 H_2O	1 Rotational	775	0.137	898	0	898
	2 6.3 μm	638	0.331	954	1 123	2 077
	3 2.1 μm	676	0.332	1012	3 254	4 266
	4 1.87 μm	171	0.594	422	5 139	5561
	5 1.38 μm	131	0.610	336	1082	1418
2 co,	1 15 μm	205	0.232	266	534	800
	2 10.4 μm	10	0.90	100	910	1010
	3 9.4 μm	10	0.90	100	1010	1110
	4 4.3 μm	260	0.161	310	2100	2410
	5 2.7 μm	220	0.400	366	3471	3 843
	6 1.9 μm	9	0.90	90	5515.5	5 245
3 co	1 4.7 μm	89	0.527	188	2 049	2231
	2 2.35 pm	3	0.90	34	4 243	4 277

[a] From Edwards [19].
[b] 0.18 H_2O, 0.06 CO,, 0.03 CO, 0.73 N_2, P = 1 atm, L = 3 m, T_g = 1400 K.

© 1983 Hemisphere. Publishing Corporation

Table 3 Block calculation of total emissivity and absorptivity[a,b]

Block number k	Lower limit ν_k	Upper limit ν_{k+1}	Block transmissivity $\tau_{g,k}$	Fractional function $f(T_g/\nu_k)$	Block fraction $\epsilon_{g,k}\Delta f_k$	Fractional function $f(T_s/\nu_k)$	Block fraction $\alpha_{g,k}\Delta f_k$
1	0	534	0.137	1.000	0.006	1.000	0.013
2	534	800	0.032	0.993	0.014	0.985	0.023
3	800	898	0.137	0.979	0.007	0.961	0.011
4	898	910	1.000	0.971	0.000	0.948	0.000
5	910	1110	0.900	0.970	0.001	0.946	0.003
6	1110	1 123	1.000	0.957	0.000	0.920	0.000
7	1 123	2 049	0.331	0.950	0.102	0.909	0.156
8	2 049	2 077	0.174	0.797	0.004	0.676	0.007
9	2 077	2 100	0.527	0.792	0.002	0.668	0.003
10	2 100	2 237	0.085	0.787	0.027	0.662	0.036
11	2 237	2 410	0.161	0.758	0.033	0.623	0.040
12	2 410	3 254	1.000	0.719	0.000	0.575	0.000
13	3 254	3 477	0.332	0.534	0.032	0.357	0.032
14	3 477	3 843	0.133	0.486	0.063	0.309	0.058
15	3 843	4 243	0.332	0.413	0.049	0.242	0.040
16	4 243	4 266	0.299	0.339	0.003	0.182	0.002
17	4 266	4 277	0.335	0.335	0.002	0.179	0.001
18	4 277	5 139	1.000	0.332	0.000	0.177	0.000
19	5 139	5 155	0.594	0.211	0.001	0.090	0.000
20	5 155	5 245	0.535	0.209	0.005	0.089	0.003
21	5 245	5 561	0.594	0.199	0.014	0.083	0.008
22	5 561	7 082	1.000	0.165	0.000	0.064	0.000
23	7 082	7 418	0.610	0.063	0.005	0.016	0.002
24	7418	∞	1.000	0.050	0.000	0.012	0.000
					0.370		0.438

[a] From Edwards [19].
[b] 0.18 H_2O, 0.06 CO_2, 0.03 CO, 0.73 N_2, $P = 1$ atm, $L = 3$ m, $T_g = 1\,400$ K, $T_e = 1\,100$ K.

5. Order the band limits in ascending order of wave number, starting with zero, and find the transmissivity in each block between limits. For the kth block, the transmissivity is

$$\tau_{g,k} = \prod \tau_{g,i} \qquad (63)$$

where the product is over all bands within the block (the bands outside the block have a transmissivity of 1.0 within the block).

6. Use the blocked-out $\tau_{g,k}$ as desired to calculate total transfer factors or total absorptivity and emissivity. For example, for total emissivity,

$$\epsilon_g = \int_0^1 [1 - \tau_g]\, df_e\left(\frac{T_g}{\nu}\right) \qquad (64a)$$

$$\epsilon_g = \sum_{k=1}^{n} (1 - \tau_{g,k})\left(f_e\left(\frac{T_g}{\nu_k}\right) - f_e\left(\frac{T_g}{\nu_{k+1}}\right)\right) \qquad (64b)$$

Note that the block procedure outlined here is preferable to using Eq. (32) or (35), even when a pure species (with or without transparent broadener diluent gas) is involved, when the absorption bands are wide.

Tables 2 and 3 show a sample block calculation.

Nomenclature for Section 2.9.5 appears at the end of Section 2.9.8.

BIBLIOGRAPHY FOR SECTION 2.9.5

The equation of transfer

1. Davidson, N., ***Statistical Thermodynamics,*** pp. 220-226, McGraw-Hill, New York, 1962.
2. Goody, R. M., ***Atmospheric Radiation,*** pp. 17–44, Oxford, London, 1964.
3. Zeldovich, Y. B., and Razier, ***Y. P., Physics of Shock Waves and High-Temperature Hydrodynamic Phenomena,*** vol. I, pp. 107-133, Academic Press, New York, 1966.

© 1983 Hemisphere Publishing Corporation

Reviews of experimental measurement techniques

4. Hottel, H. C., and Sarofim, A. F., ***Radiation Transfer,*** chap. 6, McGraw-Hill, New York, 1967.
5. Edwards, D. K., Thermal Radiation Measurements, chap. 9 ***in Measurements in Heat Transfer,*** ed. E. R. G. Eckert and R. J. Goldstein, chap. 9, Hemisphere, Washington, D.C., 1976. See also [19].

Properties of particulates (see also [3], chap. 7)

6. Van de Hulst, H. ***C., Light Scattering by Small Particles,*** Wiley, New York, 1957.
7. Hottel, H. C., and Sarotim, A. F., ***Radiative Transfer,*** chap. 12, McGraw-Hill, New York, 1967. See also Sarofim, A. F., and Hottel, H. C., Radiative Transfer in Combustion Chambers: Influence of Alternative Fuels, ***6th Int. Heat Transfer Conf., Toronto, Canada,*** vol. 6, pp. 199-217, 1978.
8. Howarth, C. R., Foster, P. J., and Thring, M. W., The Effect of Temperature on the Extinction of Radiation by Soot Particles, ***Proc. 3d Int. Heat Transfer Conference, Chicago,*** vol. 5, pp. 122-128, 1966.
9. Penner, S. S., and Olfe, D. B., ***Radiation and Reentry,*** chap. 4, Academic Press, New York, 1968.
10. Hubbard, G. L., and Tien, C. L., Infrared Mean Absorption Coefficients of Luminous Flames and Smoke, ***J. Heat Transfer,*** vol. 100, pp. 235-239, 1978.

Gas properties

Narrow-band models

11. Plass, G. N., Useful Representation for Measurements of Spectral Band Absorption, ***J. Opt. Soc. Am.,*** vol. 50, pp. 868-875, 1960.
12. Tiwari, S. N., and Gupta, S. K., Accurate Spectral Modeling for Infrared Radiation, ***J. Heat Transfer,*** vol. 100, pp. 240-246, 1978.

Wide-band models

13. Schack, A., ***Industrial Heat Transfer,*** Wiley, New York, 1927.
14. Edwards, D. K., and Menard, W. A., Comparison of Models for Correlation of Total Band Absorption, ***Appl. Opt.,*** vol. 3, pp. 621-625, 1964.
15. Edwards, D. K., and Balakrishnan, A., Thermal Radiation by Combustion Gases, ***Int. J. Heat Mass Transfer,*** vol. 16, pp. 25-40, 1973.
16. Chu, H. K., and Grief, R., Theoretical Determination of Band Absorption for Nonrigid Rotation with Applications to CO, NO, N_2O, and ***CO_2, J. Heat Transfer,*** vol. 100, pp. 230-234, 1978.

Total emissivity charts

17. Hottel, H. C., Radiant Heat Transmission, in ***Heat Transmission,*** 3d ed., ed. W. H. McAdams, chap. 4, McGraw-Hill, New York, 1954.
18. Eckert, E. R. G., and Drake, R. M., ***Analysis of Heat and Mass Transfer,*** pp. 653-656, McGraw-Hill, New York, 1972.
19. Edwards, D. K., Molecular Gas Band Radiation, ***Adv. Heat Transfer,*** vol. ***12,*** pp. 115-193, 1976.

Ultra-high-temperature gases (see also [9], chaps. 1, 3)

20. Menard, W. A., Thomas, G. M., and Helliwell, T. M., Experimental and Theoretical Study of Molecular, Continuum, and Line Radiation from Planetary Atmospheres, ***AIAA J.,*** vol. 6, pp. 655-664, 1968.

© 1983 Hemisphere Publishing Corporation

2.9.6

Radiation transfer with an isothermal gas

D. K. Edwards

A. Heat transfer at a black wall

Often for design purposes a combustion chamber or chemical reactor can be modeled as containing a well-mixed gas, one with uniform temperature and composition, excluding the wall boundary layer. Suppose, for now, that the boundary layer has a negligible effect. The net spectral radiant heat flux across any plane can be written

$$q = \int_0^{2\pi} \int_0^{\pi/2} (I^+ - I^-) \cos\theta \sin\theta \, d\theta \, d\phi \tag{1}$$

At a black wall,

$$I^+ = I_b(T_w) = \frac{B_w}{\pi} \tag{2}$$

and, from the solution to Eq. 2.9.5(6) with $I = I_b(T_w)$ at $s = 0$,

$$I^- = I_b(T_w) e^{-k_a L(\theta,\phi)} + I_b(T_g)(1 - e^{-k_a L(\theta,\phi)}) \tag{3}$$

Here the term $I_b(T_w)$ is the intensity of the wall across the chamber a distance $L(\theta,\phi)$ away, $e^{-k_a L(\theta,\phi)}$ is the transmissivity of the gas, and $1 - e^{-k_a L(\theta,\phi)}$ is the emissivity of the gas. The irradiation is seen to be made up of two contributions, transmitted wall radiation and emitted gas radiation. Substitution into Eq. (1) gives, assuming that the wall is isothermal,

$$q = (B_w - B_g) \frac{1}{\pi} \int_0^{2\pi} \int_0^{\pi/2} \text{X} \, (1 - e^{-k_a L(\theta,\phi)}) \cos\theta \sin\theta \, d\theta \, d\phi \tag{4}$$

The heat flow is

$$\dot{Q} = (B_w - B_g) \int_{A_w} \frac{1}{\pi} \int_0^{2\pi} \int_0^{\pi/2} \text{X} \, (1 - e^{-k_a L(\theta,\phi)}) \cos\theta \sin\theta \, d\theta \, d\phi \, dA_w$$

which may be expressed as

$$\dot{Q} = (B_w - B_g) A_w \, \mathfrak{F}_{wg} \tag{5}$$

where the wall-to-gas transfer factor is

$$\mathfrak{F}_{wg} = \frac{1}{A_w} \int_{A_w} \frac{1}{\pi} \int_0^{2\pi} \int_0^{\pi/2} \text{X} \, [1 - e^{-k_a L(\theta,\phi)}] \cos\theta \sin\theta \, d\theta \, d\phi \, dA_w \tag{6a}$$

Because, from Eq. 2.9.1(4),

$$d\Omega = \frac{\cos\theta' \, dA'_w}{L^2}$$

one can write equally well

$$\mathfrak{F}_{wg} = \frac{1}{A_w} \int_{A_w} \int_{A'_w} (1 - e^{-k_a L}) \frac{\cos\theta \cos\theta'}{\pi L^2} \, dA'_w \, dA_w \tag{6b}$$

One finds that the transfer from a black isothermal wall to an isothermal gas is the shape factor-weighted gas emissivity along all possible paths from the wall through the gas. Of course, Eq. (5) requires spectral integration. For now we focus on the geometric aspects of the transfer process.

© 1983 Hemisphere 1 blishing Corporation

B. The mean-beam-length concept

In view of Eq. (6b), it is natural to define a mean beam length L_{mb} such that

$$\mathfrak{F}_{wg} = (1 - e^{-k_a L_{mb}}) F_{w-w'} = 1 - e^{-k_a L_{mb}} \qquad (7)$$

where for a complete enclosure $F_{w-w'} = 1$. A strong motivation in defining L_{mb} is the expectation that an engineering approximation for it will be easily found.

Consider, as a specific example, the situation for the sphere as pictured in Fig. 1. There it is clear that $L(\theta, \phi) = 2R\cos\theta$. Thus, Eq. (7) reduces to

$$(1 - e^{-k_a L_{mb}})_{\text{sphere}} = \int_0^{\pi/2} (1 - e^{-2k_a R\cos\theta}) \times 2\cos\theta \sin\theta \, d\theta \qquad (8)$$

The answer for $k_a L_{mb}$ is seen to be a function of the optical depth, say, across the diameter, $k_a D$. It may be written formally as

$$\frac{L_{mb}}{D} = \frac{1}{t} \ln \frac{t^2/2}{(1 - e^{-t}) - te^{-t}} \qquad t = k_a D \qquad (9)$$

but the form of Eq. (8) shows the situation more physically. The possible paths are seen to range in length from zero to one diameter. Clearly the mean beam length of the sphere will be less than the diameter.

In the limit as absorption coefficient goes to zero, that is, when the gas is optically thin, the approximation can be made:

$$1 - e^{-k_a L_{mb}} \doteq k_a L_{mb}$$

$$1 - e^{-k_a L} \doteq k_a L$$

Then Eq. (8) with $\mu = \cos\theta$ reduces to

$$L_{mbg,\text{sphere}} = D \int_0^1 2\mu^2 \, d\mu = \frac{2}{3} D \qquad (10)$$

The subscript g here denotes the geometric mean beam length,

$$L_{mbg} = \lim_{k_a \to 0} L_{mb} \qquad (11)$$

so called because the value of k_a cancels out, and only the geometry governs the value.

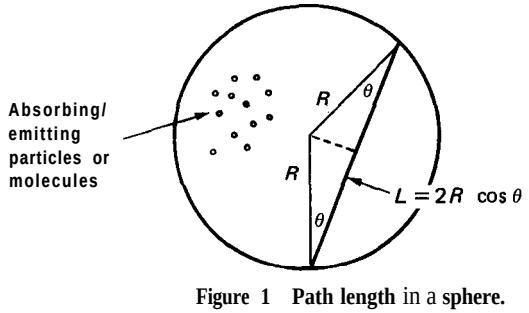

Figure 1 Path length in a sphere.

If one tries the approximation

$$\mathfrak{F}_{wg} \equiv 1 - e^{-k_a L_{mb}} \doteq 1 - e^{-k_a L_{mbg}} \qquad (12)$$

and compares it with exact calculation of Eq. (8), one finds for the sphere that the approximate value of $\mathfrak{F}_{wg}$ is within 1% of the true value when $k_a L_{mbg}$ is less than 0.25 and at worst is only 5.2% high. If one repeats the comparison for the infinite cylinder and slab, one finds that the accuracy is not as good, but if one uses $L_{mb} \doteq 0.9 L_{mbg}$ when $k_a L_{mbg}$ exceeds, say, 0.1, then the error is less than 7%.

We see that an estimate of the geometric mean beam length leads easily to an engineering estimate of the transfer factor via Eq. (12). Thus it is of considerable interest to know that L_{mbg} is very readily found for the one-wall, one-gas enclosure. Recall that in finding a transfer factor one can think of the source blackbody radiosity, here B_g, as having the value unity and the sink, here B_w, as having the value zero. Using this concept and combining Eqs. (5), (7), and (11) gives

$$L_{mbg} = \lim_{k_a \to 0} \frac{Q}{A_w k_a B_g}$$

But we have found that for an optically thin sphere,

$$\dot{Q} = 4\pi R^2 B_g \tfrac{2}{3} D k_a = \tfrac{16}{3} \pi R^3 k_a B_g$$

$$\dot{Q} = 4 V k_a B_g \qquad V = \tfrac{4}{3} \pi R^3$$

Any arbitrary volume of gas V_g can be filled with spheres with a spectrum of sizes as closely as desired. Since the volumes sum to V_g, the total power emitted sums to

$$\dot{Q} = 4 V_g k_a B_g \qquad (13)$$

Substituting into the expression for L_{mbg} gives

$$L_{mbg} = \frac{4 V_g}{A_w} \qquad (14)$$

Equation (14) states that the geometric mean beam length is simply four times the gas volume divided by the wall area totally enclosing it. With this easily calculated value, the transfer factor is readily approximated via Eq. (12), and the heat transfer is found from Eq. (5). Note that for a long duct or tunnel, where $A_w = P_w L$ and $V_g = A_c L$, the geometric mean beam length is identical to the hydraulic diameter $4A_c/P_w$.

The mean-beam-length concept, derived here on a spectral basis, can be put on a band or total basis. Integrate Eq. (4) or (5) over the spectrum. If the band approximation is suitable, one obtains

$$\dot{Q} = \sum_k (B_{w,k} - B_{g,k}) A_w \omega_k A_k^* (\rho_a L_{mb,k}) \qquad (15)$$

© 1983 Hemisphere Publishing Corporation

where

$$A_k^*(\rho_a L_{mb,k}) = \frac{1}{A_w}\int_{A_w}\frac{1}{\pi}\int_0^{2\pi}\int_0^{\pi/2} \times A_k^*(\rho_a L)\cos\theta\sin\theta\,d\theta\,d\phi\,dA_w \quad (16)$$

In general, the exact value of the mean beam length is different for each of the absorption bands, but, in practice, one may approximate $L_{mb,k}$ with L_{mbg}, or a fraction of L_{mbg} appropriate to the most important band. This fraction has been found for the exponential band model with overlapped lines ($\eta = \beta P_e > 1$) for the sphere, cylinder, and slab geometries as shown in Table 1. The table shows that for a strong band, $L_{mb} = 0.9L_{mbg}$ will do nicely for the cylinder or sphere, but for a slab, $L_{mb} = 0.83L_{mbg}$.

C. Wall layer transmission

Section 2.9.7 deals with radiation transfer within a nonisothermal gas. At a cold black wall exposed to hot gases, the irradiation upon the wall is less when a cold boundary layer exists, because not all increments of path along an incident beam are at the high temperature. Based on an analysis of thermally developing entrance flow of an absorbing-emitting molecular gas in a parallel-plate duct, Balakrishnan and Edwards [9] proposed that Eq. (15) be multiplied by a wall layer transmission factor $\tau_{WL,k}$,

$$\frac{Q_{0-x}}{A_w} = \sum_k (B_{w,k} - B_{g,k})\omega_k A_k^*(\rho_a L_{mb,k})\tau_{WL,k} \quad (17)$$

Table 1 Mean beam length for the slab, cylinder, and sphere

Optical depth at band head (based on plate spacing or diameter)	Ratio of mean beam length to geometric mean beam length L_{mb}/L_{mbg}		
	Slab	Cylinder	Sphere
0.00	1.00	1.00	1.00
0.01	0.99	1.00	1.00
0.02	0.98	1.00	1.00
0.05	0.96	1.00	1.00
0.10	0.95	1.00	1.00
0.20	0.93	1.00	1.00
0.50	0.88	0.98	0.99
1.0	0.86	0.95	0.98
2.0	0.84	0.93	0.91
5.0	0.83	0.91	0.94
10.0	0.83	0.90	0.92
	0.83	0.89	0.91

where

$$\tau_{WL,k} \doteq \frac{\ln(1+\tau_{HD,k}) - \ln(1+\tau_{HD,k}r_{WL})}{\ln(1+\tau_{HD,k})} \quad (18a)$$

$$r_{WL} \doteq \frac{1.37}{\mathrm{Re}^{0.37}}\left[1-\exp\left(-\left(\frac{x}{10D}\right)^{0.6}\right)\right] \quad (18b)$$

where D is hydraulic diameter, Re is Reynolds number based on hydraulic diameter, x is the length from the beginning of the developing thermal boundary layer, and $\tau_{HD,k}$ is the optical depth at the kth band head based on the hydraulic diameter (identical to the geometric mean beam length), $\alpha_k\rho_a D/\omega_k$. Note that Eq. (17) is not for the local heat flux at a value of x, but the average heat flux for the region between 0 and x.

D. Radiosity-irradiation formulation at an isothermal-gas-filled-enclosure wall

On a true spectral basis, Eqs. (2) and (3) may be replaced with

$$I_i^+ = \epsilon_i I_b(T_i) + (1-\epsilon_i)I_i^- \quad (19)$$

$$I_i^- = I_j^+ e^{-k_a L} + I_b(T_g)(1-e^{-k_a L}) \quad (20)$$

When these expressions are substituted into Eq. (1) and a mean-beam-length concept is invoked, the *flux* is

$$q_i = q_i^+ - q_i^- \quad (21)$$

$$q_i^+ = \epsilon_i B_i + (1-\epsilon_i)q_i^- \quad (22)$$

$$q_i^- = \sum_{j=1}^{n} F_{i-j}[q_j^+\tau_{g,i-j} + (1-\tau_{g,i-j})B_g] \quad (23)$$

where

$$\tau_{g,i-j} = e^{-k_a L_{i-j}} = \frac{1}{A_i F_{i-j}}\int_{A_i}\int_{A_j} e^{-k_a L} \times \frac{\cos\theta_i\cos\theta_j}{\pi L^2}\,dA_j\,dA_i \quad (24)$$

The path L is the distance between differential areas dA_j and dA_i, and L_{i-j} is the mean beam length for the finite areas A_j and A_i.

Oppenheim and Bevans [7] derived expressions for the geometric mean L_{i-j} for adjacent and opposite rectangles, and Dunkle [8] integrated the expressions and provided numerical values. Table 2 gives the integrated expressions, and Table 3 some numerical values. Dunkle goes on to state that the $L_{g,1-2}$ for a finite sphere of radius R to a rectangle is the value for the point sphere minus $(2/3)R$. He also recommends approximating the human form as a sphere with $(2/3)R$ = 0.26 m. The values of geometric mean beam length between areas i and j, $L_{g,i-j}$ is a close upper limit to the true mean beam length L_{i-j}.

© 1983 Hemisphere Publishing Corporation

Table 2 Closed-form expressions for geometric mean beam lengths between rectangles[a]

Geometry	Expression
1. Opposite rectangles 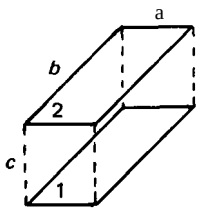 $X = a/c$ $Y = b/c$ $Z = L_{g,1-2}/c$	$$ZF_{1-2} = \frac{4}{\pi XY}\left[XY\tan^{-1}\frac{XY}{\sqrt{1+X^2+Y^2}} + X\ln\frac{X+\sqrt{1+X^2+Y^2}}{(X+\sqrt{1+X^2})\sqrt{1+Y^2}} + Y\ln\frac{Y+\sqrt{1+X^2+Y^2}}{(Y+\sqrt{1+Y^2})\sqrt{1+X^2}} + \sqrt{1+X^2}+\sqrt{1+Y^2}-\sqrt{1+X^2+Y^2}-1\right]$$
2. Adjacent rectangles 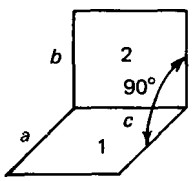 $X = a/c$ $Y = b/c$ $Z = L_{g,1-2}/c$	$$ZF_{1-2} = \frac{1}{3\pi X}\left[3X^2\ln\frac{(1+\sqrt{1+X^2})\sqrt{X^2+Y^2}}{X(1+\sqrt{1+X^2+Y^2})} + 3Y^2\ln\frac{(1+\sqrt{1+Y^2})\sqrt{X^2+Y^2}}{Y(1+\sqrt{1+X^2+Y^2})} + 3X^2(\sqrt{1+X^2+Y^2}-\sqrt{X^2+Y^2}-\sqrt{1+X^2}) + 3Y^2(\sqrt{1+X^2+Y^2} - \sqrt{X^2+Y^2}-\sqrt{1+Y^2}) + (1+X^2)^{3/2} + (1+Y^2)^{3/2} + (X^2+Y^2)^{3/2} - (1+X^2+Y^2)^{3/2} + 2X^3 + 2Y^3 - 1\right]$$

[a] See Table 2.9.3(1) for F_{12} expressions.

The rules of shape factor algebra, illustrated in Figs. 2.9.3(1)-2.9.3(3), apply to geometric mean beam lengths when G is understood to be

$$G_{i-j} = G_{j-i} = L_{g,i-j}A_iF_{i-j} \tag{25}$$

It is clear that Eqs. (22) and (23) are of the same form as Eqs. 2.9.3(13) and 2.9.3(14), and solution by matrix inversion (or reiteration) may be accomplished as explained in Sec. 2.9.3B.

E. The radiation network with a gas

Just as a network interpretation exists for Eqs. 2.9.3(12)-2.9.3(14), so does one exist for Eqs. (21)-(23). Since Eqs. (21) and (22) are exactly Eqs. 2.9.3(12) and 2.9.3(13), Eqs. 2.9.3(49) and 2.9.3(50) remain in force, showing that each surface has a surface resistance as depicted in Fig. 2.9.3(5). Equations 2.9.3(47) and 2.9.3(48) are based on Eqs. 2.9.3(12) and 2.9.3(14), and must be replaced by relations following from Eqs. (21) and (23).

$$\dot{Q}_i = q_iA_i = \sum_{j=1}^{n} A_iF_{i-j}\tau_{g,i-j}(q_i^+ - q_j^+) + \sum_{j=1}^{n} A_iF_{i-j}(1-\tau_{g,i-j})(q_i^+ - B_g) \tag{26}$$

This relation shows (1) that the internodal resistances R_{i-j} become

$$R_{i-j} = \frac{1}{A_iF_{i-j}\tau_{g,i-j}} \tag{27}$$

and (2) that for every internodal resistance R_{i-j} (including R_{i-i}), there is a node-to-gas-node resistance in parallel. Since parallel conductances add,

$$\frac{1}{R_{i-g}} = \sum_{j=1}^{n} A_iF_{i-j}(1-\tau_{g,i-j}) \tag{28}$$

It is imperative that the F_{i-i} contribution (if any) not be overlooked. As an aid to the memory in this regard, Oppenheim advocated drawing the otherwise useless appendage $R_{i-i} = 1/A_iF_{i-i}\tau_{g,i-i}$ on the network as shown in Fig. 2, which summarizes the rules for drawing a radiation network. Figure 3 shows a complete network for the case $n = 2$.

F. Some useful results

For a gas containing spray droplets or particles, the spectral variation in absorption coefficient may often be overlooked. A gas such as H_2O vapor with several wide, weak bands may be similarly treated to a lower level of approximation. For the particle-laden gas, $\tau_{g\,i-j}$ is $e^{-k_aL_{i-j}}$ as given by Eq. (24), and $\epsilon_{g,i-j}$ is $1-\tau_{g,i-j}$. For the H_2O vapor, $\epsilon_{g,i-j}$ is found from Fig. 2.9.5(7) using the mean beam length L_{i-j} and $\tau_{g,i-j} = 1-\epsilon_{g,i-j}$. Using the radiation network, one can quickly develop working relations for the following cases:

© 1983 Hemisphere Publishing Corporation

1. A gaseous source and a sink
2. A gaseous source, a refractory, and a sink
3. A source, a sink, and an adiabatic gas
4. A source, a sink, a refractory, and an adiabatic gas
5. A source, a sink, and a gaseous source or sink

As in Sec. 2.9.3E, the results are subject to assumptions of perfectly diffuse gray surfaces and, in addition, to well-stirred gray gas. Note that when the gas is a source or sink, it is presumably due to flow, perhaps with chemical reaction or change of phase, so that the heat flow from the gas $\dot{Q}_g$ is provided (or taken up) by an enthalpy change as follows:

$$\dot{m}_g(\hat{h}_{g,i} - \hat{h}_{g,o}) = \dot{Q}_g \qquad (29)$$

where $\dot{m}_g$ is the mass flow rate of the gas mixture through the enclosure, $\hat{h}_{g,i}$ is the specific enthalpy of the entering gas mixture including heats of formation or combustion, and $\hat{h}_{g,o}$ is the specific enthalpy of the exiting gas mixture at temperature T_g. As an approximation, it is frequently possible to write Eq. ***(29)*** in the form

$$\dot{m}_g c_{p,g}(T_{gf} - T_g) = \dot{Q}_g \qquad (30)$$

where T_{gf} is a fictitious gas temperature (not the completion-limited adiabatic flame temperature, it is emphasized) found from

$$T_{gf} = \frac{\dot{m}_f c_{p,f} T_{f,i} + \dot{m}_f \Delta\hat{h} + \dot{m}_a c_{p,a} T_a}{m_g c_{p,g}} \qquad (31)$$

Table 3 A short table of geometric mean beam lengths

1. Opposite rectangles

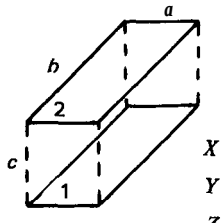

$X = a/c$
$Y = b/c$
$Z = L_{g,1-2}/c$

	Z				
$Y = 0.0$	**0.1**	**1**	10	∞	
$X = 0$	**1.00**	1.00	1.05	1.23	1.27
0.1		1.00	1.06	1.23	1.27
1			**1.11**	1.30	1.35
10				1.62	1.75
					2.00

2. Adjacent rectangles

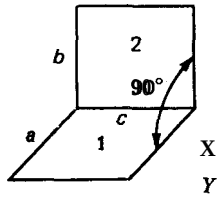

$X = a/c$
$Y = b/c$
$Z = L_{g,1-2}/c$

	Z					
$Y = 0.1$	**0.2**	**1**	**2**	10	20	
x = 0.1	**0.072**	**0.098**	**0.15**	0.17	**0.18**	**0.18**
0.2		**0.14**	**0.24**	**0.27**	**0.30**	**0.30**
1			**0.56**	**0.70**	**0.89**	**0.92**
2				**0.95**	**1.38**	**1.47**
10				**3.20**		**3.96**
20						**5.49**

3. Point sphere to rectangles

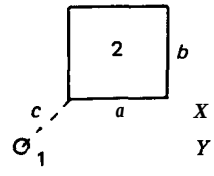

$X = a/c$
$Y = b/c$
$Z = L_{g,1-2}/c$

	Z			
$Y = 0$	1	2	3	
$X = 0$	**1.00**	1.11	1.25	1.32
1		1.22	1.37	1.45
2			**1.52**	**1.63**
3				**1.76**

© 1983 Hemisphere Publishing Corporation

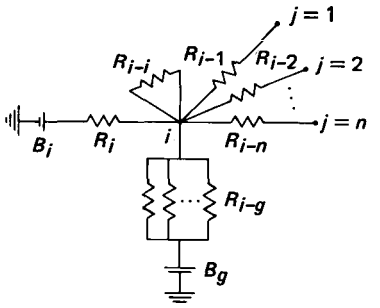

Figure 2 Radiation network connections for node 1 with isothermal gas g.

where $\dot{m}_f$ is the fuel flow rate, $c_{p,f}$ is its specific heat, $\hat{A}h$ is the heat of reaction based on $\dot{m}_f$, $\dot{m}_a$ is the air flow rate, $c_{p,a}$ is its specific heat, $\dot{m}_g$ is the gas product flow rate $(\dot{m}_g = \dot{m}_f + \dot{m}_a)$, and $c_{p,g}$ is its specific heat. The point is that, whereas in what follows we assume that we know T_g and solve for $\dot{Q}_g$, in fact we usually do not know T_g but instead $\hat{h}_{g,i}$ or T_{gf} and have to use Eq. (29) or (30) together with $\dot{Q}_g$ as a function of T_g to solve for T_g.

A gaseous source and a sink model a combustion chamber or reactor with a cooled wall. With $F_{w-w} = 1$, the network is simply a surface resistance and gas-to-wall resistance. Hence

$$A_w \mathfrak{F}_{w-g} = \frac{Q_g}{C_s T_g^4 - C_s T_w^4} = \frac{A_w}{[(1-\epsilon_w)/\epsilon_w] + 1/\epsilon_g} \tag{32}$$

A gaseous source, a refractory, and a sink models a direct-fired furnace. Figure 2 applies with battery B_2 open circuit to make the refractory wall 2 radiatively adiabatic :

$$A_1 \mathfrak{F}_{1-g} = 1/\{[(1-\epsilon_1)/\epsilon_1 A_1] + 1/[1/R_{1-g} + 1/(R_{1-2} + R_{2-g})]\} \tag{33a}$$

where

$$\frac{1}{R_{1-g}} = A_1 F_{1-1} \epsilon_{g,1-1} + A_1 F_{1-2} \epsilon_{g,1-2} \tag{33b}$$

$$R_{1-2} = \frac{1}{A_1 F_{1-2} \tau_{g,1-2}} \tag{33c}$$

$$\frac{1}{R_{2-g}} = A_1 F_{1-2} \epsilon_{g,1-2} + A_2 F_{2-2} \epsilon_{g,2-2} \tag{33d}$$

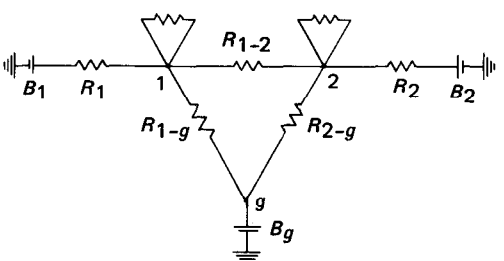

Figure 3 Radiation network for $n = 2$ with isothermal gas g.

If one needs to know the temperature of the refractory, one can solve for B_2 as follows:

$$q_1^+ = B_1 + \frac{A_1 \mathfrak{F}_{1-g}(B_g - B_1)(1-\epsilon_1)}{\epsilon_1 A_1} \tag{34a}$$

$$Q_{1-2-g} = \frac{B_g - q_1^+}{R_{1-2} + R_{2-g}} \tag{34b}$$

$$B_2 = q_2^+ = B_g - \dot{Q}_{1-2-g} R_{2-g} \tag{34c}$$

$$T_2 = \left(\frac{B_2}{C_s}\right)^{1/4} \tag{34d}$$

A source, a sink, and an adiabatic gas may model a nuclear accident scenario where hot fuel rods radiate to cold surface (spacers, carmister walls, etc.) through dry stagnant steam. Figure 2 again applies, with battery B_g open circuit to place the gas in radiative equilibrium.

$$A_1 \mathfrak{F}_{1-2} = 1/\{[(1-\epsilon_1)/\epsilon_1 A_1] + [1/R_{1-g} + 1/(R_{1-g} + R_{2-g})]^{-1} + [(1-\epsilon_2)/\epsilon_2 A_2]\} \tag{35}$$

where R_{1-2}, R_{1-g}, and R_{2-g} are as shown in Eqs. (33b-d).

A source, a sink, a refractory wall, and an adiabatic gas may be used to evaluate the effect of a dusty or otherwise absorbing atmosphere on the performance of an electric or muffle furnace, for example. Figure 4 applies with batteries B_3 and B_g open circuit. Although the network is more intricate, it remains a two-node one; only B_1 and B_2 are connected. One proceeds to simplify the network by converting the $R_{1-3}, R_{2-3}, R_{3-g}$ *wye* into a delta by means of the wye-delta transformation in Fig. 2.9.3(7). Denote the delta resistances $R_{1-2,\Delta}$, $R_{1-g,\Delta}$, and $R_{2-g,\Delta}$. Then adding the conductances in parallel gives

$$\frac{1}{R_{1-2(3)}} = \frac{1}{R_{1-2}} + \frac{1}{R_{1-2,\Delta}} \tag{36a}$$

$$\frac{1}{R_{1-g(3)}} = \frac{1}{R_{1-g}} + \frac{1}{R_{1-g,\Delta}} \tag{36b}$$

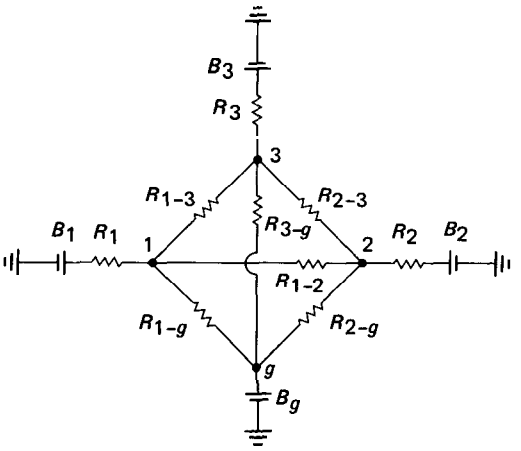

Figure 4 Radiation network for $n = 3$ with isothermal gas g.

© 1983 Hemisphere Publishing Corporation

$$\frac{1}{R_{2-g(3)}} = \frac{1}{R_{2-g}} + \frac{1}{R_{2-g,\Delta}} \tag{36c}$$

These resistances are entered into Eq. (35) to find the desired transfer factor.

A source, a sink, and a gaseous source or sink may model a direct-fired furnace where the refractory is made nonadiabatic by convection, or a nuclear accident scenario when spray cooling droplets are evaporating, for example. Note that an additional truly adiabatic surface may be included by using $R_{1-2(3)}, R_{1-g(3)}$, and $R_{2-g(3)}$ given by Eqs. (36*a-c*) in place of R_{1-2}, R_{1-g}, and R_{2-g} shown on Fig. 3. With or without the addition of a truly adiabatic surface, the network is no longer a simple two-node one, because three nodes are nonadiabatic. One proceeds by converting the $1-2-g$ delta in Fig. 3 into a wye according to Fig. 2.9.3(7). Denote the result as $R_{1,Y}, R_{2,Y}$, and $R_{g,Y}$. Then the resistances in series are added to give total values in each branch of a larger wye:

$$R_{1(T)} = R_1 + R_{1,Y} \quad R_{2(T)} = R_2 + R_{2,Y}$$
$$R_{g(T)} = R_{g,Y} \tag{37}$$

Finally, the wye is converted back to a delta according to Fig. 2.9.3(7):

$$A_1 \mathfrak{F}_{1-2} = \frac{R_{1(T)}^{-1} R_{2(T)}^{-1}}{R_{1(T)}^{-1} + R_{2(T)}^{-1} + R_{g(T)}^{-1}} \tag{38a}$$

$$A_1 \mathfrak{F}_{1-g} = \frac{R_{1(T)}^{-1} R_{g(T)}^{-1}}{R_{1(T)}^{-1} + R_{2(T)}^{-1} + R_{g(T)}^{-1}} \tag{38b}$$

$$A_2 \mathfrak{F}_{2-g} = \frac{R_{2(T)}^{-1} R_{g(T)}^{-1}}{R_{1(T)}^{-1} + R_{2(T)}^{-1} + R_{g(T)}^{-1}} \tag{38c}$$

G. Sample calculation

Suppose that a 6-m-diameter furnace is fired by 0.15 kg/s of gaseous fuel having a lower heating value of 5 X 10 J/kg and 2.7 kg/s of air, both air and fuel entering at 500 K. The load is at 900 K covered by slag 6 mm thick having a thermal conductivity of 2 W/m K and an emissivity of 0.48. The refractory roof is 50 m^2 in area. The furnace gas has a specific heat of 1 200 J/kg K and, for the calculated mean beam length and at an estimated gas temperature, an emissivity $\epsilon_g = 0.25$. It is desired to calculate T_g, T_1, and the heat transfer rate into the load.

If we neglect convection, we have case 2, a gaseous source, a refractory, and a sink. We begin by calculating $A_1 \mathfrak{F}_{1-g}$ from Eq. (33). The following values pertain (assuming that $\epsilon_{g,1-2} \doteq \epsilon_{g,2-2}$):

$$R_1 = \frac{1-\epsilon_1}{\epsilon_1 A_1} = \frac{1 - 0.48}{(0.48)(28.3)} = \mathbf{3.83\ X\ 10^{-2}\ m^{-2}}$$

$$R_{1-2} = \frac{1}{A_1 F_{1-2} \tau_{g,1-2}} = \frac{1}{(28.3)(1)(0.75)}$$
$$= \mathbf{4.72\ X\ 10^{-2}\ m^{-2}}$$

$$R_{1-g} = \frac{1}{A_1 \epsilon_{g,1-2}} = \frac{1}{(28.3)(0.25)} = 14.15 \text{ X } 10^{-2}\ m^{-2}$$

$$R_{2-g} = \frac{1}{A_2 F_{2-1} \epsilon_{g,2-1} + A_2 F_{2-2} \epsilon_{g,2-2}} = \frac{1}{(50)(0.25)}$$
$$= \mathbf{8.00\ X\ 10^{-2}\ m^{-2}}$$

A, $\mathfrak{F}_{1-g} = 1/[3.83 \text{ X } 10^{-2} + 1/\{[1/(14.15 \text{ X } 10^{-2})] + 1/[(4.72 + 8.00) \text{ X } 10^{-2}]\}] = 9.5\ m^2$

Next, Eq. (30) is written for the heat balance on the gas:

$$\dot{m}_g c_{p,g} (T_{gf} - T_g) = A_1 \mathfrak{F}_{1-g} (C_s T_g^4 - C_s T_1^4) \tag{39}$$

where

$\dot{m} c_{p,g} = (2.85)(1\,200) = 3\,420$ W/K

$$T_{gf} = 500 + \frac{0.15(5 \text{ x } 10^{\quad})}{3420} = 2\,693 \text{ K}$$

A heat balance on the surface between the *s* and *m* interfaces is written for area A_1:

$$A_1 \mathfrak{F}_{1-g} (C_s T_g^4 - C_s T_1^4) = \frac{kA_1}{\delta} (T_1 - T_0) \tag{40}$$

where

$$\frac{kA_1}{\delta} = \frac{(2)(28.3)}{6\ X\ 10^{-3}} = 9\,425 \text{ W/K}$$

The two nonlinear equations must be solved simultaneously for T_g and T_1. In a hand calculation one assumes an independent value $\dot{Q}_{g-1}^{(i)}$ for the heat transfer rate,

$$\dot{Q}_{g-1} = A_1 \mathfrak{F}_{1-g} (C_s T_g^4 - C_s T_1^4) \tag{41}$$

enters it into the right-hand side of Eq. (39), and solves for T_g and then into the left-hand side of Eq. (40) and solves for T_1. The values of T_g and T_1 are used to find a dependent value of $\dot{Q}_{g-1}^{(d)}$ from Eq. (41). Correct values of Q_{g-1}, T_1, and T_g are obtained when $\dot{Q}_{g-1}^{(i)} = \dot{Q}_{g-1}^{(d)}$. The following table completes the example :

$\dot{Q}_{g-1}^{(i)}$, W	T_g, K	T_1, K	$\dot{Q}_{g-1}^{(d)}$, W
3 x 10^6	1 816	1218	4.61 X 10
4 x 10^6	1523	1 324	1.24 X 10^6
3.3 x 10^6	1728	1250	3.49 x 10^6
3.34 x 10^6	1716	1 254	3.34 x 10^6

The answers are seen to be $\dot{Q}_{g-1} = 3.34 \text{ X } 10^6$ W, $T_g = 1\,716$ K, and $T_1 = 1\,254$ K. Having calculated a value of T_g, one should redetermine the value of ϵ_g and repeat the calculation.

If we considered convective coupling, we would

© 1983 Hemisphere Publishing Corporation

have to use case 5, a source, a sink, and a gaseous source. Then $A_1\mathfrak{F}_{1-2}$, $A_1\mathfrak{F}_{1-g}$, and $A_2\mathfrak{F}_{2-g}$ would be found, and one would have three simultaneous nonlinear equations to solve for T_1, T_2, and T_g:

$$\dot{m}_g c_{p,g}(T_{gf}-T_g)=h_1A_1(T_g-T_1)+h_2A_2(T_g-T_2)+A_1\mathfrak{F}_{1-g}(C_sT_g^4-C_sT_1^4)+A_2\mathfrak{F}_{2-g}(C_sT_g^4-C_sT_2^4) \quad (42)$$

$$h_2A_2(T_g-T_2)+A_2\mathfrak{F}_{2-g}(C_sT_g^4-C_sT_2^4)=A_1\mathfrak{F}_{1-2}(C_sT_2^4-C_sT_1^4) \quad (43)$$

$$h_1A_1(T_g-T_1)+A_1\mathfrak{F}_{1-g}(C_sT_g^4-C_sT_1^4)+A_1\mathfrak{F}_{1-2}(C_sT_2^4-C_sT_1^4)=\frac{kA_1}{\delta}(T_1-T_0) \quad (44)$$

H. Monte Carlo solution

How is the working engineer going to solve a more general radiation heat transfer problem than those five cases enumerated in Sec. F? A general method easy to grasp is the Monte Carlo one [10, 11]. Suppose that the temperature and composition field in the medium is known well enough to fix the properties. Divide the medium into M subvolumes and the surface into N areas. If only the heat flows for the areas are required, one need find only the transfer factor from area to area and area to volume. If one needs to know the heat flows for the volumes also, one will have to find the transfer factors from volume to volume as well. To find a transfer factor, one imagines that only one source area or volume i is turned on, $B_i=\pi I_{bi}=1$, and all the others are off. Then in the Monte Carlo sense one chooses randomly a source point and a direction of emission for the ray to be traced. For a surface, the ray is weighted by its directional emissivity, and $dA\cos\theta\,d\Omega$, as explained previously. For a volume of isotropic emitting material, the weighting is $k_a\,dV\,d\Omega$; that is, the points chosen within the volume should be uniformly distributed over the volume, and the direction should be uniform in solid angle. Thus, given two random numbers P_1 and P_2, the direction with respect to an arbitrary polar-azimuthal coordinate system would be

$$\theta=\cos^{-1}(2P_1-1) \quad (45)$$

$$\phi=2\pi P_2 \quad (46)$$

since $d\Omega=\sin\theta\,d\theta\,d\phi=-d(\cos\theta)\,d\phi$.

The ray tracing proceeds as described in Sec. 2.9.4, except that it is necessary to move along a ray in steps of As instead of going the entire distance R from surface to surface. The increment As is taken so that there are, say, an integer number of steps across the jth volume element being traversed. With each step As, the probability of absorption or scattering is compared to a random number P. From Eq. 2.9.5(8), this probability is $(1-e^{-k_e\Delta s})$. If P is greater than this probability, the ray continues along its original direction unchanged. If P is less than $\omega_s(1-e^{-k_es})$, the photon bundle is scattered. If it is not transmitted or scattered, it is absorbed. If the ray is scattered, a new direction is chosen according to Eqs. (45) and (46) (the ray energy is weighted by the phase function p if anisotropic scattering is considered), and the ray tracing continues until the requisite number of absorptions are scored.

Suppose that in a Monte Carlo calculation of 10 000 rays from surface i (weighted by, say, directional emissivity divided by hemispherical emissivity), 3 000 were absorbed by surface or volume j. Call f_{ij} the fraction 3 000/10 000. Then the heat flow transfer factor is

$$\mathcal{S}_{ij}=A_i\mathfrak{F}_{ij}=\epsilon_iA_if_{ij} \quad (47)$$

Suppose that, of 10 000 rays sent out from volume i, 2 000 were absorbed by surface or volume j. Call g_{ij} the fraction 2 OOO/lO 000. The surface emission is weighted by ϵ_iA_i, because the emitted heat flux is ϵ_iB_i, and the emitted heat flow is the flux times the area. An equivalent weighting is necessary for a volume.

Recall Eq. (13). The emitted radiation per unit volume is

$$Q_{V,\text{emitted}}=\frac{\dot{Q}_{\text{emitted}}}{V_g}=4k_aB_g \quad (48)$$

Thus the emission from the ith volume element is $4k_{a,i}V_iB_i$, and of that emission a fraction g_{ij} is absorbed by element j. Hence the heat flow transfer factor is

$$\mathcal{S}_{ij}=4k_{a,i}V_ig_{ij} \quad (49)$$

We need not be concerned that in a large volume some of the emitted radiation is scattered or reabsorbed. That fact was accounted for in the Monte Carlo calculation Of g_{ii} and g_{ij}.

The notation adopted here for $\mathcal{S}_{ij}$ does not distinguish between a volume and a surface. After all, a surface is a volume, the volume between the s and m thermodynamic control surfaces (where k_a is large). Because a photon can traverse a path from i to j equally well as from j to i, reciprocity holds,

$$\mathcal{S}_{ij}=\mathcal{S}_{ji} \quad (50)$$

regardless of whether i and j are both surfaces, or one or both are volumes.

With knowledge that the heat flow emitted by i and absorbed by j is $B_i\mathcal{S}_{ij}$, one can find the *net* heat flow between i and j:

$$\dot{Q}_{ij}=\mathcal{S}_{ij}(B_i-B_j)$$

If temperatures T_i and T_j are equal *so* that $B_i=B_j$, then $Q_{ij}=0$. The total heat flow out of element i is the sum

$$\dot{Q}_i=\sum_j\mathcal{S}_{ij}(B_i-B_j) \quad (51)$$

© 1983 Hemisphere Publishing Corporation

Note that the heat flux factor S_{ii} is of no consequence. However, in addition to Eq. (51), a good check for a Monte Carlo calculation is to sum S_{ij} over all j, including $j = i$. Since the sum of f_{ij} or g_{ij} over all j is unity, the sum of S_{ij} over all N surfaces and M volumes is

$$\sum_{j=1}^{N+M} S_{ij} = \begin{cases} \epsilon_i A_i & i = 1, \ldots, N \\ 4k_{a,i}V_i & i = n+1, \ldots, N+M \end{cases} \quad (52)$$

A zone method akin to the Monte Carlo method is to subdivide the volume into M zones and the surface into N subsurfaces just as for the Monte Carlo method, but instead of computing the transfer factor directly, the radio&y-irradiation problem is formulated. In the absence of scattering, the procedure is relatively straightforward, but it is tedious if more than one gas volume is involved, because shape factors involving gas transmission must be computed. Indeed, *one* way of computing such factors is to employ the Monte Carlo concept, so it is difficult to see why the transfer factor should not be computed directly via that algorithm. With scattering, the volume-to-volume and volume-to-surface shape factors are computed much as described in the Monte Carlo method, but scattered rays need not be traced, giving some computational advantage. One considers only the straight-line paths and scores rays either scattered or absorbed. The radiosity formulation is then broadened to include the source function S_i of each of the M volumes as well as the radiosity q_i^+ of the N surfaces. Just as the product of the shape factor F_{i-j} and reflectivity ρ_i gives the contribution to the radiosity of surface i by the radiosity at surface j for transfer in a diathennanous medium, so the products of the albedos and computed factors, call them $\omega_i F_{i-j}^{**}$, *gives* the contribution to the source function at volume i by the radiosity q_j^+ (for a surface) or source function S_j (for a volume). Matrix inversion or iterative solution then gives the set of S_i $(i = 1, M)$ and q_i^+ $(i = m+1, M+N)$.

Nomenclature for Section 2.9.6 appears at the end of Section 2.9.8.

BIBLIOGRAPHY FOR SECTION 2.9.6

The engineering enclosure problem

1. Hottel, H. C., Radiant Heat Transmission, in ***Heat Transmission***, ed. W. H. McAdams, 3d ed, chap. 4, McGraw-Hill, New York, 1954. See also Hottel, H. C., and A. F. Sarofim, ***Radiative Transfer,*** McGraw-Hill, New York, 1967.
2. Oppenheim, A. K., The Engineering Radiation Problem-An Example of the Interaction Between Engineering and Mathematics, ***Z. Angew. Math. Mech.***, vol. 36, pp.81-93, 1956.
3. Bevans, J. T., and Dunkle, R. V., Radiant Interchange Within an Enclosure, ***J. Heat Transfer, vol. 82,*** pp. l-19,1960.
4. Edwards, D. K., Molecular Gas Band Radiation, ***Adv. Heat Transfer***, vol. 12, pp. 115-193, 1976.
5. Becker, H. B., A Mathematical Solution for Gas-to-Surface Radiative Exchange Area for a Rectangular Parallelepiped Enclosure Containing a Gray Medium, ***J. Heat Transfer,*** vol. 99, pp. 203-211, 1977.
6. Nelson, D. A., Band Radiation Within Diffuse-Walled Enclosures, ***J. Heat Transfer, vol.*** 101, pp. 81-89, 1979.

Mean beam lengths (see also [1,4])

7. Oppenheim, A. K., and Bevans, J. T., Geometric Factors for Radiant Heat Transfer Through an Absorbing Medium in Cartesian Coordinates, ***J. Heat Transfer***, vol. 82, pp. 360-368, 1960.
8. Dunkle, R. V., Geometric Mean Beam Lengths for Radiant Heat Transfer Calculations, ***J. Heat Transfer, vol. 86,*** pp. 75-80, 1964.

Wall layer transmission

9. Balakrishnan, A., and Edwards, D. K., Molecular Gas Radiation in the Thermal Entrance Region of a Duct, ***J. Heat Transfer***, vol. 101, pp. 489-495, 1979.

Monte Carlo

10. Howell, J. R., and Perlmutter, M., Monte Carlo Solution of Thermal Transfer through Radiant Media Between Gray Walls, ***J. Heat Transfer,*** vol. 86, pp. 116-122, 1964.
11. Stockham, L. W., and Love, T. J., Radiative Heat Transfer from a Cylindrical Cloud of Particles, ***AIAA J., vol. 6,*** pp. 1 935-1940, 1968.

© 1983 Hemisphere Publishing Corporation

2.9.7

Nonisothermal gas radiation

D. K. Edwards

A. Solution of the equation of transfer

Recall that Eq. 2.9.5(6) for the change of intensity along slant path increment ds,

$$\frac{dI}{ds} = -k_a I + k_a I_b \qquad (k_s = 0) \tag{1}$$

had a solution for the homogeneous isothermal gas given by Eq. 2.9.6(3),

$$I = I_0 e^{-k_a s} + I_b(T_g)(1 - e^{-k_a s}) \quad (I_b = \text{const}) \tag{2}$$

Here $e^{-k_a s}$ is seen to be the transmissivity of a path s long, and $1 - e^{-k_a s}$ is the emissivity. When k_a varies with distance s, for example, if the composition varies, one merely transforms from distance s to optical depth t,

$$t = \int_0^s k_a \, ds \tag{3}$$

and obtains in place of Eq. (1),

$$\frac{dI}{dt} = -I + I_b \tag{4}$$

The transmissivity of the nonhomogeneous gas is accordingly e^{-t}, and the emissivity is $1 - e^{-t}$. The transformation simply says that the radiation doesn t care whether the radiating species is dilutely distributed over a large path or swept up into a short one. Meteorologists frequently describe the amount of water vapor in a path by giving the value of precipital centimeters of liquid water (actually the value of $X = \rho_a L$ in grams per square centimeter, since $\rho_{liq} = 1\ g/cm^3$). Of course, we know that the collision broadening as measured by the effect of P_e [recall Eq. 2.9.5(57)] on k_a would be affected if a molecular gas were swept up into a short path, but one considers the value of P_e as unchanged in transforming from s to t.

When T_g and hence $I_b(T_g)$ vary along the path, one finds the solution to Eq. (4) in a formal mathematical manner by variation of parameters. However, the engineer can picture the formal mathematical solution, and easily remember how to construct it, from the following physical considerations. Take an increment of path ds' at distance s (optical depth t') along the path. According to Eq. (2), that element emits $I_b[T_g(s')]k_a\,ds'$ because $1 - e^{dt} = dt' = k_a\,ds'$ is the emissivity of the increment. The, fraction transmitted from optical depth t' to t is $e^{-(t-t')}$. Thus the contribution from increment ds' to the intensity at s is

$$dI = e^{-(t-t')} I_b(t')\, dt'$$

$$= e^{-\int_{s'}^{s} k_a(s'')\, ds''} I_b(s') k_a(s')\, ds'$$

Summing (integrating) over all such increments and adding on the transmitted beam $I_0 e^{-t}$ gives

$$I = I_0 e^{-\int_0^s k_a(s')\, ds'} + \int_0^s e^{-\int_{s'}^{s} k_a(s'')\, ds''} \times I_b(s') k_a(s')\, ds' \tag{5}$$

It should be noted that when radiators of different temperatures are present, for example, particles of various sizes, each size with a different temperature, one simply sums the k_a's to obtain the total k_a, and replaces I_b with an effective value given by

© 1983 Hemisphere 1 ublishing Corporation

$$I_b = \frac{\sum_{i=1}^{n} k_{a,i} I_b(T_i)}{\sum_{i=1}^{n} k_{a,i}} \tag{6}$$

When isotropic scattering is a consideration, Eq. 2.9.5(8) applies instead of Eq. 2.9.5(6). Let the mean radiant intensity be S:

$$S = \frac{1}{4\pi} \int_0^{4\pi} I \, d\Omega \tag{7}$$

Then Eq. 2.9.5(8) can be written

$$\frac{dI}{dt_e} = -I + (1 - \omega_s) I_b + \omega_s S \tag{8}$$

where the optical depth for extinction is

$$t_e = \int_0^s (k_a + k_s) \, ds' \tag{9}$$

and ω_s is the albedo for single scatter,

$$\omega_s = \frac{k_s}{k_a + k_s} \tag{10}$$

The quantity $1 - \omega_s$ is sometimes given a name such as particle emissivity. Comparison of Eq. (8) with Eq. (4) shows them to have the same form, where the source function $(1 - \omega_s) I_b + \omega_s S$ replaces I_b. Thus Eq. (5) can be rewritten for nonzero k_s by replacing k_a with $k_a + k_s$ and I_b with $(1 - \omega_s) I_b + \omega_s S$:

$$I = I_0 e^{-\int_0^s (k_a + k_s) \, ds'} + \int_0^s e^{-\int_{s'}^s (k_a + k_s) \, ds'} \times [(1 - \omega_s) I_b + \omega_s S](k_a + k_s) \, ds' \tag{11}$$

Equation (5) for $\omega_s = 0$ or Eq. (11) for $\omega_s \neq 0$ constitutes the formal mathematical solution to the equation of transfer for a nonhomogeneous and/or nonisothermal gas. The equation is seen to be directly useful when the source function is known as a function of position. For example, when one knows the temperature and soot-concentration distributions in a burner flame, one can find the radiant intensity emerging from the flame (neglecting scattering) by using Eq. (5) and carrying out the integrations numerically. Of course, if one wants the net flux, one integrates I over $\cos\theta \, d\Omega$ as in Eq. 2.9.6(1) or 2.9.1(8),(9),

$$q_{\text{net}} = \int_0^{4\pi} I \cos\theta \, d\Omega = \int_0^{2\pi} (I_+ - I_-) \cos\theta \, d\Omega \tag{12}$$

and, if one wants the volumetric heat source, one integrates I over $d\Omega$ and subtracts the volume emission given by Eq. 2.9.6(13):

$$\dot{Q}_{V,\,\text{net absorbed}} = k_a \int_0^{4\pi} I \, d\Omega - 4\pi k_a I_b = 4\pi k_a (S - I_b) \tag{13}$$

Often one wants not the intensity at the end of a path but the intensity incident at $s = 0$. The distance through the gas from s' to $s = 0$ is then s , and the transmitted intensity is $I_L e^{-t}$. Hence Eq. (5) becomes

$$I^-(0) = I_L e^{-\int_0^L k_a(s') \, ds'} + \int_0^L e^{-\int_0^s k_a(s'') \, ds''} \times I_b(s') k_a(s') \, ds' \tag{14}$$

Also, Eq. (14) is often in a more convenient form for use when integration by parts is performed. Let $u = I_b(s')$ and

$$v = 1 - e^{-\int_0^{s'} k_a(s'') \, ds''} \qquad dv = e^{-\int_0^{s'} k_a(s'') \, ds''} k_a \, ds'$$

Then

$$\int_0^L u \, dv = uv\Big|_0^L - \int_0^L v \, du = u_L v_L - \int_0^L v \, du$$

Hence

$$I^-(0) = I_b(0) + (I_L - I_{bL}) e^{-\int_0^L k_a \, ds'} + \int_0^L e^{-\int_0^{s'} k_a \, ds''} \frac{dI_b}{ds'} \, ds' \tag{15}$$

If the backward intensity I^- is desired at a distance s along the path, one simply replaces each zero in Eq. (14) or Eq. (15) by s.

B. Geometric considerations

The equation of transfer and its solution are simple. What complicates the subject of radiation heat transfer are geometric complexities and spectral variations. We defer considering spectral variations and consider some geometric effects. One may classify a problem as one dimensional when the source function varies with one dimension only and multidimensional when it varies in more than one dimension. In the former case, four special geometries stand out: (1) the slab with variations in the z direction only; (2) the sphere with variations in r only; (3) the cylinder with variations in r only; and (4) the cone with absorption coefficient varying with $1/z$, where z is the distance from the apex, times a function of angle from the axis, and temperature varies with angle only. The slab may be applied to layers that are thin compared to any radius of curvature; the sphere to some

© 1983 Hemisphere Publishing Corporation

chemical reactors, fireballs, and stellar interiors; the cylinder to pipes, combustion chambers, and cylindrical plumes; and the cone, as an idealization, to conical plumes and jets.

Even when a problem is one dimensional in source function variation, the radiative transfer is three dimensional in that rays in all directions contribute to the net flux. The slab and sphere possess azimuthal symmetry so that integration over solid angle reduces to integration over polar angle θ only, that is, $d\Omega = 2\pi \sin\theta\, d\theta$. The cylinder and cone require integration over both base angle γ and axial angle β [recall Fig. 2.9.1(3)].

Turning attention to the slab, one sees in Fig. 1 that the length of a ray varies from one slab thickness to infinity as angle θ varies from zero to n/2. Rays of all possible lengths between these limits contribute to the heat transfer. One can obtain satisfactory numerical answers by choosing a few discrete directions, attributing to each a finite solid angle, and replacing the integrals over solid angle with weighted summations. Such approximations are referred to as discrete ordinates or "multiflux" approximations. However, exact integral expressions can be employed for the simple geometries.

For the slab one simply recognizes that slant path length s is related to normal distance z by $s = z/\cos\theta$ as shown in Fig. 1. For the cylinder the trigonometric law of cosines is used to relate the change of radial distance r to the increment of path length ds, and, for a given ray and point of origin, s is double valued in r. For a ray moving inward, one integrates from the radius at the point of origin to r_{min} and then from r_{min} to r_w as illustrated in Fig. 1. Note that polar angle is appropriate for the sphere, but base-axial angle coordinates are more convenient for the cylinder and cone.

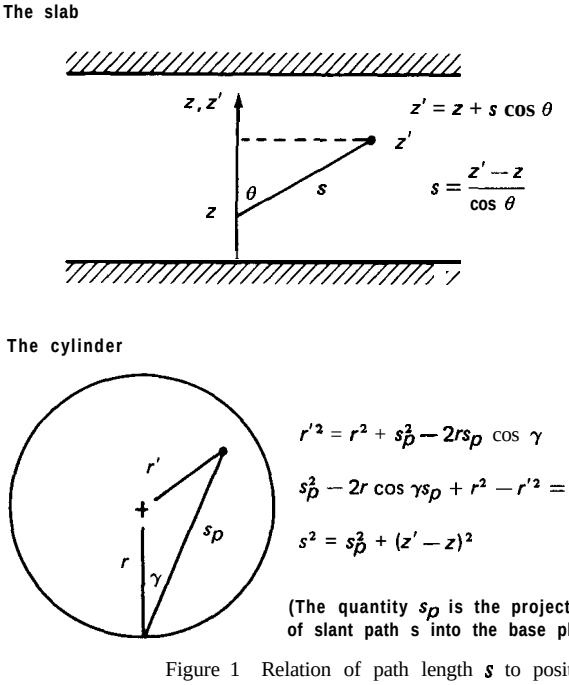

Figure 1 Relation of path length s to position.

C. The slab geometry

Introducing Eqs. (5) and (14) for location s in Eq. (12) gives rise to such terms as

$$\int_{\theta=0}^{\pi/2} e^{-k_a z/\cos\theta} \cos\theta \sin d\theta$$

One customarily denotes cos θ by μ or $1/\cos\theta$ by u. Hence a special function,

$$E_n(t) \equiv \int_0^1 e^{-t/\mu}\mu^{n-2}\, d\mu = \int_0^\infty e^{-ut}\frac{du}{u^n} \qquad (16)$$

is defined where, in the example given, $t = k_a z$. The exponential integral has properties from the definition as follows:

$$\frac{dE_n(t)}{dt} = E_n'(t) = -E_{n-1}(t) \qquad E_1'(t) = \frac{-e^{-t}}{t} \qquad (17)$$

$$\int E_n(t)\, dt = -E_{n+1}(t) \qquad (18)$$

$$E_n(0) = \frac{1}{n-1} \qquad E_1(t) = \ln\frac{1}{t} - \gamma \quad \text{as } t \to 0 \qquad (19)$$

$\gamma = 0.577\ 215\ 6\ldots$

$$E_n(t) = \frac{1}{t}e^{-t} \quad \text{as } t \to \infty \quad (t \gg n) \qquad (20)$$

A short table of exponential integrals is given in Table 1.

Rutting Eq. (5) for I^+ $(0 \leqslant \theta \leqslant \pi/2)$ and its equivalent for I^- $(\pi/2 < \theta \leqslant \pi)$ into Eq. (12) and identifying the exponential integrals gives, for diffuse boundaries,

$$q(t) = q_0^+ 2E_3(t) - q_L^+ 2E_3(t_L - t) + \int_0^t E_2(t - t')B(t')2\, dt' - \int_t^{t_L} E_2(t' - t)B(t')2\, dt' \qquad (21)$$

Here q_0^+ is the radiosity of wall at $z = 0$ ($t = 0$ in terms of optical depth) and q_L^+ is the radiosity (directed in the negative z direction) of the wall at z = L ($t = t_L$) and B is πI_b. Inspection of the equation and consideration of a differential slab of thickness dt' shows that $2E_3(t)$ is the hemispherical transmissivity for *diffuse* radiation through a slab of optical thickness t, and $1 - 2E_3(t)$ is the hemispherical absorptivity or (if the gas is isothermal) emissivity. The quantity $E_2(t - t')$ is the

© 1983 Hemisphere Publishing Corporation

Table 1 Values of the first five exponential integrals

t	$E_1(t)$	$E_2(t)$	$E_3(t)$	$E_4(t)$	$E_5(t)$
0	∞	1.000 0	0.500 0	0.333 3	0.250 0
0.01	4.037 9	0.949 7	0.490 3	0.3284	0.246 7
0.02	3.354 7	0.913 1	0.481 0	0.323 5	0.2434
0.03	2.959 1	0.881 7	0.472 0	0.318 8	0.240 2
0.04	2.6813	0.853 5	0.463 3	0.314 1	0.237 1
0.05	2.461 9	0.827 8	0.454 9	0.309 5	0.233 9
0.06	2.295 3	0.804 0	0.446 8	0.305 0	0.230 9
0.08	2.026 9	0.761 0	0.431 1	0.296 2	0.224 9
0.10	1.8229	0.722 5	0.416 3	0.287 7	0.219 0
0.20	1.222 7	0.574 2	0.351 9	0.249 4	0.192 2
0.30	0.905 7	0.469 1	0.300 0	0.216 9	0.168 9
0.40	0.702 4	0.389 4	0.257 3	0.189 1	0.148 7
0.50	0.559 8	0.326 6	0.221 6	0.165 2	0.131 0
0.60	0.454 4	0.276 2	0.191 6	0.144 6	0.115 5
0.80	0.3106	0.200 9	0.144 3	0.111 3	0.090 1
1.00	0.219 4	0.148 5	0.1091	0.086 1	0.0705
2.00	0.048 9	0.037 5	0.030 1	0.025 0	0.021 3
3.00	0.013 0	0.010 6	0.008 9	0.007 7	0.006 7

transmissivity for a ***nondiffuse*** source, where $I = I_b k_a\, dz/\cos\theta$ from optical depth t' to optical depth t. The quantity $2\,dt'$ is the hemispherical emissivity of a slab of differential optical thickness $k_a\, dz'$. Recall that the mean beam length for an optically thin slab of thickness dz' is $2\,dz'$; or, equivalently, the volume emission is $4k_a\, dz'\, B$, of which half goes forward and half backwards.

Just as Eq. (5) or (14) is often put in a more convenient form by integration by parts, so is Eq. (21). Let $v = 1 - 2E_3(t - t')$ and $u = B(t')$ in the first integral and $v' = 1 - 2E_3(t' - t)$ and $u' = B(t')$ in the second one. Then integration by parts gives

$$q(t) = (q_0^+ - B(0))2E_3(t) - (q_L^+ - B(t_L)) \times 2E_3(t_L - t) + \int_0^{t_L} 2E_3(|t - t'|) \times \left(-\frac{dB}{dt'}\right) dt' \qquad (22)$$

Note that, if $B(t')$ is discontinuous, the integral in Eq. (22) is taken in the Stieltjes sense.

For example, consider a gas in a black flat plate duct of total thickness L with uniform absorption coefficient k_a whose temperature varies in such a way that the gas blackbody radiosity B rises linearly from the value B_w at each wall over boundary layer thickness δ_{BL} to a constant value of B_g throughout the remainder of the duct. Find the heat flux at the wall. With black walls and no temperature jump at the wall, $q_0^+ - B(0) = 0$ and $q_L^+ - B(t_L) = 0$. Thus Eq. (22) at the wall becomes

$$q(0) = \int_0^{t_{BL}} 2E_3(t') \left(-\frac{B_g - B_w}{t_{BL}}\right) dt' + \int_{t_{BL}}^{t_L - t_{BL}} 2E_3(t')j(0)\, dt' + \int_{t_L - t_{BL}}^{t_L} 2E_3(t') \left(+\frac{B_g - B_w}{t_{BL}}\right) dt'$$

$$-q(0) = \epsilon_{\text{channel}}(B_g - B_w) \qquad (23a)$$

$$\epsilon_{\text{channel}} = \frac{1}{t_{BL}}\left[\frac{2}{3}(1 - 3E_4(t_{BL})) - 2(E_4(t_L - t_{BL}) - E_4(t_L))\right] \qquad (23b)$$

where $\epsilon_{\text{channel}}$ is called the effective channel emissivity. One may easily insert some numbers; for example, if $T_g = 1\,000$ K, $T_w = 500$ K, $L = 10$ cm, $\delta_{BL} = 1$ cm, and $k_a = 100\ \text{m}^{-1}$ [independent of λ over the spectrum of concern as defined by Table 2.9.1(1)], the net radiant flux at the wall is

$$-q(0) = (5.67 \times 10^{-8})(1000^4 - 500^4)\frac{1}{100(0.01)} \times \left[\frac{2}{3}(1 - 3E_4(1)) - 2(E_4(9) - E_4(10))\right] = (5.316 \times 10^4)(0.494\ 5) = 2.628 \times 10^4\ \text{W/m}^2$$

The example was chosen not just to illustrate Eq. (22), but also to give insight into a sometimes important phenomenon, self-absorption. In the numerical example the core of the gas between $t_{BL} = 1$ and $t_L - t_{BL} = 9$ was essentially opaque. Thus the irradiation q^- at the edge of the boundary layer was the full $B_g = C_s T_g^4$, and the radiosity at the wall $C_s T_w^4$ was $(0.5)^4 = 0.062\ 5$ of the gas. Yet the net flux at the wall was only 0.494 5 of the difference between $C_s T_g^4$ and $C_s T_w^4$, not $1 - 0.062\ 5 = 0.937\ 5$. In the boundary layer the irradiation upon the wall was reduced by absorption exceeding emission. For a fixed value of δ_{BL}/L, one may increase $t_L = k_a L$ from zero to infmity. If δ_{BL}/L is zero, one finds that the channel emissivity rises as $1 - 2E_3(t_L)$, linearly at first as $2t_L$ (since the geometric mean beam length is 2) and then more slowly to a maximum value of 1. When δ_{BL}/L is nonzero, one finds from Eq. (23b) that the channel emissivity rises linearly at first, as $(2 - \delta_{BL}/L)t_L$, then more slowly until a maximum is reached, and then returns to zero, as $2/[3(\delta_{BL}/L)t_L]$, as

© 1983 Hemisphere Publishing Corporation

t_L goes to infinity. Qualitatively, the same effect occurs in sooty flames from petroleum fires and in combustion chambers; that is, as the size of the flame increases, the radiant flux from it at first rises but then falls as the cold boundary layer becomes absorbing.

D. Differential formulations

When the source function is known, as it is in a nonscattering medium with known temperature profile, one simply integrates the equation of transfer along a path to obtain I, and integrates I over angles θ and ϕ (if required) or γ and β to find the heat flux. The integrations can be done numerically if necessary, or with the aid of special functions such as the exponential integrals if they apply. When the source function is unknown, as for the case of appreciable scattering, or when radiative heating or cooling affects the temperature given by the general energy equation, one may be able to execute an iterative solution based on estimating the source function, using the solution to the equation of transfer to find I, and improving the estimate of the source function by integrating I over 4π steradians and repeating. Such a procedure is convergent for albedo less than one in a medium of known temperature profile. Differential formulation may be a more convenient alternative. Some of the various differential methods are briefly described here as they would be applied to the classic engineering problem of predicting the radiant heat transfer through a layer of porous or fibrous insulation.

The situation considered is a layer of insulation L thick in radiative equilibrium. The material is imagined to be an isotropic gray emitter-absorber-scatterer with absorption coefficient $k = k_a + k_s$. Under conditions of gray radiative equilibrium ($dq_R/dz = 0$), there is no need to distinguish between isotropic scattering and absorption-reradiation. The bounding walls are taken as black. As for the adiabatic-walled passage, provision for nonblack surface emissivities can be made by adding surface resistances $(1-\epsilon_1)/\epsilon_1$ and $(1-\epsilon_2)/\epsilon_2$ to the insulation resistance $1/\mathfrak{F}_{1-2,b}$ as shown in Eq. 2.9.3(59). Optical depth $t = kz$ is measured from one wall and varies from 0 to $t_L = kL$.

For comparison we can first derive the solution for the optically thin medium $t_L \ll 1$. For the optically thin case the medium is isothermal, and the network solution for a source, a sink, and an adiabatic gas applies with $\tau_g = e^{-2t_L} \doteq 1 - 2t_L$ and $\epsilon_g = 1 - \tau_g \doteq 2t_L$, where the factor of 2 appears because the mean beam length is $2L$. The result is

$$\mathfrak{F}_{1-2} = \tau_g + \frac{1}{2}\epsilon_g = 1 - t_L \qquad \text{as } t_L \to 0 \tag{24}$$

The network solution clearly breaks down as t_L becomes large, because the assumption of an isothermal medium is then invalid.

(a) Radiation diffusion

At a wavelength where k_a is large so that (1) $1/k_a$ is short compared to any radius of curvature, (2) $k_a z_w$ is large, where z_w is the distance to any wall, and (3) the quantity dB/dz is constant over a few multiples of $1/k_a$, where z is length measured in the direction of the temperature gradient, and B is πI_b of the medium at the wavelength of concern; Eq. (22) shows that the spectral radiant heat flux reduces to a simple expression in the form of Fourier s law of heat conduction. The terms $2E_3(t)$ and $2E_3(t_L - t)$ go to zero because the optical depths t and t_L -t to the walls are large. The term $dB/dt' = (1/k_a)\,dB/dz'$ is regarded as constant at $(1/k_a)\,dB/dz$ over the range in which $2E_3(|t - t'|)$ drops to zero, and the integration with respect to t' is transformed to $t - t'$ and $t' - t$. Since both t and $t_L - t$ are large, the limits on the integrals are taken as effectively ∞. Then

$$q_\lambda = -\frac{1}{k_a}\frac{dB_\lambda}{dz}\left(4\int_0^\infty E_3(t'')\,dt''\right)$$

$$\frac{4}{3k_a}\frac{\partial B_\lambda}{\partial T}\frac{dT}{dz} \tag{25}$$

The quantity $(4/3k_a)(\partial B_\lambda/\partial T)$ is a spectral radiation conductivity. If large k_a applies to the entire spectrum of interest defined by temperature T and the internal fraction in Table 2.9.1(1), then one can integrate spectrally to obtain

$$q = -K_R\frac{dT}{dz} \tag{26}$$

where

$$K_R = \int_0^\infty \frac{4}{3k_a}\frac{\partial B_\lambda}{\partial T}\,d\lambda$$

$$= \frac{16}{3}C_s T^3\int_0^1 \frac{1}{k_a}\,df_i(\lambda T) \tag{27}$$

The quantity K_R, which is seen to be $(16/3)C_s T^3$ times the internal fraction-weighted average of $1/k_a$, is the Rosseland radiation conductivity.

The above relation was derived for a nonscattering medium. However, for a gray medium, isotropic scattering, and radiative equilibrium, it is easy to see that the albedo of single scatter is of no concern (just as the emissivity of a perfectly diffuse gray refractory wall is of no concern), and k_a is replaced with the extinction coefficient $k_a + k_s$. For nongray anisotropic scattering the situation is not so simple, but an approximation is to use a $(1 - \cos\theta)$-weighted average of the bidirectional scattering coefficient in place of k_s.

© 1983 Hemisphere 1 blishing Corporation

For the slab of insulation under consideration, one has merely

$$\frac{d}{dz}(q_R) = 0 \qquad q_R = -\frac{16}{3}\frac{1}{k} C_s T^3 \frac{dT}{dz}$$

Recognizing that $C_s T^3\, dT = dB$ permits writing

$$\frac{d}{dz}\left(\frac{4}{3k}\frac{dB}{dz}\right) = 0 \qquad \frac{d^2B}{dz^2} = 0$$

subject to $B = B_1$ at z = 0 and $B = B_2$ at z = L, if an extrapolation length is not applied. Obtaining the general solution for B, using the boundary conditions to solve for the constants, and finding $q_R = -(4/3k)\, dB/dz = \mathfrak{F}_{1-2}(B_1 - B_2)$ gives

$$\mathfrak{F}_{1-2} = \frac{4}{3t_L} \qquad \text{as } t_L \to \infty \tag{28a}$$

The solution clearly breaks down as t_L goes to zero.

To improve the accuracy of the radiation diffusion approximation, the notion of an extrapolation length is sometimes applied. Writing Eq. (22) at the wall z = 0 and letting k become large gives $q_R = -(2/3k)\, \partial B/\partial z$ versus $-(4/3k)\, \partial B/\partial z$ some distance from the wall. Extrapolating the far-from-wall slope to the wall value suggests imposing B_w at distance $2/3k$ behind the wall. In the present example L is replaced by $L + 4/3k$, giving

$$\mathfrak{F}_{1-2} \doteq \frac{1}{1 + (3/4)t_L} \qquad t_L \gg 1 \tag{28b}$$

This result is a good engineering approximation. However, it is not clear how to use the extrapolation length concept in a combined radiation and conduction-convection problem.

(b) Multiflux methods

The idea is simply to choose a few discrete directions (sometimes called discrete ordinates) and use the equation of transfer to give intensities in those directions and then form approximate expressions for S and q_R by summing them (finite quadrature). For the slab of insulation under consideration, the lowest level of this approximation is the Schuster two-flux model, which is equivalent to using a so-called substitute kernel, that is, approximating $E_2(t)$ with e^{-at}. The choice of directions is arbitrary. At the two-flux level, one might choose the directions back and forth along the geometric mean beam length (which would give correct results as $t_L \to 0$) or a somewhat shorter slant path. At the two-flux level we might number the two intensities as I_1 and I_2 and the fluxes as q_1 and q_2. The net flux would be approximated with

$$q_R \doteq \pi I_1 - \pi I_2 = q_1 - q_2$$

and the source function with

$$S \doteq \frac{1}{2}(I_1 + I_2) = \frac{1}{2\pi}(q_1 + q_2)$$

At radiative equilibrium $I_b = S$, and the equation of transfer for I_1 and I_2 is

$$\frac{dI_1}{dt_1} = -I_1 + S \qquad \frac{dq_1}{dt_1} = -q_1 + \frac{1}{2}(q_1 + q_2)$$

$$\frac{dI_2}{dt_2} = -I_2 + S \qquad \frac{dq_2}{dt_2} = -q_2 + \frac{1}{2}(q_1 + q_2)$$

We let $t_1 = akz = at$, $t_2 = -akz = -t_1$, and choose a = 2, thus aligning I_1 and I_2 along the geometric mean beam length. The two-flux equations become

$$\frac{dq_1}{dt} = q_2 - q_1 = q_R \qquad \frac{dq_2}{dt} = q_2 - q_1 = q_R$$

subject to $q_1 = B_1$ at $t = 0$ and $q_2 = B_2$ at $t = t_L$. Solving the two equations simultaneously and imposing the boundary conditions to solve for unknown constants gives q_1 and q_2. Then the net flux is found. The result for $\mathfrak{F}_{1-2}$ is

$$\mathfrak{F}_{1-2} = \frac{1}{1 + t_L} \tag{29}$$

The result is seen to be correct as $t_L \to 0$, because the geometric mean beam length was chosen, but comparison to Eq. (28a) shows that it underpredicts by 25% as $t_L \to \infty$.

If, say, six fluxes are used, the accuracy of the multiflux method becomes quite acceptable for engineering purposes. With the selection of $2n$ fluxes, one must choose $2n$ directions and attribute to each direction a weighting coefficient a_i for the net flux and b_i for the source function ($i = 1, n$).

$$q = \sum_{i=1}^{2n} a_i q_i \qquad S = \sum_{i=1}^{2n} b_i q_i \tag{30}$$

A primitive selection is to use equally spaced values of μ^2 ($\mu = \cos\theta$) over the interval 0 to + 1; that is,

$$\mu_i = \left(1 - \frac{i - 1/2}{n}\right)^{1/2} \qquad 1 \leqslant i \leqslant n$$

$$= -\left(\frac{i - \frac{1}{2}}{n} - 1\right)^{1/2} \qquad n + 1 \leqslant i \leqslant 2n \tag{31}$$

Then, because $\cos\theta\, d\Omega/\pi$ is $d\mu^2$ and $d\Omega/4\pi$ is $d\mu/2$,

$$a_i = \frac{1}{n} \qquad b_i = \frac{1}{2}\left[\left(1 - \frac{i-1}{n}\right)^{1/2} - \left(1 - \frac{i}{n}\right)^{1/2}\right]$$

$$1 \leqslant i \leqslant n$$

$$a_i = \frac{-1}{n} \qquad b_i = \frac{1}{2}\left[\left(\frac{i}{n} - 1\right)^{1/2} - \left(\frac{i-1}{n} - 1\right)^{1/2}\right]$$

$$n + 1 \leqslant i \leqslant 2n \tag{32}$$

© 1983 Hemisphere Publishing Corporation

Other selection schemes have been examined; see, for example, [8].

(c) Embedding

The embedding concept is used to formulate differential equations for the bidirectional reflectivity and transmissivity in conjunction with the use of discrete ordinates. Consider the problem of finding the bidirectional reflectivity and transmissivity of a layer of snow. The problem is related to our layer of insulation because in the limit as albedo for single scatter ω_s goes to unity, the scattering layer becomes the same as the scattering-reradiating layer in radiative equilibrium. The layer then absorbs nothing, and the hemispherical transmissivity becomes one minus the hemispherical reflectivity. The hemispherical transmissivity is thus identical to $\mathfrak{F}_{1-2,b}$ of a layer in radiative equilibrium.

Formulating by embedding is accomplished by imagining that the bidirectional properties of a slab of optical depth t are known and then asking what change would occur upon adding an infinitesimal layer dt. The layer can be imagined as added to the top (the irradiated side) or the bottom (the dark side). The procedure is referred to as embedding from above or embedding from below accordingly. Figure 2 shows the situation for calculating the reflectivity by embedding from above.

Because dt is infinitesimal, only first-order terms are retained. The figure shows all the first-order rays and the zeroth-order one. The slab is irradiated by intensity I^- in solid angle $d\Omega^-$ about angle θ^-. We want to know the intensity I^+ in direction θ^+. The five rays shown are all parallel in the emergent direction of interest θ^+. The first was scattered directly into the θ^+ direction. The slant path in that direction is $dt/\cos\theta^+$, and the source strength in the slab is $\omega_s I^- d\Omega^-/4\pi$. Hence

$$dI_1^+ = \frac{\omega_s}{4\pi} I^- d\Omega^- \frac{dt}{\cos\theta^+} \tag{33}$$

The second was scattered downward into some arbitrary direction θ_1^- and then bidirectionally reflected into the desired angle θ^+. The second-order attenuation by the thin slab dt is neglected. From the definition of the bidirectional reflectivity, Eq. 2.9.2(14),

$$dI_2^+ = \frac{1}{\pi}\rho(\theta^+, \theta_1^-) dI_1^- \cos\theta_1^- d\Omega_1^-$$

The downward scattered intensity dI_1^- is of the form of Eq. (33) with the angle θ_1^- replacing θ^+. We integrate over all possible θ_1^- directions. Accordingly,

$$dI_2^+ = \left(\frac{1}{\pi}\int_{2\pi}\rho(\theta^+, \theta_1^-) d\Omega_1^-\right)\frac{\omega_s}{4\pi} I^- d\Omega^- dt \tag{34}$$

where

$$d\Omega_1^- = 2\pi \sin\theta_1^- d\theta; = 2\pi d(\cos\theta_1^-)$$

The third ray was transmitted through the added layer dt, bidirectionally reflected into the desired angle θ^+, and transmitted again through dt. Upon each transmission an attenuation occurs.

$$I_3^+ = \left(1 - \frac{dt}{\cos\theta^+}\right)\frac{1}{\pi}\rho(\theta^+, \theta^-)\left(1 - \frac{dt}{\cos\theta^-}\right) I^- d\Omega^-$$

Upon neglect of the dt^2 term,

$$I_3^+ = \frac{1}{\pi}\rho(\theta^+, \theta^-) I^- d\Omega^- \left[1 - \left(\frac{1}{\cos\theta^+} + \frac{1}{\cos\theta^-}\right) dt\right] \tag{35}$$

This contribution is seen to contain the zeroth-order term and a first-order one.

Rays 4 and 5 arise from bidirectional reflection of the transmitted beam and subsequent scattering. For ray 4 the scattering is into the direction of interest θ^+, and for ray 5 the scattering is downward at angle θ_1^- followed by bidirectional reflection into the desired direction θ^+. Since first-order scattering occurs, the higher-order attenuations are neglected. Integration over possible scattering angles is made.

$$dI_4^+ = \frac{1}{\pi}\int_{2\pi}\rho(\theta_1^+, e\text{-}j\text{-} d\Omega_1^+ I^- \cos\theta^- d\Omega^- \frac{\omega_s dt}{4\pi\cos\theta^+} \tag{36}$$

$$dI_5^+ = \frac{1}{\pi}\int_{2\pi}\rho(\theta_1^+, \theta^-) d\Omega_1^+ I^- \cos\theta^- d\Omega^- \left(\frac{\omega_s dt}{4\pi}\right) \times \frac{1}{\pi}\int_{2\pi}\rho(\theta^+, \theta_1^-) d\Omega_1^- \tag{37}$$

Summing the five terms and dividing by $(I^- \cos\theta^- d\Omega^-/\pi)$ gives $\rho(\theta^+, \theta^-)$ for thickness $t + dt$. Denoting $\cos\theta^+$ as u, $\cos\theta^-$ as v, $\cos\theta_1^+$ as u , and $\cos\theta_1^-$ as v'; sub-

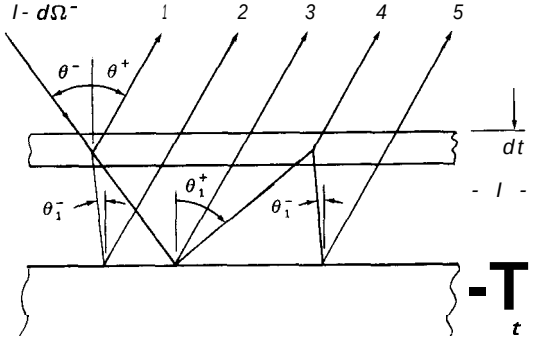

Figure 2 Embedding from above, reflectivity.

© 1983 Hemisphere Publishing Corporation

tracting $\rho(u,v,t)$; dividing by dt; and taking the limit as dt goes to zero gives

$$\frac{\partial \rho(u,v,t)}{\partial t} = \omega_s \left(\frac{1}{2u} + \int_0^1 \rho(u,v',t)\, dv' \right) \times \left(\frac{1}{2v} + \int_0^1 \rho(u',v,t)\, du' \right) - \left(\frac{1}{u} + \frac{1}{v} \right) \rho(u,v,t) \tag{38}$$

Choosing n discrete directions, say, those given by Eq. (31), and understanding a_i and b_i to be as given by Eq. (32) gives n^2 simultaneous ordinary differential equations:

$$\frac{\partial \rho_{i,j}(t)}{\partial t} = \omega_s \left(\frac{1}{2u_i} + \sum_{k=1}^{n} b_k \rho_{i,k}(t) \right) \times \left(\frac{1}{2v_j} + \sum_{k=1}^{n} b_k \rho_{k,j}(t) \right) - \left(\frac{1}{u_i} + \frac{1}{v_j} \right) \rho_{i,j}(t) \tag{39}$$

These are solved with a forward-marching Runge-Kutta integration commencing with $\rho_{i,j}(0) = 0$ for a black boundary. Once $\rho_{i,j}(t_L)$ is found, the hemispherical reflectance is

$$\rho_H(t_L) = \sum_{i=1}^{n} \sum_{j=1}^{n} a_i a_j \rho_{i,j}(t_L) \tag{40}$$

and for $\omega_s = 1$,

$$\mathfrak{F}_{1-2,b} = 1 - \rho_H(t_L) \tag{41}$$

(d) Other differential methods

Various other approximate methods have been used to analyze radiative transfer with scattering. In the classical Milne Eddington approximation the equation of transfer, Eq. (8) with $dt_e = k\, ds = k\, dz/\mu = dt/\mu$, is integrated with respect to $d\Omega$ over 4π steradians and then with respect to eos $\theta\, d\Omega$ over the same interval. The two integrations are the zeroth and first moment, respectively. Hence the method is a moment method. The approximation is made that

$$K = \int_{-1}^{+1} I\mu^2\, d\mu \doteq \frac{2}{3} \left(\frac{1}{2} \int_{-1}^{+1} I\, d\mu \right) = \frac{2}{3} S \tag{42}$$

Thus two simultaneous equations are obtained in net flux q_R and source function S:

$$\frac{dq_R}{dt} = 4\pi(1-\omega_s)(I_b - S) \tag{43}$$

$$\frac{dS}{dt} \doteq -\frac{3}{4\pi} q_R \tag{44}$$

For the insulation problem proposed, radiative equilibrium applies, and I_b = S so Eq. (43) becomes

$$\frac{dq_R}{dt} = 0 \tag{43a}$$

The two equations can be solved at once to show q_R is a constant and S a linear function in t,

$$S = S_0 - \frac{3}{4\pi} q_R t \tag{45}$$

The two unknown constants q_R and S_0 must be found from boundary conditions. At this point, as is characteristic with approximate differential methods, the problem becomes somewhat complex. One returns to the equation of transfer and solves for I_L^+ and I_0^-, Eqs. (11) and (14), respectively; and, knowing $I_0^+ = B_1/\pi$ and $I_L^- = B_2/\pi$, finds S at t = 0 and $t = t_L$ by integrating with respect to μ; and equates them to Eq. (45), thus obtaining two simultaneous equations in the two unknowns. Other moment methods have been explored [10].

E. Spectral considerations and scaling approximations

We turn our attention now away from geometric (directional and spatial) considerations to consideration of spectral variations. We have seen that the equation of transfer is readily solved, for example, Eq. (5), on a true spectral basis. The solution is useful as it stands when one is dealing with a continuum source such as soot or particulates. But when the source is a molecular gas, the spectral absorption coefficient k_a may vary by several orders of magnitude over the spectral region between lines and over a band. In such a case, Eq. (5) or (14) is of no practical use. Recall that one often has no knowledge of k_a but only of narrow-band model parameters S/d (line intensity-to-spacing ratio) and β (line width-to-spacing ratio parameter), and in some cases no knowledge of those parameters but only of wide-band parameters α_k (integrated band intensity), β_k (line width-to-spacing ratio parameter), and ω_k (band width parameter). Accordingly, one resorts to what is called "narrow-band scaling or wide-band scaling to arrive at working relations.

(a) Narrow-band scaling: the Curtis-Godson approximation

Consider the spectrally smoothed transmissivity of a path L of gas whose temperature, composition, and/or pressure varies along L. From Eqs. (2), (3), and 2.9.5(18),

© 1983 Hemisphere Publishing Corporation

$$\bar{\tau}_g = \frac{1}{d}\int_{\nu-d/2}^{\nu+d/2} e^{-\int_0^X k_a\,dX}\,d\nu \tag{46}$$

where k_a is given by a sum of Lorentz lines according to Eq. 2.9.5(15) and X is the path length-absorber gas density product. For the homogeneous gas where k_a does not vary along the path, the smoothed transmissivity $\bar{\tau}_g$ was given by an equation such as Eq. 2.9.5(19) as a function of S/d and γ/d or $\eta = \pi\gamma/d$, where S/d was the spectral average of k_a over the d interval. It is clear that for the optically thin nonhomogeneous gas, where $k_a L \ll 1$ everywhere in the spectral range u-d/z to $\nu + d/2$,

$$\bar{\tau}_g = \frac{1}{d}\int_{\nu-d/2}^{\nu+d/2}\left(1 - \int_0^X k_a\,dX\right)d\nu$$

$$= 1 - \int_0^X \left(\frac{S}{d}\right)dX = 1 - \tilde{\xi}$$

whereas the corresponding relation for the homogeneous gas is

$$\bar{\tau}_{g,\text{homo}} = 1 - \left(\frac{S}{d}\right)X$$

Hence, for the optically thin nonhomogeneous gas,

$$\bar{\tau}_g = \bar{\tau}_{g,\text{homo}}(\xi = \tilde{\xi})$$

where ξ is $(S/d)X$ for the homogeneous gas, and

$$\tilde{\xi} = \int_0^X \left(\frac{S}{d}\right)dX = \left(\frac{\tilde{S}}{d}\right)X \tag{47}$$

When the lines are strong, that is, optically thick near $\nu = \nu_i$ in Eq. 2.9.5(15), the transmissivity is low there. Appreciable transmissivity is contributed only when $(\nu - \nu_{o,i})^2$ greatly exceeds γ^2. Under this condition, comparison of Eq. (46) for the nonhomogeneous gas with that for the homogeneous gas suggests that

$$\bar{\tau}_g = \bar{\tau}_{g,\text{homo}}(\zeta = \tilde{\zeta}) \tag{48}$$

$$\tilde{\zeta} = \int_0^X \left(\frac{S}{d}\right)\left(\frac{\pi\gamma}{d}\right)dX = \left(\frac{\tilde{S}}{d}\right)(\tilde{\eta})X \tag{49}$$

The Curtis-Godson approximation is to assume that

$$\bar{\tau}_g \doteq \bar{\tau}_{g,\text{homo}}(\xi = \tilde{\xi},\ \zeta = \tilde{\zeta}) \tag{50}$$

In-terms of Eq. 2.9.5(19), the Curtis-Godson approximation is

$$\bar{\tau}_g \doteq \exp\frac{-\tilde{\xi}}{(1 + \tilde{\xi}^2/\tilde{\zeta})^{1/2}} \tag{51}$$

To obtain a working formula for nonisothermal gas intensity, one spectrally smooths Eq. (5) or (14). Comparison of the spectrally smoothed Eq. (14) with Eq. (46) shows that

$$\bar{I}_{sm}(0) = I_L\bar{\tau}_g + \int_0^{L'}\left(-\frac{d\bar{\tau}_g}{ds}\right)I_b(s)\,ds$$

$$L' = \frac{L}{\cos\theta} \tag{52}$$

Here it has been assumed that I_L is spectrally slowly varying, which really restricts the development to low reflecting boundaries. Integration by parts [or spectrally smoothing Eq. (15)] gives

$$\bar{I}_{sm}(0) = I_b(0) + [I_L - I_b(L)]\bar{\tau}_g(L) + \int_0^{L'}\bar{\tau}_g\,dI_b(s) \tag{53}$$

Now it is clear how to make a practical calculation having narrow-band model data S/d and $\eta = \pi\gamma/d$ versus ν and T_g. One marches along a line of sight computing $\tilde{\xi}$ and $\tilde{\zeta}$, $\bar{\tau}_g(\tilde{\xi},\tilde{\zeta})$ and $\int \tau_g\,dI_b(s)$ as one goes. When the end of the path is reached, the needed values are substituted into Eq. (53).

(b) Wide band scaling

Equation (53) can be put in the form

$$\bar{I}_{sm}(0) = I_L - (I_b(L) - I_L)(1 - \bar{\tau}_g) - \int_0^{L'}(1 - \bar{\tau}_g)\,dI_b(s) \tag{54}$$

Integration over all wave numbers and introduction of the band approximation [recall Eqs. 2.9.5(26) and 2.9.6(15)] gives the total intensity incident upon the wall:

$$\bar{I}_T(0) = I_{L,T} + \sum_k [I_b(\nu_k, T_L) - I_L(\nu_k)]A_k(L) - \sum_k \int_0^{L'} A_k(s)\,dI_b(\nu_k, s) \tag{55}$$

where the subscript T denotes a total quantity ($I_{L,T} = C_s T_L^4/\pi$) and where A_k is the band absorption for the nonisothermal gas. Use of Eq. (55) depends on being able to calculate the band absorption A_k of a nonisothermal gas path.

A wide-band-scaling rule proposed by Edwards and Morizumi [13] is to find ξ_1, ξ_2, and ξ_3 and compute $\tilde{\alpha}, \tilde{\omega}$, and $\tilde{\eta}$, which are used in place of α, ω, and η in Eq. 2.9.5(58) to find band absorption A:

$$\xi_{1,k} = \int_0^s \alpha_k \rho_a\,ds = \int_0^X \alpha_k\,dX = \tilde{\alpha}_k X \tag{56a}$$

© 1983 Hemisphere Publishing Corporation

$$\xi_{2,k} = \int_0^s \omega_k \alpha_k \rho_a \, ds = \int_0^{\xi_{1,k}} \omega_k \, d\xi_{1,k} = \tilde{\omega}_k \xi_{1,k} \tag{56b}$$

$$\xi_{3,k} = \int_0^s \eta_k \omega_k \alpha_k \rho_a \, ds = \int_0^{\xi_{2,k}} \eta_k \, d\xi_{2,k} = \tilde{\eta}_k \xi_{2,k} \tag{56c}$$

In a test comparison with actual nonisothermal gas emission data, the wide-band-spacing rule gave good engineering accuracy [13].

F. Molecular gas radiation in the slab

Consider now the problem of accounting for the combined effects of spectral and directional variations in a nonisothermal slab of molecular gas. One must integrate over both the spectrum and the forward and backward hemispheres to find the net radiant flux.

$$q_R = \int_{\nu=0}^{\infty} \int_{\mu=0}^{1} [I_\nu^+(\mu) - I_\nu^-(\mu)] 2\pi\mu \, d\mu \, d\nu \tag{57}$$

Thus far only one or the other of the two integrations has been considered, the hemispherical integration yielding Eq. (22) and the spectral integration (at the wall) yielding Eq. (5.5). Since the order of the integrations is interchangeable, one can find the desired relation for q_R by integrating either Eq. (22) spectrally or Eq. (55) (generalized to an arbitrary location) hemispherically. We choose the latter route because Eq. (55) already incorporates the idea of wide-band scaling, whereas Eq. (22) does not.

(a) No tation

To generalize Eq. (55) to an arbitrary location y measured from one wall, we must consider paths from y to y. Hence Eqs. (56*a-c*) are written

$$\xi_{1,k}(y, Y) = \int_{y'}^{Y} \alpha_k \rho_a \, dy'' = \xi_{1,k}(y) - \xi_{1,k}(y') \tag{58a}$$

$$\xi_{2,k}(y, y') = \int_{y'}^{Y} \omega_k \alpha_k \rho_a \, dy'' = \xi_{2,k}(y) - \xi_{2,k}(y') \tag{58b}$$

$$\xi_{3,k}(y, y') = \int_{y'}^{Y} \eta_k \omega_k \alpha_k \rho_a \, dy'' = \xi_{3,k}(y) - \xi_{3,k}(y') \tag{58c}$$

The band absorption for a slant path inclined by angle θ ($\mu = \cos\theta$) between y and y is then

$$A_{k,\mu}(y, y') = \tilde{\omega}_k A_k^*\left(\frac{\tilde{t}_k}{\mu}, \eta_k\right) \tag{59}$$

where

$$\tilde{\omega}_k = \frac{\xi_{2,k}(y, y')}{\xi_{1,k}(y, y')} \tag{60a}$$

$$\tilde{t}_k = \frac{\xi_{1,k}^2(y, y')}{\xi_{2,k}(y, y')} \tag{60b}$$

$$\tilde{\eta}_k = \frac{\xi_{3,k}(y, y')}{\xi_{2,k}(y, y')} \tag{60c}$$

Recall that the band absorptance A_k^* for the exponential-tailed band model is defined by Eqs. 2.9.5-(19), 2.9.5(23), and 2.9.5(24) as follows:

$$A_k^*(t_k, \eta_k) = \int_0^{\infty} \left[1 - \exp\left[\frac{-t_k e^{-\nu^*}}{\sqrt{1 + (t_k/\eta_k)e^{-\nu^*}}}\right]\right] d\nu^* \tag{61}$$

where $\nu^* = (\nu - \nu_k)/\omega_k$. When η_k is large, as it is at high temperatures because of the behavior of Eqs. 2.9.5(47) and 2.9.5(48), Eq. (61) reduces to

$$A_k^*(t_k) = \ln t_k + E_1(t_k) + \gamma \qquad \eta_k \gg 1 \tag{62}$$

Recall also the discussion following Eq. 2.9.5(58); when Eq. (62) is used, the values of ω_k from Table 2.9.5(1) are to be increased by 20%.

(b) Forward and backward intensities

With y understood to go from 0 at one wall to L at the other, Eq. (55) is generalized to location y by integrating from y to L instead of from 0 to L. Subscript T for total is dropped to simplify notation:

$$I_\mu^-(y) = I_L + \sum_k (I_{b,k,L} - I_{L,k}) A_{k,\mu}(L, y) - \sum_k \int_y^L A_{k,\mu}(y', y) \frac{dI_{b,k}}{dy'} \, dy' \tag{63}$$

Provision for the physically unreal idea of discontinuities in $I_{b,k}$ withy is dropped.

The forward intensity follows from Eq. (63) upon reversing the coordinate system from y to $L - y$.

$$I_\mu^+(y) = I_0 + \sum_k (I_{b,k,0} - I_{0,k}) A_{k,\mu}(y, 0) + \sum_k \int_0^Y A_{k,\mu}(y, y') \frac{dI_{b,k}}{dy'} \, dy' \tag{64}$$

© 1983 Hemisphere Publishing Corporation

(c) Slab band absorptance

Integration of $(I^+ - I^-)$ over μ converts the band absorption A_k to slab band absorption A_s. The corresponding dimensionless quantities are band absorptance A_k^* and slab band absorptance A_s^*.

$$A_s(t_k, \eta_k) = \int_0^1 A_k\left(\frac{t_k}{\mu}, \eta_k\right) 2\mu\, d\mu \tag{65a}$$

$$A_s^*(t_k, \eta_k) = \int_0^1 A_k^*\left(\frac{t_k}{\mu}, \eta_k\right) 2\mu\, d\mu \tag{65b}$$

Substitution of Eq. (62) into Eq. (65b) gives the result for large η_k:

$$A_s^*(t_k) = \ln t_k + E_1(t_k) + \gamma + \tfrac{1}{2} - E_3(t_k)$$
$$\eta_k \gg 1 \tag{66}$$

For diffuse walls, substitution of Eq. (64) minus Eq. (63) for

$$\int_0^\infty (I_\nu^+ - I_\nu^-)\, d\nu$$

into Eq. (57) then gives

$$q_R(y) = q_0^+ - q_L^+ + \sum_k (B_{k,0} - q_{k,0}^+) A_s(y, 0)$$
$$- \sum_k (B_{k,L} - q_{k,L}^+) A_s(L, y)$$
$$+ \sum_k \int_0^Y A_s(y, y') \frac{dB_k}{dy'}\, dy'$$
$$+ \sum_k \int_y^L A_s(y', y) \frac{dB_k}{dy'}\, dy' \tag{67}$$

where the notation $A_s(y, y')$ has the meaning

$$A_s(y, y') = \tilde{\omega}_k A_s^*(\tilde{t}_k, \tilde{\eta}_k) \tag{68}$$

with $\tilde{\omega}_k$, $\tilde{t}_k$, and $\tilde{\eta}_k$ given by Eqs. (60a-c).

(d) The symmetrical black-walled slab

For black walls at identical temperatures, only the last two terms of Eq. (67) remain. If in addition symmetry exists in gas temperature about the center, y = δ = L/2; that is,

$$B_k(y') = B_k(y'') \qquad y'' = L - y' \tag{69}$$

the integral from y to L is written from y to δ, δ to $26 - y$, and $26 - y$ to L = 26. Consider the integral from δ to 26 − y,

$$\int_\delta^{26-y} A_s(y', Y) \frac{dB_k}{dy'}\, dy' =$$
$$- \int_Y^\delta A_s(2\delta - y'', y) \frac{dB_k}{dy''}\, dy''$$

Similarly,

$$\int_{26-y}^{26} A_s(y', Y) \frac{dB_k}{dy'}\, dy' =$$
$$- \int_0^Y A_s(2\delta - y'', y) \frac{dB_k}{dy''}\, dy''$$

Thus Eq. (67) becomes

$$q_R(y) = -\sum_k \left\{ \int_0^y [A_s(2\delta - y'', y) - A_s(y, y'')] \frac{dB_k}{dy''}\, dy'' + \int_Y^6 [A_s(2\delta - y'', y) - A_s(y'', y)] \frac{dB_k}{dy''}\, dy'' \right\} \tag{70}$$

It remains to specify $A_s(2\delta - y'', y)$, $A_s(y, y'')$, and $A_s(y'', y)$ in terms of ξ integrals defined over the half channel. With reference to Eq. (58), it is clear that the integral from y to 26 − y is the difference of integrals from 0 to δ and 0 toy plus the difference of 0 to δ and 0 to y. Hence

$$\xi_{i,k}(2\delta - y'', y) = 2\xi_{i,k}(\delta) - \xi_{i,k}(y) - \xi_{i,k}(y'') \tag{71a}$$

$$\xi_{i,k}(y, y'') = \xi_{i,k}(y) - \xi_{i,k}(y'') \tag{71b}$$

$$\xi_{i,k}(y'', y) = \xi_{i,k}(y'') - \xi_{i,k}(y) \tag{71c}$$

With this clarification, Eqs. (60) and (68) give the desired terms.

(e) Channel emissivity

Consider a black-walled channel containing a gas with a trapezoidal source profile B, rising linearly from B_w over distance δ_{BL} to a constant value B_g in the range $\delta_{BL} \leqslant y \leqslant L - \delta_{BL}$ and then decreasing symmetrically from B_g back to B,. Assume that $(T_g - T_w)/T_w \ll 1$ so that *all* of the $B[\nu_k, T(y)]$ vary withy in the trapezoidal way proposed. Consistent with this assumption, we consider α_k, β_k, and ω_k as independent of y, and we take η_k large. Accordingly,

© 1983 Hemisphere Publishing Corporation

$$\tilde{\omega}_k = \omega_k \tag{72a}$$

$$\tilde{t}_k(2\delta - y'', y) = t_{L,k}(1 - y^* - y^{*''}) \tag{72b}$$

$$\tilde{t}_k(y, y') = t_{L,k}(y^* - y^{*'}) \tag{72c}$$

where

$$t_{L,k} = \frac{\alpha_k \rho_a L}{\omega_k} \qquad y^* = \frac{y}{L} \qquad y^{*'} = \frac{y'}{L} \tag{72d-f}$$

The wall heat flux is given by Eq. (70) at y = 0, and with $dB_k/dy'' = (B_g - B_w)/\delta_{BL}$ *in* the 0 to δ_{BL} interval and zero elsewhere,

$$q_R(0) = -\sum_k \frac{B_{g,k} - B_{w,k}}{\delta_{BL}} \times \int_0^{\delta_{BL}} [A_s(t_{L,k}(1 - y^{*''})) - A_s(t_{L,k} y^{*''})]\, dy''$$

Changing variables of integration from y to $y^{*''}$ to t_k'' gives

$$q_R(0) = -\sum_k \frac{\omega_k (B_{g,k} - B_{w,k})}{t_{BL,k}} \times \int_0^{t_{BL,k}} (A_s^*(t_{L,k} - t_k'') - A_s^*(t_k''))\, dt_k''$$

The integrals require knowing

$$S^*(t) = \int_0^t A_s^*(t')\, dt' \tag{73}$$

From Eq. (66) for large η_k,

$$S^*(t) = t(\ln t + \gamma - \tfrac{1}{2}) + (1 - E_2(t)) - (\tfrac{1}{3} - E_4(t)) \tag{74}$$

Hence

$$q_R(0) = -\sum_k \omega_k (B(\nu_k, T_g) - B(\nu_k, T_w)) \times C^*(t_{L,k}, t_{BL,k}) \tag{75a}$$

where

$$C^*(t_L, t_{BL}) = \frac{1}{t_{BL}} (S^*(t_L) - S^*(t_L - t_{BL}) - S^*(t_{BL})) \tag{75b}$$

Table 2 lists values of channel emissivity for various pairs of t_L and t_{BL}. For comparison there is shown Eq. (23) for spectral radiation at the band head (or for a gray band). For a fixed value of δ_{BL}/L, as one increases t_L from zero to infinity by increasing the density of absorber ρ_a, Eq. (75) indicates the heat flux rises monotonically to an asymptotic limit, whereas Eq. (23) rises to a maximum and then falls to zero. The difference in total band behavior and spectral behavior arises from the fact that the spectral flux at spectral locations in the tail or wings of the band increases with increasing optical depth and overcomes any decrease in spectral flux at the band head. The spectral location of the maximum spectral flux shifts farther and farther into the tail or wings of the band as the optical depth is increased. Only when the optical depth is enormous and adjacent bands overlap or the bands become so wide that $B(\nu, T_g)$ *can* no longer be approximated by $B(\nu_k, T_g)$ will a maximum in total flux be reached with increasing density. Thus a cold boundary layer does not completely shield the wall from hot molecular gas radiation.

(f) Wall layer transmissivity

More insight into the effect of a cold boundary layer can be gained -by defining a wall layer transmissivity. For a single spectral wavelength,

$$\tau_{WL} = \frac{\epsilon_{\text{channel}}(B_{g,\text{center}} - B_w)}{(1 - 2E_3(t_L))(B_{g,\text{volume}} - B_w)} \tag{76}$$

With the assumed trapezoidal profile in ***B,*** the wall layer transmissivity is

$$\tau_{WL} = \frac{\epsilon_{\text{channel}}(t_L, t_{BL})}{(1 - 2E_3(t_L))[1 - (t_{BL}/t_L)]} \tag{77}$$

In contrast, for an entire exponential-tailed band,

$$\tau_{WL} = \frac{C^*(t_L, t_{BL})}{A_s^*(t_L)[1 - (t_{BL}/t_L)]} \tag{78}$$

Table 2 shows the τ_{WL} behaviors of Eq. (77) and (78). The spectral value at the band head drops rapidly with increasing absorber density as t_{BL} grows past unity, whereas the integrated band value falls more slowly as $1/\ln(t_L)$ instead of $1/t_{BL}$.

One practical consequence of this behavior is that if one scales up the size of a combustion chamber or furnace under nonluminous combustion conditions, one expects the radiant heat flux at the wall to increase somewhat. Furthermore, regions of hot gas at distances far removed from the wall can be radiatively cooled by the cold wall because the optical depth in the band wings is not great, and the increase of $\tilde{\omega}_k$ in hot regions is marked. In contrast, in highly sooty combustion conditions the wall heat flux may decrease with scale-up in size, and regions of flame remote from the wall cannot see the wall and thus receive no radiative cooling. This latter effect can lead to increased nitric oxide pollutant formation.

© 1983 Hemisphere Publishing Corporation

Table 2 Channel emissivity and wall layer transmissivity for an exponential-tailed gas band with overlapped lines

Optical depth at band head		Channel emissivity		Wall layer transmissivity	
Across channel t_L	Across one boundary layer t_{BL}	Exponential band C^*	Spectral value at band head $\epsilon_{channel}$	Exponential band τ_{WL}	Spectral value at band head $\tau_{WL,\lambda}$
2.0	0.0	1.789	0.940	1.00	1.00
	0.1	1.672	0.848	0.98	0.95
	0.2	1.563	0.770	0.97	0.91
	0.4	1.362	0.643	0.95	0.86
	1.0	0.832	0.372	0.93	0.79
20.0	0.0	4.013	1 .ooo	1.00	1.00
	0.1	3.977	0.913	0.98	0.92
	0.2	3.891	0.839	0.96	0.85
	0.4	3.736	0.721	0.94	0.14
	1.0	3.366	0.494	0.87	0.52
	2.0	2.924	0.308	0.80	0.34
	4.0	2.335	0.161	0.12	0.21
	10.0	1.320	0.067	0.65	0.13
200.0	0.0	6.376	1 .ooo	1.00	1.00
	0.1	6.282	0.913	0.99	0.91
	0.2	6.198	0.839	0.91	0.84
	0.4	6.048	0.121	0.95	0.72
	1.0	5.692	0.494	0.90	0.50
	2.0	5.213	0.308	0.84	0.31
	4.0	4.735	0.161	0.76	0.11
	10.0	3.904	0.061	0.64	0.07
	20.0	3.218	0.033	0.56	0.04
	40.0	2.485	0.011	0.49	0.02
	100.0	1.380	0.007	0.43	0.01

Nomenclature for Section 2.9.7 appears at the end of Section 2.9.8.

BIBLIOGRAPHY FOR SECTION 2.9.7

Geometric considerations

The slab

1. Kourganoff, V., ***Basic Methods in Transfer Problems,*** Oxford, London, 1952.

The cylinder

2. Kestin, A. S., Radiant Heat Flux Distribution in a Cylindrically Symmetric Nonisothermal Gas with Temperature Dependent Absorption Coefficients, ***J. Quant. Spectrosc. Radiative Transfer,*** vol. 8, pp. 419-434, 1968.
3. Wassel, A. T., and Edwards, D. K., Molecular Gas Band Radiation in Cylinders, ***J. Heat Transfer,*** vol. 96, pp. 21-26, 1914.

Differential formulations

Radiation diffusion

4. Deissler, R. G., Diffusion Approximation for Thermal Radiation in Gases with Jump Boundary Conditions, ***J. Heat Transfer,*** vol. 86, pp. 240-246, 1964.

Multiflux methods

5. Larkin, B. K., and Churchill, S. W., Heat Transfer by Radiation Through Porous Insulations, *AIChE J.*, vol. 5, pp. 467-474, 1959.
6. Incropera, B. K., and Houf, W. G., A Three-Flux Method for Predicting Radiative Transfer in Aqueous Suspensions, ***J. Heat Transfer,*** vol. 101, pp. 497-501, 1979.
7. Modest, M. F., A Simple Differential Approximation for Radiative Transfer in Non-Gray Gases, ***J. Heat Transfer,*** vol. 101, pp. 735-736, 1979.

© 1983 Hemisphere Publishing Corporation

Embedding

8. Bellman, R. E., Kalaba, R. E., and Prestrud, M. *C., Invariant Imbeddingand Radiative Transfer in Slabs of Finite Thickness,* American Elsevier, New York, 1963.
9. Rogers, J. E., and Edwards, D. K., Bidirectional Reflectance and Transmittance of a Scattering-Absorbing Medium with Rough Surface, *Prog. Astronaut. Aeronaut,,* vol. 49, pp. 3-24, 1976.

Other methods

10. Ozisik, M. *N., Radiative Transfer,* chaps. 9 and 10, Wiley, New York, 1973.

Spectral considerations

Narrow-band scaling

11. Goody, R. M., *Atmospheric Radiation,* pp. 234-243, Oxford, London, 1964.
12. Tiwari, S. N., and Gupta, S. K., Accurate Spectral Modeling for Infrared Radiation, *J. Heat Transfer,* vol. 100, pp. 240–246, 1978.

Wide-band scaling

13. Edwards, D. K., and Morizumi, S. J., Scaling of Vibration-Rotation Band Parameters for Nonhomogeneous Gas Radiation, *J. Quant. Spectrosc. Radiative Transfer,* vol. 10, pp. 175-188, 1970.
14. Edwards, D. K., and Balakrishnan, A., Slab Band Absorptance for Molecular Gas Radiation, *J.Quant. Spectrosc. Radiative Transfer,* vol. 12, pp. 1 379-l 387, 1972. See also Self-Absorption of Radiation in Turbulent Molecular Gases, *Combustion and Flame,* vol. 20, pp. 401–417, 1973.

© 1983 Hemisphere Publishing Corporation

2.9.8

Radiation acting with conduction or convection

D. K. Edwards

A. Combined phenomena

Radiation heat fluxes are linear in blackbody radiosity B on a spectral basis, and, when spectral property variations are not severe, this linearity carries over to the total radiosity $B_T = C_s T^4$. Conduction heat fluxes are linear in heat flux potential $\Phi = \int K\, dT$ and are thus linear in temperature T when thermal conductivity K is constant. Convection is likewise linear in T when property variations are secondary. The result is that a linear problem in conduction or convection is generally made into a nonlinear problem when radiation is added. Closed-form analytical solutions are thus rare, and numerical calculations are commonly required. Even when a closed-form result is not derivable, putting the nonlinear problem into dimensionless form may disclose that the number of parameters is sufficiently small so that numerical calculation of general results can be made.

In special circumstances linearization is an appropriate procedure. With the radiation linearized in T (or more rarely the conduction or convection linearized in B) a closed-form result may be obtainable, and such a result, even if not directly useful, may convey insight to sharpen design intuition. Even when a problem is strongly nonlinear, quasilinearization will prove useful in constructing a solution procedure.

In what follows, the simpler combined problems are considered, ones for which a closed-form solution exists or ones that are parameterized in a small number of parameters. The linearization procedure and the useful concepts of a radiation heat transfer coefficient and equivalent environmental temperature are described.

B. Thermal network analysis

Consider the thermal analysis of a simple system involving both radiation and convection. For example, consider a small room whose exterior wall of 12 m^2 is shaded singleglazed window and whose interior walls, ceiling, and floor of 60 m^2 are roughly adiabatic. The room contains heat sources of 1 kW, and the outside air is 30° C. The room air is cooled to 22° C by supply air at 12° C. It is agreed to calculate convective heat transfer coefficients on all surfaces with the approximate relation $h_c = 1.3\ \Delta T^{1/3}\ W/m^2\,°C$. Suppose that the outside surface surrounds are infrared-black and are solar heated to 50°C, the shape factor from the outside of the window to the surrounds being 0.5 and the remainder to the sky. The outside air is at 60% relative humidity. The thermal designer wants to know how much cold air must be supplied to the room, and what energy savings there might be from installation of doubleglazed window and/or insulated exterior wall.

The problem can be divided into three segments: (1) radiation analysis of the exterior, (2) radiation analysis of the interior, and (3) thermal analysis of the system. These three segments illustrate a number of features of elementary thermal system analysis, with combined phenomena: (1) definition of the mean radiant temperature, (2) the radiation heat transfer coefficient, (3) definition of the mean equivalent temperature, (4) the distinction between the radiation network and the thermal network, and (5) convergence problems.

(a) Radiation analysis of the exterior

Under the assumption that the radiosity of the exterior surface has negligible influence on the radiosity of the

© 1983 Hemisphere Publishing Corporation

surrounds, the net radiant heat flux into the exterior surface 1 is

$$q_{r,0} = \alpha_{IR} q_{IR}^{-} + \alpha_S q_S^{-} - \epsilon_1 C_s T_1^4 \quad (1)$$

Note that the glass is treated as an opaque surface, because its characteristic wavelength for cutoff of transmission is approximately $\lambda_{CO} = 2.7$ μm, and $\lambda_{CO} T \doteq$ 8 10 μm K in Table 2.9.1(1) indicates a negligible internal fraction at wavelengths shorter than λ_{CO}. We begin by making the approximation $\alpha_{IR} \doteq \epsilon_1 \doteq 0.82$ and calculating the infrared irradiation

$$q_{IR}^{-} = F_{1-s} q_s^{+} + F_{1-sky} q_{sky}^{+} \quad (2)$$

According to the problem statement, $q_s^{+} = C_s T_s^4$ and F_{1-s} and F_{1-sky} are known from the geometry. The sky radiosity is

$$q_{sky}^{+} = \epsilon_{sky} C_s T_o^4 \quad (3)$$

where ϵ_{sky} for the atmospheric CO_2, H_2O, and dust is given approximately by the Brunt equation

$$\epsilon_{sky} \doteq 0.55 + 1.8 \sqrt{\frac{P_{H_2O}}{P_o}} \leqslant 1 \qquad P_o = 1 \text{ atm} \quad (4)$$

Since the partial pressure of H_2O is given by the product of the relative humidity and vapor pressure of water at the outside air temperature T_o, we have with the aid of a steam table $\epsilon_{sky} = 0.836$ and $q_{sky}^{+} = 401$ W/m^2. From Eq. (2), $q_{IR}^{-} = 509$ W/m^2. According to the problem statement, the solar irradiation is zero; thus all terms in Eq. (1) except the unknown T_1 are available.

The next step may be to calculate the mean radiant temperature of the surrounds, defined by

$$q_{r,o} = \epsilon_1 (C_s T_r^4 - C_s T_1^4) \quad (5)$$

so by comparison with Eq. (1),

$$C_s T_r^4 = \frac{\alpha_{IR} q_{IR}^{-} + \alpha_S q_S^{-}}{\epsilon_1} \quad (6)$$

For the example at hand, $T_r = 307.9$ K (34.7°C). Here T_r is somewhat above T_o because of the shape factor to the hot T_s.

(b) The radiation heat transfer coefficient

The next step may be to write Eq. (5) in the form

$$q_{r,o} = h_{r,o}(T_r - T_o) \quad (7)$$

where $h_{r,o}$ is the radiation heat transfer coefficient. By factoring Eq. (5),

$$h_{r,o} = \epsilon_1 C_s (T_r^2 + T_1^2)(T_r + T_1) \quad (8)$$

Note that the value depends on the unknown temperature T_1. In the example here, common experience of touching a window under the conditions cited suggests that $T_1 \doteq (T_i + T_o)/2 = 26$°C. Thus $h_{r,o} \doteq 5.20$ W/m^2 °C. Note that it is essential to use absolute temperatures (K) in Eq. (8), but once $h_{r,o}$ is known, relative temperatures can be used in Eq. (7).

In general, when we have

$$\dot{Q}_{r,i-j} = A_i \mathfrak{F}_{i-j} (C_s T_i^4 - C_s T_j^4) \quad (9)$$

we can, if it suits our purposes, write

$$\dot{Q}_{r,i-j} = A_i h_{r,i-j} (T_i - T_j) \quad (10)$$

where

$$h_{r,i-j} = \mathfrak{F}_{i-j} C_s (T_i^2 + T_j^2)(T_i + T_j) \quad (11)$$

(c) The mean equivalent temperature

It is convenient to consider the sum of the convective and radiative heat transfer into the exterior surface as coming from a single equivalent source. Accordingly, one writes

$$q_{1,0} = h_{c,o}(T_o - T_1) + h_{r,o}(T_r - T_1) = h_o(T_e - T_1) \quad (12)$$

Again with $h_{c,o} \doteq 1.3(T_o - T_1)^{1/3}$ (say), the value depends on T_1. We use our estimate of $T_1 \doteq 26$°C to find $h_{c,o} \doteq 2.06$ W/m^2 C. From inspection of Eq. (12),

$$h_o = h_{c,o} + h_{r,o} \quad (13)$$

$$T_e = \frac{h_{c,o} T_o + h_{r,o} T_r}{h_{c,o} + h_{r,o}} \quad (14)$$

With the estimates we find $h_o = 7.26$ W/m^2 °C and $T_e = 33.4$°C, the latter somewhat above T_o because of the hot value of T_s.

(d) Radiation analysis of the interior

Let node 2 be the inside of the exterior wall, node 3 the remaining wall surface, and node 4 the interior gas. The first step is to make a radiation analysis to fmd the transfer factors. Neglecting the gas emissivity (the reader should redo the more intricate problem when the gas is absorbingemitting), we have, from a radiation network,

$$A_2 \mathfrak{F}_{2-3} = 1/\{[(1-\epsilon_2)/\epsilon_2 A_2] + (1/A_2 F_{2-3}) + [(1-\epsilon_3)/\epsilon_3 A_3]\} \quad (15)$$

For the values given, and assuming that $\epsilon_2 = 0.82$, $\epsilon_3 = 0.87$, we obtain $\mathfrak{F}_{2-3} = 0.800$. The radiation heat transfer coefficient $h_{r,2-3}$ is then found from Eq. (11) using estimated values of $T_2 = 26$°C (299.15 K) and $T_3 = 24$°C (297.15 K), $h_{r,2-3} \doteq 4.81$ W/m^2 C.

(e) Construction and solution of the thermal network

The thermal network is now readily constructed as shown in Fig. 1. The exterior environment at equivalent

© 1983 Hemisphere Publishing Corporation

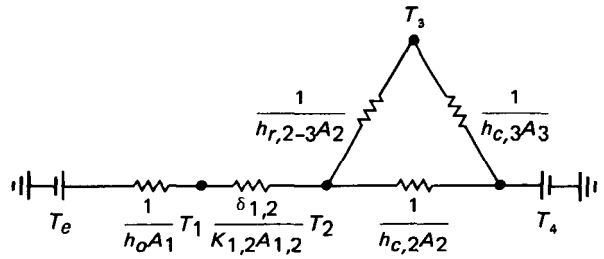

Figure 1 Thermal network for a room.

temperature T_e drives heat through outside thermal resistance $1/h_oA_1$ by convection and radiation, through the exterior wall by conduction, from the inside of the exterior wall to the air directly by convection and indirectly by radiation to the interior walls and then convection to the room air. Note that the radiation network is a prelude to the thermal network. The thermal network includes both radiation and convection resistances, both nonlinear.

The heat transfer is given by

$$\dot{Q} = (T_e - T_4)/\{(1/h_oA_1) + (\delta_{1,2}/K_{1,2}A_{1,2}) + 1/[h_{c,2}A_2 + 1/h_{r,2-3}A_2 + 1/h_{c,3}A_3)^{-1}]\} \tag{16}$$

Note that the order of the subscripts in the $A_ih_{r,i-j}$ terms must correspond to the order in the $A_i\mathfrak{F}_{i-j}$ term on which the former is based.

The unknown temperatures T_1, T_2, and T_3 follow from the network:

$$T_1 = T_e - \dot{Q}\left(\frac{1}{h_oA_1}\right) \tag{17a}$$

$$T_2 = T_e - \dot{Q}\left(\frac{1}{h_oA_1} + \frac{\delta_{1,2}}{K_{1,2}A_{1,2}}\right) \tag{17b}$$

$$T_3 = T_4 + [\dot{Q} - (T_2 - T_4)h_{c,2}A_2\ 1\ \frac{1}{h_{c,3}A_3} \tag{17c}$$

To solve we may execute a simple relaxation scheme; however, convergence is not guaranteed, but in this example there is no problem. We estimate $h_{c,2}$ as 2.06 $W/m^2\,°C$ and $h_{c,3}$ as 1.64 $W/m^2\,°C$, and for soda-lime glass 3 mm thick, $\delta_{1,2}/K_{1,2}$ = 0.003 4 $(W/m^2\,°C)^{-1}$, a negligible value. Using these values, we obtain $\dot{Q}$ = 405 W from Eq. (16), and find T_1, T_2, and T_3. Then we return to the defining equations and refine T_e, h_o, $h_{r,2-3}$, $h_{c,2}$, and $h_{c,3}$ and repeat the process until convergence is attained. Note that our assumed problem had no outside forced convection and no leakage of outside air into the room, hence the low value of $\dot{Q}$.

The rate of air circulation required is given by the first law of thermodynamics written for the open-flow room air system :

$$\dot{m}c_p(T_4 - T_{4,i}) = \dot{Q} \tag{18}$$

Taking c_p = 1006 $J/kg\,°C$ and $T_{4,i} = 12°C$, we find $\dot{m}$ = 0.040 kg/s for the 405 W, and $\dot{m}$ = 0.140 kg/s for 405 W plus 1 kW.

Convergence in the above procedure may not be achieved in a simple relaxation scheme, because an underprediction of an h_r may lead to an overprediction of a T, which may then lead to an overprediction of the h_r followed by an underprediction of the T with no closure. Convergence may be achieved by using a damping factor d; that is, the new estimate of T_1 is taken to be the last estimate times $(1 - d)$ plus d times the newly calculated value. Alternatively, one may try constructing a thermal network (still distinct from the radiation network used to get the transfer factors) in which the driving potentials are $B = C_sT^4$ instead of T, and instead of using h_r one uses the $A_i\mathfrak{F}_{i-j}$ factors directly and replaces the $1/h_{c,i}A_i$ resistances with $1/A_i\mathfrak{F}_{c,i-j}$, where

$$A_i\mathfrak{F}_{c,i-j}(C_sT_i^4 - C_sT_j^4) \equiv A_ih_{c,i}(T_i - T_j)$$

$$\mathfrak{F}_{c,i-j} = \frac{h_{c,i}}{C_s(T_i^2 + T_j^2)(T_i + T_j)} \tag{19}$$

C. Radiationcoupled transient heating or cooling

Consider a mass m with specific heat c initially at temperature T_o suddenly exposed to a radiant environment at temperature T_r via an area A and transfer factor $\mathfrak{F}$ and simultaneously heated (+) or cooled (-) internally at the rate Q. If the internal resistance due to conduction (or convection if the mass is liquid) is small compared to the surface radiation resistance, that is, if $\delta/KA \ll 1/A\mathfrak{F}4C_sT^4$, where δ is an appropriate length for internal conduction and K is the internal thermal conductivity, then the mass remains sufficiently isothermal to write

$$mc\frac{dT}{dt} = \dot{Q} - A\mathfrak{F}(C_sT^4 - C_sT_r^4) \tag{20}$$

The equation is simplified into dimensionless form by writing

$$T_e = \left(T_r^4 + \frac{\dot{Q}}{A\mathfrak{F}C_s}\right)^{1/4} \tag{21a}$$

$$\beta = \frac{T_e}{T_\theta} \tag{21b}$$

$$T^* = \frac{T}{T_o} \tag{21c}$$

$$t^* = \frac{t}{t_c} \tag{21d}$$

$$t_c = \frac{mc}{A\mathfrak{F}C_sT_o^3} \tag{21e}$$

The dimensionless form of Eq. (20),

$$\frac{dT^*}{dt^*} = -(T^{*4} - \beta^4) \tag{22}$$

© 1983 Hemisphere Publishing Corporation

is separable and integrable into closed form for t^* versus T^*.

$$t^* = \frac{1}{2\beta^3}\left[\frac{1}{2}\ln\frac{(\beta+T^*)(\beta-1)}{(\beta-T^*)(\beta+1)} + \tan^{-1}\frac{T^*-1}{\beta+(T^*/\beta)}\right] \quad (23)$$

The solution obviously applies to a spacecraft radiator whose power is suddenly switched on or off, to a hot casting that is suddenly quenched by radiation, or to a cold object that is suddenly placed into a hot radiant furnace. One calculates T_e, β, and T_c via Eq. (21) and knowing the desired T or guessing the value, finds T^* from Eq. (21c) and then t^* from Eq. (23) and finally t from Eq. (21d).

If convection acts also, a linear term in T appears on the right side of Eq. (20), and the equation still separates. The required integral appears subject to closed-form integration, but is tedious. If the convection is slight, one can write it in B according to Eq. (19) and modify $A\mathfrak{F}$ and T_e accordingly. If the convection is dominant, one could introduce h,. For a practical calculation, numerical integration can be readily carried out to obtain a table of t^* versus T^* with parameters β and $h^* = h_c/\mathfrak{F}C_sT_o^3$.

D. Radiant heat exchanger

Suppose that a fluid at temperature T_o with specific heat c_p flows at a mass flow rate of $\dot{m}$ through a tube or passage of total length L exposed on perimeter p with transfer factor $\mathfrak{F}$ to a radiator at temperature T_r. If the overall heat transfer is radiation controlled, that is, $1/\mathfrak{F}4C_sT^3 \gg \delta_w/k_w$ or $1/h_i$, where δ_w is the tube wall thickness and k_w is its conductivity and h_i is the inside heat transfer coefficient, then the equation giving the temperature change with direction of flow z is

$$\dot{m}c_p\frac{dT}{dz} = -p\mathfrak{F}(C_sT^4 - C_sT_r^4) \quad (24)$$

Using Eq. (19) one can make allowance for h_i and δ_w/k_w by finding equivalent transfer factors and summing the radiation resistances. Equation (24) is seen to be in the form of Eq. (20). Hence the solution obtained can be adopted. Let

$$\beta = \frac{T_r}{T_o} \quad (25a)$$

$$T^* = \frac{T}{T_o} \quad (25b)$$

$$z^* = \frac{pL\mathfrak{F}C_sT_o^3}{\dot{m}c_p} \quad (25c)$$

Then $z^* = t^*$ is given by Eq. (23).

The form of Eq. (23) giving z^* versus T^* is that desired for design. It tells the designer the length of exchanger needed to achieve a desired outlet temperature. In conventional heat exchanger design terminology, z^* is the number of transfer units, and T^* is related to the effectiveness ϵ_{eff} by

$$T^* = 1 + (\beta^* - 1)\epsilon_{\text{eff}} \quad (26)$$

where ϵ_{eff} has its usual meaning:

$$\epsilon_{\text{eff}} = \frac{T_{\text{out}} - T}{T_r - T_o} \quad (27)$$

For example, how much area is needed for a spacecraft waste heat exchanger to cool a stream having $\dot{m}c_p$ = 100 W/K from 450 K to 350 K? The exchanger is shaded from the sun, is remote from planetary bodies, but receives 100 W/m^2 irradiation from a sun shield. The transfer factor to the surrounds is 0.90. One begins by fmding $T_r = (100/5.67 \times 10^{-8})^{1/4}$ = 205 K; hence $\beta = 205/450 = 0.455$. The desired value of T^* is 350/450 = 0.778. From Eq. (23), $t^* = z^*$ = 0.407, hence from Eq. (25c), $pL = (100)(0.407)/0.90(5.67 \times 10^{-8})(450^3) = 8.76\ m^2$.

E. The radiating fin

In the example just described it was tacitly assumed that every element of perimeter was fully effective. In actuality one might use the skin of the vehicle for the radiator surface with tubes carrying the fluid stream spaced distance $2l$ apart as sketched in Fig. 2. Such an arrangement provides the fluid conduits some micrometeorite protection. Although it would be reasonable to assume that the segment of perimeter l_0 is isothermal, the l segments of perimeter on either side of the conduits are clearly nonisothermal when b is small.

Let x be the distance from the midpoint between conduits in the l direction. Let the radiating area of a dx element be $p\,dx$ (in Fig. 2, p is perpendicular to the cross section shown and could be called Az). Let the conduction cross section be A, $(= b\,Az)$ in Fig. 2). The transfer factor to the surrounds is called e, and the equivalent radiant temperature, given by Eq. (6), is T_r. At $x = l$, the base temperature is T_B, and at x = 0, by symmetry, dT/dx = 0. For constant conductivity K of the material in area A,, the governing equation is

$$KA,\frac{d^2T}{dx^2} = \epsilon pC_s(T^4 - T_r^4) \quad (28)$$

Here the fin approximation, that the surface temperature and area A, average temperature are indistinguish-

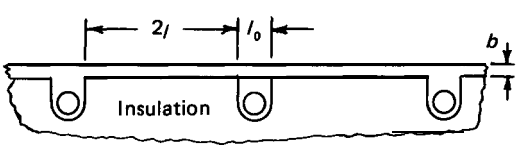

Figure 2 A radiating fin configuration.

© 1983 Hemisphere Publishing Corporation

able, has been made. In dimensionless form, one has

$$\frac{d^2T^*}{dx^{*2}} = N(T^{*4} - \beta^4) \tag{29}$$

subject to

$$x^* = 0 \quad \frac{dT^*}{dx^*} = 0 \quad x^* = 1 \quad T^* = 1$$

where

$$T^* = \frac{T}{T_B} \tag{30a}$$

$$\beta = \frac{T_r}{T_B} \tag{30b}$$

$$x^* = \frac{x}{l} \tag{30c}$$

$$N = \frac{\epsilon p C_s T_B^3 l^2}{K A_r} = \frac{\epsilon C_s T_B^3 l^2}{Kb} \tag{30d}$$

The parameter N is like a radiation Biot number $h_r b/K$ times the square of a slenderness ratio Z/b.

Fin effectiveness η is defined as

$$\eta \equiv \frac{\int_0^l \epsilon p C_s (T^4 - T_r^4)\, dx}{\epsilon p C_s (T_B^4 - T_r^4) l} \tag{31a}$$

$$= \int_0^1 \left(\frac{T^{*4} - \beta^4}{1 - \beta^4} \right) dx^* \tag{31b}$$

From a heat balance η is also related to dT^*/dx^* at $x^* = 1$.

It is clear that η is a function of N and β. Numerical calculations can be made readily by rescaling with respect to the temperature T_o at x = 0, that is, replacing T^* with $\theta = T/T_o$ and β with $\theta_r = T_r/T_o$ in Eq. (29) and introducing $\Phi = d\theta/dx^*$. Then moving θ_r ($0 \leqslant \theta_r < 1$) as an arbitrary parameter gives one an initial value problem, thus avoiding the split boundary condition, as follows:

$$x^* = 0 \quad \theta = 1 \ (\theta_r \text{ assumed}) \quad \Phi = 0$$

$$\frac{d\Phi}{dx^*} = N(\theta^4 - \theta_r^4) \quad \frac{d\theta}{dx^*} = \Phi$$

The two equations are solved simultaneously by a Runge-Kutta integration, keeping the running sum $S^* = \int \theta^4\, dx^*$, to find $\theta = \theta_B$ at $x^* = 1$. With θ_B known, $\beta = \theta_r/\theta_B$ and

$$\eta = \frac{(S^* + 1)/\theta_B^4) - \beta^4}{1 - \beta^4}$$

Thus η can be plotted versus β for desired values of N. Figure 3 shows a cross plot of η versus N with parameter β from [4].

If, instead of the uniform thickness b shown in Fig. 2, the thickness b is tapered, a lighter fin can be achieved. With variable A_r, Eq. (28) becomes

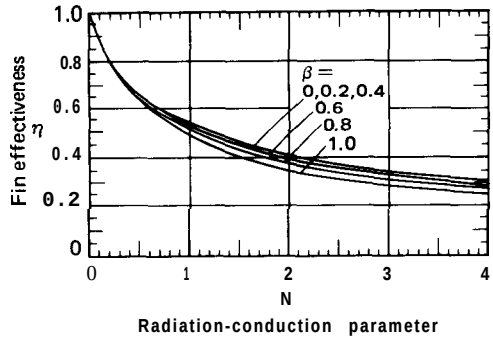

Figure 3 Fin effectiveness for the simple radiating fin.

$$K \frac{d}{dx}\left(A, \frac{dT}{dx}\right) = \epsilon p C_s (T^4 - T_r^4) \tag{32}$$

With dT/dx taken constant at $(T_B - T_o)/l$, T is known as a function of x, and the designer can integrate to find how A_r should vary with x. Let

$$A^* = \frac{A_c}{A_B} = \frac{b}{b_B} \tag{33a}$$

$$T^* = \frac{T}{T_B} \tag{33b}$$

$$x^* = \frac{x}{L} \tag{33c}$$

$$\beta = \frac{T_r}{T_B} \tag{33d}$$

$$N_B = \frac{\epsilon p C_s T_B^3 l^2}{K A_B} = \frac{\epsilon C_s T_B^3 l^2}{K b_B} \tag{33e}$$

Here it is convenient to regard T_o^* ($\beta < T_o^* < 1$) as a parameter. For a value of T_o^*, N_B is given by

$$N_B = \frac{5(1 - T_o^*)^2}{(1 - T_o^{*5}) - 5\beta^4(1 - T_o^*)} \tag{34}$$

and

$$A^* = \frac{(T^{*5} - T_o^{*5}) - 5(T^* - T_o^*)}{(1 - T_o^{*5}) - 5(1 - T_o^*)} \tag{35}$$

where

$$T^* = T_o^* + (1 - T_o^*)x^* \tag{36}$$

Fin effectiveness η is given by

$$\eta = \frac{(1 - T_o^{*5}) - 5\beta^4(1 - T_o^*)}{5(1 - \beta^4)(1 - T_o^*)} \tag{37}$$

For example, what thickness b_B is needed for a 90% effective fin with $K = 200$ W/m K, l = 5 cm, T_B = 450 K, and T_r = 225 K, and ϵ = 0.903, and how should b/b_B vary with x/l? One begins by finding β = 0.50 and using Eq. (37) to find T_o^* = 0.950 76. From Eq. (34),

© 1983 Hemisphere Publishing Corporation

N_B = 0.058 36. From Eq. (33e), b_B = 0.996 mm. The fin profile is given by Eq. (35) as follows:

x^*	b/b_B
1.00	1.00
0.80	0.958
0.60	0.835
0.40	0.633
0.20	0.354
0.0	0.0

Needless to say, there are many permutations of the radiating fin problem. Sparrow and Cess [4] give a review of many of them. The next section considers (in the linearized limit) a fin that views itself so that the irradiation upon it depends on the temperature distribution along the fin.

F. Linearized radiation and conduction around the hollow cylinder

Hollow cylinders are often used as booms or struts for space vehicles. When one is exposed to solar heating from one side, it may bend into a bow shape from the greater thermal expansion of the hot side. The problem is taken up here to give an example of an exact solution of the diffuse-walled enclosure problem and to show how linearizing a combined radiation and conduction problem facilitates analysis. Sparrow and Cess [4] pointed out that the hollow circular cylinder was one of the few enclosures for which an exact solution of the radiosity problem can be readily found. Hrycak and Helgans [5] considered the hollow conducting cylinder with a black interior. Edwards [6] treated the hollow cylinder with gray diffuse interior and an anisotropically conducting wall.

Consider a hollow cylinder of wall thickness b and radius R having temperature $T(\theta)$ close to T_o and with b sufficiently thin so that $b/R \ll 1$ and $4C_sT_o^3b/K \ll 1$. The angle θ is measured from the solar stagnation line; $\theta = \pm\pi/2$ occurs on the shadow lines, and $\theta = \pi$ is on the dark side. The fin equation is obtained from a heat balance on an element between θ and $\theta + d\theta$,

$$\frac{Kb}{R^2}\frac{d^2T}{d\theta^2} = \epsilon_o C_s T^4 + q_i - \alpha_S G_S \cos\beta \cos\theta\, U \qquad (38)$$

where ϵ_o is the total hemispherical emissivity of the outside surface, q_i is the net internal heat flux by radiation, $\alpha_S(\theta)$ is the solar absorptivity, G_S is the solar irradiation at normal incidence $I_S\,\Delta\Omega_S$, and β is the angle of the solar ray from the base plane normal to the cylindrical axis [recall Fig. 2.9.1(3); the half angle subtended by the sun is assumed to be small], and U is the unit step function, unity in the sun ($0 \leqslant \theta < n/2$) and zero in the shade ($n/2 < \theta \leqslant n$).

The first step in simplifying the problem for solution is linearization. One writes

$$C_sT^4 \doteq C_sT_o^4 + 4C_sT_o^3(T - T_o) \qquad (39)$$

and introduces

$$T^* = \frac{T - T_o}{T_o} \qquad (40)$$

Eq. (38) becomes

$$K^*\frac{d^2T^*}{d\theta^2} = 4T^* + q_i^*(\theta) - G^*(\theta) \qquad (41)$$

where

$$K^* = \frac{Kb}{R^2\epsilon_o C_s T_o^3} \qquad (42a)$$

$$q_i^* = \frac{q_i}{\epsilon_0 C_s T_o^4} \qquad (42b)$$

$$G^* = \frac{1}{\epsilon_o C_s T_o^4}(\alpha_S G_S \cos\beta \cos\theta\, U - \epsilon_o C_s T_o^4) \qquad (42c)$$

To proceed, the internal enclosure problem is analyzed, subject to the assumption that the interior is diffuse with uniform internal total hemispherical emissivity ϵ_i. The irradiation is found via Eq. 2.9.3(8) in integral form,

$$q^-(\theta) = \int_{-\pi}^{+\pi} q^+(\theta')\,dF(\theta,\theta')$$

where, from Eq. 2.9.3(4),

$$dF(\theta,\theta') = \tfrac{1}{2}\cos\gamma\, d\gamma$$

and γ is given by

$$\gamma = \frac{\pi}{2} - \frac{1}{2}|\theta' - \theta|$$

Thus the irradiation-radio&y equations are

$$q^-(\theta) = \int_{-\pi}^{\theta} q^+(\theta')\frac{1}{4}\sin\left(\frac{\theta-\theta'}{2}\right)d\theta' + \int_{\theta}^{\pi} q^+(\theta')\frac{1}{4}\sin\left(\frac{\theta'-\theta}{2}\right)d\theta' \qquad (44a)$$

$$q^+(\theta) = \epsilon_i C_s T^4 + (1-\epsilon_i)q^-(\theta\,\text{j-}$$
$$= \epsilon_i C_s T_o^4 + 4\epsilon_i C_s T_o^4 T^* + (1-\epsilon_i)q^-(\theta) \qquad (44b)$$

The net transfer is

$$q_i = q^+ - q^- = \epsilon_i C_s T_o^4(4T^* - q^*)$$

$$q_i^* = \frac{\epsilon_i}{\epsilon_o}(4T^* - q^*) \qquad (45)$$

© 1983 Hemisphere Publishing Corporation

where

$$q^* = \frac{q^- - C_s T_o^4}{C_s T_o^4} \tag{46}$$

Substitution of Eq. *(44b)* into Eq. (44*a*) and introduction of Eq. (46) gives a linear integral equation in q^* coupled through T^* to the linear differential equation, Eq. (41).

$$q^*(\theta) = \int_{-\pi}^{\pi} [4\epsilon_i T^*(\theta') + (1-\epsilon_i) q^*(\theta')] \times \frac{1}{4} \sin\left(\frac{|\theta-\theta'|}{2}\right) d\theta' \tag{47}$$

A series solution is obtained by expanding G* in a Fourier cosine series,

$$G^* = \sum_{n=1} a, \cos n\theta \tag{48}$$

where T_o is chosen to make $a,$ be zero.

$$C_s T_o^4 = \frac{1}{\pi \epsilon_o} \int_{\theta}^{\pi/2} \alpha_S G_S \cos\beta \cos\theta \, d\theta \tag{49}$$

The coefficients a,, are found by multiplying both sides of Eq. (48), written with m replacing n, by cos $n\theta$ and integrating from $\theta = 0$ to π.

$$a_n = \frac{2}{\pi} \int_{\theta}^{\pi/2} \frac{\alpha_S G_S \cos\beta}{\epsilon_o C_s T_o^4} \cos\theta \cos n\theta \, de - \frac{2}{\pi} \int_{/\theta}^{\pi} \cos n\theta \, de \tag{50}$$

The last term is clearly zero. For constant α_S (a diffuse exterior), Eqs. (49) and (50) give

$$C_s T_o^4 = \frac{\alpha_S G_S \cos\beta}{\epsilon_o \pi} \tag{49a}$$

$$\text{a,} = \frac{\pi}{2} \quad a_{2m} = \frac{2(-1)^{m+1}}{2(m)^2 - 1} \tag{50a}$$

$$a_3 = a_5 = a_7 = \cdots = 0$$

Then it is clear that Eqs. (41) and (47) are satisfied by

$$T^* = \sum_{n=1} b_n \cos n\theta \tag{51}$$

$$q^* = \sum_{n=1} c_n \cos n\theta \tag{52}$$

when the coefficients b_n and c_n are made compatible with a,. For convenience the integral S_n is defined:

$$S_n = \frac{1}{\cos n\theta} \int_{-\pi}^{\pi} \frac{1}{4} \sin\left(\frac{|\theta-\theta'|}{2}\right) \cos n\theta' \, d\theta' \tag{53}$$

$$= \frac{-1}{4n^2 - 1} \tag{54}$$

Equation (47) then gives

$$c_n = 4\epsilon_i S_n b_n + (1-\epsilon_i) S_n c_n = \frac{4\epsilon_i S_n}{1-(1-\epsilon_i)S_n} b_n \tag{55}$$

and Eqs. (41), (45), and (47) give

$$-K^* n^2 b_n = 4b_n + \frac{\epsilon_i}{0\epsilon_o} (4b_n - c_n) - a,$$

Substituting Eq. (55) and solving for b_n gives

$$b_n = \frac{1}{4(1 + (\epsilon_i/\epsilon_o)\{(1-S_n)/[1-(1-\epsilon_i)S_n]\}) + n^2 K^*} \times a_n \tag{56}$$

The solution to the problem is now complete. In a practical engineering calculation, two terms suffice. Hence the temperature is given by

$$T \doteq T_o [1 + b_1 \cos\theta + b_2 \cos 2\theta] \tag{51a}$$

where T_o is given by Eq. *(49a)* and

$$b_1 = \frac{\pi/2}{4[1 + 4\epsilon_i/\epsilon_o(4-\epsilon_i)] + Kb/R^2 \epsilon_o C_s T_o^3} \tag{56a}$$

$$b_2 = \frac{213}{4[1 + 16\epsilon_i/\epsilon_o(16-\epsilon_i)] + 4Kb/R^2 \epsilon_o C_s T_o^3} \tag{56b}$$

The design implications of the above relations are clear. The maximum temperature at $\theta = 0$ minus the minimum temperature at $\theta = \pi$ is simply $2b_1 T_o$. To minimize it one wants a small b_1. Hence a large ϵ_i and small ϵ_o are desirable, as is a large value of Kb/R^2 consistent with design weight and strength requirements. To use a small ϵ_o while maintaining a design goal for T_o requires adjusting α_S according to Eq. (49). As explained in Sec. 2.9.21, stripes of white paint or metallized tape may be used to trim the α_S/ϵ_o ratio.

For example, suppose that $\epsilon_i = 0.9$, $\epsilon_o = 0.2$, $K = 50$ W/m K (graphite-reinforced phenolic), $b = 0.5$ mm, $R = 4$ cm, and $T_o = 300$ K. Equations (56*a*) and *(56b)* give $b_1 = 0.020\ 1$ and $b_2 = 0.002\ 93$. Then Eq. *(51a)* gives $T(\theta = 0) = 306.9$ K and $T(\theta = \pi) = 294.9$ K for the maximum and minimum temperatures, respectively.

G. Convection of a radiating molecular gas

A final example is taken to illustrate how a combined convection-radiation problem is analyzed. A molecular gas at inlet temperature T_o is imagined to enter a section

© 1983 Hemisphere Publishing Corporation

of plane-parallel duct with wall temperature T_w. For simplicity the flow is assumed to be fully developed hydrodynamically; the radiation is linearized; the gas has a single exponential-tailed band (or a number of identical such bands) with overlapped lines; the duct walls are black. Balakrishnan and Edwards [18] analyzed this problem, and the nonlinear and multiband gas cases have also been examined. The general subject of coupled convection and radiation fills a fairly large literature, for example, [9-18].

(a) Formulation

The governing energy equation for low-speed, steady, hydrodynamically established (negligible viscous dissipation and flow work) forced convection when axial conduction and radiation are neglected is

$$\rho c_p u \frac{\partial T}{\partial x} = \frac{\partial}{\partial y}\left[\rho c_p(\alpha_m + \epsilon_H)\frac{\partial T}{\partial y}\right] + \frac{\partial}{\partial y}(-q_R) \quad (57)$$

where ρ is density, c_p is specific heat at constant pressure, and α_m is molecular thermal diffusivity $K_m/\rho c_p$ (all at an appropriate reference temperature); u is velocity in the x direction of flow; y is distance from one wall; ϵ_H is eddy diffusivity for heat; $T(x, y)$ is gas temperature; and q_R is radiative heat flux in the y direction. The velocity distribution $u(y)$ under hydrodynamically established conditions ($\partial u/\partial x \doteq 0$; hence $v \doteq 0$ from continuity) is

$$0 = -\frac{dP}{dx} + \frac{\partial}{\partial y}\left[\rho(\nu_m + \epsilon_M)\frac{\partial u}{\partial y}\right] \quad (58)$$

where ν_m is molecular kinematic viscosity and ϵ_M is eddy diffusivity for momentum. The pressure gradient is related to the skin friction coefficient c_f (or the Blasius friction factor $f = 4c_f$) by

$$-\frac{dP}{dx} = \frac{c_f(1/2)\rho U^2}{\delta} \quad (59)$$

where U is the average velocity and δ is the channel half width.

The eddy diffusivity for turbulent flow is taken to be given by

$$\nu_m + \epsilon_M = \nu_m \epsilon^+ \quad (60)$$

where

$$\epsilon^+ = 1 + \frac{1}{1+by^*}\left\{\frac{1}{2}\left(1 + 4K^2 y^{+2}\left[1 - e^{-y^+/A^+}\right]^2\right)^{1/2} - \frac{1}{2}\right\} \quad (61)$$

and dimensionless distance is scaled with channel half width or turbulent mixing length:

$$y^* = \frac{y}{\delta} \quad (62a)$$

$$y^+ = y^* R_t \quad (62b)$$

Turbulent Reynolds number is

$$R_t = \delta^+ = \frac{(c_f/2)^{1/2} U\delta}{\nu_m} = \left(\frac{f}{128}\right)^{1/2} \mathrm{Re} \quad (63)$$

and is related as shown to Reynolds number based on hydraulic diameter:

$$\mathrm{Re} = \frac{U(4\delta)}{\nu_m} \quad (64)$$

The Mei and Squire, von Karman, and Van Driest constants are

$$b = 3.4 \quad (65a)$$

$$K = 0.4 \quad (65b)$$

$$A^+ = 26 \quad (65c)$$

The eddy diffusivity for heat is taken to be given by

$$\alpha_m + \epsilon_H = \frac{\nu_m}{\mathrm{Pr}_m}\left[1 + \frac{\mathrm{Pr}_m}{\mathrm{Pr}_t}(\epsilon^+ - 1)\right] \quad (66)$$

where Pr, is molecular Prandtl number ν_m/α_m and Pr_t is turbulent Prandtl number ϵ_M/ϵ_H. Radiation affects Pr_t somewhat [16], but the usually accepted value is approximately 0.9.

The radiant heat flux is written in terms of the slab band absorption by means of Eq. 2.9.7(70):

$$q_R = -\sum_{k=1}^{n} \omega_k B'_k \int_0^\delta K^*(y, y')\frac{\partial T}{\partial y'}\,dy' \quad (67)$$

where ω_k is band width parameter and B is the Planck function; $B'_k = \partial B(\nu_k, T)/\partial T$ at the reference temperature. Linearization of the radiation is thus assumed in factoring B'_k from under the integral. The kernel K^* is given by Eq. (70) as

$$K^*(y, y') = A_s^*(t_H(2 - y^* - y^{*\prime})) - A_s^*(t_H|y^* - y^{*\prime}|) \quad (68)$$

where A_s^* is given by Eq. 2.9.7(66) and t_H is the optical depth at the band head for half width 6. In terms of integrated band intensity α_k, the band-head half depth is

$$t_H = \frac{\alpha_k \rho_a \delta}{\omega_k} \quad (69)$$

To proceed we make the governing equations dimensionless. Let

$$u^+ = \frac{u\delta}{\nu_m R_t} \quad (70a)$$

$$T^* = \frac{T - T_,}{T_o - T_w} \quad (70b)$$

© 1983 Hemisphere Publishing Corporation

$$R_{dm} = \frac{\delta}{K_m} \sum_{k=1}^{n} \omega_k B'_k A^*_s \tag{70c}$$

$$q^*_R = \frac{-q_R}{\sum_{k=1}^{n} \omega_k B'_k A^*_s (T_o - T_w)} \tag{70d}$$

where, to shorten the notation,

$$A^*_s = A^*_s(2t_H) \tag{70e}$$

and

$$x^* = \frac{x}{\delta \, \mathrm{Pr}, \, R_t} \tag{70f}$$

Note that the $A^*_s(2t_H)$ parameter is introduced as a convenience for later extracting a wall layer transmissivity τ_{WL} from the results. The dimensionless equations become

$$0 = R_t + \frac{d}{dy^*}\left(\epsilon^+ \frac{du^+}{dy^*}\right) \tag{71}$$

$$u^+ \frac{\partial T^*}{\partial x^*} = \frac{\partial}{\partial y^*}\left(\epsilon^+ \frac{\partial T^*}{\partial y^*}\right) + R_{dm} \frac{a}{\partial y^*} q^*_R \tag{72}$$

where

$$q^*_R = \sum_{k=1}^{n} \int_0^1 \frac{K^*(y^*, y^{*\prime})(\partial T^*/\partial y^{*\prime})\, dy^{*\prime}}{A^*_s} \tag{73}$$

Boundary conditions are $u^+ = 0$ and $T^* = 0$ at $y^* = 0$, du^+/dy^* and $dT^*/dy^* = 0$ at $y^* = 1$, and $T^* = 1$ at $x^* = 0$.

(b) Numerical solution

The momentum equation, Eq. (71), is solved by numerical integration:

$$u^+ = R_t \int_0^{y^*} \frac{1}{\epsilon^+}(1 - y^*)\, dy^*$$

The energy equation is solved by finite difference calculations after a coordinate transformation from y^* to z^* to stretch the wall region relative to the central region. The main result of engineering interest is the average total Nusselt number, defined by

$$\overline{\mathrm{Nu}}_T = \frac{\mathrm{Re}\,\mathrm{Pr}_m}{4(x/D)} \ln\left(\frac{1}{T^*_b}\right) \tag{74}$$

where T^*_b is the dimensionless bulk temperature,

$$T^*_b = \frac{\int_0^1 T^*(x^*, y^*) u^+(y^*)\, dy^*}{\int_0^1 u^+(y^*)\, dy^*} \tag{75}$$

and D is hydraulic diameter. An engineering correlation was proposed [18] in the form

$$\overline{\mathrm{Nu}}_T \doteq \overline{\mathrm{Nu}}_C + \overline{\mathrm{Nu}}_R \tag{76}$$

where

$$\overline{\mathrm{Nu}}_C = 0.020\, \mathrm{Re}^{0.8}\, \mathrm{Pr}_m^{0.33}\, \bar{F} \tag{77}$$

$$F = 1 + \frac{0.88}{1 + 0.4(x/D)} \tag{78}$$

$$\overline{\mathrm{Nu}}_R = \frac{D}{K_m} \sum_{k=1}^{n} \omega_k B'_k A^*_s \bar{\tau}_{WL,k} \tag{79}$$

$$\bar{\tau}_{WL,k} \doteq \frac{\ln(1 + t_{D,k}) - \ln(1 + t_{D,k}\bar{r}_{WL})}{\ln(1 + t_{D,k})} \tag{80}$$

$$\bar{r}_{WL} = \frac{1.37}{\mathrm{Re}^{0.37}}\left[1 - \exp\left(-\left(\frac{x}{10D}\right)^{0.6}\right)\right] \tag{81}$$

where A^*_s is the slab band absorptance for $(1/2)t_{D,k}$, where $t_{D,k}$ is optical depth based on hydraulic diameter. The suggestion was made that the results could be applied to either a parallel-plate duct or pipe [18].

(c) Sample application

For example, let us estimate the average heat transfer coefficient due to combined radiation and turbulent convection of steam at a pressure of 60 atm and a reference temperature of 1 000 K flowing at 10 m/s inside a 60-mm-inside diameter, 1 -m-long black-walled tube. Nominal property values are assumed as follows: $K_m = 0.09$ W/m K, $\nu_m = 2.6 \times 10^{-6}$ m^2/s, Pr, = 0.9. For simplicity, contributions from only the 6.3-e ($k = 1$) and 2.7-m ($k = 2$) bands will be considered.

We begin by reading values of $\tau_{H,k}$ from Fig. 2.9.5(10) for a 1 atmm PL value. For $P=$ 60 atm and $L_{mbg} = D = 60$ mm, we obtain

$$t_{D,1} \doteq (60)\left(\frac{60}{1\,000}\right)(50) = 180$$

$$t_{D,2} \doteq (60)\left(\frac{60}{1\,000}\right)(30) = 1\,0\,0$$

From Table 2 9 S(l), the band-width parameters are

$$\omega_1 = 56.4\left(\frac{1\,000}{100}\right)^{1/2}(1.2) = 214 \text{ cm-}$$

$$\omega_2 = 60\left(\frac{1\,000}{100}\right)^{1/2}(1.2) = 228 \text{ cm}^{-1}$$

Since Eq. 2.9.7(66) is derived from spectral integration, the w values were increased by 20% per the discussion following Eq. 2.9.5(58). From Eq. 2.9.7(66),

$$A^*_{s,1} = \ln\frac{180}{2} + 0.577 + 0.500 = 5.58$$

© 1983 Hemisphere Publishing Corporation

$$A^*_{s,2} = \ln \frac{100}{2} + 0.577 + 0.500 = 4.99$$

Next we determine $\bar{r}_{WL}$ and $\bar{\tau}_{WL,k}$. To do so we need the Reynolds number.

$$\mathrm{Re} = \frac{UD}{\nu_m} = \frac{(10)(60 \times 10^{-3})}{2.6 \times 10^{-6}} = 2.3 \times 10^5$$

From Eq. (81),

$$\bar{r}_{WL} = \frac{1.37}{(2.3 \times 10^5)^{0.37}} (1 - e^{-(1\,000/600)^{0.6}}) = 0\ 011$$

From Eq. (80),

$$\bar{\tau}_{WL,1} = \frac{\ln (1 \text{ t } 180) - \ln (1 \text{ t } 1.9)}{\ln (1 + 180)} = 0.80$$

$$\bar{\tau}_{WL,2} = \frac{\ln (1 + 100) - \ln (1 + 1.1)}{\ln (1 + 100)} = 0.84$$

Because the values of $\omega_k A^*_s$ are so large, that is, because the H_2O bands are so wide, we prefer to introduce the internal fraction from Sec. 29.1. Thus we make the following substitution in Eq. (79):

$$\omega_k A^*_s B'_k = 4 C_s T^3 \Delta f_{i,k} \qquad (82)$$

To find $\Delta f_{i,k}$ in Table 2.9.1(1) as a function of $XT = T/\nu$, we need the upper and lower limits on v for each band. Returning to Table 2.9.5(1), we see that the 6.3-μm band is to be centered at 1 600 cm- , and the 2.7-μm band at 3 760 cm- . Thus

$$\nu_{1,u} = \nu_{1,c} + \tfrac{1}{2}\omega_1 A^*_{s,1}$$
$$= 1600 \text{ t } \tfrac{1}{2}(214)(5.58) = 2\ 197 \text{ cm}^{-1}$$

$$\nu_{1,l} = \nu_{1,c} - \tfrac{1}{2}\omega_1 A^*_{s,1}$$
$$= 1\ 600 - \tfrac{1}{2}(214\text{X}5.58) = 1\ 003 \text{ cm}^{-1}$$

$$\nu_{2,u} = 3\ 760 + \tfrac{1}{2}\ (228\text{x}4.99) = 4\ 329 \text{ cm}^{-1}$$

$$\nu_{2,l} = 3\ 760 - \tfrac{1}{2}(228)(4.99) = 3\ 191 \text{ cm}^{-1}$$

The limits on XT and f_i are thus

Band 1: $AT = 0.455\text{-}0.997$

$f_i = 0.741\text{-}0.965$ $\quad \Delta f_i = 0.224$

Band 2: $\lambda T = 0.231\text{-}0.313$

$f_i = 0.237\text{-}0.478$ $\quad \Delta f_i = 0.241$

Substituting Eq. (82) into Eq. (79) and entering the numerical values gives

$$\overline{\mathrm{Nu}}_R = \frac{60 \text{ X } 10^{-3}}{0\ 09} (4)(5.67 \text{ X } 10^{-8})(1000^3)$$
$$\text{X } [0.224(0.80) + 0.241(0.84)] = 57.7$$

The convective contribution is given by Eqs. (77) and (78):

$$\overline{\mathrm{Nu}}_C = 0.020(2.3 \text{ X } 10^5)^{0.8}(0.9)^{0.33}\left(1 + \frac{0.88}{7.67}\right)$$
$$= 4193$$

Thus the total Nusselt number is 477. To complete the example, we find the average heat transfer coefficient:

$$\bar{h} = \frac{K_m}{D}\,\mathrm{Nu}_T = \frac{0.09}{60 \times 10^{-3}}\,(477) = 715 \text{ W/m}^2 \text{ K}$$

NOMENCLATURE FOR SECTIONS 2.9.1-2.9.8

a	length between surface roughness asperities, μm
A, A_i, A_j	area, m^2
A_c	cross-sectional area, m^2
A_k	band absorption of kth band, cm^{-1}
A^*_k	band absorptance of kth band
A^+	Van Driest s constant, 26
b	thickness, m; Mei and Squire constant, 3.4
B	blackbody heat flux, $\mathrm{W/m}^2$, or spectral blackbody heat flux, $\mathrm{W/m}^2$ cm- or $\mathrm{W/m}^2\,\mu$m; rotational constant, cm^{-1}
B	magnetic induction
c	velocity of light, 2.997 925 X 10^8 m/s
c_1	first radiation constant, 3.741 5 X $10^{-16}\,\mathrm{J\,m}^2/\mathrm{s}$
c_2	second radiation constant, 1.438 8 cm K
c_f	skin friction coefficient
c_p	specific heat at constant pressure, J/kg K
C^*	channel emissivity
C_s	Stefan-Boltzmann constant, 5.67 X 10^{-8} W/$\mathrm{m}^2\,\mathrm{K}^4$
d	spectral line spacing, cm^{-1}
D	diameter, m; optical collision diameter
D	electric induction
E	energy, J or eV
E_n	exponential integral of order n
E	electric field strength
f	function or fractional function; friction factor
f_e	external fractional function
f_i	internal fractional function
F	collision frequency, s^{-1}; entry length factor
F_{i-j}	shape factor from area i to area j
$\mathfrak{F}_{i-j}$	transfer factor from area i to area j
g	statistical weight
G	normal irradiation of a beam, $\int I\,d\Omega$, $\mathrm{W/m}^2$
G_{i-j}	area-shape factor product, $A_i F_{i-j}$, m^2
$\mathcal{G}_{i-j}$	area-transfer factor product $A_i \mathfrak{F}_{i-j}$; area-to-volume or volume-to-volume quantity, m^2
h	Planck s constant, 6.625 6 X10^{-34} J s
h_c	convective heat transfer coefficient
h_r	radiative heat transfer coefficient

© 1983 Hemisphere I blishing corporation
HEDH

$\hat{h}$ specific enthalpy, J/kg
H magnetic field strength
I intensity, W/m^2 sr; spectral intensity, W/m^2 cm^{-1} sr or W/m^2 μm sr
I_b blackbody intensity (units as above)
s imaginary part of complex number
j electric current density
k absorptive index
k_a absorption coefficient, m^{-1}
k_e extinction coefficient, m^{-1}
k_s scattering coefficient, m^{-1}
K thermal conductivity, W/m K; second moment of the radiant intensity; von Karman s constant, 0.4
K_R radiation conductivity, W/m K
K^* radiation kernel
L length, m
L_{mb} mean beam length, m
L_{mbg} geometric mean beam length, m
m mass, kg
$\dot{m}$ mass flow rate, kg/s
n refractive index
N radiation conductivity to molecular conductivity ratio
N_V number density, m^{-3}
Nu Nusselt number
P perimeter, m
P pressure, N/m^2 or atm
P_e dimensionless equivalent line-broadening pressure
P_i partial pressure of species i
Pr_m Prandtl number
Pr_t turbulent Prandtl number
q heat flux, W/m^2
q^+ radiosity, W/m^2
q^- irradiation, W/m^2
Q heat energy, J
Q heat flow, W
Q_a absorption efficiency
Q_e extinction efficiency
Q_s scattering efficiency
r_e electrical resistivity, ohm m
r_{WL} wall layer thickness-to-hydraulic diameter ratio
R radius, m
$\Re$ real part of complex number
R_t turbulent Reynolds number
Re Reynolds number based on hydraulic diameter
s slant path length, m
S integrated line intensity; mean radiant intensity
t time, s; optical depth
t_H optical depth at band head
T temperature, K
T_e environmental temperature or equivalent mean temperature, K
T_g gas temperature, K
T_r mean radiant temperature, K
T_w wall temperature, K
u $\sec\theta$; $\cos\theta$; velocity in x direction, m/s
U unit step function; average velocity in x direction, m/s
v $\cos\theta$
V detector signal, V
x length coordinate, m; mole fraction
X density-path-length product, kg/m^2 or g/m^2
Y length coordinate, m
z length coordinate, m
α absorptivity; thermal diffusivity, m^2/s
α_k integrated band intensity, $cm^{-1}/(g/m^2)$
α_m molecular thermal diffusivity, m^2/s
β line width-to-spacing parameter; dimensionless temperature ratio
γ line half width, cm- ; Euler s constant, 0.577 215 6 . . .
δ thickness or half thickness, m; vibrational quantum number change
ϵ emissivity
ϵ_{eff} heat exchanger effectiveness
ϵ_H eddy diffusivity for heat
ϵ_M eddy diffusivity for momentum
η line width-to-spacing parameter; fin effectiveness
θ polar angle
κ mass absorption coefficient, $(kg/m^2)^{-1}$
λ wavelength, μm [m in Eq. 2.9.2(73)-(76)]
μ cos θ
μ_m magnetic permeability
ν wave number, cm^{-1}; kinematic viscosity, m^2/s
ν_f frequency, s^{-1}
ν_m molecular kinematic viscosity, m^2/s
π 3.141 592 6.. .
ρ reflectivity; density, kg/m^3
ρ_a absorber partial density, kg/m^3
ρ_e electric charge density
σ_e electrical conductivity
σ_r surface roughness, μm
τ transmissivity
$\tau_{H,k}$ optical depth at band head
τ_{WL} wall layer transmissivity
ϕ azimuthal angle
Φ hot band line spacing parameter; heat flux potential
Ψ hot band intensity parameter
ω exponential band width, cm^{-1}
ω_s albedo for single scatter
Ω solid angle, sr

© 1983 Hemisphere Publishing Corporation

BIBLIOGRAPHY FOR SECTION 2.9.8

Thermal system analysis

1. Buchberg, H., Electric Analogue Prediction of the Thermal Behavior of an Inhabitable Enclosure, ***Trans.*** *ASHACE*, vol. 61, pp. 339-386, 1955.
2. Ishimoto, T., and Bevans, J. T., Temperature Variance in Spacecraft Thermal Analysis, ***J. Spacecraft Rockets,*** vol. 5, pp. 1 372-1 376, 1968.

Combined surface radiation and conduction

3. Bartas, J. G., and Sellers, W. H., Radiation Fin Effectiveness, ***J. Heat Transfer,*** vol. 82, pp. 73-75, 1960.
4. Sparrow, E. M., and ***Cess,*** R. D., ***Radiation Heat Transfer,*** pp. 180-190, Hemisphere, Washington, DC., 1978.
5. Hrycak, P., and Helgans, R. E., Jr., Equilibrium Temperature of Long Thin-Walled Cylinders in Space, *Chem.* ***Eng. Prog. Symp. Ser.,*** vol. 61, pp. 172-178, 1968.
6. Edwards, D. K., Anisotropic Conduction and Surface Radiation Around a Hollow Cylinder, ***J. Heat Transfer,*** vol. 102, pp. 706-708, 1980.

Combined gas radiation and conduction (see also [4], chap. 9)

7. Viskanta, R., Heat Transfer by Conduction and Radiation in Absorbing and Scattering Materials, ***J. Heat Transfer,*** vol. 87, pp. 143-150, 1965. See also [9].
8. Cess, R. D., The Interaction of Thermal Radiation with Conduction and Convection Heat Transfer, *Adv. Heat Transfer*, vol. 1, pp. l-50, 1964.

Combined gas radiation and convection (see also [4], pp. 190-I 96 and chap. 10)

9. Viskanta, R., Interaction of Heat Transfer by Conduction, Convection, and Radiation in a Radiating Fluid, ***J.*** Heat ***Transfer,*** vol. 85, pp. 318-328, 1963. *See* also *Adv.* ***Heat Transfer,*** vol. 3, pp. 176-251, 1966.
10. Nichols, L. D., Temperature Profile in the Entrance Region of an Annular Passage Considering the Effects of Turbulent Convection and Radiation, ***Int. J. Heat Mass Transfer,*** vol. 8, pp. 589-607, 1965.
11. deSoto, S., Coupled Radiation, Conduction, and Convection in Entrance Region Flow, ***Znt. J. Heat Mass Transfer,*** vol. 11, pp. 39-53, 1968.
12. Greif, R., and McEligot, D. M., Influence of Optically Thin Radiation on Heat Transfer in the Thermal Entrance Region of a Narrow Duct, ***J. Heat Transfer,*** vol. 93, pp. 473-475, 1971.
13. Habib, I. S., and Greif, R., Heat Transfer to a Flowing Nongray Radiating Gas: An Experimental and Theoretical Study, *Int.* ***J. Heat Mass Transfer,*** vol. 13, pp. 1 571-l 582, 1970.
14. Pearce, B. E., and Emery, A. F., Heat Transfer by Thermal Radiation and Laminar Forced Convection to an Absorbing Fluid in the Entry Region of a Pipe, ***J. Heat Transfer,*** vol. 92, pp. 221-230, 1970.
15. Kurosaki, Y., Heat Transfer by Simultaneous Radiation and Convection in an Absorbing and Emitting Medium in a Flow Between Parallel Plates, ***Heat Transfer*** 1970, vol. III, paper R2.5, 4th Int. Heat Transfer Conf., Paris/Versaille, 1970.
16. Edwards, D. K., and Wassel, A. T., Interpretation of a Turbulent Radiating Gas as a Low-Prandtl-Number Fluid, *Lett.* ***Heat Muss Transfer,*** vol. 1, pp. 19-24, 1974.
17. Wassel, A. T., and Edwards, D. K., Molecular Gas Radiation in a Laminar or Turbulent Pipe Flow, ***J. Heat Transfer,*** vol. 98, pp. 101-107, 1976.
18. Balakrishnan, A., and Edwards, D. K., Molecular Gas Radiation in the Thermal Entrance Region of a Duct, ***J. Heat Transfer,*** vol. 101, pp. 489-495, 1979.

© 1981 Hemisphere Publishing Corporation

INDEX

A

Absorption of thermal radiation:
  in gases, 2.9.5-1/2.9.5-12
    gas mixtures, 2.9.5-11/2.9.5-12
    measurement, 2.9.5-2/2.9.5-4
    molecular, 2.9.5-8/2.9.5-11
  in solids, 2.9.2-2/2.9.2-3
    characteristics, 2.9.2-1/2.9.2-2
    measurement, 2.9.2-3
Absorption coefficient, 2.9.5-2
Absorption spectra in gases, 2.9.5-4/2.9.5-8
Absorptivity:
  of particles, 2.9.5-l
  of surfaces: definition, 2.9.2-l
    measurement of, 2.9.2-3
Acentric factor:
  definition, 5.1.1-1, 5.2.1-3
  in hydrocarbons, 5.2.1-3/5.2.1-4
Acetic acid saturation properties, 5.5 .l-27
Acetone saturation properties, 5.5.1-27
Acetylene saturation properties, 5.5.1-15
Ackerman correction factor in condensation, 2.6.36
Acoustic vibration of heat exchangers, 4.6.4-3/4.6.4-4
Active systems for augmentation of heat transfer:
  in condensation, 2.6.6-1/2.6.6-3
  definition, 2.5 .1 l-3
  in forced convection, 2.5.11-4/2.5.1 l-9
  in free convection, 2.5 .11-8/2.5.1 l-9
Additives:
  effect on friction factor, 2.2.2-7
  use in heat transfer augmentation, 2.5.1 l-2, 2.7.94
Adiabatic flows, compressible, in duct, 2.2.2-l 3
Advanced models for furnaces, 3.11.7-1/3.1 1.7-5
Aggregative fluidization, 2.2.6-l
Agitated beds, heat transfer to, 2.8.34

A slash between two page numbers (e.g., 2.7.3-22/2.7.3-26) indicates a range of those pages.

Agitated vessels, 3.14.1-1
  approximate overall heat transfer coefficients in, 2.1.2-5
  equipment used in, 3.14.2-1/3.14.2-4
    gas sparging, 3.14.2-1/3.14.2-2
    mechanical agitators, 3.14.2-1
    vessel internals, 3.14.2-2/3.14.2-4
  heat exchanger, description of, 3.1.2-5/3.1.2-6
  heat transfer correlations for, 3.14.3-1/3.14.3-8
    with anchors and helical ribbons, 3.14.3-1/3.14.3-4
    with nonproximity agitators, 3.14.3-1/3.14.3-3
    scraped-wall pipe and related equipment, 3.14.3-4/3.14.3-6
Ahmad scaling method for critical heat flux *in flow* boiling of nonaqueous fluids, 2.7.3-8
Air:
  properties of dry and saturated, 3.12.2-6
  saturated liquid/vapor properties, 5.5 .l-29
  superheated gaseous, thermodynamic properties, 5.5.2-8/5.5.2-9
Air-activated gravity conveyor, 2.3.3-2
Air-cooled heat exchangers:
  comparison of air and water as coolants, 3.8.1-1
  cooling air supply: by fans, 3.8.7-1/3.8.7-3
    by natural draft, 3.8.8-l
  costing, 4.8.3-1/4.8.3-3
  custom built, 3.8.2-1/3.8.2-2
  description, 3.1.2-4/3.1.2-5
  finned *tube* bundles for, 3.8.4-1/3.8.4-2
  finned tube systems for, 3.8.3-1/3.8.3-3
  mechanical design, 4.4.1-1/4.4.1-7
    for cold climates and viscous fluid, 4.4.1-7
    components, 4.4.1-2/4.4.1-6
    nomenclature for, 4.4.1-2
    structural design factors, 4.4.1-6/4.4.1-7
  special features, 3.8.9-1/3.8.9-4
    sound emission from, 3.8.9-l
  thermal rating, 3.8.5-1/3.8.5-5
  tubeside flow arrangements, 3.8.6-l
Albedo for single scatter in radiation, 2.9.7-2
Aluminum, spectral characteristics of anodized surfaces, 2.9.2-16
Ammonia, saturated properties of, 5.5.1-29

© 1983 Hemisphere Publishing Corporation

AMTD (see Arithmetic mean temperature difference)
Analogy between heat and mass and momentum transfer, 1.2.3-6/1.2.3-7, 2.1.5-1/2.1.5-4
Analytic solutions for heat exchangers, 1.3.1-1/1.3.2-1
Analytical solution of groups, for calculation of thermodynamic properties of nonhydrocarbons, 5.2.2-3/5.2.2-9
tables of constants for, 5.5.4-1/5.5.4-6
Anchor agitators:
description, 3.14.2-1/3.14.2-2
heat transfer with, 3.14.3-3/3.14.3-4
Andrade equation for variation of viscosity with temperature, 5.1.4-3
Anelasticity, 5.4.5-5
Angled tubes, use in increasing flooding rate in reflux condensation, 2.6.2-8/2.6.2-9
Aniline, saturation properties, 5.5.1-26
Anisotropy of elastic properties, 5.4.5-4/5.4.5-5
Annular dispersed flow (see Annular flow)
Annular distributor in shell-and-tube heat exchangers, 3.3.5-11
Annular ducts:
critical heat flux in flow in, 2.7.3-20
forced convective heat transfer in single phase flow:
laminar flow, 2.5.1-3/2.5.1-4
with liquid metals, 2.5.13-1/2.5.13-2
turbulent heat transfer in, 2.5.1-6, 2.5.1-10/2.5.1-11
free convective heat transfer in closedend: horizontal, 2.5.8-14/2.5.8-16
vertical (heated on vertical curved surfaces), 2.5.8-13/2.5.8-14
single phase flow and pressure drop in, 2.2.2-7/2.2.2-10
laminar flow, 2.2.2-7/2.2.2-9
turbulent flow, 2.2.2-9/2.2.2-10
Annular fins, efficiency, 2.5.3-9
Annular flow:
critical heat flux in, 2.7.3-22/2.7.3-30
hydrodynamics in horizontal tubes, 2.3.2-25/2.3.2-26
hydrodynamics in vertical tubes, 2.3.2-19/2.3.2-21
deposition and entrainment correlations, 2.3.2-21
interfacial roughness relationship, 2.3.2-20
triangular relationship for, 2.3.2-10
regimes of occurrence of: in horizontal flow, 2.3.2-3/2.3.2-4
in inclined tubes, 2.3.2-4/2.3.2-5
in systems with phase change, 2.3.2-6/2.3.2-7
Annuli (see Annular ducts)
Arc welding of tubes into tube sheets:
on inner face, 4.2.6-10
on outer face, 4.2.6-8
Archimedes number, 2.2.1-11
Area of tube outside surface in shell-and-tube heat exchangers: charts for, 3.1.4-6, 3.3.10-5
Argon, saturated properties, 5.5.1-30
Arithmetic mean temperature difference, definition, 3.1.4-2
Armstrong, Robert C., 2.2.8-1/2.2.8-13, 2.5.12-1/2.5.12-16
ASME VIII code, for mechanical design of shell-and-tube heat exchangers:
description, 4.3.1-1/4.3.1-2
index to, 4.3.2-1/4.3.2-11
ASOG (see Analytical solution of groups)
Assisted convection:
around immersed bodies, 2.5.9-1/2.5.9-4
in vertical channels, 2.5.9-2/2.5.9-6
Asymmetric loading, in heat exchangers, 4.1.2-2/4.1.2-9
Augmentation of heat transfer, 2.5.11-1/2.5.1 1-12, 2.6.6-1/2.6.6-4, 2.7.9-1/2.7.9-5
active systems for: definition, 2.5 .1 l-3
in forced convection, 2.5.11-8/2.5.11-9
in free convection, 2.5.114
compound systems for, 2.5.1 l-9
in boiling, 2.7.9-1/2.7.9-5
pool boiling, 2.7.9-1/2.7.9-2
within tubes, 2.7.9-3/2.7.9-4
in condensation, 2.6.6-1/2.6.6-4
in forced convection, 2.6.6-2/2.6.6-3
in vapor space, 2.6.6-1/2.6.6-2
in kettle reboilers, 3.6.26
in shell-and-tube heat exchangers using low finned tubes, 3.3.1 l-2/3.3.1 1-3
passive systems for: definition, 2.5.1 1-1/2.5.11-3
in forced convection, 2.5.11-4/2.5.11-8
in free convection, 2.5 .1 l-3
performance evaluation criteria for, 2.5.1 l-912.5.1 l-10
Austenitic chromium-nickel steels, as material of construction, 45.24
Average phase velocity in multiphase flows, 2.3.1-4

B

Baffle leakage in shell-and-tube heat exchangers:
numerical methods for predictions of, 1.4.2-3
recommended design procedures for accounting for, 3.3.1-1/3.3.11-5
Baffle pipes in agitated vessels, 3.14.2-3/3.14.2-4
Baffles in shell-and-tube heat exchangers:
constructional features affecting thermal design:
clearances, 4.2.5-7
cross type, 4.2.5-4/4.2.5-5
longitudinal type, 4.2.5-8
maximum pitch, 4.2.5-7
support type, 4.2.5-5/4.2.5-6
thickness, 4.2.5 -7
disk-and-doughnut, 3.3.11-2
double segmental, 3.3.11-2
leakage effects associated with (see Baffle leakage, Leakage effects)
number of, calculation of, 3.3.6-4
segmental, recommended characteristics of, 3.3.5-7/3.3.5-10
Baker flow regime map for horizontal gas-liquid flow, 2.3.2-3
Balance equation (applied to complete equipment), 1.2.4-1/1.2.4-7
average interaction coefficients and driving forces for, 1.2.4-2/1.2.4-3
conventional representations of heat exchanger performance by, 1.2.4-4/1.2.4-5
differential form of, 1.2.5-1/1.2.5-3
for enthalpy, temperature and concentration, 1.2.5-1/1.2.5-3
solution and closure, 1.2.5-2/1.2.5-3
for enthalpy, temperature and concentration changes, 1.2.4-1/1.2.4-2
NTU and effectiveness in, 1.2.4-3/1.2.4-4
Band dryer:
description, 3.13.24
practical design, 3.13.7-1/3.13.7-2
Banks of tubes (see Tube banks)
Barrels for shell-and-tube heat exchangers (see Shells)
Basket-type evaporator, 3.5.2-1/3.5.2-3
Bauer, R., 2.8.1-1/2.8.1-14, 2.8.2-1/2.8.2-8
Bayonet tube heat exchangers, constructional features of, 4.2.3-9/4.2.3-10

© 1983 Hemisphere Publishing Corporation

Beer-Lambert law, 2.9.5-S
Bell, Kenneth J., 3.1.1-1/3.1.4-9
Bell-Delaware method for shell-side heat transfer and pressure drop in shell-and-tube heat exchangers, 3.3.2-5/3.3.2-6
modified form as basis for recommended procedure, 3.3.3-1/3.3.11-5
Bell and Ghaly method for calculation of multicomponent systems:
condensation, 2.6.3-4/2.6.3-5
evaporation, 2.7.8-5
Bellows, expansion, for shell-and-tube heat exchangers:
analytic basis for codes for, 4.3.3-2
constructional features, 4.2.6-10/4.2.6-11
index to U.S., U.K., and F.R.G. codes for, 4.3.2-10/4.3.2-11
Benard cells in free convection in horizontal fluid layers, 2.5.8-1/2.5.8-3
Bends:
boiling heat transfer in tubes with, 2.7.4-4/2.7.4-6
dryout in tubes with, 2.7.4-2/2.7.4-4
enhancement of condensation in, 2.6.6-3
multiphase pressure loss in: gas-liquid systems, 2.3.2-l 7
solid-gas systems, 2.3.3-7
solid-liquid systems, 2.3.4-4
single-phase fluid flow and pressure drop in, 2.2.2-16/2.2.2-17
loss coefficients for, 2.2.2-16
use ofvaned bends, 2.2.2-16/2.2.2-17
Benedict-Webb-Rubin equation of state, 5.2.2-3
Benzene saturation properties, 5.5.1-12
Berenson equation for pool film boiling from a horizontal surface, 2.7.2-14
Bergles, Arthur E., 2.5.1 1-1/2.5.11-12, 2.6.6-1/2.6.6-4, 2.7.9-1/2.7.9-5
Bernoulli equation, application to flow across cylinders, 2.2.4-I
Bimetal tubes, use of in shell-and-tube heat exchangers, 4.2.5-2
Binary mixtures:
bubble growth in, 2.7.6-5/2.7.6-7
bubble nucleation in, 2.7.6-5
condensation of 2.1.6-2/2.1.6-3, 2.6.3-7
condensers for, 3.4.4-1/3.4.4-2
constants for, for use in calculation of multicomponent systems, 5.5.4-1/5.5.4-9
diffusion and mass transfer in, 2.1.5-1/2.1.5-4
forced convection boiling of, 2.7.8-1/2.7.8-10
combined heat and mass transfer in, 2.7.8-3/2.7.8-6
critical heat flux in, 2.7.8-6/2.7.8-7
saturated nucleate, 2.7.8-1/2.7.8-2
two-phase forced convective, 2.7.8-2/2.7.8-3
phase equilibria in, 2.7.6-1/2.7.6-3
pool boiling of, 2.7.7-1/2.7.7-7
critical heat flux, 2.7.7-4/2.7.7-5
film boiling, 2.7.7-6
minimum heat flux, 2.7.7-5/2.7.7-6
nucleate boiling, 2.7.7-1/2.7.7-4
transition boiling, 2.7.7-5
Bingham fluid (non-Newtonian), 2.2.8-7
Biot number:
in conduction, 2.4.3-2
in melting and solidification, 2.4.4-1/2.4.4-2
Black surface:
heat transfer between gas and, 2.9.6-1/2.9.6-2
spectral characteristics of reflectance from selective, 2.9.2-17
Blackbody radiation, 2.9.1-3/2.9.1-5
Blake-Carmen-Kozeny equation, 2.2.5-2
Blasius equation for friction factor, 2.2.2-3
Block-type heat exchanger, 4.4.4-4
Blowing (see Injection)
Blunt bodies, drag coefficients for, 2.2.3-7
Boilers:
combustion systems for firing, 3.11.2-2/3.11.2-3
as type of heat exchanger, 1.1.5-2
(See also Reboilers)
Boiling:
augmentation of heat transfer in, 2.7.9-1/2.7.9-5
pool boiling, 2.7.9-1/2.7.9-2
within tubes, 2.7.9-3/2.7.9-5
in axial flow reboilers, 3.6.2-6
basic processes, 2.7.1-1/2.7.1-9
bubble detachment and frequency, 2.7.1-7/2.7.1-8
bubble growth, 2.7.1-6/2.7.1-7
evaporation, 2.7.1-2
heterogeneous nucleation, 2.7.1-3/2.7.1-5
homogeneous nucleation, 2.7.1-2/2.7.1-3
sizing of active nucleation sites, 2.7.1-5/2.7.1-6
vapor formation, 2.7.1-1/2.7.1-2
of binary and multicomponent mixtures:
basic process in, 2.7.6-1/2.7.6-7
forced convective boiling, 2.7.8-1/2.7.8-10
pool boiling, 2.7.7-1/2.7.7-7
in evaporators, 3.5.7-2/3.5.7-3
in horizontal tubes, 2.7.4-1/2.7.4-7
dryout in (including bends and coils), 2.7.4-1/2.7.4-4
heat transfer rates in, 2.7.4-4/2.7.4-6
in kettle and horizontal thermosiphon reboilers, 3.6.2-1/3.6.2-6
pool boiling, 2.7.2-1/2.7.2-17
boiling curve for, 2.7. l-l
critical heat flux in, 2.7.2-9/2.7.2-13
film boiling in, 2.7.2-14/2.7.2-15
minimum heat flux in, 2.7.2-13/2.7.2-14
nucleate boiling in, 2.7.2-3/2.7.2-9
onset of nucleate boiling in, 2.7.2-2/2.7.2-3
transition boiling in, 2.7.2-l 3
outside tubes and tube bundles, 2.7.5-1/2.7.5-7
single tube in crossflow, 2.7.5-1/2.7.5-4
tube bundles, 2.7.5-4/2.7.5-7
in vertical tubes, 2.7.3-1/2.7.3-37
critical heat flux, 2.7.3-12/2.7.3-30
heat transfer in the region where critical heat flux has been exceeded, 2.7.3-30/2.7.3-34
regimes of flow and heat transfer in, 2.7.3-1/2.7.3-5
saturated boiling, 2.7.3-10/2.7.3-12
subcooled boiling, 2.7.3-5/2.7.3-10
Boiling curve:
in binary mixtures, 2.7.7-l
in pool boiling, 2.7.2-l
effect of surface finish on, 2.7.2-3
for single horizontal tube in crossflow, 2.7.5-l
for tube banks, 2.7.5-4
Boiling length:
definition, 2.7.3-15
quality/boiling length correlations, 2.7.3-15
application of nonuniform heating cases, 2.7.3-19
Boiling number, definition, 2.7.4-5
Boiling point, normal, 5.1.3-1
of commonly used fluids, 5.5.1-1/5.5.1-40
Boiling range (in multicomponent mixtures), influence on selection of reboilers, 3.6.1-6
very wide, effect on reboiler design, 3.6.4-3
Boiling surface in boiling in vertical tubes, 2.7.34
Bolted channel head in shell-and-tube exchanger, 4.2.4-l
Bolted cone head in shell-and-tube heat exchanger, 4.2.4-2

© 1983 Hemisphere I blishing Corporation

Bolting of flanges in shell-and-tube heat exchangers, 4.2.6-4/4.2.6-5
Boltzmann s constant, 2.9.1-3
Bonnet head, in shell-and-tube heat exchanger, 4.2.4-l/4.2.4-2
Borishanski, V. M., 2.5.13-1/2.5.13-4
Borishanski correlation for nucleate pool boiling, 2.7.2-S
Botterill, J. S. M., 2.8.4-1/2.8.4-8
Boundary layer:
in combined free and forced convection heat transfer to immersed bodies, 2.5.9-1/2.5.9-3
concept, 2.2.1-16/2.2.1-17
equations, 2.2.1-17/2.2.1-18
continuity, 2.2.1-17
internal energy, 2.2.1-18
internal forms of, 2.2.1-20
Levy-Lees transformation of, 2.2.1-18/2.2.1-20
mean kinetic energy, 2.2.1-17
momentum, 2.2.1-17
solutions of, 2.2.1-20/2.2.1-22
turbulent kinetic energy, 2.2.1-18
on flat plate, 2.2.1-22/2.2.1-30
in flow over cylinders, 2.2.3-312.2.3-s
in flow over immersed bodies, 2.2.3-1/2.2.3-2
in heat transfer to flat plates: laminar boundary layer, 2.5.2-1/2.5.2-2
turbulent, 2.5.2-2
theory, 2.2.1-16/2.2.1-30
as example of theory of models, 2.2.1-13
Thickness of (displacement, momentum, energy, density, temperature); 2.2.1-20
Turbulent: prediction methods for, 2.2.1-26/2.2.1-29
universal laws for, 2.2.1-25/2.2.1-26
Boussinesq approximations:
application in free convective flows, 2.5.7-1
for gravity effect, 2.2.1-10
application to laminar flow in circular duct, 2.2.2-5
Boussinesq number, definition, 2.5.7-2
Bowring correlations for critical heat flux, 2.7.3-16/2.7.3-18
Bracket supports for heat exchangers, index to U.S., U.K., and F.R.G. codes for, 4.3.2-7
Branches, mechanical design aspects, 4.1.8-1/4.1.8-2
Brazing in plate fin heat exchanger construction, 4.4.3-3/4.4.3-4
Bricks, drying of, 3.13.5-2/3.13.5-5
Brinkman number, 2.5.12-6
British Standards Institute code for mechanical design of heat exchangers (see BS 1500 code)
Bromley equation for film boiling from horizontal cylinders, 2.7.2-14
BS 1500 code for mechanical design of shell-and-tube heat exchangers:
description, 4.3.1-1/4.3.1-3
index to, 4.3.2-1/4.3.2-11
Bubble crowding as mechanism of critical heat flux, 2.7.3-22
Bubble flow:
drift flux model for, in vertical flow, 2.3.2-18/2.3.2-19
regions of occurrence: in horizontal flow, 2.3.2-2/2.3.2-4
in inclined tubes, 2.3.2-4/2.3.2-5
in shell-and-tube heat exchangers, 2.3.2-5/2.3.2-6
in systems with phase change, 2.3.2-6/2.3.2-7
in vertical flow, 2.3.2-1/2.3.2-2
Bubbles:
in boiling of binary mixtures: growth, 2.7.6-5/2.7.6-7
nucleation, 2.7.6-5
in boiling of single components: detachment and frequency, 2.7.1-712.7.1-g
growth, 2.7.1-6/2.7.1-7
nucleation, 2.7.1-1/2.7.1-6
in fluidized beds, 2.2.6-4/2.2.6-7
coalescence, 2.2.6-5/2.2.6-6
single bubbles, 2.2.6-4/2.2.6-5
spatial distribution, 2.2.6-6/2.2.6-7
in gas-liquid flow: horizontal tubes, 2.3.2-2/2.3.2-4
vertical tubes, 2.3.1-1/2.3.2-2,2.3.2-18/2.3.2-19
rise velocity of gas bubbles in liquid, 2.3.2-18/2.3.2-19
Buffer layer in duct flow, 2.2.2-l
Bulk viscosity, 2.2.1-2
Bundle-induced convection in kettle reboilers, 3.6.2-2/3.6.2-3
Buoyancy effects:
on developing flows in ducts, 2.2.2-l 1
on flows, 2.2.1-10/2.2.1-11
inducing flow in channels, free convection heat transfer with, 2.5.7-19/2.5.7-20
on laminar flow over flat plate, 2.2.1-24
Buoyancy-induced flow in channels, free convective heat transfer with, 2.5.7-19/2.5.7-20
Burnout (see Critical heat flux)
1,2-Butadiene saturation properties, 5.5.1-16
1,3-Butadiene saturation properties, 5 .5.1-17
Butane saturation properties, 5.5.1-7
Butanol saturation properties, 5.5 .l-19
Butterworth, D., 2.6.1-1/2.6.3-10
t-Butyl alcohol saturation properties, 5.5.1-20
By pass (shell-to-tube bundle):
clearances in shell-and-tube heat exchangers, 3.3.5-14
heat transfer and pressure drop correction factors for, 3.3.6-8/3.3.6-9
BWR equation of state (see Benedict-Webb-Rubin equation of state)

C

Cabin heater, 3.11.2-2
Calorically perfect gas, 2.2.1-8
Carbon dioxide:
emissivity of gaseous, 5.5.5-2
saturation properties, 5.5.1-30
superheated gaseous, thermodynamic properties, 5.5.2-2
Carbon monoxide saturation properties, 5 .5.1-31
Carbon steel as material of construction, 4.5.2-2/4.5.2-3
Carbon tetrachloride saturation properties, 5.5.1-31
Carmen-Kozeny equation (see Blake-Carmen Kozeny equation)
Carrean fluid (non-Newtonian), 2.2.8-7
Carryover of solids in fluidized beds, 2.2.6-3
Cavitation as source of damage in heat exchangers, 4.5.3-l
Centrifugal dryer, 3.13.2-4
Ceramics, spectral characteristics of reflectance from, 2.9.2-18
Certification of heat exchangers, 4.7.7-l
Channel emissivity, 2.9.7-11/2.9.7-12
Channel flow, heat and mass transfer in, 2.1.7-1/2.1.7-2
Chapman-Rubescin formula for viscosity variation with temperature, 2.2.1-9
Chemical formulas of commonly used fluids, 5.5.1-1/5.5.1-40
Chemical reactions, numerical calculation of flows involving, 1.4.3-2/1.4.3-3
Chen correlation for forced convective boiling, 2.7.3-11/2.7.3-13
Chenoweth, J. M., 4.6.1-1/4.6.6-3
Chevron troughs as corrugation design in plate heat exchangers, 3.7.1-1, 3.7.3-1/3.7.3-2,3.7.6-2
CHF (see Critical heat flux)
Chillers, construction features of, 4.2.3-9

© 1983 Hemisphere Publishing Corporation

Chilton-Colburn analogy, 1.2.3-6
Chisholm, D., 2.6.7-1/2.6.7-4, 3.10.1-1/3.10.7-9, 4.8.1-1
Chisholm correlations:
for frictional pressure drop in straight channels, 2.3.2-l 1
for pressure drop in singularities, 2.3.2-15/2.3.2-18
Chlorine, saturation properties, 5.5 .1-32
Chloroform, saturation properties, 5.5.1-26
Choice of heat transfer equipment (see Selection of heat transfer equipment)
Chugging flow (gas-liquid), in shell-and-tube heat exchangers, 2.3.2-5/2.3.2-6
Churchill, S. W., 2.5.7-1/2.5.10-12
Churchill and Chu correlations for free convective heat transfer:
horizontal cylinders, 2.5.7-21
vertical plates: laminar flow, 2.5.7-3
turbulent flow, 2.5.7-4
Churn flow, regions of occurrence of, 2.3.2-1/2.3.2-2
Circles, radiative heat transfer shape factors between parallel coaxial, 2.9.3-3
Circular cylinders (see Cylinders)
Circulation, modes of in free convection: in enclosures heated from below, 2.5.8-6
CISE correlations for void fractions, 2.3.2-14/2.3.2-15
Clapeyron-Clausius relationship (see Clausius-Clapeyron relationship)
Clausius-Clapeyron relationship:
application in evaporation, 2.7.1-2
in homogeneous nucleation, 2.7.1-3
Cleaning of shell-and-tube heat exchangers, 3.3.4-5
Climbing film evaporator, 3.5.24
Closed distillation process, 2.1.7-8
Coalescence of bubbles in fluidized beds, 2.2.6-5 /2.2.6-6
Coatings for corrosion protection, 4.5.2-5/4.5.2-6
Cocurrent flow:
F-factor chart for, 1.5.2-3
heat exchangers, 1.1.1-1/1.1.1-2
single-phase temperature pattern in, 1.1.3-l
solutionsfor, 1.3.1-1/1.3.1-4
θ-NTU chart for, 1.5.2-3
Codes, mechanical design:
analytic basis of code rules, 4.3.3-1/4.3.3-2
comparison of principal codes, 4.3.4-1/4.3.4-3
cylinders: external pressure, 4.3.4-1/4.3.4-2
flanges, 4.3.4-2/4.3.4-3
nozzles, 4.3.4-3
stresses, 4.3.4-l
tubesheets, 4.3.4-2
example of applications, 4.3.6-1/4.3.6-23
guides to national practice in application of, 4.3.5-1/4.3.5-9
France (SNCT), 4.3.5-6
Germany (Merkblatter), 4.3.54
Holland (Stoomwesen), 4.3.5-5
Italy (ANCC), 4.3.5-7
Japan: high pressure, 4.5.3-9
standard, JIS-B8243, 4.3.5-8
U.K. (BS 1500), 4.3.5-3
U.S. (ASME VIII), 4.3.5-2
index to U.S., U.K., and F.R.G. codes, 4.3.2-1/4.3.2-l 1
conical shell, 4.3.2-3/4.3.2-4
cylindrical shell and channel, 4.3.2-2/4.3.2-3
dished head, 4.3.24
flanges, 4.3.2-5/4.3.2-7
flat head, 4.3.2-4/4.3.2-5
floating head, 4.3.2-5
nozzles, 4.3.2-9/4.3.2-10
shell bellows, 4.3.2-10/4.3.2-11
supports, 4.3.2-7
tubes, 4.3.2-3
tubesheets, 4.3.2-714.3.2-g
introduction, 4.3.1-1/4.3.1-3
Coiled tubes (see Helical coils, Curved ducts)
Coiled wire inserts for enhancement of heat transfer in boiling, 2.7.9-3
Colburn and Drew method for binary vapor condensation, 2.6.3-7
Colburn and Hougen method for condensation in presence of noncondensable gases, 2.6.3-6
Colburn equation for single-phase heat transfer outside tube banks, 3.3.2-l
Colburn j factor:
application in heat exchangers, 3.3.1-2
definition, 2.1.3-4
for flow over tube banks, 3.3.7-1/3.3.7-4
in plate fin exchangers, 3.9.4-1/3.9.6-2
values of heat transfer in tubes, 2.1.3-7
Colebrook-White equation for friction factor in rough circular pipe, 2.2.2-3
Coles, law of the wake, 2.2.1-26
Collier, J. G., 2.7.1-1/2.7.8-10
Column internal reboiler (see Internal reboilers)
Combined conductive, convective, and radiative heat transfer, 2.9.8-1/2.9.8-10
Combined free and forced convection heat transfer:
in channels, 2.5.10-1/2.5.10-10
horizontal channels, 2.5.10-7/2.5.10-12
vertical channels: laminar assisted convection, 2.5.10-2/2.5.10-6
laminar opposing convection, 2.5.10-6
turbulent, 2.5.10-6/2.5.10-7
around immersed bodies, 2.5.9-1/2.5.9-6
creeping flow regime (assisting convection), 2.5.9-3
horizontal plates (transverse flow), 2.5.9-4/2.5.9-6
immersed bodies (transverse flow), 2.5.9-6
opposing convection, 2.5.9-4
slightly inertial flow regime (assisting convection), 2.5.9-3/2.5.9-4
thin boundary layer regime (assisting convection), 2.5.9-1/2.5.9-3
turbulent regime (assisting convection), 2.5.9-4
Combined heat and mass transfer, 2.1.6-1/2.1.6-4
in condensation of mixtures, 2.1.6-2/2.1.6-4
in drying, 2.1.6-1/2.1.6-2
in evaporation of binary and multicomponent mixtures, 2.7.8-2/2.7.8-6
in heat exchangers, 1.1.2-1, 1.2.2-3/1.2.2-4
in single-phase free convection, 2.5.7-12/2.5.7-13
Combining flow, loss coefficients in, 2.2.2-20
Combustion chambers (see Furnaces)
Combustion model for furnaces, 3.11.7-3/3.11.7-4
Compact heat exchangers (see Plate fin heat exchangers)
Compartment dryers, 3.13.2-3
Compound systems for augmentation of heat transfer, 2.5.11-9
Compressible flow:
in ducts, 2.2.2-12/2.2.2-14
adiabatic (Fanno) flow, 2.2.2-13
basic equations for, 2.2.2-12/2.2.2-13
with constant heat transfer, 2.2.2-12/2.2.2-13
over cylinders, 2.2.3-6
inviscid flow with heat addition, 2.2.2-13
low density effect in, 2.2.2-13
Computer methods for heat exchanger design:
discussion of, 3.3.10-1/3.3.10-2
logic of, 3.1.3-3/3.1.3-4

© 1983 Hemisphere Publishing Corporation

Computer methods for heat exchanger design, logic of (Cont.):
design, 3.1.3-3/3.1.3-4
rating, 3.1.3-3
plate exchangers, 3.7.104
Computer program for Monte Carlo calculations of radiative heat transfer, 2.9.4-4/2.9.4-5
Concentration, choice of evaporator type for, 3.5.5-1/3.5.5-2
Concentric spheres, free convective heat transfer in, 2.5.8-16
Concurrency corrections in plate heat exchangers, 3.7.8-1/3.7.8-2
Condensation:
combined heat and mass transfer in, 2.1.6-2/2.1.6-4
dropwise, 2.6.5-1/2.6.5-4
calculation of heat transfer in, 2.6.5-2/2.6.5-3
introduction to, 2.1.7-6
mechanism of, 2.6.5-1/2.6.5-2
order of magnitude heat transfer coefficient in, 2.6.5-l
promoters for, 2.6.5-3/2.6.5-4
film, introduction to, 2.1.7-4/2.1.7-6
filmwise, of pure vapor, 2.6.2-1/2.6.2-19
outside horizontal and inclined tubes, 2.6.2-9/2.6.2-12, 3.4.6-3
inside horizontal tubes, 2.6.2-12/2.6.2-15, 3.4.6-2
interfacial resistance in, 2.6.2-15
liquid metals, 2.6.2-15/2.6.2-16
on vertical surfaces, 2.6.2-2/2.6.2-9, 3.4.6-3
on finned tubes, 3.4.6-3
fogging in, 2.6.7-1/2.6.7-4
conditions producing supersaturation, 2.6.7-2/2.6.7-3
design to minimize, 2.6.7-3
effects of, 2.6.7-3
nuclei formation, 2.6.7-1/2.6.7-2
supersaturation, 2.6.1-l
in horizontal tubes, flow regimes in, 2.3.2-7
in plate exchangers, 3.7.12-1
in plate fin heat exchangers, 3.9.13-1/3.9.13-2
introduction to, 2.6.1-1
heat transfer resistances in, 2.6.1-2
modes of, 2.6.1-1/2.6.1-2
of vapor mixture, 2.6.3-1/2.6.3-10, 3.4.64
approximate method, 2.6.3-2/2.6.3-5
binary vapor mixtures, 2.6.3-7
multicomponent mixtures, 2.6.3-7/2.6.3-9
single vapor with noncondensable gas, 2.6.3-5/2.6.3-7
of vapor mixtures forming immiscible liquids, 2.6.4-1/2.6.4-7
eutectic mixtures, 2.6.4-2/2.6.4-3
with incondensable gases, 2.6.4-5/2.6.4-7
non-eutectic mixtures, 2.6.4-3/2.6.4-5
Condensation curves:
description, 2.6.3-1/2.6.3-2
differential, 2.6.3-4/2.6.3-5
integral, 2.6.3-312.6.3-S
Condensers:
approximate overall heat transfer coefficients in, 2.1.2-3
design procedures for, 3.4.9-1/3.4.9-4
overall, 3.4.9-1/3.4.9-2
inside tubes, 3.4.9-2/3.4.9-3
outside tubes, 3.4.9-3/3.4.9-4
discussion of types of, 3.4.3-1/3.4.3-6
horizontal in-tube, 3.4.3-3/3.4.3-4
horizontal, outside tube, 3.4.3-4/3.4.3-6
vertical m-tube, downflow, 3.4.3-1/3.4.3-2
vertical m-tube, upflow, 3.4.3-2/3.4.3-3
vertical, outside tube, 3.4.36
fogging in, 2.6.7-1/2.6.7-4, 3.4.5-2
heat transfer in, 3.4.6-1/3.4.6-4
finned tubes, 3.4.6-3
outside horizontal tubes, 3.4.6-3
with mixtures, 3.4.64
subcooling in, 3.4.6-4
inside tubes, 3.4.6-1/3.4.6-2
outside vertical tubes, 3.4.6-3/3.4.6-4
introduction to, 3.4.1-1
mean temperature difference in, 3.4.8-1/3.4.8-3
operational problems in, 3.4.5-1/3.4.5-2
fogging, 3.4.5-2
due to limited vapor load, 3.4.5-1/3.4.5-2
pressure control, 3.4.5-1
venting, 3.4.5-2
pressure drop in, 3.4.7-1/3.4.7-2
selection of type of, 3.4.2-1/3.4.2-4
temperature patterns in, 1.1.3-1/1.1.3-2
as type of heat exchanger, 1.1.5-2
for use in association with evaporators, 3.5.4-2
for vapor mixtures, 3.4.3-1/3.4.4-2
(See also Condensation)
Conduction, heat:
basic equations for, 2.4.1-1/2.4.1-2
in melting and solidification, 2.4.4-l/2.4.4-3
periodic change of temperature in, 2.4.5-1/2.4.5-4
steady state, 2.4.2-1/2.4.2-3
in bodies with internal heat sources, 2.4.2-3
plane, cylindrical and spherical shells without internal heat sources, 2.4.2-1/2.4.2-3
thermal contact resistance in, 2.4.6-1/2.4.6-2
transient response to a step change in temperature, 2.4.3-1/2.4.3-12
one-dimensional systems, 2.4.3-1/2.4.3-10
multidimensional systems, 2.4.3-10/2.4.3-11
Conductors, thermal conductivity of, 5.4.3-2/5.4.3-3
Cones, vertical:
free convective heat transfer from, 2.5.7-24
Conical shells, mechanical design of:
analytic basis for codes, 4.3.3-l
basic principles of, 4.1.3-2
index to U.K., U.S., and F.R.G. codes for, 4.3.2-3/4.3.2-4
Connors equation for fluid elastic instability, 4.6.4-2
Conservation equations:
for chemical species, 1.2.1-3
in differential form, 2.2.1-5/2.2.1-7
in duct flow, 2.2.1-3/2.2.1-5
in furnaces, 3.11.7-1/3.1 1.7-2
for gas-liquid flows, 2.3.2-8/2.3.2-9
homogeneous model, 2.3.2-8
separated flow model, 2.3.2-8/2.3.2-9
in integral form, 2.2.1-2/2.2.1-5
for multiphase flows, 2.3.1-4/2.3.1-7
homogeneous model for, 2.3.1-4/2.3.1-7
separated flow model for, 2.3.1-6/2.3.1-7
for turbulent flows, 2.2.1-13/2.2.1-14
Construction elements of heat exchangers, 4.1.1-2/4.1.2-3
Contact angle, 2.3.1-2
influence in nucleate boiling, 2.7.1-5, 2.7.2-2
Contact resistance:
influence on particle-to-wall heat transfer in packed beds, 2.8.3-3
thermal, 2.4.6-1/2.4.6-4
Continuity equation:
applications in heat exchanger calculations, 1.2.6-5
in boundary layer, 2.2.1-17
in compressible duct flows, 2.2.2-12
differential form in single phase flow, 2.2.1-5/2.2.1-7

© 1983 Hemisphere Publishing Corporation

Continuity equation (Cont.):
in gas-liquid flows, 2.3.2-8/2.3.2-9
integral form in single phase flow, 2.2.2-2
in multiphase flows: homogeneous, 2.3.1-5
separated flow, 2.3.1-25
in turbulent flow, 2.2.1-14
Continuum model, for fluids, 2.2.1-1
Continuum theories, for non-Newtonian fluids, 2.2.8-6/2.2.8-9
Lodge s rubber-like liquid, 2.2.8-8
Maxwell model, 2.2.8-7
Oldroyd eight constant model, 2.2.8-8
White-Metzner model, 2.2.8-8
Contraction, sudden, pressure drop in: single-phase flow, 2.2.2-20
two-phase gas-liquid flow, 2.3.2-16/2.3.2-17
two-phase gas-liquid flow, 2.3.2-16/2.3.2-17
Control:
of heat pipes, 3.10.7-1/3.10.7-2
of reboilers, 3.6.4-2
Convection effects, on heat transfer in kettle reboilers:
bundle induced, 3.6.2-2/3.6.2-3
externally induced, 3.6.2-3
Convective boiling (see Boiling)
Convective heat transfer, single phase:
around immersed bodies: single bodies, 2.5.2-3/2.5.2-8
smooth flat plates, 2.5.2-1/2.5.2-3
augmentation of, 2.5.11-1/2.5.11-12
in combined free and forced convection (see Combined free and forced convection)
channel flows, 2.5.10-1/2.5.10-12
immersed bodies, 2.5.9-1/2.5.9-7
effect of radiation on, 2.9.8-1/2.9.8-10
in fixed beds, 2.8.2-1/2.8.2-8, 2.8.3-1/2.8.3-3
in flow over tube banks, 2.5.3-1/2.5.3-16
finned tubes, 2.5.3-6/2.5.3-16
plain tubes, 2.5.3-1/2.5.3-6
forced convection in ducts, 2.5.1-1/2.5.1-13
laminar flow, 2.5.1-2/2.5.1-5
turbulent flow, 2.5.1-5/2.5.1-13
in free convection: immersed bodies, 2.5.7-1/2.5.7-31
layers and enclosures, 2.5.8-l/2.5.8-25
with impinging jets, 2.5.6-1/2.5.6-10
in liquid metal systems, 2.5.13-1/2.5.13-4
with non-Newtonian fluids, 2.5.12-1/2.5.12-16
in channels with viscous heating, 2.5.12-10/2.5.12-14
in channels without viscous heating, 2.5.12-6/2.5.12-10
with dilute polymer solution, 2.5.12-14/2.5.12-15
in packed and agitated beds, 2.8.3-1/2.8.3-9
Conversion factors, for physical properties, 5.5.1-3
Conveyor, gravity:
air activated, 2.3.3-2
fluidized bed, 2.3.3-7/2.3.3-9
Cooling towers:
effect of variation in atmospheric pressure on, 3.12.6-2/3.12.6-3
hybrid, 3.12.5-1/3.12.5-5
assisted draft, 3.12.5-3/3.12.5-4
closed-circuit evaporative coolers, 3.12.5-4/3.12.5-5
dry, 3.12.5-1/3.12.5-2
wet-dry, 3.12.5-2/3.12.5-3
introduction to, 3.12.1-l
mechanical draft, 3.12.4-1/3.12.4-4
natural draft: dry, 3.8.2-1/3.8.2-2, 3.8.8-l
wet, structural design, 3.12.3-6/3.12.3-7
wet, thermal design, 3.12.3-1/3.12.3-6
main features of, 3.12.4-1/3.12.4-2
thermal performance and design, 3.12.2-4/3.12.4-4
packing region in, 3.12.2-1/3.12.2-13
departures from uniform counter flow in, 3.12.2-12/3.12.2-13
heat and mass transfer in, 3.12.2-1/3.12.2-3
packings in, 3.12.2-8/3.12.2-11
state of air leaving, 3.12.2-11/3.12.2-12
theory of thermal design of, 3.12.2-3/3.12.2-8
testing and acceptance of, 3.12.6-1/3.12.6-2
as type of heat exchanger, 1.1.5-2
water loss from, 3.12.6-2
Cooper, Anthony, 3.7.1-1/3.7.12-2
Copper-base alloys, as material of construction, 4.5.2-4/4.5.2-5
Correlation, general nature of, 1.2.3-5/1.2.3-6
Correspondence principle, in physical properties, 5.1.1-1
Corrosion:
associated with phase separation, 4.5.3-5
associated with welds, 4.5.3-S /4.5.3-6
erosion/corrosion, 4.5.3-1/4.5.3-2
fretting, 4.5.3-2
gas-vapor phase, 4.5.3-6/4.5.3-7
materials of construction to avoid, 4.5.2-2/4.5.2-6
in shell-and-tube heat exchangers, 3.3.4-5
vapor blanketing as cause, 4.5.34
in various equipment: reboilers, 4.5.3-S
waste heat boilers, 4.5.34
Corrugation design, for plate heat exchangers, 3.7.3-1/3.7.3-2, 4.4.2-3/4.4.2-4
Costing of heat exchangers:
air-cooled, 4.8.3-1/4.8.3-3
introduction to, 4.8.1-1
plate, 4.8.4-1/4.8.4-2
shell-and-tube, 4.8.2-1/4.8.2-5
Countercurrent flow:
critical heat flux in, 2.7.3-26
gas-liquid, in vertical channels, 2.3.2-21/2.3.2-22
heat exchangers, 1.1.1-1
temperature pattern for in single-phase flow, 1.1.3-1
θ-NTU chart for, 1.5.2-2
Counterflow (see Countercurrent flow)
Coupled thermal fields, in transient conduction, 2.4.3-12
Cowie, R. C., 4.8.2-114.8.2-s
Creeping flow, in combined free and forced convection around immersed bodies, 2.5.9-3
Critical density, of commonly used fluids, 5.5.1-1/5.5.1-40
Critical flow, in gas-liquid systems, 2.3.2-26/2.3.2-29
Henry-Fauske model for, 2.3.2-28/2.3.2-29
homogeneous models for, 2.3.2-28
Critical heat flux:
in axial flow reboilers, 3.6.2-7/3.6.2-8
in counter-current flow, 2.7.3-26
enhancement of, in boiling in tubes, 2.7.9-3/2.7.9-4
pool boiling, 2.7.9-1/2.7.9-2
in evaporators, 3.5.7-3
in flow in vertical annuli, 2.7.3-20/2.7.3-21
in flow in vertical tubes, 2.7.3-13/2.7.3-30
nomenclature for, 2.7.3-13
with non-uniform heat flux, 2.7.3-18/2.7.3-20
with uniform heat flux, 2.7.3-13/2.7.3-18
in forced convective boiling of binary and multicomponent mixtures, 2.7.8-6/2.7.8-7
departure from nucleate boiling, 2.7.8-6/2.7.8-7
dryout, 2.7.8-7
in kettle reboilers, 3.6.2-4/3.6.2-5
mechanisms of, 2.7.3-22/2.7.3-26
annular flow prediction methods for, 2.7.3-23/2.7.3-26

© 1983 Hemisphere Publishing Corporation

Critical heat flux (Cont.):
with nonaqueous fluids, 2.7.3-26/2.7.3-30
in pool boiling, 2.7.2-9/2.7.2-13
geometric effects in, 2.7.2-10/2.7.2-l 1
liquid viscosity effects on, 2.7.2-12
subcooling effects on, 2.7.2-12/2.7.2-13
surface condition effects on, 2.7.2-13
Zuber analysis for, 2.7.2-9/2.7.2-10
in pool boiling of binary and multicomponent mixtures, 2.7.7-4/2.7.7-5
in rectangular channels, 2.7.3-20
in rod bundles, 2.7.3-21/2.7.3-22
outside single tubes in crossflow, 2.7.5-2/2.7.5-3
outside tubes in tube banks, 2.7.5-5/2.7.5-7
correlations for, 2.7.5-6/2.7.5-7
mechanisms of, 2.7.5-5/2.7.5-6
Critical pressure:
of commonly used fluids, 5.5.1-1/5.5.1-40
in hydrocarbon mixtures, 5.2.1-3
Kesler and Lee equation for, 5.2.1-6
in pure fluids, 5.1.1-2
Critical Rayleigh number, in free convection, 2.5.8-2/2.5.8-3, 2.5.8-3/2.5.8-6
Critical temperature:
of commonly used fluids, 5.5.1-1/5.5.1-40
in hydrocarbon mixtures, 5.2.1-3
Kesler and Lee equation for, 5.2.1-5
in pure fluids, 5.1.1-1/5.1.1-2
Critical velocity, in stratification in bends and horizontal tubes, 2.7.4-1/2.7.4-3
Critical volume, 5.1.1-2
Crocco s integral, application to boundary layer equations, 2.2.1-19
Cross counter flow heat exchangers, 1.1.1-2
solutions for, 1.3.1-1/1.3.1-4
Crossflow:
in air-cooled heat exchangers, 3.8.5-1/3.8.5-5
boiling in over horizontal tubes and tube banks, 2.7.5-1/2.7.5-4
in cooling towers, 3.12.2-12/3.12.2-13
over cylinders (see Cylinders)
flow induced vibration in, 4.6.1-1/4.6.6-3
heat exchangers: definition of, 1.1.1-2
solutions for heat transfer in, 1.2.64, 1.3.14
pressure drop in gas-liquid, 2.3.2-12
in shell-and-tube heat exchangers, 3.3.6-3/3.3.6-4
temperature difference correction (F-correction) and θ-NTU charts for various configurations of, 1.5.3-1/1.5.3-13
with both streams mixed, 1.5.3-3
one tube row, unmixed, 1.5.34
four tube rows, four passes, unmixed, 1.5.3-11
four tube rows, two passes, mixed, 1.5.3-12
three tube rows, one pass, unmixed, 1.5.36
three tube rows, three passes, unmixed, 1.5.3-10
two tube rows, one pass, unmixed, 1.5.3-5
two tube rows, two passes, unmixed, 1.5.3-9
over tube banks (see Tube banks)
Crossflow shells (see X-shells)
Crystallization, choice of evaporator type for, 3.5.5-2
Curved ducts:
dryout in evaporative heat transfer in, 2.7.4-2/2.7.4-4
single-phase fluid flow and pressure drop in, 2.2.2-14/2.2.2-16
flow characteristics in, 2.2.2-14/2.2.2-15
laminar flow in, 2.2.2-15/2.2.2-16
turbulent flow in, 2.2.2-16
Cut-and-twist factor, in enhancement of heat transfer in double pipe heat exchangers, 3.2.3-l
Cyclohexane, saturation properties of, 5.5.1-l 1
Cyclopentane, saturation properties of, 5.5.1-l 1
Cylinders:
banks of cylinders (see Tube banks)
boiling from outside horizontal in crossflow, 2.7.5-1/2.7.5-4
characteristics of as packings for fixed beds, 2.2.5-2
combined free and forced convective heat transfer from, 2.5.9-1/2.5.9-6
fixed beds of, heat transfer in, 2.8.1-1/2.8.1-14, 2.8.2-1/2.8.2-8
flow across, 2.2.3-3/2.2.3-7
circular, 2.2.2-3/2.2.2-6
noncircular, 2.2.3-6/2.2.3-7
pressure coefficient in, 2.2.4-2
free convective heat transfer from, 2.5.7-20/2.5.7-24
horizontal, 2.5.7-20/2.5.7-23
vertical and inclined, 2.5.7-23/2.5.7-24
free convective heat transfer inside horizontal, 2.5.8-14
hollow, radiation and conduction around, 2.9.8-6/2.9.8-7
pool boiling from, 2.7.2-1/2.7.2-15
critical heat flux in, 2.7.2-9/2.7.2-12
radiative heat transfer on nonisothermal gas in, 2.9.7-3
steady-state thermal conduction in, 2.4.2-l/2.4.2-3
transient conduction in, 2.4.3-1/2.4.3-10
numerical methods for, 2.4.3-8/2.4.3-10
series solution for, 2.4.3-1/2.4.3-7
single-phase heat transfer in flow over, 2.5.2-4/2.5.2-5
solution using internal heat transfer coefficient, 2.4.3-712.4.3-g
under external pressure, comparison of mechanical design codes for, 4.3.4-1/4.3.4-2

D

Damage, sources of in heat exchangers, 4.5.3-1/4.5.3-7, 4.6.1-l/4.6.1-2
Damköhler number:
definition, 2.2.1-l 1
modified form for compressible flows with heat transfer, 2.2.2-12
Damping:
capacity, anelasticity, and, 5.4.5-5
of flow-induced vibration, 4.6.2-4
Davis and Anderson criterion, for onset of nucleate boiling, 2.7.3-6
Decane, saturation properties of, 5.5.1-10
Degradation temperature, of polymers, 2.5.12-l
Del operator (see Differential vector operators)
Delaware method, for shell-side heat transfer and pressure drop, (see Bell-Delaware method)
Dengler and Addoms correlation, for forced convective heat transfer in two-phase flow, 2.7.3-8
Density:
definition, 2.2.1-1
fluid with constant, 2.2.1-8/2.2.1-9
fluid with small variations of, 2.2.1-8
of liquid water, 5.5.3-2
of multicomponent liquid mixtures, 5.2.3-1/5.2.3-2
relation with viscosity for gases, 2.2.1-9
of saturated Liquids and vapors, 5.5.1-1/5.5.1-40
of solids, 5.4.1-1/5.4.1-2
graphite and carbon, 5.4.1-l

© 1983 Hemisphere I blishing Corporation

Density, of solids (Cont.):
metal alloys, 5.4.1-l
organics, 5.4.1-2
refractories, 5.4.1-1/5.4.1-2
Deposition of droplets in annular flow, 2.3.2-21, 2.7.3-24
Design of heat exchangers, introduction, 3.1.1-1/3.1.4-9
Design procedures, for segmentally baffled heat exchangers, 3.3.10-1/3.3.10-8
Desuperheaters for use in association with evaporators, 3.5.4-2
Developing flow in ducts:
single-phase flow and pressure drop in, 2.2.2-10/2.2.2-11
hydrodynamic entrance region in, 2.2.2-10/2.2.2-11
various forms and effects on, 2.2.2-11
Diathermanous fluid, 2.9.1-1
Differential condensation:
calculation of condensation curves, 2.6.3-4
description, 2.6.3-l/2.6.3-3
Differential formulations for nonisothermal gas radiation, 2.9.7-5/2.9.7-8
embedding, 2.9.7-712.9.7-g
multiflex methods, 2.9.7-6/2.9.7-7
radiation diffusion, 2.9.7-5/2.9.7-6
Differential resistance term in heat exchanger design, 3.3.9-2
Differential vector operators in heat conduction, 2.4.1-2
Diffraction models for radiative heat transfer from surfaces, 2.9.4-712.9.4-g
Diffuse surfaces, radiative heat transfer between, 2.9.3-1/2.9.3-17
Diffuse wall passages, radiative heat transfer in, 2.9.3-13/2.9.3-16
Diffusers, single-phase flow and pressure drop in, 2.2.2-17/2.2.2-19
effect of inlet conditions, 2.2.2-18/2.2.2-19
with free discharge, 2.2.2-17/2.2.2-18
methods of improving performance in, 2.2.2-19
performance, 2.2.2-17
Diffusion coefficients:
in gases, 5.2.5-3/5.2.5-4
in liquids, 5.2.5-1/5.2.5-3
Dimensional analysis:
pi theorem for, 2.2.1-11/2.2.1-12
and theory of similarity, 2.2.1-10/2.2.1-13
Dimensionless groups:
equivalent groups in heat and mass transfer, 2.1.5-2
in fluidization, 2.2.6-2/2.2.6-3
in free convective heat transfer to immersed bodies, 2.5.7-2/2.5.7-3
table of, 2.2.1-11
Dimensionless numbers (see Dimensionless groups)
Dimensionless time (see Fourier number)
Dimethyl propane saturated properties, 5 .5 .l-6
Direct contact condensation:
introduction, 2.6.1-l
mechanical construction, 4.4.4-6/4.4.4-7
Direct contact cooling, 4.4.4-8
Direct contact evaporation, 4.4.4-7
Dirt (see Fouling)
Disnetization in numerical analysis:
for cases where flow patterns must be calculated, 1.4.2-l
in design of heat exchangers with prescribed flow patterns, 1.4.1-1/1.4.1-6
effect of fineness, 1.4.1-5/1.4.1-6
subdivision of space, 1.4.1-1/1.4.1-2
subdivision of time, 1.4.1-2/1.4.1-3
Disk-and-doughnut baffled heat exchangers, 3.3.11-2
Disk turbine agitator, 3.14.2-1/3.14.2-2
heat transfer in vessel agitated by, 3.14.3-l
Disks, free convective heat transfer from inclined, 2.5.7-25
Dispersed bubble flow (see Bubble flow)
Dissipation of turbulent energy, 2.2.1-20
Distillation, closed distillation process, 2.1.7-8
Distribution:
annular, in shell-and-tube heat exchangers, 3.3.5-l 1
design in fluidized beds, 2.2.6-7/2.2.6-8
Dittus-Boelter equation, for single-phase forced convective heat transfer, 2.7.3-5
Dividing flow, loss coefficients in, 2.2.2-19
DNB (departure from nucleate boiling) (see Critical heat flux)
Donohue method, for shell-side heat transfer in shell-and-tube heat exchangers, 3.3.2-2
Double-pipe heat exchanger:
approximate overall heat transfer coefficients, 2.1.2-3
description, 3.1.2-1/3.1.2-2
design, 3.2.1-1/3.2.6-2
applications of, 3.2.2-l
construction/mechanical design, 3.2.5-1/3.2.5-2, 4.4.4-1/4.4.4-2
design parameters for, 3.2.3-1/3.2.3-6
introduction, 3.2.1-l
operational advantages of, 3.2.6-1/3.2.6-2
types available, 3.2.4-1/3.2.4-2
Double segmental baffled heat exchangers, 3.3.1 l-2
Downward facing surfaces, free convective heat transfer from, 2.5.7-13/2.5.7-15
Downward flow in vertical tubes, flow patterns in gas/liquid, 2.3.2-2
Dowtherm A saturation properties, 5.5.1-28
Dowtherm J saturation properties, 5.5.1-28
Drag coefficient:
for circular cylinder, 2.2.3-3/2.2.3-4
definition, 2.2.3-2
in fluidized beds, 2.2.6-2
for sphere, 2.2.3-3
on tube in tube bank, 2.2.4-3/2.2.4-5
Drag force:
on immersed bodies, 2.2.3-2/2.2.3-4
on tube in tube bank, 2.2.4-3/2.2.4-5
Drag reduction, 2.2.8-11/2.2.8-12
effect on heat transfer, 2.5.12-14/2.5.12-15
Drift flux model for two-phase flows, 2.3.1-7/2.3.1-9
Droplets:
deposition and entrainment of, in annular flow, 2.3.2-21
nucleation of in supersaturated vapors, 2.6.7-l/2.6.7-2
use in augmentation of heat transfer, 2.5.11-8
Dropwise condensation:
calculation of heat transfer in, 2.6.5-2/2.6.5-3
introduction, 2.1.7-6,2.6.1-l, 2.6.5-l
mechanisms of, 2.6.5-1/2.6.5-2
order of magnitude heat transfer coefficient in, 2.6.5-l
promotors for, 2.6.5-3/2.6.5-4
Dry cooling towers, 3.8.2-1/3.8.2-2, 3.8.8-1, 3.12.5-1/3.12.5-2
Dry-wall convection, in evaporation (see Postdryout heat transfer)
Dryers:
classification and selection, 3.13.2-l/3.13.2-4
introduction, 3.13.1-1/3.13.1-2
layout and performance data, 3.13.3-1/3.13.3-5
description of drying process in the Mollier chart, 3.13.3-4/3.13.3-5
energy and mass balances, 3.13.3-1/3.13.3-2
Mollier chart, 3.13.3-l
wet bulb temperature in, 3.13.3-2/3.13.3-4
practical design, 3.13.7-1/3.13.7-3
band dryers, 3.13.7-1/3.13.7-2

© 1983 Hemisphere Publishing Corporation

Dryers, practical design (Cont.):
fluid bed dryers, 3.13.7-2
pneumatical conveying dryers, 3.13.7-2
rotary dryers, 3.13.7-2
spray dryers, 3.13.7-2/3.13.7-3
prediction of drying rates in, 3.13.4-1/3.13.4-5
prediction of residence time in: with nonprescribed material flow, 3.13.6-1
with prescribed material flow, 3.13.5-1/3.15.5-5
as type of heat exchange equipment, 1.1.5-3
Drying, combined heat and mass transfer in, 2.1.6-1/2.1.6-2
Drying loft, 3.13.2-3
Drying plant (see Dryers)
Drying rates, prediction of, 3.13.4-1/3.13.4-5
Dryout:
introduction, 2.7.3-2
as mechanism for critical heat flux: of liquid film, 2.7.3-22/2.7.3-30
under a vapor clot, 2.7.3-22
(See also Critical heat flux)
Ductile fracture as failure mode of heat exchanger, 4.1.1-3
Ducts, single-phase fluid flow and pressure drop in, 2.2.2-1/2.2.2-25
circular pipes, fully developed flow, 2.2.2-1/2.2.2-7
compressible flow in, 2.2.2-12/2.2.2-14
curved ducts, 2.2.2-14/2.2.2-17
developing flow in, 2.2.2-10/2.2.2-11
losses in piping components in, 2.2.2-14/2.2.2-20
noncircular ducts, fully developed flow, 2.2.2-7/2.2.2-10
unstead flow in, 2.2.2-14
Durand correlation for heterogeneous conveyance in solid/liquid flow, 2.3.4-6

E

E-type shells in shell-and-tube heat exchangers:
recommended calculation methods for pressure drop and heat transfer in, 3.3.1-1/3.3.10-8
temperature difference correction (F) and θ-NTU charts for, 1.5.2-5/1.5.2-10
Eckert number, 2.2.1-11
Eddy viscosity:
definition, 2.2.2-2
relation to mixing length, 2 2.24
Edwards, D. K., 2.9.1-1/2.9.8-12,5.5.5-l/5.5.54
EEC code for thermal design of heat exchangers, 4.3.1-3
Effective thermal conductivity of fixed beds, 2.8.1-1/2.8.1-14, 2.8.2-2/2.8.2-5
Effective tube length in shell-and-tube heat exchangers, 3.3.5-17
Effectiveness of a heat exchanger, definition, 1.2.4-3, 2.1.2-2
Efficiency of fins, 2.5.3-6/2.5.3-7
Elastic analysis, in mechanical design, 4.1.2-l 1
Elastic properties of solids:
anelasticitydamping capacity, 5.4.5-5
anisotropy, 5.4.5-4/5.4.5-5
introduction to, 5.4.5-l
isotropic materials, 5.4.5-3/5.4.5-4
static and dynamic properties, 5.4.5-2
stress-strain curve, 5.4.5-2/5.4.5-3
tables of, 5.5.8-1/5.5.8-3
Electric fields, effect on properties of rheologically complex materials, 5.3.8-1/5.3.8-2
Electromagnetic theory of radiation, 2.9.2-7/2.9.2-10
Electrostatic fields in augmentation of heat transfer, 2.5.11-3/2.5.11-4, 2.5.11-8/2.5.11-9, 2.7.94
Elhadidy relation between heat and momentum transfer, 1.2.3-6
Embedding methods for radiative heat transfer in nonisothermal gases, 2.9.7-7/2.9.7-8
Emission of thermal radiation, in solids, 2.9.2-1/2.9.2-3
characteristics of, 2.9.2-1/2.9.2-2
measurement of, 2.9.2-3
Emissivity:
of gaseous combustion products, 3.11.34
of gases, 2.9.5-1/2.9.5-13
table, 5.5.5-1/5.5.5-4
of solids, 5.4.4-1/5.4.4-6
of surfaces: definition, 2.9.2-1
measurement of, 2.9.2-3
tables, 5.5.7-1/5.5.7-3
total, of solids, table, 3.11.3-6
EMTD (effective mean temperature difference) in air-cooled heat exchangers, 3.8.5-4/3.8.5-5
Enclosures:
annuli, free convective heat transfer in: horizontal, 2.5.8-14/2.5.8-16
vertical (heated on vertical curved surfaces), 2.5.8-13/2.5.8-14
concentric spheres, free convective heat transfer in, 2.5.8-16
free convection heat transfer in, when heated from below, 2.5.8-3/2.5.8-6
critical Rayleigh number, 2.5.8-3/2.5.8-6
heat transfer rates, 2.5.8-6
modes of circulation, 2.5.8-6
honeycombs, free convective heat transfer in, 2.5.8-20/2.5.8-23
horizontal cylinders, free convective heat transfer inside, 2.5.8-14
inclined, free convective heat transfer in, 2.5.8-17/2.5.8-20
large aspect ratios, 2.5.8-17/2.5.8-19
moderate aspect ratios, 2.5.8-20
rectangular, free convective heat transfer in, when heated from the sides, 2.5.8-6/2.5.8-13
flow patterns in, 2.5.8-6/2.5.8-8
large aspect ratios, 2.5.8-8/2.5.8-10
with local heating, 2.5.8-13
low aspect ratios, 2.5.8-10/2.5.8-13
Energy, internal (see Specific internal energy)
Energy equation:
in boundary layers, 2.2.1-18
in compressible duct flow, 2.2.2-12
differential form in single-phase flow, 2.2.1-5/2.2.1-7
in gas-liquid flows, 2.3.2-8/2.3.2-9
homogeneous flow, 2.3.2-8
separated flow, 2.3.2-812.3.2-v
in heat exchangers, 1.2.6-2/1.2.6-3
integral form in single-phase flow, 2.2.1-3
in multiphase flows: homogeneous, 2.3.1-5/2.3.1-6
separated flow, 2.3.1-7
in non-Newtonian flow, 2.5.12-5
in turbulent flow, 2.2.1-14
Enhancement devices:
for condensation, 2.6.6-1/2.6.6-4
for single-phase heat transfer, 2.5.11-1/2.5.11-12
Enhancement of heat transfer (see Augmentation)
Enlargements in pipes:
single-phase flow and pressure drop in, 2.2.2-17/2.2.2-19
diffusers, 2.2.2-17/2.2.2-19
sudden enlargements, 2.2.2-19

© 1983 Hemisphere Publishing Corporation

Enlargements in pipes (Cont.):
two-phase flow and pressure drop in, 2.3.2-15/2.3.2-16
slow change, 2.3.2-15/2.3.2-16
sudden enlargement, 2.3.2-16
Enthalpy:
changes in streams in heat exchangers, 1.2.4-1/1.2.4-2
of saturated liquids and vapors, 5.5.1-1/5.5.1-40
(See *also* Specific enthalpy)
Enthalpy balance equations for cooling towers, 3.12.2-5
Entrainment in annular gas-liquid flow, 2.3.2-l 1, 2.7.3-24
Entrance effects in heat and mass transfer:
comparison of laminar and turbulent flows, 2.1.7-1/2.1.7-2
in turbulent flow heat transfer, 2.5.1-7
Entrance lengths, hydrodynamic in pipe flow, 2.2.2-10/2.2.2-11
Entrance losses for tube inlet in shell-and-tube heat exchanger, 2.2.7-7/2.2.7-8
Entropy (see Specific entropy)
Eötvos number:
in bubble departure, 2.7.1-8
definition, 2.3.2-19
Equations of state:
Benedict-Webb-Rubin, 5.2.2-3
Peng-Robinson, 5.1.24
Redlich-Kwong, 5.1.24
Redlich-Kwong-Soave, 5.1.24
van der Waals, 5.1.2-3/5.1.2-4
Equilibrium interphase:
in binary and multicomponent mixture, 2.7.6-1/2.7.6-4, 5.2.1-1/5.2.1-8
hydrocarbon phase behavior, 5.2.1-3/5.2.1-5
in mixtures of undefined components, 5.2.1-515.2.1-s
nonhydrocarbon phase behavior, 5.2.1-5
vapor-liquid, 5.2.1-2/5.2.1-3
introduction, 1.2.1-3
metastable and stable, 2.7.1-1
Equilibrium vapor nucleus, 2.7.1-3
Equivalent sand roughness, 2.2.1-29/2.2.1-30
Ergun equation, for pressure drop in fixed beds, 2.2.5-2
Ethane:
saturation properties, 5.5 .1-5
superheated gaseous, thermodynamic properties of, 5.5.2-2
Ethanol:
critical heat flux table for flow boiling of in vertical tube, 2.7.3-29
saturation properties of, 5.5.1-18
Ethyl acetate saturation properties, 5.5.1-25
Ethyl benzene saturation properties, 5.5 .l-14
Ethyl ether saturation properties, 55.1-23
Ethylene:
saturation properties of, 5.5.1-15
superheated gaseous, thermodynamic properties, 5.5.2-3
Ethylene oxide saturation properties, 5.5.1-24
Euler number:
definition, 2.2.1-11
effect of roughness on, in flow over tube banks, 2.2.4-14/2.2.4-15
in flow over tube banks, 2.2.4-5/2.2.4-12
European Economic Community (see EEC code for thermal design of heat exchangers)
Eutectic mixtures, condensation of forming immiscible liquids, 2.6.4-2/2.6.4-3
Evaporation:
flow regimes in, 2.3.2-6/2.3.2-7
at an interface, 2.7.1-2
interfacial resistance in, 2.1.7-8
introduction to, 2.1.7-6/2.1.7-8
in plate fin heat exchangers, 3.9.13-1/3.9.13-2
in plate heat exchangers, 3.7.12-1
(See also Boiling)
Evaporative coolers, 3.12.5-4/3.12.5-5
Evaporators:
arrangements for, 3.5.3-1/3.5.3-2
flash evaporation, 3.5.3-2
multiple effect, 3.5.3-1/3.5.3-2
vapor recompression, 3.5.3-2
choice of type of, 3.5.5-1/3.5.5-2
concentration, 3.5.5-1/3.5.5-2
crystallization, 3.5.5-2
vaporization, 3.5.5-l
design aspects, 3.5.4-1/3.5.4-2
condensers for, 3.5.4-2
desuperheaters for, 3.5.4-2
hot fluid space in, 3.5.4-l
separators for, 3.5.4-1/3.5.4-2
estimation of heat transfer coefficients in, 3.5.7-1/3.5.7-3
estimation of pressure drop and circulation in, 35.6-l
estimation of surface area in, 3.5.8-1
introduction to, 3.5.1-l
as type of heat exchanger, 1.1.5-2
types, 3.5.2-1/3.5.2-7
basket type, 3.5.2-l/3.5.2-3
climbing film, 3.5.24
falling film, 3.5.2-4/3.5.2-5
horizontal shell side, 3.5.2-l
horizontal tube side, 3.5.2-5/3.5.2-6
long-tube vertical, 3.5.2-3/3.5.2-4
plate-type, 3.5.2-6
short-tube vertical, 3.5.2-l
Exit losses for tubes in shell-and-tube exchanger, 2.2.7-8
Expansion joints, mechanical design of:
basic principles of, 4.1.6-I
constructional details of, 4.2.6-1014.2.6-l 1
Expansion of tubes into tube sheets:
explosive, 4.2.6-7
roller, 4.2.6-6/4.2.6-7
Explosive welding of tubes into tube sheets, 4.2.6-8/4.2.6-10
Extended surfaces (see Fins)
Externally induced convection, in kettle reboilers, 3.6.2-3
Extinction coefficient, 2.9.5-1
Extinction efficiency, 2.9.5-1
Extruders, heat transfer in, 3.14.3-5/3.14.3-6
Eyring fluid (non-Newtonian), 2.2.8-7

F

F-correction method:
application to single-pass cocurrent and countercurrent flow exchangers, 1.3.1-2/1.3.1-4, 1.5.2-1/1.5.2-2
F-factor charts and equations for various heat exchanger configurations, 1.5.2-2/1.5.3-12
crossflow (both streams mixed), 1.5.3-3
four tube rows, four passes, unmixed, 1.5.3-11
four tube rows, one pass, unmixed, 1.5.3-7
four tube rows, two passes, mixed, 1.5.3-12
one tube row, unmixed, 1.5.34
three tube rows, one pass, unmixed, 1.5.3-6
three tube rows, three passes, unmixed, 1.5.3-10

© 1983 Hemisphere Publishing Corporation

F-correction method, F-factor charts and equations for various heat exchanger configurations, crossflow (Cont.):
two tube rows, one pass, unmixed, 1.5.3-5
two tube rows, two tube passes, unmixed, 1.5.3-9
double-pipe heat exchangers, 3.2.3-4/3.2.3-5
E-shell with even number of passes, 1.5.2-5
five E-shells in series, 1.5.2-9
four E-shells in series, 1.5.2-8
Gshell, even number of tube passes, 1.5.2-l 3
J-shell, even number of tube passes, 1.5.2-12
J-shell, one tube pass, 1.5.2-l 1
single pass cocurrent, 1.5.2-3
six E-shells in series, 1.5.2-10
three E-shells in series, 1.5.2-7
two E-shells in series, 1.5.2-6
for calculation of heat exchangers, 1.2.44, 1.5.1-1/1.5.3-12
F-factor method:
for temperature difference (see F-correction method)
tong, for critical heat flux with non-uniform heat flux, 2.7.3-19/2.7.3-20
F-type shells:
calculation of heat transfer and pressure drop in, 3.3.11-2
discussion of, 3.3.4-3
thermal leakage in, 1.5.2-14/1.5.2-15
Failure modes of heat exchangers, 4.1.1-3/4.1.1-5
corrosion and other damage mechanisms, 4.5.3-1/4.5.3-7
ductile fracture, 4.1.1-3
high strain fatigue, 4.1.1-5
incremental collapse, 4.1.1-3/4.1.1-5
Falling film evaporator:
description of, 3.5.2-4/3.5.2-5
mass transfer in, 2.1.7-8
Fanning friction factor (see Friction factor)
Fanno flow, 2.2.2-13
Fans in air-cooled heat exchangers:
drive design, 3.8.7-2, 4.4.1-4/4.4.1-6
noise emission, 3.8.9-l
power consumption, 3.8.7-1/3.8.7-2
selection and sizing, 3.8.7-l
Fatigue as failure mode of a heat exchanger, 4.1.1-5, 4.5.3-2/4.5.3-3, 4.6.1-2
Ferritic stainless steels, as material of construction, 4.5.2-3/4.5.2-4
Fick s law for diffusion, 2.1.1-2
extensions to multicomponent system, 2.1.5-1
limitations in, 2.1.1-1/2.1.1-4
Film boiling:
in axial flow reboilers, 3.6.2-9
in cross flow over single cylinder, 2.7.5-3/2.7.5-4
in forced convective boiling on vertical surfaces, 2.7.3-30/2.7.3-31
vertical flat plate, 2.7.3-30/2.7.3-31
vertical rod, 2.7.3-31
in kettle reboilers, 3.6.2-5
in pool boiling, 2.7.2-14/2.7.2-15
Film cooler, approximate overall heat transfer coefficients in, 2.1.24
Film temperature, definition of for turbulent flow over flat plate, 2.2.1-29
Films in heat exchangers, 1.1.4-2
Filmwise condensation:
description of, 2.6.1-I
of pure vapors, 2.6.2-1/2.6.2-19
inside horizontal tubes, 2.6.2-12/2.6.2-15
outside horizontal tubes, 2.6.2-9/2.6.2-12
interfacial resistance in, 2.6.2-15
with liquid metals, 2.6.2-15/2.6.2-16
on vertical surfaces, 2.6.2-2, 2.6.2-9
Finite difference equations:
application to natural convection in enclosures, 2.5.8-8
for flow pattern calculation, 1.4.2-1/1.4.2-4
for heat exchangers, 1.4.1-3/1.4.1-4
Finned-tube banks (see Tube banks finned)
Fins:
application in enhancement of boiling heat transfer, 2.7.9-1/2.7.9-4
as augmentation devices, 2.5.1 l-2
in condensation, 2.6.6-2/2.6.6-3
internally finned tubes, 2.5.11-5/2.5.11-6, 2.6.6-2/2.6.6-3
in natural convection, 2.5.11-3/2.5.11-4
on cylinders in tube banks: pressure drop in, 2.2.4-13/2.2.4-14
effect on flow over cylinders, 2.2.3-6/2.2.3-7
free convective heat transfer from, 2.5.7-25
longitudinal (straight): application in double-pipe heat exchangers, 3.2.1-1/3.2.6-2
efficiency of, 2.5.3-9, 3.2.1-1/3.2.6-2
low finned tubes: applications in shell-and-tube heat exchangers, 3.3.11-2/3.3.11-4
correlation for single-phase heat transfer in flow over, 2.5.3-12/2.5.3-13
use in boiling augmentation, 2.7.9-l/2.7.9-2
radiating, 2.9.8-4/2.9.8-6
single-phase forced convective heat transfer to banks of tubes with, 2.5.3-6/2.5.3-16
efficiency of fiis in, 2.5.3-6/2.5.3-11
experimental data compared with correlations for, 2.5.3-13/2.5.3-15
heat transfer correlations for high fins, 25.3-l l/2.5.3-12
heat transfer correlations for low fins, 2.5.3-12/2.5.3-13
types, in heat exchangers, 1.1.4-1
types used in an-cooled heat exchangers, 3.8.3-1/3.8.3-3
Fire-tube boiler, 3.11.2-3
Fired heaters, 3.11.2-1/3.11.2-2
Firsova, E. V., 2.5.13-1/2.5.13-4
Fittings, pipe (see Piping components)
Fixed beds:
characteristics of packings in, 2.2.5-2
heat transfer in, with gas flowing through, 2.8.2-1/2.8.2-7, 2.8.3-1/2.8.3-3
contact area resistance in, 2.8.3-2
effective thermal conductivity in, 2.8.2-2/2.8.2-5
fluid-to-particle heat transfer in, 2.5.4-1/2.5.4-6
heat transfer from walls of, 2.8.2-5/2.8.2-7, 2.8.3-1/2.8.3-3
molecular gas conduction influence in, 2.8.3-1/2.8.3-2
one-dimensional temperature field in, 2.8.2-7
radiative heat transfer in, 2.8.3-2
two-dimensional temperature field in, 2.8.2-1/2.8.2-2
heat transfer in stagnant (with no flow through), 2.8.1-1/2.8.1-14
effective thermal conductivity of, 2.8.1-3/2.8.1-5
heat transfer coefficient from walls to, 2.8.1-5/2.8.1-10
onedimensional temperature field in, 2.8.1-10/2.8.1-14
twodimensional temperature field in, 2.8.1-1/2.8.1-2
non-uniform heat transfer in, 2.1.4-3/2.1.4-4
single-phase flow and pressure drop in, 2.2.5-1/2.2.5-5
voidage in, 2.2.5-l
Fixed tubesheet, shell-and-tube exchangers:
comparison of codes, 4.3.4-2
mechanical features, 4.2.3-1/4.2.3-4
Flanges, mechanical design of in heat exchangers:
basic principles, 4.1.7-1/4.1.7-2

© 1983 Hemisphere Publishing Corporation

Flanges, mechanical design of in heat exchangers (*Cont.*):
comparison of codes, 4.3.4-2/4.3.4-3
constructional features, 4.2.6-3/4.2.6-5
index to U.S., U.K., and F.R.C. codes, 4.3.2-5/4.3.2-7
Flash evaporation, 3.5.3-2
Flat absorber of thermal radiation, 2.9.2-15
Flat plate:
free convective heat transfer on: inclined and horizontal plates, 2.5.7-13/2.5.7-19
vertical plates, 2.5.7-2/2.5.7-13
laminar flow along, 2.2.1-22/2.2.1-24
effect of buoyancy forces, 2.2.1-24
effect of density-viscosity function, 2.2.1-22
effect of Mach number, 2.2.1-23
effect of Prandtl number, 2.2.1-23
effect of suction or injection, 2.2.1-23
effect of wall temperature, 2.2.1-22
effect of wall temperature distribution, 2.2.1-23/2.2.1-24
higher order effects, 2.2.1-24
reference temperature, 2.2.1-23
single-phase forced convective heat transfer in, 2.5.2-1/2.5.2-3
transition flow along, 2.2.1-24/2.2.1-25
effect of outer flow turbulence, 2.2.1-24
effect of pressure gradient, 2.2.1-24
heat transfer in, 2.2.1-25
suction on blowing effect, 2.2.1-25
surface roughness, 2.2.1-25
turbulent flow along, 2.2.1-29/2.2.1-30
effect of suction or injection, 2.2.1-30
heat transfer on, 2.2.1-29/2.2.1-30
Mach number effect on, 2.2.1-30
skin friction on, 2.2.1-29
Flat reflector of thermal radiation, 2.9.2-14
Floating head designs for shell-and-tube heat exchangers:
analytical basis for codes for, 4.3.3-l
comparison of codes for, 4.3.4-2
detailed constructional features, 4.2.3-4/4.2.3-7
outside packed type, 4.2.3-7
packed-lantern ring type, 4.2.3-5/4.2.3-6
pull through type, 4.2.3-5
split backing ring type, 4.2.3-4/4.2.3-5
discussion, 3.3.5-12/3.3.5-13
example of calculation of heat exchanger mechanical design with, 4.3.6-l/4.3.6-23
flanges in, 4.2.6-3
mechanical design of: basic principles of, 4.1.4-2/4.1.4-4
Flooding phenomena:
in gas-liquid flow in vertical tubes, 2.3.2-21/2.3.2-23
in reflux condensation, 2.6.2-7/2.6.2-9, 3.4.3-2/3.4.3-3
Pushkina and Sorokin correlation for, 2.3.2-22
as source of critical heat flux limitation in countercurrent flow: in tube banks, 2.7.5-5/2.7.5-6
in tubes, 2.7.3-26
Wallis correlation for, 2.3.2-22, 2.6.2-8
Flow distribution in plate heat exchangers, 3.7.6-2, 3.7.8-3/3.7.8-4, 4.4.3-3
Flow-induced vibration, 4.6.1-1/4.6.6-3
design considerations, 4.6.6-1/4.6.6-3
introduction, 4.6.1-1/4.6.1-2
sources of damage by, 4.6.1-1/4.6.1-2
prediction procedure, 4.6.5-1/4.6.5-2
shell-side velocities causing, 4.6.3-l
tube bundle vibration characteristics, 4.6.2-1/4.6.2-4
amplitude of vibration, 4.6.24
damping, 4.6.24
finned-tube natural frequencies, 4.6.2-3
span lengths, 4.6.2-3
straight tube natural frequencies, 4.6.2-1/4.6.2-3
U-bend tube natural frequencies, 4.6.2-3
vibration phenomena, 4.6.4-1/4.6.4-4
acoustic vibration, 4.6.4-3/4.6.4-4
combined phenomena, 4.6.44
fluid elastic whirling, 4.6.4-2
parallel flow eddy formation, 4.6.4-3
turbulent buffeting, 4.6.4-2
vortex shedding, 4.6.4-1/4.6.4-2
Flow patterns (see Flow regimes)
Flow quality (see Quality)
Flow regimes:
in combined free and forced convection in channels:
circular pipes, 2.5.10-1/2.5.10-2
rectangular channels, 2.5.10-11
in combined free and forced convection around immersed bodies, 2.5.9-1/2.5.9-4
in condensation forming immiscible liquids, 2.6.4-2
in fixed beds, 2.8.2-2
in fluidized beds, 2.2.6-1, 2.2.6-3
in gas-liquid flow, 2.3.2-1/2.3.2-7
horizontal tubes, 2.3.2-2/2.3.2-4
inclined tubes, 2.3.2-4/2.3.2-5
shell-and-tube heat exchangers, 2.3.2-5/2.3.2-6, 3.4.7-2
systems with phase change, 2.3.2-6/2.3.2-7
vertical tubes, 2.3.2-1/2.3.2-2
influence of free convection on, in horizontal pipe flow, 2.2.2-6
in natural convection in enclosures, 2.5.8-6/2.5.8-8
in single-phase flow in tube banks, 2.2.4-1/2.2.4-3
in single-phase flow over immersed bodies:
boundary layer regime, 2.2.3-1/2.2.3-2
over circular cylinders, 2.2.3-3
over noncircular cylinders, 2.2.3-6/2.2.3-7
in solid-gas flow, 2.3.3-2
Fluid elastic instability as source of flow-induced vibration, 4.6.4-2
Fluid elastic whirling (see Fluid elastic instability as a source of flow induced vibration)
Fluid mechanics, Eulerian formulation for, 2.2.1-l
Fluid-to-particle heat transfer in fluidized beds, 2.5.5-1/2.5.5-6
Fluidized bed dryer:
description, 3.13.24
practical design, 3.13.7-2
Fluidized bed gravity conveyors, 2.3.3-712.3.3-g
Fluidized beds:
bed-to-immersed tube heat transfer in, 2.8.4-6/2.8.4-7
bed-to-wall heat transfer in, 2.8.4-1/2.8.4-8
interphase gas convective component, 2.8.4-3
particle convective component, 2.8.4-2/2.8.4-3
predictive methods for, 2.8.4-4/2.8.4-6
radiative component, 2.8.4-3
fluid-to-particle heat transfer in, 2.5.5-1/2.5.5-6
introduction, 2.5.1-1/2.5.5-2
low Peclet numbers, 2.5.3-3/2.5.3-6
recommended equations, 2.5.5-2/2.5.5-3
single-phase fluid flow and pressure drop in, 2.2.6-112.2.6-g
local structure in, 2.2.6-6/2.2.6-8
minimum velocity for fluidization in, 2.2.6-2/2.2.6-3
pressure drop, 2.2.6-2
state diagram for, 2.2.6-2/2.2.6-3
types of fluidization, 2.2.6-1/2.2.6-2
use in augmentation of heat transfer, 2.5.1 l-8
Fluids:
models for, 2.2.1-7/2.2.1-10

© 1983 Hemisphere Publishing Corporation

Fluids, models for (Cont.):
calorifically perfect, 2.2.1-8
constant density, 2.2.1-812.2.1-g
continuum, 2.2.1-1
perfect gas (ideal gas), 2.2.1-7/2.2.1-8
small density variation, 2.2.1-8
physical properties: mixtures of fluids, 5.2.1-1/5.2.5-5
pure fluids, 5.1.1-1/5.1.5-3
rheologically complex, 5.3.1-1/5.3.8-3
tables, 5.5.1-1/5.5.5-4
Fluorine saturation properties, 5.5.1-32
Fluted tubes, application in evaporators, 2.7.9-3
Flux method, for modeling radiation in furnaces, 3.11.7-5
Flux relationships in heat exchangers, 1.2.2-1/1.2.2-4
Fog formation (see Fogging in condensation)
Fogging in condensation, 2.6.7-1/2.6.7-4
design to minimize, 2.6.7-3, 3.4.5-2
effects of, 2.6.7-3, 3.4.5-2
nuclei formation, 2.6.7-1/2.6.7-2
supersaturation, 2.6.7-1/2.6.7-3
Forced convection heat transfer, single-phase (see Convection heat transfer)
Forced convective boiling (see Boiling)
Forced flow reboilers:
characteristics, advantages, and disadvantages of, 3.6.1-5
heat transfer characteristics of, 3.6.2-6/3.6.2-10
Forster and Zuber correlation for nucleate boiling, 2.7.24
Fouling:
in double-pipe heat exchangers, 3.2.6-l
in evaporators, 3.5.7-1/3.5.7-2
influence in selection of reboiler type, 3.6.1-6
numerical methods in the prediction of, 1.4.2-4
in plate heat exchangers, 3.7.9-l
in reboiler design, 3.6.4-1/3.6.4-2
fouling resistances in reboilers, 3.6.4-2
in shell-and-tube heat exchangers, 3.3.4-5, 3.3.5-14/3.3.5-15
asliiiting factor in design, 3.3.10-7/3.3.10-8
as source of damage, 4.5.3-5
Four phase flows, examples, 2.3.1-2
Fourier law for conduction, 2.1.1-2,2.4.1-l
limitations in, 2.1.1-1/2.1.1-4
Fourier number (Fo):
definition, 1.2.3-5, 2.1.3-2
in packed beds, 2.8.3-1/2.8.3-3
in solidification and melting, 2.4.4-1/2.4.4-2
in transient conduction, 2.4.3-1/2.4.3-7
Frames for plate heat exchangers, 4.4.2-5/4.4.2-7
France, guide to national practice for mechanical design, 4.3.5-6
Free convection:
augmentation of heat transfer in: active systems for, 2.5.114
passive systems for, 2.5.1 1-3
combined with forced convection (see Combined free and forced convection)
effect on laminar flow heat transfer in channels, 2.5.1-4/2.5.1-5
effect of, on single-phase flow in vertical ducts, 2.2.2-11
heat transfer around immersed bodies, 2.5.7-1/2.5.7-3 1
generalized solutions for, 2.5.7-25/2.5.7-28
horizontal cylinders, 2.5.7-20/2.5.7-23
inclined and horizontal surfaces, 2.5.7-13/2.5.7-19
open ended channels, 2.5.7-19/2.5.7-20
other shapes, 2.5.7-25
spheres, 2.5.7-24/2.5.7-25
vertical cones, 2.5.7-24
vertical and inclined cylinders, 2.5.7-23/2.5.7-24
vertical plates, 2.5.7-2/2.5.7-13
influence on friction factor in circular pipe flow, 2.2.2-5/2.2.2-7
in layers and enclosures, 2.5.8-1/2.5.8-25
circular vertical annuli heated and cooled on vertical curved surfaces, 2.5.8-13/2.5.8-14
concentric spheres, 2.5.8-16
enclosures heated from below, 2.5.8-3
honeycombs, 2.5.8-20/2.5.8-23
horizontal annuli, 2.5.8-14/2.5.8-16
horizontal cylinders, 2.5.8-14
inclined enclosures, 2.5.8-17/2.5.8-20
infinite horizontal layers, 2.5.8-1/2.5.8-3
rectangular enclosures heated and cooled on the sides, 2.5.8-6/2.5.8-13
occurrence in flow in horizontal circular pipe, Metais and Eckert diagram for, 2.2.2-6
Free-fall velocity of particles, 2.3.3-3
Free molecule conditions, maximum shear stress, heat flux, and mass flux in, 2.1.1-2
Free-stream turbulence, effect on flow over cylinders, 2.2.36
Freeze protection of air-cooled heat exchangers, 4.4.1-1/4.4.1-2, 4.4.1-7
Fresnel relations in reflection of radiation, 2.9.2-9
Fretting corrosion, 4.5.3-2
Friction coefficient (see Friction factor)
Friction factor:
in circular pipe flow, 2.2.2-1/2.2.2-2
definition, 2.2.2-l
Moody chart for, 1.2.3-3, 2.2.2-2
definition, 1.2.3-2
in fixed beds, 2.2.5-3
in flow over tube banks, 3.3.7-1/3.3.7-4
interfacial, 2.3.2-21/2.6.2-6
liquid film, 2.3.2-10
in plate fin exchangers, 3.9.4-1/3.9.6-2
in plate heat exchangers, 3.7.4-1/3.7.4-2
on the shell side of double-pipe heat exchangers, 3.2.3-5/3.2.3-6
of solid in solid gas flow, 2.3.3-5/2.3.3-7
definition, 2.3.3-5
in horizontal pneumatic conveyance, 2.3.3-5/2.3.3-6
in vertical pneumatic conveyance, 2.3.3-5
in systems with heat transfer augmentation: coiled tubes, 2.5.11-7
internally finned tubes, 2.5.11-6
roughened surfaces, 2.5 .11-2/2.5.11-5
twisted tape systems, 2.5.11-7
Friction multipliers in gas-liquid flow:
correlation for: in singularities, 2.3.2-15/2.3.2-18
in straight channels, 2.3.2-9/2.3.2-12
definition, 2.3.2-9
Friction velocity definition, 2.2.1-25
Frictional pressure drop (see Pressure drop)
Friedel correlation for frictional pressure gradient in straight channels, 2.3.2-l 1
Froude number:
definition, 1.2.3-5, 2.2.1-11
in fluidized beds, 2.2.6-2/2.2.6-3
Fuels, properties of, 3.11.3-2/3.11.3-3
Fugacity, 5.2.1-2
Furnaces:
advanced models for, 3.11.7-1/3.11.7-6
in boilers, 3.11.2-2/3.11.2-3
heat transfer in, 3.11.3-6
heat sink, 3.11.3-3/3.11.3-6
heat source, 3.11.3-1/3.1 1.3-3

© 1983 Hemisphere Publishing Corporation

Furnaces, heat transfer in (Cont.):
heat transfer of the sink, 3.11.3-6
refractory surfaces, 3.11.3-6
introduction, 3.11.1-l
multizone model for, 3.11.6-1/3.11.6-4
plug flow model for, 3.11.5-1/3.11.5-2
in process heaters, 3.11.2-1/3.1 1.2-2
radiation characteristics of row of cylinders backed by refractory wall in, 2.9.3-12/2.9.3-13
stirred reactor model for, 3.11.4-1/3.1 1.4-6
as type of heat exchange equipment, 1.1.5-3

G

G-type shells in shell-and-tube heat exchangers:
description, 3.3.4-3
temperature difference correction factor (F) and θ-NTU chart for, 1.5.2-13
Galileo number, 2.2.1-11
in bubble rise in liquids, 2.3.2-19
Gas heater, approximate overall heat transfer coefficients in, 2.1.2-3
Gas-liquid flows:
applications of one-dimensional equations, 2.3.2-7/2.3.2-18
conservation equations, 2.3.2-8/2.3.2-9
correlation for void fraction, 2.3.2-13/2.3.2-15
frictional pressure drop in straight channels, 2.3.2-9/2.3.2-12
pressure changes across singularities, 2.3.2-15/2.3.2-18
pressure drop in heat exchangers, 2.3.2-12/2.3.2-13
critical two-phase flow, 2.3.2-26/2.3.2-29
flow patterns in, 2.3.2-1/2.3.2-7
horizontal tubes, 2.3.2-2/2.3.2-4
shell-and-tube heat exchangers, 2.3.2-5/2.3.2-6
in systems with phase change, 2.3.2-6/2.3.2-7
inclined tubes, 2.3.2-4/2.3.2-5
vertical tubes, 2.3.2-1/2.3.2-2
hydrodynamics of specific flow regimes (horizontal), 2.3.2-23/2.3.2-26
annular flow, 2.3.2-25/2.3.2-26
slug flow, 2.3.2-24/2.3.2-25
stratified flow, 2.3.2-23/2.3.2-24
hydrodynamics of specific flow regimes (vertical), 2.3.2-18/2.3.2-23
annular flow, 2.3.2-19/2.3.2-21
bubble flow, 2.3.2-18/2.3.2-19
counter-current flow and flooding, 2.3.2-21/2.3.2-23
plug-slug flow, 2.3.2-19
in plate heat exchangers, 3.7.12-1
Gas-solid flow (see Solid-gas flow)
Gas sparging, for agitation of vessels:
description, 3.14.2-1/3.14.2-2
heat transfer with, 3.14.3-3
Gaseous fuels, properties of, 3.11.3-2
Gases:
as constituent of multiphase flows, 2.3.1-2
combined radiative and convective heat transfer to, 2.9.8-7/2.9.8-10
diffusion coefficients in, 5.2.5-3/5.2.5-4
emissivity of, 2.9.5-1/2.9.5-13
table of, 5.5.5-1/5.5.5-4
emissivity of combustion product mixtures of, 3.11.34, 5.5.5-3/5.5.5-4
isothermal, radiative heat transfer in, 2.9.6-l/2.9.6-9
nonisothermal, radiative heat transfer in, 2.9.7-l/2.9.7-13
P-$\tilde{V}$-T relationships for, 5.1.2-1/5.1.2-4
radiation properties, 2.9.5-1/2.9.5-12
equation of transfer for, 2.9.5-1/2.9.5-2
gas mixtures, 2.9.5-11/2.9.5-12
measurement of, 2.9.5-2/2.9.5-4
molecular, 2.9.5-8/2.9.5-11
physics of, 2.9.5-4
spectral, band and total property definition, 2.9.5412.9.5-g
superheated, thermodynamic properties of, tables, 5.5.2-l/5.5.2-11
thermodynamic properties, 5.1.3-l/5.1.3-7
transport properties, 5.1.3-1/5.1.3-7
Gasketed plate heat exchangers (see Plate heat exchangers)
Gaskets:
for flanges in shell-and-tube heat exchangers, 4.2.6-3/4.2.6-4
for graphite block exchangers, 4.4.44
in plate heat exchangers, design and properties, 4.4.2-4/4.4.2-5
Geometric optics models for radiative heat transfer from surfaces, 2.9.4-8
Germany, Federal Republic of, mechanical design of heat exchangers in:
guide to national practice, 4.3.54
index to Merkblatter code, 4.3.2-1/4.3.2-1 1
Gersten, K., 2.2.1-112.2.3-g
Gibbs phase rule, 5.2.1-l
Girth flanges, in shell-and-tube heat exchangers:
analytical basis for code for, 4.3.3-2
constructional details of, 4.2.6-3
Gn (heat generation number), 2.5.12-6
Gnielinski, V., 2.5.1-1/2.5.4-6
Goodness factor, as a basis for comparison of plate fin heat exchanger surfaces, 3.9.7-1/3.9.7-3
Goody narrow band model for gas radiation properties, 2.9.5-5
Graetz number:
definition, 1.2.3-5, 2.1.3-2
in non-Newtonian flows, 2.5.12-6/2.5.12-7
Graetz problem (see Nusselt-Graetz problem)
Graphite, density of, 5.4.1-l
Graphite block heat exchanger, 4.4.44
Grashof number, 1.2.34,2.2.1-l 1, 2.2.2-6
in free convection over immersed bodies, 2.5.7-2
Gravitational acceleration, effect in pool boiling, 2.7.2-9
Gravity conveyor:
air-activated, 2.3.3-2
fluidized bed, 2.3.3-7/2.3.3-9
Gregorig effect in enhancement of condensation, 2.6.6-l/2.6.6-2
Griffith, P., 2.6.5-1/2.6.5-4
Groeneveld correlation for postdryout heat transfer, 2.7.3-31
Groeneveld and Delorme correlation for postdryout heat transfer, 2.7.3-32/2.7.3-33
Group contribution parameters tables, 5.5.4-10
Guerrieri and Talty correlations for forced convective heat transfer in two-phase flow, 2.7.3-g
Guldberg s rule for critical temperature, 5.1.1-l
Guy, A. R., 3.2.1-1/3.2.6-2

H

Hagen-Poseville law, 2.1.1-2,2.2.2-l, 2.2.2-3
Hagen-Rubens relation, between electrical and optical constants, 2.9.2-10

© 1983 Hemisphere Publishing Corporation

Hampson **coils (see Helical** coils)
Handley and Heggs equation for fixed bed pressure drop, 2.2.5-3
Harris, D., 4.3.6-1/4.3.6-23
Hausen equation for developing laminar flow, 2.5.1-2
Headers in shell-and-tube heat exchangers, 2.2.7-1/2.2.7-2
inlet distribution header, 2.2.7-5 /2.2.7-6
outlet combining headers, 2.2.7-6/2.2.7-7
tube entry/exit pressure loss, 2.2.7-7/2.2.7-8
Heads, in heat exchangers:
analytic basis for codes, 4.3.3-l
constructional features of affecting mechanical design, 4.2.6-1/4.2.6-2
index of U.K., U.S.A., and F.R.G. codes for, 4.3.2-4/4.3.2-5
mechanical design of, 4.1.8-1
types of, in shell-and-tube exchangers, 4.2.4-1/4.2.4-2
bolted channel, 4.2.4-l
bolted cone, 4.2.4-2
Bonnett type, 4.2.4-1/4.2.4-2
high pressure, 4.2.4-2/4.2.4-3
welded channel, 4.2.4-l
Heat and mass transfer:
combined, 2.1.6-1/2.1.6-4
in condensation, 2.1.6-2/2.1.6-4
in cooling towers, 3.12.2-1/3.12.2-3
in drying, 2.1.6-1/2.1.6-2
in heat exchangers, 1.1.2-1, 1.2.2-3/1.2.2-4
in single-phase free convection, 2.5.7-12/2.5.7-13
relations between, 1.2.3-6/1.2.3-7
state of the art, 2.1.7-1/2.1.7-8
Heat capacity (see Specific heat capacity)
Heat conduction (see Conduction, heat)
Heat exchanger design, introduction, 3.1.1-1/3.1.4-9
approximate sizing of shell-and-tube heat exchangers, 3.1.4-1/3.1.4-9
basic design equation, 3.1.4-1
estimation of heat load, 3.1.4-1/3.1.4-2
estimation of mean temperature difference, 3.1.4-2/3.1.4-3
estimation of overall heat transfer coefficient, 3.1.4-3/3.1.4-6
estimation of surface area, 3.1.4-6/3.1.4-7
example, 3.1.4-7/3.1.4-9
fundamental concepts, 3.1.1-1/3.1.1-3
basic design equation, 3.1.1-2
heat transfer coefficients, 3.1.1-1
mean temperature difference, 3.1.1-2/3.1.1-3
logic of the design process, 3.1.3-1/3.1.3-4
criteria for successful design, 3.1.3-1/3.1.3-2
relationship among selection rating and design, 3.1.3-2/3.1.3-4
simplified example of design modification algorithm for computer, 3.1.3-3/3.1.3-4
types of heat exchangers and their applications, 3.1.2-1/3.1.2-6
air-cooled, 3.1.2-4/3.1.2-5
double-pipe, 3.1.2-1/3.1.2-2
mechanically aided, 3.1.2-5
plate fin or matrix, 3.1.2-5
plate heat, 3.1.2-3/3.1.2-4
shell-and-tube, 3.1.2-2/3.1.2-3
Heat exchangers:
agitated vessels, 3.14.1-1/3.14.3-8
air-cooled, thermal design, 3.8.1-1/3.8.9-4
condensers, 3.4.1-1/3.4.9-5
corrosion and other damage, 4.5.3-1/4.5.3-7
costing, 4.8.1-1/4.8.4-2
air-cooled, 4.8.3-1/4.8.3-3
plate, 4.8.4-1/4.8.4-2
shell-and-tube, 4.8.2-1/4.8.2-5
definitions and quantitative relationships, 1.2.0-1/1.2.6-7
balance equations for equipment, 1.2.4-1/1.2.4-7
differential equations for streams in, 1.2.5-1/1.2.5-3
flux relationships, 1.2.2-1/1.2.2-4
partial differential equations for interpenetrating continua in, 1.2.6-1/1.2.6-7
thermodynamic concepts, 1.2.1-1/1.2.1-3
transfer coefficient dependences,1.2.3-1/1.2.3-7
description of, 1.1.0-1/1.1.6-1
equipment forms, 1.1.5-1/1.1.5-3
interactions between streams in, 1.1.2-1/1.1.2-2
interfaces between streams in, 1.1.4-1/1.1.4-2
temperature change patterns, 1.1.3-1/1.1.3-2
types of flow configuration, 1.1.1-1/1.1.1-4
unsteady operation, 1.1.6-1
design, 3.1.1-1/3.1.4-9
double pipe, 3.2.1-1/3.2.6-2
application of, 3.2.2-l
construction/mechanical design, 3.2.5-1/3.2.5-2, 4.4.4-1/4.4.4-2
design parameters, 3.2.3-1/3.2.3-6
introduction, 3.2.1-1
operational advantages, 3.2.6-1/3.2.6-2
types available, 3.2.4-1/3.2.4-2
F-correction method for, 1.2.4-4, 1.3.1-2/1.3.1-4
F-factor charts for, 1.5.2-3/1.5.3-12
gas-liquid pressure drop in, 2.3.2-12/2.3.2-13
liquid metal heat transfer in, 2.5.13-8/2.5.13-4
materials of construction, 4.5.2-1/4.5.2-6
mechanical design: air-cooled, 4.4.1-1/4.4.1-7
basic principles, 4.1.1-1/4.1.8-3
block type, 4.4.4-4
direct contact, 4.4.4-6/4.4.4-8
double-pipe, 3.2.5-1/3.2.5-2, 4.4.4-1/4.4.4-2
example of design, 4.3.6-1/4.3.6-23
heat pipes, 4.4.4-9/4.4.4-11
helical (Hampson) coils, 4.4.4-8/4.4.4-9
jacketed heaters, 4.4.4-3/4.4.4-4
plate fin heat exchangers, 4.4.3-1/4.4.3-9
plate heat exchangers, 4.4.2-1/4.4.2-8
scraped surface, 4.4.4-5/4.4.4-6
shell-and-tube (codes), 4.3.1-1/4.3.5-1
shell-and-tube (construction), 4.2.1-1/4.2.6-13
spiral plate, 4.4.4-5
tubular and panel immersion, 4.4.4-2/4.4.4-3
numerical solution methods for: with calculation of flow pattern, 1.4.2-1/1.4.2-4
with prescribed flow patterns, 1.4.1-1/1.4.1-6
plate fin, 3.9.1-1/3.9.13-4
plate, thermal design of, 3.7.1-1/3.7.12-2
P-NTU method for, 1.2.4-4/1.2.4-5, 1.3.1-2
pressure drop in headers, nozzles, and turnarounds, 2.2.7-l
radiant, 2.9.84
representation as interpenetrating continua, 1.2.6-1/1.2.6-7
shell-and-tube (single phase), thermal design of, 3.3.1-1/3.3.11-5
θ method chart for, 1.5.2-1/1.5.3-12
θ method for, 1.2.4-5, 1.3.1-2/1.3.1-4
Heat generation number (Cn), 2.3.12-6
Heating media, for reboilers, 3.6.2-10
Heat of vaporization, 5.1.3-2/5.1.3-4
of commonly used fluids, 5.5.1-1/5.5.1-40

© 1983 Hemisphere Publishing Corporation

Heat pipes:
axial heat transfer and operational envelope for, 3.10.4-l
characteristics of wicks for, 3.10.6-1/3.10.6-2
circulation and axial heat transfer in, 3.10-2-1/3.10.2-3
introduction to, 3.10.1-1/3.10.1-2
mechanical design of exchangers using, 4.4.4-914.4.4-l 1
selection of working fluid for, 3.10.5-1/3.10.5-2
start-up and control of, 3.10.7-1/3.10.7-2
temperature distribution and radial heat flux in, 3.10.3-1/3.10.3-2
Heat transfer:
analogy with mass transfer, 2.1.5-1/2.1.5-4
augmentation of (see Augmentation of heat transfer)
in cooling towers, 3.12.2-1/3.12.2-2
enhancement of, (see Augmentation of heat transfer)
in fluidized beds, fluid-to-particle, 2.5.5-2/2.5.5-6
in non-uniform systems, 2.1.4-1/2.1.4-4
in packed beds, 2.1.4-3/2.1.4-4
in shell-and-tube heat exchangers, 2.1.4-1/2.1.4-3
single phase convective (see Convective heat transfer, single phase)
in transition flow over flat plate, 2.2.1-25
in tubes: Colburn *j*-factor (laminar and turbulent), 2.1.3-7
correlations for, 2.5.1-1/2.5.1-11
Nusselt numbers for (laminar and turbulent), 2.1.36
in turbulent flow over flat plates, 2.2.1-29/2.2.1-30
by radiation (see Radiative heat transfer)
Heat transfer coefficient:
in agitated vessels, 3.14.3-1/3.14.3-8
in air-cooled heat exchangers, 3.8.5-1/3.8.5-5
average and overall values for, discussion, 1.2.4-2/1.2.4-3
in bed-to-wall heat transfer in fluidized beds, 2.8.4-1/2.8.4-7
in boiling in a vertical tube, 2.7.3-1/2.7.3-37
variation with quality of, 2.7.3-3
in boiling in horizontal tubes, bends, and coils, 2.7.4-1/2.7.4-7
in boiling of binary and multicomponent mixtures: forced convective, 2.7.8-1/2.7.8-10
pool boiling, 2.7.7-1/2.7.7-7
in boiling on outside of single tubes and tube banks, 2.7.5-1/2.7.5-7
in combined free and forced convection: in channels, 2.5.10-1/2.5.10-10
over immersed bodies, 2.5.9-1/2.5.9-6
in condensation, 2.6.1-2
in double-pipe exchangers, 3.2.3-3/3.2.3-3
in evaporators, 3.5.6-1/3.5.7-3
in fixed beds: between wall and bed, stagnant (no flow) conditions, 2.8.1-5/2.8.1-10
particle-to-fluid, 2.5.4-1, 2.8.3-1/2.8.3-3
in flow over tube banks, 2.5.3-1/2.5.3-8
in fluidized beds: particle-to-fluid heat transfer, 2.5.5-1/2.5.5-6
in free convection: in layers and enclosures, 2.5.8-1/2.5.8-25
over immersed bodies, 2.5.7-1/2.5.7-31
individual, definition of, 1.2.2-1/1.2.2-2, 2.1.2-6
typical values of, 2.1.2-6
internal, use in transient conduction calculations, 2.4.3-7/2.4.3-8
with liquid metals, 2.5.13-1/2.5.13-4
local, definition, 2.5.1-1
mean, along duct, 2.5.1-1
in moving, agitated, and vibrated beds of particles, 2.8.3-3/2.8.3-9
in non-Newtonian flows, 2.5.12-1/2.5.12-16
numerical calculation of, 1.4.3-3/1.4.3-4
overall definition of, 1.2.2-1/1.2.2-2, 2.1.2-1, 3.1.1-1
in various heat exchangers, 2.1.2-3/2.1.2-4
in plate fin exchangers, 3.9.4-1/3.9.6-2
in plate heat exchangers, 3.7.5-l
in pool boiling, 2.7.2-1/2.7.2-17
radiation, 2.9.8-2
in reboilers, 3.6.2-1/3.6.2-10
on the shell side in shell-and-tube heat exchangers, 3.3.1-1/3.3.11-5
in single-phase flow in ducts: laminar flow, 2.5.1-3/2.5.1-4
turbulent flow, 2.5.1-5/2.5.1-11
volumetric, 1.1.2-2
Heat transfer regimes:
in boiling in a vertical tube, 2.7.3-2
in free and forced single-phase convection, 2.5 .10-2
Heated cavity reflectometer, 2.9.2-7
Heggs, P. J., 2.2.5-1/2.2.5-5
Helical coils:
in agitated vessels, 3.14.2-2/3.14.2-3
heat transfer to, 3.14.3-1/3.14.3-2
augmentation of boiling heat transfer using, 2.7.94
convective boiling in, 2.7.4-5/2.7.4-6
cooler, approximate overall heat transfer coefficients in, 2.1.24
dryout in evaporative heat transfer in, 2.7.4-3/2.7.4-4
Hampson-type for heat exchangers, 4.4.4-8/4.4.4-9
single-phase flow and pressure drop in, 2.2.2-14/2.2.2-16, 2.5.11-6/2.5.11-7
single-phase heat transfer in, 2.5.11-6/2.5.11-7
Helical inserts, for enhancement of heat transfer in boiling, 2.7.9-3
Helical ribbon agitator:
description, 3.14.2-1/3.14.2-2
heat transfer with, 3.14.3-3/3.14.3-4
Helium:
saturation properties, 5.5.1-33
superheated, thermodynamic properties, 5.5.2-1/5.5.2-2
Helmholtz reciprocity principle, in radiative heat transfer, 2.9.2-6
Henry, J. A. R., 2.2.7-112.2.7-l 1
Henry-Fauske model, for critical two-phase flow, 2.3.2-28/2.3.2-29
Henry s law, for partial pressure, 2.7.6-l
Heptane saturation properties, 5.5 .l-9
Heterogeneous conveyance in horizontal pipes, 2.3.4-3/2.3.4-6
Heterogeneous nucleation in boiling, 2.7.1-3/2.7.1-5
Hewitt, Geoffrey F., 2.3.1-1/2.3.2-33
Hexagonal cells, in free convection, 2.5.8-2
Hexane saturation properties, 5 .5 .l-8
Hicks equation, for fixed-bed pressure drop, 2.25-3
High finned tubes, correlations for single-phase heat transfer in flow over, 2.5.3-11/2.5.3-12
Hohlraum cavity, 2.9.1-3
Holland, guide to national practice for mechanical design of heat exchangers, 4.3.5-5
Homogeneous condensation (fog formation), 2.6.1-1
effects, 2.6.7-3
nuclei formation, 2.6.7-1/2.6.7-2
supersaturation, 2.6.7-1/2.6.7-3
Homogeneous model:
conservation equations for, in multiphase flows, 2.3.1-4/2.3.1-7
in gas-liquid flows: conservation equations, 2.3.2-8
critical flow estimation by, 2.3.2-28
frictional pressure drop correlations based on, 2.3.2-10
pressure drop in singularities calculated by, 2.3.2-15/2.3.2-18

© 1983 Hemisphere Publishing Corporation

Homogeneous model (Cont.):
in solid-liquid flow, 2.3.4-2/2.3.4-3
Homogeneous nucleation:
of droplets in supersaturated vapor, 2.6.7-1/2.6.7-2
of vapor bubbles in liquids, 2.7.1-2/2.7.1-3
table of values of temperature for various substances, 2.7.1-4
Honeycombs:
free convective heat transfer in, 2.5.8-20/2.5.8-23
loss coefficients in, 2.2.2-20
Horizontal cylinders:
free convective heat transfer inside, 2.5.8-14
(See *also* Cylinders, Horizontal tubes)
Horizontal layers, of fluid, free convection heat transfer in, 2.5.8-1/2.5.8-3
Horizontal pipes:
hydraulic conveyance in, 2.3.4-1/2.3.4-6
pneumatic conveyance in, 2.3.3-1/2.3.3-2
(See also Pipes, circular; Horizontal tubes)
Horizontal plates (see Horizontal surfaces; Flat plates)
Horizontal shell-side evaporator, 3.5.2-l
Horizontal surfaces:
combined free and forced convection in transverse flow over, 2.5.9-4/2.5.9-6
free convective heat transfer from, 2.5.7-13/2.5.7-18
downward facing surfaces, 2.5.7-13/2.5.7-15
upward facing surfaces, 2.5.7-15 /2.5.7-18
pool boiling from, 2.7.2-1/2.7.2-15
Horizontal thermosiphon reboilers:
calculation procedures for, 3.6.5-2/3.6.5-3
characteristics, advantages and disadvantages of, 3.6.1-3
thermal design, 3.6.2-1/3.6.2-6
bubbleinduced convection effects, 3.6.2-2/3.6.2-3
critical heat flux and film boiling, 3.6.2-4/3.6.2-5
effective mean temperature difference, 3.6.24
externally induced convection effects, 3.6.2-3
finned tubes in, 3.6.26
flow distribution and hydraulics of, 3.6.2-6
mixture effects, 3.6.2-3/3.6.2-4
single tube nucleate boiling, 3.6.2-1/3.6.2-2
vapor liquid disengagement in, 3.6.2-6
Horizontal tube-side evaporator, 3.5.2-5/3.5.2-6
Horizontal tubes:
boiling outside with crossflow, 2.7.5-1/2.7.5-4
combined free and forced convection in, 2.5.10-7/2.5.10-l 1
with uniform heat flux, 2.5.10-7/2.5.10-l 1
with uniform wall temperature, 2.5.10-7
combined free and forced convective heat transfer from outside, 2.5.9-1/2.5.9-6
condensation on inside, 2.6.2-12/2.6.2-15, 3.4.6-1/3.4.6-2
annular flow, 2.6.2-15
flow regimes, 2.6.2-12/2.6.2-13, 3.4.6-2
stratifying flow, 2.6.2-13/2.6.2-14, 3.4.6-2
condensation on outside of, 2.6.2-9/2.6.2-12, 3.4.6-3
in bundles, 2.6.2-1012.6.2-l 2
effect of vapor shear, single tube, 2.6.2-9/2.6.2-10
laminar flow, single tube, 2.6.2-9
condensers with condensation inside, 3.4.3-3/3.4.3-4, 3.4.9-3
condensers with condensation outside, 3.4.3-5/3.4.3-6, 3.4.9-3/3.4.9-4
convective boiling in, 2.7.4-1/2.7.4-7
dryout in, 2.7.4-1/2.7.4-4
heat transfer in, 2.7.4-4/2.7.4-6
flow regimes in gas-liquid flow in, 2.3.2-2/2.3.2-4
free convective heat transfer from outside of, 2.5.7-20/2.5.7-23
heat transfer to, in fluidized beds, 2.8.4-6/2.8.4-7
hydrodynamics of various two-phase flow regimes in, 2.3.2-23/2.3.2-26
annular flow, 2.3.2-25/2.3.2-26
slug flow, 2.3.2-24/2.3.2-25
stratified flow, 2.3.2-23/2.3.2-24
pool boiling from, 2.7.2-1/2.7.2-15
(See also Horizontal pipes; Pipes, circular)
Hottel s rule, in absorption of radiation by gases, 2.9.5-7
Hsu criterion, for onset of nucleate boiling, 2.7.2-2
Hybrid cooling towers, 3.12.5-1/3.12.5-5
assisted draft towers, 3.12.5-3/3.12.5-4
closed circuit evaporative coolers, 3.12.5-4/3.12.5-5
wet-dry towers, 3.12.5-2/3.12.5-3
Hydraulic conveyance:
homogeneous and pseudohomogeneous, 2.3.4-2/2.3.4-3
in horizontal tubes: flow regimes in, 2.3.4-l/2.3.4-2
heterogeneous conveyance in, 2.3.4-3/2.3.4-6
Hydraulically smooth surface, 2.2.2-l
Hydrocarbons:
phase behavior, 5.2.1-3/5.2.1-4
thermodynamic properties, 5.2.2-115.2.2-g
Hydrodynamic entrance length, in single-phase flow in ducts, 2.2.2-10/2.2.2-11
Hydrogen:
saturated properties, 5.5.1-33
supersaturated gaseous, thermodynamic properties, 5 5.24
Hydrogen chloride saturation properties, 5.5.1-34
Hydrogen fluoride saturation properties, 5.5.1-34
Hydrogen sulfide saturation properties, 5.5 .1-35
Hydrostatic testing of shell-and-tube heat exchangers, 4.2.6-11/4.2.6-13
Hysteresis: in boiling curve, 2.7.2-8
reduction of, using porous surfaces, 2.7.9-3

I

Ideal gas law, 2.2.1-7
Ideal gas, velocity of sound in, 2.2.1-8
Illingworth, A., 4.7.1-1/4.7.10-1
Immersed bodies:
combined free and forced convection around, 2.5.9-1/2.5.9-6
creeping flow regime (assisting convection), 2.5.9-3
opposing convection, 2.5.94
slightly inertial regime (assisting convection), 2.5.9-3/2.5.9-4
thin boundary layer regime (assisting convection), 2.5.9-1/2.5.9-3
transverse flow, 2.5.9-4/2.5.9-6
turbulent regime (assisting convection), 2.5.94
free convective heat transfer to, 2.5.7-1/2.5.7-31
generalized solutions for, 2.5.7-25/2.5.7-28
horizontal cylinders, 2.5.7-20/2.5.7-23
inclined and horizontal surfaces, 2.5.7-l 312.5.7-l 9
open-ended channels, 2.5.7-19/2.5.7-20
other shapes, 2.5.7-25
spheres, 2.5.7-24/2.5.7-25
vertical cones, 2.5.7-24
vertical and inclined cylinders, 2.5.7-23/2.5.7-24
vertical plates, 2.5.7-2/2.5.7-13
single-phase flow over, 2.2.3-1/2.2.3-9
circular cylinder, 2.2.3-3/2.2.3-6
flow regimes in, 2.2.3-l/2.2.3-2
forces exerted on, in, 2.2.3-2/2.2.3-3

© 1983 Hemisphere Publishing Corporation

immersed bodies (Cont.):
noncircular cylinders, 2.2.3-612.2.3-l
single-phase forced convective heat transfer to: flat plates, 2.5.2-1/2.5.2-3
single bodies, 2.5.2-3/2.5.2-8
Immersed tubes, heat transfer to, in fluidized beds, 2.8.4-6/2.8.4-7
Immersion exchangers, 4.4.4-2/4.4.4-3
Immersion heaters, 4.4.4-2/4.4.4-3
Immiscible liquids, condensation of vapors producing, 2.6.4-1/2.6.4-7
description, 2.6.1-1, 2.6.4-l
eutectic mixtures, 2.6.4-2/2.6.4-3
Imperfectly diffuse surfaces:
definition, 2.9.4-l
radiative heat transfer between specular surfaces and, 2.9.4-1/2.9.4-l 1
Impingement damage in heat exchangers, 4.5.3-l
Impingement plate:
constructional features of, 4.2.5-7/4.2.5-8
effect on inlet pressure drop in shell-and-tube heat exchangers, 2.2.7-4/2.2.7-5
in condensers, 3.4.3-5
(See also Impingement protection)
Impingement protection, in shell-and-tube heat exchangers, 3.3.5-10/3.3.5-11
with condensation, 3.4.3-5
Impinging jets:
single-phase heat transfer in, 2.5.6-1/2.5.6-10
average coefficients in, 2.5.6-3/2.5.6-4
local coefficients in, 2.5.6-2/2.5.6-3
Inclined cylinders (see Inclined pipes; Cylinders)
Inclined enclosures, free convective heat transfer in, 2.5.8-17/2.5.8-20
large aspect ratios, 2.5.8-17/2.5.8-19
moderate aspect ratios, 2.5.8-20
Inclined flow, effect of on heat transfer to cylinders, 2.5.2-4/2.5.2-5
Inclined pipes:
flow regimes in gas-liquid flow in, 2.3.2-4/2.3.2-5
free convection heat transfer on outside of, 2.5.7-23/2.5.7-24
pneumatic conveying (solid/gas flow) in, 2.3.3-2
(See ***also*** Pipes, circular)
Inclined plates (see Inclined surfaces; Flat plates)
Inclined surfaces, free convective heat transfer from, 2.5.7-13/2.5.7-18
downward facing surfaces, 2.5.7-13/2.5.7-15
upward facing surfaces, 2.5.7-15/2.5.7-18
Inclined tubes (see Pipes, circular; Pipes, noncircular; Inclined Pipes; Cylinders)
Incondensables (see Noncondensables)
Inconel, spectral characteristics of reflectance from oxidized surface of, 2.9.2-15
Incremental collapse, as failure mode in heat exchanger, 4.1.1-3/4.1.1-5
Inert gases, effect on condensation, 2.1.6-3/2.1.6-4
Injection:
effect in transition flow over flat plate, 2.2.1-25
effect in turbulent flow over flate plates, 2.2.1-30
effect on laminar flow on flat plate, 2.2.1-23
use in augmentation of heat transfer, 2.5 .l 1-3/2.5 .l l-9
Inlet effects in shell-and-tube heat exchangers, 3.3.6-9/3.3.6-10
In-life flow, bundles of tubes (see Tube banks)
In-line tube banks:
correction for heat transfer in, 2.5.3-1/2.5.3-16
finned tubes, 2.5.3-l 1
plain tubes, 2.5.3-2
drag coefficients for tubes in, 2.2.44
pressure drop in with finned tubes, 2.2.4-14
pressure drop in with plain tubes, 2.2.4-7/2.2.4-8
correction factors for small number of tube rows, 2.2.4-10
effect of yawing on, 2.2.4-12
Inspection (see Testing and inspection)
Insulators, thermal conductivity of, 5.4.3-l/5.4.3-2
Integral condensation:
calculation of condensation curves for, 2.6.3-3/2.6.3-4
description, 2.6.3-1/2.6.3-3
Integral fined tubes:
as augmentation device in natural convection, 2.5 .ll-3
use in shell-and-tube heat exchangers, 4.2.5-3
Interaction coefficients in heat exchangers, 1.1.2-1/1.1.2-2
Interaction parameters for binary systems, tables, 5.5.4-8/5.5.4-9
Interfacial resistance, in condensation, 2.6.2-15
Interfacial roughness, relationships for, in annular gas-liquid flow, 2.3.2-20/2.3.2-21
Interfacial shear stress, effect on filmwise condensation:
on vertical surface, 2.6.2-5/2.6.2-7
Interfacial tension (see Surface tension)
Intermating troughs, as corrugation design in plate heat exchangers, 3.7.1-1, 3.7.3-1/3.7.3-2, 3.7.6-l
Intermittent flows:
gas liquid, in horizontal and inclined flows, 2.3.2-2/2.3.2-5
plug flow, in vertical pipes, 2.3.2-19
slug flow, in horizontal pipes, 2.3.2-24/2.3.2-25
Internal energy (see specific internal energy)
Internal heat sources, temperature distribution in bodies with, ***2.4.2-3***
Internal heat transfer coefficient, use in transient conduction calculations, 2.4.3-7/2.4.3-8
Internal reboilers (in distillation columns), characteristics, advantages and disadvantages of, 3.6.1-2/3.6.1-3
Internally finned tubes, heat transfer and pressure drop in, 2.5.11-5/2.5.11-6
International Standards Organization (see ISO)
Interpenetrating continua (as representation of heat exchangers):
partial differential equations for, 1.2.6-1/1.2.6-7
porosity in, 1.2.6-2
Intertube velocity, in tube banks, 2.2.4-3
Inviscid flow, compressible, with heat addition, 2.2.2-13/2.2.2-14
Irvine, T. F., Jr., 2.4.6-1/2.4.6-4
ISO codes for mechanical design of heat exchangers, 4.3.1-3
Isobutane saturated properties, 5 .5.1-6
Isopentane saturation properties, 5.5.1-7
Isothermal flow, compressible, in ducts, 2.2.2-13
Isothermal gas, radiation heat transfer to walls from, 2.9.6-1/2.9.6-9
Isotropic materials, elastic properties, 5.4.5-3/5.4.5-4
Isotropic scattering, 2.9.5-2
Italy, guide to national practice for heat exchanger mechanical design, 4.3.5-7

J

J-type shells, in shell-and-tube heat exchangers:
calculation of heat transfer and pressure drop in, 3.3 .1 l-l
description of, 3.3.4-3
temperature difference correction (F) and θ-NTU charts for, 1.5.2-11/1.5.2-12
Jacket-type heaters, 4.4.4-3/4.4.4-4

© 1983 Hemisphere Publishing Corporation

Jacob number, 2.7.1-8
Japan, guide to national practice for heat exchanger mechanical design:
high-pressure gas control law, 4.3.5-9
standard construction (JISB8243), 4.3.5-8
Jayatillaka relation, between heat and momentum transfer, 1.2.3-6
Jens and Lottes correlation for subcooled forced convective boiling of water, 2.7.3-8
Jet impingement dryer, 3.13.24
Jets, impinging (see Impinging jets)

K

Kapitza number, 2.1.7-4/2.1.7-5
Kern method, for shell-side heat transfer in shell-and-tube heat exchangers, 3.3.2-2
Kesler and Lee equations, for critical temperature, critical pressure, acentric factor and molecular weight, 5.2.1-6/5.2.1-8
Kettle reboilers:
calculation procedures for, 3.6.5-1/3.6.5-2
characteristics, advantages and disadvantages of, 3.6.1-2
constructional features of, 4.2.3-7/4.2.3-8
thermal design, 3.6.2-1/3.6.2-6
bubble-induced convection effects, 3.6.2-2/3.6.2-3
critical heat flux and film boiling, 3.6.2-4/3.6.2-5
effective mean temperature difference, 3.6.2-4
externally induced convection effects, 3.6.2-3
finned tubes in, 3.6.2-6
flow distribution and hydraulics, 3.6.2-6
mixture effects, 3.6.2-3/3.6.2-4
single tube nucleate boiling, 3.6.2-1/3.6.2-2
vapor-liquid disengagement in, 3.6.2-6
Kirchoff s law, in radiative heat transfer, 2.9.2-2
Knudsen number, 2.2.1-11
K-values, in phase equilibrium, 5.2.1-3

L

Lamella heat exchangers, 3.1.2-3/3.1.2-4
Laminar boundary layers (see Boundary layers)
Laminar flow:
combined free and forced convective heat transfer in, 2.5.10-1/2.5.10-11
condensation in vertical surfaces, 2.6.2-2/2.6.2-4
heat transfer in ducts in, 2.5.1-2/2.5.1-5
augmentation of, 2.5.11-4/2.5.11-8
in concentric annular ducts, 2.5.1-3
free convection effects in, 2.5.1-4/2.5.1-5
with liquid metals, 2.5.13-l/2.5.13-2
between parallel plates, 2.5.1-3
in straight circular pipes, 2.5.1-2
heat transfer in free convection on a vertical surface in, 2.5.7-3
heat transfer in tube bundles in, 2.5.13-2/2.5.13-3
in circular pipes, 2.2.2-1/2.2.2-2
in ducts, characteristic of plate fin heat exchangers, 3.9.5-1/3.9.5-3
in noncircular pipes, 2.2.2-7/2.2.2-9
Laminar flow control, of boundary layers, 2.2.1-25
Laminar sublayer (see Viscous sublayer)
Lancaster, J. F., 4.5.1-1/4.5.3-7
Large eddy simulation, in prediction of turbulent boundary layers, 2.2.1-29
Latent heat (see Heat of vaporization)
Laws for turbulent flows:
of the wake, 2.2.1-26
of the wall, 2.2.1-25
velocity defect, 2.2.1-26
Layers of fluid, free convection heat transfer in, 2.5.8-1/2.5.8-3
Le Fevre equations for free convective heat transfer, 2.5.7-3
Leakage between streams, in shell-and-tube heat exchangers, 3.3.4-4/3.3.4-5, 4.6.1-2
Leakage effects, on heat transfer and pressure drop in shell-and-tube heat exchangers, 3.3.1-1/3.3.11-5
shell-to-baffle: correction factors, 3.3.6-6/3.3.6-8
leakage area, 3.3.6-4/3.3.6-5
tubes-to-baffle: correction factors, 3.3.6-6/3.3.6-8
leakage area, 3.3.6-5
Lessing rings, characteristic of, as packings for fixed beds, 2.2.5-2
Lienhard and Dhir analysis of critical heat flux in pool boiling, 2.7.2-10/2.7.2-12
Lienhard and Eichhorn criterion, for transition in critical heat flux mechanism in crossflow over single tube, 2.7.5-3
Lift force:
in flow in tube banks, 2.2.4-16
in flow over immersed bodies, 2.2.3-3
Liley, P. E., 5.5.6-1/5.5.7-3
Liquid fuels, properties of, 3.11.3-3
Liquid hold-up, 2.3.1-3
Liquid metals:
heat transfer in, 2.5.13-1/2.5.13-4
in channel flows, 2.5.13-1/2.5.13-4
condensation of, 2.6.2-15/2.6.2-16
in heat exchangers, 2.5.13-3
Liquid-solid flow (see Solid-liquid flow)
Liquids:
as constituent in multiphase flows, 2.3.1-1/2.3.1-2
physical properties of:
in multicomponent mixtures, 5.2.3-1/5.2.4-4
rheologically complex, 5.3.1-1/5.3.8-3
saturated property tables for, 5.5.1-1/5.5.1-40
specific heat capacity, 5 .1.3-7
specific volume, 5.1.2-1/5.1.2-2
surface tension, 5.1.5-1/5.1.5-3
thermal conductivity, 5.1.4-6/5.1.4-7
thermal expansion coefficient, 5 .1.2-2
viscosity, 5.1.4-1/5.1.4-5
LMTD (see Logarithmic mean temperature difference)
Loads, types of in heat exchangers, 4.1.1-1
Local conditions hypothesis, for critical heat flux in flow boiling, 2.7.3-18/2.7.3-19
Lockhart and Martinelli correlations:
for frictional pressure gradient, 2.3.2-10
for void fraction, 2.3.2-l 7
Lodge s rubber-like liquid (non-Newtonian), 2.2.8-8
Logarithmic driving force in mass transfer, 2.1.5-3
Logarithmic law region, 2.2.2-l
Logarithmic Mean Temperature Difference, 1.2.4-2/1.2.4-3, 2.1.2-2, 2.5.1-1, 3.1.1-2
Longitudinal fins (see Straight fins)
Long-tube vertical evaporator, 3.5.2-3/3.5.2-4
Loss coefficient, 2.2.2-14
for bends, 2.2.2-16
in combining and dividing flow, 2.2.2-19/2.2.2-20
for diffusers, 2.2.2-17/2.2.2-18
values for various fittings, 2.2.2-19/2.2.2-20

© 1983 Hemisphere I ublishing Corporation

Louvered fins, in plate fin exchangers, 3.9.3-l
Low-alloy steels, as material of construction, 4.5.2-3
Low-finned tubes:
application in shell-and-tube heat exchangers, 3.3.1 l-2/3.3.1 1-3
correlations for single phase heat transfer in flow over, 2.5.3-12/2.5.3-11
use in boiling augmentation, 2.7.9-1/2.7.9-2
Lubricants, physical properties of:
classification, 5.3.2-l
lubricant-cooling liquids, 5.3.5-1/5.3.5-2
oils, 5.3.3-1/5.3.3-2
plastic lubricants, 5.3.4-1/5.3.4-2
Ludwieg-Tillmann formula, for skin friction, 2.2.1-26
Lydersen's incremental method, for critical parameters, 5.1.1-1/5.1.1-2

M

Macdonald equation, for fixed-bed pressure drop, 2.2.5-3
Mach number, 2.2.1-11
effect on turbulent flow over flat plate, 2.2.1-30
incompressible duct flows with heat transfer, 2.2.2-12
Maddox, R. N., 5.2.1-1/5.2.5-5, 5.5.1-1/5.5.2-11, 5.5.4-1/5.5.4-9
Magnetic fields, effect on properties of rheologically complex materials, 5.3.8-1/5.3.8-2
Manifolds (see Headers)
Martin, H., 2.4.1-1/2.4.5-4, 2.5.5-1/2.5.6-10
Martinelli and Boelter equations for combined free and forced convection, 2.5.10-2/2.5.10-3
Martinelli and Nelson correlations:
for frictional pressure gradient, 2.3.2-10/2.3.2-l 1
for void fraction, 2.3.2-14
Mass absorption coefficient, 2.9.5-2
Mass and heat transfer, combined:
in condensation, 2.1.6-2/2.1.6-4
in drying, 2.1.6-1/2.1.6-2
Mass extinction coefficient, 2.9.5-2
Mass fraction, in multicomponent mixtures, 1.2.1-2
Mass scattering coefficient, 2.9.5-2
Mass transfer:
analogy with heat transfer, 2.1.5-1/2.1.5-4
in cooling towers, 3.12.2-2/3.12.2-3
in condensation: in multicomponent mixtures, 2.6.3-7/2.6.3-8
of binary mixtures, 2.6.3-7
of single vapor with noncondensables, 2.6.3-5/2.6.3-7
with impinging jets, 2.5.6-1/2.5.6-10
in fixed beds, 2.5.4-2/2.5.2-6
in fluidized beds, 2.5.5-3/2.5.5-6
in nonuniform systems, 2.1.4-1/2.1.4-4
volumetric coefficient for, 1.1.2-2
Mass transfer coefficient:
in fixed beds, 2.5.4-1/2.5.4-6
individual definition of, 1.2.2-2/1.2.2-3, 2.1.5-2/2.1.5-3
Matovosian, Robert, 5.5.5-1/5.5.5-4
Materials of construction, for heat exchangers, 4.5.1-1/4.5.3-7
materials for corrosive service, 4.5.2-2/4.5.2-6
austenitic stainless steels, 4.5.24
carbon steel, 4.5.2-2/4.5.2-3
coatings, 4.5.2-5/4.5.2-6
copper base alloys, 4.5.2-4/4.5.2-5
ferritic chromium stainless steels, 4.5.2-3
low alloy steels, 4.5.2-3
nickel based alloys, 4.5.2-5
non-metallic materials, 4.5.2-6
titanium, 4.5.2-5
materials for noncorrosive service, 4.5.2-2
product forms, 4.5.2-1/4.5.2-2
shells, channels, covers, and bonnets, 4.5.2-1/4.5.2-2
tubes, 4.5.2-l
tubesheets, 4.5.2-1
testing and inspection of, 4.7.2-l
Matrix heat exchangers (see Plate fin heat exchangers)
Matrix inversion techniques, in radiative heat transfer, 2.9.3-7/2.9.3-8
Maximum bed-to-surface heat transfer, in fluidized beds, 2.8.4-4/2.8.4-5
Maximum heat flux:
by conduction in solids, 2.1.1-2
in condensation, 2.1.7-4/2.1.7-6
under free molecule conditions in gases, 2.1.1-2
Maximum mass flux:
in condensation, 2.1.7-4/2.1.7-6
under free molecule conditions, 2.1.1-2
Maximum shear stress, under free molecule conditions, 2.1.1-2
Maximum velocities (in shell-and-tube heat exchangers), 3.3.5-15, 4.5.3-3
Maxwell model, for non-Newtonian fluid, 2.2.8-7
Maxwell velocity of a vapor, as limiting phenomenon in condensation, 2.1.7-4/2.1.7-6
Maxwell s equations, for electromagnetic radiation, 2.9.2-7/2.9.2-8
Mean-beam-length concept, in radiative heat transfer:
tables of geometric mean beam lengths, 2.9.6-5
theory of, 2.9.6-2/2.9.3
theory of, 2.9.6-2/2.9.6-3
Mean equivalent temperature, of a surface in combined convective and radiative heat transfer, 2.9.8-2
Mean phase content, 2.3.1-3
Mean temperature difference:
application in shell-and-tube heat exchangers, 3.3.5-l 7
concept of, 3.1.1-2/3.1.1-3
effective, in kettle reboilers, 3.6.2-4
in condensers, 3.4.8-1/3.4.8-3
(See *also* Logarithmic mean temperature difference, Arithmetic mean temperature difference)
Mechanical agitators, for agitated vessels, 3.14.2-1/3.14.2-2
heat transfer correlations for, 3.14.3-1/3.14.3-6
Mechanical design of heat exchangers:
air cooled heat exchangers, 4.4.1-1/4.4.1-7
basic principles, 4.1.1-1/4.1.8-3
expansion joints, 4.1.6-1
flanges, 4.1.7-1/4.1.7-2
heads, openings and branches, 4.1.8-l/4.1.8-2
introduction to, 4.1.1-1/4.1.1-5
methods of analysis, 4.1.2-1/4.1.2-9
shells, 4.1.3-1/4.1.3-3
tube plates, 4.1.4-1/4.1.4-3
tubes, 4.1.5-I
block type, 4.4.4-4
direct contact, 4.4.4-6/4.4.4-8
double-pipe exchangers, 3.2.5-l/3.2.5-2,4.4.4-1/4.4.4-2
heat pipes, 4.4.4-9/4.4.4-11
helical (Hampson) coils, 4.4.4-8/4.4.4-9
jacketed heaters, 4.4.4-3/4.4.4-4
plate fin heat exchangers, 4.4.3-1/4.4.3-9
plate heat exchangers, 4.4.2-1/4.4.2-8
shell-and-tube exchangers: constructional features, 4.2.1-1/4.2.6-13

© 1983 Hemisphere Publishing Corporation

Mechanical design of heat exchangers, shell-and-tube exchangers:
constructional features (Cont.):
design codes for, 4.3.1-1/4.3.5-l
example of design, 4.3.1-6/4.3.6-23
scraped surface, 4.4.4-5/4.4.4-7
spiral plate, 4.4.4-5
tubular and panel immersion, 4.4.4-2/4.4.4-3
Mechanical draft cooling towers, 3.12.4-1/3.12.4-2
thermal performance and design, 3.12.4-2/3.12.4-4
Mechanical draft fan coolers (see Air-cooled heat exchangers)
Melting, thermal conduction in, 2.4.4-1/2.4.4-2
Melting point of commonly used substances, 5.5.1-1/5.5.1-40
Mercury:
saturation properties, 5.5.1-35
superheated gaseous, thermodynamic properties of, 5.5.2415.5.2-j
Merkblatter (German) code, for mechanical design of heat exchangers, 4.3.1-3
index to, 4.3.2-1/4.3.2-4
Merkel s equation, in cooling tower design, 3.12.2-3
Metais and Eckert diagrams, for regimes of convection:
in horizontal pipes, 2.2.6-6, 2.5.10-1/2.5.10-2
in vertical pipes, 2.5.10-2
Metastable equilibrium, of vapor and liquid, 2.7.1-1
Methane saturation properties, 5 .5.1-4
Methanol saturation properties, 5.5.1-17
Methyl acetate saturation properties, 5.5.1-25
Methyl-t-butyl ether saturation properties, 5.5 .1-23
Metals:
condensation of, 2.6.2-15/2.6.2-16
density, 5.4.1-1
liquid, single-phase heat transfer in, 2.5.13-1/2.5.13-4
spectral absorptivity, 2.9.2-11/2.9.2-12
Microlayer evaporation, in boiling of binary mixtures, 2.7.6-7
Minimum heat flux in pool boiling:
of binary and multicomponent mixtures, 2.7.7-5/2.7.7-6
of pure components, 2.7.2-13/2.7.2-14
Minimum tubeside velocity, in shell-and-tube heat exchangers, 3.3.5-16
Minimum velocity for fluidization, 2.2.6-2
Minimum wetting rate, for binary mixtures, 2.7.8-7
Mirror-image concept, in radiative heat transfer, 2.9.4-1/2.9.4-2
Mirrors, spectral characteristics of reflectance from, 2.9.2-17
Mist flow:
in axial flow reboilers, 3.6.2-9
heat transfer in (see Post-dryout heat transfer)
onset, as mechanism for critical heat flux in reboilers, 3.6.2-8/2.6.2-9
Mixed convection, occurrence in horizontal circular pipe, Metais and Eckert diagram for, 2.2.2-6
Mixing length, 2.2.24
table of turbulent flow in circular pipes, 2.2.2-3
Mixing vessel (see Agitated vessel)
Mixtures:
of gases, radiation properties, 2.9.5-l l/2.9.5-12
condensers for, 3.4.4-1/3.4.4-2
(See ***also*** Binary mixtures, Multicomponent mixtures)
Models, theory of, 2.2.1-12/2.2.1-13
Modes of heat transfer, Nusselt description, 2.1.0-2
Molecular gas radiation properties, 2.9.5-8/2.9.5-1 1
Molecular weight:
of commonly used fluids, 5.5.1-1/5.5.1-40
Kesler and Lee equation for estimation of in hydrocarbon mixtures, 5.2.1-7
Molerus, O., 2.2.6-1/2.2.6-9
Mollier chart, for humid air, 3.13.1-1
description of drying processes in terms of, 3.13.3-4/3.13.3-5
Momentum equation:
in boundary layer, 2.2.1-17
in compressible duct flow, 2.2.1-12
differential form for single-phase flow, 2.2.1-5/2.2.1-7
in gas-liquid flows, 2.3.2-8/2.3.2-9
homogeneous model, 2.3.2-8
separated flow model, 2.3.2-8/2.3.2-9
in heat exchanger calculations, 1.2.6-5/1.2.6-7
integral form for single-phase flow, 2.2.1-2/2.2.1-3
in multiphase flows: homogeneous flow, 2.3.1-5
separated flow, 2.3.1-7
in non-Newtonian flow, 2.5.12-5
in turbulent flow, 2.2.1-14
Monte Carlo methods, in radiative heat transfer, 2.9.4-2/2.9.4-5
for radiative heat transfer with an isothermal gas, 2.9.6-8/2.9.6-9
Moody chart:
for critical two-phase flow, 2.3.2-28
for single-phase friction factor in circular pipes, 1.2.3-3, 2.2.2-2
Morcos and Bergles equation, for influence of free convection of friction factor, 2.2.2-6
Morris, M., 4.3.1-1/4.3.5-11
Mostinski correlations:
for critical heat flux, 3.6.2-5
for nucleate boiling, 2.7.2-6
application to kettle reboilers, 3.6.2-l
Moving bed, heat transfer to, 2.8.3-3/2.8.3-4
Moving belt, heat transfer to, 2.1.3-2/2.1.3-3
Muchowski, E., 2.8.3-1/2.8.3-9
Mueller, A. C., 3.4.1-1/3.4.9-5
Multicomponent mixtures:
an-cooled condensers for, 3.8.9-2/3.8.9-4
boiling of, in kettle reboilers, 3.6.2-3/3.6.2-4
condensation of, 2.6.3-7/2.6.3-9, 2.6.4-1/2.6.4-7
condensers for, 3.4.4-1/3.4.4-2
diffusion in, 2.1.5-1/2.1.5-4
forced convective boiling of, 2.7.8-1/2.7.8-10
combined heat and mass transfer in, 2.7.8-3/2.7.8-6
critical heat flux in, 2.7.8-6/2.7.8-7
saturated nucleate, 2.7.8-1/2.7.8-2
two-phase forced convective, 2.7.8-2/2.7.8-3
of gases, radiation properties of, 2.9.5-11/2.9.5-12
phase equilibria in, 2.7.6-3/2.7.6-5
physical properties of, 5.2.1-1/5.2.5-5
diffusion coefficients, 5.2.5-1/5.2.5-5
equilibria, 5.2.1-1/5.2.1-8
interfacial tension, 5.2.4-1/5.2.4-3
thermodynamic properties, 5.2.2-1/5.2.2-9
thermophysical properties, 5.2.3-1/5.2.3-9
pool boiling of, 2.7.7-1/2.7.7-7
critical heat flux, 2.7.7-412.7.7-j
film boiling, 2.7.7-6
minimum heat flux, 2.7.7-5/2.7.7-6
nucleate boiling, 2.7.7-1/2.7.7-4
transition boiling, 2.7.7-5
Multidimensional systems, heat conduction in, 2.4.3-10/2.4.3-12
Multiflux methods, for radiative heat transfer in non-isothermal gases, 2.9.7-6/2.9.7-7
Multipass shell-and-tube heat exchangers, 1 .1 .l-2
Multiphase fluid flow and pressure drop:
introduction and fundamentals, 2.3.1-1/2.3.1-10

© 1983 Hemisphere Publishing Corporation

Multiphase fluid flow and pressure drop, introduction and fundamentals (Cont.):
classification of multiphase flows, 2.3.1-1/2.3.1-2
conservation equations for, 2.3.1-3/2.3.1-7
design parameters in, 2.3.1-2/2.3.1-3
drift flux models for, 2.3.1-7/2.3.1-10
solid-gas flow, 2.3.3-1/2.3.3-10
flow patterns in, 2.3.3-2
pressure drop in, 2.3.3-2, 2.3.3-4/2.3.3-8
principles of pneumatic conveyance, 2.3.3-1/2.3.3-2
solid-liquid flow, 2.3.4-1/2.3.4-7
flow regimes in, 2.3.4-1/2.3.4-2
pressure drop in, 2.3.4-3/2.3.4-6
Multiple effect evaporation, 3.5.3-1/3.5.3-2
Multirod clusters (see Rod bundles)
Multizone model, for furnaces, 3.11.6-1/3.11.6-4
Murray, I., 4.4.4-1/4.4.4-11

N

Nabla operator (see Differential vector operators)
Nahme-Griffith number, 2.5.12-6
National practice, in mechanical design, guide to, 4.3.5-1/4.3.5-9
Natural convection:
as precursor to nucleate boiling, 2.7.2-1/2.7.2-2
(See ***also*** Free convection)
Natural draft cooling towers:
dry, 3.8.2-1/3.8.2-2, 3.8.8-1, 3.12.5-1/3.12.5-2
main features of, 3.12.3-1/3.12.3-2
structural design, 3.12.3-6/3.12.3-7
thermal performance and design of, 3.12.3-2/3.12.3-6
design optimization of, 3.12.3-5/3.12.3-6
performance away from design point, 3.12.3-6
pressure losses in, 3.12.3-3/3.12.3-5
thermal design equation, 3.12.3-2/3.12.3-3
Natural draft heat exchangers (see Air cooled heat exchangers, Cooling towers)
Natural frequency of tube vibration in heat exchangers, 4.6.2-1/4.6.2-4
Navier-Stokes equation, 2.2.1-5
Neon saturation properties, 5.5 .1-36
Neopentane saturated properties, 5.5 .l-6
Net free area, in double-pipe heat exchangers, 3.2.3-l
Netherlands, guide to national mechanical design practice, 4.3.5-5
Newton s law, for momentum transfer, 2.1.1-2
limitations in, 2.1.1-1/2.1.1-4
NFA (see Net free area)
Nickel-base alloys, as material of construction, 4.5.2-5
Nitrogen:
critical heat flux table for flow boiling of in vertical tube, 2.7.3-29
saturation properties, 5.5 .l-36
superheated gaseous, thermodynamic properties, 5.5.2-5
Noise, in air-cooled heat exchangers, 3.8.9-l
Nonane saturation properties, 5.5.1-10
Nonaqueous fluids, critical heat flux in, 2.7.3-6/2.7.3-30
Noncircular cylinders (see Cylinders)
Noncondensables:
in boiling, 2.7.2-8
in condensation, 2.1.6-2, 2.6.1-2, 2.6.3-5/2.6.3-7, 2.6.4-5 /2.6.4-6, 2.6.5-2/2.6.5-3
Nondestructive testing, of heat exchangers, 4.7.6-1/4.7.6-2
Nonmetallic materials, for heat exchangers, 4.5.26
Non-Newtonian flow:
free convective heat transfer from: spheres, 2.5.7-25
vertical plates, 2.5.7-10/2.5.7-11
properties of rheologically complex fluids in, 5.3.1-1/5.3.8-3
single-phase fluid flow and pressure drop in, 2.2.8-1/2.2.8-13
experimental characterization of non-Newtonian fluids 2.2.8-1/2.2.8-6
models for non-Newtonian fluids, 2.2.8-6/2.2.8-9
turbulent flow of non-Newtonian fluids, 2.2.8-l I
volume flow rate/pressure drop relations, 2.2.8-912.2.8-l 1
single-phase forced convective heat transfer with, 2.5.12-1/2.5.12-16
in channel flows, 2.5.12-6/2.5.12-15
equations and dimensionless groups for, 2.5.12-5/2.5.12-6
governing physical properties in, 2.5.12-2/2.5.12-5
Non-uniform heat flux, critical heat flux with, 2.7.3-18/2.7.3-22
North, C., 4.8.3-1/4.8.3-3
No-tubes-in-window shells, calculation of heat transfer and pressure drop in, 3.3.1 I-113.3.1 l-3
Nozzles:
analytic basis for codes for, 4.3.3-2
comparison of codes for, 4.3.4-2
impinging jets from, heat transfer in, 2.5.6-1/2.5.6-10
arrays of nozzles, 2.5.6-5/2.5.6-6
optical spatial arrangement, 2.5.6-6/2.5.6-9
single nozzles, 2.5.6-4/2.5.6-5
in shell-and-tube heat exchangers: constructional features of, 4.2.5-12, 4.2.6-2/4.2.6-3
description of, 2.2.7-l
impingement protection for, 3.3.5-10/3.3.5-11
pressure change across inlet nozzle, 2.2.7-2/2.2.7-3
pressure change across outlet nozzle, 2.2.7-3/2.2.7-4
index to U.S., U.K., and F.R.G. codes for, 4.3.2-9/4.3.2-10
loss coefficients in, 2.2.2-20
NTU (see Number of transfer units)
Nuclear fuel suspensions, properties of, 5.3.1-2/5.3.1-3
Nucleate boiling:
augmentation of, 2.7.9-1/2.7.9-4
in axial flow reboilers, 3.6.2-6/3.6.2-7
in evaporators, 3.5.7-2/3.5.7-3
in forced convective boiling of binary and multicomponent mixtures, 2.7.8-1/2.7.8-2
in forced convective heat transfer in vertical tubes, 2.7.3-1/2.7.3-12
in horizontal tubes, 2.7.4-1/2.7.4-7
in kettle reboilers, 3.6.2-1/3.6.2-4
outside tubes and tube bundles in crossflow, 2.7.5-1/2.7.5-7
in pool boiling of binary and multicomponent mixtures, 2.7.7-1/2.7.7-4
in pool boiling systems, 2.7.2-3/2.7.3-9
correlations for, 2.7.2-3/2.7.3-7
hysteresis in, 2.7.2-8
influence of dissolved gases on, 2.7.2-8
influence of gravitational acceleration on, 2.7.2-9
influence of liquid subcooling on, 2.7.2-9
influence of size and orientation of surface on, 2.7.2-8/2.7.2-9
influence of surface conditions on, 2.7.2-7/2.7.2-8
influence of system pressure on, 2.7.2-7
influence of wettability of surface on, 2.7.2-9
Nucleation:
augmentation devices for, 2.7.9-1/2.7.9-2
in binary systems, 2.7.6-5
heterogeneous, in boiling, 2.7.1-3/2.7.1-4
homogeneous, of vapor bubble in liquid, 2.7.1-2/2.7.1-3
in supersaturated vapor, 2.6.7-1/2.6.7-2

© 1983 Hemisphere Publishing Corporation

Nucleation sites:
critical size for nucleation: in pool boilii, 2.7.2-2/2.7.2-3
in subcooled forced convective boiling, 2.7.3-6
enhancement of number and activity of, 2.7.9-1/2.7.9-2
size in binary mixtures, 2.7.6-5
sizing of active, 2.7.1-5/2.7.1-6
Nuclei, formation in supersaturated vapor, 2.6.7-1/2.6.7-2
Number of transfer units (NTU):
in air-cooled heat exchangers, 3.8.5-1/3.8.5-5
average value in nonuniform heat transfer in shell-and-tube heat exchangers, 2.1.4-1/2.1.4-3
as basis for design of plate heat exchangers, 3.7.2-l
rating in, 3.7.7-l
in cooling of slab, 2.1.3-1/2.1.3-2
in cooling towers, 3.12.2-4/3.12.2-5
in heat exchangers, 1.2.4-3
in particle-to-fluid heat transfer in fluidized beds, 2.5.5-2/2.5.5-3
in transient heat transfer, definition of, 2.1.2-2/2.1.3-7
(See also θ or θ-NTU method)
Numerical methods:
application in furnace prediction, 3.11.7-5
for cases in which flow patterns must be calculated, 1.4.2-1/1.4.2-2
applications, 1.4.2-3/1.4.2-4
discretization, 1.4.2-1
finite difference equations for, 1.4.2-1/1.4.2-2
solution procedure, 1.4.2-2/1.4.2-3
for the solution of heat exchangers with a prescribed flow pattern, 1.4.1-1/1.4.1-6
discretization, 1.4.1-1/1.4.1-3
finite difference equations for, 1.4.1-3/1.4.1-4
influence of fineness of discretization, 1.4.1-5/1.4.1-6
special applications of, 1.4.3-1/1.4.3-6
calculations of heat transfer coefficients, 1.4.3-3/1.4.3-4
flows with chemical reactions, 1.4.3-2/1.4.3-3
flows with radiation, 1.4.3-3
turbulent flow in empty spaces, 1.4.3-2
two-phase flows, 1.4.3-l
in transient conduction calculations, 2.4.3-8/2.4.3-10
Nusselt:
description of modes of heat transfer, 2.1.9-2
equations for condensation: inside horizontal tube, 2.6.2-13
outside horizontal tube, 2.6.2-9
vertical surface, 2.6.2-2
Nusselt-Graetz problem, in laminar heat transfer in ducts, 2.5.1-2
Nusselt number:
in combined and free and forced convection: around immersed bodies, 2.5.9-1/2.5.9-6
in channels, 2.5.10-2/2.5.10-11
definition, 1.2.3-2
in finned tube banks, 2.5.3-l 1
in flow over tube banks, 2.5.3-1/2.5.3-6
forms of correlation for, 2.1.34
in free convection over immersed bodies, 2.5.7-2
for heat transfer in tubes, 2.1.36
in laminar flow in ducts, 2.5.1-2/2.5.1-5
in liquid metal flow, 2.5.13-1/2.5.13-4
in non-Newtonian flows, 2.5.12-7/2.5.12-16
in nonuniform heat transfer in packed beds, 2.1.4-3/2.1.4-4
in particle to fluid heat transfer in fixed beds, 2.5.4-l
in plate heat exchangers, 3.7.5-l
in single-phase flow over immersed bodies, 2.5.2-1/2.5.2-8
in systems with heat transfer augmentation, 2.5.11-1/2.5.11-12
in turbulent flow in ducts, 2.5.1-5/2.5.1-11

O

Oblate spheroids, free convective heat transfer from, 25.7-25
Octane saturation properties, 5.5.1-9
Oldroyd eight constant model, for non-Newtonian fluid, 2.2.8-8
ONB (onset of nucleate boiling):
in pool boiling, 2.7.2-12
in subcooled boiling in vertical tubes, 2.7.3-5/2.7.3-7
One equation models, for turbulent boundary layers, 2.2.1-28
Openings, mechanical design aspects, 4.1.8-1/4.1.8-2
Operational envelope of a heat pipe, 3.10.4-I
Opposed convection:
around immersed bodies, 2.5.9-11
in vertical tubes, 2.5.10-6
Optimization methods, for heat exchanger design, 3.3.4-2
Organic solids, density, 5.4.1-2
Orifices:
loss coefficients in, 2.2.2-21
two-phase gas liquid flow, 2.3.2-17/2.3.2-18
OTL (see Outer tube limit)
Outer tube limit, in shell-and-tube heat exchangers, 4.2.5-9
Outlet effects, in shell-and-tube heat exchangers, 3.3.6-9/3.3.6-10
Overall heat transfer coefficient, 2.1.2-1
approximate values: in shell-and-tube exchangers, 3.1.4-4/3.1.4-5
in liquid metal heat exchangers, 2.5.13-3
in various heat exchangers, 2.1.2-3/2.1.2-4
in air-cooled heat exchangers, 3.8.5-1/3.8.5-5
Overall power hypothesis, for critical heat flux in flow boiling, 2.7.3-19
Oxygen:
saturation properties, 5.5.1-37
superheated gaseous, thermodynamic properties of, 5.5.2-6

P

Packed beds (see Fixed beds)
Packing relationship, in cooling tower design, 3.12.2-3/3.12.2-4
Packings, for cooling towers, 3.12.2-8/3.12.2-10
Packings, for fixed beds:
characteristics, 2.2.5-2
effective conductivity of various in fixed beds: beds with gas flow, 2.8.2-212.8.2-S
stagnant beds, 2.8.1-3/2.8.1-5
Paikert, P., 3.8.1-1/3.8.9-4
Paints, spectral characteristics of reflectance of surfaces treated with, 2.9.2-14/2.9.2-17
Palen and Small correlation, for critical heat flux in tube banks, 2.7.5-6
Palen, J. W., 3.6.1-1/3.6.5-6
Panel immersion exchangers, 4.4.4-2/4.4.4-3
Parallel flow (see Cocurrent flow)
Parallel plates, (see Plates)
Partial boiling in subcooled forced convective heat transfer, 2.7.3-812.7.3-g
Particle convective component, in heat transfer from fluidized beds, 2.8.4-2/2.8.4-3
Particle emissivity, 2.9.7-2
Particle Reynolds number in fixed beds, 2.2.5-2
Particles:
fluid-to-particle heat transfer in fluidized beds, 2.5.5-1/2.5.5-6
free fall velocity of, 2.3.3-3

© 1983 Hemisphere I blishing Corporation

Particles (Cont.):
particle-to-wall heat transfer in fluidized beds, 2.8.4-1/2.8.4-8
Particulate fluidization, 2.2.6-l
Pass arrangements, in plate heat exchangers, 3.7.8-1/3.7.8-3
Passes, tube side, 4.2.5-3/4.2.5-4
boxed in, 4.2.5-4
number of, 4.2.5-3/4.2.5-4
partition plates between, 4.2.5-3
Passive methods, for augmentation of heat transfer, 2.5.11-1/2.5.11-3
in condensation, 2.6.6-1/2.6.6-4
in forced convection, 2.5.11-4/2.5.11-8
in free convection, 2.5.1 l-3
Pearson number, 2.5.12-6
Peclet number, 1.2.3-2/1.2.3-3, 2.1.5-2
heat and mass transfer at low, in fluidized beds, 2.5.5-3/2.5.5-5
in heat transfer in liquid metal systems, 2.5.13-1/2.5.13-4
in non-Newtonian flow, 2.5.12-6
Peng-Robinson equation of state, 5.1.2-4
application to hydrocarbons, 5.2.2-2
Penner s rule, in absorption of radiation by gases, 2.9.5-7
Pentane:
normal, critical heat flux for flow boiling of in vertical tube, 2.7.3-29
saturation properties of, 5.5 .l-8
Perfect gas (see Ideal gas)
Perforated fins, in plate fin heat exchangers, 3.9.3-l
Perforated plates, loss coefficients in, 2.2.2-20
Periodic variations in temperature, thermal conduction in bodies with, 2.4.5-1/2.4.5-4
Petroleum properties, 5.3.1-3
Phase change number, 2.4.4-l
Phase envelope, for natural gas mixture, 5.2.1-4
Phase equilibrium:
in binary mixtures, 2.7.6-1/2.7.6-3
in multicomponent mixtures, 2.7.6-3/2.7.6-4
(See also Equilibrium, phase)
Phase rule (Gibbs), 5.2.1-I
Phase separation, as source of corrosion problems, 4.5.3-5
PHE (see Plate heat exchanger)
Phenol saturation properties, 5.5 .l-20
Phonons, in thermal conductivity of solids, 5.4.3-1/5.4.3-3
Physical properties:
of mixtures of fluids, 5.2.1-1/5.2.5-5
of pure fluids, 5.1.1-1/5.1.5-3
of rheologically complex media, 5.3.1-1/5.3.8-3
of solids, 5.4.0-1/5.4.5-5
tables of, 5.5.1-1/5.5.8-3
variation with temperature: effect in developing flow, 2.2.2-11
effect on flow in tube banks, 2.2.4-10/2.2.4-12
effect on flow over cylinder, 2.2.3-6
effect on friction factor in circular pipe flow, 2.2.2-7/2.2.2-8
effect in heat transfer of flat plates, 2.5.2-2/2.5.2-3
effect in laminar flow heat transfer in channels, 2.5.1-4
effect in turbulent flow heat transfer in channels, 2.5.1-6/2.5.1-7
nature of variation, 2.2.1-9
in polymers, 2.5.12-2/2.5.12-4
Pin fins (see Spine fins)
Pi theorum, in dimensional analysis, 2.2.1-11
Pipe fittings (see Piping components)
Pipes, circular:
augmentation of heat transfer in, 2.5 .1 l-412.5 .11-9
internally finned for, 2.5.11-5/2.5.11-6
boiling of binary and multicomponent mixtures in, 2.7.8-1/2.7.8-7
critical heat flux, 2.7.8-6/2.7.8-7
forced convective (including mass transfer effects), 2.7.8-2/2.7.8-6
nucleate boiling, 2.7.8-1/2.7.8-2
combined free and forced convection in, 2.5.10-1/2.5.10-12
in condensers, 3.4.1-1/3.4.9-5
horizontal channels, 2.5.10-7/2.5.10-11
vertical pipes, 2.5 .10-2/2.5.10-7
flow boiling in: horizontal pipes, 2.7.4-1/2.7.4-7
vertical pipes, 2.7.3-1/2.7.3-37
free convective heat transfer from outside of, 2.5.7-20/2.5.7-24
horizontal, 2.5.7-20/2.5.7-23
vertical and inclined, 2.5.7-23/2.5.7-24
heat transfer to, in fluidized beds, 2.8.4-6/2.8.4-7
heat transfer to liquid metals in, 2.5.13-1
laminar heat transfer in, 2 .5.1-2
in hydrodynamically developed flow, 2.5.1-1
in thermally and hydrodynamically developing flow, 2.5.1-2
pneumatic conveyance (gas solids flow) in, 2.3.3-1/2.3.3-2
radiative heat transfer along, 2.9.3-15/2.9.3-16
roughened surface, radiative heat transfer along, 2.9.4-9/2.9.4-10
single-phase fluid flow and pressure drop in fully developed flow in, 2.2.2-1/2.2.2-7
effect of free convection on, 2.2.2-5/2.2.2-7
effect of temperature dependent fluid properties on, 2.2.2-7
friction factor, 2.2.2-1/2.2.2-2
influence of additives on, 2.2.2-7
turbulence characteristics in, 2.2.2-1/2.2.2-5
turbulent heat transfer in, 2.5.1-512.5.1-g
two-phase gas-liquid flow in, 2.3.2-1/2.3.2-33
flow regimes in, 2.3.2-1/2.3.2-5
hydrodynamics of flow in, 2.3.2-7/2.3.2-26
use in shell-and-tube heat exchangers for single-phase flow, 3.3.1-1/3.3.11-5
Pipes, noncircular:
triangular ducts: single-phase fluid flow and pressure drop in, 2.2.2-7/2.2.2-10
laminar flow, 2.2.2-7/2.2.2-8
turbulent flow, 2.2.2-9/2.2.2-10
(See also Rectangular ducts, Square ducts)
Piping components:
gas-liquid flow and pressure drop in, 2.3.2-15/2.3.2-18
bends, 2.3.2-17
open valves, 2.3.2-18
orifice plates, 2.3.2-17/2.3.2-18
slow changes in cross section, 2.3.2-15/2.3.2-16
sudden contractions, 2.3.2-16/2.3.2-17
sudden enlargements, 2.3.2-16
single-phase fluid flow and pressure drop in, 2.2.2-14/2.2.2-20
curved ducts, 2.2.2-14/2.2.2-17
enlargements, 2.2.2-17/2.2.2-19
miscellaneous fittings, 2.2.2-19/2.2.2-20
Plain tube banks (see Tube banks, plain)
Planck's constant, 2.9.1-3
Planck s law, for spectral distribution of blackbody radiation, 2.9.1-3
Plane shells: steady-state thermal conduction in, 2.4.2-1/2.4.2-3

© 1983 Hemisphere Publishing Corporation

Plastic analysis, in mechanical design, 4.1.2-1/4.1.2-2
Plate-and-frame heat exchangers (see Plate heat exchangers)
Plate coil baffles, in agitated vessels, 3.14.2-3/3.14.2-4
Plate fin heat exchangers, 1.1.4-2, 3.9.1-1/3.9.1-2
approximate overall heat transfer coefficients in, 2.1.24
calculation procedure for a rating problem, 3.9.9-l
correlation of heat transfer and friction data for, 3.9.6-1/3.9.6-2
definition of geometric terms for, 3.9.2-l
description of, 3.1.2-5
goodness factor comparisons for, 3.9.7-1/3.9.7-3
laminar flow surfaces, 3.9.5-1/3.9.5-3
mechanical design, 4.4.3-1/4.4.3-9
brazing, 4.4.3-3/4.4.3-4
construction, 4.4.3-1/4.4.3-3
flow distributors, 4.4.3-3
materials, 4.4.3-7/4.4.3-8
plate fin-tube construction, 4.4.3-5/4.4.3-7
multifluid service in, 3.9.12-1/3.9.12-2
pressure drop calculation in, 3.9.10-1/3.9.10-2
procedures for the thermal sizing problems in, 3.9.11-1/3.9.11-2
recent theory and data on vaporization and condensation in, 3.9.13-1/3.9.13-4
specifications of sizing and rating problems in, 3.9.8-1/3.9.8-2
surface geometries for, 3.9.3-l
surface performance data for, 3.9.4-1/3.9.4-2
Plate fins, efficiency of, 2.5.3-9/2.5.3-10
Plate heat exchangers:
approximate overall heat transfer coefficients in, 2.1.24
construction and operation of, 3.7.1-1/3.7.1-3
corrugation design, 3.7.3-1/3.7.3-2
costing, 4.8.4-1/4.8.4-2
description, 3.1.2-3/3.1.2-4
gasketed plate, 3.1.2-3
lamella (Ramen), 3.1.2-3/3.1.2-4
spiral plate, 3.1.2-3
factors affecting plate design, 3.7.6-1/3.7.6-2
corrugation geometry, 3.7.6-1/3.7.6-2
distribution, 3.7.6-2
factors governing plate specification, 3.7.2-l
fouling, 3.7.9-l
friction factor correlations, 3.7.4-l/3.7.4-2
heat transfer correlations, 3.7.5-1/3.7.5-2
mechanical design, 4.4.2-1/4.4.2-8
frame design, 4.4.2-5/4.4.2-7
gasket design and properties, 4.4.2-4/4.4.2-5
plate arrangements, 4.4.2-l
plate construction features, 4.4.2-1/4.4.2-2
plate design features, 4.4.2-3/4.4.2-4
methods of surface area calculation, 3.7.10-1/3.7.10-4
overall plate design for, 3.7.7-1/3.7.7-2
plate arrangements and correction factors for, 3.7.8-1/3.7.8-4
concurrency corrections, 3.7.8-1/3.7.8-2
distribution along port manifolds, 3.7.8-3/3.7.8-4
end effects, 3.7.8-2/3.7.8-3
types of pass arrangements, 3.7.8-l
thermal mixing in, 3.7.11-1/3.7.11-2
two-phase flow applications, 3.7.12-l
Plates:
characteristic of, as packings for fixed beds, 2.2.5-2
parallel, laminar heat transfer in flow between, 2.5 J-3
in hydrodynamically developed flow, 2.5.1-3
in thermally and hydrodynamically developing flow, 2.5.1-3
Plate-type evaporator, 3.5.2-6
Plug flow:
regions of occurrence of: in horizontal flow, 2.3.2-2/2.3.2-4
in inclined tubes, 2.3.2-4/2.3.2-5
in systems with phase change, 2.3.2-6/2.3.2-7
in vertical flow, 2.3.2-1/2.3.2-2
in vertical channels, 2.3.2-19
bubble rise velocity in, 2.3.2-19
Plug flow model, for furnaces, 3.11.5-1/3.11.5-2
Pneumatic conveyance, 2.3.3-1/2.3.3-2
in horizontal pipes, 2.3.3-1/2.3.3-3
in inclined pipes, 2.3.3-2
in vertical pipes, 2.3.3-l
Pneumatic conveying dryer, 3.13.7-2
P-NTU method:
application to single pass exchangers, 1.3.1-2/1.3.1-4
for calculation of heat exchangers, 1.2.4-4/1.2.4-5
Poiseuille law (see Hagen Poiseuille law)
Polarization, of thermal radiation, 2.9.2-12/2.9.2-14
Polymers:
degradation temperature, 2.5.12-l
physical properties, 2.5.12-2/2.5.12-4, 5.3.6-1/5.3.7-2
specific heat capacity, 2.5.12-3
thermal conductivity, 2.5.12-2
viscosity, 2.5.12-2/2.5.12-4
non-Newtonian heat transfer to, 2.5.12-1/2.5.12-15
Pool boiling, 2.1.7-6/2.1.7-8
augmentation of heat transfer in, 2.7.9-1/2.7.9-2
boiling curve for, 2.7.2-1/2.7.2-2
critical heat flux in, 2.7.2-9/2.7.2-13
geometric effects on, 2.7.2-11/2.7.2-12
liquid viscosity effect on, 2.7.2-12
subcooling effects on, 2.7.2-12/2.7.2-13
surface condition effects on, 2.7.2-13
film boiling in, 2.7.2-14/2.7.2-15
minimum heat flux in, 2.7.2-13/2.7.2-14
nucleate boiling, 2.7.2-3/2.7.3-9
correlations for, 2.7.2-3/2.7.3-7
hysteresis in, 2.7.2-8
influence of dissolved gas on, 2.7.2-8
influence of gravitational acceleration on, 2.7.2-9
influence of liquid subcooling on, 2.7.2-9
influence of size and orientation of surface on, 2.7.2-8/2.7.2-9
influence of surface conditions on, 2.7.2-7/2.7.2-8
influence of system pressure on, 2.7.2-7
influence of wettability of surface on, 2.7.2-9
of binary and multicomponent mixtures, 2.7.7-1/2.7.7-7
critical heat flux, 2.7.7-4/2.7.7-5
film boiling, 2.7.7-6
minimum heat flux, 2.7.7-5/2.7.7-6
nucleate boiling, 2.7.7-1/2.7.7-2
transition boiling, 2.7.7-5
onset of nucleate boiling in, 2.7.2-2/2.7.2-3
transition boiling in, 2.7.2-13
Porous surfaces, for enhancement of boiling heat transfer, 2.7.9-l
Post-burnout heat transfer (see Postdryout heat transfer, Transition boiling, Film boiling)
Post-dryout heat transfer:
correlations for in vertical tubes, 2.7.3-31/2.7.3-34
with departure from thermodynamic equilibrium, 2.7.3-32/2.7.3-33
empirical correlations, 2.7.3-31/2.7.3-32
semi-theoretical, 2.7.3-33/2.7.3-34
in evaporators, 3.5.7-3

© 1983 Hemisphere Publishing Corporation

Powders:
classification of types of, in fluidized beds, 2.2.6-3/2.2.6-4
thermal conductivity under vacuum, 2.1.1-2
Power law fluid (non-Newtonian), 2.2.8-7
forced convective heat transfer to, 2.5.12-1/2.5.12-16
free convective heat transfer to bodies immersed in, *2.5.7-10, 2.5.7-25*
Prandtl number, 1.2.34, 2.1.3-3
effect on laminar flow over flat plate, 2.2.1-23
formulas for, 5.1.4-7
of liquid water, 5.5.34
of saturated vapors and liquids, 5.5.1-1/5.5.5.1-40
shell-side, in shell-and-tube heat exchangers, 3.3.5-17
turbulent, 2.2.1-19
Pressure coefficient:
for flow over single cylinder, 2.2.4-2
for flow over tube in tube bank, 2.2.4-2
Pressure control of condensers, 3.4.5-l
Pressure drop:
in condensers, 3.4.7-1/3.4.7-2
in double-pipe heat exchangers, 3.2.3-5/3.2.3-6
in evaporators, 3.5.6-1
in fluidized beds, 2.2.6-2
in gas-liquid flow, 2.3.2-7/2.3.2-18
frictional, in straight pipes, 2.3.2-9/2.3.2-12
in shell-and-tube heat exchangers, 2.3.2-12/2.3.2-13
in singularities, 2.3.2-15/2.3.2-18
in stratified flow, 2.3.2-23/2.3.2-24
in vertical annular flow, 2.3.2-19
in headers, nozzles and turnarounds in shell-and-tube heat exchangers, 2.2.7-1/2.2.7-11
in internally finned tubes, 2.5.11-5/2.5.11-6
in multiphase systems, 2.3.1-1/2.3.1-10
in gas-solid flow, 2.3.3-2, 2.3.3-4/2.3.3-7
overall, in cooling towers, 3.12.3-3/3.12.3-5
in the packings of cooling towers, 3.12.2-10/3.12.2-11
in plate fin heat exchangers, 3.9.10-1/3.9.10-2
in plate heat exchangers, 3.7.4-1/3.7.4-2
and pumping power in heat exchangers, 1.2.4-5/1.2.4-6
in reboilers, 3.6.3-l
on the shell side of shell-and-tube heat exchangers, 3.3.1-1/3.3.11-5
as limitation in design, 3.3.10-6
in single phase systems: in ducts and fittings, 2.2.2-1/2.2.2-25
in fixed beds, 2.2.5-1/2.2.5-5
introduction and fundamentals, 2.2.1-l/2.2.1-35
in non-Newtonian fluid flow, 2.2.8-9/2.2.8-11
in tube banks, 2.2.4-1/2.2.4-17, 3.3.7-1/3.3.7-4
in vertical tubes with subcooled boiling, 2.7.3-9/2.7.3-10
Pressure gradient:
effect in transition boundary layer flow over flat plate, 2.2.1-24
(See ***also*** Pressure drop)
Process heaters, fired, 3.11.2-1/3.11.2-2
Prolate spheroids, free convective heat transfer from, *2.5.7-25*
Promoters, for dropwise condensation, 2.6.5-3/2.6.5-4
Propane:
saturation properties, 5.5.1-5
superheated gaseous, thermodynamic properties of, *5.5.2-615.5.2-l*
1-Propanol saturation properties, 5.5.1-18
2-Propanol saturation properties, 5.5 .1-19
Propeller agitator, 3.13.2-1/3.14.2-2
heat transfer in agitated vessels with, 3.14.3-1
Propylene:
saturation properties, 5.5.1-6
superheated gaseous, thermodynamic properties, 5.5.2-7
Propylene oxide saturation properties, 5.5.1-24
Proximity agitators, 3.14.2-1
heat transfer in agitated vessels with, 3.14.3-3/3.14.3-6
Pugh, S. F., 5.4.5-1/5.4.5-5, 5.5.8-1/5.5.8-3
Pulsations, use in augmentation of heat transfer, 2.5 .ll-8
Pushkina and Sorokin correlation, for flooding in vertical tubes, *2.3.2-22*
P-$\tilde{V}$-T correlations, for pure fluids, 5.1.2-1/5.1.2-4
Pyramid, free convective heat transfer from, 2.5.7-25

Q

Quality, in multiphase flows:
flow quality, 1.2.1-1, 2.3.14, 2.7.3-l
static quality, 1.2.1-1, 2.3.14

R

Radiant heat exchanger, 2.9.84
Radiating fin, 2.9.8-4/2.9.8-6
Radiation:
diffusion method, for calculation of nonisothermal gas radiation, 2.9.7-5/2.9.7-6
effect in film boiling, 2.7.2-15
effect on heat transfer in packed beds, 2.8.3-2
heat transfer coefficient, 2.9.8-2
in heat transfer from fluidized beds, 2.8.4-3, 2.8.4-6/2.8.4-7
models for, in furnaces, 3.11.7-4/3.11.7-5
networks, 2.9.3-8/2.9.3-10
with a gas, 2.9.64
numerical calculation of flows involving, 1.4.3-3
(See ***also*** Radiative heat transfer)
Radiation shields, in radiation heat transfer, 2.9.3-12/2.9.3-13
Radiative heat transfer:
acting with conduction and convection, 2.9.8-1/2.9.8-10
combined phenomena in, 2.9.8-l
around hollow cylinder, 2.9.8-6/2.9.8-7
in molecular gas convection, 2.9.8-7/2.9.8-10
in radiant heat exchanger, 2.9.84
from radiating tin, 2.9.8-4/2.9.8-6
radiation coupled transient heating or cooling, 2.9.8-3/2.9.8-4
thermal network analysis of, 2.9.8-1/2.9.8-3
gas radiation properties, 2.9.5-1/2.9.5-13
equation of transfer for, 2.9.5-1/2.9.5-2
gas mixtures, 2.9.5-11/2.9.5-12
measurement of, 2.9.5-2/2.9.5-4
molecular, 2.9.5-8/2.9.5-11
physics, of, 2.9.5-4
spectral, band and total property definitions, 2.9.5-4/2.9.5-8
in furnaces, 3.11.3-1/3.11.7-6
introduction to, 2.9.1-1/2.9.1-5
blackbody radiation, 2.9.1-3/2.9.1-5
radiant intensity and flux, 2.9.1-2/2.9.1-3
thermodynamic surfaces and surface systems, 2.9.1-1/2.9.1-2
nonisothermal gas radiation, 2.9.7-1/2.9.7-13

© 1983 Hemisphere I blishing Corporation

Radiative heat transfer, nonisothermal gas radiation (Cont.):
differential formulations for, 2.9.7-5/2.9.7-8
equation of transfer for, 2.9.7-1/2.9.7-2
geometric considerations, 2.9.7-2/2.9.7-3
molecular gas radiation in, 2.9.7-10/2.9.7-13
slab geometry, 2.9.7-3/2.9.7-5
spectral considerations and scaling approximations in, 2.9.7-8/2.9.7-10
radiation transfer between perfectly diffuse surfaces, 2.9.3-1/2.9.3-17
diffuse-walled passages, 2.9.3-13/2.9.3-16
radiation network, 2.9.3-8/2.9.3-10
radiosity-irradiation formulations, 2.9.3-4/2.9.3-8
refractory surfaces, 2.9.3-8
selected working relations for, 2.9.3-10/2.9.3-13
shape factors for, 2.9.3-1/2.9.3-4
radiation transfer between specular and imperfectly diffuse surfaces, 2.9.4-1/2.9.4-l 1
mirror-image concept, 2.9.4-1/2.9.4-2
Monte Carlo algorithms, 2.9.4-2/2.9.4-5
rough walled passages, 2.9.4-9/2.9.4-10
specular and imperfectly diffuse surfaces, 2.9.4-l
specular walled passages, 2.9.4-5/2.9.4-7
surface models, 2.9.4-7/2.9.4-9
surface radiation characteristics, 2.9.2-1/2.9.2-20
absorption and emission characteristics, 2.9.2-1/2.9.2-3
approximations, 2.9.2-10/2.9.2-12
electromagnetic theory and the Fresnel relations, 2.9.2-7/2.9.2-10
polarization, 2.9.2-12/2.9.2-15
radiation characteristics in thermal design, 2.9.2-15/2.9.2-20
reflection and transmission characteristics, 2.9.2-312.9.2-l
between surfaces and isothermal gas, 2.9.6-1/2.9.6-9
calculation of, 2.9.6-4/2.9.6-8
heat transfer at black wall, 2.9.6-l
mean beam length concept for, 2.9.6-2/2.9.6-3
Monte Carlo solutions for, 2.9.6-8/2.9.6-9
radiation network in, 2.9.6-4
radiosity-irradiation formulation for gas filled enclosure wall, 2.9.6-3/2.9.6-4
wall layer transmission in, 2.9.6-3
Radiators, automotive, construction, 4.4.3-5/4.4.3-7
Radiometers, application in gas radiation property measurement, 2.9.5-3
Radiosity, Stephan s law for, 2.9.1-3
Radiosity-irradiation formulations in radiative heat transfer, 2.9.3412.9.3-g
for gas-filled enclosure wall, 2.9.6-3/2.9.6-4
Ramen heat exchanger (see Lamella heat exchanger)
Raoult s law for partial pressure, 2.7.6-l
Rating of heat exchangers, 3.1.3-2, 3.3.4-1
computer program structure for, 3.1.3-3
Raybigh instability, in free convection, 2.5.8-2
Rayleigh number, 1.2.34, 2.2.1-16, 2.2.2-6
critical, for instability in free convection: in enclosures heated from below, 2.5.8-3/2.5.8-6
in horizontal layers, 2.5.8-2/2.5.8-3
in free convection over immersed bodies, 2.5.7-3
Reay, D., 3.13.7-1/3.13.7-3
Reboilers:
approximate overall coefficients in, 2.1.2-3
shell-and-tube, 3.6.1-1/3.6.5-6
calculation procedures for, 3.6.5-1/3.6.5-6
pressure drop in, 3.6.3-l
special design considerations for, 3.6.4-1/3.6.4-4
thermal design of, 3.6.2-1/3.6.2-10
as type of heat exchanger, 1.1.5-2
(See also Boilers)
Reciprocal mode integrating sphere, for reflection and transmission measurements in radiation, 2.9.2-7
Rectangles:
closed form solutions for mean beam lengths between, 2.9.64
radiative heat transfer shape factors for opposite and adjacent, 2.9.3-3
table of mean beam lengths, 2.9.6-5
Rectangular ducts:
combined free and forced convective heat transfer in, 2.5.10-11, 3.9.5-1/3.9.3-3
critical heat flux in flow boiling in, 2.7.3-20
laminar flow in, 2.2.2-7/2.2.2-9
radiative heat transfer along, 2.9.3-16/2.9.3-17
turbulent flow in, 2.2.2-10
Rectangular enclosures, free convective heat transfer in:
when heated and cooled on vertical sides, 2.5.8-6/2.5.8-13
when heated from below, 2.5.8-3/2.5.8-6
Rectangular fins, for plate fin exchangers, 3.9.3-l
Redlich-Kwong and Redlich-Kwong-Soave equations of state, 5.1.24
application to hydrocarbons, 5.2.2-1/5.2.2-2
Reduced pressure, correlations for pool boiling using, 2.7.2-5/2.7.2-7
Reentrance cavities, for enhancement of boiling, 2.7.9-1/2.7.9-2
Reference temperature:
in calculation of friction factor in circular duct, 2.2.2-7
for laminar flow over flat plates, 2.2.1-23
for turbulent flow over flat plates, 2.2.1-29
Reflectance (see Reflectivity)
Reflection, of thermal radiation, from solid surfaces:
characteristics of, 2.9.2-3/2.9.2-6
measurement of, 2.9.2-6/2.9.2-7
Reflectivity, of solid surfaces, 2.9.2-3
measurement of, 2.9.2-6/2.9.2-7
Reflectometer, heated cavity, 2.9.2-7
Reflux condensers, 3.4.3-2
flooding phenomena in, 2.6.2-9, 3.4.3-2/3.4.3-3
Refractories, density of, 5.4.1-1/5.4.1-2
Refractory services, 2.9.3-8
in furnaces, 3.11.3-6
heat transfer by radiation between source, sink and, 2.9.3-11/2.9.3-12
Refrigerant 12:
critical heat flux table for flow of in vertical tube, 2.7.3-29
saturation properties, 3.5.1-21
Refrigerant 13 saturation properties, 5 .5 .l-2 1
Refrigerant 21 saturation properties, 5.5 .l-22
Refrigerant 22 saturation properties, 5.5.1-22
Regenerative heat exchangers, 1.1.1-3/1.1.1-4
periodic operation of, 1.1.6-1
Regimes of heat transfer, in ducts, single phase flow, 2.5.1-1
Relaminarization, of turbulent flow, 2.2.1-16
Residence times, in dryers:
with non-prescribed material flow, 3.13.6-1
with prescribed material flow, 3.13.5-1/3.13.5-2
Retrograde behavior, in phase envelope for natural gas, 5.2.1-4/5.2.1-5
Reynolds number, 2.1.1-3
as limiting criteria for applicability of molecular flux relationship, 2.1.1-3

© 1983 Hemisphere Publishing Corporation

Reynolds number (*Cont.*):
bubble, 2.3.2-19
definition of, 1.2.3-2/1.2.3-3
in finned tube bundles, 2.5.3-11
in condensation on vertical surface, 2.6.2-3
in cross flow over tube banks, 2.2.4-1/2.2.4-12, 2.5.3-1/2.5.3-8, 3.3.7-1/3.3.7-4
particle, fixed beds, 2.2.5-2
fluidized beds, 2.2.6-2
shell-side, in shell-and-tube heat exchangers, 3.3.5-16
in two-phase gas-liquid flow, 2.3.2-10
Rheologically complex materials, properties of:
disperse compositions, 5.3.1-1/5.3.1-3
nuclear fuel suspensions, 5.3.1-2/5.3.1-3
petroleum, 5.3.1-3
two-component compositions, 5.3.1-1/5.3.1-2
effect of external electric and magnetic fields on, 5.3.8-1/5.3.8-2
lubricants: classification of, 5.3.2-l
lubricant-cooling liquids, 5.3.5-1/5.3.5-2
oils, 5.3.3-1/5.3.3-2
polymers, 5.3.6-1/5.3.7-2
Rheology, shear flow experiments used in, 2.2.8-3
Richardson number, 2.2.1-11
Ring cells, in free convection, 2.5.8-2
Ring stiffness, in shell-and-tube heat exchangers, 4.1.2-8/4.1.2-9
Rod bundles:
critical heat flux in flow in, 2.7.3-21/2.7.3-22
turbulent longitudinal flow in, 2.2.2-10
Rohsenow correlation, for nucleate boiling, 2.7.24
application in forced convection boiling in vertical tubes, 2.7.3-712.7.3-g
Roll cells, in free convection, 2.5.8-2
Roller expansion, of tubes into tube sheets, 4.2.6-6/4.2.6-7
Room, thermal network for combined radiation and convection in, 2.9.8-3
Rossby number, 2.2.1-11
Rotary dryer, 3.13.24
practical design of, 3.13.7-2
Rotating drums, heat transfer to particle bed in, 2.8.3-4/2.8.3-5
Rotation, as device for heat transfer augmentation, 2.5.11-4, 2.5.11-8
Roughness, surface:
in augmentation of condensation, 2.6.6-1/2.6.6-2
in augmentation of heat transfer, 2.5.11-2, 2.5.11-3/2.5.11-4
as enhancement device in boiling, 2.7.9-2
completely rough surface, 2.2.2-2
effect in flow in fixed beds, 2.2.5-4
effect on flow over cylinders, 2.2.3-6
effect in pool boiling: critical heat flux, 2.7.2-13
nucleate boiling, 2.7.2-3/2.7.2-8
effect on pressure drop in tube banks, 2.2.4-14/2.2.4-15
effect on skin friction in turbulent flow over flat plate, 2.2.1-29
effect in transition flow over flat plate, 2.2.1-25
radiative heat transfer from, 2.9.4-7/2.9.4-10
values for commercial surfaces, 2.2.24
Rough walled passages, radiative heat transfer down, 2.9.4-9/2.9.4-10
Ruiz, C., 4.1.1-1/4.1.8-3

S

Saddle supports, for heat exchangers, as source of assymetric loading, 4.1.2-2/4.1.2-9
Sand roughness, equivalent, 2.2.1-29/2.2.1-30
Sardesai, R. G., 2.6.4-1/2.6.4-7
Saturated boiling:
in pool boiling, 2.7.2-1/2.7.2-17
in vertical tubes, 2.7.3-10/2.7.3-12
nucleate, 2.7.3-10/2.7.3-11
two-phase forced convective, 2.7.3-11/2.7.3-12
Saturated fluids, tables of physical properties, 5.5.1-1/5.5.1-40
Saturation pressure, 2.7.1-1
Saturation temperature, 2.7.1-1
Saunders, E. A. D., 4.2.1-1/4.2.6-13
Scaling approximations, in nonisothermal gas radiation, 2.9.7-8/2.9.7-10
narrow band scaling: the Curtis Godson approximation, 2.9.7-8/2.9.7-9
wide-band scaling, 2.9.7-9/2.9.7-10
Scattering bed models, for radiative heat transfer from surfaces, 2.9.4-8/2.9.4-9
Scattering coefficient, 2.9.5-2
Schack wide-band model, for gas radiation properties, 2.9.5-6
Schlünder, E. U., 2.1.1-1/2.1.7-8, 3.13.1-1/3.13.6-l
Schlünder equations:
for developing laminar flow, 2.5.1-2
for gas conduction in packed beds, 2.8.3-l
Schmidt number, 1.2.34
Schrock and Grossman correlations, for forced ***convective*** heat transfer in two-phase flow, 2.7.3-8
Schunk, M., 5.1.1-1/5.1.5-3, 5.4.1-1/5.4.4-6
Schwier, K., 5.5.3-1/5.5.3-5
Scraped surfaces:
in augmentation of heat transfer, 2.5 .11-3
heat exchangers, description of, 3.1.2-6
in heat exchangers, 1.1.4-2
heat transfer coefficients with, 3.14.3-4/3.14.3-6
mechanical design for, 4.4.4-5/4.4.4-6
Scaling devices, in shell-and-tube heat exchangers, 4.2.5-8/4.2.5-9
Seider-Tate equation, for heat transfer in heat exchangers, 3.3.2-2
Selection of heat transfer equipment:
for condensation duty, 3.4.2-1/3.4.2-4
dryers, 3.13.2-1/3.13.2-4
for evaporation, 3.5.5-1/3.5.5-2
general introduction to, 3.1.2-1/3.1.2-6
reboilers, 3.6.1-2/3.6.1-6
selection table, 3.6.1-6
Semiconductors, thermal conductivity, 5.4.3-3
Separated flow model:
application to stratified flow prediction, 2.3.2-23/2.3.2-24
conservation equations for: in gas-liquid flow, 2.3.2-8/2.3.2-9
in multiphase flows, 2.3.1-6/2.3.1-7
Separators, for use in association with evaporators, 3.5.4-1/3.5.4-2
Series solutions, for one-dimensional transient conduction, 2.4.3-1/2.4.3-7
Serrated fms, in plate fin heat exchangers, 3.9.3-l
Shah correlation, for boiling in horizontal tubes, 2.7.4-5
Shape factor, in radiative heat transfer between diffuse surfaces, 2.9.3-1/2.9.3-4
Shear flow, of non-Newtonian fluids, 2.2.8-1/2.2.8-3
Shear free flow, of non-Newtonian fluids, 2.2.8-3/2.2.8-6
Shear rate, in fluid, 2.2.8-l
Shear stress:
distribution of wall, in flow over single cylinder, 2.2.3-5
interfacial effect on filmwise condensation: on vertical surfaces, 2.6.2-5/2.6.2-7
turbulent, in pipe flow, 2.2.2-5
Shelf dryer, 3.13.24

© 1983 Hemisphere I blishing Corporation

Shell-and-tube heat exchanger:
application of low-fin tubes in, 3.3.1 l-2/3.3.1 1-3
approximate overall coefficient in, 2.1.2-3
approximate sizing of, 3.1.4-1/3.1.4-9
basic design equation for, 3.1.4-9
estimation of heat load, 3.1.4-1/3.1.4-2
estimation of mean temperature difference, 3.1.4-2/3.1.4-3
estimation of overall heat transfer coefficient, 3.1.4-3/3.1.4-6
estimation of surface area, 3.1.4-6/3.1.4-7
example of, 3.1.4-7/3.1.4-9
baffle leakage in, numerical calculation of, 1.4.2-3
condensation in, 3.4.1-1/3.4.1-5
corrosion and other damage of, 4.5.3-1/4.5.3-7
description of 3.1.2-2/3.1.2-3
F-factor and θ-NTU charts for, 1.5.2-1/1.5.2-15
E-shell with even number of passes, 1.5.2-5
five E-shells in series, 1.5.2-9
four E-shells in series, 1.5.2-8
G-shell, even number of tube passes, 1.5.2- 13
J-shell, even number of tube passes, 1.5.2-12
J-shell, one tube pass, 1.5.2-11
six E-shells in series, 1.5.2-10
three E-shells in series, 1.5.2-7
two E-shells in series, 1.5.2-6
F-type shells, thermal leakage in, 1.5.2-14/1.5.2-15
introduction to design features, 1.1.5-1/1.1.5-2
materials of construction, 4.5.2-1/4.5.2-6
mechanical design: basic principles, 4.1.1-1/4.1.8-3
constructional features of, 4.2.1-1/4.2.6-13
design codes for, 4.3.1-1/4.3.5-11
example of calculations, 4.3.6-1/4.3.6-23
multipass, 1.1.1-2
non-uniform heat transfer in, 2.1.4-l/2.1.4-3
numerical solutions for: with flow pattern calculation, 1.4.2-1/1.4.2-4
with prescribed flow patterns, 1.4.1-1/1.4.1-6
pressure drop in headers, nozzles and turnarounds in, 2.2.7-1/2.2.7-11
thermal design, 3.3.1-1/3.3.11-5
auxiliary calculations, 3.3.6-1/3.3.6-11
calculation of shell-side heat transfer coefficient and pressure drop, 3.3.8-1/3.3.8-3
extension to other shell, baffle and tube bundle geometries, 3.3.11-1/3.3.11-3
ideal tube-bank correlations for, 3.3.7-1/3.3.7-4
input data and recommended practices, 3.3.5-1/3.3.5-17
objectives and background, 3.3.1-1/3.3.1-2
performance evaluation when geometry specified, 3.3.9-1/3.3.9-6
practices of design, 3.3.4-1/3.3.4-5
procedures for segmentally baffled exchangers, 3.3.10-1/3.3.10-8
recommended method: principles and limitations, 3.3.3-1/3.3.3-5
survey of shell-side flow correlations, 3.3.2-l/3.3.2-6
Shells, for shell-and-tube heat exchangers:
costing, 4.8.2-1/4.8.2-5
inside diameter: metric practice for, 3.3.5-3
U.S. practice for, 3.3.5-3
materials of construction, 4.5.2-l/4.5.2-2
mechanical design: analytical basis for codes, 4.3.3-l
basic principles, 4.1.3-l
constructional features of, 4.2.6-l
index to U.S., U.K., and F.R.G. codes for, 4.3.2-2/4.3.2-3
Shell-to-baffle clearance, in shell-and-tube heat exchangers, 3.3.5-13/3.3.5-14
Sherwood number, 1.2.3-2, 2.1.5-2
in particle-to-fluid mass transfer in fixed beds, 2.5.4-1/2.5.4-6
Shipes, K. V., 4.4.1-1/4.4.1-7
Short-tube vertical evaporator, 3.5.2-l
Shulman, Z. P., 5.3.1-1/5.3.8-3
Silver method, for calculation of multicomponent condensation, 2.6.3-4/2.6.3-5
Similarity, theory of, 2.2.1-10/2.2.1-13
Simultaneous heat and mass transfer (see Heat and mass transfer, combined)
Singham, J. R., 3.12.1-1/3.12.6-4
Single-phase convective heat transfer (see Convective heat transfer, single-phase)
Single-phase fluid flow:
in ducts and fittings, 2.2.2-1/2.2.2-25
in fixed beds, 2.2.5-1/2.2.5-5
over immersed bodies, 2.2.3-112.2.3-g
introduction and fundamentals, 2.2.1-1/2.2.1-35
in headers, nozzles and turnarounds, 2.2.7-1/2.2.7-11
in tube banks, 2.2.4-1/2.2.4-17
Singularities, two-phase gas-liquid pressure drop across, 2.3.2-15/2.3.2-18
bends, 2.3.2-17
open valves, 2.3.2-18
orifice plates, 2.3.2-17/2.3.2-18
slow changes in cross section, 2.3.2-15/2.3.2-16
sudden contraction, 2.3.2-16/2.3.2-17
sudden enlargement, 2.3.2-16
Sink, in radiation:
heat transfer between source, refractory and, 2.9.3-11/2.9.3-12
heat transfer from source to, 2.9.3-10/2.9.3-11
Skin friction coefficient, 2.2.1-20
in flow over cylinders, 2.2.3-5
in flow over tube banks, 2.2.4-3/2.2.4-5
Ludwieg-Tillman formula for, 2.2.1-26
Stratford formulas for, in boundary layers, 2.2.1-21
in turbulent flow over flat plates, 2.2.1-29
Slab:
heat transfer in cooling of, 2.1.3-1/2.1.3-2
leaching process in, 2.1.5-2
radiative heat transfer in non-isothermal gas in, 2.9.7-3/2.9.7-5, 2.9.7-10/2.9.7-13
transient conduction in, 2.4.3-1/2.4.3-10
numerical methods for, 2.4.3-8/2.4.3-10
series solution for, 2.4.3-1/2.4.3-7
solution using internal heat transfer coefficient, 2.4.3-7/2.4.3-8
Slip ratio (see Velocity ratio)
Slot, radiative heat transfer along, 2.9.3-15/2.9.3-16
Slug flow:
hydrodynamics of, 2.3.2-24/2.3.2-25
mechanism of critical heat flux in, 2.7.3-22
regions of occurrence of, in gas-liquid flow in horizontal tubes, 2.3.2-1/2.3.2-5
Slugging, in fluidized beds, 2.2.6-l
Smith, R. A., 3.5.1-1/3.5.8-3
Smoluchowski effect, 2.1.1-2
Snell's law, in radiation, 2.9.2-9
Solar absorber, 2.9.2-15/2.9.2-16
Solar reflector, 2.9.2-16
Soldered fins, in double pipe exchangers, 3.2.5-l
Solid fuels, properties of, 3.11.3-3

© 1983 Hemisphere I blishing Corporation

Solid-gas flow:
flow patterns in, 2.3.3-2
free-fall velocity in, 2.3.3-3
pressure drop in, 2.3.3-2, 2.3.3412.3.3-g
principles of pneumatic conveyance by, 2.3.3-1/2.3.3-2
horizontal pipes, 2.3.3-1/2.3.3-2
inclined pipes, 2.3.3-2
vertical pipes, 2.3.3-l
velocity ratio in, 2.3.34
Solidification, heat conduction in, 2.4.4-1/2.4.4-2
Solid-liquid flow:
flow patterns in, 2.3.4-1/2.3.4-2
pressure drop in, 2.3.4-2/2.3.4-6
principles of hydraulic conveyance, 2.3.4-l
Solids:
as constituents in multiphase flows, 2.3.1-1
physical properties, 5.4.1-1/5.4.5-5
density, 5.4.1-1/5.4.1-2
elastic properties, 5.4.5-1/5.4.5-5
emissivity, 5.4.4-1/5.4.4-4
specific heat, 5.4.2-1/5.4.2-2
thermal conductivity, 5.4.3-1/5.4.3-3
total emissivities, 3.11.3-6
Solids circulation, in fluidized beds, 2.2.6-6/2.2.6-7
Sound velocity:
in ideal gas, 2.2.1-8
in two-phase gas-liquid flow, 2.3.2-27
Source, in radiation:
radiative heat transfer between refractory, sink and, 2.9.3-11/2.9.3-12
radiative heat transfer between sink and, 2.9.3-10/2.9.3-1 1
Spacers, in shell-and-tube heat exchangers, 4.2.5-8/4.2.5-9
Spalding, D. B., 1.1.1-1/1.4.3-6
sparging:
for agitation of vessels, 3.1.4-2
of reboilers, 3.6.4-3
Specific enthalpy, 1.2.1-l
of saturated liquids and vapors, 5.5.1-1/5.5.1-40
of superheated gases, 5.5.2-115.5.2-I 1
Specific entropy, of superheated gases, tables of, 5.5.2-1/5.5.2-l 1
Specific heat (see Specific heat capacity)
Specific heat capacity, 1.2.1-2/1.2.1-3
in polymers, 2.5.12-8, 5.3.6-2
in pure fluids, 5.1.3-4/5.1.3-7
of liquid water, 5.5.3-2
of multicomponent mixtures, 5.2.3-8/5.2.3-9
of saturated liquids and vapors, 5.5.1-1/5.5.1-5
of solids, 5.4.2-1/5.4.2-2
Specific internal energy, 1.2.1-1
Specific volume:
of polymers, 5.3.6-2
of superheated gas, tables of, 5.5.2-1/5.5.2-1 1
of the gas phase, 5.1.2-2/5.1.2-3
of the liquid phase, 5.1.2-l
Spectral absorptivity:
in gases, 2.9.5-5
of metals at room temperatures, 2.9.2-l l/2.9.2-12
Spectral emissivity, in gases, 2.9.5-5
Specular surface, 2.9.4-l
radiative heat transfer between imperfectly diffuse surfaces and, 2.9.4-1/2.9.4-11
Specular-walled passages, radiative heat transfer in, 2.9.4-5/2.9.4-7
with adiabatic sides, 2.9.4-6/2.9.4-7
with isothermal sides, 2.9.4-5/2.9.4-6
with non-isothermal sides, 2.9.4-6
Spheres:
characteristics of, as packings for fixed beds, 2.2.5-2
combined free and forced convective heat transfer from, 2.5.9-1/2.5.9-6
in transverse flow, 2.5.9-6
in vertical flow, 2.5.9-1/2.5.9-4
concentric, free convective heat transfer in, 2.5.8-16
drag coefficients for, 2.2.3-2
fixed beds of, heat transfer in, 2.8.1-1/2.8.1-14, 2.8.2-1/2.8.2-8, 2.5.4-1/2.5.4-7
free convective heat transfer from, 2.5.7-24/2.5.7-25
heat transfer to beds of moving, agitated and vibrated, 2.8.3-3/2.8.3-8
single-phase forced convection heat transfer to, 2.5.2-5/2.5.2-8, 2.5.4-l
combined correlation for, 2.5.2-5, 2.5.4-1
in restricted channel, 2.5.2-5
transient conduction in, 2.4.3-1/2.4.3-10
numerical methods for, 2.4.3-8/2.4.3-10
series solutions for, 2.4.3-1/2.4.3-7
solutions using internal heat transfer coefficient, 2.4.3-7/2.4.3-8
Spherical shells:
mechanical design, of, 4.1.3-1/4.1.3-2
steady-state thermal conduction in, 2.4.2-1/2.4.2-3
Spheroids (oblate and prolate), free convective heat transfer from, 2.5.7-25
Spine fins:
efficiency, 2.5.3-9
in plate fin exchangers, 3.9.3-l
Spiral heat exchanger:
approximate overall heat transfer coefficients in, 2.1.24
description of, 3.1.2-3/3.1.2-4
mechanical design of, 4.4.4-4/4.4.4-5
Spray dryers, 3.13.7-2/3.13.7-3
Sprays, in heat exchangers, 1.1.4-2
Square ducts:
laminar flow in, 2.2.2-712.2.2-g
roughened wall, radiative heat transfer along, 2.9.4-9/2.9.4-10
Stable equilibrium, of vapor and liquid, 2.7.1-1
Staggered tube banks:
application in shell-and-tube heat exchangers, 3.3.5-5
correlations for heat transfer in, 2.5.3-l/2.5.3-16
finned tubes, 2.5.3-11
plain tubes, 2.5.3-2
drag coefficients for tubes in, 2.2.4-4
pressure drop in, with plain tubes, 2.2.4-8/2.2.4-9
correction factors for overall number of tube rows, 2.2.4-10
effect of yawing on, 2.2.4-12
pressure drop with tinned tubes, 2.2.4-13/2.2.4-14
Stagnant packed beds (see Fixed beds)
Stainless steels:
as materials of construction, 4.5.2-3/4.5.2-4
austenitic, 4.5.2-4
ferritic, 4.5.2-3/4.5.2-4
spectral characteristics of reflectance from oxidized surface of, 2.9.2-15
Stanton number, 1.2.3-1, 2.2.1-11
startup:
of heat pumps, 3.10.7-1/3.10.7-2
of reboilers, 3.6.4-2
State diagram, for fluidized beds, 2.2.6-2
Static mixer inserts, as enhancement device in condensation, 2.6.6-3
Static quality (see Quality)

© 1983 Hemisphere Publishing Corporation

Steels, as material of construction, 4.5.2-2/4.5.2-4
austenitic stainless, 4.5.24
carbon steel, 4.5.2-2/4.5.2-3
ferritic stainless, 4.5.2-3/4.5.2-4
low alloy steels, 4.5.2-3
Stefan-Boltzmann constant, 2.9.1-3
Stefan s law, for blackbody radiation, 2.9.1-3
Stegmaier, W., 2.3.3-1/2.3.3-10
Stephan and Korner correlation, for boiling of binary mixtures, 2.7.7-2
Stephan-Maxwell equations for diffusion, 2.1.5-I
Stirred beds, heat transfer to, 2.8.3-4
Stirred reactor model, for furnaces, 3.11.4-1/3.11.4-6
Stirred tanks (see Agitated vessels)
Straight fins (longitudinal fins)
application in double-pipe heat exchangers, 3.2.1-1/3.2.6-2
efficiency of, 2.5.3-9, 3.2.3-1/3.2.3-3
Stratfords method, for solution of boundary layer equations, 2.2.1-21
Stratification, in gas-liquid flow (see Stratified flow)
Stratified flow:
as source of dryout in evaporative heat transfer, 2.7.4-1/2.7.4-4
in bends, 2.7.4-2/2.7.4-3
in helical coils, 2.7.4-3/2.7.4-4
in horizontal tubes, 2.7.4-1/2.7.4-2
prediction of, in horizontal and inclined tubes, 2.3.2-23/2.3.2-24
regions of occurrence of: in condensation, 2.3.2-7
in horizontal tubes, 2.3.2-2/2.3.2-4
in inclined tubes, 2.3.2-4/2.3.2-5
in shell-and-tube heat exchangers, 2.3.2-5/2.3.2-6
Stream analysis methods, for shell-side heat transfer and pressure drop in shell-and-tube heat exchangers, 3.3.2-3/3.3.2-6
Stress equation models, for turbulent boundary layers, 2.2.1-29
Stresses:
allowable, comparison of codes for, in mechanical design of heat exchangers, 4.3.4-l
types of, in heat exchangers, 4.1.1-1/4.1.1-2
Stress tensor:
in non-Newtonian fluids, 2.2.8-2
in single phase fluid flow, 2.2.1-2
in turbulent flow, 2.2.1-15
Stress-strain curve, for solids, 5.4.5-2/5.4.5-3
Strouhal number, 2.2.3-3
values for: banks of tubes, 2.2.4-15/2.2.4-16
flow over blunt bodies, 2.2.3-7
flow over single cylinders, 2.2.3-4, 2.2.4-l
in vortex shedding as source of tube vibration, 4.6.4-1/4.6.4-2
Subchannel analysis, for critical heat flux in rod bundles, 2.7.3-21
Subcooled boiling:
in pool boiling, 2.7.2-1/2.7.2-17
in vertical tubes, 2.7.3-5/2.7.3-10
fully developed, 2.7.3-7/2.7.3-8
onset of, 2.7.3-5/2.7.3-7
partial, 2.7.3-812.7.3-g
single phase convection, 2.7.3-S
void fraction in, 2.7.3-9/2.7.3-10
Subcooling:
in condensers, 3.4.6-4
of liquid: effect on critical heat flux, 2.7.3-13
effect on forced convective boiling, 2.7.3-5/2.7.3-10
effect on pool boiling: critical heat flux, 2.7.2-12/2.7.2-13
nucleate boiling, 2.7.2-9
of vapor in condensation, 2.6.7-1
Sublayer, viscous, 2.2.2-l
Suction:
effect in transition flow over flat plate, 2.2.1-25
effect in turbulent flow over flat plate, 2.2.1-30
effect on laminar flow over flat plate, 2.2.1-23
use in augmentation of heat transfer, 2.5 .11-3, 2.5.11-9
Sudden contractions (see Contraction)
Sudden enlargements (see Enlargement)
Superficial velocity, in multiphase flow, 2.3.14
Superheated liquid, in metastable state, 2.7.1-1
Superheated gases, thermodynamic properties of, 5.5.2-1/5.5.2-11
Superheated vapor, condensation of, on vertical surface, 2.6.2-3
Supersaturation, as cause of fogging in condensers:
conditions producing, 2.6.7-2/2.6.7-3
description of, 2.6.7-J
Supports, for heat exchangers (see Saddle supports, Bracket supports)
Suppression of nucleate boiling, 2.7.3-10/2.7.3-11
Surface condensers, 3.4.3-5
Surface finish:
effect in pool boiling:
critical heat flux, 2.7.2-13
nucleate boiling, 2.7.2-3/2.7.2-8
(See also Roughness, surface)
Surface, hydraulically smooth, 2.2.2-l
Surface models, in radiative heat transfer, 2.9.4-7/2.9.4-9
diffraction models, 2.9.4-7/2.9.4-8
geometric optics models, 2.9.4-8
scattering bed models, 2.9.4-8/2.9.4-9
Surface roughness (see Roughness, surface)
Surface tension:
devices depending on, for heat transfer augmentation, 2.5.11-2
methods of estimating, 5.1.5-1/5.1.5-2
in mixtures of fluids, 5.2.4-1/5.2.4-3
tables of, for saturated fluids, 5.5.1-1/5.5.1-40
Sutherland formula, for viscosity variation with temperature, 2.2.1-9
Sutterby fluid (non-Newtonian), free convective heat transfer to, 2.5.7-11
Swirling flow, in augmentation of heat transfer, 2.5.11-2

T

Taborek, J., 1.5.2-1/1.5.3-12, 3.3.1-1/3.3.11-5
Taitel and Dukler flow regime map, for horizontal and inclined gas-liquid flows, 2.3.2-3/2.3.2-4
Tapes, twisted (see Twisted tapes)
Teflon, use in heat transfer enhancement:
in boiling, 2.7.9-l
in condensation, 2.6.6-l
TEMA (Tubular Exchanger Manufacturers Association):
example of calculation of mechanical design of TEMA type AJS, 4.3.6-1/4.3.6-23
mechanical design standards, 4.3.1-2/4.3.1-3
index to, 4.3.2-1/4.3.2-11
recommended baffle characteristics in segmentally baffled exchangers, 3.3.5-8
specification sheet for exchanger, 3.3.4-2
standards, 3.3.1-l
type designation system, 4.2.2-1/4.2.2-3
Temperature-dependent physical properties (see Physical properties, variation with temperature)

© 1983 Hemisphere Publishing Corporation

Temperature distribution:
in condensation, 2.6.1-2
in fixed beds: in stagnant conditions, 2.8.1-1/2.8.1-2, 2.8.1-10/2.8.1-14
with flow-through bed, 2.8.2-1/2.8.2-2, 2.8.2-7
series solutions for, in transient conduction, 2.4.3-112.4.3-l
Ternary mixtures, diffusion and mass transfer in, 2.1.5-4
Testing and inspection of heat exchangers:
certification, 4.7.7-l
cleanliness and storage, 4.7.9-l
constructions, 4.7.5-l
fittings, 4.7.8-l
materials, 4.7.2-l
nondestructive testing, 4.7.6-1/4.7.6-2
objectives of, 4.7.1-1/4.7.1-2
preparation and dispatch, 4.7.10-l
stages of inspection, 4.7.4-l
welding, 4.7.3-l
Thermal conduction (see Conduction, heat)
Thermal conductivity:
effective, in fixed beds: with flow, 2.8.2-2/2.8.2-5
with no flow (stagnant), 2.8.1-1/2.8.1-14
effective, of wicks in heat pipes, 3.10.3-l
of liquid water, 5.5.3-3
of multicomponent mixtures, 5.2.3-7/5.2.3-8
of polymers, 2.5.12-2
of pure fluids, 5.1.4-5 /5.1.4-7
gases, 5.1.4-5/5.1.4-6
liquids, 5.1.4-l
of rheologically complex materials, 5.3.1-1/5.3.2-3
of saturated vapors and liquids, 5.5.1-1/5.5.1-40
of solids, 5.4.3-1/5.4.3-3
electrical conductors, 5.4.3-2/5.4.3-3
electrical insulators, 5.4.3-1/5.4.3-2
semiconductors, 5.4.3-3
tables of, 5.5.6-1/5.5.6-4
of typical tube materials in heat exchangers, 3.3.5-5
Thermal contact resistance, 2.4.6-1/2.4.6-4
Thermal design, constructional features affecting, in shell-and-tube heat exchangers, 3.1.1-1/3.1.4-9, 4.2.5-1/4.2.5-23
Thermal diffusivity of liquid water, 5.5.3-5
Thermal expansion, effect of, in shell-and-tube heat exchangers, 3.3.4-4
Thermal expansion coefficient:
in gases, 5.1.2-3
of liquid water, 5.5.3-3
in liquids, 5.1.2-2
in saturated liquids, tables of, 5.5.1-1/5.5.1-40
Thermal leakage in F-type shell-and-tube heat exchangers, 1.5.2-14/1.5.2-15
Thermal mixing in plate heat exchangers, 3.7.11-1/3.7.11-2
Thermal network analysis of radiation acting with conduction and convection, 2.9.8-1/2.9.8-3
Thermal stress:
in heat exchanger shells, 4.1.3-2
numerical methods in the production of, 1.4.24
in tube plates, 4.1.4-4
Thermodynamic properties:
of saturated fluids, 5.5.1-1/5.5.1-40
of superheated gases, 5.5.2-1/5.5.2-4
Thermodynamic surface in radiative heat transfer, 2.9.1-1/2.9.1-2
Thermoexel surface, for enhancement of boiling, 2.7.9-1/2.7.9-2
Thermosiphon, as form of heat pipe, 3.10.1-l
Thermosiphon reboilers (see Vertical thermosiphon reboilers, Horizontal thermosiphon reboilers)
θ-NTU method:
application to single pass counter and cocurrent flow exchangers, 1.3.1-2/1.3.1-4, 1.5.2-1/1.5.2-2
charts and equations for heat exchanger design, 1.5.2-2/1.5.3-12
for counter flow, 1.5.2-2
cross flow (both streams mixed), 1.5.3-3
four tube rows, four passes, unmixed, 1.5.3-l 1
four tube rows, two passes, mixed, 1.5.3-12
one tube row, unmixed, 1.5.3-4
three tube rows, one pass, unmixed, 1.5.3-6
three tube rows, three passes, unmixed, 1.5.3-10
two tube rows, one pass, unmixed, 1.5.3-5
two tube rows, two tube passes, unmixed, 1.5.3-9
E-shell with even number of passes, 1.5.2-5
five E-shells in series, 1.5.2-g
four E-shells in series, 1.5.2-8
G-shell, even number of tube passes, 1.5.2-13
J-shell, even number of tube passes, 15.2-12
J-shell, one tube pass, 1.5.2-l 1
single pass cocurrent, 1.5.2-3
six E-shells in series, 1.5.2-10
three E-shells in series, 1.5.2-7
two E-shells in series, 1.5.2-6
for calculation of heat exchangers, 1.2.4-5, 1.5.2-1/1.5.3-12
Thickness of boundary layers (displacement, momentum, energy, density, temperature), 2.2.1-20
Three-phase flows:
classification, 2.3.1-2
gas-liquid-liquid, 2.3.1-2
gas-liquid-solid, 2.3.1-2
solid-liquid-liquid, 2.3.1-2
Thwaites method for solution of boundary layer equations, 2.2.1-21
Tie rods in shell-and-tube heat exchangers, 4.2.5-814.2.5-g
Tinker method for shell-side heat transfer in shell-and-tube heat exchangers, 3.3.2-3/3.3.2-6
Titanium as material of construction, 4.5.2-5
T-junctions, loss coefficients in, 2.2.2-20
Toluene saturation properties, 5.5.1-12
Tong F-factor method, for critical heat flux with nonuniform heating, 2.7.3-19/2.7.3-20
Toroidal shells, mechanical design, 4.1.3-2
Total emissivity in gases, 2.9.5-5
Transcendental equations in transient conduction, 2.4.34
Transient behavior:
in free convective heat transfer on vertical plates, 2.5.7-9/2.5.7-10
of heat exchangers, 1.1.6-1
in radiation-coupled heating or cooling, 2.9.8-3/2.9.8-4
Transition boiling:
in binary and forced convective boiling, 2.7.7-5
in forced convection over vertical surfaces, 2.7.3-30
in pool boiling, 2.7.2-13
Transition flow, heat transfer in free convective flow over vertical surfaces in, 2.5.7-4/2.5.7-5
Transmission of thermal radiation in solids:
characteristics, 2.9.2-3/2.9.2-6
measurement, 2.9.2-612.9.2-l
Transmissivity of solids:
definition, 2.9.2-3
measurement, 2.9.2-612.9.2-l
Transport phenomena, approximate model for in dilute gases, 2.1.1-1

© 1983 Hemisphere Publishing Corporation

Transport properties:
of pure fluids, 5.1.4-1/5.1.4-7
turbulent, 2.1.1-3
Transverse flow, combined free and forced convection in, 2.5.9-4/2.5.9-6
Treated surfaces, for augmentation of heat transfer, 25.1 J-l
Triangular duct:
laminar flow in, 2.2.2-9
laminar heat transfer in, 3.9.5-1/3.9.5-3
Triangular fins, in plate tin exchangers, 3.9.3-l
Triangular relationship, in annular gas-liquid flow, 2.3.2-20
Triple interface (gas/solid/liquid), 2.3.1-2
Trouton s rule, for heat of vaporization, 5.1.3-3
Truelove, J. S., 3.11.1-1/3.11.7-6
True temperature difference, in double pipe exchangers, 3.2.34
Tube-baffle damage, in heat exchangers, 4.5.3-3
Tube banks, finned:
application in kettle reboilers, 3.6.2-6
mechanical design, in air cooled heat exchangers, 4.4.1-2/4.4.1-5
single-phase flow and pressure drop in, 2.2.4-13/2.2.4-15
correlation for pressure drop for staggered banks with annular (ring shaped) fins, 2.2.4-13/2.2.4-14
correlation for staggered banks with helical fins, 2.2.4-14
single-phase heat transfer in, 2.5.3-6/2.5.3-16
comparison of experimental data and correlations for, 2.5.3-13/2.5.3-15
fm efficiency in, 2.5.3-6/2.5.3-11
heat transfer correlations for, with high-finned tubes, 2.5.3-11/2.5.3-12
heat transfer correlations for, with low-fumed tubes, 2.5.3-12/2.5.3-13
types used in air-cooled heat exchangers, 3.8.4-1/3.8.4-2
Tube banks, plain:
boiling on outside of tubes within, 2.7.5-4/2.7.5-7
critical heat flux in, 2.7.5-5/2.7.5-7
heat transfer coefficients in, 2.7.5-4/2.7.5-5
condensation in horizontal, 2.6.2-10/2.6.2-12
condensation in vertical, 2.6.2-2/2.6.2-10
flow induced vibration in, 4.6.1-1/4.6.6-3
single-phase flow and pressure drop in, 2.2.4-1/2.2.4-12, 3.3.7-1/3.3.7-4
description of, 2.2.4-1/2.2.4-3
drag and pressure drop in, 2.2.4-3/2.2.4-12, 3.3.7-1/3.3.7-4
Strouhal numbers in, 2.2.4-15/2.2.4-16
single-phase heat transfer to, 2.5.3-1/2.5.3-8
with liquid metals, 2.5.13-2
single row of tubes, 2.5.3-1/2.5.3-2, 2.5.3-3
tube banks, 2.5.3-2/2.5.3-8, 3.3.7-1/3.3.7-4
Tube banks, roughened tubes, effect of roughness on Euler number in, 2.2.4-14/2.2.4-15
Tube bundles:
characteristics of in shell-and-tube heat exchangers, 3.3.4-3/3.3.4-4
(See *also* Rod bundles, Tube banks)
Tube counts, in shell-and-tube heat exchangers:
constructional features affecting, 4.2.5-9/4.2.5-12
simplified equations for, 3.3.5-11/3.3.5-12
tables of, 4.2.5-13/4.2.5-23
Tube end attachment, in shell-and-tube heat exchangers:
arc welding: on inner face, 4.2.6-10
on outer face, 4.2.6-8
explosive expansion, 4.2.6-7/4.2.6-8
explosive welding, 4.2.6-8/4.2.6-10
roller expansion, 4.2.6-6/4.2.6-7
Tube-in-plate extended surface configurations, fin efficiency of, 2.5.3-10
Tube plates, in shell-and-tube heat exchangers:
analytic basis for codes for, 4.3.3-2
basic mechanical principles of design of, 4.1.4-1/4.1.4-4
equivalent plates, 4.1.4-1
perforated, stresses in, 4.1.4-3/4.1.4-4
plates connected by tubes, 4.1.4-2
stresses and edge rotation of unperforated, 4.1.4-1/4.1.4-2
thermal stresses, 4.1.4-4
comparison of codes for, 4.3.4-2
constructional features of, 4.2.6-5/4.2.6-6, 4.5.3-3
double, constructional features of, 4.2.3-10/4.2.3-11
index to U.S., U.K., and F.R.G. codes for, 4.3.2-714.3.2-g
materials of construction for, 4.5.2-l
Tubes:
characteristics of, in shell-and-tube heat exchangers, 4.2.5-1/4.2.5-3
bimetal, 4.2.5-2
diameter and thickness, 4.2.5-l
integrally finned, 4.2.5-3
length, 4.2.5-1/4.2.5-2
pitch, 4.2.5-2
circular (see Pipes, circular)
codes for mechanical design of:
analytical basis of, 4.3.3-l
index to U.S., U.K., and F.R.G. codes, 4.3.2-3
flow-induced vibration of, 4.6.2-1/4.6.6-3
natural frequency of, 4.6.2-1/4.6.2-4
materials of construction for, 4.5.2-l
mechanical design characteristics of, 4.1.5-1
noncircular (see Pipes, noncircular)
recommended dimensions of, in shell-and-tube heat exchangers, 3.3.5-4/3.3.5-5
thermal conductivity of typical materials for, 3.3.5-5
Tubesheets, in shell-and-tube heat exchangers (see Tube plates)
Tube-side passes (see Passes, tube-side)
Tubular Exchanger Manufacturers Association (see TEMA)
Tubular immersion exchangers, 4.4.4-2/4.4.4-3
Tubular reactor, nonuniform heat and mass transfer in, 2.1.4-3/2.1.4-4
Tunnel dryer, 3.13.2-4
Turbine agitators:
axial flow, 3.14.2-2
disk, 3.14.2-1/3.14.2-2
flat blade, 3.14.2-1/3.14.2-2
glass coated, 3.14.2-1
heat transfer in vessels agitated by, 3.14.3-1
pitched blade, 3.14.2-1
Turbine exhaust condensers, air cooled, 3.8.9-2
Turbulence:
characteristics in circular pipe flow, 2.2.2-1/2.2.2-5
effect in film condensation, 2.6.2-4/2.6.2-5
integral scale of, 2.2.1
limitation of phenomenological transport laws by, 2.1.1-3/2.1.1-4
modeling of, 2.2.1-14/2.2.1-16
in furnace prediction, 3.11.7-2/3.11.7-3
origin of, 2.2.1-16
relaminarization of, 2.2.1-16
Turbulent boundary layers:
differential methods for, 2.2.1-28/2.2.1-29
large-eddy simulations, 2.2.1-29
one-equation models, 2.2.1-28
stress-equation models, 2.2.1-29

© 1983 Hemisphere Publishing Corporation

Turbulent boundary layers: differential methods for (Cont.):
two-equation models, 2.2.1-28
zero-equation models, 2.2.1-28
integral methods for, 2.2.1-26/2.2.1-27
Turbulent buffeting, as source of tube vibration, 4.6.4-2
Turbulent energy, integral equation for, 2.2.1-20
dissipation of, 2.2.1-20
production of, 2.2.1-20
Turbulent flow:
in boundary layers, 2.2.1-18
in circular pipes, 2.2.2-1/2.2.2-5
combined free and forced convective heat transfer in channels in, 2.5.10-6/2.5.10-11
combined radiative and convective heat transfer to, 2.9.8-7/2.9.8-10
in condensation, on vertical surfaces, 2.6.2-4/2.6.2-5
conservation equations for, 2.2.1-13/2.2.1-14
averaging in, 2.2.1-13
in empty spaces, numerical calculation of, 1.4.3-2
fundamentals of, 2.2.1-13/2.2.1-16
heat transfer in free convective flow over vertical surfaces in, 2.5.74
modeling of, 2.2.1-14/2.2.1-16
of non-Newtonian fluids, 2.2.8-11/2.2.8-12
in noncircular pipes, 2.2.2-9/2.2.2-10
in plate heat exchangers, 3.7.10-2/3.7.10-3
relaminarization in, 2.2.1-16
single-phase heat transfer in ducts in, 2.5.1-5/2.5.1-13
augmentation of, 2.5.11-412.5.11-g
concentric annuli, 2.5.1-10/2.5.1-11
in liquid metal systems, 2.5.13-1/2.5.13-2
smooth tubes, 2.5.1-5/2.5.1-9
Turbulent transport properties, 2.1.1-3
Turnarounds, in heat exchangers, 2.2.7-l
pressure losses in, 2.2.7-812.2.7-g
Twisted tapes:
enhancement of boiling heat transfer by, 2.7.9-3/2.7.9-4
enhancement of condensation by, 2.6.6-3
as inserts for augmentation of heat transfer, 2.5.11-7/2.5.11-8
Two-equation models, for turbulent boundary layers, 2.2.1-28
Two-phase flows:
classification of, 2.3.1-2
liquid-liquid flows, 2.3.1-2
numerical calculation of, 1.4.3-l
(See *also* Gas-liquid flow, Solid-gas flow, Solid-liquid flow)
Two-shell pas exchanger (see F-shells)

U

$\bar{U}$-$\tilde{\alpha}$ method, 2.1.2-5
$\bar{U}$ method, 2.1.2-712.1.2-g
Ulinskas, R., 2.2.4-1/2.2.4-17
Unequal baffle spacing, correction factor for, 3.3.6-11
UNIFAC method, for estimation of thermodynamic properties of mixtures, 5.2.2-615.2.2-g
tables of constants for use with, 5.5.4-6/5.5.4-7
Uniform heat flux:
combined free and forced convection in channels with:
horizontal channels, 2.5.10-7/2.5.10-11
vertical channels, 2.5.10-4/2.5.10-7
critical heat flux in vertical tubes with, 2.7.3-12/2.7.3-18
solutions and correlations for free convective heat transfer within: horizontal and inclined plates, 2.5.7-18
vertical plates, 2.5.1-612.5.7-g
Uniform wall temperature, combined forced and free convection in channels with:
horizontal channels, 2.5.10-7
vertical channels, 2.5.10-3/2.5.10-4
Uniheads, as form of double-pipe heat exchanger, 3.2.4-l
United Kingdom, mechanical design of heat exchangers in:
guide to national practice, 4.3.5-3
index to BS1500 code, 4.3.2-1/4.3.2-11
United States of America (see U.S.)
Universal laws, for turbulent boundary layers, 2.2.1-25/2.2.1-26
law of the wake of D. Coles, 2.2.1-26
law of the wall, 2.2.1-25
table of, 2.2.1-27
universal velocity profile, 2.2.1-26
velocity defect law of von Karman, 2.2.1-26
Universal velocity profile, 2.2.1-26
Universal velocity defect law, 2.2.2-2
Unsteady flows:
in ducts, 2.2.2-14
over cylinders, 2.2.3-6
Upward facing surfaces, free convective heat transfer from, 2.5.7-15/2.5.7-18
U.S., mechanical design of heat exchangers in:
guide to national practice, 4.3.5-2
index to ASME VIII code and TEMA standards, 4.3.2-114.3.2-l 1
Usher, J. Dennis, 3.7.1-1/3.7.12-2, 4.4.2-1/4.4.2-8, 4.8.4-1/4.8.4-2
U.S.S.R. Academy of Sciences, tables of critical heat flux data for water, 2.7.3-17/2.7.3-18
U-tube bundles, for shell-and-tube heat exchangers, 3.3.5-12/3.3.5-13, 4.2.3-4
vibration of, natural frequencies in, 4.6.2-3

V

Vacuum condensers, air cooled, 3.8.9-2
Vacuum operation, of reboilers, 3.6.4-3
Valves:
loss coefficients in, 2.2.2-20
open, two-phase gas-liquid flow pressure losses in, 2.3.2-18
van der Waals equation of state, 5.1.2-3/5.1.2-4
Vaned bends, single-phase flow and pressure drop in, 2.2.2-16/2.2.2-17
Vapor belt, in condensers, 3.4.3-5
Vapor blanketing, as mechanism of critical heat flux, 2.7.3-22
in kettle reboilers, 3.6.2-5
as source of accelerated corrosion, 4.5.34
Vapor injection, effect of on boiling heat transfer in tube bundles bundles, 2.7.5-5
Vaporization, choice of evaporator type for, 3.5.5-l
in plate-fin heat exchangers, 3.9.13-1/3.9.13-2
Vaporization, heat of (see Heat of vaporization)
Vaporizer, double bundle, constructional features, 4.2.3-9
Vapor-liquid disengagement, in kettle reboilers, 3.6.2-6
Vapor-liquid separation, for evaporators, 3.5.4-1/3.5.4-2
3.5.4-1/3.5.4-2
Vapor pressure, variation with temperature, 5.1.3-1/5.1.3-2
Vapor recompression, in evaporation, 3.5.3-2

© 1983 Hemisphere Publishing Corporation

Velocity defect law:
for turbulent boundary layers, 2.2.1-26
universal, 2.2.2-2
Velocity distribution:
in circular pipe flow, 2.2.2-3
distorted inlet, effect on single phase flow and pressure drop, 2.2.2-l 1
Velocity fluctuations, in turbulent pipe flow, 2.2.2-4/2.2.2-5
Velocity ratio (slip ratio):
in gas-liquid flow, 2.3.2-13
in solid-gas flow, 2.3.3-4
Venting of condensers, 3.4.5-2
Vertical cones (see Cones, vertical)
Vertical cylinders (see Cylinders, Vertical pipes, Pipes, circular)
Vertical cylindrical fired heater, 3.11.2-1
Vertical pipes:
annular flow in, 2.3.2-19/2.3.2-21
boiling in, 2.7.3-1/2.7.3-37
critical heat flux, 2.7.3-12/2.7.3-30
heat transfer in region where critical heat flux has been exceeded, 2.7.3-30/2.7.3-34
regimes of flow and heat transfer in, 2.7.3-1/2.7.3-5
saturated boiling, 2.7.3-10/2.7.3-12
subcooled boiling, 2.7.3-5/2.7.3-10
bubble flow in, 2.3.2-18/2.3.2-19
combined free and forced convective heat transfer in:
laminar flow (assisting convection), 2.5 .10-2/2.5.10-6
laminar flow (opposing convection), 2.5.10-6
regimes in, 2.5.10-2
turbulent convection, 2.5.10-6
condensation in, 2.6.2-212.6.2-g
effect of interfacial shear, 2.6.2-5/2.6.2-7
effect of waves and turbulence, 2.6.2-4/2.6.2-5
laminar flow, 2.6.2-2/2.6.2-4
reflux condensation, 2.6.2-712.6.2-g
condensers with condensation inside, 3.4.3-1/3.4.3-3
downflow, 3.4.3-1/3.4.3-2, 3.4.9-2/3.4.9-3
upflow, 3.4.3-2/3.4.3-3, 3.4.9-3
condensers with condensation outside, 3.4.3-6, 3.4.94
flooding in: in gas liquid vertical flow, 2.3.2-21/2.3.2-23
in reflux condensation, 2.6.2-712.6.2-g
flow regimes in gas-liquid flow in, 2.3.2-1/2.3.2-2
free convective heat transfer from outside of, 2.5.7-23/2.5.7-24
hydraulic conveyance in, 2.3.4-1/2.3.4-3
plug (or slug) flow in, 2.3.2-19
pneumatic conveyance in, 2.3.3-l
(See *also* Pipes, circular; Pipes, noncircular)
Vertical plates (see Vertical surfaces)
Vertical surfaces:
combined free and forced convective heat transfer to, 2.5.9-1/2.5.9-4
combined heat and mass transfer on, 2.5.7-12
film boiling in forced convection on, 2.7.3-30/2.7.3-31
filmwise condensation on, 2.6.2-212.6.2-g
free convective heat transfer from, 2.5.7-2/2.5.7-13
combined equation for uniform wall temperature case, 2.5.7-5/2.5.7-6
dimensionless groupings for, 2.5.7-2/2.5.7-3
laminar flow with uniform wall temperature, 2.5.7-3/2.5.7-4
non-Newtonian, 2.5.7-1012.5.7-l 1
solution for uniform heat flux, 2.5.7-612.5.7-g
transient behavior of, 2.5.7-912.5.7-l 1
transition flow with uniform wall temperature, 2.5.7-4/2.5.7-5
turbulent flow with uniform wall temperature, 2.5.7-4/2.5.7-5
free convective mass transfer to, 2.5.7-11/2.5.7-12
pool boiling, from 2.7.2-1/2.7.2-15
Vertical thermosiphon reboilers:
calculation procedures for, 3.6.5-3/3.6.5-4
heat transfer characteristics of, 3.6.2-6/3.6.2-10
convective and nucleate boiling, 3.6.2-6/3.6.2-7
film boiling in, 3.6.2-9
heat flux limitations in, 3.6.2-713.6.2-g
mist flow, 3.6.2-9
temperature profiles in, 3.6.2-9/3.6.2-10
shell-side characteristics, advantages and disadvantages, 3.6.1-5
tube-side characteristics, advantages and disadvantages, 3.6.1-3/3.6.1-5
Vertical tubes (see Vertical pipes)
Vibrated beds, heat transfer to, 2.8.3-5/2.8.3-6
Vibration:
in augmentation of heat transfer, 2.5.11-3, 2.5.11-4, 2.5.11-8, 2.7.9-4
numerical methods for prediction of occurrence of, 1.4.2-4
(See *also* Flow-induced vibration)
Viscometric functions (non-Newtonian flow), methods of determining, 2.2.84
Viscosity:
liquid, effect on critical heat flux in pool boiling, 2.7.2-12
of liquid water, 5 5.34
of multicomponent mixtures, 5.2.3-2/5.2.3-6
non-Newtonian, 2.2.8-2
of pure fluids, 5 .1.3-1
gases, 5.1.4-l
liquids, 5.1.4-1/5.1.4-5
relation with density for gases, 2.2.1-9
of saturated liquids and vapors, 5 .5.1-1/5.5.1-40
small variations in, 2.2.1-9/2.2.1-10
variation with temperature:
Chapman-Rubescin formula for, 2.2.1-9
Sutherland formula for, 2.2.1-9
Viscosity number (Vi), 2.3.2-19
Viscous dissipation, influence on heat transfer in non-Newtonian flows, 2.5.12-10/2.5.12-14
Viscous sublayer, in duct flow, 2.2.2-l
Voidage, in fixed beds, definition, 2.2.5-l
Void fraction, 2.3.1-3
correlations for in gas-liquid flow, 2.3.2-13/2.3.2-15
CISE correlations for, 2.3.2-14/2.3.2-15
drift flux models for, 2.3.2-13/2.3.2-14
homogeneous, 2.3.2-l 3
Martinelli correlations for, 2.3.2-14
models for in gas-liquid flow :
horizontal stratified flow, 2.3.2-23/2.3.2-24
vertical bubble flow, 2.3.2-18/2.3.2-19
vertical plug flow, 2.3.2-19
in subcooled boiling, 2.7.3-9/2.7.3-10
Volumetric heat transfer coefficient, 1.1.2-2
Volumetric mass transfer coefficient, 1.1.2-2
von Karman friction factor equation for fully rough surface, 2.2.2-3
von Karman velocity defect law, 2.2.1-26
Vortex shedding:
from single cylinders, 2.2.3-3
as source of tube vibration, 4.6.4-1/4.6.4-2
in tube banks, 2.2.4-15/2.2.4-16

© 1983 Hemisphere Publishing Corporation

Votator, agitator, 3.14.2-1
heat transfer with, 3.14.3-6

W

Wallis correlations:
for flooding, 2.3.2-22
application in reflux condensation, 2.6.2-8
for interfacial friction factor, 2.3.2-21
Wallis criterion, for transition from stratified to annular flow, applications in condensation, 3.4.6-2
Wall baffles, in agitated vessels, 3.14.2-2
Wall layer transmissivity, 2.9.7-12/2.9.7-13
Wall temperature:
effect in laminar flow along flat plate, 2.2.1-22
effect of distribution of, in laminar flow along flat plate, 2.2.1-23/2.2.1-24
Wake, Coleslaw of the, 2.2.1-26
Waste heat boilers, corrosion and failure in, 4.5.3-4/4.5.3-5
Water:
critical heat flux values for, in tubes (table), 2.7.3-17/2.7.3-18
emissivity of gaseous, 5.5.5-1/5.5.5-2
liquid, properties of, 5.5.3-1/5.5.3-5
pool boiling curve for, at atmospheric pressure, 2.7.2-l
saturated properties: (0°–50°C), 3.12.2-6
(O-647 K), 5.5.1-37
superheated gaseous, thermodynamic properties of, 5.5.2-915.5.2-l 1
Water loss, from cooling towers, 3.12.6-2
Water tube boiler, 3.11.2-3
Wavelengths, of blackbody radiation, 2.9.1-4/2.9.1-5
Waves, interfacial, effect on film condensation on vertical surface, 2.6.2-4/2.6.2-5
Wavy fins, in plate fin exchangers, 3.9.3-l
Webb, R. L., 3.9.1-1/3.9.13-4, 4.4.3-1/4.4.3-9
Weber, M., 2.3.3-1/2.3.4-7
Weber number, 1.2.3-5
Welded channel head, in shell-and-tube heat exchanger, 4.2.4-l
Welded fins, in double pipe exchangers, 3.2.5-l
Welding:
testing and inspection of, 4.7.3-l
of tubes into tube sheets: arc, 4.2.6-8, 4.2.6-10
explosive, 4.2.6-8/4.2.6-10
Welds, corrosion of, 4.5.3-5/4.5.3-6
Wentz and Thodos equation, for fixed-bed pressure drop, 2.2.5-3
Wet-bulb temperature, 3.13.3-2/3.13.3-4
Wettability, of surface, effect on pool boiling, 2.7.2-9
Whalley and Hewitt correlations:
for entrainment, 2.3.2-22
for interfacial roughness, 2.3.2-21
White-Metzner model, for non-Newtonian fluid, 2.2.8-8
Wicking, in enhancement of heat transfer, 25.11-2
Wicks, for heat pipes:
characteristics of, 3.10.6-1/3.10.6-2
effective thermal conductivity of, 3.10.3-l
Window zone, in shell-and-tube heat exchangers:
calculation of effective areas of, for flow through, 3.3.6-1/3.3.6-2
pressure drop in gas-liquid flow in, 2.3.2-12/2.3.2-13
Winter, H. H., 2.5.12-1/2.5.12-16
Wire inserts, coiled, for enhancement of heat transfer in boiling, 2.7.9-3
Wispy annular flow, regions of occurrence of, 2.3.2-1/2.3.2-2
Working fluid, selection of for heat pipe, 3.10.5-1/3.10.5-2

X

m-Xylene saturation properties, 5.5.1-13
o-Xylene saturation properties 5.5.1-13
p-Xylene saturation properties, 5.5.1-14
X-type shells (cross flow shells):
application in condensers, 3.4.9-3
description of, 3.3.4-3

Y

Yawed tube banks, pressure drop in, 2.2.4-12
Youngs modulus, 5.4.5-3
table of values of, 5.5.8-2

Z

Zero equation models, for turbulent boundary layers, 2.2.1-28
Zivi equation, for void fraction, 2.6.2-14
Zone model, for furnaces (see Multizone model)
Zuber-Findlay model, for two-phase flows, 2.3.1-9/2.3.1-10
Zuber theory, for critical heat flux in pool boiling, 2.7.2-10
Žukauskas, A., 2.2.4-1/2.2.4-17, 2.5.3-1/2.5.3-16

© 1983 Hemisphere Publishing Corporation